MALLA REDDY ENGINEERING COLLEGE

(Autonomous) - Main Campus

(A UGC Autonomous Institution, Approved by AICTE, New Delhi & Affiliated to JNTUH, Hyderabad).
Accredited by NAAC with 'A++' Grade (Cycle- III),
NIRF Rank Band 101-150, ARIIA Band Performer,
NBA Tier-I Accredited (B.Tech- CE, EEE, ME, ECE & CSE, M.Tech - CSE, EPS, TE)
Maisammaguda, Medchal-Malkajgiri District, Secunderabad– 500100,
Telangana State. www.mrec.ac.in

SCI - INDEXED JOURNAL PUBLICATIONS IN THE CALENDAR YEAR-2022

MALLA REDDY ENGINEERING COLLEGE (AUTONOMOUS)
(UGC Autonomous Institution, Approved by AICTE, New Delhi & Affiliated to JNTUH, Hyderabad). Accredited by NAAC with 'A++' Grade,
Maisammaguda (H), Medchal-Malkajgiri District, Secunderabad,
Telangana State – 500100, www.mrec.ac.in

Faculty Research Publication in the Calendar Year - 2022

LIST OF SCI JOURNALS

S.No	Department	No.of Journals
1	Civil Engineering	03
2	Electrical and Electronics Engineering	18
3	Electronics and Communication Engineering	06
4	Computer Science and Engineering	06
5	Humanities and Science	14
6	Mechanical Engineering	06
7	Information Technology	01
8	CSE-Data Science	01
9	Mining Engineering	01
Total		**56**

MALLA REDDY ENGINEERING COLLEGE (AUTONOMOUS)

(UGC Autonomous Institution, Approved by AICTE, New Delhi & Affiliated to JNTUH, Hyderabad). Accredited by NAAC with 'A++' Grade,

Maisammaguda (H), Medchal-Malkajgiri District, Secunderabad,

Telangana State – 500100, www.mrec.ac.in

Sl. No	Title of paper	Name of the author/s	Department	Name of journal	Year of publication	ISSN number
1	Experimental Testing on Mechanical, Durability, and Adsorption Dispersion Properties of Concrete with Multiwalled Carbon Nanotubes and Silica Fumes	Dr.B.Sudharshan Reddy	Civil Engg	Hindawi,Adsorption Science & Technology	3/1/2022	ISSN: 0263-6174 (Print),ISSN: 2048-4038 (Online)
2	Effect of Fiber Mixing and Nanoclay on the mechanical properties of Biodegradable Natural Fiber – Based Nano composites	Dr. C. Selin Ravi Kumar	Civil Engg	Hindawi,Adsorption Science & Technology	3/1/2022	ISSN: 0263-6174 (Print),ISSN: 2048-4038 (Online)
3	Applying ANN – PSO algorithm to maximize the compressive strength and split tensile strength of blended self curing concrete on the impact of supplementary cementitious materials	J.S.S.K.Vasa	Civil Engg	Hindawi,Adsorption Science & Technology	Apr, 2022	ISSN 2193-1801 (
4	Comparative Performance Assessment of Different Energy Storage Devices in Combined LFC and AVR Analysis of Multi-Area Power System	Dr. Ch. Rami Reddy	EEE	Energies	Feb, 2022	1996-1073

5	SMES and TCSC Coordinated Strategy for Multi-area Multi-source System with Water Cycle Algorithm Based 3DOF-PID Controller	Dr. Ch. Rami Reddy	EEE	Smart science	Mar, 2022	2308-0477
6	Faulted Section Identification and Fault Location in Power Network Based on Histogram Analysis of Three-phase Current and Voltage Modulated	Dr. Ch. Rami Reddy	EEE	Journal of Electrical Engineering & Technology	Apr, 2022	
7	Distribution System Service Restoration Using Electric Vehicles	Dr. Ch. Rami Reddy	EEE	Energies	Apr, 2022	1996-1073
8	FPGA Implementation of AI-Based Inverter IGBT Open Circuit Fault Diagnosis of Induction Motor Drives	Dr. N. Rajeswaran Dr. T. Rajesh	EEE	Micromachines	Apr, 2022	2072-666X
9	A Hybrid AOSAOA Scheme Based on the Optimal Location for Electric Vehicle Parking Lots and Capacitors in a Grid to Care of Voltage Profile and Power Loss	Dr. Ch. Rami Reddy	EEE	Energies	June, 2022	1996-1073
10	Comparative Performance Analysis of Deregulated Hydrothermal System With Dual Mode Controller and Diverse Source of Generation Employing Imperialistic Competition Algorithm	Dr. P Marimuthu, Dr. T Rajesh Dr. N Rajeswaran	EEE	IEEE Access	May, 2022	2169-3536
11	Performance Assessment of Open-Loop and Closed-Loop Generation Rate Constraint Models for Optimal LFC of the Three-Area Reheat Thermal System	Dr. Ch. Rami Reddy	EEE	Frontiers in Energy Research	June, 2022	2296-598X

12	Implementation of a Novel Tabu Search Optimization Algorithm to Extract Parasitic Parameters of Solar Panel	Dr. P. Sarala	EEE	Energies	June, 2022	1996-1073
13	Seagull Optimization Algorithm–Based Fractional-Order Fuzzy Controller for LFC of Multi-Area Diverse Source System With Realistic Constraints	Dr. Ch. Rami Reddy	EEE	Frontiers in Energy Research	July, 2022	2296-598X
14	Location Determination of Electric Vehicles Parking Lot With Distribution System by Mexican AXOLOTL Optimization and Wild Horse Optimizer	Dr. Ch. Rami Reddy	EEE	IEEE Access	May, 2022	2169-3536
15	Comparison of Principal-Component-Analysis-Based Extreme Learning Machine Models for Boiler Output Forecasting	Dr. Ch. Rami Reddy	EEE	Applied Sciences	July, 2022	2076-3417
16	PV/WT Integrated System Using the Gray Wolf Optimization Technique for Power Quality Improvement	Dr. Ch. Rami Reddy	EEE	Frontiers in Energy Research	Aug, 2022	2296-598X
17	Improving the power quality of island microgrid with voltage and frequency control based on a hybrid genetic algorithm and PSO	Dr. Ch. Rami Reddy	EEE	IEEE Access	Aug, 2022	2169-3536
18	Experimental Investigation and Performance Characteristics of Francis Turbine with Different Guide Vane Openings in Hydro Distributed Generation Power Plants	Dr. P. Sarala Dr. Ch Rami Reddy	EEE	Energies	Sept., 2022	1996-1073

19	A deep CNN approach for islanding detection of integrated DG with time series data and scalogram	Dr. Ch Rami Reddy	EEE	Soft Computing	Oct, 2022	1433-7479
20	Challenges in achieving sustainable development goal 7: Affordable and clean energy in light of nascent technologies	Dr. K. Prasada Rao	EEE	Sustainable Energy Technologies and Assessments	Sept., 2022	2213-1388
21	Solving the environmental/economic dispatch problem using the hybrid FA-GA multi-objective algorithm	Dr. Ch. Rami Reddy	EEE	Energy Reports	Oct., 2022	2352-4847
22	MRI de-noising using improved unbiased NLM filter	S. Sahu A. Anand A. K. Singh A. K. Agrawal M. P. Singh	ECE	Journal of Ambient Intelligence and Humanized Computing	2022	1868-5145
23	Enhanced security to MANETs using digital codes	Syed Jalal Ahmad, Ishrath Unissa, M. ShoukathAli, AbhayKumar	ECE	Journal of Information Security and Applications	2022	2214-2126
24	Forecasting Solar Energy Production Using Machine Learning	C.Vennila, Anita Titus, T.Sri Sudha, U.Sreenivasulu, N.Pandu Ranga Reddy, K.Jamal, Dayadi Lakshmaiah, P.Jagadeesh, Assefa Belay	ECE	International Journal of Photoenergy	2022	1687-529X
25	An Optimized Deep-Learning-Based Low Power Approximate Multiplier Design	M. Usharani, B. Sakthivel, S. Gayathri Priya, T. Nagalakshmi,	ECE	Computer Systems Science and Engineering	2022	0267-6192

		J. Shirisha				
26	Design and Implementation of Smart Hydroponics Farming Using IoT-Based AI Controller with Mobile Application System	S.V.S.Ramakrishnam Raju , Bhasker Dappuri, P.Ravi Kiran Varma, Murali Yachamaneni, D.Marlene Grace Verghese, Manoj Kumar Mishra	ECE	Journal of Nanomaterials	2022	1687-4129
27	Impact of a Thermal Barrier Coating in Low Heat Rejection Environment Area of a Diesel Engine	Megavath Vijay Kumar, Thumu Srinivas Reddy, Ch.Rami Reddy, S.Venkata Rami Reddy, Mohammad Alsharef, Yasser Alharbi, Basem Alamri	ECE	Sustainability	2022	2071-1050
28	A New Framework for Simulating and Modeling Cloud Computing Infrastructures and Services is Cloudsim	Mrs.A Rasgnya	CSE	TELEMATIQUE	22-Sep	1856-4194
29	A Study on Inside Views of Cloud Computing Tools	Dr.A Ramaswami Reddy Dr.Arun Kumar Kandru	CSE	Chield Studies in Asia Pacific Context	Aug-22	2288-601X
30	Wind Driven Optimization-Based Medical Image Encryption for Blockchain-Enabled Internet of Things Environment	N. Supriya	CSE	Computers, Materials & Continua	22-Jun	DOI:10.32604/cmc.2022.030267
31	Iot for analyzing and investigating digital forensics tools using cloud computing	N.Supriya,S.Shivaprasad	CSE	IJHS	12-Apr	1934-1955

32	Dynamic Resource Allocation in Cloud Infrastructure using ant Lion - Based Auto Regression Model	J.Kavitha	CSE	IJCYE	22-Feb	1074-5351
33	Enhanced security to MANETs using digital codes	Syed Jalal Ahmad, Ishrath Unissa, M. ShoukathAli, AbhayKumar	CSE	Journal of Information Security and Applications	2022	2214-2126
34	Rheological investigations on cholesterol derivative mesogens	Dr LNVH Soma Sundar	Physics	Molecular Crystals and Liquid Crystals	2022	1542-1406
35	Investigation of Physical properties of Ca doped MgTiO3 Ceramics for microwave applicatiuos	GuruSampath Kumar A	Physics	Digest Journal of Nanomaterials and Biostructures	2022	1842-3582
36	Ni0.48Cu0.12Zn0.4Fe2O4 + Paraformaldehyde nanocomposites as microwave absorbent dominent materials	A.Thirupathi	Physics	Elsevier Solid State Communication	2022	0038-1098
37	Electronic Spectra (Experimental and Simulated), and DFT Investigation of NLO, FMO, NBO, and MESP Characteristics of Some Biphenylcarboxaldehydes	Dr. L. Ravindranath	Physics	Polycyclic Aromatic Compounds (Taylor & Francis)	2022	1563-5333
38	Experimental and DFT Quantum Chemical Studies on Structural, Vibrational and Molecular Properties of Some Substituted 4-Phenylphenols	Dr. L. Ravindranath	Physics	Polycyclic Aromatic Compounds (Taylor & Francis)	2022	1563-5333
39	Enhanced photocatalytic hydrogen evolution from reduced graphene oxide-defect rich TiO2-x nanocomposites	Jagadeesh BabuS., Murthy Muniyappa, Navakoteswara RaoV., Ravi Mudike, Mahesh Shastria, Sardar	Department of PHYSICS	International Journal of Hydrogen Energy	2022	1879-3487

		Tathagata, Prasanna D.Shivaramu, ShankarM.V., Ananda Kumar C.S., DineshRangappa.				
40	Copper zinc tin sulfide and multi-walled carbon nanotubes nanocomposite for visible-light-driven photocatalytic applications	RaviMudike, ChetanaSabbanahalli, Jagadeesh Babu Sriramoju, Amarnath Bheemaraju, Guddappa Halligudra, Murthy Muniyappa, Manikanta P.Narayanaswamy, Ananda Kumar CS, Prasanna D.Shivaramu, DineshRangappa.	Department of PHYSICS	Materials Research Bulletin	2022	1873-4227
41	Cocatalyst free nickel sulphide nanostructure for enhanced photocatalytic hydrogen evolution	MurthyMuniyappa, SagaraN. Kalegowda, ManjunathShetty, Jagadeesh Babu Sriramoju, MaheshShastri, Navakoteswara RaoS.V., Debasis De, ShankarM.V., DineshRangappa.	Department of PHYSICS	International Journal of Hydrogen Energy	2022	1879-3487
42	Study on the DC supply and charging effect on the growth of carbon nanotubes and their electrochemical properties	S. Chetana, Manjunath Shetty, Kunal Roy, Jagadeesh Babu Sriramoju, Guddappa Halligudra, Prasanna D. Shivaramu, C. S. Ananda Kumar, K. G.	Department of PHYSICS	Journal of Materials Science: Materials in Electronics volume	2022	1573-482X

		Basavakumar & Dinesh Rangappa				
43	FPGA Implementation of AI Based Inverter IGBT Open Circuit Fault Diagnosis of Induction Motor Drives	Kesava Vamsi Krishna Vajjala	Physics	Micromachines	2022	2072-666X
44	Analysis of Joule heating and chemical reaction effects in electroosmosis peristaltic transport of couple-stress and micropolar fluids	Dr.K.Venugopal Reddy	H&S MATHS	Heat Transfer	2022	2688-4542
45	Recent Development of Heat and Mass Transport in the presence of Hall, ion slip and thermo diffusion in radiative second grade material	N.Ravi Kumar	H&S MATHS	*Micromachines*	2022	2072-666X
46	Novel metformin complexes: Geometry optimization, non-isothermal kinetic parameters, DNA binding, on–off light switching and docking studies	Dr.B.Shekhar	chemistry	Applied organometalic chemistry	2022	1099-0739
47	Metformin-Derived Water-Soluble Cobalt Complexes:Thermal, Spectroscopic, DNA Interaction, and Molecular Docking Studies	Dr.B.Shekhar	chemistry	Applied Biochemistry and Biotechnology	2022	0885-4513
48	Experimental Investigation and Performance Characteristics of Francis Turbine with Different Guide Vane Openings in Hydro Distributed Generation Power Plants	Megavath Vijay Kumar, T. Subba Reddy, P. Sarala, P. Srinivasa Varma, Obbu Chandra Sekhar, Abdulrahman Babqi, Yasser Alharbi, Basem Alamri, and Ch. Rami Reddy	Mechanical	*Energies*	Sept., 2022	1996-1073

49	Impact of a Thermal Barrier Coating in Low Heat Rejection Environment Area of a Diesel Engine	Megavath Vijay Kumar, Thumu Srinivas Reddy, Ch. Rami Reddy, S. Venkata Rami Reddy, Mohammad Alsharef, Yasser Alharbi, Basem Alamri	Mechanical	*Sustainability*	November, 2022	2071-1050
50	Investigation of the combustion of exhaust gas recirculation in diesel engines with a particulate filter and selective catalytic reactor technologies for environmental gas reduction	Megavath Vijay Kumar, Alur Veeresh Babu, Ch. Rami Reddy, A. Pandian, Mohit Bajaj, Hossam M. Zawbaa, Salah Kamel	Mechanical	*Case Studies in Thermal Engineering*	November, 2022	2214-157X
51	Influence of Post-heat Treatment on Friction Stir-Processed AA7075/SiC Surface Composite Properties	D.S. Chandra Mouli , R. Umamaheswara Rao, A. Raveendra, P. Saritha, and G. Parthasarathi	Mechanical	Journal of Materials Engineering and Performance	December, 2022	1059-9495
52	Inflence of Milling Process Parameters and Significance of Tools to Improve the Surface Quality of GFRP Composites	I.S.N.V.R.Prasanth, D.V.Ravishankar, M.Manzoor Hussain, Chandra Mouli Badiganti	Mechanical	Machining Science and Technology(Taylor & Francis Ltd-SCI)	January,2022	1091-0344
53	Study of friction and wear behavior of Graphite reinforced AA7075 Nanocomposites by Machine learning	I. S. N. V. R. Prasanth, P.Jevanandam, Selavaraju P, Sateesh K, Sujatha P	Mechanical	Journal of nano materials(Hindawi)	February, 2023	1687-4110
54	Deep Convolution Neural Networks Learned Image Classification for Early Cancer Detection Using Lightweight	Dr.Deena Babu Mandru	IT	Spinger	2022	ISSN 2193-1801 (

55	Iot for analyzing and investigating digital forensics tools using cloud computing	S.Shivaprasad	CSE-DS	IJHS	12-Apr	1934-1955
56	XG Boost Algorithm to Simultaneous Prediction of Rock Fragmentation and Induced Ground Vibration Using Unique Blast Data	Dr.N.Sri Chandrahas	MINING	MDPI	2022	ISSN 2304-6775

Hindawi
Adsorption Science & Technology
Volume 2022, Article ID 4347753, 13 pages
https://doi.org/10.1155/2022/4347753

Research Article

Experimental Testing on Mechanical, Durability, and Adsorption Dispersion Properties of Concrete with Multiwalled Carbon Nanotubes and Silica Fumes

Naga Dheeraj Kumar Reddy Chukka,[1] **B. Sudharshan Reddy**,[2] **K. Vasugi**,[3] **Yeddula Bharath Simha Reddy**,[4] **L. Natrayan**,[5] **and Subash Thanappan**[6]

[1]*Department of Civil Engineering, Aditya College of Engineering and Technology, Surampalem, Affiliated to Jawaharlal Nehru Technological University Kakinada, Kakinada, East Godavari District, Andhra Pradesh, India*
[2]*Department of Civil Engineering, Malla Reddy Engineering College, Secunderabad, India*
[3]*School of Civil Engineering, Vellore Institute of Technology, Chennai, Tamil Nadu, 600 127, India*
[4]*School of Civil Engineering, REVA University, Bengaluru, India*
[5]*Department of Mechanical Engineering, Saveetha School of Engineering, SIMAT, Tamil Nadu, 602105, Chennai, India*
[6]*Department of Civil Engineering, Ambo University, Ambo, Ethiopia*

Correspondence should be addressed to Naga Dheeraj Kumar Reddy Chukka; dheerukumbi@gmail.com, L. Natrayan; natrayan07@gmail.com, and Subash Thanappan; thanappansubash@gmail.com

Received 14 January 2022; Revised 18 February 2022; Accepted 4 March 2022; Published 25 March 2022

Academic Editor: Lakshmipathy R

The major goal of this research is to see how carbon nanotubes and silica fume affect the durability and mechanical qualities of high-performance concrete (HPC). Mechanical properties, such as split tensile strength, compressive strength, elasticity modulus, and flexural strength, and durability properties like water absorption, abrasion, chloride penetration, acid, and sea water resistance, impact resistance of HPC consisting silica fume (SF), and carbon nanotubes (CNT) were examined in this study. Varied trail combinations with different proportions of CNT and SF admixtures were created for this reason. Portland cement was partially replaced with 1 percent, 1.5 percent, 2 percent, and 3 percent CNT, while SF was substituted with 5 percent, 7.5 percent, and 10 percent. Both CNT and SF outperform conventional concrete in terms of mechanical and durability attributes, according to the findings. CNT produces superior results than SF due to its smaller size.

1. Introduction

In India, concrete is the most extensively used building material, with annual use of more than 1000 lakh m^3. It is generally recognized that traditional concrete fails to satisfy numerous functional criteria such as permeability, environmental resistance, frost resistance, and thermal cracking. As a result, additional material developments have been produced. To meet the current demand, it is thought essential to increase the performance and strength of concrete using appropriate admixtures. HPC has gained popularity in construction because to its improved mechanical qualities and endurance. It is generally understood that admixtures such as CNT, SF, nanosilica (NS), fly ash (FA), and ground granulated glass blast-furnace slag (GGBS) are required for the manufacturing of HPC. These admixtures can increase one or both of concrete's durability and strength attributes [1].

HPC is a type of concrete with the best qualities in the fresh and hardened concrete stages. HPC is considerably better than traditional concrete because the components in HPC contribute to the different qualities most effectively and efficiently. It contains concrete that offers significantly higher structural capacity while maintaining appropriate durability or substantially better resistance to environmental impacts

Figure 1: Silica fume.

Table 1: Physical features of SF.

Property	Value
Specific gravity	2.22
Bulk density	480–720 kg/m^3
Surface area	13,000–30,000 m^2/kg
Particle size	<1 μm
Fineness modulus	20,000 m^2/kg
Bulk modulus	240 kg/m^3
Colour	Dark grey

Table 2: Chemical features of SF.

Oxides	Percentage
SiO_2	92.1
Al_2O_3	0.5
Fe_2O_3	1.4
CaO	0.5
MgO	0.3
K_2O	0.7
Na_2O	0.3
SO_3	0.17
C	0.5-1.4
S	0.1-2.5
Loss of ignition (C+S)	0.7-2.5

Table 3: Properties of fine aggregate.

Specific gravity	2.66
Fineness modulus	2.7
Bulk density	1.65 kg/m^3
Type of sand	Medium sand (zone 2)

Table 4: Superplasticizer properties.

Appearance	Light brown liquid
Relative density	1.08 ± 0.01 at 25°C
pH	>6
Chloride ion content	<0.2%

Table 5: Mix proportions of trial mixes.

S. no.	Identification of mix	Replacement of CNT (%)	Replacement of SF (%)	Superplasticizer (%)
1	Normal mix	—	—	0.4
2	1 CNT	1	—	0.4
3	1.5 CNT	1.5	—	0.45
4	2 CNT	2	—	0.5
5	3 CNT	3	—	0.6
6	5 SF	—	5	0.5
7	7.5 SF	—	7.5	0.7
8	10 SF	—	10	0.8

Table 6: Results of workability tests.

Identification of mix	Superplasticizer (%)	Workability in terms of		
		Slump (mm)	Compaction factor	Vee-bee (secs)
Normal mix	0.4	56	0.95	4.3
1 CNT	0.4	29	0.83	22.4
1.5 CNT	0.45	32	0.85	20.4
2 CNT	0.5	35	0.88	17.2
3 CNT	0.6	39	0.9	12.5
5 SF	0.5	26	0.8	18.2
7.5 SF	0.7	38	0.88	11.1
10 SF	0.8	45	0.93	10.2

(durability in service). Nanotechnology is a burgeoning topic of study with applications in various fields. To improve the performance of nanocomposites, only a minimal amount of nanomaterial is required. Fibers are introduced into the cementitious matrix to overcome these flaws, and the application of this microfiber reinforcement improves the mechanical characteristics of cement-based products. This microfiber addition will assist to postpone the onset of microcracks, but it will not stop them from forming. This problem can be solved by including nanofibers or nanoparticles in cement. It has paved the way for the development of "nanoengineered ultra-high-performance materials" and the development of a new era of "crack-free materials." Conventional concrete will be transformed into a self-monitoring, crack-resistant, multipurpose smart material.

One of the most significant components in improving the microstructure of concrete is silica. In concrete, adding microsilica pozzolan gives the greatest results. This substance is made of 0.01 millimeter spherical grains that include 90% percent amorphous silica. Because it has a larger percentage of amorphous silica (greater than 99 percent) and smaller particles, its performance can be better than microsilica (1-50 nanometer). Compared to other pozzolan, it has the smallest particle size and the highest amount of amorphous silica, so its reactivity should be stronger. Because of its great reactivity, its usage is substantially lower than others'.

The goal of this study is to look at the mechanical and durability qualities of M60 grade HPC after replacing 1 percent, 1.5 percent, 2 percent, and 3 percent of the mass of

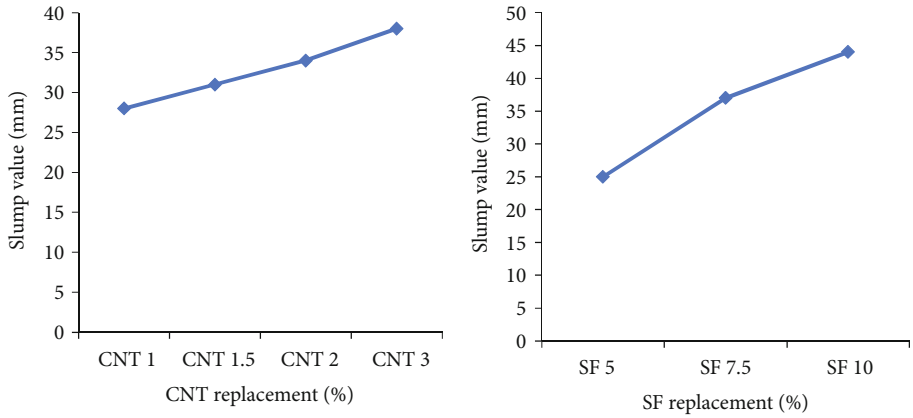

(a) % of CNT replacement (b) % of SF replacement

Figure 2: Variation of slump value.

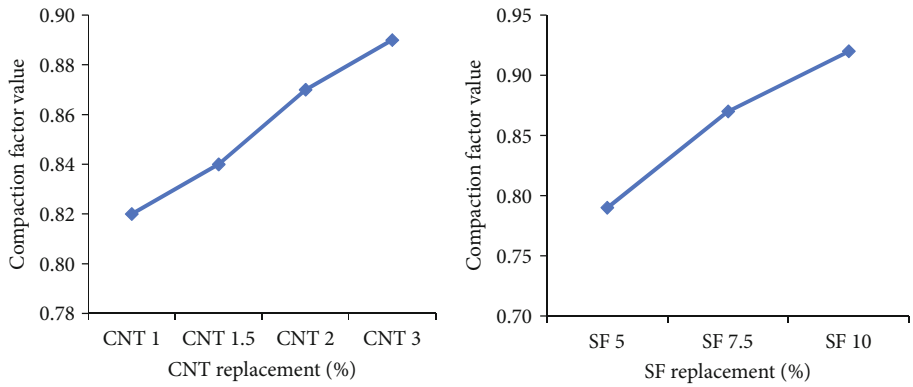

(a) % of CNT replacement (b) % of SF replacement

Figure 3: Variation of compaction factor value.

cement with CNT and 5 percent, 7.5 percent, and 10 percent of mass of cement with SF at a fixed water to binder (W/B) ratio, i.e., 0.31. This study is aimed at discovering the optimum amount of CNT and SF for cement substitution that would offer HPC exceptional durability and mechanical properties.

2. Literature Review

Wille and Loh studied the influence of CNT on the fresh and rheology characteristics of cement paste and mortar [2]. The influence of amorphous CNT particles added in cement pastes is investigated. Rheological experiments reveal after 75 minutes of mixing, mortar containing 2.5 percent by weight CNT has inadequate flowability to be monitored continuously in a Viskomat PC viscometer. Compared to plastic viscosity, the effect of CNT concentration on yield stress is more noticeable. When CNT was added, the spread, setting time, and time to achieve maximum temperature all lowered by 33 percent, 60 percent, and 51.3 percent, compared to specimens that did not have CNT. After 9 hours, X-ray diffraction in the sample containing 2.5 weight percentage CNT reveals the existence of calcium hydroxide. When CNT is introduced, the air content increases by 79 percent but the apparent density decreases by 2.4 percent.

Elahi et al. [3] investigated the mechanical and long-term durability of HPC adding extra cementitious materials. The compressive strength was used to evaluate the mechanical features, while the electrical resistivity, chloride diffusion, water absorption, and air permeability were used to study the durability characteristics. The kind and amount of extra cementitious materials were among the test variables (GGBS, FA, and SF). GGBS, FA, and SF were used to substitute portland cement up to 70 percent, 40 percent, and 15 percent, respectively. According to the findings, in terms of bulk resistivity and strength development, SF outperforms other supplemental cementitious materials. The mixes comprising GGBS, FA, and SF performed the best of all the mixes to resist chloride diffusion. Permeation findings were favourable in the mix including FA. All of the ternary mixes have produced HPC with good durability.

Coppola et al. [4] published a research that compared the impacts of CNT and NS in concrete. The local mechanical characteristics of cement pastes with 0 percent and 15 percent CNT replacement were measured using nanoindentation and scanning probe microscope imaging. The

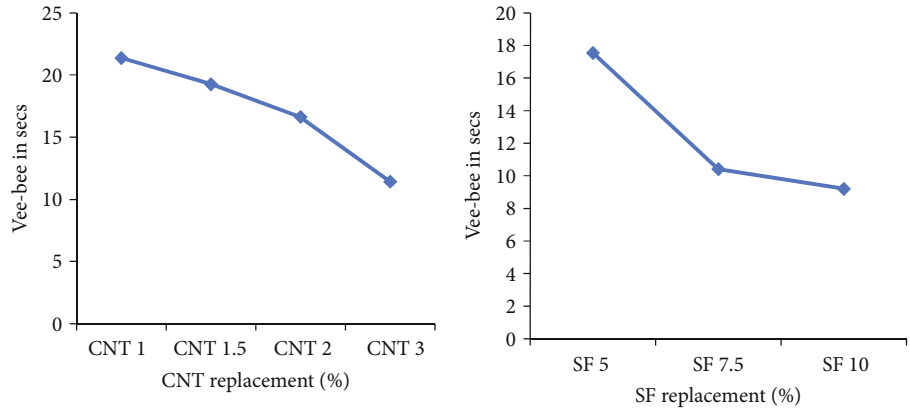

(a) % of CNT replacement (b) % of SF replacement

Figure 4: Variation of vee-bee consistometer.

Table 7: Results of compressive strength.

Identification of mix	Average compressive strength (N/mm^2)					
	1st day	3rd day	7th day	28th day	56th day	90th day
Normal mix	12.6	37.1	38.8	62.4	64.9	67.4
1 CNT	18	40	46	67	70.2	70.5
1.5 CNT	21.5	44	48.3	69	70.7	71.9
2 CNT	22	48	52.6	72.1	73.2	78.9
3 CNT	21.9	48.4	51.7	70.2	71	72.9
5 SF	13.3	40.1	44	63.9	74.7	77.1
7.5 SF	13.7	42.6	46.2	69	76.7	78.3
10 SF	16.1	38.7	45.7	64.6	75.2	77.9

presence of pozzolanic reaction is demonstrated by a decrease in volume percentage of $Ca(OH)_2$ in sample containing CNT. NS considerably enhances the durability of concrete, according to a parallel investigation of cement pastes containing NS. The impacts of NS on cement paste nanostructure are described in this paper and their impact on concrete durability. According to the nanoindentation investigation, the volume percentage of the high-stiffness calcium silicate hydrate (C-S-H) gel rose dramatically with the addition of NS. The findings of nanoindentation on cement paste samples containing equivalent amounts of CNT and NS are compared. CNT samples contained about double the quantity of high-stiffness C-S-H as NS samples. The volume proportion of high-stiffness C-S-H was as high as 50% in samples containing 15 percent CNT.

Lu et al. [5] studied the impact of polypropylene fibers on physical and mechanical characteristics of CNT mortars. Four fiber fractions 0 percent, 0.1 percent, 0.3 percent, and 0.5 percent are taken. In the first phase of the research, 6 batches were made to determine the optimal quantity of CNT in regular cement mortar. In the second stage, 0.1 percent, 0.3 percent, and 0.5 percent polypropylene fibers were added to the ordinary and optimum mixtures selected in the first stage, to determine the impact of the polypropylene fibers on the shrinkage and strength properties. According to the findings, using polypropylene fibers in the cement matrix resulted in a small increase in flexural and compressive strength. The influence of increasing the fiber content to mechanical strength was negative. The inefficient dispersion of polypropylene fibers in mortar, which increases pore volume and causes additional micro flaws in the cement matrix, might be one explanation for this result. The addition of CNT particles boosted the efficiency of the fiber reinforcement in terms of mechanical strength. This might be owing to a decrease in internal porosity, particularly in the fiber/matrix transition zone, which has a greater contact surface and thus friction between 2. The addition of CNT to mortars reduced water absorption. The inclusion of CNT in the cement matrix enhanced the dying shrinkage of mortar. Fiber reinforcing in cement mortar might help to mitigate this impact. However, using a high fiber content (more than 0.3 percent) did not affect shrinkage strain.

The mechanical characteristics of concrete containing CNT and NS were examined by Hawreen and Bogas [6]. This study is aimed at looking at the impact of adding NS to regular concrete and compare it to CNT. CNT and NS are partly replaced with cement in this study by 2 percent, 4.5 percent, and 7.5 percent cubic samples of 10 cm with breaking three samples from each plan for seven compressive strength experiment mixtures aged 3, 7, 28, 90, and 180 days. In primary ages, the importance of CNT in compressive strength is inferred. However, as time passes, this decreases, and its peak activity is between 7 and 28 days old. They discovered that adding 3 to 12 percent CNT to mortar increases its strength by three to four times.

The influence of CNT on the mechanical characteristics and microstructure of cement mortar was studied by Baloch et al. [7]. The impact of the size and amount of CNT particles on the mechanical characteristics and microstructure of manufactured cement mortar are examined in this work. The measurements are taken on the 7th day after the cement mortar is produced. Compared to the pure cement mortar, the cement mortar incorporating CNT had improved mechanical qualities. Because the manufacturing procedure utilized here resulted in a uniform spreading of CNT in cement, its mechanical characteristics improved even when

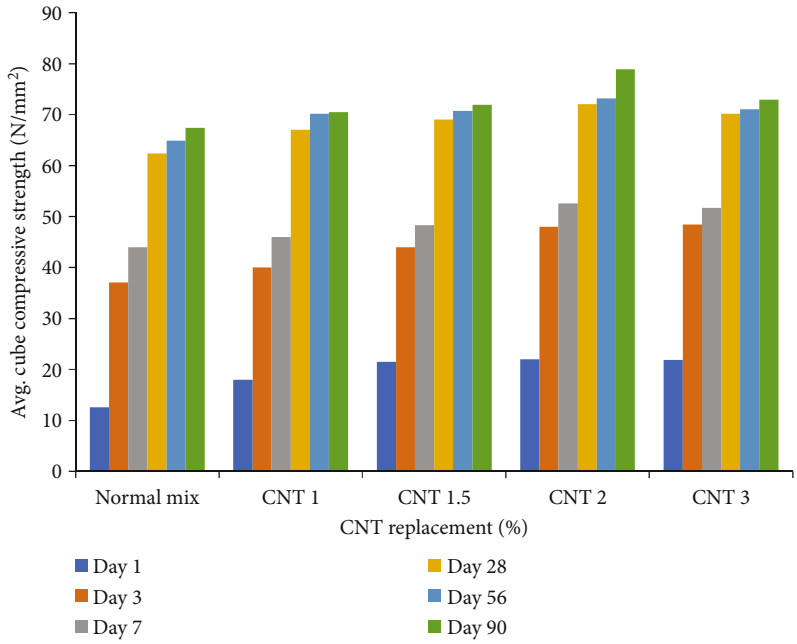

Figure 5: Fluctuation of compressive strength for % of CNT replacement.

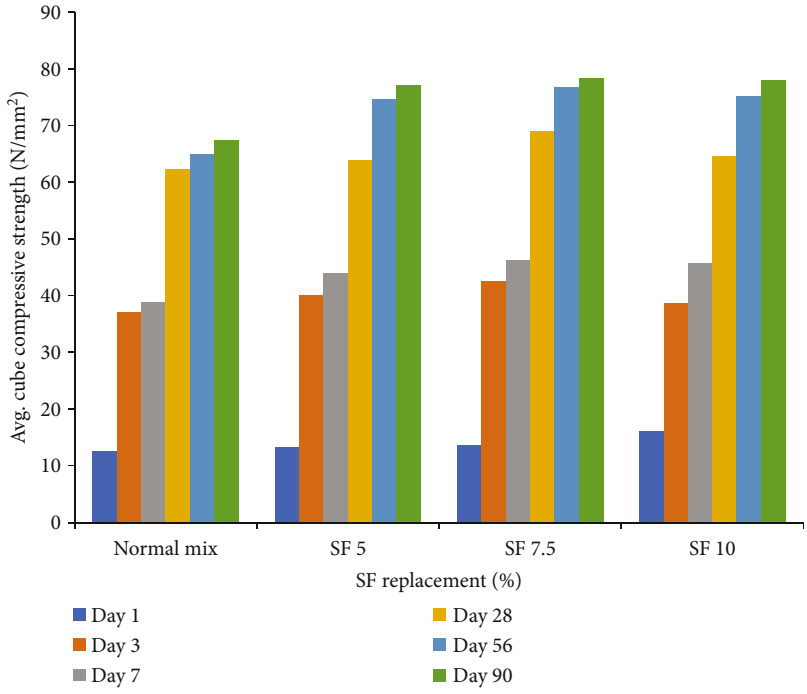

Figure 6: Fluctuation of compressive strength for % of SF replacement.

just 1% CNT were added. In other words, adding a critical quantity of CNT enhanced the compressive strength. The addition of CNT to regular cement mortar improves its mechanical qualities (compressive, flexural, and tensile strengths).

The influence of CNT on concrete with ordinary cement and ordinary cement + Class F fly ash binders was examined in this study. Hawreen and Bogas [8] studied the characteristics of CNT-infused concrete. In terms of strength development, reactivity, densification of the interfacial transition zone, and pore refinement mixes including CNT showed significant improvement. The enormous surface area of CNT particles, which has pozzolanic and filling effects on the cementitious matrix, is primarily responsible for this enhancement. According to microstructural and thermal studies, the impact of filler and pozzolanic effects on pore

Table 8: Split tensile strength of concrete at the 28th day.

Identification of mix	CNT (%)	SF (%)	Split tensile strength (N/mm^2)
Normal mix	0	0	5.78
1 CNT	1	0	6.6
1.5 CNT	1.5	0	6.83
2 CNT	2	0	7.21
3 CNT	3	0	7
5 SF	0	5	6.30
7.5 SF	0	7.5	7.25
10 SF	0	10	6.89

structure improvement was shown to be dependent on the dose of CNT.

Electrical resistivity, water absorption, and chloride penetration of HPC incorporating NS and SF were studied by Jalal et al. [9]. This work explored the durability-related aspects of high strength self-compacting concrete incorporating NS and SF, including electrical resistivity, water absorption, and chloride penetration. Varied combinations with different SF and NS admixtures are created for this purpose. Microsilica, NS, and a combination of micro- and nanosilica are used to substitute portland cement in varied proportions of 10 percent, 2 percent, and 10 percent + 2 percent, respectively. The influence of binder content on concrete qualities is also explored using different binder contents. Capillary absorption, water absorption, resistivity tests, and chloride ion percentage are used to assess durability attributes. The findings demonstrate that in combinations including admixtures, such as a blend of SF and NS, capillary absorption, water absorption, and chloride ion percentage, all fell dramatically. The admixtures boosted the resistivity of the self-compacting concrete mixes, which might reduce corrosion risk.

The influence of W/C ratio on permeability, porosity, and abrasive strength of CNT concrete was studied by Hawreen et al. [10]. This study is aimed at seeing how the water-cement ratio affects the porosity, abrasive strength, and coefficient of hydraulic conductivity of CNT concrete. The water-cement ratios directly or indirectly affect abrasion resistance, porosity, efficiency, and other properties. When CNT was combined with cement mortar, it resulted in an upgraded concrete with great strength and abrasion resistance. The water-cement ratios were adjusted in this study to analyze and assess concrete specimens' abrasive and compressive strength. The water-cement ratios in the mixture ranged from 0.33, 0.36, 0.4, 0.44, and 0.5 in the produced concrete samples, which contained 3 percent CNT. In all concrete samples, the other components of the mixture were kept constant. The abrasion strength of concrete was enhanced by 36 percent by lowering the W/C ratio from 0.5 to 0.33. The hydraulic conductivity coefficient of concrete decreases from 31.71×10^{15} to 2×10^{15} m/sec when the W/C ratio is decreased from 0.5 to 0.33. In addition, the concrete's porosity was lowered, and the W/C ratio was decreased from 0.5 to 0.33. The abrasion depth decreased as the W/C ratio grew from 0.33 to 0.5 for silica fume and natural pozzolanas on sulfuric acid.

The characteristics of concrete adding SF and NS were given by Tavakoli and Heidari [11]. The study looks at the usage of NS and SF in concrete simultaneously. To achieve this, SF in concentrations of 5 and 10% and NS in concentrations of 0.5 and 1% were substituted with cement and a total of eight mixture designs were used to conduct compressive strength and water absorption tests. Compared to the control sample, using both 10 percent SF and 1 percent NS as a cement substitute resulted in a 42.2 percent improvement in compressive strength. Furthermore, it was discovered that using these components simultaneously had a greater impact than using them separately. Finally, the findings revealed that employing such components enhances concrete quality.

3. Materials Used in HPC

3.1. Cement. The cement utilized in this investigation was 53 grade ordinary portland cement, often used in the construction sector. The physical characteristics of cement were determined using a pycnometer and Vicat's apparatus, as per IS 12269:1987 (reaffirmed 2004). The results show that cement's specific gravity, initial, final setting time, and standard consistency are 3.12, 125 min, 281 min, and 32%, respectively.

3.2. Silica Fume. For many years, SF has already been employed worldwide in the construction of high-strength, long-lasting concrete. Both fresh and hardened concretes benefit from the addition of SF. SF is a by-product of the smelting process in silicon and ferrosilicon industries. At high temperatures approximately 2,000°C, the reduction of high-purity quartz to silicon produces SiO_2 vapours, which oxidize and condense in the low-temperature zone to microscopic particles. The SF is indicated in Figure 1.

Tables 1 and 2 show SF physical and chemical features.

3.3. Carbon Nanotubes. CNTs are a relatively new addition to the concrete industry as a nanoscale reinforcement. These materials are single-walled or multiwalled hollow cylinder graphite sheets [12]. In this study, multiwalled carbon nanotubes were used. With Young's modulus of one TPa, these materials have a high rigidity. It has a tensile strength of above 100GPa and can endure strain elongation of up to 15%-16% [13]. It also offers greater adsorption capabilities due to its larger specific area (approx. 1000 m^2/g). CNT acts in cement-based composites because it increases the interfacial contact area and efficiently stabilizes the concrete mixture.

3.4. Coarse Aggregate. The aggregate strength and the binding between the aggregate and paste become crucial considerations in HPC. Crushed-stone aggregates have a greater compressive strength than gravel aggregate in concrete. Crushed aggregate with a size of 12.5 mm and an angular form was employed in this investigation.

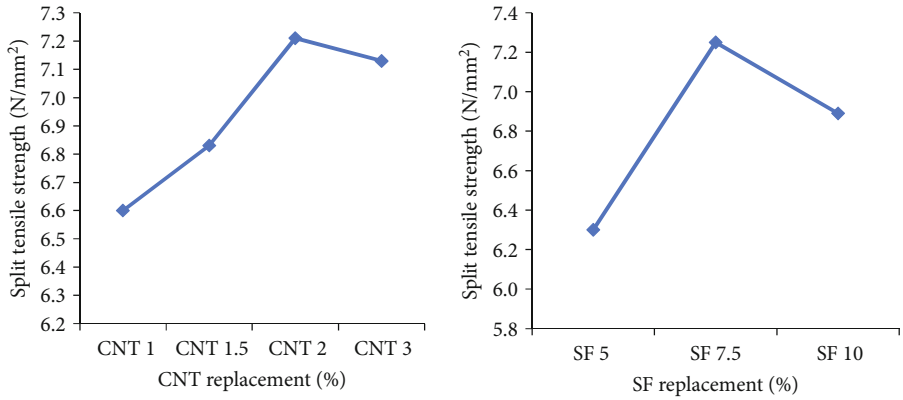

(a) % of CNT replacement

(b) % of SF replacement

Figure 7: Split tensile strength variation at the 28th day.

Table 9: Concrete flexural strength at the 28th day.

Identification of mix	CNT (%)	SF (%)	Flexural strength (N/mm^2)
Normal mix	0	0	7.5
1 CNT	1	0	8.0
1.5 CNT	1.5	0	8.5
2 CNT	2	0	10.5
3 CNT	3	0	9
5 SF	0	5	8
7.5 SF	0	7.5	9.5
10 SF	0	10	9

3.5. Fine Aggregate. According to the IS:2386 (Part-3):1963 limitations, the fine aggregate was examined. Table 3 give the properties of fine aggregates.

3.6. Water. Water is a significant component of cement paste because it participates chemically in the events that lead to the formation of the hydration product, C-S-H gel. The binding activity of C-S-H gel is primarily responsible for the strength of cement paste. The compatibility of the provided cement with the chemical and mineral admixtures and the water used for mixing is critical for HPC. The quality and quantity of water must be constantly monitored.

3.7. Superplasticizer. Chemical admixtures like superplasticizers, water reducers, and retarders are required. They assist in getting the least practicable W/B ratio by making better use of enormous quantities of cement in HPC.

GLENIUM B233 polycarboxylic ether based superplasticizer is employed in this work. Table 4 lists the characteristics of GLENIUM B233. The product was designed particularly for use in HPC applications that demand excellent workability, performance, and durability. GLENIUM B233 keeps rheoplastic concrete workable for more than 45 minutes at +25°C. Temperature and the kind of cement, the manner of transport, the nature of aggregates, and starting workability all influence workability loss. Trial mixes should be used to find the best dose of GLENIUM B233.

4. Experimental Investigations

4.1. Proportion of Mix Achieved by Phase I. Various mixes for M60 grade are determined using the ACI [14] technique of mix design. The mix percentage is determined by testing both fresh and hardened concretes based on the trail mixes. The compressive strength and workability tests are used to determine the mix percentage. The final mix percentage for partial cement replacement by SF of 5 percent, 7.5 percent, and 10 percent and CNT of 1 percent, 1.5 percent, 2 percent, and 3 percent is chosen to achieve both compressive strength and workability of concrete. With a W/B ratio of 0.31, the mix percentage obtained from the trail mixes is 1 : 0.82 : 2.07.

4.2. Mix Proportions for Replacement. At a steady water-binder ratio of 0.31, the cement was partially substituted with CNT by 1 percent, 1.5 percent, 2 percent, and 3 percent and SF by 5 percent, 7.5 percent, and 10 percent, based on the mix proportions determined in phase I. For the M60 grade, a total of 7 trail mixes have arrived. A polycarboxylic ether-based superplasticizer is utilized in all of the combinations above to make workable concrete. The amount of superplasticizer used varies by % to obtain the desired slump. Table 5 shows the varying percentages of CNT and SF replacement.

The details of concrete specimens cast for the M60 grade of HPC mixes are as follows:

(i) 144 nos. of cube specimen of size 100 × 100 mm

(ii) 28 nos. of cylindrical specimens of size 150 mm × 300 mm

(iii) 32 nos. of cylindrical specimens of size 100 mm × 200 mm

(iv) 21 nos. of prisms of size 100 mm × 100 mm × 500 mm

(v) 21 nos. of cylindrical specimens of size 150 mm × 63 mm

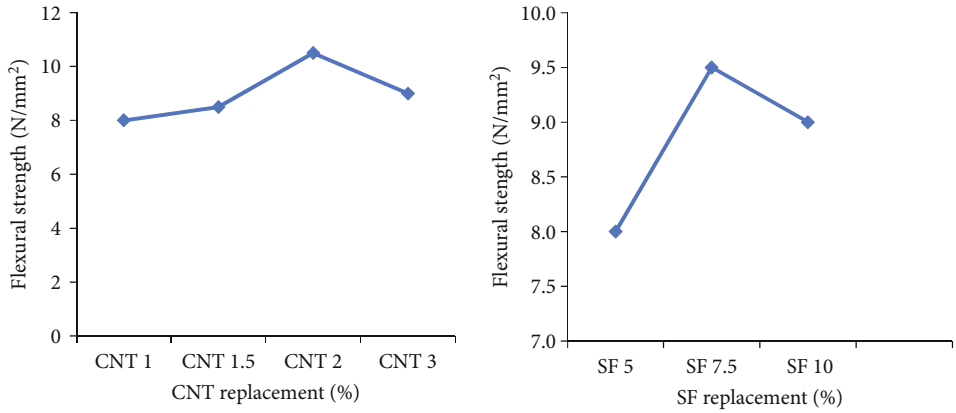

(a) % of CNT replacement (b) % of SF replacement

Figure 8: Variation of flexural strength at the 28th day.

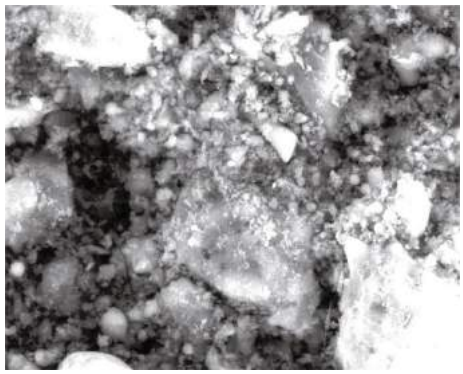

Figure 9: SEM image.

Table 10: Modulus of elasticity of concrete at the 28th day.

Identification of mix	CNT (%)	SF (%)	Modulus of elasticity (N/mm^2)
Normal mix	0	0	45000
1 CNT	1	0	55000
1.5 CNT	1.5	0	68000
2 CNT	2	0	77000
3 CNT	3	0	71000
5 SF	0	5	50000
7.5 SF	0	7.5	68000
10 SF	0	10	60000

(vi) 21 nos. of cylindrical specimens of size 70 mm × 70 mm × 35 mm

(vii) 42 nos. of cube specimens of size 150 mm

5. Results and Discussions

5.1. Workability of Concrete. The results of workability tests on fresh concrete such as the compaction factor test, vee-bee consistometer test, and slump test were done according to BIS [15] requirements, and the results are displayed in Table 6.

For all of the mixtures, the W/B ratio was kept consistent at 0.31. The test findings show that increasing the superplasticizer content improved the workability of concrete when CNT and SF were largely replaced for cement. Workability is reduced because of the inclusion of CNT and microsilica with a high specific surface area. To maintain a consistent slump, such an impact may increase water use. To keep water demand equivalent to that of the control, superplasticizers should be dosed by weight of CNT and microsilica. Figures 2–4 depict the variance of workability test results.

5.2. Concrete Compressive Strength. Compressive strength tests were performed on cube specimens at various ages including 1, 3, 7, 28, 56, and 90 days, and the findings are presented in Table 7.

When CNT and SF are introduced to concrete, the compressive strength of the mixture changes dramatically. This is mostly owing to improved aggregate-paste bonding and microstructure. The test findings show that when CNT is partially replaced with cement, the compressive strength of concrete is enhanced at an earlier age. The blend containing 3 percent CNT and 7.5 percent SF yielded the highest compressive strength. The synthesis of C–S–H was generated by the interaction of CNT and SF with calcium hydroxide created during the hydration of cement. It was partly because of the filling role of very tiny CNT and SF particles. Furthermore, early compressive strength gains were lower in concrete containing various amounts of SF. Figures 5 and 6 demonstrate the fluctuation in compressive strength for a mix including CNT and SF at various ages.

5.3. Split Tensile Strength. Table 8 shows the split tensile strength of concrete containing CNT and SF after 28 days of testing.

According to the test findings, the split tensile strength improved steadily as the % of CNT content was raised. When SF was partially replaced, however, the split tensile strength was raised until it reached 7.5 percent replacement, after which it was lowered. The variation of split tensile strength for the mix containing CNT and SF is shown in Figure 7.

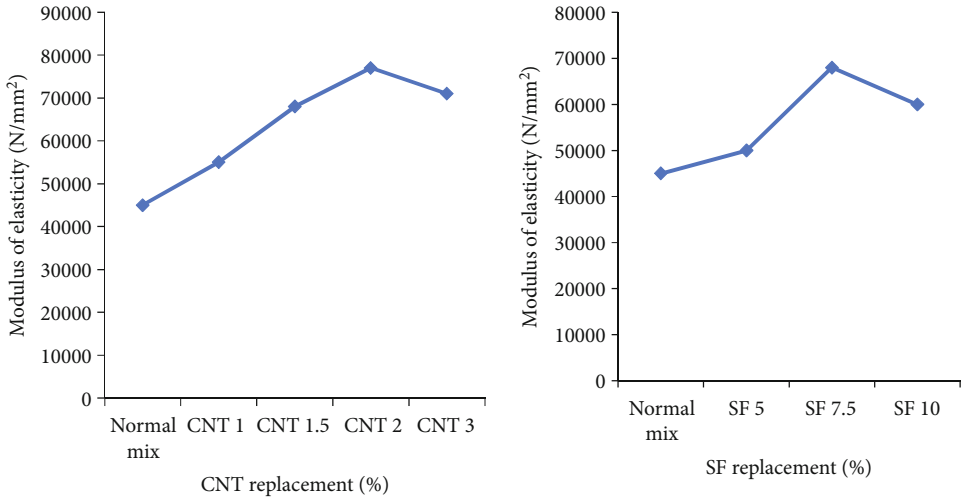

(a) % of CNT replacement (b) % of SF replacement

Figure 10: Variation of modulus of elasticity.

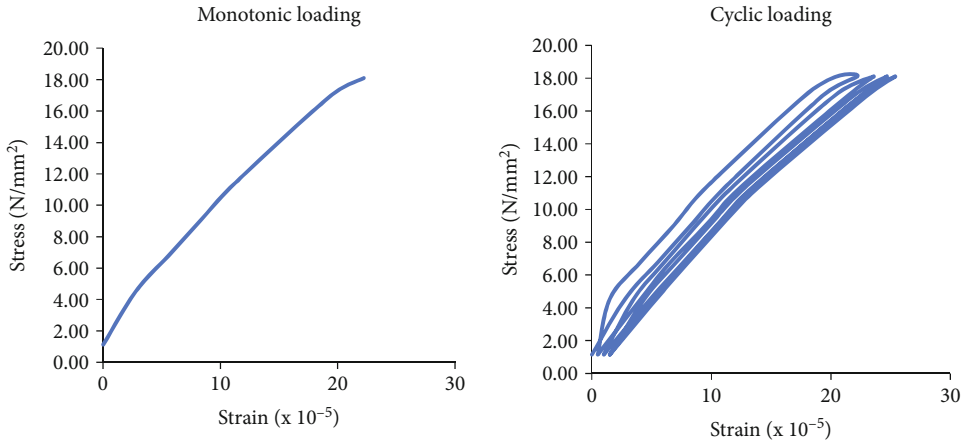

(a) Monotonic loading (b) Cyclic loading

Figure 11: Stress-strain curve for 1% of CNT.

5.4. Flexural Strength. Table 9 shows the concrete flexural strength test results on the 28th day.

The variation of the flexural strength concrete containing CNT and SF is depicted in Figure 8.

Compared to splitting tensile strength, adding CNT and SF to the concrete significantly influences flexural strength. Even extremely high percentages of CNT and SF boost flexural strengths dramatically. It was also discovered that the flexural strength increased steadily when the SF replacement % was increased.

5.5. Adsorption Characteristics of Carbon Nanotubes. A micrograph of shattered concrete species was seen after the compressive strength test at 28 days. The CNT samples with dispersion with other components may be observed. The CNT samples, as well as SF samples, are visible in Figure 9. A closed cluster of CNT can be seen in some parts of the micrograph.

5.6. Modulus of Elasticity of Concrete. The test results of the modulus of elasticity of concrete containing CNT and SF are shown in Table 10.

The slope of a stress-strain curve formed during compressive testing on a sample of the material can be calculated experimentally. According to the test findings, the concrete elastic modulus was raised for the concrete containing CNT and SF. The rise in Young's modulus of CNT-containing concrete is greater than that of SF-containing concrete due to the higher specific surface. Figure 10 depicts the modulus of elasticity change for CNT and SF mixes.

Strain curve under monotonic loading and cyclic loading are shown in Figure 11.

5.7. Saturated Water Absorption. Table 11 shows the saturation water absorption test results for HPC trail mixes at the ages of 28 and 90 days.

On the 28th and 90th days, the trail mixes' saturation water absorption varied from 1.5 to 1.65%. The Concrete

Table 11: Saturated water absorption test results.

Identification of mix	CNT (%)	SF (%)	Saturated water absorption (%)	
			28th day	90th day
Normal mix	0	0	1.656	1.652
1 CNT	1	0	1.59	1.551
2 CNT	2	0	1.565	1.519
3 CNT	3	0	1.517	1.51
5 SF	0	5	1.586	1.576
7.5 SF	0	7.5	1.553	1.591
10 SF	0	10	1.541	1.576

Table 12: Results of porosity.

Identification of mix	CNT (%)	SF (%)	Effective porosity (%)	
			28th day	90th day
Normal mix	0	0	2.534	2.529
1 CNT	1	0	2.413	2.411
2 CNT	2	0	2.316	2.312
3 CNT	3	0	2.312	2.309
5 SF	0	5	2.514	2.510
7.5 SF	0	7.5	2.418	2.412
10 SF	0	10	2.396	2.391

Table 13: Results of sorptivity.

Identification of mix	CNT (%)	SF (%)	Sorptivity $(mm/min)^{0.5}$ 28th day
Normal mix	0	0	0.085
1 CNT	1	0	0.073
2 CNT	2	0	0.06
3 CNT	3	0	0.05
5 SF	0	5	0.081
7.5 SF	0	7.5	0.064
10 SF	0	10	0.053

Table 14: Rapid chloride permeability results.

Identification of mix	CNT (%)	SF (%)	Charge passed as per ASTM equivalent (coulombs)	Chloride ion penetrability
Normal mix	0	0	1368	Low
1 CNT	1	0	917.1	Very low
2 CNT	2	0	982.8	Very low
3 CNT	3	0	1053	Low
5 SF	0	5	909	Very low
7.5 SF	0	7.5	881.1	Very low
10 SF	0	10	558.9	Very low

Table 15: Acid resistance test results.

Identification of mix	CNT (%)	SF (%)	Acid resistance Loss in weight (%)
Normal mix	0	0	0.39
1 CNT	1	0	0.3
2 CNT	2	0	0.35
3 CNT	3	0	0.3
5 SF	0	5	0.56
7.5 SF	0	7.5	0.45
10 SF	0	10	0.43

Society of the United Kingdom describes that concrete with a saturated water absorption limit of roughly 3%, as excellent concrete. This indicates that the performance of CNT and SF in filling the pores in the concrete was excellent due to their particle size. According to the test findings, the combination CNT 3 and SF 10 has the lowest saturated water absorption value [16].

5.8. Porosity. The porosity test results at the 28th and 90th day for the various HPC trail mixes are given in Table 12.

The effective porosities for the trail mixes at the 28th day are ranged from 2.31 to 2.53 percent. The results show that the effective porosity value is lower for the mix containing 3% of CNT and 10% of SF [17]. This was due to the microfilling effect of CNT and SF, and it concludes that CNT and SF have a good durability characteristic [18].

5.9. Sorptivity. The test results of sorptivity are given in Table 13 for HPC trail mixes at the age of 28 days.

The results are varied from 0.05 to 0.08 for both CNT and SF replacements. The test results can be concluded that CNT replacement performs better than the SF [19].

5.10. Rapid Chloride Permeability Test. Table 14 shows the results of the rapid chloride permeability test on the 28th day for the various HPC trail mixes.

The test results show that the lowest amount of charge is passed for the specimens containing 3% of CNT and 10% of SF [20]. The charges that passed through the specimens are ranged from 550 to 1050 coulombs [21]. The chloride penetration resistance is much higher for the mix containing 3% of CNT and 10% SF [22]. The charges that passed through the conventional concrete are higher than the HPC mix containing CNT and SF. This is due to the pozzolanic reactivity and microfilling effects of CNT and SF [23].

5.11. Acid Resistance. The test results of acid resistance are shown in Table 15 for the various HPC trail mixes at the age of 28 days.

The percentage loss in weight for the mixes containing CNT ranges from 0.3 to 0.35 and for SF ranges from 0.43 to 0.56 [24]. The test results show that the CNT performs better than the SF against acid attack [25].

Table 16: Sea water resistance test results.

Identification of mix	CNT (%)	SF (%)	Sea water resistance Loss in weight (%)
Normal mix	0	0	0.86
1 CNT	1	0	0.5
2 CNT	2	0	0.60
3 CNT	3	0	0.7
5 SF	0	5	0.7
7.5 SF	0	7.5	0.52
10 SF	0	10	0.4

Table 17: Abrasion resistance test results.

Identification of mix	CNT (%)	SF (%)	Abrasion resistance Average loss of thickness (mm)
Normal mix	0	0	0.92
1 CNT	1	0	0.42
2 CNT	2	0	0.35
3 CNT	3	0	0.29
5 SF	0	5	0.67
7.5 SF	0	7.5	0.48
10 SF	0	10	0.35

Table 18: Impact resistance test results.

Identification of mix	Average number of drops for initial crack	Average number of drops at failure	Energy at initial crack (E_1) (N mm)	Energy at failure (E_2) (N mm)	Ductility index (s)
Normal mix	301	305	6327517	6411604	1.01329
1 CNT	346	351	7273492	7378600	1.01445
2 CNT	367	372	7714947	7820055	1.01362
3 CNT	384	390	8072315	8198445	1.01562
5 SF	396	402	8324574	8450704	1.015
7.5 SF	338	342	7105319	7189405	1.01183
10 SF	352	366	7399622	7693925	1.03977

5.12. Sea Water Resistance. The results of sea water resistance are shown in Table 16 for the various trail mixes of HPC at the age of 28 days.

The percentage loss in weight for CNT ranges from 0.5 to 0.7 and for SF is 0.4 to 0.7 [26]. The test results have been observed that the HPC trail mixes have high resistance against sea water. Especially for 1% of CNT and 10% of SF, they are less attacked by the sea water [27].

5.13. Abrasion Resistance. The results of abrasion resistance also shown in Table 17 for various trail mixes of HPC at the age of 28 days.

The average loss of thickness for the HPC mix containing CNT ranges from 0.29 to 0.42 mm and for SF ranges from 0.35 to 0.67 mm [28]. Thus, the mixes containing CNT showed less average thickness loss than those containing SF [29]. Both CNT and SF have high abrasion resistance than the normal mix concrete [30].

5.14. Impact Resistance. The impact resistance tests are given in Table 18 for the HPC trail mixes at the age of 28 days.

Due to admixtures like SF and CNT, the concrete was well packed. The average number of drops at failure for the mixes is ranged from 305 to 402. The mix containing 3% of CNT shows better resistance than the other mixes. The impact resistance of the concrete is increased due to the conversion of calcium hydroxide to the calcium hydrates by CNT and SF in the concrete.

6. Conclusions

From the acquired experimental data, the following conclusions may be drawn:

(i) The HPC mixes require more water due to the specific surface area and particle size of SF and CNT. The superplasticizer dose is adjusted from 0.4 to 0.8 percent by weight of cement to produce the desired workability

(ii) When utilizing SF, the superplasticizer dose is greater than when using CNT

(iii) The average compressive strength at 28 days rose by 1.41 percent, 1.8 percent, 2.2 percent, and 2 percent for the mixes containing 1 percent, 1.5 percent, 2 percent, and 3 percent of CNT, respectively. At the 56^{th} and 90^{th} days, the compressive strength increases

(iv) The average cube compressive strength increases until it reaches 2 percent of CNT, which begins to decline. As a result, predicting the optimal CNT replacement content is challenging

(v) The average compressive strength at 28 days rose by 1.2 percent, 1.5 percent, and 0.8 percent for the mixes containing 5 percent, 7.5 percent, and 10 percent of SF, respectively

(vi) The flexural strength and split tensile strength of the mix comprising 1 percent, 1.5 percent, 2 percent, and 3 percent CNT are rising up to 2 percent CNT. The flexural strength and split tensile strength of the mix including SF only increase up to 7.5 percent SF

(vii) Concrete having CNT has a greater elasticity modulus than concrete containing SF. Substantial deformation increases in a linear fashion

(viii) Porosity, sorptivity, and water absorption are lower in trail mixes with the CNT substitution than in SF. This suggests that the size of the CNT

particles is important in making the concrete impermeable

(ix) Concrete mixes including SF and CNT are more resistant to abrasion, impact load, acid, and seawater assault and chloride penetration. This is owing to the microstructure improvement brought about by the filler actions of SF and CNT, which result in discontinuous and fine pore structure

(x) The performance level of CNT is superior to that of SF and normal concrete in terms of durability and mechanical qualities. As a result, it can be inferred that CNT replacement has higher durability and mechanical properties by up to 3 percent. According to the test results, the ideal SF replacement content is just 7.5 percent

(xi) The partial substitution of SF and CNT with cement results in a reduction in cement use

Data Availability

The data used to support the findings of this study are included within the article. Should further data or information be required, these are available from the corresponding author upon request.

Conflicts of Interest

The authors declare that there are no conflicts of interest regarding the publication of this paper.

Acknowledgments

The authors thank Aditya College of Engineering and Technology, Surampalem, and Saveetha School of Engineering, SIMATS, Chennai, for the technical assistance. The authors appreciate the supports from Ambo University, Ethiopia.

References

[1] P. C. Aitcin, *High Performance Concrete*, E & FN Spon An imprint of routledge publications, 1998.

[2] K. Wille and K. J. Loh, "Nanoengineering ultra-high-performance concrete with multiwalled carbon nanotubes," *Transportation Research Record*, vol. 2142, no. 1, pp. 119–126, 2010.

[3] A. Elahi, M. Basheer, S. Nanukuttan, and Q. U. Z. Khana, "Mechanical and durability properties of high performance concretes containing supplementary cementitious materials," *Construction and Building Materials*, vol. 24, no. 3, pp. 292–299, 2010.

[4] L. Coppola, A. Buoso, and F. Corazza, "Electrical properties of carbon nanotubes cement composites for monitoring stress conditions in concrete structures," *Applied Mechanics and Materials*, vol. 82, pp. 118–123, 2011.

[5] L. Lu, D. Ouyang, and W. Xu, "Mechanical properties and durability of ultra high strength concrete incorporating multi-walled carbon nanotubes," *Materials*, vol. 9, no. 6, p. 419, 2016.

[6] A. Hawreen and J. A. Bogas, "Influence of carbon nanotubes on steel–concrete bond strength," *Materials and Structures*, vol. 51, no. 6, p. 155, 2018.

[7] W. L. Baloch, R. A. Khushnood, and W. Khaliq, "Influence of multi-walled carbon nanotubes on the residual performance of concrete exposed to high temperatures," *Construction and Building Materials*, vol. 185, pp. 44–56, 2018.

[8] A. Hawreen and J. A. Bogas, "Creep, shrinkage and mechanical properties of concrete reinforced with different types of carbon nanotubes," *Construction and Building Materials*, vol. 198, pp. 70–81, 2019.

[9] M. Jalal, A. R. Pouladkhan, H. Norouzi, and G. Choubdar, "Chloride penetration, water absorption and electrical resistivity of high performance concrete containing nano silica and silica fume," *Journal of American Science*, vol. 8, no. 4, pp. 278–284, 2012.

[10] A. Hawreen, J. A. Bogas, and R. Kurda, "Mechanical characterization of concrete reinforced with different types of carbon nanotubes," *The Arabian Journal for Science and Engineering*, vol. 44, no. 10, pp. 8361–8376, 2019.

[11] D. Tavakoli and A. Heidari, "Properties of concrete incorporating silica fume and nano-SiO_2," *Indian Journal of Science and Technology*, vol. 6, no. 1, pp. 1–5, 2013.

[12] M. Jung, Y. S. Lee, S. G. Hong, and J. Moon, "Carbon nanotubes (CNTs) in ultra-high performance concrete (UHPC): dispersion, mechanical properties, and electromagnetic interference (EMI) shielding effectiveness (SE)," *Cement and Concrete Research*, vol. 131, p. 106017, 2020.

[13] P. Mudasir and J. A. Naqash, "Impact of Carbon Nano Tubes on Fresh and Hardned Properties of Conventional Concrete," *Materials Today: Proceedings*, pp. 1–6, 2021.

[14] N. D. K. R. Chukka and M. Krishnamurthy, "Seismic performance assessment of structure with hybrid passive energy dissipation device," *Structure*, vol. 27, pp. 1246–1259, 2020.

[15] N. D. K. R. Chukka, L. Natrayan, and W. D. Mammo, "Seismic fragility and life cycle cost analysis of reinforced concrete structures with a hybrid damper," *Advances in Civil Engineering*, vol. 2021, Article ID 4195161, 17 pages, 2021.

[16] S. Praburanganathan, N. Sudharsan, Y. B. S. Reddy, N. D. K. R. Chukka, L. Natrayan, and P. Paramasivam, "Force-deformation study on glass fiber reinforced concrete slab incorporating waste paper," *Advances in Civil Engineering*, vol. 2022, Article ID 5343128, 10 pages, 2022.

[17] S. Justin Abraham Baby, S. Suresh Babu, and Y. Devarajan, "Performance study of neat biodiesel-gas fuelled diesel engine," *International Journal of Ambient Energy*, vol. 42, no. 3, pp. 269–273, 2021.

[18] V. S. Nadh, C. Krishna, L. Natrayan et al., "Structural behavior of nanocoated oil palm shell as coarse aggregate in lightweight concrete," *Journal of Nanomaterials*, vol. 2021, Article ID 4741296, 7 pages, 2021.

[19] Y. Devarajan, G. Choubey, and K. Mehar, "Ignition analysis on neat alcohols and biodiesel blends propelled research compression ignition engine," *Energy Sources, Part A: Recovery, Utilization, and Environmental Effects*, vol. 42, no. 23, pp. 2911–2922, 2020.

[20] A. Sedaghatdoost and K. Behfarnia, "Mechanical properties of Portland cement mortar containing multi-walled carbon nanotubes at elevated temperatures," *Construction and Building Materials*, vol. 176, pp. 482–489, 2018.

[21] A. Naqi, N. Abbas, N. Zahra, A. Hussain, and S. Q. Shabbir, "Effect of multi-walled carbon nanotubes (MWCNTs) on the strength development of cementitious materials," *Journal of Materials Research and Technology*, vol. 8, no. 1, pp. 1203–1211, 2019.

[22] A. B. H. Bejaxhin, G. Paulraj, and M. Prabhakar, "Inspection of casting defects and grain boundary strengthening on stressed Al6061 specimen by NDT method and SEM micrographs," *Journal of Materials Research and Technology*, vol. 8, no. 3, pp. 2674–2684, 2019.

[23] C. M. Kansal and R. Goyal, "Analyzing mechanical properties of concrete with nano silica, silica fume and steel slag," *Materials Today: Proceedings*, vol. 45, no. 6, pp. 4520–4525, 2021.

[24] H. Y. Leung, J. Kim, A. Nadeem, J. Jaganathan, and M. P. Anwar, "Sorptivity of self-compacting concrete containing fly ash and silica fume," *Construction and Building Materials*, vol. 113, pp. 369–375, 2016.

[25] A. B. H. Bejaxhin and G. Paulraj, "Experimental investigation of vibration intensities of CNC machining centre by microphone signals with the effect of TiN/epoxy coated tool holder," *Journal of Mechanical Science and Technology*, vol. 33, no. 3, pp. 1321–1331, 2019.

[26] A. S. Rassokhin, A. N. Ponomarev, and O. L. Figovsky, "Silica fumes of different types for high-performance fine-grained concrete," *Magazine of Civil Engineering*, vol. 2, pp. 151–160, 2018.

[27] Y. Lin, J. Yan, Z. Wang, F. Fan, and C. Zou, "Effect of silica fumes on fluidity of UHPC: experiments, influence mechanism and evaluation methods," *Construction and Building Materials*, vol. 210, pp. 451–460, 2019.

[28] Y. Devarajan, D. B. Munuswamy, B. T. Nalla, G. Choubey, R. Mishra, and S. Vellaiyan, "Experimental analysis of Sterculia foetida biodiesel and butanol blends as a renewable and eco-friendly fuel," *Industrial Crops and Products*, vol. 178, p. 114612, 2022.

[29] S. M. M. Karein, A. A. Ramezanianpour, T. Ebadi, S. Isapour, and M. Karakouzian, "A new approach for application of silica fume in concrete: wet granulation," *Construction and Building Materials*, vol. 157, pp. 573–581, 2017.

[30] V. Gayatri, N. Bhanu Teja, D. K. Sharma, J. Thangaraja, and Y. Devarjan, "Production of biodiesel from phoenix sylvestris oil: Process optimisation technique," *Sustainable Chemistry and Pharmacy*, vol. 26, p. 100636, 2022.

Hindawi
Journal of Nanomaterials
Volume 2022, Article ID 4994658, 7 pages
https://doi.org/10.1155/2022/4994658

Research Article

Effect of Fiber Mixing and Nanoclay on the Mechanical Properties of Biodegradable Natural Fiber-Based Nanocomposites

Razan A. Alshgari,[1] K. Sargunan,[2] C. Selin Ravi Kumar,[3] M. V. Vinayagam,[4] J. Madhusudhanan,[5] S. Sivakumar,[6] Saikh Mohammad Wabaidur,[1] M. A. Islam,[7] and G. Ramasubramanian[8]

[1]*Chemistry Department, College of Science, King Saud University, Riyadh 11451, Saudi Arabia*
[2]*Department of Civil Engineering, Vidya Academy of Science & Technology Technical Campus, Kilimanoor, Kerala 695602, India*
[3]*Department of Civil Engineering, Malla Reddy Engineering College (Autonomous), Hyderabad, Telangana 500100, India*
[4]*Department of Mechanical Engineering, Sree Krishna College of Engineering, Vellore, Tamil Nadu, India*
[5]*Department of Biotechnology, Anand Institute of Higher Technology, Kazhipattur, Tamil Nadu 603103, India*
[6]*Department of Civil Engineering, PSNA College of Engineering and Technology, Dindigul, Tamil Nadu 624622, India*
[7]*Faculty of Biology, University of Manchester, UK*
[8]*Department of Chemistry, Seenu Atoll School, Maldives*

Correspondence should be addressed to G. Ramasubramanian; raman@satollschool.edu.mv

Received 20 May 2022; Revised 17 July 2022; Accepted 30 July 2022; Published 7 September 2022

Academic Editor: Ram Prasad

Combining two types of fibers may aid in improving the fundamental properties of organic fiber-reinforced hybrid polymeric materials. Biomaterials created from raw materials are gaining appeal in the industrial sector due to their high quality, as well as sustainability and environmental considerations. Natural fiber-reinforced hybrid nanocomposites were created in this work using a compression moulding technique with wood particles, hemp fiber, polypropylene, and montmorillonite nanoclay. Following that, the impacts of fiber mixture and vermiculite on mechanical and compostable qualities were studied. Both the coir and the hemp fibers were alkali-treated to minimize their hydrophilic nature before even being employed. Using universal tensile testing equipment, the mechanical characteristics of the prepared composites were investigated and found to be improved following fiber blending and nanoparticle inclusion. The maximum strength was occurred at the combinations like 10 wt. % of wood particle, hemp, nanoclay, and 70% of polypropylene matrix. Scanning electron microscopy showed that nanoclay significantly increased the adherence and interoperability between fiber and the polymer matrices. The good biocompatibility and water absorption capabilities of the nanocomposite were increased by mixing fibers, but nanoparticle additions seemed to have the opposite impact.

1. Introduction

Agricultural leftovers that are plentiful and present difficulties when processed have recently been the topic of investigation due to growing awareness of environmental concerns. Field crop leftovers are frequently generated in billions of tonnes and are cheap; though solitary, a minor percentage of the waste is used as domestic petroleum or nourishment, while the majority is charred in the turf, polluting both the air and the environment. The challenge might be solved by using these leftovers as reinforcement material in polymer composites. It will also increase the value of the agrifood stream restraint. Fabric-based polymer matrix composites have lately been enough to substitute high strength concrete in the building and construction industry. Natural fibers are replacing traditional synthetic materials as reinforcing agents because of their nonpollutant, anticorrosiveness, good mechanical properties, light

Table 1: Natural fibers and their mechanical properties.

Fibers	Density (g/cm^3)	Tensile strength (MPa)	Young's modulus (GPa)	Elongation at break (%)
Abaca	1.5	980	—	—
Banana	1.35	355	33.8	5.3
Coir	1.25	220	6	15-25
Cotton	1.51	400	12	3-10
Flax	1.4	800-1500	60-80	1.2-1.6
Hemp	1.48	550-900	70	1.6
Jute	1.46	400-800	10-30	1.8
Kenaf (bast)	1.2	295	—	2.7-6.9
Pineapple	1.5	170	82	1-3
Ramie	1.5	500	44	2
Sisal	1.33	600-700	38	2-3

Figure 1: Abstraction of cannabis fiber from cannabis shrub.

weight, low price, recyclability, and good biocompatibility, as well as their good ecological effects [1, 2]. The use of renewable resources in polymeric composites may aid in reducing CO_2 emissions from plastic burning. Despite its usefulness, organic fiber-based composite materials have lesser elasticity, tensile strength, durability, and water resistance than artificial fiber-based composite materials. To address these challenges, natural materials might be combined with a tougher inorganic or organic fiber in polymer matrices. This will result in hybrid composites that make better use of the best attributes of the components, resulting in an optimal, superior, and more cost-effective combination [3]. Manufacturers may customize composites using organic fiber-reinforced hybrid polymeric materials at a cheap cost, which is not possible with binary mixtures of one fiber and one filler spread in the matrices [4]. Organic cellulosic fibers are reusable, nonabrasive, have good mechanical qualities, and are ecologically benign, making them desirable in engineering disciplines including automobiles and construction. Wood, jute, ramie, and hemp, out of all natural materials, have the greatest opportunity as hybrid composite reinforcement across the globe [5]. Due to its light weight, specific strength, biodegradability, simple accessibility, recyclability, and low price, wood fiber has achieved tremendous popularity as a filler in polymeric materials. Wood-reinforced polymers of various kinds have previously been developed and marketed [6]. The inclusion of wood fiber increased the elasticity, rigidity, toughness, durability, and flame retardancy of the polymers [7]. Hemp, on the other hand, is the toughest natural fiber since it is derived from the stem of the hemp plant. Cannabis is a millennia plant that is today regarded as one of the most environmentally friendly commercial

Table 2: Parameters and their constraints of nanocomposites.

Sample No.	Wood particle (wt. %)	Hemp (wt. %)	Nanoclay (wt. %)	Polypropylene matrix (wt. %)
1	30	0	0	70
2	0	30	0	70
3	15	15	0	70
4	15	0	15	70
5	0	15	15	70
6	10	10	10	70

materials. Herbs were sometimes mistakes to their resemblance to marijuana indica. Hemp could be grown in a wide range of climatic areas on a variety of extremely good, upgrading circumstances with such a wonderful yield even without agrochemicals, attaining elevations of 2-3 meters and a radius of 6-internal diameter. The cannabis seeds are regarded as a poor socioeconomic organic metabolic end due to its high hygroscopicity and tannin content. Processing techniques could result in better cannabis strands with an undigested surface of the fiber and more customization. Cannabis threads implanted in a lignocellulosic or phenolic foundation are produced into various architectural configurations [8, 9]. Cannabis fiber building has previously been extensively researched, resulting in useful, in-depth information being available in cultural canon. Hemp fibers are longer, stronger, and harder than other plant fabrics like silk, and they are also coarser; so, they are used in engineering fields. As a result, composites (airline sector, sporty products, etc.), structural and building materials, geotextiles,

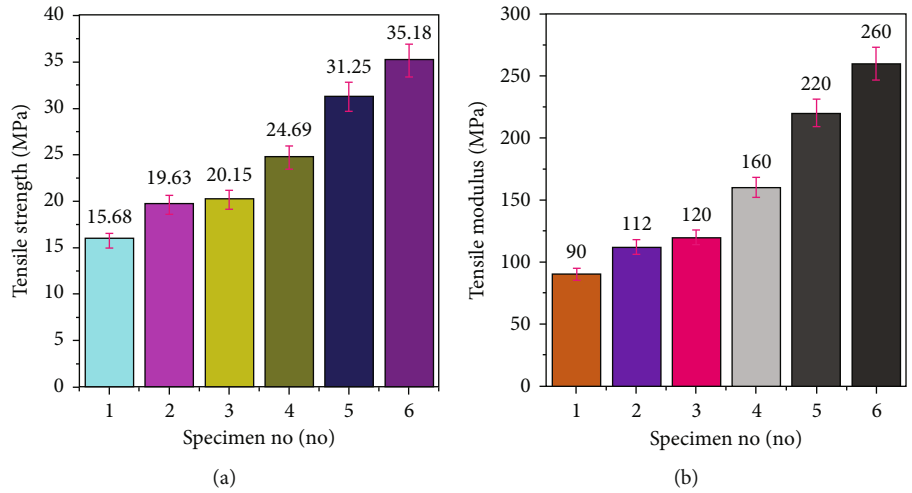

Figure 2: (a) Tensile strength. (b) Tensile modulus of nanohybrid composite.

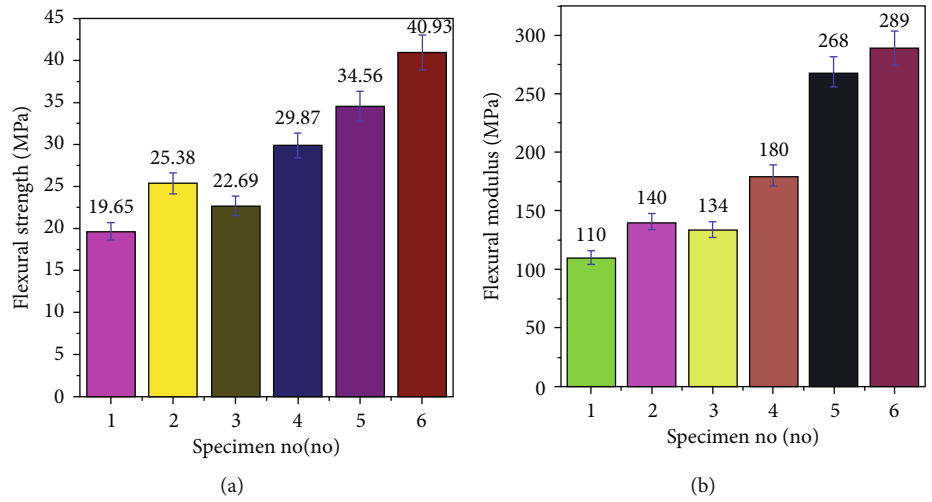

Figure 3: (a) Flexural strength. (b) Flexural modulus of nanohybrid composite.

and other uses account for nearly a quarter of the marijuana fibers utilized in commercial processes. Throughout their life span, hemp fibers exhibit a variety of forms, thicknesses, topologies, and characteristics. In comparison to other cellulosic fibers, this has a considerable lignin content, moderate cellulose content, and a large microfibril inclination, which results in poorer tension strength and increased elasticity. This chemical structure minimizes the product's reactivity with polymeric radical generated throughout manufacturing, as well as its serviceability [10, 11], and the mechanical possessions of different threads is revealed in Table 1.

Nanocomposites outperform conventional polymers in terms of weight, durability, and simplicity of processing [12]. Nanomaterials are made up of tiny components with the lowest single measurement in the nanometric variety (i.e., less than 100 nm) that permits them to fill a matrix more efficiently. The nanoparticles known as "nano clays" are made up of stacked crystalline silicon dioxide. The nanoclay seems to have a higher surface area and a porous structure, resulting in significant interface contact between the polymers and the nanofiller, enhancing the polymer characteristics dramatically. Because of their exceptional mechanical, visual, electronic, and fire reserve capabilities, nanocomposites supplemented using biological and chemical nanostructures have attracted a lot of interest [13, 14]. Nanocomposites are a new type of nanocrystalline hybridization material made up of biodegradable polymers with one or more inorganic nanoparticles. They constitute the nexus of nanotechnology, materials engineering, and biology [15]. The creation of nanocomposites with improved thermodynamic, physical, and multifunctional qualities has been pursued. Furthermore, biopolymer-based materials made using renewable technologies have demonstrated digestibility and biocompatibility in pharmaceuticals, packaged food, and agricultural applications. Numerous research have been directed on normal fabric-strengthened polymeric materials that have been hybridized with synthetic fiber [16, 17]. On the other hand, natural fiber hybrid nanocomposite and their combination with natural fibers and nanoclay, on the other hand, have received much interest. The primary purpose of this work was to determine how combining fiber types and adding nanoclay to wood/hem/nanoclay hybrid

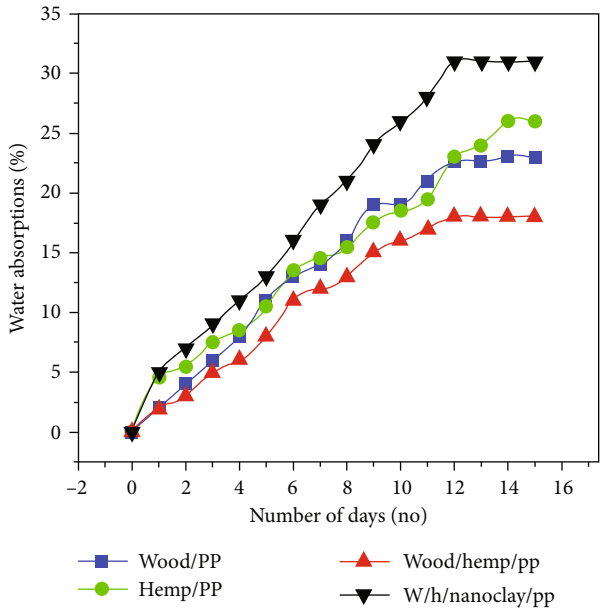

FIGURE 4: Water absorption behavior of wood/hemp/nanoclay/PP-based hybrid composites.

polypropylene biomaterials influenced their mechanical and biodegradable properties.

2. Resources and Techniques

2.1. Resources. In the composite system, wood fiber, hemp fiber, and nanoclay were employed as reinforcing fillers. Rithu Timber Industry in Madurai, Tamil Nadu, India, processed and gathered wood fiber. A GVR fiber factory in Madurai, Tamilnadu, India, processed and gathered hemp fiber. The nanoclay, sodium hydroxide, and polypropylene (PP) were provided by the Naga chemical company in Chennai, Tamilnadu, India. Figure 1 shows demonstrations of the subtraction procedure of hemp fiber from the hemp plant.

2.2. Alkaline Treatment. Unprocessed cannabis was washed in 2-3% scrubbing chemicals for 30 minutes at 50-60°C and disinfected with plain water before curing in an elevated furnace at around 80°C for 30 minutes, as stated. Washed threads became referred to as "raw threads." The threads are then disinfected via immersing them in a 2 : 1 combination of toluene and methanol for 60 to 78 h at 35°C, followed by a vigorous rinsing in 24 hours. Finally, the fibers were again engrossed in a 5 percent NaOH solvents at ambient conditions for 4 hours.

2.3. Fabrication of Hybrid Composites. Firstly, a stainless-steel mould with a size of 300 × 300 × 3 mm was refined. The matrix material was mixed well with the hardener to create a good matrix system. The compression moulding technique was used to construct the composite from wood/hemp/nanoclay combinations. By hand stirring with a glass rod, varying weight percents of nanoclay powder were disseminated in the produced polypropylene. This matrix mixture was scattered over the mould's layers of fibers. The combinations were warmed to 170°C inside the compression moulding machine for 15 minutes. The composite was chilled in the atmospheric air for numerous proceedings to avoid any contraction that may have occurred throughout the abstraction method. The parameters of the nanocomposites are listed in Table 2. That parameter provides better improvement with mechanical properties which was proved by the various researchers [15–17].

2.4. Testing of Hybrid Composites. For tension behavior, the produced laminate specimens were taken and converted to ASTM D 638-03 analogues and ASTM D-790 for bending behavior [7]. Morphological examinations of cracked laminate material were carried out using SEM. Prior to SEM analysis, the samples were being laved, desiccated, and then chemically covered using tens of nanometers of golden to improve the ionic properties of the mixtures. The models were dehydrated for 1 hour at 70°C in a microwave and then cooled to a consistent weight in the outdoors. Following that, the composite samples were submerged in purified water for 10 days, as per ASTM D570 [18]. Each and every day, the models were detached from the aquatic, cleaned with tissue paper, reweighed and quantified, and then returned to the liquid. The below formula was used to compute the water uptake rates in Equation (1).

$$\text{Moisture absorption} = \left(\frac{W_2 - W_1}{W_1}\right) * 100. \quad (1)$$

W_2 is the heaviness of the model after immersing, and W_1 is the heaviness of the model before absorption. Each kind of sample was subjected to five experiments, with the average results provided.

3. Result and Discussion

3.1. Tensile Strength. The tension properties and tensile modulus of different nanocomposites are shown in Figures 2(a) and 2(b). As shown in the figure, the tensile strength and tensile modulus of the hemp and polypropylene composite and the wood and polypropylene composite were almost identical. This might be related to the fact that wood and hemp fibers have comparable cellulose content [18]. Owing to its increased hemi cellulose concentration, hemp fiber is much more hydrophilic than wood fiber, while polypropylene is hydrophobic by nature. As a consequence, the hydrophilic hemp/wood and the hydrophobic polypropylene did not adhere properly, leading to a reduction in tensile strength and tensile modulus. When hemp fiber was mixed with wood fiber in PP and nanoclay was added, hybrid composites outperformed wood/PP and hemp/PP composites in terms of tensile strength and modulus. It is thought that composite materials with hemp or wood have higher tensile characteristics than other compositions because of fiber/matrix bonding, resulting in an even and efficient stress distribution across fibers. In addition, once nanoclay was added, the hybrid composites had the highest tensile strength and modulus. The nanoclay improved the mechanical characteristics of the composites by increasing

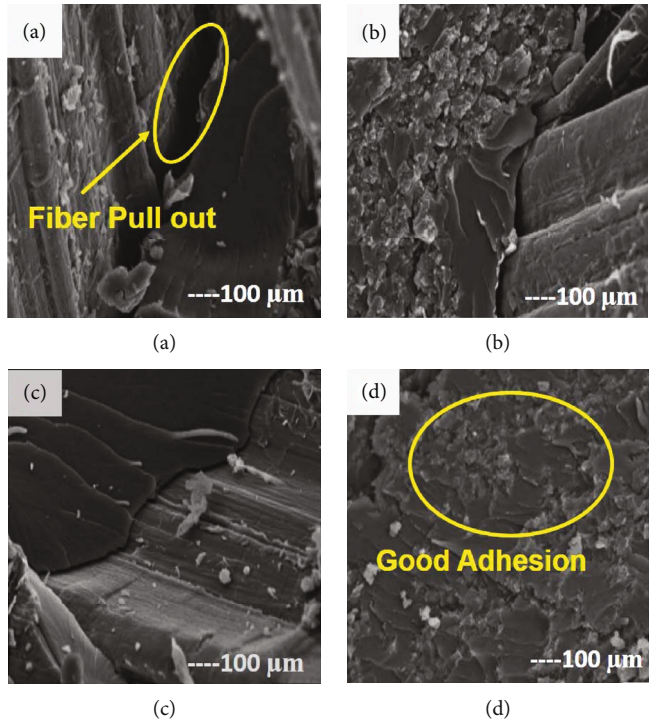

Figure 5: SEM image of (a) wood/PP, (b) hemp/PP, (c) wood/hemp/PP, and (d) wood/hemp/nanoclay/PP-based hybrid composite.

interfacial contact and adherence between both the fiber and the polymer matrices. A prior study had shown similar findings [19].

3.2. Flexural Strength. Flexural loading seems to be the most popular application rate of the deformation technique, which involves stretching a square sample to fracture or using a multiple point flexural evaluation technique. The maximal strain inside the substance at its yielding point is reflected in the flexural strength, and it is shown in Figures 3(a) and 3(b). It shows wood/PP composites, and the hemp/PP composites revealed the highest flexural strength. This result demonstrates that the adherence of hemp fiber was good compared to wood. Polypropylene composites' three-point bending strength increased with the addition of nanoclay. The addition of nanoclay increased the strength properties of the composite material, with a combination of wood/hemp/nanoclay/PP having the maximum bending strength value. The trends observed in the bending strength of the composite show the high surface area exhibited by the small filler particles, which improves the dispersion between the filler and the matrix and improves the interfacial bond [20, 21]. The SEM image discernibly shows the above trends. Polypropylene has brilliant adhesion to a variety of materials and can be further supported by adding fibers and particles. The outcomes show that hybrid nanoclay and wood/hemp/PP composites provide the finest consequences in both tensile and bending cases compared to other combinations.

3.3. Moisture Absorption Behavior. Figure 4 shows demonstrations of the moisture content levels of dissimilar composite materials. At the beginning, the rate of water updating for all composite materials was high, but this level has become almost consistent and reduced in the end phase. According to the findings, all the composite materials exhibit a high moisture uptake rate with the increased time durations. After the first day, moisture content ranged from 7 to 14%, and it climbed to 17 to 33% for various produced composites. The hybrid nanocomposites produced with nanoclay had the greatest percentage of water fascination of all the composite materials. This could be owing to the hybrid nanocomposite's enhanced hydrophilic character after fiber blending and nanoclay inclusion. In comparison to the other composites, the hemp/PP amalgamated had the maximum aquatic preoccupation standards. This is owing to the enormous number of OH groups found on the interfaces of hemp fibers. In the hemp/PP composites, the quantity of hydroxyl groups and microvoids increased, resulting in a significant increase in moisture fascination. The hybrid combination of wood and hemp, on the other hand, absorbed the least quantity of water. However, the accumulation of hydrophilic fillers to the hybrid nanocomposite occasioned in greater moisture absorption than the hybrid composite [15].

3.4. Fractography Analysis. The morphologies of nanomaterials were examined using SEM. Figure 5 presents the tension fracture boundaries of nanomaterials and hybridized nanofiber. The timber mixture as well as the hemp/PP mixture seemed to have the smoothest interfaces of all manufactured configurations, as illustrated in Figures 5(a) and 5(b), resulting in reduced material characteristics. The aspect of timber nanocomposites was equivalent to that of the timber

and hemp/PP hybrids, as can be seen in Figure 5(c). Because the energy spent was low, the intermediate connection between the fibers and resin was not really able to withstand fiber pull-out after collision [22]. The hybrid composite had a more flawless texture than the individual materials, as shown in Figure 5(d). The introduction of nanoclay to the hybrid mixture enhances the material characteristics of the bio-based nanomaterials by increasing interfacial interaction and superficial roughness.

4. Conclusion

The mechanical and water absorption evaluation of many wood, hemp, nanoclay, and polypropylene-based nanocomposites was identified, and the following conclusions were obtained. Wood/hemp/nanoclay/PP hybrid composites outperformed wood/PP, hemp/PP, and wood/hemp/PP composites in terms of tensile and flexural strength. This might clearly demonstrate how effectively the polymer matrix and fibers interact. The nanoclay filler advances hybrid composite mechanical strength by boosting adhesive bonding strength. This is immediately apparent in SEM analysis. The wood/hemp/PP combination absorbs the most water when compared to other combinations. Nanoclay addition, on the other hand, has the opposite effect on these characteristics.

Data Availability

The data used to support the findings of this study are included within the article. Further data or information is available from the corresponding author upon request.

Conflicts of Interest

The authors state that the publishing of this paper does not include any conflicts of interest.

Acknowledgments

The authors appreciate the supports from Seenu Atoll School, Maldives, for the research and preparation of the manuscript. The authors thank the University of Manchester, Vidya Academy of Science & Technology Technical Campus, Malla Reddy Engineering College, PSNA College of Engineering and Technology for providing assistance in this work. This work was funded by the Researchers Supporting Project Number (RSP-2021/265), King Saud University, Riyadh, Saudi Arabia.

References

[1] M. N. M. Layth Mohammed, G. P. Ansari, M. Jawaid, and M. S. Islam, "A review on natural fiber reinforced polymer composite and its applications," *International Journal of Polymer Science*, vol. 2015, Article ID 243947, 15 pages, 2015.

[2] V. Mohanavel, S. Suresh Kumar, J. Vairamuthu, P. Ganeshan, and B. Nagaraja Ganesh, "Influence of stacking sequence and fiber content on the mechanical properties of natural and synthetic fibers reinforced penta-layered hybrid composites," *Journal of Natural Fibers*, pp. 1–13, 2021.

[3] A. K. Saravanan, A. Rajendra Prasad, D. Muruganandam, G. Saravanan, S. Vivekanandan, and M. Sudhakar, "Study on natural fiber composites of jute, pine apple and banana compositions percentage of weight basis for thermal resistance and thermal conductivity," *Materials Today: Proceedings*, vol. 37, no. 2, pp. 147–151, 2021.

[4] D. Logendran, K. Gurusami, M. C. Anand Chakaravarthi, G. Puthilibai, M. Suresh, and M. Sudhakar, "Experimental research on glass fibres / caustic soda treated banana fibers hybrid composite," *Materials Today: Proceedings*, vol. 33, no. 7, pp. 4408–4411, 2020.

[5] L. Karikalan, M. Chandrasekran, S. Ramasubramanian, and S. Baskar, "Hybridization of composites using natural and synthetic fibers for automotive application," *International Journal of Scientific Research in Science and Technology*, vol. 3, no. 7, pp. 916–920.

[6] V. Ganesan, V. Shanmugam, B. Kaliyamoorthy et al., "Optimisation of mechanical properties in saw-dust/woven-jute fibre/polyester structural composites under liquid nitrogen environment using response surface methodology," *Polymers (Basel).*, vol. 13, no. 15, p. 2471, 2021.

[7] M. Boopalan, M. Niranjanaa, and M. J. Umapathy, "Study on the mechanical properties and thermal properties of jute and banana fiber reinforced epoxy hybrid composites," *Composites. Part B, Engineering*, vol. 51, pp. 54–57, 2013.

[8] G. Velmurugan, K. Babu, L. I. Flavia, C. S. Stephy, and M. Hariharan, "Utilization of grey Taguchi method to optimize the mechanical properties of hemp and coconut shell powder hybrid composites under liquid nitrogen conditions," *IOP Conf. Ser. Mater. Sci. Eng.*, vol. 923, no. 1, p. 012045, 2020.

[9] G. Velmurugan, T. Shaafi, and M. S. Bhagavathi, "Evaluate the tensile, flexural and impact strength of hemp and flax based hybrid composites under cryogenic environment," *Mater. Today Proc.*, vol. 50, pp. 1326–1332, 2022.

[10] X. Li, L. G. Tabil, and S. Panigrahi, "Chemical treatments of natural fiber for use in natural fiber-reinforced composites: a review," *Journal of Polymers and the Environment*, vol. 15, no. 1, pp. 25–33, 2007.

[11] F. Tanasă, M. Zănoagă, C. A. Teacă, M. Nechifor, and A. Shahzad, "Modified hemp fibers intended for fiber-reinforced polymer composites used in structural applications—a review. I. Methods of modification," *Polymer Composites*, vol. 41, no. 1, pp. 5–31, 2020.

[12] A. Sreenivasulu, S. Rajkumar, S. Sathyanarayana, S. S. Kumar, G. V. Gaurav, and B. D. I. Premkumar, "Impact of nano-filler WC on the fracture strength of epoxy resin," *Materials Today: Proceedings*, vol. 59, no. 2, pp. 1420–1424, 2022.

[13] N. E. Zafeiropoulos, C. A. Baillie, and J. M. Hodgkinson, "Engineering and characterisation of the interface in flax fibre/polypropylene composite materials. Part II. The effect of surface treatments on the interface," *Composites. Part A, Applied Science and Manufacturing*, vol. 33, no. 9, pp. 1185–1190, 2002.

[14] M. S. Ravi Theja, P. Ramshankar, M. C. Sashikkumar et al., "Investigation into mechanical properties of EPDM/SBR-nanoclay nanocomposites," *Materials Today: Proceedings*, vol. 59, pp. 1508–1512, 2022.

[15] N. A. Rahman, A. Hassan, R. Yahya, R. A. Lafia-Araga, and P. R. Hornsby, "Polypropylene/glass fiber/nanoclay hybrid composites: morphological, thermal, dynamic mechanical

and impact behaviors," *Journal of Reinforced Plastics and Composites*, vol. 31, no. 18, pp. 1247–1257, 2012.

[16] K. Majeed, M. Jawaid, A. Hassan et al., "Potential materials for food packaging from nanoclay/natural fibres filled hybrid composites," *Materials and Design*, vol. 46, pp. 391–410, 2013.

[17] E. M. Fernandes, R. A. Pires, J. F. Mano, and R. L. Reis, "Bio-nanocomposites from lignocellulosic resources: properties, applications and future trends for their use in the biomedical field," *Progress in Polymer Science*, vol. 38, no. 10-11, pp. 1415–1441, 2013.

[18] V. Ganesan and B. Kaliyamoorthy, "Utilization of Taguchi Technique to Enhance the Interlaminar Shear Strength of Wood Dust Filled Woven Jute Fiber Reinforced Polyester Composites in Cryogenic Environment," *Journal of Natural Fibers*, vol. 19, no. 6, pp. 1–12, 2022.

[19] M. Saiful Islam, S. Hamdan, I. Jusoh, M. Rezaur Rahman, and A. S. Ahmed, "The effect of alkali pretreatment on mechanical and morphological properties of tropical wood polymer composites," *Materials and Design*, vol. 33, pp. 419–424, 2012.

[20] G. Velmurugan and K. Babu, "Statistical analysis of mechanical properties of wood dust filled jute fiber based hybrid composites under cryogenic atmosphere using Grey-Taguchi method," *Materials Research express.*, vol. 7, no. 6, 2020.

[21] F. Sarker, P. Potluri, S. Afroj, V. Koncherry, K. S. Novoselov, and N. Karim, "Ultrahigh performance of nanoengineered graphene-based natural jute fiber composites," *ACS Applied Materials & Interfaces*, vol. 11, no. 23, pp. 21166–21176, 2019.

[22] X. Wang, H. Sun, H. Bai, and L. P. Zhang, "Thermal, mechanical, and degradation properties of nanocomposites prepared using lignin-cellulose nanofibers and poly (lactic acid)," *BioResources*, vol. 9, no. 2, pp. 3211–3224, 2014.

International Journal on Interactive Design and Manufacturing (IJIDeM)
https://doi.org/10.1007/s12008-022-00907-z

ORIGINAL PAPER

Applying ANN – PSO algorithm to maximize the compressive strength and split tensile strength of blended self curing concrete on the impact of supplementary cementitious materials

C. Vivek Kumar[1] · K. Sargunan[2] · J. S. S. K. Vasa[2] · V. Praveen Jesuraj[3] · A. Punitha[4] · R. Karthikeyan[5]

Received: 8 April 2022 / Accepted: 25 April 2022

Abstract
This study was intended to get the optimized Compressive strength and split tensile strength of Blended Self CuringConcrete(BSCC) on the impact of Supplementary Cementitious Materials (SCM's). The experiments were conducted by varying the quantity of Cement, Flyash, Ground Granulated Blast Furnace Slag (GGBFS), Silica Fume and Slump with fixed quantity of Fine aggregate, Coarse aggregate, S.P and Water. Totally 13 different mix proportions were prepared and tested for Compressive Strength (CS) and Split Tensile Strength (STS). Both strengths were calculated for 7, 14 and 28 days. To optimize the compressive strength and split tensile strength, a feed forward Artificial Neural Network (ANN) model was developed, and Particle Swarm Optimization (PSO) algorithm was used by optimizing the weighing factors of the network in the neural power software. Finally, with a root mean square error of 0.008223, 0.006559, and 0.009743 for CS and 0.008905, 0.006999, and 0.008745 for STS, the model was obtained for 7, 14, and 28 days. The percentage contribution of input parameters is also discussed separately for compressive strength and split tensile strength of 7, 14 and 28 days of curing. Finally, the optimized compressive strength and split tensile strength were found to be 42.3552 N/mm^2 and 4.3113 N/mm^2 respectively for 28 days.
.

Keywords Blended self curing concrete · Cementitious materials · ANN · PSO

1 Introduction

Blended cement concrete is a mixture of cement replaced with supplementary cementitious materials with different proportioning mixes based upon the utility of concrete. SCMs like fly ash (FA), silica fume (SF), metakaolin (MK), bentonite, and ground granulated blast-furnace slag (GGBFS) were used to replace cement up to 60% without the need of alkaline solution in the investigation done by Halit Yazıcı [1]. Due to this SCMs the rheological, durability, and mechanical qualities of concrete can be enhanced by adding up to 40% mineral additive to the mixture and keeps costs down by reducing the amount of cement used in the concrete. Utilising pozzolanic materials and transforming them into useful materials can help conserve the environment while also assisting in the development of high-performance concrete thorough the literature on unary, binary, and triple blended pozzolans which was employed as concrete replacements explained by Athiyamaan [2].

Ternary blended concrete reveals the addition of several pozzolanic materials to the concrete, including cement acting as the primary binding agent. Metakaolin as well as fly ash from power stations are both important ingredients for modern concrete. Increasing the use of SCMs including such fly ash, silica fume, GGBFS, rice husk ash, and metakaolin during concrete production, precedes to the idea of blended cements and concretes. By reorienting the mix design parameters for enhanced structural characteristics of concrete, with an emphasis on regulating OPC content while increasing

✉ C. Vivek Kumar
vivekkumarcr@gmail.com

1 Civil Engineering, Gokaraju Rangaraju Institute of Engineering and Technology, Hyderabad, India

2 Civil Engineering, Malla Reddy Engineering College, Hyderabad, India

3 Civil Engineering, SSM Institute of Engineering and Technology, Dindigul, India

4 Computer Science & Engineering, Annamalai University, Chidambaram, India

5 Mechanical Engineering, Gokaraju Rangaraju Institute of Engineering and Technology, Hyderabad, India

Published online: 13 June 2022

the overall cementitious material and limiting water content while obtaining chemical admixture for improved workability and compensating concerted hydration using SCMs. Due to the intensified utilization of performance built concrete, concrete incorporating self-curing agents could mean a new range of trend in construction throughout the modern era. For the inclusion of internal or self-curing water in concrete, newer techniques can also be used.

Most researchers suggested using saturated aggregates to perform internal concrete curing using polyethylene glycol PEG 400 mostly as self-curing agent for concrete mixes. Supplementary Cementitious Materials (SCMs) such as Flyash, Ground Granulated Furnace Slag, and Silica Fume improve the stiffness, ductility, and load bearing capability of concrete structures while reducing crack strengthening and dissemination. Thus according to the cement composite philosophy, a new composite material has high structural implementation and exceptional economic advantages can be produced by combining positive synergy with different admixtures. Suryawanshi et al. [3] investigated the incorporation of mineral admixtures to cement concrete enhances the amount of water required for curing, and this requirement can be much higher than those in ordinary Portland cement concrete mixes. Chemical shrinkage happens when there is water shortage for hydration also because inner relative humidity decreases.The key property of hardened concrete, durability, is profoundly affected by curing as it has a significant impact upon its hydration of Portland cement.

Using soft computing techniques, Feizbakhsh et al. [4] investigated the prediction model of compressive strength of self–compacting concrete (SCC). Adaptive neuro–based fuzzy inference method (ANFIS), artificial neural network (ANN), and PSOPC–ANFIS, a combination of particle swarm optimization with passive congregation (PSOPC) and ANFIS, are among the techniques used. Khademi et al. [5] developed three different models of multiple linear regression (MLR), artificial neural network (ANN), and adaptive neuro-fuzzy inference system (ANFIS), trained, and tested in the MATLAB programming environment for forecasting the 28-day compressive strength of concrete for 173 different mix designs, based upon the experimental results. Numerous regression, neural networks (NNT), and ANFIS models are developed, trained, and tested using concrete constituents as input variables in determining the 28-day compressive strength of no-slump concrete (28-CSNSC) by Sohbani et al. [6]. When the results are compared, perhaps the NNT and ANFIS models are more capable of predicting the 28-CSNSC than the conventional regression models suggested.

Nikoo et al. [7] studied about numerous experimental data patterns were used to build models from observations of cylindrical concrete components with different aspects. Uysal [8] researched the forecasting of the loss in compressive strength of SCC, an artificial neural network (ANN) model based specific formulation had been proposed, which would be defined in terms with cement, mineral additives, aggregates, heating degree, and with or without PP fibres and the analytical model developed with ANN appeared to have a strong prediction capability of CS. Ahmet Raif Boğaa [9] investigated concrete containing GGBFS and CNI, the effects of cure form and curing time were investigated along with compressive strength, splitting tensile strength, and chloride ion permeability were all tested extensively and formulated four-layered artificial neural network approach (ANN) and adaptive neuro-fuzzy inference system (ANFIS). Lingam et.al [10] developed Artificial Neural Networks (ANN) to forecast the compressive strength of HPC comprising binary and quaternary blended mixes. Gulbandilar et al. [11] formulated the prediction models for flexural strength of cement mortars were created using Artificial Neural Networks (ANN) and Adaptive Network-based Fuzzy Inference Systems (ANFIS)with four input parameters Portland cement, GGBFS, WTRP, and sample age and one output parameter flexural strength of cement mortars.

2 Materials and methods

In this investigation, the self curing blended concrete was planned to prepare with the following ingredients such as Cement, Fly ash, Ground Granulated Blast Furnace Slag, Silica Fume, Fine Aggregate, Coarse Aggregate, S.P, Water and Slump. To prepare the SCBC, different quantities of cement, fly ash, ground granulated blast furnace, silica fume, and slump were maintained, while the remainder of the materials were kept constant. Table 1 shows the proportioning of standard self-curing concrete of M30 grade, while Table 2 shows the various mix proportions of Blended Self Curing Concrete for M30 Grade as per IS10262:2019 [12] codal provisions. It should be noted that the slump was measured from the bottom of the mould. Finally compressive and split tensile strength tests were performed on the specimens for seven, fourteen, and twenty-eight days of curing.

From the literature, the factors which are having considerable influence on the performance of Compressive Strength and Split tensile Strength for 7, 14 and 28 dayswere identified. They are (i) Cement (kg/m^3), Fly Ash (kg/m^3) (iii) GGBFS (kg/m^3) and (iv) Silica Fume (kg/m^3) and these factors were controlled during mixing process. A series of trial experiments were undertaken to determine the functional range of the supplementary Cementitious Materials (SCM's). Totally 13 different combinations was mentioned as M1 to M13 in Table 2 of BSCC specimens in Cube and Cylindrical forms were prepared. Each cube mould of the size is 150 × 150 × 150 mm for CS and STS with cylinder 150 mm in diameter and 300 mm long. For each blended mix, in a fresh state, the slump value (in mm) and for a hardened state, the strength

Table 1 Proportioning of Standard Self Cured mix for M30 Concrete (unit expressed as kg/m^3)

Materials	Cement	Fine Aggregate	Coarse Aggregate	PEG 400	Water	Water-Cement Ratio
Quantity	350	744.3	1314.2	2.28	175	0.4

Table 2 Mix proportions of Blended Self Curing Concrete for M30 Grade

Mix	Cement	FlyAsh	GGBFS	SF	Fine Agg	Coarse.Agg	S.P	Water	Slump (mm)
Quantity in kg/m^3									
M1	350	0	0	0	744.3	1314.2	3.5	140	244
M2	227.5	87.5	35	0	744.3	1314.2	3.5	140	255
M3	227.5	0	87.5	35	744.3	1314.2	3.5	140	255
M4	227.5	87.5	0	35	744.3	1314.2	3.5	140	256
M5	227.5	70	52.5	0	744.3	1314.2	3.5	140	251
M6	227.5	0	70	52.5	744.3	1314.2	3.5	140	251
M7	227.5	70	0	52.5	744.3	1314.2	3.5	140	254
M8	227.5	35	0	87.5	744.3	1314.2	3.5	140	252
M9	227.5	35	87.5	0	744.3	1314.2	3.5	140	255
M10	227.5	0	35	87.5	744.3	1314.2	3.5	140	252
M11	227.5	70	0	52.5	744.3	1314.2	3.5	140	248
M12	227.5	70	52	0	744.3	1314.2	3.5	140	251
M13	227.5	70	0	52.5	744.3	1314.2	3.5	140	253

parameters were calculated and noted down. Finally, the characteristic compressive strength and split tensile strength was calculated by using formula shown in Eqs. (1)and (2) [13] respectively.

$$\mathrm{CS}\left(\frac{\mathrm{N}}{\mathrm{mm}^2}\right) = \frac{\mathrm{AppliedLoad\ overCubeSpecimen}}{\mathrm{CrossSectionalArea}} \tag{1}$$

$$\mathrm{STS}\left(\frac{\mathrm{N}}{\mathrm{mm}^2}\right) = \frac{2^{*}\mathrm{AppliedLoad\ over\ Cylindrical\ Specimen}}{\pi\ ^{*}\mathrm{diameter\ of\ cylinder}^{*}\mathrm{length\ of\ cylinder}} \tag{2}$$

The calculated (experimental) values of compressive strength and split tensile strength for BSCC are displayed in the Table 3 for 7, 14 and 28 days. Figs. 1 and 2 show specimens in Cube and Cylindrical forms of BSCC, whereas Figs. 3 and 4 are the tested specimens of compressive strength and split tensile strength respectively.

3 Developing a model and an optimization

In this investigation, it was planned to optimize the characteristic compressive strength and split tensile strengthfor 7, 14 and 28 days of Blended SCC using SCMs and finding the optimized process parameters after the model was created. Here, the model was created by Artificial Neural Network (ANN) and the model was optimized by Particle Swarm Optimization (PSA) algorithm. The role played by ANN and PSO in the field of modeling and optimization is discussed below. Figure 5 illustrates the integrated attempt of artificial neural network and particle swarm optimization algorithm.

3.1 Artificial neural network

The ANN methodology outperforms all other model, including linear and exponential regression. Many researchers have supported the use of ANN as a forecasting model because of its exceptional learning algorithm and balancing of input and output associations, including for non-linear and complicated systems [15, 16]. According to Ebrahimpour et al. [17], the ANN methodology has tremendous modelling potential due to its ability to identify the relationships at the core of complex systems. HadiMashhadban et al. [18] investigated whether a neural network could be designed to perform a specific role by changing the values of the connections (weights) between the components. Tavakoli et al. [19] explored into the use of artificial neural networks (ANN) to forecast the mechanical properties and energy dissipation capacity of fibre reinforced self-compacting concrete. They mentioned that now the ANN outcomes are really like the experimental information. To train the data, ANN uses various learning algorithms such as "Fast Propagation," "Batch Back

Table 3 Experimental Results of various Mix Proportions of Blended Self Curing Concrete

Mix	Compressive Strength (N/mm^2)			Split Tensile Strength (N/mm^2)		
	7 days	14 days	28 days	7 days	14 days	28 days
M1	12.48	20.15	31.21	1.34	2.1	3.4
M2	16.04	26.67	41.12	1.48	3.11	4.21
M3	16.79	25.6	38.16	1.54	3	4.18
M4	15.52	25.89	37.85	1.47	2.99	4.13
M5	13.06	24.52	35.21	1.42	2.6	4.03
M6	13.97	22.52	36.76	1.39	2.48	4.1
M7	14.03	20.78	35.07	1.35	2.56	4.19
M8	13.36	21.42	34.25	1.47	2.49	3.94
M9	14.08	20.76	33.53	1.49	2.44	3.91
M10	14.64	23.78	34.86	1.45	2.5	3.86
M11	15.97	25.29	38.95	1.33	2.24	3.54
M12	15.17	23.9	35.29	1.29	2.19	3.68
M13	14.25	21.19	33.93	1.3	2.28	3.79

Fig. 1 Cubical test specimens for compressive strength

Fig. 2 Cylindrical test specimens for split tensile strength

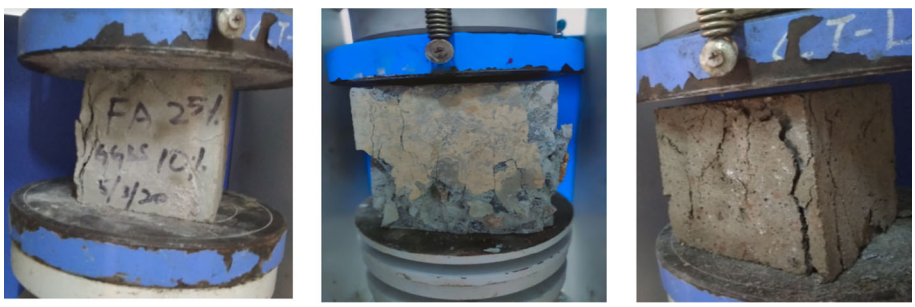

Fig. 3 Cubical tested specimens for compressive strength

Fig. 4 Cylindrical tested specimens for split tensile strength

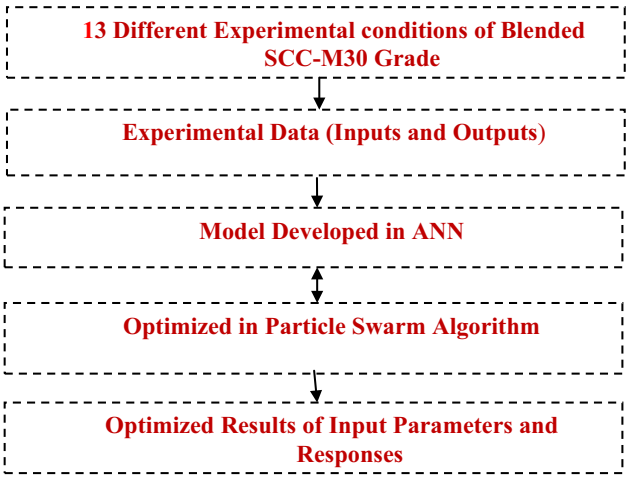

Fig. 5 Flow Chart of Hybrid ANN—PSO [14]

Propagation," "Incremental Back Propagation," and "Levenberg Marquadt." Nonlinear transfer functions such as Linear, Threshold Linear, Bipolar Linear, Gaussian, Tanh, and sigmoid are also included [20].This investigation's programme supports two separate link types: "multilayer regular feed forward" and "multilayer full feed forward." The RMSE divergence was used as a deciding factor as to when to stop training [21].

3.2 Particle swarm optimization

The PSO is a population-based optimization algorithm invented by Eberhart and Kennedy in 1995 and inspired by social behaviour such as bird flocking or fish schooling. In PSO, each particle in dimensional solution space is treated as an individual even amongst the population. The velocity and position of each particle are randomly chosen, and the very first position of each particle is determined using the target functions [22]. Then, amongst these results generated by all particles throughout the populations, gbest is found. The pbest particle is fixed which is based on the gbest. The pbest particle is assigned a velocity and a new population is formed, defining the new (second) position among all particles. Then gbest is discovered among the outcomes of the newly formed population, which is based on the most recent

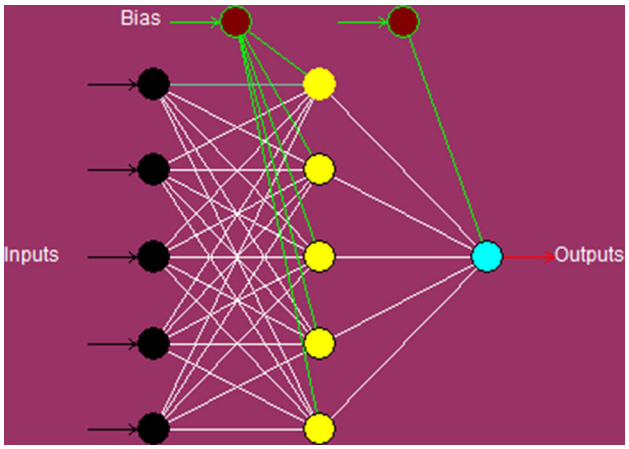

Fig. 6 Configuration of Three-Layered Neural Network

pbest particle. This process is repeated before the stop criterion, either the number of variables or no adjustments in the gbest value, take effect upon this algorithm.

3.3 Solutions of ANN & PSO

CPC-X Neural Power [20] was used to model and optimize the problem in this study. Engineering fields are also aware of the implementation of ANN and PSOA throughout the engineering world [23]. In ANN, the Levenberg Marquadt algorithm and multilayer normal feed forward propagation have been used as learning algorithm and connection type, meanwhile.Both the learning rate and the momentum were set to 0.8. For the hidden layer and output layer, the sigmoid transfer feature has been used. The sigmoid function was found to be the most used function by Muthupriya et al. [24]. There is no standard method for determining the number of neurons in the network's hidden layer; instead, trial and error can be used, which was investigated by Singh et.al [25] and Kennedy et al.[26].

According to Das et al. [27], the number of neurons in the hidden layer can be based on the number of input sources n, and the number of neurons in the hidden layer can vary between n, n/2, 2n, 2n + 1, and 2n + 2. Kutanaei et al. [28] investigated PSOA's ability to model the mechanical properties of fibre reinforced cement sand. Xuesong [29] explained the use of the PSO algorithm to solve the TSP and the experiment results show that the new algorithm is successful for this problem, despite the drawbacks of genetic algorithms such as being easily locked into a local optimum. The total number of hidden layer is 1 and node on the hidden layer is 5. Finally, the model was achieved with the root mean square error of 0.008223, 0.006559 and 0.009743 for CS and 0.008905, 0.006999 and 0.008745 for STS respectively for 7, 14 and 28 days. Figure 6 shows the model which was used in this investigation.

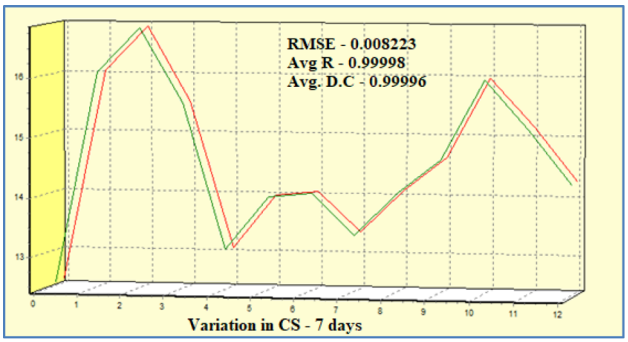

(a) ANN Model for CS – 7 days

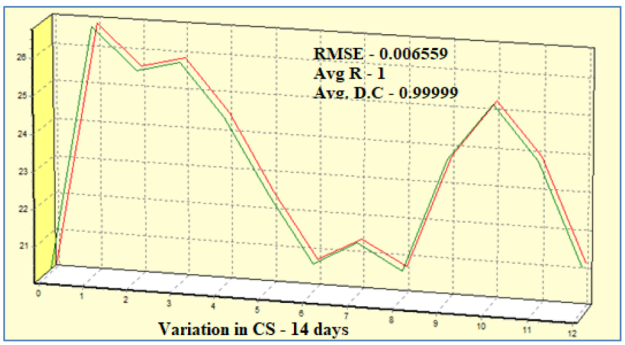

(b) ANN Model for CS – 14 days

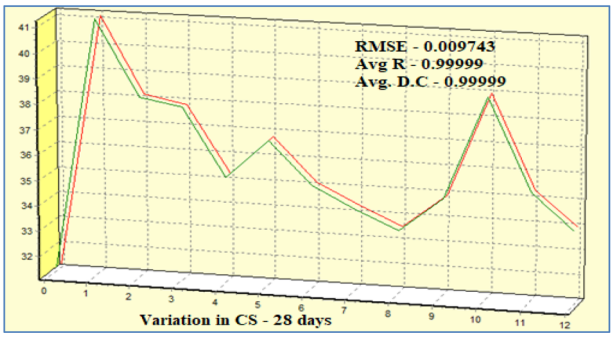

(c) ANN Model for CS – 28 days

Fig. 7 **a** ANN Model for CS—7 days. **b** ANN Model for CS—14 days. **c** ANN Model for CS—28 days

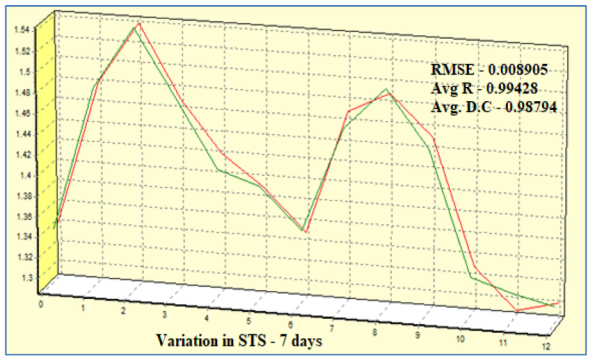

(a) ANN Model for STS – 7 days

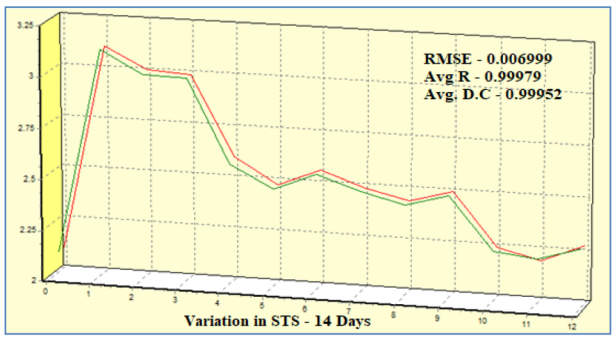

(b) ANN Model for STS – 14 days

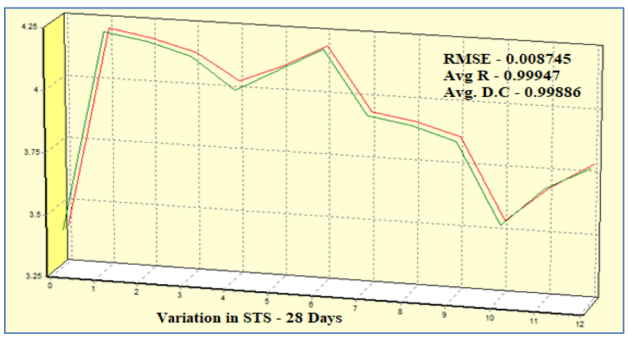

(c) ANN Model for STS – 28 days

Fig. 8 **a** ANN Model for STS—7 days. **b** ANN Model for STS—14 days. **c** ANN Model for STS—28 days

Figures 7(a) through (c) and 8(a) through (c) show the results of model created by ANN for CS and STS respectively, whereas Table 4 and 5 show the statistical significance of the model for CS and STS respectively.

To execute the optimization in PSO the following parameters were used [29]. The population size, inertia weight, learning factors such as cognitive factor (C1) and social factor (C2) are 10, 0.1, 2and 2 respectively. Finally, it was observed that the optimized values of Compressive strength are 17.3288, 27.4850 and 42.3553 N/mm^2 for 7, 14 and

Table 4 ANN Model's Statistical values of CS for different curing days

	7 Days	14 Days	28 Days
RMSE	0.008223	0.006559	0.009743
Avg R	0.99998	1	0.99999
Avg. D.C	0.99996	0.99999	0.99999

Table 5 ANN Model's Statistical values of STS for different curing days

	7 Days	14 Days	28 Days
RMSE	0.008905	0.006999	0.008745
Avg R	0.99428	0.99979	0.99947
Avg. D.C	0.98794	0.99952	0.99886

Table 6 Optimized CS and optimized input values for different curing days

	7 Days	14 Days	28 Days
Compressive strength (N/mm^2)	17.3288	27.4850	42.3553
Cement	240.96	290.0097	229.4345
Fly ash	40.6751	86.0072	87.3342
GGBFS	67.3086	38.7017	2.4941
Silica fume	6.4172	73.4944	1.3895
Slump	253.3402	252.2067	251.1089

Table 7 Optimized STS and optimized input values for different curing days

	7 Days	14 Days	28 Days
Split Tensile Strength (N/mm^2)	1.5713	3.2363	4.3113
Cement	304.3145	319.9055	284.9032
Flyash	66.0441	20.6085	61.2320
GGBFS	59.6020	80.7960	83.9702
Silica fume	33.3184	32.2040	54.7132
Slump	251.3592	254.1756	247.2356

28 days respectively. Moreover it was found that the optimized values of Split Tensile Strength are 1.5713, 3.2363 and 4.3113 N/mm^2 for 7, 14 and 28 days respectively. Table 6 and 7 show the optimized input parameters for compressive strength and split tensile strength respectively for different curing days.

Figures 9(a) through (c) and 10(a) through (c) show process parameters importance (%) for CS and STS respectively. Whereas Tables 8 and 9 show the importance of each input factor (%) on compressive strength and split tensile strength respectively for different curing days. From the Tables 8 and 9 it can be found that the importance of cement contribution is low irrespective of strength and number of curing days.

As the CS and STS are dependent on the quantity of GGBFS, fly ash, silica fume, and slump and the heat of hydration of concrete, the contribution of GGBFS, fly ash, silica fume, and slump vary in different curing periods (long term and early-age). The CS of concrete mixtures including GGBFS increases when the amount of GGBFS is increased [30]. The presence of GGBFS provides greater early strength, whereas fly ash provides greater strength after a long time of curing. Fly ash particles interact with free lime in the cement to obtain more cementitious material, which improves long-term strength [31]. The type and quantity of cementing material, the water content, the aggregate grading, the existence of entrained air, and using chemical admixtures have a significant impact on the fresh and hardened properties of fly ash-based concrete [32].

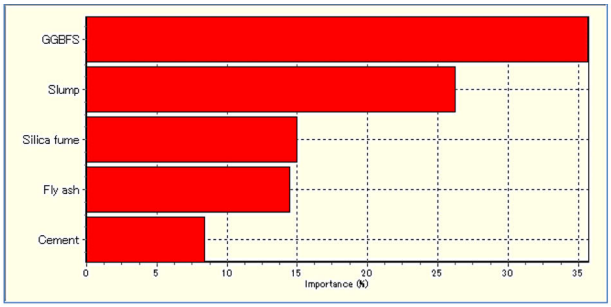

(a) Factors Importance (%) on CS – 7 days

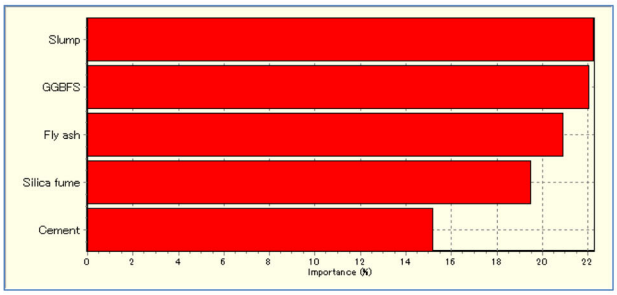

(b) Factors Importance (%) on CS – 14 days

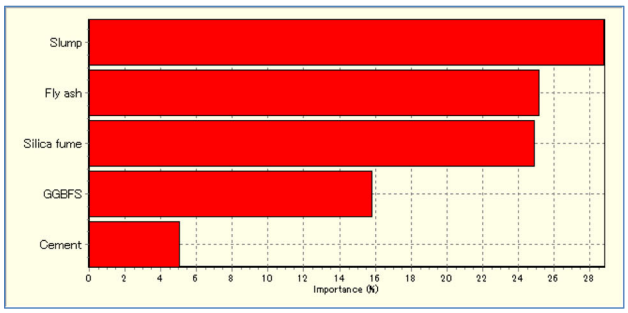

(c) Factors Importance (%) on CS – 28 days

Fig. 9 **a** Factors Importance (%) on CS—7 days. **b** Factors Importance (%) on CS—14 days. **c** Factors Importance (%) on CS—28 days

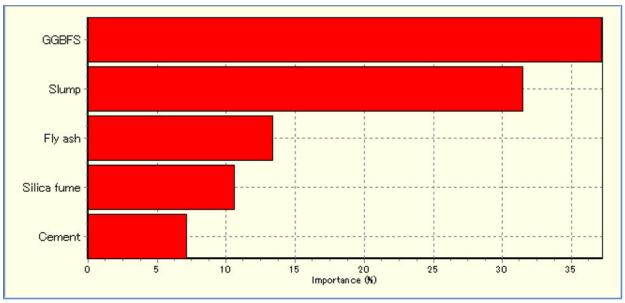

(a) Factors Importance (%) on STS – 7 days

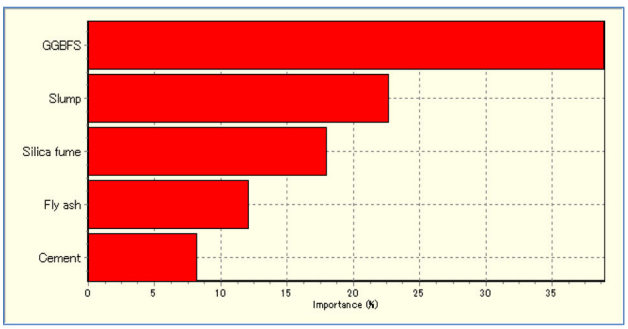

(b) Factors Importance (%) on STS – 14 days

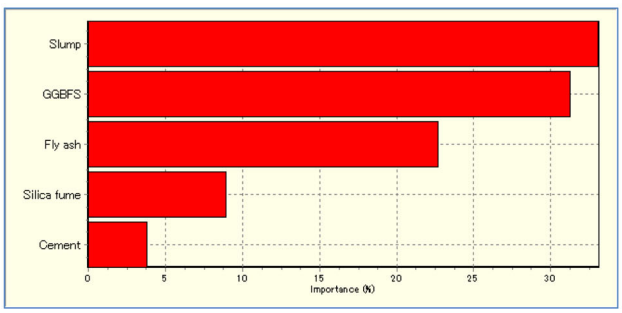

(c) Factors Importance (%) on STS – 28 days

Fig. 10 **a** Factors Importance (%) on STS—7 days. **b** Factors Importance (%) on STS—14 days. **c** Factors Importance (%) on STS—28 days

4 Conclusions

- The self-curing blended concrete was prepared with the following ingredients such as Cement, Fly ash, Ground Granulated Blast Furnace Slag, Silica Fume, Fine Aggregate, Coarse Aggregate, S.P, Water and Slump.
- Cement, Fly ash, Ground Granulated Blast Furnace, Silica Fume and Slump were maintained with different proportions and the rest of the ingredients were fixed constant.
- The compressive strength and split tensile strength tests were conducted on the respective specimens for three different curing days of 7, 14 and 28.
- The model was constructed between the process factors and output values by artificial neural network. Finally, the model was achieved with the root mean square error of 0.008223, 0.006559 and 0.009743 for CS and 0.008905, 0.006999 and 0.008745 for STS respectively for 7, 14 and 28 days.
- The model trained by ANN was suitably incorporated with the evolutionary computational techniques of particle swarm optimization.
- It was observed that the optimized value of compressive strength is 17.3288, 27.4850 and 42.3553 N/mm^2 for 7, 14 and 28 days respectively. Moreover it was found that the optimized value of split tensile strength is 1.5713, 3.2363 and 4.3113 N/mm^2 for 7, 14 and 28 days respectively.
- The percentage importance was found separately for optimized compressive strength and split tensile strength. It was also found that irrespective of curing days cement has the least importance on compressive strength and split tensile strength.

Table 8 Importance of each input factor in % on CS for different curing days

Parameters	7 Days	Parameters	14 Days	Parameters	28 Days
GGBFS	35.73	Slump	22.27	Slump	28.84
Slump	26.3	GGBFS	22.09	Fly ash	25.24
Silica fume	15.01	Fly ash	20.93	Silica fume	24.95
Fly ash	14.52	Silica fume	19.52	GGBFS	15.87
Cement	8.439	Cement	15.19	Cement	5.106

Table 9 Importance of each input factor in % on STS for different curing days

Parameters	7 Days	Parameters	14 Days	Parameters	28 Days
GGBFS	37.23	GGBFS	38.95	Slump	33.12
Slump	31.55	Slump	22.69	GGBFS	31.29
Fly ash	13.42	Silica fume	18.01	Fly ash	22.76
Silica fume	10.62	Fly ash	12.13	Silica fume	8.98
Cement	7.175	Cement	8.23	Cement	3.85

Declarations

Conflict of interest On behalf of all authors, I hereby disclose that no potential competing interest is involved with this technical paper.

References

1. Yazıcı, H.: The effect of silica fume and high-volume Class C fly ash on mechanical properties, chloride penetration and freeze–thaw resistance of self-compacting concrete. Constr. Build. Mater. **22**(4), 456–462 (2008). https://doi.org/10.1016/j.conbuildmat.2007.01.002
2. Athiyamaan, V.: Admixture-based self-compacted concrete with self-curing concrete techniques a state of art of review. Cleaner Eng. Technol. (2021). https://doi.org/10.1016/j.clet.2021.100250
3. Suryawanshi, N.T., Thakare, S.B., Jain, R.K.: Self-curing possibilities of blended concrete using water soluble polymer. Int. J. Adv. Sci. Technol. **29**(9s), 3829–3835 (2020)
4. Feizbakhsh, A., Khatibinia, M.: A comparative study of Traditional and Intelligence Soft Computing methods for predicting Compressive strength of Self Compacting concretes. Int. J. Optim. Civil Eng. **7**(3), 367–382 (2017)
5. Khademi, F., Akbari, M., Jamal, S.M., Nikoo, M.: Multiple linear regression, artificial neural network, and fuzzy logic prediction of 28 days compressive strength of concrete. Front. Struct. Civil Eng. (2017). https://doi.org/10.1007/s11709-016-0363-9
6. Sobhani, J., Najimi, M., Pourkhorshidi, A.R., Parhizkar, T.: Prediction of the compressive strength of no-slump concrete: a comparative study of regression, neural network and ANFIS models. Constr. Build. Mater. **24**(5), 709–718 (2010)
7. Nikoo, M., Torabian Moghadam, F., Sadowski, L.: Prediction of concrete compressive strength by evolutionary artificial neural networks. Adv. Mater. Sci. Eng. (2015). https://doi.org/10.1155/2015/849126
8. Uysal, M., Tanyildizi, H.: Estimation of compressive strength of self compacting concrete containing polypropylene fiber and mineral additives exposed to high temperature using artificial neural network. Constr. Build. Mater. **27**(1), 404–414 (2012)
9. Boğa, A.R., Öztürk, M., Topcu, I.B.: Using ANN and ANFIS to predict the mechanical and chloride permeability properties of concrete containing GGBFS and CNI. Compos. Part B Eng. **45**(1), 688–696 (2013)
10. Lingam, A., Karthikeya, J.: Prediction of compressive strength for HPC mixes containing different blends using ANN. Comput. Concr. **13**(5), 621–632 (2014)
11. Gulbandilar, E., Kocak, Y.: Application of expert systems in prediction of flexural strength of cement mortars. Comput. Concr. **18**(1), 1–16 (2016)
12. IS 10262: 2019, Concrete mix proportioning—guidelines (2nd Revision), Bereau of Indian Standards, New Delhi
13. Jagannadha Kumar, M.V., Srikanth, M., Jagannadha Rao, K.: Strength characteristics of self-curing concrete. Int. J. Res. Eng. Technol. **1**(1), (2012), ISSN: 2319–1163
14. Karthikeyan, R., Senthil Kumar, V., Punitha, A., Chavan, U.M.: An integrated ANN - GA approach to maximize the material removal rate and to minimize the surface roughness of wire cut EDM on Titanium alloy. Adv. Mater. Process. Technol. (2020). https://doi.org/10.1080/2374068X.2020.1793267
15. Alavala, CR: Fuzzy logic and neural networks: basic concepts and applications. Daryaganj, Delhi: New Age International; (2008)
16. Pilkington, J.L., Prestonb, C., Gomesa, R.L.: Comparison of response surface methodology (RSM) and artificial neural networks (ANN) towards efficient extraction of artemisinin from Artemisia annual. Ind. Crop. Prod. **58**, 15–24 (2014)
17. Ebrahimpour, A., Abd, R.R., Chng, D.H., et al.: A modeling study by response surfacemethodologyandartificial neural network on culture parameters optimization for thermostable lipase production from a newly isolated thermophilic Geobacillus sp. Strain ARM. BioMedCentral **8**, 96 (2008)
18. Mashhadban, H., Kutanaei, S.S., Sayarinejad, M.A.: Prediction and modeling of mechanical properties in fiber reinforced self-compacting concrete using particle swarm optimization algorithm and artificial neural network. Constr. Build. Mater. (2016). https://doi.org/10.1016/j.conbuildmat.2016.05.034
19. Tavakoli, H.R., Omran, O.L., Shiade, M.F., Kutanaei, S.S.: Prediction of combined effects of fibers and nano-silica on the mechanical properties of selfcompacting concrete using artificial neural network. Lat. Am. J. Solids Struct. **11**(11), 1906–1923 (2014)
20. CPC-X Software, Neural Power User Guide (2003) Available: http://www.geocities.com/neuralpower, https://www2.southeastern.edu/Academics/Faculty/pmcdowell/matlab_nnet_help.pdf
21. Awolusi, T.F., Oke, O.L., Akinkurolere, O.O., et al.: Performance comparison of neural networktraining algorithms in the modeling properties of steel fiber reinforced concrete. Heliyon. **5**, e01115 (2019)
22. Bharathi Raja, S., Baskar, N.: Particle swarm optimization technique for determining optimalmachining parameters of different work piece materials in turning operation. Int. J. Adv. Manuf. Technol. **54**, 445–463 (2011)
23. Tavakoli, H.R., Omran, O.L., Kutanaei, S.S., Shiade, M.F.: Prediction of energy absorption capability in fiber reinforced self-compacting concrete containing nano-silica particles using artificial neural network. Lat. Am. J. Solids Struct. **11**(6), 966–979 (2014)
24. Muthupriya, P., Subramanian, K., Vishnuram, B.G.: Prediction of compressive strength and durability of high performance concrete by artificial neural networks. Int. J. Optim. Civil Eng. **1**, 189–209 (2011)
25. Singh, A.K., Singhal, D., Kumar, R.: Machining of aluminum 7075 alloy using EDM process: an ANN validation. Mater. Today (2020). https://doi.org/10.1016/j.matpr.2020.02.591

26. Kennedy, J., Clerc, M.: Standard PSO 2006. . info/ Standard-PSO-2006.c.
27. Das, K., Kumar, K., Barman, T.K., Sahoo, P.: Application of artificial bee colony algorithm for optimization of MRR and surface roughness in EDM of EN31 tool steel, Procedia. Mater. Sci. **6**, 741–751 (2014). https://doi.org/10.1016/j.mspro.2014.07.090
28. Kutanaei, S.S., Choobbasti, A.J.: Prediction of combined effects of fibers and cement on the mechanical properties of sand using particle swarm optimization algorithm. J. Adhes. Sci. Technol. **29**(6), 487–501 (2015)
29. Yan, X., Zhang, C., Luo, W., Li, W., Chen, W., Liu, H.: Solve traveling salesman problem using particle swarm optimization algorithm. Int. J. Comput. Sci. **9**(6), 264 (2012)
30. Samad, S., Shah, A., Limbachiya, M.C.: Strength development characteristics of concrete produced with blended cement using ground granulated blast furnace slag (GGBS) under various curing conditions. Sādhanā **42**, 1203–1213 (2017). https://doi.org/10.1007/s12046-017-0667-z
31. https://www.fhwa.dot.gov/pavement/recycling/fach03.cfm#:~:text=Fly%20ash%20particles%20react%20with,to%20increase%20long%2Dterm%20strength
32. https://www.pci.org/PCI_Docs/Design_Resources/Guides_and_manuals/references/bridge_design_manual

Terms and Conditions

Springer Nature journal content, brought to you courtesy of Springer Nature Customer Service Center GmbH (“Springer Nature”).
Springer Nature supports a reasonable amount of sharing of research papers by authors, subscribers and authorised users (“Users”), for small-scale personal, non-commercial use provided that all copyright, trade and service marks and other proprietary notices are maintained. By accessing, sharing, receiving or otherwise using the Springer Nature journal content you agree to these terms of use (“Terms”). For these purposes, Springer Nature considers academic use (by researchers and students) to be non-commercial.
These Terms are supplementary and will apply in addition to any applicable website terms and conditions, a relevant site licence or a personal subscription. These Terms will prevail over any conflict or ambiguity with regards to the relevant terms, a site licence or a personal subscription (to the extent of the conflict or ambiguity only). For Creative Commons-licensed articles, the terms of the Creative Commons license used will apply.
We collect and use personal data to provide access to the Springer Nature journal content. We may also use these personal data internally within ResearchGate and Springer Nature and as agreed share it, in an anonymised way, for purposes of tracking, analysis and reporting. We will not otherwise disclose your personal data outside the ResearchGate or the Springer Nature group of companies unless we have your permission as detailed in the Privacy Policy.
While Users may use the Springer Nature journal content for small scale, personal non-commercial use, it is important to note that Users may not:

1. use such content for the purpose of providing other users with access on a regular or large scale basis or as a means to circumvent access control;
2. use such content where to do so would be considered a criminal or statutory offence in any jurisdiction, or gives rise to civil liability, or is otherwise unlawful;
3. falsely or misleadingly imply or suggest endorsement, approval , sponsorship, or association unless explicitly agreed to by Springer Nature in writing;
4. use bots or other automated methods to access the content or redirect messages
5. override any security feature or exclusionary protocol; or
6. share the content in order to create substitute for Springer Nature products or services or a systematic database of Springer Nature journal content.

In line with the restriction against commercial use, Springer Nature does not permit the creation of a product or service that creates revenue, royalties, rent or income from our content or its inclusion as part of a paid for service or for other commercial gain. Springer Nature journal content cannot be used for inter-library loans and librarians may not upload Springer Nature journal content on a large scale into their, or any other, institutional repository.
These terms of use are reviewed regularly and may be amended at any time. Springer Nature is not obligated to publish any information or content on this website and may remove it or features or functionality at our sole discretion, at any time with or without notice. Springer Nature may revoke this licence to you at any time and remove access to any copies of the Springer Nature journal content which have been saved.
To the fullest extent permitted by law, Springer Nature makes no warranties, representations or guarantees to Users, either express or implied with respect to the Springer nature journal content and all parties disclaim and waive any implied warranties or warranties imposed by law, including merchantability or fitness for any particular purpose.
Please note that these rights do not automatically extend to content, data or other material published by Springer Nature that may be licensed from third parties.
If you would like to use or distribute our Springer Nature journal content to a wider audience or on a regular basis or in any other manner not expressly permitted by these Terms, please contact Springer Nature at

onlineservice@springernature.com

energies

MDPI

Article

Comparative Performance Assessment of Different Energy Storage Devices in Combined LFC and AVR Analysis of Multi-Area Power System

CH. Naga Sai Kalyan [1], B. Srikanth Goud [2,*], Ch. Rami Reddy [3], Mohit Bajaj [4], Naveen Kumar Sharma [5], Hassan Haes Alhelou [6,7,*], Pierluigi Siano [8,9] and Salah Kamel [10]

1 Department of Electrical and Electronics Engineering, Vasireddy Venkatadri Institute of Technology, Guntur 522508, India; kalyanchallapalli@gmail.com
2 Department of Electrical and Electronics Engineering, Anurag College of Engineering, Ghatkesar 501301, Telangana, India
3 Department of Electrical and Electronics Engineering, Malla Reddy Engineering College (A), Maisammaguda, Secunderabad 500100, Telangana, India; crreddy229@gmail.com
4 Department of Electrical and Electronics Engineering, National Institute of Technology, Delhi 110040, India; mohitbajaj@nitdelhi.ac.in
5 Department of Electrical Engineering, I. K. Gujral Punjab Technical University, Jalandhar 144603, India; naveen31.sharma@gmail.com
6 School of Electrical and Electronic Engineering, University College Dublin, D04 V1W8 Dublin, Ireland
7 Department of Electrical and Computer Systems Engineering, Monash University, Clayton, VIC 3800, Australia
8 Department of Management & Innovation Systems, University of Salerno, 84084 Fisciano, Italy; psiano@unisa.it
9 Department of Electrical and Electronic Engineering Science, University of Johannesburg, Johannesburg 2006, South Africa
10 Electrical Engineering Department, Faculty of Engineering, Aswan University, Aswan 81542, Egypt; skamel@aswu.edu.eg
* Correspondence: srikanth.b@anuraghyd.ac.in (B.S.G.); hassan.haesalhelou@ucd.ie (H.H.A.)

check for updates

Citation: Kalyan, C.N.S.; Goud, B.S.; Reddy, C.R.; Bajaj, M.; Sharma, N.K.; Alhelou, H.H.; Siano, P.; Kamel, S. Comparative Performance Assessment of Different Energy Storage Devices in Combined LFC and AVR Analysis of Multi-Area Power System. *Energies* **2022**, *15*, 629. https://doi.org/10.3390/en15020629

Academic Editor: Adrian Ilinca

Received: 1 October 2021
Accepted: 5 January 2022
Published: 17 January 2022

Abstract: This paper made an attempt to put forward the comparative performance analysis of different energy storage devices (ESDs), such as redox flow batteries (RFBs), superconducting magnetic energy storage (SMES) device and ultra-capacitors (UCs), in the combined frequency and voltage stabilization of a multi-area interconnected power system (MAIPS). The investigative power system model comprises two areas, and each area consists of the power-generating sources of thermal, hydro and gas units. The intelligent control mechanism of fuzzy PID was used as a secondary controller optimized with a hybridized approach of the artificial electric field algorithm (HAEFA) subjected to the minimization of integral time absolute error (ITAE) objective function. However, the superiority of fuzzy PID in dampening the deviations of combined load frequency control (LFC) and automatic voltage regulator (AVR) responses was revealed upon comparison with conventional PI and PID. Further, the LFC-AVR combined analysis was extended to incorporate different ESDs one after the other. The simulation results reveal the efficacy of incorporating ESDs with the LFC-AVR system and the supremacy of RFBs in damping out the fluctuations in frequency and voltage.

Keywords: energy storage devices; combined LFC-AVR; ITAE; fuzzy PID; HAEFA algorithm

1. Introduction

One of the central issues that practicing engineers face in electrical power systems is the simultaneous control of terminal voltage and area frequency. The impairment of any of these parameters strongly impairs the life expectancy and performance of other operating equipment associated with the power system. Controlling devices that have been installed in large complex power systems are intended to deal with small load disturbances

in order to hold system frequency and terminal voltage at specified limits. In this regard, the generating units are always provided with two operating loops. Among them, one is load frequency control (LFC) loop, which deals with reducing the gap among real power generation and load, thereby regulating the frequency. The other is the automatic voltage regulator (AVR) loop, which deals with controlling the reactive power in the system and thereby the terminal voltage [1].

Elgerd and Fosha [2] are the two researchers who pioneered the work on the LFC of power system networks. Since then, a huge base of literature has been published in this domain, some of which is mentioned in this paper. Dhanasekaran et al. [3] designed the ant colony optimization (ACO)-based traditional PID controller with different cost functions for the stability assessment of an isolated nuclear power plant. Due to the implementation simplicity of traditional PI [4,5]/PID [6–10]/PIDD [11] controllers, they have been widely implemented for different models of multi-area power systems. Moreover, the authors implemented different optimization approaches such as the chemical reaction-based particle swarm optimizer (CRPSO) [4], Harris Hawks optimizer (HHO) [5], grey wolf optimizer (GWO) [6], flower pollination algorithm [7], genetic algorithm (GA) [8], improved (I) PSO (IPSO) [9], differential evolution (DE) [10] and grey wolf optimization (GWO) [11]. In [4,6,7], the authors performed an analysis on a dual-area system with hydro-thermal generating units, whereas in [8–11], the authors considered a multi-area system with conventional thermal–hydro–gas units. Further, with the benefit of providing additional tuning parameters in fractional order (FO), controllers are also gaining momentum, especially in LFC schemes, and are widely accepted by researchers [12]. In [13,14], the authors implemented the FOPID controller in a multi-area system for retaining stability under load disturbances using the gases Brownian optimizer (GBO) [13] and big bang—big crunch (BBBC) [14] techniques, respectively. Moreover, the researchers also designed fuzzy (F) and other cascaded (C) controllers such as FPI [15]/FPID [16]/type-2 FPID [17]/FPIDN-FOI [18], etc., listed in the literature. Despite that, these controllers are also needed to optimize for better operation efficiency [19]. Previous research has employed searching approaches such as the bacterial foraging optimizer (BFO) [15], firefly pattern search (FA-PS) [16], symbiotic organism search (SOS) [17], imperialist competitive approach (ICA) [18], etc.

The researchers of the abovementioned literature only focused on stabilizing system frequency, which is only concentrated on the LFC issue and AVR coupling is not considered. A huge quantity of literature is available on LFC and AVR independently. Nowadays, authors are concentrating on conducting research work with combined LFC-AVR models but are restricted to a certain extent. Gupta et al. [19] performed an analysis of an LFC-AVR combined model and regulated the performance by incorporating damper winding in the synchronous generator rotor of AVR loop but was limited to only single area. Rakhshani et al. [20] carried out a combined analysis on an isolated thermal power unit with the regulation of a traditional PI controller. Chandrakala and Balamurugan extended the combined LFC-AVR analysis to the multi-area system incorporated with traditional hydro-thermal power generation units in each area under the supervision of simulated annealing (SA) [21]-based traditional PID control. In [22], the authors carried out the analysis of combined LFC-AVR to a three-area system with an F-based controller fine-tuned with the lightening search algorithm (LSA), but each area comprised only thermal and diesel units. In [23,24], the researchers employed multi-generation units in a multi-area system for combined analysis, but the research was limited to the design of classical PID using the moth flame optimizer (MFO) [23] and DE-AEFA [24], respectively.

This motivated the authors in this paper to design an intelligent-based fuzzy PID controller for a combined LFC-AVR model for a multi-area system with multiple generation units to stabilize voltage and frequency simultaneously. Till now, in the stream of LFC-AVR combined analysis, authors have only been focused on the implementation of traditional and FO-based controllers. The combined LFC-AVR system is more complex, so traditional controllers are no longer supportable, especially for large perturbations. Thus, fuzzy

PID fine-tuned with the HAEFA mechanism was implemented as a secondary regulatory technique in both the loops of LFC and AVR.

However, the design and implementation of the secondary regulator mechanism alone is not sufficient for the power system network to maintain stability during load perturbations [25]. These secondary regulators are only capable of restoring stability during small perturbations. So, the complex power system definitely needs an ancillary strategy as a territorial control approach to overcome the hunting mechanism of the power system apparatus during large load disturbances. Ancillary strategies include overlying the DC line with the existing AC transmission line (AC/DC links) [26] in parallel and the incorporation of ESDs [27,28] with the system. In this paper, different ESDs were incorporated with the system one after the other to assess their performance in obtaining the simultaneous stabilization of voltage and frequency. A comparison of different ESDs' performances in a multi-area combined LFC-AVR system has so far not been reported in the literature, and the intelligent fuzzy PID regulator for a combined system is also a maiden attempt.

In light of the abovementioned aspects, this paper contributes the following:

a. An LFC-AVR combined model of a two-area system was designed for simultaneous voltage and frequency stabilization.
b. Intelligent-based fuzzy PID was implemented as a secondary regulator in the loops of LFC and AVR.
c. The implementation of fuzzy PID for a combined system has not been reported in the literature so far.
d. The HAEFA algorithm was utilized to tune the parameters of the secondary controller.
e. The supremacy of fuzzy PID was demonstrated with controllers of traditional PI/PID.
f. The necessity of coupling AVR with LFC loop was clearly demonstrated and justified.
g. The performance assessment of different ESDs in a combined effect was analyzed.

2. Methodology

A HAEFA-based fuzzy PID control approach is presented in this paper for a combined LFC-AVR analysis. To carry out the analysis, the LFC-AVR system was designed and developed in MATLAB/Simulink version of (R2016a). Disturbance of 10%SLP was injected in area-1 of test system to analyze fuzzy PID control performance. Efficacy of fuzzy PID was revealed with traditional PI/PID controllers. Moreover, the efficacy of the controller depends on the selection of optimization approach. The newest technique of HAEFA was implemented in this paper after testing it on different benchmark standard functions. Further, various ESDs were considered individually with the LFC-AVR system as territorial controllers to boost the performance. Simulation results reveal the supremacy of RFBs over other ESDs.

3. System Modeling

3.1. Modeling of LFC Loop

The power system displayed in Figure 1 considered for investigation consists of two areas of equal generation capacity. Each area comprises identical generation sources of thermal, hydro and gas units. The dynamical analysis of the power system was carried out upon laying area-1 with 10%SLP. The parameters of generation units such as gain and time constants in the investigated power system are provided in [29]. The modeling of the power-generating utilities employed in this work is given as follows:

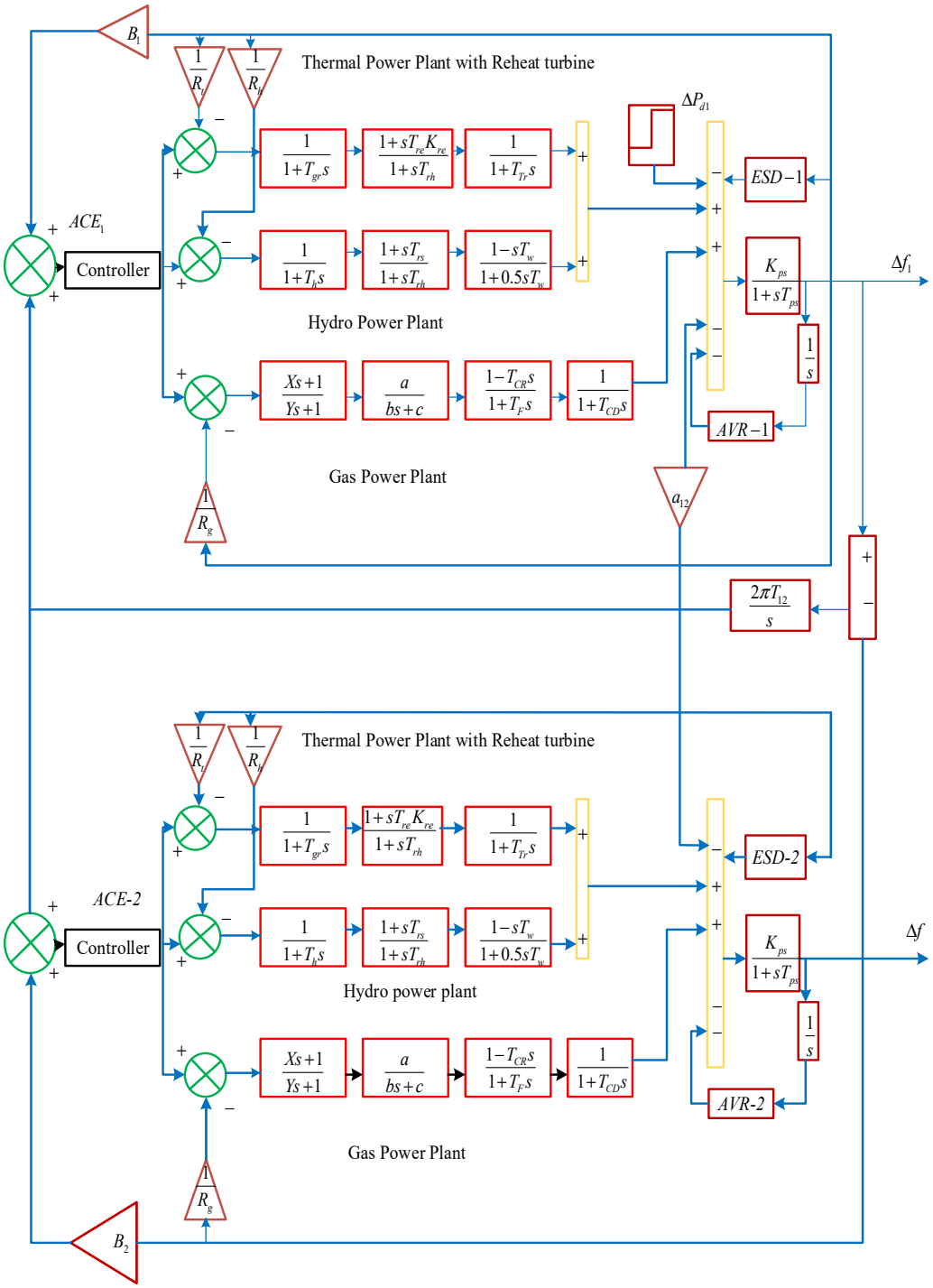

Figure 1. Combined LFC-AVR model of multi-area system.

Thermal system:

$$G_T(s) = \frac{(1 + sT_{re}K_{re})}{(1 + T_{gr}s)(1 + sT_{re})(1 + T_{tr}s)} \tag{1}$$

Hydro system:

$$G_H(s) = \frac{(1 + sT_{rs})(1 - sT_W)}{(1 + T_h s)(1 + T_{rh}s)(1 + 0.5T_W s)} \tag{2}$$

Gas system:

$$G_G(s) = \frac{(1+Xs)(1-T_{CR}s)a}{(1+Ys)(c+bs)(1+T_Fs)(1+T_{CD}s)} \quad (3)$$

3.2. Modeling of AVR Loop

AVR safeguards the voltage of the synchronous generator to prevent the violation of predetermined limits. The model of AVR with coupling coefficients is displayed in Figure 2. The AVR system mainly consists of a sensing unit, generator field, amplifier unit and excitation units. The sensor continuously senses the terminal unit and generates the error voltage (ΔV) signal upon comparing it with the reference voltage signal. The error voltage signal can then be amplified and fed to the excitation unit to change the synchronous generator field excitation. With this the terminal voltage deviation is quickly compensated in order to make the system stable. The detailed mathematical modeling of AVR unit is as follows [30]:

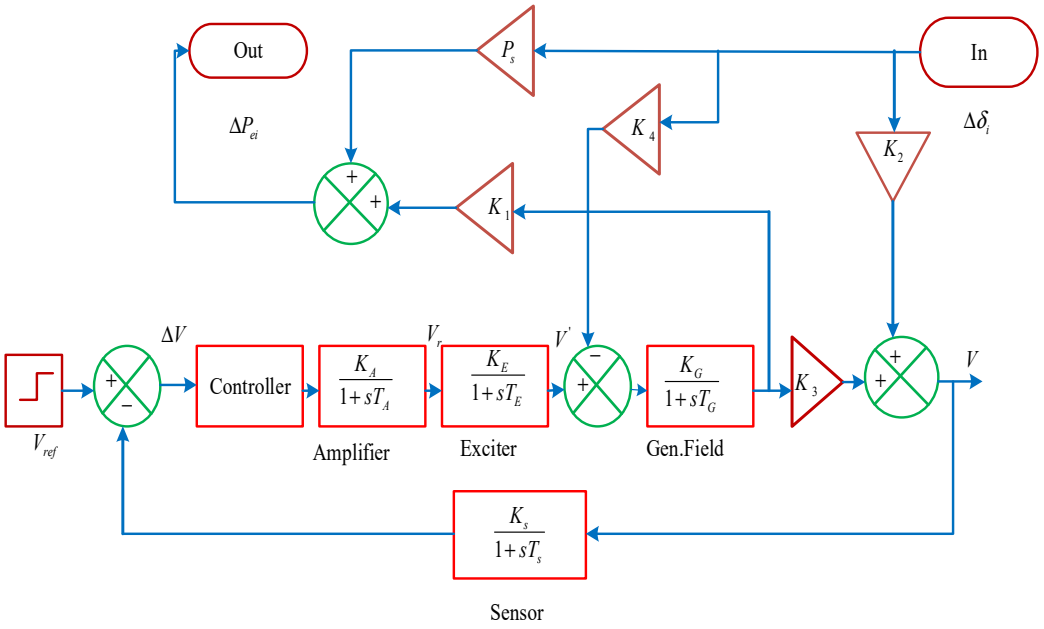

Figure 2. AVR with coupling coefficients.

Amplifier:

$$G_A(s) = \frac{K_A}{1+sT_A} \quad (4)$$

Exciter:

$$G_E(s) = \frac{K_E}{1+sT_E} \quad (5)$$

Generator:

$$G_F(s) = \frac{K_S}{1+sT_S} \quad (6)$$

Sensor:

$$G_S(s) = \frac{K_S}{1+sT_S} \quad (7)$$

3.3. Modeling of LFC and AVR Coupling

The main aim of analyzing the effect of the combined LFC and AVR system is to control frequency and terminal voltage simultaneously. Frequency can be controlled by regulating real power generation, and terminal voltage is maintained by controlling the generator field excitation system. However, as the actions taken by the AVR system result in

'V' variation, there is a considerable effect of terminal voltage on real power generation [22], given by

$$P_e = \frac{|V|\,|E'|}{X_S}\sin\delta \tag{8}$$

So, the automatic voltage regulator has an instantaneous considerable impact on load frequency control loop. From [1] it was found that under dynamic load (ΔP_d) conditions, there will be deviation in the system frequency (Δf), resulting in a shift in the generator load angle $(\Delta\,\delta)$. On incorporating these effects, the change in real power generation is mathematically expressed as

$$\Delta P_e = P_S\Delta\delta + K_1E' \tag{9}$$

where E' is EMF induced in the generator stator winding, K_1 is the deviation in 'V' for a small deviation in E', and the field output voltage of the generator, P_S, is synchronizing the power coefficient chartered as power angle characteristics slope at initial operating angles. The variation in voltage with respect to the alteration in the rotor angle is termed as

$$\Delta V = K_2\Delta\delta + K_3E' \tag{10}$$

The transfer function of the generator field considering the change in load angle is approximated by

$$E' = \frac{K_G}{1+sT_G}(V' - K_4\,\Delta\delta) \tag{11}$$

K_1, K_3, K_4 Coefficients are positive, but K_2 may be negative depending on total system reactance (X_S).

Where $X_S = X_1 + X_2 + X_{12}$, The K coefficients are mentioned in [30].

4. Controller and Objective Function

In general, classical PID regulators are widely accepted and utilized for the monitoring and regulation of power system frequency, owing to the benefits of design simplicity. However, these traditional controllers are not effective or competent for a system with uncertainties. Intelligent-based fuzzy regulators are more effective in dealing with complex realistic power system networks. Despite that, the performance of fuzzy controllers strongly relies on the design of appropriate fuzzy rule base interface system and membership functions (MFs), which is a complex job. The structure of the fuzzy-assisted PID regulator employed for the combined LFC and AVR study in this paper is displayed in Figure 3 [31]. The fuzzy logic controller (FLC) is provided with the input as area control error (ACE) and derivative of ACE. Usually, triangular, bell-shaped and trapezoidal MFs are utilized for FLC systems because of their simplicity in real-time execution and requirement of low-level memory. Thus, triangular MFs were utilized in this paper for the FLC as both the input and output. Five fuzzy linguistic variables that were considered for the FLC system were zero (Z), small negative (SN), big negative (BN), small positive (SP) and big positive (BP), as displayed in Figure 4 [32], and the rules are noted in Table 1. The center of gravity method of the defuzzification procedure was used in this study to calculate the fuzzy output. The output of the FLC system was then fed to the traditional PID to present the final output. However, the parameters of the traditional PID needed to be optimally rendered and were thus subjected to the time-domain-based performance index. Out of all the performance indices, ITAE is meant to be the most effective in reducing response overshoots and settling time to be implemented in this work, as given in Equation (12) [33].

$$J_{ITAE} = \int_0^{T_{sim}} t.(\Delta f_1 + \Delta f_2 + \Delta P_{tie_{12}} + \Delta V_1 + \Delta V_2)dt \tag{12}$$

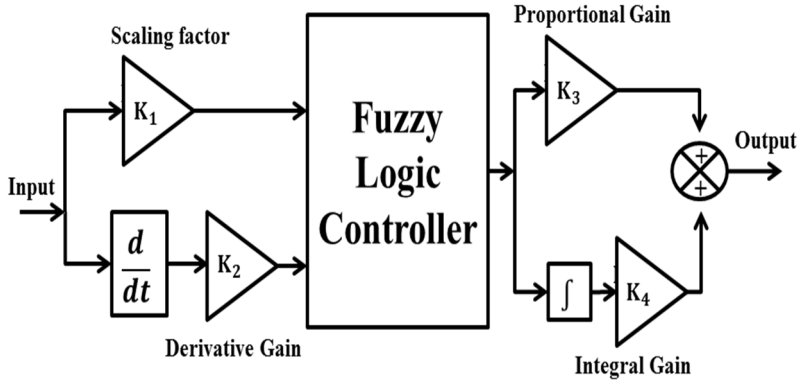

Figure 3. Fuzzy assisted PID controller.

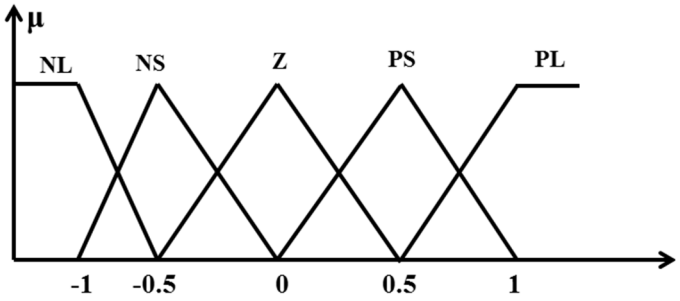

Figure 4. MFs for FLC.

Table 1. FLC input and output rules.

ACE	ΔACE				
	BN	**SN**	**Z**	**SP**	**BP**
BN	BN	BN	BN	SN	Z
SN	BN	BN	SN	Z	SP
Z	BN	SN	Z	SP	BP
SP	SN	Z	SP	BP	BP
BP	BP	Z	SP	BP	BP

5. Discussion

5.1. Ultra Capacitors

UCs, usually called super capacitors, possess the tendency to store bulk power by charge separation between the metallic plates of a large surface area. Though the UCs are more costly compared to other ESDs, they have been extensively utilized with the benefits of a large power density and extravagant specific power. With a longer cycle time and lower and easy maintenance, they are suitable for peak demand situations. However, the UC is very clean and eco-friendly with zero emissions, which facilitates its extensive application. The transfer function of UCs utilized in this paper is provided in Equation (13).

$$G_{UC} = \frac{K_{UC}}{1 + ST_{UC}} \tag{13}$$

5.2. Superconducting Magnetic Energy Storage

SMES devices are one of the most prominent ESDs, as their static nature leads to higher efficiency. SMES involves no chemical reactions, and thus no harmful gases are exposed to atmosphere. This device comprises a magnetic circuit enclosed in a closed chamber, which is maintained at a cryogenic temperature to attain super conductivity. SMES devices also comprise power converter unit and a step-down transformer. The

magnetic coil charging and discharging can be achieved through the transformer, and the interface between the SMES and grid is facilitated by the power converter unit. The charging of coil in SMES will be done during off-peak load durations and discharging at peak demands. The compensator model of SMES utilized in this paper for stabilizing frequency is displayed in Figure 5 [34]. The SMES device parameters are stabilization gain K_{SMES}, and T_1, T_2, T_3 and T_4 are time constants.

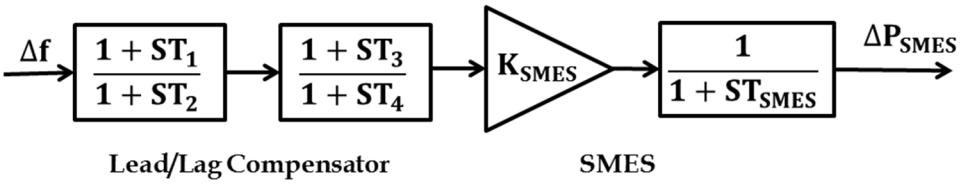

Figure 5. SMES structure.

5.3. Redoxflow Batteries

RFBs are one of the most effective ESDs based on the electrochemical reaction theory. Due to the benefits of a quick response nature and load-leveling characteristics, they have an extensive range of applications. Sulfuric acid solution with ions of vanadium acts as an electrolytic solution in RFBs for chemical reactions. RFBs comprising of two isolation chambers eliminate the problem of self-discharge. The oxidation and reduction reactions of the electrolytic solution in RFBs are responsible for the charging and discharging process. Its operation range depends upon the quantity of the electrolyte solution employed. In this paper, the workings of RFBs for the LFC study are given in Equation (14) [35].

$$\Delta P_{rfb} = \left\{ (ACE * K_{rfb}) - \left(\frac{K_{ri}}{1 + sT_{ri}}\right) \right\} \left(\frac{1}{1 + sT_{di}}\right) - (set\ value) \tag{14}$$

6. HAEFA Algorithm

HAEFA is one of the newest meta-heuristic searching strategies developed by the researchers in [25]. Based on Coulomb's law of electric field theory, the AEFA approach was implemented by the authors in [36]. This AEFA algorithm was implemented by the researchers especially for the control and operation of modern power system analysis and LFC studies and detected a drawback of updating the step size, which affects the effective utilization of search space. To overcome the above and to make the AEFA more effective in obtaining solutions for engineering optimization problems, the researchers in [25] put forward the hybridization mechanism and termed it the HAEFA algorithm. The implementation of this HAEFA approach is explained as follows:

First, initially randomize the gains of the controller in both LFC-AVR loops of the considered power system model as K_{PN}, K_{IN}, K_{DN} $\forall$ N = 1,2,3 . . . . n

$$X = \begin{bmatrix} K_{P1} & K_{I1} & K_{D1} \\ K_{P2} & K_{I2} & K_{D2} \\ \cdots & \cdots & \cdots \\ \cdots & \cdots & \cdots \\ K_{PN} & K_{IN} & K_{DN} \end{bmatrix} \tag{15}$$

The particles of each of the populations are updated in simulation. After performing the simulation for a given time period, the objective function values are calculated for each of the populations and treat them as local best solutions. The objective function conceived in this paper was ITAE, and the corresponding fitness function was evaluated as

$$fitness\ function\ = \frac{1}{1 + ITAE\ Index} \tag{16}$$

Among the local best solutions, select the population that results in the lowest objective function value with the highest fitness value as the global best population. The respective solution is considered to be the global best solution, as the formulated objective function handles frequency and power deviations pertaining to multiple areas, which increases the problem complexity. Due to this the diversity of the solutions is increased. In order to bring the local best solutions towards the global best solution a novel velocity equation is formulated. In this equation the chaotic constants C_1 and C_2 are generated dynamically to change the particles' velocity to favor the local and global best solutions. Using these local and global best solutions, the velocity of each of the populations can be calculated as

$$V_i^{(t+1)} = rand() * V_i^{(t)} + a_i^{(t)} + C_1 * rand_1() * (P_{best} - P_{current}) + C_2 * rand_2() * (G_{best} - G_{current}) \quad (17)$$

Later, the particles position will be updated using

$$X_i^{(t+1)} = X_i^{(t)} + V_i^{(t+1)} \quad (18)$$

where $V_i^{(t+1)}$ and $X_i^{(t+1)}$ represent velocity and the position of ith particle in the $(t + 1)$ iteration, respectively. The chaotic parameters are varied dynamically to limit the chances of solution divergence using

$$C_i = 1 + \frac{1}{1 + \exp(\frac{-iter}{iter\ \max})}, \quad i = 1, 2 \quad (19)$$

The acceleration (a) and electric field (E) of ith particle at the $(t + 1)$ iteration will be calculated as shown below.

$$a_i^{(t+1)} = \frac{Q_i^{(t+1)} * E_i^{(t+1)}}{M_i^{(t+1)}} \quad (20)$$

$$E_i^{(t+1)} = \frac{F_i^{(t+1)}}{Q_i^{(t+1)}} \quad (21)$$

The total force exerting on ith particle in $(t + 1)$ iteration as

$$F_i^{(t+1)} = \sum_{j=1, j\neq i}^{n} rand() * F_{ij}^{(t+1)} \quad (22)$$

The force magnitude exerted on ith due to the jth particle in the $(t + 1)$ iteration is

$$F_{ij}^{(t+1)} = K^{(t+1)} \frac{Q_i^{(t+1)} * Q_j^{(t+1)} * (P_j^{(t+1)} - X_j^{(t+1)})}{R_{ij}^{(t+1)}} \quad (23)$$

where 'K' represents Coulomb's constant, which can be calculated as

$$K^{(t+1)} = K_0 * \exp(-\alpha \frac{Current\ iteration}{iteration\ \max}) \quad (24)$$

where K_0 and α are constant parameters.

In order to maximize the force exerted by the electric field on the particles, half of the equivalent Euclidian distance is considered, as follows.

$$R_{ij}^{(t+1)} = 0.5 * \| X_i^{(t+1)} - X_j^{(t+1)} \|_2 \quad (25)$$

$$Q_i^{(t+1)} = \frac{q_i^{(t+1)}}{\sum_{i=1}^{n} q_i^{(t+1)}} \tag{26}$$

The charge of the *i*th and *j*th particles as indicated with $Q_i^{(t+1)}$ and $Q_j^{(t+1)}$ at the $(t + 1)$ iteration is as follows.

$$q_i^{(t+1)} = \exp\left(\frac{fitness_i^{(t+1)} - worst^{(t+1)}}{best^{(t+1)} - worst^{(t+1)}}\right) \tag{27}$$

The problem formulated in this paper is a minimization one, and hence the best and worst fitness values will be evaluated as

$$best^{(t+1)} = \min\left(fitness_j^{(t+1)}\right), \ \ j \in (1, 2, 3 \ldots . n) \tag{28}$$

$$worst^{(t+1)} = \max\left(fitness_j^{(t+1)}\right), \ \ j \in (1, 2, 3 \ldots . n) \tag{29}$$

This procedure is repeated for three iterations to train the populations to increase the searching capability. This is considered to be the first stage of the proposed algorithm. Here, after starting the iterative process, it takes a minimum of three iterations to obtain the decreased variance of deviation of the solutions. Using this statistical analysis, the developed algorithm generated first-stage solutions after three iterations. After this, the pair-wise comparison process was initiated to divide the total populations in half. The populations related to these solutions were forwarded to the second stage of the proposed methodology. Due to this, the remaining iterative process was performed with maximum efficacy to obtain the best solution within fewer iterations. The process of pair-wise comparison is as follows below:

Let $fitness_1$, $fitness_2$, $fitness_3 \ldots \ldots \ldots \ldots fitness_n$ be the fitness values of the solution for 'n' particles;

If $fitness_1 > fitness_2$, then send $fitness_1$ to the next stage;

If $fitness_3 > fitness_4$, then send $fitness_3$ to the next stage;

If $fitness_5 > fitness_6$, then send $fitness_5$ to the next stage;

If $fitness_{(n-1)} > fitness_{(n)}$, then send $fitness_{(n-1)}$ to the next stage.

This process of pair-wise comparison was performed on all populations to obtain the best half of the entire population. The remaining algorithmic operations were performed on these populations.

After reviewing the literature carefully, it was noticed that the hybridization of multiple algorithms increases the algorithm's performance to the maximum extent. From this, it was determined that in this paper a new hybridization approach was established by taking the advantage of crossover operation. As the considered objective function makes the problem more complex, it was necessary to obtain a converged solution instead of a diverged solution. From the fourth iteration onwards the existing crossover operation was performed on second-stage populations to minimize the solution divergence with updated velocity. Crossover can also be called recombination, which works to create offspring from two parents by combining the genetic information in a specified manner. It is the only way of generating new offspring stochastically from an existing population, which is analogous to the biological human reproduction system. There are various types of crossover operations available in the literature; however, after the conclusion of an extensive literature survey, it was determined that uniform crossover operation may yield better results, and it was thus implemented.

$$\Upsilon^{new} = (1 - \lambda) \times \Upsilon^{ref} + \lambda \times \Upsilon^{old} \tag{30}$$

where λ is the random number between [0, 1] and Table 2, given below, indicates the uniform crossover operation.

Table 2. Uniform crossover operation.

Parent1	0 1 0 0 0 1 0 1
Parent2	0 0 1 1 0 1 0 0
Mask	1 0 0 1 0 1 1 0
Child1	0 1 0 1 0 1 0 1
Child2	0 0 1 0 0 1 0 0

After crossover operation the positions are updated; this whole procedure will be repeated till the completion of the maximum number of iterations, and then the best values are displayed. HAEFA flowchart is displayed in Figure 6.

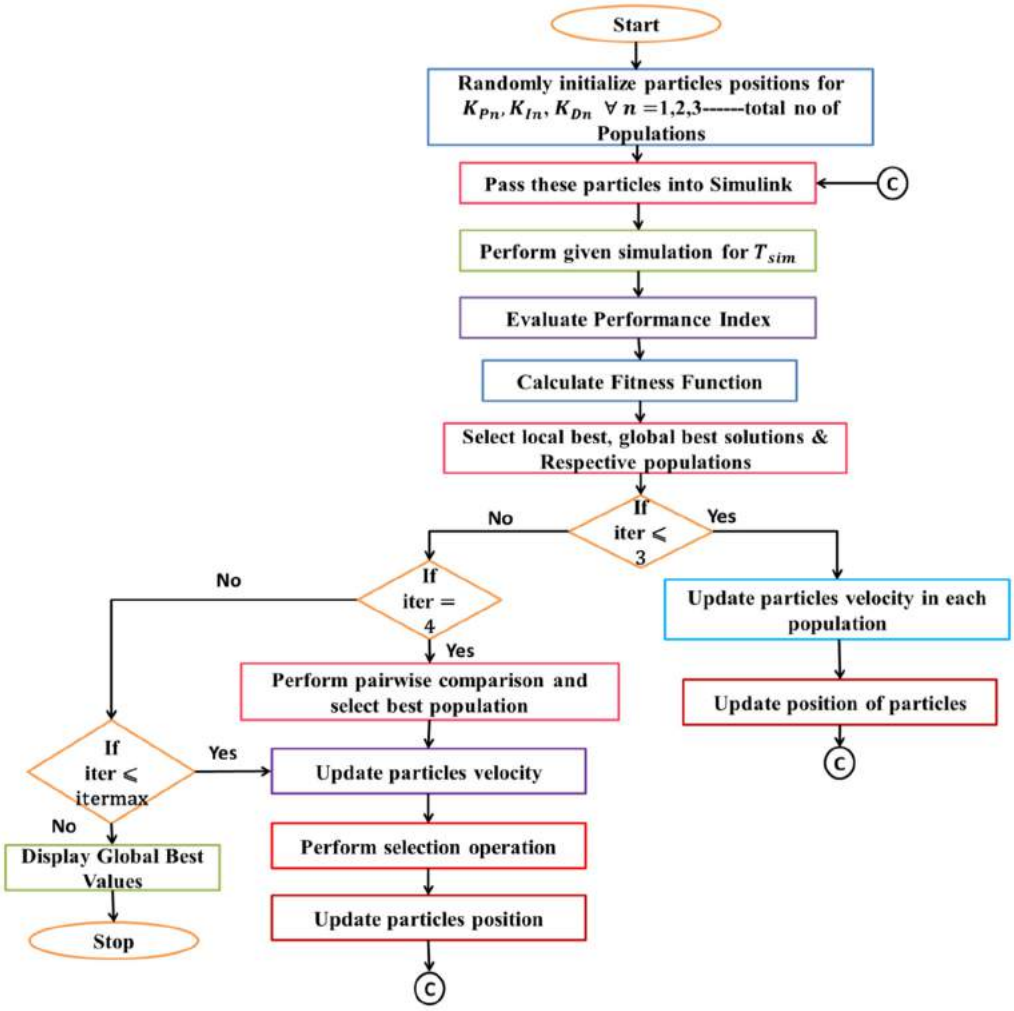

Figure 6. HAEFA flowchart.

Before implementing this strategy for power system optimization, the efficacy of hybridization was tested on the benchmark function of sphere function given in Equation (31). Both the algorithms were implemented with a population of 100 for 100 trials. The efficacy of the algorithm was assessed in terms of initial and final function values, as displayed in Figure 7. From Figure 7, it can be concluded that the function values at the initial and final instants were good, but a better solution was found using HAEFA as compared to the AEFA approach. Moreover, the final values of the function with HAEFA were almost below the mean value, which shows its effectiveness and tendency to maintain exploration and exploitation.

$$f(x) = \sum_{i=1}^{2} x_i^2 \tag{31}$$

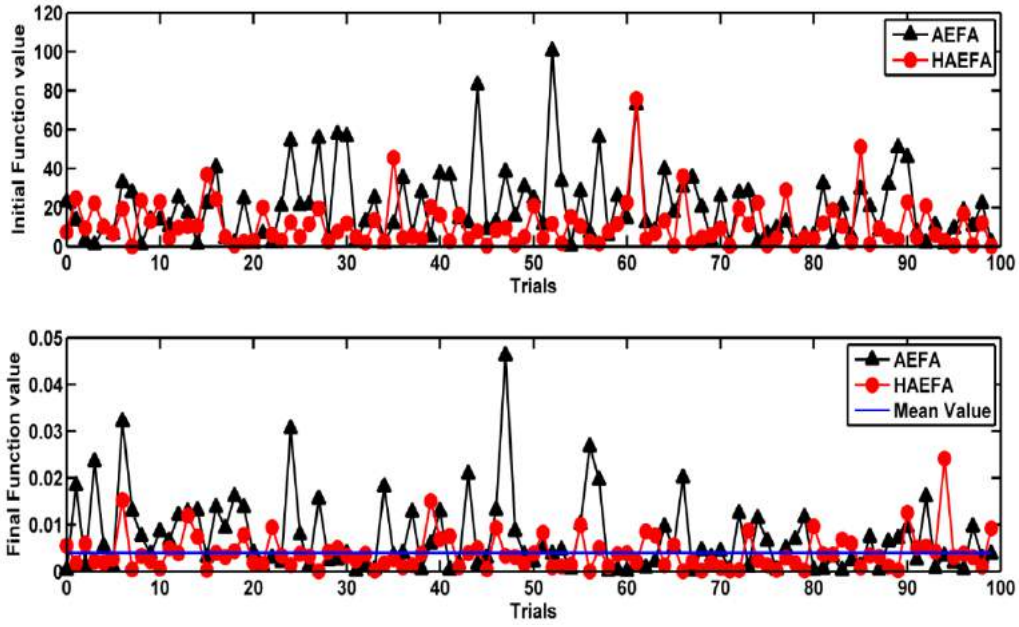

Figure 7. Sphere function objective value at initial and final instant using AEFA and HAEFA methods for 100 trials.

7. Simulation Results

The simulation of the combined LFC and AVR system of MAIPS was designed in the domain of MATLAB/Simulink version (2016a), and the HAEFA optimization algorithm was developed in a (.m file) format. In order to assess the dynamical analysis, the combined LFC and AVR system was targeted with 10%SLP on area-1. The HAEFA algorithm was implemented with a population size of 50 for 100 iterations.

7.1. Case-1: Analysis of Combined LFC and AVR System with HAEFA-Tuned Controllers

The combined LFC and AVR model of MAIPS were analyzed with different controllers such as traditional PI/PID and intelligent-based fuzzy PID in both the loops of LFC and AVR one at a time by injecting area-1 with a load of 10% SLP. The parameters of these controllers were rendered optimally with a hybridized algorithm of the HAEFA approach. Figure 8 depicts the responses of the combined LFC-AVR system under various controllers fine-tuned with the HAEFA approach, and these responses were interpreted in terms of settling time, as provided in Table 3. After observing the responses rendered in Figure 8, we came to the decision that the undershooting and overshooting of the responses were very comfortably mitigated by the fuzzy PID compared to traditional PI/PID controllers. Moreover, the terminal voltages quickly reached specified values with the HAEFA-tuned fuzzy PID regulator. From Table 3, it is obvious that the responses reached the steady condition in much less time with the fuzzy PID controller than traditional PI/PID. Thus, the intelligent fuzzy PID showed its predominance in regulating the behavior of complex MAIPS of the LFC-AVR combined model. The parameters of PI/PID/fuzzy PID controllers that were retrieved optimally with the HAEFA technique are noted in Table 4. Further, the ITAE index value of the HAEFA-tuned fuzzy PID controller was improved by 54.19% with the HAEFA-based PI and 41.66% with HAEFA-based PID controllers.

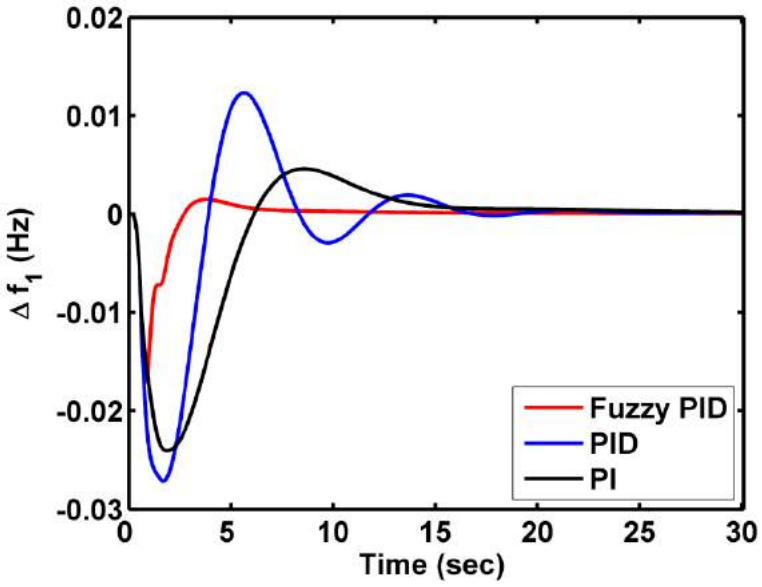

(**a**)

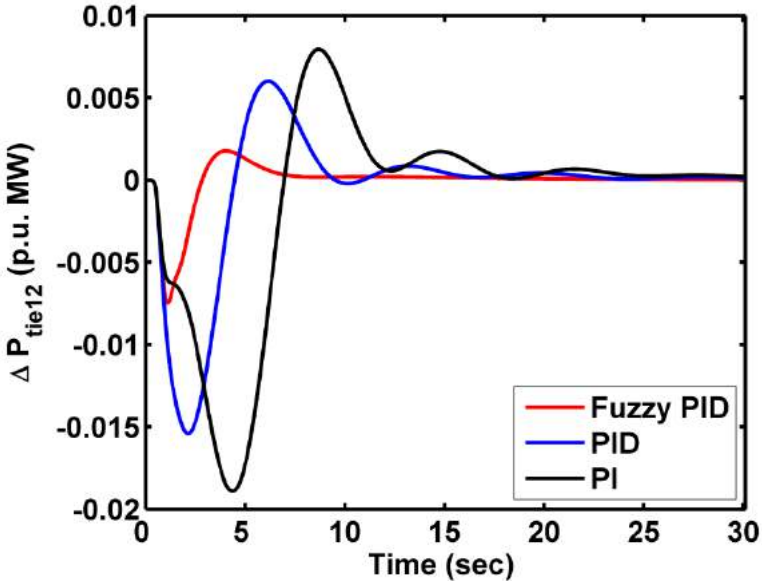

(**b**)

Figure 8. *Cont*.

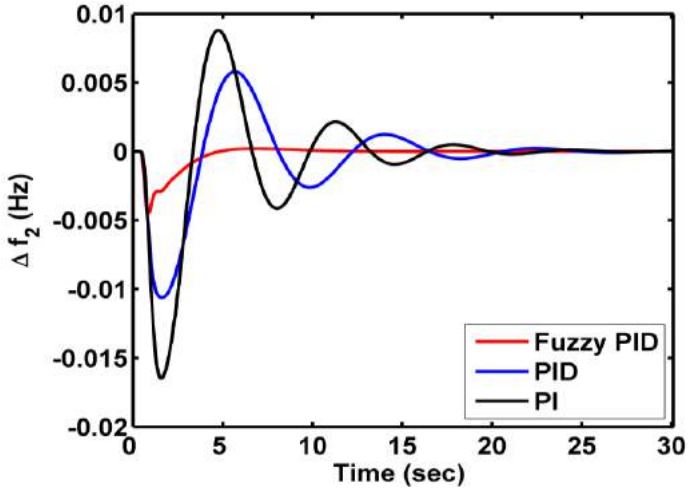

(**c**)

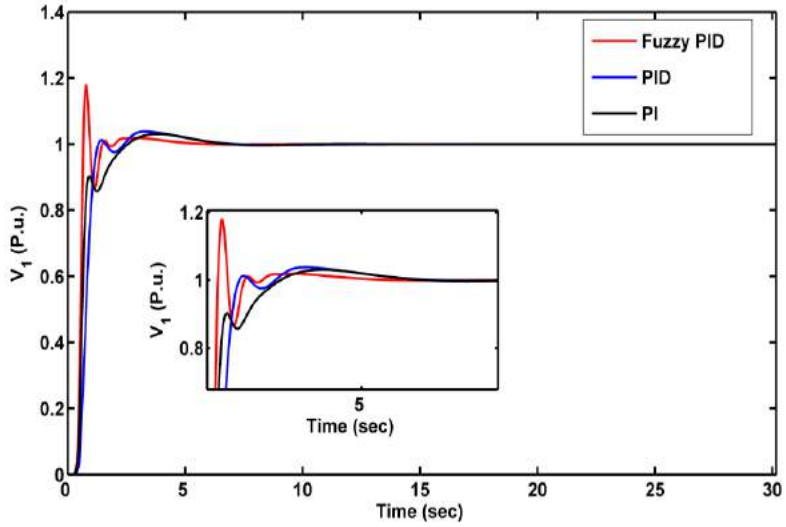

(**d**)

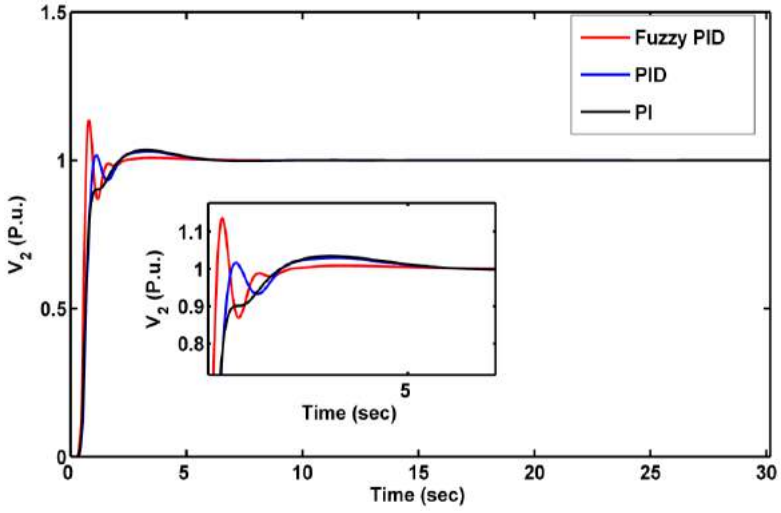

(**e**)

Figure 8. Responses for case-1: (**a**). Δf_1, (**b**). $\Delta Ptie_{12}$, (**c**). Δf_2, (**d**). V_1 and (**e**). V_2.

Table 3. Settling time of responses in case-1.

HAEFA-Based Controllers	Settling Time T_S (Sec)					ITAE
	Δf_1	Δf_2	ΔP_{tie12}	V_1	V_2	
PI	26.88	26.62	27.94	8.124	8.791	36.134
PID	23.45	24.11	22.93	6.524	7.811	28.376
Fuzzy PID	15.23	11.03	17.34	5.127	4.157	16.552

Table 4. Controller optimal gains found with HAEFA technique.

HAEFA Tuned Controller	Area-1		Area-2	
	LFC Loop	AVR Loop	LFC Loop	AVR Loop
PI	K_P = 3.1324 K_I = 2.1487	K_P = 2.0119 K_I = 1.1576	K_P = 2.9034 K_I = 1.8270	K_P = 1.9085 K_I = 1.0864
PID	K_P = 3.3517 K_I = 2.4854 K_D = 0.9649	K_P = 2.2510 K_I = 1.3472 K_D = 0.4976	K_P = 2.8909 K_I = 2.1869 K_D = 0.9595	K_P = 2.3413 K_I = 1.3718 K_D = 0.8693
Fuzzy PID	K_P = 3.7679 K_I = 1.9755 K_D = 1.2769	K_P = 2.0457 K_I = 1.0844 K_D = 0.9961	K_P = 3.4509 K_I = 1.9924 K_D = 0.9133	K_P = 2.3015 K_I = 1.1554 K_D = 0.9419

7.2. Case-2: Analysis of System Performance with and without Considering AVR Coupling

In this sub section, a comparison has been made between the responses of the considered MAIPS without and with considering AVR coupling under the supervision of the HAEFA-tuned fuzzy PID controller. In order to obtain the analysis in more comparative approach, the power system with and without AVR coupling was analyzed for the same load disturbance, 10%SLP on area-1, and the responses are displayed in Figure 9. From the responses rendered in Figure 9, it can be noticed that the deviations in system behavior were slightly heightened with the consideration of AVR coupling, which can be justified by Equation (8). The stability of the power system depends on both terminal voltage and area frequency. The monitoring and regulation of voltage and frequency of the power system must be carried out with intense care. The mathematical analysis given in Equation (8) demonstrates the cumulative and simultaneous impact of variations in the AVR loop leading to the fluctuations in the LFC loop and vice versa. Considering all these analyses the ITAE objective function provided in Equation (12) is formulated for simultaneous voltage and frequency stabilization.

7.3. Case-3: Analysis of Combined LFC and AVR System with Different ESDs

The fuzzy PID regulator based on the HAEFA mechanism showed the supreme performance; as revealed in aforementioned cases, further analysis was performed under its supervision. The design of the secondary regulator alone was not sufficient to maintain the stability of the large complex interconnected power system networks. Thus, territorial control strategy was needed. Different ESDs such as RFBs, UCs and SMES were placed in both the areas of the LFC loop one after the other for the same load disturbances. The responses of the combined LFC-AVR system with different ESDs are compared in Figure 10 and were assessed numerically from a settling time point of view, as noted in Table 5, and they are further compared in the bar chart displayed in Figure 11 for easy observation. Analyzing the results depicted in Figure 11, we came to know that the deviations in frequency and line power flow were mitigated further, and the respective area terminal voltages were enhanced to a great extent. We also observed that for the different ESDs, such as RFBs, SMES and UCs, the RFBs showed more predominance in bringing the deviations in system responses to a steady condition more effectively. This was possible only because the quick response nature and lower cycle time of RFBs facilitates the complex combined LFC-AVR system to prevent hunting during load fluctuations compared to other ESDs.

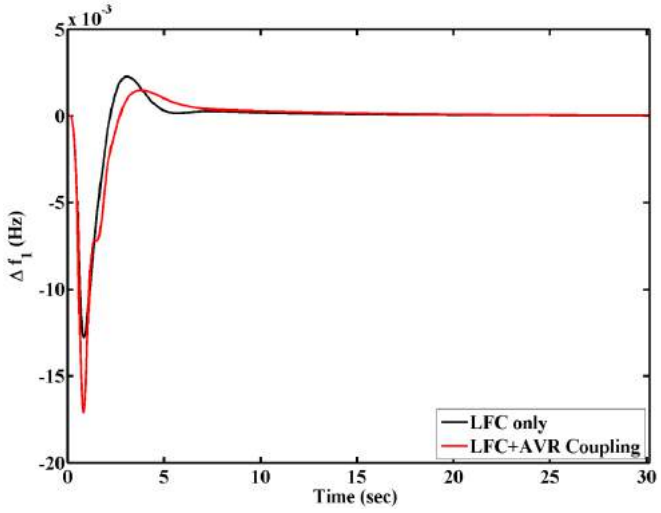

(**a**)

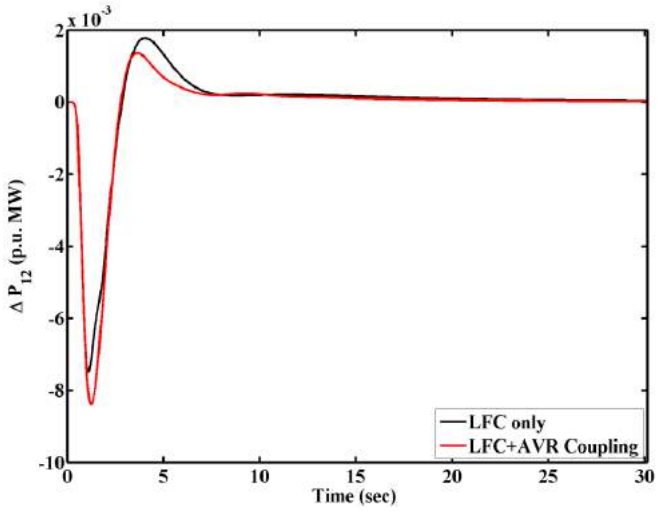

(**b**)

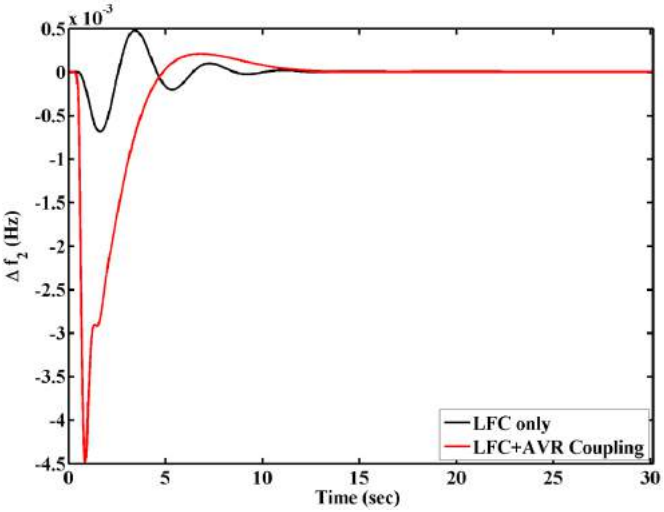

(**c**)

Figure 9. Responses for case-2: (**a**). Δf_1, (**b**). $\Delta Ptie_{12}$ and (**c**). Δf_2.

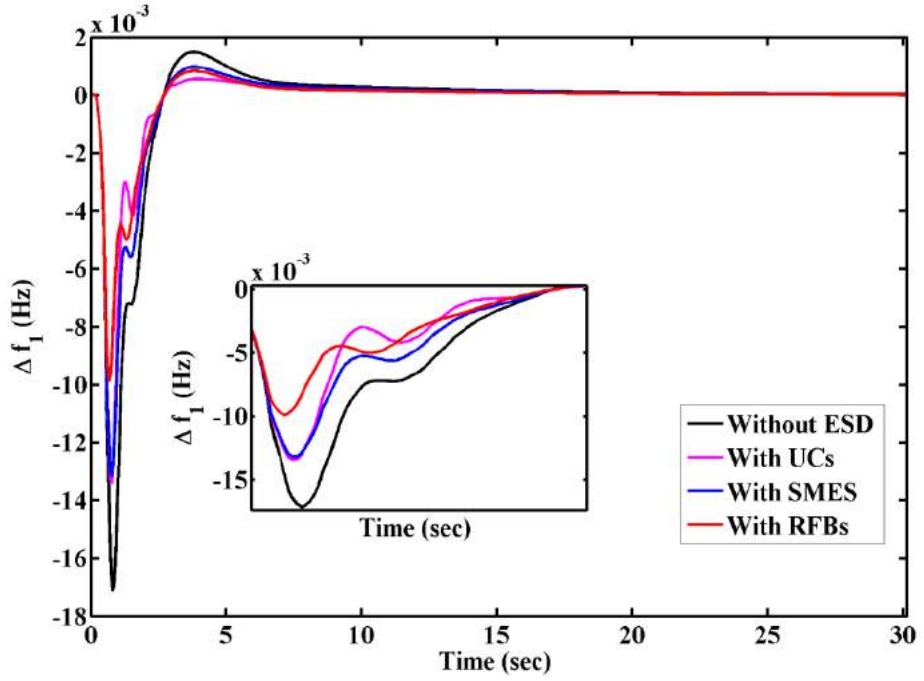

(**a**)

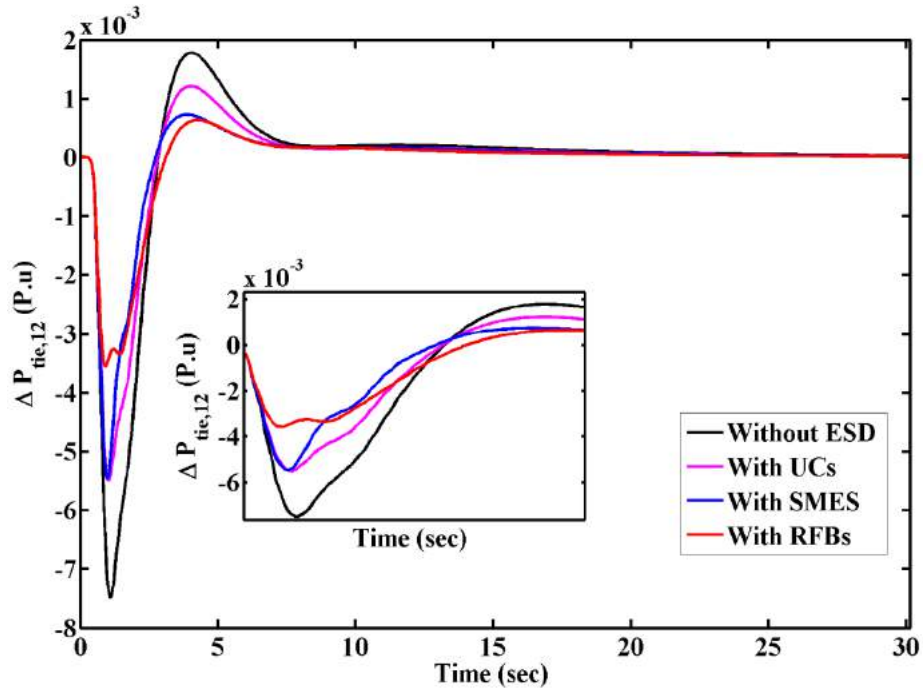

(**b**)

Figure 10. *Cont.*

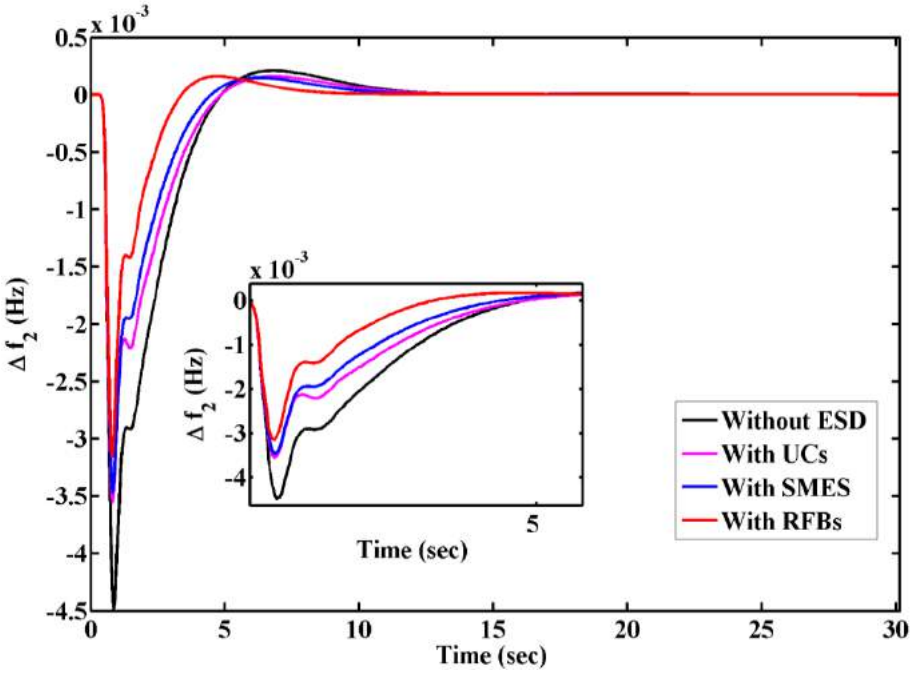

(**c**)

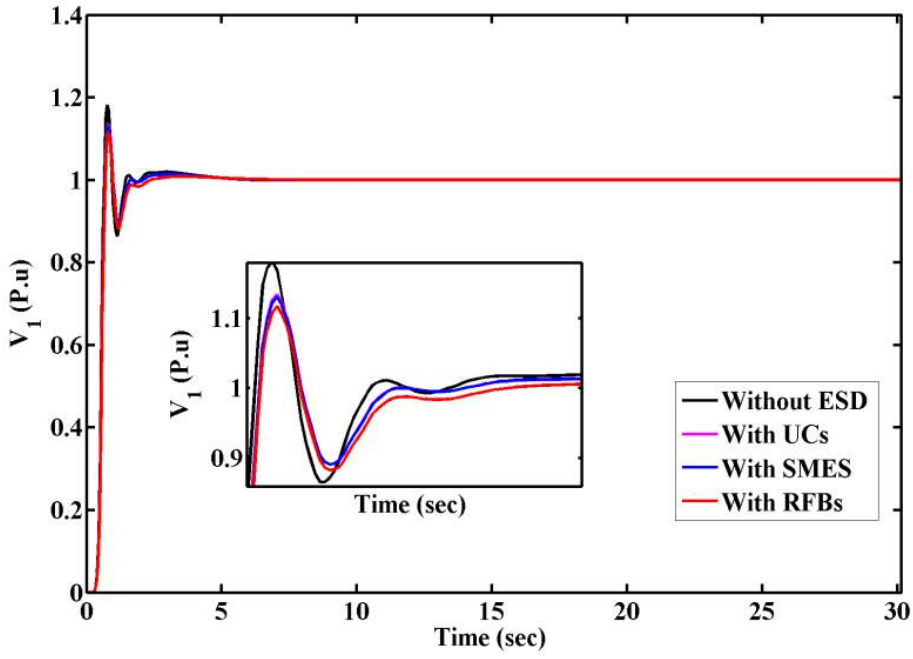

(**d**)

Figure 10. *Cont*.

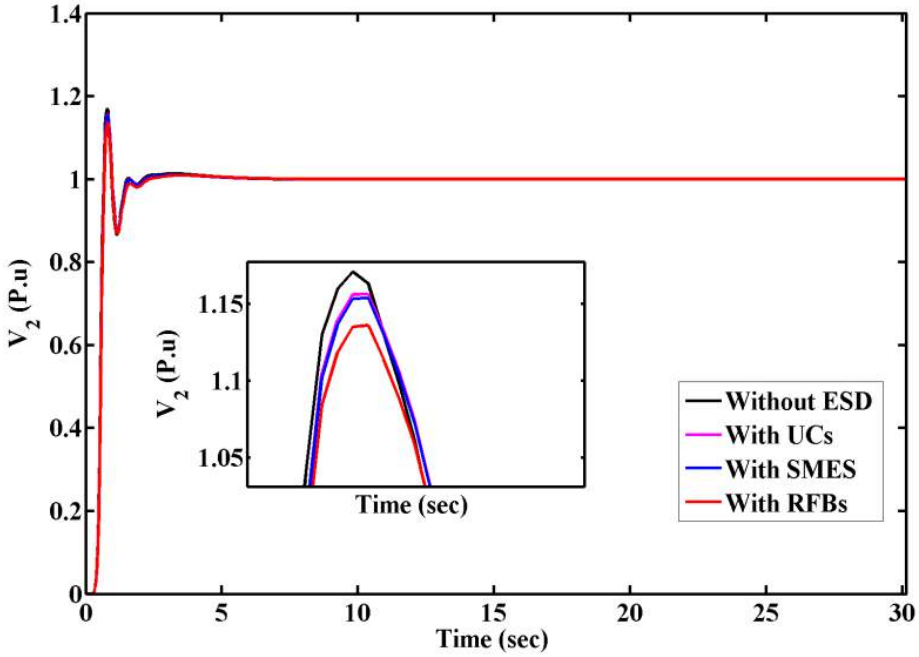

(**e**)

Figure 10. Responses for case-3: (**a**). Δf_1, (**b**). $\Delta Ptie_{12}$, (**c**). Δf_2, (**d**). V_1 and (**e**). V_2.

Table 5. Settling time of responses for case-3.

HAEFA: Fuzzy PID	Settling Time T_S (Sec)				
	Δf_1	Δf_2	ΔP_{tie12}	V_1	V_2
Without ESD	15.23	11.03	17.34	5.127	4.157
With UCs	14.55	9.92	16.90	4.125	3.821
With SMES	12.89	9.81	16.25	3.240	2.801
With RFBs	11.61	8.28	15.59	2.214	2.026

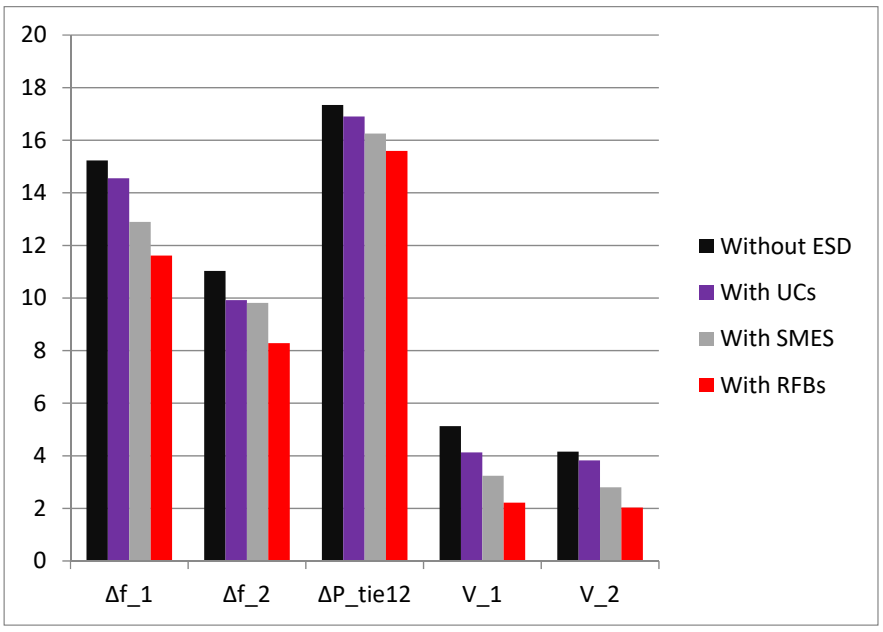

Figure 11. Comparison of responses' settling time (in seconds on Y-axis) for different ESDs.

8. Conclusions

The stability of frequency and voltage of the interconnected power system can be addressed simultaneously by connecting the AVR loop with the LFC using coupling coefficients. In this paper a HAEFA-tuned fuzzy PID was employed as a secondary regulator in both the LFC and AVR loops, and the dynamical analysis was carried out by laying area-1 with 10% SLP. The responses of LFC and AVR showcase the supremacy of fuzzy PID over classical PI and PID. Moreover, with fuzzy PID the ITAE function value was enhanced by 54.19% with PI and 41.67% with PID. However, the necessity of considering AVR coupling with the LFC loop was demonstrated and justified. Further, the combined system was incorporated with different ESDs such as RFBs, SMES and UCs one after the other in both the areas, and the system dynamical responses were compared to reveal the best one. The comparative results reveal that there as an enhancement in system dynamical behavior when incorporating ESDs in the view of the reduction in peak undershoot, overshoot and settling time. Moreover, out of all the ESDs the RFBs showed more predominance in the enhancement of system deviations and is recommended as the preferred territorial controller for the stability of interconnected power systems over the other ESDs.

Author Contributions: Conceptualization, C.N.S.K.; methodology, C.N.S.K.; validation, C.N.S.K., C.R.R., M.B. and S.K.; formal analysis, C.N.S.K., H.H.A. and P.S.; investigation, N.K.S. and M.B.; resources, B.S.G., S.K., H.H.A. and P.S.; writing—original draft preparation, C.N.S.K., C.R.R. and M.B.; writing—review and editing, N.K.S., C.N.S.K., M.B. and C.R.R.; visualization, B.S.G. and M.B. All authors have read and agreed to the published version of the manuscript.

Funding: This research received no external funding.

Institutional Review Board Statement: Not Applicable.

Informed Consent Statement: Not Applicable.

Data Availability Statement: No supplementary data available.

Acknowledgments: The authors thank the support of the National Research and Development Agency of Chile (ANID), ANID/Fondap/15110019.

Conflicts of Interest: The authors declare no conflict of interest.

References

1. Kalyan, C.S.; Rao, G. Demonstrating the Effect of Excitation Cross Coupling and Communication Time Delays on Automatic Generation Control. In Proceedings of the 2021 4th Biennial International Conference on Nascent Technologies in Engineering (ICNTE), Virtual, 15–16 January 2021; pp. 1–6. [CrossRef]
2. Fosha, C.E.; Elgerd, O.I. The Megawatt-Frequency Control Problem: A New Approach Via Optimal Control Theory. *IEEE Trans. Power Appar. Syst.* **1970**, *PAS-89*, 563–577. [CrossRef]
3. Dhanasekaran, B.; Siddhan, S.; Kaliannan, J. Ant colony optimization technique tuned controller for frequency regulation of single area nuclear power generating system. *Microprocess. Microsyst.* **2020**, *73*, 102953. [CrossRef]
4. Mohanty, B.; Hota, P.K. A hybrid chemical reaction- particle swarm optimization technique for automatic generation control. *J. Electr. Syst. Inf. Technol.* **2018**, *5*, 229–244. [CrossRef]
5. Yousri, D.; Babu, T.S.; Fathy, A. Recent methodology based Harris Hawks optimizer for designing load frequency control incorporated in multi-interconnected renewable energy plants. *Sustain. Energy Grids Netw.* **2020**, *22*, 100352. [CrossRef]
6. Guha, D.; Roy, P.; Banerjee, S. Load frequency control of interconnected power system using grey wolf optimization. *Swarm Evol. Comput.* **2016**, *27*, 97–115. [CrossRef]
7. Madasu, S.D.; Kumar, M.L.S.S.; Singh, A.K. A flower pollination algorithm based automatic generation control of inter-connected power system. *Ain Shams Eng. J.* **2018**, *9*, 1215–1224. [CrossRef]
8. Hakimuddin, N.; Khosla, A.; Garg, J.K. Centralized and decentralized AGC schemes in 2-area interconnected power system considering multi source power plants in each area. *J. King Saud Univ. Eng. Sci.* **2020**, *32*, 123–132. [CrossRef]
9. Barisal, A.; Mishra, S. Improved PSO based automatic generation control of multi-source nonlinear power systems interconnected by AC/DC links. *Cogent Eng.* **2018**, *5*, 1422228. [CrossRef]
10. Kalyan, C.N.S.; Rao, G.S. Performance comparison of various energy storage devices in combined LFC and AVR of multi area system with renewable energy integration. *Int. J. Renew. Energy Res.* **2020**, *10*, 933–944.

11. Kalyan, C.S.; Suresh, C.V. PIDD controller for AGC of nonlinear system with PEV integration and AC-DC links. In Proceedings of the 2021 International Conference on Sustainable Energy and Future Electric Transportation (SEFET), Virtual, 21–23 January 2021; pp. 1–6. [CrossRef]
12. Tasnin, W.; Saika, L.C. Comparative performance of different energy storage devices in AGC of multi-source system in-cluding geothermal power plant. *J. Renew. Sustain. Energy* **2018**, *10*, 024101. [CrossRef]
13. Zamani, A.; Barakati, S.M.; Yousofi-Darmian, S. Design of a fractional order PID controller using GBMO algorithm for load–frequency control with governor saturation consideration. *ISA Trans.* **2016**, *64*, 56–66. [CrossRef] [PubMed]
14. Jain, S.; Hote, Y.V. Design of fractional PID for Load frequency control via Internal model control and Big bang Big crunch optimization. *IFAC Pap. Line* **2018**, *51*, 610–615. [CrossRef]
15. Arya, Y.; Kumar, N. Design and analysis of BFOA- optimized fuzzy PI/PID controller for AGC of multi-area tradition-al/restructured electrical power systems. *Soft Comput.* **2017**, *121*, 6435–6452. [CrossRef]
16. Rajesh, K.; Dash, S.; Rajagopal, R. Hybrid improved firefly-pattern search optimized fuzzy aided PID controller for automatic generation control of power systems with multi-type generations. *Swarm Evol. Comput.* **2019**, *44*, 200–211. [CrossRef]
17. Nayak, J.R.; Shaw, B.; Sahu, B.K. Application of adaptive-SOS (ASOS) algorithm based interval type-2 fuzzy-PID controller with derivative filter for automatic generation control of an interconnected power system. *Eng. Sci. Technol. Int. J.* **2018**, *21*, 465–485. [CrossRef]
18. Arya, Y. Improvement in automatic generation control of two-area electric power systems via a new fuzzy aided optimal PIDN-FOI controller. *ISA Trans.* **2018**, *80*, 475–490. [CrossRef] [PubMed]
19. Gupta, A.; Chauhan, A.; Khanna, R.; Gupta, A.; Chauhan, A.; Khanna, R. Design of AVR and ALFC for single area power system including damping control. In Proceedings of the 2014 Recent Advances in Engineering and Computational Sciences (RAECS), Chandigarh, India, 6–8 March 2014; pp. 1–5. [CrossRef]
20. Rakhshani, E.; Rouzbehi, K.; Sadeh, S. A New Combined Model for Simulation of Mutual Effects between LFC and AVR Loops. In Proceedings of the 2009 Asia-Pacific Power and Energy Engineering Conference, Wuhan, China, 28–30 March 2009; pp. 1–5. [CrossRef]
21. Chandrakala, K.V.; Balamurugan, S. Simulated annealing based optimal frequency and terminal voltage control of multi source multi area system. *Int. J. Electr. Power Energy Syst.* **2016**, *78*, 823–829. [CrossRef]
22. Rajabongshi, R.; Saikia, L.C. Conbined control of voltage and frequency of multi-area multisource system incorporating solar thermal power plant using LSA optimized classical controllers. *IET Gener. Transm. Distrib.* **2017**, *11*, 2489–2498. [CrossRef]
23. Lal, D.K.; Barisal, A.K. Combined load frequency and terminal voltage control of power systems using moth flame optimization algorithm. *J. Electr. Syst. Inf. Technol.* **2019**, *6*, 1–24. [CrossRef]
24. Kalyan, C.H.N.S.; Rao, G.S. Impact of communication time delays on combined LFC and AVR of a multi-area hybrid system with IPFC-RFBs coordinated control strategy. *Prot. Control. Mod. Power Syst.* **2021**, *6*, 1–20. [CrossRef]
25. Kalyan, C.N.S.; Rao, G.S. Coordinated SMES and TCSC Damping Controller for Load Frequency Control of Multi Area Power System with Diverse Sources. *Int. J. Electr. Eng. Inform.* **2020**, *12*, 747–769. [CrossRef]
26. Kalyan, C.N.S.; Rao, G.S. Frequency and voltage stabilisation in combined load frequency control and automatic voltage regulation of multiarea system with hybrid generation utilities by AC/DC links. *Int. J. Sustain. Energy* **2020**, *39*, 1009–1029. [CrossRef]
27. Rajbongshi, R.; Saikia, L.C. Coordinated performance of interline power flow controller and superconducting magnetic energy storage in combined ALFC and AVR system under deregulated environment. *J. Renew. Sustain. Energy* **2018**, *10*, 044102. [CrossRef]
28. Kalyan, C.N.S.; Venkateswarlu, A.N.; Reddy, C.R.; Goud, B.S.; Prasad, A.G.; Sriram, C.; Aymen, F. Frequency reg-ulation of multi area renewable energy source system with practical constraints under fractional-order fuzzy controller. *Int. J. Renew. Energy Res.* **2021**, *11*, 992–1002.
29. Kalyan, C.N.S.; Rao, G.S. Performance Index-Based Coordinated Control Strategy for Simultaneous Frequency and Voltage Stabilization of Multi-area Interconnected System. In *Control Applications in Modern Power System*; Singh, A.K., Tripathy, M., Eds.; Lecture Notes in Electrical Engineering; Springer: Singapore, 2021; pp. 45–55. [CrossRef]
30. Kalyan, C.N.S.; Rao, G.S. Coordinated control strategy for simultaneous frequency and voltage stabilisation of the multi-area interconnected system considering communication time delays. *Int. J. Ambient. Energy* **2021**, 1–13. [CrossRef]
31. Kalyan, C.N.S.; Suresh, C.V. Differential Evolution based Intelligent Control Approach for LFC of Multiarea Power System with Communication Time Delays. In Proceedings of the 2021 International Conference on Computing, Communication, and Intelligent Systems (ICCCIS), Greater Noida, India, 19–20 February 2021; pp. 868–873. [CrossRef]
32. Kalyan, C.N.S.; Goud, B.S.; Reddy, C.R.; Ramadan, H.S.; Bajaj, M.; Ali, Z.M. Water Cycle Algorithm Optimized Type II Fuzzy Controller for Load Frequency Control of a Multi-Area, Multi-Fuel System with Communication Time Delays. *Energies* **2021**, *14*, 5387. [CrossRef]
33. Kalyan, C.N.S.; Rao, G.S. Stabilizing Frequency and Voltage in Combined LFC and AVR System with Coordinated Performance of SMES and TCSC. In *Control Applications in Modern Power System*; Singh, A.K., Tripathy, M., Eds.; Lecture Notes in Electrical Engineering; Springer: Singapore, 2021; pp. 65–76. [CrossRef]
34. Kalyan, C.N.S. UPFC and SMES based Coordinated Control Strategy for Simultaneous Frequency and Voltage Stability of an Interconnected Power System. In Proceedings of the 2021 1st International Conference on Power Electronics and Energy (ICPEE), Bhubaneswar, India, 2–3 January 2021; pp. 1–6. [CrossRef]

35. Shankar, R.; Bhushan, R.; Chatterjee, K. Small-signal stability analysis for two-area interconnected power system with load frequency controller in coordination with FACTS and energy storage device. *Ain Shams Eng. J.* **2016**, *7*, 603–612. [CrossRef]
36. Anita; Yadav, A. AEFA: Artificial electric field algorithm for global optimization. *Swarm Evol. Comput.* **2019**, *48*, 93–108. [CrossRef]

SMES and TCSC Coordinated Strategy for Multi-area Multi-source System with Water Cycle Algorithm Based 3DOF-PID Controller

Article *in* Smart Science · March 2022

DOI: 10.1080/23080477.2022.2054199

CITATIONS
2

READS
133

6 authors, including:

Kalyan Challapalli
vvit
44 PUBLICATIONS **243** CITATIONS
SEE PROFILE

Srikanth Goud .B
Anurag College of Engineering
53 PUBLICATIONS **200** CITATIONS
SEE PROFILE

Mohit Bajaj
Graphic Era University
160 PUBLICATIONS **953** CITATIONS
SEE PROFILE

G Srinivasa Rao
CMR College of Engineering & Technology
35 PUBLICATIONS **57** CITATIONS
SEE PROFILE

Smart Science

ISSN: (Print) (Online) Journal homepage: https://www.tandfonline.com/loi/tsma20

SMES and TCSC Coordinated Strategy for Multi-area Multi-source System with Water Cycle Algorithm Based 3DOF-PID Controller

Ch. Naga Sai Kalyan, B. Srikanth Goud, Ch. Rami Reddy, Mohit Bajaj & G. Srinivasa Rao

To cite this article: Ch. Naga Sai Kalyan, B. Srikanth Goud, Ch. Rami Reddy, Mohit Bajaj & G. Srinivasa Rao (2022): SMES and TCSC Coordinated Strategy for Multi-area Multi-source System with Water Cycle Algorithm Based 3DOF-PID Controller, Smart Science, DOI: 10.1080/23080477.2022.2054199

To link to this article: https://doi.org/10.1080/23080477.2022.2054199

Published online: 21 Mar 2022.

SMART SCIENCE
https://doi.org/10.1080/23080477.2022.2054199

Taylor & Francis
Taylor & Francis Group

SMES and TCSC Coordinated Strategy for Multi-area Multi-source System with Water Cycle Algorithm Based 3DOF-PID Controller

Ch. Naga Sai Kalyan [a], B. Srikanth Goud [b], Ch. Rami Reddy [c], Mohit Bajaj [d] and G. Srinivasa Rao [e]

[a]Department of Electrical and Electronics Engineering, Vasireddy Venkatadri Institute of Technology, Guntur, India; [b]Department of Electrical and Electronics Engineering, Anurag College of Engineering, Ghatkesar, India; [c]Department of Electrical and Electronics Engineering, Malla Reddy Engineering College (A), Secunderabad, India; [d]Department of Electrical and Electronics Engineering, National Institute of Technology Delhi, New Delhi, India; [e]Department of Electrical and Electronics Engineering, CMR College of Engineering & Technology, Kandlakoya, Medchal, India

ABSTRACT

This paper attempted to assess the supremacy of designed higher-order degree of freedom (DOF) proportional(P)-integral(I)-derivative(D) (PID) (3DOF-PID) controller making use of a new meta-heuristic optimization approach of water cycle algorithm (WCA) in the study of load frequency control. For this, two test system models of dual area hydro-thermal system system and multiarea multisource systems are believed for investigative purposes. The investigation is performed by imparting the area-1 of test system models with a disturbance of 10% step load (10%SLP). Parameters of 3DOF-PID are rendered optimally over the index of integral square error. Efficacy of the presented 3DOF-PID regulator fine-tuned with WCA is demonstrated with other control schemes that have been implemented on the same test systems. Moreover, superconducting magnetic energy storage and Thyristor controlled series compensator territorial schema is implemented for the MSMA system for performance enhancement. Finally, the robustness of the presented approach is demonstrated through sensitivity analysis.

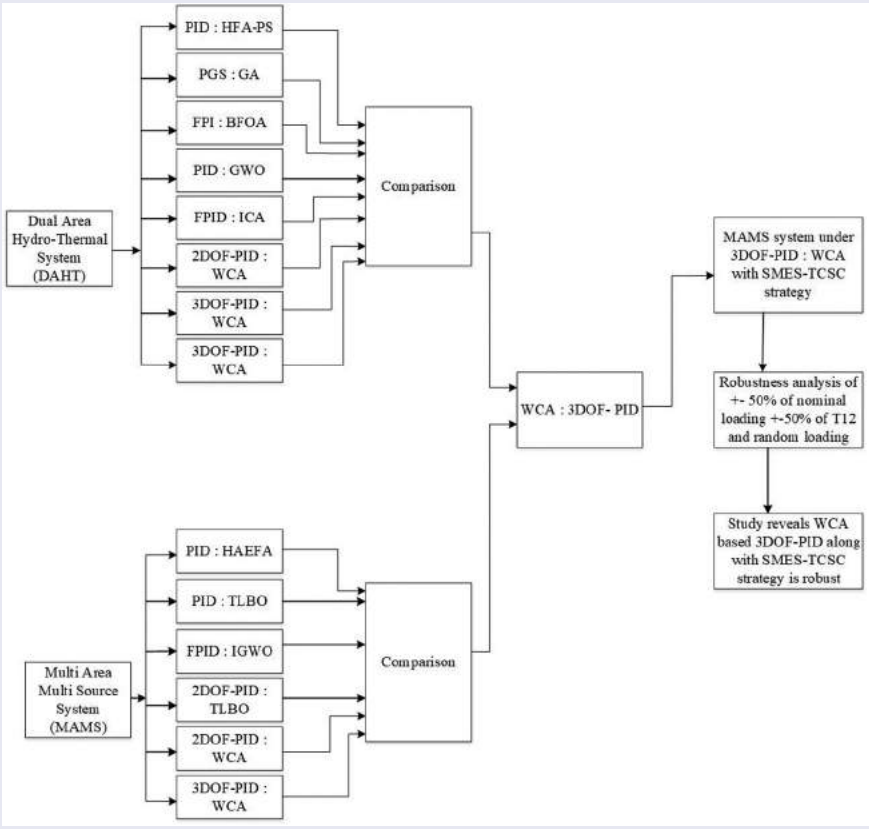

ARTICLE HISTORY
Received 11 July 2021
Accepted 4 March 2022

KEYWORDS
3DOF-PID controller; water cycle algorithm; 10%SLP; LFC; SMES-TCSC

CONTACT B. Srikanth Goud srikanth.b@anuraghyd.ac.in Department of Electrical and Electronics Engineering, Anurag College of Engineering, Ghatkesar 501301, India

1. Introduction

In the modern power system in today's era, more generation units are penetrating the existing power grid to fulfill everlasting power demand. The power generating sources integrated with the grid are together running in synchronism and forms coherent groups named control areas. Each control area is intended to connect with other areas of different power generation sources through a tie-line for making the power system more reliable. These tie-lines facilitates the flow of power among inter areas, normally from surplus to deficit areas. During load fluctuations, the frequency of the area and power flow in a line will also fluctuate and sometimes they may even go beyond the pre-specified limits, which affect system stability. The stability of the power system will be maintained by dragging down the real power mismatch among generation and demand near-zero [1]. Up to a certain extent, this will be performed by the governor in the power generation unit by altering the operating point of the system to match the real power generation with demand. But, this governor can't handle the situations of huge demands. Therefore, during large disturbances, a redundant action is necessary to maintain the system stable. Hence, to overthrow these problems, load frequency controller is manifested.

Some of the control strategies that have been utilized by the researchers in the domain of LFC in recent studies are traditional PI/PID/PIDN [2,3], controllers with double derivative (DD) gain of IDD/PIDD [4], modified (M) PID (MPID) [5], fractional-order (FO) FOPI/FOPID [6], FOPI-FOPD, PIDN-FOID, intelligent fuzzy (F) designs of FPI/FPID [7,8], fuzzy gain scheduling (FGS) [9], FFOPI-FOPD [10], artificial neural network (ANN) [11], etc. Even though several intelligent and ANN-based controllers are initiated to govern power system frequency fluctuations, most of the researchers are focused on the implementation of traditional control schemes because of design simplicity. However, to accommodate the performance of large interconnected systems, these traditional controllers are not adequate. Moreover, designing fuzzy involves plenty of assumptions that directly affect the controller efficacy. However, ANN-based regulator design needs a proper selection of non-linear activation functions and conceiving of hidden layers, which is the most complex task [12]. Degree of freedom (DOF) controllers involve independent control loops that facilitate effective and robust control schemes. Although 2DOF-PID/3DOF-PID [13] regulators are implemented in the study of LFC, their usage is limited to a certain extent only. The efficacy of DOF controllers especially 3DOF-PID possessing three independent regulatory loops has to be analyzed rigorously, especially for multiarea multisource (MAMS) systems so far. This motivates the authors to implement the 3DOF-PID regulator in this work as a load frequency controller.

Literature survey demonstrates that the performance of power system not solely resides on the construction of the controller but also relies on the appropriate selection of soft computing methods. Different natural inspired meta-heuristic approaches that have been implemented for controller optimizations in study of LFC are genetic algorithm (GA) [9], pattern search technique (PS) [14], bacteria foraging optimization algorithm (BFOA) [8], imperialist competitive algorithm (ICA) [10], biogeography-based optimizer (BBO) [13], grey wolf optimizer (GWO) [3], grass hopper optimization (GHO) [5], differential evolution (DE) [15], teaching learning-based optimizer (TLBO) [16], firefly algorithm (FA) [17], whale optimization algorithm (WOA) [18], particle swarm optimization (PSO), artificial field algorithm (AEFA) [2], and some other hybrid (h) approaches of DE-AEFA [12], hFA-PS [19], improved (I) IGWO [20], etc.

In the present era, several stochastic-based and population-based optimization methods are evolving. Different domains of fields have been researched with rapidly evolving optimization techniques. The soft computing methods that are evolved so far are encountered with several demerits such as slow convergence, the tendency of getting trapped into local minimum solution, unable to hold the equilibrium between the phases of exploration and exploitation, etc. This facilitates the scope of implementing new evolving techniques, especially for engineering optimizations. In this regard, a natural meta-heuristic approach of the water cycle algorithm (WCA) inspired by the water cycle, proposed by researchers [21], is implemented in this paper for power system optimization. This algorithm is equipped with evaporation and rain loop especially to maintain the equilibrium among the phases of exploration and exploitation, and it is having the capability to overcome the aforementioned demerits that most of the optimization algorithms are suffering.

The major contributions of this paper are

(a) Designed the 3DOF-PID controller optimized with the WCA approach and is implemented to the LFC study successfully.
(b) Working of the presented 3DOF-PID is tested on widely utilized DAHT and MAMS power system models.
(c) The supremacy of WCA-based 3DOF-PID in regulating system stability is revealed by comparing it with other controllers reported in literature.
(d) Superconducting magnetic energy storage (SMES)-thyristor controlled series compensator (TCSC) territorial control schema is established with MAMS system for performance boost up.
(e) A robustness test is finally conducted to validate the strength of the presented control approach.

2. Power system model

Considered two interconnected power system models in this paper to test the performance efficacy of 3DOF-PID based on the WCA presented control approach. The first test system is the DAHT model named test system-1 and the other is the MAMS system termed as test system-2 in this work. Test system-1 incorporates both hydro-thermal units in each area with unique generation capacities. However, the MAMS system comprises two areas having generation sources like hydro-thermal -gas in each area with equal capacity. The DAHT system and MAMS system displayed in Figures 1 and 2, respectively, are constructed in the platform of MATLAB/SIMULINK (R2016a). The parameters that are necessary to design these models had been taken from [2,19].

3. 3DOF-PID controller

In the study of LFC, traditional PID is employed in a widespread because of design simplicity. However, these traditional PIDs are no longer capable enough to govern the system with realistic uncertainties. But, higher-order DOF regulators can easily handle the nonlinear systems with their adjustable loops. DOF indicates the number of closed loops that can be aligned independently. 3DOF involves three independent loops that are accountable for responses shaping, stability improvement, and elimination of disturbances. The structure of 3DOF-PID [13] implemented in this work is displayed in Figure 3, where U(S) indicates the signal generated by 3DOF-PID to alter generator set point valves, R(S) represents reference signal, Y(S) indicates feedback from interconnected power system output, and D(S) indicates load disturbance. Moreover, the integral square error (ISE) constraint given in Equation (1) is adopted to find the optimal parameters using the WCA approach.

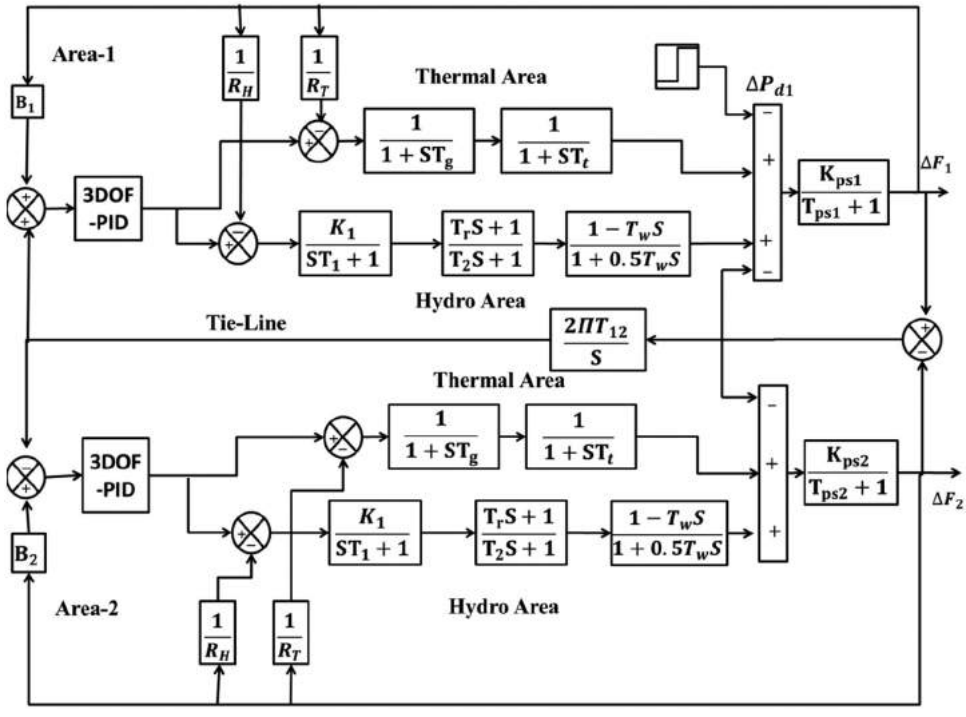

Figure 1. Model of DAHT system (test system-1).

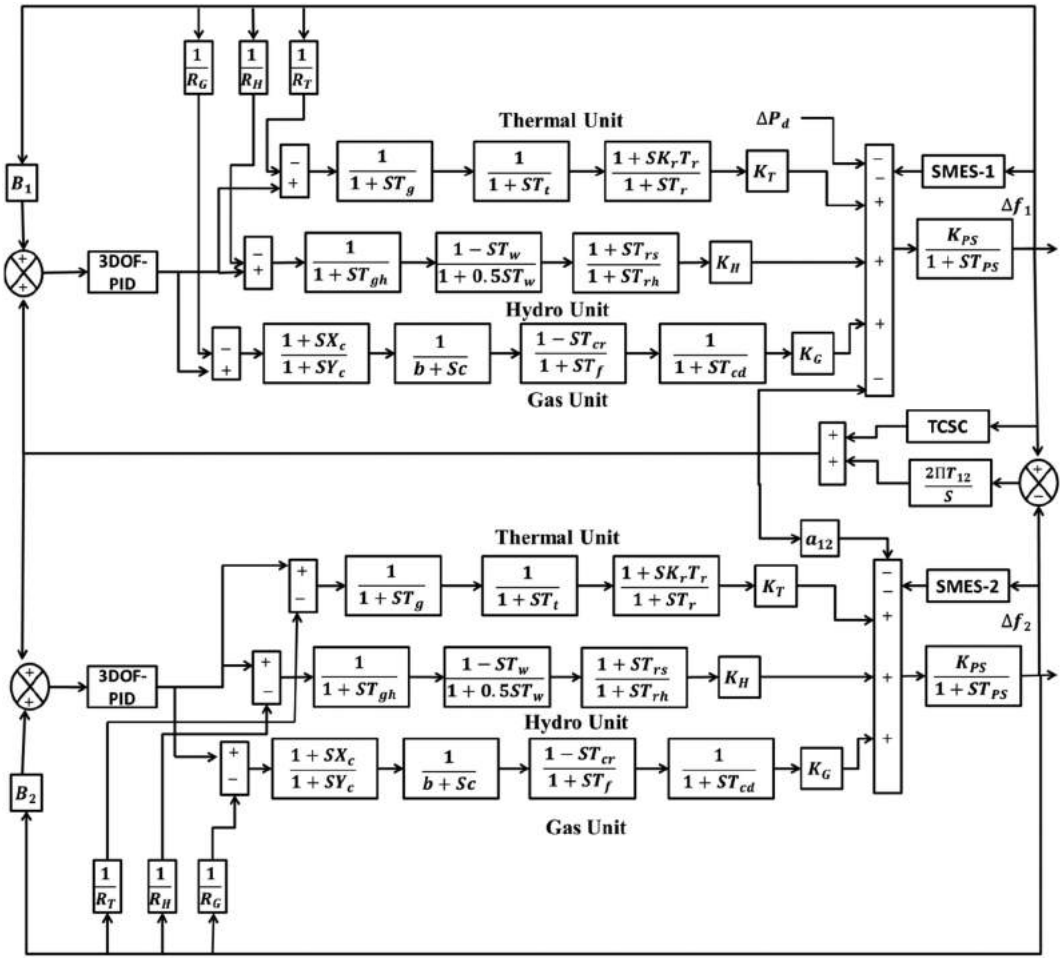

Figure 2. Model of MAMS system with SMES-TCSC strategy (test system-2).

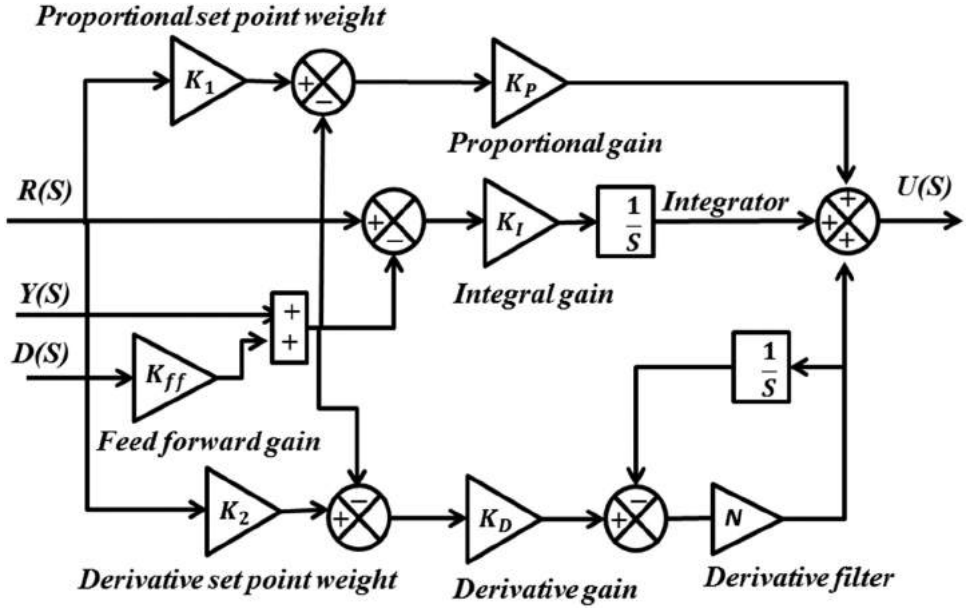

Figure 3. Structure of 3DOF-PID.

$$J_{ISE} = \int_0^T (\Delta f_1^2 + \Delta P_{tie,12}^2 + \Delta f_2^2)dt \quad (1)$$

4. SMES

Among all the ESDs, SMES devices will always be treated as the most prominent ones because of their static operation in the wide time range. The conductors in SMES possess the quality of superconductivity with almost zero resistance by enclosing them in a closed chamber containing liquid nitrogen or helium gas at cryogenic temperature. The conductors in SMES are wounded on a magnet, and the energy stored in the device is of a DC nature. Moreover, SMES also incorporates a power conversion unit (PCU) along with one step-down transformer. The PCU acts as interfacing between device and grid, whereas the charging/discharging of the conductor which is wounded around the magnet will be done through a step-down transformer. Normally, SMES devices get charged up at off-peak load durations and discharged immediately when there is a real power mismatch of demand and generation. The capability of storing bulk power, less cycle time, and negligible power loss motivates the authors to incorporate SMES devices in this work. The transfer function of SMES employed in this paper has been considered by [2] and is given in Equation (2).

$$G_{SMES} = \frac{K_{SMES}}{1 + ST_{SMES}} \quad (2)$$

5. TCSC

TCSC device can be designed by connecting thyristor controller reactor (TCR) with a capacitor in parallel. This TCSC is one of the inventions in FACTS devices of first-generation. TCSC is having the ability to alter the line parameters, thereby can regulate the line power flow. TCSC is induced with a tie-line of the interconnected system to regulate the dynamic flow of power during load disturbances to maintain system stability. TCSC is capable of handling dynamic, transient stability issues along with stabilizing the voltage in distant lines economically. Power flow control mechanism will be easily achieved by this TCSC device through adjusting capacitive reactance, thereby reducing in line reactance and enhancement in loading ability. The structure of TCSC implemented as a damping controller in this paper for the interconnected system is displayed in Figure 4.

The power flow deviation in tie-line ΔP^0_{tie12}, in general, be stated as

$$\Delta P^0_{tie12}(s) = \frac{2\pi T^0_{12}}{s}(\Delta f_1(s) - \Delta f_2(s)) \quad (3)$$

The flow of current in tie-line from area-1 to area-2 when incorporating TCSC in series can be stated as

$$i_{12} = \frac{|V_1|\langle\delta_1 - |V_2|\langle\delta_2}{j(X_{12} - X_{TCSC})} \quad (4)$$

Where X12 and XTCSC indicate the reactance of tie-line and TCSC, respectively.

The net tie-line power flow can be modeled as

$$P_{tie} - jQ_{tie} = V_1^* i_{12} = |V_1|\langle -(\delta_1) \left[\frac{|V_1|\langle\delta_1 - |V_2|\langle\delta_2}{j(X_{12} - X_{TCSC})}\right] \quad (5)$$

Equation (5) can be modified by separating the real power flow in tie-line be given as

$$P_{tie} = \frac{|V_1||V_2|}{(X_{12} - X_{TCSC})}\sin(\delta_1 - \delta_2) \quad (6)$$

Let, the compensation provided by the device TCSC be expressed as

$$k_c = \frac{X_{TCSC}}{X_{12}} \quad (7)$$

With Equation (7), Equation (6) can be modified as

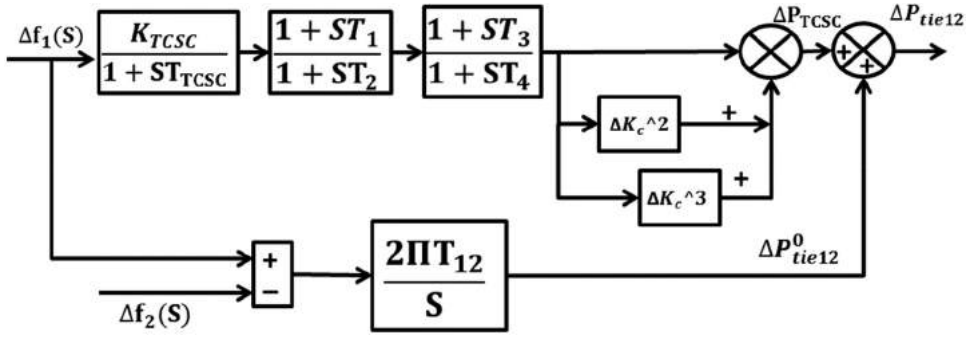

Figure 4. TCSC as damping controller.

$$P_{tie} = \frac{|V_1||V_2|}{X_{12}(1-k_c)}\sin(\delta_1 - \delta_2) \quad (8)$$

Usually, the parameters δ_1, δ_2, k_c are perturbed with small magnitudes i.e. $\Delta\delta_1$, $\Delta\delta_2$, Δk_c respective form nominal quantities of $\delta_1^0, \delta_2^0, k_c^0$. The incremental form of Equation (8) can be restated as

$$\Delta P_{tie} = \frac{|V_1||V_2|}{X_{12}(1-k_c^0)^2}\sin(\delta_1^0 - \delta_2^0)\Delta k_c + \frac{|V_1||V_2|}{X_{12}(1-k_c^0)}\cos(\delta_1^0 - \delta_2^0)(\Delta\delta_1 - \Delta\delta_2) \quad (9)$$

If $J_{12}^0 = \frac{|V_1||V_2|}{X_{12}(1-k_c^0)^2}\sin(\delta_1^0 - \delta_2^0)$ and $T_{12}^0 = \frac{|V_1||V_2|}{X_{12}(1-k_c^0)}\cos(\delta_1^0 - \delta_2^0)$ the above equation can be rewritten as

$$\Delta P_{tie} = \frac{J_{12}^0}{(1-k_c^0)^2}\Delta k_c + \frac{T_{12}^0}{(1-k_c^0)}(\Delta\delta_1 - \Delta\delta_2) \quad (10)$$

Since, $\Delta\delta_1 = 2\pi\ \Delta f_1 dt$ and $\Delta\delta_2 = 2\pi\ \Delta f_2 dt$ taking Laplace to transform to Equation (10) would become as

$$\Delta P_{tie} = \frac{J_{12}^0}{(1-k_c^0)^2}\Delta k_c(s) + \frac{T_{12}^0}{s(1-k_c^0)}(\Delta f_1(s) - \Delta f_2(s)) \quad (11)$$

Let, the input signal to the TCSC device be considered as ΔError(s) and the expression of $\Delta k_c(s)$ will be modeled by considering the transfer function of the TCSC power conditioning unit as follows [22]:

$$\Delta k_C(s) = \frac{K_{TCSC}}{1+sT_{TCSC}}\left(\frac{1+sT_1}{1+sT_2}\right)\left(\frac{1+sT_3}{1+sT_4}\right)\Delta\text{Error}(s) \quad (12)$$

Equation (12) be modified by considering $\Delta f_1(s)$ as error signal,

$$\Delta k_C(s) = \frac{K_{TCSC}}{1+sT_{TCSC}}\left(\frac{1+sT_1}{1+sT_2}\right)\left(\frac{1+sT_3}{1+sT_4}\right)\Delta f_1(s) \quad (13)$$

The change in power injected by the TCSC device in tie-line through compensation factor and is approximated [23] to third-degree polynomial in this work as

$$\Delta P_{TCSC} = \Delta K_C + \Delta K_C^2 + \Delta K_C^3 + - - - - - \quad (14)$$

Where the parameters T_1, T_2, T_3, and T4 indicate time constants of lag-lead compensator that are responsible for improving the system frequency response and the parameters K_{TCSC} and T_{TCSC} indicates gain and time constants of TCSC, respectively.

6. WCA algorithm

WCA algorithm is one of the newest naturally inspired meta-heuristic optimization approaches from the movement of water cycle proposed in the year 2012 in [21]. The procedure of searching in this WCA mechanism is started by initiating the raindrops as particles. These raindrops continuously flow downwards and gather to form streams/rivers. The content of streams/rivers lastly joined the sea. The water in streams, rivers, and sea gets evaporated forms the clouds and with raining the waters will again fall on earth. This procedure will be repeated until the global best solution, which is the sea is obtained. Moreover, the WCA has the strength to allocate maximum/minimum function values accurately with a high convergence rate. So, in this work, WCA is implemented for optimization of the power system through fine-tuning the parameters of the 3DOF-PID controller, which is employed as a secondary regulator. In detail, the problem is to render parameters of 3DOF-PID optimally to hold the stability of interconnected power systems especially even the generation units are targeted with heavy load disturbances.

The raindrops are initialized as follows for the problem having Nvar variables

$$RD_i = Y_i = [y_1, y_2 \ldots\ldots\ldots y_{Nvar}] \quad (15)$$

$$\text{RD Population} = \begin{bmatrix} RD_1 \\ - \quad - \quad - \\ RD_i \\ - \quad - \quad - \\ RD_{N_{POP}} \end{bmatrix} \quad (16)$$

However, the performance index of each raindrop is evaluated by employing equation (ISE), and later the raindrops are flown downwards and gathered from streams or rivers. The positions of streams and rivers are initialized assuming that these streams and rivers will join the sea at last.

$$P_{stream}^{new} = P_{stream} + \text{rand}() * C * (P_{river} - P_{stream}) \quad (17)$$

$$P_{river}^{new} = P_{river} + \text{rand}() * C * (P_{sea} - P_{river}) \quad (18)$$

Where "C" indicates constant takes the value from [0–2] and rand () takes from [0–1]. Suppose, the solution produced by the streams are by far beneficial than the solution generated by the river then the positions of rivers and streams are interchanged. A similar performa will apply to rivers and the sea. Furthermore, the loop of evaporation and rain is incorporated in the searching procedure to avoid the chances of getting trapped into minimum local value. This loop possesses a specific role

in this WCA approach and made the WCA algorithm most prominent in comparison to other recent optimization approaches. The process of evaporation end if

$$|P_{sea} - P_{river}| < d_{max} \tag{19}$$

$$d_{max}^{new} = d_{max} - (d_{max}//\max.\text{iteration}) \tag{20}$$

After the end of the evaporation process, the procedure of raining starts immediately as follows

$$P_{stream}^{new} = P_{sea} + \sqrt{U}\, X\, \text{rand}(1, N_{var}) \tag{21}$$

'U' represents the search rate closer to sea. After this, the termination of the main loop gets started when the algorithm satisfies the convergence criteria and the global best solutions are displayed. The flowchart of the WCA algorithm is displayed in Figure 5.

However, the efficacy of the WCA algorithm is tested on the standard benchmark function of Himmelblau's test function given in Equation (22).

$$f(x_1,x_2) = (x_1^2 + x_2 - 11)^2 + (x_1 + x_2^2 - 7)^2 \tag{22}$$

Along with the WCA algorithm, other algorithms such as PSO, gravitational search algorithm (GSA), ICA, and sine cosine algorithm (SCA) are also utilized to find the optimal values for x_1 and x2 one after the other for 100 iterations with a total population of 100. The convergence characteristics of all the algorithms are compared in Figure 6 and are concluded that the WCA approach finds the optimal solution within fewer iterations compared to other algorithms. Moreover, the function value starts low with WCA and yields an optimal solution with a high convergence rate.

7. Simulation results

Case-1: Performance analysis of DAHT system under various control approaches

To validate the performance efficacy of the proposed 3DOF-PID controller fine-tuned with the WCA approach, a widely accepted power system model of the DAHT system is believed. Area-1 of the DAHT system is targeted with a disturbance of 10%SLP for dynamical analysis. Different secondary controllers that are implemented to the same DAHT system by the researchers in the study of LFC such as PID-based hFA-PS [19], FGS-based GA [9], FPI tuned with BFOA [8], GWO-based PID [3], FPID rendered with ICA [7], and 2DOF-PID with WCA are considered one after the other. System responses under these methodologies are compared with the responses of the proposed 3DOF-PID rendered with the WCA approach in Figure 7. DAHT system dynamical behavior is interpolated numerically in terms of settling time placed in Table 1 to assess the stability. Pointing out the responses settling time in Table 1, elucidated that responses that are undergone deviations at the time of load disturbances are dragged to steady-state positions very effectively in quick time by proposed WCA-tuned 3DOF-PID secondary regulator compared to other controllers reported in recent literature. Furthermore, noticing Figure 7 visualized that under the monitoring of WCA-based 3DOF-PID, the deviations in system responses like undershoot/overshoots are lessened with various controllers that are proposed by the authors on the same test system model. This is possible due to the inheritance of three independent control loops in the 3DOF-PID regulator in shaping out the responses with oscillation free and dragging the deviations to a steady position. Moreover, the efficacy of the WCA metaheuristic approach also boosts up 3DOF-PID monitoring by rendering optimal parameters. Optimal gains of different regulators implemented in this case are noted in Table 2.

Case-2: Performance analysis of MAMS system under various control approaches

Later, the presented WCA optimized 3DOF-PID controller is implemented to another frequently utilized model of the MAMS system by the researchers. The MAMS system displayed in Figure 2, is also examined by targeting area-1 with 10% SLP. Various control schemes such as PID optimized with HAEFA [2] and TLBO [16], techniques, FPID using the IGWO approach [20], 2DOF-PID fine-tuned with TLBO [16], and WCA mechanisms are implemented to get the comparative analysis with the proposed regulatory scheme. The responses for this case are displayed in Figure 8, and the respective optimal gains are reciprocated in Table 3. System behavior under the supervision of aforementioned control approaches in terms of settling times, which are noted in Table 3 are interpolated, came to know that deviations with WCA-based 3DOF-PID are very less fluctuated and also reached a steady position in quick time. Moreover, the convergence characteristics of different soft computing technique-based controllers are rendered in Figure 9 and came into conclusion that with control strategy of proposed method yields the optimum solution in very less number of iterations, and the function value initially starts with less value by proposed scheme compared to other control techniques. Optimal gains of controllers employed in this subsection are noted in Table 4. The designed 3DOF-PID optimized with WCA metaheuristic approach outperforms intelligent FPID tuned with IGWO and traditional PID rendered with

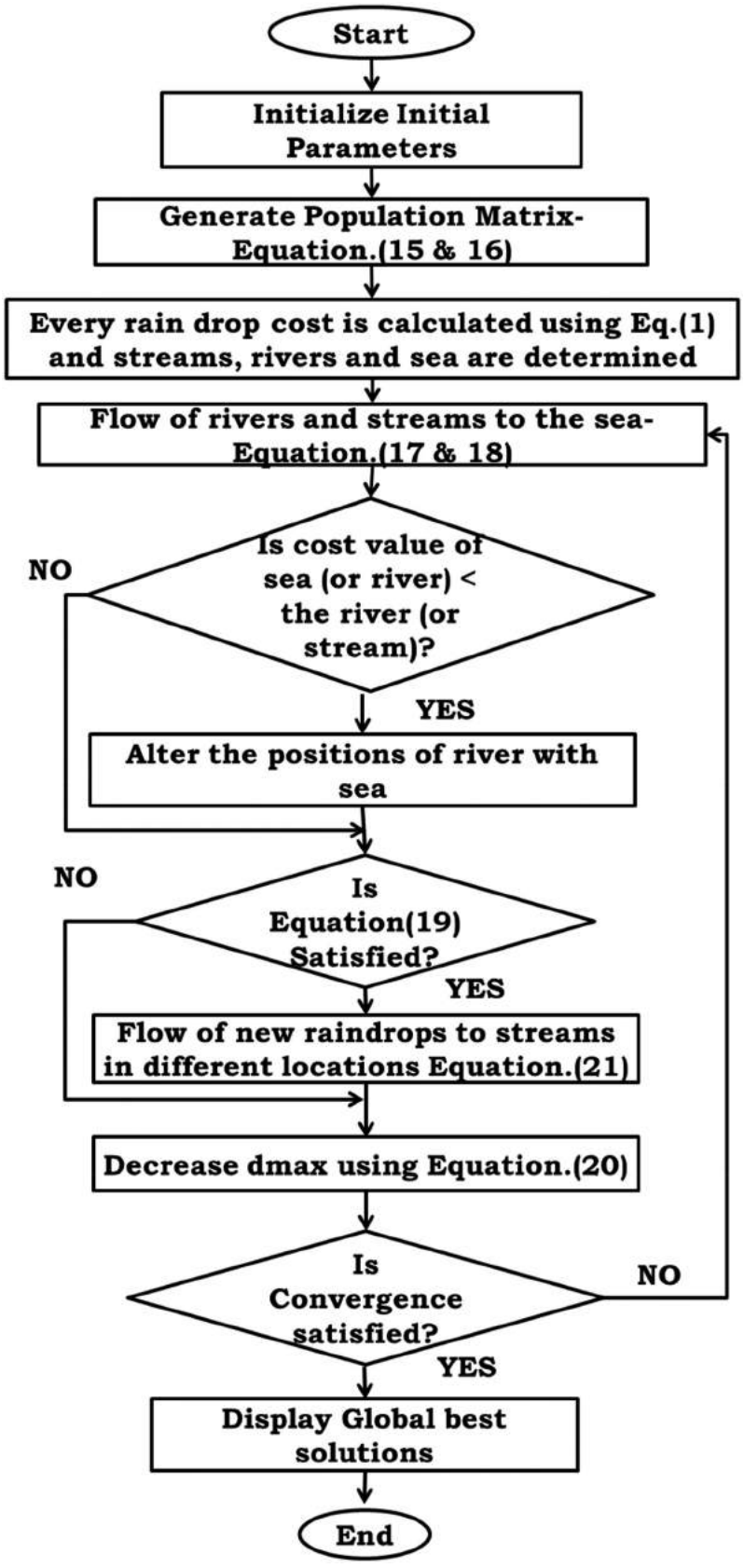

Figure 5. WCA flowchart.

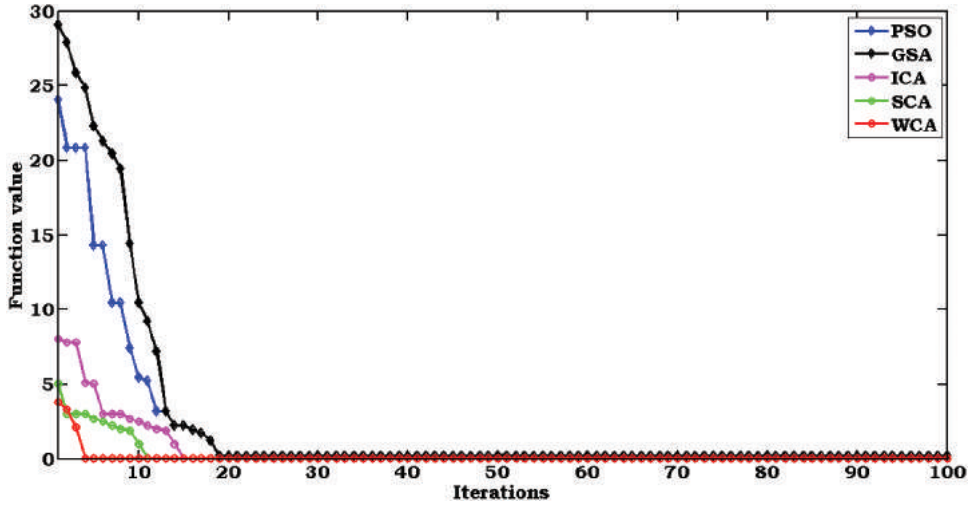

Figure 6. Convergence characteristics of various algorithms tested on Himmelblau's test function.

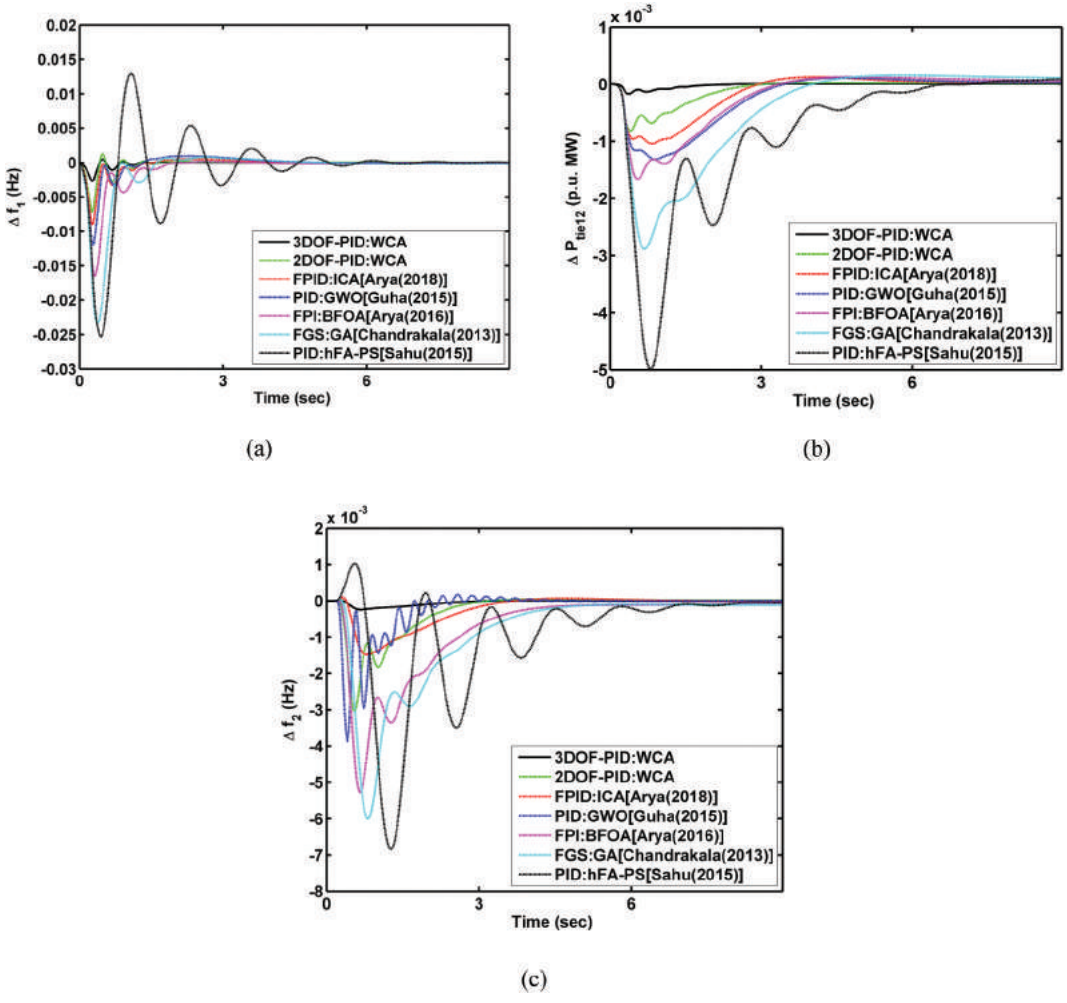

Figure 7. DAHT system responses for case-1. (a) Δf_1, (b) ΔP_{tie12}, (c) Δf_2.

Table 1. Objective value and settling time of responses for DAHT system under various controllers.

Settling Time	PID: hFA-PS	FGS: GA	FPI: BFOA	PID: GWO	FPID: ICA	2DOF-PID: WCA	3DOF-PID: WCA
Δf_1	10.585	8.513	6.312	4.779	4.037	3.525	2.865
ΔP_{tie12}	9.869	8.418	7.160	5.612	4.892	3.970	3.013
Δf_2	9.905	8.610	7.764	5.698	4.664	3.914	3.116
Index value	11.6E-02	9.71E-03	8.01E-03	6.11E-03	3.92E-03	6.73E-04	2.39E-04

Table 2. Optimal gains of controllers employed for DAHT system.

Gains		PID: hFA-PS	FGS: GA	FPI: BFOA	PID: GWO	FPID: ICA	2DOF-PID: WCA	3DOF-PID: WCA
Area-1	K_P	2.2161	1.1489	1.9761	1.4228	1.9067	1.3370	1.1434
	K_I	1.3464	0.6691	0.3386	0.8878	1.3257	1.1180	0.8781
	K_D	0.4912	0.3886	-	0.3989	0.9199	0.8155	0.3125
	K_1	-	-	-	-	-	0.3556	0.4300
	K_2	-	-	-	-	-	0.2512	0.5155
	K_{ff}	-	-	-	-	-	-	0.0740
Area-2	K_P	2.0228	0.9720	2.0244	1.2564	1.9136	1.4379	1.2367
	K_I	1.4206	0.7682	0.3287	0.6132	0.9752	1.2137	1.0912
	K_D	0.6006	0.3536	-	0.4509	0.8428	1.0144	0.4254
	K_1	-	-	-	-	-	0.3456	0.5054
	K_2	-	-	-	-	-	0.3542	0.3353
	K_{ff}	-	-	-	-	-	-	0.1908

Table 3. Objective value and settling time of responses for MAMS system under various controllers.

Settling Time	WCA: 3DOF-PID	WCA: 2DOF-PID	TLBO: 2DOF-PID	IGWO: FPID	IGWO: FPID	HAEFA: PID
Δf_1	7.23	8.52	11.93	14.97	14.97	21.31
ΔP_{tie12}	6.70	8.47	11.06	14.72	14.72	20.81
Δf_2	5.682	8.08	10.82	13.38	13.38	21.75
Index value	2.28 E-05	4.88 E-05	3.26 E-04	9.04 E-04	9.04 E-04	6.64 E-03

HAEFA and TLBO mechanisms. However, fuzzy inherits lot more assumptions in considering MFs and designing rule-base interface which affects its performance and traditional PID is not adequate to cope up with system during large disturbances.

Case-3: Performance analysis of MAMS system with coordinated SMES and TCSC control strategy

To exert power system monitoring and governing at another level, secondary regulator alone is not sustainable. Performance boost up in power system will be attained through the adoption of territory control schema. So, in this work, SMES-TCSC schema is implemented for the MAMS system to achieve performance enhancement, especially during heavy disturbances. Initially, only SMES devices are incorpo-

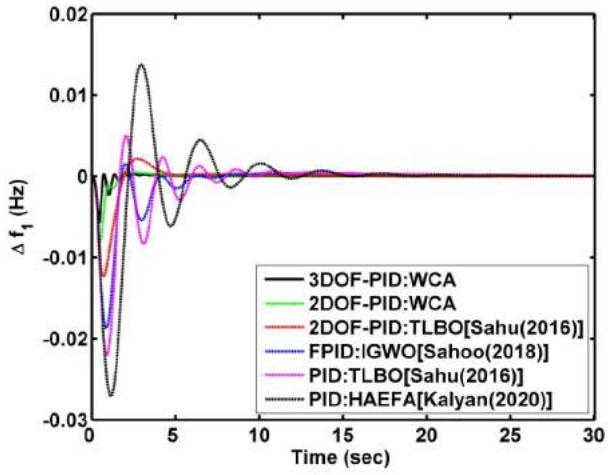

(a)

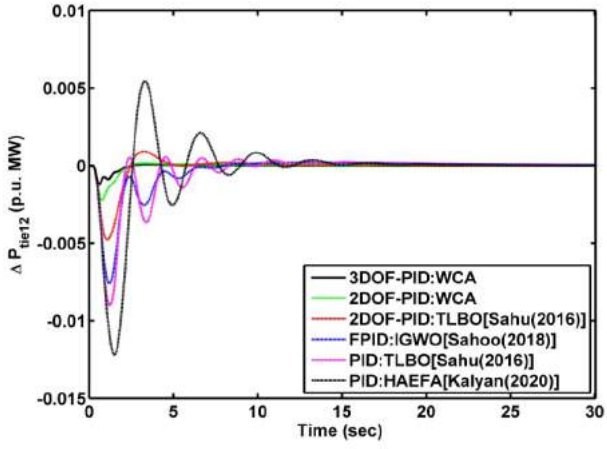

(b)

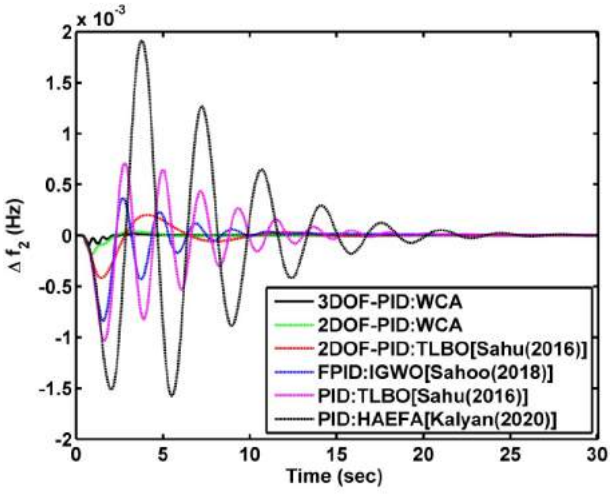

(c)

Figure 8. MAMS system responses for case-2. (a) Δf_1, (b) ΔP_{tie12}, (c) Δf_2.

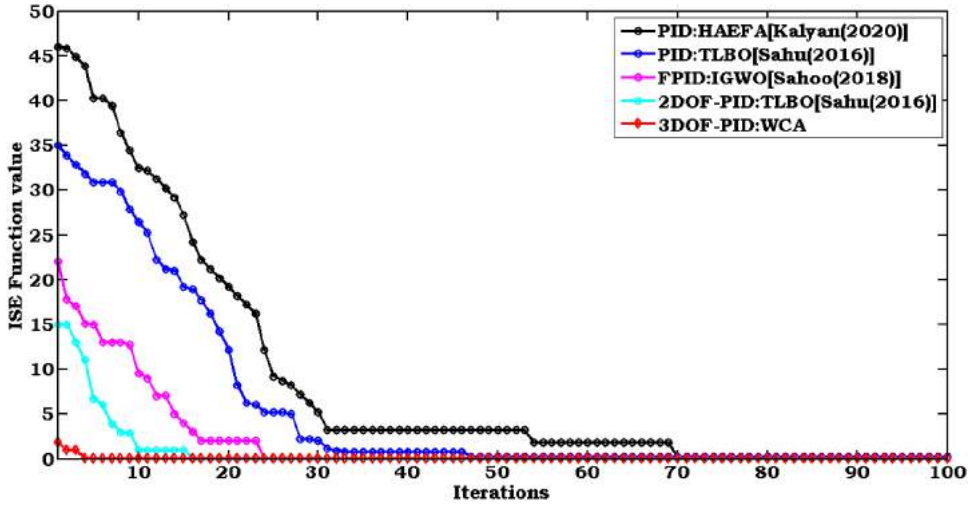

Figure 9. Convergence characteristics of different control approaches implemented to MAMS system.

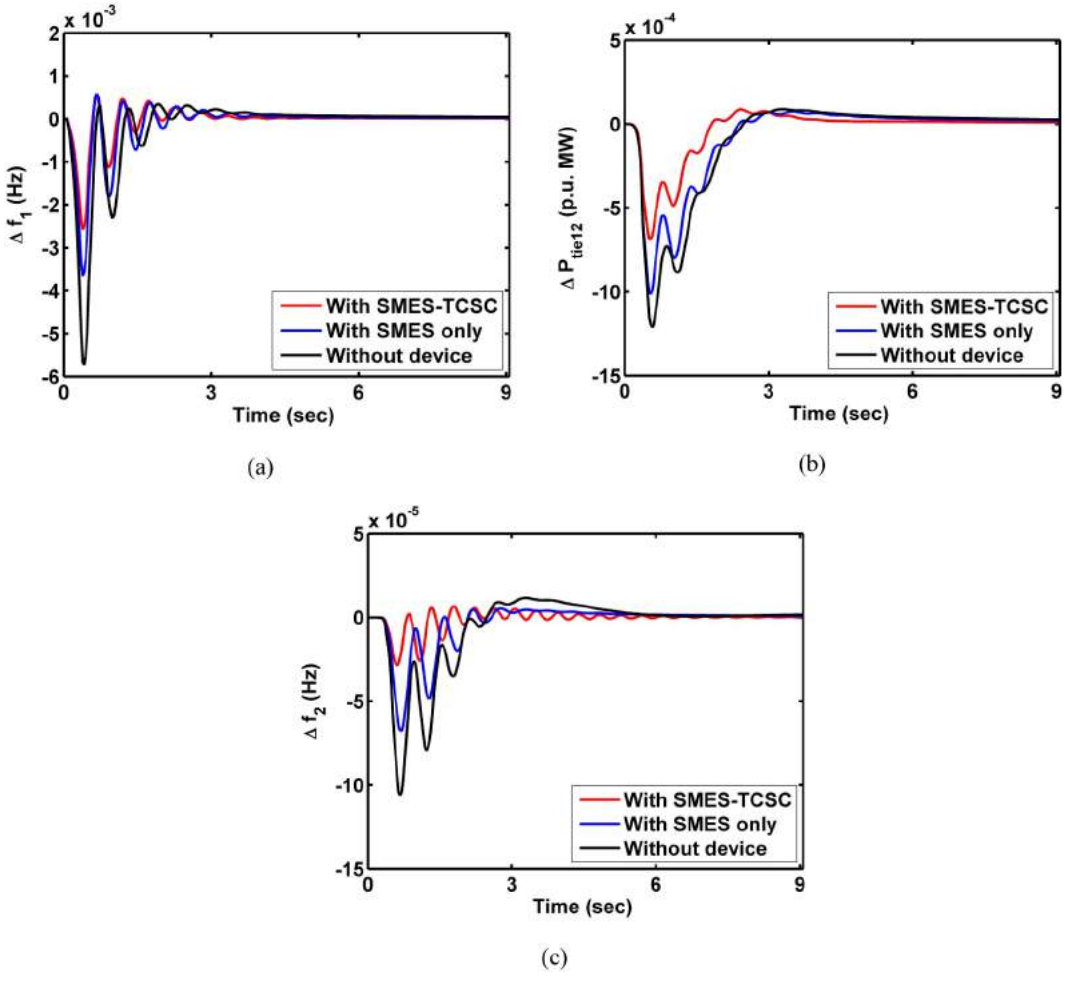

Figure 10. MAMS system responses for case-3. (a) Δf_1, (b) ΔP_{tie12}, (c) Δf_2.

Table 4. Optimal gains of controllers employed for MAMS system.

Parameters		WCA: 3DOF-PID	WCA: 2DOF-PID	TLBO: 2DOF-PID	IGWO: FPID	TLBO: PID	HAEFA: PID
Area-1	K_P	1.3129	1.1922	2.0278	2.1617	2.0921	3.7724
	K_I	1.3387	1.3592	1.7677	1.1025	1.1353	2.20348
	K_D	0.9232	0.8241	0.6135	0.8977	0.8368	0.7188
	K_1	0.3363	0.4334	0.3187	-	-	-
	K_2	0.3271	0.7794	0.2144	-	-	-
	K_{ff}	0.6755	-	-	-	-	-
Area-2	K_P	1.2153	1.6288	1.8177	2.0823	2.1021	2.3000
	K_I	1.2788	1.4289	1.5759	1.6975	1.7096	1.2446
	K_D	0.6376	0.4613	0.5599	0.5674	0.7321	0.7027
	K_1	0.2266	0.2048	0.2383	-	-	-
	K_2	0.5122	0.0368	0.2244	-	-	-
	K_{ff}	0.7881	-	-	-	-	-

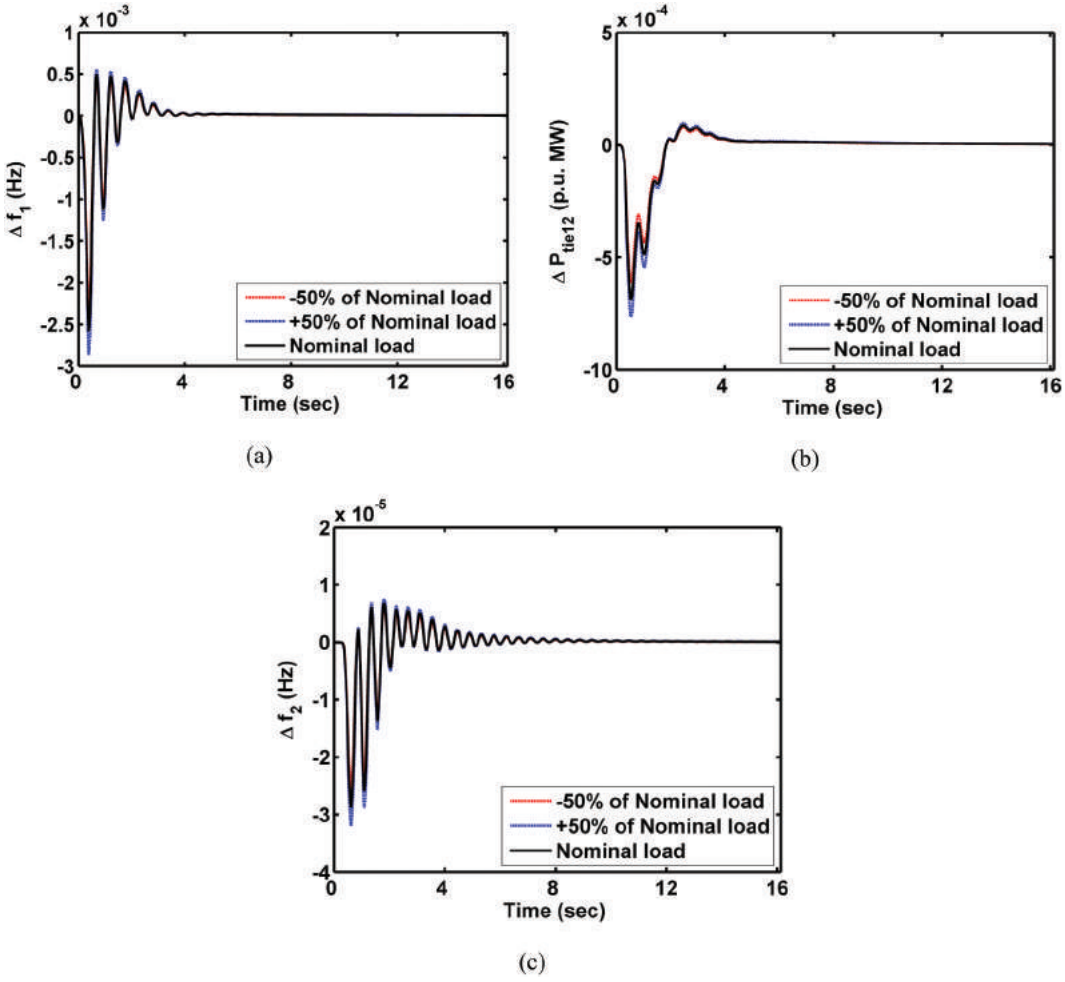

Figure 11. MAMS system responses for case-4 of load variations (a) Δf_1, (b) ΔP_{tie12}, (c) Δf_2.

rated in both the areas and the system responses are visualized. Later, TCSC is established with a tie-line and the SMES devices are unchanged. Behaviors of the system with these devices are displayed in Figure 10 and showcased more enhancements in responses with SMES-TCSC schema rather than of only SMES and without SMES-TCSC schema. This is achieved because of the quick discharging time of SMES and its capability of storing bulk power, also the features of TCSC in compensating the variations in power flow by altering line parameters. Numerical results for this case along with corresponding SMES-TCSC device parameters that are rendered optimally in the range of [0–1] are disclosed in Table 5.

Table 5. Settling time of MAMS system responses with SMES-TCSC scheme.

Parameters	Without Device	With only SMES	With SMES-TCSC
Δf_1	7.23	5.12	4.23
ΔP_{tie12}	6.70	6.047	5.305
Δf_2	5.682	5.25	4.71
Device Parameters	–	$K_{SMES} = 1.000$, $T_{SMES} = 0.9985$	$T_1 = 0.346, T_2 = 0.890$, $T_3 = 0.651, T_4 = 0.923$ $K_{TCSC} = 0.998, T_{TCSC} = 1.000$

Table 6. Numerical results of MAMS system responses for sensitivity analysis.

		Setting time (Ts)Sec			Peak undershoot (Us)		
Parameter	% Change	Δf_1	ΔP_{tie12}	Δf_2	Δf_1 (Hz) $\times 10^{-3}$	Δf_2 (Hz) $\times 10^{-5}$	$_{\Delta Ptie12} \times 10^{-4}$ (Pu. MW)
	Nominal Conditions	4.23	5.305	4.71	2.49	2.706	6.86
B_i	+50% of nominal value	4.12	5.21	4.63	2.32	2.67	6.29
	−50% of nominal value	4.38	5.65	5.31	2.51	2.90	7.21
T_t	+50% of nominal value	4.36	5.47	4.89	2.67	2.91	6.98
	−50% of nominal value	3.89	5.11	4.53	2.34	2.65	6.66
T_w	+50% of nominal value	4.49	5.66	4.98	2.71	2.89	6.96
	−50% of nominal value	4.12	5.22	4.66	2.19	2.56	6.29
T_{CD}	+50% of nominal value	5.07	5.98	5.32	2.76	3.01	7.08
	−50% of nominal value	3.99	5.19	4.39	2.34	2.18	5.89

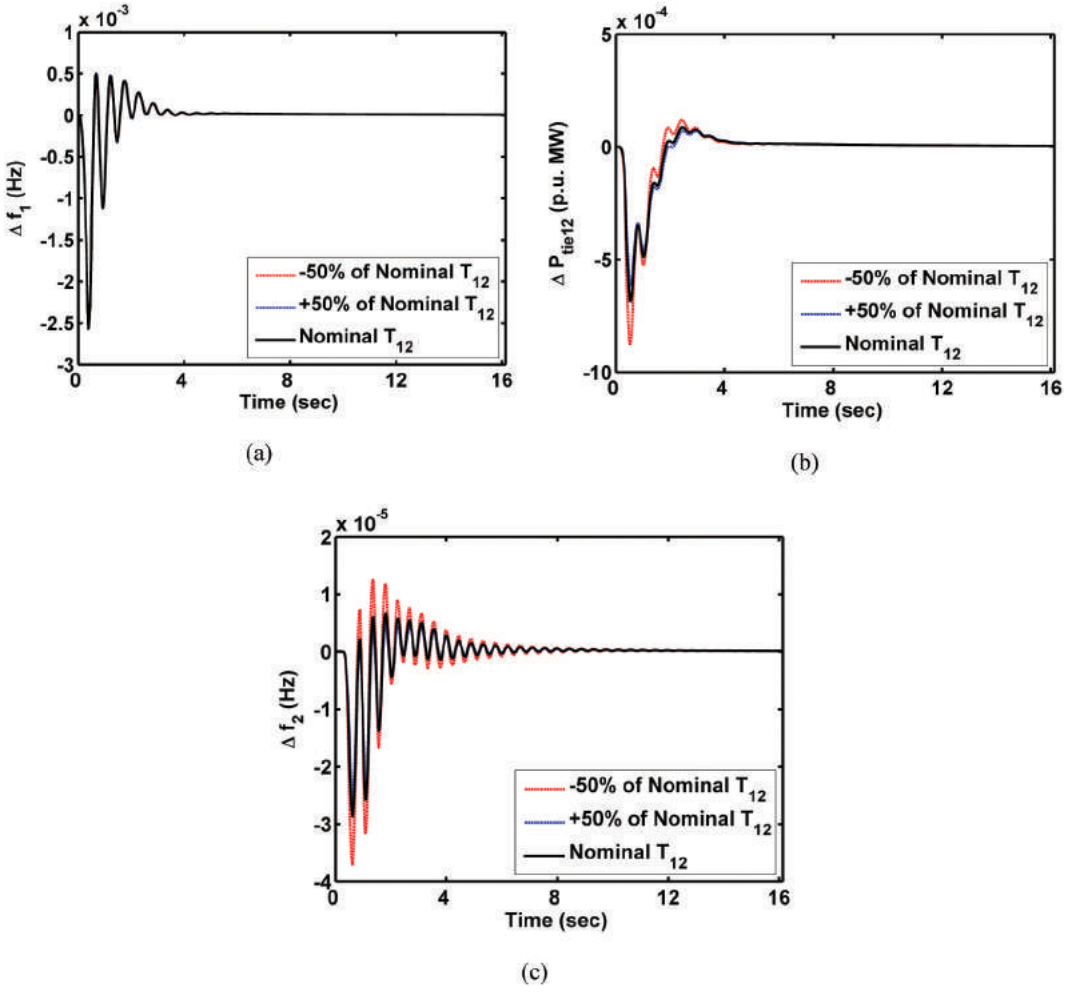

Figure 12. MAMS system responses for case-4 of variations in tie-line coefficient (a) Δf_1, (b) ΔP_{tie12}, (c) Δf_2.

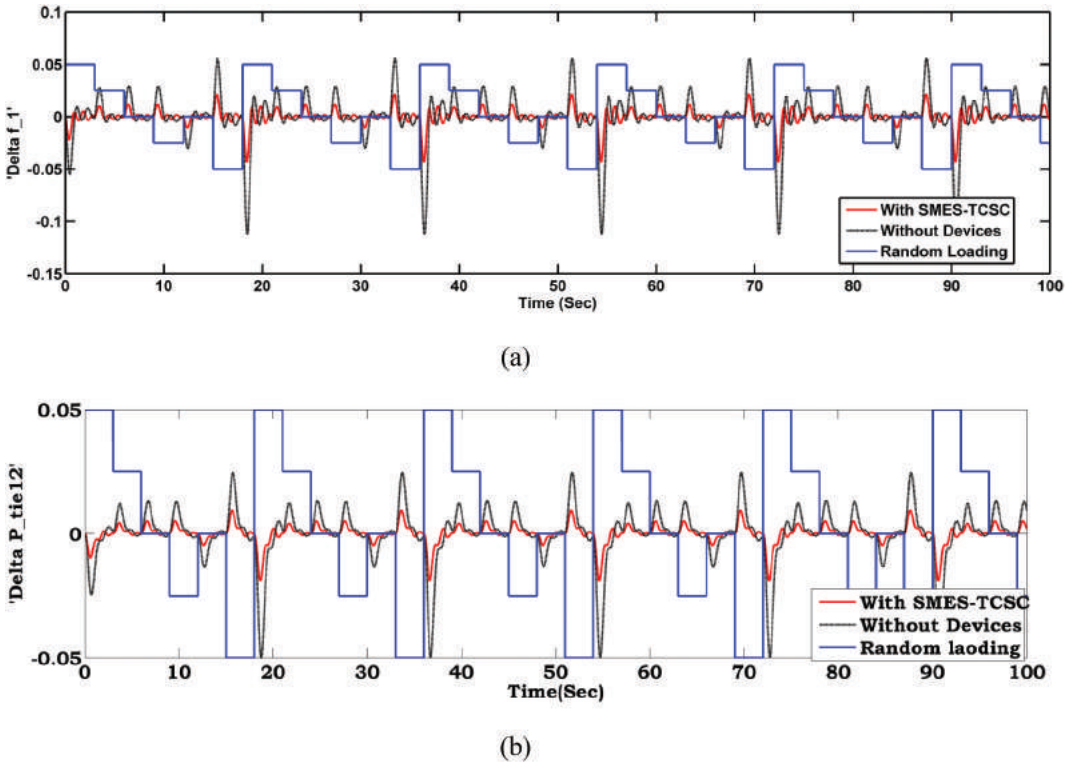

Figure 13. MAMS system responses for case-4 of random loadings (a) Δf_1, (b) ΔP_{tie12}.

Case-4: Sensitivity test on MAMS system

Finally, a sensitivity test is enforced to exhibit the robustness of the presented strategy. For this purpose, MAMS system parameters are varied to a wide extent and the system is targeted with large load fluctuations and also with random loadings. Figures 11 and 12 indicate the MAMS system responses for large load variations and also with variations in tie-line coefficient. Responses for random loadings are displayed in Figure 13. The numerical results for system responses of other parametric variations are listed in Table 6. This sensitivity analysis elucidated that the presented territorial schema along with WCA-based 3DOF-PID is good at holding system stability even in the case of system targeted with random loadings.

8. Conclusion

This paper demonstrated the sovereign of WCA-tuned 3DOF-PID regulator in ruling out the deviations in frequency and power flow in line with the interconnected power system in the study of LFC. This presented approach is tested on widely utilized power system models of DAHT system and MAMS systems. Sovereignty of WCA-tuned 3DOF-PID is established with controllers like hFA-PS-based PID, FGS based on GA, BFOA-based FPI, GWO-tuned PID, ICA-based FPID approaches on DAHT system and HAEFA-tuned PID, TLBO-tuned PID, IGWO-based FPID, and TLBO-based 2DOF-PID regulatory approaches on MAMS system reported in the literature. Simulation results visualized the extreme monarchy of 3DOF-PID based on the WCA algorithm in outperforming other traditional and intelligent-based controllers in maintaining the stability of power systems under disturbance conditions. Later, SMES-TCSC territorial schema is implemented for the MAMS system to boost up the performance. Finally, the MAMS system is subjected to random loadings and the parameters are also varied to a wide extent to test the presented approach robustness. The robustness test reveals the presented control schema can withstand the system stability even the parameters and loadings are varied to large extent.

Disclosure Statement

No potential conflict of interest was reported by the author(s).

ORCID

Ch. Naga Sai Kalyan http://orcid.org/0000-0002-9863-3580
B. Srikanth Goud http://orcid.org/0000-0002-5107-9738

Ch. Rami Reddy http://orcid.org/0000-0003-1941-0766
Mohit Bajaj http://orcid.org/0000-0002-1086-457X
G. Srinivasa Rao http://orcid.org/0000-0002-4776-5524

References

[1] Saadat H. 1999. Power system analysis. 1st ed. NY: McGraw-Hill.
[2] Kalyan CNS, Rao GS. Coordinated SMES and TCSC damping controller for load frequency control of multi area power system with diverse sources. Int J Elect Eng Inform. 2020;12(4):747–769.
[3] Guha D, Roy PK, Banerjee S. Load frequency control of interconnected power system using grey wolf optimization. Swarm evol comput. 2016;27:97–115.
[4] Raju M, Saikia LC, Sinha N. Automatic generation control of a multi-area system using ant lion optimizer algorithm based PID plus second order derivative controller. Elect Power Energy Syst. 2016;80:52–63.
[5] Nosratabadi SM, Bornapour M, Gharaei MA. Grasshopper optimization algorithm for optimal load frequency control considering modified PID controller in restructured multi-resource multi-area power system with redox flow battery units. Control Eng Pract. 2019;89:204–227.
[6] Tasnin W, Saikia LC. Comparative performance of different energy storage devices in AGC of multi-source system including geothermal power plant. J Renewable Sustainable Energy. 2018;10 (2):024101.
[7] Arya Y. Automatic generation control of two-area electrical power systems via optimal fuzzy classical controller. J Franklin Inst. 2018;355(5):2662–2688.
[8] Arya Y, Kumar N. Design and analysis of BFOA-optimized fuzzy PI/PID controller for AGC of multi-area traditional/restructured electrical power systems. Soft comput. 2016;21(21):6435–6452.
[9] Chandrakala KRMV, Balamurugan S, Sankaranarayana K. Variable structure fuzzy gain scheduling based load frequency controller for multi-source multi-area hydro thermal system. Elect Power Energy Syst. 2013;53:375–381.
[10] Arya Y. A new optimized fuzzy FOPI-FOPD controller for automatic generation control of electrical power systems. J Franklin Inst. 2019;356 (11):5611–5629.
[11] Kassem AM. Neural predictive controller of a two area load frequency control for interconnected power system. Ain Shams Eng J. 2010;1(1):49–58.
[12] Kalyan CNS, Rao GS. Impact of communication time delays on combined LFC and AVR of a multi-area hybrid system with IPFC-RFBs coordinated control strategy. Protect Cont Mod Power Syst. 2021;6(7). DOI:10.1186/s41601-021-00185-z
[13] Rahman A, Saikia LC, Sinha N. Automatic generation control of an unequal four area thermal system using biogeography based optimized 3DOF-PID Controller. IET Generat Transm Dist. 2016;10(16):4118–4129.
[14] Khamari D, Sahu RK, Sekhar GT, et al. Automatic generation control of power system in deregulated environment using hybrid TLBO and pattern search technique. Ain Sham Eng J. 2020;11(3):553–573.
[15] Sahu RK, Panda S, Rout UK. DE optimized parallel 2-DOF PID controller for load frequency control of power system with governor dead-band nonlinearity. Elect Power Energy Syst. 2013;49:19–33.
[16] Sahu RK, Panda S, Rout UK, et al. Teaching learning based optimization algorithm for automatic generation control of power system using 2-DOF PID controller. Elect Power Energy Syst. 2016;77:287–301.
[17] Pradhan PC, Sahu RK, Panda S. Firefly algorithm optimized fuzzy PID controller for AGC of multi-area multi-source power systems with UPFC and SMES. Eng Sci Technol Int J. 2016;19(1):338–354.
[18] Saha A, Saikia LC. Renewable energy source based multi area AGC system with integration of EV utilizing cascade controller considering time delay. Int Trans Elect Energy Syst. 2018. DOI:10.1002/etep.2646
[19] Sahu RK, Panda S, Padhan S. A hybrid firefly algorithm and pattern search technique for automatic generation control of multi area power systems. Elect Power Energy Syst. 2015;64:9–23.
[20] Sahoo BP, Panda S. Improved grey wolf optimization technique for fuzzy aided PID controller design for power system frequency control. Sust Energy Grids Net. 2018;16:278–299.
[21] Eskanda H, Sadollah A, Bahereininejad A, et al. Water cycle algorithm- a novel meta-heuristic optimization method for solving constrained engineering optimization problems. Comput Struct. 2012;110 :151–166.
[22] Nandi M, Shiva CK, Mukherjee V. TCSC based automatic generation control of deregulated power system using quasi-oppositional harmony search algorithm. Eng Sci Technol Int J. 2017;20(4):1380–1395.
[23] Lal DK, Barisal AK. Comparative performance evaluation of FACTS devices on AGC with diverse sources of energy generation and SMES. Cog Eng. 2017;4(1):1318466.

Journal of Electrical Engineering & Technology
https://doi.org/10.1007/s42835-022-01079-2

ORIGINAL ARTICLE

Faulted Section Identification and Fault Location in Power Network Based on Histogram Analysis of Three-phase Current and Voltage Modulated

Masoud Dashtdar[1] · K. Sarada[2] · Seyed Mohammad Sadegh Hosseinimoghadam[1] · C. H. Naga Sai Kalyan[3] · A. N. Venkateswarlu[4] · B. Srikanth Goud[5] · C. H. Rami Reddy[6] · Youcef Belkhier[7] · Mohit Bajaj[8] · B. Nagi Reddy[9]

Received: 26 May 2021 / Revised: 7 March 2022 / Accepted: 21 March 2022

Abstract
In the discussion of fault location due to the existence of multiple branches in the distribution network, different locations are obtained and this shows the importance of detecting the faulted section in the distribution network. In this paper, the new idea of modulating the current and three-phase voltage of the line's beginning and histogram analysis has been used for fault location in the power network. First, threephases of current and voltage of the line's beginning are converted separately through convolution into a modulated current signal and a voltage signal, respectively. Then by dividing the density ratio of the modulated voltage by the modulated current, the distance to fault location can be estimated; but there is the possibility of obtaining several fault locations in the distribution network. In the following, the faulted section can be estimated through a histogram analysis of the modulated voltage. Simulation results show that by modulating the three-phase voltage, there is a possibility to eliminate the effects of fault resistance, fault occurrence angle, fault type on the algorithm's accuracy. In the end, the suggested algorithm was implemented on a 735 kV transmission network and an IEEE-15bus distribution network whose results demonstrate the appropriate accuracy of the suggested algorithm.

Keywords Fault location · Distribution network · Histogram analysis · Convolution · Current and voltage modulated

1 Introduction

Considering the huge dependency of urban industries and consumers on electric energy, a power outage would cause severe economic damages to industries and would disrupt the daily life of subscribers. On the other hand, the possibility of random and unpredicted faults in the national electricity network exists and by reducing the fault location the time, the damages of a power outage could be minimized. So far and to accelerate the network repair and improve reliability,

✉ B. Srikanth Goud
srikanth.b@anuraghyd.ac.in

[1] Electrical Engineering Department, Bushehr Branch, Islamic Azad University, Bushehr, Iran

[2] Department of Electrical and Electronics Engineering, KLEF Deemed to Be University, Guntur 522502, India

[3] Department of Electrical and Electronics Engineering, VasireddyVenkatadri Institute of Technology, Guntur 522508, India

[4] Department of Electrical and Electronics Engineering, Vignan's Lara Institute of Technology and Sciences, Vadlamudi, Guntur 522213, India

[5] Department of Electrical and Electronics Engineering, Anurag College of Engineering, Ghatkesar, Telangana 501301, India

[6] Department of Electrical and Electronics Engineering, Malla Reddy Engineering College (A), Maisammaguda, Telangana 500100, India

[7] Department of Computer Science, Faculty of Electrical Engineering, Czech Technical University, Karlovo Namesti 13, Praha 2, 121 35 Prague, Czechia

[8] Department of Electrical and Electronics Engineering, National Institute of Technology, Delhi 110040, India

[9] Department of Electrical and Electronics Engineering, Vignana Bharathi Institute of Technology, Hyderabad, India

Published online: 07 April 2022

various methods have been presented for fault location [1]. But, nowadays, due toliving in a restructured environment and competition between companies in order to increasing energy access for consumers, system faults have received more attention. In addition in fault location approaches, methods have been presented for determining the fault section or distance especially in distribution networks [2–4].

Fault location methods can be classified into impedance methods, traveling waves and high-frequency components of fault current and voltage, and learning-based smart methods. Traveling wave methods have a complicated structure and are very expensive due to their use of sampling filters [5, 6]. Impedance methods have a relatively simple structure and employing them in protective relays is easily possible [7, 8]. But due to existence of multiple branches in the distribution network, using this method will lead to the estimation of multiple points in the network. Therefore, using this method in the distribution network depends on combining will a method that is capable of estimating the faulted section [4].

Along with existing approaches, methods based on learning algorithms can also be used as replacements for fault locating in the distribution network. In these methods, extracting effective features and employing appropriate learning algorithms are two major and effective issues in establishing learning methods [2, 3]. The problem with smart methods based on neural networks is when the power network has expanded or has changed its topology for whatever reason; in which case, all our train data must be reproduced and redesigned for the new network.

Nowadays, signal processing techniques have been used for fault location. One of the most used functions in signal processing is wavelet transform which enables us to extract the signal's high and low-frequency components which can play an important role in fault location. For instance, we can determine the fault location by applying wavelet transform on high-frequency samples of the fault signal recorded at the beginning of medium-voltage feeders and their endpoints [9]. A method has been presented in [10], which uses the wavelet transform for determining fault location using information recorded before and after the fault in the transmission network; which enables wavelet transform with high-resolution time for high-frequency components of fault transients. In [11–25], smart meter devices and artificial neural network techniques are used to detect the faulted section and fault location in the distribution network.

One of the techniques of signal processing in the domain of time is multiplying two signals and converting them into one signal, in a way that the new signal will have the features of both signals. On the other hand, high-frequency components are created in a fault occurrence, and therefore, in the frequency domain, the multiplication of two signals should be done through convolution. In this paper, the idea of convolution has been used to convert threephases of current and voltage into one current signal and one voltage signal; in a way that they will have all the frequency information of those threephases. Then, the fault location is estimated by the impedance method. The main difference is that in the impedance method, multiple fault locations are estimated and the accuracy of this method is highly dependent on line parameters. But in our proposed method, the fault location can be easily estimated using the histogram analysis technique which is not dependent on line parameters. In Sect. 2, the proposed method is described based on modulating the signal and histogram analysis. Section 3 discusses the implementation of the network and the fault location algorithm. In section 4, the results of this approach are presented and the conclusion is provided in section V.

2 Proposed Method

In this paper, the work foundation is based on the current histogram analysis and modulated voltage at the line's beginning, before and after the fault. Then in the first step and using convolution, the three-phase current and voltage recorded by measuring devices are converted into one current signal and one modulated voltage signal that preserves the frequency information of all three signals. Then, by dividing the density ratio of modulated voltage in the modulated current, the distance to fault location can be estimated. But the possibility of obtaining several points in the distribution network exists, and it could be estimated the fault location through histogram analysis of the modulated voltage (before and after the fault). Thus, our algorithm consists of three stages: modulating threephases of current and voltage, calculating the density of the modulated signal and in the end, histogram analysis to detect the faulted section.

2.1 Signal Convolution

In the time domain andduring multiple two signals performing, it couldbe done in a simple mathematical way. But in the frequency domain, multiplying two signals should be done through convolution. Convolution is a mathematical operator that acts on two functions of Va and Vb (a, b phase voltage) a third function (z) create that can be considered as the modified version of one of the main functions. Convolution is similar to the correlation function. Applications of this operator include statistics, computer vision, image processing, signal processing, electrical engineering, and differential equations. Convolution of two mathematical functions is obtained using Eq. (1):

$$Z = V_a * V_b \tag{1}$$

The sign * is the symbol for convolution. Convolution has some interesting features and properties:

$$V_a * \left(V_b * V_c\right) = \left(V_a * V_b\right) * V_c \quad (2)$$

A. Commutative property: commutative property exists in convolution; which means that if two signals or two functions swap places in the convolution, the result will not change.
B. Associative property: the associative property is also presentedin the convolution of three signals or three functions; considerat the following equation: Eq. (2) represents the associative property in which V_a, V_b, and V_c are respectively voltages for phases a, b and c.
C. Distributive property: The distribution property is also presentedin the convolution of three signals or three functions.
D. Impact of time shift: Timeshift in two signals will affect the convolution of two signals and convolution will shift with the same amount as the shifting of the signals.
E. Coefficient Effect: If a constant value is multiplied by the convolution of two signals or two functions, it will eventually affectin the convolution of these two signals and two functions and will be multiplied by the same amount.

Thehigh-frequency components are produced during a fault occurrence and considering the mentioned issues, a simple solution for reducing calculations and also preserving frequency information in one signal is using convolution to convert three-phase signals into one signal with the same frequency properties. Figure 1 shows an example of converting a three-phase voltage into a modulated voltage through convolution.One of the signal processing techniques to derive the fault property from the current or voltage signal is the use of wavelet transform which is capable of displaying signal sharp changes when the fault is in a small scale. Which is obtained by multiplying the original signal in a wavelet at a different scale fromthe original signal. Now, the convolution technique is similar to the wavelet transform at the time of the fault andcould beapproporiatedisplay in the changes at the time of the fault, such that it was able to detect single-phase fault of a one wave peak, two-phase fault two-wave peak, and three-phase fault two-wave peak with less amplitude of two-phase fault extraction. So in this scheme, instead of wavelet transforms that are only able to

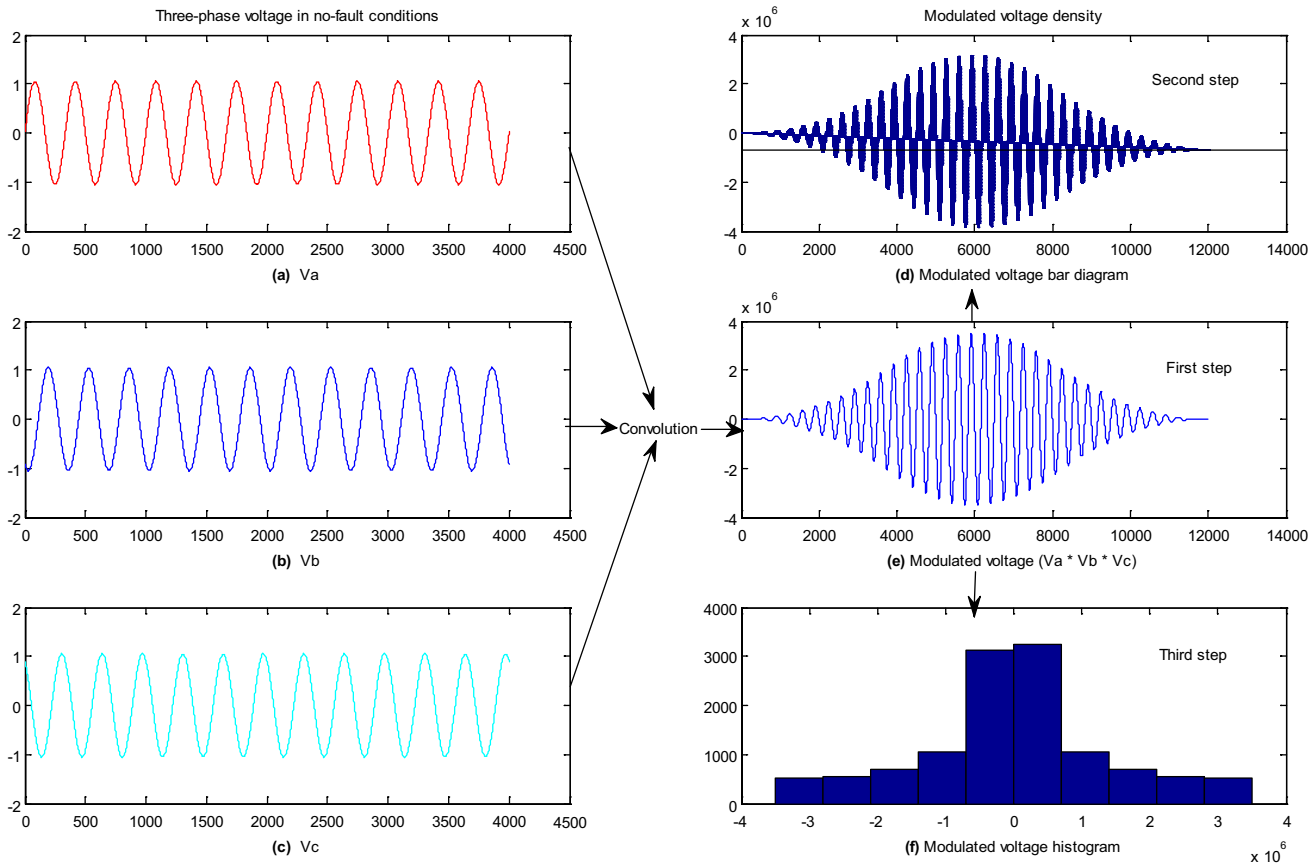

Fig. 1 Converting a three-phase voltage into one modulated voltage in a no-fault condition in the network

apply individually to each of the phases. Use the convolution to apply the voltage and current three-phases, the same wavelet transform features to one-scale only at form a modulated voltage and current signal obtain and then comparing these two modulated signals fault location estimated. The difference in wavelet transform is that,it could be dividedthe signal into several domains, but in the convolution instead of using the mother wavelet, it has createdtwo modulated signals with the same characteristics by applying together threephases of voltage and current.

2.2 Calculating the Fault Candidate Points in the Network

One of the common methods in fault location is the impedance method which estimates the fault location as two-terminal or single-terminal using the measured voltage and current. This method depends on being aware of the line parameters and the more information which are on the line's resistance, reactance, and capacitor, the algorithm will be more approporiate and the calculations will be more complicated. In this research and to reduce the calculations and ignoring the line parameters, the idea of convolution and calculating the density of the converted signals has been presented. Our studies show that this density is different between no-fault conditions and fault conditions it will have different single-phase, two-phase, and three-phase for different faults. Therefore, in this design, the first step after a fault occurrence is to calculate the modulated voltage and current at the line's beginning; in the next step, the density of modulated voltage and current is obtained and then by dividing the density ratio of the voltage by the current, a constant value is achieved and multiplied that value by the line's length, the distance to fault location is estimated.

Figure 1shows the density of the modulated voltage for a three-phase voltage in a normal (no-fault) condition. Here, the density of the modulated signal shows the number of changes in the surface beneath the signal; which is measurable using the "bar" command on MATLAB. Figure 2 shows the changes in the area under the curve of the modulated voltage in a no-fault condition.

$$V_{co} = V_a * V_b * V_c \tag{3}$$

$$I_{co} = I_a * I_b * I_c \tag{4}$$

$$X = \frac{d(V_{co})}{d(I_{co})} \times L \tag{5}$$

$$d(V_{co}) = \sum_{k=1}^{N} V_{co} \tag{6}$$

$$d(I_{co}) = \sum_{k=1}^{N} I_{co} \tag{7}$$

$K = 1, 2, \ldots, N$; N is the number of moments (coefficients).

Equation (3), (4) show the convolution of voltage and current, respectively; Eq. (5) shows how to calculate the fault location, and Eqs. (6), (7) represent the density of modulated voltage and current, respectively; in which I_{co}, V_{co} are respectively the modulated current and voltage; V_a, V_b and V_c are respectively the voltages for phases a, b and c at the line's beginning; I_a, I_b, and I_c are respectively the currents for phases a, b and c at the line's beginning; x is the distance to fault location; L is the line's length; $d(V_{CO})$ and $d(I_{co})$ are respectively the densities of modulated voltage and current.Eq. (5) is a criterion for the fault location in

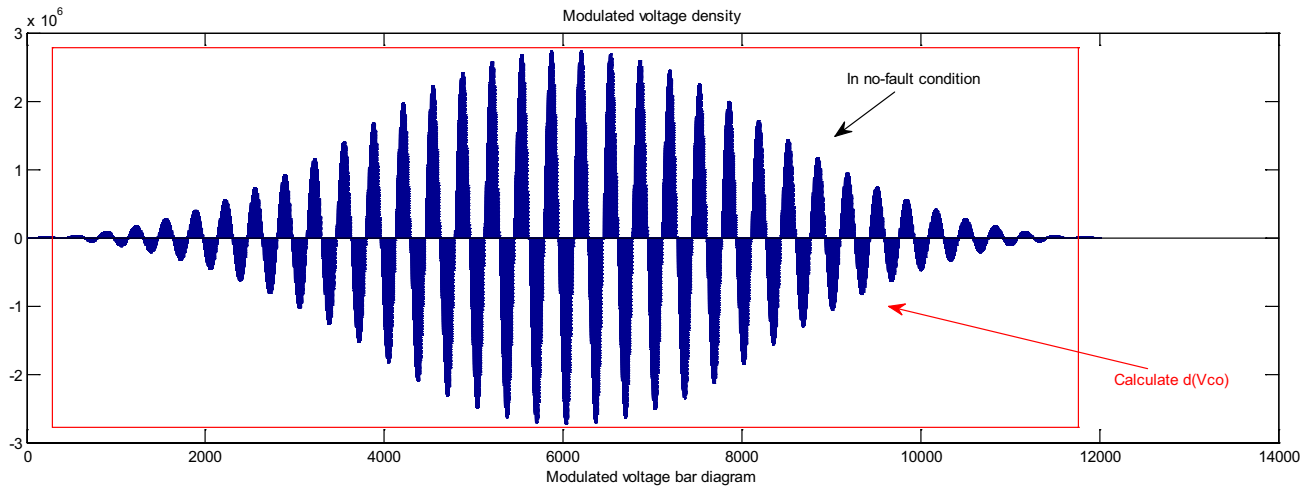

Fig. 2 Changes in the area under the curve of the modulated voltage in normal condition

a transmission network. It should be noted that the amount of $d(V_{CO})$ and $d(I_{co})$ are equal in a no-fault condition and when a fault occurs, their values will be different based on the fault type, fault resistance, and fault angle. But since our processing is occurring simultaneously on the current and voltage, the ratio of these changes will be in a way that won't create problems for the algorithm's accuracy. Because for each fault type, the resistance, or angle, the current will changeproportional to the voltage and therefore, our estimation will not be wrong.

Figures 3, 4 show the results are different for different fault types.the voltage is decreased and current id increased during a fault occurrence which could be properly seen in the modulated voltage and current; so that when the fault intensifies (from single-phase to three-phase), the amplitude of the modulated voltage will decrease, and the modulated current increases. Also, the obtained waveform is different in different faults; in a way that we will have one wave peak in a single-phase fault and two wave peaks with different amplitudes in two-phase and three-phase faults. From the convolution's feature, it is completely clear that the waveform of the modulated voltage has become similar to the waveform of the modulated current which helps us significantly in calculating the fault location. As it can be be can seenin Fig. 3, the peak amplitude of the modulated voltage in single-phase fault 2,000,000, in a two-phase fault 1,500,000, in a three-phase fault 1,200,000 is well reduced. Also, according to Fig. 4, the peak amplitude of the modulated current in single-phase fault is 40000000000, in a two-phase fault is 70000000000, in a three-phase fault is 150000000000, which is aapproporiate increase of amplitude.

The feature of this scheme is the simultaneous processing of the current and voltage at the beginning of the line at the time the fault occurs. Therefore, depending on the type ofpower network (distribution or transmission) at the time of the fault, their voltage or current proportionallystaylow or high, and since the current and voltage density of the threephases are calculated simultaneously, then the power network type will have a not effect on this. Because the two density ratios will have a for each network the fault current and voltage ratios change at the same time, so Eq. (5) does not have trouble estimating the distance (X). So ifit deal with a large power network, voltage and current changes at the time the fault occurred, though limited, still have and will not have an effect on the algorithm. For example, Fig. 5 shows the voltage and current measured at the time of the

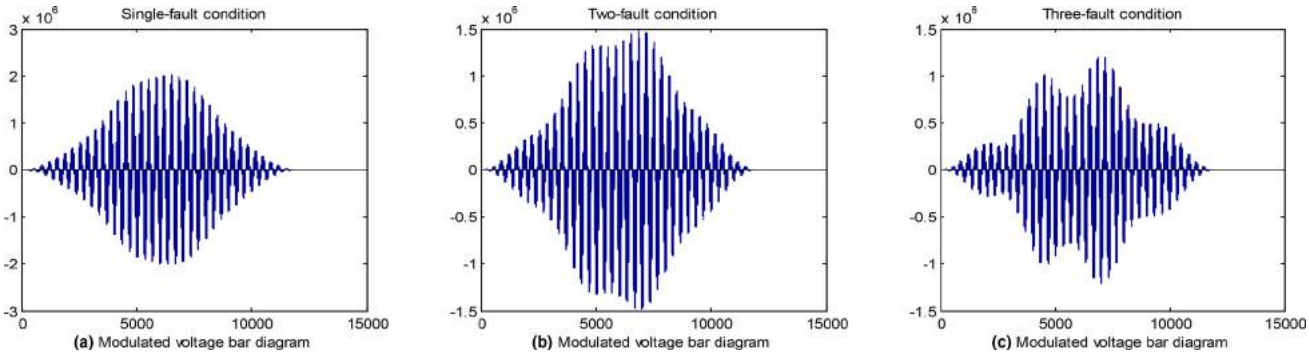

Fig. 3 Changes in density of the modulated voltage **a** in a single-phase fault condition, **b** in a two-phase fault condition, and **c** in a three-phase fault condition

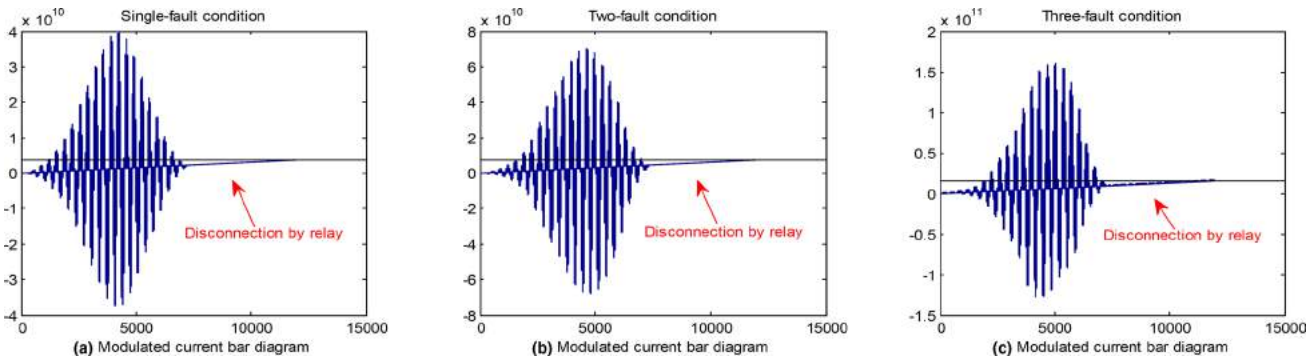

Fig. 4 Changes in density of the modulated current **a** in a single-phase fault condition, **b** in a two-phase fault condition, and **c** in a three-phase fault condition

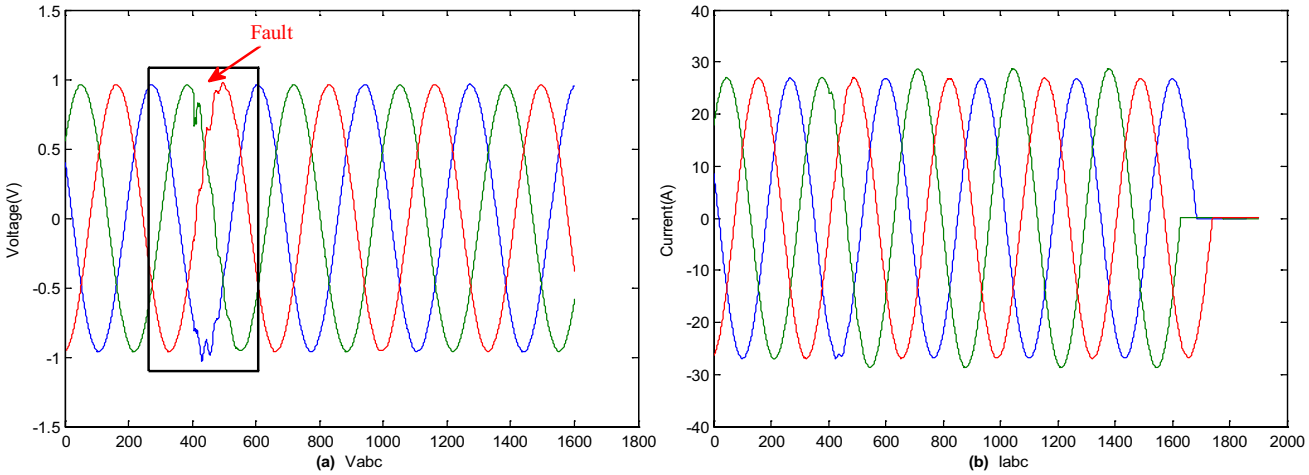

Fig. 5 Fault voltage and current measured in the large transmission network

fault in a large transmission network. As it can be can seen, the amplitude of voltage and current changes is very small. Now, in Fig. 6, the modulated voltage and current density are shown, and the ratio of these two values at the line is $x = 49.93$, so the proposed method in large networks and even for high impedance faults where the voltage changes are very small, it will perform well. This is because the convolution is similar to the wavelet transform, which multiplies the original signal in a mother wavelet, thereby extracting the small and sharp edges of the signal. Convolution also these small changes is magnification in the modulated signal by multiplying the three-phase signal. This magnification in the voltage and the current signal is done in the same proportion, so the proposed method does not have a problem in estimating the fault location.

3 Estimating the Faulted Section in the Distribution Network

As ithas mentioned in the previous section, Eq. (5) is a criterion for calculating the fault location in a transmission network. Now, if we want to use this equation in the distribution network, due to the presence of different branches, it is possible to obtain several points; therefore, detecting the fault location is very important in the distribution network. In this design, the idea of histogram analysis of the modulated voltage at the line's beginning has been presented; and the faulted section can be easily detected by comparing the histogram of the modulated voltage before and after the fault. An analysis conducted by a histogram

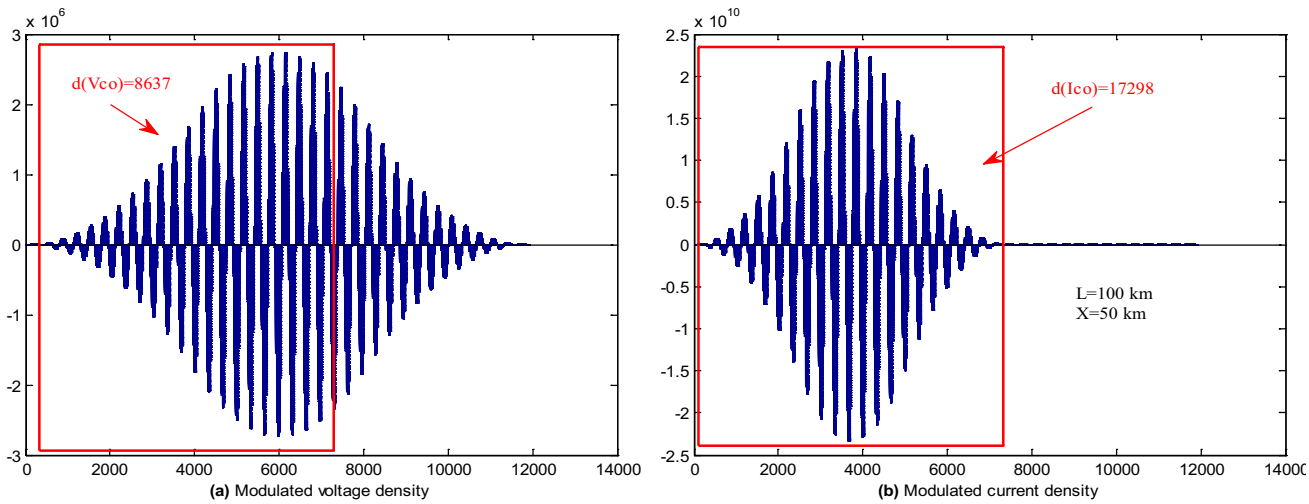

Fig. 6 Measured voltage and current density in the large transmission network

diagram is an initial or even general analysis. In the histogram diagram, there is an overall look at the data frequency in groups. The basis of the histogram is composed of a vertical axis that always represents frequency and a horizontal axis thatrepresents continuous data (numerical) as parts with different amounts (the minimum being 20 parts). The size of each bar shows the frequency of that bar between ranges. A histogram chart is similar to a bar chart' which data range has decided to be used at looking the histogram chart, it can quickly infer four factors:

- Peak: it shows the range of highest frequency.
- Gap: gap means that there is no information available in a range or ranges and gaps usually present the information associate with importance in the analysis.
- Concentration: When two or three bars have similar sizes, then the data are concentrated in those ranges.

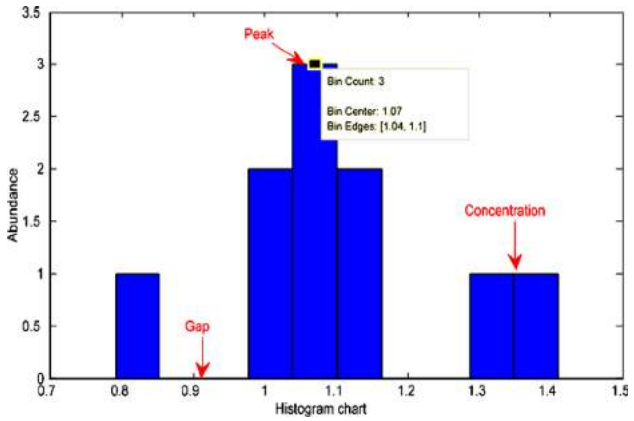

Fig. 7 An example of a histogram chart

- Outliner: ranges in which data frequency is very unlikely to happen and exist.

Figure 7 shows three important properties of a histogram chart. In regards to fault location in the distribution network, our studies show that the peak and partitioning of the histogram are different depending on the fault type and the faulted section and they will be appropriate criteria for detecting the faulted section. Therefore, in our design, first, the fault candidate points are obtained using Eq. (5), and then by comparing the histogram in the candidate section before and after the fault, the faulted section is detected. Our studies show that the histogram of each section is different for different faults and by detecting the candidate sections, in which the faulted section can easily be detected. The results are shown in the following.

Figure 8 shows a sample of fault candidate points in the power transmission and distribution network. It can be seenin Fig. 8a, one candidate point X is obtained for each fault along the transmission line, but in the distribution network of Fig. 8b, for each fault along the line, many candidate points may be obtained, as in Fig. 8b it seen that there is only one candidate point to the distance X, and for the distance greater than X, there will be three branches, so three candidate points, such as X1, X2, and X3, will be obtained, thus detecting the faulted branch seen in the distribution network of particular importance.

Suppose in Fig. 8a that a fault occurred and the voltage and current information of the fault was at the beginning of the line, it can now be easily obtained by Eq. (5) of the fault distance X. Now, if a fault occurs in Fig. 8b distribution network and the voltage and current information at the beginning of the Substation are available, Eq. (5) can obtainedthe fault distance to the Substation, but due to the

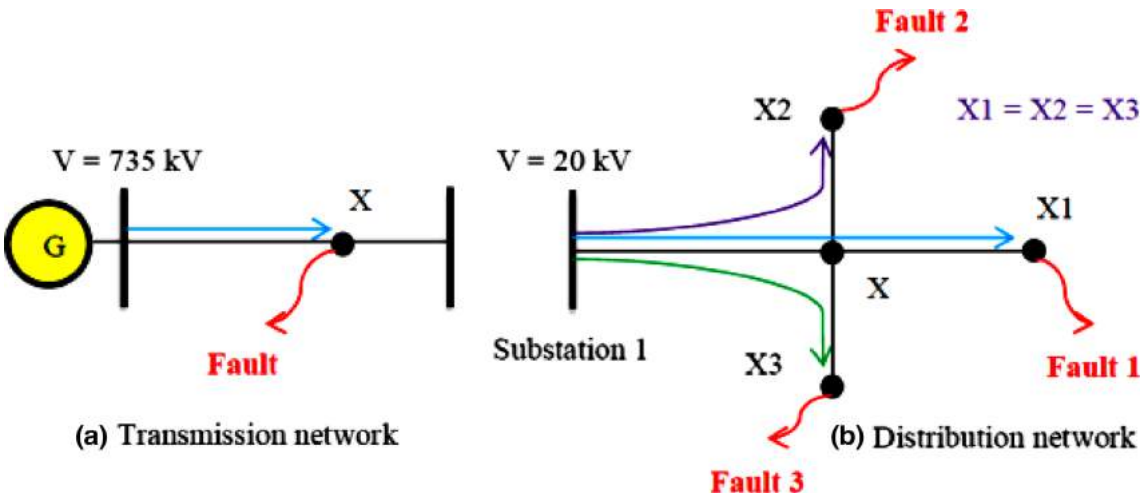

Fig. 8 Fault candidate points in **a** Transmission network, **b** Distribution network

different branches in the distribution network, several candidate points may be presented. For example, if the fault distance X1 is obtained since X1 = X2 = X3, then three candidate points (i.e. Fault 1, Fault 2, Fault 3) will be obtained, that to accurately diagnose faulted branch in this paper of histogram analytics idea of the modulated three-phase voltage is provided at the beginning of Substation.

Suppose a two-phase fault to ground occurs at distance X1 from Substation in Fig. 8b. In this case, three X1, X2, X3 candidate points will be obtained for the fault location, followed by observation and matching of the modulated voltage histogram at the beginning of the Substation can detect the exact point of fault location. Asit can be seen in Fig. 9, the modulated voltage histograms are different before and after the fault and vary for each branch. Before the fault (Fig. 9a) the peak of the histogram is above 3000 and after the fault, at each point (ie Fig. 9b–d) the peak of the histogram is lower than 3000, also to detect the faulted branch seen from Peak 1, Peak 2 is used. In Fig. 9b (main branch) Peak 2 is below 2500 and in Fig. 9c (lateral branch) Peak 2 is above 2500 while in Fig. 9d (mutual lateral branch) is replaced by Peak 1, Peak 2. So it is easy to see the value of Peak 1, Peak 2 faulted branch detected. Our studies show that the modulated voltage histogram varies for different faults and the number of main and lateral branches of the distribution network and it is easy to identify the fault location by matching the histogram of each section as described in Sect. 4 of the article.

One of the common techniques in fault location argument is the impedance method, whose accuracy depends on the knowledge of line parameters such as resistance, reactance, and capacitance, and if two types of line (in terms of line resistance and reactance) are used in different parts of the network, impedance method in fault location is difficult. But in the histogram analysis method there is no need for line parameters and only need to record three-phase voltage information at the beginning of the line. It has no problems and will even be able to provide different histograms for each network section. Thus, in this scheme, by comparing the histograms of each section, one can easily obtain the faulted branch by matching the histogram. Because it was able to present different histograms for each section. What is meant here is the non-dependence of the proposed method on line parameters such as resistance, inductance, and line capacitor to calculate the fault location. Figure 10 shows how x is calculated in the impedance method. It is clear from its comparison with Eq. (5) that the proposed method is not dependent on line information and only estimates the fault location with voltage and current at the beginning of the line.

The existence of power quality issues in the distribution network not only disturbs but also makes the voltage histogram unique in that part of the distribution network. Also, since our processing of the voltage and current at the beginning of the network is synchronous and any change in voltage causes a change in current, so Eq. (5) will not occure the

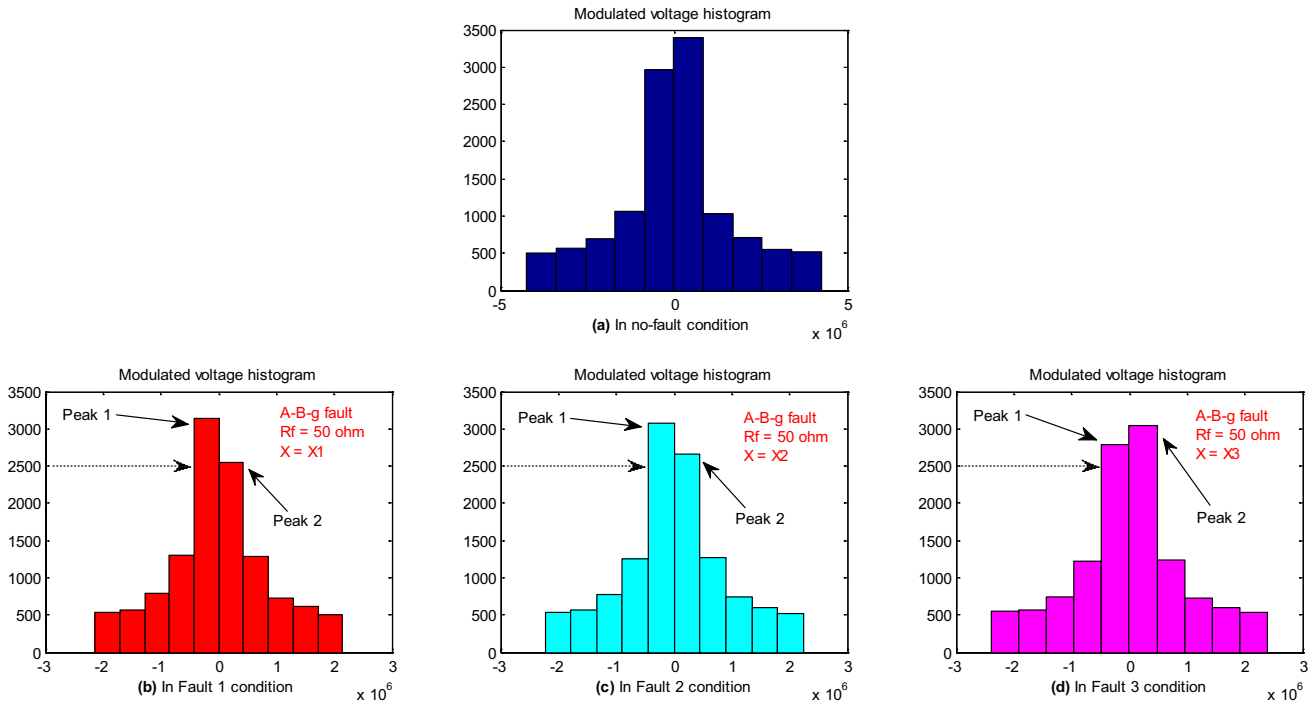

Fig. 9 Modulated voltage histogram at the beginning of Substation before and after a fault for fault candidate points

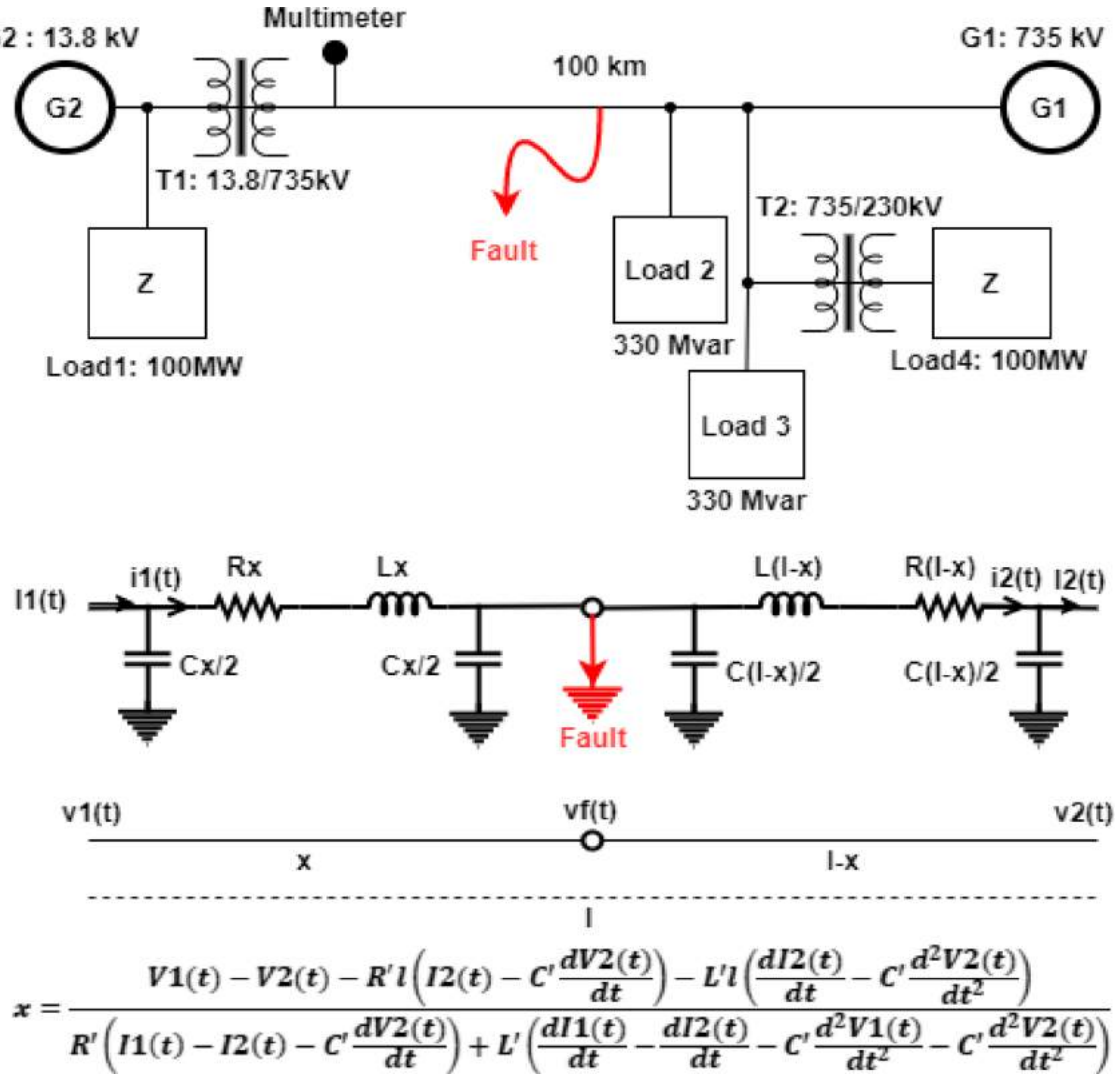

$$x = \frac{V1(t) - V2(t) - R'l\left(I2(t) - C'\frac{dV2(t)}{dt}\right) - L'l\left(\frac{dI2(t)}{dt} - C'\frac{d^2V2(t)}{dt^2}\right)}{R'\left(I1(t) - I2(t) - C'\frac{dV2(t)}{dt}\right) + L'\left(\frac{dI1(t)}{dt} - \frac{dI2(t)}{dt} - C'\frac{d^2V1(t)}{dt^2} - C'\frac{d^2V2(t)}{dt^2}\right)}$$

Fig. 10 Transmission network study under

difficulty. For example, in the same IEEE 15-bus network, there is a DG unit in bus 3, which causes the modulated voltage histogram peak to increase in that branch instead of decreasing the histogram peak. Therefore, the presence of new devices in its distribution network has made the histogram of that section unique, which can be very helpful in detecting the faulted section.

4 Network Implementation

In this paper, the suggested algorithm was first implemented on a 735 kV transmission network and then on an IEEE-15bus distribution network. The transmission network under study is the same standard network designed by G. Sybille (Hydro-Quebec) which can be observed by entering the power_3phseriescomp.mdl command on MATLAB. Also, the line length of the transmission network is considered 100 km is shown in Fig. 10. Regarding the distribution network under study, it should be mentioned that this network consists of 14 sections which include the main branch (with 4 sections) and 5 lateral-branches (consisted of 9 sections) and in this paper, (like [2, 3]) sections are named as binary numbers. So the main branch will include Sections 0001, 0010, 0011, 0100 and lateral-branches will include Sections 0101, 0111, 0110, 1110, 1000, 1001, 1010, 1011, 1100, 1101. Figure 11 shows the single-linear diagram of the distribution network under study. Also, the length of each section is considered 10 km, and all the modeling in this paper arecarried out on MATLAB. The reason for naming each section is that, in our study, it will be showedthat each section has a specific property, and to show these distinctions, we named the sections. Finally, the complete flowchart of the proposed fault locator algorithm is shown in Fig. 12.

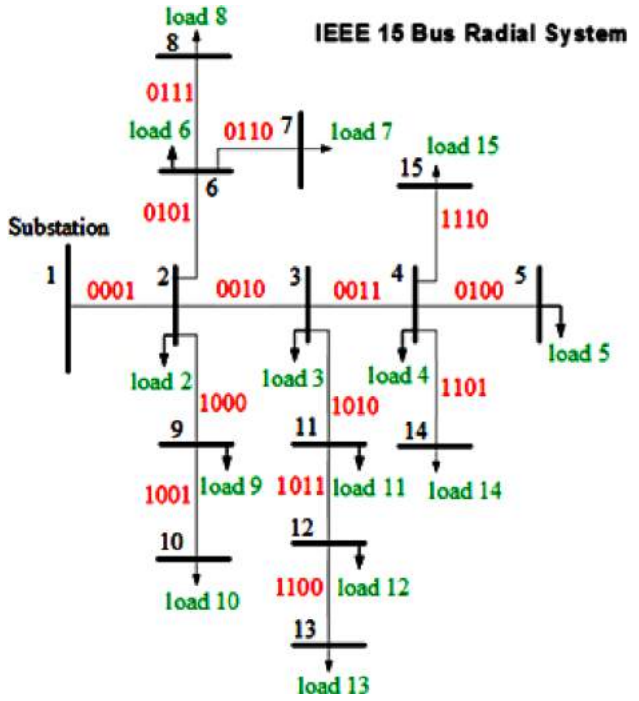

Fig. 11 Distribution network study under

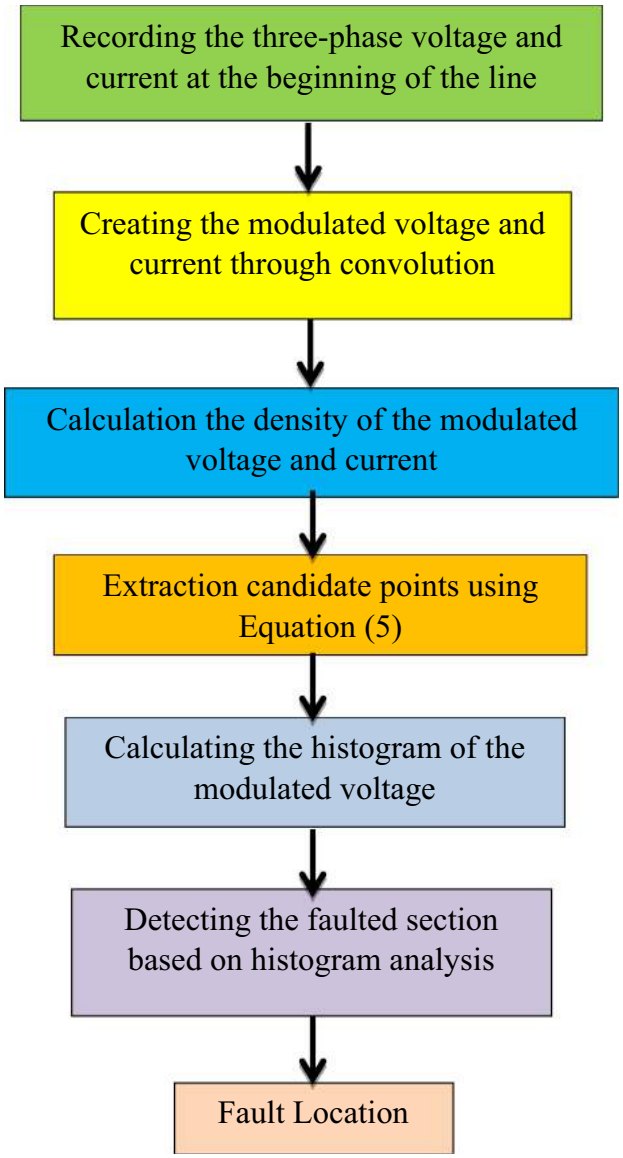

Fig. 12 Flowchart of the suggested locator algorithm

5 Simulation Results

Imagine that a three-phase fault has occurred at a distance of 50 km to the transmission line understudy and waveform of voltage and current recorded by measuring devices at the line's beginning is as Fig. 13 shows. In the first step, the modulated voltage and current are calculated along with the density of each signal. Figure 14 shows the density of the modulated voltage and current. As it can be seen, the density of the modulated voltage has been calculated up to the moment of the relay's performance.Then after a fault in the network, the relay detects the fault and removes the fault current by disconnecting it. This cuts off the branch current, but the voltage may still be measured at the beginning of the line. Therefore, to avoid reducing the accuracy of Eq. (5), it is calculatedthe modulated voltage density until the current is interrupted by the relay. As Seen Figs. 13, 14 for a better understanding of the subject. Asit can be seen from Fig. 13, at the instant of 2500 the current is interrupted by the relay but the network voltage remains. Therefore, according to Fig. 14, the modulated voltage density up to the moment of relay operation is calculated according to the modulated current density up to 7500. This is done because Eq. (5) has no problem and the exact location of the fault is obtained. Therefore, the modulated voltage and current density must be calculated until the moment of the relay operation. The densities of the modulated voltage and current were respectively 6573 and 13,166. Now, by dividing the former value by the latter, and multiply the answer by the line's length, the amount of 49.9240 has been estimated for the fault location.

With familiar about the idea of the design,itis implementedthe suggested algorithm on the distribution network. The difference is that by employing this idea, several candidate points in the distribution network are provided and to detect the faulted section, the idea of a histogram analysis has been presented. Our studies show that the histogram of the modulated voltage at the line's beginning (before and after the fault) is different for each different fault in each section. Here,are the considering limited article pages, the results of the study on the main branch (0001, 0010, 0011) and a lateralbranch (0101, 1000) have been briefly presented. Figure 15 shows the histogram of the modulated voltage at

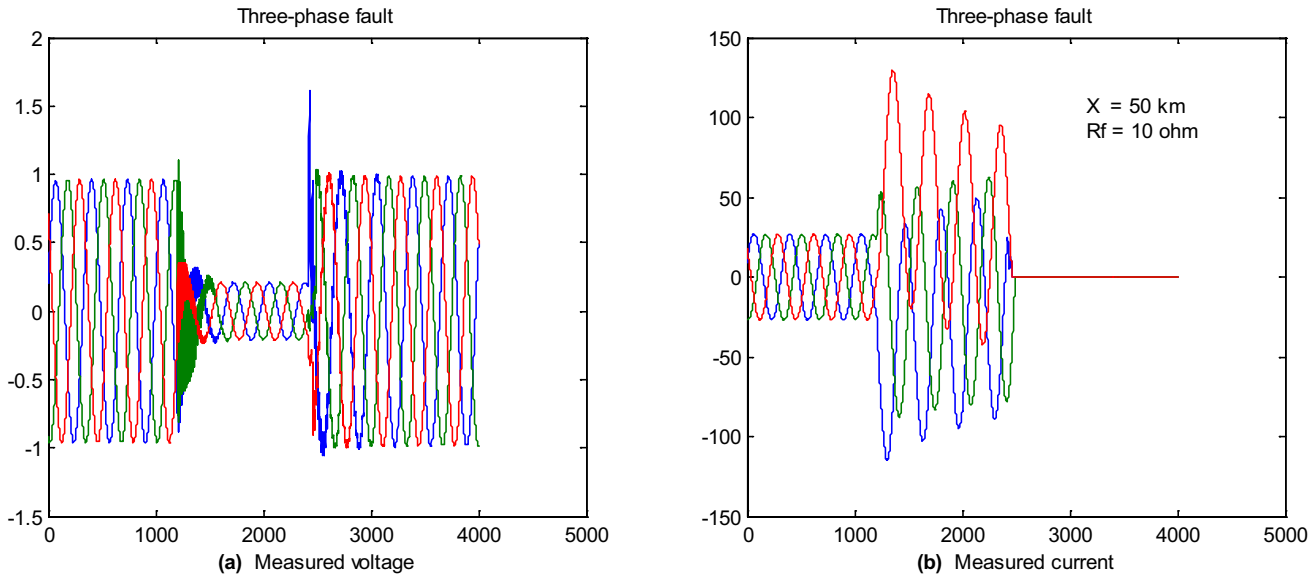

Fig. 13 Voltage and current are measured at the line's beginning

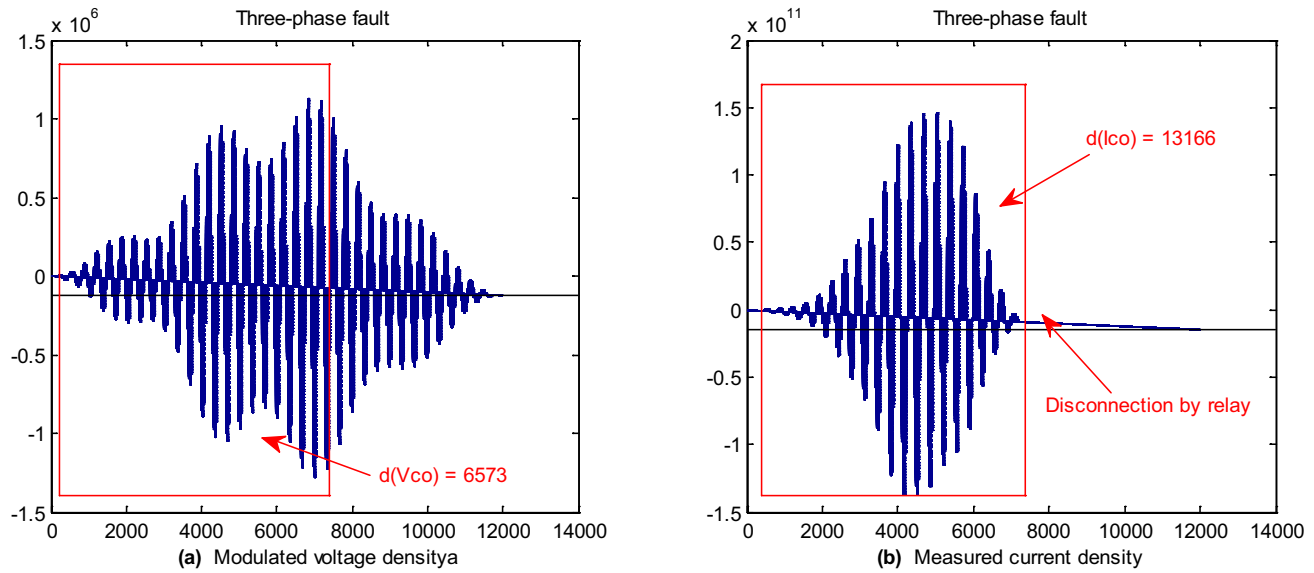

Fig. 14 The density of modulated voltage and current

the line's start before the fault occurrence. By comparing it to Figs. 16, 17, 18, 19, 20 that have happened after the fault occurrence, fault detection is easily possible.

Figures 16, 17, 18 show the histogram changes of the modulated voltage in the main branch of the network for single-phase fault, two-phase fault, and three-phase fault, respectively. Figure 19 and Fig. 20 respectively show the histogram changes of the modulated voltage in the lateral-branch 0101, 1000 for single-phase fault, two-phase fault, and three-phase fault. As you can see, histogram changes can help us detect the fault type (single-phase, two-phase and three-phase fault). Therefore, it can be statedthat the histogram of each fault type is unique.

In this design and to conduct histogram analysis, it has considered twoimportant components of the histogram: partitioning (range of the horizontal axis) and the peak amount. As it can be seen, the range of the horizontal axis is between ± 3,500,000 in normal condition (no-fault), between ± 2,500,000 in single-phase fault, between ± 2,000,000 in two-phase fault, and between ± 1,500,000 is in three-phase fault. Therefore, the intensification of a fault reduced the histogram partitioning.

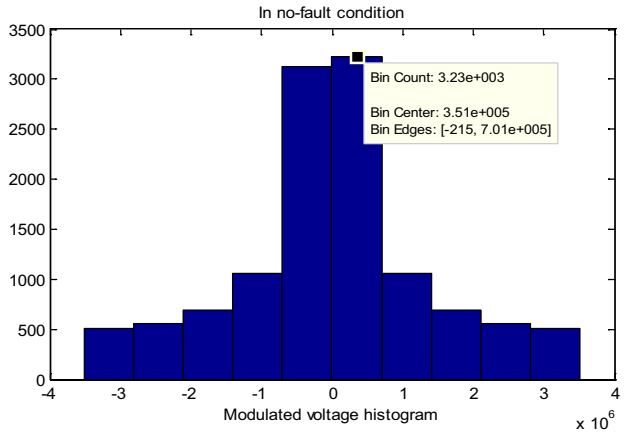

Fig. 15 Histogram of the modulated voltage before the fault

The next component is the peak amount which is different in the main branch and the lateralbranch of the network and changes in the sections of each branch. Figures 16, 17, 18 clearly show that the peak amount increases in each section that gets far from the feeder's beginning. The reason is the presence of a source in bus 3 of the network that has led to improved voltage drop. Figures 19, 20 clearly shows that the peak amount in the lateral-branch 0101, 1000 has moved and the more it gets far from the sources, the more it decreases.

With the concept of the design, imaging that a two-phase fault has occurred ata 5 km distance from the feeder's beginning. First, candidate points are extracted using Eq. (5). Since the length of each section is considered 10 km, three candidate sections of 0001, 0101, 1000 are presented. The candidate points are determined, the faulted section is detected by histogram analysis; in a way that by comparing Figs. 17a, 19b, 20b, the faulted section can be detected. Therefore, in this design, the fault location in the distribution

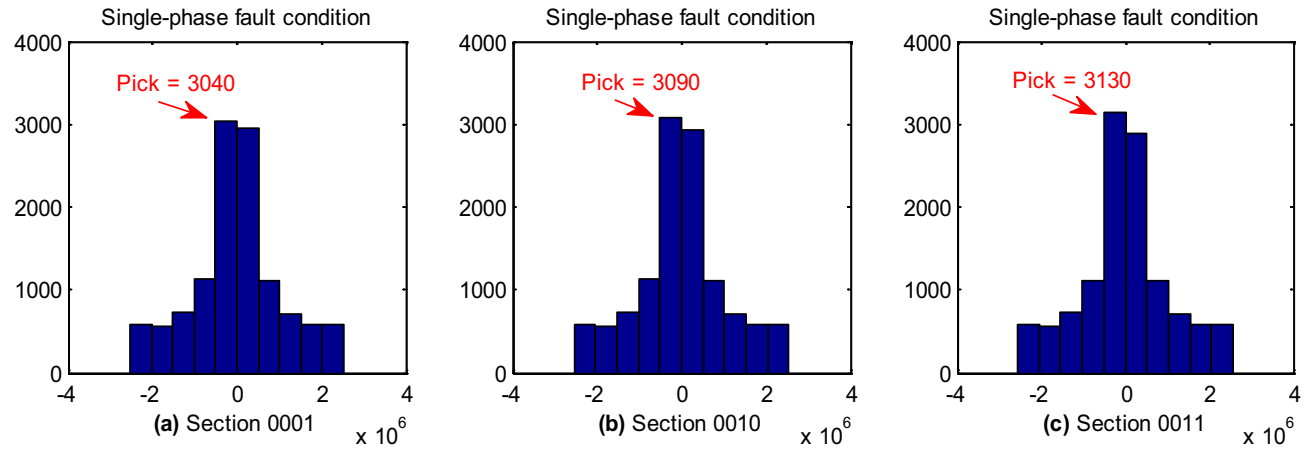

Fig. 16 Histogram changes of the modulated voltage for a single-phase fault in Sections 0001, 0010, 0011

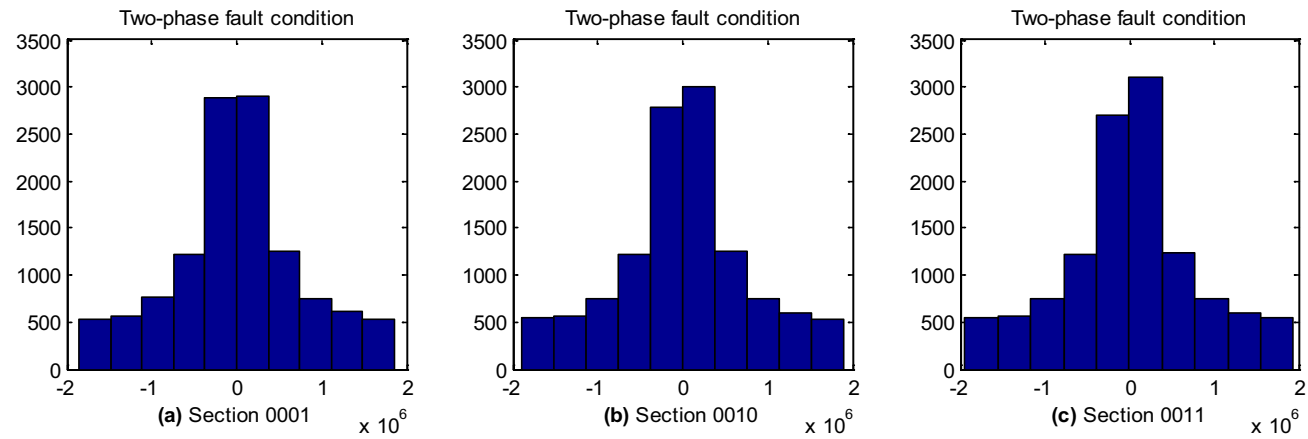

Fig. 17 Histogram changes of the modulated voltage for a two-phase fault in Sections 0001, 0010, 0011

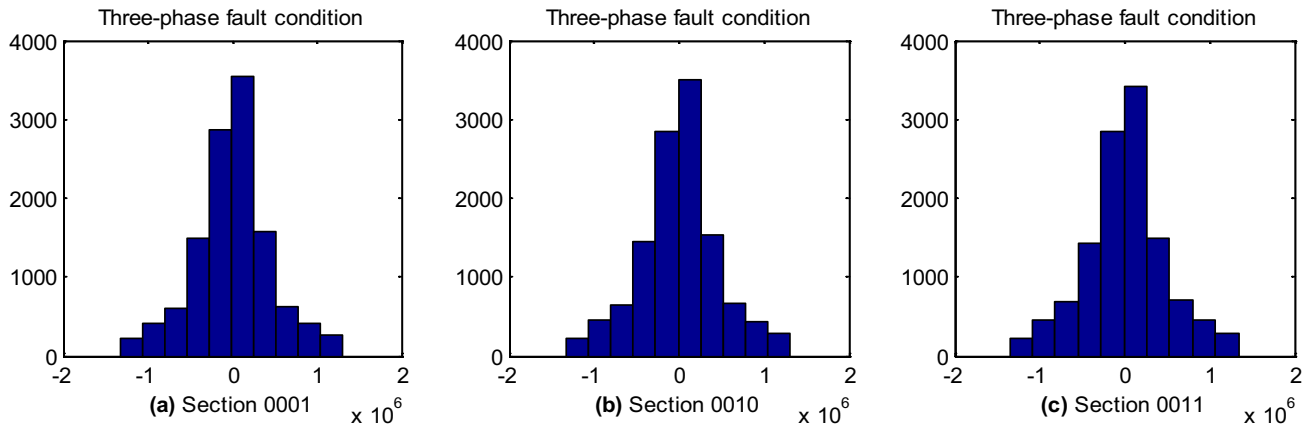

Fig. 18 Histogram changes of the modulated voltage for a three-phase fault in Sections 0001, 0010, 0011

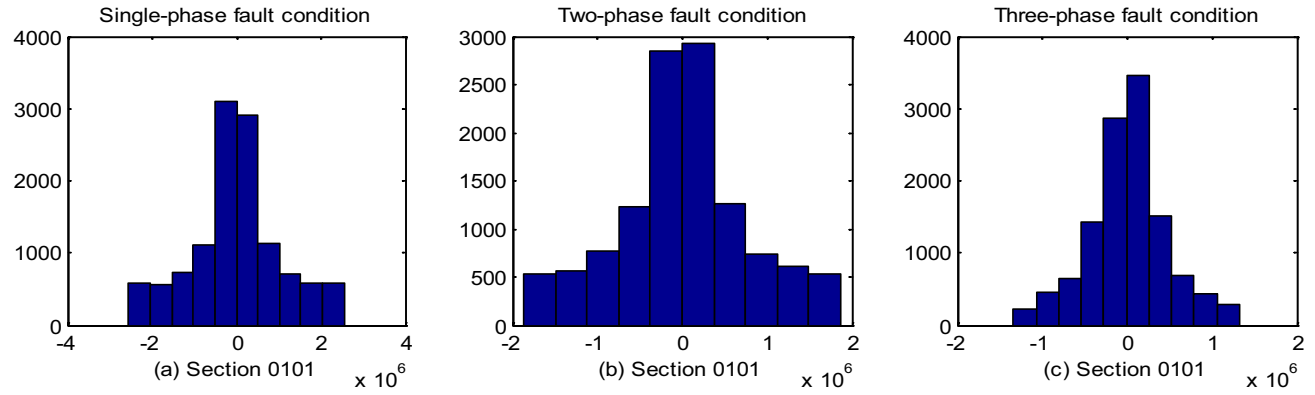

Fig. 19 Histogram changes of the modulated voltage for single-phase, two-phase and three-phase fault in Section 0101

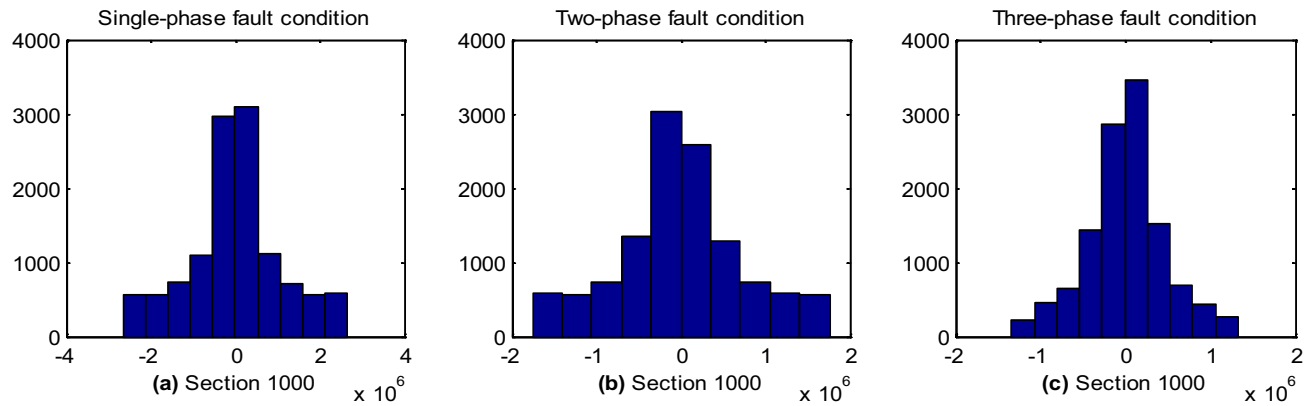

Fig. 20 Histogram changes of the modulated voltage for single-phase, two-phase and three-phase fault in Section 1000

network can be properly estimated using three ideas of calculating convolution, density, and histogram analysis.

In the following and to investigate the accuracy of the suggested algorithm, different faults in different distances were tested on transmission and distribution networksand the results has showedin Tables 1, 2. Also, the estimation error percentage can be calculated using Eq. (8) whose results are put in Tables 1, 2.

Table 1 Results from testing the suggested algorithm in the transmission network

Estimated values		Actual values	Estimated values	RE(%)
X (km)	R_f (ohm)	Fault type	X_e (km)	
30	0.5	A-g	30.3261	0.3261
20	8	A-B-g	20.4025	0.4025
50	10	A-B-C-g	49.9240	0.0760
70	85	C-g	70.1235	0.1235
65	100	A-C-g	65.1123	0.1123
10	–	B-C	9.9702	0.0298
40	75	B-g	40.0916	0.0916
80	150	B-C-g	79.9379	0.0621
30	–	A-C	29.7712	0.2288
85	–	A-B	85.1793	0.1793
15	15	A-g	15.1078	0.1078
90	95	A-C-g	90.1634	0.1634
40	–	A-B-C	40.1546	0.1546

$$RE = \frac{|Actual\ Location - Estimated\ Location|}{Length\ of\ Line} \times 100\% \quad (8)$$

The results clearly show that changes in fault location, fault resistance, and fault type do not influence detecting the faulted section and fault location in the network using the suggested algorithm. Because, it is simultaneously process threephases of current and voltage, any change in fault type will cause a simultaneous change in the voltage and current and thus the suggested algorithm will not face any problems. As it can be seen in Tables 1, 2, the maximum estimation error in the transmission network is 0.4025% and in the distribution network, the maximum estimation error is 0.9910% which is an appropriate percentage. Although the error percentage has gone up slightly in lateralbranches of the distribution network, because the faulted section is easily extractable, the performance of the suggested algorithm is appropriate.

6 Conclusion

In this paper, a new method based on signal processing techniques was used to fault location in the power system. Three techniques of convolution, density calculation, and histogram analysis were used to detect faulted section and fault location, especially in the distribution network. In a way that in the first step, three-phase voltage and current at the line's beginning will be modulated through convolution and then the density of each modulated signal is calculated and by calculating the ratio of these two values, the distance to fault location is obtained; and in the end, the faulted section in the distribution network can be estimated by analyzing the histogram of the modulated voltage at the line's beginning. The design's features include:

- Not being dependent on line parameters.

Table 2 Results from testing the suggested algorithm in the distribution network

Section	Actual values		Estimated values			RE (%)
	X (km)	R_f (ohm)	Fault type	S_e	X_e (km)	
0001	6	0.5	A-g	0001	5.9622	0.378
0010	5	7	A-B-g	0010	4.9763	0.237
0011	8	–	A-B-C	0011	7.9682	0.318
0100	7	25	B-g	0100	7.0301	0.301
0101	9	35	C-g	0101	8.9321	0.679
0110	0.5	45	B-C-g	0110	0.4552	0.448
0111	5	–	A-B	0111	5.0991	0.991
1000	3	65	A-C-g	1000	2.9823	0.177
1001	4	–	A-B-C	1001	3.9756	0.244
1010	6	85	C-g	1010	6.0623	0.623
1011	7	95	A-g	1011	7.0256	0.256
1100	8	10	B-g	1100	8.0978	0.978
1101	3	75	A-B-g	1101	2.9243	0.757
1110	2	55	B-C-g	1110	2.0611	0.611
0011	4	100	A-C-g	0011	4.0237	0.237
0111	9	14	B-g	0111	9.0178	0.178
1001	6	2	A-B-g	1001	5.9813	0.187
1011	8	–	B-C	1011	7.9817	0.183
0110	5	–	A-C	0110	4.9423	

- Fault type, faulted phase, fault resistance, fault occurrence angle has no effects on the suggested algorithm. Because a change in the mentioned parameters will cause a simultaneous change in the voltage and current of the threephases and since the processes on voltage and current are done simultaneously in this design through convolution, the design will not face any problems.
- Using convolution to create modulated voltage and current with a similar waveform.
- Presenting a unique histogram for each fault and faulted section.
- Appropriate algorithm accuracy: maximum estimation error of 0.4025% for the transmission network and 0.9910% for the distribution network was achieved.

References

1. Dashtdar M, Hosseinimoghadam SMS, Dashtdar M (2021) Fault location in the distribution network based on power system status estimation with smart meters data. Int J Emerg Electric Power Syst. https://doi.org/10.1515/ijeeps-2020-0126
2. DMasoud, RDashti, and HR Shaker (2018) "Distribution network fault section identification and fault location using an artificial neural network. In: 2018 5th International Conference on Electrical and Electronic Engineering (ICEEE). IEEE
3. Dashtdar M (2018) Fault location in distribution network based on fault current analysis using artificial neural network. Mapta J Electric Comput Eng (MJECE) 1(2):18–32
4. Dashti R, Sadeh J (2014) Fault section estimation in power distribution network using impedance-based fault distance calculation and frequency spectrum analysis. IET Gener Transm Distrib 8(8):1406–1417
5. Lopes FV, Kusel BF, Silva KM (2016) Traveling wave-based fault location on half-wavelength transmission line. IEEE Latin Am Trans 14:248
6. Hosseinimoghadam SMS, Dashtdar M, Dashtdar M (2020) Fault location in distribution networks with the presence of distributed generation units based on the impedance matrix. J Inst Eng Ser B 102:1–10
7. Rao A, Bogale B (2015) Accurate Fault Location Technique on Power Transmission Lines with use of Phasor Measurements. International Journal of Engineering Research and Technology. 4(2)
8. Dashtdar M, Dashtdar M (2021) Fault location in the distribution network based on scattered measurement in the network. Energy Syst 11:1–24
9. Magnago FH, Abur A (1998) Fault location using wavelet. IEEE Trans Power Deliv 13(4):1475–1480
10. Dashtdar M, Dashtdar M (2019) Fault location in the transmission network using a discrete wavelet transform. Am J Electric Comput Eng 3(1):30–37. https://doi.org/10.11648/j.ajece.20190301.14
11. Kapoor G (2018) A fault-location evaluation method of a 330 kv three-phase transmission line by using discrete wavelet transform. Int J Eng Des Anal 1(1):5–10
12. Dashtdar M, Esmaeilbeig M, Najafi M, Nezhad Bushehri ME (2020) Fault location in the transmission network using artificial neural network. Auto Control Comput Sci 54(1):39–51
13. Chen YQ, Fink O, Sansavini G (2018) Combined fault location and classification for power transmission lines fault diagnosis with integrated feature extraction. IEEE Trans Ind Electron 65:561–569
14. Wang M, Changfeng X, Huimin L (2018) fault location without wave velocity influence using wavelet and Clark transform. Springer, Cham, pp 321–326
15. Sarkar A, Patel B (2018) RBF neural network-based wavelet packet energy-aided fault localization on a hybrid transmission line. Springer, Singapore, pp 807–815
16. Saini M et al (2018) Algorithm for fault location and classification on parallel transmission line using wavelet based on Clarke's transformation. Int J Electric Comput Eng 8:699–710
17. Samantaray SR, Panigrahi BK, Dash PK (2008) High impedance fault detection in power distribution networks using time-frequency transform and probabilistic neural network. IET Gener Transm Distrib 2(2):261–270
18. He Z, Ling Fu, Lin S, Bo Z (2010) Fault detection and classification in EHV transmission line based on wavelet singular entropy. IEEE Trans Power Deliv 25(4):2156–2163
19. Ekici S, Yildirim S, Poyraz M (2008) Energy and entropy-based feature extraction for locating the fault on transmission lines by using neural network and wavelet packet decomposition. Expert Syst Appl 34:2937–2944
20. Dashtdar M, Dashtdar M (2019) Fault location in distribution network based on phasor measurement units (PMU). Sci Bull Electric Eng Faculty 19(2):38–43
21. Dashtdar M, Dashtdar M (2019) Detecting the fault section in the distribution network with distributed generators based on optimal placement of smart meters. Sci Bull Electric Eng Faculty 19(2):28–34
22. Dashtdar M, Dashtdar M (2019) Fault location in the transmission network based on extraction of fault components using wavelet transform. Sci Bull Electric Eng Faculty 19(2):1–9
23. Dashtdar M, Esmailbeag M, Najafi M (2019) Fault location in the transmission network based on zero-sequence current analysis using discrete wavelet transform and artificial neural network. Am J Electr Comput Eng 3:30
24. Dashtdar M, Dashtdar M (2020) Fault location in radial distribution network based on fault current profile and the artificial neural network. Sci Bull Electric Eng Faculty 20(1):14–21
25. Dashtdar M, Dashtdar M (2020) Fault location in distribution network based on fault current profile and the artificial neural network. Mapta J Electric Comput Eng (MJECE) 2(1):30–41

Masoud Dashtdar was born in Bushehr, Iran, on September 20, 1986. He received an M.Sc. in power electrical engineering from Islamic Azad University of Bushehr, Iran, in 2013. He is holding a Ph.D. degree from Islamic Azad University, Bushehr, Iran, in 2020. He is an assistant professor as a faculty member of the Islamic Azad University, Bushehr Branch. He is a reviewer of ISI journals with the "Journal of Electrical Engineering & Technology (JEET)", "Artificial Intelligence Review", "Soft Computing", "Electrical Engineering", "Iranian Journal of

Science and Technology, Transactions of Electrical Engineering", "International Transactions On Electrical Energy Systems", "Canadian Journal of Electrical and Computer Engineering", "IEEE Access" and "IEEE Transactions on Circuits and Systems II" cooperation. His research interests are distribution systems, including fault diagnosis in power systems, artificial neural network computing, power electronics, electric machines, renewable energy, microgrid, smart grids, harmonic analysis, power quality, optimization, and meta-heuristic algorithms.

K. Sarada received B.Tech degree in Electrical and Electronics Engineering from Sri Vidya Niketan Engineering College, Andhra Pradesh, India in 2001and M.Tech degrees in Electrical and Electronic Engineering from Sri Venkateswara University, Andhra Pradesh, India in 2004 and pursing her PhD in the area of Deregulated electricity market. Currently she is an Associate Professor in KLEF, Andhra Pradesh, India. Her research interests includes Deregulation, power system stability.

Seyed Mohammad Sadegh Hosseinimoghadam was born in Bushehr, Iran, on July 1, 1990. He holds a Bachelor in power electrical engineering from the Islamic free university of Bushehr, Iran, in 2014. He holds M.Sc. from the science and research free university of Tehran, Iran in 2016, in power system engineering. He is holding a Ph.D. from the Islamic university of Bushehr, Iran, in power systems. His research interests are Distribution systems, including fault diagnosis and Protection in power systems. Renewable Energy, MicroGrid, Harmonic analysis, Optimization Algorithms.

C. H. Naga Sai Kalyan received his Ph.D from Acharya Nagarjuna University and M.Tech degree from JNTUK, Kakinada, India. His research interest includes design of controllers for interconnected power system models using soft computing techniques and application of FACTS devices in power system operation and control. Currently he is working as Associate Professor in EEE Department of VasireddyVenkatadri Institute of Technology, Guntur, India.

A. N. Venkateswarlu studied B.Tech, Electrical and Electronics Engineering, in JNTUK, Kakinada, Andhra Pradesh, India, M.Tech., Instrumentation, in IIT., Kharagpur, and obtained Ph.D from JNTUH, Hyderabad, in Power Systems (FACTS). Interests are Power Systems, Electrical Vehicles and Renewable Energy Sources.

B. Srikanth Goud (member, IEEE) received his B. Tech degree in Electrical and Electronics Engineering and M. Tech degree in Control Systems from JNT University, Hyderabad, in 2009 and 2012 respectively. He has done his Ph.D degree in Electrical and Electronics Engineering from KoneruLakshmaiah Education Foundation in 2022. He is currently working as Assistant Professor in Electrical and Electronics Engineering, Anurag College of Engineering, Hyderabad, India. He has published over 30 research articles in reputed journals, international conferences, and book chapters. His research interests are Distribution Generation, Power Quality, Smart Grids, Power Electronic Converters and their applications to Power Systems.

C. H. Rami Reddy (member, IEEE) received his B.Tech. degree in Electrical and Electronics Engineering, M.Tech. degree in Electrical Machines and Drives from Jawaharlal Nehru Technological University, Kakinada, Andhra Pradesh, in 2011, 2014 respectively and the Ph.D. degree in Electrical and Electronics Engineering from K. L. University, Andhra Pradesh, India, in February 2022. He is currently working as an Assistant Professor in Electrical and Electronics Engineering with Malla Reddy Engineering College (Autonomous), Secunderabad, Telangana, India. He published more than 45 articles in various Web of

Science and Scopus indexed journals. His current research interests include integrated renewable energy systems, FACTS devices, power converters and their applications to energy systems. He is an editorial board member, Reviewer of various Web of Science and Scopus Indexed Journals.

Youcef Belkhier received his Masters degree in automatic from the University of Bejaia, Algeria, in 2017 and a PhD from the same university in 2021. He currently works as a researcher at the Faculty of Electrical Engineering, Czech Technical University in Prague. His research interests include designing and testing electrical machines and their control, renewable energy systems, and the Internet of Things.

Mohit Bajaj (member, IEEE & PES) was born in Roorkee, India, in 1988. He received the Bachelor degree in electrical engineering from the FET, Gurukula Kangri Vishwavidhyalya, Haridwar, India, in 2010 and the M.Tech. degree in power electronics and ASIC design from NIT Allahabad, U.P., India in 2013. He is currently pursuing the PhD degree with the Department of Electrical and Electronics Engineering, NIT Delhi, India. He has academic experience of 5 years. He has published over 30 research articles in reputed journals, international conferences, and book chapters. His research interests include power quality improvement in renewable DG systems, distributed generations planning, application of multi-criteria decision making in power system, custom power devices, IoT and smart grids

B. Nagi Reddy received his B. Tech degree in Electrical and Electronics Engineering, in 2010 and M.Tech degree in Power Electronics, in Jan' 13 from Jawaharlal Nehru Technological University, Hyderabad. He has done his Full-Time PhD from KoneruLakshmaiah Education Foundation (KLEF – Formerly K L University) in 2020. He assisted a book called Electrical Machines, written by Dr. M. Ramamoorty& Dr. O. Chandra Sekhar, which is published in 2017. He is the co-author of a "monograph on Reactive Power" published in 2020. He also published more than 25 Technical papers in the SCI & Scopus indexing Journals.Now, he is currently working as Associate Professor in electrical and electronics engineering department in Vignana Bharathi Institute of Technology (VBIT), Hyderabad. His area of interests are design & control of Power converters & Drives, Electric vehicals, Renewable energy sources etc.

energies

MDPI

Article

Distribution System Service Restoration Using Electric Vehicles

Swapna Ganapaneni [1], Srinivasa Varma Pinni [1,*], Ch. Rami Reddy [2], Flah Aymen [3], Mohammed Alqarni [4], Basem Alamri [5] and Habib Kraiem [6]

[1] Electrical and Electronics Engineering, Koneru Lakshmaiah Education Foundation, Vaddeswaram 522302, India; swapna@kluniversity.in
[2] Electrical and Electronics Engineering, Malla Reddy Engineering College (A), Maisammaguda, Secunderabad 500100, India; crreddy229@mrec.ac.in
[3] National Engineering School of Gabès, Processes, Energy, Environment and Electrical Systems, University of Gabès, LR18ES34, Gabes 6072, Tunisia; aymen.flah@enig.u-gabes.tn
[4] College of Engineering, University of Business and Technology (UBT), Jeddah 23435, Saudi Arabia; m.alqarni@ubt.edu.sa
[5] Department of Electrical Engineering, College of Engineering, Taif University, P.O. Box 11099, Taif 21944, Saudi Arabia; b.alamri@tu.edu.sa
[6] Department of Electrical Engineering, College of Engineering, Northern Border University, Arar 73222, Saudi Arabia; habib.kraiem@yahoo.fr
* Correspondence: pinnivarma@kluniversity.in

Abstract: Nowadays the utilization of Electric Vehicles (EVs) has greatly increased. They are attaining greater attention due to their impacts on the grid at the distribution level. However, due to the increased need for electricity, EVs are also used to serve the load in the instance of electrical failure in the distribution systems. This paper presents a new approach to a service restoration method for a low-voltage distribution network at the time of a power outage using existing EVs available in a parking place. The objective function formulated here was a constrained linear optimization model. It aimed to develop priority-based scheduling of the residential user appliances while meeting all the operational constraints if the EV's power was in a deficit at the hour of the outage. Weight factors were assigned to various residential appliances to decide their priority while scheduling. To substantiate the proposed methodology, a day load profile of a 20 kVA distribution transformer feeding eight residential users is considered. This was tested during an hour-long power outage scenario in the MATLAB and LINGO platforms, with four EVs available during the outage period. This method restored the maximum power to the residential appliances.

Keywords: Electric Vehicles; service restoration; distribution system; priority-based scheduling; residential appliances

Citation: Ganapaneni, S.; Pinni, S.V.; Reddy, C.R.; Aymen, F.; Alqarni, M.; Alamri, B.; Kraiem, H. Distribution System Service Restoration Using Electric Vehicles. *Energies* **2022**, *15*, 3264. https://doi.org/10.3390/en15093264

Academic Editor: Carlos Bordons

Received: 11 April 2022
Accepted: 26 April 2022
Published: 29 April 2022

Publisher's Note: MDPI stays neutral with regard to jurisdictional claims in published maps and institutional affiliations.

1. Introduction

Recently, the electricity demand has increased the utilization of power systems. As customers always expect uninterruptible quality power, it poses a challenge to power utility companies to increase their power supply to meet the additional loads. If proper planning is not done, the system gets stressed, which leads to the risk of outages and blackouts. The increased utilization of EVs becomes a promising strategy for service restoration at the distribution level. After a major outage, the distribution system generally requires a long time for maintenance. Dependency on a utility operator for its repair may not result in quick management of an outage. However, a benefit associated with EVs is that the batteries in the EVs help to serve the loads at the time of the outage.

Various potential services offered by EVs for distribution systems are mentioned in [1] and are called EV distribution system services (EVs-DSS). They categorized the services into three main groups. It was suggested that active power support from EVs can be considered for congestion management, loss minimization, peak shaving, valley filling, and

voltage regulation and load shifting. Various aspects of EVs, such as technical, economical, regulatory, and user-related issues and their associated barriers, are discussed in [2].

Mixed-integer linear programming was implemented in [3] for fast restoration of a distribution system with different penetration levels of Plug-in Hybrid Electric Vehicles (PHEVs). They analyzed coordination for the restoration of transmission and distribution systems for bringing the system back to normal conditions. A decentralized multi-agent system approach was proposed in [4] for service restoration. It was used to account for uncertainty in load demand and renewable energy resources in 38 bus and 119 bus distribution systems. They highlighted the use of EVs to support the energy uncertainties at the time of restoration.

To improve the resilience of the distribution system, a two-stage optimization model was proposed by [5] for the routing and scheduling of mobile power sources (MPSs), such as EVs. This solution demonstrated its effectiveness when tested on IEEE 33-node and 123-node test systems. A resilient scheme was proposed in [6] for the proper dispatch of repair crews and MPSs for disaster recovery logistics, optimizing the distribution system restoration by forming dynamic microgrids powered by the MPSs. A smart transformer architecture for a solid-state transformer was proposed in [7] to improve the services of the electric grid and the resilience of the system by initiating a restoration procedure after a blackout.

Mobile energy resources (MERs) connected to the distribution system through the transportation system are used for dynamic service restoration to serve critical loads. MERs' dispatching schedule is obtained from a mixed-integer linear programming optimization problem in [8]. The faster self-healing process of a distribution system for reliable load pickup by PHEVs is presented in [9], where a Markov chain process was used to generate the driving behavior of PHEVs and an optimization problem was formulated to restore the maximum load.

Power system restoration was achieved in [10] by locating distributed generators (DGs) optimally. They considered this as a problem of constrained optimization and applied it to both sub-transmission and distribution systems for the minimization of the service area at the time of restoration. A hybrid multi-agent system approach with six agents was implemented for service restoration in [11], using both DGs and EVs. The optimal location of DGs was obtained by using an Open DSS network simulator and proposing an R&M algorithm for finding optimal island ranges.

A real-time household load priority scheduling algorithm was implemented in [12] based on the availability of renewable energy sources to minimize the energy cost and satisfy the comfort of the customers. Assigned priority to home appliances was achieved dynamically for hour-to-hour energy consumption of various home appliances. A strategy for service restoration at multiple levels was proposed in [13] with microgrids and EVs and a fault was created on 3 feeders and 18 nodes of an IEEE distribution system. They not only restored the service in a much quicker time but also improved the reliability of the system.

Classification of DGs and models of service restoration methods were discussed in [14]. They implemented it for an active distribution network as a complex optimization problem by considering the priority levels of users, the number of switching operations, and losses of the network after restoration. The Pareto genetic algorithm, which was implemented to choose the optimal path for service restoration, gave effective results.

Table 1 shows the comparison of computational methods of service restoration in distribution systems, along with their solution approaches, merits, and demerits. The optimal coordinated operation of dc microgrids connected to a distribution system followed by a major power disturbance to sustain the distribution system resilience was proposed in [15] as a multi-objective mixed-integer linear programming optimization problem. They considered the impact of PHEVs and demonstrated the effectiveness of different methodologies on a 34-bus test distribution system.

Table 1. Comparison of computational methods of service restoration in distribution systems.

Ref. No.	Problem	Solution Approach	Merits	Demerits
[3]	Distribution system restoration using PHEVs	Mixed-integer linear programming is implemented. 100-bus test system was considered.	Coordination between transmission and distribution restoration was obtained.	The availability of a large number of PHEVs and their participation were concerns.
[4]	Service restoration using DGs	The decentralized multi-agent system (MAS) framework and service restoration was formulated as the multi-objective optimization problem.	Addressed the uncertainty in load demand and renewable distributed generators (RDGs) for service restoration.	Powerful control architecture was required for communication between the agents of the MAS.
[6]	Co-optimized distribution system restoration	Co-optimized repair crew and mobile power sources. A mixed-integer linear programming method was proposed.	Methods to reduce the computational time, the repair tasks, and MPS connection pre-processing were proposed.	Needed good coordination at every stage of implementation and involved many data variables.
[10]	Smart service restoration with distributed generation	The Tabu search approach was proposed to solve constrained objective functions.	Sub-transmission and distribution systems were considered with all crucial objectives.	Many data variables were involved and needed more input data.
[11]	Service restoration in distribution systems using a hybrid multi-agent approach	Used DGs and EVs. Multi-objective, multi-constraint, combinatorial, nonlinear optimization problem.	The optimal positions of DGs and islanding ranges were determined.	Required a powerful control architecture of a hybrid MAS. Fewer switching operations are not taken care of.
[13]	Multi-level service restoration strategy of a distribution network	Utilized the microgrid (MG) and EVs. An optimal power flow (OPF) model was constructed to minimize the net loss after the service restoration.	A potential aspect of EVs and MGs was considered.	The availability of sufficient capacity from MGs and the number of EVs to participate readily were concerns.
[14]	Service restoration of an active distribution network using DGs	A multi-objective, multiple-constraint, complex optimization problem was proposed.	Prioritized loads were restored, improved the economic benefits of the grid, and reduced the loss of the network fault recovery.	The intermittent nature of renewable DGs may not provide support all the time.

An optimal operation of the local energy community (LEC) placed in the distribution network consisting of the number of EVs, which are treated as flexible energy resources, are used for manual frequency restoration [16]. An EV Markov adequacy model was proposed in [17] to estimate the reliability of the system in both cases, i.e., home-to-vehicle and grid-to-vehicle, as well as vehicle-to-home and vehicle-to-grid, based on the mobility of EVs, capacity available from EVs, stochastic behavior of driving EVs, etc.

In [18], the authors identified the optimal location of EV charging stations, along with DGs, using artificial intelligence-based hybrid golf and particle swarm optimization methods in IEEE 33- and 69-bus systems to enhance the reliability of the distribution systems. In [19], the authors implemented a two-step, self-optimizing method for charging and discharging a large-scale fleet of EVs in a microgrid for a real-time network based on an estimated process of the Ontario energy network.

In [20], the authors developed a model for estimating the power demand of EVs while they were charging to calculate the total charging demand in a distribution system. An EVs' state of charge (SoC)-based dynamic charge coordination method in a distribution network was proposed in [21]. PHEVs were modeled as an energy storage system and their impact

on power distribution systems was analyzed in [22] by considering different penetration levels, periods, and variations of load in a day. Batteries of EVs are used as energy storage devices. The different topologies of single energy storage systems and hybrid energy storage systems were presented in [23]. The lifetime of distribution components, mainly on a distribution transformer, was investigated in [24] due to the increased charging impact of EVs and PHEVs. They gave suggestions to reduce the negative impacts on a distribution transformer. Regarding PHEVs charging and discharging, their impact was studied in two areas by [25]. They evaluated the reliability indices and proposed a reliability index expected energy not charged (EENC) to find a better location for the charging station. They also presented two discharging strategies to inject power into the grid to restore the system during a power failure. Regarding the concept of vehicle-to-grid (V2G), the possible ancillary services, potential benefits, challenges, impacts, and future market penetration were discussed clearly in [26]. The role of EVs connected in V2G mode in a distribution system was analyzed by calculating the reliability indices and the proposed model estimated the energy available from EVs during a day to supply the grid during emergency conditions [27]. The results showed an improvement in the reliability of the system while EVs inject power into the grid.

Significant approaches are discussed in the literature to handle service restoration traditionally, where some of them implemented network reconfiguration, formed suitable islanding, identified best switch indices, used a graph-based method, used an optimal load shed during restoration, integrated renewable energy resources (RERs), implemented of heuristic methods to obtain optimal restoration, used PHEVs along with DGs, etc. The implementation of the above methods needs a lot of analysis and verification [28]. They pose certain technical challenges in terms of the system operating conditions, equipment availability, time to restore, and operation success rate. All these methods are heavily focused on medium- and high-voltage standard IEEE distribution networks and extended distribution systems but are not concentrated on the low-voltage distribution systems to satisfy the needs of the individual residential user.

In recent years, most studies have only focused on various issues related to EVs, such as coordinated and uncoordinated charging of EVs, demand-side management with EVs, enhancement of reliability, and voltage and frequency regulation using EVs. PHEVs and EVs are used to feed power back to the grid, i.e., V2G technology. However, its control is more complex and needs the grid operator to coordinate the operations, as well as requires good communication infrastructure [29]. The concepts of vehicle-to-building (V2B) or vehicle-to-home (V2H) technologies require simple infrastructure that feeds power to a building or home, respectively. The V2B and V2H can be used as a backup during emergencies. Therefore, for outage management, EVs can be used to restore power to a home or building and it is a good alternative for V2G during an emergency condition [30]. With the advent of the increased use of EVs, quick power restoration is possible from the side of a low-voltage distribution system during a power outage, which can avoid dependency on utility operators. We believe that no other authors have focused on service restoration from the perspective of a low-voltage distribution system, i.e., a distribution transformer serving the residential area to satisfy their individual needs solely using parked Electric Vehicles, utilizing the potential aspect of V2B or V2Hand their state of charge. Without the intervention of the grid, service restoration of residential loads is possible according to their priorities by using parked EVs during the period of a power outage. The optimization problem formulated here is a linear model to achieve priority-based scheduling of residential appliances if EVs' power is a deficit to serve the required load. The model is less complex and involves fewer computations. Thus, this studyaimed at service restoration of the residential loads served by a distribution transformer using parked Electric Vehicles in that area, according to the resident's priority for individual appliances of the residential loads.

This paper is organized as follows. Section 2 presents the description of the test system, the methodology for the priority-based schedule of appliances is explained in Section 3,

Section 4 presents the discussion on the results, and finally, the conclusion is presented in Section 5.

2. Description of the Test System

At the end of 2020, 10 million electric cars were on the world's roads and there was a significant rise in the new electric car registrations, which was nearly 41%.By 2030, EV stock in all modes on the road will be around 7% [31]. Almost 95% of the time, EVs are parked at homes or parking lots in the U.S. [32]. While the vehicles are parked in the parking lot, they can be used to provide power to the grid, which helps with service restoration.

For this investigation, eight residential users served by a 20KVA distribution transformer and its residential load profile of a location in Texas, USA, in summer were considered from [33]. The residential area served by the distribution transformer and its load profile for a day is shown in Figures 1 and 2, respectively. It was assumed that each residential user had an EV, along with various appliances, such as a freezer, washing machine, refrigerator, microwave oven, various lighting loads, water heater, and air conditioners. Their wattages and power consumption, considered from [34], are tabulated in Table 2.

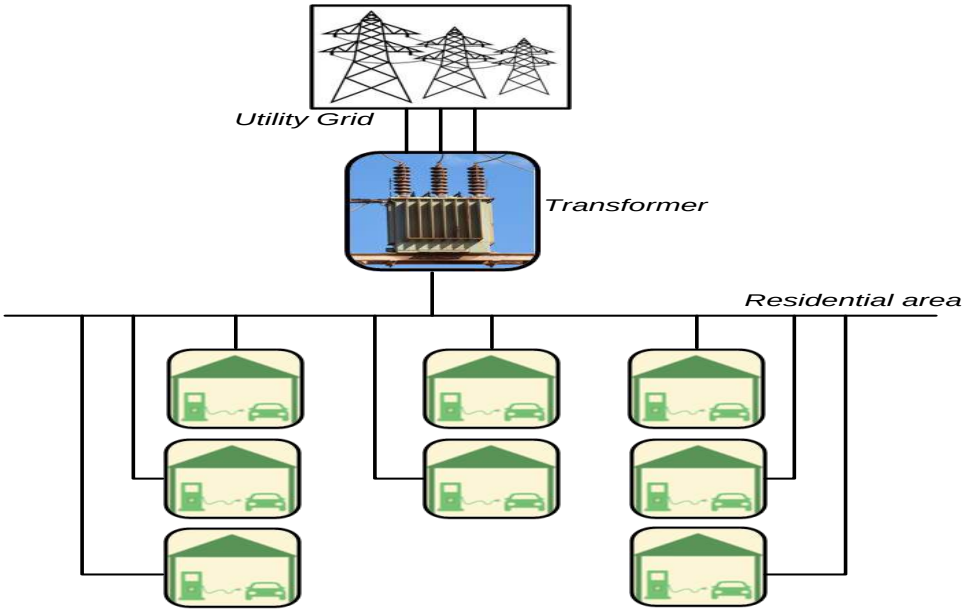

Figure 1. Distribution transformer serving residential loads.

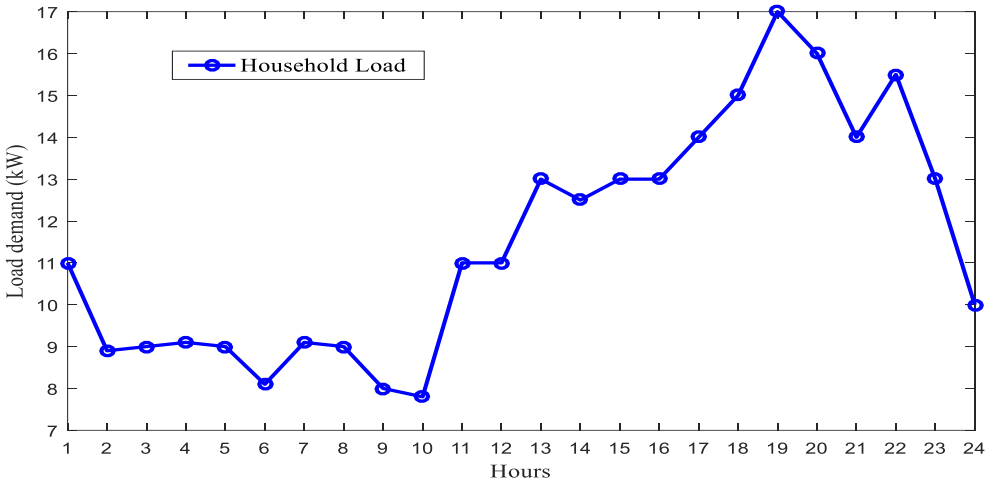

Figure 2. Residential load profile during the day.

Table 2. Wattage and quantity of various appliances in the residences.

S.No.	Appliances	Wattage(W) × Quantity							
		Residential User-1	**Residential User-2**	**Residential User-3**	**Residential User-4**	**Residential User-5**	**Residential User-6**	**Residential User-7**	**Residential User-8**
1	Refrigerator	100 × 1	150 × 1	100 × 1	130 × 1	130 × 1	130 × 1	150 × 1	100 × 1
2	freezer	500 × 1	400 × 1	400 × 1	500 × 1	50 × 1	50 × 1	50 × 1	400 × 1
3	Tube lights	None	22 × 3	22 × 3	22 × 3	22 × 3	22 × 3	22 × 3	22 × 3
4	Lamps	15 × 4	15 × 3	15 × 3	15 × 3	15 × 3	15 × 3	15 × 3	15 × 3
5	LED TV	85 × 1	116 × 1	120 × 1	110 × 1	60 × 1	85 × 1	90 × 1	110 × 1
6	Desktop	150 × 1	150 × 1	150 × 1	150 × 1	200 × 1	150 × 1	150 × 1	200 × 1
7	Laptop	60 × 1	60 × 1	60 × 1	-	60 × 1	60 × 1	100 × 1	60 × 1
8	Phones	25 × 2	25 × 2	25 × 2	25 × 2	25 × 2	25 × 3	25 × 1	25 × 1
9	Blender	250 × 1	250 × 1	250 × 1	250 × 1	250 × 1	250 × 1	250 × 1	-
10	Electric kettle	-	-	1200 × 1	1200 × 1	1200 × 1	1200 × 1	1200 × 1	1200 × 1
11	Microwave	900 × 1	900 × 1	900 × 1	900 × 1	900 × 1	600 × 1	900 × 1	900 × 1
12	Iron	1000 × 1	1000 × 1	1000 × 1	1000 × 1	800 × 1	1000 × 1	1000 × 1	1000 × 1
13	Security light	25 × 6	25 × 6	25 × 6	25 × 6	25 × 6	25 × 6	25 × 6	25 × 6
14	Waterpump	750 × 1	750 × 1	750 × 1	750 × 1	750 × 1	750 × 1	750 × 1	750 × 1
15	Waterheater	1000 × 1	1000 × 1	1000 × 1	1000 × 1	-	1000 × 1	1000 × 1	1000 × 1
16	Washing Machine	900 × 1	900 × 1	900 × 1	900 × 1	900 × 1	500 × 1	900 × 1	900 × 1
17	Dishwasher	1200 × 1	1200 × 1	1200 × 1	1200 × 1	1200 × 1	1200 × 1	1200 × 1	1200 × 1
18	Electricstove	2000 × 1	2000 × 1	2000 × 1	2000 × 1	2000 × 1	2000 × 1	2000 × 1	2000 × 1
19	ElectricpressureCooker	1000 × 1	1000 × 1	1000 × 1	1000 × 1	1000 × 1	1000 × 1	1000 × 1	1000 × 1
20	Coffee maker	1400 × 1	1400 × 1	1400 × 1	1400 × 1	1400 × 1	1400 × 1	800 × 1	1400 × 1
21	Air Conditioner	1500 × 1	1500 × 1	1500 × 1	1500 × 1	1000 × 1	1000 × 1	1000 × 1	1000 × 1
22	Internet Router	-	15 × 1	15 × 1	15 × 1	15 × 1	15 × 1	15 × 1	15 × 1
23	Waterpurifier	100 × 1	100 × 1	100 × 1	100 × 1	100 × 1	100 × 1	100 × 1	100 × 1

The EV model considered was the Nissan Leaf 2016, which has a 24 kWh battery capacity. Generally, the driving behavior of EVs decides the available SoC in the EVs. To retain a high life for batteries, the SoC must be maintained in the range of 20 to 80% of its capacity. In the present work, it was assumed that EVs were initially available in the range of 30 to 60% of SoC. Therefore, the percentage of SoC available from each EV was estimated in the range of 10% to 40% by using a random function in the PYTHON platform for every hour. Further, it was assumed that at least one EV was available in the parking lot at any instant.

Therefore, the total power available from EVs in the parking lot could be aggregated based on their SoC and could be treated as a single source of generation to serve the residential loads instantly at the time of an outage. The aggregated power of all EVs in an hour is the sum of the power of the individual vehicle and is given as P_{agg}.

$$P_{agg} = \sum_{i=1}^{N} P_i \tag{1}$$

where P_i is the power available from ith EV during the hour of outage in kW.

3. Problem Formulation and Methodology

The restoration problem was formulated as a constrained linear programming problem. It aimed to serve maximum power to the residential users who were served by a distribution transformer at the time of the outage based on the availability of EVs. In the case of deficit power from the EVs, appliances in the individual house were served based on the priorities assigned by that resident. The weight factor assigned to appliances decided the priority of the appliance during the hour of restoration. The higher the value of the weight factor, the higher the priority of the appliance.

Therefore, the objective function was formulated as shown in Equation (2) to restore maximum available power to the connected appliances. Further, it was subjected to various operational constraints, such as power available from EVs, limits on the bus voltage,

connectivity of the appliance at the time of the outage, and power ratings of the appliance, as shown in Equations (3)–(5).

$$\text{Max} \sum_{i=1}^{N} \sum_{j=1}^{K} W_{ij} * P_{ij} * C_{ij} \quad (2)$$

$$\text{Subjected to } V_i\text{min} \leq V_i \leq V_i\text{max} \; \forall \; i \ldots \quad (3)$$

$$\sum_{i=1}^{N} \sum_{j=1}^{K} P_{ij} * C_{ij} \leq P_{agg} \; \forall i, j \ldots \quad (4)$$

$$P_{ij} \leq R_{ij} \forall \; i, j \ldots \quad (5)$$

where P_{ij} is the power scheduled for the ith residential user's jth appliance in kW.

W_{ij} is the priority factor of the ith residential user's jth appliance.

C_{ij} indicates the on or off condition of the jth appliance for the ith residential user.

$C_{ij} = 1$ when the jth appliance is turned on by the ith residential user at the time of restoration.

$C_{ij} = 0$ when the jth appliance is turned off by the ith residential user at the time of restoration.

V_i is the ith bus voltage in pu.

$V_i$min and $V_i$max are the lower and upper limits of the bus voltage, which are considered as 0.9 pu and 1 pu, respectively.

The values of bus voltages were obtained from the power flow analysis.

R_{ij} is the power rating of the ith residential user's jth appliance in kW.

The distribution transformer serving the eight residential users was modeled as a 9-bus radial distribution system. Its single-line diagram is represented in Figure 3 before the outage. The system shows that the transformer fed the nine buses B1 to B9, out of which, buses B2 to B9 represent the residential users 1 to 8, respectively, and their corresponding loads are represented as L1 to L8. As shown in Table 2, the list of appliances, their wattages, and the quantity used by each residential user was considered. The power rating of every appliance of a residential user (R_{ij}) can be obtained from Table 2. It was considered that residential users separated from each other by 10 m, the resistance was 20 ohms per kilometer, and the reactance was twice the value of the resistance.

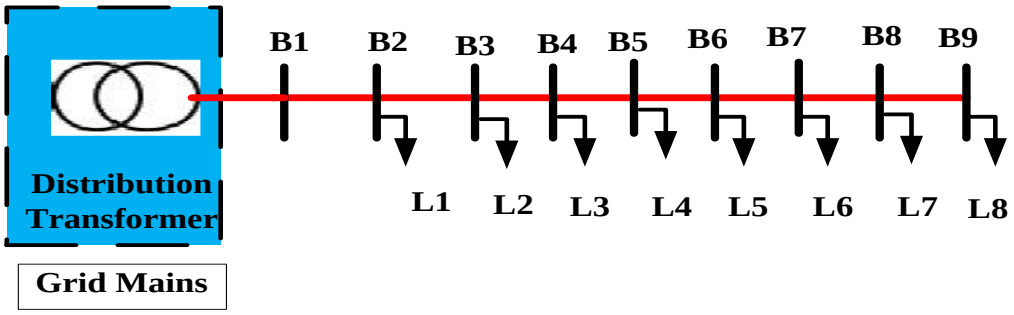

Figure 3. Single-line diagram of the radial distribution system under consideration.

At the time of the blackout, for the service restoration, the EVs' total energy was aggregated as per their availability in the parking lot. Then, the aggregated power from EVs was treated as a source of generation to serve the residential loads. The test system at the time of restoration is shown in Figure 4. The base MVA of the system was considered as per the availability of the number of EVs at the hour of the outage. First, the residential load profile of every resident was estimated using the residential load profile for a day.

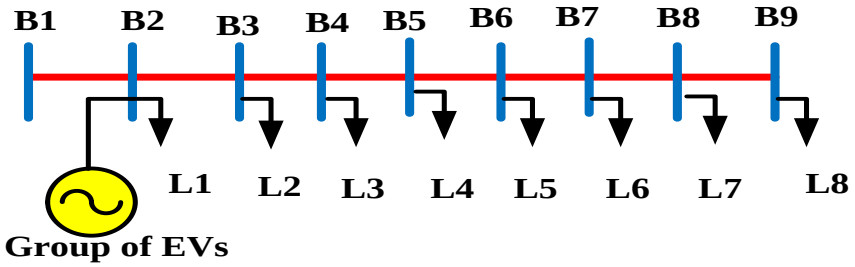

Figure 4. Single-line diagram of the radial distribution system at the time of restoration.

Later, Newton's method of power flow was implemented in the test system to identify the voltage violations in the MATLAB/MATPOWER environment. If no violations were found, appliances were powered per their requirements. If violations existed, then prioritization of appliances was required. Every appliance in all residences was indexed and their corresponding weight factors were assigned according to the individual residential user priorities. The sum of the weight factors assigned to connected appliances of every residential user must be equal to 1. Figure 5 shows the flowchart of the methodology to follow for implementing priority-based scheduling of the appliances using EVs in this study.

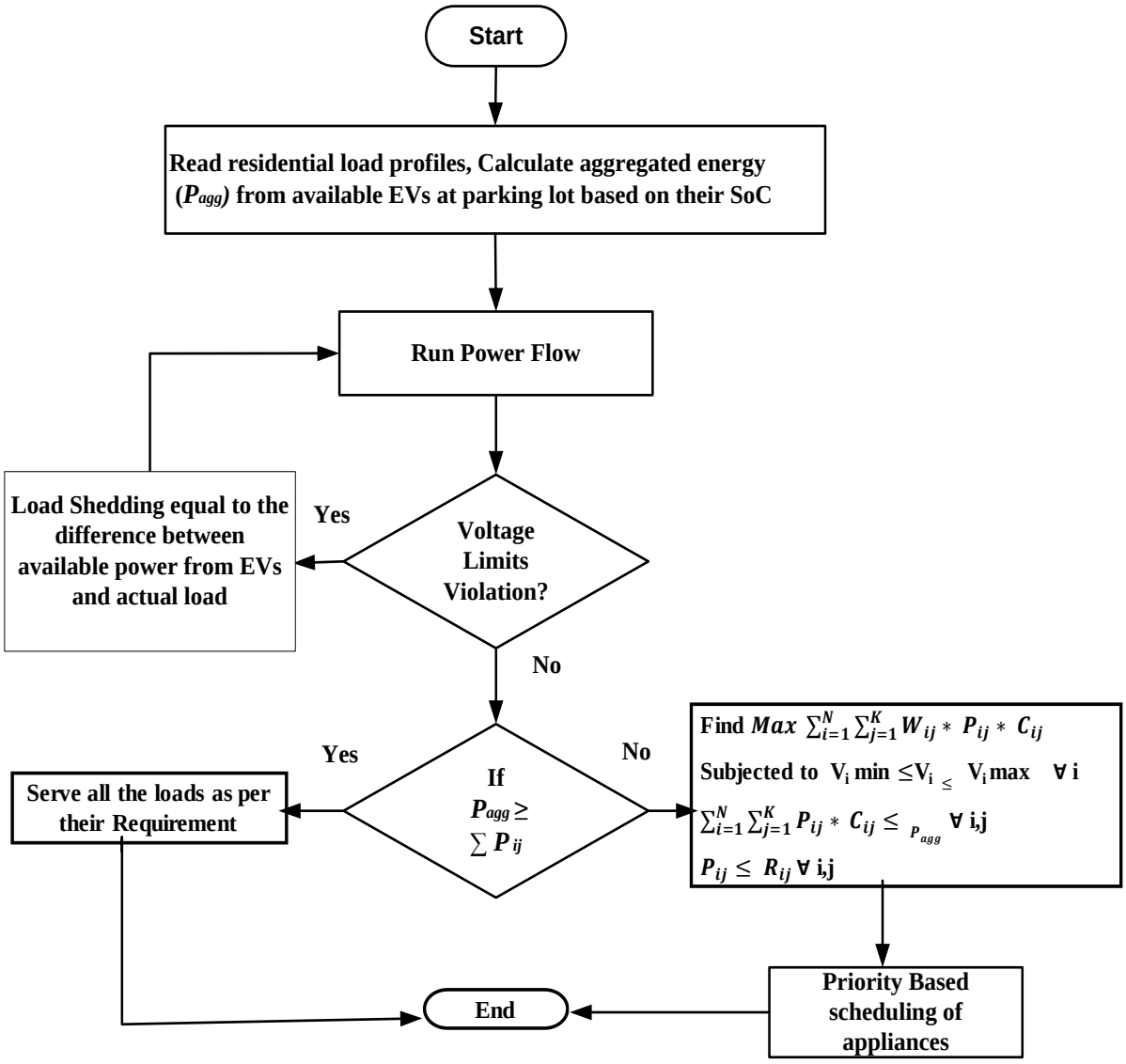

Figure 5. The flowchart of the priority-based scheduling of the appliances.

If the voltage magnitudes were within the limits, it implied that the power available from EVs was more abundant than the actual load. Otherwise, load shedding was made equivalent to the difference between the available EVs' power and the actual residential need for power at the time of restoration. Thereby, the load shedding ensured that the bus voltages were within the limits and the objective function was calculated, which gave the schedule for maximum energy restored to the appliances according to their weight priority factors for every residence by using LINGO optimization modeling.

4. Results and Discussions

The proposed methodology was implemented in the distribution system, as shown in Figure 4. The total residential load profile at any given time was considered as k based on [35]; then the residential load profile of k, individual residents was determined as 0.15 k times for the residential users 1 to 4 and 0.1 k times for residential users 5 to 8. In the instance of a blackout, the number of EVs available in the parking lot was considered to estimate the available energy from EVs based on their SoC. A random function was used to generate the random number of EVs available for 24 h in PYTHON. Power flow was implemented with the estimated power from EVs to observe the voltage deviations. Table 3 shows the randomly generated number of EVs, their estimated power, and the status of the voltage limits after the power flow with available EVs power for each hour. It was observed that the voltage magnitudes were in bounds if the available power from the EVs was higher than the total load. While the voltage magnitudes were within the limits, there was no need to provide weight factors for the appliances and the required load could be served as it is. Prioritization of appliances was required in the case of bus voltage limit violations. To validate the effectiveness of the proposed methodology, a scenario was considered to implement service restoration when the EVs' power was insufficient and the load shedding was done based on the priorities assigned to appliances and voltages to satisfy the limits.

The Scenario at Hour 16

Under an outage condition at hour 16, it was estimated that the total power available from EVs was 9.41 kW and the residential load to meet was 14.09 kW. Power flow was run with a base MVA of 0.096 MVA, as four EVs were available whose battery capacity was 24 kWh each. It was observed that the voltage at buses 6–9 had deviated from the limits. Therefore, load shedding was required. The amount of load shedding was calculated as the difference between the total residential load and the available power from EVs here, it was 4.68 kW. Afterload shedding power flow resulted from the imposed voltage at every bus. Figure 6 shows the voltage profiles before and after the load shedding conditions at hour 16. It is seen that those bus voltages were within the specified limits after the load shedding.

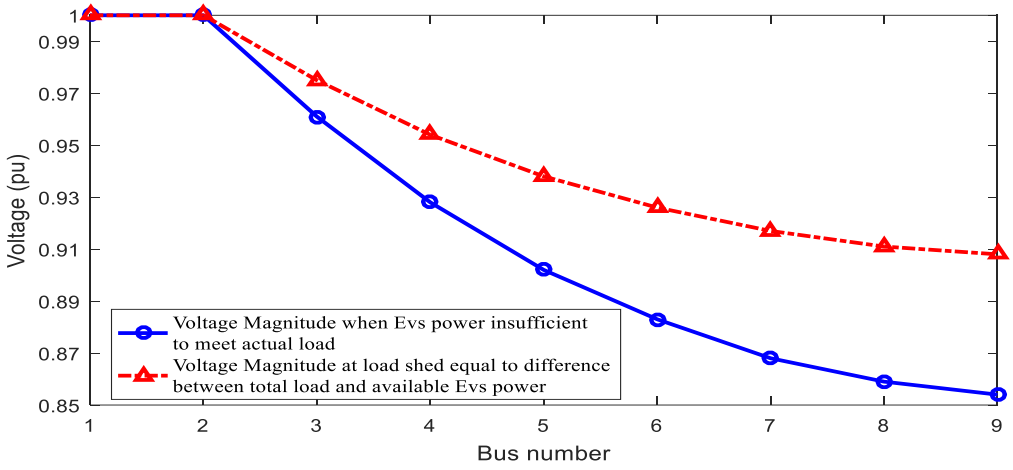

Figure 6. Voltage profile at hour 16 before and after load shedding.

Table 3. Available number of EVs, power from EVs, total actual load, and status of voltage limits during each hour.

Sl.No.	Hour Number	Number of EVs Available	Available Power from EVs (kW)	Total Load (kW)	Status of Voltage Limits before Load Shedding
1	1	2	7.49	10.33916	Violated
2	2	5	24.19	9.7942246	Not violated
3	3	5	18.62	9.2970252	Not violated
4	4	3	15.56	8.885042	Not violated
5	5	3	12.29	8.5883301	Not violated
6	6	3	15.74	8.4295185	Not violated
7	7	4	20.35	8.4238109	Not violated
8	8	5	22.85	8.5789847	Not violated
9	9	2	12.67	8.8953919	Not violated
10	10	2	11.33	9.3659586	Not violated
11	11	5	25.73	9.9761853	Not violated
12	12	3	11.72	10.704147	Violated
13	13	5	11.52	11.520491	Violated
14	14	2	10.18	12.388442	Violated
15	15	3	12.1	13.263797	Violated
16	16	4	9.41	14.094927	Violated
17	17	2	7.3	14.822779	Violated
18	18	5	11.52	15.380871	Violated
19	19	5	12.1	15.6953	Violated
20	20	2	8.07	15.684732	Violated
21	21	2	10.95	15.260411	Violated
22	22	4	12.1	14.326153	Violated
23	23	5	11.52	12.778351	Violated
24	24	3	10.75	10.505969	Violated

Subsequently, the individual residential load was approximated to be 2.115 kW for the residents 1 to 4, which was 0.15 times the 14.09 kW, and for residents 5 to 8, it was 1.409 kW, which was 0.1 times the 14.09 kW, as per our assumption. While a sufficient load was shed, priority-based scheduling was implemented by running the objective function in the LINGO platform. LINGO is an inclusive tool that solves the linear, nonlinear, quadratic, quadratically constrained, second-order cone, semi-definite, stochastic, and integer optimization models with fast built-in solvers. Thus, the maximum power was restored to the appliances from the available EVs. The actual individual residential load profiles, weight factor assigned for priority of appliances, and power restored to appliances from EVs after load shedding are shown in Figures 7–14 for residential users 1–8, respectively.

The amount of load shedding for individual residential users was done as their percentage of the actual load. Hence, the load shedding required for residents 1 to 4 and residents 5–8 was 0.702 kW and 0.468 kW, respectively. Based on the weight factors assigned to the appliances, it was observed that appliances with higher weight factors were scheduled first and the appliances with lower weight factors were scheduled later. Thus, the load shedding for a particular appliance happened according to its priority index. Since there was a deficit of power from EVs compared to the actual load, not all appliances were scheduled as per their requirements. The power restored to the eight residential users was 1.36 kW, 1.4 kW, 1.219 kW, 1.4 kW, 0.945 kW, 0.91 kW, 0.94 kW, and 0.942 kW, respectively. The power restored to individual residents was according to the load pattern of their actual loads. However, maximum power was restored from the available EVs' power. Tables 4 and 5 show the actual power needed during the period of the outage and

the power restored from the four available EVs. Therefore, the load served by a low voltage distribution system could be met with the help of parked EVs without any help from the grid during emergency power outages. An abundant number of EVs at the hour of the outage would further meet the total load required during the outage period.

Table 4. Status of the test system during an outage without EVs.

Number of residential users interrupted	8
Duration of the power outage	1 h
Power needed in kW	14.09
Total residential appliances to run	69

Table 5. Status of the test system during the outage with EVs.

Number of residential users interrupted	0
Duration of the power outage	1 h
Power restored from EVs in kW	9.116
Total residential appliances served	39

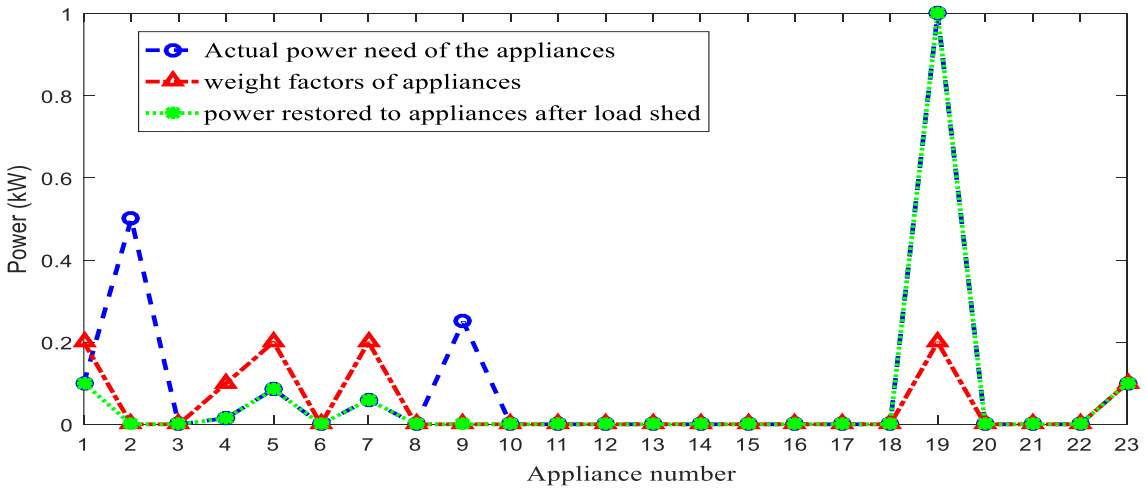

Figure 7. Actual load to meet, weight factors assigned for priority of appliance, and power restored due to EVs for residential user 1.

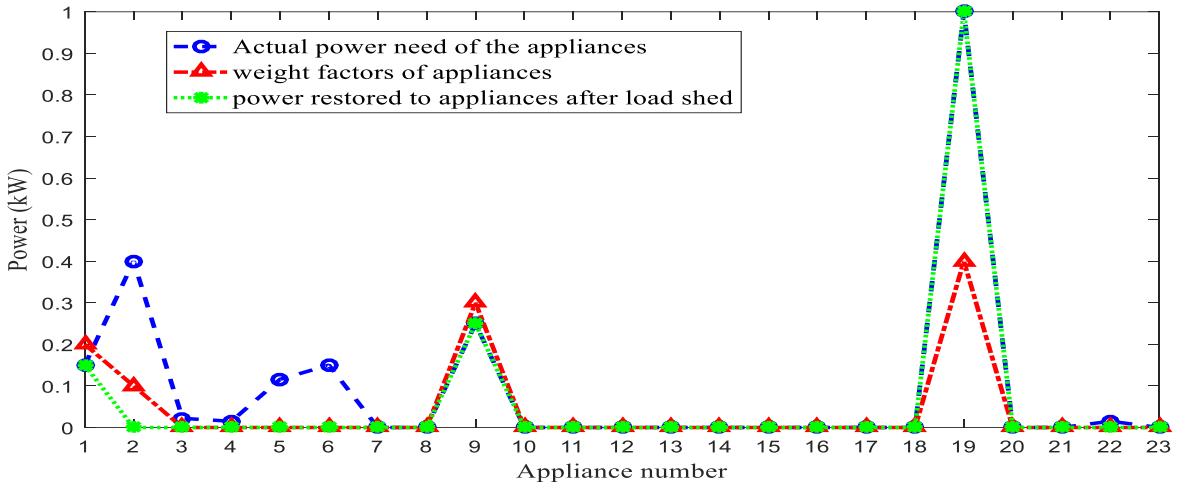

Figure 8. Actual load to meet, factors assigned for priority of appliance, and power restored due to EVs for residential user 2.

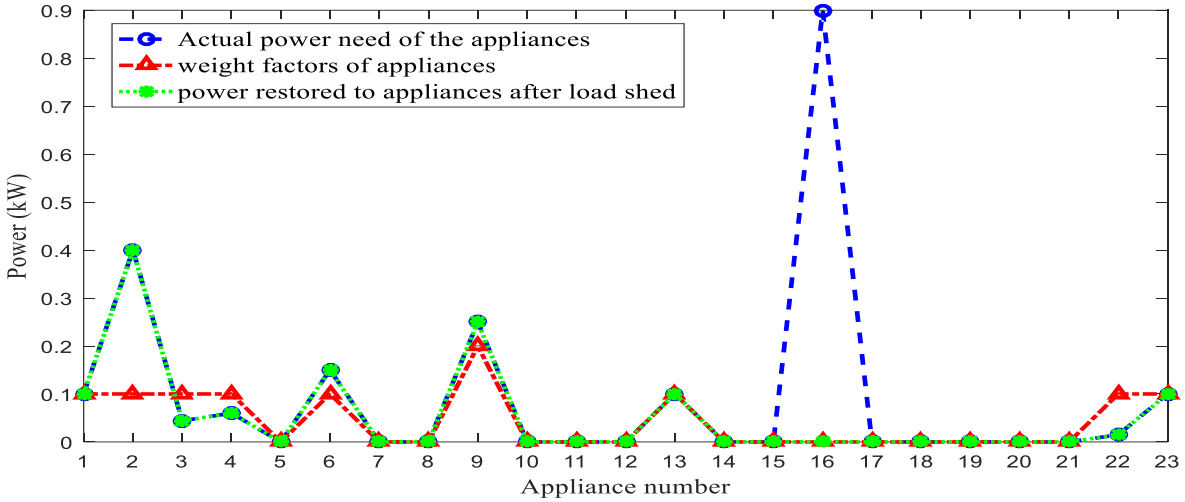

Figure 9. Actual load to meet, weight factors assigned for priority of appliance, and power restored due to EVs for residential user 3.

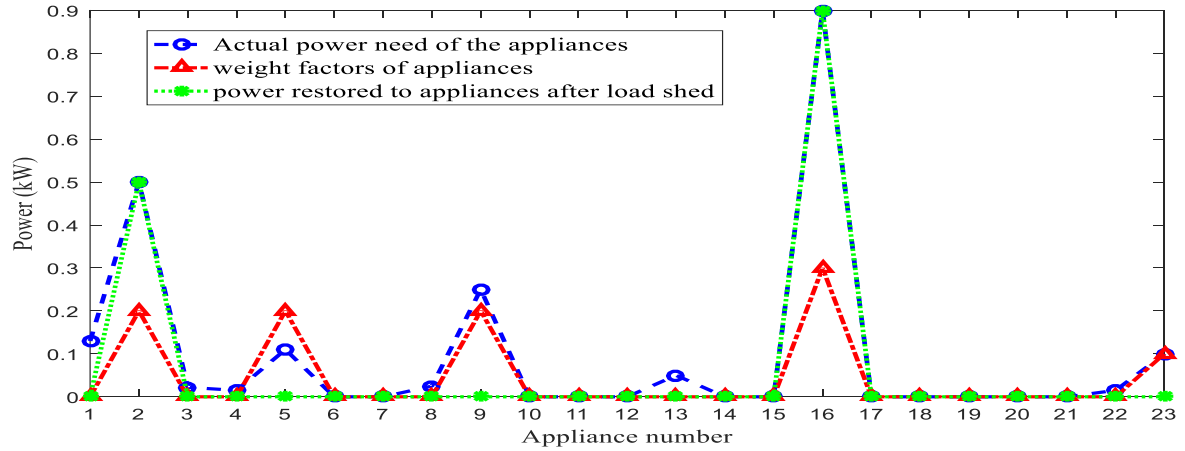

Figure 10. Actual load to meet, weight factors assigned for priority of appliance, and power restored due to EVs for residential user 4.

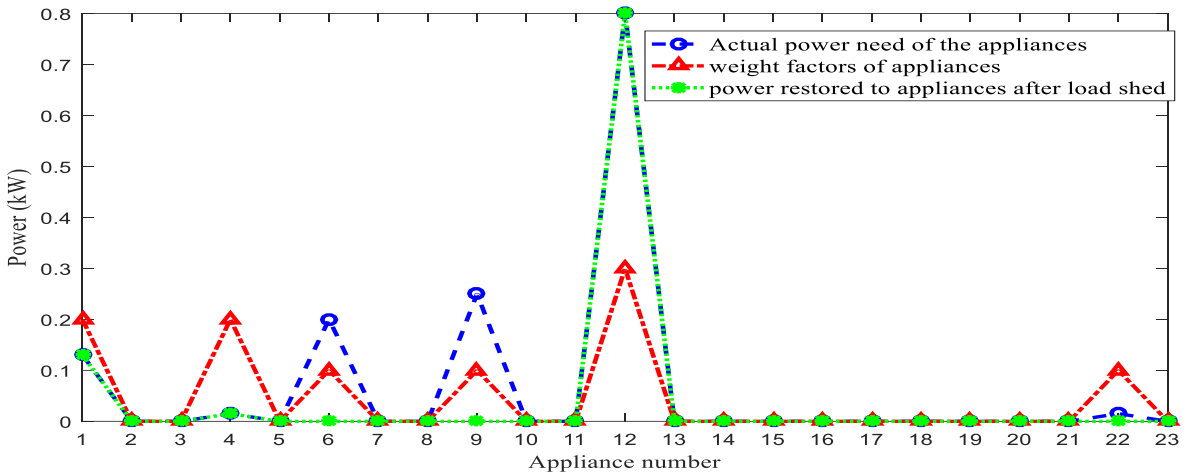

Figure 11. Actual load to meet, weight factors assigned for priority of appliance, and power restored due to EVs for residential user 5.

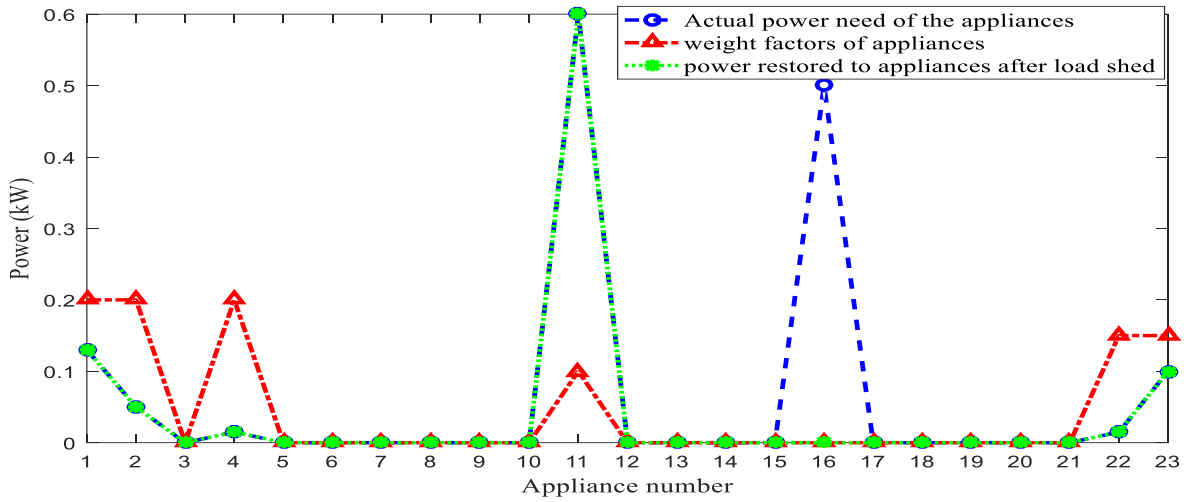

Figure 12. Actual load to meet, weight factors assigned for priority of appliance, and power restored due to EVs for residential user 6.

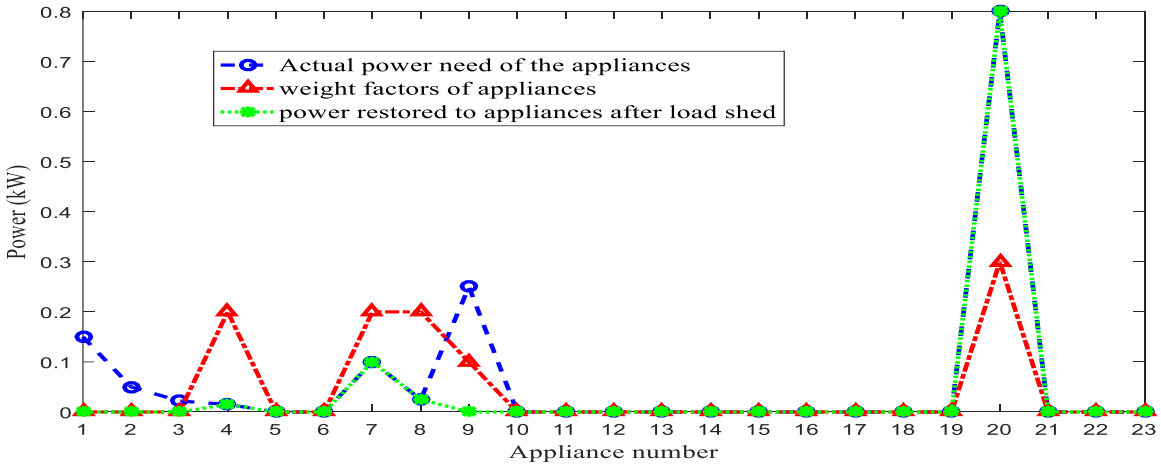

Figure 13. Actual load to meet, weight factors assigned for priority of appliance, and power restored due to EVs for residential user 7.

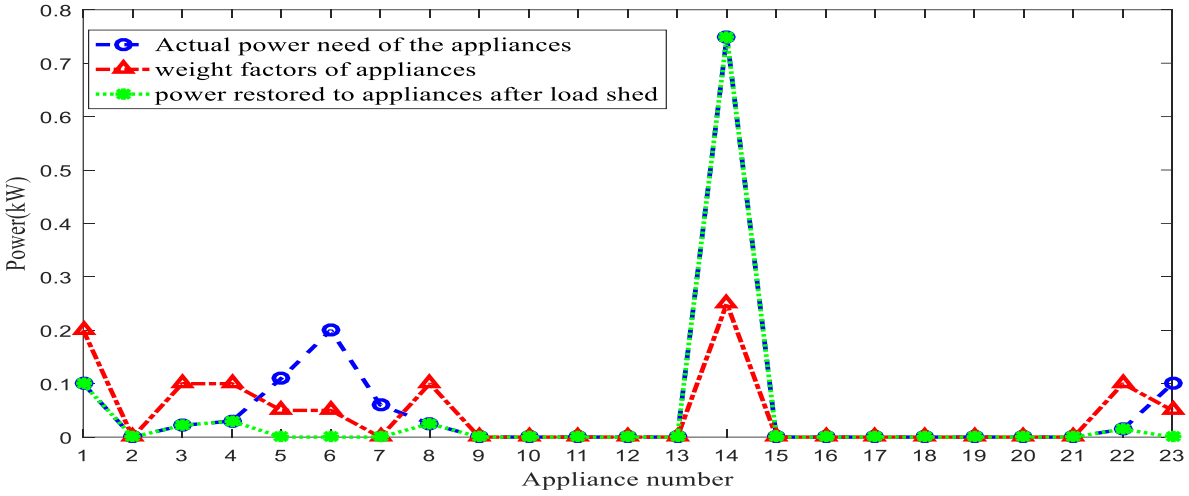

Figure 14. Actual load to meet, weight factors assigned for priority of appliance, and power restored due to EVs for residential user 8.

5. Conclusions

This study proposed a restoration strategy for LT distribution systems by tapping into the potential of parked EVs in a residential area served by a distribution transformer. The proposed methodology was tested on eight residential users by considering a 24 h residential load profile served by a 20 KVA distribution transformer. With the accessible power from EVs, at the time of the outage, priority-based scheduling of the residential appliances at every residence was performed. The results obtained exhibited the need for load shedding when the EVs' predicted power was lower than the actual load and scheduling of appliances was required according to the assigned priorities of each residential user. However, a significant number of EVs contributed to the maximum load restoration. Thus, the restoration strategy using the parked EVs in the LT distribution system improved the resilience and reliability of the distribution system. The uncertainty in the availability of EVs during power outages and a willingness to participate in the service restoration by EVs, the dynamics of EV batteries, and a multi-agent system approach can be implemented in the future to improve the efficiency and stability of the system.

Author Contributions: Conceptualization, S.G. and S.V.P.; methodology, S.G.; software, M.A. and S.G.; validation, B.A., C.R.R., S.G. and F.A.; formal analysis, H.K. and S.G.; investigation, S.G.; resources, M.A. and S.G.; data curation, B.A. and C.R.R.; writing—original draft preparation, M.A., B.A. and S.G.; writing—review and editing, S.G. and C.R.R.; visualization, F.A.; supervision, F.A. and S.V.P.; project administration, M.A. and C.R.R.; funding acquisition, B.A. and M.A. All authors have read and agreed to the published version of the manuscript.

Funding: The authors would like to acknowledge the financial support received from Taif University Researchers Supporting Project Number (TURSP-2020/278), Taif University, Taif, Saudi Arabia.

Institutional Review Board Statement: Not applicable.

Informed Consent Statement: Not applicable.

Data Availability Statement: Not applicable.

Acknowledgments: The authors would like to acknowledge the financial support received from Taif University Researchers Supporting Project Number (TURSP-2020/278), Taif University, Taif, Saudi Arabia. Also authors extend their appreciation to the Deputyship for Research& Innovation, Ministry of Education in Saudi Arabia for funding this research work through the project number "IF_2020_NBU_304" and to the grant number PAQ2022 from the university of gabes, Tunisia.

Conflicts of Interest: The authors declare no conflict of interest.

References

1. Arias, N.B.; Hashemi, S.; Andersen, P.B.; Træholt, C.; Romero, R. Distribution System Services Provided by Electric Vehicles: Recent Status, Challenges, and Future Prospects. In *IEEE Transactions on Intelligent Transportation Systems*; IEEE: Boston, MA, USA, 2019; Volume 20, pp. 4277–4296. [CrossRef]
2. Venegas, F.G.; Petit, M.; Perez, Y. Active integration of electric vehicles into distribution grids: Barriers and frameworks for flexibility services. *Renew. Sustain. Energy Rev.* **2021**, *145*, 111060. [CrossRef]
3. Sun, W.; Kadel, N.; Alvarez-Fernandez, I.; Nejad, R.R.; Golshani, A. Optimal distribution system restoration using PHEVs. *IET Smart Grid* **2019**, *2*, 42–49. [CrossRef]
4. Sharma, A.; Srinivasan, D.; Trivedi, A. A Decentralized Multi-Agent Approach for Service Restoration in Uncertain Environment. In Proceedings of the 2018 IEEE Power & Energy Society General Meeting (PESGM), Portland, OR, USA, 24 December 2018. [CrossRef]
5. Shunbo, L.; Chen, C.; Zhou, H.; Hou, Y. Routing and Scheduling of Mobile Power Sources for Distribution System Resilience Enhancement. In *IEEE Transactions on Smart Grid*; IEEE: Boston, MA, USA, 2019; Volume 10, pp. 5650–5662. [CrossRef]
6. Lei, S.; Chen, C.; Li, Y.; Hou, Y. Resilient Disaster Recovery Logistics of Distribution Systems: Co-Optimize Service Restoration with Repair Crew and Mobile Power Source Dispatch. In *IEEE Transactions on Smart Grid*; IEEE: Boston, MA, USA, 2019; Volume 10, pp. 6187–6202. [CrossRef]
7. Zhu, R.; Andresen, M.; Langwasser, M.; Liserre, M.; Lopes, J.P.; Moreira, C.; Rodrigues, J.; Couto, M. Smart transformer/large flexible transformer. In *CES Transactions on Electrical Machines and Systems*; CES: Seoul, Korean, 2020; Volume 4, pp. 264–274. [CrossRef]

8. Wang, Y.; Xu, Y.; Li, J.; Li, C.; He, J.; Liu, J.; Zhang, Q. Dynamic load restoration considering the interdependencies between power distribution systems and urban transportation systems. *CSEE J. Power Energy Syst.* **2020**, *6*, 772–781. [CrossRef]
9. Golshani, A.; Sun, W.; Zhou, Q. PHEVs contribution to the self-healing process of distribution systems. In *2016 IEEE Power and Energy Society General Meeting (PESGM)*; IEEE: Boston, MA, USA, 2016; pp. 1–5. [CrossRef]
10. Ferreira Neto, L.H.T.; Pereira, B.R.; da Costa, G.R.M. Smart Service Restoration of Electric Power Systems. In Proceedings of the 2016 IEEE Power and Energy Society General Meeting (PESGM), Boston, MA, USA, 14 November 2016; pp. 1–5. [CrossRef]
11. Abilkhassenov, M.; Auketayeva, A.; Berikkazin, N.; Jamwal, P.K.; Nunna, H.S.V.S.K. Service Restoration in Power Distribution Systems using Hybrid Multi-Agent Approach. In Proceedings of the 2018 International Conference on Computing and Network Communications (CoCoNet), Astana, Kazakhstan, 15–17 August 2018; pp. 144–151. [CrossRef]
12. Liu, X.; Ivanescu, L.; Kang, R.; Maier, M. Real-time household load priority scheduling algorithm based on prediction of renewable source availability. In *IEEE Transactions on Consumer Electronics*; IEEE: Boston, MA, USA, 2012; Volume 58, pp. 318–326. [CrossRef]
13. Jia, H.; Jin, X.; Mu, Y.; Yu, X. A multi-level service restoration strategy of distribution network considering microgrids and electric vehicles. In Proceedings of the 2014 International Conference on Intelligent Green Building and Smart Grid (IGBSG), Taipei, Taiwan, 23–25 April 2014; pp. 1–4. [CrossRef]
14. Hong, X.; Xia, M.; Han, Y. A service restoration method for active distribution network. *Energy Procedia* **2014**, *61*, 339–344. [CrossRef]
15. Parast, M.E.; Nazari, M.H.; Hosseinian, S.H. Resilience Improvement of Distribution Networks Using a Two-Stage Stochastic Multi-Objective Programming via Microgrids Optimal Performance. In *IEEE Access*; IEEE: Boston, MA, USA, 2021; Volume 9, pp. 102930–102952. [CrossRef]
16. Firoozi, H.; Khajeh, H.; Laaksonen, H. Optimized Operation of Local Energy Community Providing Frequency Restoration Reserve. In *IEEE Access*; IEEE: Boston, MA, USA, 2020; Volume 8, pp. 180558–180575. [CrossRef]
17. Al-Muhaini, M. Electric Vehicle Markov-Based Adequacy Modeling for Electric Microgrids. In *IEEE Access*; IEEE: Boston, MA, USA, 2020; Volume 8, pp. 132721–132735. [CrossRef]
18. Bilal, M.; Rizwan, M.; Alsaidan, I.; Almasoudi, F.M. AI-Based Approach for Optimal Placement of EVCS and DG With Reliability Analysis. In *IEEE Access*; IEEE: Boston, MA, USA, 2021; Volume 9, pp. 154204–154224. [CrossRef]
19. Rezaeimozafar, M.; Eskandari, M.; Savkin, A.V. A Self-Optimizing Scheduling Model for Large-Scale EV Fleets in Microgrids. In *IEEE Transactions on Industrial Informatics*; IEEE: Boston, MA, USA, 2021; Volume 17, pp. 8177–8188. [CrossRef]
20. Boudina, R.; Wang, J.; Benbouzid, M.; Yao, G.; Zhou, L. A Review on Stochastic Approach for PHEV Integration Control in a Distribution System with an Optimized Battery Power Demand Model. *Electronics* **2020**, *9*, 139. [CrossRef]
21. Akil, M.; Dokur, E.; Bayindir, R. The SOC Based Dynamic Charging Coordination of EVs in the PV-Penetrated Distribution Network Using Real-World Data. *Energies* **2021**, *14*, 8508. [CrossRef]
22. Aljanad, A.; Mohamed, A.; Shareef, H. Impact study of plug-in electric vehicles on electric power distribution system. In Proceedings of the 2015 IEEE Student Conference on Research and Development (SCOReD), Kuala Lumpur, Malaysia, 13–14 December 2015; pp. 339–344. [CrossRef]
23. Hanschek, A.J.; Bouvier, Y.E.; Jesacher, E.; Grbović, P.J. Analysis and Comparison of Power Distribution System Topologies for Low-Voltage DC–DC Automated Guided Vehicle Applications. *Energies* **2022**, *15*, 2012. [CrossRef]
24. Yan, Q.; Kezunovic, M. Impact analysis of Electric Vehicle charging on distribution system. In Proceedings of the 2012 North American Power Symposium (NAPS), Champaign, IL, USA, 22 October 2012; pp. 1–6. [CrossRef]
25. Galiveeti, H.R.; Goswami, A.K.; Choudhury, N.B. Impact of plug-in electric vehicles and distributed generation on reliability of distribution systems. *Eng. Sci. Technol. Int. J.* **2018**, *21*, 50–59. [CrossRef]
26. Ravi, S.S.; Aziz, M. Utilization of Electric Vehicles for Vehicle-to-Grid Services: Progress and Perspectives. *Energies* **2022**, *15*, 589. [CrossRef]
27. Ammous, M.; Khater, M.; AlMuhaini, M. Impact of Vehicle-to-Grid Technology on the Reliability of Distribution Systems. In Proceedings of the 2017 9th IEEE-GCC Conference and Exhibition (GCCCE), Manama, Bahrain, 8–11 May 2017; pp. 1–6. [CrossRef]
28. Liu, Y.; Fan, R.; Terzija, V. Power system restoration: A literature review from 2006 to 2016. *J. Mod. Power Syst. Clean Energy* **2016**, *4*, 332–341. [CrossRef]
29. Vadi, S.; Bayindir, R.; Colak, A.M.; Hossain, E. A Review on Communication Standards and Charging Topologies of V2G and V2H Operation Strategies. *Energies* **2019**, *12*, 3748. [CrossRef]
30. Mao, T.; Zhang, X.; Zhou, B. Modeling and Solving Method for Supporting 'Vehicle-to-Anything' EV Charging Mode. *Appl. Sci.* **2018**, *8*, 1048. [CrossRef]
31. Global EV Outlook. *Accelerating Ambitions Despite the Pandemic*; International Energy Agency: Paris, France, 2021.
32. Tomić, J.; Kempton, W. Using fleets of electric-drive vehicles for grid support. *J. Power Sources* **2007**, *168*, 459–468. [CrossRef]
33. Affonso, C.M.; Kezunovic, M. Probabilistic Assessment of Electric Vehicle Charging Demand Impact on Residential Distribution Transformer Aging. In Proceedings of the 2018 IEEE International Conference on Probabilistic Methods Applied to Power Systems (PMAPS), Boise, ID, USA, 24–28 June 2018; pp. 1–6. [CrossRef]
34. US Department of Energy. Estimating Appliance and Home Electronic Energy Use. Available online: https://www.energy.gov/energysaver/estimating-appliance-and-home-electronic-energy-use (accessed on 19 April 2022).
35. Mou, Y.; Xing, H.; Lin, Z.; Fu, M. Decentralized Optimal Demand-Side Management for PHEV Charging in a Smart Grid. In *IEEE Transactions on Smart Grid*; IEEE: Boston, MA, USA, 2015; Volume 6, pp. 726–736. [CrossRef]

micromachines

MDPI

Article

FPGA Implementation of AI-Based Inverter IGBT Open Circuit Fault Diagnosis of Induction Motor Drives

Nagalingam Rajeswaran [1,*], Rajesh Thangaraj [1], Lucian Mihet-Popa [2,*], Kesava Vamsi Krishna Vajjala [3] and Özen Özer [4]

[1] Electrical and Electronics Engineering, Malla Reddy Engineering College, Secunderabad 500100, India; rajesh.t@mrec.ac.in
[2] Faculty of Information Technology, Engineering, and Economics, Oestfold University College, 1757 Halden, Norway
[3] Department of Physics, Malla Reddy Engineering College, Secunderabad 500100, India; media@mrec.ac.in
[4] Department of Mathematics, Faculty of Science and Arts, Kırklareli University, Kırklareli 39100, Turkey; ozenozer39@gmail.com
* Correspondence: rajeswarann@gmail.com (N.R.); lucian.mihet@hiof.no (L.M.-P.); Tel.: +91-73822211597 (N.R.)

Abstract: In modern industrial manufacturing processes, induction motors are broadly utilized as industrial drives. Online condition monitoring and diagnosis of faults that occur inside and/or outside of the Induction Motor Drive (IMD) system make the motor highly reliable, helping to avoid unscheduled downtimes, which cause more revenue loss and disruption of production. This can be achieved only when the irregularities produced because of the faults are sensed at the moment they occur and diagnosed quickly so that suitable actions to protect the equipment can be taken. This requires intelligent control with a high-performance scheme. Hence, a Field Programmable Gate Array (FPGA) based on neuro-genetic implementation with a Back Propagation Neural network (BPN) is suggested in this article to diagnose the fault more efficiently and almost instantly. It is reported that the classification of the neural network will provide the output within 2 µs although the clone procedure with microcontroller requires 7 ms. This intelligent control with a high-performance technique is applied to the IMD fed by a Voltage Source Inverter (VSI) to diagnose the fault. The proposed approach was simulated and experimentally validated.

Keywords: condition monitoring; Induction Motor Drive; fault diagnosis; FPGA; Back Propagation Neural Network; Discrete Wavelet Transforms

Citation: Rajeswaran, N.; Thangaraj, R.; Mihet-Popa, L.; Krishna Vajjala, K.V.; Özer, Ö. FPGA Implementation of AI-Based Inverter IGBT Open Circuit Fault Diagnosis of Induction Motor Drives. *Micromachines* **2022**, *13*, 663. https://doi.org/10.3390/mi13050663

Academic Editor: Piero Malcovati

Received: 22 March 2022
Accepted: 21 April 2022
Published: 23 April 2022

1. Introduction

Industrial induction motors are highly reliable and easy to operate; hence, they are extensively used as industrial drives [1,2]. They work under harsh and severe conditions, and as a result, they are subject to both internal and exterior faults and breakdowns [3]. These faults must be sensed at the earliest stage; otherwise, catastrophic failure of the machine may result in disruptions to production [4,5]. It was this need that necessitated online supervision and fault analysis design to be integrated with the drive system [6,7].

According to conventional wisdom, the maintenance of Induction Motor Drive (IMD) happens at a certain interval. However, the performance of IMD may decline at irregular intervals as a result of environmental and operational factors. As a result, online monitoring of instant messaging is required to increase efficiency. In new evolving methodologies, predictive maintenance via condition monitoring (CM) is a critical component, intending to project the maintenance schedule based on the state of the plant or process [8–10]. It is possible to improve the performance and efficiency of an IMD by using condition-based monitoring. Such monitoring also extends the life and productivity of the system and reduces internal and external damages. It has become vital to use CM and fault detection in IMDs to prevent unexpected failures and reduce unplanned downtime. There are many

ways for condition monitoring of IM, including Acoustic Emission (AE) monitoring, vibration signature analysis, and Motor Current Signature Analysis (MCSA). However, these monitoring techniques are complicated and need costly sensors [10]. When a CM system is efficient, it is capable of delivering early warning and forecasting errors. The CM system obtains basic data information from the motor via the use of signal processing or data analysis methods as described before. Although the method does not need human interpretation, it does have a fundamental downside [11–13]. The automation of the fault detection and diagnosis process is a natural evolution in the development of CM technologies [14,15]. An intelligent system, such as artificial intelligence methods, Genetic Algorithms (GA), Fuzzy Logic (FL), Artificial Neural Networks (ANN), and expert systems, is required for the autonomous fault detection system [16]. In an industry-based comprehensive assessment of high voltage IMD failures, multiple types of classification were used to identify the causes of the failures [17]. These categories included protection system, machine size, age, number of poles, maintenance regime, and operating hours. Induction machines have been subjected to an investigation into the causes of both stator and bearing failures, which together account for about 75% of all failures [18].

To gather information regarding CM and diagnostic measures, a survey on IM drives for industrial applications was conducted [19]. The research focused on the challenges that are now being addressed and those that will be addressed in the future in the development of autonomous diagnostic methods. The LabVIEW platform was used to produce cutting-edge capabilities for online control of induction motors [20–22]. It has been determined that the use of stator current analysis-based demodulation methods is the most suited method for diagnosing bearing faults.

There are many noncontact CM approaches that may be used to diagnose inductor motor failures. Specifically, it was discovered that the park vector analysis and instantaneous power analysis procedures are the most effective methods for recognizing motor failure signals. The Support Vector Machine (SVM)-based algorithms have demonstrated that they provide improved results for the classification and fault diagnosis of a three-phase induction motor [23]. The Bearing Damage Index (BDI), which is based on the wavelet packet node energy coefficient analysis method, has been proposed not only to detect faults in bearings but also to detect the severity level of the fault [24]. The Bearing Damage Index (BDI) is based on the wavelet packet node energy coefficient analysis method. A review of the most current literature has been published on the automation of condition monitoring in IMD [25]. When it comes to directing maintenance for electrical machines, one of the factors that has been identified as a barrier is the cost-to-benefit ratio between capital and operating expenses [26–28].

In the last two decades or so, condition supervision and fault identification of IMD attracted the attention of many researchers who developed AI-based control schemes such as expert systems, fuzzy interference systems, neural network and neuro-fuzzy techniques. All these techniques when implemented in real time are computationally complex, time-consuming, and lacking in optimal switching strategies. Hence, a new method, neuro-genetic design and implementation of fault diagnosis of induction motors based on a FPGA are proposed in this article [29,30]. The measured signals are processed through DWT for feature extraction. These features are used to detect the type of fault that occurred in the system.

The remaining article is structured as follows. The proposed test system model is presented in Section 2. Section 3 details the proposed method, and Section 4 presents the experimental results. Lastly in Section 5 the conclusions are presented.

2. Proposed System Description

The schematic diagram of the IMD with a FPGA-based neuro-genetic implementation is shown in Figure 1. The proposed system consists of a power supply block having an AC to DC converter node and a DC to AC inverter node, a squirrel cage induction motor, a flux and signal estimation (Programmable Cascaded Low Pass Filter (PCLPF)) block, a

neuro-genetic based fault diagnosis block, a controller block, a neuro-genetic-based Space Vector Pulse Width Modulation (SVPWM) block, and a binary block. The input signals corresponding to the induction motor's terminal voltages and currents are transformed into output signals indicating torque and flux by the lux and signal estimation block. These signals are sent into the controller block, which creates input signals for the SVPWM block, which processes and generates suitable pulses for the binary logic block. The fault diagnosis block receives signals matching the Insulated Gate Bipolar Transistor (IGBT) inverter's output voltages.

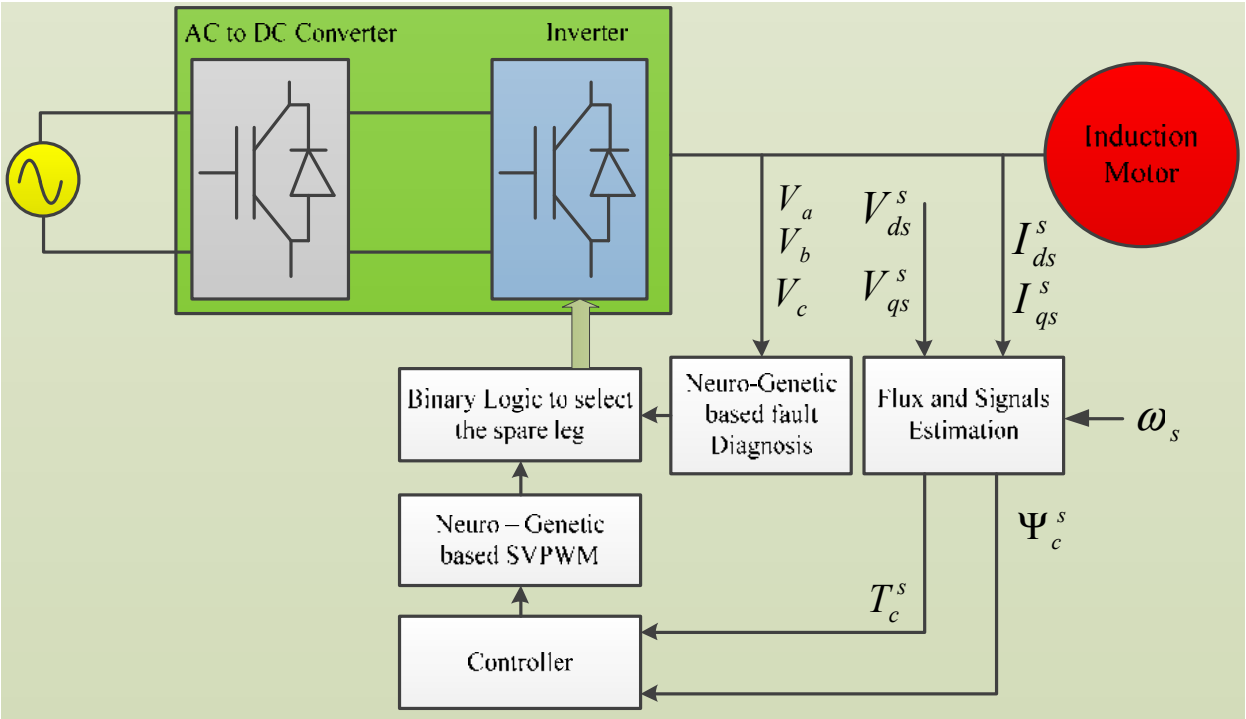

Figure 1. Schematic of Neuro-Genetic-based fault diagnosis drive system.

It processes them in the neural network to produce TRIAC signals for the modified structure of the IGBT inverter. These, together with the output signal of the SVPWM block, are input to the binary logic block, the output signals of which are utilized to transfer the jurisdiction from the faulty leg to the backup leg.

2.1. Reconfiguration of Inverter Topology

IGBT inverter topology is shown in Figure 2. The inverter structure has three legs, with every leg carrying two switches, **S1**, **S2**, **S3**, **S4**, and **S5**, **S6**, correspondingly. The fourth leg has another two switches, **S7** and **S8**. Three Triacs, **T1**, **T2** and **T3**, are utilized for configuring the inverter later fault existence and its elimination. If there is a misfiring in power switch **Sn**, the fault identification part finds this fault and separates the corresponding fault leg by disconnecting the gate signals to the switch **Sn**. The phase current '$\mathbf{i_{sn}}$' is reduced to zero by the freewheeling diodes **Dn** in the faulted leg. Then the restructuring module fires **Tn** which interconnects '**n**' (Leg) and '**o**' (**C1** and **C2**).

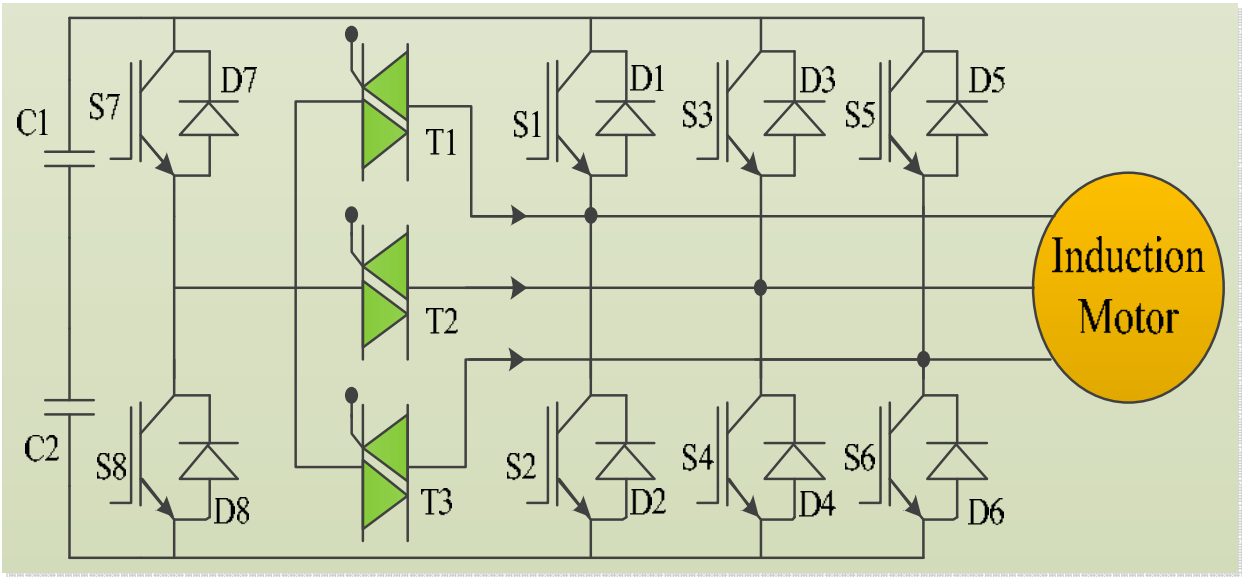

Figure 2. IGBT Inverter topology.

2.2. Fault Diagnosis Based on a FPGA

To accurately diagnose the fault when it occurs, the trend or changes in the monitoring signals must be sensed unambiguously so that the same could be converted into binary code. These coded signals could be used to translate the fault category and its position. Then appropriate gate signals can be generated for suitable action on the system. To carry out the above processes, the control scheme should consist of facilities such as a signal or feature eradication, neural network regulation, fault identification, and gating signals. For the drive system under consideration, the fault diagnosis is performed as follows. The backfire in any one of the switches in a leg of the inverter can be recognized by an error in the corresponding leg voltage. The neural network is experienced with ordinary and extraordinary data for the inverter operation, and so outputs of the neural network are almost '0' and '1' as binary code. Then, corresponding to the error signal of the faulty leg voltage, binary code is generated and sent to the fault identification structure which senses and decodes the fault category and its location. Thereupon, the neural network selects the switches to isolate the faulty leg and bring in the spare leg so that the inverter regains its normal state as a three phase **VSI** to supply the IMD, making it fault tolerant. Suppose if the fault occurred in leg '**n**', causing a deviation in the leg voltage $\pm\Delta Vno$. Then, the leg voltage after fault occurrence can be given as Equation (1),

$$V'no = Vno \pm \Delta Vno \quad (1)$$

This signal may not distinguish itself from Vno, and so a signal transformation technique is required to accurately diagnose the fault. The feature or signal extractor should be such that it provides adequate and significant details about the trend of the signal to enable the neural network to diagnose the fault type and its location with a high degree of accuracy. To achieve this, a feature extractor using a Discrete Wavelet Transform (DWT) technique is employed. The Register Transfer Language (RTL) schematic diagram of the DWT technique is shown in Figure 3. Discrete wavelet transformation is good in time resolution of high frequencies [11].

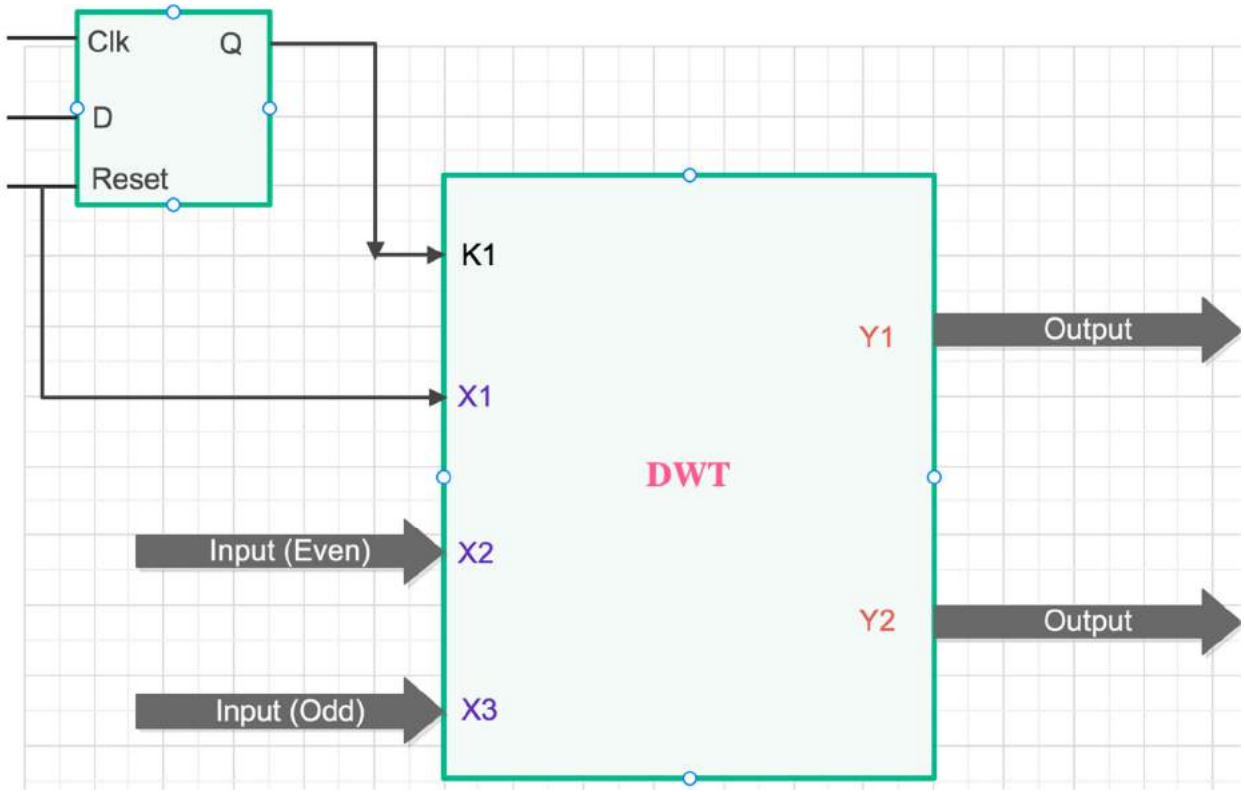

Figure 3. Schematic view of DWT.

3. Neuro-Genetic Approach for Fault Classification

For accurate fault isolation, the signals (voltage, current, and speed) are transformed with the DWT technique for feature extraction [8]. After transformation, the output voltage variations are classified by using the neuro-genetic approach which continues to feedback the signals until desired (target) output is obtained representing the fault situation.

Neuro-Genetic Architecture Design

The structure of the BPN classification based on a FPGA is shown in Figure 4. For the given drive system fed by a **VSI**, there are seven states to represent the conditions, i.e., normal, fault on **S1**, fault on **S2**, fault on **S3**, fault on **S4**, fault on **S5**, fault on **S6**, and fault on **S7**. It requires a seven-layer neural structure. In addition, there are three hidden nodes and one yield node.

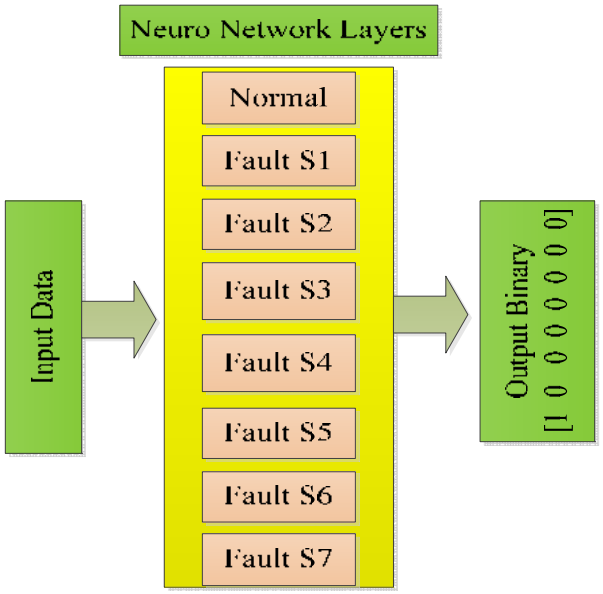

Figure 4. Development of BPN classification structure.

The neuro-genetic-SVPWM has double subnets. One is the voltage amplitude subnet with a 1-3-1 structure, and the other is the angle subnet with the architecture of 1-18-3 to produce a three-phase yield. The sigmoid activation function is used. Every structure is experienced with one set of normal data and four sets of faulted data.

The use of GA helps achieve an optimized weight value for BPN to obtain the desired output for the fault situation. Thus, the neuro-genetic technique based on a FPGA when implemented functions in such a way that the control scheme is capable of fast processing to achieve fault diagnosis almost instantly [12,13]. Here, the mixed design of neural networks and genetic algorithms is developed and implemented in the FPGA process as given by the flow diagram in Figure 5. The idle, birth, selection, crossover, mutation, and store states are used in GA. Linear feedback shift register (LFSR) is used to produce arbitrary numbers [13,14]. A fitness value is designated to every part in the community depending on the discrepancy in the set and original output of the structure. The total number of Pins in the FPGA appliance is 208 and utilized pins in the suggested structure are only 49. The experimental setup presented in Figure 6 is verified on the xc3s500e-4-pq208 board (Xilinx, San Jose, CA, USA). The three-phase induction motor specifications are listed in Table 1.

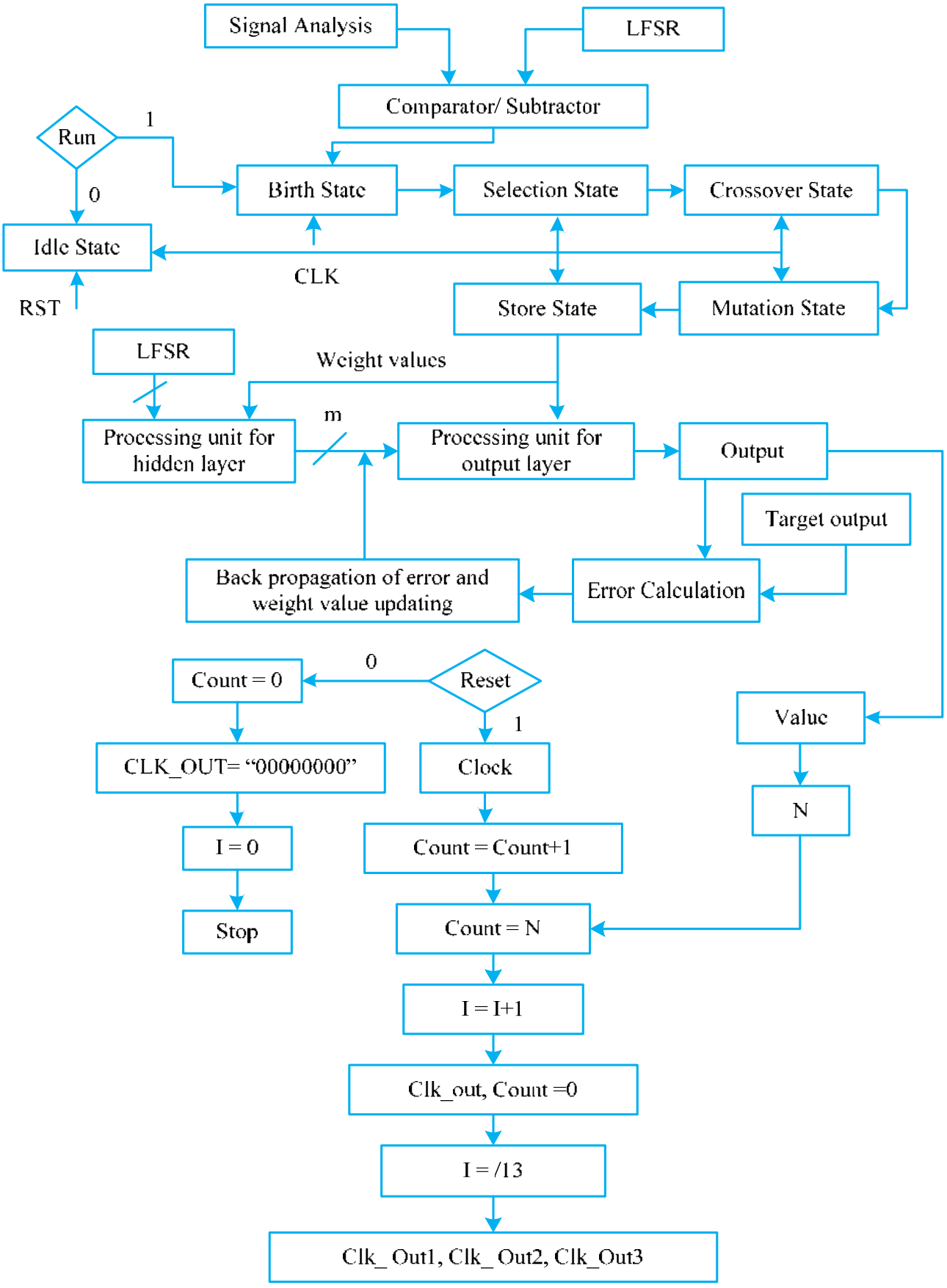

Figure 5. Flow chart of neuro-genetic design.

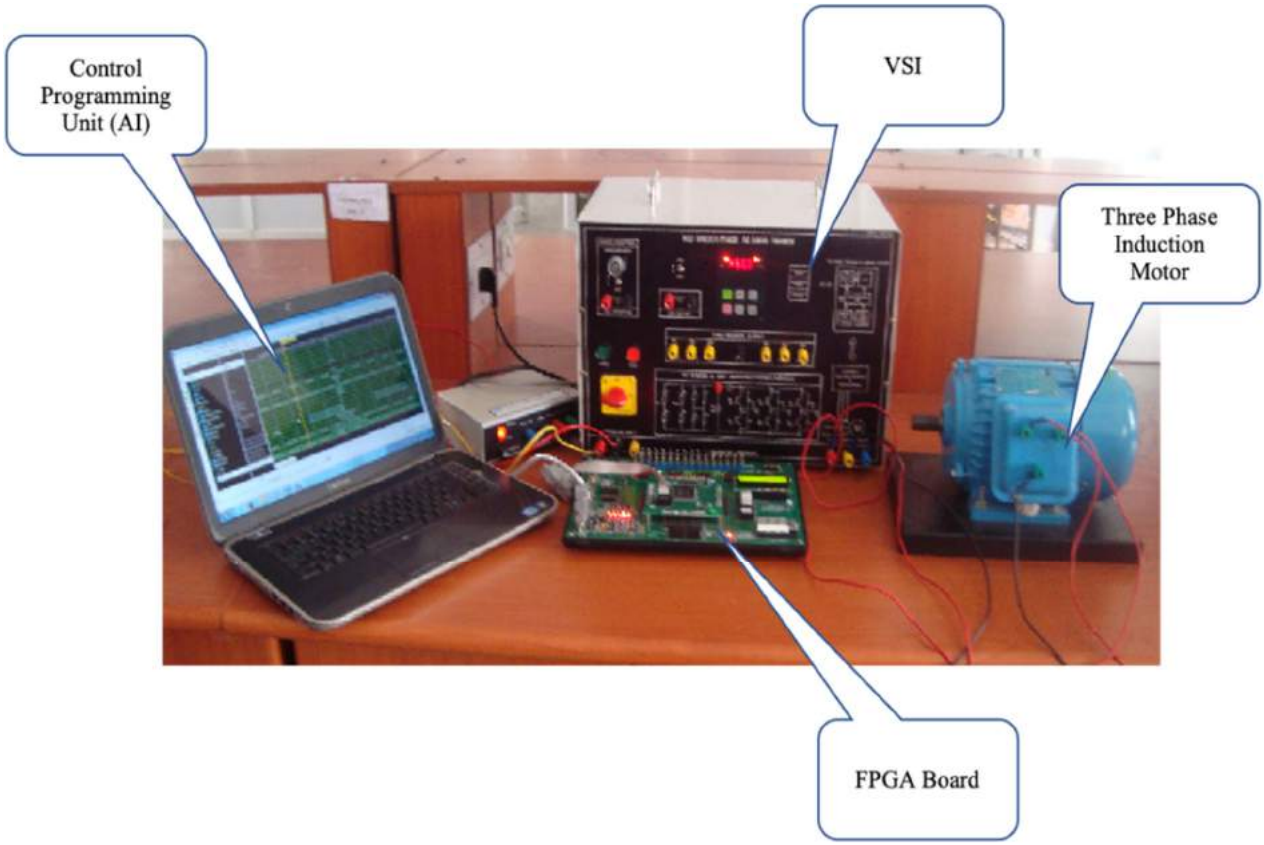

Figure 6. Neuro-genetic implementation based on a FPGA.

Table 1. Induction motor specifications.

Parameter	Range
Speed	1390 rpm
Volts	415 V
Frequency	50 Hz
Power	0.75 kW
Pole	4

4. Results and Discussion

The problem associated with ANN concerning weight optimization to train the network is adequately addressed using GA. The use of DWT as a feature extractor provides significant details in the pattern set to the neural network, enabling it to perform with a high degree of accuracy in fault diagnosis.

With successful configuration by a FPGA, the neuro-genetic-SVPWM processes the signals such that the variation of the neural network provides the yield with minimum and maximum time of 10.85 ns and 11.99 ns. It is reported that the classification of the neural network will provide the output within 2 µs although the clone procedure with a microcontroller requires 7 ms [17]. However, the neuro-genetic approach obtained the low and high period of yield as 10.857 ns (7.440 ns logic, 3.417 ns route, 68.5% for logic and 31.5% for route) and 11.99 ns (8.042 ns for logic, 3.952 ns for route, 67.1% for logic and 32.9% for route), respectively. The result simulations are performed by using integer numbers. The selected device power information is shown in Table 2. The prototype requirement of the proposed method device utilization summary is provided in Table 3. According to the defective and normal conditions, the output voltage waveform reveals how quickly the neuro-genetic process will produce the switching wave shape. A total of 173,524 kilobytes of RAM are used. The suggested design achieves the use of hardware and efficiency to

minimize power consumption in different aspects. Table 4 shows the full clock reports and timing summary. The simulation timing and real-time clock utilization by VHDL is a hardware description language (HDL) software and is tabulated below in Table 5.

Table 2. Power summary.

Parameter	Power (W)	Voltage	Range	Icc (A)	Iccq (A)
Vccint	0.031	1.20	1.14 to 1.25	0.000	0.026
Vccaux	0.045	2.5		0.000	0.018
Vcco25	0.005	2.5		0.000	0.002

Table 3. Device utilization summary.

Logic Utilization	Used	Available	Range
Total number of slice registers	188	9312	2%
Number used as flip flops	105		
Number used as latches	83	2.5	
Number of 4 input LUTs	270	9312	2%
Logic Distribution	**Used**	**Available**	**Range**
Number of occupied slices	217	4656	4%
Number of slices containing only related logic	217	217	100%
Number of slices containing unrelated logic	0	217	0%
Total Number of 4 input LUTs	303	9312	3%
Number used as logic	270		
Number used as a route-through	33		
Number of bonded IOBs	81	159	51%
IOB latches	11		
Number of BUFGMUXs	3	24	12%
Number of M | ULT | I18X18SIOs	4	20	20%

Table 4. Clock Report.

Clock Net	Resource	Locked	Fanout	Net Skew (ns)	Max Delays (ns)
X4/y0_not001	BUFGMUX_X2Y10	No	12	0.011	0.142
Clk1_BUFGP	BUFGMUX_X2Y11	No	75	0.076	0.196
State_out1_1_OBUF	BUFGMUX_X1Y10	No	11	0.030	0.148
x3/ov4	Local		16	0.045	1.249
x3/ov1	Local		6	0.211	1.988
x3/ov3	Local		5	0.460	1.124
x3/ov2	Local		6	0.224	2.235

Table 5. Timing Summary.

Parameters	Frequency
Minimum period	10.857 ns
Maximum frequency	92.108 MHz
Minimum input arrival time before clock	20.18 ns
Maximum output required time after clock	11.99 ns
Maximum combinational path delay	8.610 ns
Total REAL time to Xst completion	11.00 s
Total CPU time to Xst completion	10.41 s

5. Conclusions

Fault diagnosis of IMD has been attempted for fault occurrence in VSI by using a neuro-genetic technique based on a FPGA. The neuro-genetic algorithm (BPN with GA)

processes the error to diagnose the fault type and its location to transfer the switching from faulty leg to spare leg of the IGBT inverter, thereby making the system a fault tolerant IMD. The implementation of this technique is found to increase the speed of response for situational observation and fault identification, thereby enhancing the reliability of the drive system in modern industrial processes. With successful configuration by a FPGA, the neuro-genetic-SVPWM processes the signals such that the variation of the neural network provides the yield with minimum and maximum time of 10.85 ns and 11.99 ns. The proposed techniques can be extended in the near future with various machine-learning methods and switching response can be improved.

Author Contributions: N.R. and R.T.; methodology, N.R.; software, R.T.; validation N.R., L.M.-P. and K.V.K.V.; formal analysis, L.M.-P.; investigation, R.T.; resources, N.R.; data creation, R.T.; writing—original draft preparation, Ö.Ö.; writing—review and editing, N.R., R.T. and K.V.K.V.; visualization, N.R.; supervision, K.V.K.V. and L.M.-P.; project administration, R.T.; funding acquisition. All authors have read and agreed to the published version of the manuscript.

Funding: This research received no external funding.

Institutional Review Board Statement: Not applicable.

Informed Consent Statement: Not applicable.

Conflicts of Interest: The authors declare no conflict of interest.

References

1. Gangsar, P.; Tiwari, R. Signal based condition monitoring techniques for fault detection and diagnosis of induction motors: A state-of-the-art review. *Mech. Syst. Signal Process.* **2020**, *144*, 106908. [CrossRef]
2. Khoualdia, T.; Lakehal, A.; Chelli, Z.; Khoualdia, K.; Nessaib, K. Optimized multi-layer perceptron artificial neural network-based fault diagnosis of induction motor using vibration signals. *Diagnostyka* **2021**, *22*, 65–74.
3. Popa, L.M.; Jensen, B.B.; Ritchie, E.; Boldea, I. Condition monitoring of Wind Generators. In Proceedings of the 38th IAS Annual Meeting on Conference Record of the Industry Applications Conference, Salt Lake City, UT, USA, 12–16 October 2003; Volume 3, pp. 1839–1846. [CrossRef]
4. Al-Janabi, S.; Rawat, S.; Patel, A.; Al-Shourbaji, I. Design and evaluation of a hybrid system for detection and prediction of faults in electrical transformers. *Int. J. Electr. Power Energy Syst.* **2015**, *67*, 324–335. [CrossRef]
5. Sica, F.C.; Guimarães, F.G.; de Oliveira Duarte, R.; Reis, A.J. A cognitive system for fault prognosis in power transformers. *Electr. Power Syst. Res.* **2015**, *127*, 109–117. [CrossRef]
6. Uddin, M.N.; Hao, W. Development of a self- tuned neuro-fuzzy controller for induction motor drives. *IEEE Trans. Ind. Appl.* **2007**, *43*, 1108–1116. [CrossRef]
7. Mihet-Popa, L.; Bak-Jensen, B.; Ritchie, E.; Boldea, I. Current Signature Analysis to Diagnose Incipient Faults in Wind Generator Systems. In Proceedings of the 5th International Symposium on Advanced Electromechanical Motion Systems-Electromotion, ELECTROMOTION 2003, Marrakech, Morocco, 26–28 November 2003; Volume 2, pp. 647–652.
8. Zhong, B. Developments in intelligent condition monitoring and diagnostics in System Integrity and Maintenance. In Proceedings of the 2nd Asia-Pacific Conference (ACSIM2000), Nanjing, China, 1 January 2000; Queensland University of Technology: Brisbane, Australia, 2000; pp. 1–6.
9. Naber, N.; Getz, T.; Kim, Y.; Petrosky, J. Real-Time Fault Detection and Diagnostics Using FPGA-Based Architectures. In Proceedings of the 2010 International Conference on Field Programmable Logic and Applications, Milan, Italy, 31 August–2 September 2010; IEEE Computer Society. pp. 346–351.
10. Mihet-Popa, L.; Pacas, J.M. Failure Detection in Converter Fed Induction Machines under Different Operation Conditions. In Proceedings of the International Electric Machines and Drives Conference (IEMDC), San Antonio, TX, USA, 15–18 May 2005; Volume 3, pp. 967–974.
11. Verucchi, C.J.; Acosta, G.G. Fault Detection and Diagnosis Techniques in Induction Electrical Machines. *Lat. Am. Trans.* **2007**, *5*, 41–49. [CrossRef]
12. Qiao, Z.; Elhattab, A.; Shu, X.; He, C. A second-order stochastic resonance method enhanced by fractional-order derivative for mechanical fault detection. *Nonlinear Dyn.* **2021**, *106*, 707–723. [CrossRef]
13. Mihet-Popa, L.; Prostean, O.; Szeidert, I.; Filip, I.; Vasar, C. Fault Detection Methods for Frequency Converters Fed Induction Machines. In Proceedings of the 12th IEEE Conference on Emerging Technologies and Factory Automation-ETFA, Patras, Greece, 25–28 September 2007; pp. 161–168. [CrossRef]
14. Zidani, F.; Diallo, D.; Benbouzid, M.E.H.; Said, R.N.A. Fuzzy-based approach for the diagnosis of fault modes in a voltage-fed PWM inverter induction motor drive. *IEEE Trans. Ind. Electron.* **2008**, *55*, 586–593. [CrossRef]

15. Wu, Y.; Jiang, B.; Wang, Y. Incipient winding fault detection and diagnosis for squirrel-cage induction motors equipped on CRH trains. *ISA Trans.* **2020**, *99*, 488–495. [CrossRef]
16. Mihet-Popa, L. Current Signature Analysis as Diagnosis Media for incipient fault detection. *J. Adv. Electr. Comput. Eng.* **2007**, *7*, 11–15. [CrossRef]
17. Tatikonda, S.; Agarwal, P. Field Programmable Gate Array (FPGA) based neural network implementation of Motion Control and fault diagnosis of induction motor drive. In Proceedings of the 2008 IEEE International Conference on Industrial Technology, Chengdu, China, 21–24 April 2008; pp. 1–6.
18. Toma, R.N.; Prosvirin, A.E.; Kim, J.M. Bearing fault diagnosis of induction motors using a genetic algorithm and machine learning classifiers. *Sensors* **2020**, *20*, 1884. [CrossRef] [PubMed]
19. Ali, M.Z.; Shabbir, M.N.S.K.; Zaman, S.M.K.; Liang, X. Single-and multi-fault diagnosis using machine learning for variable frequency drive-fed induction motors. *IEEE Trans. Ind. Appl.* **2020**, *56*, 2324–2337. [CrossRef]
20. Kumar, P.; Hati, A.S. Review on machine learning algorithm-based fault detection in induction motors. *Arch. Comput. Methods Eng.* **2021**, *28*, 1929–1940. [CrossRef]
21. Zaman, S.M.K.; Liang, X. An effective induction motor fault diagnosis approach using graph-based semi-supervised learning. *IEEE Access* **2021**, *9*, 7471–7482. [CrossRef]
22. Kabul, A.; Ünsal, A. A diagnosis method of multiple faults of induction motors based on vibration signal analysis. In Proceedings of the 2021 IEEE 13th International Symposium on Diagnostics for Electrical Machines, Power Electronics and Drives (SDEMPED), Dallas, TX, USA, 22–25 August 2021; Volume 1.
23. Bazan, G.H.; Goedtel, A.; Duque-Perez, O.; Morinigo-Sotelo, D. Multi-Fault Diagnosis in Three-Phase Induction Motors Using Data Optimization and Machine Learning Techniques. *Electronics* **2021**, *10*, 1462. [CrossRef]
24. Zamudio-Ramirez, I.; Antonino-DAVIU, J.A.; Osornio, R.A.; Dunai, L. Tracking of high-order stray-flux harmonics under starting for the detection of winding asymmetries in wound-rotor induction motors. *IEEE Trans. Ind. Electron.* **2021**, *69*, 8463–8471. [CrossRef]
25. Wong, P.K.; Biao, J.S. Fault Diagnosis of Induction Motors Under Untrained Loads with a Feature Adaptation and Improved Broad Learning Framework. *IEEE/ASME Trans. Mechatron.* **2021**, 1–12. [CrossRef]
26. Mauricio, A.; Smith, W.A.; Randall, R.B.; Antoni, J.; Gryllias, K. Improved Envelope Spectrum via Feature Optimization-gram (IESFOgram): A novel tool for rolling element bearing diagnostics under non-stationary operating conditions. *Mech. Syst. Signal Process.* **2020**, *144*, 106891. [CrossRef]
27. Mohammed, O.A.; Abed, N.Y.; Ganu, S. Modelling and Characterization of Induction Motor Internal Faults Using Finite Element and Discrete Wavelet Transforms. *IEEE Trans. Magnet.* **2006**, *42*, 3434–3436. [CrossRef]
28. AlShorman, O.; Alkahatni, F.; Masadeh, M.; Irfan, M.; Glowacz, A.; Althobiani, F.; Kozik, J.; Glowacz, W. Sounds and acoustic emission-based early fault diagnosis of induction motor: A review study. *Adv. Mech. Eng.* **2021**, *13*, 1687814021996915. [CrossRef]
29. Cerda, J.C.; Martinez, C.D.; Comer, J.M.; Hoe, D.H.K. An efficient FPGA random number generator using LFSRs and cellular automata. In Proceedings of the 2012 IEEE 55th International Midwest Symposium on Circuits and Systems (MWSCAS), Boise, ID, USA, 5–8 August 2012; pp. 912–915.
30. Choudhary, A.; Goyal, D.; Shimi, S.L.; Akula, A. Condition monitoring and fault diagnosis of induction motors: A review. *Arch. Comput. Methods Eng.* **2019**, *26*, 1221–1238. [CrossRef]

energies

MDPI

Article

A Hybrid AOSAOA Scheme Based on the Optimal Location for Electric Vehicle Parking Lots and Capacitors in a Grid to Care of Voltage Profile and Power Loss

Ch. S. V. Prasad Rao [1], A. Pandian [1,*], Ch. Rami Reddy [2], A. Giri Prasad [3], Ahmad Alahmadi [4] and Yasser Alharbi [4]

[1] Department of Electrical and Electronics Engineering, Koneru Lakshmaiah Education Foundation, Vaddeswaram, A.P., Guntur 522302, India; prasad.chsv@gmail.com
[2] Department of Electrical and Electronics Engineering, Malla Reddy Engineering College (A), Secunderabad 500100, India; crreddy229@mrec.ac.in
[3] Department of Electrical and Electronics Engineering, VNR Vignana Jyothi Institute of Engineering and Technology, Secunderabad 500090, India; giriprasad_a@vnrvjiet.in
[4] Department of Electrical Engineering, College of Engineering, Taif University, P.O. Box 11099, Taif 21944, Saudi Arabia; aziz@tu.edu.sa (A.A.); y.alharbi@tu.edu.sa (Y.A.)
* Correspondence: pands07@kluniversity.in

Abstract: In this manuscript, a hybrid system depending on the optimal location of electric vehicle parking lots (PL) and capacitors under voltage profile care and power loss is proposed. The proposed hybrid scheme is the joint execution of both the atomic orbital search (AOS) and arithmetic optimization algorithm (AOA). Commonly it is called the A OSAOA technique. In the paper, the allocation of the parking lot and capacitor is introduced to congestion management with reactive power compensation. To optimally regulate that parking lot size, the AOSAOA technique is adopted. Furthermore, parking lot and capacitor allocation are introduced to congestion management and reactive power compensation. With this proper control, the perfect sitting of capacitor and EV parking lots under the grid, including the deterioration of real and reactive power loss and voltage profiles are optimally chosen. Furthermore, the implementation of the proposed AOSAOA model is developed by the MATLAB/Simulink platform, and the efficiency of the proposed model is likened to other techniques.

Keywords: electric vehicles parking lot; voltage and power loss; atomic orbital search; arithmetic optimization algorithm

Citation: Rao, S.V.P.C.; Pandian, A.; Reddy, R.C.; Prasad, A.G.; Alahmadi, A.; Alharbi, Y. A Hybrid AOSAOA Scheme Based on the Optimal Location for Electric Vehicle Parking Lots and Capacitors in a Grid to Care of Voltage Profile and Power Loss. *Energies* **2022**, *15*, 4202. https://doi.org/10.3390/en15124202

Academic Editor: Giovanni Lutzemberger

Received: 23 April 2022
Accepted: 2 June 2022
Published: 7 June 2022

1. Introduction

Today, in countries that rely heavily on imported crude oil, key anxieties regarding climate change and increasing oil prices have pushed energy efficiency to become a basic standard. At present, the transportation sector accepts a large part of oil consumption, a large part of which is utilized for road vehicles [1]. As a result, oil prices are rising day by day, bringing burdens to the lives of ordinary people. With the protection of energy and the environment, the worldwide focus in the future will be on alternative transportation, such as electric vehicles (EV) [2]. The invention of rechargeable batteries was applied to electric vehicles that used electric motors and distributed electricity in the 19th century. By charging the battery when necessary, people will feel comfortable driving such electric cars in the city. The top probable position also allows the frame to alleviate voltage problems at different nodes while reducing current leakage from capacitive components. With the increasing popularity of electric vehicles [3], it is necessary to improve the charging infrastructure and provide new affordable models. Since cleaner solutions help people live in a healthy environment, the government provides incentives acceptance of electric vehicles and prolongs investment in infrastructure [4].

Today, electric vehicles have become the hopeful option of powered motor vehicles for general transportation, so charging points need to expand locally in the future. Electric vehicles will be related through a power distribution network that uses charging stations. According to [4], a multi objective optimization method is implemented for modeling difficult assignments. However, in [4], the authors considered the vehicle-to-grid (V2G) under its work but they did not consider the impact of the use of electric vehicles on congestion management. Furthermore, in [5], the allocation of electric vehicle parking was proposed with a detailed probability model of EVPL on the distribution network. In [6], a parking-based allocation system was utilized to catch the best parking location in the Nordic region. Additionally, the impact of EVPL demand on power distribution network losses was studied in depth in [7]. In [8], the restricted distribution of the electric vehicle distribution network was studied. In [9], GA and particle swarms were used to perform the reliability-driven distribution optimization (PSO) of electric vehicle charging points. In [10], the authors proposed a comparable work. A loading system was recommended in [11] to change the maximum load to off-peak hours. Regarding the problems of voltage violation and minimizing power loss, dissimilar load plans are expected. S. Pazouki et al. [12] proposed the simultaneous optimal planning (placing and sizing) of charging stations and distributed generations to address new challenges. They used a genetic algorithm for a simulation study on a 33-bus radial distribution network. The simulation results show the effects of the installation of charging stations in the presence/absence of distributed generations on total costs, reliability, loss, voltage profile, and emission. K. Karmaker et al. [13] proposed an electric vehicle charging station (EVCS) based on solar and biogas to reduce the burden on the national grid. This proposed EVCS integrates a combination of a solar PV module, three biogas generators, 25 lead-acid batteries, a converter, and charging assemblies. They analyzed the economic, technical, and environmental feasibility of the proposed EVCS using Hybrid Optimization of Multiple Energy Renewable Pro software [14]. This proposed method was investigated on a 33-bus system to validate the optimal sitting and sizing of RES and EV charging stations simultaneously. M. Atwa et al. [15] proposed a methodology for the optimal allocation of different types of renewable distributed generation units to reduce annual energy loss in the distribution system.

India and other developing economies have also adopted these collection strategies. J. Teng et al. [16] designed optimal charging/discharging scheduling for battery storage systems (BSSs) that minimizes the distribution systems' losses. Using the genetic algorithm-based method, the results demonstrated the validity of the proposed mathematical model and optimal charging/discharging schedule. M. Mazidi et al. [17] proposed a method in which the reserve requirement for compensating renewable forecast errors was provided by both responsive loads and distributed generation units. The reserve requirement for compensating renewable forecast errors was provided by both responsive loads and distributed generation units. J. GeunKim and M. Kuby [18] developed a linear programming model for optimizing the locations of refueling stations by considering a vehicle's driving range and the necessary deviations of drivers. It shows the maximization of total flows refueled on deviation paths and the decrease of the captured demand flows with an increase in deviation distances, which led to the fragmentation of the global auto market, such as India and Southeast Asia. Two- and three-wheelers are attractive short-term targets. In China, Europe, the United States, and the rest of the world, it is closely followed due to active government measures and continues to lead electric vehicles across the board. It can be clearly seen from the literature review that the distribution grid voltage curve is kept within limits by the smart charging of electric vehicles. V2G apps have yet to do that job. Using the best location for electric vehicle parking lots, it turns out that execution does not rely solely on incentives. Therefore, economically and the geologically convenient charge is a must, as are homes, shopping malls, workplaces, and charging station parking lots. The key feature implies the time variable that consumers value the most. The loss can also be reduced using multiple

generators. 22Kmeans clustering technology was abandoned to analyze the best PL citations at the same time that the ECCRP mathematical formula was described, and a probability-based method was developed to optimize EVPL appointment and size [19]. All CS designs, as a planning model for the distribution network overlay, are concerned with the optimal configuration of CS under the overlay grid. The current work attempts to propose [20] a classification that outlines certain planning models for difficult CS placement as the overlap of the distribution.

2. Recent Research Work: A Brief Review

In the literature, based on the use of various technologies and aspects of the optimal configuration of electric vehicle charging points, various research works can be carried out. Some of them seek feedback: S. Sachan et al. [21] proposed a new method of occasionally charging electric vehicles. In the study, it is recommended to allocate parking lots and condensers congestion management and reactive power compensation. To do this, they performed an analysis by assessing the inverse Jacobian matrix of current research. Biogeography-based optimization technology is used to optimize parking lot size. The expected technology effectiveness was tested on a custom IEEE 34-bus distribution network. Surbhi Aggarwal and Amit Kumar Singh [22] studied the installation of rapid charging stations, a case study on a 24-bus system. This work demonstrates the location of charging stations through dissimilar nominal powers of 5, 25, 50, and 100 MW in different systems of test cases on the load bus line, taking into account the violation of the voltage amplitude limits ($0.95 < V < 1.05$) ratings. Appropriate site selection and size adjustments were made for the DG, and four different test cases were considered, among which charging stations were pre-installed to overcome network loss and maintain system stability. Mohd Bilal and Mohammad Rizwan [23] demonstrated a new hybrid technology to study the best location for electric vehicle charging stations. In addition, this article performs a thorough inspection of the vehicle's facilities to the network. The proposed hybrid method contains Particle Swarm Optimization and Hybrid Gray Wolf Optimization. With the mix of these algorithms of ideal properties and development capabilities, M. Ahmadi et al. [24] proposed the difficulty of the optimal allocation of parking lots of electric vehicles and programming of the optimal operation of electric vehicles under an intelligent distribution network. Different factors involving technical and economic aspects were considered in the questions posed to achieve real solutions. In terms of technical issues, it was considered to lessen network losses and lessen voltage drop between feeders, as well as meet network requirements wholly. In addition, in the questions posed, the total cost of purchasing power and the total cost of loading and unloading the electric vehicle parking lots around the Pearl River Delta was considered based on price.

L. Chen et al. [25] proposed an electric vehicle charging station (EVCS) and explained a new optimized allocation and size adjustment under the Allahabad power distribution system in India. Their key impression considers the reduction in reactive power loss index, improvement in voltage power index, reduction in actual power loss index, and initial cost to optimize EVCS configuration to obtain the smallest installation. To solve the nonlinear optimization mixed-integer difficulty, a new meta-heuristic algorithm is proposed, called the balanced Mayfly algorithm. The modification is to improve precision and solve the problem of algorithm scanning. Charles Raja S [26] demonstrated a two-layer hybrid programming method that improves system reliability using optimizing vehicle charging stations (VCS) that integrate plug-in hybrid electric vehicles and renewable distributed power generation (RDG) at the same time. In the presence of RDG volatility, there are extensive requirements among customers to ensure continuity of supply. Therefore, based on various emergency analyses, a non-linear objective function was developed to lessen the lack of power supply (ENS) provided to customers. Two notable contributions stand out from existing efforts. First, identify the best location for selecting both the RDG and the charging station. Considering the simultaneous integra-

tion of VCS and RDG, a method based on the hybrid Nelder Mead Cuckoo Search algorithm is adopted to minimize ENS, smoothly reduce power loss, and increase the voltage range in the system. P. Rajesh and F.H. Shajin [27] proposed an innovative method for charging stations (CS) with optimal planning and capacitors in the new technology. To accomplish a better balance between the exploration and development of the Dragonfly (DA) algorithm, Gaussian and quantum mutation strategies are used in DA performance. This is the novelty of the work we have shown. Therefore, it is called the quantum effect Gaussian mutation Dragonfly Algorithm. Here, this algorithm is recommended to allocate parking spaces and capacitors and reactive power compensation for congestion management.

Background of Research Work

A review of current research work portrays the optimal configuration of charging stations of an electric vehicle as an important influencing factor. With the quick expansion of EV charging technology, numerous charging facilities are being used at electric vehicle charging stations (EVCS). Charging through dissimilar charging powers may meet the charging needs of different electric vehicles and affect the temporal at the same time and spatial distribution of electric vehicle charging requirements, posing challenges to the rationality and economics of the EVCS allocation plan. To improve the charging efficiency of electric vehicles and alleviate the aforementioned pain points, optimal EVCS planning is becoming an extremely important issue. The optimized configuration scheme of EVCS can meet the charging needs of different electric vehicle owners at the minimum social cost, thus promoting the development of the electric vehicle industry. Genetic Algorithms (GA), Heuristic algorithms, Particle Swarm Optimization (PSO), GAPSO Hybrid Algorithm, and Chemical Reaction Optimization, in addition to Differential Evolution (DE), are techniques commonly used. In addition, the optimization model with a linear integer is utilized to regulate the location of the EVCS and is competently resolved through an optimization solver. Furthermore, in real life, EVCS always mixes and installs multiple charging facilities to meet diversified charging needs. This phenomenon complicates the electric vehicle charging needs, which is why it is great to seek an efficient method to optimize the planning of electric vehicles with multiple charging facilities. These above-mentioned shortcomings are produced in the existing system that carries on this research work.

3. System Modeling of EV

In this article, we consider a smart grid that powers commercial consumers. These buildings are equipped with wind energy and photovoltaic units related to the grid. In addition, electric vehicle charging stations have been set up in the parking area of the workplace and are powered by photovoltaic and wind generators. The goal of the proposed system is to measure the optimal size of electric vehicle parking lots and capacitors on the power distribution system. When the load suddenly has a high demand, the DC bus capacitor is located on the DC side to stabilize the DC bus voltage. An overview of the electric vehicle parking lot (PL) based on the proposed approach is shown in Figure 1. The major part of the electric vehicle charging station (EVCS) is the DC bus, where all the electric vehicles (EVs) are situated for charging. The modeling and mathematical formulations of the sources are described as follows.

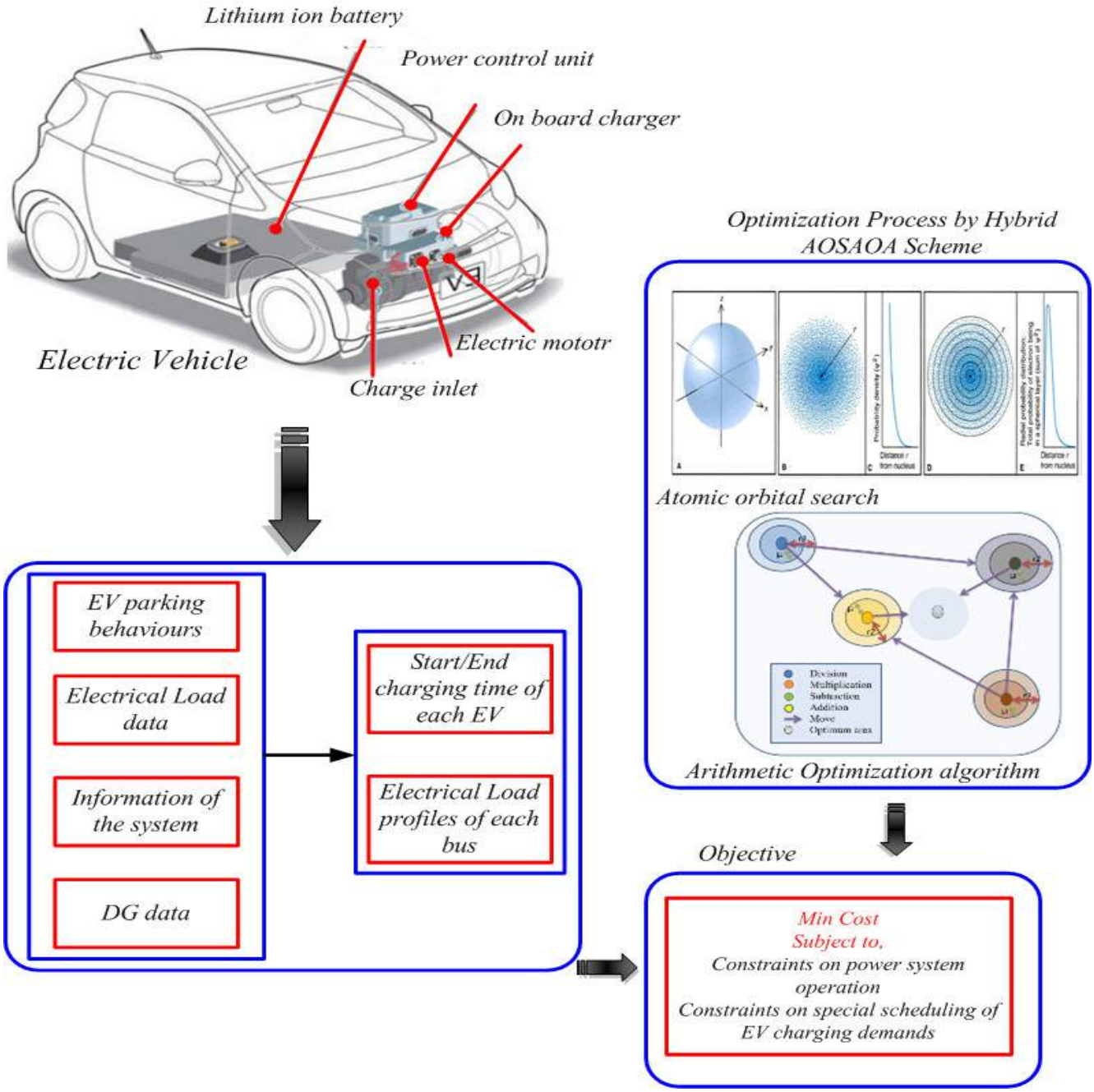

Figure 1. Overview of electric vehicle parking lot based on the proposed approach.

3.1. Modeling of EV

The vehicle model includes a driver, vehicle dynamics, and a power system. A driver's model with input is the actual vehicle speed compared to the reference speed. The output of the driver model is the positions of the brake pedal and the accelerator pedal. The power system receives the instruction from the driver's pedal position and fulfills it through EM and ICE.

The combined active power of the internal combustion engine (ICE) and energy management (EM) acts as a result of the power system and input model of the vehicle's dynamics, namely drag, force, traction, rolling resistance, and gravitational force presented by the slopes of the road [28]. Figure 1 show an overview of an EVCS with parking spaces. The deviation of EV is estimated based on Equation (1)

$$EV_d(t) = \frac{1}{\sigma^* \sqrt{2\Pi}} e^{-(t-\mu^*)/2\sigma^{*2}}, 0 < t < 24 \quad (1)$$

where σ^* is the standard deviation and its value is 3.1, and μ^* is the mean value and its value is 16.97. The arrival of the EV is estimated based on Equation (2)

$$EV_a(t) = \frac{1}{\sigma^* \sqrt{2\Pi}} e^{-(t-\mu^*)/2\sigma^{*2}}, 0 < t < 24 \quad (2)$$

where the value of μ^* and σ^* are 17.01 and 3.2. The EV distance is estimated using the following Equation (3).

$$EV_d(d) = \frac{1}{d\sigma^* \sqrt{2\Pi}} e^{-(\ln d-\mu^*)/2\sigma^{*2}}, d > 0 \quad (3)$$

Here, d shows the travel distance and the values of μ^* and σ^* are 3.2 and 0.9.

3.2. Mathematical Formulation of PV System

Solar cells are basic elements for generating PV systems. Solar cells are coupled in series or in parallel to create a solar cell matrix with the required rating. Figure 2 show the circuit of the solar energy system. In the photovoltaic energy subsystem, sunlight stored with a solar power panel becomes electrical energy [29]. Y. Song, Y. Zheng, and D. Hill (2016) proposed a convexified model, converted using convex relaxation techniques from the conventional model[30], which is applied for 15-bus distribution networks and reduces the total energy and charging cost. In this model, high computational efficiency and optimal solution can be achieved [31]. S. Fazeli, S. Venkatachalam, R. Chinnam, and A. Murat (2020) proposed an embedded two-stage stochastic model which determines the types of EV supply and optimal layout [32]. H. Zhang et al. developed an algorithm using a Gaussian operator and mixed an algorithm for different variations. These algorithms are applied in practical locating planning projects and reduce social costs [33]. L. Gong et al. proposed an optimal charging technique based on a dynamic spike pricing policy with distribution transformer normal operation for reducing the charging cost. They used a genetic algorithm (GA) to reduce charging costs with effective peak sharing [34]. Using Equation (4), the power generated through the photovoltaic system was calculated

$$P_{pv} = R_t \eta_{pv} A_{pv} \quad (4)$$

where P_{pv} represents the power output of the photovoltaic panel, R_t represents the solar radiation in the inclined plane module, η_{pv} represents the efficiency of the photovoltaic panel, and A_{pv} is the area of the photovoltaic panel. The following Equation (5) clarifies the efficiency of photovoltaic panels,

$$\eta_{pv} = \eta_{r-pv} \eta_{PC} \left[1 - N_T \left(T_C - T_{ref}\right)\right] \quad (5)$$

where photovoltaic panel implies η_{pv}, reference module implies η_{r-pv}, power condition implies η_{PC}, photovoltaic panel temperature coefficient denotes N_T, cell temperature (°C) implies T_C as in Equation (6), and the cell temperature on reference conditions is T_{ref}. Likewise, T_{ref} is placed through 25 °C and takes on N_T's value of −3.7 × 10^{-3} °C^{-1} for the temperature of mono and poly crystalline silicon.

$$T_C = T_A + \left[\frac{NOCT - 20}{800}\right] R_t \tag{6}$$

where, T_A implies temperature of ambient air and $NOCT$ implies nominal cell operating temperature.

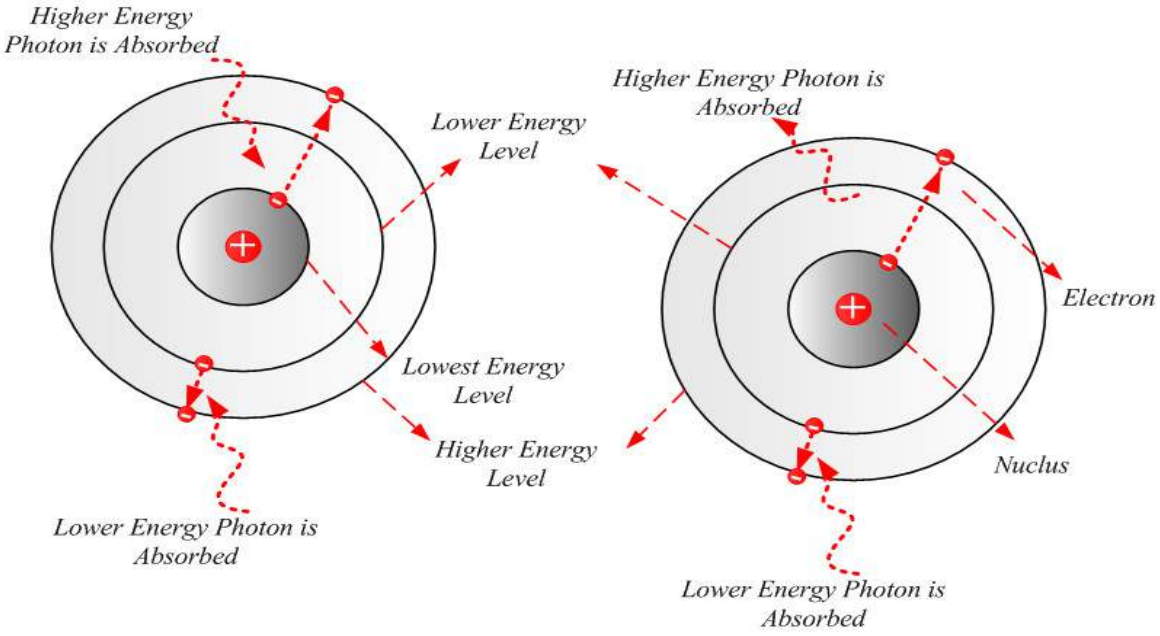

Figure 2. Structure of AOA.

The PV module current is articulated as Equation (7)

$$I^* = I_L^* - I_{sat}^* \left[\exp\left\{q^* \frac{V_{pv}^* + I_{pv}^* . R_s^*}{\upsilon k T_c}\right\} - 1\right] - \frac{V_{pv}^* + I_{pv}^* . R_s^*}{R_{sh}^*} \tag{7}$$

where I_L^* signifies the created current for Light A, R_{sh}^* and R_s^* are series and shunt resistances in Ω, k represents Boltzmann's constant, υ signifies the ideal factor of p-n, V_{pv}^* and I_{pv}^* are the solar cell output voltage and current, and I_{sat}^* indicates the reverse saturation current in A. I_{sat}^* shows the reverse saturation current and I_L^* shows the light-generated current illustrated in Equations (8) and (9)

$$I_L^* = \left[I_{sc} + \gamma(T_c - T_c^*)\right] \frac{C_T}{C_T^*} \tag{8}$$

$$I_{sat}^* = \frac{I_{sc}\gamma(T_c - T_c^*)}{\exp\left[\frac{V_{oc}\gamma(T_c - T_c^*}{V_T}\right] - 1} \tag{9}$$

where T_c are the PV cell's ambient temperature, C_T implies irradiance, γ is the temperature coefficient under short circuit current, V_T is the thermal voltage, and V_{oc} is the open-circuit voltage at standard temperature.

3.3. Modeling of Parking Lot and Capacitor

Electric vehicle charging infrastructure plays a very important role in electric vehicle parking locations, including capacitors, because in electric vehicle parking, as active power loss reduces, system performance improves reliability and efficiency. Charging infrastructure includes all the tools and procedures used to transfer electricity from the grid to the vehicle. A charging area with an acceptable charging time system can improve the performance of electric vehicles and reduce public charging requirements. The following Equation (10) shows the power loss.

$$P_L^* = \sum_{i,j=1}^{n} \left[\upsilon_{ij} (P_i^* P_j^* + Q_i^* Q_j^*) + \varsigma_{ij} (Q_i^* P_j^* - P_i^* Q_j^*) \right] \tag{10}$$

Here, P_i^* and Q_i^* specifythat bus i is active and has reactive power injections, P_j^* and Q_j^* implicate that bus j is active with reactive power injections, and n denotes the number of buses. The υ_{ij} and ς_{ij} can be expressed by (11)

$$\upsilon_{ij} = \left(\frac{x_{ij}}{V_i^* V_j^*} \right) \cos(\beta_i - \beta_j) \tag{11}$$

$$\varsigma_{ij} = \left(\frac{x_{ij}}{V_i^* V_j^*} \right) \sin(\beta_i - \beta_j). \tag{12}$$

Here, the voltage of buses *i* and *j* is shown as V_i and V_j, the bus admittance matrix is represented as Y_{ij}, the load angles of buses *i* and *j* are β_i and β_j, ς_{ii} and υ_{ii} are the susceptance and conductance values, *N* is thenumber of buses. Where, V_i^* and V_j^* imply i and j bus voltage and x_{ij} denotes the impedance matrix.

$$\frac{\partial P_L^*}{\partial P_i^*} = 2\upsilon_{ii} P_i^* + 2 \sum_{\substack{j \neq i \\ j=1}}^{n} \left(\upsilon_{ij} P_j^* - \varsigma_{ij} Q_j^* \right) = 0 \tag{13}$$

$$P_i^* = -\frac{1}{\upsilon_{ii}} \left[\sum_{\substack{j \neq i \\ j=1}}^{n} \left(\upsilon_{ij} P_j^* - \varsigma_{ij} Q_j^* \right) \right] \tag{14}$$

Also

$$P_i^* = P_i^{*EV} + P_{Gi}^* - P_{Di}^* \tag{15}$$

The EVs, PL size, and the size of the capacitor are presented in Equations (16) and (17)

$$P_i^{*EV} = P_{Di}^* - P_{Gi}^* - \frac{1}{\upsilon_{ii}} \left[\sum_{\substack{j \neq i \\ j=1}}^{n} \left(\upsilon_{ij} P_j^* - \varsigma_{ij} Q_j^* \right) \right] \tag{16}$$

$$Q_i^{*EV} = Q_{Di}^* - Q_{Gi}^* - \frac{1}{\upsilon_{ii}}\left[\sum_{\substack{j\neq i \\ j=1}}^{n}\left(\upsilon_{ij}Q_j^* + \varsigma_{ij}P_j^*\right)\right] \tag{17}$$

where P_{Gi}^* implies the grid power in bus *i* and P_{Di}^* specifies bus *I* power demand. The active and reactive power of bus i and j are estimated using Equations (18) and (19)

$$P_i^* = V_i^{*2}G_{ii}^* + \sum_{\substack{j=1 \\ \overline{j\neq 1}}}^{n}\left|V_i^*V_j^*Y_{ij}\right|\cos\left(\theta_{ij} - \beta_i + \beta_j\right) \tag{18}$$

$$Q_i^* = -V_i^{*2}B_{ii}^* - \sum_{\substack{j=1 \\ \overline{j\neq 1}}}^{n}\left|V_i^*V_j^*Y_{ij}\right|\sin\left(\theta_{ij} - \beta_i + \beta_j\right). \tag{19}$$

Here, P_i^* implies the bus *i* active power and Q_i^* implies the bus *i* reactive power. Where G_{ii}^* implies the conductance of bus i, θ_{ij} implies the angle magnitude of self-admittance at line i to j and B_{ii}^* implies the susceptance at bus i. The indexes of sensitivity in the form of the voltage angles and magnitudes are illustrated by

$$\begin{bmatrix}\Delta P^* \\ \Delta Q^*\end{bmatrix} = \begin{bmatrix}J_{11}^* & J_{12}^* \\ J_{21}^* & J_{22}^*\end{bmatrix}\begin{bmatrix}\Delta\beta \\ \Delta V\end{bmatrix} \tag{20}$$

$$\begin{bmatrix}\Delta\beta \\ \Delta V\end{bmatrix} = \begin{bmatrix}U_1^* & U_2^* \\ U_3^* & U_4^*\end{bmatrix}\begin{bmatrix}\Delta P^* \\ \Delta Q^*\end{bmatrix}. \tag{21}$$

ΔP^* is denoted as active power deviation, ΔQ^* is represented as reactive power deviation, ΔV signifies the voltage deviation, $\Delta\beta$ denotes the deviation of load angles of bus *i* and bus *j* as β_i and β_j where, J^* shows matrices and U_1^*, U_2^*, U_3^*, and U_4^* are the voltage variation impacts regarding power on every distribution network bus which is illustrated by the following Equations (22)–(25).

$$U_1^* = \begin{bmatrix}\frac{\partial\beta_2}{\partial P_2^*} & \frac{\partial\beta_2}{\partial P_3^*} & \cdots\cdots & \frac{\partial\beta_2}{\partial P_n^*} \\ \cdot & \cdot & \cdot & \cdot \\ \cdot & \cdot & \cdot & \cdot \\ \frac{\partial\beta_n}{\partial P_2^*} & \frac{\partial\beta_n}{\partial P_3^*} & \cdots\cdots & \frac{\partial\beta_n}{\partial P_n^*}\end{bmatrix} \tag{22}$$

$$U_2^* = \begin{bmatrix} \frac{\partial \beta_2}{\partial Q_2^*} & \frac{\partial \beta_2}{\partial Q_3^*} & \cdots\cdots & \frac{\partial \beta_2}{\partial Q_n^*} \\ \cdot & \cdot & \cdot & \cdot \\ \cdot & \cdot & \cdot & \cdot \\ \frac{\partial \beta_n}{\partial Q_2^*} & \frac{\partial \beta_n}{\partial Q_3^*} & \cdots\cdots & \frac{\partial \beta_n}{\partial Q_n^*} \end{bmatrix} \tag{23}$$

$$U_3^* = \begin{bmatrix} \frac{\partial V_2^*}{\partial P_2^*} & \frac{\partial_2^* V_2^*}{\partial P_3^*} & \cdots\cdots & \frac{\partial V_2^*}{\partial P_n^*} \\ \cdot & \cdot & \cdot & \cdot \\ \cdot & \cdot & \cdot & \cdot \\ \frac{\partial V_n^*}{\partial P_2^*} & \frac{\partial V_n^*}{\partial P_3^*} & \cdots\cdots & \frac{\partial V_n^*}{\partial P_n^*} \end{bmatrix} \tag{24}$$

$$U_4^* = \begin{bmatrix} \frac{\partial V_2^*}{\partial Q_2^*} & \frac{\partial V_2^*}{\partial Q_3^*} & \cdots\cdots & \frac{\partial V_2^*}{\partial Q_n^*} \\ \cdot & \cdot & \cdot & \cdot \\ \cdot & \cdot & \cdot & \cdot \\ \frac{\partial V_n^*}{\partial Q_2^*} & \frac{\partial V_n^*}{\partial Q_3^*} & \cdots\cdots & \frac{\partial V_n^*}{\partial Q_n^*} \end{bmatrix} \tag{25}$$

After that, the subsequent four sensitivity indexes are denoted in Equations (26)–(29)

$$I_{1i}^* = \frac{\sum_{k=1}^{n} \frac{\partial \beta_k}{\partial P_i^*}}{N} \tag{26}$$

$$I_{2i}^* = \frac{\sum_{k=1}^{n} \frac{\partial V_k^*}{\partial P_i^*}}{N} \tag{27}$$

$$I_{3i}^* = \frac{\sum_{k=1}^{n} \frac{\partial \beta_k}{\partial Q_i^*}}{N} \tag{28}$$

$$I_{4i}^* = \frac{\sum_{k=1}^{n} \frac{\partial V_k^*}{\partial Q_i^*}}{N} \tag{29}$$

Here, I_{1i}^* denotes the current in the first bus, I_{2i}^* represents the current in the second bus, I_{3i}^* denotes the current in the third bus, I_{4i}^* represents the current in the fourth bus, and N denotes the count of distribution network nodes. The active and reactive power flow among the nodes is indicated via the factor of contribution from the

electric vehicle parking lot, including the capacitor. Rated power amid bus i and bus j is demonstrated using the following Equations (30) and (31)

$$P_{ij}^{*} = P_{ij}^{*b} + \Delta P_{ij}^{*} \tag{30}$$

$$\Delta P_{ij}^{*} = \sum_{N=1}^{Nb} \frac{\partial P_{ij}^{*}}{P_{N}^{*EV}} \Delta P_{N}^{*} + \sum_{N=1}^{Nb} \frac{\partial Q_{ij}^{*}}{Q_{N}^{*EV}} \Delta Q_{N}^{*}. \tag{31}$$

The above Equation (31) can be rewritten as (32)

$$\Delta P_{ij}^{*} = \sum_{N=1}^{Nb} CFP_{N}^{*EV}(ij,N) \Delta P_{N}^{*} + \sum_{N=1}^{Nb} CFP_{N}^{*EV}(ij,N) \Delta Q_{N}^{*}. \tag{32}$$

The active with reactive power factor contribution for the EVs parking lot, including the capacitor, is illustrated in Equations (33) and (34)

$$CFP_{N}^{*EV}(ij,N) = \frac{\partial P_{ij}^{*}}{\partial P_{N}^{*EV}} \tag{33}$$

$$CFP_{N}^{*EV}(ij,N) = \frac{\partial Q_{ij}^{*}}{\partial Q_{N}^{*EV}}. \tag{34}$$

Equations (33) and (34) can be substituted in Equation (30), resulting in (35) and (36)

$$CFP_{N}^{*EV}(ij,N) = \sum_{j=1}^{Nb} \frac{\partial V_{j}^{*}}{\partial P_{N}^{*EV}} \times \frac{\partial P_{ij}^{*}}{\partial V_{j}^{*}} + \sum_{j=1}^{Nb} \frac{\partial \beta_{j}}{\partial P_{N}^{*EV}} \times \frac{\partial P_{ij}^{*}}{\partial \beta_{j}} \tag{35}$$

$$CFQ_{N}^{*EV}(ij,N) = \sum_{j=1}^{Nb} \frac{\partial V_{j}^{*}}{\partial Q_{N}^{*EV}} \times \frac{\partial Q_{ij}^{*}}{\partial V_{j}^{*}} + \sum_{j=1}^{Nb} \frac{\partial \beta_{j}}{\partial Q_{N}^{*EV}} \times \frac{\partial Q_{ij}^{*}}{\partial \beta_{j}} \tag{36}$$

$CFP_{N}^{*EV}(ij,N)$ denotes and depicts the real power contribution factor and $CFQ_{N}^{*EV}(ij,N)$ shows the reactive power contribution factor of the capacitor and EVs parking lot.

3.4. Objective Function

The objective function is the optimal location of electric vehicle parking lots and capacitors to reduce energy loss. The system power loss is indicated in Equation (10), and the parking power limit can be expressed as Equations (37) and (38)

$$P_{\min}^{EV} \le P_{i,t}^{EV} \le P_{\max}^{EV} \tag{37}$$

$$Q_{\min}^{EV} \le Q_{i,t}^{EV} \le Q_{\max}^{EV} \tag{38}$$

where $P_{\min}^{EV}$ is the minimum active power of the EV and $Q_{\min}^{EV}$ is the minimum reactive power of the EV.

Power balance constraints are given below in Equation (39).

$$\sum_{i=1}^{n} P_{i}^{*EV} = \sum_{i=1}^{n} PD_{i}^{*} + P_{L}^{*} - PG_{i}^{*} \tag{39}$$

The power limits can be verified with Equation (40).

$$\left|P_{ij,L}^{*}\right| \le \left|P_{ij\max,J}^{*}\right| \tag{40}$$

4. Proposed Approach of Atomic Orbital Search and Arithmetic Optimization Algorithm (AOSAOA)

The proposed hybrid scheme will be the joint execution of both the AOS and AOA. AOS depends on certain principles of quantum mechanics and the quantum atomic model under a common configuration of electrons [35]. AOA uses the distribution behavior of major arithmetic operators in mathematics, involving (multiplication, division, subtraction, and addition) [36]. Commonly it is referred to as the AOSAOA technique. The structure of AOA is shown in Figure 2.

4.1. Step by Step Process of AOA

Step 1: Initialization

Determine the initial positions of solution candidates in the search space.

Step 2: Random generation

The initialization procedure generates input parameters randomly using the following Equation (41),

$$X = \begin{bmatrix} S_{11} & S_{12} & \ldots & S_{1n} \\ S_{21} & S_{22} & \ldots & S_{2n} \\ : & : & : & : \\ S_{n1} & S_{n2} & \ldots & S_{nn} \end{bmatrix}. \tag{41}$$

Here, X specifies the input parameters of the system.

The minimal objective function is skilled with the optimal process.

Step 3: Fitness Function

Evaluate the fitness values of initial solution candidates as in Equation (42)

$$\Phi = Min\sum_{i=1}^{n} C_i \,. \tag{42}$$

Step 4: Determine the binding state, binding energy, and lowest energy level of the atom.

Step 5: For the kth imaginary layer, determine the binding energy and binding state of the layer.

Step 6: Distribute candidates' solutions in the imaginary layers.

Step 7: Generate a random integer as the number of imaginary layers, which are around the nucleus of an atom.

Step 8: Determine the lowest energy level for the candidate in the *k*th layer.

Step 9: For the *i*th candidate solution in the *k*th layer, generate random updating parameters.

Step 10: Determine the photon rate for the *i*th candidate solution in the *k*th layer. Determine the binding state and binding energy of the atom and determine the lowest energy level for the candidate in the atom.

Step 11: Termination

If the number of subjects in the census is equal, check the end method. If not, go to step 4. If the end criteria are not met, go to step 3. If you are satisfied with the finished condition, then find the right solution. Figure 3 display the flow chart of AOA.

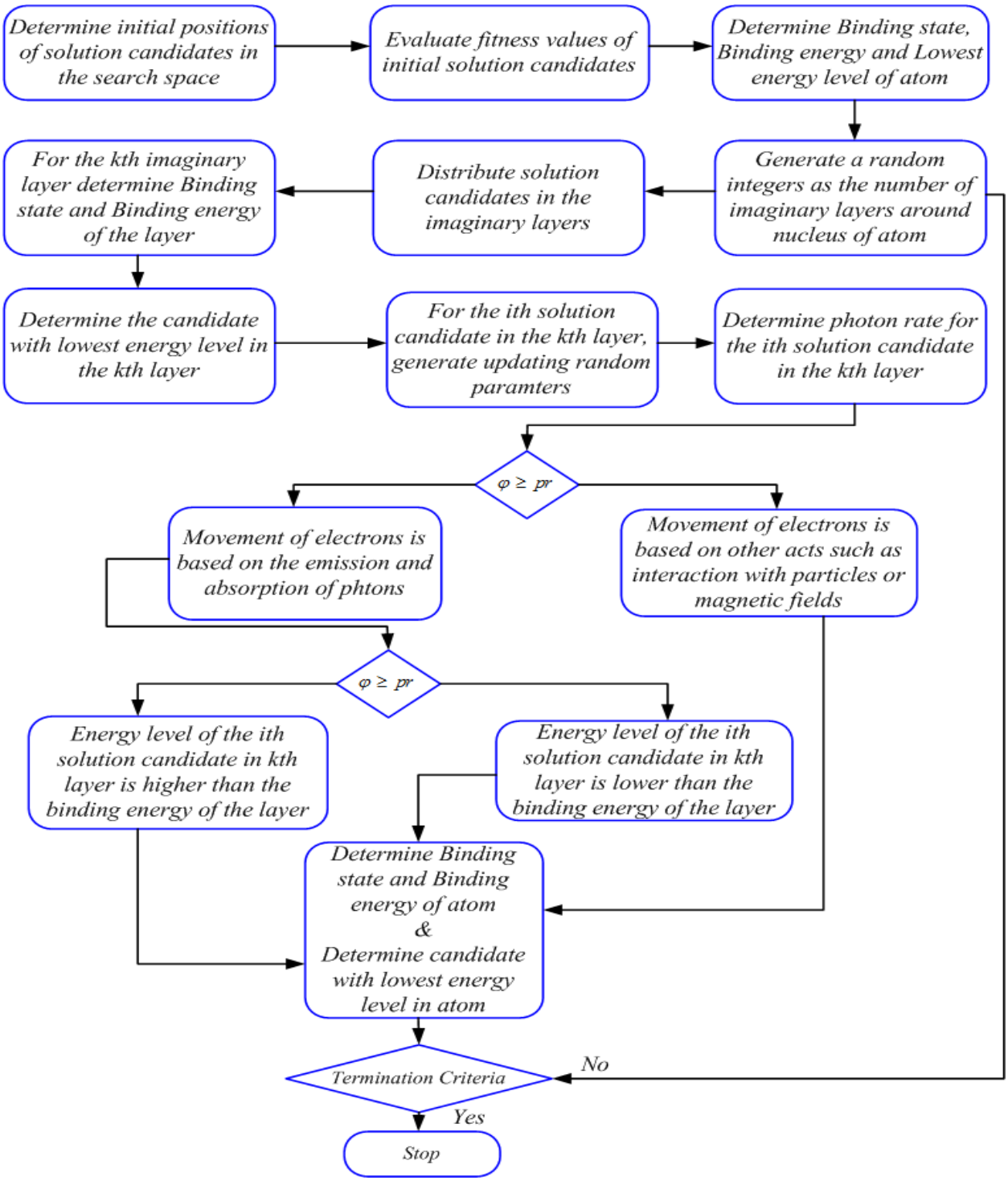

Figure 3. Flowchart of AOA.

4.2. Steps of Arithmetic Optimization Algorithm

Arithmetic is the fundamental component of numerical theory, and it is one of the most important components of modern mathematics, as well as analysis, geometry, and algebra. Arithmetic operators (i.e., subtraction, division, addition, and multiplication) are common calculation methods used to read numbers.

4.3. Step by Step Process of GRFA

Step 1: Initialization phase

In AOA, the process of optimization starts with candidate solutions (X) indicated in Matrix (43). These are randomly generated and the best solution for the candidate for each duplication is considered the most complete or best solution.

$$X = \begin{bmatrix} S_{11} & S_{12} & \ldots & S_{1n} \\ S_{21} & S_{22} & \ldots & S_{2n} \\ : & : & : & : \\ S_{n1} & S_{n2} & \ldots & S_{nn} \end{bmatrix} \quad (43)$$

Here, X Shows the systems input parameters.

Step 2: Fitness Function

Evaluate the fitness values of the initial solution candidates.

Step 3: Exploration phase

In this section, the behavior of AOA is introduced, and Figure 3 show the flowchart of AOA. According to arithmetic staff, mathematical calculators using a multiplication (M) operator or even division (D) obtain higher resolutions or distributed values (see various rules) that bind them to the testing method. Due to their high dispersion, these operators (M and D) are not able to easily approach the target.

Step 4: Exploitation phase

At this stage, the AOA exploitation strategy is introduced. Arithmetic staff and arithmetic calculators using add (A) or subtraction (S) find very dense results referring to the exploitative method. Due to their low dispersion, these operators (A and S) can easily approach the target.

Step 5: Termination

If the number of subjects in the census is equal, check the end method. If not, move to step 4. Go to step 3 if the end criteria are not met. If you satisfy the finish condition, find the right solution.

5. Results and Discussion

A hybrid scheme was proposed based on an optimal location electric vehicles parking lot (PL) and the capacitor's on-grid profile of voltage and power loss. With this proper control, the perfect placement of the capacitor on the grid and parking lot of EVs on the grid, depletion of reactive and real power loss, and voltage profile are optimally improved. Furthermore, the implementation of the proposed AOSAOA model was developed by the MATLAB/Simulink platform, and the efficiency of the proposed model was likened to other techniques.

The proposed method was tested on 31 buses with 23 kV in a distribution system consisting of 415 V permanent networks (J. Grainger and S. Civanlar) [37]. S. Deilami et al. [38] connected to several low-voltage home loads, and curves in daily loads were completed using a set of high sensitivity options. K. Clement-Nyns et al. [39] proposed integrated charging where the grid load factor is amplified, and power loss is reduced by flexible and quadratic planning techniques. D. Thukaram et al. [40] proposed a method tested to analyze the electrical levels of several distribution networks at a rate of R / X. The application of this method is for reactive power optimum location and planning network reconfiguration.

Figure 4 show PEV charging with different penetrations of no PEV, 16% PEV, and 32% PEV. Here, the no PEV is presented. The no PEV flows from 0.85 p.u at the period of 1 h, and it increases up to 0.87 p.u. at the period of 7 h. The 16% PEV flows from 0.84 p.u at the time period of 1 h, and it increases up to 0.89 p.u. at the time period of 7 h. The 32% PEV flows from 0.83 p.u at the time period of 1 h, and at the time period of 12 h, it increases up to 0.98 p.u, and then it reduces to 0.85 p.u at the time period of 24 h. Figure 5 show the PEV charging with different penetrations of no PEV, 47% PEV, and 63% PEV. Here, in

the subplot, the no PEV is presented. The no PEV flows from 0.919 p.u at the time period of 1 h, and it increases up to 0.92 at the time period of 5 h. The 47% PEV flows from 0.918 p.u at the time period of 1 h, and it reduces up to 0.81 at the time period of 5 h. The 63% PEV flows from 0.919 p.u at the time period of 1 h, and at the time period of 12 h, it increases up to 0.95 p.u, and then reduces to 0.91 p.u at the time period of 24 h. Figure 6 show the PEV penetration of the weakest power voltage of no PEV, 16% PEV, and 32% PEV. Here, in subplot (a), the no PEV is presented. The no PEV flows from 0.93 p.u at the time period of 1 h, and at the time period of 12 h, the no PV flows up to 0.97 p.u, and then reduces to 0.95 p.u at the time period of 24 h. The 16% PEV flows from 0.92 p.u at the time period of 1 h, and at the time period of 12 h, it increases up to 0.98 p.u, and then reduces to 0.96 p.u at the time period of 24 h. The 32% PEV flows from 0.94 p.u at the time period of 1 h, and at the time period of 12 h, it increases up to 0.97 p.u, and then reduces to 0.96 p.u at the time period of 24 h. Figure 7 show the PEV penetration of the weakest power voltage of No PEV, 47%% PEV and 63% PEV. Here, in the subplot, the no PEV is presented. The no PEV flows from 0.919 p.u at the time period of 1 h, and it increases up to 0.92 at the time period of 5 h. The 47% PEV flows from 0.918 p.u at the time period of 1 h, and it increases up to 0.937 p.u. at the time period of 5 h. The 63% PEV flows from 0.929 p.u at the time period of 1 h, and at the time period of 12 h, it reduces to 0.918 p.u, and then increases up to 0.948 p.u at the time period of 24 h.

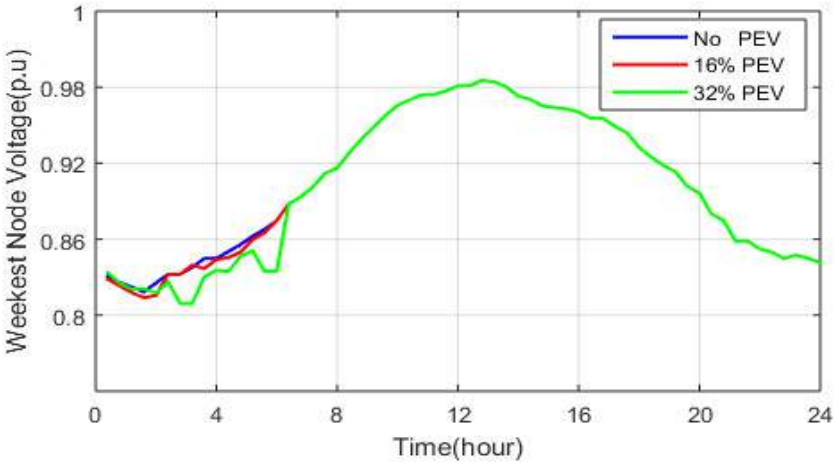

Figure 4. PEV charging with diverse penetration of no PEV, 16% PEV, and 32% PEV.

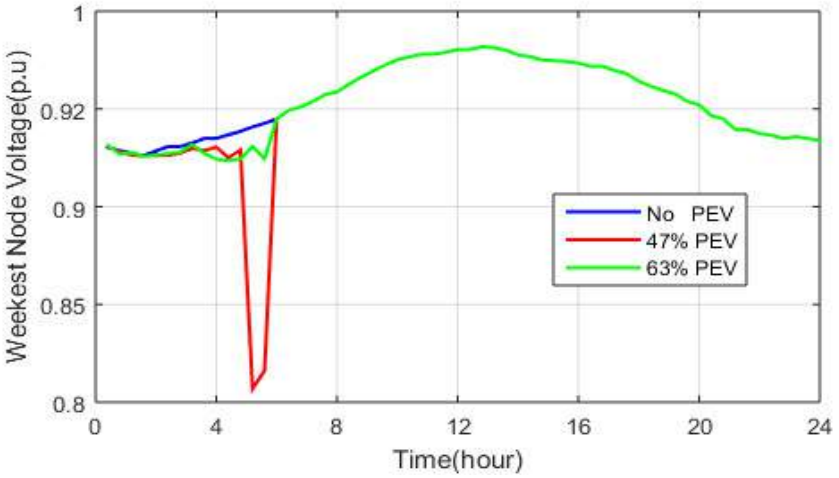

Figure 5. PEV charging with different penetration of no PEV, 47% PEV, and 63% PEV.

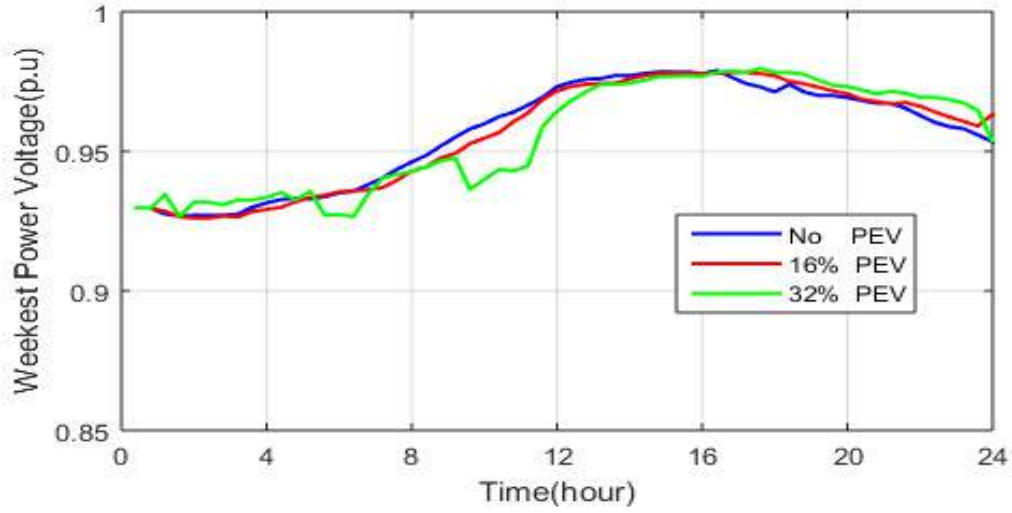

Figure 6. PEV penetration of weakest power voltage no PEV, 16% PEV, and 32% PEV.

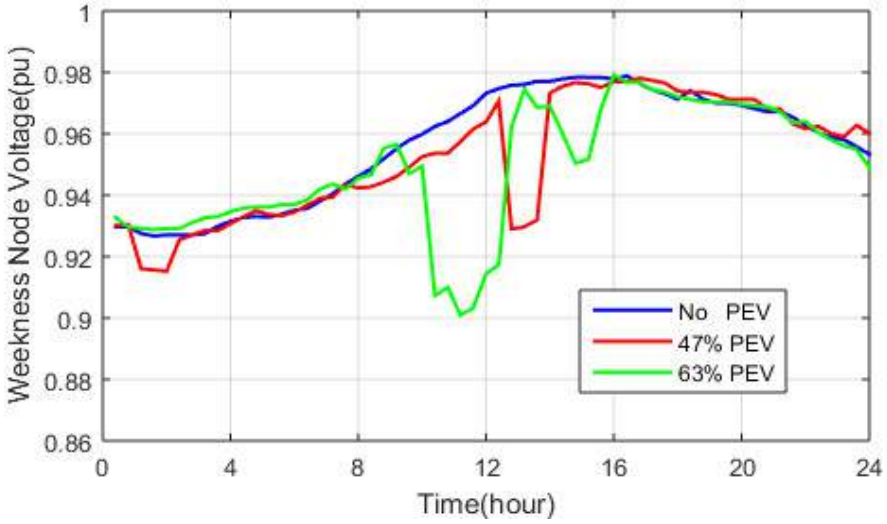

Figure 7. PEV penetration of weakest power voltage of no PEV, 47% PEV, and 63% PEV.

Figure 8 show the PEV penetration of total power loss of no PEV, 16% PEV, and 32% PEV. Here, in the subplot, the no PEV is presented. The no PEV flows from 29 kW at the time period of 1 h, and at the period of 8 h, the no PEV flows up to 6 kW, and then reduces to 3 kW at the time period of 12 h. The 16% PEV flows from 29 kW at the time period of 1 h, and at the period of 8 h, it reduces to 12 kW, and then reduces to 3 kW at the time period of 12 h. The 32% PEV flows from 30 kW at the period of 1 h, and at the time period of 12 h, it reduces to 3 kW, and then increases up to 24 kW at the time period of 24 h. Figure 9 show the PEV penetration of total power loss of no PEV, 47% PEV, and 63% PEV. Here, in the subplot, the no PEV is presented. The no PEV flows from 24 kW at the period of 1 h, and it decreases to 3 kW at the period of 12 h. The 47% PEV flows from 27 kW at the period of 1 h, and it reduces to 4 kW at the time period of 12 h. The 63% PEV flows from 26 kW at the period of 1 h, and at the period of 12 h, it reduces to 8 kW, and then increases up to 20 kW at the period of 24 h.

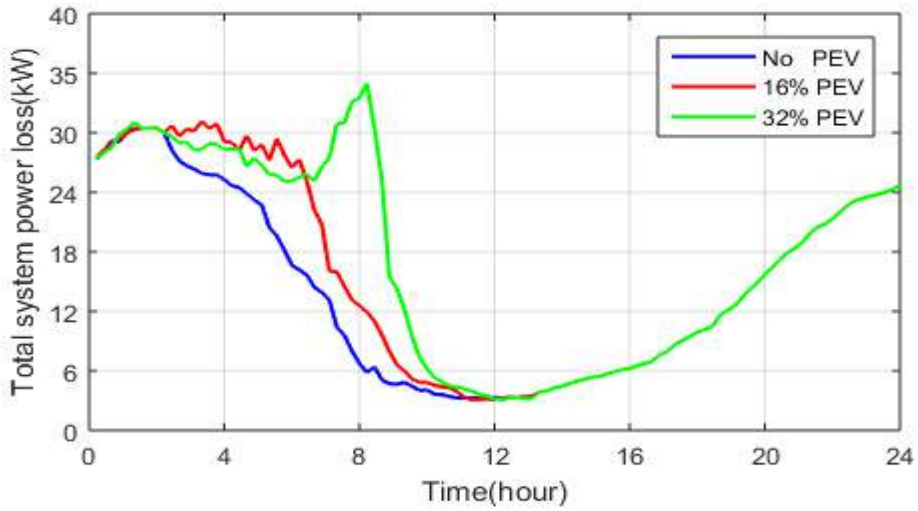

Figure 8. PEV penetration of total power loss of no PEV, 16% PEV, and 32% PEV.

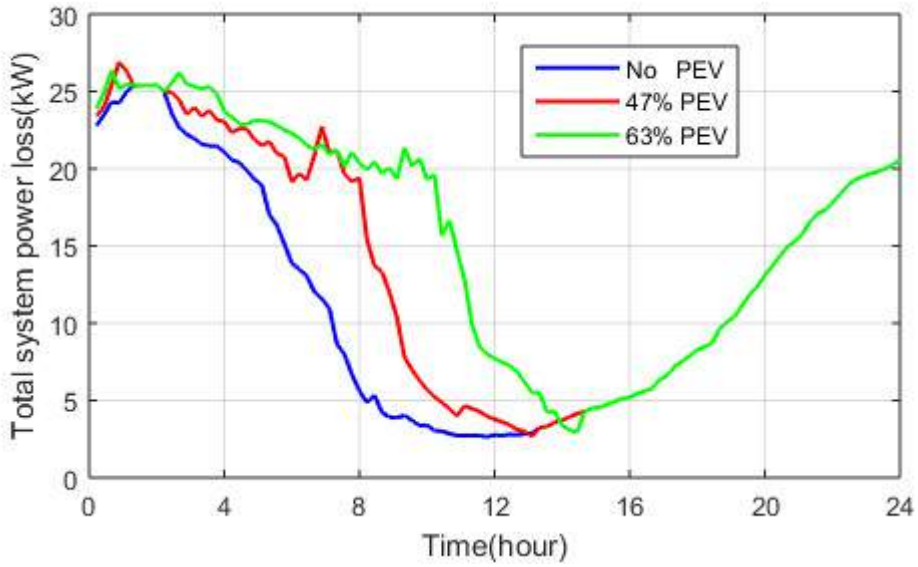

Figure 9. PEV penetration of total power loss no PEV, 47% PEV, and 63% PEV.

Figure 10 show the PEV penetration of total power consumption of no PEV, 47% PEV, and 63% PEV. Here, in the subplot, the no PEV is presented. The no PEV flows from 830 kW at the period of 1 h, and it decreases to 300 kW at the time period of 12 h. The 47% PEV flows from 820 kW at the time period of 1 h, and it reduces to 370 kW at the time period of 12 h. The 63% PEV flows from 830 kW at the period of 1 h, and at the time period of 12 h, it reduces to 450 kW, and then increases up to 700 kW at the time period of 24 h. Figure 11 show the PEV penetration of total power consumption of no PEV, 16% PEV, and 32% PEV. Here, in the subplot, the no PEV is presented. The no PEV flows from 820 kW at the time period of 1 h, and it decreases to 280 kW at the time period of 12 h. The 16% PEV flows from 830 kW at the period of 1 h, and it reduces to 340 kW at the period of 12 h. The 32% PEV flows from 840 kW at the time period of 1 h, and at the period of 12 h, it reduces to 290 kW, and then increases up to 730 kW at the time period of 24 h.

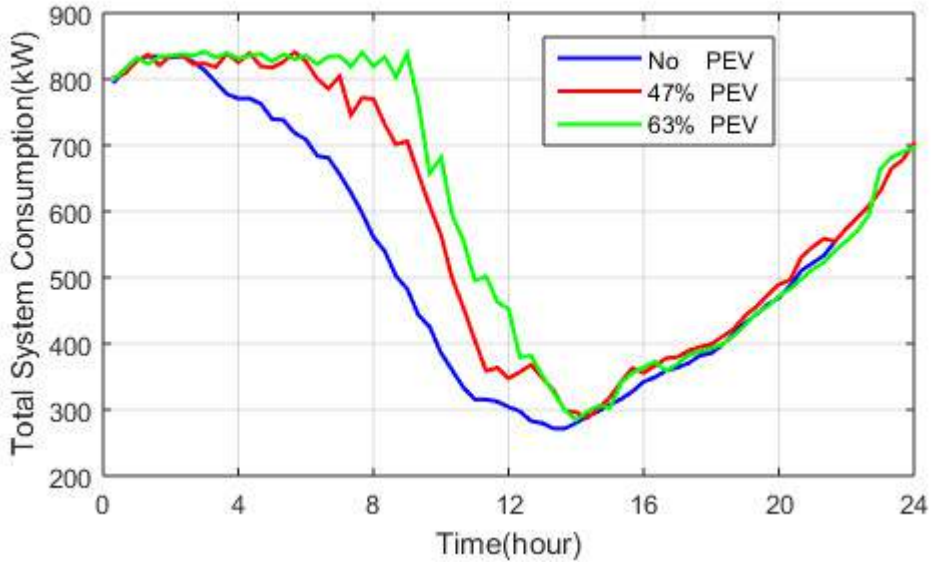

Figure 10. PEV penetration of total power consumption no PEV, 47% PEV, and 63% PEV.

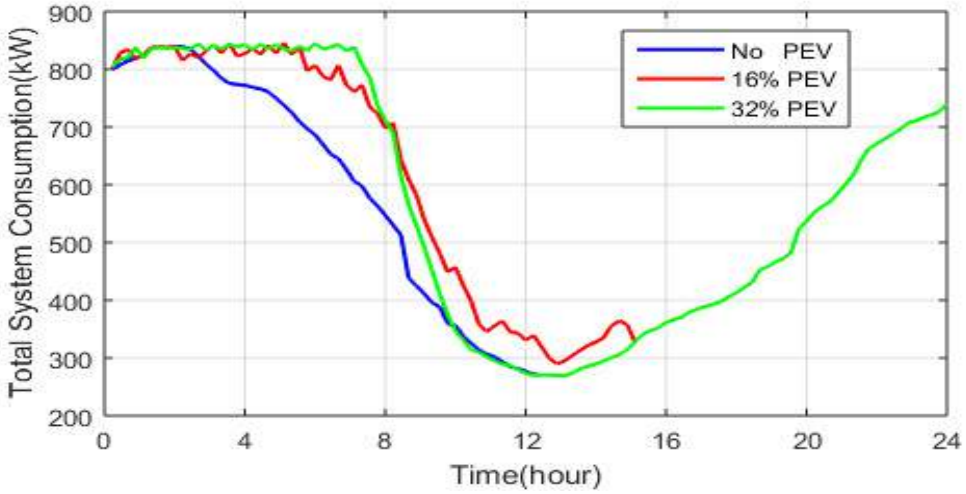

Figure 11. PEV penetration of total power consumption no PEV, 16% PEV, and 32% PEV.

Figure 12 show the fixed charge–rate coordination integrating capacitor of no PEV, 16% PEV, and 32% PEV. Here, in the subplot, the no PEV is presented. The no PEV flows from 0.93 p.u at the time period of 1 h, and it increases up to 0.976 p.u at the time period of 12 h. The 16% PEV flows from 0.956 p.u at the time period of 1 h, and it increases up to 0.981 p.u at the time period of 12 h. The 32% PEV flows from 0.95 p.u at the time period of 1 h, and at the time period of 12 h, it increases up to 0.99 p.u, and then reduces to 0.95 p.u at the time period of 24 h. Figure 13 show the fixed charge-rate coordination integrating capacitor of no PEV, 47% PEV, and 63% PEV. Here, in the subplot, the no PEV is presented. The no PEV flows from 0.928 p.u at the period of 1 h, and it increases up to 0.978 p.u at the period of 12 h. The 47% PEV flows from 0.94 p.u at the time period of 1 h, and it increases up to 0.982 p.u at the period of 12 h. The 63% PEV flows from 0.948 p.u at the time period of 1 h, and at the time period of 12 h, it increases up to 0.98 p.u, and then reduces to 0.958 p.u at the time period of 24 h.

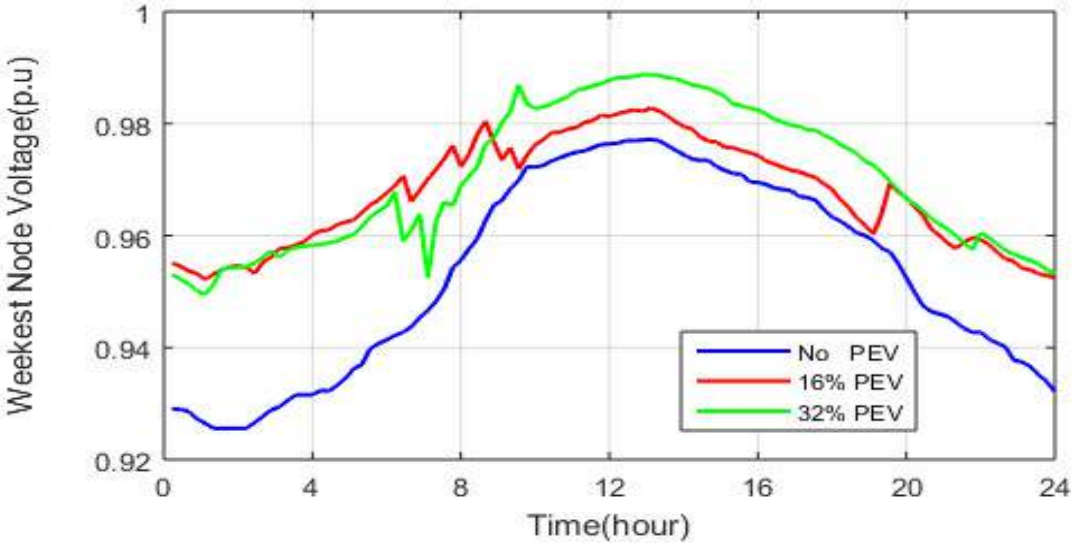

Figure 12. Fixed-charge–rate coordination integrating capacitor no PEV, 16% PEV, and 32% PEV.

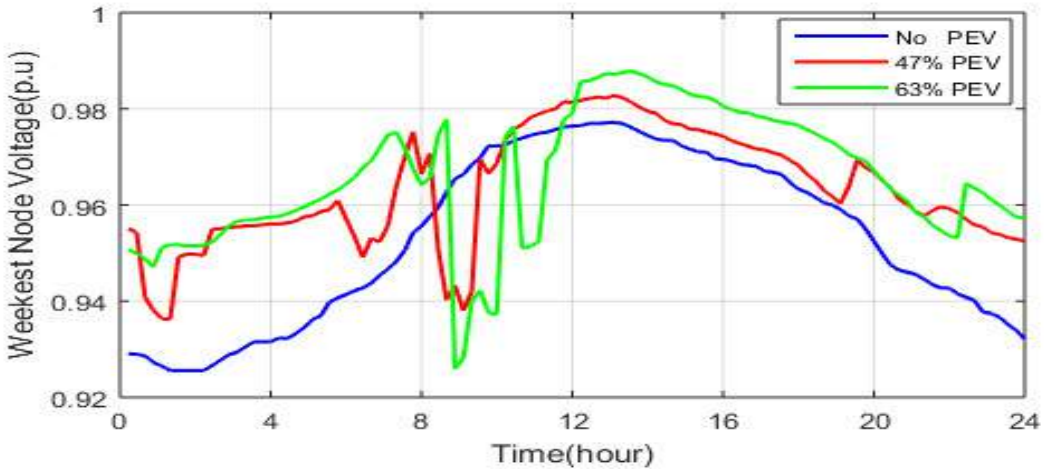

Figure 13. Fixed charge-rate coordination integrating capacitor no PEV, 47% PEV, and 63% PEV.

Figure 14 show the PEV penetration of total power loss of no PEV, 16% PEV, and 32% PEV. Here, in the subplot, the no PEV is presented. The no PEV flows from 24 kW at the time period of 1 h, and it decreases to 6 kW at the time period of 9 h. The 16% PEV flows from 24 kW at the time period of 1 h, and it reduces to 8 kW at the time period of 9 h. The 32% PEV flows from 25 kW at the time period of 1 h, and at the time period of 12 h, it reduces to 2 kW, and then increases up to 20 kW at the time period of 24 h. Figure 15 show the PEV penetration of total power loss of no PEV, 47% PEV, and 63% PEV. Here, in the subplot, the no PEV is presented. The no PEV flows from 24 kW at the time period of 1 h, and it decreases to 2.5 kW at the time period of 12 h. The 47% PEV flows from 25 kW at the time period of 1 h, and it reduces to 4 kW at the time period of 12 h. The 63% PEV flows from 24 kW at the time period of 1 h, and at the time period of 12 h, it reduces to 10 kW, and then increases up to 20 kW at the time period of 24 h. Figure 16 show the fixed charge—the rate of total power consumption of no PEV, 16% PEV, and 32% PEV. Here, in the subplot, the no PEV is presented. The no PEV flows from 820 kW at the time period of 1 h, and it reduces to 260 kW at the time period of 11 h. The 16% PEV flows from 825 kW at the time period of 1 h, and it reduces to 320 kW at the time period of 11 h. The 32% PEV flows from 830 kW at the time period of 1 h, and at the time period of 12 h, it reduces to 260 kW and then increases up to 780 kW at the time period of 24 h.

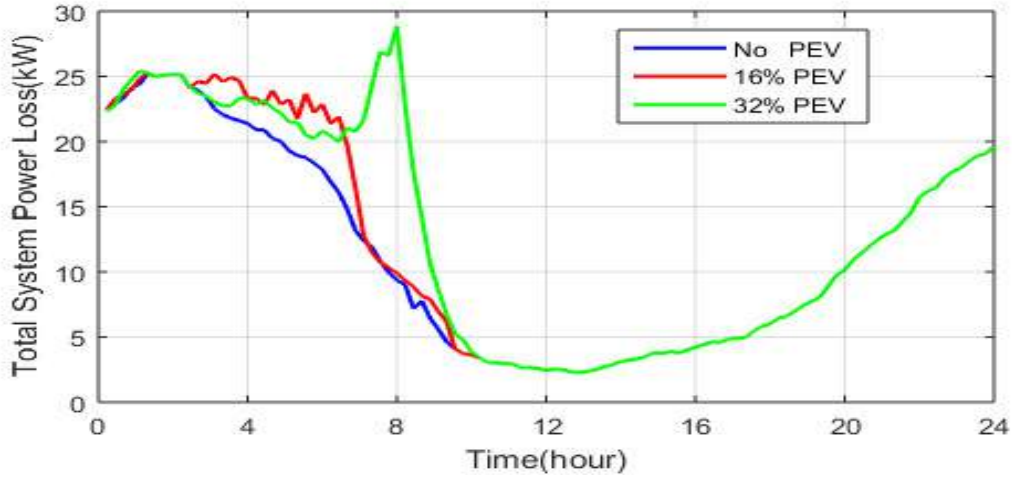

Figure 14. Fixed charge–rate of total power loss of no PEV, 16% PEV, and 32% PEV.

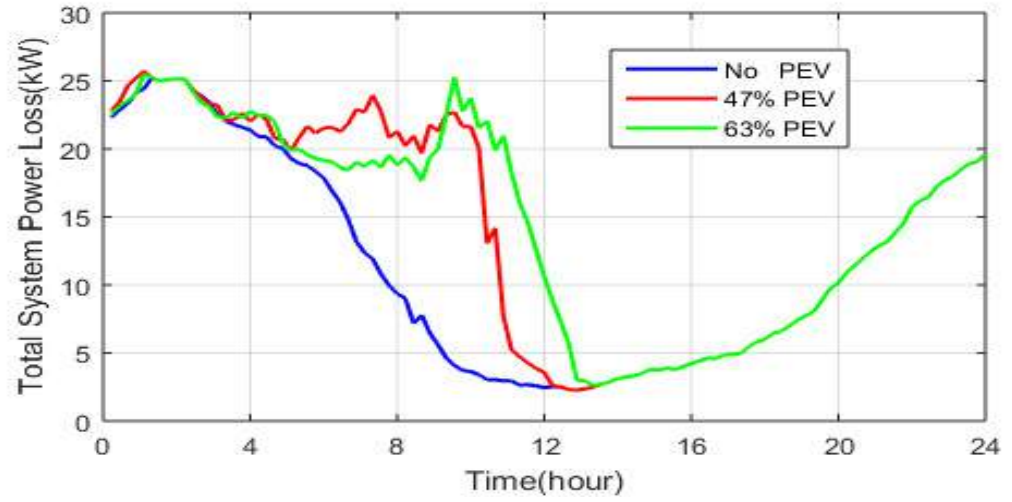

Figure 15. Fixed charge–rate of total power loss of no PEV, 47% PEV, and 63% PEV.

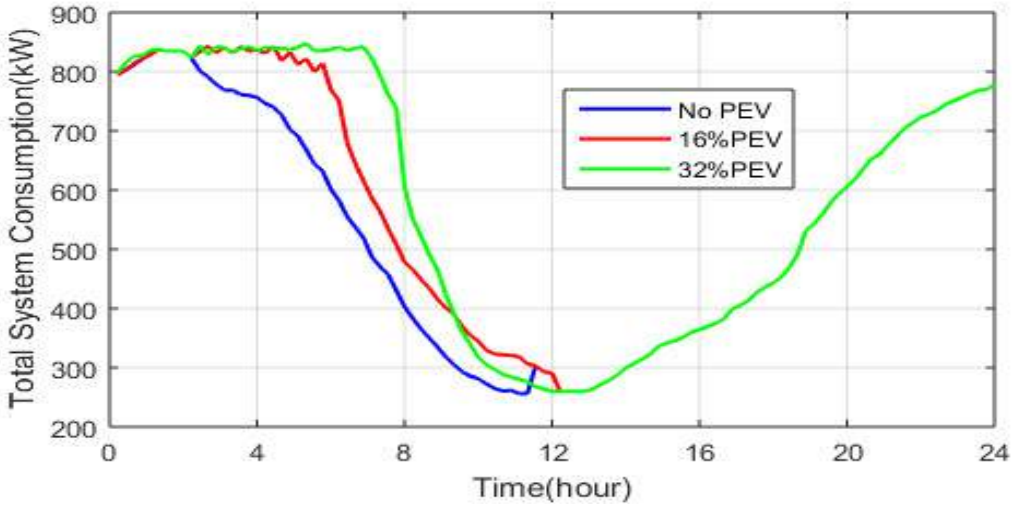

Figure 16. Fixed charge–rate of total power consumptionof no PEV, 16% PEV, and 32% PEV.

Figure 17 show the PEV penetration of total power consumption of no PEV, 47% PEV, and 63% PEV. Here, in the subplot, the no PEV is presented. The no PEV flows from

820 kW at the period of 1 h, and it decreases to 280 kW at the period of 10 h. The 47% PEV flows from 825 kW at the period of 1 h, and it reduces to 300 kW at the period of 10 h. The 63% PEV flows from 830 kW at the period of 1 h, and at the time period of 12 h, it reduces to 260 kW, and then increases up to 780 kW at the period of 24 h.

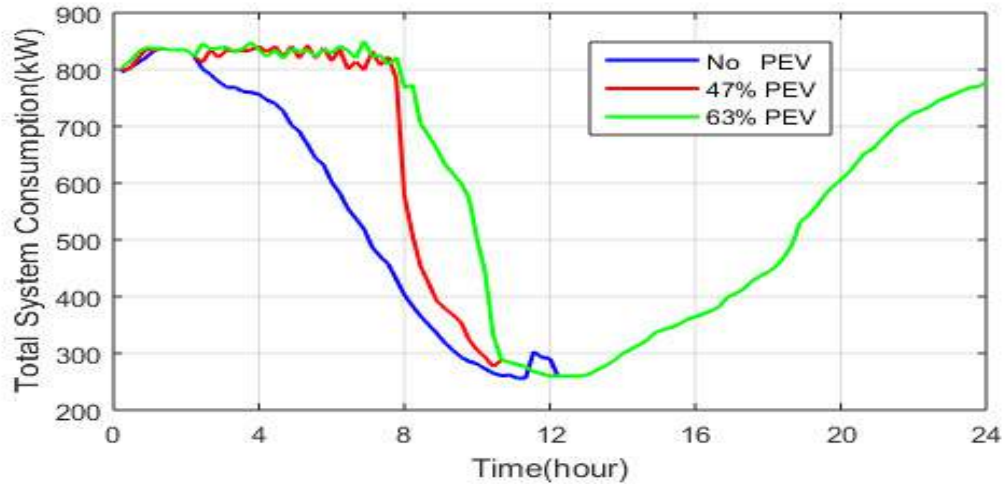

Figure 17. Fixed charge–rate of total power consumption of no PEV, 47% PEV, and 63% PEV.

The proposed analysis with uncoordinated and coordinated levels is shown in Figure 18. Figure 18 show the bar chart proposed method satisfaction level with comparison. When uncoordinated, all customers are satisfied, but the satisfaction level of service is low. When coordination is applied, the PEV customer satisfaction is only three. The success of this approach is to satisfy both the client and the customer, and a limited amount of PEV connection proposed.

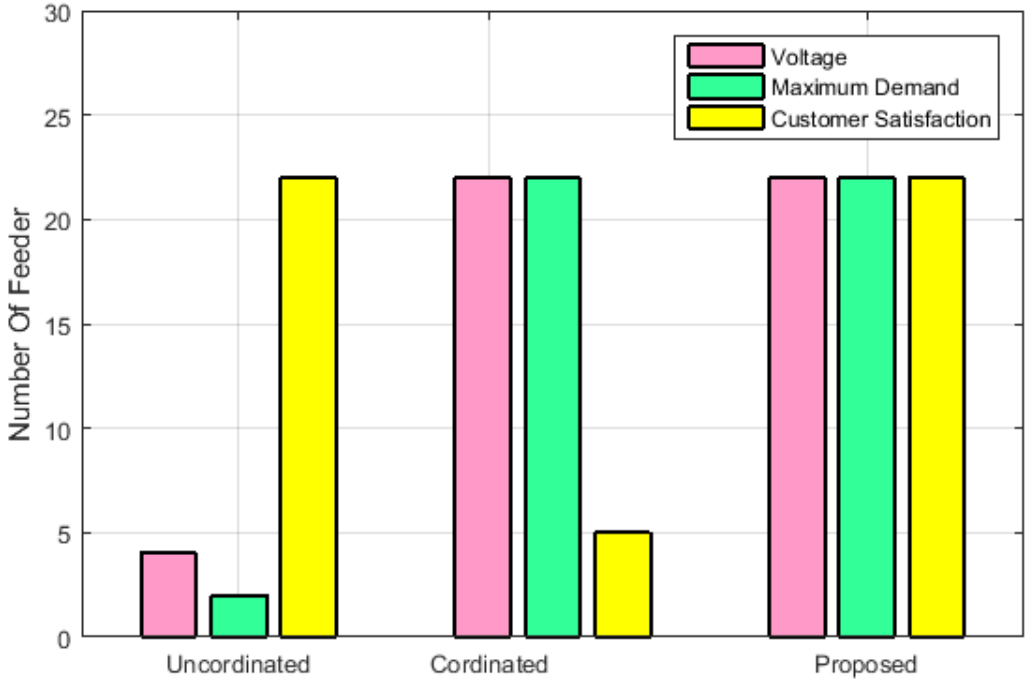

Figure 18. Analysis of proposed with uncoordinated and coordinated level.

Table 1 show the PEV charging on the distribution system. When uncoordinated, the car charging process starts immediately but randomly without following system parameters. The distribution system will deal with many problems, such as overload, high power loss, and unacceptable power outages. When coordinated, in order to overcome the harmful effects of un insulated charges of PEV on the distribution system, a real-time method of coordinating 5 min PEV charging is suggested in this paper. Once the car is connected to the charger, the charging process will start only after the central controller decision. The AOSAOA algorithm used optimizes PEV arrivals, and all system barriers are satisfied.

Table 1. PEV charging on the distribution system.

Methods	PEV (%)	ΔV (%)	Increase(%)	Satisfaction Ratio
No PEV Uncoordinated	0	7.35	0	-
	16	7.61	6.97	-
	32	8.95	14.59	-
	47	17.72	33.85	-
	63	19.16	6.96	-
Coordinated	16	7.43	13.67	18/4
	32	7.47	12.32	15/7
	47	8.61	17.53	8/14
	63	9.91	5.53	3/19
Coordinated with capacitor and OLTC switching	16	4.96	5.53	22/0
	32	4.99	11.86	22/0
	47	6.32	17.28	22/0
	63	7.34	23.03	22/0

Note: Table 1 show achieving the satisfaction of PEV customer and utility sides together.

Table 2 show the charging variation limit and charging power limit. In 100 EV, the charging power variation limit is 250 kW, and the charging power limit is 500 kW. In 200 EV, the charging power limit is 1000 kW and the charging power variation limit is 750 kW. In 300 EV, the charging power limit is 1875 kW, and the charging power variation limit is 1000 kW.

Table 2. Charging power limit and variation limit.

EV	Charging Power Limit	Charging Power Variation Limit
100	500 kW	250 kW
200	1000 kW	750 kW
300	1875 kW	1000 kW

6. Conclusions

In this manuscript, the location determination of an electric vehicles parking lot and capacitors in grid care of voltage profile and power loss by atomic orbital search and arithmetic optimization algorithm optimizer was proposed. The proposed technique performances were analyzed in the MATLAB/Simulink working platform. The performance of the proposed and existing techniques were graphically illustrated. The proposed approach was analyzed under the perfect location of capacitors and parking of electric vehicles on the network. The AOSAOA approach optimized the EVPL's participation in various energy and ancillary services markets, including the effects of capacity payments. The benefit of EVPL was obtained using the proposed approach and its performance was higher than the existing approach in terms of the analysis of the decrease in the loss of real and reactive power and the change of the voltage profile. By utilizing

the proposed hybrid technique, the system provides an optimal solution through the least calculation time. Analysis of total power loss and total power consumption of EVs in PL, the analysis of PV power at different PEVs, and fixed charge-rate were also examined. To analyze the performance of the projected approach, the simulation results were analyzed and compared with methods such as PEV uncoordinated, coordinated, and coordinated with the capacitor.

Author Contributions: Conceptualization, C.S.V.P.R., C.R.R. and A.G.P.; methodology C.S.V.P.R., A.P., C.R.R., and A.G.P.; software C.S.V.P.R. and A.P.; validation C.R.R., A.A., and Y.A.; formal analysis A.G.P.; investigation, C.S.V.P.R. and A.G.P.; resource C.S.V.P.R.; data curation C.S.V.P.R.; writing—original draft preparation, C.S.V.P.R. and C.R.R.; writing—review and editing, A.A. and Y.A.; visualization, C.R.R.; supervision, A.P.; project administration, A.P.; funding acquisition, A.G.P., A.A., and Y.A. All authors have read and agreed to the published version of the manuscript.

Funding: The authors would like to acknowledge the financial support received from Taif University Researchers Supporting Project Number (TURSP-2020/121), Taif University, Taif, Saudi Arabia.

Institutional Review Board Statement: Not applicable.

Informed Consent Statement: Not applicable.

Data Availability Statement: Not applicable.

Conflicts of Interest: The authors declare no conflict of interest.

References

1. Rajabi-Ghahnavieh, A.; Sadeghi-Barzani, P. Optimal Zonal Fast-Charging Station Placement Considering Urban Traffic Circulation. *IEEE Trans. Veh. Technol.* **2017**, *66*, 45–56.
2. Zhang, H.; Moura, S.J.; Hu, Z.; Song, Y. PEV Fast-Charging Station Siting and Sizing on Coupled Transportation and Power Networks. *IEEE Trans. Smart Grid***2018**, *9*, 2595–2605.
3. Hosseini, M.; MirHassani, S.A. Refueling-station location problem under uncertainty. *Transp. Res. Part E***2015**, *84*, 101–111.
4. Yildiz, B.; Arslan, O.; Karasan, O.E. A branch and price approach for routing and refueling station location model. *Eur. J. Oper. Res.* **2016**, *248*, 815–826.
5. MirHassani, S.A.; Ebrazi, R. A flexible reformulation of the refueling station location problem. *Transp. Sci.* **2012**, *47*, 617–628.
6. Wang, G.; Xu, Z.; Wen, F.; Wong, K.P. Traffic-Constrained Multi-objective Planning of Electric Vehicle Charging Stations. *IEEE Trans. Power Deliv.* **2013**, *28*, 2363–2372.
7. Yao, W.; Zhao, J.; Wen, F.; Dong, Z.; Xue, Y.; Xu, Y.; Meng, K. A Multi-Objective Collaborative Planning Strategy for Integrated Power Distribution and Electric Vehicle Charging Systems. *IEEE Trans. Power Syst.* **2014**, *29*, 1811–1821.
8. Moradi, M.; Abedini, M.; Tousi, S.; Hosseinian, S. Optimal siting and sizing of renewable energy sources and charging stations simultaneously based on Differential Evolution algorithm. *Int. J. Electr. Power Energy Syst.***2015**, *73*, 1015–1102.
9. Amini, M.H.; Moghaddam, M.P.; Karabasoglu, O.J.S.C. Simultaneous allocation of electric vehicles parking lots and distributed renewable resources in smart power distribution networks. *Sustain. Cities Soc.* **2017**, *28*, 332–342.
10. Aljanad, A.; Mohamed, A.; Shareef, H.; Khatib, T. A novel method for optimal placement of vehicle-to-grid charging stations in distribution power system using a quantum binary lightning search algorithm. *Sustain. Cities Soc.* **2018**, *38*, 174–183.
11. Shaoyun, G.; Liang, F.; Hong, L. Planning of charging stations considering traffic flow and capacity constraints of distribution network. *Power Syst. Technol.* **2013**, *37*, 582–589.
12. Pazouki, S.; Mohsenzadeh, A.; Ardalan, S.; Haghifam, M. Simultaneous Planning of PEV Charging Stations and DGs Considering Financial, Technical,and Environmental Effects. *Can. J. Electr. Comput. Eng.* **2015**, *38*, 238–245.
13. Karmaker, A.K.; Ahmed, M.R.; Hossain, M.A.; Sikder, M.M. Feasibility assessment & design of hybrid renewable energy based electric vehicle charging station in Bangladesh. *Sustain. Cities Soc.* **2018**, *39*, 189–202.
14. Mozafar, M.R.; Moradi, M.H.; Amini, M.H. A simultaneous approach for optimal allocation of renewable energy sources and electric vehicle charging stations in smart grids based on improved GAPSO algorithm. *Sustain. Cities Soc.***2017**, *32*, 627–637.
15. Atwa, Y.M.; El-Saadany, E.F.; Salama, M.M.A.; Seethapathy, R. Optimal Renewable Resources Mix for Distribution System Energy Loss Minimization. *IEEE Trans. Power Syst.* **2010**, *25*, 360–370.
16. Teng, J.; Luan, S.; Lee, D.; Huang, Y. Optimal Charging/Discharging Scheduling of Battery Storage Systems for Distribution Systems Interconnected With Sizeable PV Generation Systems. *IEEE Trans. Power Syst.* **2013**, *28*, 1425–1433.
17. Mazidi, M.; Zakariazadeh, A.; Jadid, S.; Siano, P. Integrated scheduling of renewable generation and demand response programs in a microgrid. *Energy Convers. Manag.* **2014**, *86*, 1118–1127.
18. GeunKim, J.; Kuby, M. The deviation-flow refueling location model for optimizing a network of refueling stations. *Int. J. Hydrog. Energy***2012**, *28*, 5406–5420.

19. Hung, D.Q.; Mithulananthan, N.; Lee, K.Y. Determining PV Penetration for DistributionSystems With Time-Varying Load Models. *IEEE Trans. Power Syst.* **2014**, *29*, 3048–3057.
20. Yu, H.; Chung, C.Y.; Wong, K.P.; Lee, H.W.; Zhang, J.H. Probabilistic Load Flow Evaluation With Hybrid Latin Hypercube Sampling and Cholesky Decomposition. *IEEE Trans. Power Syst.***2009**, *24*, 661–667.
21. Sachan, S.; Amini, M. Optimal allocation of EV charging spots along with capacitors in smart distribution network for congestion management. *Int. Trans. Electr. Energy Syst.* **2020**, *30*, e12507.
22. Aggarwal, S.; Singh, A. Impact analysis of electric vehicle charging station integration with distributed generators on power systems. *Int. J. Circuit Theory Appl.***2021**, *49*, 1811–1827. https://doi.org/10.1002/cta.2974.
23. Bilal, M.; Rizwan, M. Integration of electric vehicle charging stations and capacitors in distribution systems with vehicle-to-grid facility. *Energy Sources Part A Recovery Util. Environ. Eff.* **2021**, *41*, 1828–1837. https://doi.org/10.1080/15567036.
24. Ahmadi, M.; Hosseini, S.; Farsadi, M. Optimal Allocation of Electric Vehicles Parking Lots and Optimal Charging and Discharging Scheduling using Hybrid Metaheuristic Algorithms. *J. Electr. Eng. Technol.***2021**, *16*, 759–770. https://doi.org/10.1007/s42835-020-00634-z.
25. Chen, L.; Xu, C.; Song, H.; Jermsittiparsert, K. Optimal sizing and sitting of EVCS in the distribution system using metaheuristics: A case study. *Energy Rep.***2021**, *7*, 208–217. https://doi.org/10.1016/j.egyr.2020.12.032.
26. Raja, C.S.; Kumar, V.N.M.; Senthil, K.J.; Nesamalar, J.J. Enhancing system reliability by optimally integrating PHEV charging station and renewable distributed generators: A Bi-Level programming approach. *Energy***2021**, *229*, 120746. https://doi.org/10.1016/j.energy.2021.120746.
27. Rajesh, P.; Shajin, F. Optimal allocation of EV charging spots and capacitors in distribution network improving voltage and power loss by Quantum-Behaved and Gaussian Mutational Dragonfly Algorithm (QGDA). *Electr. Power Syst. Res.* **2021**, *194*, 107049. https://doi.org/10.1016/j.epsr.2021.107049.
28. Luo, L.; Wei, G.; Suyang, Z.; He, H.; Song, G.; Jun, H.; Zhi, W.; Xiaobo, D. Optimal planning of electric vehicle charging stations comprising multi-types of charging facilities. *Appl. Energy***2018**, *226*, 1087–1099.
29. Andrenacci, N.; Ragona, R.; Valenti, G. A demand-side approach to the optimal deployment of electric vehicle charging stations in metropolitan areas. *Appl. Energy***2016**, *182*, 39–46.
30. Zheng, Y.; Song, Y.; Hill, D.; Meng, K. Online Distributed MPC-Based Optimal Scheduling for EV Charging Stations in Distribution Systems. *IEEE Trans. Ind. Inform.* **2019**, *15*, 638–649.
31. Song, Y.; Zheng, Y.; Hill, D. Optimal Scheduling for EV Charging Stations in Distribution Networks: A Convexified Model. *IEEE Trans. Power Syst.***2016**, *32*, 1574–1575.
32. Fazeli, S.; Venkatachalam, S.; Chinnam, R.; Murat, A. Two-Stage Stochastic Choice Modeling Approach for Electric Vehicle Charging Station Network Design in Urban Communities. *IEEE Trans. Intell. Transp. Syst.* **2020**, *22*, 3038–3053.
33. Zhang, H.; Tang, L.; Yang, C.; Lan, S. Locating electric vehicle charging stations with service capacity using the improved whale optimization algorithm. *Adv. Eng. Inform.* **2019**, *41*, 100901.
34. Gong, L.; Cao, W.; Liu, K.; Zhao, J. Optimal Charging Strategy for Electric Vehicles in Residential Charging Station under Dynamic Spike Pricing Policy. *Sustain. Cities Soc.***2020**, *63*, 102474.
35. Azizi, M. Atomic orbital search: A novel metaheuristic algorithm. *Appl. Math. Model.* **2021**, *93*, 657–683. https://doi.org/10.1016/j.apm.2020.12.021.
36. Abualigah, L.; Diabat, A.; Mirjalili, S.; AbdElaziz, M.; Gandomi, A. The Arithmetic Optimization Algorithm. *Comput. Methods Appl. Mech. Eng.* **2021**, *376*, 113609. https://doi.org/10.1016/j.cma.2020.113609.
37. Grainger, J.; Civanlar, S. Volt/Var Control on Distribution Systems with Lateral Branches Using Shunt Capacitors and Voltage Regulators Part I: The Overall Problem. *IEEE Trans. Power Appar. Syst.* **1985**, *104*, 3278–3283. https://doi.org/10.1109/tpas.1985.318842.
38. Deilami, S.; Masoum, A.; Moses, P.; Masoum, M. Real-Time Coordination of Plug-In Electric Vehicle Charging in Smart Grids to Minimize Power Losses and Improve Voltage Profile. *IEEE Trans. Smart Grid***2011**, *2*, 456–467. https://doi.org/10.1109/tsg.2011.2159816.
39. Clement-Nyns, K.; Haesen, E.; Driesen, J. The Impact of Charging Plug-In Hybrid Electric Vehicles on a Residential Distribution Grid. *IEEE Trans. Power Syst.* **2010**, *25*, 371–380. https://doi.org/10.1109/tpwrs.2009.2036481.
40. Thukaram, D.; Banda, H.W.; Jerome, J. A robust three phase power flow algorithm for radial distribution systems. *Electr. Power Syst. Res.* **1999**, *50*, 227–236. https://doi.org/10.1016/s0378-779600150-3.

IEEE Access
Multidisciplinary | Rapid Review | Open Access Journal

Received April 24, 2022, accepted April 30, 2022, date of publication May 3, 2022, date of current version May 17, 2022.

Digital Object Identifier 10.1109/ACCESS.2022.3172109

Comparative Performance Analysis of Deregulated Hydrothermal System With Dual Mode Controller and Diverse Source of Generation Employing Imperialistic Competition Algorithm

PONNUSAMY MARIMUTHU[1], T. RAJESH[1], N. RAJESWARAN[1], AND HASSAN HAES ALHELOU[2], (Senior Member, IEEE)

[1]Department of Electrical and Electronics Engineering, Malla Reddy Engineering College, Secunderabad 500100, India
[2]Department of Electrical Power Engineering, Tishreen University, Latakia 2230, Syria

Corresponding author: Hassan Haes Alhelou (alhelou@ieee.org)

ABSTRACT This paper presents an accomplishment of Load Frequency Control (LFC) under deregulated environment using Imperialistic Competition Algorithm (ICA) based Dual Mode Controller (DMC). The Capacitive Energy Storage (CES) and Static Synchronous Series Compensator (SSSC) have been successfully used to improve the performance of the system dynamics. The optimization techniques are beneficial to the design of the Dual Mode Controller and overcome the drawbacks identified by the conventional controllers. The traditional Load Frequency Control system is adapted to interpret bilateral contracts on the system. The performance index is calculated by using the integral of the square of error technique to optimize the controllers of the Load Frequency Control system. The simulation analysis reveals that due to the presence of the Imperialistic Competition Algorithm-based Dual-Mode Controller, the performance of the system improves in terms of peak time, settling time, and overshoot, and also performance index is lesser than the system without the Imperialistic Competition Algorithm based Dual Mode Controller following a load disturbance in either of the areas.

INDEX TERMS Deregulation, load frequency control, capacitive energy storage, static synchronous series compensator, imperialistic competition algorithm, dual mode controller, integral controller.

NOMENCLATURE

LFC	- Load Frequency Control.
AGC	- Automatic Generation Control.
ICA	- Imperialistic Competition Algorithm.
DPM	- Disco Participation Matrix.
cpf	- Contract Participation Factor.
apf	- ACE Participation FActor.
DMC	- Dual Mode Controller.
CES	- Capacitive Energy Storage.
SSSC	- Synchronous Series Compensator.
ISO	- Independent System Operator.
FACTS	- Flexible AC Transmission Systems.
IC	- Integral Controller.
PIC	- Proportional Integral Controller.
PID	- Proportional Integral Derivative.
TCPS	- Thyristor Controlled Phase Shifters.
WOA	- Whale Optimization Algorithm.
UC	- unit commitment.
ACE	- Area Control Error.
PI	- Performance Index.
Δf_1	- Change in Frequency in Area 1.
Δf_2	- Change in Frequency in Area 2.
$\Delta P_{tie1,2}$	- Change in Tie-Line Power.
P_D	- Real Power Demand.
Q_D	- Reactive Power Demand.
ΔP_D	- Change in Real Power Demand.
ΔQ_D	- Change in Reactive Power Demand.
P – f	- Real Power – Frequency.
Q – V	- Reactive Power - Voltage.

The associate editor coordinating the review of this manuscript and approving it for publication was Nagesh Prabhu.

R - Speed Regulation.
T_P - Peak Time.
T_S - Settling Time.
M_P - Peak Overshoot.
T_R - Rise Time.
T_t - Time Constant of Turbine.
T_{12} - Synchronizing Coefficient.
T_p - Time Constant of Turbo Generator.
ΔP_{SSSC} - Change in Power Output of SSSC.
K_{SSSC} - Gain of the SSSC.
T_{SSSC} - Time Constant of SSSC.
K_{CES} - Gain of the CES.
T - Time Constants.
K_i - Gain of the Integral Controller.
K_p - Gain of the Proportional Controller.
K_P - Power System Gain.
ε - Specified limit of the Error Signal.
$Coun_i$ - Position of the i^{th} Country.
N_{coun} - No. of Countries in the Imperialistic.
C_1, C_2 - Acceleration Coefficients.
Col_n^i - Position of i^{th} Colony of the nth Empire.
Ic_n - Cost of n^{th} Empire.
IC_n - Normalized Cost.
H - Inertia Constant.
f^o - Initial Frequency.
I_n - Position of nth Empire.
IP_n - Initial Number of Colonies of the nth Empire.
n - Number of Iterations.
N_{col} - Remaining Countries form n^{th} Empire.
n_{coun} - Total Number of Countries.
$newcol_n^i$ - Updated Position of Colonies of the n^{th} Empire.
N_{imp} - Most Powerful Countries from nth Empire.
NTP_n - Normalized Cost of n^{th} Empire.
TP_n - Total Power of n^{th} Empire.
ps_n - Possession Probability of n_{th} Empire.
ζ - Positive Number Less than 1.
α, β - Weighting Factors.

I. INTRODUCTION

The effective operation of a power system has essential that its frequency is maintained constant within acceptable limits. There are two aspects to maintaining frequency as constant. One is the coordination of Generation – Load schedule, whereas the second is planned power flow in the tie-line of the system. These two are the most critical challenges in operating a hydrothermal system during the dynamic operation [1], [2]. Currently, the power sector is undergoing a deregulated market environment that affords power at controlled tariffs to a system that establishes firms demanding everyone to sell power at lesser tariffs. The Transmission Companies (TransCos), Distribution Companies (DisCos), and Generating Companies (GenCos) are the several units of such a type of system. The generation in power system control concepts under deregulation in [3]. A new framework for implementing load following contracts in price-based operation and the execution of Independent System Operator (ISO) is a practical working of the system with balancing the economics have been deliberated in [4].

It was shown that the customized AGC scheme included agreement data and measurements, which improved the control signals to be dispatched to controllers. The above scheme included Area Control Error (ACE) as a fraction of the control error signal. It satisfied the North American Reliability Council (NERC) performance criteria. It also explained an interesting case to determine if any of the contracts were violated, and this case study results with three sets were presented in [5].

The LFC problem is simulated comprehensively and has been evaluated under the deregulated environment in [6]. The automatic generation control could be simulated and optimized after deregulation. The idea of bilateral contracts and DPM was introduced and implemented in the two-area system. The system's response to contract violations was also studied and reported [7]. The dynamic response of the CES unit with a small volume to the system encouragingly progresses been presented in [8]. Several FACTS devices have been extensively active to offer enhanced stability for the control of power systems networks. The combination of Static Synchronous Series Compensator and Capacitive Energy Storage are realized as vital devices to get better dynamic response of the system [9].

The integral of the square of error is considered in the search for optimal Automatic Generation Control (AGC) parameters. The various optimization techniques used in two areas of the hydrothermal system in the presence of Static Synchronous Series Compensator (SSSC) and Capacitive Energy Storage (CES) under deregulation are considered to exemplify the optimum parameter search. The results demonstrate the superior working of PSO over others in the tuning of AGC [10]. A detailed study of the Imperialistic Competition Algorithm for optimization techniques was presented in [11].

In the hydrothermal system, the gain of the controllers are optimized by the Imperialistic Competition Algorithm with CES and Static Synchronous Series Compensator under the deregulated scenario [12]. The continuous and discrete model of Load Frequency Control of two areas hydrothermal system with the traditional level of controllers and selection of the appropriate value of sampling period and parameters of speed regulation has investigated with generation rate constraints is given in [13]. The performance of electric governor, mechanical governor, and single-stage and two-stage reheat turbines on dynamic responses has been considered. Also, the choice of the parameter of speed regulation and sampling period has been scrutinized. The performance is examined with the controller gains of Integral Controller (IC), Proportional Integral Controller (PIC), and Proportional Integral Derivative (PID) in the interconnected Automatic Generation Control system are optimized by Bacterial Foraging (BF) technique is given in [14]. The IC gains and electric governor parameters were optimized using the ISE criterion. The concept of IC and PC

are used in the design of DMC, and the main benefit of PIC is that, it reduces the error in steady-state is nearly zero but typically gives large deviations in frequency are given in [15]. The parameters of speed governors and turbines and their transfer function models can be found in the IEEE committee report [16].

Collective modeling of the reservoirs caught up in gas systems and electric power and locations of both the networks are crucial features to be well-thought-out in planning energy resources [17]. The different energy storage amenities are considered for modeling the system and system optimization to the natural gas and electric power systems. The tactic can be handled by the interdependent operation between the cascade of hydro plants, and the coordination of hydrothermal problems characterizes it. The dissimilarity of the circuit capacity and transmission line losses are also considered [18]. The studies have been conducted for models of nonlinear and linear speed governor mechanisms with the models of the turbine in hydro systems are suggested by the report of the IEEE committee [19].

The Thyristor Controlled Phase Shifters (TCPS) and CES are positioned in the tie line of the system, and their various methods of control strategy are proposed in [20]. The system has been studied with the effect of unit commitment (UC) using PIDN-FOPD for various approaches. The Whale optimization algorithm (WOA) is effectively used for concurrent optimization of various controllers mentioned above. The analysis has explored that the system dynamics are improved by using WOA [21].

The recent literature presented a critical study on the impact of AE-FC units on AGC performance of interconnected two areas non-reheat thermal system, PV-reheat thermal, and multi-source hydro-thermal system (MSHTS). Further, the effects of STG and geothermal (GT) plants are recently inspected in two and three-area deregulated systems [22]. To improve FPI performance, some researchers have implemented different optimization methods to tune the FPID controller. Hybrid harmony search-cuckoo optimization algorithms are employed efficiently to tune input/output SFs of FPID controllers for different types of systems [23]. Recently, Fractional Order (FO) controllers have been implemented in power system models, and desirable results have been observed.

A FO fuzzy PID (FOFPID) controller was tuned recently using ICA [24]. Further, the literature review indicates that the hybridization of the fuzzy controller with the FO controller shows enhanced performance compared to fuzzy hybridized with a conventional controller. A proficient frequency regulation scheme has been explored in this work for two interconnected hybrid microgrids (hμGs) comprised of multiple renewable energy sources. A new optimization algorithm has been formulated to replicate the photo-tactic swarming behavior of green leafhoppers named Green Leaf-hopper Flame optimization algorithm (GLFOA) to tune the system controllers. The superiority of GLFOA is confirmed by comparing the performance with several popular optimization algorithms [25]. A unique interconnected hybrid microgrid (IHM) double area system is developed that includes a novel combined solar gas turbine (CSGT), biodiesel generator (BDG), wind turbine generator (WTG), and energy storage units, and DC link (DCL) using tilt-integral-derivative (TID) controller. A recently developed metaheuristic algorithm, Harris's hawk optimization (HHO) technique, is used to obtain controller gain constraints. Use of CSGT in 2- area IHM for load frequency control (LFC) is a novel work and uses the TID controller and HHO technique for tuning the controllers' parameters [26].

Automatic Generation Control maintains the balance of grid power, and also it is used to strengthen the abrupt disturbance of frequency within the system power grid. The approach is implemented to plan a system controller for the depreciation of various issues in AGC within the open market structure of the system. Under deregulation, a multi-area hydrothermal system examines countless LFC problems in the open market scenario. But all of it concerning Load Frequency Control of two area systems with the competitive market environment does not examine the existence of Dual Mode Controller and Capacitive Energy Storage and Static Synchronous Series Compensator with Imperialistic Competition Algorithm. Therefore, this paper deals with designing a Dual Mode Controller for Capacitive Energy Storage and an SSSC-based multi-area interconnected system under deregulation employing the Imperialistic Competition Algorithm.

For better understanding, the novel contributions of this work are highlighted as follows:

(i) To propose a Load Frequency Control for novel ICA tuned Dual Mode Controller for multi-area based hydrothermal system.
(ii) To exemplify the proposed technique by incorporating Capacitive Energy Storage and SSSC to damp the tie-line power oscillations.
(iii) To authenticate the strength of the proposed method, the simulation results are compared to the various intelligent control strategies in the state-of-the-art literature.

This work is organized as follows: The transfer functional block diagram of LFC of two areas of the hydrothermal system under deregulated environment is discussed in the second section. The design of Capacitive Energy Storage and its block diagram is presented in the third section. The design and accomplishment of SSSC and its transfer functional block diagram is presented in section 4. The fifth Section focused on designing and implementing the dual-mode controller's continuous and discontinuous mode of operation. The incorporation of the imperialistic competition algorithm and its implementation is presented in the sixth section. Finally, the seventh section presents the results and discussions, followed by the conclusion.

II. LOAD FREQUENCY CONTROL UNDER DEREGULATED SCENARIO

The LFC of interconnected two area systems has been examined with a reheat unit in area 1 and a hydro unit in area 2.

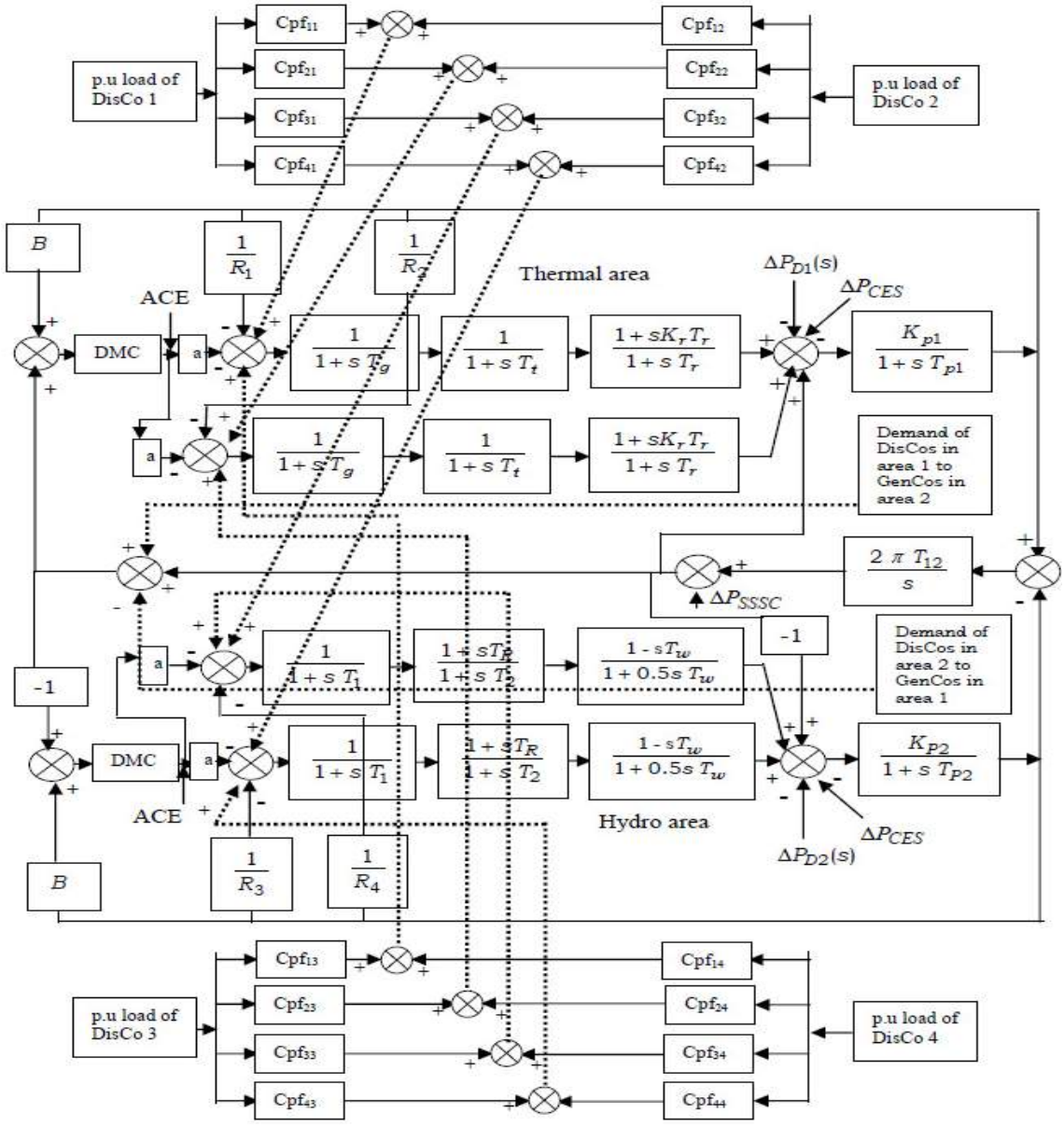

FIGURE 1. The DMC based LFC of hydrothermal system under deregulation with SSSC and CES.

The transfer function models of the Load Frequency Control system are given in the report of the IEEE committee on system dynamic models [16], and the parameters and specifications are given in Appendix. Fig. 1 indicates the model of the block diagram of the hydrothermal system with multi-area under deregulation, and each area consists of two Discos and three GenCos. The system performance with optimization is calculated through the Integral of Square of Error (ISE) technique [8], namely, Performance Index (PI) is given in (1) is used to compare the performance of the system with several techniques. Where α and β are called weighting factors.

$$PI = \int_0^t (\alpha \cdot \Delta f_1^2 + \beta \cdot \Delta f_2^2 + \Delta P_{tie\,1,2}^2) \qquad (1)$$

III. DESIGN AND IMPLEMENTATION OF CAPACITIVE ENERGY STORAGE

This exceptional ability of Capacitive Energy Source compared to the further storage of energy systems like flywheels, pumped hydro, etc., makes it a viable option to be employed in significant applications [8]. This ability of CES allows it to function as a storage entity of energy and afford stability due to disturbances and act as a spinning reserve. The capacitor plays a significant role in making the CES entity capable of damping the oscillations formed due to the abrupt rise or fall of power. The Capacitive Energy Storage unit consists of Power Conversion System (PCS) and a supercapacitor [8]. Many discrete capacitive units are connected in parallel to form the storage capacitor based on the amount of energy storage capacity required. Either frequency deviation or Area

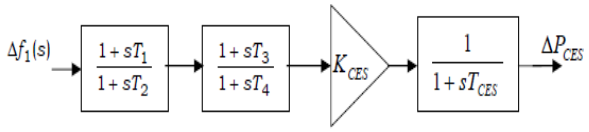

FIGURE 2. CES implemented to LFC.

Control Error (ACE) can be used as the control signal to the CES unit. Fig. 2 [8] indicates the Capacitive Energy Storage block diagram depiction of the unit to the system is given in [8]. Capacitive Energy Storage's edifice comprises gain block K_{CES}, T_{CES} is a time constant, and T_1, T_2, T_3, and T_4 are the time constants of blocks of phase compensation with two stages.

IV. DESIGN AND IMPLEMENTATION OF STATIC SYNCHRONOUS SERIES COMPENSATOR

The Static Synchronous Series Compensator influenced the tie-line power flow by emulating a capacitive or an inductive reactance. It is a voltage source switching converter with self-commutation to control a voltage in quadrature means of the line current [9]. The compensation level can be energetically controlled by altering the magnitude and polarity of the injected voltage V_S. The SSSC can also be operated together in capacitive mode or inductive mode.

Fig. 3 [9] shows the Static Synchronous Series Compensator block diagram is to be integrated into the system [9] to progress the performance. The Static Synchronous Series Compensator structure comprises gain block K_{SSSC}, T_{SSSC} is a time constant, and T_1, T_2, T_3, and T_4 are the time constants of blocks of phase compensation having two stages. The deviation of the frequency of area 1 is the input to the Static Synchronous Series Compensator.

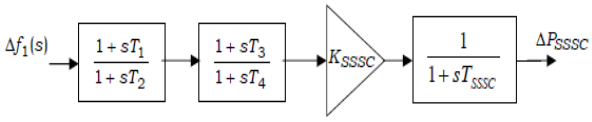

FIGURE 3. SSSC implemented to LFC.

V. DESIGN AND IMPLEMENTATION OF DUAL-MODE CONTROLLER

Integrating the Integral Controller (IC) into the system offers zero steady-state error; however, it results in abnormal settling time and the system overshoot. For the step load, small values of gain of the proportional controller results in a large steady-state error. The immense value of proportional controller gain provides improved steady-state performance except for transient response. So the gain of the proportional controller alone is not suitable for eliminating steady-state error. A general way of reducing the steady-state error is by introducing IC in the system. Suppose the gain of the integrator controller is adequately high. In that case, it gives a highly unfavorable response with a sharply rising peak overshoot and a low value of peak overshoot due to the small value of integral controller gain. Still, the rise time of the system increases. So the above concept is called DMC, which involves both a proportional and integral controller. The DMC is beneficial for the proper design of the gain of the proportional controller and integral controller. Usually, the overshoot of the system can be abridged by employing a Proportional Controller (PC) [13], [14]. So exertions have been offered in this work to construct a Dual Mode Controller, which includes both integral controller and proportional controller, as shown in Fig. 4 [13]. Based upon the $ACE(t)$ operation of control law that can be interchanged between the different control modes i.e. continuous mode and discontinuous mode. The controller's output is in (2) and (3).

$$\text{if } |ACE(t)| > \varepsilon \quad \Delta P_c(t) = -K_p \cdot ACE(t), \tag{2}$$

and,

$$\Delta P_c(t) = -K_i \int ACE(t)dt \quad \text{if } |ACE(t)| < \varepsilon \tag{3}$$

where $\Delta P_c(t) =$ the output signal of the controller
$K_p =$ proportional controller gain
$\varepsilon =$ specified limit of the error signal
$K_i =$ integral controller gain.

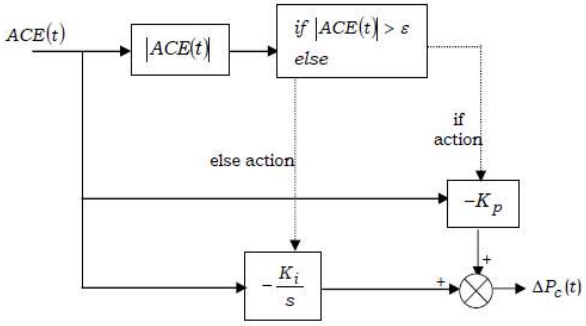

FIGURE 4. Proposed DMC control scheme.

The proposed DMC is simple in configuration and easy to put into practice, as it uses the value of Area Control Error (ACE) which is already available in the system. But care should be taken that the hyper switching plane should be specified at every load change.

VI. IMPLEMENTATION OF IMPERIALISTIC COMPETITION ALGORITHM

The concept of the Imperialistic Competition Algorithm was propounded by A. Gargari and Lucas [11]. The Imperialistic Competition Algorithm is a consequence of the conception of imperialistic competitions. The Imperialistic Competition Algorithm is initiated by a preliminary population represented as countries. Imperialists represent the countries that possess the great admirable value of the objective function,

and the discarded countries fit to be the colonies of the respective imperialists. All the respective colonies were spread among the Imperialists based on power. The colonies are afterward moving towards their appropriate imperialist, and respective imperialist's places will be improved based on the certainty. In the next stage, the competition was conducted between the empires, and based on this competition, weaker empires were eliminated. This competition leads to a further increase in the power of the strong empire and diminishes the frail empire's power also; empires are eliminated if they are unable to recover their position. The competitions are conducted for all the empires for the duration of several iterations and result in the formation of only one empire. The remaining empires turn out to be the colonies of this empire. The flowchart of the proposed algorithm implemented for Load Frequency Control of multi-area hydrothermal system under deregulation is given in Fig. 5 [12]. The simulation parameters of the Imperialistic Competition Algorithm are specified in Appendix.

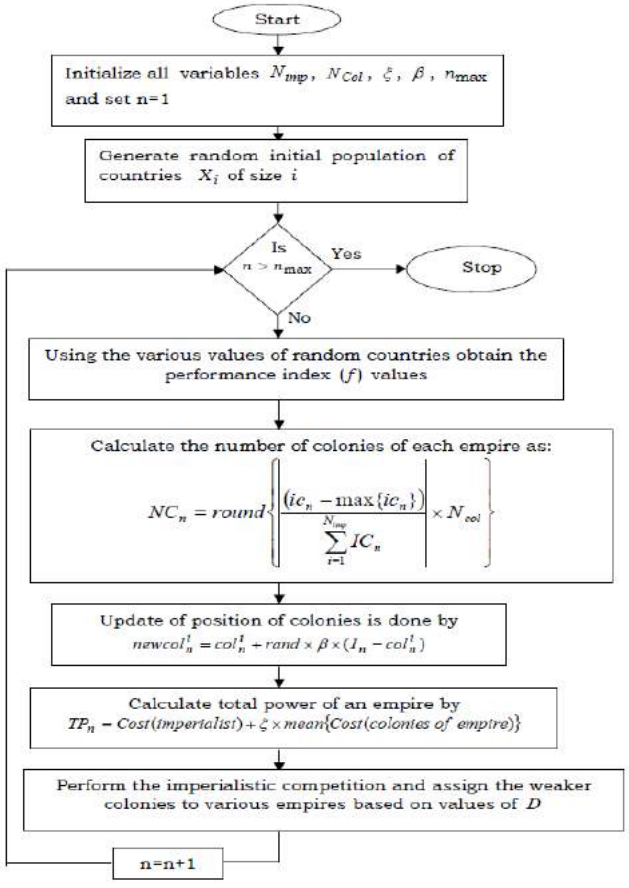

FIGURE 5. Flowchart of imperialistic competition algorithm.

A. INITIAL EMPIRES GENERATION

The initializing the algorithm, countries are generated, and it is denoted as the preliminary population [12]. Generally, in the problem of optimization, the country's position can be defined as $Coun_i = (x_i^1, x_i^2, \ldots x_i^n)$, where $i = 1, 2, 3 \ldots Ncoun$, where N_{coun} be the complete set of countries in the imperialistic.

The function of the variables can find the evaluation of the cost function of the different countries $(x_i^1, x_i^2, \ldots x_i^n)$. The individual country's cost, i.e., C_i can be computed in (4).

$$C_i = f(x_i^1, x_i^2, \ldots x_i^n) \tag{4}$$

where C_i denoted as cost of the i^{th} country.

The most commanding countries are preferred to formulate the empires, and it is symbolized as N_{imp}. The N_{col} denoted countries which have been leftover are preferred as colonies of these empires. Based on the value of objective function or power, the colonies are equally allocated to the imperialists. For minimization problems, the cost functions are inversely proportional to the individual imperialist's powers. So the value of the normalized costs can be evaluated for the empires in (5) as follows,

$$IC_n = ic_n - \max\{ic_i\} \tag{5}$$

where ic_n denoted as cost of the n^{th} imperialist and IC_n denoted as normalized cost.

The calculation of the normalized power of each imperialist in (6) is as follows,

$$IP_n = \left| \frac{IC|_n}{\sum_{i=1}^{N_{imp}} IC_n} \right| \tag{6}$$

where IP_n is denoted as the normalized power of each imperialist. Initially, the total number of colonies of each empire is calculated in (7) as follows,

$$NC_n = round(IP_n \times N_{col}) \tag{7}$$

where the NC_n is assumed to be the initial number of colonies of the n^{th} empire.

B. IMPERIALISTS AND COLONIES MOVEMENT

In this stage, the colonies are moved to the imperialists, relevant. The new positions of the colonies of n^{th} the empire are updated in (8) as follows,

$$newcol_n^i = col_n^i + rand \times \beta \times (I_n - col_n^i) \tag{8}$$

where col_n^i is the position of the i^{th}-colony of n^{th} imperialist and the rand is a random number between 0 to 1, β is a weight factor equal to 1.75, and I_n is the position of n^{th}-imperialist.

C. POSITION OF IMPERIALIST'S UPDATION

The positions of the imperialists are updated based on the cost function or the power of the imperialists. The imperialist attained lower costs than the imperialists were interchanged, and the respective colonies were also moved to the new imperialists based on the new position.

TABLE 1. Performance evaluation of proposed ICA based DMC system.

S. No.	Proposed System	Area 1- Thermal			Area 2- Hydro		
		Peak Time in (sec)	*Overshoot in (Hz)*	*Settling time in (sec)*	*Peak Time in (sec)*	*Overshoot in (Hz)*	*Settling time in (sec)*
1	Conventional Dual Mode Controller	2.21	0.00283042	7.541	0.83	0.00583379	4.241
2	Particle Swarm Optimization	2.155	0.00314339	4.120	0.895	0.00598582	2.760
3	ICA based Integral Controller	2.24	0.0029334	4.106	0.88	0.00593382	2.655
4	ICA based Dual Mode Controller	2.25	0.00287201	4.005	0.87	0.00591586	2.585

D. COMPUTATION OF TOTAL POWER

The empire's power is evaluated by the total powers of respective colonies and the corresponding imperialist. So the whole power of an empire can be determined (9) as:

$$TP_n = Cost(imperialist) + \xi \times mean\{Cost(colonies\ of\ empire)\} \quad (9)$$

where TP_n- is the total power of n^{th}-empire and ξ is considered as a positive number, less than 1.

E. CONDUCTING COMPETITIONS

The imperialistic competitions are conducted for each empire, and finally, after the completion, the empires undertake the colonies of other empires. At last, the colonies with less power in the empires can be identified, and competition is conducted to acquire these weaker colonies based on the possession probability. The normalized value of the total power of each empire can be determined in (10).

$$NTP_n = TP_n - \max\{TP_i\} \quad (10)$$

where NTP_n is the normalized power of n^{th}-empire. The possession probability of each empire is in (11).

$$ps_n = \left| \frac{NTP_n}{\sum_{i=1}^{N_{imp}} NTP_i} \right| \quad (11)$$

where ps_n is the possession probability of the n^{th}-empire. The vector PS is subdivided into the colonies of the various empires and can be determined in (12).

$$PS = \lfloor ps_1, ps_2, \ldots ps_{N_{imp}} \rfloor \quad (12)$$

where PS is denoted as possession probability of the imperialist. A random vector employing equivalent size as that of a vector PS is formed in (13) as follows,

$$R = \lfloor r_1, r_2, \ldots r_{N_{imp}} \rfloor \quad (13)$$

$$\begin{bmatrix} 0.1 & 0.0 & 0.3 & 0.4 \\ 0.0 & 0.1 & 0.0 & 0.2 \\ 0.3 & 0.4 & 0.1 & 0.0 \\ 0.2 & 0.0 & 0.2 & 0.1 \\ 0.2 & 0.3 & 0.0 & 0.1 \\ 0.2 & 0.2 & 0.4 & 0.2 \end{bmatrix}$$

FIGURE 6. Disco participation matrix.

TABLE 2. Assessment of PI values.

S. No.	Proposed Systems	Normal Case	Contract Violation
1	Conventional DMC	$2.593X10^{-5}$	$4.685X10^{-5}$
2	Particle Swarm Optimization	$1.910\ X10^{-5}$	$3.854\ X10^{-5}$
3	ICA based IC	$1.897X10^{-5}$	$3.557X10^{-5}$
4	ICA based DMC	$1.808X10^{-5}$	$3.358X10^{-5}$

where $r_1, r_2, r_3, \ldots r_{N_{imp}}$ are numbers generated randomly between 0 and 1. The D vector is determined in (14) as follows,

$$D = PS - R = \lfloor ps_1 - r_1, ps_2 - r_2, \ldots ps_{N_{imp}} - r_{N_{imp}} \rfloor \quad (14)$$

All the colonies of the empire will be shifted to the empires with a high value in the D vector.

F. POWERLESS EMPIRES AND THEIR ELIMINATION

The empires which have the least power collapsed in the imperialistic competition. Typically, the empire is declared collapsed if all colonies are lost.

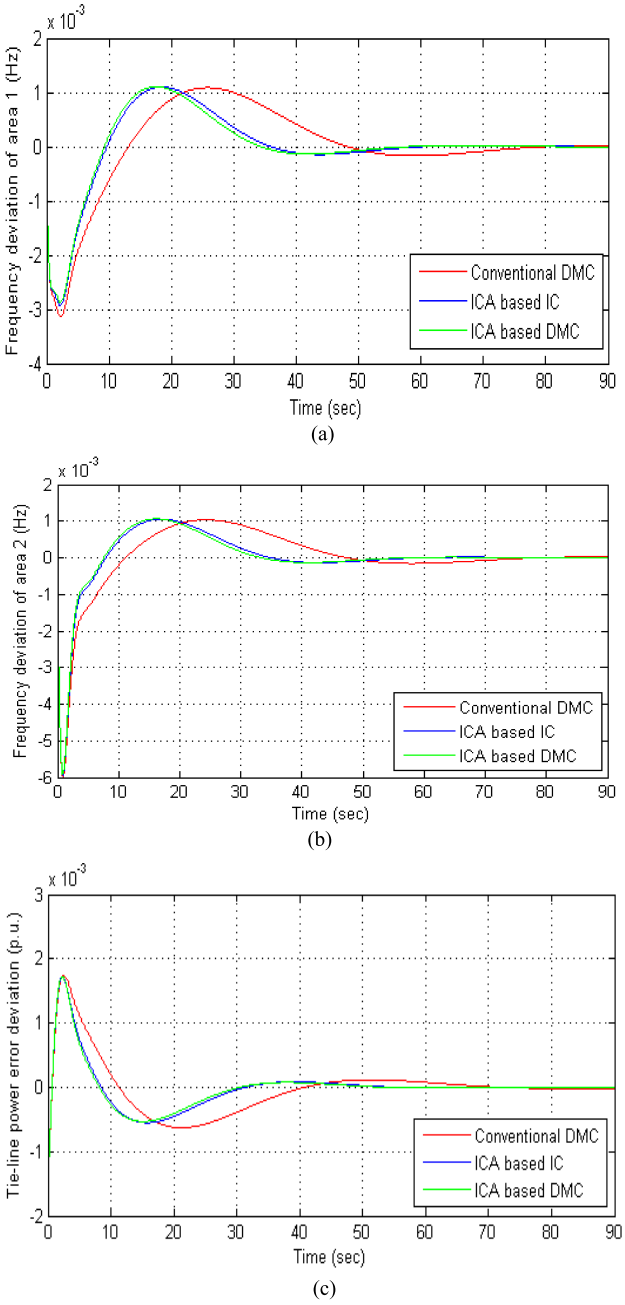

FIGURE 7. a. Deviations of area frequency in area 1 during normal condition. b. Deviations of area frequency in area 2 during normal condition. c. Tie line power error during normal condition.

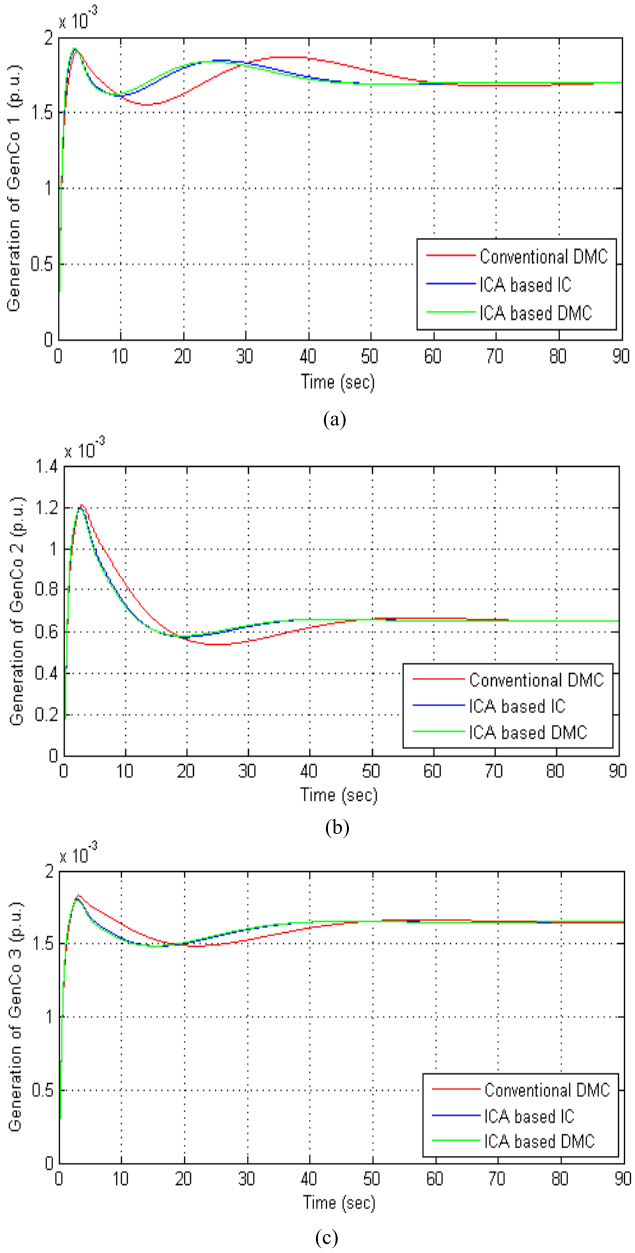

FIGURE 8. a. Generation of GenCo 1 in thermal area during normal condition. b. Generation of GenCo 2 in thermal area during normal condition. c. Generation of GenCo 3 in thermal area during normal condition.

G. CONVERGENCE

Finally, the most powerful empire is declared based on the maximum number of colonies under it. Further, there was no change in the colonies and empire after the declaration of the winner.

VII. RESULTS AND DISCUSSIONS

In this work, CES and Static Synchronous Series Compensator with the multi-area hydrothermal system are considered under deregulation. The participation of each and every GenCos in the system of Automatic Generation Control as per the mentioned participation factors: $apf_1 = apf_4 = 0.5$, $apf_2 = apf_3 =$, $apf_5 = apf_6 = 0.25$. A 0.4% step load disturbance is considered in each area. The DPM is considered in this work is given in Fig. 6.

The value of 0.5 is the nominal value of the gain setting considered for the conventional dual-mode controller in each area. So the optimized gain of the integral controllers for the Particle Swarm Optimization technique [10] is 0.3578, and 0.9335 has been attained for areas 1 and 2. The gain settings of 0.8454 and 0.91 have been attained through the

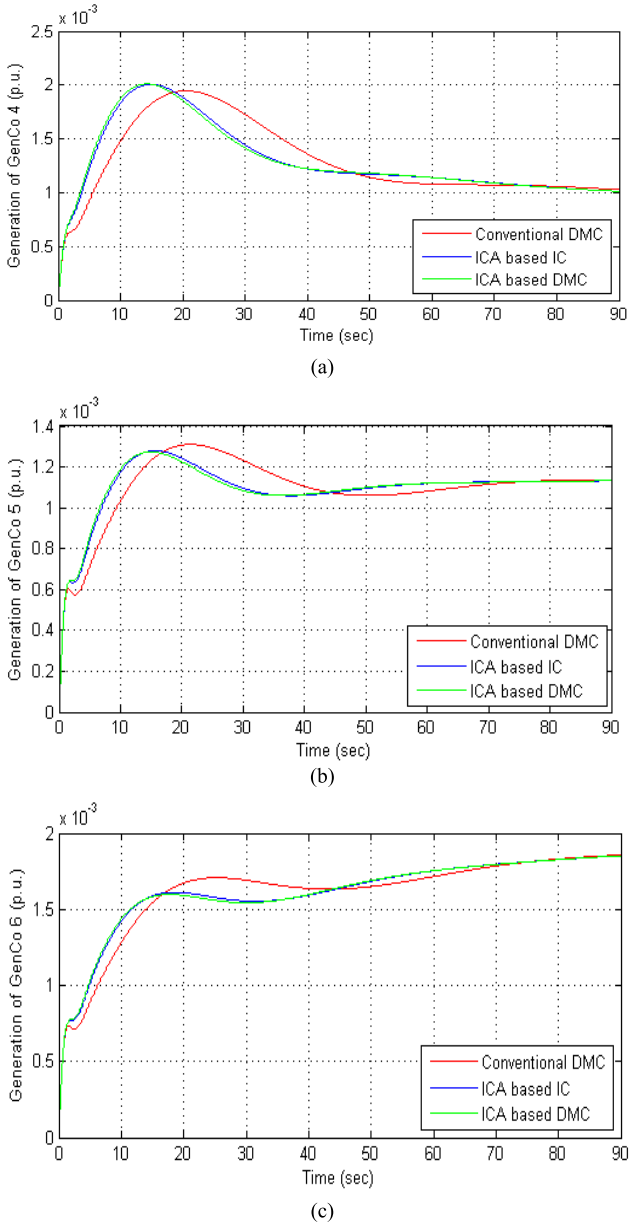

FIGURE 9. a. Generation of GenCo 4 in hydro area during normal condition. b. Generation of GenCo 5 in hydro area during normal condition. c. Generation of GenCo 6 in hydro area during normal condition.

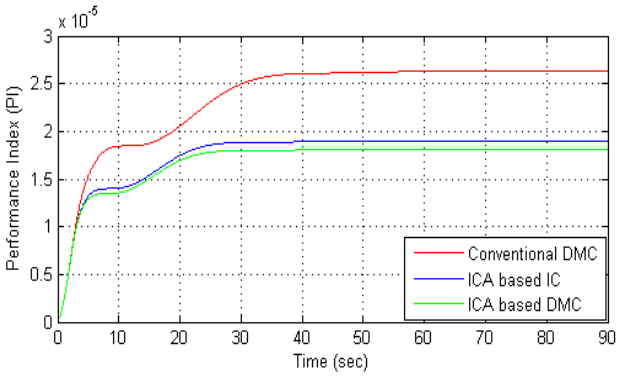

FIGURE 10. Comparison of PI values during normal condition.

Imperialistic Competition Algorithm [12] corresponding to areas 1 and 2. The optimal values of the proportional controller and integral controller gain setting of Dual Mode Controller in both the areas are $K_{i1} = K_{i2} = 0.987$ and $K_{p1} = kp2 = 0.95$ are found by the Imperialistic Competition Algorithm. The value of the proportional gain K_p determines how fast the system responds, whereas the value of the integral gain K_i determines how fast the steady-state error is eliminated. When the value of these gains are more considerable for better control performance. The specified limit of the error signal of $\varepsilon_1 = \varepsilon_2 = 0.02$ has been deliberated to design this work's Dual Mode Controller (DMC). It is also to be considered that the values of ε_1 and ε_2 might look arbitrary. Still, the values have been selected after carefully studying the system performance under various conditions. The comparison of system performance shown in Table-1 with the conventional dual-mode controller, imperialistic competition algorithm-based integral controller, and imperialistic competition algorithm-based dual-mode controller by frequency deviations in both areas are taken as reference. The overshoot of the system in the thermal area is 0.00287201 *Hz*, and the hydro area is 0.00591586 *Hz* for the imperialistic competition algorithm-based dual-mode controller. The settling time of the thermal area is 4.005 sec, and the hydro area is 2.585 sec is less compared with all other methods. The proposed controller gives a lower ripple in the output voltage, reduces the settling time, and keeps the output stable in case of step input. The overshoot of the output voltage during transient time is minimized using the pole-zero cancellation technique. For the system to be stable, the rise time must be less so that the speed of response is increased, and the maximum peak overshoot should also be less. The enhancement of overall system performance with imperialistic competition algorithm-based dual-mode controller can be perceived from Table-1; the dynamic system performance of both areas is improved.

The proposed system Performance Index (PI) value is shown in Table 2 with conventional Dual Mode Controller, Imperialistic Competition Algorithm based Integral Controller (IC), and Imperialistic Competition Algorithm based Dual Mode Controller. It is observed from Table 2 that the performance index of the Imperialistic Competition Algorithm-based Dual Mode Controller for the standard case is 1.08×10^{-5}, and the contract violation case is 3.358×10^{-5}. So the Imperialistic Competition Algorithm-based Dual Mode Controller has a lesser performance index value than all other techniques, which designates that the Imperialistic Competition Algorithm-based Dual Mode Controller has more improved control performance than all other techniques.

The frequency deviation of both the areas under the usual case is depicted in Fig. 7a and 7b. The error deviations in

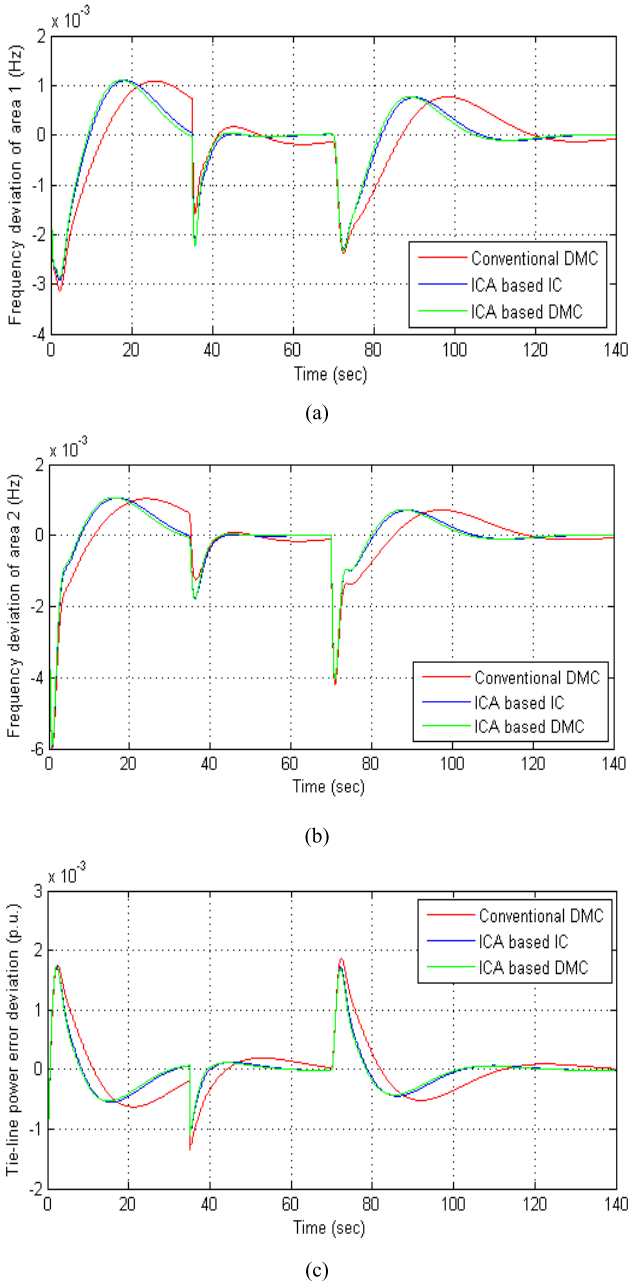

FIGURE 11. a. Deviations in area Frequency in area 1 during contract violation condition. b. Deviations in area Frequency in area 2 during contract violation condition. c. Tie line power error during contract violation condition.

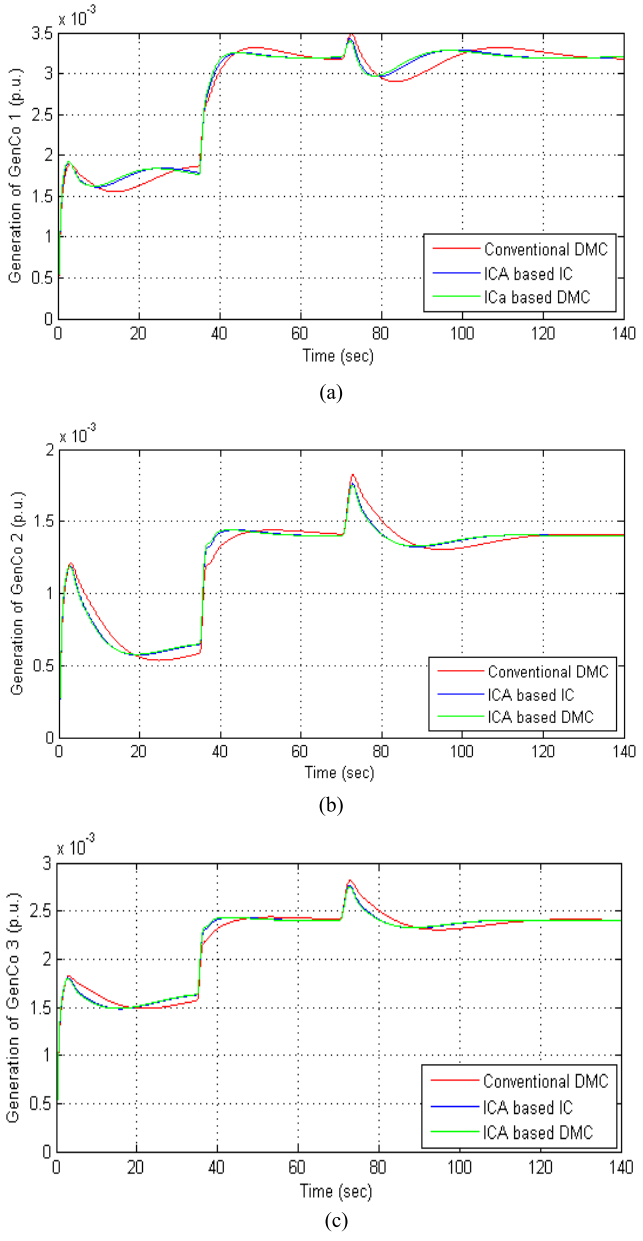

FIGURE 12. a. Generation of GenCo 1 in Thermal area during Contract violation condition. b. Generation of GenCo 2 in Thermal area during Contract violation condition. c. Generation of GenCo 3 in Thermal area during Contract violation condition.

the tie-line power in the standard case are shown in Fig. 7c. It can be perceived that the lessening of frequency deviation of the system and error of oscillations in the tie-line power is achieved due to the existence of the Imperialistic Competition Algorithm-based Dual Mode Controller. The power generations of GenCo 1, Genco 2, and Genco 3 in the thermal area under the standard case are depicted in Fig. 8a, 8b, and 8c. The power generations of GenCo 4, Genco 5, and Genco 6 in the hydro area under the usual case are depicted in Fig. 9a, 9b, and 9c. The settling time of a dynamical system is the time elapsed from applying an ideal step input to the time the dynamic system output entered and remained with a steady-state value of the system. It is realized that the oscillations of power are restricted due to the existence of the Imperialistic Competition Algorithm-based Dual Mode Controller. Fig. 10 indicates the assessment of the PI value of the hydrothermal system during normal conditions. The lesser value of PI indicates that the system acquires improved performance due to the existence of the Imperialistic Competition Algorithm based on the Dual Mode Controller.

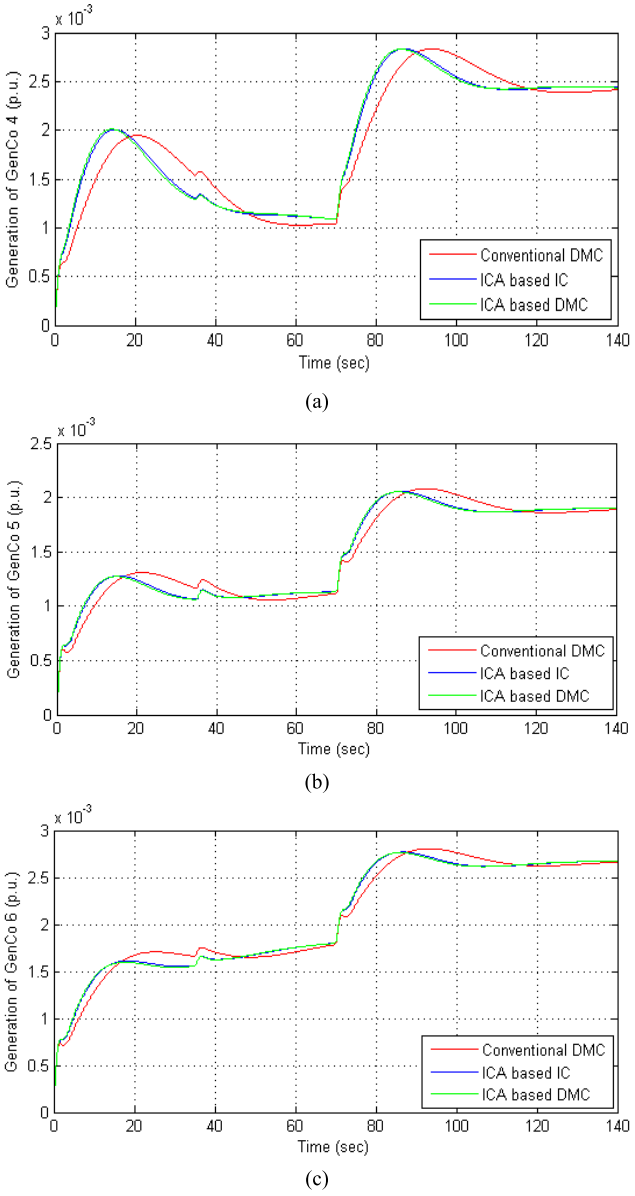

FIGURE 13. a. Generation of GenCo 4 in Hydro area during Contract violation condition. b. Generation of GenCo 5 in Hydro area during Contract violation condition. c. Generation of GenCo 6 in Hydro area during Contract violation condition.

A. CONTRACT VIOLATION

The step load increase in power demand in an LFC is supplied either from the kinetic energy of the rotating machine or increased generation. Further, following a step change in load demand in the interconnected system, the primary ALFC (Automatic Load Frequency Control) loop responds first within seconds. In contrast, the secondary ALFC loop responds rather slowly (within minutes) to compensate for the static frequency drop. During this period, undesirable perturbation oscillation may occur in the dynamic response. Incorporating SSSC and CES in the ALFC makes zero in the open loop transfer function, as the results two poles are situated at the left half of the s plane with absolute values

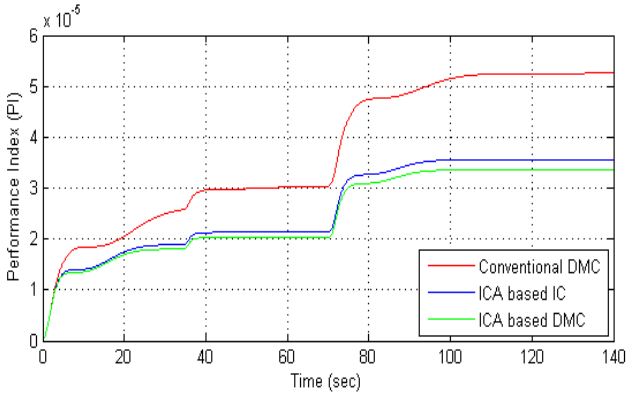

FIGURE 14. Comparison of PI values under contract violation.

improve the response. Hence, dissimilarity is occurred in the response between without and with SSSC and CES during the initial response (within 10 sec) and the response at contract violation (35 sec and 70 sec).

It possibly will arise that the DisCos are demanding more than indicated in the contract, and it may break up a contract. In this case, 0.3% of the additional step load demanded by DisCo1 after 35 sec and DisCo4 after 70 sec are considered in both areas. The add-on load is engaged by all the GenCos, which is in the same area in which defilement of agreement has arisen. The frequency deviation of both the areas under the contract violation case is depicted in Fig. 11a and 11b. The error deviations in the tie-line power in the course of contract violation are shown in Fig. 11c. It depicts that the reduction in deviation of frequency and oscillations of error in tie-line power is achieved due to the imperialistic competition algorithm-based dual-mode control.

The power generations of GenCo 1, Genco 2, and Genco 3 in the thermal area under contract violation are depicted in Fig. 12a, 12b, and 12c. The power generations of GenCo 4, Genco 5, and Genco 6 in the hydro area under contract violation are depicted in Fig. 13a, 13b, and 13c. It can be observed from the Figures the power oscillations are restricted due to the existence of the Imperialistic Competition Algorithm-based Dual Mode Controller.

The assessment of the PI values of both the systems in the course of the contract violation situation is shown in Fig. 14. It is realized that the PI value of the system acquires additionally abridged due to the existence of the Imperialistic Competition Algorithm-based Dual Mode Controller. The Performance Index value of the ICA-based integral controller and ICA-based dual-mode control under the contract violation cases are 3.557×10^{-5} and 3.358×10^{-5}. The result indicates that the Performance Index of the system with a dual-mode control-based imperialistic competition algorithm has superiority compared to all other methods.

VIII. CONCLUSION

The Imperialistic Competition Algorithm has been efficiently implemented to adjust the gain settings of the Dual Mode

Controller. A multi-area-based hydrothermal system in the competitive market environment of Capacitive Energy Storage and Static Synchronous Series Compensator has been employed to validate the system performance. The Integral Square of Error (ISE) technique has been used to evaluate the performance index for the different techniques. The system's performance was analyzed for conventional Dual-Mode Controller, Imperialistic Competition Algorithm-based integral controller, and Imperialistic Competition Algorithm based Dual Mode Controller in a two-area hydrothermal with Capacitive Energy Storage and Static Synchronous Series Compensator based system in open market scenario has been investigated. The settling time of thermal and hydro areas for conventional Dual Mode Controller is 7.541 sec and 4.241 sec; Particle Swarm Optimization technique is 4.12 sec and 2.7 sec, Imperialistic Competition Algorithm based Integral Controller is 4.106 sec and 2.655 sec. But the Imperialistic Competition Algorithm-based Dual Mode Controller is 4.005 sec and 2.585 sec. The Performance Index value for standard and Contract violation case is 1.808×10^{-5} and 3.358×10^{-5}. The simulation result indicates that the suggested Imperialistic Competition Algorithm-based Dual Mode Controller technique successfully diminishes the oscillations of frequency and tie-line power of the system. It can be understood that the Performance Index of the system with Dual Mode Controller based Imperialistic Competition Algorithm has superiority as compared to other methods.

APPENDIX

A. HYDROTHERMAL SYSTEM DATA

$$P_{r1}, P_{r2} = 1200\text{Mw}; \quad K_{p1}, K_{p2} = 120\text{Hz/p.u. Mw}; \quad T_{p1}, T_{p2} = 20\text{s} \quad \text{and Tg} = 0.08\text{s}; \quad T_t = 0.3\text{s}; \quad T_w = 1\text{s}; \quad T_r = 5s, \quad T_1 = 41.6s \quad \text{and} \quad T_2 = 0.513\text{s}; \quad B_1, B_2 = 0.4249\text{p.u Mw/Hz}; \quad R_1, R_2 = 2.4\text{Hz/p.u.} \quad \text{Mw}; \quad T_{12} = 0.0866\text{s};$$

B. CES DATA

$$K_{CES} = 0.3; \quad T_{CES} = 0.0352\text{s}; \quad T_1 = 0.279\text{s}; \quad T_2 = 0.026\text{s}; \quad T_3 = 0.411\text{s} \quad \text{and } T_4 = 0.1\text{s};$$

C. SSSC DATA

$$K_{SSSC} = 0.292; \quad T_{SSSC} = 0.03\text{s}; \quad T_1 = 0.188\text{s}; \quad T_2 = 0.039\text{s}; \quad T_3 = 0.542\text{s} \quad \text{and } T_4 = 0.14\text{s};$$

D. PARAMETERS OF ICA

$$N_{imp} = 20; \quad N_{col} = 100; \quad \xi = 0.2; \quad \beta = 1.75$$

REFERENCES

[1] C. Concordia and L. K. Kirchmayer, "Tie-line power and frequency control of electric power systems—Part II," *Trans. Amer. Inst. Electr. Eng., III, Power App. Syst.*, vol. 73, no. 2, pp. 133–146, Apr. 1954.

[2] M. L. Kothari, B. L. Kaul, and J. Nanda, "Automatic generation control of hydro-thermal system," *J. Inst. Eng.*, vol. 61, vol. 2, pp. 85–91, Oct. 1980.

[3] R. P. Schulte, "An automatic generation control modification for present demands on interconnected power systems," *IEEE Trans. Power Syst.*, vol. 11, no. 3, pp. 1286–1294, Aug. 1996.

[4] J. Kumar, K.-H. Ng, and G. Sheble, "AGC simulator for price-based operation. I. A model," *IEEE Trans. Power Syst.*, vol. 12, no. 2, pp. 527–532, May 1997.

[5] J. Kumar, K.-H. Ng, and G. Sheble, "AGC simulator for price-based operation. Part 2: Case study results," *IEEE Trans. Power Syst.*, vol. 12, no. 2, pp. 533–538, May 1997.

[6] B. H. Bukken and O. Grande, "Automatic generation control in a deregulated environment," *IEEE Trans. Power Syst.*, vol. 13, no. 4, pp. 1401–1406, Nov. 1998.

[7] V. Donde, M. A. Pai, and I. A. Hiskens, "Simulation and optimization in an AGC system after deregulation," *IEEE Trans. Power Syst.*, vol. 16, no. 3, pp. 481–489, Aug. 2001.

[8] P. Marimuthu and C. Govindaraju, "Load frequency control of hydrothermal system under open market considering capacitive energy storage," *Int. Rev. Model. Simul.*, vol. 5, no. 5, pp. 2307–2313, Oct. 2012.

[9] P. Marimuthu, S. S. Dash, and B. Basavaraja, "Performance analysis of CES and CES-SSSC in load frequency control of multi area system under open market scenario," *Int. J. Distrib. Energy Res. Smart Grids*, vol. 10, no. 1, pp. 1–13, 2014.

[10] P. Marimuthu, B. Basavaraja, and S. S. Dash, "Load frequency control of multi-area SSSC and CES based system under deregulation using particle swarm optimization," *Int. Rev. Elect. Eng.*, vol. 10, no. 1, pp. 154–162, 2015.

[11] E. Atashpaz-Gargari and C. Lucas, "Imperialist competitive algorithm: An algorithm for optimization inspired by imperialistic competition," in *Proc. IEEE Congr. Evol. Comput.*, Sep. 2007, pp. 4661–4667.

[12] M. Ponnusamy, B. Banakara, S. S. Dash, and M. Veerasamy, "Design of integral controller for load frequency control of static synchronous series compensator and capacitive energy source based multi area system consisting of diverse sources of generation employing imperialistic competition algorithm," *Int. J. Electr. Power Energy Syst.*, vol. 73, pp. 863–871, Dec. 2015.

[13] J. Nanda, A. Mangla, and S. Suri, "Some new findings on automatic generation control of an interconnected hydrothermal system with conventional controllers," *IEEE Trans. Energy Convers.*, vol. 21, no. 1, pp. 187–194, Mar. 2006.

[14] J. Nanda and L. C. Saika, "Comparison of performances of several types of classical controller in automatic generation control for an interconnected multi-area thermal system," in *Proc. Australas. Universities Power Eng. Conf.*, vol. 22, Dec. 2008, pp. 1–6.

[15] K. Chatterjee, "Design of dual mode PI controller for load frequency control," *Int. J. Emerg. Electr. Power Syst.*, vol. 11, no. 4, pp. 1–26, Sep. 2010.

[16] I. Report, "Dynamic models for steam and hydro turbines in power system studies," *IEEE Trans. Power App. Syst.*, vol. PAS-92, no. 6, pp. 1904–1915, Nov. 1973.

[17] D. M. Ojeda-Esteybar, R. G. Rubio-Barros, and A. Vargas, "Integrated operational planning of hydrothermal power and natural gas systems with large scale storages," *J. Modern Power Syst. Clean Energy*, vol. 5, no. 3, pp. 299–313, May 2017.

[18] E. J. De Oliveira, J. W. M. Lima, and K. C. De Almeida, "Allocation of FACTS devices in hydrothermal systems," *IEEE Trans. Power Syst.*, vol. 15, no. 1, pp. 272–282, Feb. 2000.

[19] N. Pathak, T. S. Bhatti, and A. Verma, "Discrete data AGC of hydrothermal systems under varying turbine time constants along with the power system loading conditions," *IEEE Trans. Ind. Appl.*, vol. 53, no. 5, pp. 4998–5013, Sep. 2017.

[20] R. Kumar and V. K. Sharma, "Whale optimization controller for load frequency control of a two-area multi-source deregulated power system," *Int. J. Fuzzy Syst.*, vol. 22, no. 1, pp. 122–137, Feb. 2020.

[21] A. Saha and L. C. Saikia, "Utilisation of ultra-capacitor in load frequency control under restructured STPP-thermal power systems using WOA optimised PIDN-FOPD controller," *IET Gener., Transmiss. Distrib.*, vol. 11, no. 13, pp. 3318–3331, Sep. 2017.

[22] W. Tasnin, L. C. Saikia, and M. Raju, "Deregulated AGC of multi-area system incorporating dish-stirling solar thermal and geothermal power plants using fractional order cascade controller," *Int. J. Electr. Power Energy Syst.*, vol. 101, pp. 60–74, Oct. 2018.

[23] M. Gheisarnejad, "An effective hybrid harmony search and cuckoo optimization algorithm based fuzzy PID controller for load frequency control," *Appl. Soft Comput.*, vol. 65, pp. 121–138, Apr. 2018.

[24] Y. Arya, "AGC performance enrichment of multi-source hydrothermal gas power systems using new optimized FOFPID controller and redox flow batteries," *Energy*, vol. 127, pp. 704–715, May 2017.
[25] S. C. Sahoo, A. K. Barik, and D. C. Das, "A novel green leaf-hopper flame optimization algorithm for competent frequency regulation in hybrid microgrids," *Int. J. Numer. Model., Electron. Netw., Devices Fields*, vol. 35, p. e2982, no. 3, May 2022, doi: 10.1002/jnm.2982.
[26] M. Bhuyan, D. C. Das, and A. K. Barik, "Proficient power control strategy for combined solar gas turbine-wind turbine generator-biodiesel generator based two area interconnected microgrid employed with DC link using Harris's hawk optimization optimised tilt-integral- derivative controller," *Int. J. Numer. Model., Electron. Netw., Devices Fields*, vol. 35, p. e2991, Feb. 2022, doi: 10.1002/jnm.2991.

PONNUSAMY MARIMUTHU received the B.E. degree in electrical and electronics engineering from the University of Madras, Chennai, the M.E. degree in power systems engineering from Anna University, Chennai, and the Ph.D. degree in electrical and electronics engineering from Jawaharlal Nehru Technological University, Hyderabad. He is currently working as a Professor with the Department of Electrical and Electronics Engineering, Malla Reddy Engineering College (Autonomous), Secundrabad, India. His research interests include economic dispatch, deregulation in power systems, optimal location and power flow control with FACTS devices, dynamic response of multi area hydrothermal systems, HVDC systems, AI techniques, and power quality. He is serving as a reviewer for reputed journals and various international conferences organized by IEEE and Springer.

T. RAJESH received the bachelor's degree in electrical and electronics engineering from the Dr. Sivanthi Aditanar College of Engineering, Manonmaniam Sundaranar University, in 1999, and the master's degree in power system engineering from the Thiagarajar College of Engineering, Madurai Kamaraj University, Madurai, in 2001, and the Ph.D. degree from Anna University, Tamil Nadu, India. He is currently working as a Professor at the Department of Electrical and Electronics Engineering, Malla Reddy Engineering College (Autonomous), Hyderabad. He has more than 18 years of teaching experience. He has many research publications in national and international journals to his credit. His research interests include power systems, power quality, and control systems. He is a member of various professional bodies, such as MIEEE, MIE, MISTE, MACM, MISCA, MIAENG, and FSIESRP.

N. RAJESWARAN received the bachelor's degree in electrical and electronics engineering from the Government College of Engineering, Bargur (Madras University), the master's degree in applied electronics from Anna University Chennai, Tamil Nadu, and the Ph.D. degree from Jawaharlal Nehru Technological University Hyderabad, Telangana, India. He is currently working as a Professor and the HoD of the Department of Electrical and Electronics Engineering, Malla Reddy Engineering College (Autonomous), Hyderabad. He has published many research papers in various international journals and conferences. His research interests include electrical machines, soft computing, fault diagnosis, power systems, and image processing. He is a Life Time Member of various professional bodies, such as MIE, ISTE, IAENG, and IACSIT.

HASSAN HAES ALHELOU (Senior Member, IEEE) received the B.Sc. degree (Hons.) from Tishreen University, Latakia, Syria, in 2011, and the M.Sc. and Ph.D. degrees (Hons.) from the Isfahan University of Technology, Iran. He is currently a Professor and a Faculty Member with Tishreen University and a Consultant with Sultan Qaboos University (SQU), Oman. He is also with the Department of Electrical and Computer Systems Engineering, Monash University, Clayton, VIC, Australia. Previously, he was with the School of Electrical and Electronic Engineering, University College Dublin (UCD), Dublin, Ireland, from 2020 to 2021, and the Isfahan University of Technology (IUT). He has published more than 200 research papers in high-quality peer-reviewed journals and international conferences. His research papers received 2550 citations with H-index of 26 and i-index of 56. He has authored/edited 15 books published in reputed publishers, such as Springer, IET, Wiley, Elsevier, and Taylor & Francis. He has participated in more than 15 international industrial projects over the globe. His major research interests include renewable energy systems, power systems, power system security, power system dynamics, power system cybersecurity, power system operation, control, dynamic state estimation, frequency control, smart grids, microgrids, demand response, and load shedding. He was a recipient of the Outstanding Reviewer Award of many journals, such as *Energy Conversion and Management* (ECM), the *ISA Transactions*, and *Applied Energy*. He was also a recipient of the Best Young Researcher Award in the Arab Student Forum Creative among 61 researchers from 16 countries from Alexandria University, Egypt, in 2011, the Excellent Paper Award from IEEE CSEE Journal of Power and Energy Systems (SCI IF: 3.938; Q1), in 2021 and 2022. He serves as an Editor in a number of prestigious journals, such as IEEE Systems Journal, *Computers and Electrical Engineering* (Elsevier), *IET Journal of Engineering*, and *Smart Cities*. He has also performed more than 800 reviews for high prestigious journals, including IEEE Transactions on Power Systems, IEEE Transactions on Smart Grid, IEEE Transactions on Industrial Informatics, IEEE Transactions on Industrial Electronics, *Energy Conversion and Management*, *Applied Energy*, and *International Journal of Electrical Power and Energy Systems*. He was included in the 2018 and 2019 Publons and Web of Science (WoS) List of the top 1% best reviewer and researchers in the field of engineering and cross-fields over the world.

frontiers | Frontiers in Energy Research

ORIGINAL RESEARCH
published: 23 June 2022
doi: 10.3389/fenrg.2022.920651

Performance Assessment of Open-Loop and Closed-Loop Generation Rate Constraint Models for Optimal LFC of the Three-Area Reheat Thermal System

CH. Naga Sai Kalyan[1], B. Srikanth Goud[2], Ch. Rami Reddy[3], M. Kiran Kumar[4], Mohit Bajaj[5], Mohamed F. El-Naggar[6,7] and Salah Kamel[8]*

[1]Electrical and Electronics Engineering, Vasireddy Venkatadri Institute of Technology, Guntur, India, [2]Department of Electrical and Electronics Engineering, Anurag University, Venkatapur, India, [3]Department of Electrical and Electronics Engineering, Malla Reddy Engineering College (A), Secunderabad, India, [4]Department of Electrical and Electronics Engineering, Koneru Lakshmaiah Education Foundation, Guntur, India, [5]Department of Electrical and Electronics Engineering, National Institute of Technology, New Delhi, India, [6]Department of Electrical Engineering, College of Engineering, Prince Sattam Bin Abdulaziz University, Al-Kharj, Saudi Arabia, [7]Department of Electrical Power and Machines Engineering, Faculty of Engineering, Helwan University, Helwan, Egypt, [8]Electrical Engineering Department, Faculty of Engineering, Aswan University, Aswan, Egypt

OPEN ACCESS

Edited by:
Xiaoshun Zhang,
Northeastern University, China

Reviewed by:
Jiawen Li,
South China University of Technology, China
Mahmoud Elsisi,
National Taiwan University of Science and Technology, Taiwan

***Correspondence:**
Mohamed F. El-Naggar
mfelnaggar@yahoo.com
m.elnaggar@psau.edu.sa

Specialty section:
This article was submitted to Smart Grids, a section of the journal Frontiers in Energy Research

Received: *14 April 2022*
Accepted: *18 May 2022*
Published: *23 June 2022*

Citation:
Sai Kalyan CHN, Goud BS, Reddy CR, Kumar MK, Bajaj M, El-Naggar MF and Kamel S (2022) Performance Assessment of Open-Loop and Closed-Loop Generation Rate Constraint Models for Optimal LFC of the Three-Area Reheat Thermal System. Front. Energy Res. 10:920651. doi: 10.3389/fenrg.2022.920651

In this article, a novel investigation is performed to showcase the best suitable structure of the generation rate constraint (GRC) for the three-area reheat thermal power system (RTPS) to obtain load frequency control (LFC) optimally. For investigation purposes, two GRC models which are widely implemented in the literature without providing any discussion of their selection and suitability are confiscated in this article. The two GRC structures deliberated in the present article are termed as open-loop and closed-loop models. The performance of the three-area reheat thermal unit is examined with these two GRC structures for a perturbation of 10% step load (10% SLP) on area-1. An investigation is performed under the governance of a three-degree-of-freedom PID (3DOFPID) controller, fine-tuned using a water cycle algorithm (WCA) subjected to index integral square error (ISE) minimization. However, the efficacy of the proposed WCA-tuned 3DOFPID controller is revealed with other control approaches available in the literature upon implementation of a widely accepted model of a two-area hydrothermal system. Finally, the simulation results and sensitivity analysis showed the suitable GRC structure for a three-area reheat thermal unit to obtain LFC optimally with high performance.

Keywords: generation rate constraint, load frequency control, 3DOFPID controller, water cycle algorithm, ISE index

INTRODUCTION

In modern power systems, LFC is an indispensable peculiar function when it comes to the regulation of the parameter frequency. However, to get the exact, precise divination of the issue LFC, it is necessary to consider the inherent requirements and main practical constraints like GRC with the power generation utilities. The physical constraint GRC compels the rate of change of opening the steam valve, which significantly influences the dynamical behavior of the power system. Thus, the GRC nonlinearity property affects the power system performance practically. In realistic nature, the

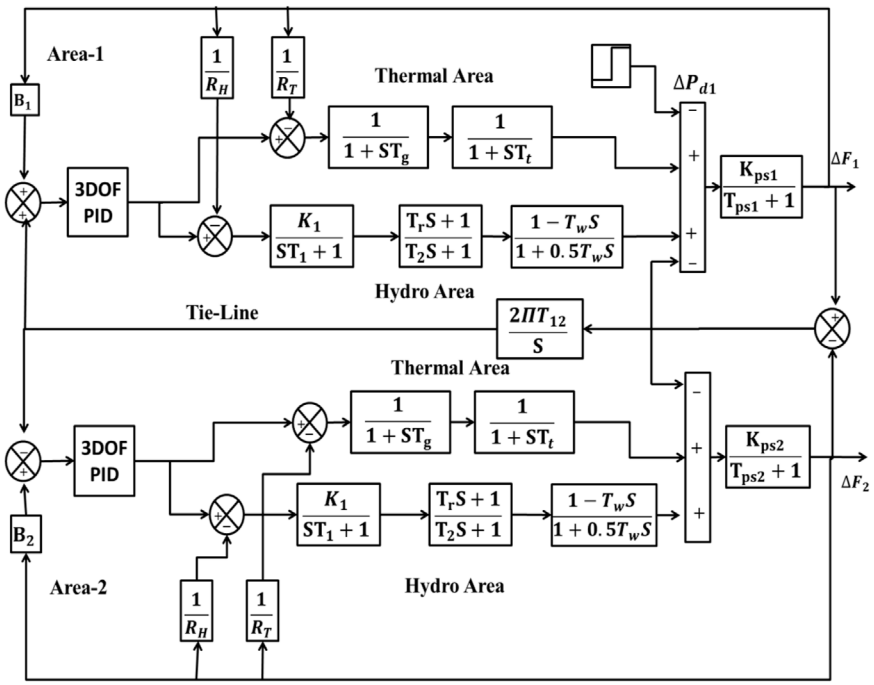

FIGURE 1 | Model of the DAHT power system (Goud et al., 2021).

rate at which the deviation in real power generated by the units in the thermal plant is cramped by the GRC maximum limits. Thus, LFC design for thermal units without considering the physical constraints like GRC may not be realistic (Kalyan and Rao, 2020a). The intention of considering thermal units with GRC is that the rapid rise in load demand brings out an excessive steam from the boiler and causes condensation because of adiabatic expansion. In general expectation, the steam condensation in thermal units is not more than 20% of the required temperature and pressure. Thus, it is only facilitated to alter power generation of about 1.2Pu of nominal power generation throughout the first few 10 s (Morsali et al., 2014). Once the generation unit reaches its maximum capacity, then the GRC restricts incremental variation in turbine power. Because of the significant impact of GRC on the performance of LFC, proper encompassment of realistic GRC constraints within the system will enhance the control mechanism. Otherwise, the power system will suffer from momentarily significant disturbances in a controller design.

The demand on the power system will never be constant and will fluctuate continuously. With these, the control signals will also deviate. The frequency deviations will be compensated by altering the actual power generation provided through ramping limits in GRC. Moreover, the effect of GRC under significant disturbances is even more noticeable, and the system tries to raise the generation to sustain the stability in a faster time horizon. However, the negative impact of GRC on the thermal units maybe even worse with the consideration of another nonlinearity such as the governor dead band (GDB). The plant may not attain a stable condition and falls into an unstable state, and then, the protective relay will operate to isolate the generation utilities. The literature survey presents that with the consideration of both GDB and GRC, the system responses will face more significant deviations in peak overshoots/undershoots and more considerable settling time for the situation of not conceiving GDB and GRC (Kalyan and Rao, 2021). Hence, the aforementioned limitations need to be considered to avoid the instability of an interconnected system. With the incorporation of GDB and GRC, the system becomes highly nonlinear, which degrades the secondary controller performance. Thus, intense care must be taken while designing regulators, especially for the thermal units with GDB and GRC.

Over the past few years, researchers have considered mainly two structures of GRC for the frequency analysis, termed as openvloop and closed loop. In Lal et al. (2016), a dual area hydrothermal (DAHT) system is considered with an open-loop GRC structure, but the effect of GDB is not incorporated. Nanda et al. (2015) regarded a dual area thermal-hydro-gas (THG) system for the investigation and employed the open-loop GRC for the thermal unit, but the ramp rate limits are not considered. Researchers in Rahman et al. (2017) evaluated GDB and GRC of open-loop for the two-area thermal system. Later, renewable sources like solar thermal and wind turbines are taken in both areas. Raju et al. (2016) and Çelik (2020) considered a three-area reheat thermal system with the GRC structure of an open loop, but the impact of GDB on the system performance is not taken into account. The impact of GDB and GRC in a three-area thermal system is investigated by the researchers in Padhy and Panda (2017), but the analysis is restricted to the deployment of an open-loop GRC structure without briefing its selection. Furthermore, the LFC of the reheat thermal system is

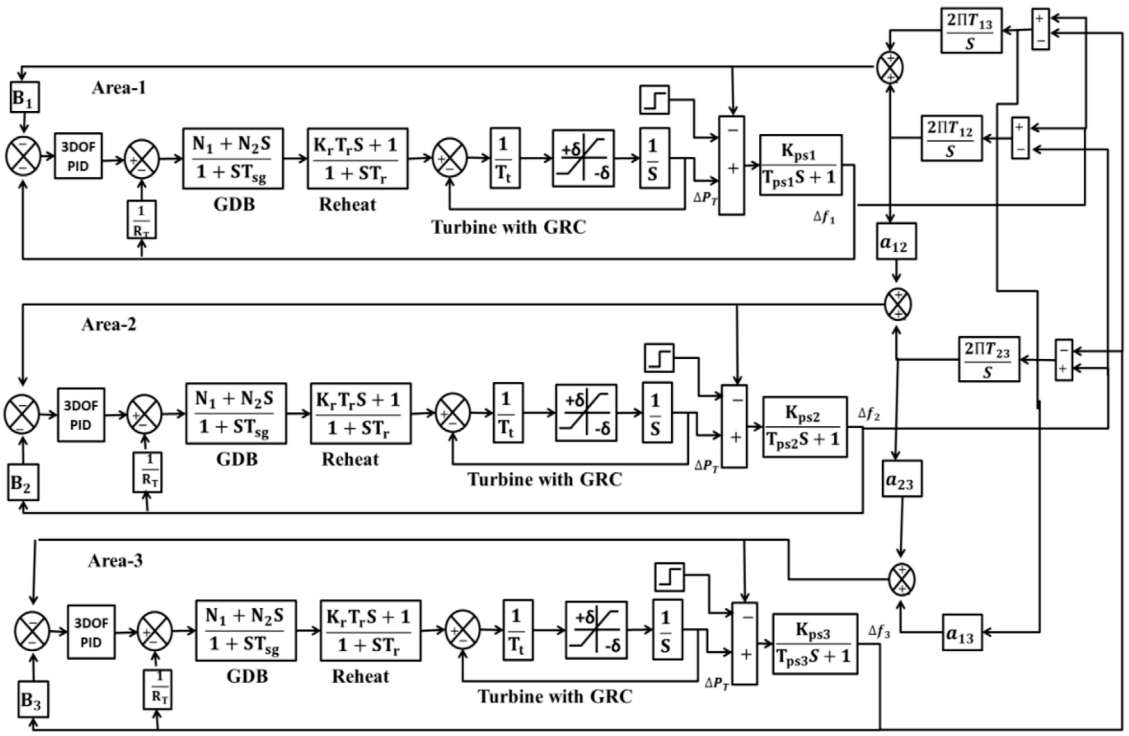

FIGURE 2 | Model of the three-area RTPS system (Morsali et al., 2014).

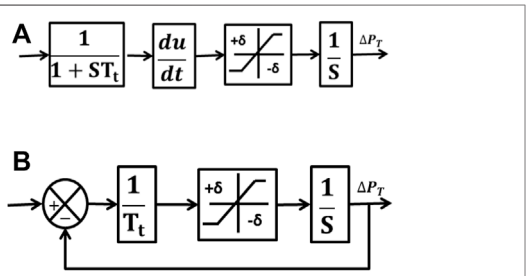

FIGURE 3 | GRC structure. **(A)** Open-loop and **(B)** closed-loop.

extended to five areas by the researchers in Shiva and Mukherjee (2016) by considering the open-loop structure of GRC and not considering the effect of GDB. In Rajesh et al. (2019), the five-area THG system is investigated by considering a thermal unit with an open-loop GRC.

Pan and Das (2015) investigated the dual area thermal system with a closed-loop GRC model, and the effect of GDB is also taken into analysis. Morsali et al. (2017) and Ahmed et al. (2022) performed the LFC of the dual area THG system and employed the closed-loop GRC for the thermal units in both the areas and considered the GDB effect on system performance. After that, the authors in Sahu et al. (2016a) considered a closed-loop GRC structure for the three areas of RTPS, and the coordination of GDB with GRC was not analyzed. Kalyan and Suresh (2021a) considered GDB and GRC of a closed-loop for the LFC analysis of the DAHT system and, the coordination of GDB and GRC impact on the performance of the system is not demonstrated.

After a careful literature survey, it is concluded that the researchers had widely utilized the GRC open loop and closed loop with and without considering the effect of GDB on the multi-area thermal units. But the proper reason for selecting the GRC structure for thermal units has not been demonstrated so far to the best. This motivates the authors in this work to analyze the performances of these two GRC structures in the LFC of the multi-area thermal units by considering the coordination of GRC and GDB. A similar kind of investigation is performed in Morsali et al. (2014), but the analysis is strictly restricted to the dual-area systems and that too under the governing of particle swarm optimization (PSO)-based traditional PID controller.

Furthermore, the literature survey discloses the wide implementation of traditional PI/PID and fractional order (FO) controllers for LFC study with different soft computing algorithms such as the seagull optimization algorithm (SOA) (Harideep et al., 2021), artificial field algorithm (AEFA) (Kalyan and Rao, 2020b), flower pollination algorithm (FPA) (Madasu et al., 2018), moth flame algorithm (MFA) (Lal and Barisal, 2019), ant–lion optimizer (ALO) (Pradhan et al., 2020), differential evolution (DE) (Kalyan and Suresh, 2021b), chemical reaction optimizer (CRO), mine blast optimizer (MBO), gravitational search algorithm (GSA) (Sahu et al., 2015), Harris Hawks optimizer (HHO) (Yousri et al., 2020), grasshopper optimizer (GHO) (Nosratabadi et al., 2019), volley ball algorithm (VBA)

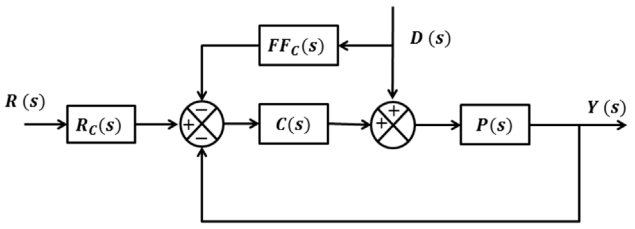

FIGURE 4 | 3DOF-PID controller closed loop expression (Elsisi, 2020).

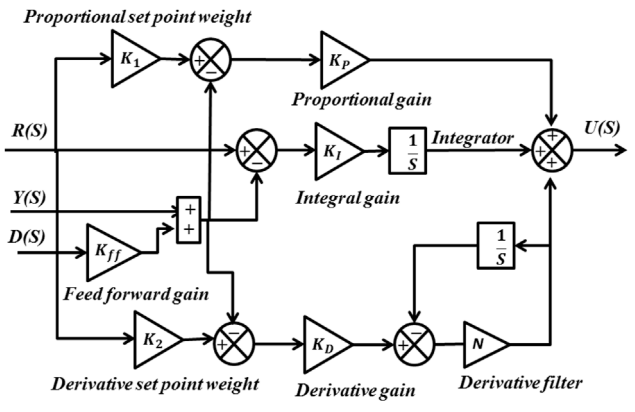

FIGURE 5 | Structure of the 3DOF-PID controller (Elsisi, 2020).

(Prakash et al., 2019), sine-cosine algorithm (SCA) (Tasnin and Saikia, 2018), water cycle algorithm (WCA) (Goud et al., 2021), teaching–learning-based (TLBO) optimizer (Sahu et al., 2016b), multi-verse optimizer (MVO) (Kumar and Hote, 2018), symbiotic asymptotic search (SAS) (Nayak et al., 2018) algorithm, slap swarm optimizer (SSO) (Sariki and Shankar, 2021), gray wolf optimizer (GWO) (Kalyan, 2021a), and hybrid (H) algorithms like DE-AEFA (Kalyan and Rao, 2020c), HAEFA (Sai Kalyan et al., 2020), whale optimization (WOA) algorithm (Elsisi, 2020), lightening search algorithm (LSA) (Elsisi and Abdelfattah, 2020), and arithmetic optimization algorithm (AOA) (Elsisi et al., 2021). are extensively reported. Furthermore, the aforementioned soft computing-based regulators are not only applied to thermal-based energy systems but also extended to the energy systems with renewable generation sources the researchers.

However, the FO and conventional controllers are not robust enough for the power system models perceived with practical constraints of GRC and GDB. In contrast to the abovementioned intelligent fuzzy systems, the controllers are widely applied to the LFC of power systems with GRC and GDB. However, membership function selections and framing of the rule-based system involve more approximations which may degrade the power system performance. Thus, researchers are more likely to tend toward higher-order DOF controllers in the LFC studies with the benefit of individual control loops. But the implementation of 3DOFPID for the LFC study is not seen much, and WCA tuned 3DOFPID is a maiden attempt.

Considering the limitations in the aforementioned literature, the contributions in this work are as follows:

(a) The three-area reheat thermal system is designed and developed in the MATLAB/SIMULINK (R2016a) platform.
(b) LFC analysis is performed by injecting 10% SLP disturbance in area-1.
(c) The performances of GRC open-loop and closed-loop models in LFC are investigated and demonstrated.
(d) The WCA-based 3DOFPID controller is implemented as a regulator in all the three areas.
(e) Efficacy of 3DOFPID tuned with WCA is showcased with other recently presented regulators such as HAEFA/TLBO-tuned PID and WCA tuned 2DOFPID by implementing on the DAHT system.
(f) Sensitivity analysis is conducted to showcase the robustness of the presented control scheme.

POWER SYSTEM MODELING

The power system model that has been initially deliberated in this work is the DAHT system with the unique generation capacities. DAHT depicted in **Figure 1** has been widely implemented by the researchers in recent years to analyze the behavior of the system with the proposed control schemes. The necessary data to design the DAHT system in MATLAB/SIMULINK are perceived from Goud et al. (2021). On the other side, the second power system model is a three-area RTPS having generation capacities in the ratio of 1:2:4 for area-1: area-2: area-3, respectively, conceived for investigation purposes. The model of the three-area system is displayed in **Figure 2**, the conceived GRC structures are depicted in **Figure 3** (Morsali et al., 2014), and the various subsystems in the reheat thermal unit are modeled as follows:

The governor dead band is expressed as follows:

$$\frac{N_1 + N_2 S}{1 + ST_{sg}}. \tag{1}$$

The reheat turbine can be expressed as follows:

$$\frac{K_r T_r S + 1}{1 + ST_r}. \tag{2}$$

The power plant can be expressed as follows:

$$\frac{K_{ps}}{T_{ps} S + 1}. \tag{3}$$

The GRC value for both the closed- and open-loop structures is considered as 10%/min and is modeled as

$$|\Delta P_T| = 0.1\,(pu/\min) = 0.0017\,(pu/\sec). \tag{4}$$

Thus, for the thermal units, the value of GRC for the closed-loop and open-loop structures can be taken into account by limiters as ±0.0017 in the reheat turbine. In general, the definition of GDB is related to a change in the speed magnitude within which there may not be any alteration in the turbine valve

TABLE 1 | WCA parameters.

Parameter	Value
N_{Var}	21
N_{POP}	100
Maximum iteration	50
d_{max}	0.001
U	0.04
C	2

position. After reviewing the literature, in this article, Fourier coefficients of N1 and N2 are modeled in GDB.

The incremental change in power flow between the *i*th and *j*th areas is modeled as

$$\Delta P_{ij}(s) = \frac{2\pi T_{ij}}{s}\left(\Delta f_i(s) - \Delta f_j(s)\right). \quad (5)$$

During the operation of the thermal plant with incremental change in the load demand, deviation in the *i*th area frequency is modeled as

$$\Delta f_i(s) = \frac{K_{ps}}{1 + sT_{ps}}\left[\Delta P_T(s) - \Delta P_d(s) - \Delta P_{ij}(s)\right]. \quad (6)$$

These deviations in area frequency will be fully damped out using a secondary regulator by changing the alternator set point valve operation by taking the area control error (ACE) as the input. The ACE signal to the regulator in the *i*th area will be modeled as

$$ACE_i = B_i \Delta f_i + \Delta P_{ij}. \quad (7)$$

3DOF-PID CONTROLLER

DOF controllers are technically elucidated as the number of closed loops that can be independently adjusted. Thus, the 3DOF-PID controller consists of three closed-loop independent transfer functions that are responsible for closed-loop stability, closed-loop response shaping, and rejection of disturbance. The three inputs to the individual control loops are R(s), which indicates the reference input signal, Y(s), which indicates the feedback taken from the output of the test system, and D(s), which represents a disturbance in the load. For the 3DOF-PID controller, the closed-loop expression is indicated in **Eq. 8** and is shown in **Figure 4** (Rahman et al., 2016).

$$Y(s) = \left[\frac{C(s)P(s)}{1 + C(s)P(s)}R_c(s)\right]R(s) + \left[\frac{P(s) - C(s)P(s)FF_c(s)}{1 + C(s)P(s)}\right]D(s). \quad (8)$$

The structure of 3DOF-PID employed as the frequency regulator in this work is depicted in **Figure 5** (Rahman et al., 2016). Out of this, the closed-loop stability is attained with component C(s), and the quality of the output response in both the static and dynamic nature is maintained by the components C(s) and $R_C(s)$. The disturbance D(s) in the interconnected system is eliminated by the component feed-forward controller FFC(s) if **Eq. 9** is satisfied.

$$P(s) - C(s)P(s)FF_C(s) = 0. \quad (9)$$

The proportional-integral-derivative parameter is indicated with K_P, K_I, and K_D, and N represents the filter coefficient. K_1 and

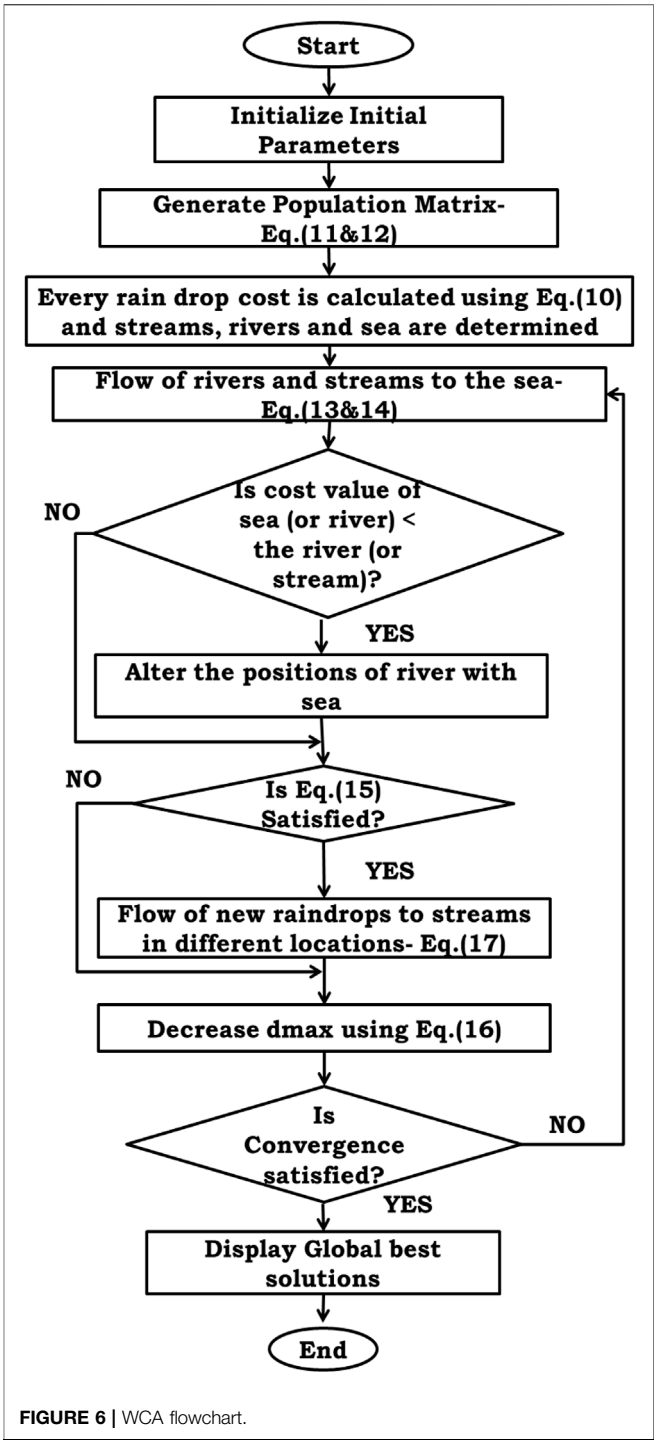

FIGURE 6 | WCA flowchart.

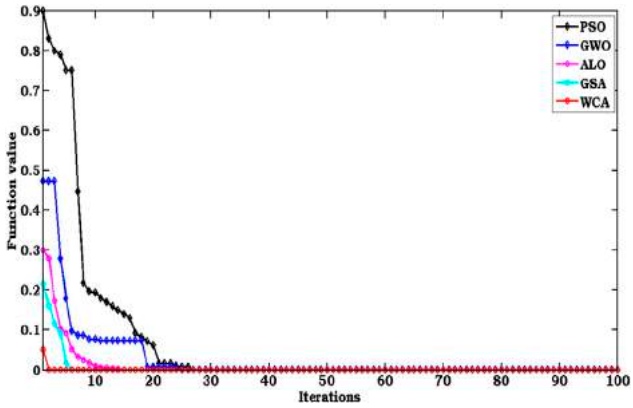

FIGURE 7 | Convergence of different optimizations tested on Booth function.

K_2 are the proportional and derivative weight signals for the component $R_C(s)$.

However, the gains of 3DOF-PID are to be rendered optimally with a heuristic optimization algorithm subjected to the minimization of the time-domain index. Owing to the benefits of maintaining the equilibrium between dampening the peak undershoot/overshoot deviations and bringing the responses to stable conditions in quick time, the ISE objective function (Naga Sai Kalyan and Sambasiva Rao, 2020) is employed in this article, as mentioned in **Eq. 10**.

$$J_{ISE} = \int_0^{T_{sim}} (\Delta f_1^2 + \Delta f_2^2 + \Delta f_3^2 + \Delta P_{tie12}^2 + \Delta P_{tie13}^2 + \Delta P_{tie23}^2)dt. \quad (10)$$

WCA ALGORITHM

In the LFC study, the selection of an optimization search algorithm is equally important to the design of a secondary controller. In this work, 3DOF-PID is taken as a secondary controller in every area. However, the optimal operation of the controller strongly depends on the optimization algorithm that has been considered. For this, a new and efficient searching methodology was proposed by Eskandar et al. (2012), named as the water cycle algorithm (WCA), which mimics the continuous water movement. Until now, the WCA mechanism is chosen by researchers all over the world as a solution to complex nonconstrained and constrained optimization problems. But implementation of the WCA approach for the optimization of modern interconnected power systems is not seen much. This motivates the authors to adopt the WCA algorithm in this article.

Moreover, WCA can locate an optimal solution for both maximization and minimization of an objective function with a high convergence rate and accuracy. In this article, WCA is utilized to optimize 3DOF-PID controller gains subjected to ISE minimization provided in **Eq. 10** so that the oscillations in system responses will be damped out completely in a short time. The strategy of WCA starts with a minute particle in the water cycle which is a raindrop or snowdrop. The raindrops or snow droplets on the mountains flow down to form streams or rivers. The rivers

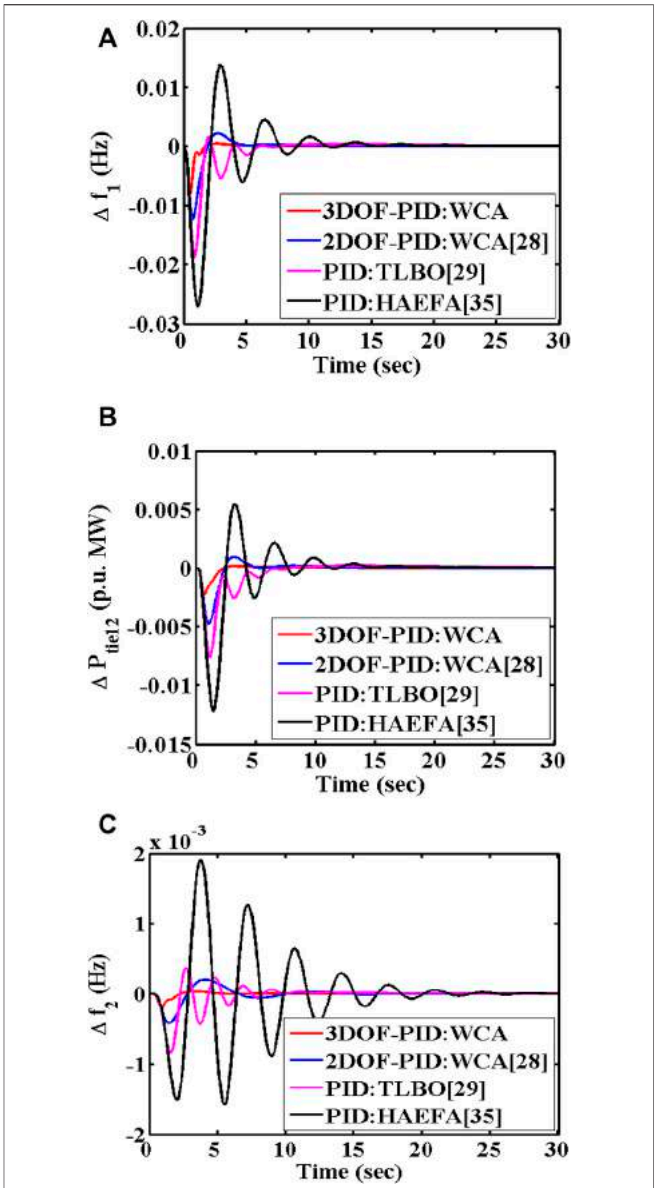

FIGURE 8 | Case 1 responses. **(A)** Δf_1, **(B)** ΔP_{tie12}, and **(C)** Δf_2.

TABLE 2 | Response settling time (in s) with various controllers for the DAHT system.

Settling time	Δf_1	Δf_2	ΔP_{tie12}
PID: HAEFA	18.93	20.66	20.95
PID: TLBO	14.26	14.95	14.89
2DOF-PID: WCA	10.41	11.96	11.09
3DOF-PID: WCA	**5.19**	**5.12**	**5.17**

TABLE 3 | Controller optimal gains employed for the DAHT system.

Parameter	PID: HAEFA	PID: TLBO	2DOF-PID: WCA	3DOF-PID: WCA
Area 1				K_{ff} = 0.1183
			K_1 = 0.7956	K_1 = 0.2293
	K_P = 0.1862	K_P = 0.2040	K_2 = 0.5337	K_2 = 0.3452
			N = 139.365	N = 144.870
	K_I = 0.0364	K_I = 0.1265	K_P = 0.6166	K_P = 0.7203
			K_I = 0.3006	K_I = 0.2027
	K_D = 0.1238	K_D = 0.2734	K_D = 0.5578	K_D = 0.7509
Area 2				K_{ff} = 0.1781
			K_1 = 0.7287	K_1 = 0.1754
	K_P = 0.1477	K_P = 0.3126	K_2 = 0.5673	K_2 = 0.1238
			N = 140.096	N = 143.786
	K_I = 0.0723	K_I = 0.3056	K_P = 0.6716	K_P = 0.5485
			K_I = 0.5428	K_I = 0.3578
	K_D = 0.2130	K_D = 0.2614	K_D = 0.4822	K_D = 0.6045

or streams continue their flow until they adjoin the sea at last. In search space, initially, the populations are the raindrops created randomly to solve the problem, and the sea is selected as the best, which is treated as the global best solution.

Evaporation and raining loop are added to impart the equilibrium of exploration and exploitation phenomena to the WCA mechanism. During evaporation, water evaporates and accumulates at the top of the atmosphere and forms a cloud, when it condenses and again returns to earth in the form of rain (Kalyan, 2021b; Kalyan, 2021c).

Initialization

The raindrops (RD) initialized for Nvar variables in this work are as follows:

$$RD_i = Y_i = [y_1, y_2 \ldots\ldots\ldots y_{Nvar}], \tag{11}$$

$$RD \quad Population = \begin{bmatrix} RD_1 \\ - \quad - \quad - \\ RD_i \\ - \quad - \quad - \\ RD_{N_{POP}} \end{bmatrix}. \tag{12}$$

The matrix "RD Population" indicates a randomly generated population, and NPOP represents the number of populations. Thereafter, the cost of every raindrop will be evaluated using **Eq. 10**.

Stream Flows Into the River (or) River Flow Into the Sea

Initially, the positions of rivers and streams are initialized subjected to the assumption that these will flow into the sea finally.

$$P_{stream}^{new} = P_{stream} + rand() * C * (P_{river} - P_{stream}), \tag{13}$$

$$P_{river}^{new} = P_{river} + rand() * C * (P_{sea} - P_{river}), \tag{14}$$

where "C" is a constant taken from Morsali et al., (2014) and Kalyan and Rao, (2020a) and rand () generated between [0–1]. Suppose, if the stream generates a solution much more compromising than its connecting river, then in this situation, the locations of the river and stream get interchanged. The aforementioned methodology will be implemented in the rivers and seas.

Evaporation and Raining

To overcome the solution getting into the trap of local minima and to impart the nature of exploration and exploitation into the searching strategy, the evaporation and raining loop was incorporated.

The process of evaporation terminates if it satisfies the following condition.

$$|P_{sea} - P_{river}| < d_{max}. \tag{15}$$

The d_{max} value will be decreased automatically using **Eq. 16**, and usually, it is nearer to zero.

$$d_{max}^{new} = d_{max} - (d_{max}/\text{max.iteration}). \tag{16}$$

The raining process will begin immediately at the end of evaporation. During rain, the new raindrops will create different new streams, which will be located as

$$P_{stream}^{new} = P_{sea} + \sqrt{U}\, X\, rand(1, N_{var}). \tag{17}$$

The parameter 'U' indicates the rate of exploration nearer to the sea. The WCA exhibits the global solution right after the completion of the maximum iteration or reaching the stopping criteria. The parameters utilized in algorithm WCA are displayed in **Table 1**, and the flowchart is depicted in **Figure 6** (Goud et al., 2021). Moreover, the WCA is applied to the Booth function given in **Eq. 18** before being discharged to the study of LFC. Along with the WCA approach, different optimizations like PSO/GWO/ALO/GSA are also implemented to optimize the Booth function one at a time for a maximum of 100 iterations with 50 populations. The characteristics of various algorithms in the criteria of convergence in an appliance to Booth function are compared in **Figure 7**. It is noticed from **Figure 7** that compared to other optimizations, the WCA converges quickly in less iteration. Furthermore, the functional value with the mechanism WCA initializes with a very low value compared to the other soft computing approaches of ALO/GWO/PSO. This

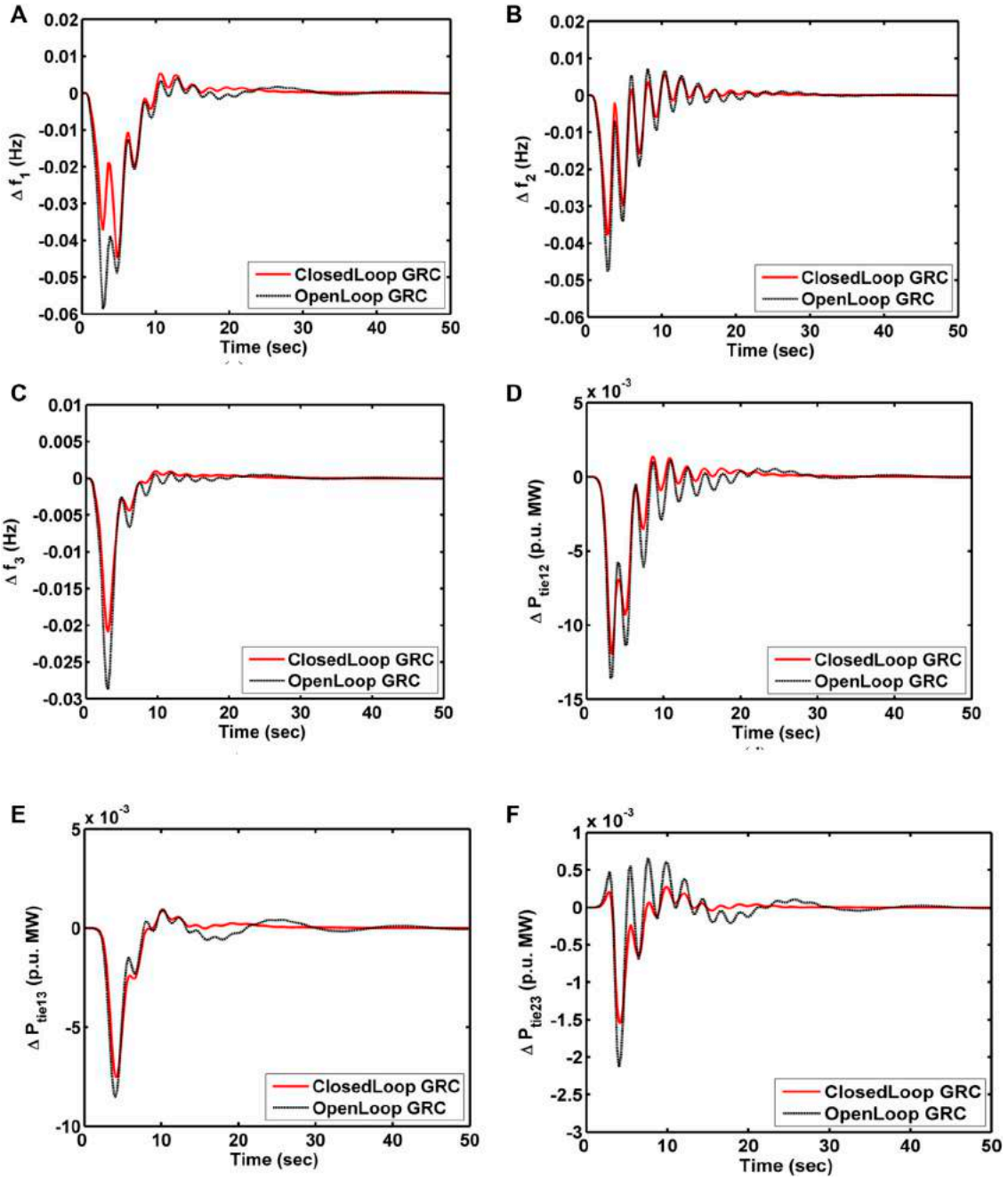

FIGURE 9 | Case 2 responses. **(A)** Δf_1, **(B)** Δf_2, **(C)** Δf_3, **(D)** ΔP_{tie12}, **(E)** ΔP_{tie13}, and **(F)** ΔP_{tie23}.

shows the inherent feature of WCA in balancing the phases of exploration and exploitation. Moreover, the benefit of the optimization process that the algorithm initiates with a low function value is that there will be less chance to get the solution diversified. Hence, considering all the aspects of the WCA mechanism urges to accomplish in the study of LFC.

$$f(x,y) = (x + 2y - 7)^2 + (2x + y - 5)^2. \quad (18)$$

RESULTS AND DISCUSSION

Case-1: Analysis of the DAHT System With Different Control Strategies

The operational efficacy of the 3DOF-PID fine-tuned WCA approach is visualized upon implementing this regulator on an extensively utilized test system DAHT model with 10% SLP on area 1. Different control mechanisms like PID tuned with

TABLE 4 | Response settling time (in s) with the WCA-tuned 3DOF-PID controller for the three-area RTPS model.

Parameter	GRC open-loop structure	GRC closed-loop structure
Δf_1	41.61	25.74
Δf_2	32.89	26.99
Δf_3	29.45	22.74
ΔP_{tie12}	42.16	27.42
ΔP_{tie13}	47.39	26.89
ΔP_{tie23}	44.08	23.63
ISE*10^{-3}	136.72	63.87

TABLE 5 | Optimal gains of the 3DOF-PID controller found using the WCA algorithm for the three-area thermal system.

Parameter	Area 1	Area 2	Area 3
GRC open-loop	K_1 = 0.4161	K_1 = 0.4057	K_1 = 0.3104
	K_2 = 0.2862	K_2 = 0.2767	K_2 = 0.3132
	K_{ff} = 0.3267	K_{ff} = 0.1937	K_{ff} = 0.2014
	N = 149.23	N = 146.17	N = 144.82
	K_P = 0.7813	K_P = 0.8844	K_P = 0.8952
	K_I = 0.1724	K_I = 0.2225	K_I = 0.1626
	K_D = 0.2887	K_D = 0.2623	K_D = 0.2872
GRC closed-loop	K_1 = 0.3634	K_1 = 0.2927	K_1 = 0.2617
	K_2 = 0.2523	K_2 = 0.2767	K_2 = 0.2841
	K_{ff} = 0.0981	K_{ff} = 0.2131	K_{ff} = 0.0836
	N = 131.64	N = 136.71	N = 135.90
	K_P = 0.8927	K_P = 0.8962	K_P = 0.9164
	K_I = 0.1171	K_I = 0.2659	K_I = 0.0851
	K_D = 0.1698	K_D = 0.3576	K_D = 0.1748

HAEFA (Sai Kalyan et al., 2020), TLBO (Sahu et al., 2016b), 2DOF-PID fine-tuned with WCA (Goud et al., 2021), and 3DOF-PID tuned with WCA are chosen as regulators in every area of the DAHT system one by one. The system responses with different soft computing-based secondary regulators under the same load disturbances are compared in **Figure 8**, to reveal the best one. Dynamic behaviors of DAHT are transliterated in settling time and noted in **Table 2**, and the respective optimum gains are provided in **Table 3**. From **Figure 8** and **Table 2**, it is concluded that the presented 3DOF-PID tuned with the WCA algorithm outperforms the recently proposed control strategies of HAEFA and TLBO-based PID and WCA-tuned 2DOF-PID. Compared to other control approaches, the proposed regulator is effective in dampening the oscillations by altering the generator's set-point valve according to the load fluctuations and is more sovereign in bringing the deviations to a steady position in a short time.

Case-2: Analysis of Three-Area RTPS With Open- and Closed-Loop GRC Structures

In this subsection, the considered three-area RTPS model of the test system is analyzed in a time-domain simulation platform upon laying a disturbance of 10% SLP on area-1. The test system model is investigated with the open- and closed-loop structures of GRC individually, under the governance of the 3DOFPID regulator, which is rendered optimally with the WCA mechanism. Dynamical responses of three-area RTPS with GRC structures of the open- and closed-loop are compared in **Figure 9**, to reveal the best. System responses that are retrieved under perturbed conditions are area frequency and power deviations in the transmission line. Numerically, these responses are analyzed in settling time and provided in **Table 4**. The gains of the 3DOF-PID regulator that are founded optimally using the WCA approach employed with the system having different GRC structures are placed in **Table 5**. Noticing the responses compared in **Figure 9**, we came to infer that the system responses are greatly diversified with the employing of the open-loop GRC model and hardly reaches stable condition. On the other hand, responses of the thermal systems with a closed-loop GRC model are less deviated in connection with peak undershoot/overshoot, and also, within less time, the responses attained a steady-state position. Moreover, the ISE index value is also improvised with a closed-loop GRC structure by 53.28% with an open-loop GRC structure. Furthermore, the time taken to find the optimal parameters of the 3DOFPID regulator using the WCA approach is more with an open loop compared to that of employing a closed loop. Thus, it is concluded that for the LFC studies the thermal units with the open-loop GRC structure are struggling a lot to regain stability during load disturbances even under the regulation of secondary controllers. Hence, this work strongly suggests employing the GRC structure of closed loop, especially for the thermal generating units in LFC studies.

Case-3: Sensitivity Test Against Wide Load Variations and Uncertainties in System Parameters

Closed-loop GRC structure performance efficacy for the thermal units in fully dampening the oscillations to zero in a short time is revealed in the aforementioned case. Therefore, a sensitivity analysis is needed to be conducted to demonstrate the robustness of the closed-loop GRC structure in coordination with the proposed WCA-based 3DOF-PID regulator. The system loading has been varied to the wide range of ±50% from nominal load, and the parameters of the thermal system like the time constant of the steam turbine (T_t) and tie-line are varied by ±50% from the normal parameter. The sensitivity analysis subjected to wide variations of loading is presented in **Figure 10**, and it has also numerically analyzed about settling time provided in **Table 4**. Perceiving from **Figure 10**, the responses are not disturbed much, even though the system is targeted with a wide variation of load from the nominal load. Moreover, almost all the responses attained stable conditions at the same time, regardless of load variations. The settling time of the system responses against uncertainty in parameters is noted in **Table 4**. From the sensitivity analysis, it is concluded that three-area RTPS possessing the closed-loop GRC structure in coordination with the WCA-based 3DOFPID regulator does not encounter any difficulty in regaining the steady-state condition despite parametric uncertainties. Thus, the obtained optimal parameters of the 3DOF-PID controller using WCA optimization are robust and not necessary to alter the 3DOF-PID parameters, even under situations of uncertainty.

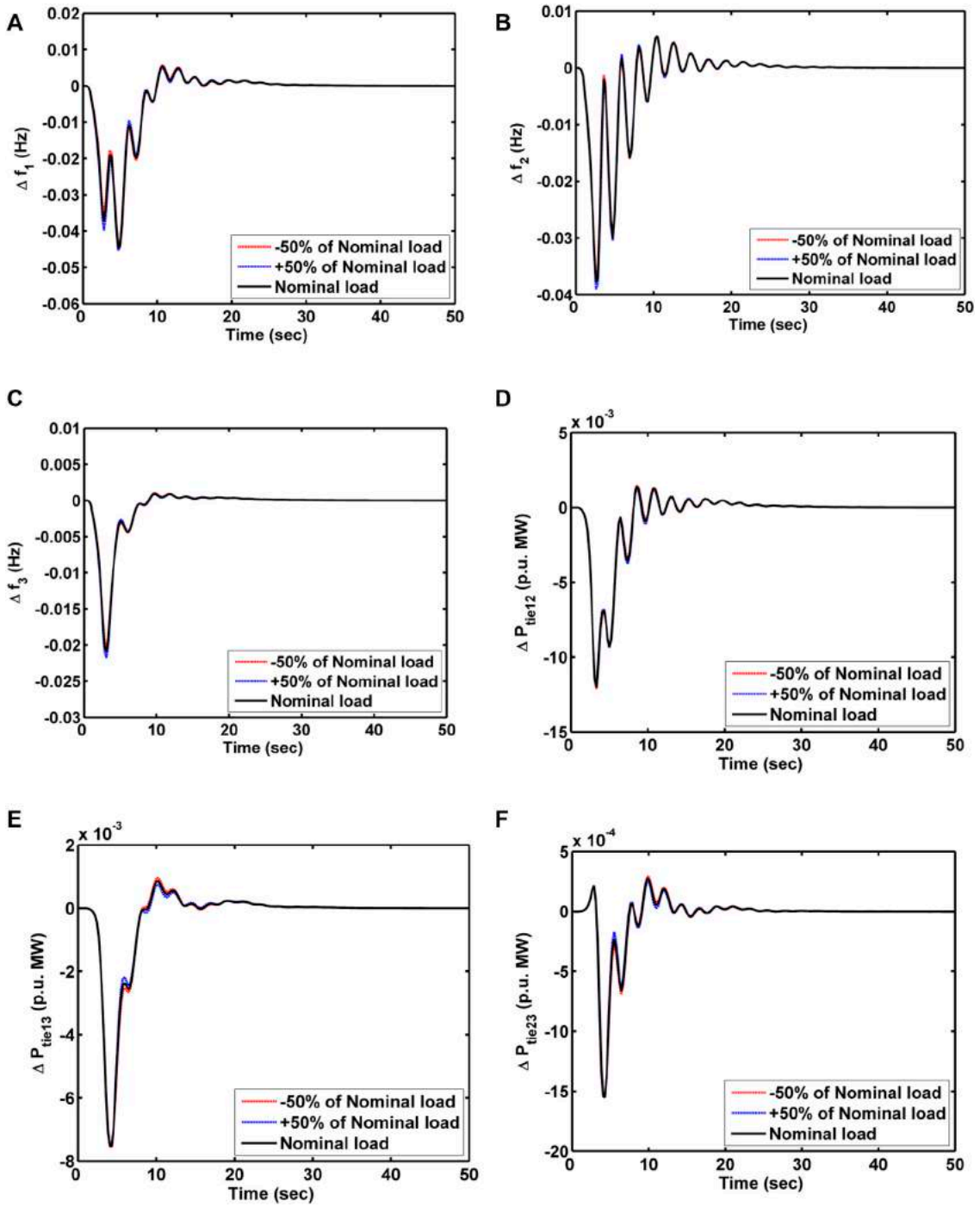

FIGURE 10 | Case 3 responses. **(A)** Δf_1, **(B)** Δf_2, **(C)** Δf_3, **(D)** ΔP_{tie12}, **(E)** ΔP_{tie13}, and **(F)** ΔP_{tie23}.

CONCLUSION

The performance of three-area RTPS considering the realistic constraints of GDB and GRC is examined with the open-loop GRC structure and the closed-loop GRC structure independently. The analysis is performed under the governance of the WCA-based 3DOFPID controller for a 10%SLP disturbance on area 1. Moreover, the efficacy of the proposed regulatory mechanism is deliberated with different soft computing-based control structures that are available in the recently reported literature on the widely utilized model of DAHT. Dynamical responses of the three-area thermal system in the time-domain reveal the efficacy of the GRC closed-loop structure in dampening the frequency deviations and transmission line power flow.

Furthermore, the investigation is stretched to the implementation of a sensitivity test to examine the rigidness of the proposed control scheme. The sensitivity test is administered for considering system loading and parameters with uncertainties. The simulation results reveal the efficacy and robustness of the WCA-based 3DOFPID regulator in performing satisfactorily even under the conditions of parametric and loading uncertainties with a closed-loop GRC structure. Fabrication of intelligent fuzzy aided regulator for the optimal LFC of the multi-area RTPS may be undertaken in future. Moreover, a similar study would be extended to the multi-area RTPS with the integration of renewable energy sources. Thus, this article recommended adopting the GRC structure of closed loop for the RTPS models in LFC studies.

DATA AVAILABILITY STATEMENT

The original contributions presented in the study are included in the article/Supplementary Material. Further inquiries can be directed to the corresponding author.

AUTHOR CONTRIBUTIONS

CK, BG, and CR contributed to the conception and design of the study. MK organized the database. MB performed the statistical analysis. ME-N and SK wrote the first draft of the manuscript. All authors contributed to manuscript revision, read, and approved the submitted version.

REFERENCES

Ahmed, M., Magdy, G., Khamies, M., and Kamel, S. (2022). Modified TID Controller for Load Frequency Control of a Two-Area Interconnected Diverse-Unit Power System. *Int. J. Electr. Power & Energy Syst.* 135, 107528. doi:10.1016/j.ijepes.2021.107528

Çelik, E. (2020). Improved Stochastic Fractal Search Algorithm and Modified Cost Function for Automatic Generation Control of Interconnected Electric Power Systems. *Eng. Appl. Artif. Intell.* 88, 103407. doi:10.1016/j.engappai.2019.103407

Elsisi, M., and Abdelfattah, H. (2020). New Design of Variable Structure Control Based on Lightening Search Algorithm for Nuclear Reactor Power System Considering Load-Following Operation. *Nucl. Eng. Technol.* 52 (3), 544–551. doi:10.1016/j.net.2019.08.003

Elsisi, M., Tran, M.-Q., Hasanien, H. M., Turky, R. A., Albalawi, F., and Ghoneim, S. S. M. (2021). Robust Model Predictive Control Paradigm for Automatic Voltage Regulators against Uncertainty Based on Optimization Algorithms. *Mathematics* 9 (22), 2885. doi:10.3390/math9222885

Elsisi, M. (2020). New Design of Robust PID Controller Based on Meta-Heuristic Algorithms for Wind Energy Conversion System. *Wind Energy* 23 (2), 391–403. doi:10.1002/we.2439

Eskandar, H., Sadollah, A., Bahreininejad, A., and Hamdi, M. (2012). Water Cycle Algorithm - A Novel Metaheuristic Optimization Method for Solving Constrained Engineering Optimization Problems. *Comput. Struct.* 110-111, 151–166. doi:10.1016/j.compstruc.2012.07.010

Goud, B. S., Kalyan, C. N. S., Keerthi, N., Reddy, C. R., Bajaj, M., and Reddy, B. N. (2021). "AGC of Multi Area Multi Fuel System with Water Cycle Algorithm Based 3DOF-PID Controller and Integration of PEVs," in 2021 International Conference on Data Analytics for Business and Industry (ICDABI). 464–469. doi:10.1109/ICDABI53623.2021.9655899

Harideep, P., Pavan Sai Reddy, V., Ganesh, G., Bhanu Prakash, O., Naga Sai Kalyan, C., and Suresh, C. V. (2021). Seagull Optimization Tuned Traditional PID Controller with Set Point Filter for LFC of Hydro Thermal System Based on Performance Indices, 2021 4th International Conference on Recent Developments in Control, Automation & Power Engineering (RDCAPE), October2021, 85–89. Noida, India. doi:10.1109/RDCAPE52977.2021.9633523

Kalyan, C. N. S., and Rao, G. S. (2020). Impact of Communication Time Delays on Combined LFC and AVR of a Multi-Area Hybrid System with IPFC-RFBs Coordinated Control Strategy. *Prot. Control Mod. Power Syst.* 6. 1. doi:10.1186/s41601-021-00185-z

Kalyan, C. N. S., and Rao, G. S. (2020). Performance Comparison of Various Energy Storage Devices in Combined LFC and AVR of Multi Area System with Renewable Energy Integration. *Int. J. Renew. Energy Res.* 10, 933–944.

Kalyan, C. N. S., and Rao, G. S. (2020). Combined Frequency and Voltage Stabilization of Multi-Area Multisource System by DE-AEFA Optimized PID Controller with Coordinated Performance of IPFC and RFBs. *Int. J. Ambient Energy*. 1. 1. doi:10.1080/01430750.2020.1860130

Kalyan, C. N. S., and Rao, G. S. (2021). Coordinated Control Strategy for Simultaneous Frequency and Voltage Stabilization of the Multi-Area Interconnected System Considering Communication Time Delays. *Int. J. Ambient Energy*. 1. 1. doi:10.1080/01430750.2021.1967192

Kalyan, C. N. S., and Suresh, C. V. (2021a). PIDD Controller for AGC of Nonlinear System with PEV Integration and AC-DC Links, January 2021 Proceedings of the International Conference on Sustainable Energy and Future Electric Transportation (SEFET), Hyderabad, India, 1–6. doi:10.1109/SeFet48154.2021.9375756

Kalyan, C. N. S., and Suresh, C. V. (2021b). Differential Evolution Based Intelligent Control Approach for LFC of Multiarea Power System with Communication Time Delays, February2021 Proceedings of the International Conference on Computing, Communication, and Intelligent Systems (ICCCIS), , 868–873. Greater Noida, India. doi:10.1109/ICCCIS51004.2021.9397112

Kalyan, C. N. S. (2021a). UPFC and SMES Based Coordinated Control Strategy for Simultaneous Frequency and Voltage Stability of an Interconnected Power System, Proceedings of the 2021 1st International Conference on Power electronics and Energy (ICPEE), January 2021, 1–6. Bhubaneswar, India. doi:10.1109/ICPEE50452.2021.9358576

Kalyan, C. N. S. (2021b). Determination of Appropriate GRC Modelling for Optimal LFC of Multi Area Thermal System, Proceedings of the 2021 IEEE International Power and Renewable energy Conference (IPRECON), September 2021, 1–6. Kollam, India. doi:10.1109/IPRECON52453.2021.9640892

Kalyan, C. N. S. (2021c). Water Cycle Algorithm Based Intelligent Controller for Frequency Regulation of Dual Area Hybrid System with Time Delays. Proceedings of the 2021 IEEE International Power and Renewable energy Conference (IPRECON), September 2021, 1–5. Kollam, India. doi:10.1109/IPRECON52453.2021.9640646

Kumar, M., and Hote, Y. V. (2018). Robust CDA-PIDA Control Scheme for Load Frequency Control of Interconnected Power Systems. *IFAC-PapersOnLine* 51, 616–621. doi:10.1016/j.ifacol.2018.06.164

Lal, D. K., and Barisal, A. K. (2019). Combined Load Frequency and Terminal Voltage Control of Power Systems Using Moth Flame Optimization Algorithm. *J. Electr. Syst. Inf Technol* 6, 8. doi:10.1186/s43067-019-0010-3

Lal, D. K., Barisal, A. K., and Tripathy, M. (2016). Grey Wolf Optimizer Algorithm Based Fuzzy PID Controller for AGC of Multi-Area Power System with TCPS. *Procedia Comput. Sci.* 92, 99–105. doi:10.1016/j.procs.2016.07.329

Madasu, S. D., Sai Kumar, M. L. S., and Singh, A. K. (2018). A Flower Pollination Algorithm Based Automatic Generation Control of Interconnected Power System. *Ain Shams Eng. J.* 9, 1215–1224. doi:10.1016/j.asej.2016.06.003

Morsali, J., Zare, K., and Tarafdar Hagh, M., (2014). Appropriate Generation Rate Constraint (GRC) Modeling Method for Reheat Thermal Units to Obtain Optimal Load Frequency Controller (LFC), 2014 5th Conference on Thermal Power Plants (CTPP), 10–11. Iran, Tehran. June 2014, . doi:10.1109/CTPP.2014.7040611

Morsali, J., Zare, K., and Tarafdar Hagh, M. (2017). Applying Fractional Order PID to Design TCSC-Based Damping Controller in Coordination with Automatic

Generation Control of Interconnected Multi-Source Power System. *Eng. Sci. Technol. Int. J.* 20, 1–17. doi:10.1016/j.jestch.2016.06.002

Naga Sai Kalyan, C., and Sambasiva Rao, G. (2020). Frequency and Voltage Stabilisation in Combined Load Frequency Control and Automatic Voltage Regulation of Multiarea System with Hybrid Generation Utilities by AC/DC Links. *Int. J. Sustain. Energy* 39, 1009–1029. doi:10.1080/14786451.2020.1797740

Nanda, J., Sreedhar, M., and Dasgupta, A. (2015). A New Technique in Hydro Thermal Interconnected Automatic Generation Control System by Using Minority Charge Carrier Inspired Algorithm. *Int. J. Electr. Power & Energy Syst.* 68, 259–268. doi:10.1016/j.ijepes.2014.12.025

Nayak, J. R., Shaw, B., and Sahu, B. K. (2018). Application of Adaptive-SOS (ASOS) Algorithm Based Interval Type-2 Fuzzy-PID Controller with Derivative Filter for Automatic Generation Control of an Interconnected Power System. *Eng. Sci. Technol. Int. J.* 21, 465–485. doi:10.1016/j.jestch.2018.03.010

Nosratabadi, S. M., Bornapour, M., and Gharaei, M. A. (2019). Grasshopper Optimization Algorithm for Optimal Load Frequency Control Considering Predictive Functional Modified PID Controller in Restructured Multi-Resource Multi-Area Power System with Redox Flow Battery Units. *Control Eng. Pract.* 89, 204–227. doi:10.1016/j.conengprac.2019.06.002

Padhy, S., and Panda, S. (2017). A Hybrid Stochastic Fractal Search and Pattern Search Technique Based Cascade PI-PD Controller for Automatic Generation Control of Multi-Source Power Systems in Presence of Plug in Electric Vehicles. *CAAI Trans. Intell. Technol.* 2, 12–25. doi:10.1016/j.trit.2017.01.002

Pan, I., and Das, S. (2015). Fractional-order Load-Frequency Control of Interconnected Power Systems Using Chaotic Multi-Objective Optimization. *Appl. Soft Comput.* 29, 328–344. doi:10.1016/j.asoc.2014.12.032

Pradhan, R., Majhi, S. K., Pradhan, J. K., and Pati, B. B. (2020). Optimal Fractional Order PID Controller Design Using Ant Lion Optimizer. *Ain Shams Eng. J.* 11, 281–291. doi:10.1016/j.asej.2019.10.005

Prakash, A., Murali, S., Shankar, R., and Bhushan, R. (2019). HVDC Tie-Link Modeling for Restructured AGC Using a Novel Fractional Order Cascade Controller. *Electr. Power Syst. Res.* 170, 244–258. doi:10.1016/j.epsr.2019.01.021

Rahman, A., Saikia, L. C., and Sinha, N. (2016). Automatic Generation Control of an Unequal Four-area Thermal System Using Biogeography-based Optimised 3DOF-PID Controller. *IET Gener. Transm. & Distrib.* 10, 4118–4129. doi:10.1049/iet-gtd.2016.0528

Rahman, A., Saikia, L. C., and Sinha, N. (2017). Automatic Generation Control of an Interconnected Two-Area Hybrid Thermal System Considering Dish-Stirling Solar Thermal and Wind Turbine System. *Renew. Energy* 105, 41–54. doi:10.1016/j.renene.2016.12.048

Rajesh, K. S., Dash, S. S., and Rajagopal, R. (2019). Hybrid Improved Firefly-Pattern Search Optimized Fuzzy Aided PID Controller for Automatic Generation Control of Power Systems with Multi-type Generations. *Swarm Evol. Comput.* 44, 200–211. doi:10.1016/j.swevo.2018.03.005

Raju, M., Saikia, L. C., and Sinha, N. (2016). Automatic Generation Control of a Multi-Area System Using Ant Lion Optimizer Algorithm Based PID Plus Second Order Derivative Controller. *Int. J. Electr. Power & Energy Syst.* 80, 52–63. doi:10.1016/j.ijepes.2016.01.037

Sahu, R. K., Panda, S., and Padhan, S. (2015). A Novel Hybrid Gravitational Search and Pattern Search Algorithm for Load Frequency Control of Nonlinear Power System. *Appl. Soft Comput.* 29, 310–327. doi:10.1016/j.asoc.2015.01.020

Sahu, R. K., Gorripotu, T. S., and Panda, S. (2016). Automatic Generation Control of Multi-Area Power Systems with Diverse Energy Sources Using Teaching Learning Based Optimization Algorithm. *Eng. Sci. Technol. Int. J.* 19, 113–134. doi:10.1016/j.jestch.2015.07.011

Sahu, R. K., Panda, S., Rout, U. K., and Sahoo, D. K. (2016). Teaching Learning Based Optimization Algorithm for Automatic Generation Control of Power System Using 2-DOF PID Controller. *Int. J. Electr. Power & Energy Syst.* 77, 287–301. doi:10.1016/j.ijepes.2015.11.082

Sai Kalyan, C. N., Rao, G. S., and Rao, G. S. (2020). Coordinated SMES and TCSC Damping Controller for Load Frequency Control of Multi Area Power System with Diverse Sources. *ijeei* 12, 747–769. doi:10.15676/ijeei.2020.12.4.4

Sariki, M., and Shankar, R. (2021). Optimal CC-2DOF(PI)-PDF Controller for LFC of Restructured Multi-Area Power System with IES-Based Modified HVDC Tie-Line and Electric Vehicles, Engineering Science and Technology. *Int. J.* 1. 1. doi:10.1016/j.jestch.2021.09.004

Shiva, C. K., and Mukherjee, V. (2016). Design and Analysis of Multi-Source Multi-Area Deregulated Power System for Automatic Generation Control Using Quasi-Oppositional Harmony Search Algorithm. *Int. J. Electr. Power & Energy Syst.* 80, 382–395. doi:10.1016/j.ijepes.2015.11.051

Tasnin, W., and Saikia, L. C. (2018). Comparative Performance of Different Energy Storage Devices in AGC of Multi-Source System Including Geothermal Power Plant. *J. Renew. Sustain. energy* 10, 024101. doi:10.1063/1.5016596

Yousri, D., Babu, T. S., and Fathy, A. (2020). Recent Methodology Based Harris Hawks Optimizer for Designing Load Frequency Control Incorporated in Multi-Interconnected Renewable Energy Plants. *Sustain. Energy, Grids Netw.* 22, 100352. doi:10.1016/j.segan.2020.100352

Conflict of Interest: The authors declare that the research was conducted in the absence of any commercial or financial relationships that could be construed as a potential conflict of interest.

Publisher's Note: All claims expressed in this article are solely those of the authors and do not necessarily represent those of their affiliated organizations, or those of the publisher, the editors, and the reviewers. Any product that may be evaluated in this article, or claim that may be made by its manufacturer, is not guaranteed or endorsed by the publisher.

NOMENCLATURE

f system frequency (60Hz)

Δf frequency deviation

i The subscript indicating the area number (i = 1, 2, 3)

ΔP_d change in the load demand (10%SLP)

ΔP_T change in thermal power generation

ΔP_{tie} change in the tie-line power flow

R_T speed regulation

B_1,B_2,B_3 area bias parameter (0.4312Pu.MW/Hz)

T_{ij} synchronizing coefficient of the tie-line between areas i and j (i ≠ j) (0.0433 pu.MW/rad)

T_{sg} steam time governor time constant (0.06s)

T_{sim} simulation time

K_r reheat steam turbine constant (0.3)

K_{ps1}, K_{ps2}, and K_{ps3} power plant model constant (80)

T_r reheat steam turbine time constant (10.2s)

T_{ps1},T_{ps2}, and T_{ps3} power plant model time constant (12s)

T_t The time constant of the steam turbine (0.3s)

N_1 and N_2 GDB Fourier coefficients (0.8, -0.6366)

±δ GRC ramp rate limits (±0.0005)

energies

Article

Implementation of a Novel Tabu Search Optimization Algorithm to Extract Parasitic Parameters of Solar Panel

Naveena Bhargavi Repalle [1,*], Pullacheri Sarala [2], Lucian Mihet-Popa [3,*], Shashidhar Reddy Kotha [1] and Nagalingam Rajeswaran [4]

[1] Electrical and Electronics Engineering, CVR College of Engineering, Hyderabad 501510, India; shashidhar.kotha5@gmail.com
[2] Electrical and Electronics Engineering, Malla Reddy Engineering College, Maisammaguda, Secunderabad 500100, India; sarala.2906@gmail.com
[3] Faculty of Information Technology, Engineering and Economics, Oestfold University College, 1757 Halden, Norway
[4] Electrical and Electronics Engineering, Malla Reddy Institute of Engineering and Technology, Maisammaguda, Secunderabad 500100, India; rajeswarann@gmail.com
* Correspondence: bhargavi.rn5@gmail.com (N.B.R.); lucian.mihet@hiof.no (L.M.-P.)

Abstract: The aging of PV cells reduces their electrical performance i.e., the parasitic parameters are introduced in the solar panel. The shunt resistance (R_{Sh}), series resistance (R_S), photo current (I_{Ph}), diode current (I_d), and diffusion constant (a_1) are known as parasitic or extraction parameters. Cracks and hotspots reduce the performance of PV cells and result in poor V–I characteristics. Certain tests are carried out over a long period of time to determine the quality of solar cells; for example, 1000 h of testing is comparable to 20 years of operation. The extraction of solar parameters is important for PV modules. The Tabu Search Optimization (TSO) algorithm is a robust meta-heuristic algorithm that was employed in this study for the extraction of parasitic parameters. Particle Swarm Optimization (PSO) and a Genetic lgorithm (GA), as well as other well-known optimization methods, were used to test the proposed method's correctness. The other approaches included the lightning search algorithm (LSA), gravitational search algorithm (GSA), and pattern search (PS). It can be concluded that the TSO approach extracts all six parameters in a reasonably short period of time. The work presented in this paper was developed and analyzed using a MATLAB-Simulink software environment.

Keywords: synthetic data (SD); pattern search (PS); absolute error; optimization technique; solar cell (SC); tabu list (TL)

Citation: Repalle, N.B.; Sarala, P.; Mihet-Popa, L.; Kotha, S.R.; Rajeswaran, N. Implementation of a Novel Tabu Search Optimization Algorithm to Extract Parasitic Parameters of Solar Panel. *Energies* **2022**, *15*, 4515. https://doi.org/10.3390/en15134515

Academic Editors: Bruno Canizes, João Soares, Sérgio Ramos and Zahra Foroozandeh

Received: 23 May 2022
Accepted: 19 June 2022
Published: 21 June 2022

1. Introduction

Photovoltaic (PV) systems are ecologically benign, cost-effective, and simple to incorporate into traditional electricity grids [1]. To diminish power lopsidedness, sunlight-based chargers are not straightforwardly connected to the load [2]. A panel-to-load power tracking strategy is recommended to avoid this problem [3]. Another major area of study is the extraction of parasitic features from the solar cell [4]. In this article, the use of the TSO approach to extract solar properties is reported.

PV systems with one diode were studied mathematically by Villalva et al. [5]. The suggested modelling is easily accessible, quick, meticulous, and emulation-friendly. Series and shunt protections, as well as how the continuous functional cluster thinks about as far as most extreme power [6], are considered in the plan. Three aspects are focused to modify the nonlinear condition contingent upon the I–V bend in an experimental manner [7].

On a solitary-diode model of a sunlight-based cell, X. Mama et al. [8] recommended an information-driven I–V strategy that was surveyed on three boundaries (short circuit current (ISC), RSh, and open-circuited voltage, VOC). For finding plan boundaries, such as ideally consistent RS, RP, photon initiation current, and dull current, Saleem et al. [9]

proposed a four-point extraction procedure [9]. Using GaAsP and SiGe tandem structures with a three-terminal assessment [10], the authors were able to derive sub-cell features. An analysis of the potential difference between the two reference cells was used to derive individual voltages in the proposed method.

Predicting the losses of sub-passive cells also alters I–V curves. Consequently, different, but similar, conditions at various input bands [11] govern the multi-performance junction's performance. Particle swarm optimization (PSO) was laid out by Wei et al. [12] to segregate the exhibition attributes of natural sun-oriented cells, combined with three-diode lumped boundaries. Muralidhar et al. [13] proposed a technique that assists with overcoming the deficiency to avoid the drifting of local optimum issues. Diab et al. [14] researched and proposed a quick and precise method for separating obscure sun-oriented properties involving tree growth algorithm for assorted sun-powered PV modules. This strategy guarantees that all recovered boundaries are processed under ideal circumstances, bringing about optimal outcomes. In the future extension for this, PV systems will be able to make use of this method in partially shaded conditions [15].

In Raba et al. [16], a definite Markov chain Monte Carlo approach was used to prove that 2-dimensional organic solar cells were devoid of uncontrolled events. Caracciolo et al. [17] developed a single-variable optimization technique for constant environmental conditions. It was found that the majority of the features, such as the R_{Sh}, IO, and panel range, were resolved when tested under extreme environmental conditions. Therefore, the proposed method is successful in all challenging circumstances.

Cervellini et al. [18] and Semero et al. [19] suggested a novel genetic algorithm (GA) that can be applied to a wide range of kelvins and irradiation (G) zones [20]. The simple and easy expression of the I–V curve and accompanying equations is achieved using the recommended GA approach [20]. This simplifies the assessment process. For single-, double-, and multi-diode plans, Liao et al. [21] developed difference vector in differential evolution with adaptive mutation. DVADE's goal is to quickly determine the extricated limits of a broad range of PV models. Each individual vector is used and reused in the mutation technique, which employs a differential evolution process and, therefore, may be reused many times. Toledo et al. proposed the two-step linear-least-square technique [22]. There is a vital benefit to the recommended approach, which is that it can gather information whether it is obtained from an I–V curve, i.e., it does not need any previous assessments and does not request information on past examinations or data about the boundaries [23,24]. It is feasible to eliminate the inherent potential (Vbi) from cells by utilizing a material-science-based model and an observational method considering I–V attributes [25,26].

The following is a summary of the remaining portion of the paper. Following the introduction, Section 2 presents a mathematical depiction of a solar panel. Section 3 illustrates the ageing effect of the solar panel. In Section 4, proposed methods are presented. Section 5 provides a comparison of the suggested method's findings and performance with those of existing meta-heuristics. Conclusions and recommendations are provided in Section 6.

2. Mathematical Modeling of PV Cell Based on Single Diode

The current produced by the sunlight is parallelized utilizing the current source from a single-diode-modeled solar cell (SC), with the diode acting as a half-wave rectifier. The model is easy to implement due to its simplest form. However, this model does not give the required information regarding the solar cell's parameters [27]. Figure 1 shows the equivalent circuit of a single-diode-modeled SC.

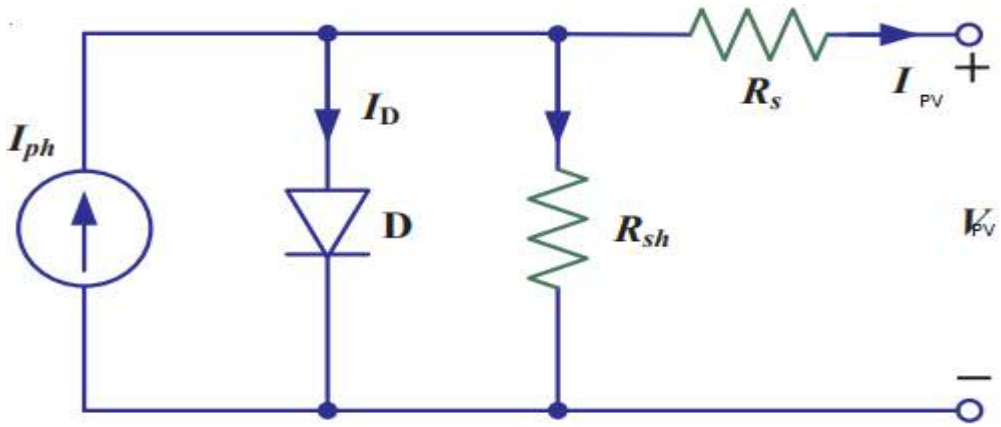

Figure 1. Circuit diagram of a single-diode-modeled solar cell.

The PV current obtained from the sunlight-based charger was determined as follows:

$$I_{PV} = I_{Ph} - I_d \tag{1}$$

where I_{PV} is the photovoltaic current, I_{ph} is the photo current, and I_d is the diode current. The I_d was obtained based on Shockley equation, which is represented as:

$$I_d = I_S\left[\exp\left(\frac{q(V_{PV} + I_{PV}R_S}{\eta K_b T_k}\right) - 1\right] \tag{2}$$

The output current of the PV cell is represented as follows:

$$I_{PV} = I_{Ph} - I_S\left[\exp\left(\frac{q(V_{PV} + I_{PV}R_S)}{\eta K_b T_k}\right) - 1\right] - \frac{V_{PV} + I_{PV}R_S}{R_P} \tag{3}$$

The following implicit form simplifies the PV cell's output characteristics:

$$F(I_{PV}, V_{PV}, T_K, G) = I_{Ph} - I_{PV} - I_S[\alpha_1] - \beta_1 \tag{4}$$

$$\left.\begin{array}{ll} where & \alpha_1 = \exp\left(\frac{q(V_{PV}+I_{PV}R_S)}{\eta K_b T_k}\right) - 1 \\ & \beta_1 = \frac{V_{PV}+I_{PV}R_S}{R_P} \end{array}\right\} \tag{5}$$

3. Aging Effect of Solar Panels

The aging of the PV module depends on the type of photovoltaic technology employed for the design of the solar cell and the environmental conditions in which it is installed. The PV panel performance is degraded due to the formation of cracks and bubbles on the panel surface. The performance of solar panels is reduced due to aging, which is mainly due to dust accumulation, humidity, UV radiation, wind speed, temperature, and certain other external factors, such as rain, snow, hail, and mechanical shocks.

Impact of Aging on Solar Cell

The aging of the PV cell reduces the electrical performance, i.e., the parasitic parameters are introduced in the solar panel. The shunt resistance (R_{Sh}), series resistance (R_S), photo current (I_{Ph}), diode current (I_d), and diffusion constant (a_1) are known as parasitic or extraction parameters. Cracks and hotspots reduce the performance of solar panel V–I characteristics. Certain tests are carried out over a span of time to determine the quality of solar cells; for example, 1000 h of testing is comparable to 20 years of operation [28].

The aging of the PV panel is described using aging laws, which are represented as follows:

$$\tau_1(T) = \tau_0(-\alpha_{opt} \cdot T + 100\%) \tag{6}$$

$$R_S(T) = R_{S0} + (\alpha_{RS} \cdot T + 100\%) \quad (7)$$

where α_{opt} represents the degradation rates of the transmissivity (glass optical losses and encapsulating losses) and the α_{R_S} of the series resistance (the deterioration of the electrical parts) are defined with accelerated test results. The degradation laws, the reduction in the transmissivity, and the augmentation of the series resistance according to time are given by expressions (6) and (7). The obtained degradation coefficients are α_{opt} = 0.6% per year and α_{R_S} = 0.23% per year. τ is the transmissivity and T is the time in years.

4. Proposed Tabu Search Optimization (TSO) Algorithm

To address the state of the issue of numerous optimizations, the meta-heuristic method is applied. During optimization, the lowest value is chosen initially, followed by a more extensive search. The tabu list (TL) memory utilitarian strategy obtains the information and stores the past arrangement while directing the following stage. For forestalling nearby improvements, irrelevant information is limited, and ideal information is isolated in aspiration criteria (AC). It is feasible to involve nearby heuristic examination tasks to concentrate on the outcome space in front of the neighborhood ideal through the TSO approach, which utilizes TL to help achieve developmental memory with appropriate limitations and goal levels.

To solve finite-solution set optimization problems, dynamic properties research is preferred because of the flexible memory consumption in tabu motions. Repeated solutions are out of the question, since these are unrepeatable activities. There are three varieties of TSO: the forbidding strategy, the freeing strategy system, and the short-term strategy (STS). By performing approximated solutions, the STS maintains a link between the FS and the FSS, while the FSS takes care of what remains after the optimization process, and the FS controls which data reach the operational zone. Figure 2 portrays the forbidden development, which depends on non-improved and nonlinear arrangements, as well as memory and neighborhood arrangements.

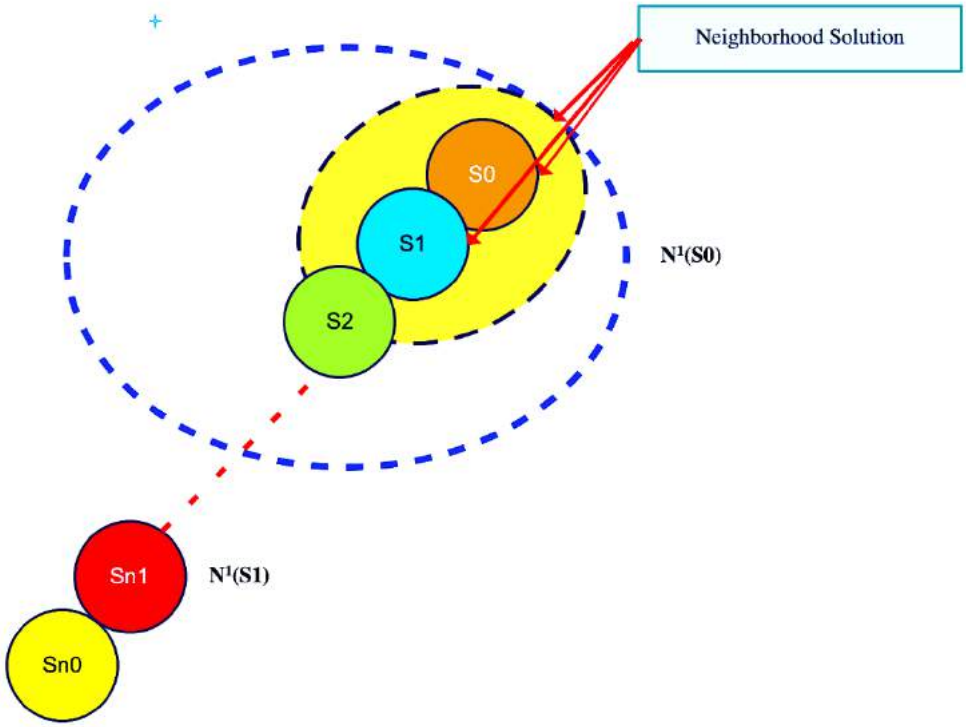

Figure 2. Tabu list neighborhood solutions for new solution.

The TL should not contain any of these options. The tabu classification may be discarded if new tabu motions are introduced.

The new set of T(S) solutions is as follows:

$$S^I \in N(S) = \{N(S) - T(S)\} + A(S) \quad (8)$$

TSO integrates goal programming and evaluates the solutions in more than one dimension, i.e., comparing the most important value with the first, second, third, and so on. The TSO framework is depicted in Figure 3.

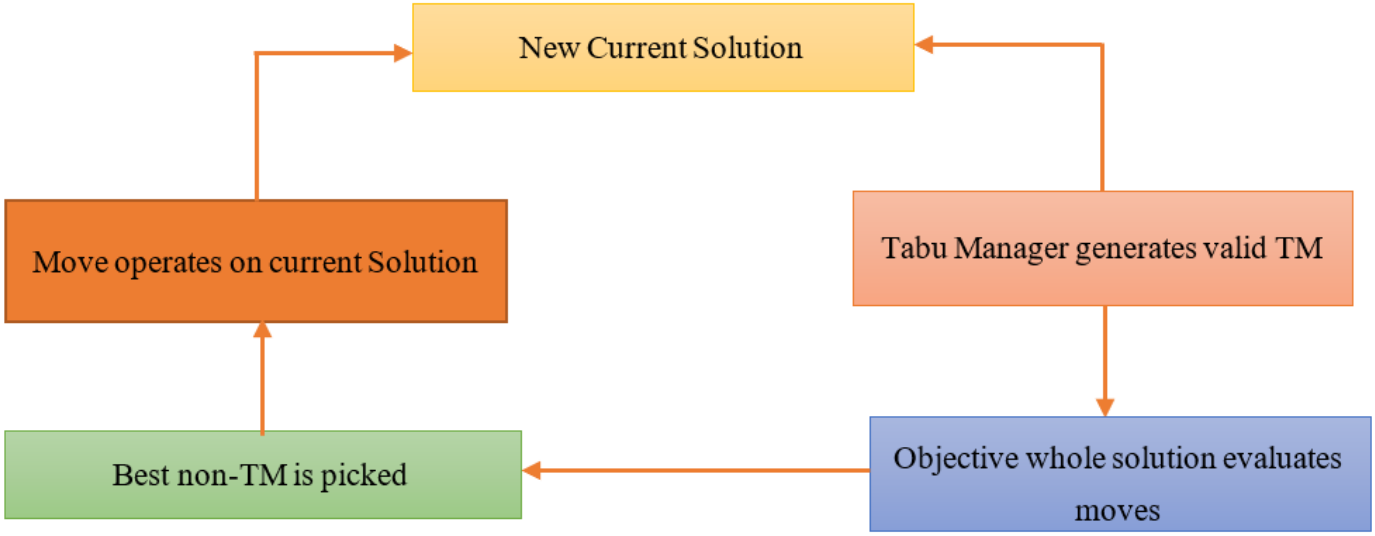

Figure 3. TSO framework for obtaining the optimal solution.

Basic TSO

The algorithm (Algorithm 1) for Basic Tabu Search Optimation is detailed step wise below.

Algorithm 1 Basic TSO	
STEP 1	Select a primary result i_o in S. Set $i_0^* = 0$ and k = 0.
STEP 2	Fix k = k + 1 and produce a subset V* of outcomes in N (i_0, k) in such a way that either one of the tabu circumstances is infringed, or even one of the aspiration conditions is clutched.
STEP 3	Select the best j in V* and put $i_0 = j$.
STEP 4	If f (i_0) < f (i_0^*) arrange $i_0^* = i_0$.
STEP 5	Update tabu and aspirational conditions.
STEP 6	Stop if a stopping condition is reached. Otherwise, go to STEP 2.
STEP 7	The stopping criteria of TS are as follows: N (i, k + 1) = 0. i.e., no possible resolution in the vicinity of result i_0. Here, k is largest than the highest numbers of rearrangements that are accepted. The number of repetitions since the last advancement of i_0^* is higher than the corresponding number. There is confirmation that an optimal result has been obtained.

The upper-band and lower-band areas are described by feasible and unfeasible parameters. The number of generations is determined by the feasibility, as indicated in Figure 4a,b.

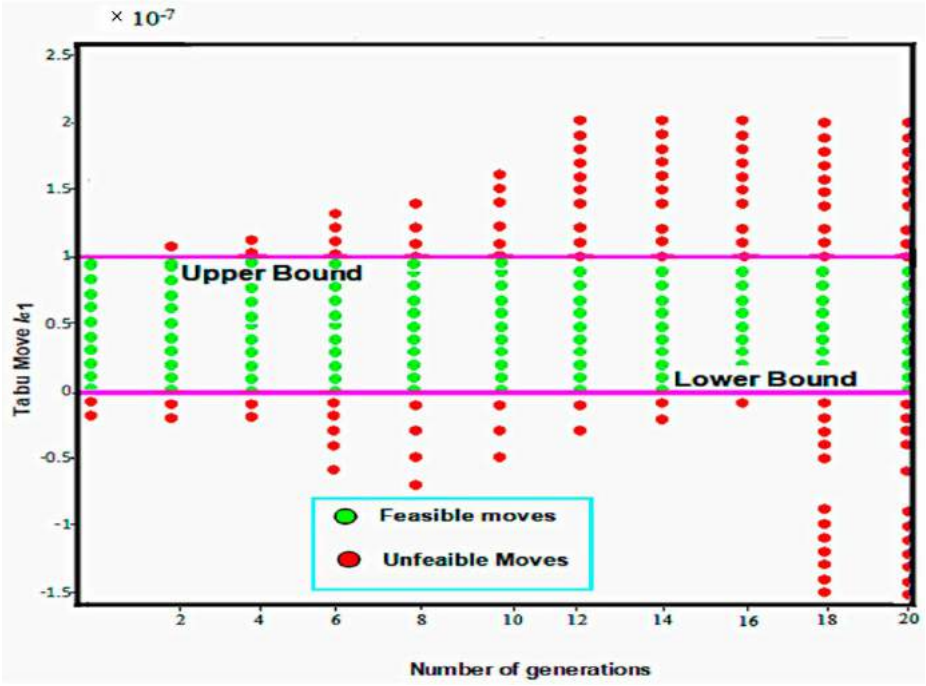

(**a**)

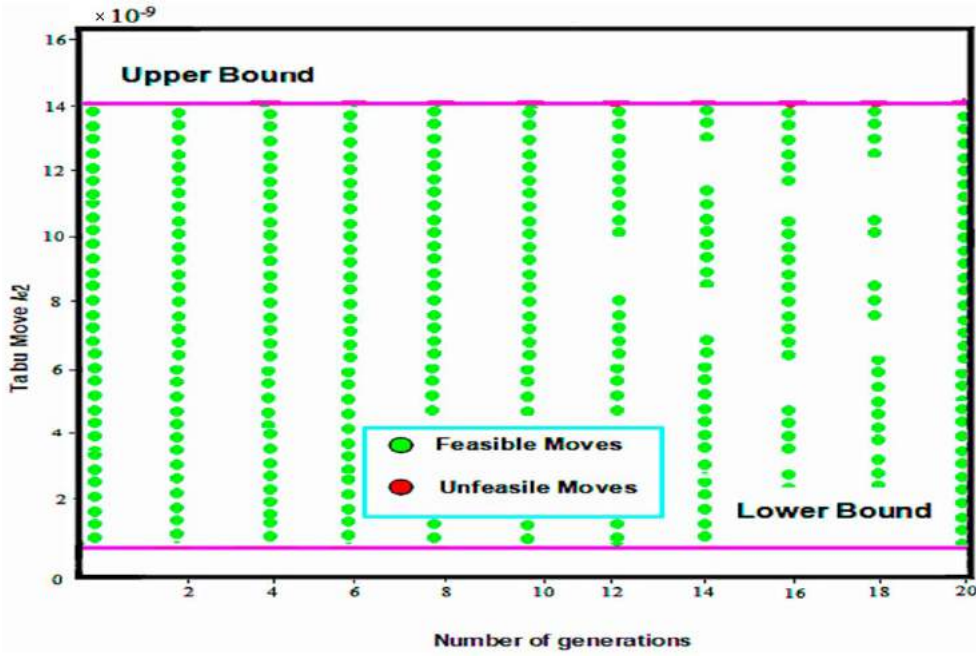

(**b**)

Figure 4. Resulting tabu movements. (**a**) Lower feasibility and (**b**) higher feasibility.

5. Results and Analysis

The numerical re-enactments of the proposed strategy were simulated in MATLAB/Simulink along with existing methods such as LSA and GSA. The obtained numerical findings and synthetic data (SD) had a significant connection. A comparison of the proposed TSO algorithm's performance on two different solar-panel wattage ranges was drawn. On Windows XP, with a 1.2 GHz Mobile Intel CPU, all of the algorithms ran on a single platform with distinct basic data. The proficiency of the boundary extraction strategy was assessed utilizing the assembly, I–V information bend, and calculation execution.

In this work, to extract the parameters, real measured V–I data of the solar cell and PV module were used in the simulation. A commercial silicon solar cell 57 mm in diameter

was taken as the prototype and V–I measurements were taken under one sun (100 W/m^2) at 33 °C. This prototype is the same as that used by AlRashidi et al. (2011) and AlHajri et al. (2012). The adjustable parameters in this simulation, determined by trial, were given by: population size (parallel number) N = 100, maximum iteration number kmax = 2500, crossover operation rate Pc = 0:5, and merging operation rate Pm = 0:5.

The information examination of a 40-watt PV board is displayed in Table 1. The values derived using the GA algorithm for the parameters I_{Ph}, I_{01}, I_{02}, R_S, R_P, and a1 were 2.69 A, 9.51×10^{-9} A, 32×10^{-7} A, 0.0794 Ω, 878.95 Ω, and 1.28. In addition, the suggested TSO method extracted 1.94 A (I_{Ph}), 6.35×10^{-9} A (I01), 11.92×10^{-7} A (I02), 0.0782 Ω (R_S), 762.68 Ω (R_P), and 1.29 A (I_{Ph}) (a1). The analysis of the pre-existing synthetic data with the numerical values gathered by the various instruments used in this study clearly yielded a statistically significant difference. When compared to other current algorithms, the TSO algorithm requires substantially less time to compute, taking just 112 s.

Table 1. Comparison of fata for a 40-watt PV panel using GA, LSA, GSA, PS, PSO, and proposed TSO algorithms.

S.NO	Parameter	Synthetic Data	GA	LSA	GSA	PS	PSO	TSO
1	I_{ph}	1.967 A	2.69 A	2.55 A	2.162 A	2.189 A	2.01 A	1.94 A
2	I_{01}	6.23×10^{-9} A	9.51×10^{-9} A	8.2×10^{-9} A	8.6×10^{-9} A	7.65×10^{-9} A	5.65×10^{-9} A	6.35×10^{-9} A
3	I_{02}	20.9×10^{-7} A	32.6×10^{-7} A	25.9×10^{-7} A	26.28×10^{-7} A	26.76×10^{-7} A	23.32×10^{-7} A	11.92×10^{-7} A
4	R_s	0.0775 Ω	0.0794 Ω	0.0975 Ω	0.097 Ω	0.0969 Ω	0.0954 Ω	0.0782 Ω
5	R_P	712.65 Ω	878.95 Ω	862.65 Ω	858.53 Ω	816.76 Ω	782.65 Ω	762.68 Ω
6	a_1	1.45	1.28	1.19	1.32	1.47	1.38	1.29
7	Time (s)	...	779	682	395	362	237	112

Table 2 shows that the suggested TSO method produced numerical results that were similar to the synthetic data, namely 5.41 A (I_{Ph}), 8.7×10^{-9} A (I01), 9.29×10^{-5} A (I_{02}), 0.942 Ω (R_S), 1281.98 Ω (R_P), and 1.01 A (I_{Ph}) (a1). When compared to current techniques, the TSO algorithm takes less time to compute (228 s). Accordingly, the proposed TSO calculation was demonstrated to be better than that of current metaheuristic calculations. Figure 5a–d shows the I–V charts of the S75, S115, SM55, and SQ150PC modules utilizing the TSO technique and test information, respectively.

Table 2. Comparison of data for a 200-watt PV panel using Ga, Lsa, Gsa, Ps, Pso, and proposed TSO algorithms.

S.No.	Parameter	Synthetic Data	GA	LSA	GSA	PS	PSO	TSO
1	I_{ph}	5.300 A	7.45 A	7.21 A	6.95 A	6.45 A	6.06 A	5.41 A
2	I_{01}	8.97×10^{-9} A	9.48×10^{-9} A	9.27×10^{-9} A	9.27×10^{-9} A	9.027×10^{-9} A	9.17×10^{-9} A	8.7×10^{-9} A
3	I_{02}	9.29×10^{-7} A	10.88×10^{-7} A	10.49×10^{-7} A	9.87×10^{-7} A	10.22×10^{-7} A	10.98×10^{-7} A	9.29×10^{-7} A
4	R_s	0.896 Ω	1.12 Ω	1.176 Ω	1.0968 Ω	1.796 Ω	1.016 Ω	0.942 Ω
5	R_P	1298.18 Ω	1498.58 Ω	1545.08 Ω	1434.78 Ω	1398.18 Ω	1386.08 Ω	1281.98 Ω
6	a_1	1	1.88	1.76	1.63	1.43	1.19	1.01
7	Time (s)	...	898	731	676	487	341	228

At various irradiance levels, including 1000 W/m^2 and 600 W/m^2, the TSO approach was utilized to inspect the effects of a few PV modules, including multi-glasslike (S75 and S115) and mono-translucent (SM55 and SQ150PC). The S75 multi-crystalline panel takes 0.5 s to compute at 1000 W/m^2 to retrieve the parameters. Different modules, such as S115, SM55, and SQ 150PC, require 0.43, 0.41, and 0.39 s, respectively. Data extracted is tabulated in Table 3. The extra boundaries of the S75 PV module, I_{Ph}, I_{01}, I_{02}, R_S, R_P, and a1, are 5.420 A, 9.97×10^{-9} A, 6.29×10^{-7} A, 0.696 Ω, 416.18 Ω, and 1.15. At G = 600 W/m^2. The situation is therefore similar. The S75 modules take up a significant amount of processing time, whereas the SM55 takes up the least. However, the S75 multi-crystalline module's total numerical values are noticeable under any irradiance levels.

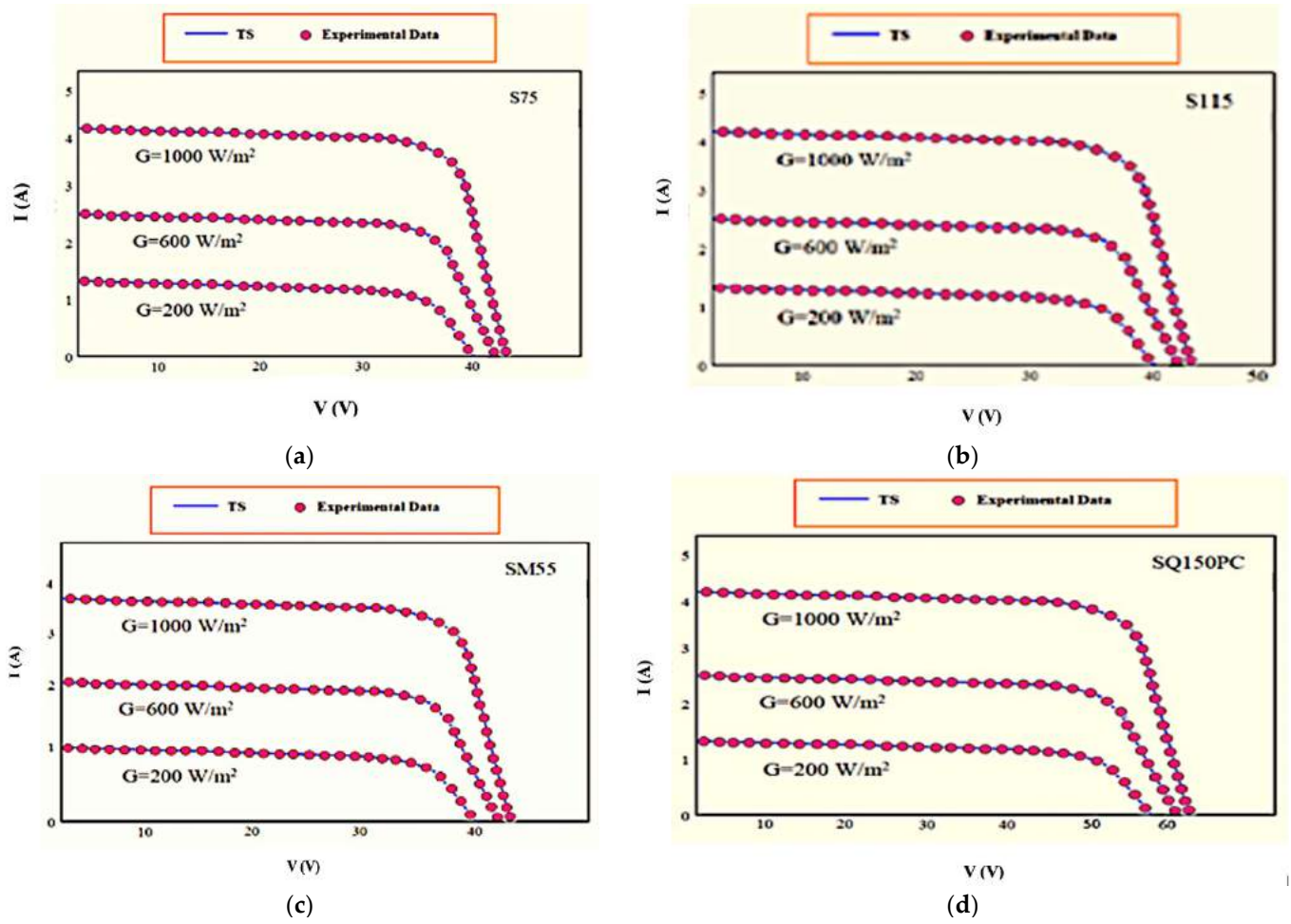

Figure 5. I–V qualities obtained by utilizing TSO calculation and trial information. (**a**) S75, (**b**) S115, (**c**) SM55, and (**d**) SQ150PC.

Table 3. Data extracted at different irradiance levels from multi-crystalline and mono-crystalline.

S. NO	Parameter	Multi-Crystalline		Mono-Crystalline	
G = 1000 W/m²		*S75*	*S115*	*SM55*	*SQ150PC*
1	I_{Ph} (A)	5.420	5.457	3.876	4.046
2	I_{01} (A)	9.97×10^{-9}	10.87×10^{-9}	1.68×10^{-9}	2.47×10^{-9}
3	I_{02} (A)	6.29×10^{-7}	6.37×10^{-7}	2.98×10^{-7}	3.049×10^{-7}
4	Rs (Ω)	0.696	0.968	0.32	0.876
5	Rp (kΩ)	416.18	434.78	598.58	345.08
6	a_1	1.15	1.23	1.08	1.76
7	Time (min)	0.5	0.43	0.41	0.39
G = 600 W/m²					
1	I_{Ph} (A)	3.420	3.457	3.876	2.546
2	I_{01} (A)	10.09×10^{-9}	8.87×10^{-9}	3.68×10^{-9}	8.47×10^{-9}
3	I_{02} (A)	8.29×10^{-7}	6.37×10^{-7}	2.98×10^{-7}	3.029×10^{-7}
4	Rs (Ω)	0.596	0.698	0.52	0.976
5	Rp (kΩ)	426.18	464.38	698.58	1345.08
6	a_1	1.15	1.13	1.28	1.36
7	Time (min)	0.41	0.36	0.36	0.39

The combination time for the TSO technique corresponds to the level of emphasis performed. As the quantity of cycles rises, so do the execution time and the rate at which

the results increase. Instances of the combination reaction of PV modules with 40-watt and 200-watt appraisals are displayed in Figure 6a,b.

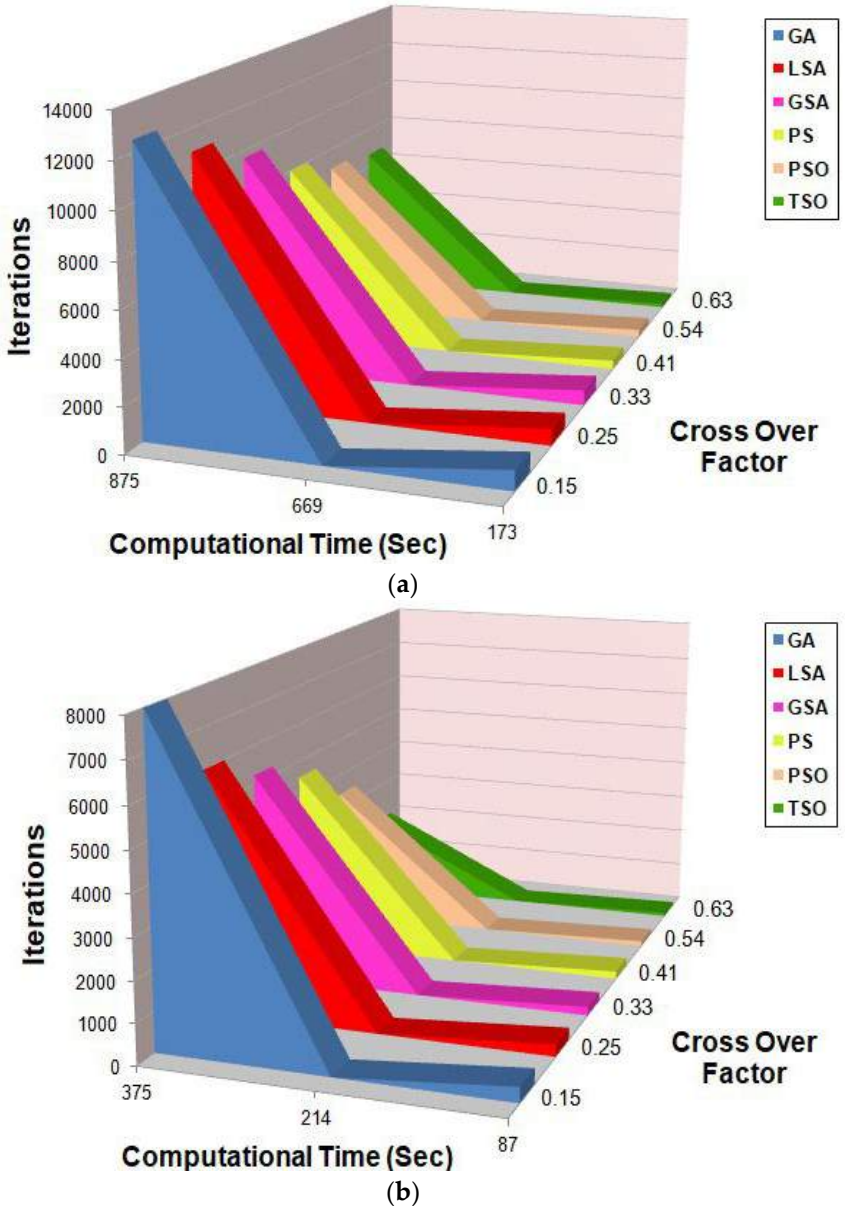

Figure 6. Convergence characteristics of (**a**) 40-watt and (**b**) 200-watt PV module.

Changes in absolute errors have a significant impact on the proposed TSO algorithm and current approaches under diverse irradiance patterns. Figure 7a,b illustrates the % absolute error on the mono-crystalline and multi-crystalline PV panels, respectively.

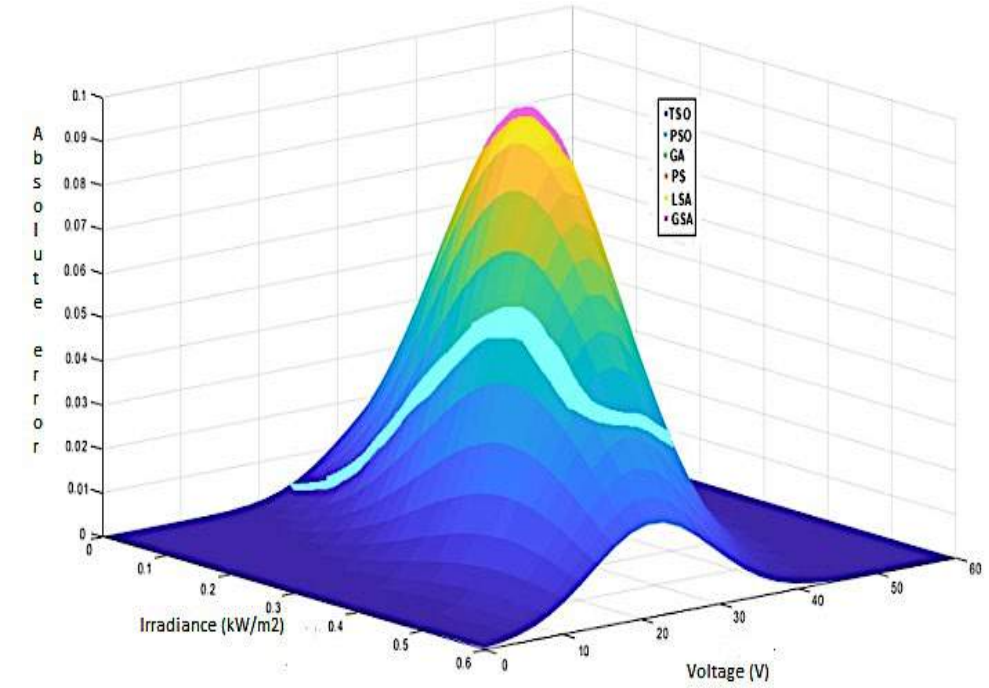

(**a**)

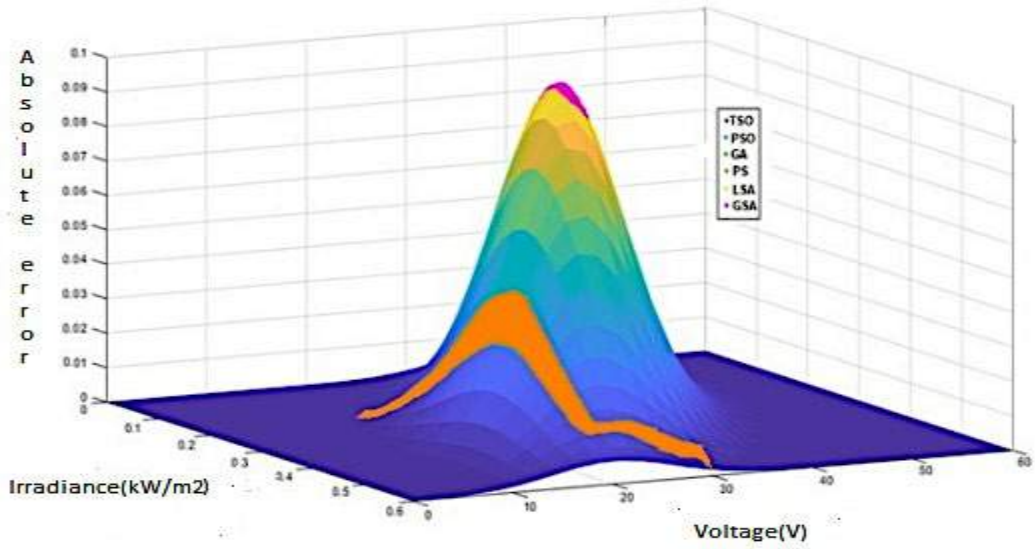

(**b**)

Figure 7. Absolute errors for (**a**) multi-crystalline and (**b**) mono-crystalline.

6. Conclusions

Under a variety of environmental conditions, the parasitic limits of PV modules may be extricated using a TSO-based approach. On an assortment of PV modules, including 40-watt and 200-watt PV modules, multi-glass-like mono clear, and small-film modules, the proposed TSO algorithm was compared with existing computation algorithms, such as the genetic algorithm, lightning search algorithm, gravitational search algorithm, pattern search algorithm (PS), and particle swarm optimization (PSO). The proposed approach is different from the other current optimization algorithms, and showed a superior calculation ability proving that the TSO calculation has superior qualities, with less intricacy and quicker combination, as displayed in Tables 1 and 2.

Author Contributions: Conceptualization, N.B.R., P.S. and S.R.K.; Data curation, N.B.R. and P.S.; Formal analysis, S.R.K. and N.R.; Funding acquisition, L.M.-P.; Investigation, N.R.; Software, N.B.R.; Supervision, N.R.; Writing—original draft, N.B.R. and P.S.; Writing—review & editing, L.M.-P. All authors have read and agreed to the published version of the manuscript.

Funding: This research received no external funding.

Conflicts of Interest: The authors declare no conflict of interest.

Nomenclature

I_{PV}	photovoltaic current (A)
I_S	diode reverse-saturation current (A)
I_d	diode currents (A)
I_{ph}	photocurrent (A)
q	charge (C)
α	number of iterations for each simplex
β	number of offspring
R_s	series resistance (Ω)
R_{sh}	shunt resistance (Ω)
K_b	Boltzmann constant ($1.3806503 \times 10^{-23}$ J/K)
η	empirical constant 1 for Ge, 2 for Si
T_K	cell temperature in kelvin

References

1. Bhukya, M.N.; Kumar, M.; Mohan, V.C.J. Design and Development of a Low-Cost Grid Connected Solar Inverter for Maximum Solar Power Utilization. In *Recent Advances in Power Electronics and Drives*; Lecture Notes in Electrical Engineering; Springer: Singapore, 2021; Volume 707. [CrossRef]
2. Bae, Y.; Vu, T.; Kim, R. Implemental Control Strategy for Grid Stabilization of Grid-Connected PV System Based on German Grid Code in Symmetrical Low-to-Medium Voltage Network. *IEEE Trans. Energy Convers.* **2013**, *28*, 619–631. [CrossRef]
3. Ali, A.; Almutairi, K.; Padmanaban, S.; Tirth, V.; Algarni, S.; Irshad, K.; Islam, S.; Zahir, M.H.; Shafiullah, M.; Malik, M.Z. Investigation of MPPT Techniques Under Uniform and Non-Uniform Solar Irradiation Condition–A Retrospection. *IEEE Access* **2020**, *8*, 127368–127392. [CrossRef]
4. Ahmad, W.; Liu, D.; Wu, J.; Ahmad, W.; Wang, Y.; Zhang, P.; Zhang, T.; Zheng, H.; Chen, L.; Chen, Z.D.; et al. Enhanced Electrons Extraction of Lithium-Doped SnO2Nanoparticles for Efficient Planar Perovskite Solar Cells. *IEEE J. Photovolt.* **2019**, *9*, 1273–1279. [CrossRef]
5. Villalva, M.G.; Gazoli, J.R.; Filho, E.R. Comprehensive Approach to Modeling and Simulation of Photovoltaic Arrays. *IEEE Trans. Power Electron.* **2009**, *24*, 1198–1208. [CrossRef]
6. Arefifar, S.A.; Paz, F.; Ordonez, M. Improving Solar Power PV Plants Using Multivariate Design Optimization. *IEEE J. Emerg. Sel. Top. Power Electron.* **2017**, *5*, 638–650. [CrossRef]
7. Kumar, N.; Saha, T.K.; Dey, J. Sliding-Mode Control of PWM Dual Inverter-Based Grid-Connected PV System: Modeling and Performance Analysis. *IEEE J. Emerg. Sel. Top. Power Electron.* **2015**, *4*, 435–444. [CrossRef]
8. Ma, X.; Huang, W.-H.; Schnabel, E.; Kohl, M.; Brynjarsdottir, J.; Braid, J.L.; French, R.H. Data-Driven II–VV Feature Extraction for Photovoltaic Modules. *IEEE J. Photovolt.* **2019**, *9*, 1405–1412. [CrossRef]
9. Saleem, H.; Karmalkar, S. An Analytical Method to Extract the Physical Parameters of a Solar Cell from Four Points on the Illuminated J-V Curve. *IEEE Electron Device Lett.* **2009**, *30*, 349–352. [CrossRef]
10. Soeriyadi, A.H.; Wang, L.; Conrad, B.; Li, D.; Lochtefeld, A.; Gerger, A.; Barnett, A.; Perez-Wurfl, I. Extraction of Essential Solar Cell Parameters of Subcells in a Tandem Structure With a Novel Three-Terminal Measurement Technique. *IEEE J. Photovolt.* **2017**, *8*, 327–332. [CrossRef]
11. Mintairov, M.; Kalyuzhnyy, N.A.; Evstropov, V.V.; Lantratov, V.M.; Mintairov, S.A.; Shvarts, M.Z.; Andreev, V.M.; Luque, A. The Segmental Approximation in Multijunction Solar Cells. *IEEE J. Photovolt.* **2015**, *5*, 1229–1236. [CrossRef]
12. Wei, T.; Yu, F.; Huang, G.; Xu, C. A Particle-Swarm-Optimization-Based Parameter Extraction Routine for Three-Diode Lumped Parameter Model of Organic Solar Cells. *IEEE Electron Device Lett.* **2019**, *40*, 1511–1514. [CrossRef]
13. Bhukya, M.N.; Kumar, M.; Depuru, S.R. A Simple Approach to Enhance the Performance of Traditional P&O Scheme under Partial Shaded Condition by Employing Second Stage to the Existing Algorithm. In *Modeling, Simulation and Optimization*; Springer: Singapore, 2021. [CrossRef]
14. Diab, A.A.Z.; Sultan, H.M.; Aljendy, R.; Al-Sumaiti, A.S.; Shoyama, M.; Ali, Z.M. Tree Growth Based Optimization Algorithm for Parameter Extraction of Different Models of Photovoltaic Cells and Modules. *IEEE Access* **2020**, *8*, 119668–119687. [CrossRef]
15. Bhukya, M.N.; Kota, V.R.; Depuru, S.R. A Simple, Efficient, and Novel Standalone Photovoltaic Inverter Configuration with Reduced Harmonic Distortion. *IEEE Access* **2019**, *7*, 43831–43845. [CrossRef]

16. Raba, A.; Leroy, Y.; Kohlstädt, M.; Würfel, U.; Cordan, A. Organic Solar Cells: Extraction of Physical Parameters by Means of Markov Chain Monte Carlo Techniques. *IEEE J. Photovolt.* **2017**, *7*, 1098–1104. [CrossRef]
17. Caracciolo, F.; Dallago, E.; Finarelli, D.G.; Liberale, A.; Merhej, P. Single-Variable Optimization Method for Evaluating Solar Cell and Solar Module Parameters. *IEEE J. Photovolt.* **2012**, *2*, 173–180. [CrossRef]
18. Cervellini, M.P.; Echeverria, N.I.; Antoszczuk, P.D.; Retegui, R.A.G.; Funes, M.A.; Gonzalez, S.A. Optimized Parameter Extraction Method for Photovoltaic Devices Model. *IEEE Lat. Am. Trans.* **2016**, *14*, 1959–1965. [CrossRef]
19. Semero, Y.K.; Zhang, J.; Zheng, D. PV power forecasting using an integrated GA-PSO-ANFIS approach and Gaussian process regression based feature selection strategy. *CSEE J. Power Energy Syst.* **2018**, *4*, 210–218. [CrossRef]
20. Bhukya, M.N.; Kumar, M. Factors Affecting the Efficiency of Solar Cell and Technical Possible Solutions to Improve the Performance. In *Modeling, Simulation and Optimization*; Springer: Singapore, 2021; pp. 623–634. [CrossRef]
21. Liao, Z.; Gu, Q.; Li, S.; Hu, Z.; Ning, B. An Improved Differential Evolution to Extract Photovoltaic Cell Parameters. *IEEE Access* **2020**, *8*, 177838–177850. [CrossRef]
22. Toledo, F.J.; Blanes, J.M.; Galiano, V. Two-Step Linear Least-Squares Method for Photovoltaic Single-Diode Model Parameters Extraction. *IEEE Trans. Ind. Electron.* **2018**, *65*, 6301–6308. [CrossRef]
23. Rossmo, K.; Harries, K. A novel P&OT-Neville's interpolation MPPT scheme for maximum PV sytem energy extraction. *Int. J. Renew. Energy Dev.* **2021**, *7*, 251–260. [CrossRef]
24. AlShabi, M.; Ghenai, C.; Bettayeb, M.; Ahmad, F.F.; Assad, M.E.H. Multi-group grey wolf optimizer (MG-GWO) for estimating photovoltaic solar cell model. *J. Therm. Anal.* **2020**, *144*, 1655–1670. [CrossRef]
25. Manda, P.K.; Ramaswamy, S.; Dutta, S. Extraction of the Built-in Potential for Organic Solar Cells from Current–Voltage Characteristics. *IEEE Trans. Electron Devices* **2017**, *65*, 184–190. [CrossRef]
26. Kota, V.R.; Bhukya, M.N. A simple and efficient MPPT scheme for PV module using 2-Dimensional Lookup Table. In Proceedings of the 2016 IEEE Power and Energy Conference at Illinois (PECI), Urbana, IL, USA, 19–20 February 2016; pp. 1–7. [CrossRef]
27. Bauer, A.; Hanisch, J.; Ahlswede, E. An Effective Single Solar Cell Equivalent Circuit Model for Two or More Solar Cells Connected in Series. *IEEE J. Photovolt.* **2013**, *4*, 340–347. [CrossRef]
28. Azizi, A.; Logerais, P.-O.; Omeiri, A.; Amiar, A.; Charki, A.; Riou, O.; Delaleux, F.; Durastanti, J.-F. Effect of the maturing of a photovoltaic module on the presentation of a framework associated framework. *Sol. Energy* **2018**, *174*, 445–454. [CrossRef]

frontiers | Frontiers in Energy Research

ORIGINAL RESEARCH
published: 05 July 2022
doi: 10.3389/fenrg.2022.921426

Seagull Optimization Algorithm–Based Fractional-Order Fuzzy Controller for LFC of Multi-Area Diverse Source System With Realistic Constraints

CH. Naga Sai Kalyan[1], *B. Srikanth Goud*[2], *Ch. Rami Reddy*[3], *Ramanjaneya Reddy Udumula*[4], *Mohit Bajaj*[5], *Naveen Kumar Sharma*[6], *Elmazeg Elgamli*[7]*, *Mokhtar Shouran*[7] *and Salah Kamel*[8]

[1]Electrical and Electronics Engineering, Vasireddy Venkatadri Institute of Technology, Guntur, India, [2]Department of Electrical and Electronics Engineering, Anurag University, Ghatkesar, India, [3]Department of Electrical and Electronics Engineering, Malla Reddy Engineering College, Secunderabad, India, [4]Department of Electrical and Electronics Engineering, SRM University, Amaravati, India, [5]Department of Electrical and Electronic Engineering, National Institute of Technology Delhi, Delhi, India, [6]Electrical Engineering Department, I. K. G. Punjab Technical University, Jalandhar, India, [7]Wolfson Centre for Magnetics, School of Engineering, Cardiff University, Cardiff, United Kingdom, [8]Electrical Engineering Department, Faculty of Engineering, Aswan University, Aswan, Egypt

OPEN ACCESS

Edited by:
Bo Yang,
Kunming University of Science and Technology, China

Reviewed by:
Jingbo Wang,
Kunming University of Science and Technology, China
Xiaoshun Zhang,
Northeastern University, China

***Correspondence:**
Elmazeg Elgamli
Elgamlies@cardiff.ac.uk

Specialty section:
This article was submitted to Smart Grids, a section of the journal Frontiers in Energy Research

Received: *15 April 2022*
Accepted: *26 May 2022*
Published: *05 July 2022*

Citation:
Naga Sai Kalyan CH, Goud BS, Reddy CR, Udumula RR, Bajaj M, Sharma NK, Elgamli E, Shouran M and Kamel S (2022) Seagull Optimization Algorithm–Based Fractional-Order Fuzzy Controller for LFC of Multi-Area Diverse Source System With Realistic Constraints. Front. Energy Res. 10:921426. doi: 10.3389/fenrg.2022.921426

This study initiates the implementation of fractional-order (FO) fuzzy (F) PID (FOFPID) controller fine-tuned using a seagull optimization algorithm (SOA) for the study of load frequency control (LFC). Initially, the SOA-tuned FOFPID regulator is implemented on the widely utilized model of dual-area reheat-thermal system (DARTS), named test system-1 in this work for a perturbation of 10% step load (10% SLP) on area-1. Dynamical analysis of the DARTS system reveals the viability of the SOA-tuned FOFPID control scheme in regulating frequency deviations effectively compared to other control schemes covered in the literature. Later, the presented regulator is implemented on the multi-area diverse sources (MADS) system possessing realistic constraints in this study, termed test system-2. The sovereignty of the presented FOFPID controller is once again evidenced with controllers of PID/FOPID/FPID fine-tuned with the SOA approach. Moreover, the effect of considering practical realistic nonlinearity constraints such as communication time delays (CTDs) on MADS system performance is visualized and the necessity of its consideration is demonstrated. Furthermore, AC-DC lines are incorporated with the MADS system to enhance the performance under heavy-load disturbances and the robustness of the proposed regulatory mechanism is deliberated.

Keywords: load frequency control, seagull optimization algorithm, FOFPID controller, 10% SLP, AC-DC lines

INTRODUCTION

In modern days, the most powerful ancillary service is the LFC, especially for the control and operation of interconnected power system networks. The electrical system is becoming more complex due to the integration of several diverse sources of generating units to meet the variable load demand. The operating point of the generation unit must be altered to keep the real power mismatch (RPM) as minimum as possible. RPM is the exact difference between the amount of real power generated by the generation units and the existing load demand. This RPM is

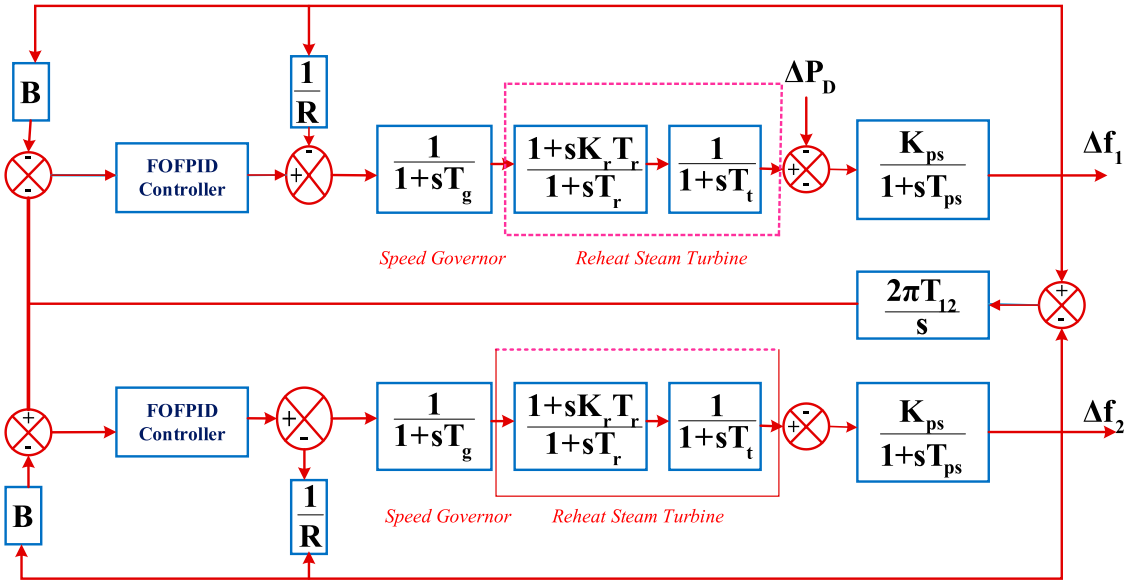

FIGURE 1 | Dual area reheat-thermal system (test system-1).

the direct analogy to one of the powerful parameters in the interconnected network, which is frequency. Thus, the minimization of RPM should be monitored continuously, as there will be continuous fluctuations in load demand. This must be done automatically; otherwise, the real power mismatch may become worse and affect the power system frequency. Frequency regulation must be done with the utmost care; if not, it adversely affects the power system stability. This task can be easily and automatically accomplished by LFC.

Researchers have put forward several control techniques in the LFC domain, and their performance was tested on numerous test system models that were elaborated by Tungadio and Sun (2019). Regardless of considering the power system networks, numerous techniques have been administered by the researchers of which standard PI, PID, PID plus filter (F), and PIDF regulators (Madasu et al., 2018; Arya, 2019a) are utilized extensively due to design simplicity. However, the performance efficacy of classical controllers is more likely to be dependent upon the optimization algorithms that have been deployed to optimize the controller gains. Several population- and stochastic-based searching algorithms reported in domain of LFC in optimizing classical controllers are chaotic atom search optimization (CASO) (Irudayaraj et al., 2022), many-objective optimization approach (MOOA) (Hajiakbari Fini et al., 2016), chaotic crow search (CCS) algorithm (Khokhar et al., 2021), gray wolf optimizer (GWO) (Sharma and Saikia, 2015), quadratic approach with pole compensator (QAWPC) (Hanwate and Hote, 2018), marine predator algorithm (MPA) (Yakout et al., 2021), Hooke–Jeeve's optimizer (HJO) (Chatterjee, 2010), quasi-oppositional harmony search algorithm (QOHSA) (Shankar and Mukherjee, 2016), chemical reaction optimizer (CRO) (Mohanty and Hota, 2018), hybrid artificial electric field algorithm (HAEFA) (Sai Kalyan et al., 2020), bacteria foraging optimization (BFOA) (Ali and Elazim, 2015), mine blast optimizer (MBO) (Alattar et al., 2019), particle swarm optimizer (PSO) (Magid and Abido, 2003), differential evolution (DE) (Kalyan and Suresh, 2021), combination of DE with pattern search (Sahu et al., 2015a) and AEFA (DE-AEFA) (Kalyan and Rao, 2021a), grasshopper optimizer (GHO), and cuckoo search approach (CSA) (Latif et al., 2018). Moreover, the conventional controllers exhibit efficacy in linearized models and could not maintain the stability of nonlinear interconnected power systems (IPS).

In contrast to classical regulators, model predictive controllers (MPC) (Zhang et al., 2020) are widely implemented by researchers. Moreover, the researchers adopted algorithms to train the model predictive network such as multiverse optimizer (MVO) (Ali et al., 2020), adaptive distributed auction algorithm (ADAA) (Zhang et al., 2021), and GHO (Nosratabadi et al., 2019). However, the design of MPC involves many control parameters, large load complexity, huge algorithmic complexity, and more computational burden. Thus, complex IPS models adapting MPC as a secondary regulator become more complex and thereby affect the automatic functioning and stability of IPS.

Owing to the advantage of possessing additional knobs in fractional order (FO)–type regulators (Delassi et al., 2018) they are also used by the researchers extensively in the LFC study. However, the uncertainty in FO parameters diluted the regulator sensitivity, thereby greatly influencing the robustness of system performance which led researchers to focus on the degree of freedom (DOF) controllers (Kalyan, 2021). Moreover, the performances of DOF regulators are also limited to only a certain extent, especially to IPS models with practical constraints such as communication time delays (CTDs), governor dead band (GDB), and generation rate constraint

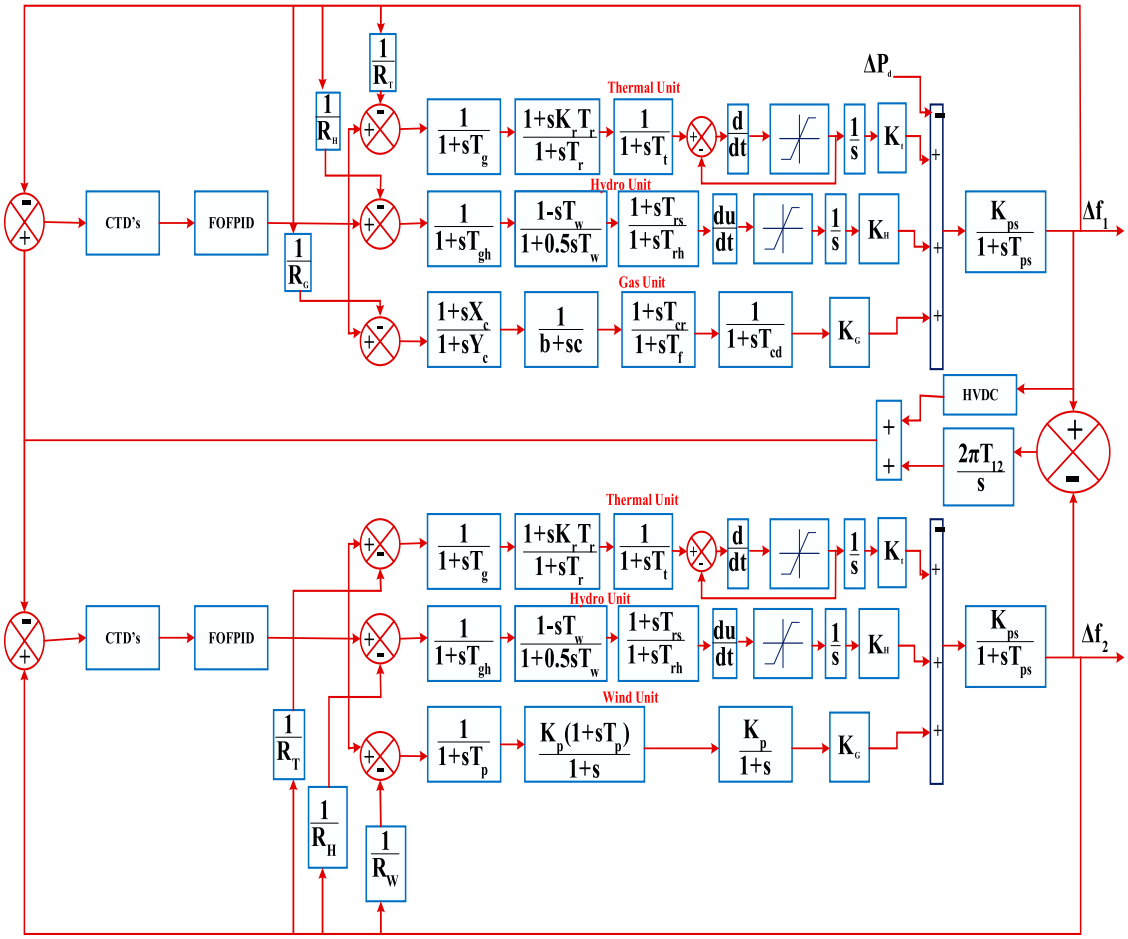

FIGURE 2 | Multi-area diverse source system with practical constraints (test system-2).

(GRC) (Arya, 2019b). Contrary to the aforementioned, fuzzy-logic controllers (FLC) exhibit more efficacy in handling nonlinearized models. Thus, FLC is suitable for IPS with practical constraints. FLC in conjunction with traditional controllers is successfully implemented in the LFC study with different optimization algorithms such as an imperialist competitive algorithm (ICA) (Arya, 2020), DE (Sahu et al., 2015b), water cycle algorithm (WCA) (Kalyan et al., 2021), sine–cosine approach (SCA) (Khezri et al., 2019), and ant lion optimizer (ALO) (Fathy and Kassem, 2019). To further enhance the ability of FLC in governing the IPS models toward stability effectively, FO nature is imparted to the FPID regulator in this work and is termed as the FOFPID regulator. From the literature on LFC, it is apparent that LFC performance is greatly handled by the optimization-based controllers. Hence, applications of new optimization algorithms for solving realistic power system problems are always welcome. In this regard, a new nature-inspired algorithm of the seagull optimization approach (SOA) is implemented in this study and is a maiden attempt, especially for power system operation and control of IPS with practical constraints. Until now, the regulators presented by the researchers so far were tested on linearized and nonlinearized power system models with and without integrating renewable energy units. To authenticate the investigative analysis of LFC closer to the nature of realistic practice, the researchers must adopt the nonlinearity constraints with power system models. Constraints of nonlinearity such as GRC and GDB are widely considered by the researchers, and less attention is given to other constraints of CTDs. In realistic practice, IPSs are widely spread and employ numerous sensing and phasor measurement devices. The measured data will be transmitted and received among different devices located in distant places via communication peripherals. The exchange of information will not be done instantly, and there exists a certain time delay. The delay might affect the IPS performance, and hence, this study tried to investigate the predominance of time delays in coordination with the constraint of GRC. Limited work is available on LFC with CTDs and is restricted to the implementation of traditional regulators (Kalyan and Rao, 2021b; Kalyan and Rao, 2021c). Thus, this study addresses the impact of the realistic constraint parameter, that is, CTDs on IPS performance in coordination with GRC under a fuzzy-aided FO-based regulator based on the newest optimization algorithm.

The following are the research contributions:

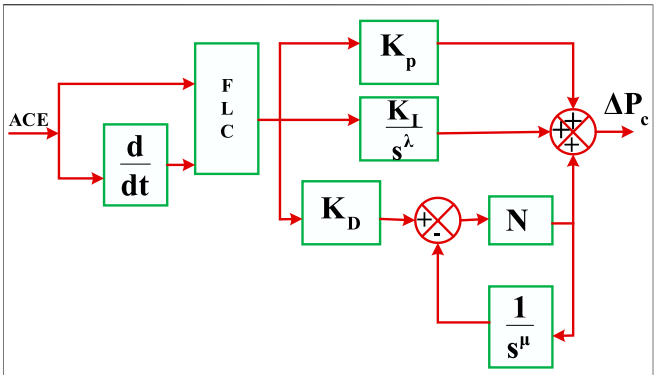

FIGURE 3 | Structure of FOFPID controller.

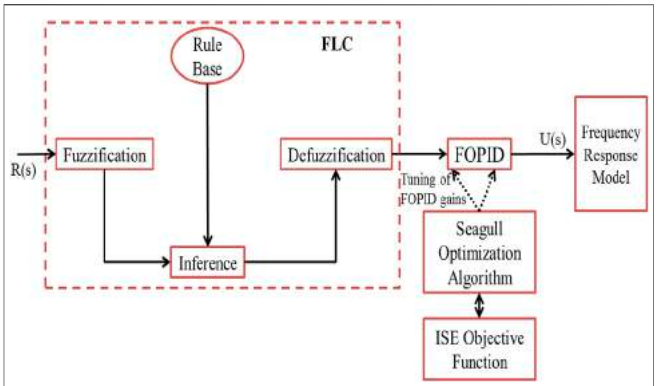

FIGURE 5 | The framework of FOFPID is based on SOA.

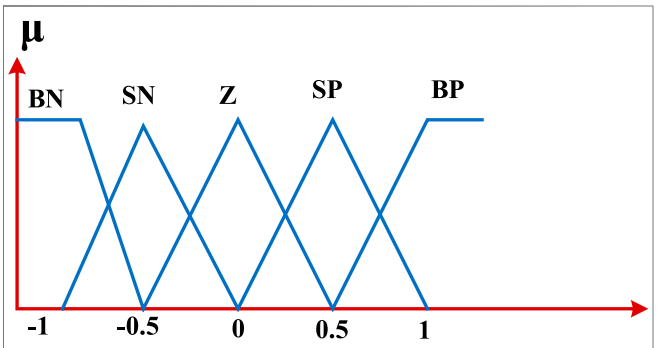

FIGURE 4 | MFs considered for FLC.

TABLE 1 | FLC input and output rules.

ACE	ΔACE				
	BN	**SN**	**Z**	**SP**	**BP**
BN	BN	BN	BN	SN	Z
SN	BN	BN	SN	Z	SP
Z	BN	SN	Z	SP	BP
SP	SN	Z	SP	BP	BP
BP	BP	Z	SP	BP	BP

1) The SOA-optimized FOFPID controller is designed and implemented for the study of LFC for the first time.
2) Supremacy of the SOA-tuned FOFPID controller is established with PSO-based PI, PID tuned with HAEFA and BFOA, GA-based FOPID, and DE-based FPID techniques available in the literature by implementing it on the test system-1 model.
3) Presented controller performance is tested on a nonlinear MADS system (test system-2) and efficacy is revealed with controllers of PID/FOPID/FPID.
4) The impact of CTDs on the performance of the MADS system is demonstrated.
5) Further AC-DC lines are enacted to enhance MADS system performance.
6) Sensitivity analysis is conducted to showcase the secondary and territorial control schemes' robustness.

POWER SYSTEM MODELS

This work considered two different power system networks to assess the FOFPID controller performance. One is DARTS termed as test system-1 and the other is MADS termed as test system-2. The DARTS model incorporates thermal units of reheat-type turbines in both areas with equal generation capacities. On the other hand, the MADS system that tests system-2 consists of two areas in area-1 and area-2 comprising thermal-hydro-wind units. The participation factor for each source of generation unit is allocated to achieve smooth load distribution and is considered as 0.6225 for thermal, 0.3 for hydro unit, and a factor of 0.075 for gas/wind unit. The required data to build the DARTS system depicted in **Figure 1** and MADS system model depicted in **Figure 2** are considered from Sai Kalyan et al. (2020) and Sahu et al. (2020), respectively. The power system models are designed in the (R2016a) version of MATLAB/SIMULINK. The mathematical modeling of MADS system is as follows:

Thermal unit:

$$\text{Reheat Turbine} = \frac{\Delta P_T(s)}{\Delta P_V(s)} = \frac{1 + sT_rK_r}{1 + sT_r}, \tag{1}$$

$$\text{Governor} = \frac{\Delta P_V(s)}{\Delta P_G(s)} = \frac{1}{1 + sT_g}. \tag{2}$$

Hydro unit:

$$\text{Governor} = \frac{\Delta P_V(s)}{\Delta P_g(s)} = \frac{1}{1 + sT_{gh}}, \tag{3}$$

$$\text{Droop} = \frac{\Delta P_{V1}(s)}{\Delta P_V(s)} = \frac{1 + sT_{rs}}{1 + sT_{rh}}, \tag{4}$$

$$\text{Penstock} = \frac{\Delta P_T(s)}{\Delta P_{V1}(s)} = \frac{1 - sT_w}{1 + 0.5sT_w}. \tag{5}$$

Gas unit:

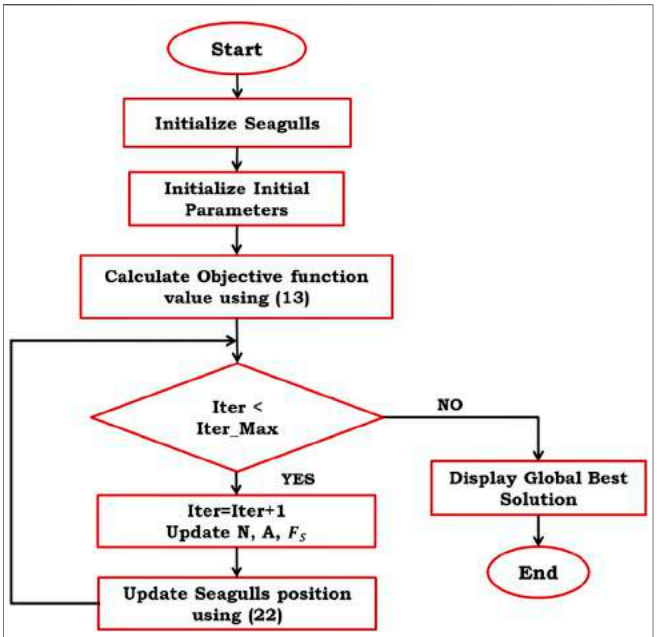

FIGURE 6 | SOA flowchart.

$$\text{Positioner Valve} = \frac{\Delta P_g(s)}{\Delta P_p(s)} = \frac{1}{c + sb}, \tag{6}$$

$$\text{Governor} = \frac{\Delta P_s(s)}{\Delta P_g(s)} = \frac{1 + sX_g}{1 + sY_g}, \tag{7}$$

$$\text{Combustion Reactor} = \frac{\Delta P_R(s)}{\Delta P_S(s)} = \frac{1 - sT_{CR}}{1 + sT_f}, \tag{8}$$

$$\text{Compressor Discharge} = \frac{\Delta P_{CD}(s)}{\Delta P_R(s)} = \frac{1}{1 + sT_{CD}}. \tag{9}$$

Wind unit:

$$\text{Wind energy converter} = \frac{\Delta P_{GW}(s)}{\Delta P_{MW}(s)} = \frac{K_p^2(1 + sT_P)}{(1 + s)(1 + s)}. \tag{10}$$

Furthermore, MADS system is employed with an additional DC line with an AC line in parallel for performance boost up. The modeling of the DC line (Kalyan and Rao, 2020) employed in this work is expressed in **Eq. 11**.

$$G_{DC} = \frac{K_{DC}}{1 + ST_{DC}}. \tag{11}$$

COMMUNICATION TIME DELAYS

Acquainted with the complexity of the modern power system, many measuring sensors which are located at remote terminal units (RTUs) are used to transmit data to the control center. Generally, information from sensors or measuring apparatus is transmitted to the control center where the command signals have been generated. Command signals are transmitted to the plant location to shift the generating unit operating point so that the real power mismatch gets minimized. Transmitting and receiving signals among measurement devices at RTUs and

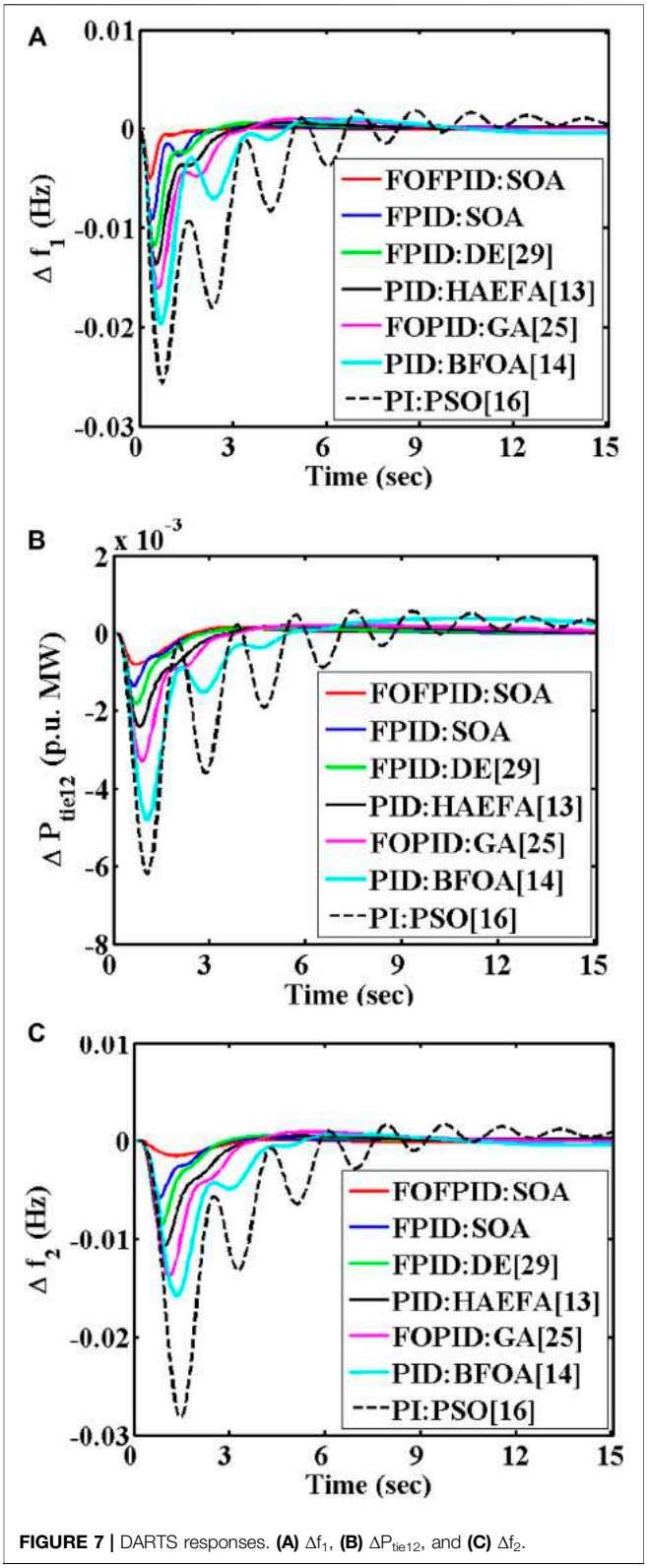

FIGURE 7 | DARTS responses. **(A)** Δf_1, **(B)** ΔP_{tie12}, and **(C)** Δf_2.

TABLE 2 | Controller optimal gains employed for DARTS system and responses settling time.

Parameter	Control technique						
	PSO: PI (Magid and Abido, 2003)	**BFOA: PID (Ali and Elazim, 2015)**	**GA: FOPID (Delassi et al., 2018)**	**HAEFA: PID (Sai Kalyan et al., 2020)**	**DE: FPID (Sahu et al., 2015b)**	**SOA: FPID**	**SOA: FOFPID**
Area-1	K_P = 3.043 K_I = 0.366	K_P = 1.714 K_I = 0.647 K_D = 0.218	λ = 0.156 μ = 0.28 K_P = 1.508 K_I = 0.621 K_D = 0.324	K_P = 1.200 K_I = 0.449 K_D = 0.413	K_P = 0.974 K_I = 0.074 K_D = 0.135	K_P = 0.765 K_I = 0.431 K_D = 0.215	λ = 0.221 μ = 0.207 K_P = 0.981 K_I = 0.109 K_D = 0.531
Area-2	K_P = 2.921 K_I = 0.244	K_P = 1.593 K_I = 0.326 K_D = 0.318	λ = 0.094 μ = 0.37 K_P = 1.419 K_I = 0.532 K_D = 0.213	K_P = 1.091 K_I = 0.348 K_D = 0.504	K_P = 1.090 K_I = 0.107 K_D = 0.204	K_P = 0.876 K_I = 0.351 K_D = 0.199	λ = 0.206 μ = 0.335 K_P = 1.017 K_I = 0.211 K_D = 0.638
Δf_1	27.19	19.53	14.64	11.57	8.155	5.788	3.960
ΔP_{tie}	26.33	17.56	13.44	11.82	9.761	7.263	5.679
Δf_2	23.61	17.25	13.76	9.554	8.155	6.902	4.988
ISE	11.85E-03	9.23E-03	7.17E-03	6.43E-03	6.07E-03	5.89E-03	5.21E-03

TABLE 3 | MADS responses settling time for case-2 and case-3.

Settling time (sec)		PID	FOPID	FPID	FOFPID
Case-2	Δf1	17.46	14.84	9.661	6.092
	ΔPtie12	18.34	15.08	11.02	8.86
	Δf2	16.05	13.10	9.86	5.645
Case-3	Δf1	32.24	19.41	14.05	9.786
	ΔPtie12	33.82	19.43	14.64	12.39
	Δf2	31.16	22.07	16.31	11.06

command centers in plant locations can be done only *via* communication channels. Inherently, these communication channels possess the feature of time delays which distinctly affect the power system performance. Designing secondary regulators for large power system networks without taking these CTDs with the system may yield unsatisfactory performance. Moreover, in the event of large CTDs the system may become unstable. Considering the aforementioned aspects, this study addresses the LFC of interconnected power systems with CTDs as expressed in **Eq. 12** (Kalyan and Rao, 2021a).

$$e^{-s\tau_d} = \frac{1 - \frac{\tau_d}{2}s}{1 + \frac{\tau_d}{2}s}. \tag{12}$$

FRACTIONAL-ORDER FUZZY PID CONTROLLER

Implementation of traditional PID controllers in the domain of LFC has been reported extensively because of its robustness, simplicity in design, and efficiency, especially for linear systems. Despite that, traditional PID regulators are not suitable for the system with time delays and nonlinear features of uncertainties. On the contrary, fuzzy-logic controllers (FLC) are one of the finest regulators and are best suitable for obtaining the performance of nonlinear control systems optimally. Researchers proved that FLC systems can effectively change the system operating point compared to many classical controllers like PI/PID/PIDD to sustain stability. FLC has been provided with input as area control error (ACE) and its derivative. During the phase of transients, the FPI regulator exhibited low performance due to the internal integrator for the higher-order process. This motivated the authors in this study to implement FPID, and to further enhance the performance of FLC in a closed-loop system where the FO gains are incorporated (Sharma et al., 2021). Thus, FOFPID is designed, whose architecture is shown in **Figure 3**, and implemented for the stability of the interconnected power systems. The membership functions (MFs) perceived in this work for both error and change in error are five linguistic variables termed as (BP) big positive, (SP) small positive, (Z) zero, (BN) big negative, and (SN) small negative, as depicted in **Figure 4**. Mamdani type of fuzzy engine has been perceived, and the FLC output is calculated by employing the defuzzification method of the center of gravity. FLC rule base in two dimensional is noted in **Table 1**. Moreover, a time domain–based integral square error (ISE) index is enacted to optimize the FOFPID controller gains in this work as given in **Eqn. 13**. The framework of FOFPID based on SOA is depicted in **Figure 5**.

$$J_{ISE} = \int_0^{T_{Sim}} \left(\Delta f \frac{2}{1} + \Delta P_{tie,12}^2 + \Delta f \frac{2}{2} \right) dt. \tag{13}$$

SEAGULL OPTIMIZATION ALGORITHM

Seagulls are intelligent and are technically called Laridae, normally living on the banks of seas and oceans all over the globe. The species of seagulls can be differentiated based on their length and mass. Usually, seagulls come under the food chain of omnivorous and are likely to feed on amphibians, reptiles, earthworms, fish, and insects. The body of seagulls is covered with feathers of white color and possesses specialized glands at the bottom of their neck. Seagulls possess the ability to feed on saltwater and by making use of the glands behind the neck, the

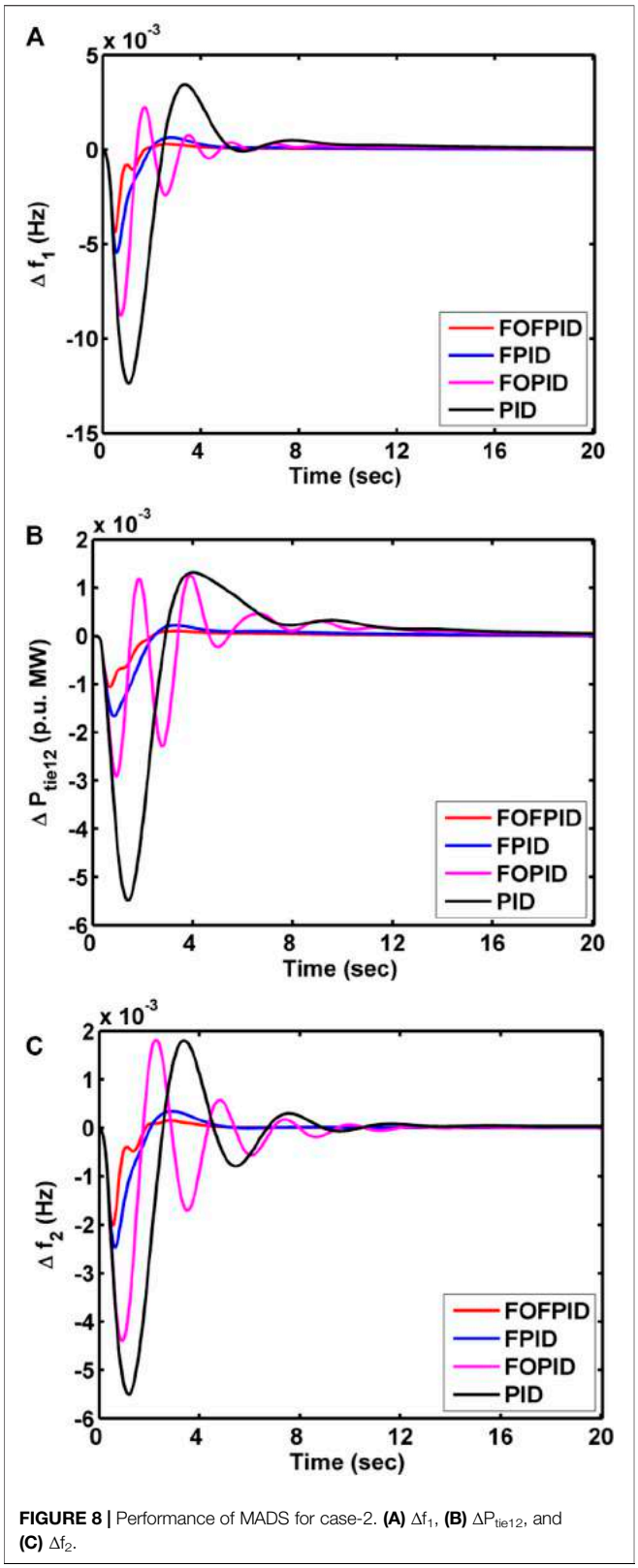

FIGURE 8 | Performance of MADS for case-2. **(A)** Δf_1, **(B)** ΔP_{tie12}, and **(C)** Δf_2.

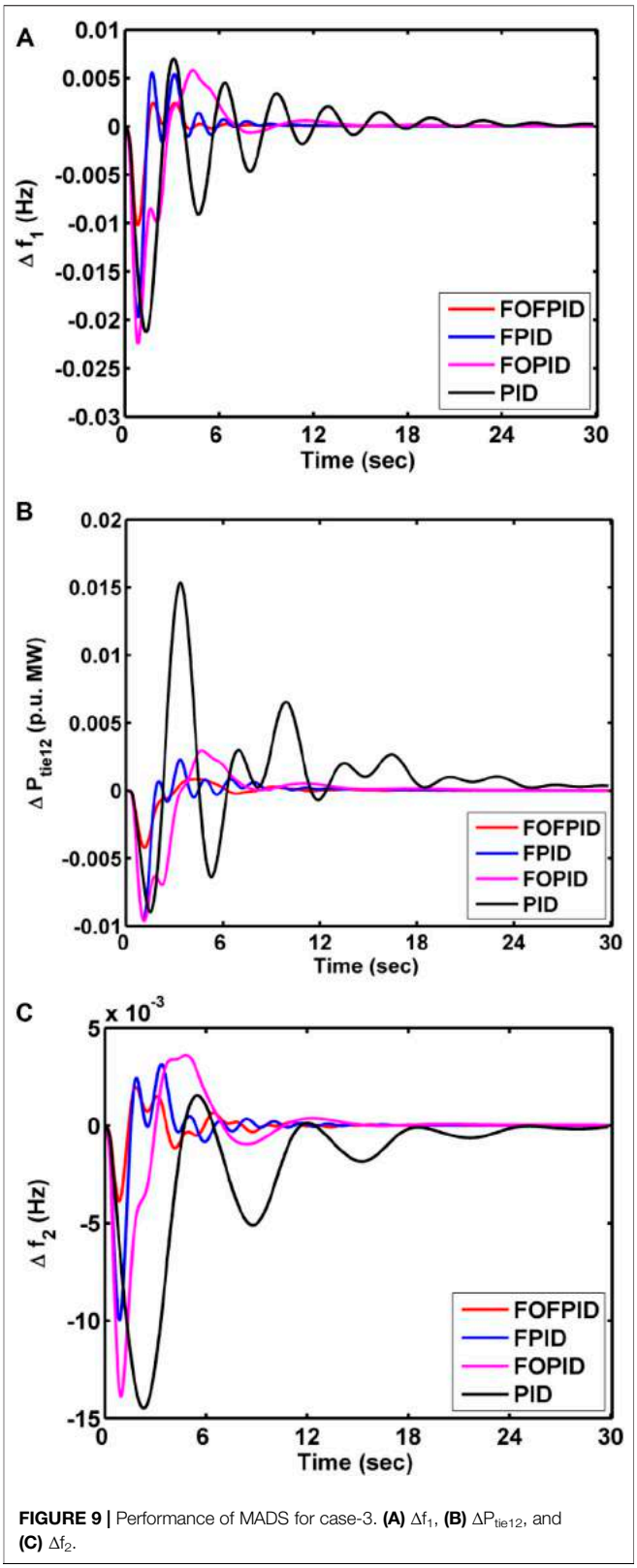

FIGURE 9 | Performance of MADS for case-3. **(A)** Δf_1, **(B)** ΔP_{tie12}, and **(C)** Δf_2.

excess salt in the body can be flushed out. This is the unique ability of these birds, something that no other bird can do. Seagulls are very clever and make raining sounds through their feet to trap the prey that hide underwater. Moreover, seagulls sprinkle the bread crumbs that have been collected from nearby neighborhoods for catching fish.

TABLE 4 | Controller optimum gains employed for MADS system using SOA algorithm.

Parameter		Optimum value										
		K_{P1}	K_{I1}	K_{D1}	λ_1	μ_1	K_{P2}	K_{I2}	K_{D2}	λ_2	μ_2	ISE*10^{-3}
Case-2	PID	1.983	0.595	0.305	—	—	1.885	0.664	0.295	—	—	98.61
	FOPID	1.171	0.721	0.508	0.318	0.264	1.127	0.913	0.543	0.407	0.189	72.16
	FPID	0.929	0.775	0.666	—	—	1.199	0.983	0.657	—	—	52.21
	FOFPID	0.988	0.477	0.894	0.073	0.298	1.298	0.619	0.527	0.120	0.139	29.18
Case-3	PID	1.804	0.778	0.672	—	—	1.762	0.998	0.880	—	—	135.3
	FOPID	1.060	0.834	0.699	0.407	0.359	1.299	1.013	0.781	0.316	0.217	107.1
	FPID	1.092	0.588	0.762	—	—	1.388	1.016	0.771	—	—	93.2
	FOFPID	0.889	0.578	0.987	0.136	0.179	1.328	0.917	0.786	0.210	0.246	67.4

Depending on attacking prey and the migration nature of seagulls, the SOA was put forward by the authors Dhiman and Kumar (2019). The coding of this algorithm has been carried out based on a group of seagulls shifting from one place to another during the migration phase, and the strategies that are implemented by them while attacking the prey. In SOA, collision avoidance among searching agents can be achieved by employing an additional parameter "N" to find the position of the new search agent ($\vec{F}_S$) given as

$$\vec{F}_S = N\chi\vec{D}_S(t). \tag{14}$$

The current position of the seagull is represented with $\vec{D}_S$, and "t" indicates the current iteration. The collision avoidance variable "N" can be modeled as

$$N = E_c - (t*(E_c/\text{Max.Iter})). \tag{15}$$

The value of the collision avoidance parameter is chosen as "2" in this work to govern the change in a variable that can be reduced linearly from E_c to 0. Upon finishing the phenomena of avoidance in the collision mechanism, the search agents try to move closer to the position of the best individual using

$$\vec{M}_S = A\chi\left(\vec{P}_{bs}(t) - \vec{D}_S(t)\right). \tag{16}$$

The parameter "A" is randomized to achieve the tendency of equilibrium among the phases of exploitation and exploration and can be calculated as

$$A = 2*N^2*\text{rand}(). \tag{17}$$

Later, the position of each search agent will be updated as follows:

$$\vec{R}_S = \left|\vec{F}_S + \vec{M}_S\right|. \tag{18}$$

While migrating, seagulls regularly change their speed and attacking angle based on experience. In the plane of three dimensions, the behavior of seagull's migration can be modeled as

$$S' = r*\text{Cos}(j), \tag{19}$$

$$T' = r*\text{Sin}(j), \tag{20}$$

$$U' = r*j. \tag{21}$$

"r" indicates the radius of seagulls' movement in spiral, and "j" is the randomized number chosen in the range of (0–2). After saving the best solution, the remaining searching agent's positions will be updated as

$$\vec{D}_S(k) = \left(\vec{M}_S*S'*T'*U'\right) + \vec{P}_{bs}(k). \tag{22}$$

The procedure involved in SOA optimization is pictorially represented in **Figure 6**. SOA is implemented for other engineering optimization problems and no literature has been reported so far in the domain of LFC to the best of the authors' knowledge. The intelligent behavior of seagulls motivated the authors to implement the searching strategy of SOA for the LFC study.

RESULTS AND DISCUSSIONS

Case-1: Dynamical Analysis of Test System-1

Evidently, the supremacy of the proposed FOFPID controller optimized with the SOA approach, a rigorously utilized model of the DARTS system in the literature, is considered and the analysis is carried out upon laying 10% SLP in area-1. In addition to the proposed control scheme, other control approaches that are listed in the literature such as PSO-based PI (Magid and Abido, 2003), BFOA-optimized PID (Ali and Elazim, 2015), FOPID ($PI^{\lambda}D^{\mu}$) fine-tuned with GA (Delassi et al., 2018), HAEFA-based PID (Sai Kalyan et al., 2020), and FPID rendered with DE (Sahu et al., 2015b) are used as regulators one after the other. System responses under various approaches to the same disturbance are displayed in **Figure 7** to obtain a comparative analysis. Responses are numerically interpolated because of settling time and the optimal controller gains are placed in **Table 2**. Observing **Figure 7** and explaining the numerical results in **Table 2** exposed the dominance of the presented SOA-based FOFPID controller in minimizing the response deviations and also the time taken to reach a steady condition. This is possible only because the SOA searching mechanism that inherits the potentiality of keeping equilibrium between exploration and exploitation facilitates optimally locating the parameters of FOFPID in reducing control error. The objective value with the presented searching scheme is also greatly enhanced by 56.23% with PSO, 43.5% with BFOA, 27.3% with GA, 23.4%

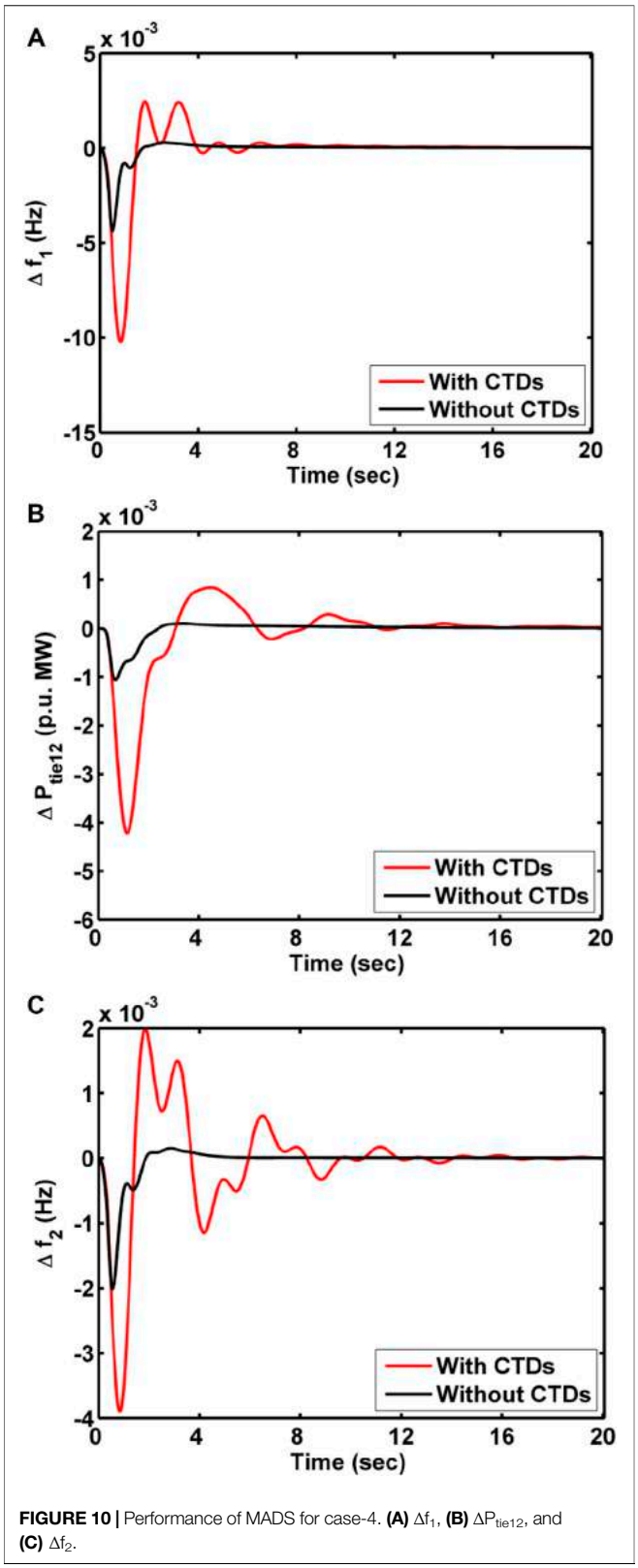

FIGURE 10 | Performance of MADS for case-4. **(A)** Δf_1, **(B)** ΔP_{tie12}, and **(C)** Δf_2.

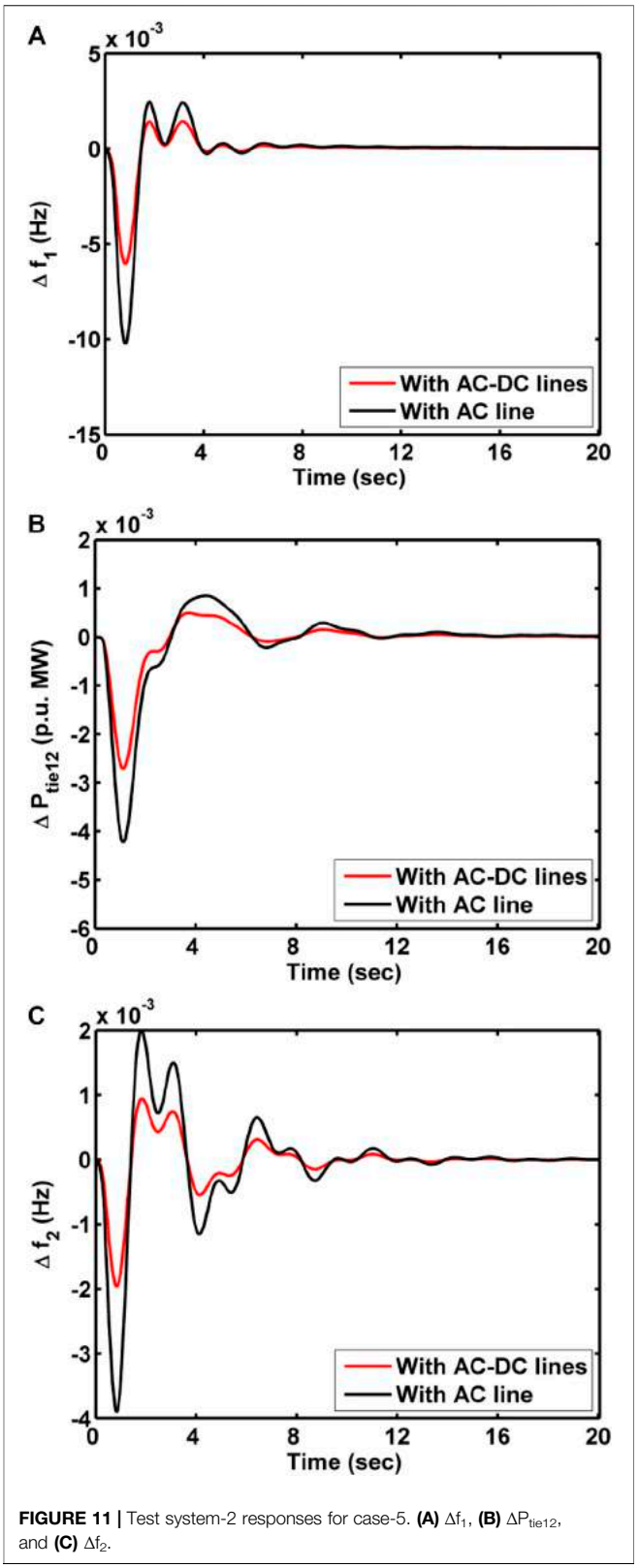

FIGURE 11 | Test system-2 responses for case-5. **(A)** Δf_1, **(B)** ΔP_{tie12}, and **(C)** Δf_2.

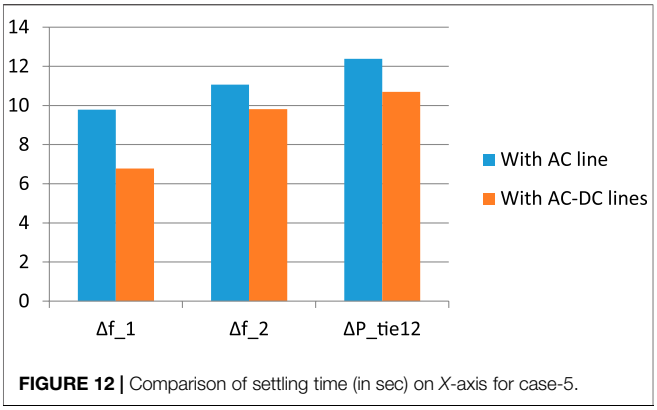

FIGURE 12 | Comparison of settling time (in sec) on *X*-axis for case-5.

with HAEFA, and 16.5% with DE approaches available in the literature.

Case-2: Dynamical Analysis of Test System-2 Without Considering CTDs

Later, the implementation of the proposed SOA-tuned FOFPID controller is assessed on another realistic test system model of MADS system, the practical constraint of GRCs is considered, and the CTDs are not perceived for this case. Controllers such as PID/FOPID/FPID/FOFPID are consecrated as regulators in every area one after the other, and the parameters are optimally located with the SOA searching strategy. The dynamical analysis is conducted by applying MADS system with 10% SLP on area-1, and the responses are comparatively rendered in **Figure 8**. Noting the MADS system dynamical behavior displayed in **Figure 8**, that the FOFPID regulator outperforms PID/FOPID/FPID controllers is visualized and is more dominant in regulating system dynamical behavior in aspects of settling time noted in **Table 3**. Moreover, the responses peak undershoots are improvised with FOFPID (Δf_1 = 0.0041 Hz, ΔP_{tie12} = 0.0009 Pu.MW, Δf_2 = 0.0019 Hz) compared to those of FPID (Δf_1 = 0.0051 Hz, ΔP_{tie12} = 0.0016 Pu.MW, and Δf_2 = 0.0024 Hz), FOPID (Δf_1 = 0.0087 Hz, ΔP_{tie12} = 0.00285 Pu.MW, and Δf_2 = 0.0043 Hz), and traditional PID (Δf_1 = 0.0123 Hz, ΔP_{tie12} = 0.00537 Pu.MW, and Δf_2 = 0.0054 Hz).

Case-3: Dynamical Analysis of Test System-2 With Considering CTDs

The MADS system is considered with CTDs along with another nonlinear feature of GRCs, for analysis purposes in this case. Variations of MADS system responses under different controllers optimized with SOA strategy are shown in **Figure 9**, and the employed gains are displayed in **Table 4**. Responses are interpreted numerically from a settling time point of view and are placed in **Table 3**. Observing **Figure 9** and **Table 3**, we concluded that under the situations of nonlinearity also, the proposed controller exhibits superior performance in damping out the oscillations that are induced in the system responses due to CTDs consideration. Moreover, the proposed controller drags down the system response deviations to a steady-state position quickly compared to other methodologies. Furthermore, the peak undershoots of the responses are improvised with FOFPID (Δf_1 = 0.0099 Hz, ΔP_{tie12} = 0.0040 Pu.MW, and Δf_2 = 0.0036 Hz) compared to those of FPID (Δf_1 = 0.0193 Hz, ΔP_{tie12} = 0.0089 Pu.MW, and Δf_2 = 0.0095 Hz), FOPID (Δf_1 = 0.022 Hz, ΔP_{tie12} = 0.0094 Pu.MW, and Δf_2 = 0.01373 Hz), and traditional PID (Δf_1 = 0.0212 Hz, ΔP_{tie12} = 0.0088 Pu.MW, and Δf_2 = 0.0144 Hz).

Case-4: Revealing the CTDs Impact on Test System-2 Performance

To visualize the constraint CTD's impact on system performance, MADS system responses under the supervision of the FOFPID regulator, which was already established as the best from the aforementioned analysis, are compared in **Figure 10** for the same disturbance conditions. From **Figure 10**, it is revealed that the CTDs have a significant impact on frequency fluctuations and deviations in power flow through the tie-line in the LFC problem. Because considering CTDs means a delay in signal reception and transmission between different devices at various locations. CTDs delay the sending of area control error signal (ACE) to the secondary controller, resulting in the shift of the power system operating point with some delay. This results in more deviations in the frequency and tie-line power of the system. Even though the responses of the system are more deviated while perceiving CTDs, it is very much recommended to adopt the nonlinear features of CTDs in the course of designing secondary regulators. Because considering CTDs while designing a secondary controller can regulate the system dynamics to maintain stability. In this work, the parameter of CTDs is deliberated as 0.25 sec of real value. The designed regulator without considering CTDs may not be robust and cannot maintain stability in case of any unpredicted delays induce with the network.

Case-5: Dynamical Analysis of Test System-2 With CTDs and AC-DC Lines

To suppress fluctuations in the power flow of interconnected lines further and to damp out the variations in area frequency, an additional DC is installed with the existing AC line in parallel. During sudden heavy load disturbances, the demand for exchange of power *via* intralines is more and the secondary regulator alone is not adequate to govern frequency deviations. Therefore, a territorial control strategy needs to be employed with the system. Simulation results depicted in **Figure 11** reveal that with the incorporation of the DC line, the fluctuations in system dynamical behavior are damped and undergo steady position in less time compared to the case of employing only the AC line. The settling time of MADS responses with AC and AC-DC lines is indicated in the bar chart in **Figure 12**.

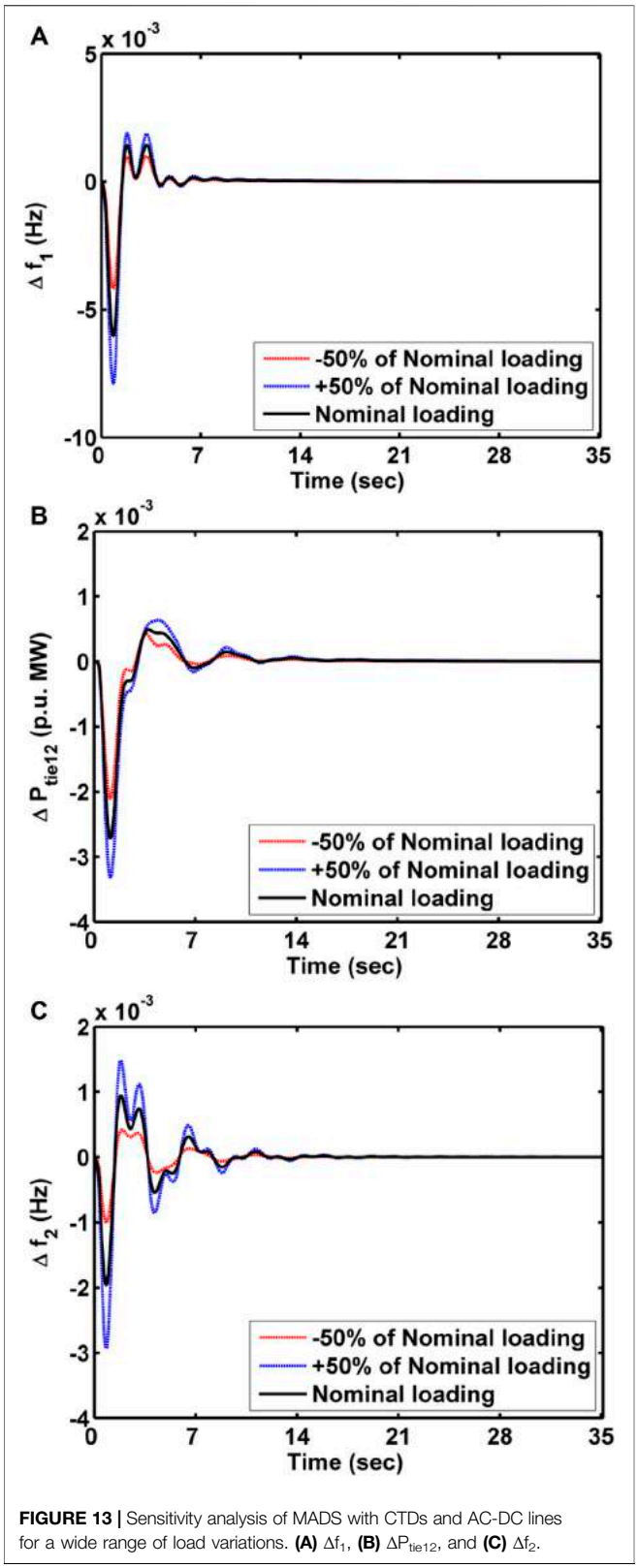

FIGURE 13 | Sensitivity analysis of MADS with CTDs and AC-DC lines for a wide range of load variations. **(A)** Δf_1, **(B)** ΔP_{tie12}, and **(C)** Δf_2.

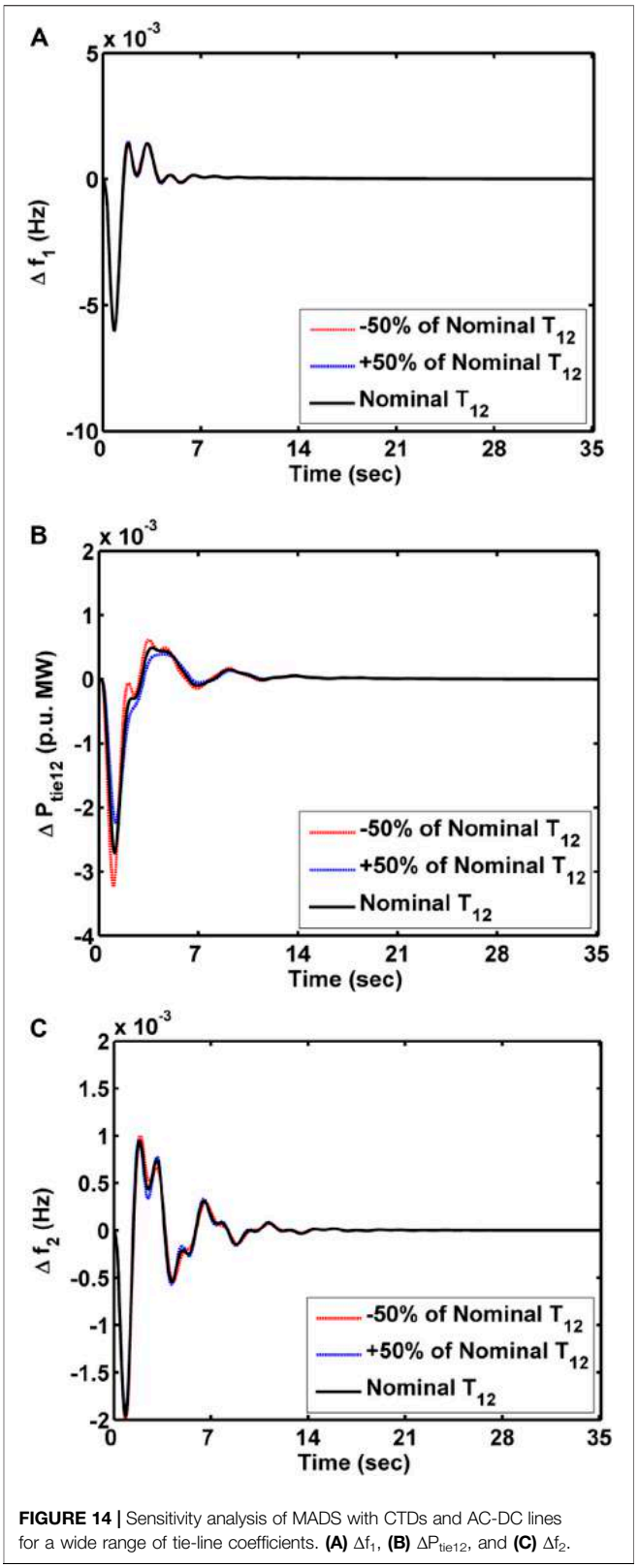

FIGURE 14 | Sensitivity analysis of MADS with CTDs and AC-DC lines for a wide range of tie-line coefficients. **(A)** Δf_1, **(B)** ΔP_{tie12}, and **(C)** Δf_2.

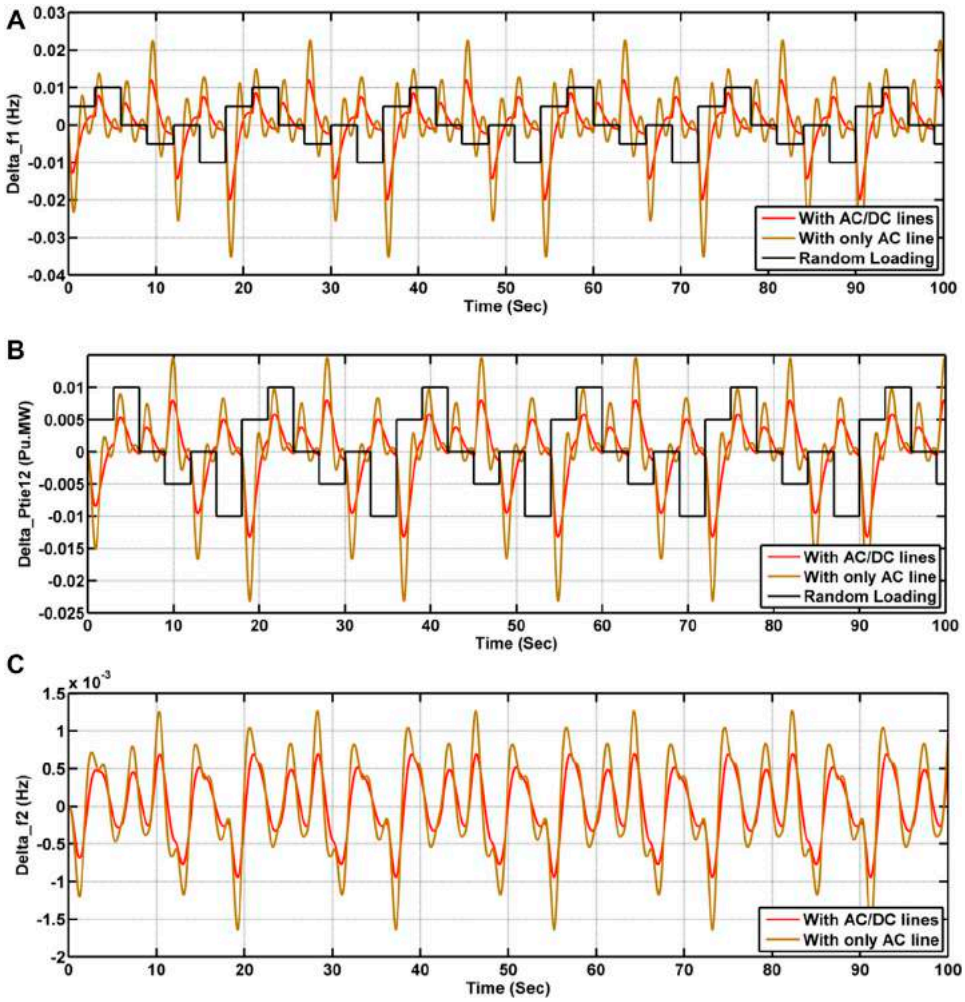

FIGURE 15 | MADS responses under random loading. **(A)** Δf_1, **(B)** ΔP_{tie12}, and **(C)** Δf_2.

Case-6: Sensitivity Analysis

System parameters have been subjected to deviations in ± 50% from nominal parametric values to manifest the robustness of implemented secondary and territorial control schemes. Responses of the system under the control of SOA-tuned FOFPID along with the territorial scheme of AC-DC lines for variations in loading and tie-line coefficient are displayed, respectively, in **Figure 13** and **Figure 14**. The responses are shown in **Figure 13** and **Figure 14**, which conclude that the deviations in responses for wide range loadings do not affect the system performance much. Furthermore, the system is subjugated with a pattern of random loading, and the responses are shown in **Figure 15**. It has been deliberated that the oscillations are supposed to be more damped with the AC-DC line rather than only the AC line. Hence, the presented secondary and territorial control schemes are robust.

CONCLUSION

A novel control scheme of SOA tuned FOFPID is designed and implemented successfully for regulating the frequency of interconnected power system networks. However, the supremacy of the presented control schema is established with other controllers that are implemented on the same power system model of the test system-1 available in recent literature. Moreover, the presented SOA-based FOFPID controller shows remarkable performance in damping out oscillation in tie-line power and frequency of MADS effectively even though the system is perceived with realistic constraints. Moreover, the minimization of the objective function is very finely performed under the presented controller and is enhanced by 70.40, 59.56, and 44.11% with PID, FOPID, and FPID for the case of the MADS system not conceiving CTDs. For the case of conceiving CTDs, the improvisation in objective

function minimization was 50.18, 37.06, and 27.28%, respectively. The CTDs' impact on the performance of MADS is demonstrated clearly and the necessity of perceiving CTDs is justified and convinced. Furthermore, AC-DC tie-lines are established with the MADS system and the performance is enhanced especially due to the ability of the DC line in transferring bulk power during heavy load disturbances. Finally, robustness is validated by conducting the sensitivity test. In the future, there is a lot of scope for assessing the effect of CTDs on LFC performance and the implementation of SOA-based FOFPID for the optimization of IPS in the restructured environment.

DATA AVAILABILITY STATEMENT

The original contributions presented in the study are included in the article/Supplementary Material; further inquiries can be directed to the corresponding author.

AUTHOR CONTRIBUTIONS

The authors have contributed the same in producing this manuscript.

REFERENCES

Alattar, A. H., Selem, S. I., Metwally, H. M. B., Ibrahim, A., Aboelsaud, R., Tolba, M. A., et al. (2019). Performance Enhancement of Micro Grid System with SMES Storage System Based on Mine Blast Optimization Algorithm. *Energies* 12 (16), 3110. doi:10.3390/en12163110

Ali, E. S., and Elazim, S. M. A. (2015). BFOA Based Design of PID Controller for Two Area Load Frequency Control with Nonlinearities. *Int. J. Electr. Power Energy Syst.* 51, 224–231. doi:10.1016/j.ijepes.2013.02.030

Ali, H. H., Kassem, A. M., Al-Dhaifallah, M., and Fathy, A. (2020). Multi-verse Optimizer for Model Predictive Load Frequency Control of Hybrid Multi-Interconnected Plants Comprising Renewable Energy. *IEEE Access* 8, 114623–114642. doi:10.1109/access.2020.3004299

Arya, Y. (2020). A Novel CFFOPI-FOPID Controller for AGC Performance Enhancement of Single and Multi-Area Electric Power Systems. *ISA Trans.* 100, 126–135. doi:10.1016/j.isatra.2019.11.025

Arya, Y. (2019). AGC of PV-Thermal and Hydro-Thermal Power Systems Using CES and a New Multi-Stage FPIDF-(1+PI) Controller. *Renew. Energy* 134, 796–806. doi:10.1016/j.renene.2018.11.071

Arya, Y. (2019). Impact of Hydrogen Aqua Electrolyzer-Fuel Cell Units on Automatic Generation Control of Power Systems with a New Optimal Fuzzy TIDF-II Controller. *Renew. Energy* 139, 468–482. doi:10.1016/j.renene.2019.02.038

Chatterjee, K. (2010). Design of Dual Mode PI Controller for Load Frequency Control. *Int. J. Emerg. Electr. Power Syst.* 11. doi:10.2202/1553-779x.2452

Delassi, A., Arif, S., and Mokrani, L. (2018). Load Frequency Control Problem in Interconnected Power Systems Using Robust Fractional PI λ D Controller. *Ain Shams Eng. J.* 9, 77–88. doi:10.1016/j.asej.2015.10.004

Dhiman, G., and kumar, V. (2019). Seagull Optimization Algorithm: Theory and its Applications for Large-Scale Industrial Engineering Problems. *Knowledge-Based Syst.* 165, 169–196. doi:10.1016/j.knosys.2018.11.024

Fathy, A., and Kassem, A. M. (2019). Antlion Optimizer-ANFIS Load Frequency Control for Multi-Interconnected Plants Comprising Photovoltaic and Wind Turbine. *ISA Trans.* 87, 282–296. doi:10.1016/j.isatra.2018.11.035

Hajiakbari Fini, M., Yousefi, G. R., and Alhelou, H. (2016). Comparative Study on the Performance of Many-objective and Single-objective Optimisation Algorithms in Tuning Load Frequency Controllers of Multi-area Power Systems. *IET Gener. Transm. & Distrib.* 10, 2915–2923. doi:10.1049/iet-gtd.2015.1334

Hanwate, S. D., and Hote, Y. V. (2018). Optimal PID Design for Load Frequency Control Using QRAWCP Approach. *IFAC-PapersOnline.* 51, 651–656. doi:10.1016/j.ifacol.2018.06.170

Irudayaraj, A. X. R., Wahab, N. I. A., Premkumar, M., Radzi, M. A. M., Sulaiman, N. B., Veerasamy, V., et al. (2022). Renewable Sources-Based Automatic Load Frequency Control of Interconnected Systems Using Chaotic Atom Search Optimization. *Appl. Soft Comput.* 119, 108574. doi:10.1016/j.asoc.2022.108574

Kalyan, C., Goud, B., Reddy, C., Ramadan, H., Bajaj, M., and Ali, Z. (2021). Water Cycle Algorithm Optimized Type II Fuzzy Controller for Load Frequency Control of a Multi-Area, Multi-Fuel System with Communication Time Delays. *Energies* 14, 5387. doi:10.3390/en14175387

Kalyan, C. H. N. S., and Rao, G. S. (2021). Impact of Communication Time Delays on Combined LFC and AVR of a Multi-Area Hybrid System with IPFC-RFBs Coordinated Control Strategy. *Prot. Control Mod. Power Syst.* 6. doi:10.1186/s41601-021-00185-z

Kalyan, C. N. S. (2021). "Determination of Appropriate GRC Modelling for Optimal LFC of Multi Area Thermal System," in 2021 IEEE International Power and Renewable Energy Conference (IPRECON), Kollam, India, 24-26 Sept. 2021 (IEEE), 1–6. doi:10.1109/IPRECON52453.2021.9640892

Kalyan, C. N. S., and Rao, G. S. (2021). "Demonstarting the Effect of Excitation Cross Coupling and Communication Time Delays on Automatic Generation Control," in 2021 4th Biennial International Conference on Nascent Technologies in Engineering (ICNTE), NaviMumbai, India, 15-16 Jan. 2021 (IEEE), 1–6. doi:10.1109/ICNTE51185.2021.9487779

Kalyan, C. N. S., and Rao, S. G. (2021c). Coordinated Control Strategy for Simultaneous Frequency and Voltage Stabilisation of the Multi-Area Interconnected System Considering Communication Time Delays. *Int. J. Ambient Energy* 1, 13. doi:10.1080/01430750.2021.1967192

Kalyan, C. N. s., and Suresh, C. V. (2021). "Differential Evolution Based Intelligent Control Approach for LFC of Multiarea Power System with Communication Time Delays," in 2021 International conference on Computing, Communication, and intelligent Systems (ICCCIS), Greater Noida, India, 19-20 Feb. 2021 (IEEE), 868–873. doi:10.1109/ICCCIS51004.2021.9397112

Kalyan, N. S. C., and Rao, S. G. (2020). Frequency and Voltage Stabilisation in Combined Load Frequency Control and Automatic Voltage Regulation of Multiarea System with Hybrid Generation Utilities by AC/DC Links. *Int. J. Sustain. Energy* 39, 1009–1029. doi:10.1080/14786451.2020.1797740

Khezri, R., Oshnoei, A., Oshnoei, S., Bevrani, H., and Muyeen, S. M. (2019). An Intelligent Coordinator Design for GCSC and AGC in a Two-Area Hybrid Power System. *Appl. Soft Comput.* 76, 491–504. doi:10.1016/j.asoc.2018.12.026

Khokhar, B., Dahiya, S., and Parmar, K. P. S. (2021). A Novel Hybrid Fuzzy PD-TID Controller for Load Frequency Control of a Standalone Microgrid. *Arab. J. Sci. Eng.* 46, 1053–1065. doi:10.1007/s13369-020-04761-7

Latif, A., Pramanik, A., Das, D. C., Hussain, I., and Ranjan, S. (2018). Plug in Hybrid Vehicle-Wind-Diesel Autonomous Hybrid Power System: Frequency Control Using FA and CSA Optimized Controller. *Int. J. Syst. Assur Eng. Manag.* 9, 1147–1158. doi:10.1007/s13198-018-0721-1

Madasu, S. D., Kumar, M. L. S. S., and Singh, A. K. (2018). A Flower Pollination Algorithm Based Automatic Generation Control of Interconnected Power System. *Ain Shams Eng. J.* 09 (04), 1215–1224. doi:10.1016/j.asej.2016.06.003

Magid, Y. L. A., and Abido, M. A. (2003). "AGC Tuning of Interconnected Reheat Thermal Systems with Particle Swarm Optimization," in 10th IEEE International conference on Electronics, Circuits and Systems., Sharjah, United Arab Emirates, 14-17 Dec. 2003 (IEEE), 376–379. doi:10.1109/ICECS.2003.1302055

Mohanty, B., and Hota, P. K. (2018). A Hybrid Chemical Reaction-Particle Swarm Optimisation Technique for Automatic Generation Control. *J. Electr. Syst. Inf. Technol.* 5, 229–244. doi:10.1016/J.JESIT.2017.04.001

Nosratabadi, S. M., Bornapour, M., and Gharaei, M. A. (2019). Grasshopper Optimization Algorithm for Optimal Load Frequency Control Considering Predictive Functional Modified PID Controller in Restructured Multi-Resource Multi-Area Power System with Redox Flow Battery Units. *Control Eng. Pract.* 89, 204–227. doi:10.1016/j.conengprac.2019.06.002

Sahu, P. C., Prusty, R. C., and Panda, S. (2020). Approaching Hybridized GWO-SCA Based Type-II Fuzzy Controller in AGC of Diverse Energy Source Multi Area Power System. *J. King Saud Univ. - Eng. Sci.* 32, 186–197. doi:10.1016/j.jksues.2019.01.004

Sahu, R. K., Chandra Sekhar, G. T., and Panda, S. (2015). DE Optimized Fuzzy PID Controller with Derivative Filter for LFC of Multi Source Power System in Deregulated Environment. *Ain Shams Eng. J.* 6, 511–530. doi:10.1016/j.asej.2014.12.009

Sahu, R. K., Gorripotu, T. S., and Panda, S. (2015). A Hybrid DE-PS Algorithm for Load Frequency Control under Deregulated Power System with UPFC and RFB. *Ain Shams Eng. J.* 6, 893–911. doi:10.1016/j.asej.2015.03.011

Sai Kalyan, C. N., Rao, G. S., and Rao, G. S. (2020). Coordinated SMES and TCSC Damping Controller for Load Frequency Control of Multi Area Power System with Diverse Sources. *ijeei* 12, 747–769. doi:10.15676/ijeei.2020.12.4.4

Shankar, G., and Mukherjee, V. (2016). Load Frequency Control of an Autonomous Hybrid Power System by Quasi-Oppositional Harmony Search Algorithm. *Int. J. Electr. Power & Energy Syst.* 78, 715–734. doi:10.1016/j.ijepes.2015.11.091

Sharma, M., Dhundhara, S., Arya, Y., and Prakash, S. (2021). Frequency Stabilization in Deregulated Energy System Using Coordinated Operation of Fuzzy Controller and Redox Flow Battery. *Int. J. Energy Res.* 45 (2), 7457–7475. doi:10.1002/er.6328

Sharma, Y., and Saikia, L. C. (2015). Automatic Generation Control of a Multi-Area ST - Thermal Power System Using Grey Wolf Optimizer Algorithm Based Classical Controllers. *Int. J. Electr. Power & Energy Syst.* 73, 853–862. doi:10.1016/j.ijepes.2015.06.005

Tungadio, D. H., and Sun, Y. (2019). Load Frequency Controllers Considering Renewable Energy Integration in Power System. *Energy Rep.* 5, 436–453. doi:10.1016/j.egyr.2019.04.003

Yakout, A. H., Attia, M. A., and Kotb, H. (2021). Marine Predator Algorithm Based Cascaded PIDA Load Frequency Controller for Electric Power Systems with Wave Energy Conversion Systems. *Alexandria Eng. J.* 60, 4213–4222. doi:10.1016/j.aej.2021.03.011

Zhang, X., Tan, T., Zhou, B., Yu, T., Yang, B., and Huang, X. (2021). Adaptive Distributed Auction-Based Algorithm for Optimal Mileage Based AGC Dispatch with High Participation of Renewable Energy. *Int. J. Electr. Power & Energy Syst.* 124, 106371. doi:10.1016/j.ijepes.2020.106371

Zhang, X., Xu, Z., Yu, T., Yang, B., and Wang, H. (2020). Optimal Mileage Based AGC Dispatch of a Genco. *IEEE Trans. Power Syst.* 35 (04), 2516–2526. doi:10.1109/tpwrs.2020.2966509

Conflict of Interest: The authors declare that the research was conducted in the absence of any commercial or financial relationships that could be construed as a potential conflict of interest.

Publisher's Note: All claims expressed in this article are solely those of the authors and do not necessarily represent those of their affiliated organizations, or those of the publisher, the editors, and the reviewers. Any product that may be evaluated in this article, or claim that may be made by its manufacturer, is not guaranteed or endorsed by the publisher.

IEEE Access
Multidisciplinary | Rapid Review | Open Access Journal

Received April 25, 2022, accepted May 13, 2022, date of publication May 18, 2022, date of current version May 27, 2022.

Digital Object Identifier 10.1109/ACCESS.2022.3176370

Location Determination of Electric Vehicles Parking Lot With Distribution System by Mexican AXOLOTL Optimization and Wild Horse Optimizer

CH. S. V. PRASAD RAO[1], A. PANDIAN[1], (Senior Member, IEEE), CH. RAMI REDDY[2], (Member, IEEE), FLAH AYMEN[3], MOHAMMED ALQARNI[4], AND MOSLEH M. ALHARTHI[5]

[1]Department of Electrical and Electronics Engineering, Koneru Lakshmaiah Education Foundation, Guntur, Andhra Pradesh 522502, India
[2]Department of Electrical and Electronics Engineering, Malla Reddy Engineering College (Autonomous), Secunderabad, Telangana 500100, India
[3]National Engineering School of Gabès, Processes, Energy, Environment and Electrical Systems, LR18ES34, University of Gabès, Gabès 6072, Tunisia
[4]College of Engineering, University of Business and Technology (UBT), Jeddah 21361, Saudi Arabia
[5]Department of Electrical Engineering, College of Engineering, Taif University, Taif 21944, Saudi Arabia

Corresponding author: A. Pandian (pands07@kluniversity.in)

This work was supported in part by the University of Business and Technology Researchers Supporting Program, Jeddah, Saudi Arabia; in part by Taif University, Taif, Saudi Arabia, through the Taif University Researchers Supporting Project under Grant TURSP 2020/122; and in part by the National Engineering School of Gabès, University of Gabès, Tunisia, under Project PEJC2022.

ABSTRACT In this manuscript proposes a hybrid approach for locating and sizing Electric vehicle charging stations (EVCSs) optimally and managing the vehicle charging process. The proposed hybrid approach is to work in conjunction with Mexican Axolotl optimization (MAO) and Wild Horse Optimizer (WHO) hence it is named as MAOWHO approach. The major purposes of the proposed approach are to site and size of the electric vehicle parking lot (EVPL) and to improve the benefit of EVPL for the participation of the reserve market. In addition, power loss and voltage fluctuations occur due to the stochastic nature of renewable energy sources (RES) and electric vehicles (EV) demand load, which is reduced by the proposed approach. To optimally determine the size of the parking lot, the MAOWHO approach is adopted. The integration of the EV and PV systems, especially in parking lots, enhances the reliability and flexibility of the electrical system at critical moments. Multiple objective optimization problems are calculated to achieve objective variables to reduce power losses, voltage fluctuations, charging and supply costs, and EV costs. The location and capacity of the RES and EV charging stations in this optimization problem are objective variables. The MAOWHO approach enhances Solar Powered Electric Vehicle Parking Lot (EVSPL) participation in various energy and ancillary service markets that includes the effects of capacity payments. Besides, the implementation of MAOWHO approach is done by the MATLAB/Simulink platform and the performance of the MAOWHO approach is compared to the existing approaches. From the simulation outcome, it concludes that the proposed approach based performance provides a profit of 880 €compared to other approaches like SMO, CGO, SBLA.

INDEX TERMS Ancillary service, electric vehicles, photovoltaic panels, electric vehicle charging stations, EV parking lot, EV owners.

I. INTRODUCTION

In recent years, the demand for fossil fuels has increased with the transportation sector and power plants [1]. Utilizing these resources not only leads to higher costs but hence also causes greenhouse gas (GHG) emissions along with environmental pollution [2]. The demand for fuel in the transportation sector is increasing year by year, and this significant demand is increasing the cost as well as air pollution [3]. Therefore, several countries prefer green vehicles over internal

The associate editor coordinating the review of this manuscript and approving it for publication was Muhammad Zakarya.

combustion cars. Compared to petrol vehicles, electric vehicles (EVs) are more environmentally peaceful and economically viable [4].In the construction of these vehicles, advanced battery and power electronics equipment are used, which allows the use of EVs in the network as controllable loads, which play the role of energy saving systems (ESS) to support the network. [5]. This can be done by vehicle to grid (V2G), and it is initially used by participating in market and ancillary services that regulate the revenue and expenditure model [6]. Because of high load and drop voltage across specific sensitivity network buses, the penetration of EVs into the power grid presents challenges like thermal control violation of the transmitting lines and uncertainty of demand [7].

According to various studies, 95% of vehicles during the day are in the parking system, therefore, by V2G this capability is used for frequency and voltage control [8]. Revenue for vehicle owners is available through the participation of vehicles in V2G [9]. Moreover, V2G mode is also utilized to mitigate network challenges using the capabilities of EVs and PHEV charging stations [10]. At these stations, vehicles reap the benefits of recharging their batteries and selling the surplus storing energy on the grid [11]. Controlling the charging and discharging of vehicles in different ways such as altering energy charges at dissimilar time intervals [12]. RES has been gaining value in recent years as an alternative to fossil fuel power plants [13]. Due to the present of these resources close to the load, minimization of losses, voltage fluctuations and investment costs is obtained [14].

Because of the randomness of the RES production can pose challenges to the wide penetration, and grid of these resources [15]. Hence, to support the network must be required the high capacity energy storage systems [16]. On this basis, charging stations with V2G on the network are established like ESS. The excess energy generated from RES is stored in the charging stations as well as in a timely manner the stored energy is transmitted to the power grid [17]. This will distribute these resources and diminish the pressure on the distribution network [18]. Smart grid with the best possible arrangement of RES and PHEV charging stations can diminish emissions rates and effectively meet many technical and economic challenges [19]. There are various approaches like optimization, linear modeling, etc., are introduced based on V2G usage in power systems as well as charging stations. Some optimization algorithms like GA, PSO, and other optimization algorithms could not be modified to provide the total solution depending on valve point impact, restricted operating zones, and functional quadratic cost by parts. Optimization indicates the ruling procedure of better feasible solutions to particular problems [20]. The above-alluded optimization strategies have often been determinable including major problems, and local optimum entrapment. They are obliquity in terms of algorithm, and derivation of search space required. It creates inefficiency in solving real problems. This refers to the motivation of these processes, which are inspired by nature and implemented by new algorithms competing with the current optimization model. Here, a newly suggested hybrid optimization algorithm like Mexican Axolotl optimization (MAO) and Wild Horse Optimizer (WHO), named as MAOWHO approach. An integrated method is used to avoid the weakness caused by the optimization strategies' application. Hence, the hybrid approach provides a better outcome.

This manuscript proposes a hybrid MAOWHO for locating and sizing Electric vehicle charging stations (EVCSs) optimally and managing the vehicle charging process. The proposed hybrid approach is to work in conjunction with MAO and WHO hence it is named as MAOWHO approach. In addition, power loss and voltage fluctuations occur due to the stochastic nature of renewable energy sources (RES) and electric vehicles (EV) demand load, which is reduced by the MAOWHO approach. The remaining manuscript is described below. Section 2 describes the bibliographic survey and its background. Section 3 describes the configuration of the integrated PV and EV system in SG. Section 4 describes the proposed approach-based power quality improvement; Section 5 describes the result and discussion. Section 6 concludes the manuscript.

II. RECENT RESEARCH WORK: A BRIEF REVIEW

In the literature, various research works were available depending on the optimal allocation of electric vehicle charging space using various techniques and aspects. Some of them are reviews were followed:

Biogeography-based optimization (BBO) approach for EV charging spots was presented by S. Sachan *et al.* [21]. The concurrent management of congestion and the compensation of reactive power were achieved by allocating parking and a capacitor. Through the utilization of inverse Jacobian matrix, performed the sensitivity analysis of the system. Aggarwal and A. Kumar [22] have studied the installation of a fast-charging station in the IEEE 24-bus testing system. The major aim of the transportation sector was the achievement of low-carbon, green transportation, and sustainable development. The introduced model analysis the placement of CS based on various power rates like 5, 25, 50, and 100 MW with consideration of the limit of voltage magnitude as well as a rating of line.

Newton–Raphson (NR) approach was utilized by the introduced model to analyze the case studies. The power fluctuations, problems of power quality etc. were occurring the random charging of EVs. The losses were eliminated by the correct sitting and sizing of DGs. Berg*et al.* [23] have suggested a method for calculating the future EV fleets demand and the flexibility in the office area. Compared to residential charging, office charging was different. There was 42 EVs charging was considered to analyze the demand of the system. By considering the network capacity and forecasted load because of EV charging, the placement of charging stations was performed. Turan*et al.* [24] has studied the integration of PV, EVPL based on consumption of power, losses, and operating condition of the distribution system. The design

of the parking lot was performed for EVs as well as energy was given from the grid and PV. The design of the energy management system was performed for the management of EVs charging under day and seasons with solar radiation data. Through the consideration of the charging sequence of the various car brands, power consumption dependent on EV was calculated. The main purpose of the introduced system is to reduce power consumption, and voltage level improvement; minimize the peak and continuous demand of power of the EVPL.

Bouguerra*et al.* [25] have suggested 5 Integer Linear Programs depending on a weighted set covering models for planning of EV charging infrastructure. The major purpose of the introduced approach was to site and size EVCSs, to access EV chargers easily by drivers in a small range. The introduced model was considered the investment cost reduction and convenience of EV users'. Li *et al.* [26] have suggested an improved genetic algorithm (GA) for locating the public CSs. The introduced approach was considering the investment and travel costs of EV owners. Through the feedback integration among the CS and the geographical area, the demand for electric ride-hailing was considered. The introduced approach was considering the multi-population GA. Mohammadi *et al.* [27] have suggested optimization-dependent issues for the calculation of size and place of EVPL and the scheduling of charging and discharging of EVs in PLs. The introduced approach has considered the costs like purchasing energy from the grid, and EV charging in PLs. Moreover, the distribution system constraints were considered by the introduced approach. Here is proposed the hybrid MAOWHO approach. The advantage of the MAO approach is very good with unimodal and multimodal optimization functions, Easy to implement, Bypass local minima, does not require information about the gradient of the objective function, and solves a wide range of problems in various fields. The disadvantage of MAO is, that for composite functions, it has an average performance. The advantage of the WHO approach is good ability to solve the problems, greater efficiency, used to solve several real problems use in different fields of study, simplicity, ease of use, along with its effective and efficient results. The disadvantage of WHO is, that it is a single-objective algorithm, it will be essential to develop a binary and multi-objective version of the proposed algorithm. Mortaz *et al.* [46] have suggested mixed-integer nonlinear programming for investment planning for Vehicle-to-Grid (V2G) technology in a microgrid. The economic reliability of EV was enhanced by the V2G technology because it permitted the microgrid to take advantage of temporal arbitrage in the electricity market. Effects of uncertainty, investors preferred payback period, market price fluctuations, and electric vehicles arrival and departure rates were analyzed. The author only focused on the V2G facilitates while its facilities to participate in ancillary services markets could further enhance economic benefits. H Khalkhali and S Hosseinian [47] have developed a three-stage scheduling framework based on stochastic programming and MPC for operating the EV parking lots. This work only focused on the price of energy for the economic inputs and did not consider participating in ancillary services markets. Li*et al.* [48] have suggested spatiotemporal interaction of EVs with RES power system. The major contribution of the introduced approach was cost reduction. This work focused on RES but the storage technologies were not utilized.

A. BACKGROUND OF THE RESEARCH WORK

The implementation of EVPL is a challenging one which has been demonstrated in a review of recent research work. In the power system, RESs provide various advantages but EV integration with RES is challenging. It causes the instability of the system. Variability and uncertainty are the disadvantages of PV and the quality of power is decreased by EVs, therefore, it overloads the power system and interferes with the regular power system. To reduce the impact of the integration of RES and EVs, at the same time increase the flexibility of the power system, mitigating the environmental impacts various approaches are introduced. The integration of EV into the parking lot and optimizing their charging against time-of-use tariffs is important recently. Various approaches are utilized to reduce the cost and increase the profit of the system. Some of them are GA, particle swarm optimization (PSO), GA-PSO hybrid algorithm, differential evolution (DE), and chemical reaction optimization (CRO). Additionally, the location of EVCS is determined by the linear integer optimization model but because of low voltage huge current flows, power loss in a distribution network was extreme. Moreover, different types of charging facilities are adjusted to meet different charging requests, which complicate the spatial and temporary distribution of EV charging requests, thus emphasizing the need to identify effective approaches for optimal planning for EVCSs.

III. CONFIGURATION OF ELECTRIC VEHICLE WITH PV SYSTEM

In this manuscript, the smart grid utilizing commercial buildings is considered. These buildings are comprised of PV related to the grid. Moreover, the EVCS is set up in the parking area which is powered by photovoltaic [28]. The major purposes of MAOWHO are the site and sizing of EVPL and to improve the benefit of EVPL for the participation of the reserve market. For this purpose, this manuscript proposed a hybrid approach, which is the joint operation of both the MAO and WHO. Fig. 1 depicts the configuration of EV and PV. The MAOWHO approach investigates the energy market problems, EVPL characteristics depend on input data such as transportation patterns and energy market prices. EVPL's profit is maximized by the utilization of EVPL by the owner's contracts of the EVs, which are interconnected between revenues. The distribution system supplies power to existing EVPL charging stations in various locations. EVs are connected to a power supply system for charging/discharging EVs through charging stations [29].

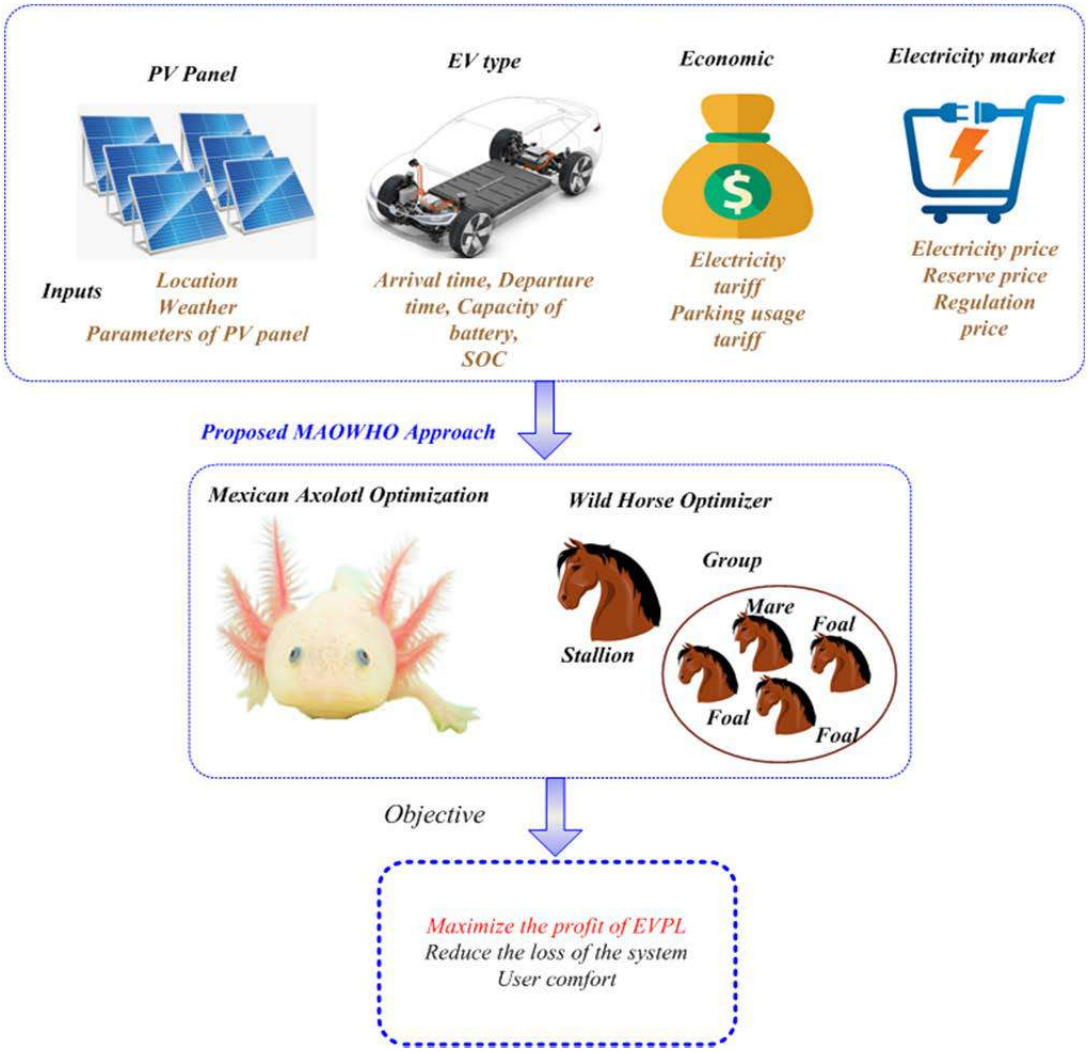

FIGURE 1. Configuration of proposed EVPL With distribution system.

Based on the uncertainty associated with the weather conditions, various PV power generation scenarios are constructed.

The proposed approach is to determine the output of energy such as V2G, G2V, revenue, and EVSPL operating costs. The MAOWHO approach considers parameters such as weather conditions and owners' uncertainty tables for EVs. Furthermore, it provides an optimal strategy for EVSPL implementation, taking into account the perspective of the owners of the EVs and the EVSPL operator, as well as for the convenience of the owner of EVs, it increases the profitability of providing services to the grid. Therefore, EVPL's optimal site is used to promote sustainable transportation systems and buildings to promote electric vehicles and sustainable buildings. Energy efficiency, as well as sustainable energy production and consumption, is improved by the EVPL. EV input is considered as arrival/departure time, EV battery capacity, and SoC, the input of PV is the radiation of the solar, which is considered the season and location, economically electricity tariff, parking utility tariff, and energy price in the electricity market, reserve price, and regulatory price increase/decrease are considered in the proposed system.

A. MODELING OF PV MODULE

PV power generation is high based on the local weather during the day, solar radiation varies [30]–[33]. The maximum outcome of the PV system is obtained by using the PV module parameters which are described in the following equations (1),

$$p_{t,\varphi}^{pv} = v_{t,\varphi}^{op} \times i_{t,\varphi}^{sc} \times f_f \tag{1}$$

Here, fill factor is denoted as f_f, PV unit short circuit current is denoted as $i_{t,\varphi}^{sc}$, PV unit open circuit voltage is denoted as $v_{t,\varphi}^{op}$, tilt angle is denoted as φ and time as t, the open circuit voltage of the PV is described by (2),

$$v_{t,\varphi}^{op} = v_{stc}^{op} - k_v \times T_t^c \tag{2}$$

Here, open circuit voltage of the PV system in standard test condition is denoted as v_{stc}^{op}, voltage coefficient is denoted as k_v, the instantaneous cell temperature is denoted as T_t^c., the above equation is rewritten as (3),

$$v_{t,\varphi}^{op} = \left\{ i_{t,\varphi}^{sc} + k_i \times \left[T_t^c - 25^o C \right] \right\} \times \frac{g_{t,\varphi}}{1000} \tag{3}$$

Here, short-circuit current temperature coefficient is denoted as k_i, global solar irradiance is denoted as $g_{t,\varphi}$. The instantaneous cell temperature is described by (4),

$$T_t^c = T^A + \left(T^{noct} - 20^o C \right) \times \frac{g_{t,\varphi}}{800} \tag{4}$$

Here, ambient temperature is denoted as T^A, the nominal operating cell temperature is denoted as T^{noct}. The fill factor is described by (5),

$$f_f = \frac{p^{mpp}}{v^{op} \times i^{sc}} \tag{5}$$

Here, power at maximum power point is denoted as p^{mpp}, open circuit voltage is denoted as v^{op}, and short circuit current implies i^{sc}. The total PV power is described as (6),

$$p_{t,\varphi}^{Tot.pv} = \eta^{pv} \times n^s \times n^p \times p_{t,\varphi}^{pv} \tag{6}$$

Here, the efficiency of the PV module is denoted as η^{pv}, the count of the PV module connected in series is denoted as n^s, count of the PV module connected in parallel is denoted as n^p. Additional control was provided to control the transmission of electricity as PV to the parking lot which is described by (7),

$$\begin{aligned} p_{t,\varphi}^{Tot.pv} &\le p_{W,t}^{pv2pl} \\ &\le SoC^{Max} \times \alpha_{tot,t}^{EVs} - \left(SoC_{W,t-1} + \beta_{tot,t}^{Soc,EV} \right) \end{aligned} \tag{7}$$

Here, net EVs SoC is denoted as $\beta_{tot,t}^{Soc,EV}$, the total Capacity of EVs in EVPL is denoted as $\alpha_{tot,t}^{EVs}$, W as a scenario, under the maximum SoC of the EVPL, the power transmission to EVPL is based on the newly arrived/departed EVs state of charge (SOC).

B. MODELING OF ELECTRIC VEHICLE PARKING LOT (EVPL)

Because of the various uncertainties like every EV arrival/departure times, and the arrival time EV SoC [34], the EVPL operation is controlled by various limits. Power injection from the grid to PL is described by (8),

$$p_{W,t}^{g2pl} + p_{W,t}^{pv2pl} + p_{W,t}^{r-down} \le \chi^{Ch} \times N_{W,t}^{EV} \tag{8}$$

Here, the rate of charge of the parking lot is denoted as χ^{Ch}, the amount of parked EVs is denoted as $N_{W,t}^{EV}$, power from PV to PL is denoted as $p_{W,t}^{pv2pl}$, power from the grid to PL is denoted as $p_{W,t}^{g2pl}$, Ramp down power is denoted as $p_{W,t}^{r-down}$, the number of EV in EVPL is denoted as $N_{W,t}^{EV}$. Power injection from PL to the grid is described by (9),

$$p_{W,t}^{pl2g} + p_{W,t}^{Rsr,Act} + p_{W,t}^{r-up} \le \chi^{DCh} \times N_{W,t}^{EV} \tag{9}$$

Here, Ramp up-regulation power is denoted as $p_{W,t}^{r-up}$, rate of discharge of the parking lot is denoted as χ^{DCh}, and injection on the reserve activated by ISO is denoted as $p_{W,t}^{Rsr,Act}$. EVSPL cannot simultaneously transfer and inject power which is described by (10),

$$u_t^{g2pl} + u_t^{pl2g} \le 1 \tag{10}$$

The SoC of EVPL based on scenario and time is described by (11),

$$\begin{aligned} SoC_{W,t}^{pl} = SoC_{W,t-1}^{pl} &+ SoC_{W,t}^{Arr} - SoC_{W,t}^{Dep} \\ &+ \left(p_{W,t}^{pl2g} + p_{W,t}^{pv2pl} + p_{W,t}^{r-down} \right) \times \eta^{Ch} \\ &- \frac{p_{W,t}^{pl2g} + p_{W,t}^{Rsr-Act} + p_{W,t}^{r-up}}{\eta^{DCh}} \end{aligned} \tag{11}$$

The SoC of EVPL is depending on the factors like SoC as before, the power interactions utilize the grid [35], [36], EVs SoC is one of the arriving/departing EVs. The arriving EV SoC is described as (12)

$$SoC_{W,t}^{Arr} = \begin{cases} 0, & SoC_{W,t}^{Scenar} \le SoC_{W,t-1}^{Scenar} \\ SoC_{W,t}^{Scenar} - SoC_{W,t-1}^{Scenar}, & SoC_{W,t}^{Scenar} < SoC_{W,t-1}^{Scenar} \end{cases} \tag{12}$$

The departing EV SoC is described as (13),

$$SoC_{W,t}^{Dep} = \begin{cases} 0, & SoC_{W,t-1}^{Scenar} \le SoC_{W,t}^{Scenar} \\ \dfrac{\left(SoC_{W,t-1}^{Scenar} - SoC_{W,t}^{Scenar} \right) SoC_{W,t}}{SoC_{W,t}^{Scenar}}, & SoC_{W,t}^{Scenar} < SoC_{W,t-1}^{Scenar} \end{cases} \tag{13}$$

Here, the energy stored in EVPL achieved as input displays are denoted as $SoC_{W,t}^{Scenar}$ which is described by (14),

$$SoC_{W,t}^{Scenar} = \sum \alpha_{W,t}^{EVs} \times SoC_{W,t}^{EV} \tag{14}$$

Here, the capacity of the EV battery is denoted as $\alpha_{W,t}^{EVs}$, SoC of the EV battery is denoted as $SoC_{W,t}^{EV}$. The additional EV SoC, while EV stays in EVPL, is described by (15),

$$SoC_{W,t}^{Up} = \begin{cases} 0, & SoC_{W,t}^{Dep} \le SoC_{W,t}^{Scenar} - SoC_{W,t-1}^{Scenar} \\ SoC_{W,t}^{Dep} - SoC_{W,t}^{Scenar} - SoC_{W,t-1}^{Scenar}, & Otherwise \end{cases} \tag{15}$$

The amount of energy absorbed from an EV is described by (16),

$$SoC_{W,t}^{Down} = \begin{cases} 0, & SoC_{W,t}^{Scenar} - SoC_{W,t-1}^{Scenar} \le SoC_{W,t}^{Dep} \\ SoC_{W,t}^{Dep} - SoC_{W,t}^{Scenar} - SoC_{W,t-1}^{Scenar}, & Otherwise \end{cases} \tag{16}$$

The constraint of SOC of EVPL is described as (17),

$$\sum SoC_{Min}^{EV} \le SoC_{W,t} \le \sum SoC_{Max}^{EV} \tag{17}$$

C. MODELING OF DISTRIBUTION SYSTEM

By utilizing the energy balance equation, the proposed EVPL should meet and maintain the integrity of distribution systems [37]–[39]. Here considered the active as well as reactive power of the system. The purpose of the energy balance modeling is the minimization the loss of the system. The active power based on the power flow is described by (18),

$$\begin{aligned} p_{l,t,W}^{Sub.tx} + P_{l.t,W}^{RES} - \sum_{m}\left(p_{l,m,t,W}^{+} + P_{l.m,t,W}^{-}\right) + r_{l,m} \\ \times i_{l.m,t,W}^{2} + \sum_{m}\left(p_{l,m,t,W}^{+} + P_{l.m,t,W}^{-}\right) + p_{W,t}^{pl2g} \\ = p_{l,t}^{d} + p_{W,t}^{g2pl} \end{aligned} \tag{18}$$

Here, active powers of the branch lm when going downstream and upstream is denoted as $p_{l,m,t,W}^{+}, P_{l.m,t,W}^{-}$, Sub transmission power is denoted as $p_{l,t,W}^{Sub.tx}$, RES power is denoted as $P_{l.t,W}^{RES}$, resistance is denoted as $r_{l,m}$, the square of the current flow is denoted as $i_{l.m,t,W}^{2}$. The reactive power balance of the system is described by (19),

$$\begin{aligned} Q_{l,t,W}^{Sub.tx} + Q_{l.t,W}^{RES} - \sum_{m}\left(Q_{l,m,t,W}^{+} + Q_{l.m,t,W}^{-}\right) + x_{l,m} \\ \times i_{l.m,t,W}^{2} + \sum_{m}\left(Q_{l,m,t,W}^{+} + Q_{l.m,t,W}^{-}\right) + p_{W,t}^{pl2g} \\ = Q_{l,t}^{d} + p_{W,t}^{g2pl} \end{aligned} \tag{19}$$

Here, reactive powers of branch lm when going downstream and upstream is denoted as $Q_{l,m,t,W}^{+} + Q_{l.m,t,W}^{-}$.

The constraints of active and reactive power is described as (20-21),

$$0 \geq (p_{l,m,t,W}^{+} - p_{l.m,t,W}^{-}) \leq V^{Nom} \times i_{l,m}^{Max} \tag{20}$$

$$0 \geq (Q_{l,m,t,W}^{+} - Q_{l.m,t,W}^{-}) \leq V^{Nom} \times i_{l,m}^{Max} \tag{21}$$

Here, the nominated amount of voltage is denoted as V^{Nom} maximum transfer capacity is denoted as $V^{Nom} \times i_{l,m}^{Max}$. As described by the equations above, the apparent power flow in each line does not exceed the maximum transmission capacity. System voltage balance is described by (22),

$$\begin{aligned} v_{l,t,W}^{2} - v_{m,t,W}^{2} - z_{l,m}^{2} \times i_{l,m,t,W}^{2} \\ - 2r_{l,m}(p_{l,m,t,W}^{+} - p_{l.m,t,W}^{-}) \\ - 2x_{l,m}(Q_{l,m,t,W}^{+} - Q_{l.m,t,W}^{-}) = 0 \end{aligned} \tag{22}$$

Linear constraints for active and reactive power are described as follows (23),

$$\begin{aligned} v_{l,t,W}^{2,nom} \times v_{l,m,t,W}^{2} \\ = \sum_{f}\left((2F-1) \times \Delta s_{l,m,F,t,W} \times \Delta p_{l,m,F,t,W}\right) \\ + \sum_{f}\left((2F-1) \times \Delta s_{l,m,F,t,W} \times \Delta Q_{l,m,F,t,W}\right) \end{aligned} \tag{23}$$

The power flow constraints is described by (24-28),

$$(p_{l,m,t,W}^{+} - p_{l.m,t,W}^{-}) = \sum_{F} \Delta p_{l,m,F,t,W} \tag{24}$$

$$(Q_{l,m,t,W}^{+} - Q_{l.m,t,W}^{-}) = \sum_{F} \Delta Q_{l,m,F,t,W} \tag{25}$$

$$0 \leq \Delta p_{l,m,F,t,W} \leq \Delta s_{l,m,F,t,W} \tag{26}$$

$$0 \leq \Delta Q_{l,m,F,t,W} \leq \Delta s_{l,m,F,t,W} \tag{27}$$

$$\Delta s_{l,m,F,t,W} = \frac{v^{nom} \times i_{l,m}^{Max}}{f} \tag{28}$$

The distribution system model also includes constraints related to voltage restrictions by $v^2 \leq (v^{nom})^2$. The inequality constraint is described by (29),

$$\Delta s_{l,m,F,t,W} = \frac{v^{nom} \times i_{l,m}^{Max}}{f} \tag{29}$$

D. OBJECTIVE FORMULATION

The objective function of this paper is to reduce the loss of the system and increase the revenue of EVPL. The power loss is shown in the following equation (30).

$$P_{L}^{*} = \sum_{l,m=1}^{n}\left[\upsilon_{lm}(p_{l}^{*}p_{m}^{*} + Q_{l}^{*}Q_{m}^{*}) + \varsigma_{lm}(Q_{l}^{*}p_{m}^{*} - p_{l}^{*}Q_{m}^{*})\right] \tag{30}$$

Here, p_{l}^{*} and q_{l}^{*} implicates active with reactive power injections in bus l, p_{m}^{*} and Q_{m}^{*} specifies active with reactive power injections in bus m, and n specifies the number of buses. There are nine cost function is considered to increase the profit of EVPL, which is described by (31),

$$\begin{aligned} & p_{W,t}^{pv2pl}, p_{W,t}^{pl2g}, p_{W,t}^{g2pl}, p_{W,t}^{Rsr}, p_{W,t}^{Rsr,Act}, \\ & SoC_{W,t}^{Up}, SoC_{W,t}^{Down}\{benefit\ of\ PL\} \\ & = MAX\sum\nolimits_{i}\pi_{i}\sum\nolimits_{t}\left\{p_{W,t}^{pl2g} \times \gamma_{t}^{e} + p_{W,t}^{Rsr} \times \gamma_{W,t}^{c^{EV},Rsr}\right. \\ & \left. + p_{W,t}^{r-Up,Act} \times \gamma_{t}^{r-Up} + p_{W,t}^{r-down,Act} \times \gamma_{t}^{r-down}\right\} \\ & + p_{W,t}^{Rsr,Act} \times \gamma_{t}^{e} + SoC_{W,t}^{Up} \times \gamma_{t}^{tarif,G2V} + N_{t}^{PL} \\ & \times \gamma_{t}^{tarif,sty} - p_{W,t}^{g2pl} \times \gamma_{t}^{e} \\ & - \left(p_{W,t}^{Rsr,Act} \times \zeta^{Rsr} + p_{W,t}^{r-Up} \times \zeta^{r-Up} + p_{W,t}^{r-down}\right. \\ & \left. \times \zeta^{r-down}\right)\gamma_{t}^{e} \times \pi^{unvail} \\ & - p_{W,t}^{Rsr,Act} \times \gamma_{t}^{tarif,V2G} - SoC_{W,t}^{Down} \times \gamma_{t}^{tarif,V2G} \\ & - \left(p_{W,t}^{pl2g} + p_{W,t}^{reg,Act}\right) \times C_{e}^{Degr} - p_{W,t}^{r-Up} \times C_{Reg}^{Degr} \end{aligned} \tag{31}$$

The first cost function depends on providing energy to the electricity market, which means an infusion of energy considering the PL2G, which is described as (32),

$$In(PL_{1}) = \sum_{t} p_{W,t}^{pl2g} \times \gamma_{t}^{e} \tag{32}$$

Here, the electricity cost function is denoted as γ

The second cost function depends on participation in the reserve market which is described as,

$$In(PL_2) = \sum_t p_{W,t}^{Rsr,pl2g} \times \gamma_{W,t}^{c^{EV},Rsr} \quad (33)$$

The third cost function depends on the probability that the system operator will call EVPL to produce the offered reserve which is described as (34),

$$In(PL_3)_{t,W} = \sum_t p_{W,t}^{Rsr,pl2g} \times \gamma_t^{Rsr} \times \pi^{call} \quad (34)$$

The fourth one depends on the charging process of the EV, which means the EV batteries are charged by the EV owner, and the charging cost is paid to PL is described. The income is represented as (35),

$$In(PL_4)_{t,W} = \sum_t \left(p_{W,t}^{pv2pl} + p_{W,t}^{g2pl}\right) \times \gamma_t^{tarif,G2V} \quad (35)$$

Here charging tariff of G2Vis denoted as $\gamma_t^{tarif,G2V}$.

Income obtained from regulation up/ down the phase in the regulatory market is described in the five and sixth incomes (36-37).

$$In(PL_5)_{t,W} = \sum_t p_{W,t}^{reg,pl2g} \times \gamma_t^{c^{EV},r-Up} \quad (36)$$

$$In(PL_6)_{t,W} = \sum_t p_{W,t}^{reg,g2pl} \times \gamma_t^{c^{EV},r-Down} \quad (37)$$

Here, capacity payment regulation up market is denoted as $\gamma_t^{c^{EV},r-Up}$, capacity payment regulation down market is denoted as $\gamma_t^{c^{EV},r-Down}$. The benefit obtained at EVPL usage tariff is defined in the 7th income. That means the owner pay to PL for parking in the EVPL (38).

$$In(PL_7)_{t,W} = \sum_t N_t^{PL} \times \gamma_t^{tarif,sty} \quad (38)$$

Here, the number of EV in EVPL is denoted as N_t^{PL}, average usage tariff is denoted as $\gamma_t^{tarif,sty}$.

Probability of call through the system operator to create regulation in the offered manner as described in 8th and 9th income which is described by (39-40),

$$In(PL_8)_{t,W} = \sum_t p_{W,t}^{reg,g2pl} \times \gamma_t^{r-down} \times \pi^{call} \quad (39)$$

$$In(PL_9)_{t,W} = \sum_t p_{W,t}^{reg,pl2g} \times \gamma_t^{r-up} \times \pi^{call} \quad (40)$$

Consider the cost of the system is also nine terms such as degradation of EV cost, energy buy from the grid, payment of EV owner cost, penalty payable by EVPL, cost of discharge of batteries while participating in the reserve market [40]–[43], cost because of the V2G mode degradation of batteries in energy and regulatory market, lack of EVPL to deliver the energy offered in the regulatory market. Degradation of EVs battery because of the V2G functionality in the reserve market is described by (41),

$$(C_{PL1})_{t,W} = \sum_t p_{W,t}^{Rsr,pl2g} \times C_e^{Degr} \times \pi^{Unvail} \quad (41)$$

The buying energy from the grid means the transmission of energy from the grid to PL is described by (42),

$$(C_{PL2})_{t,W} = \sum_t p_{W,t}^{g2pl} \times \gamma_t^e \quad (42)$$

Participating in V2G mode pays the EV owner for discharging EV batteries is described in the third cost function which describes by (42),

$$(C_{PL3})_{t,W} = \sum_t p_{W,t}^{pl2g} \times \gamma_t^{tariff.G2V} \quad (43)$$

The offered reserves are not delivered due to the unavailability of EVPL's. When the offered reserves are not delivered by the EVPL then it undergoes the penalty cost. It is described by (44),

$$(C_{PL4})_{t,W} = \sum_t p_{W,t}^{Rsr.pl2g} \times \zeta^{Rsr} \times F_{OR}^{PL} \times \gamma_t^{c^{EV},Rsr} \times \pi^{Unvail} \quad (44)$$

Here, EVPL forced outage rate is denoted as F_{OR}^{PL}. Describes the cost of discharging the batteries while participating in the reserve market required for the grid system operator by (45),

$$(C_{PL5})_{t,W} = \sum_t p_{W,t}^{Rsr.pl2g} \times \gamma_t^{tariff,G2V} \times \pi^{Unvail} \quad (45)$$

Because of the V2G mode, degradation of batteries in energy and the regulatory market dependent cost is described by (46-47),

$$(C_{PL6})_{t,W} = \sum_t p_{W,t}^{pl2g} \times C_e^{Degr} \quad (46)$$

$$(C_{PL7})_{t,W} = \sum_t p_{W,t}^{reg.pl2g} \times C_e^{reg} \quad (47)$$

Here, the degradation cost of EV batteries due to the operation of the energy market is denoted as C_e^{Degr}; the degradation cost of EV batteries due to the operation of regulation V2G mode is denoted as C_e^{reg}.

The unavailability of EVPL to deliver the energy supplied in the regulatory market depends on the last 2 cost functions. If EVPL offer regulations are unavailability then it has the penalty cost, which is described by (48-49),

$$(C_{PL8})_{t,W} = \sum_t p_{W,t}^{reg.pl2g} \times \zeta^{r-Up} \times \pi^{Unvail} \times F_{OR}^{PL} \times \gamma_t^e \quad (48)$$

$$(C_{PL9})_{t,W} = \sum_t p_{W,t}^{reg.pl2g} \times \zeta^{r-down} \times \pi^{Unvail} \times F_{OR}^{PL} \times \gamma_t^e \quad (49)$$

IV. LOSS REDUCTION AND PROFITINGENHANCEMENT OF EVPL USING THE PROPOSED MAOWHO APPROACH

The proposed EVPL model is utilized the hybrid MAOWHO Approach. it is the combined execution of MAO and WHO. The major purposes of the proposed approach are site and sizing of EVPL and improving the benefit of EVPL for the participation of the reserve market. The proposed approaches

investigate the energy market problems, EVPL characteristics depend on input data such as transportation patterns and energy market prices. EVPL's profit is maximized by the utilization of EVPL by the owner's contracts of the EVs, which are interconnected between revenues. The distribution system supplies power to existing EVPL charging stations in various locations. EVs are connected to a power supply system for charging/discharging EVs through charging stations. Based on the uncertainty associated with the weather conditions, various PV power generation scenarios are constructed. The proposed approach is to determine the output of energy such as V2G, G2V, revenue, and EVSPL operating costs. The MAOWHO approach considers parameters such as weather conditions and owners' uncertainty tables for EVs. Furthermore, it provides an optimal strategy for EVSPL implementation, taking into account the perspective of the owners of the EVs and the EVSPL operator, as well as for the convenience of the owner of EVs, it increases the profitability of providing services to the grid. A detailed description of the proposed approach is given below.

A. MEXICAN AXOLOTL OPTIMIZATION ALGORITHM BASED LOSS REDUCTION

The MAO algorithm is the metaheuristic algorithm inspired by the life of the axolotl [44]. It is inspired by the birth, breeding, and restoration of the tissues of the axolotls, as well as the way they live in the aquatic environment. As axolotls are sexed creatures, the population is divided into males and females. Also, consider the ability of axolotls to alter their color, and we consider they alter their body parts' color to camouflage them and avoid predators. The MAO algorithm operates in four iterative stages, defined by the TIRA acronym: Transition from larvae to the adult state, Injury and restoration, Reproduction, and Assortment. In this paper, the loss is minimized by the algorithm for maximum power extraction and increases the efficiency of the proposed system. The step-by-step process is described below.

1) STEP 1: INITIALIZATION

Initialize the size, female population, male population, damage probability, regeneration probability, differential constant, tournament size, termination criteria.

2) STEP 2: RANDOM GENERATION

Generate the population in a random manner

3) STEP 3: FITNESS CALCULATION

It is based on the objective function, in which the loss of the system is minimized (50).

$$F_c = Min\left(P_L^*\right) \tag{50}$$

4) STEP 4: CLASSIFICATION OF MALE FEMALE POPULATION

The individuals are assigned as male and female due to axolotls developing according to their sex, and two subpopulations are obtained.

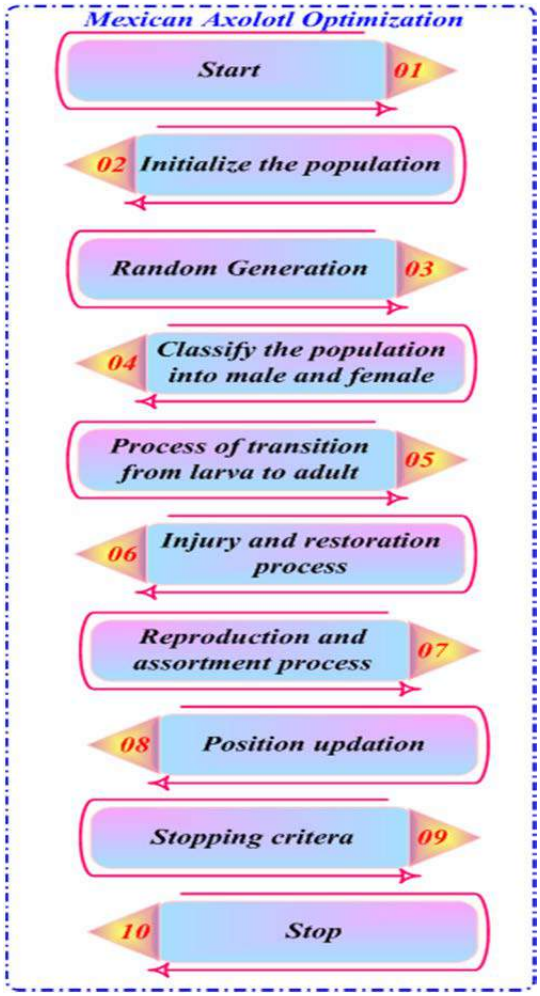

FIGURE 2. Flow chart of proposed Mao approach.

5) STEP 5: TRANSITION FROM LARVAE TO ADULT STATE

Then, the Transition from larvae to adult begins. Male individuals will transition in water, from larvae to adult, by adjusting their body parts 'color towards the male who is best adapted to the environment.

In this stage, choose the best male and female axolotls based on the objective function

Find the inverse probability of transition for male and female (51)

$$p(M, F)_j = \frac{Obj(M_j, F_j)}{\sum Obj(M_j, F_j)} \tag{51}$$

- Update the male and female populations

If the probability value of males is greater than the random value then update the male population by (52),

$$M_{ji} = M_{ji} + M_{best,i} - M_{ji} * \alpha \tag{52}$$

Otherwise, Change the body color of male axolotl by (53),

$$M_{ji} = Min_i + Max_i - Max_j * R_i \tag{53}$$

Here, Transition parameter is represented as α, male axolotl is denoted as M_j, random number as R_i

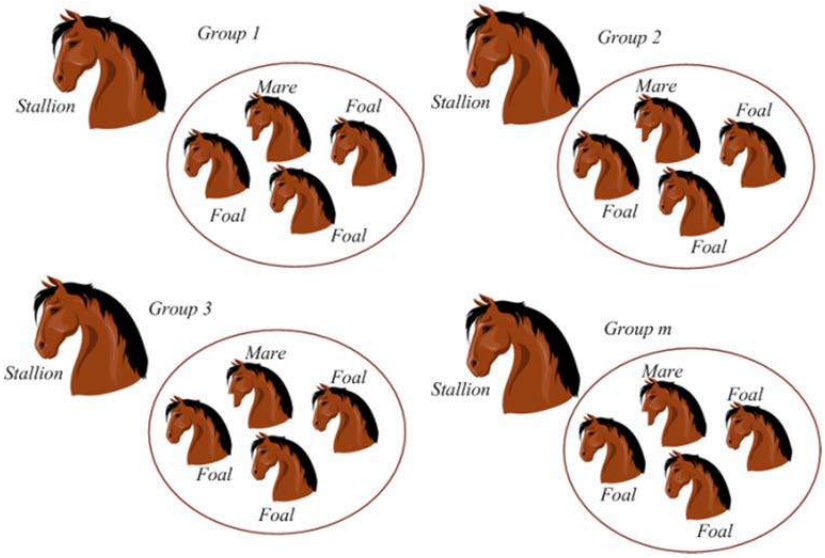

FIGURE 3. Formation of horse groups tailored to the initial population.

If the probability value of female is less than the random value then update the female population by (54),

$$F_{ji} = F_{ji} + F_{best,i} - F_{ji} * \alpha \tag{54}$$

Otherwise find the coloured axolotl value (55),

$$F_{ji} = Min_i + (Max_i - Max_i) * R_i \tag{55}$$

Through this calculation update the best value of male and female.

6) STEP 6: PROCESS OF INJURY AND RESTORATION

When moving the axolotls into the water, they can be prone to accidents and injuries it is the injury stage of axolotls. When the probability is damaged then, its part is lost. Then go to the regeneration process which is described as (56)

$$\bar{P}_{ji} = Min_i + (Max_i - Max_i) * R_i \tag{56}$$

7) STEP 7: PROCESS OF REPRODUCTION AND ASSORTMENT

The male lays the sperm and the female collects them Gloca to put them in her sperm. Assume it lays two eggs. After hatching the eggs, then starts the assortment process. If the young larva is best then it is replaced in the best position.

8) STEP 8: CHECK THE STOPPING CRITERIA

If terminations criteria are satisfied then find the optimal solution otherwise go to step 3.

B. WILD HORSE OPTIMIZER BASED MAXIMIZATION OF PROFIT OF EVPL

The wild horse is a species of the genus Equus, which includes as subspecies the modern domesticated horse as well as the undomesticated European wild horse, and the endangered Przewalski's horse [45]. Fig. 3 shows the Formation of horse groups tailored to the initial population.

1) STEP 1: INITIALIZATION

Initialize the input parameters like arrival/departure time, EV battery capacity, SoC, electricity tariff, parking utility tariff and energy price in the electricity market, reserve price, and regulatory price up/down, iteration demandEVPL numbers.

2) STEP 2: RANDOM GENERATION

Randomly generate the initialized parameter in the matrix form

$$Y = \begin{bmatrix} f_1\left[cd^{11}(t) & cd^{12}(t) & \dots & cd^{1m}(t)\right] \\ f_2\left[cd^{21}(t) & cd^{22}(t) & \dots & cd^{2m}(t)\right] \\ \vdots & & \vdots & \\ f_n\left[cd^{n1}(t) & cd^{n2}(t) & \dots & cd^{nm}(t)\right] \end{bmatrix} \tag{57}$$

3) STEP 3: FITNESS EVALUATION

The fitness is chosen based on the objective function

$$F(t) = Min(C) + MAx(\text{Pr}\,ofit\ \ PL) \tag{58}$$

Here, C indicate as the addition of degradation of EV cost, energy buy from the grid, payment of EV owner cost, penalty payable by EVPL, cost of discharge of batteries while participating in the reserve market, cost because of the V2G mode degradation of batteries in energy and regulatory market, lack of EVPL to deliver the energy offered in the regulatory market.

4) STEP 4: GRAZING BEHAVIOR

As mentioned in the previous section, foals generally spend most of their time grazing around their company. To practice

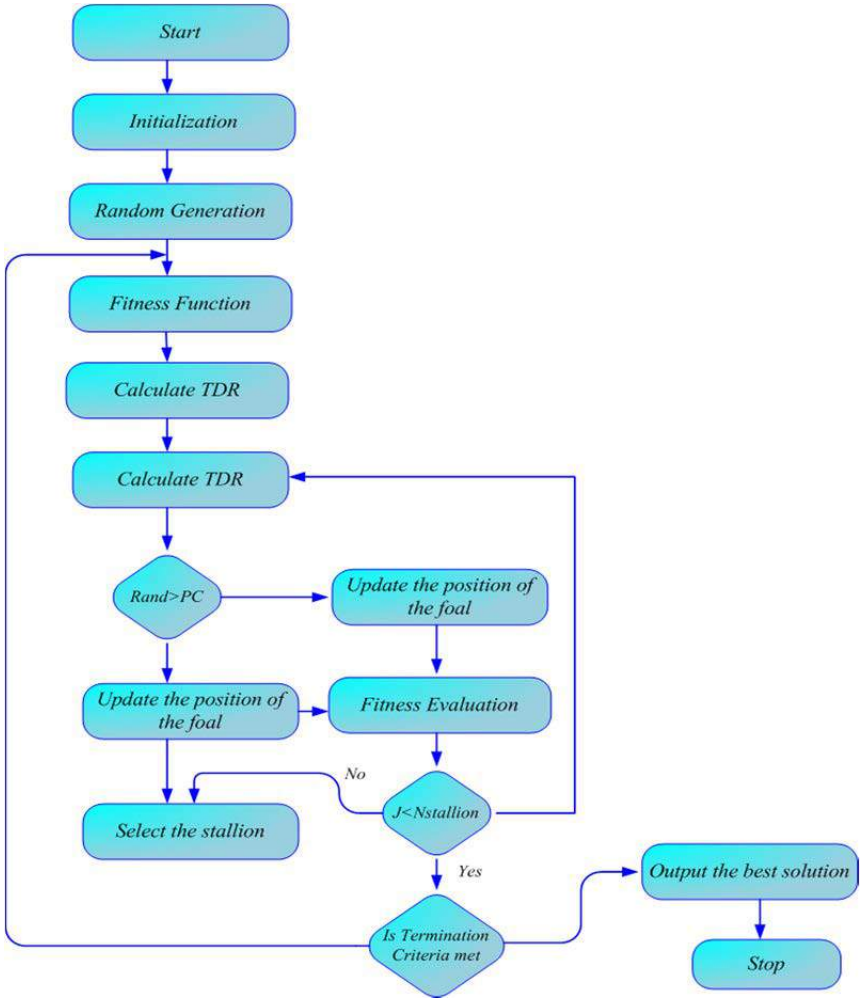

FIGURE 4. Flow chart of wild horse optimization.

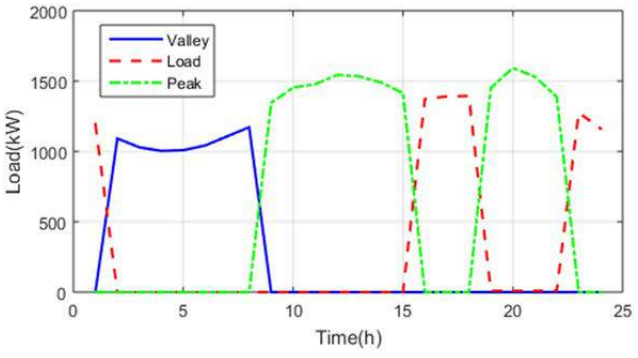

FIGURE 5. Analysis of load with different periods.

grazing behavior, remember that the stallion must be the center of the grazing area, and the individuals of the company are looking for the center (grazing).

5) STEP 5: HORSE MATING BEHAVIOR

One of the most precise behaviors of horses, when compared to different animals, is the behavior of isolating foals and mating. Foals leave the institution earlier than achieving puberty, male foals be a part of the institution of unmarried horses, and lady foals be a part of some other own circle of relatives institution to attain puberty and locate their mate.

6) STEP 6: GROUP LEADERSHIP

The institution chief ought to lead the institution to an appropriate place. We remember this appropriate place to be the water hollow. The institution ought to circulate in the direction of this water hollow. Other businesses circulate in an equal manner in the direction of the water hollow. The leadership is competing for this water hollow as the dominant institution utilizes this water hollow, different businesses aren't allowed to apply the water hollow till the domination institution actions away.

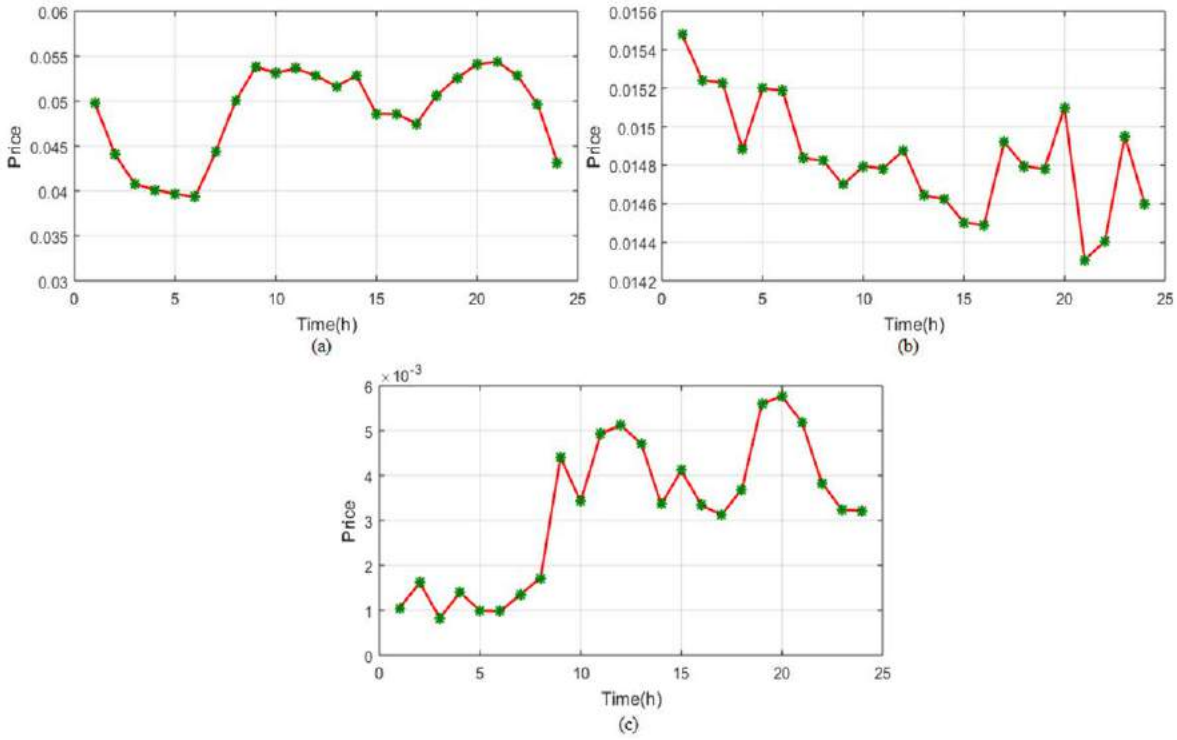

FIGURE 6. Analysis of prices of electricity market in winter (A) Energy price (B) Reserve price (C) Capacity payment.

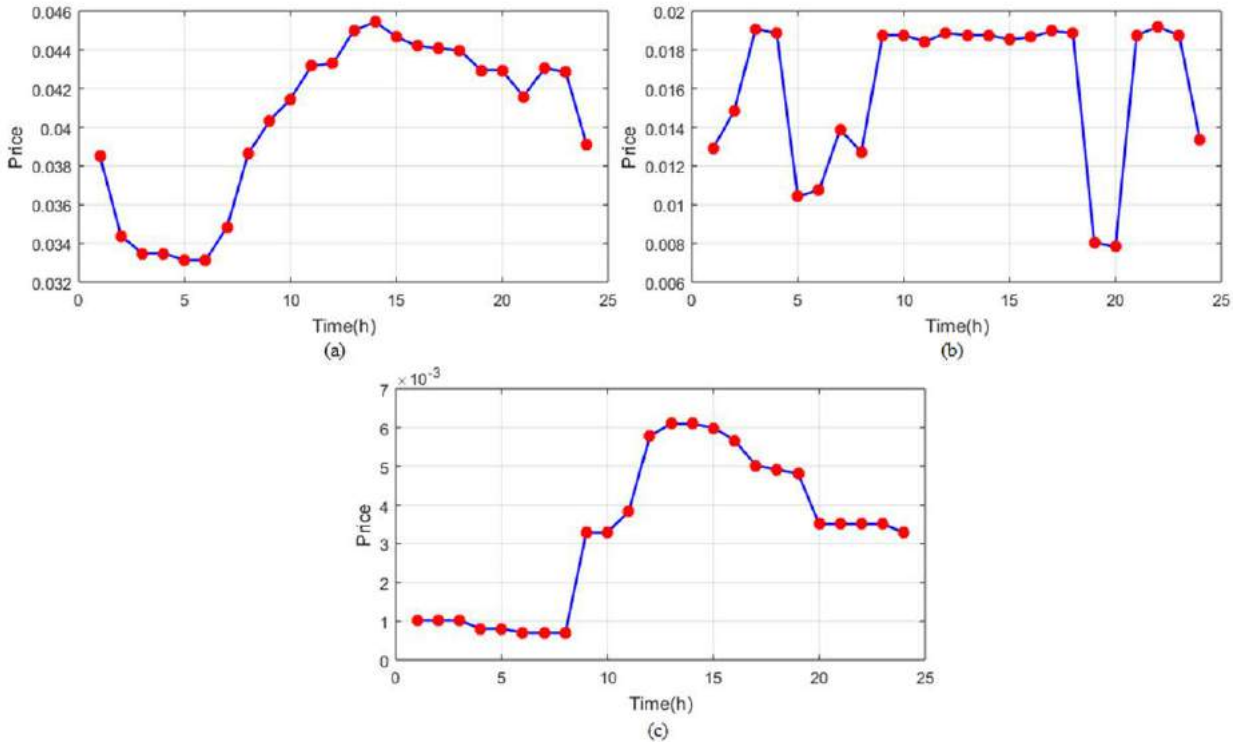

FIGURE 7. Analysis of prices of electricity market in summer (A) Energy price (B) Reserve price (C) Capacity payment.

7) STEP 7: EXCHANGE AND CHOICE OF LEADERS

First, the leadership must be randomly selected keeping in mind the randomness of the algorithm. In the later levels of the algorithm, leadership is primarily purely dependent on health. If one of the institution participants is healthier than the institution chief, the chief location and its members

will change. Fig. 4 shows the flow chart of the proposed WHO approach.

V. RESULTS AND DISCUSSIONS

In this manuscript, describe the performance of the proposed MAOWHO based on the simulation outcome. To increase the profit, and reduce the loss, the cost in this paper proposed a hybrid MAOWHO approach. The proposed approach is simulated in MATLAB Simulink Platform and the performance of the proposed approach is analyzed under three scenarios Without PV generation on both summer and winter seasons, PV on a winter day, PV on a summer day. The capacity payment was also analyzed. The cases with and without capacity payment are considered for the analysis of the proposed system. Finally, the proposed approach is compared to the existing approach. Parameters of the MAO-WHO Approach are tabulated in Table 1.

TABLE 1. Parameters of the MAO-WHO approach.

Parameters of WHO	
Number of population	100
Stallion % or Number of groups	0.2
Crossover %	0.13
Maximum number of iteration	100
Parameters of MAO	
Male population	60
Female population	60
Maximum number of iteration	100

Analysis of load with different periods is shown in Fig.5. Here the load is analyzed under three different periods like valley-period (2 to 8h), off-peak period (16 to 18 h and 23 to 1 h), and peak period (9 to 15 h, 19 to 22 h). In the valley period, the load varies up to 1200 kW, and during the peak hours the load is varied up to 1600 kW and in the off-peak periods, the load is varied up to 1400 kW. Analysis of prices of the electricity market in winter is shown in Fig.6. Subplot 6(a) shows the energy price. The energy price starts at 0.05 €/kWh, then it decreased to reach 0.04 €/kWh at 6 h. After the price is increased to 0.054 €/kWh at 9h and it slowly reduced to 0.0455€/kWh at 17 h. Again the price is increased to 0.054 €/kWh at 21 h, then reduced to 0.044 at 24 h. Subplot 6(b) shows the reserve price. Here, the price is varied from 0.0155 €/kWh in the first hour. Then it reduced and varied from time to time. Subplot 6 (c) displays the capacity of payment. The capacity of payment starts at $1*10^{-3}$€/kWh at 1h. The price is increased at 9 to 20 h. At 12 h, the capacity payment is $5*10^{-3}$€/kWh and At 20 h, the capacity payment is $5.8*10^{-3}$€/kWh. The reserve price is varying from hour to hour.

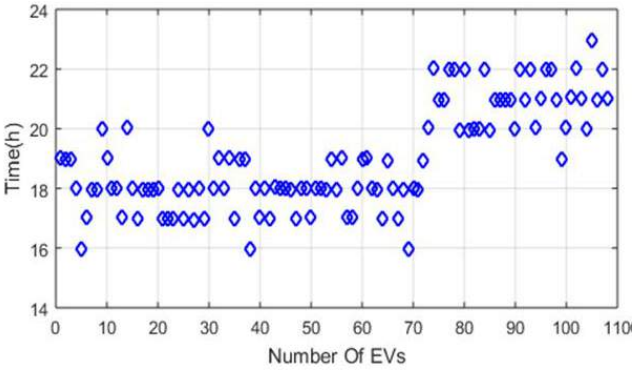

FIGURE 8. Analysis of arrival time of EVS in Pl.

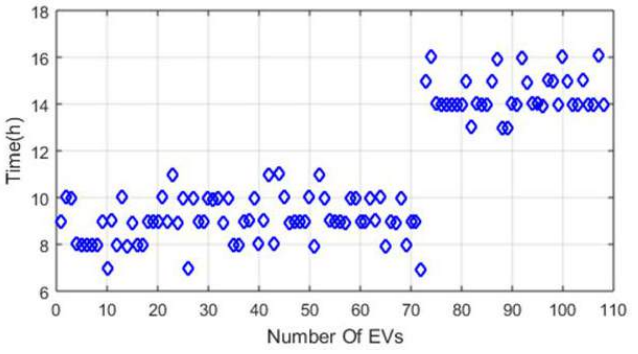

FIGURE 9. Analysis of departure time of EVS in Pl.

Analysis of prices of the electricity market in winter is shown in Fig.7. Subplot 7(a) shows the energy price. The energy price starts at 0.039 €/kWh, then it decreased to reach 0.033 €/kWh at 6 h. After the price is increased to 0.0455 €/kWh at 14 h and it slowly reduced to 0.0415€/kWh at 21 h. Again the price is increased to 0.043 €/kWh at 22 h, then reduced to 0.039 €/kWh at 24 h. Subplot 7(b) shows the reserve price. Here, the price is varied from 0.013 €/kWh in the first hour. Then it increased to 0.019€/kWh in 3rd hour. Then it reduced to 0.012 0.013 €/kWh at 5th hour and it constant to 0.019€/kWh from 9 to 18 h. Again it reduced to 0.008 €/kWh at 20th h. Again it increased to 0.019 €/kWh at 21h. Subplot 7(c) displays the capacity of payment. The capacity of payment starts at $1*10^{-3}$€/kWh at 1 to 3h. The price is increased from 8 to 14 h. At 13 h, the capacity of payment is $6*10^{-3}$€/kWh and At 19 h, the capacity of payment is $4.9*10^{-3}$€/kWh.

Analysis of the arrival time of EVs in PL is displayed in Fig.8. The arrival count of EV is high at the period of 16 to 20 h and the 21 to 22h. Analysis of the departure time of EVs in PL is displayed in Fig.9. Analysis of PV power output during the winter season as well as summer season is displayed in Fig.10. Subplot 10(a) displays winter season PV power. From 1 to 8 h, the PV power is zero. From 9 h onwards, the PV power is increased and it reaches 16 kW at 14 h. After 14 h, the PV power is gradually decreased to reach 0 at 18 h. Subplot 10(b) displays the summer season PV power. From 1 to 5 h, the PV power is zero. From 6 h

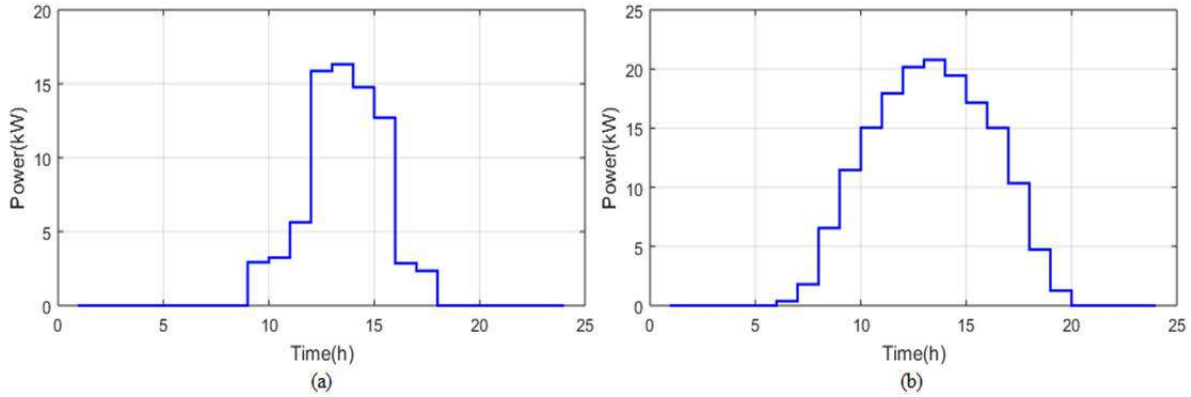

FIGURE 10. Analysis of PV power at (A) Winter (B) Summer.

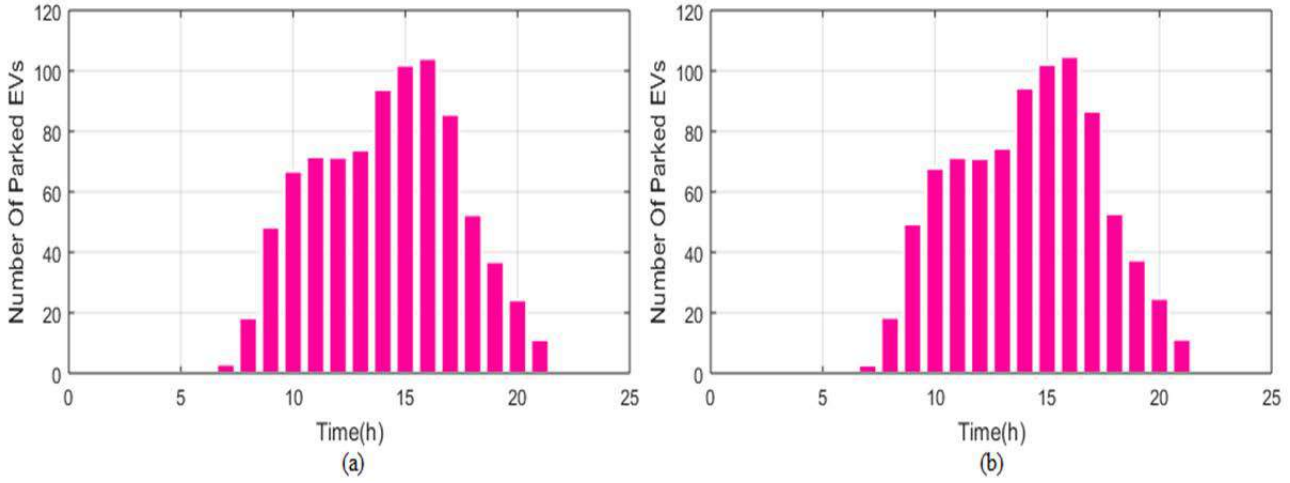

FIGURE 11. Analysis of number of parked EVS (A) Winter (B) Summer.

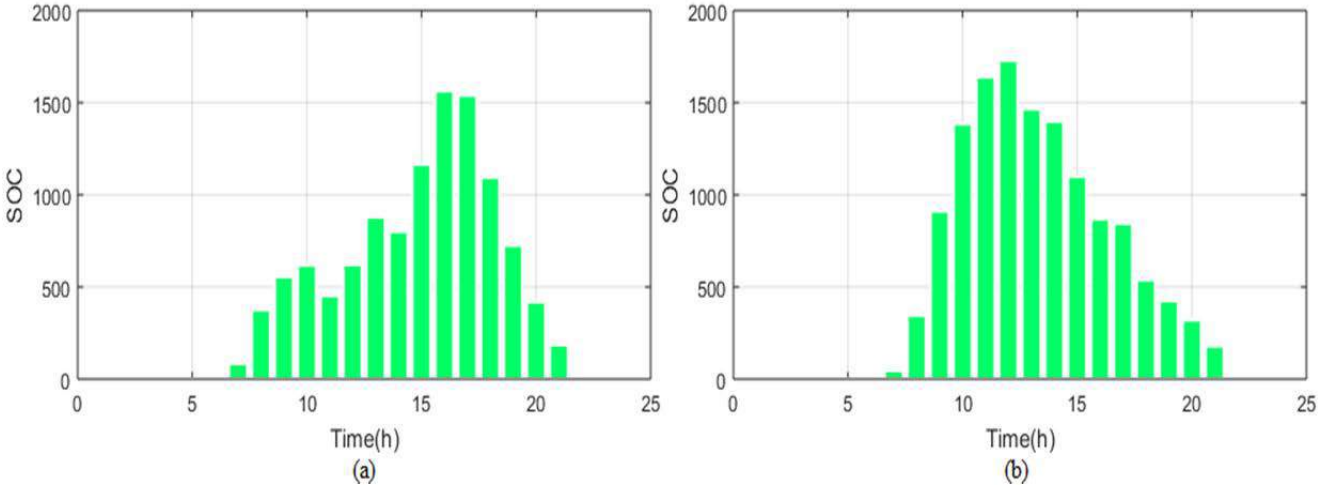

FIGURE 12. Analysis of SOC of EVPL (A) PV in winter (B) PV in summer.

onwards, the PV power is increased and it reaches 21 kW at 14 h. After 14 h, the PV power is gradually decreased to reach 0 at 20 h.

Analysis of several parked EVs during the summer and winter seasons are shown in Fig. 11. Subplot 11(a) displays the number of parked EVs in winter. The number of parked

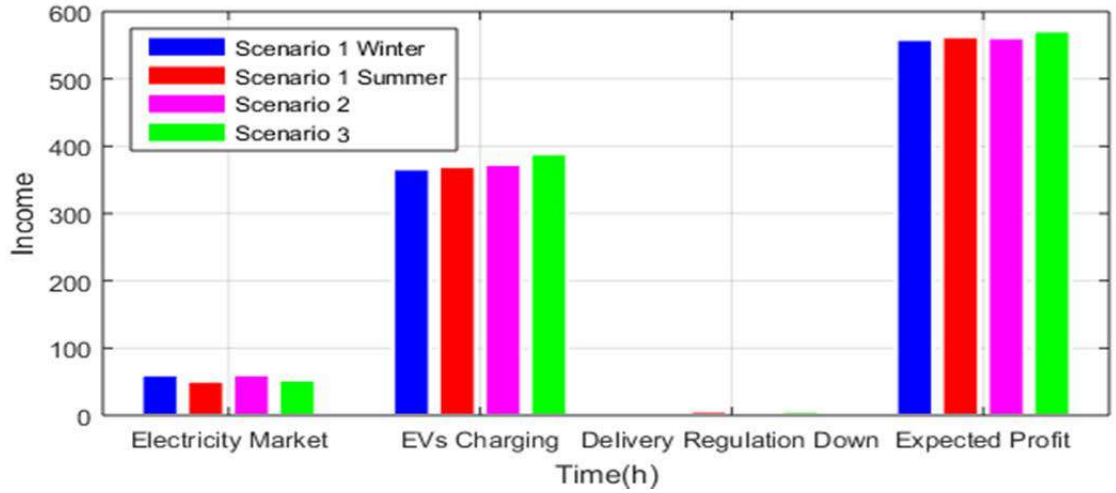

FIGURE 13. Analysis of various EVPL profits.

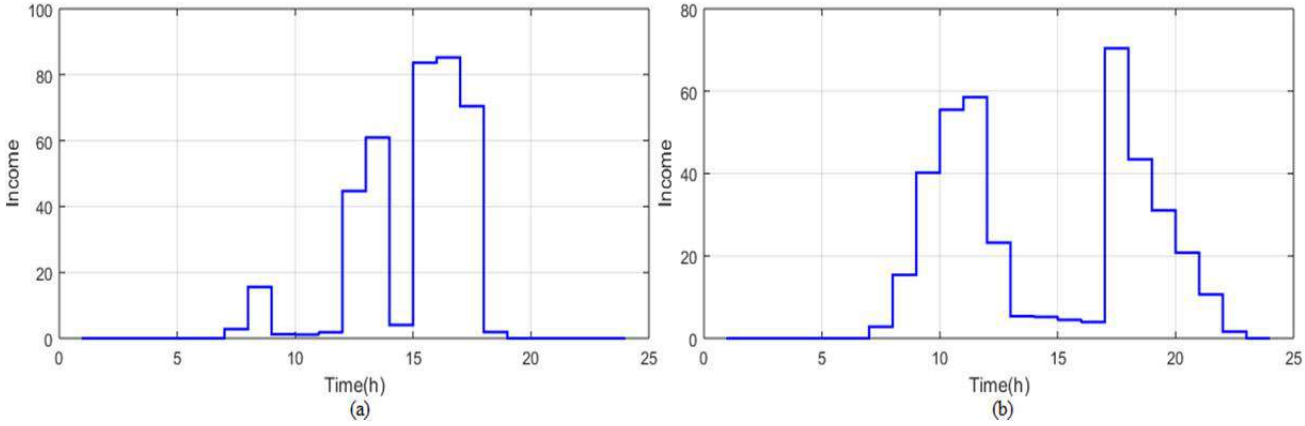

FIGURE 14. Analysis of income from EV Charging (A) PV in winter (B) PV in summer.

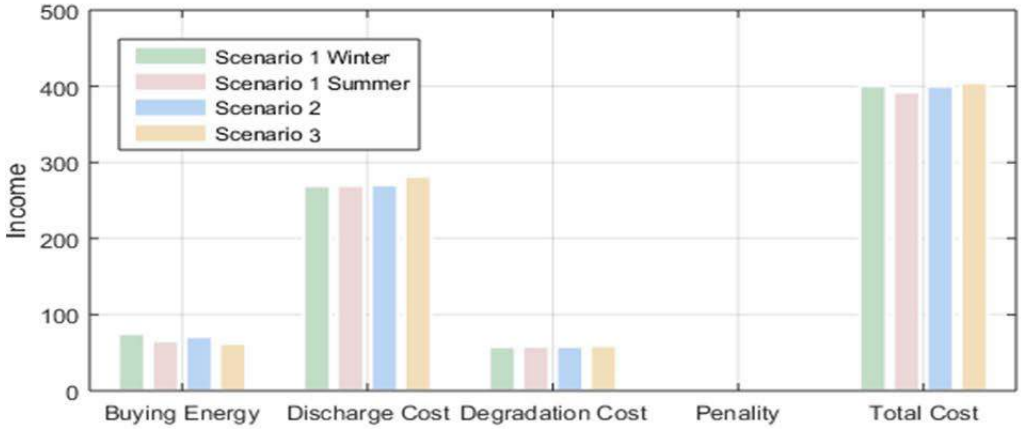

FIGURE 15. Analysis of cost breakdown of EVPL without capacity payment.

EVs at 1 to 6 hours is zero, at 6 h onwards, it is increasing from 1. The number of parked EVs is 70 at 11h, and then it increased to 105 at 16 h. Then it decreased to reach 10 at 21 h. Subplot 11(b) displays the number of parked EVs in summer. From the winter season, it has slight variations. Analysis of SOC of EVPL in winter and summer seasons is displayed

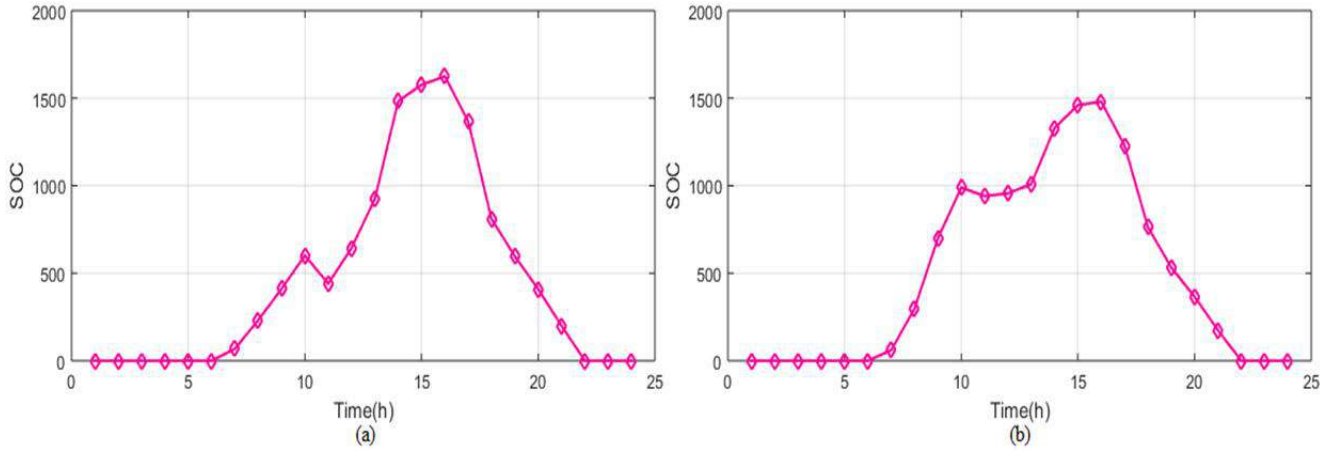

FIGURE 16. Analysis of EVPLSOC with capacity payment (A) Winter (B) Summer.

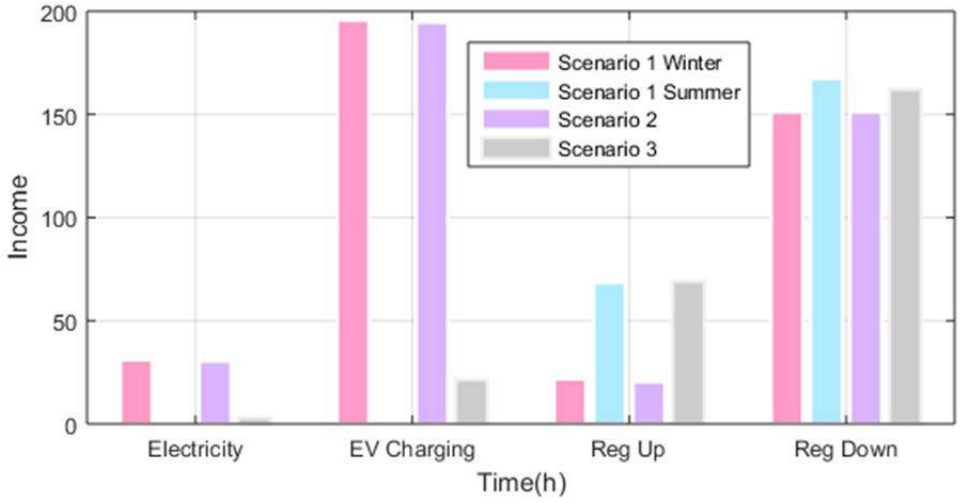

FIGURE 17. Analysis of cost breakdown of EVPL with capacity payment.

in Fig. 12. The SOC of EVPL in the winter season is displayed in Fig. 12(a). Inthe winter season, the SOC is 50 at 7 h, and it increased to reach 600 Wh. After it reduced and increased to reach 800 Wh and it reduced Again increased to 1600 Wh at 16 h. Then SOC of EVPL is reduced to 200 Wh at 21h.

The SOC of EVPL in the summer season is shown in Fig. 12(b). In the summer season, the SOC is 50 at 7 h, and it increased to reach 1700 kWh at 12 h. After it reduced gradually to reach 200 Wh at 21h. Analysis of various EVPL profits is displayed in Fig. 13. Without PV in the winter and summer season income from the electricity market is 60 €, 50 €. With PV in the winter and summer seasons income from the electricity market is 60 €, 50 €. Without PV in the winter and summer season income from EV charging is 360 €, 365 €. With PV in the winter and summer season income from EV charging is 370 €, 375 €. The income from delivery regulation and down is around 2 to 6 €. Without PV in the winter and summer season income from expected profit is 560 €, 565 €. With PV in the winter and summer season income expected is 565 €, 570 €. Do not treat income from EVs utility charges as EVSPL. From this result, it is concluded that PV in winter is one of the most lucrative for EVPL, while the winter baseline is the minimum profitable environment. Considering the resulting revenue in the electricity market, the display of PV in winter provides higher returns.

Analysis of income from EV charging with PV in the winter and summer seasons is displayed in Fig. 14. The high income in winter is 85 € and the PV in summer, the high income is 70€. Analysis of the cost breakdown of EVPL without capacity payment is shown in Fig. 15. Without PV in the winter and summer season income from buying energy is 70 €, 60 €. With PV in the winter and summer season income from buying energy is 65 €, 60 €. Without PV in the winter and summer season income from discharging is 270 €, 270 €. With PV in the winter and summer season income from discharging is 270 €, 280 €. Income from degradation is 60 € in all cases. The total cost Without PV in the winter

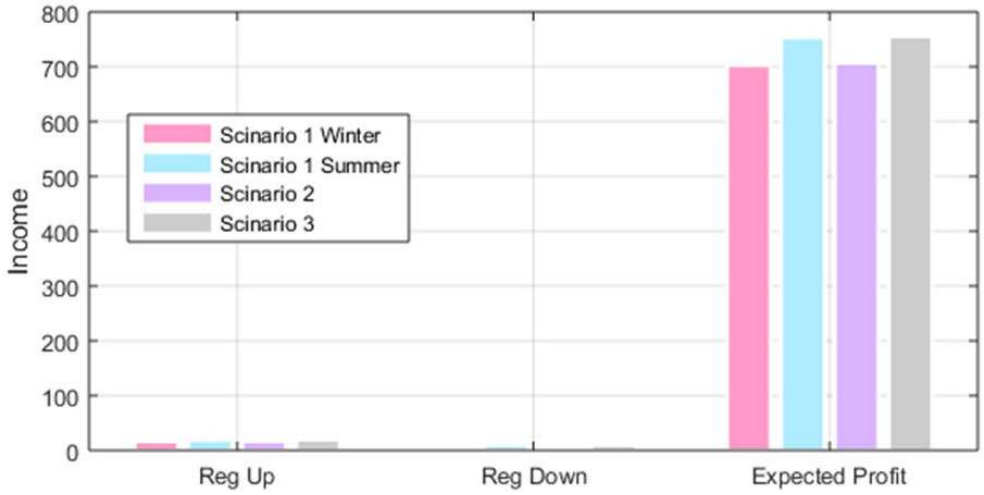

FIGURE 18. Analysis of cost breakdown of EVPL with capacity payment under delivery offered and expected profit.

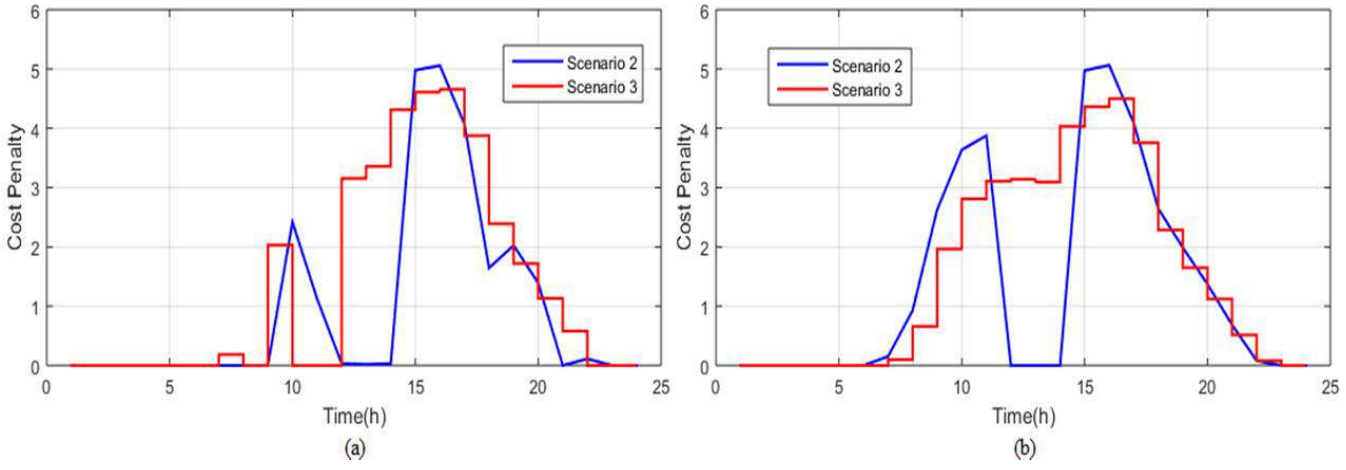

FIGURE 19. Analysis of the EVPL'S hourly penalty cost for not generating the energy provided (a) regulatory-up (b) regulatory-down.

and summer seasons is 400 €, 380€. The total cost With PV in the winter and summer seasons is 390 €, 400€.

The main goal is the high cost associated with the discharge charges of EVs. Due to the high level of PV power generation, the most expensive electric vehicles in the electricity market are discharged in the early morning and evening hours. There is a perfect change in grid purchasing energy. Analysis of EVPL SOC with capacity payment in summer and winter seasons is displayed in Fig. 16. Subplot 16(a) shows the SOC of EVPL in winter. The SOC of EVPL is zero at 0 to 6 h. Then the SOC is increased and reaches the maximum of 1600 kWh and it decreased to zero at 22 h. In the summer season shows subplot 16(b), SOC of EVPL high value is 1500 kWh.

Analysis of cost breakdown of EVPL with capacity payment under without and with PV in winter is shown in Fig. 17. Without PV in the winter and summer season income from the electricity market is 30 € and 0. With PV in the winter and summer season income from the electricity market is 30 €, 0 €. Without PV in the winter and summer seasons income from EV charging is 180 € and 0. With PV in the winter and summer season income from EV charging is 175 €, 25 €. Without PV in the winter and summer season income from regulation up participation is 25 € and 70. With PV in winter and summer season income from regulation up participation is 20 €, 75 €. Without PV in the winter and summer season income from regulation down participation is 150 € and 170€. With PV in winter and summer seasons income from regulation up participation is 150 € and 170€.

Analysis of the cost breakdown of EVPL with capacity payment under-delivery offered and expected profit is shown in Fig. 18. Without PV in the winter and summer season income from delivery offered regulation up participation is 5€, 5 €. With PV in winter and summer season income from delivery offered regulation up participation is 5€, 5 €. Without PV in the winter and summer season income from delivery offered regulation down participation is 2€, 1 €. With PV in winter and summer season income from expected is 700 €, 750 €. Without PV in the winter and summer season

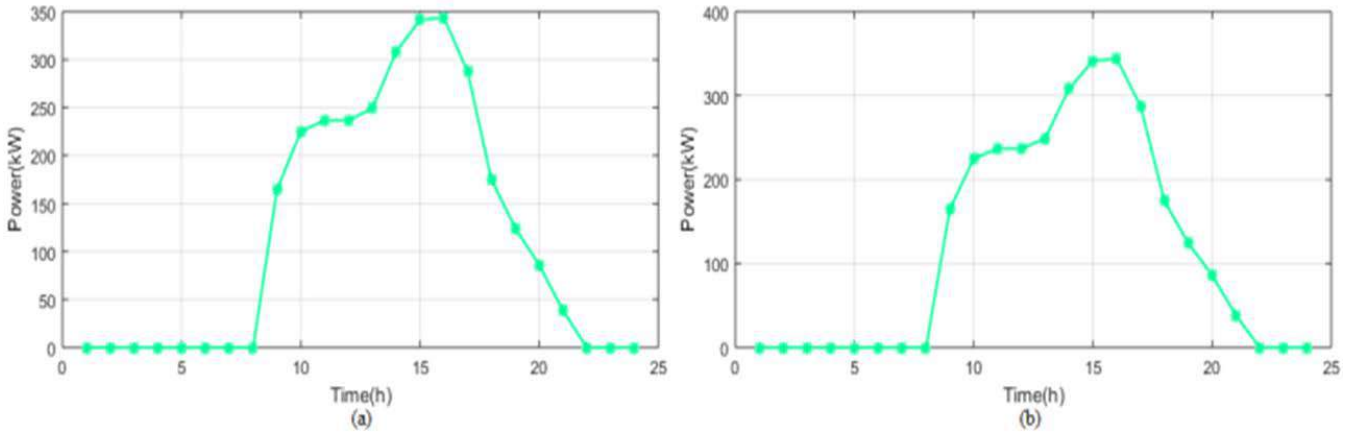

FIGURE 20. Analysis of EVPL'S reserve market participation in considering the increase in capacity payments (A) Without PV in winter (B) with PV in winter.

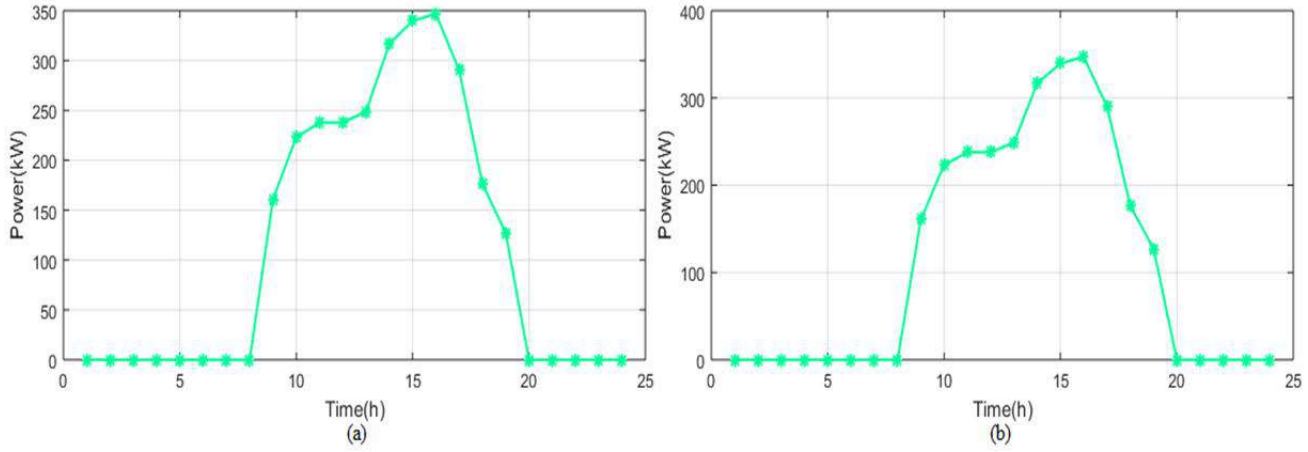

FIGURE 21. Analysis of EVPL's reserve market participation in considering the increase in capacity payments (A) Without PV in summer (B) With PV in summer.

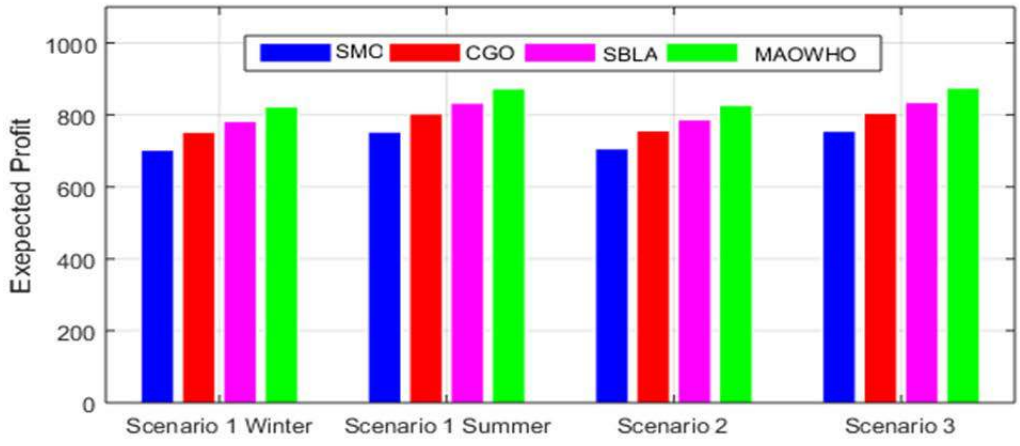

FIGURE 22. Comparison of proposed and existing approach expected profit.

income from delivery offered expected is 700 €, 750 €. From this analysis, it is concluded that the PV with summer is balanced one than the other cases. Analysis of EVPL's hourly penalty cost did not generate the energy provided (a) Regulatory-up and (b) Regulatory -down is shown in Fig. 19. The penalty cost is high for the PV in winter Analysis of EVPL's reserve market participation in considering the increase in capacity payments (a) Without PV in winter (b) With PV in winter is displayed in Fig.20. Its peak power is 350 kW. Analysis of EVPL's reserve market participation in

considering the increase in capacity payments (a) Without PV in summer (b) With PV in summer is shown in Fig. 21. From Fig. 21, it is concluded without PV in summer power and PV in summer power are considered the same. Fig. 22 shows the comparison of the proposed and existing approach expected profit. The profit of the proposed approach under Without PV in winter is 850 €. The existing approach like SMO, CGO, and SBLA profit becomes 700 €, 750 €, and 790 €. In all the scenarios the proposed approach profit is high than the existing is proved in Fig. 22.

VI. CONCLUSION

In this manuscript, a hybrid MAOWHO approach for locating and sizing of EVCSs optimally as well as managing the vehicle charging process. The proposed approach is the joint operation of MAO and WHO. The major aim of the MAOWHO approach is to maximize the profit of EVPL and reduces the cost of the EV user. The proposed approach considers the demand of the load and the uncertainty of PV. Using the MATLAB Simulink platform the proposed approach is implemented. The proposed approach is analyzed under three scenarios Without PV in summer and winter, With PV in summer, and With PV in winter. Then the proposed approach analyzes the nine varieties of costs and income of the system. The MAOWHO approach enhances EVSPL's participation in many energy and ancillary service markets, including the effects of capacity payments. The benefit of EVPL is obtained using the proposed approach and the proposed approach performance is high than the existing approach as proved by the comparison outcome.

ACKNOWLEDGMENT

This work was supported in part by the University of Business and Technology Researchers Supporting Program, Jeddah, Saudi Arabia; in part by Taif University, Taif, Saudi Arabia, through the Taif University Researchers Supporting Project under Grant TURSP 2020/122; and in part by the National Engineering School of Gabès, University of Gabès, Tunisia, under Project PEJC2022.

REFERENCES

[1] A. Rajabi-Ghahnavieh and P. Sadeghi-Barzani, "Optimal zonal fast-charging station placement considering urban traffic circulation," *IEEE Trans. Veh. Technol.*, vol. 66, no. 1, pp. 45–56, Jan. 2017.

[2] H. Zhang, S. J. Moura, Z. Hu, and Y. Song, "PEV fast-charging station siting and sizing on coupled transportation and power networks," *IEEE Trans. Smart Grid*, vol. 9, no. 4, pp. 2595–2605, Jul. 2018.

[3] M. Hosseini and S. MirHassani, "Refueling-station location problem under uncertainty," *Transp. Res. E, Logistics Transp. Rev.*, vol. 84, pp. 101–116, Dec. 2015.

[4] B. Y. O. Arslan and O. E. Karaşan, "A branch and price approach for routing and refueling station location model," *Eur. J. Oper. Res.*, vol. 248, no. 3, pp. 815–826, 2016.

[5] S. A. MirHassani and R. Ebrazi, "A flexible reformulation of the refueling station location problem," *Transp. Sci.*, vol. 47, no. 4, pp. 617–628, 2012.

[6] G. Wang, Z. Xu, F. Wen, and K. P. Wong, "Traffic-constrained multi-objective planning of electric vehicle charging stations," *IEEE Trans. Power Del.*, vol. 28, no. 4, pp. 2363–2372, 2013.

[7] W. Yao, J. Zhao, F. Wen, Z. Dong, Y. Xue, Y. Xu, and K. Meng, "A multi-objective collaborative planning strategy for integrated power distribution and electric vehicle charging systems," *IEEE Trans. Power Syst.*, vol. 29, no. 14, pp. 1811–1821, Jul. 2014.

[8] M. H. Moradi, M. Abedini, S. R. Tousi, and S. M. Hosseinian, "Optimal siting and sizing of renewable energy sources and charging stations simultaneously based on differential evolution algorithm," *Int. J. Elect. Power Energy Syst.*, vol. 73, pp. 1015–1024, Dec. 2015.

[9] M. H. Amini, M. P. Moghaddam, and O. Karabasoglu, "Simultaneous allocation of electric vehicles parking lots and distributed renewable resources in smart power distribution networks," *Sustain. Cities Soc.*, vol. 28, pp. 332–342, Jan. 2017.

[10] A. Aljanad, A. Mohamed, H. Shareef, and T. Khatib, "A novel method for optimal placement of vehicle-to-grid charging stations in distribution power system using a quantum binary lightning search algorithm," *Sustain. Cities Soc.*, vol. 38, pp. 174–183, Apr. 2018.

[11] G. Shaoyun, F. Liang, and L. Hong, "Planning of charging stations considering traffic flow and capacity constraints of distribution network," *Power Syst. Technol.*, vol. 37, no. 3, pp. 582–589, 2013.

[12] S. Pazouki, A. Mohsenzadeh, S. Ardalan, and M.-R. Haghifam, "Simultaneous planning of PEV charging stations and DGs considering financial, technical, and environmental effects," *Can. J. Electr. Comput. Eng.*, vol. 38, no. 3, pp. 238–245, 2015.

[13] A. K. Karmaker, M. R. Ahmed, M. A. Hossain, and M. M. Sikder, "Feasibility assessment & design of hybrid renewable energy based electric vehicle charging station in Bangladesh," *Sustain. Cities Soc.*, vol. 39, pp. 189–202, Apr. 2018.

[14] M. R. Mozafar, M. H. Moradi, and M. H. Amini, "A simultaneous approach for optimal allocation of renewable energy sources and electric vehicle charging stations in smart grids based on improved GA-PSO algorithm," *Sustain. Cities Soc.*, vol. 32, pp. 627–637, Jul. 2017.

[15] Y. M. Atwa, E. F. El-Saadany, M. M. A. Salama, and R. Seethapathy, "Optimal renewable resources mix for distribution system energy loss minimization," *IEEE Trans. Power Syst.*, vol. 25, no. 1, pp. 360–370, Feb. 2010.

[16] J. H. Teng, S. W. Luan, D. J. Lee, and Y. Q. Huang, "Optimal charging/discharging scheduling of battery storage systems for distribution systems interconnected with sizeable PV generation systems," *IEEE Trans. Power Syst.*, vol. 28, no. 2, pp. 1425–1433, May 2013.

[17] M. Mazidi, A. Zakariazadeh, S. Jadid, and P. Siano, "Integrated scheduling of renewable generation and demand response programs in a microgrid," *Energy Convers. Manage.*, vol. 86, pp. 1118–1127, Oct. 2014.

[18] J.-G. Kim and M. Kuby, "The deviation-flow refueling location model for optimizing a network of refueling stations," *Int. J. Hydrogen Energy*, vol. 37, no. 6, pp. 5406–5420, Mar. 2012.

[19] D. Q. Hung, N. Mithulananthan, and K. Y. Lee, "Determining PV penetration for distribution systems with time-varying load models," *IEEE Trans. Power Syst.*, vol. 29, no. 6, pp. 3048–3057, Nov. 2014.

[20] G. W. Hua and Y. D. Xu, "Optimal deployment of charging stations and movable charging vehicles for electric vehicles," *J. Syst. Manage. Sci.*, vol. 9, no. 1, pp. 105–116, 2019, doi: 10.33168/jsms.2019.0106.

[21] S. Sachan and M. Amini, "Optimal allocation of EV charging spots along with capacitors in smart distribution network for congestion management," *Int. Trans. Electr. Energy Syst.*, vol. 30, no. 9, 2020, Art. no. e12507.

[22] S. Aggarwal and A. K. Singh, "Impact analysis of electric vehicle charging station integration with distributed generators on power systems," *Int. J. Circuit Theory Appl.*, vol. 49, no. 6, pp. 1811–1827, Jun. 2021, doi: 10.1002/cta.2974.

[23] M. A. van den Berg, I. Lampropoulos, and T. A. AlSkaif, "Impact of electric vehicles charging demand on distribution transformers in an office area and determination of flexibility potential," *Sustain. Energy, Grids Netw.*, vol. 26, Jun. 2021, Art. no. 100452, doi: 10.1016/j.segan.2021.100452.

[24] M. T. Turan, Y. Ates, O. Erdinc, E. Gokalp, and J. P. S. Catalão, "Effect of electric vehicle parking lots equipped with roof mounted photovoltaic panels on the distribution network," *Int. J. Electr. Power Energy Syst.*, vol. 109, pp. 283–289, Jul. 2019, doi: 10.1016/j.ijepes.2019.02.014.

[25] S. Bouguerra and S. BharLayeb, "Determining optimal deployment of electric vehicles charging stations: Case of Tunis City, Tunisia," *Case Stud. Transp. Policy*, vol. 7, no. 3, pp. 628–642, 2019, doi: 10.1016/j.cstp.2019.06.003.

[26] J. Li, Z. Liu, and X. Wang, "Public charging station location determination for electric ride-hailing vehicles based on an improved genetic algorithm," *Sustain. Cities Soc.*, vol. 74, Nov. 2021, Art. no. 103181, doi: 10.1016/j.scs.2021.103181.
[27] M. MohammadiLandi, M. Mohammadi, and M. Rastegar, "Simultaneous determination of optimal capacity and charging profile of plug-in electric vehicle parking lots in distribution systems," *Energy*, vol. 158, pp. 504–511, Sep. 2018, doi: 10.1016/j.energy.2018.06.065.
[28] H. Yu, C. Y. Chung, K. P. Wong, H. W. Lee, and J. H. Zhang, "Probabilistic load flow evaluation with hybrid Latin hypercube sampling and Cholesky decomposition," *IEEE Trans. Power Syst.*, vol. 24, no. 2, pp. 661–667, May 2009.
[29] M. Ahmadi, S. Hosseini, and M. Farsadi, "Optimal allocation of electric vehicles parking lots and optimal charging and discharging scheduling using hybrid metaheuristic algorithms," *J. Electr. Eng. Technol.*, vol. 16, no. 2, pp. 759–770, 2021.
[30] A. Pal, A. Bhattacharya, and A. Chakraborty, "Allocation of electric vehicle charging station considering uncertainties," *Sustain. Energy, Grids Netw.*, vol. 25, Mar. 2021, Art. no. 100422.
[31] A. Goswami and P. Kumar Sadhu, "Stochastic firefly algorithm enabled fast charging of solar hybrid electric vehicles," *Ain Shams Eng. J.*, vol. 12, no. 1, pp. 529–539, Mar. 2021.
[32] A. Amer, M. Azzouz, A. Azab, and A. Awad, "Stochastic planning for optimal allocation of fast charging stations and wind-based DGs," *IEEE Syst. J.*, vol. 15, no. 3, pp. 4589–4599, Sep. 2021.
[33] Y. Zhou, A. Ravey, and M. Péra, "Real-time cost-minimization power-allocating strategy via model predictive control for fuel cell hybrid electric vehicles," *Energy Convers. Manage.*, vol. 229, Feb. 2021, Art. no. 113721.
[34] R. Aghapour, M. S. Sepasian, H. Arasteh, V. Vahidinasab, and J. P. S. Catalão, "Probabilistic planning of electric vehicles charging stations in an integrated electricity-transport system," *Electr. Power Syst. Res.*, vol. 189, Dec. 2020, Art. no. 106698.
[35] L. Luo, Z. Wu, W. Gu, H. Huang, S. Gao, and J. Han, "Coordinated allocation of distributed generation resources and electric vehicle charging stations in distribution systems with vehicle-to-grid interaction," *Energy*, vol. 192, Feb. 2020, Art. no. 116631.
[36] S. D. Vidhya and M. Balaji, "Modelling, design and control of a light electric vehicle with hybrid energy storage system for Indian driving cycle," *Meas. Control*, vol. 52, nos. 9–10, pp. 1420–1433, Nov. 2019.
[37] Y. Kim, M. Figueroa-Santos, N. Prakash, S. Baek, J. Siegel, and D. Rizzo, "Co-optimization of speed trajectory and power management for a fuel-cell/battery electric vehicle," *Appl. Energy*, vol. 260, Feb. 2020, Art. no. 114254.
[38] H. A. Yavasoglu, Y. E. Tetik, and H. G. Ozcan, "Neural network-based energy management of multi-source (battery/UC/FC) powered electric vehicle," *Int. J. Energy Res.*, vol. 44, no. 15, pp. 12416–12429, Dec. 2020.
[39] J. Hu, D. Liu, C. Du, F. Yan, and C. Lv, "Intelligent energy management strategy of hybrid energy storage system for electric vehicle based on driving pattern recognition," *Energy*, vol. 198, May 2020, Art. no. 117298.
[40] J. Hu, X. Niu, X. Jiang, and G. Zu, "Energy management strategy based on driving pattern recognition for a dual-motor battery electric vehicle," *Int. J. Energy Res.*, vol. 43, no. 8, pp. 3346–3364, Jun. 2019.
[41] M. Montazeri-Gh and M. Mahmoodi-K, "Optimized predictive energy management of plug-in hybrid electric vehicle based on traffic condition," *J. Cleaner Prod.*, vol. 139, pp. 935–948, Dec. 2016.
[42] Z. Luo, F. He, X. Lin, J. Wu, and M. Li, "Joint deployment of charging stations and photovoltaic power plants for electric vehicles," *Transp. Res. D, Transp. Environ.*, vol. 79, Feb. 2020, Art. no. 102247.
[43] R. Mehta, D. Srinivasan, A. Khambadkone, J. Yang, and A. Trivedi, "Smart charging strategies for optimal integration of plug-in electric vehicles within existing distribution system infrastructure," *IEEE Trans. Smart Grid*, vol. 9, no. 1, pp. 299–312, Jan. 2016.
[44] H. Haghighat, "Energy loss reduction by optimal distributed generation allocation in distribution systems," *Int. Trans. Electr. Energy Syst.*, vol. 25, no. 9, pp. 1673–1684, Sep. 2015.
[45] Y. Villuendas-Rey, J. L. Velázquez-Rodríguez, M. D. Alanis-Tamez, M.-A. Moreno-Ibarra, and C. Yáñez-Márquez, "Mexican axolotl optimization: A novel bioinspired heuristic," *Mathematics*, vol. 9, no. 7, p. 781, Apr. 2021.
[46] I. Naruei and F. Keynia, "Wild horse optimizer: A new meta-heuristic algorithm for solving engineering optimization problems," *Eng. With Comput.*, pp. 1–32, Jun. 2021.
[47] E. Mortaz, A. Vinel, and Y. Dvorkin, "An optimization model for siting and sizing of vehicle-to-grid facilities in a microgrid," *Appl. Energy*, vol. 242, pp. 1649–1660, May 2019.
[48] H. Khalkhali and S. H. Hosseinian, "Multi-stage stochastic framework for simultaneous energy management of slow and fast charge electric vehicles in a restructured smart parking lot," *Int. J. Electr. Power Energy Syst.*, vol. 116, Mar. 2020, Art. no. 105540.
[49] M. Li, M. Lenzen, D. Wang, and K. Nansai, "GIS-based modelling of electric-vehicle–grid integration in a 100% renewable electricity grid," *Appl. Energy*, vol. 262, Mar. 2020, Art. no. 114577.

CH. S. V. PRASAD RAO received the B.E. degree in electrical and electronics engineering (EEE) from the Gandhi Institution of Technology and Management (GITAM), Visakhapatnam, Andhra Pradesh, India, affiliated to Andhra University, Visakhapatnam, in 1999, and the M.Tech. degree in specialization high voltage engineering from the Department of Electrical and Electronics Engineering (EEE), JNTU, Kakinada, Andhra Pradesh, in 2002. He is currently pursuing the Ph.D. degree with the Department of Electrical and Electronics Engineering (EEE), Koneru Lakshmaiah Education Foundation (Deemed to be University), Guntur, Andhra Pradesh. His research interest includes electric vehicles application in power system engineering.

A. PANDIAN (Senior Member, IEEE) received the B.E. degree from the Department of Electrical and Electronics Engineering, Bharathiar University, Coimbatore, Tamil Nadu, in 1999, the M.E. degree in electrical machines from the P. S. G. College of Technology, Coimbatore, in 2006, and the Ph.D. degree from Anna University, Chennai, in 2015. He is currently working as a Professor and the Research Group Head in power electronics with the Department of Electrical and Electronics Engineering, Koneru Lakshmaiah Education Foundation (Deemed to be University), Guntur, Andhra Pradesh, India. He is having 20 years of teaching experience in different cadre as department head, research and development activities, and administrative work. He has published more than 38 articles in reputed international and national journals, such as *Sci*, *Web of Science*, and *Scopus Indexed Journal*. He has also presented ten papers in international conferences and published three patents in IPR. His current research interests include power converters, smart grids, EV technology, electrical drives, and optimization. He is a member of the Editorial Board/Reviewer Board of IEEE Transactions, Taylor & Francis, Elsevier, Sage, and many reputed journal publishers.

CH. RAMI REDDY (Member, IEEE) received the B.Tech. degree in electrical and electronics engineering and the M.Tech. degree in electrical machines and drives from Jawaharlal Nehru Technological University, Kakinada, Andhra Pradesh, India, in 2011 and 2014, respectively, and the Ph.D. degree in electrical and electronics engineering from K. L. University, Andhra Pradesh, in 2022. He is currently working as an Assistant Professor in electrical and electronics engineering with the Malla Reddy Engineering College (Autonomous), Secunderabad, Telangana, India. His current research interests include integrated renewable energy systems, distributed generation, FACTS devices, and power converters applications to energy systems. He is an Editorial Board Member and a Reviewer of various *Web of Science* and *Scopus Indexed Journals*. He is also a Guest Editor of *Energies* journal (MDPI) for a Special Issue "Advancement in Renewable Energy Technologies and Smart Grid."

FLAH AYMEN was born in Gabès, Tunisia, in 1983. He received the bachelor's and M.Tech. degrees in electrical engineering from the National Engineering School of Gabès (ENIG), University of Gabès, Tunisia, in 2007 and 2009, respectively, and the Ph.D. degree from the Department of Electrical Engineering, ENIG, University of Gabès, in 2012. In 2021, he becomes an Associate Professor. He is currently an Associate Professor with ENIG, University of Gabès. He has academic experience of 11 years. He has published more than 40 research articles in international cited journals and conferences and book chapters. His research interests include regroups and electrical vehicle.

MOHAMMED ALQARNI received the B.Sc. degree in electrical engineering-power and machines from King Abdulaziz University, Jeddah, Saudi Arabia, in 2008, and the M.Sc. degree in engineering management and the Ph.D. degree in electrical power engineering from Brunel University London, U.K., in 2010 and 2016 respectively. Since 2016, he has been with the University of Business and Technology (UBT), Jeddah, where he was the Chairman of the Department of Electrical Engineering and the Dean of the College of Engineering. He is also an Assistant Professor. His research interests include power systems, renewable energy integration, clean energy technologies, electricity market, electric vehicle, and smart grid.

MOSLEH M. ALHARTHI was born in Taif, Saudi Arabia, in 1966. He received the B.Sc. and M.S. degrees in electronics technology and engineering from Indiana State University, Terre Haute, IN, USA, in 1996 and 1997, respectively, and the Ph.D. degree in electrical engineering from Arkansas University, Fayetteville, AR, USA, in 2001. He was an Assistant Professor with the Jeddah College of Technology, Jeddah, Saudi Arabia, from 2001 to 2009. He is currently working as a Professor with the Department of Electrical Engineering, Taif University. He also works as the Dean of the College of Engineering, Taif University. His research interests include control engineering, electronics, and signal processing.

applied sciences

MDPI

Article

Comparison of Principal-Component-Analysis-Based Extreme Learning Machine Models for Boiler Output Forecasting

K. K. Deepika [1], P. Srinivasa Varma [2,*], Ch. Rami Reddy [3,4], O. Chandra Sekhar [4], Mohammad Alsharef [5], Yasser Alharbi [5] and Basem Alamri [5]

[1] Electrical and Electronics Engineering, Vignan's Institute of Information Technology, Duvvada, Visakhapatnam 530049, India; keerthi.deepika@gmail.com
[2] Electrical and Electronics Engineering, Koneru Lakshmaiah Education Foundation, Guntur 522302, India
[3] Electrical and Electronics Engineering, Malla Reddy Enginering College, Secunderabad 500100, India; crreddy229@mrec.ac.in
[4] Electrical Engineering, National Institute of Technology, Srinagar 190006, India; obbuchandra@nitsri.net
[5] Department of Electrical Engineering, College of Engineering, Taif University, P.O. Box 11099, Taif 21944, Saudi Arabia; m.alsharef@tu.edu.sa (M.A.); y.alharbi@tu.edu.sa (Y.A.); b.alamri@tu.edu.sa (B.A.)
* Correspondence: pinnivarma@kluniversity.in

Abstract: In this paper, a combined approach of Principal Component Analysis (PCA)-based Extreme Learning Machine (ELM) for boiler output forecasting in a thermal power plant is presented. The input used for this prediction model is taken from the boiler unit of the Yermarus Thermal Power Station (YTPS), India. Calculation of the accurate electrical output of a boiler in an operating system requires the knowledge of hundreds of operating parameters. The dimensionality of the input dataset is reduced by applying principal component analysis using IBM@SPSS Software. In the process of principal component analysis, a dataset of 232 parameters is standardized into 16 principal components. The total dataset collected is divided into training and testing datasets. The extreme learning machine is designed for various activation functions and the number of neurons. Sigmoid and hyperbolic tangent activation functions are studied here. Its generalization performance is examined in terms of the Mean Square Error (MSE), Mean Absolute Error (MAE), Root Mean Square (RMSE), and Mean Absolute Percentage Error (MAPE). ELM and PCA–ELM are compared. In both the ELM and PCA–ELM models, when the extreme learning machine was designed with a sigmoid activation function with 100 nodes in the hidden layer, RMSE was 5.026 and 4.730, respectively. Therefore, the developed combined approach of PCA–ELM proved as a promising technique in forecasting with reduced errors and reduced time.

Keywords: extreme learning machine (ELM); principal component analysis (PCA); boiler output forecasting; activation function; hidden neurons; sigmoid function

Citation: Deepika, K.K.; Varma, P.S.; Reddy, C.R.; Sekhar, O.C.; Alsharef, M.; Alharbi, Y.; Alamri, B. Comparison of Princpal-Component-Analysis-Based Extreme Learning Machine Models for Boiler Output Forecasting. *Appl. Sci.* **2022**, *12*, 7671. https://doi.org/10.3390/app12157671

Academic Editor: Christian W. Dawson

Received: 23 June 2022
Accepted: 27 July 2022
Published: 29 July 2022

1. Introduction

The growing decentralization and digitization of the power industry is driving the relevance of artificial intelligence and data analysis in particular. Today's data science studies include a wide range of topics along the value chain, from generation and trade through transmission, distribution, and consumption. Diverse applications and different methodologies, such as various types of artificial neural networks, have also been studied. From the applications of data analysis, it can be used in four ways:

- Forecasting and Prediction.
- Monitoring and Controlling.
- Clustering.
- Others [1].

Any industrial growth story includes the thermal power industry. However, it now functions in a complicated context characterized by significant unpredictability in operational circumstances such as grid changes, a competitive market (alternative sources), fuel input, regulatory constraints, and changing staff. This creates a difficult operating environment and reduces plant profitability. Bhangu [2] proposed that with a greater rate of growth, more maintenance is required, and a complete availability analysis will aid in identifying components that are primarily responsible for low availability. It can be useful in the installation of future power plants. It is critical for the efficient and economic operation of a power plant to properly anticipate the full load electrical power output of a base load power plant. It is useful for getting the most money out of the available resources. In contrast to earlier research publications that explored data analytics in power plants and their components, Tüfekci [3] made a comparison study on multiple machine learning (ML) algorithms for predicting combined cycle power plant (CCPP) full load electrical power outputs. The prediction was done for the same using the Genetic Algorithm by Lorencin [4]. When the supplied findings were examined, artificial neural networks have much greater Root Mean Squared Error (RMSE) than other approaches, including basic regression functions. For a proper system analysis utilizing thermodynamical approaches, a significant number of assumptions are necessary, such that these assumptions account for the unpredictability of the outcome. Without these assumptions, a thermo-dynamical analysis of a real-world application would demand hundreds of nonlinear equations, the solution to which would either be impossible or would take too much time and effort. So, Kesgin [5] highlighted that machine learning algorithms are increasingly being used as an alternative to thermo-dynamical approaches to analyze systems with unpredictable input and output patterns to overcome this barrier. As a result, when considering a machine learning approach for predicting output in a power plant, various algorithms or methods can be used, but selecting the most efficient and appropriate method is critical. In [6], a hybrid Machine Learning algorithm for the prediction of landslide displacement was proposed. It was implemented for Shuping and Baishuihe landslides to calculate the hyperparameters. Ref. [7] demonstrates a support Vector Machine for the prediction of seepage-driven landslides.

As power plant equipment is complicated and difficult to predict precisely, Yuliang Dong [8] proposed an artificial neural network for condition prediction that was developed using principal component analysis (PCA). Author Wang Feiin [9] demonstrated a viable prediction model of power for grid-connected solar plants based on artificial neural networks. This neural model gives the hourly prediction value of power in steps, using the input vector as well as the past power value and other impact elements. In [10], R Mei proposed a new network model which consists of Elman Neural Networks (ENN) and principal component analysis (PCA). This prediction model helped to improve the wind power usage while also developing the stability and safety of the plant. A two-stage neural network using an Elman recurrent neural network and BP neural network was developed by L. Ma [11] to predict typical values of fault feature variables and fault types. To anticipate short-term wind power, Gang Chen [12] developed a prediction model based on a convolutional neural network (CNN) and genetic algorithm (GA) wind power prediction model for the development of wind power generation and the research status of wind power prediction technology.

Different prediction methods such as logistic regression, rule-based method, simple Bayesian classifier, artificial neural network method, k-nearest neighbor method [13], decision tree, support vector machine [14], and extreme learning machine (ELM) [15–18] can be used.

Zhou [15] found out that for small- to medium-sized training data, the user can select to utilize a method based on the training data's size (complexity of calculation is dependent on the amount of training data) or hidden nodes' size (complexity of computation is based on the number of hidden nodes). The dimensionality of the mapped space is determined by the number of hidden nodes. In general, the more sophisticated the training examples are, the more hidden nodes are needed to train a generalized model to estimate the target functions for a large data issue. When dealing with highly big and complicated training datasets, this causes challenges for ELM. Huang [16] found that due to the enormous number of hidden nodes required, the ELM network is quite massive, and the computing process becomes very expensive.

Huang [17] discussed the ELM method, which can be utilized to directly train neural networks using threshold functions. Many academics have lately researched extreme learning machines (ELM) as a sort of generalized single-hidden-layer feed-forward network in theory and applications. ELM's hidden node parameters (input weights and hidden layer biases) are generated at random, and the output weights are then computed analytically using the generalized inverse approach. An ELM-based equality-constrained optimization approach with two solutions for different training data sizes was illustrated.

However, out of all these methods, Tan [19] proposed ELM. It is more efficient as ELM has a swift learning rate. ELM was applied to find out the correlation between operational parameters and nitrogen oxide emissions of the boiler. Results illustrated that the ELM model was shown to be more exact and quicker than the common artificial neural network and support vector regression models in modeling nitrogen oxide emissions.

In [20], the power flow, active power, and reactive power models of electric springs to regulate voltage were replaced by three data-driven models based on the extreme learning machine (ELM). To develop the final control strategies, an ELM-based control model was provided. In [21], an extreme learning machine (ELM) artificial neural network and four eddy current sensors were used to develop a measuring technique for the rotation angle of the spherical joint. The developed prototype showed measurement accuracy as well as offered a high-precision measuring approach. Through the determination of the picture coordinates of ripe fruits and fruit trees, the extreme learning machine algorithm was incorporated into the agricultural equipment navigation system, together with the BP neural network algorithm in [22], to accomplish the speedy navigation of the operation of agricultural machinery. The test findings reveal that employing the extreme learning machine, which can match the design criteria of contemporary agricultural machinery and equipment, has enhanced picking efficiency and accuracy significantly.

The authors addressed accurate Maximum Power Point Tracking (MPPT) for PV-based Distributed Generation (DG) in [23] using an error-optimized (via Improved Water Cycle) Extreme Learning Machine with Ridge Regression (IWC–ELMRR). The effectiveness of the suggested method is demonstrated by an improved Error-MPP profile and decreased dynamic oscillation at the DG (Distributed Generation) coupling bus. In [24], an extreme learning machine (ELM) with Neural Networks was incorporated in Cooperative Spectrum Sensing (CSS) for cognitive radio networks (CRN) for detecting false alarms. The findings show that the NN–ELM approach offers a superior balance of training duration and detection performance. The overfitting issue raised in the ELM approach was overcome in [25]. It combines bound optimization theory with Variational Bayesian (VB) inference to create new L1 norm-based ELMs. It exhibited the best prediction performance on the testing dataset.

To reduce the memory and complicated data issues, principal component analysis (PCA) is employed on complex datasets. To understand the PCA in its raw form and its applications, the paper written by Sidharth et al. [26] is helpful as it contains a detailed explanation of the step-by-step procedure of the PCA with an explanation. In [26], authors defined PCA as a multivariate approach for analyzing a data set in which observa-

tions are characterized by numerous inter-correlated quantitative dependent variables. Its purpose is to extract key information from statistical data and express it as a set of new orthogonal variables known as principal components. The application of PCA was mostly found in image processing, so some extensions are known as 2DPCA and modular PCA are developed that are better than PCA in terms of their accuracy in feature extraction and facial recognition, respectively [27,28]. A comparison between ICA (Individual Component Analysis) and PCA is performed in terms of facial recognition [29]. The application of PCA for its very purpose, i.e., to reduce dimensions of data, is performed on bio-medical data [30]. PCA can also be used in power plants for fault detection and identification [31]. Ref. [32] shows that the application of PCA to detect faults in superheaters using the temperature data from tubes is successful, and an extended PCA method known as Kernel PCA works better for non-linear data. PCA and wavelet approaches were combined in [33] and extended for fault analysis in electrical machines. The other capability of PCA is an estimation. Ref. [34] is an example of estimating sag from data obtained from 17 sub-stations.

The method has been used in various fields such as image processing [25], medical [30], in which PCA had been used both as a reduction method and a data filter, chemical processing [31], and facial recognition [26–36].

Castaño suggested that the PCA–ELM algorithm in [37] train any SLFN with hidden nodes that has linear activation functions. With the information acquired via PCA on the training dataset, it calculates the hidden node parameters. The network structure can be simplified in this way to enhance prediction precision. Miao [38] found that the rationale for combining PCA and ELM is to make use of the two algorithms' strengths, such that the combined method has the neural network's stability and learning capacity while reducing the input neurons' complexity. The applications of a PCA–ELM-based prediction model in different domains are:

Ji in [39] used the PCA–ELM network model to predict the blast furnace gas utilization rate to optimize the operation of a blast furnace. Yuan [40] suggested the usage of terahertz time-domain technology in conjunction with the PCA–GA–ELM model to assess the thickness of TBCs. The research by Sun [41] offered a unique hybrid model that combines principal component analysis (PCA) and a regularized extreme learning machine (RELM) to predict carbon dioxide emissions in China from 1978 to 2014.

To recapitulate the novelty of the work in this paper, the idea is to investigate the prediction of boiler output power in a thermal power plant using an extreme learning machine. Calculation of the electrical output of a boiler in the operating system requires the knowledge of 232 operating parameters. To reduce the dimensionality of the input dataset, principal component analysis is performed. Finally, an extreme learning machine is established to predict the boiler output power, whose inputs are the 16 principal components. To validate the effectiveness of the combined approach of PCA–ELM, it is compared with ELM in testing accuracy and simulation time. Further, the ELM model is designed with various activation functions, and the number of hidden neurons and the results for simulation time and testing accuracy are compared. From earlier statements, the following hypotheses can be levied:

i. to investigate the prediction of boiler output power in a thermal power plant using an extreme learning machine
ii. to reduce the dimensionality of the input dataset by performing principal component analysis
iii. to validate the effectiveness of the combined approach of PCA–ELM over ELM and
iv. to determine the simulation time and testing accuracy of PCA–ELM designed for various ELM network architectures.

2. Methodology

2.1. Extreme Learning Machine

To answer huge and complicated data issues using ELM without running out of memory, the network size should be kept minimal while maintaining acceptable generalization accuracy. Its architecture is shown in Figure 1.

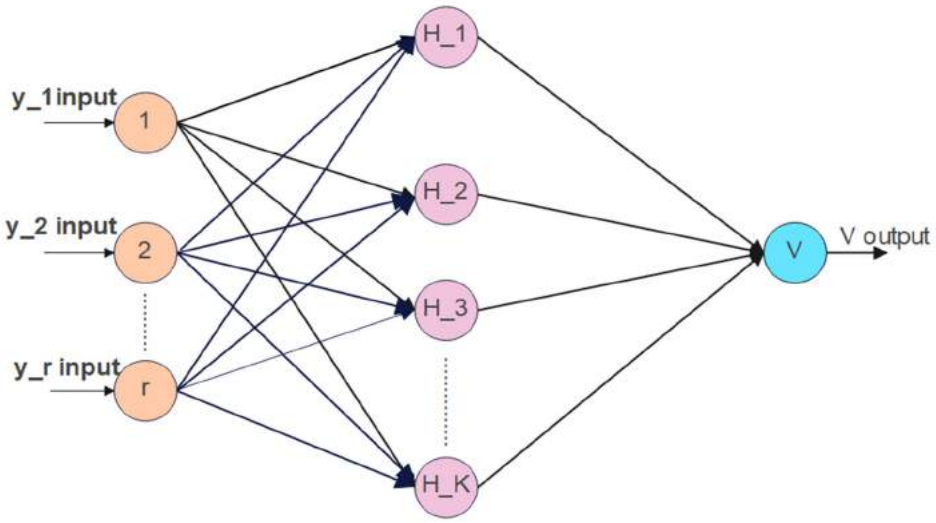

Figure 1. Extreme learning machine architecture.

ELM Algorithm

For different samples—(y_r,u_r), in which $y_r = [y_{r1}, y_{r2}, y_{r3}, \ldots\ldots, y_{ri}]T$, $u_r = [u_{r1}, u_{r2}, u_{r3}, \ldots\ldots, u_{rt}]T$ are the unified single-layer feed-forward neural network containing the number of hidden layer nodes ($\bar{k}$) and the activation function $f(x)$.

$$\sum_{r=1}^{\bar{k}} \delta_r f(y_r) = \sum_{r=1}^{\bar{k}} \delta_r f(w_r y_r + d_r) = z_s, s = 1,2, \ldots . km \quad (1)$$

where $\delta_r = [\delta_{r1}\delta_{r2}, \delta_{r3}, \ldots\ldots \delta_{rt}]^T$ denotes the output weights for connecting the ith hidden node and the output node; $w_r * y$ denotes the inner product. $w_r = [w_{r1}, w_{r2,} \ldots . . w_{ri}]^T$ denotes the weights of the input $f(x)$, which connects the nth hidden node. d_r denotes the deviation of the nth hidden node; $f(x)$ is the activation function, and the output of the hidden nodes is (2).

$$f(w_r, d_r, y) = f(w_r * y + d_r) \quad (2)$$

A single-hidden-layer feed-forward neural network containing the number of hidden layer nodes ($\bar{k}$) and the activation function $f(r)$ can approximate the k samples $\{y_r,b_r\}$ without deviation, namely as in Equation (3).

$$\sum_{s}^{k} \|z_s - u_s\| = 0 \quad (3)$$

The relationship of $\delta_r w_r, d_r$ is given by (4):

$$\sum_{r=1}^{\bar{k}} \delta_r f(w_r y_s + d_r) = u_s, s = 1,2, \ldots . . k \quad (4)$$

The above Formula (4) can be represented by the matrix below in (5).

$$[v][\delta] = [u] \quad (5)$$

where matrix (6).

$$v(w_1, \ldots\ldots, w_{\bar{k}}, d_1 \ldots\ldots, d_{\bar{k}}, y_1, \ldots\ldots, y_{\bar{k}}) = \begin{vmatrix} f(w_1 y_1 + d_1) & \ldots & f(w_{\bar{k}} y_1 + d_{\bar{K}}) \\ & \ldots & \\ f(w_1 y_N + b_K) & \ldots & f(w_{\bar{K}} y_{\bar{K}} d_{\bar{K}}) \end{vmatrix}_{\bar{K} * \bar{K}} \quad (6)$$

where $\hat{w}_r, \hat{d}_r \hat{\delta}_r$ (r = 1, 2, K) denotes the output matrix of the hidden layer (7):

$$\delta = \begin{vmatrix} \delta_1^T \\ \vdots \\ \delta_{\bar{K}}^T \end{vmatrix}_{\bar{K} * t} \quad u = \begin{vmatrix} u_1^U \\ \vdots \\ u_K^U \end{vmatrix}_{K * t} \quad (7)$$

The matrix v can adjust network parameters constantly by solving the following minimization problem (8):

$$min \| v\delta - u \| \quad (8)$$

The traditional single-layer feedforward network (SLFN) needs to find a set of optimal parameters $\hat{w}_r, \hat{d}_r \hat{\delta}_r$ (r = 1, 2… K) following (9):

$$\| v(w_1, \ldots\ldots, w_{\bar{k}}, d_1 \ldots\ldots, d_{\bar{k}})\delta - u \| = min_{\hat{w}_r, \hat{d}_r \hat{\delta}_r} \| v(w_1, \ldots\ldots, w_{\bar{k}}, d_1 \ldots\ldots, d_{\bar{k}})\delta - u \| \quad (9)$$

2.2. Principal Component Analysis

Principal component analysis is a dimensionality-reduction technique, and its goal is to minimize the data's dimensionality while preserving as much variety as possible from the original dataset.

Steps to perform PCA are:

(a) Data standardization

The matrix Y is standardized using the following calculation Formula (10):

$$x_{ij} = \frac{y_{ij} - \overline{y_j}}{\sqrt{var(y_j)}} \quad (10)$$

where, $Y = \{Y_{ii}\}$, $X = \{X_{ij}\}$, i = 1,2, 3…, n, j = 1,2,3…, p.

$$\bar{y} = \frac{1}{n} \sum_{i=1}^{n} y_{ij} \text{ and } Var(y_j) = \frac{1}{n-1} \sum_{i=1}^{n} (y_{ij} - \overline{y_j})^2 \quad (11)$$

(b) Calculating covariance matrix

The formula for covariance concerning variance is (12) and (13).

$$Var(X) = \frac{\sum_{i=1}^{n} (X_i - X')(X_i - X')}{(\mathrm{n} - 1)} \quad (12)$$

$$Cov(X, Y) = \frac{\sum_{i=1}^{n} (X_i - X')(Y_i - Y')}{(\mathrm{n} - 1)} \quad (13)$$

where

X' = Arithmetic mean of data X.
Y' = Arithmetic mean of data Y.
n = Number of observations.

The Covariance matrix can be obtained as (14):

$$\sum = \begin{bmatrix} Var(X) & Cov(x, y) \\ Cov(Y, X) & Var(Y) \end{bmatrix} \quad (14)$$

The correlation coefficient matrix R is solved as follows (15):

$$R = \frac{X^T X}{n - 1} \quad (15)$$

(c) Eigenvalues are determined by solving

$$|(S - \lambda I)| = 0 \tag{16}$$

Eigenvectors of λ_1 are given below

$$(S - \lambda I)U_1 = 0$$

The eigenvalue and eigenvector of the coefficient matrix are calculated as follows:

$$|R - \lambda I_n| = 0 \tag{17}$$

The calculated eigenvector is $a_i = (a_{i1}, a_{i2,} a_{i3,} \ldots \ldots a_{in}), for\ i = 1,2,3 \ldots\ldots, n$, and the eigenvalue is λ_i. Eigenvalues are sorted in descending order to obtain a set of principal components F_i, as in (18):

$$F_i = a_{i1}X_1 + a_{i2}X_2 + a_{i3}Y_3 + \cdots \ldots\ldots + a_{in}X_n \tag{18}$$

(d) Choosing new components

The principal components are determined as follows: the rate of contribution of the *k*th principal component is given as (19):

$$\lambda_k \left(\sum_{j=1}^{n} \lambda_j \right) \tag{19}$$

The rate of the accumulating contribution of the first *k* principal component is given as (20):

$$\sum_{j=1}^{k} \lambda_j \left(\sum_{j=1}^{n} \lambda_j \right) \tag{20}$$

2.3. PCA–ELM

Figure 2 indicates the approach to the integration of PCA and ELM, which is split into three segments. Segment 1 is the selection of the input dataset. A thermal power plant is built with huge machines and other equipment, where a lot of parameters will affect their efficiency. The efficiency of the machines and equipment affects the efficiency of the thermal power plant. A boiler's efficiency is purely based on parameters such as the inlet steam pressure, inlet steam temperature, outlet steam pressure, and outlet steam temperature, etc. So, a dataset consisting of the values of these parameters is selected as the input data. The principal component analysis is performed in Segment 2 on the selected input data. The principal components i.e., a new dataset with reduced dimensions, are set as the input to ELM. Segment 3 details ELM development and execution. The new data obtained by Segment 2 is further divided into training and testing datasets. The ELM model is simulated, and errors are calculated.

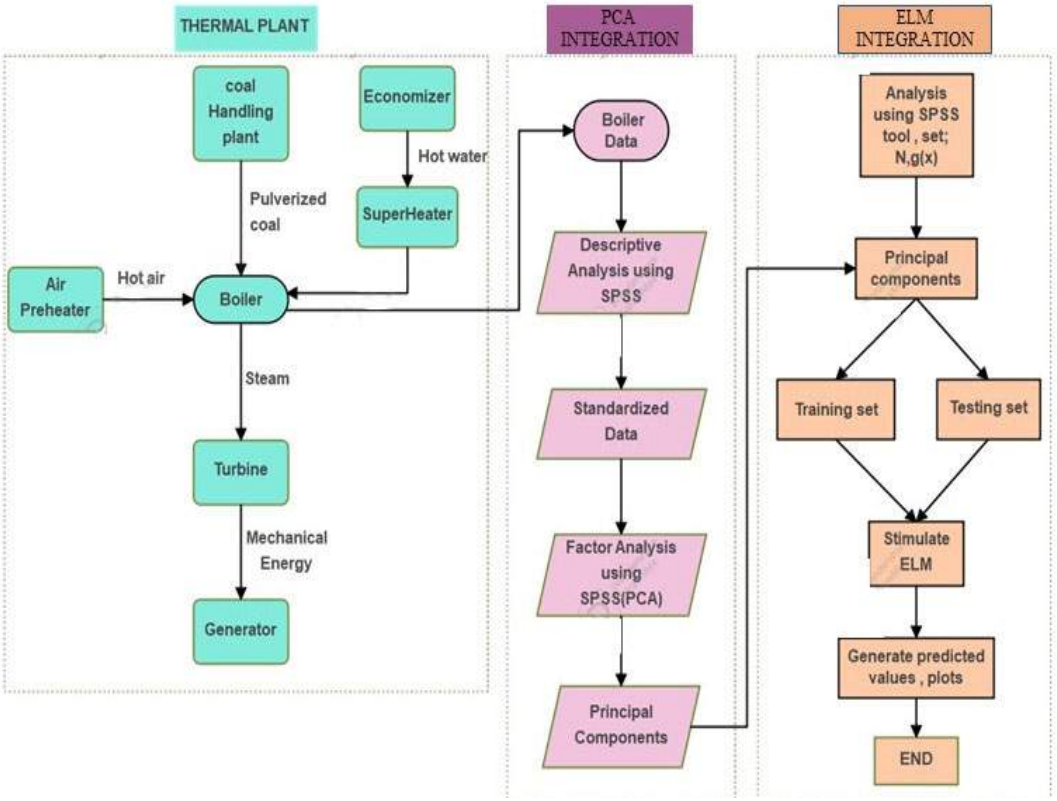

Figure 2. PCA–ELM Integration Approach.

The testing accuracy of the developed model can be determined from several errors such as the Mean Square Error—mean of the square of the resulted error; Mean Absolute Error—mean of the absolute values of the error; Root Mean Square Error—square root of the mean square error; Mean Absolute Percentage Error—percentage value of the mean absolute error. For K number of samples, the actual and predicted value for each sample u are given by $y_u, \hat{y}_u$, respectively. Then, the errors are determined using Equations (21)–(24). At last, the network model with the least errors is preferable.

$$\text{Mean Squared Error (MSE)} = \frac{1}{K}\sum(y_u - \hat{y}_u)^2 \quad (21)$$

$$\text{Mean Absolute Error (MAE)} = \frac{1}{K}\sum(y_u - \hat{y}_u) \quad (22)$$

$$\text{Root Mean Squared Error (RMSE)} = \sqrt{\frac{1}{K}\sum(y_u - \hat{y}_u)^2} \quad (23)$$

$$\text{Mean Absolute Percentage Error (MAPE)} = \frac{100}{K}\sum\left|\frac{y_u - \hat{y}_u}{y_u}\right| \quad (24)$$

3. Model Approach

This research is based on the boiler consumption at the Yermarus Thermal Power Station (YTPS) located in India. The Yermarus Thermal Power Station is a coal-fired thermal power station in the Raichur district of Karnataka. The Karnataka Power Corporation owns the power facility. Bharat Heavy Electricals is the EPC contractor for this power project, which is India's first 800 MW supercritical thermal power plant. The plant has two units in it. The installed capacity of the power plant is 1600 MW (2 × 800 MW).

The equipment of a thermal power plant has different operating parameters to generate the maximum capacity. For a boiler, the operating parameters are the inlet steam pressure, inlet steam temperature, outlet steam pressure, outlet steam temperature, at re-heater, super-heater, de-super-heater, air pre heater, forced draft and load, total coal flow, total primary air flow, total secondary air flow, separated overfire air, heavy

fuel oil pump current, seal air fan current, Air Pre-Heater (APH) main motor current, and APH standby motor current, and the levels of various gases are the parameters fed as inputs to perform PCA. From the widely deployed measuring devices, sensors, and recorders, the boiler log is summarized. Further, data from this boiler log for January 2022 from the Yermarus thermal power station were given as the input to the network model. It consists of nine coal mills. The data consist of 232 parameters and 96 samples each.

The PCA calculation was performed on SPSS 19.0 software. Upon performing the eigenvalue decomposition technique for the input data covariance matrix, 232 parameters were reduced to 16 principal components based upon the covariance factor. The variance of each parameter can be explained using Table 1.

Table 1. Variance of the obtained 16 principal components.

Component Number	Eigenvalue	% of Variance	Cumulative %
1	75.245	32.433	32.433
2	54.165	23.347	55.780
3	34.359	14.810	70.590
4	19.495	8.403	78.993
5	11.663	5.027	84.020
6	5.936	2.559	86.579
7	4.683	2.018	88.597
8	3.185	1.373	89.970
9	2.416	1.042	91.012
10	2.184	0.941	91.953
11	1.697	0.731	92.685
12	1.625	0.701	93.385
13	1.550	0.668	94.053
14	1.370	0.591	94.644
15	1.252	0.540	95.184
16	1.056	0.455	95.639

For all the 232 variables, there will be 232 components, but the characteristics of the original variables will be reduced to 16 components. Key information about the 232 variables is mined from these components. The percentage of the variance of the first principal component (PC1) is 32.433. It signifies that the first principal component has 32.433% of the characteristics of the original data. The second principal component (PC2) has the second highest variance percentage of 23.347%. These 16 principal components form the inputs to the input layer of the modeled ELM network. The modeling of the ELM includes the selection of the number of hidden neurons and activation function and the division of data for training and testing. The modeled ELM consists of one hidden layer, and a variety of activation functions are considered. All the data are divided into two parts—one part is for training, and the other for testing. The ELM model is built for predicting the output. First, the ELM has been trained on some samples by giving both inputs and outputs. After that, it has been tested on some inputs, and the outputs obtained are compared with the original outputs in the data.

The PC1 vs PC2 results are depicted in Figure 3. The type of activation function and number of hidden neurons affect the prediction capability and speed of the ELM model. If the accuracy and speed of the model is good, then the network model can be used for further greater analysis. By using SPSS, the principal components are randomly assigned as training samples and testing samples for different ranges of hidden nodes (i.e., 3, 30, 50, 80, 100) and activation functions (sigmoid and hyperbolic tangent) when the PCA–ELM model is stimulated and tested.

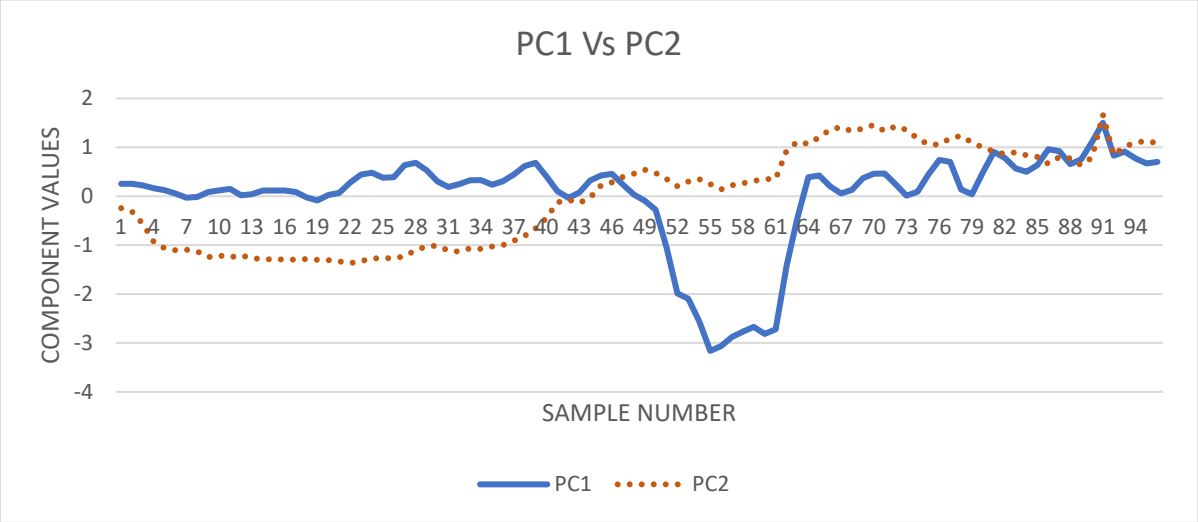

Figure 3. Principal component 1 vs. principal component 2.

4. Results and Discussion

To determine the best approach between ELM and PCA–ELM, initially, the dataset of 232 variables and 96 samples is standardized. Then, principal component analysis is performed, and the spread of the obtained components can be observed in Figure 4. The first 16 components have a greater percentage of the variance than the rest of the components, meaning all the characteristics of the original dataset are present in those 16 principal components.

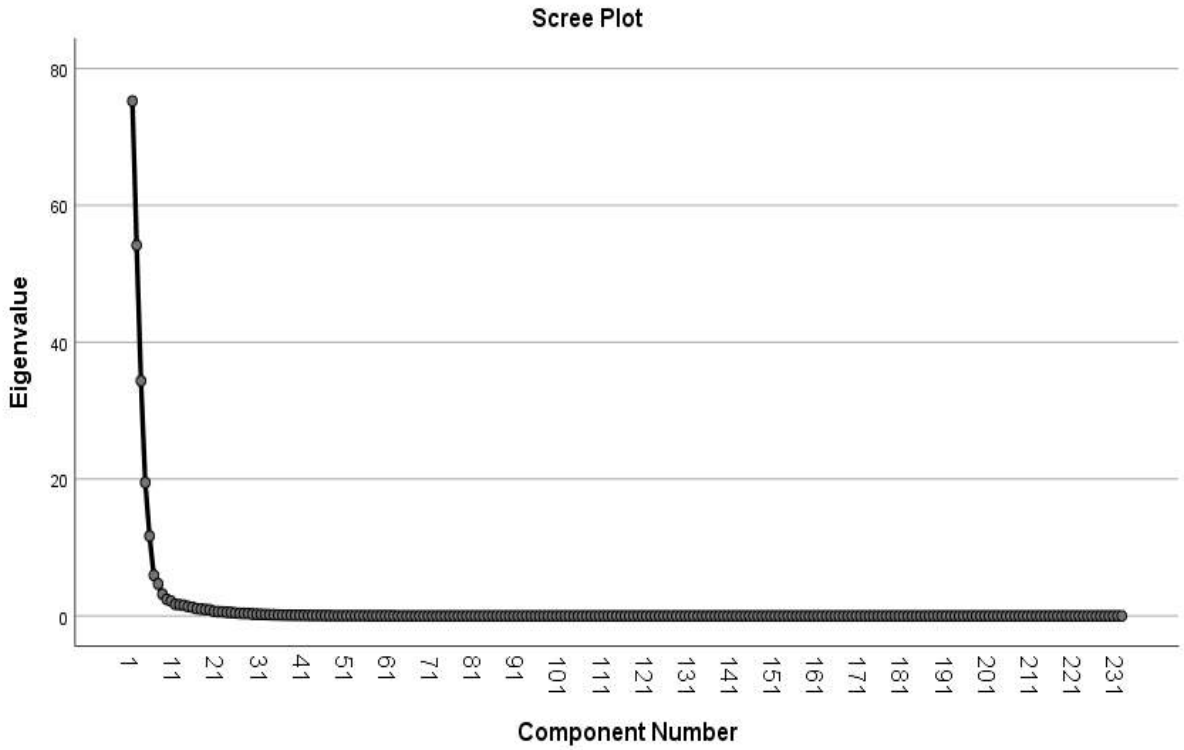

Figure 4. Scree plot explaining the spread of principal components.

From Table 1 the percentage variance of the obtained 16 principal components is as follows: 32.4, 23.3, 14.8, 8.4, 5.02, 2.5, 2.01, 1.3, 1.04, 0.94, 0.73, 0.701, 0.668, 0.59, 0.54, 0.455, and the cumulative contribution rate is 95.639%. It signifies that the 16 principal com-

ponents represent 95.639% of the original dataset characteristics. A conventional ELM model using a sigmoid activation function with 50 hidden nodes is developed, and the original data of 232 variables is given as training and testing samples.

In the next part of the simulation, the dimensionality of the huge input data is reduced using PCA and then integrated into ELM, continuing with the same ELM design of a sigmoid activation function and 50 hidden nodes. A comparison of the predictions using both the approaches—ELM and PCA–ELM, during training and testing—consists of 2 general parts: relative errors and training time.

Results shown in Table 2 highlight that the conventional ELM model takes 13 ms, whereas PCA–ELM takes only 2 ms.

Table 2. ELM model and PCA–ELM integration model using a sigmoid activation function with 50 hidden neurons.

Parameters/Approach	ELM	PCA–ELM
training sum of squares error	0.02	0.015
training time (in milliseconds)	13	2
training relative error	0.009	0.01
the testing sum of squares error	0.05	0.023
testing relative error	0.065	0.017
MSE	39.932	14.711
MAE	3.902	2.969
MAPE	0.696	0.526
RMSE	6.319	3.835

More time for training and the relative errors are high compared to the PCA–ELM integrated model, and the cause of high-dimensional data can be observed on a network model. So, the PCA–ELM integrated model has the best prediction capability and is more accurate towards training time. In addition, the ELM and PCA–ELM models using a sigmoid activation function with 100 hidden nodes are developed. From Table 3, the relative errors and training time for both the models can be observed.

Table 3. ELM model and PCA–ELM integration model using a sigmoid activation function with 100 hidden neurons.

Parameters/Approach	ELM	PCA–ELM
training sum of squares error	0.002	0.015
training time (in milliseconds)	45	2
training relative error	0.001	0.01
testing sum of squares error	0.038	0.023
testing relative error	0.053	0.017
MSE	25.269	22.380
MAE	2.726	3.626
MAPE	0.481	0.639
RMSE	5.026	4.730

Now, an accurate prediction model is established, but the choice of the number of hidden nodes and activation functions is a failing factor. To begin, PCA–ELM models using a sigmoid activation function with different ranges of hidden neurons of 3, 30, 50, 80, and 100 were created, with mean square errors of 160, 23, 14, 33, and 22 respectively. From Table 4, the results show that the prediction model using the sigmoid function should be implemented with a high range of hidden nodes (mostly 30 or more hidden nodes).

Table 4. Sigmoid-function-based PCA–ELM model for a various number of hidden neurons.

Parameter/Model	S-3	S-30	S-50	S-80	S-100
training sum of squares error	0.094	0.022	0.015	0.018	0.015
training time (in milliseconds)	0	0	2	2	2
training relative error	0.045	0.012	0.01	0.013	0.01
testing sum of squares error	0.158	0.018	0.023	0.034	0.023
testing relative error	0.278	0.018	0.017	0.027	0.017
MSE	160.063	23.487	14.714	33.224	22.379
MAE	8.0185	3.531	2.969	4.282	3.626
MAPE	1.436	0.621	0.526	0.767	0.639
RMSE	12.655	4.841	3.835	5.764	4.730

PCA–ELM models using a hyperbolic tangent activation function with different ranges of hidden neurons of 3, 30, 50, 80, and 100 are developed, and the mean square errors of the models are 107, 42, 61, 110, and 668, respectively. From Tables 4 and 5, in the case of 30 hidden nodes, the MSE is 23.487 with the sigmoid-function-based PCA–ELM model, whereas it is 42.206 with the hyperbolic-tangent-function-based PCA–ELM model. In the case of 100 hidden neurons, the MSE is 22.379 with the sigmoid-function-based PCA–ELM model, whereas it is 668.565 with the hyperbolic-tangent-function-based PCA–ELM model. This shows that the prediction model using the sigmoid function is more reliable from the lower range of hidden nodes.

Table 5. Hyperbolic-tangent-function-based PCA–ELM model for a various numbers of hidden neurons.

Parameter/Model	H-3	H-30	H-50	H-80	H-100
training sum of squares error	0.288	0.021	0.008	0.125	2.268
training time (in milliseconds)	2	2	6	5	9
training relative error	0.037	0.002	0.001	0.025	0.288
testing sum of squares error	0.386	0.272	0.415	0.733	1.939
testing relative error	0.135	0.019	0.135	0.094	0.678
MSE	107.124	42.206	61.051	110.047	668.565
MAE	7.249	3.200	3.141	6.609	21.095
MAPE	1.300	0.572	0.557	1.180	3.668
RMSE	10.350	6.496	7.813	10.490	25.857

The Mean Absolute Error (MAE), Mean Absolute Percentage Error (MAPE), and Root Mean Square Error (RMSE) are determined from the predicted values. An extensive comparison of these values for various numbers of hidden nodes and both activation functions —hyperbolic tangent and sigmoid functions—is illustrated in Figure 5. Notations used in Figure 5 represent *activation function-number of neurons*, where 'H', 'S' represent the hyperbolic tangent function and sigmoid function, respectively. For example, H-3—represents a hyperbolic tangent activation function with 3 hidden neurons, and S-3—a sigmoid activation function with 3 hidden neurons.

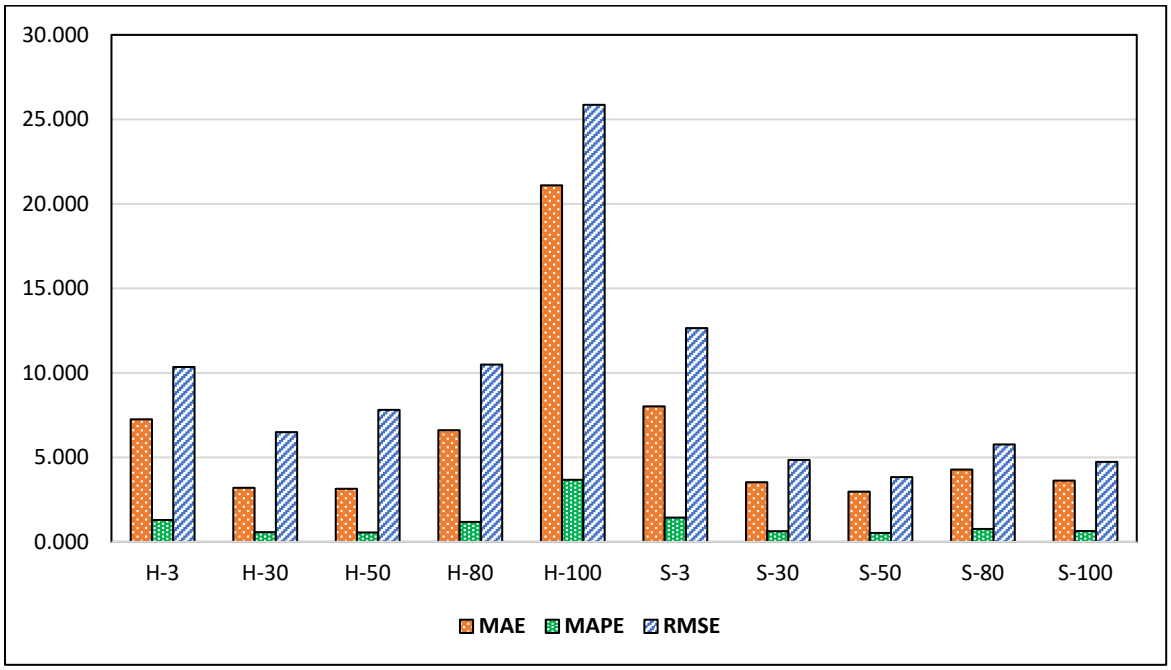

Figure 5. Comparison of the errors for various models.

The developed PCA–ELM network's workings have been tested in three aspects:

- The performance of the conventional ELM has been compared with that of PCA–ELM.
- The PCA–ELM network was compared by varying the range of hidden neurons.
- The two PCA–ELM networks using the hyperbolic tangent function and sigmoid function are developed and compared.

The PCA–ELM network was built using the hyperbolic tangent function, and the range of neurons is varied. As the range of neurons increased, the error also increased, and the efficiency of the model decreased, whereas in the PCA–ELM network using a sigmoid function when the range of hidden neurons is varied, as the range is increased, the error decreased. The number of hidden neurons is varied from 3, 30, 50, 80, and 100. In addition, the training time for a neural network model is crucial, and a conventional ELM network is challenging. So, by using the PCA technique, the large boiler data are reduced to minimal data without losing any of their features, and those acquired principal components are integrated into the ELM network; this PCA–ELM is accurate and fast compared to the conventional ELM network. This can be observed from training time in the comparison Table 6.

Table 6. PCA–ELM models using a hyperbolic tangent function and sigmoid function with different ranges of hidden neurons.

H/S	H	H	H	H	H	S	S	S	S	S
Number of hidden neurons	3	30	50	80	100	3	30	50	80	100
training sum of squares error	0.288	0.021	0.008	0.125	2.268	0.094	0.022	0.015	0.018	0.015
training time (ms)	2	2	6	5	9	0	0	2	2	2
training relative error	0.037	0.002	0.001	0.025	0.288	0.045	0.012	0.01	0.013	0.01
testing sum of squares error	0.386	0.272	0.415	0.733	1.939	0.158	0.018	0.023	0.034	0.023
testing relative error	0.135	0.019	0.135	0.094	0.678	0.278	0.018	0.017	0.027	0.017
MSE	107.12	42.206	61.051	110.04	668.56	160.063	23.487	14.711	33.224	22.3799

MAE	7.2494	3.2004	3.1415	6.6091	21.095	8.01854	3.5317	2.9691	4.2829	3.62697
MAPE	1.3001	0.5720	0.5574	1.1800	3.6681	1.43662	0.6339	0.5260	0.7671	0.63997
RMSE	10.35008	6.496684	7.813519	10.49037	25.85701	12.6516305	4.846391	3.835549	5.764049	4.73075014

5. Conclusions

In this paper, a combined approach of principal component analysis with extreme learning machines is investigated to predict boiler output power in a thermal power plant. The electrical output of a boiler in the operating system requires knowledge of 232 operating parameters. Principal component analysis is performed to reduce the dimensionality of the input dataset. These principal components form the input matrix for the extreme learning machine. Total inputs are divided into two parts—training and testing datasets. To validate the effectiveness of the combined approach of PCA–ELM, it is compared with ELM in terms of its testing accuracy and simulation time. Further, the ELM model is designed with various activation functions and several hidden neurons, and the results for simulation time and testing accuracy are compared. In summary, according to the predictions made, the following conclusions can be drawn:

i. To predict the boiler output power in a thermal power plant, PCA–ELM is superior to ELM in predicting accuracy and learning speed. This is because with PCA, the dimension of the inputs is reduced while maintaining the properties of the data points using variance, thereby reducing the computation time.
ii. In terms of prediction precision, PCA–ELM shows superior performance over ELM because of the eigenvalue decomposition technique for the input data covariance matrix. In this way, correlated input parameters are carefully converted into linearly uncorrelated ones. Thus, this shows the necessity for dimensionality reduction methods to enhance forecasting.
iii. The generalization ability of the ELM is corroborated with changes in ELM parameters' activation function and the number of hidden nodes. In a comparison of PCA–ELM models with a hyperbolic tangent function and those with a sigmoid function, the latter shows better performance in terms of errors. However, the performance of the hyperbolic tangent function deteriorates with the increasing number of hidden neurons.

This paper primarily studies the forecasting of boiler output based on thermal power plant operating parameters. It can further be extended to the optimization of the input parameters. For the fact of serious air pollution caused by thermal plants, these outcomes may also be considered in the production planning. Hence there are numerous other ways to incorporate this study.

Author Contributions: Conceptualization, K.K.D., C.R.R. and P.S.V.; methodology, O.C.S.; software, M.A.; validation, K.K.D., P.S.V., C.R.R., O.C.S., M.A., Y.A. and B.A.; formal analysis, O.C.S.; investigation, K.K.D.; resources, C.R.R.; data curation, P.S.V.; writing—original draft preparation, K.K.D. and C.R.R.; writing—review and editing, O.C.S. and P.S.V.; visualization, C.R.R.; supervision, O.C.S.; project administration, P.S.V.; funding acquisition, M.A., Y.A. and B.A. All authors have read and agreed to the published version of the manuscript.

Funding: The authors would like to acknowledge the financial support received from Taif University Researchers Supporting Project Number (TURSP-2020/278), Taif University, Taif, Saudi Arabia.

Institutional Review Board Statement: Not applicable.

Informed Consent Statement: Not applicable.

Data Availability Statement: Not applicable.

Conflicts of Interest: The authors declare no conflict of interest.

References

1. Vom Scheidt, F.; Medinová, H.; Ludwig, N.; Richter, B.; Staudt, P.; Weinhardt, C. Data analytics in the electricity sector – A quantitative and qualitative literature review. *Energy AI* **2020**, *1*, 100009.
2. Bhangu, S.N.; Singh, R.; Pahuja, G.L. Availability performance analysis of thermal power plants. *J. Inst. Eng. India Ser. C* **2019**, *100*, 439–448.
3. Tüfekci, P. Prediction of full load electrical power output of a base load operated combined cycle power plant using machine learning methods. *Int. J. Electr. Power Energy Syst.* **2014**, *60*, 126–140.
4. Lorencin, I.; Anđelić, N.; Mrzljak, V.; Car, Z. Genetic Algorithm Approach to Design of Multi-Layer Perceptron for Combined Cycle Power Plant Electrical Power Output Estimation. *Energies* **2019**, *12*, 4352.
5. Kesgin, U.; Heperkan, H. Simulation of thermodynamic systems using soft computing techniques. *Int. J. Energy Res.* **2005**, *29*, 581–611.
6. Ma, J.; Xia, D.; Guo, H.; Wang, Y.; Niu, X.; Liu, Z.; Jiang, S. Metaheuristic-based support vector regression for landslide displacement prediction: a comparative study. *Landslides* **2022**, 1–23. https://doi.org/10.1007/s10346-022-01923-6.
7. Ma, J.; Wang, Y.; Niu, X.; Jiang, S.; Liu, Z. A comparative study of mutual information-based input variable selection strategies for the displacement prediction of seepage-driven landslides using optimized support vector regression. *Stoch. Hydrol. Hydraul.* **2022**, 1–21. https://doi.org/10.1007/s00477-022-02183-5.
8. Dong, Y.; Gu, Y.; Yang, K.; Zhang, J. Applying PCA to establish artificial neural network for condition prediction on equipment in power plant. In Proceedings of the Fifth World Congress on Intelligent Control and Automation (IEEE Cat. No.04EX788), Shenyang, China, 15–19 June 2004, pp. 1715–1719, Volume 2. https://doi.org/10.1109/WCICA.2004.1340965.
9. Fei, W.; Mi, Z.; Shi, S.; Zhang, C. A practical model for single-step power prediction of grid-connected PV plant using artificial neural network. In Proceedings of the 2011 IEEE PES Innovative Smart Grid Technologies, Perth, WA, Australia, 13–16 November 2011; pp. 1–4. https://doi.org/10.1109/ISGT-Asia.2011.6167097.
10. Mei, R.; Lv, Z.; Tang, Y.; Gu, W.; Feng, J.; Ji, J. Short-term prediction of wind power based on principal component analysis and Elman neural network. In Proceedings of the 2021 IEEE Sustainable Power and Energy Conference (iSPEC), Nanjing, China, 23–25 December 2021; pp. 3669–3674. https://doi.org/10.1109/iSPEC53008.2021.9735980.
11. Ma, L.; Wang, X.; Cao, X. Feedwater heater system fault diagnosis during dynamic transient process based on two-stage neural networks. In Proceedings of the 32nd Chinese Control Conference, Xi'an, China, 26–28 July 2013; pp. 6148–6153.
12. Chen, G.; Shan, J.; Li, D.Y.; Wang, C.; Li, C.; Zhou, Z.; Wang, X.; Li, Z.; Hao, J.J. Research on Wind Power Prediction Method Based on Convolutional Neural Network and Genetic Algorithm. In Proceedings of the 2019 IEEE Innovative Smart Grid Technologies—Asia (ISGT Asia), Chengdu, China, 21–24 May 2019; pp. 3573–3578. https://doi.org/10.1109/ISGT-Asia.2019.8880918.
13. Dong, Y.; Ma, X.; Fu, T. Electrical load forecasting: A deep learning approach based on K-nearest neighbors. *Appl. Soft Comput.* **2020**, *99*, 106900.
14. Malhotra, R. Comparative analysis of statistical and machine learning methods for predicting faulty modules. *Appl. Soft Comput.* **2014**, *21*, 286–297.
15. Zhou, H.; Huang, Gu.; Lin, Z.; Wang, H.; Soh, Y.C. Stacked extreme learning machines. *IEEE Trans. Cybern.* **2014**, *45*, 2013–2025.
16. Huang, G.-B.; Zhou, H.; Ding, X.; Zhang, R. Extreme Learning Machine for Regression and Multiclass Classification. *IEEE Trans. Syst. Man Cybern. Part B Cybern.* **2012**, *42*, 513–529.
17. Huang, G.-B.; Zhu, Qi.; Mao, K.Z.; Siew, C.; van Saratchandran, P.; Sundararajan, N. Can threshold networks be trained directly? *IEEE Trans. Circuits Syst. II Express Briefs* **2006**, *53*, 187–191.
18. Miche, Y.; Sorjamaa, A.; Lendass, A. OP-ELM: Theory, experiments and a toolbox. In *International Conference on Artificial Neural Networks*; Springer: Berlin/Heidelberg, Germany, 2008; pp. 145–154.
19. Tan, P.; Xia, J.; Zhang, C.; Fang, Q.; Chen, G. Modeling and reduction of NOX emissions for a 700 MW coal-fired boiler with the advanced machine learning method. *Energy* **2015**, *94*, 672–679.
20. Zhao, H.; Zhao, J.; Zheng, Y.; Qiu, J.; Wen, F. A Hybrid Method for Electric Spring Control Based on Data and Knowledge Integration. *IEEE Trans. Smart Grid* **2019**, *11*, 2303–2312. https://doi.org/10.1109/TSG.2019.2951585.
21. Shi, X.; Kang, Q.; An, J.; Zhou, M. Novel L1 Regularized Extreme Learning Machine for Soft-Sensing of an Industrial Process. *IEEE Trans. Ind. Inform.* **2021**, *18*, 1009–1017. https://doi.org/10.1109/TII.2021.3065377.
22. Yu, H.; Yang, L.; Zhou, Y. Navigation System Research and Design Based on Intelligent Image Classification Algorithm of Extreme Learning Machine. In Proceedings of the 2020 IEEE International Conference on Power, Intelligent Computing and Systems (ICPICS), Shenyang, China, 28–30 July 2020; pp. 930–933. https://doi.org/10.1109/ICPICS50287.2020.9202157.
23. Patnaik, S.; Tripathy, L.; Dhar, S. An Improved Water Cycle Optimized Extreme Learning Machine with Ridge Regression towards Effective Maximum Power Extraction for Photovoltaic based Active Distribution Grids. In Proceedings of the 2020 International Conference on Computational Intelligence for Smart Power System and Sustainable Energy (CISPSSE), Keonjhar, Odisha, 23–35 April 2020; pp. 1–6. https://doi.org/10.1109/CISPSSE49931.2020.9212281.
24. Giri, M.K.; Majumder, S. Extreme Learning Machine Based Cooperative Spectrum Sensing in Cognitive Radio Networks. In Proceedings of the 2020 7th International Conference on Signal Processing and Integrated Networks (SPIN), Noida, India, 27–28 February 2020; pp. 636–641. https://doi.org/10.1109/SPIN48934.2020.9071418.
25. Tang, Zhenhao, Shikui Wang, Xiangying Chai, Shengxian Cao, Tinghui Ouyang, and Yang Li. Auto-encoder-extreme learning machine model for boiler NOx emission concentration prediction. *Energy* **2022**, *256*, 124552.

26. Mishra, P.S.; Sarkar, U.; Taraphder, S.; Datta, S.; Swain, D.; Saikhom, R.; Panda, S.; MenalshLaishramMultivariate statistical data analysis-principal component analysis (PCA). *Int. J. Livest. Res.* **2017**, *7*, 60–78.
27. Yang, J.; Zhang, D.; Frangi, A.; Yang, J.-Y. Two-dimensional pca: a new approach to appearance-based face representation and recognition. *IEEE Trans. Pattern Anal. Mach. Intell.* **2004**, *26*, 131–137. https://doi.org/10.1109/TPAMI.2004.1261097.
28. Gottumukkal, R.; Asari, V.K. An improved face recognition technique based on modular PCA approach. *Pattern Recognit. Lett.* **2004**, *25*, 429–436. https://doi.org/10.1016/j.patrec.2003.11.005.
29. Draper, B.A.; Baek, K.; Bartlett, M.S.; Beveridge, J. Recognizing faces with PCA and ICA. *Comput. Vis. Image Underst.***2003**, *91*, 115–137. https://doi.org/10.1016/S1077-3142(03)00077-8.
30. Daffertshofer, A.; Lamoth, C.J.; Meijer, O.G.; Beek, P.J. PCA in studying coordination and variability: A tutorial. *Clin. Biomech.* **2004**, *19*, 415–428.
31. Choi, S.W.; Lee, C.; Lee, J.-M.; Park, J.H.; Lee, I.-B. Fault detection and identification of nonlinear processes based on kernel PCA. *Chemom. Intell. Lab. Syst.* **2005**, *75*, 55–67. https://doi.org/10.1016/j.chemolab.2004.05.001.
32. Yu, J.; Yoo, J.; Jang, J.; Park, J.H.; Kim, S. A novel plugged tube detection and identification approach for final super heater in thermal power plant using principal component analysis. *Energy* **2017**, *126*, 404–418. https://doi.org/10.1016/j.energy.2017.02.154.
33. Ferracuti, F.; Giantomassi, A.; Ippoliti, G.; Longhi, S. Multi-Scale PCA Based Fault Diagnosis for Rotating Electrical Machines. In Proceedings of the European Workshop on Advanced Control and Diagnosis, 8th ACD, Ferrara, Italy, 18–19 November 2010; pp. 296–301.
34. Filho, J.M.; Filho, J.M.D.C.; Paiva, A.P.; de Souza, P.V.G.; Tomasin, S. A PCA-based approach for substation clustering for voltage sag studies in the Brazilian new energy context. *Electr. Power Syst. Res.* **2016**, *136*, 31–42. https://doi.org/10.1016/j.epsr.2016.02.012.
35. Bhutto, J.A.; Lianfang, T.; Du, Q.; Soomro, T.A.; Lubin, Y.; Tahir, M.F. An Enhanced Image Fusion Algorithm by Combined Histogram Equalization and Fast Gray Level Grouping Using Multi-Scale Decomposition and Gray-PCA. *IEEE Access* **2020**, *8*, 157005–157021. https://doi.org/10.1109/ACCESS.2020.3018264.
36. Serna, Ignacio, Aythami Morales, Julian Fierrez, and Nick Obradovich. Sensitive loss: Improving accuracy and fairness of face representations with discrimination-aware deep learning. *Artif. Intell.* **2022**, *305*, 103682.
37. Castaño, A.; Fernández-Navarro, F.; Hervás-Martínez, C.PCA-ELM: A robust. *Neural Processing Lett.* **2013**,*37*, 377–392.
38. Miao, Y.Z.; Ma, X.P.; Bu, S.P. Research on the Learning Method Based on PCA-ELM. *Intell. Autom. Soft Comput.* **2017**, *23*, 637–642.
39. Ji, Y.; Zhang, S.; Yin, Y.; Su, X. Application of the improved the ELM algorithm for prediction of blast furnace gas utilization rate. *IFAC-PapersOnLine* **2018**, *51*, 59–64.
40. Yuan, B.; Wang, W.; Ye, D.; Zhang, Z.; Fang, H.; Yang, T.; Wang, Y.; Zhong, S. Nondestructive Evaluation of Thermal Barrier Coatings Thickness Using Terahertz Technique Combined with PCA–GA–ELM Algorithm. *Coatings* **2022**, *12*, 390.
41. Sun, W.; Sun, J. Prediction of carbon dioxide emissions based on principal component analysis with regularized extreme learning machine: The case of China. *Environ. Eng. Res.* **2017**, *22*, 302–311.

frontiers | Frontiers in Energy Research

ORIGINAL RESEARCH
published: 08 August 2022
doi: 10.3389/fenrg.2022.957971

PV/WT Integrated System Using the Gray Wolf Optimization Technique for Power Quality Improvement

B. Srikanth Goud[1], Ch. Rami Reddy[2], Ch. Naga Sai kalyan[3], Ramanjaneya Reddy Udumula[4], Mohit Bajaj[5,6], Bdereddin Abdul Samad[7], Mokhtar Shouran[7] and Salah Kamel[8]*

[1]Department of Electrical and Electronics Engineering, Anurag University, Ghatkesar, India, [2]Department of Electrical and Electronics Engineering, Malla Reddy Engineering College, Secunderabad, India, [3]Department of Electrical and Electronics Engineering, Vasireddy Venkatadri Institute of Technology, Guntur, India, [4]Department of Electrical and Electronics Engineering, SRM University, Amaravathi, India, [5]Department of Electrical Engineering, Graphic Era University, Dehradun, India, [6]Department of Electrical Engineering, National Institute of Technology, Delhi, India, [7]Wolfson Centre for Magnatics, School of Engineering, Cardif University, Cardiff, United Kingdom, [8]Department of Electrical Engineering, Faculty of Engineering, Aswan University, Aswan, Egypt

This paper presents the integration of renewable energy sources such as photovoltaics, wind, and batteries to the grid. The hybrid shunt active power filter (HSHAPF) is optimized with the Gray wolf optimization (GWO) and fractional order proportional integral controller (FOPI) for harmonic reduction under nonlinear and unbalanced load conditions. With the use of GWO, the parameters of FOPI are tuned, which effectively minimizes the harmonics. The proposed model has effectively compensated the total harmonic distortions when compared with without the filter and with the passive filter, the active power filter with a PI controller, and the GWO-FOPI-based controller. The performance of the proposed controller is tested under nonlinear and unbalanced conditions. The parameters of the FOPI controller are better tuned with the GWO technique. The comparative results reflect the best results of GWO-FOPI-based HSHAPF. The suggested controller is built in the MATLAB/Simulink Platform.

Keywords: hybrid shunt active power filter, Gray wolf optimization, fractional-order PI controller, renewable energy sources, power quality, harmonic compensation

OPEN ACCESS

Edited by:
Hadi Taghavifar,
UiT The Arctic University of Norway, Norway

Reviewed by:
Hamid Taghavifar,
Urmia University, Iran
Mohd Ashraf Ahmad,
Universiti Malaysia Pahang, Malaysia

****Correspondence:***
Bdereddin Abdul Samad
abdulsamadbf@cardiff.ac.uk

Specialty section:
This article was submitted to Process and Energy Systems Engineering, a section of the journal Frontiers in Energy Research

Received: *07 June 2022*
Accepted: *22 June 2022*
Published: *08 August 2022*

Citation:
Goud BS, Rami Reddy C, Naga Sai kalyan C, Udumula RR, Bajaj M, Abdul Samad B, Shouran M and Kamel S (2022) PV/WT Integrated System Using the Gray Wolf Optimization Technique for Power Quality Improvement. Front. Energy Res. 10:957971. doi: 10.3389/fenrg.2022.957971

1 INTRODUCTION

Power quality (PQ) problems that occur in the distribution system occur when using nonlinear loads. With the development in semiconductor technology, the modeling and usage of power electronic devices are increasing on the end-user side (Mosobi et al., 2015). Because of the usage of power electronic devices, they give rise to many problems like a disturbance in reactive power, a poor power factor, harmonic distortion, and so on (Dash et al., 2018). These problems cause severe effects on the distribution system which result in PQ. To mitigate PQ issues, we have many controlling techniques which ensure harmonic-free systems (Hussain et al., 2019). There are mainly two approaches: load

Abbreviations: APF, active power filter; BESS, battery as the energy storing system; CC-VSI, current controlled voltage source inverter; DG, distributing generation; FOPI, fractional order proportional integral; GWO, Gray wolf optimization; HPFC, hybrid power filter compensation; HSHAPF, hybrid shunt active power filter; PCC, point of common coupling; PV, photovoltaic; PWM, pulse width modulation; PQ, power quality; RES, renewable energy sources; THD, total harmonic distortion.

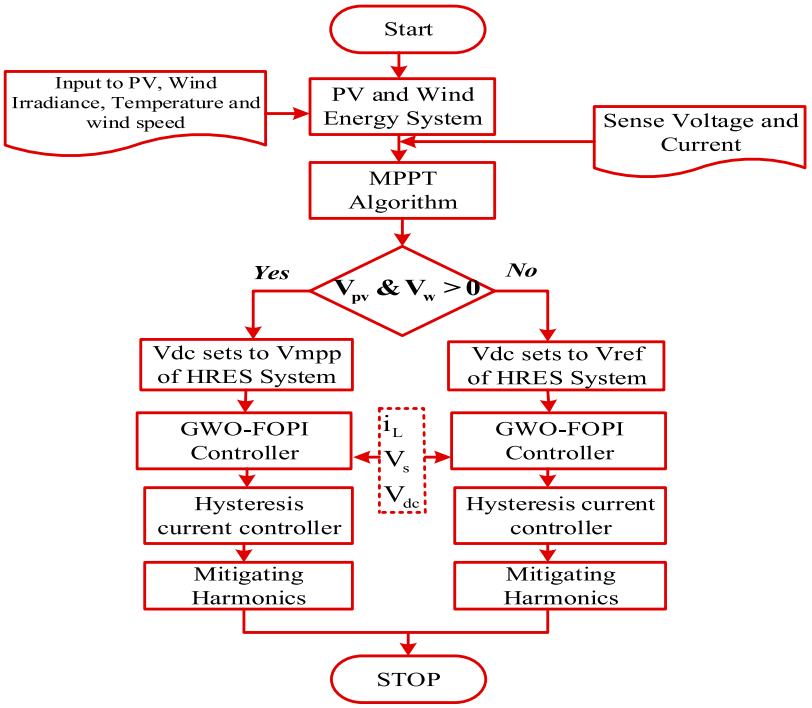

FIGURE 1 | Flow chart of the proposed system.

conditioning and power line conditioning (Amir and Srivastava, 2019). Most of the equipment used nowadays is more sensitive to the adverse effects of PQ problems (Goud and Reddy, 2020).

In this approach, at the point of common coupling (PCC), the proposed approach minimizes the effect produced by nonlinear loads. Initially, passive filter usage was widely considered for harmonic elimination and reactive power compensation. Due to various remarkable disadvantages like constant compensation performance, a large size, resonance, and so on, later on, the usage became less. To mitigate the reactive power compensation and harmonics (Jamil et al., 2019), active power filters (APFs) became more prominent as the performance characteristics are very effective when compared with the conventional filters (Meral and Celik, 2018).

APFs are devices that generally produces an equal quantity of harmonics when compared with the load with a phase shift of 180^0. These harmonics are injected into the linear PCC, and load current harmonics are mitigating and supply becomes sinusoidal (Pang et al., 2019). They are broadly classified as series APF and shunt APF. Shunt APF is used to mitigate the load current harmonics by inserting equal and opposite harmonic compensating current. **Table 1** presents the brief research works carried out in the literature. This literature mainly focuses on grid integration using RES, APFs, PQ issues, and various types of controllers designed to mitigate in the hybrid integrated system.

The designed system is a combination of photovoltaics (PVs), wind, and batteries as energy-storing devices (Arkhangelski et al., 2019). The purpose of using a battery is not only to provide backup but also to store the excess amount of generated energy to meet the demand. **Figure 1** shows the structure of HSHAPF CC-VSI which is grid interfaced through a DC-link capacitor (Naresh et al., 2018; Muthukumar and Balamurugan, 2019; Goud and Rao, 2020; Kuchibhatla et al., 2020). To increase the voltage if required, a step-up transformer is connected to the AC side of the inverter at the PCC. At the PCC, an uncontrolled bridge rectifier nonlinear load is connected. To minimize the load current harmonics, an inverter control is being utilized and transfers the DG power flow to the PCC.

1.1 Primary Aim and Structure of the Paper

In this paper, total harmonic distortion (THD) reduction under nonlinear load and unbalanced load without the filter, with the passive filter, and with APF using a PI controller and the proposed controller is introduced, which results in the best reduction of harmonics under various load conditions.

The following is the paper's primary contribution:

- The DG is the combination of PV, wind, and batteries as storing devices. Energy can be stored in the batteries when an excess amount is generated and can be used to compensate for the required load under various conditions.
- The system is an integrated system. The dynamic performance is observed under various load conditions when connected at the PCC. This integration creates the harmonics, which causes the affect the system's stability
- A metaheuristic algorithm known as the Gray wolf optimization (GWO) technique is introduced, which generates the best optimal pulse for the proposed

TABLE 1 | Review of recent research works.

Contribution	Authors	References
• They designed the PV and wind model with and without APF when connected to the nonlinear load. • They developed a DC-DC boost converter and inverter which convert to AC with the same frequency, amplification, and phase of the grid that will be connected to PV and wind system fundamental elements.	Aljendy et al.	Aljendy et al. (2019)
• They represented the performance, operational concepts, and analysis of D-STATCOM, which is widely used power electronic equipment designed to improve the PQ in low-voltage distribution systems. • They used VSC to improve the PF and THD reduction when LCL passive filters are employed.	E. Rambabu et al.	Rambabu et al. (2011)
• They designed an intelligent controller with SHAPF in the integrated hybrid energy system to mitigate the PQ issues. During the distribution of power, most of the PQ issues are raised due to the nonlinear loads. • Intelligent techniques are developed in the PV, wind, and fuel cell integrated system. Based on neuro-fuzzy system dynamics, pf SHAPF is optimized using adaptive control algorithms.	Ravinder et al.	Ravinder and Bansal, (2019)
• They developed a hybrid renewable energy source system integrated to the grid with UPQC, which is effectively used to mitigate PQ problems such as sag, swell, and disturbances. • They implemented an atom search optimization-based fractional order proportional integral controller.	C. R. Reddy et al.	Reddy et al. (2021)
• They proposed a microgrid power system that is boosted with a dual-voltage source inverter. • It mainly consists of two inverters for enabling the grid to exchange power produced by RES and offset the nonlinear load and unbalanced loads. • One inverter reduces the cost by implementing the filter voltage and increasing the usage of microgrid power, and the other inverter reduces the DC link voltage.	N. Kumar et al.	Bhupesh et al. (2019)
• They proposed a three-phase SHAPF nonlinear control approach. This design minimized the reactive, harmonic current components and unbalances. • To mitigate the disturbances of the conventional method, they proposed a conventional delay compensation approach which produces reference current with less precise delays. • Synchronous reference frame theory is used in the first stage to remove reference currents from nonlinear loads to compensate for the delay; a three-phase R-L loaded diode rectifier is used.	Rahmani S et al.	Rahmani et al. (2010)
• The proposed fast load voltage control and efficient voltage mitigation using a PWM voltage source inverter (VSI). • The control approach is designed based on a hybrid linear with a voltage controller for variable structure control and a dead bear controller. • The proposed system is used to balance voltage at PCC with VSI-based DG.	Mohamed et al.	Mohamed and El-Saadany, (2009)
• They designed a VSC-based hybrid power filter compensator (HPFC) for mitigating the harmonics and reactive power compensation in wind energy-based DG systems. • The multi-loop dynamic error control unit is designed with a DC voltage tracking loop to ensure robust and rapid control over the HPFC.	Imam et al.	Imam et al. (2020)
• They proposed UPQC and mainly focused on the distribution network problems such as reducing losses, voltage drop, overloads, and unbalance in line currents. • To improve the reliability, reduce losses, and increase the voltage profile, UPQC with reliability indices has been designed.	Dashtdar et al.	Dashtdar et al. (2021a)
• To meet the PQ requirements and mitigate them, they designed reliable power filters. They discussed SHAPF with the conventional PI controller to regulate DC link voltage and PQ enhancement. • For reference current extraction, instantaneous eference frame theory is used. To obtain gate pulses, hysteresis current control is used to generate the gate pulses to the VSI.	A. Sharaf et al.	Sharaf et al. (2010)

fractional order proportional integral (FOPI) controller, which effectively functions to mitigate the PQ issues and reduce THD.

The following sections of the papers are categorized as follows: **Section 2** describes the proposed system and design, **Section 3** proposes the mathematical modeling of the controller, **Section 4** describes the proposed HSHAPF, **Section 5** illustrates the GWO technique and FOPI controller, **Section 6** deals with results and discussion, and **Section 7** is the conclusion.

2 PROPOSED TEST SYSTEM

The proposed modeling is designed using both passive and active filters. The designed model improves the compensation characteristics of the filter, which reduces the disadvantages of both active and passive filters. **Figure 1** represents the flow chart of the proposed system. **Section 2** describes the detailed construction of the system design. In this proposed paper, HSHAPF is implemented with the combination of the LC passive filter and voltage source PWM converter illustrated in **Figure 2**, which illustrates the renewable energy resources (RES) and HSHAPF connected to the grid. **Table 2** illustrates the design parameters. **Figure 3** depicts the basic structure of SHAPF. This design is tested at various loads such as nonlinear loads and unbalanced loads. The characteristics of both filters are designed in providing the best performance under various operating conditions. To filter out the harmonics, the designed structure is modeled with storage systems using the battery, DC link, and switches with antiparallel diodes (Goud and Rao, 2021). At PCC, compensating current is injected using a voltage source converter to mitigate the harmonics. To overcome the power rating required for the PWM converter, the system is modeled using both active and passive filters to mitigate the harmonics. Here, power MOSFETs are used in

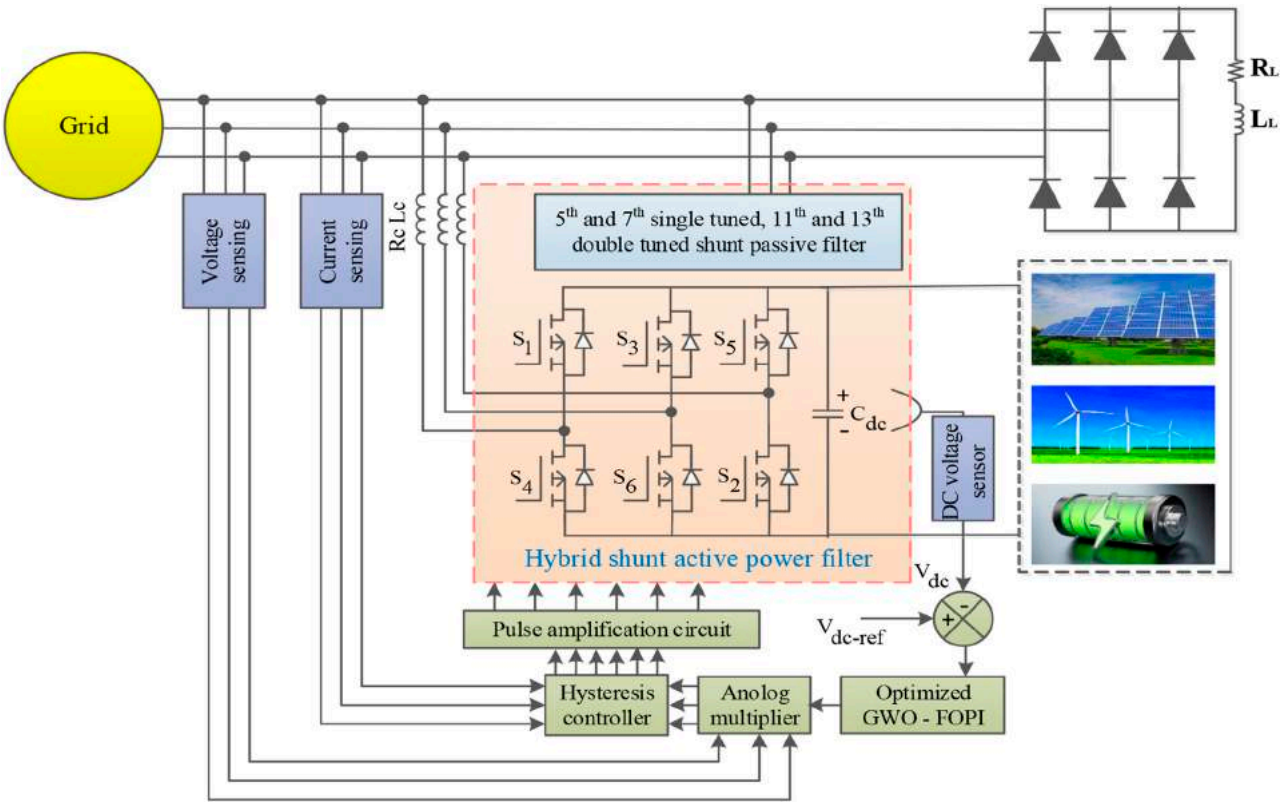

FIGURE 2 | Schematic diagram of RES-based HSHAPF.

TABLE 2 | System parameters.

S.No	Description	Parameters	Values
1		Voltage source	230 V
		Frequency	50 Hz
2	PV	Irradiance	1000
3		Diode resistance	595.5 Ω
4		Forward voltage	0.8 V
6	Wind	Base wind speed	12 m/s
7		Base rotational speed	0.4 m/s
8		Stator phase resistance	1.5 Ω
9		Armature inductance	8.5e-3H
10	Battery	Type	Nickel-metal-hydride
		The initial state of charge	100
11	Load	Nominal voltage	230 V

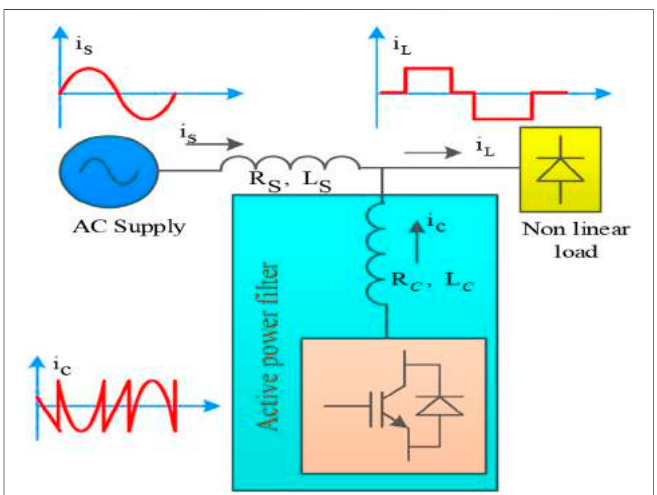

FIGURE 3 | Basic structure of shunt APF.

designing the PWM converters, which is cost-effective. To eliminate the harmonic at the PCC, equal and opposite magnitude harmonic current has to be injected, which also improves the PQ in the distribution system.

2.1 Equivalent Circuit of the Photovoltaic

The structure of PV is depicted in **Figure 4**, whose panel terminal current and voltage are computed based on the below equation (Mosobi et al., 2015; Dash et al., 2018)

$$I_p = I_{sc} - I_o\left\{\exp\left[\frac{Q}{akt}\left(V_p + I_p R_{SE}\right) - 1\right]\right\} - \frac{V_p + I_{sc}R_{se}}{R_{sh}} \quad (1)$$

$$V_p = \frac{akt}{Q}\ln\left\{\frac{I_{sc}}{I_p} + 1\right\} \quad (2)$$

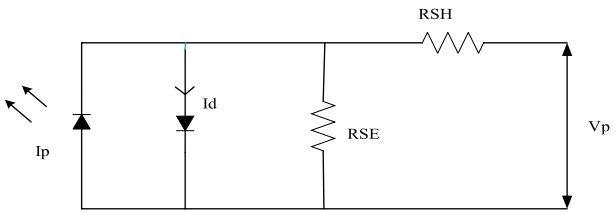

FIGURE 4 | Schematic diagram of PV.

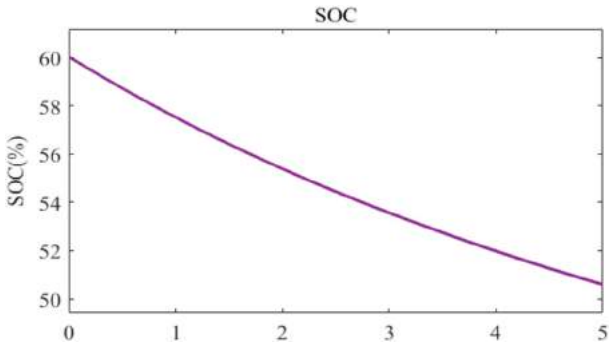

FIGURE 5 | Performance of the battery under the SOC.

where k is Boltzmann's constant, Q is the electron charge, a is the diode ideality factor, R_{SE} is the series resistance, t is the temperature in Kelvin, R_{SH} is the shunt resistance, V_P is the voltage of the cell, and I_{Sc} is the current. The power of a PV panel is described as follows:

$$P_{PV}(t) = N_{pv}(t) \times I_{pv}(t) \times V_{pv}(t) \tag{3}$$

where $N_{pv}(t)$ are several cells in the PV array, $P_{pv}(t)$ is the power of PV, $V_{pv}(t)$ $V_{pv}(t)$ is the voltage of PV, and $I_{pv}(t)$ is the current of PV. Maximum power extraction from the grid does not occur at any time as it is concerned with the allocation of current and load. MPPT is a standard method for capturing the maximum power from PV under load. There are many other sorts of methods; in this case, perturb and observer approaches are applied.

2.2 Modeling of the Wind Turbine

The wind turbine (WT) generates the output power, which was determined by wind speed as well as the hub's height. The WT is reliant on wind speed, which is calculated using the below equation (Amir and Srivastava, 2019)

$$P_{wind} = \begin{cases} 0 \\ P_R \bullet \dfrac{v - v_c}{v_R - v_c} \text{for} (V_c \le v \le v_R) \\ P_R \text{for} \left(V_R \le v \le v_f \right) \end{cases} \tag{4}$$

where P_R is the electrical power rating, v_C is the decrease in wind speed, v_R is the wind speed predicted, and v_F is the wind speed cut off. The impacts of WT installation height must be taken into account while calculating WT performance.

2.3 Modeling of the Battery as an Energy Storing System

The battery size is computed and developed using the reference autonomy day in the event of a required power requirement (AD) shown in the below equation (Goud and Reddy, 2020)

$$B^{capacity} = \frac{\text{Autonomyday} \times P^L}{\eta^I * \eta^B * \text{DOD}} \tag{5}$$

where η^B is the efficiency of the battery, DOD is the depth of discharge rate of the battery, P^L is the demand power, and η^I is the inverter efficiency. The amount of time a battery can produce electricity to meet load demand is described as AD. When RES generates excess electricity, it is used to charge a battery in the HRES system. The following equation is used to calculate battery power

$$B^P = P_{PV}(t) + P_{WT}(t) - \frac{P_L(t)}{\eta^I} \tag{6}$$

where B^P is the battery power. In the battery, $P_L(t)$ is the load demand of the system. As stated below, state of charge (SOC) is a critical parameter in HRES that is linked to additional energy creation and energy shortage. **Figure 5** depicts SOC

$$SOC(t) = \begin{Bmatrix} SOC(t-1)(1-\mu) + \\ \left(P_{pv}(t) + P_{WT}(t) - \dfrac{P_L(t)}{\eta^I} \right) \times \\ \eta^B, P_{pv}(t) + P_{WT}(t) > P_L(t) \\ SOC(t-1)(1-\mu) + \\ \left(\dfrac{P_L(t)}{\eta^I} - P_{pv}(t) + P_{WT}(t) \right) \times \\ \eta^B, P_{pv}(t) + P_{WT}(t) < P_L(t) \end{Bmatrix} \tag{7}$$

where μ is the battery self-discharge rate.

3 MATHEMATICAL MODELING OF THE PROPOSED SYSTEM

A set of n harmonics with n = {1,2,3,. . ..N} is proposed. At the same position, components are found, and they are current I_L (t) and Voltage V_s (t), which can be expressed as the equation that follows (Pang et al., 2019 and Aljendy et al., 2019). **Figures 6**, **7** depict the mathematical modeling of the controller

$$V_s(t) = \begin{bmatrix} V_{s1} \\ V_{s2} \\ V_{s3} \end{bmatrix} = \begin{bmatrix} \sum_{n=1}^{N} V_{sn1} \sin(n(\omega t)) \\ \sum_{n=1}^{N} V_{sn2} \sin\left(n\left(\omega t - 120^0\right)\right) \\ \sum_{n=1}^{N} V_{sn3} \sin\left(n\left(\omega t - 240^0\right)\right) \end{bmatrix} \tag{8}$$

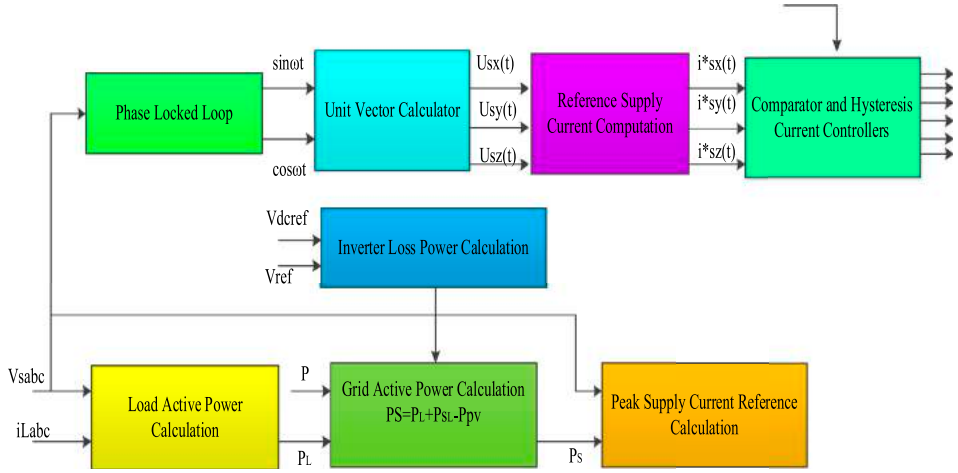

FIGURE 6 | Control structure of the proposed system.

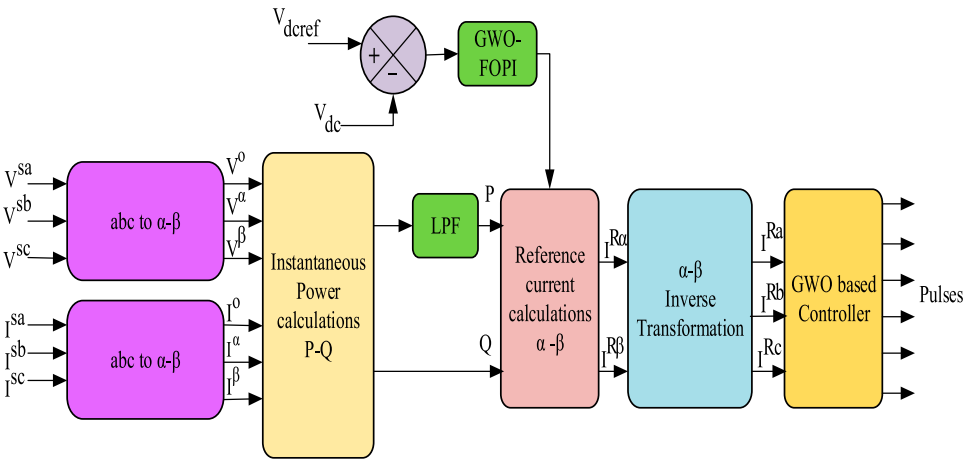

FIGURE 7 | HSHAPF control structure.

$$i_L(t) = \begin{bmatrix} i_{l1} \\ i_{l2} \\ i_{l3} \end{bmatrix} = \begin{bmatrix} \sum_{n=1}^{N} I_{Ln1} \sin\left(n\omega t - \phi_{n1}\right) \\ \sum_{n=1}^{N} I_{Ln2} \sin\left(n\left(\omega t - 120^0\right) - \phi_{n2}\right) \\ \sum_{n=1}^{N} I_{Ln3} \sin\left(n\left(\omega t + 120^0\right) - \phi_{n3}\right) \end{bmatrix} \quad (9)$$

(I_{Ln1}, I_{Ln2}, I_{Ln3}) are load current peak values; (V_{sn1}, V_{sn2}, V_{sn3}) are PCC voltage peak values; and ϕ_{n1}, ϕ_{n2}, and ϕ_{n3} are harmonic component phase angles of the nth order.

The real power delivered by the grid P_s should be similar to the grid power provided for compensating at a high power factor using the below equation (Aljendy et al., 2019)

$$P_s = P_L + P_l - P = \frac{3}{2} V_{s1} I_{s1}^* \quad (10)$$

where the real loss of power is P_l, the actual power delivered by the RES is P, and the real power of the load is P_L; as a result, the maximum value of the basic aspect of typical point voltage is a key component, and Is* is an essential component and is the source current component expressed in the below equation (Ravinder and Bansal, 2019)

$$I_{s1}^* = \frac{2P_s}{3V_{s1}} \quad (11)$$

$$\begin{aligned} I_{sx}^*(t) &= I_{s1}^* u_{sx} \\ I_{sy}^*(t) &= I_{s1}^* u_{sy} \\ I_{sz}^*(t) &= I_{s1}^* u_{sz} \end{aligned} \quad (12)$$

$$\begin{aligned} u_{sx}(t) &= u_a(t) \\ u_{sy}(t) &= -\frac{1}{2} u_a(t) + \frac{\sqrt{3}}{2} u_b(t) \\ u_{sz}(t) &= -\frac{1}{2} u_a(t) - \frac{\sqrt{3}}{2} u_b(t) \end{aligned} \quad (13)$$

where $u_a(t) = \sin\omega t$ and $u_b(t) = \cos\omega t$ as expressed by the equations (Bhupesh et al., 2019; Reddy et al., 2021) indicate the

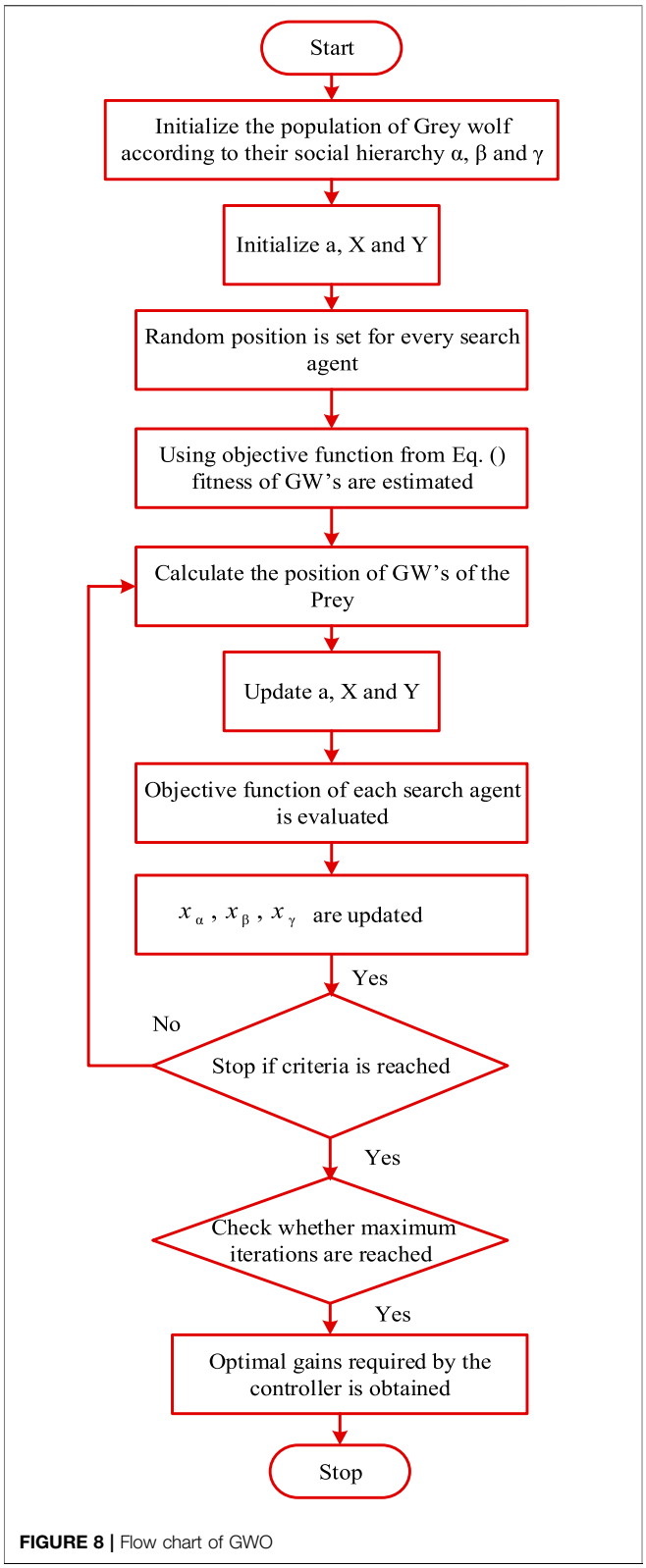

FIGURE 8 | Flow chart of GWO

distance between adjacent reference currents. The current inverter and standard inverter current errors are sent to the HCC ($\Delta ic_a, \Delta ic_b, \Delta ic_c$), which adjusts the duty ratio of the

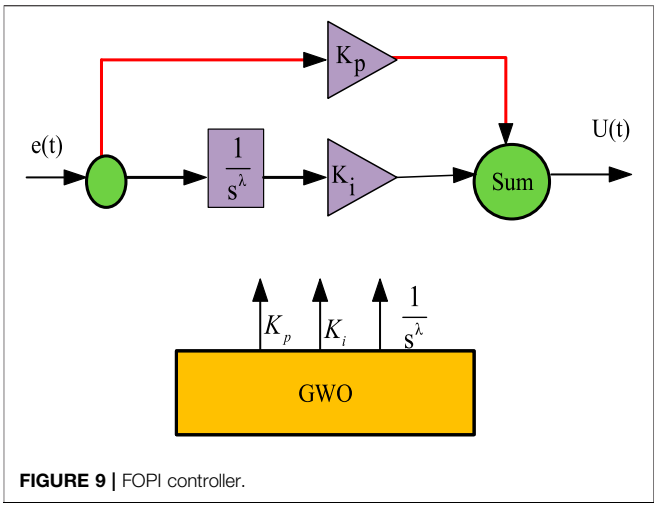

FIGURE 9 | FOPI controller.

PWM inverter expressed in the below equation (Rahmani et al., 2010)

$$\begin{aligned}\Delta i_{ca} &= I^*_{c1}(t) - i_{c1}\\ \Delta i_{cb} &= I^*_{c2}(t) - i_{c2}\\ \Delta i_{cc} &= I^*_{c3}(t) - i_{c3}\end{aligned} \tag{14}$$

Determined by the difference between the real and perceived currents of the inverter, the hysteresis regulator regulates and modulates pulse in both gate actuators of a grid-connected adapter. In phase A of the inverter, the S_1 switch is on, while $\Delta_{ic1} > H_b$ and S4 are off, and vice versa if $\Delta_{ic1} < H_b$.H_b the hysteresis band's width. The period of the switching pulses for either leg will be the same.

4 HYBRID SHUNT ACTIVE POWER FILTER CONTROL STRUCTURE

The p-q theory is used, which is mainly based on a-b-c conversion into α-β-0 coordinates and α-β-0 conversation into a-b-c parameters, which are familiarly known as Clark's transformation and inverse transformation, respectively (Durairasan and Balasubramanian, 2020; Hari Prabhu and Sundararaju, 2020; Sureshkumar and Ponnusamy, 2020). The transformation is shown in **Figures 6**, **7**, from which compensating currents are generated.

In this transformation, three-phase source voltage and load current are converted to stationary reference frame α-β-0 using the below equations (Mohamed and El-Saadany, 2009; Imam et al., 2020)

$$\begin{bmatrix} V^{s0} \\ V^{s\alpha} \\ V^{s\beta} \end{bmatrix} = \sqrt{\frac{2}{3}} \begin{bmatrix} \frac{1}{\sqrt{2}} & \frac{1}{\sqrt{2}} & \frac{1}{\sqrt{2}} \\ 1 & -\frac{1}{2} & -\frac{1}{2} \\ 0 & \frac{\sqrt{3}}{2} & -\frac{\sqrt{3}}{2} \end{bmatrix} \begin{bmatrix} V^{sa} \\ V^{sb} \\ V^{sc} \end{bmatrix} \tag{15}$$

TABLE 3 | FOPI controller parameters.

Parameter	Value
Search agents	50
No of iterations	10
Dim	3
K_p	5.9537
K_i	11.1470
λ	0.8798

$$\begin{bmatrix} I^{l0} \\ I^{l\alpha} \\ I^{l\beta} \end{bmatrix} = \sqrt{\frac{2}{3}} \begin{bmatrix} \frac{1}{\sqrt{2}} & \frac{1}{\sqrt{2}} & \frac{1}{\sqrt{2}} \\ 1 & -\frac{1}{2} & -\frac{1}{2} \\ 0 & \frac{\sqrt{3}}{2} & -\frac{\sqrt{3}}{2} \end{bmatrix} \begin{bmatrix} I^{La} \\ I^{Lb} \\ I^{Lc} \end{bmatrix} \tag{16}$$

where $I^{l\alpha}$ and $I^{l\beta}$ are phase-neutral currents, while I^{La}, I^{Lb}, and I^{Lc} are three-phase load currents. Three-phase supply voltages are V^{Sa}, V^{Sb}, and V^{Sc}, whereas the phase-neutral voltages are $V^{S\alpha}$, $V^{S\beta}$. The instantaneous values of actual and unconsidered powers are determined using phase neutral voltages and load currents (Hari Prabhu and Sundararaju, 2020; Sureshkumar and Ponnusamy, 2020). In the shunt active filter, the actual and reactive power is determined using the below equation (Dashtdar et al., 2021a)

$$\begin{bmatrix} P \\ Q \end{bmatrix} = \begin{bmatrix} V^{s\alpha} & V^{s\beta} \\ -V^{s\beta} & V^{s\alpha} \end{bmatrix} \begin{bmatrix} I^{l\alpha} \\ I^{l\beta} \end{bmatrix} \tag{17}$$

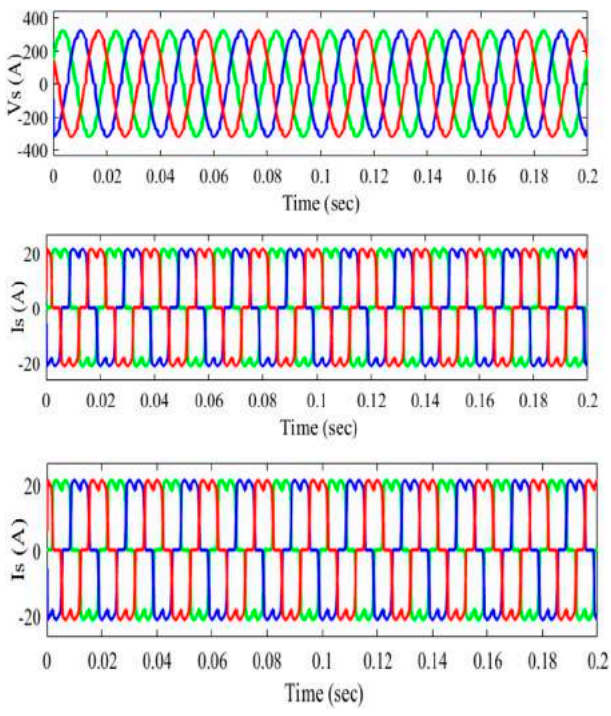

FIGURE 10 | Without the filter for nonlinear load source voltage (V_s), source current (I_s), and load current (I_L).

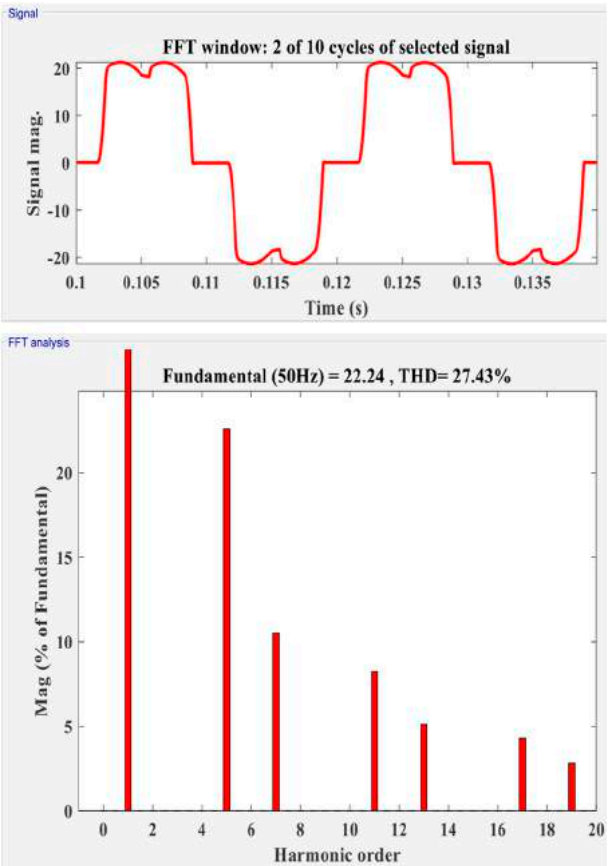

FIGURE 11 | Without the filter for unbalanced load source voltage (V_s), source current (I_s), and load current (I_L).

Using the below equation (Sharaf et al., 2010), the reference currents are evaluated

$$\begin{bmatrix} I^{Ra} \\ I^{Rb} \\ I^{Rc} \end{bmatrix} = \sqrt{\frac{2}{3}} \begin{bmatrix} 1 & 0 \\ -\frac{1}{2} & \frac{\sqrt{3}}{2} \\ -\frac{1}{2} & -\frac{\sqrt{3}}{2} \end{bmatrix} \begin{bmatrix} I^{R\alpha} \\ I^{R\beta} \end{bmatrix} \tag{18}$$

I^{Ra}, I^{Rb}, and I^{Rc} represent the reference currents of an HSHAPF. The reference current is used to calculate the erroneous current, which must be modified using the GWO-optimized PI controller. Based on system error reduction, the SHAPF creates optimal pulses. The GWO is utilized to compute the optimal solution and the best pulses for adjusting the FOPI controller. The next section describes a detailed description of the recommended strategy as well as a flow chart.

5 GRAY WOLF OPTIMIZATION TECHNIQUE

GWO is new optimization that is supported by the swarm intelligence which is inspired by the psychology of GW to

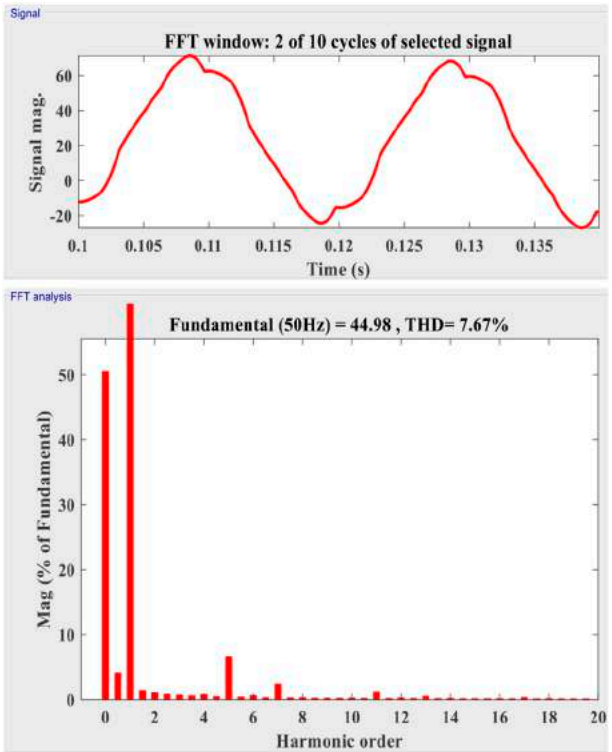

FIGURE 12 | With the passive filter for nonlinear load source voltage (V_s), source current (I_s), and load current (I_L).

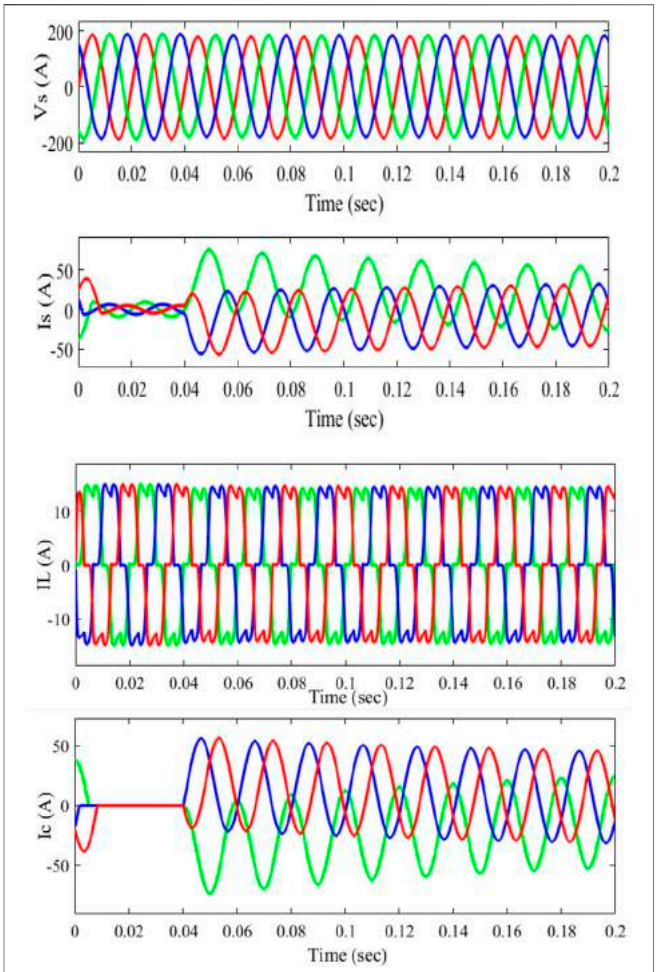

FIGURE 13 | Analysis of PV irradiance, PV power, wind speed, and wind power.

hunt prey illustrated in **Figure 8**. GWs are always in groups and adjusted in a location during the hunting process. To model the hunting procedure mathematically, the optimal best solution is given to the alpha group act following beta and delta packs (Goud et al., 2020). GWs create a kink around the injured to start hunting the prey, generally written as

$$\vec{d} = \left|\vec{c}.\vec{x}_p(t) - \vec{x}(t)\right| \tag{19}$$

$$\vec{x}(t+1) = \left|\vec{x}_p(t) - \vec{a}.\vec{d}\right| \tag{20}$$

't' in **Eq. 19** indicates the current iteration. The vectors x and x_p indicate the GW and the wound location, respectively, and coefficient vectors X and Y are framed from the below equations (Naresh et al., 2018; Goud and Rao, 2020)

$$\vec{X} = 2.\vec{a}.\vec{r}_1 - \vec{a} \tag{21}$$

$$\vec{Y} = 2.\vec{r}_2 \tag{22}$$

r_1 and r_2 indicate the random vector, which varies between (0, 1), while the component "a" falls from 2 to 0 throughout the iteration. Using the below equations (Durairasan and Balasubramanian, 2020; Kuchibhatla et al., 2020; Goud and Rao, 2021), the hunting process is calculated

$$\left.\begin{aligned}\vec{d}_\alpha &= \left|\vec{c}_1.\vec{x}_\alpha - \vec{x}\right| \\ \vec{d}_\beta &= \left|\vec{c}_2.\vec{x}_\beta - \vec{x}\right| \\ \vec{d}_\gamma &= \left|\vec{c}_3.\vec{x}_\gamma - \vec{x}\right|\end{aligned}\right\} \tag{23}$$

$$\left.\begin{aligned}\vec{x}_1 &= \vec{x}_\alpha - \vec{a}_1\left(\vec{d}_\alpha\right) \\ \vec{x}_2 &= \vec{x}_\beta - \vec{a}_2\left(\vec{d}_\beta\right) \\ \vec{x}_3 &= \vec{x}_\gamma - \vec{a}_3\left(\vec{d}_\gamma\right)\end{aligned}\right\} \tag{24}$$

Using the below equation (Durairasan and Balasubramanian, 2020), the α, β, and γ mean value positions are found

$$\vec{x}(t+1) = \frac{\vec{x}_1 + \vec{x}_2 + \vec{x}_3}{3} \tag{25}$$

The procedure of the suggested approach is as follows:

Step 1: Create the populations.
Step 2: Using **Eqs 21**, **22**, calculate the values of Y, a, and Z.

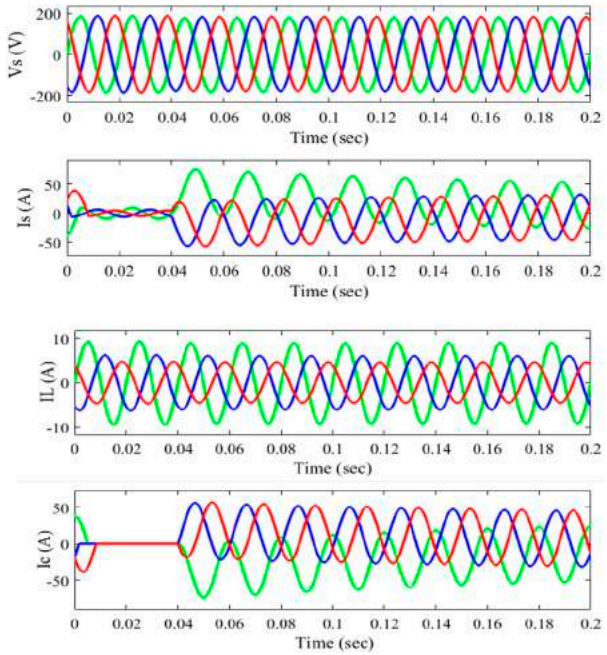

FIGURE 14 | With the passive filter for unbalanced load source voltage (V_s), source current (I_s), and load current (I_L).

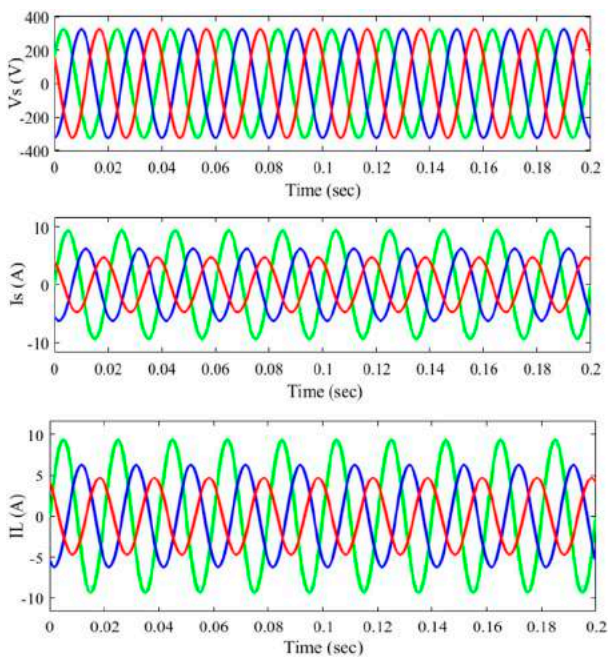

FIGURE 15 | Total harmonic distortion with the passive filter.

Step 3: A random location is created from the Search agent.
Step 4: The fitness values of Gray wolves are computed using an objective function.

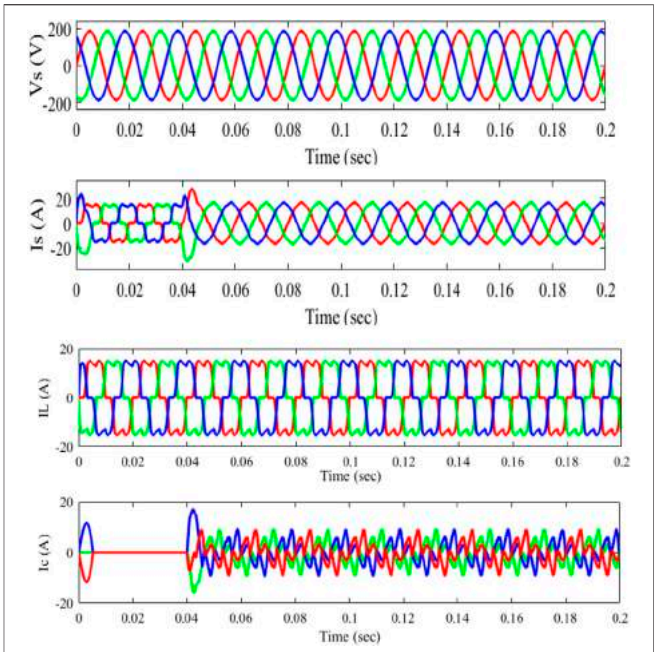

FIGURE 16 | With SHAPF for nonlinear load source voltage (V_s), source current (I_s), load current (I_L), and compensating current (I_c).

Step 5: The position of the Gray wolves as well as the parameters A, a, and C, are changed.
Step 6: Using fitness calculations, the optimal option for the next generation is selected.
Step 7: x_α, x_β, and x_γ are all updated.
Step 8: If the halting condition is not met, the preceding steps are repeated.
Step 9: The controller's optimal settings are determined.

5.1 Fractional Order Proportional Integral Controller

The FOPI controller's transfer function is represented by the below equation (Goud et al., 2021a; Dashtdar et al., 2021b; Goud et al., 2021b; Goud et al., 2021c). The FOPI controller design is seen in **Figure 9**

$$U(t) = K_p e(t) + K_i \int_t^{\lambda} e(t) \tag{26}$$

The values of the controller depend on K_p, K_i, and fractional-order λ and are represented in **Table 3**.

6 SIMULATION RESULTS

HSHAPF performance is analyzed in MATLAB/Simulink. Two different loads are considered: nonlinear load and unbalanced load. Without the filter, the THD was 27.43%, and after HSHAPF

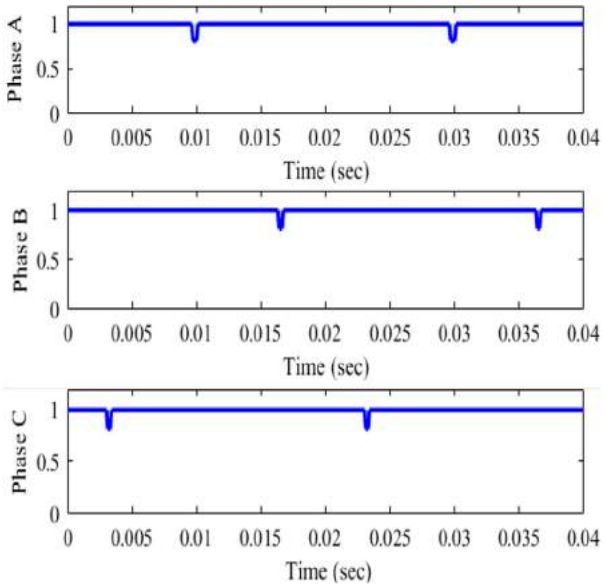

FIGURE 17 | Total harmonic distortion without the filter.

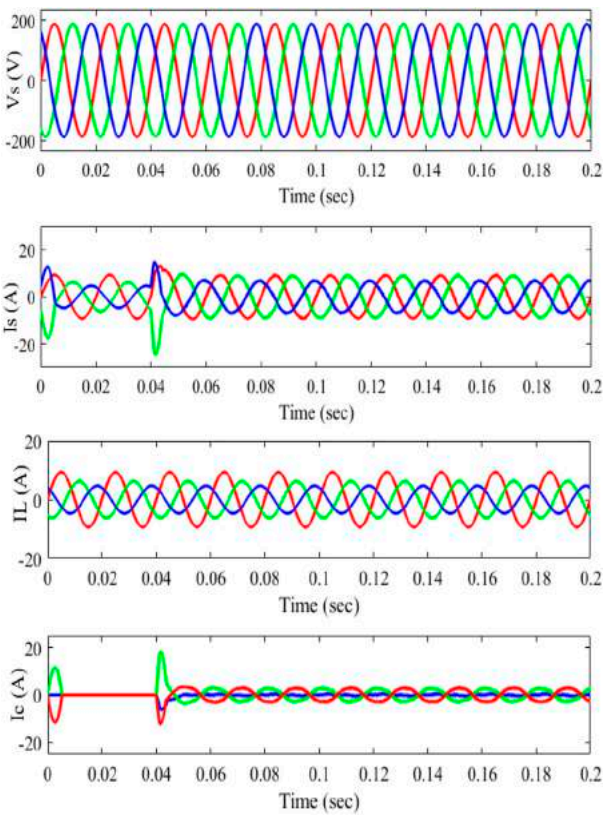

FIGURE 18 | Total harmonic distortion with GWO-based SHAPF.

with the GWO-based FOPI controller, the THD is reduced to 1.74%. Similarly, with a passive filter, the THD is 7.67%, and with APF with the PI controller, the THD is 5.85%.

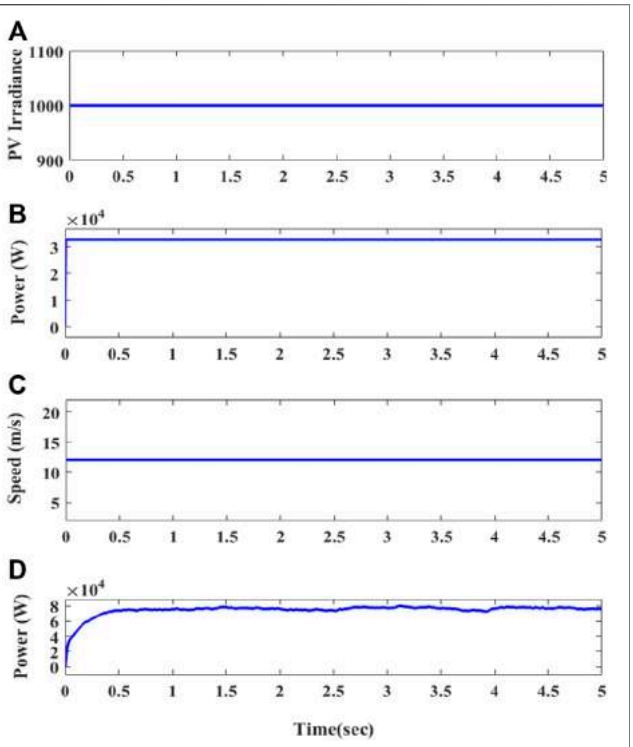

FIGURE 19 | Power factor for phases A, B, and C.

6.1 Case I: Without the Filter for Nonlinear Load

At PCC, nonlinear load is connected, which is generally time-varying and difficult to observe system dynamic performances. At the first diode, the rectifier load is connected to the PCC. During t = 0.01 s to t = 0.2 s, an additional RL segment is added. The figure shows that the inputs to PV and wind are 800–1000 w/m^2 and 12–15 m/s, respectively.

In this case, the system dynamic performance of the system without using the filter is analyzed. **Figure 10** shows that the harmonics are not eliminated. It represents the source voltage (Vs.), source current (I_s), and load current (I_L). During time intervals t = 0.01 s to t = 0.04 s, harmonics are observed in both the source current and load current when the design is employed without the filter. **Figure 8** represents the THD of about 27.43%. For the sudden change in load at the PCC, it is observed that the system has high dynamic performance.

6.2 Case II: Without the Filter for Unbalanced Load

Initially, the load connected at the PCC is the diode rectifier which is then replaced with a single-phase diode rectifier which behaves as an unbalanced load during t = 0.01 s and is removed at t = 0.2 s. From **Figure 11**, PCC voltage V_s, supply current I_s, and unbalanced current I_L show the dynamic performances of the system.

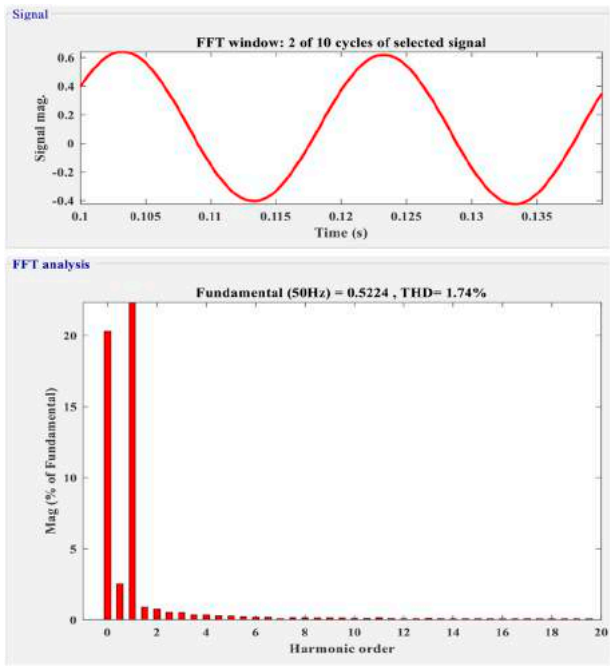

FIGURE 20 | With SHAPF for unbalanced linear load source voltage (V_s), source current (I_s), load current (I_L), and compensating current (I_c).

6.3 Case III: With the Passive Filter for Nonlinear Load

Sudden changes in loads are nonlinear, so it is important to analyze the system's dynamic characteristics. A diode rectifier load is first connected to the PCC. From t = 0.01 s to t = 0.04 s, an extra load of the RL circuit is added to the previous load. During the nonlinear load, the current decreases from 45A to 5A at time t = 0.01 s and then climbs from 5 to 45A at time t = 0.04 s. The voltage at PCC V_s, supply current I_s, variable load current I_L, and compensating current I_c between t = 0.01 s and t = 0.04 s are shown in **Figure 12**. The findings show that nonlinear control has high dynamic performance for fast-changing loads.

6.4 Case IV: With Passive Filter Unbalanced Load

The imbalance, harmonics, and reactive power of an unbalanced nonlinear load must be rectified at PCC. A three-phase diode is used as the load at first. At t = 0.01 s, a one-phase rectifier is connected in series to the PCC and removed at t = 0.04 s. The input values for PV are 1000 w/m^2 and a wind speed of 12 m/s, depicted in **Figure 13**. Between t = 0.01 s and t = 0.04 s, the PCC is connected to a resistor between phases a and b and then withdrawn. In **Figure 14**, V_s represents the PCC voltage, I_s represents the source current, I_L represents the current at load, and I_c represents the inverter. Even with erratic supply currents, PCC's source currents are balanced. As a consequence, the recommended control may be able to balance line currents while simultaneously correcting for reactive and harmonic components of a load. **Figure 15** shows that the THD is 7.67%, which is lowered by using a passive filter.

TABLE 4 | Comparison of THDs.

Total harmonic distortion	
Without the filter	27.43 (%)
With the passive filter	7.67
APF with PI controllers	5.85
With the GWO-FOPI controller	1.74

6.5 Case V: With the Shunt Active Power Filter for Nonlinear Load

Because rapid change loads are nonlinear, time-varying loads, it is critical to analyze the system's dynamic characteristics. The PCC is initially linked to a three-phase diode rectifier load. An extra load of the RL circuit is added to the current load from t = 4 s to t = 5 s. At time t = 0.01 s, the nonlinear load current rises from 45A to 5A, and at time t = 0.04 s, it climbs from 5 to 45A. **Figure 16** represents the voltage at PCC V_s, the supply current I_s, the variable load current IL, and the compensating current I_c between periods t = 0.01 s and t = 0.04 s. The findings show that nonlinear control has high dynamic performance for fast-changing loads. As the PCC load current increases, the THD value rises. The THD is 27.43%, depicted in **Figure 17** without the filter, 7.67% depicted in **Figure 15** with the passive filter, and 1.74% with the suggested GWO-FOPI controller with SHAPF depicted in **Figure 18**. The power factors for phases A, B, and C are all 0.99, as shown in **Figure 19**.

6.6 Case VI: With Hybrid Shunt Active Power Filter Unbalanced Load

The variations, reactive power, and harmonics of an unbalanced load must be rectified at PCC. In the beginning, a single-phase diode is used as the load. A single-phase rectifier is connected in series to the PCC at = 0.01 s. Between t = 0.01 s and t = 0.04 s, the PCC is connected to a resistor between phases a and b and then withdrawn. **Figure 20** represents the voltage at PCC V_s, the supply current I_s, the variable load current I_L, and the inverter current I_c. The supply current is balanced at PCC even during irregularities. As a consequence, the recommended control may be able to balance line currents while simultaneously correcting for reactive and harmonic load current components. **Table 4** compares THDs without a filter to THDs with a filter.

Finally, under the IEEE 519 standards, the suggested GWO-based FOPI controller with decreased THD is proposed. With the suggested controller, the THD is decreased by 1.74%.

7 CONCLUSION

PQ in a grid-connected hybrid system with the battery as an energy storing device is proposed with the GWO-based FOPI controller with SHAPF circuit to mitigate the issues. The optimal pulses required for the FOPI controller are attained with the GWO technique. This system has been considered in three different practices: without a filter, the THD is 27.43%; with a passive filter, the THD is 7.67%; the APF with the PI controller is 5.85%, and with the proposed GWO-FOPI controller, it resulted in 1.74% total harmonic reduction. The recommended method's simulation results are then validated in the MATLAB/Simulink software. The final results of the hybrid system proved the GWO controller's practicality and effectiveness in decreasing PQ concerns including THD.

DATA AVAILABILITY STATEMENT

The original contributions presented in the study are included in the article/supplementary material; further inquiries can be directed to the corresponding author.

AUTHOR CONTRIBUTIONS

All authors listed have made a substantial, direct, and intellectual contribution to the work and approved it for publication.

REFERENCES

Aljendy, R., Nasyrov, R. R., Abdelaziz, A. Y., and Diab, A. A. Z. (2019). Enhancement of Power Quality with Hybrid Distributed Generation and FACTS Device. *IETE J. Res.*, 1–12. doi:10.1080/03772063.2019.1698321

Amir, M., and Srivastava, S. K. (2019). "Analysis of Harmonic Distortion in PV-Wind-Battery Based Hybrid Renewable Energy System for Microgrid Development," in *Applications of Computing, Automation and Wireless Systems in Electrical Engineering* (Singapore: Springer), 1223–1231. doi:10.1007/978-981-13-6772-4_107

Arkhangelski, J., Roncero-Sánchez, P., Abdou-Tankari, M., Vázquez, J., and Lefebvre, G. (2019). Control and Restrictions of a Hybrid Renewable Energy System Connected to the Grid: A Battery and Supercapacitor Storage Case. *Energies* 12, 2776. doi:10.3390/en12142776

Bhupesh, N. K., Kotaiah Chowdary, K., and Subrahmanyam, V. (2019). Renewable Energy Hybrid Power System with Improvement of Power Quality in Grid by Using DVSI. *Renew. Energy* 6, 1300.

Dash, S. K., Ray, P. K., and Ray, P. K. (2018). Power Quality Improvement Utilizing PV Fed Unified Power Quality Conditioner Based on UV-PI and PR-R Controller. *Cpss Tpea* 3, 243–253. doi:10.24295/cpsstpea.2018.00024

Dashtdar, M., Bajaj, M., Hosseinimoghadam, S. M. S., Sami, I., Choudhury, S., Rehman, A. U., et al. (2021a). Improving Voltage Profile and Reducing Power Losses Based on Reconfiguration and Optimal Placement of UPQC in the Network by Considering System Reliability Indices. *Int. Trans. Electr. Energy Syst.* 31 (11), e13120. doi:10.1002/2050-7038.13120

Dashtdar, M., Nazir, M. S., Hosseinimoghadam, S. M. S., and Bajaj, M. (2021b). Improving the Sharing of Active and Reactive Power of the Islanded Microgrid Based on Load Voltage Control. *Smart Sci.* 10, 1–16. doi:10.1080/23080477.2021.2012010

Durairasan, M., and Balasubramanian, D. (2020). An Efficient Control Strategy for Optimal Power Flow Management from a Renewable Energy Source to a Generalized Three-phase Microgrid System: A Hybrid Squirrel Search Algorithm with Whale Optimization Algorithm Approach. *Trans. Inst. Meas. Control* 42, 1960–1976. doi:10.1177/0142331220901628

Goud, B. S., and Rao, B. L. (2021). Power Quality Enhancement in Grid-Connected PV/wind/battery Using UPQC: Atom Search Optimization. *J. Electr. Eng. Technol.* 16, 821–835. doi:10.1007/s42835-020-00644-x

Goud, B. S., and Rao, B. L. (2020). Power Quality Improvement in Hybrid Renewable Energy Source Grid-Connected System with Grey Wolf Optimization. *Int. J. Renew. Energy Res. (IJRER)* 10, 1264–1276. doi:10.20508/ijrer.v10i3.11318.g8004

Goud, B. S., Rao, B. L., Reddy, B. N., Rajesh, N., Anjan, B., and Reddy, C. R. (2020). "Optimization Techniques in PV-Wind Based Distribution Generation-A Brief Review," in 2020 IEEE 17th India Council International Conference (INDICON), India, 10-13 Dec. 2020, 1–6.

Goud, B. S., Rao, B. L., and Reddy, C. R. (2021a). An Intelligent Technique for Optimal Power Quality Reinforcement in a Grid-connected HRES System: EVORFA Technique. *Int. J. Numer. Model. Electron. Netw. Devices Fields* 34, e2833. doi:10.1002/jnm.2833

Goud, B. S., Reddy, C. R., Bajaj, M., Elattar, E. E., and Kamel, S. (2021b). Power Quality Improvement Using Distributed Power Flow Controller with BWO-Based FOPID Controller. *Sustainability* 13, 11194. doi:10.3390/su132011194

Goud, B. S., and Reddy, C. R. (2020). Essentials for Grid Integration of Hybrid Renewable Energy Systems: a Brief Review. *Int. J. Renew. Energy Res. (IJRER)* 10, 813–830. doi:10.20508/ijrer.v10i2.10772.g7950

Goud, B. S., Reddy, C. R., Rakesh, T., Rajesh, N., Reddy, B. N., and Aymen, F. (2021c). Grid Integration of Renewable Energy Sources Using GA Technique for Improving Power Quality. *Int. J. Renew. Energy Res. (IJRER)* 11 (3), 1390–1402. doi:10.20508/ijrer.v11i3.12292.g8283

Hari Prabhu, M., and Sundararaju, K. (2020). Power Quality Improvement of Solar Power Plants in Grid Connected System Using Novel Resilient Direct Unbalanced Control (RDUC) Technique. *Microprocess. Microsystems* 75, 103016. doi:10.1016/j.micpro.2020.103016

Hussain, J., Hussain, M., Raza, S., and Siddique, M. (2019). Power Quality Improvement of Grid Connected Wind Energy System Using DSTATCOM-BESS. *Int. J. Renew. Energy Res.* 9, 1388–1397. doi:10.20508/ijrer.v9i3.9802.g7717

Imam, A. A., Sreerama Kumar, R., and Al-Turki, Y. A. (2020). Modeling and Simulation of a PI Controlled Shunt Active Power Filter for Power Quality Enhancement Based on P-Q Theory. *Electronics* 9 (4), 637. doi:10.3390/electronics9040637

Jamil, E., Hameed, S., Jamil, B., and Qurratulain (2019). Power Quality Improvement of Distribution System with Photovoltaic and Permanent Magnet Synchronous Generator Based Renewable Energy Farm Using Static Synchronous Compensator. *Sustain. Energy Technol. Assessments* 35, 98–116. doi:10.1016/j.seta.2019.06.006

Kuchibhatla, S. M., Padmavathi, D., and Rao, R. S. (2020). An Elephant Herding Optimization Algorithm-Based Static Switched Filter Compensation Scheme for Power Quality Improvement in Smart Grid. *J. Circuit Syst. Comp.* 29, 2050066. doi:10.1142/s0218126620500668

Meral, M. E., and Celik, D. (2018). DSOGI-PLL Based Power Control Method to Mitigate Control Errors under Disturbances of Grid Connected Hybrid Renewable Power Systems. *Adv. Electr. Electron. Eng.* 16, 81–91. doi:10.15598/aeee.v16i1.2485

Mohamed, Y. A.-R. I., and El-Saadany, E. F. (2009). A Control Method of Grid-Connected PWM Voltage Source Inverters to Mitigate Fast Voltage Disturbances. *IEEE Trans. Power Syst.* 24 (1), 489–491. doi:10.1109/tpwrs.2008.2006996

Mosobi, R. W., Chichi, T., and Gao, S. (2015). Power Quality Analysis of Hybrid Renewable Energy System. *Cogent Eng.* 2, 1005000. doi:10.1080/23311916.2015.1005000

Muthukumar, R., and Balamurugan, P. (2019). A Model Predictive Controller for Improvement in Power Quality from a Hybrid Renewable Energy System. *Soft Comput.* 23, 2627–2635. doi:10.1007/s00500-018-3626-7

Naresh, M., Soni, U. K., and ripathi, R. K. (2018). Power Flow Control and Power Quality Improvement in DFIG Based Wind Energy Conversion System Using Neuro Fuzzy System. *Int. J. Appl. Eng. Res.* 13, 5236–5243.

Pang, M., Shi, Y., Wang, W., and Pang, S. (2019). Optimal Sizing and Control of Hybrid Energy Storage System for Wind Power Using Hybrid Parallel PSO-GA Algorithm. *Energy Explor. Exploitation* 37, 558–578. doi:10.1177/0144598718784036

Rahmani, S., Mendalek, N., and Al-Haddad, K. (2010). Experimental Design of a Nonlinear Control Technique for Three-phase Shunt Active Power Filter.

IEEE Trans. Ind. Electron. 57 (10), 3364–3375. doi:10.1109/tie.2009.2038945

Rambabu, E., Praveena, E., and Kishore, P. V. (2011). Mitigation of Harmonics in Distribution System Using D-STATCOM. *Int. J. Sci. Eng. Res. IJSER* 2, 1–5.

Ravinder, K., and Bansal, H. O. (2019). Investigations on Shunt Active Power Filter in a PV-Wind-FC Based Hybrid Renewable Energy System to Improve Power Quality Using Hardware-In-The-Loop Testing Platform. *Electr. Power Syst. Res.* 177, 105957. doi:10.1016/j.epsr.2019.105957

Reddy, C. R., Goud, B. S., Aymen, F., Rao, G. S., and Bortoni, E. C. (2021). Power Quality Improvement in HRES Grid Connected System with FOPID Based Atom Search Optimization Technique. *Energies* 14 (18), 5812. doi:10.3390/en14185812

Sharaf, A. M., Wang, W., and Altas, I. H. (2010). A Novel Hybrid Active Filter Compensator for Stabilization of Wind-Utility Grid Interface Scheme. *Euro. Trans. Electr. Power* 20 (3), 306–326. doi:10.1002/etep.313

Sureshkumar, K., and Ponnusamy, V. (2020). Hybrid Renewable Energy Systems for Power Flow Management in Smart Grid Using an Efficient Hybrid Technique. *Trans. Inst. Meas. Control* 42, 2068–2087. doi:10.1177/0142331220904818

Conflict of Interest: The authors declare that the research was conducted in the absence of any commercial or financial relationships that could be construed as a potential conflict of interest.

Publisher's Note: All claims expressed in this article are solely those of the authors and do not necessarily represent those of their affiliated organizations or those of the publisher, the editors, and the reviewers. Any product that may be evaluated in this article or claim that may be made by its manufacturer is not guaranteed or endorsed by the publisher.

IEEE Access
Multidisciplinary | Rapid Review | Open Access Journal

Date of publication xxxx 00, 0000, date of current version xxxx 00, 0000.

Digital Object Identifier 10.1109/ACCESS.2017.Doi Number

Improving the power quality of island microgrid with voltage and frequency control based on a hybrid genetic algorithm and PSO

Masoud Dashtdar[1], Aymen Flah[2], Seyed Mohammad Sadegh Hosseinimoghadam[1], CH Ramy Reddy[3], Hossam Kotb[4], and Kareem M. AboRas[4], Bortoni Edson C[5]

[1]Electrical Engineering Department, Bushehr Branch, Islamic Azad University, Bushehr, Iran
[2]Energy Processes Environment and Electrical Systems Unit, National Engineering School of Gabes, University of Gabes, Gabes 6029, Tunisia
[3]Electrical and Electronics Engineering, Malla Reddy Engineering College (A), Maisammaguda, Secunderabad 600119, India
[4]Department of Electrical Power and Machines, Faculty of Engineering, Alexandria University, Alexandria 21544, Egypt
[5]Electric and Energy Systems Institute, Itajubá Federal University, Itajubá 37500, Brazil

Corresponding author: Aymen Flah (aymen.flah@enig.u-gabes.tn)

ABSTRACT An efficient power control technique for inverter-based distributed generation (DG) in an islanded microgrid is investigated in this work. The objective is to raise the caliber of the electricity pumped from network-connected DGs. The characteristics that are taken into consideration include voltage and frequency control, dynamic response, and steady-state response, particularly when the microgrid is operating in island mode or when there is a load change. The control method consists of an internal current control loop and an external power control loop based on a synchronous reference frame and a conventional PI controller. The power controller is designed based on voltage-frequency (VF) control. In addition, an intelligent search technique that combines Particle Swarm Optimization (PSO) and Genetic Algorithm (GA) is utilized to automatically modify power controller parameters. The control technique in this research is that the DG modifies its control mode to modify the system voltage and frequency when the microgrid is islanded or load conditions change. The simulation results in MATLAB/SIMULINK software show that the proposed control system has been able to improve the power quality well.

INDEX TERMS Microgrid, PI controller, Voltage control, Frequency control, Genetic algorithm, PSO.

I. INTRODUCTION

A microgrid typically consists of a local set of DGs, energy storage systems, and different thermal and electric loads. Which represents the complementary power grid infrastructure due to the rapid increase in load demand. The microgrid can operate in two modes of network connection and islands. In addition, the infiltration of micro-sources such as wind, photovoltaics, water, and fuel cells has emerged as alternatives in the electricity market that provide green energy and scalability in the power system. However, such sources are usually connected by PWM-VSI (Pulse Width Modulation-Voltage Source Inverter) systems, whose semiconductor components have a non-linear voltage-current characteristic and provide a high switching frequency, which increases the quality of power in end consumers [1-2]. In microgrids, to achieve high-efficiency operation, achieve the desired power quality, and the possibility of connecting DGs to the network, we need a strong control system. As a result, one of the most essential components of modern electronic power converters is the current control strategy of the PWM-VSI system. Hysteresis Current Control (HCC) is a nonlinear controller that is widely utilized for a three-phase network-connected VSI system. The current controller which is linear Spatial Vector PWM (SVPWM) is a suitable controller that compensates for current error using a proportional-integral controller (PI) or a predictive control technique that can correct and generate PWM independently. This controller features a high-quality sine waveform, outstanding steady-state response, and low current ripple. Furthermore, because SVPWM has good qualities such as a stable switching frequency, appropriate switching pattern, and excellent use of DC-link voltage, it can improve controller behavior [3-4].

In addition, to generate PWM reference voltage signals, an external power control loop is commonly paired with a current control loop. In the combined control method, the power control strategy, to provide acceptable power quality, plays a key role. One of the following two power control

strategies can be used by the DG unit. In network connection mode, an active-reactive power control method is used, while in island mode, a voltage-frequency control technique is used. In this instance, the DG unit must provide maximum power while maintaining system stability [5-7]. Researchers have recently developed power controllers based on the internal current control loop that improves network configuration. In [8-9] a controller is investigated that seeks to improve dynamic stability and provides all the information needed for analysis and design. In [10-13], a power control strategy is applied to a microgrid, which can be analyzed and compared. Although dynamic performance and load sharing are taken into account, as well as controller details, this procedure lacks automatic parameter adjustment to maximize performance during rapid changes.

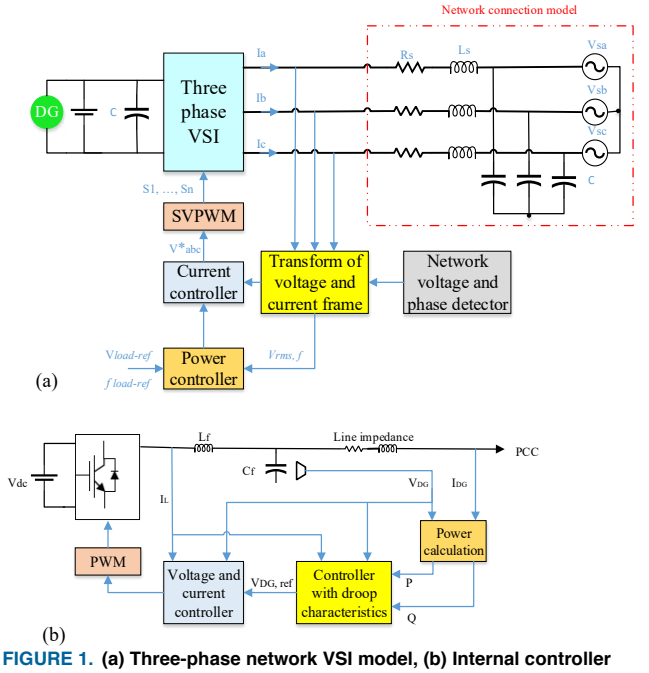

FIGURE 1. (a) Three-phase network VSI model, (b) Internal controller structure in inverter-based DGs.

Since the operation of microgrids is based on DG with a low power generation level, frequency control is done in cooperation with several DG units. DGs, like solar and wind cells, are not able to participate in frequency control due to their uncertain nature [14]. In such a case, one of the units (diesel generator or voltage source inverter) is considered as a reference of voltage and frequency, and the storage is used with a frequency compensation strategy. The basis of diesel generator performance is based on the droop characteristic. In this method, the synchronous generator or inverter voltage source, based on its primary control, the more frequency drop occurs in the microgrid, the more power is injected into the microgrid to compensate for load changes [15-16]. In such cases, for secondary frequency control (automatic control), the no-load frequency in the drop method must be increased. The controller used is usually a proportional-integral (PI) controller [17-20]. In reference [21-23], a fuzzy controller is used to improve frequency control. The fuzzy controller provides a better response than the simple PI controller, which is designed for only one working point. In [24] a new hybrid method is used for secondary control in microgrids based on robust control methods. In [25] presents a self-regulating controller based on human emotional behaviors for the frequency controller in microgrids. In [26] a fuzzy controller is proposed to control the microgrid frequency in the presence of electric vehicles and it is claimed that the proposed robust controller can be used for different network topologies. In [27] a fuzzy controller optimized with PSO in [28] of the combination of PSO with artificial neural network and in [29] of fuzzy adaptive model predictive control in [30] of a robust firefly-swarm hybrid optimization in [31] a hybrid cuckoo search and pattern search algorithm is used to control the microgrid frequency.

The combination of evolutionary algorithms has been investigated in many studies. In this research, a real-time optimization-based power controller for inverter-based DG in an island microgrid is examined. Based on the synchronous reference frame, this controller is connected to the present control loop. This design employs a traditional PI controller with a feed-forward compensation applied to the internal control loop to provide a quick dynamic response. When switching from microgrid to island mode or changing loads, the DG unit uses the VF control mode, which uses the GA-PSO meta-heuristic algorithm to regulate the system voltage and frequency. The GA-PSO algorithm is used to automatically adjust the parameters in real-time. The main purpose of this study is to improve the quality of the power supply by keeping the voltage and frequency in the acceptable range. The most important features of the proposed controller can be stated as follows:

- Real-time PI controller design using hybrid PSO-GA algorithm.
- Optimum setting of microgrid VF controller parameters using PSO-GA algorithm.
- Including non-linear factors and uncertainties in the microgrid model to approach the real behavior of the microgrid.
- In the proposed controller, no telecommunication link or timing is used to detect the start of the modification process and its implementation, and the start time of the process is determined locally and separately for each DG.
- There is no need for a master unit to control voltage and switch between inverter controllers during islanding.
- The proposed controller has a robust performance against changes in the working points of DGs that may have occurred due to load changes, the arrival of new DGs, or changing the operation mode of the microgrid, and it causes proper power sharing between DGs.

So, the paper was built to present six parts. The first one is related to the introduction section, then in the second part, the three-phase network-connected mathematical model is presented and explained. Then, in the third part, the proposed

control technic is detailed and discussed. Next, the concept of GA-PSO for controlling this system is explained. In the fifth part, the results are demonstrated and explained. Finally, a conclusion part closes the paper

II. THE THREE-PHASE NETWORK-CONNECTED VSI SYSTEM MODEL

A three-phase network-connected VSI with an LC filter is depicted in this model in "Figure 1a" where R_S and L_S are the equivalent resistance and inductance of the filter. C is the filter capacitor and V_s is the network voltage. The equations are written assuming that the zero point on the DC side is connected to the zero point on the AC side.

The equivalent circuit of the system in the abc reference frame is represented by the state-space equations as Equation (1) [32]:

$$\frac{d}{dt}\begin{bmatrix} i_a \\ i_b \\ i_c \end{bmatrix} = -\frac{R_s}{L_s}\begin{bmatrix} i_a \\ i_b \\ i_c \end{bmatrix} + \frac{1}{L_s}\left(\begin{bmatrix} V_a \\ V_b \\ V_c \end{bmatrix} - \begin{bmatrix} V_{sa} \\ V_{sb} \\ V_{sc} \end{bmatrix}\right) \quad (1)$$

Using the park transform, Equation (1) can be transferred to the dq reference frame as Equation (2):

$$\frac{d}{dt}\begin{bmatrix} i_d \\ i_q \end{bmatrix} = \begin{bmatrix} -\frac{R_s}{L_s} & -\omega \\ \omega & -\frac{R_s}{L_s} \end{bmatrix}\begin{bmatrix} i_d \\ i_q \end{bmatrix} + \frac{1}{L_s}\left(\begin{bmatrix} V_d \\ V_q \end{bmatrix} - \begin{bmatrix} V_{sd} \\ V_{sq} \end{bmatrix}\right) \quad (2)$$

where ω is the angular frequency. Park transform can be defined as Equation (3):

$$i_{dq0} = T i_{abc}$$

$$i_{dq0} = \begin{bmatrix} i_d \\ i_q \\ i_0 \end{bmatrix}, i_{abc} = \begin{bmatrix} i_a \\ i_b \\ i_c \end{bmatrix}$$

$$T = \sqrt{\frac{2}{3}}\begin{bmatrix} cos\theta & \cos(\theta - \frac{2\pi}{3}) & \cos(\theta + \frac{2\pi}{3}) \\ -sin & -\sin(\theta - \frac{2\pi}{3}) & -\sin(\theta + \frac{2\pi}{3}) \\ \frac{1}{\sqrt{2}} & \frac{1}{\sqrt{2}} & \frac{1}{\sqrt{2}} \end{bmatrix} \quad (3)$$

where $\theta = \omega_s t + \theta_0$ is the angle of rotation of the synchronous and θ_0 represents the initial value.

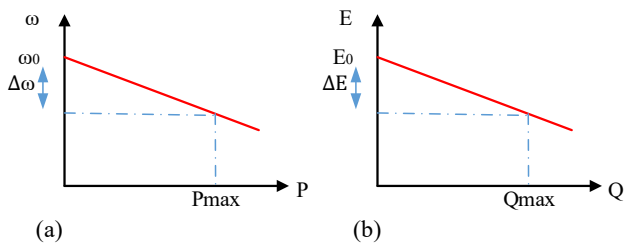

FIGURE 2. (a) Droop characteristic P-ω, (b) Droop characteristic Q-E.

A. CONVENTIONAL DROOP CONTROL PRINCIPLES

The usual method of resource local control is to implement the controller in synchronous coordinates, in which the various parameters of the balanced network are permanently mode converted to dc, and as a result, the PI controller can be used to control the source. Figure 1b shows the control structure of an inverter-based DG source with a droop controller. Since the performance of the microgrid in the island mode is considered, it is expected that the DG units will be able to supply the microgrid load optimally. Assuming that the rated power of the sources is the same, each DG unit will supply the load power at a certain level in proportion to the network arrangement and the size of its feeder impedance. As can be seen in Figure 2, by increasing the active and reactive power produced by the source and in proportion to the slope of the characteristic droop, the frequency, and amplitude of the output voltage of the inverter source decrease relative to its nominal value, respectively. But the problem of power-sharing in frequency and voltage characteristics is faced with different conditions.

$$P_i = \frac{E_i V_i}{X_i} \sin \delta_i \quad (4)$$

$$\Delta\omega = \frac{d\delta}{dt} \quad (5)$$

Depending on the amount of active power provided by each source, the frequency or in other words the voltage angle of the sources will differ from each other. Thus, the voltage of higher frequency sources is leading than that of lower frequency sources, and according to Equation (4), this leading leads to an increase in output at the source with less power output. Given that in the permanent state the frequency of all sources reaches the same value and on the other hand, there is a relationship between frequency and voltage angle according to Equation (5), the voltage angle of different sources relative to each other changes rapidly and this process eventually leads to equal active power production of DG units and ideal sharing of this power in the microgrid. However, because the drop at the source voltage will vary due to the different impedances of the source feeder, the output voltage range of the DG units will not be equal and as a result, the reactive power will not be properly shared between the sources.

B. V/F CONTROL STRATEGY

DG units can be classified into three sorts of energy sources when compared to large generators: 1- Variable speed sources (variable frequency) such as wind energy, 2- High-speed sources (high frequency) such as microturbines, 3- Direct energy conversion sources such as photovoltaics and fuel cells. For this reason, it is necessary to use VSI to connect DG to the network to achieve flexible performance. The DG power circuit is based on the VSI with a control structure, as illustrated in Figure 1a, thus the DG unit's performance is

based on the inverter control model. For example, in grid-connected mode, the DG acts as a PQ generator, and the inverter must follow the active-reactive power control mode, while there is no need to adjust the voltage and frequency because the grid voltage is constant. But in island mode, DG is expected to meet load demand for power quality. The voltage and frequency are not constant in this scenario, so the inverter must use control mode V/F to solve the nominal power-sharing problem. Therefore, with good DG performance, a proper control mode can be achieved.

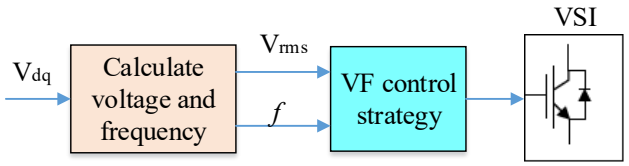

FIGURE 3. VSI based on V/F power controller.

It is required to ensure an uninterrupted shift of control modes according to the conditions for the microgrid to operate reliably, and stable operation in the island mode should be provided according to the voltage and frequency regulation of the microgrid. In this case, the DG must meet the load demand and keep the voltage and frequency in the acceptable range, so the VF control mode must be adopted by one or more DGs to meet the system needs. Figure 3 depicts the block diagram for this application. As a result, the voltage and frequency reference values must be calculated locally or via the microgrid control center. Loop-Locked-Phase can be used to determine the frequency and the voltage can be obtained by Equation (6):

$$V_{rms} = \sqrt{V_d^2 + V_q^2} \quad (6)$$

VSI is commonly used as an interface for distributed generation sources in the distribution network. The VSI behaves like a synchronous machine and controls the frequency and voltage of the system through the controllers. The complete model of the VSI control system based on DG units is shown in Figure 4. The power circuit contains the inverter and the output LC filter, while the control circuit includes the power controller based on the drop technique, the voltage and frequency controller, the current controller, and the power calculation loop. The power control loop includes a droop controller which indicates that the active and reactive power in the DG units is divided by the droop coefficient based on the frequency and voltage of the system, respectively. According to the power controller diagram block the relationship between frequency and active power and voltage and reactive power (as shown in Figure 2) can be written as Equation (7):

$$\begin{aligned} \omega &= \omega_n - m_p P \\ V &= V_n - n_q Q \end{aligned} \quad (7)$$

where ω_n is the nominal value of the frequency, V_n is the nominal value of the voltage, and m_p and n_q are the active and reactive power droop gain, respectively. To achieve the correct regulation of voltage and frequency using existing controllers, DC values must be used for the input of the controller. Therefore, the abc values must be converted to dq0 values using the park transform. Equation (8) calculates the instantaneous powers of active P and reactive Q based on the measured output voltage and current [33]:

$$\begin{aligned} P &= \frac{\omega_c}{s+\omega_c} \times \left(v_{od}\, i_{od} + v_{oq}\, i_{oq}\right) \\ Q &= \frac{\omega_c}{s+\omega_c} \times \left(v_{od}\, i_{oq} - v_{oq}\, i_{od}\right) \end{aligned} \quad (8)$$

where v_{od}, v_{oq}, and i_{od}, i_{oq} are the output voltages and currents in the form dq, respectively. A low-pass filter is used to eliminate the instantaneous fluctuations in active and reactive power.

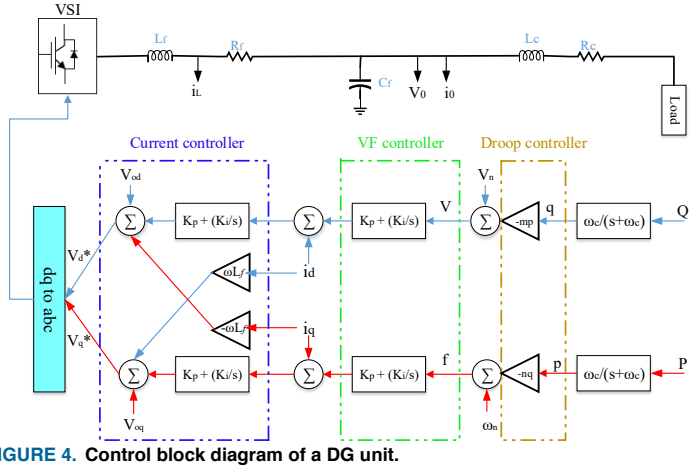

FIGURE 4. Control block diagram of a DG unit.

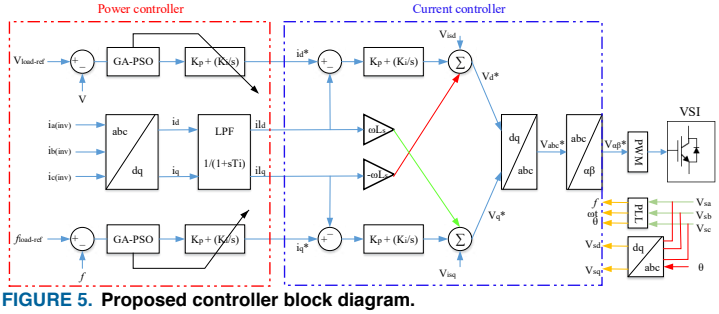

FIGURE 5. Proposed controller block diagram.

III. CONTROL TECHNIQUE PROPOSITION

The power controller for a three-phase network-connected VSI system is described in this section. The controller architecture, as shown in Figure 5, consists of three main blocks: a power controller, a current linear controller, and a GA-PSO algorithm for automatic and real-time power control parameter modification. The details of each of these blocks will be described below.

A. POWER CONTROL STRATEGY

The goal of putting this strategy in place is to increase power quality under the desired control mode. The power controller

based on the two PI controllers is illustrated on the left side of the block diagram in Figure 5. This controller denotes an external control loop that is applied to create reference currents i_d* and i_q*. As a result, a relatively moderate shift in the reference current path could result in a higher quality inverter output power, indicating that the target is under control. In this paper, the VF control strategy based on the GA-PSO hybrid algorithm for VSI-based DG is presented. The voltage and frequency of the system are the main objectives of the control that must be achieved in the case of island operation. This technique is offered to respond to unexpected events such as the microgrid being disconnected from the main network or the loads connected to the microgrid changing. The controller changes the voltage and frequency depending on the f_{ref} and V_{ref} reference values, and the GA-PSO algorithm finds the control parameters to provide the appropriate reference current vectors. According to the reference frame and based on the PI controller, Equation (9) can be used to obtain the reference current vectors.

$$i_d^* = (V_{ref} - V)\left(K_{pv} + \frac{K_{iv}}{s}\right)$$
$$i_q^* = (f_{ref} - f)\left(K_{pf} + \frac{K_{if}}{s}\right) \quad (9)$$

B. CURRENT CONTROL LOOP

The goal of putting this controller in place is to ensure that transient inverter output currents are tracked accurately and quickly. The present control loop, which is based on the synchronous reference frame, is shown on the right side of the block diagram in Figure 5. This controller is normally set up so that voltage is applied to the impedance R-L. The voltage angle is measured by the PLL block, which is then employed in the park transformation frame. To eliminate the current error, two PI controllers are employed, and the inverter current loop and the network voltage feed-forward loop are both used to improve steady-state and dynamic performance. As a result, the output signals in the dq frame indicate the reference voltage signals. By converting the park frame to Clarke, reference voltage signals are generated by combining six pulses for SVPWM in the stationary reference frame. In addition, the use of the SVPWM method ensures that the output voltage vectors have the least harmonic. Based on Equation (2), the relation of the reference voltage signals in the dq synchronous frame can be written as Equation (10):

$$\begin{bmatrix} V_d^* \\ V_q^* \end{bmatrix} = \begin{bmatrix} -K_p & -\omega L_s \\ \omega L_s & -K_p \end{bmatrix} \begin{bmatrix} i_d \\ i_q \end{bmatrix} + \begin{bmatrix} K_p & 0 \\ 0 & K_p \end{bmatrix} \begin{bmatrix} i_d^* \\ i_q^* \end{bmatrix} + \begin{bmatrix} K_i & 0 \\ 0 & K_i \end{bmatrix} \begin{bmatrix} X_d \\ X_q \end{bmatrix} + \begin{bmatrix} V_{sd} \\ V_{sq} \end{bmatrix} \quad (10)$$

The uppercase * represents the reference values and $dX_d/dt = i_d^* - i_d$, $dX_q/dt = i_q^* - i_q$. According to Equation (11), using the Clarke transform, Equation (10) can be transferred to the static frame α-β. In addition, induction current is obtained using a low-pass filter (LPF) LC. Here, the LPF is represented by a first-order transform function.

$$\begin{bmatrix} V_\alpha \\ V_\beta \\ V_0 \end{bmatrix} = \frac{2}{3} \begin{bmatrix} V_a \\ V_b \\ V_c \end{bmatrix} \begin{bmatrix} 1 & -\frac{1}{2} & -\frac{1}{2} \\ 0 & \frac{\sqrt{3}}{2} & -\frac{\sqrt{3}}{2} \\ \frac{1}{2} & \frac{1}{2} & \frac{1}{2} \end{bmatrix} \quad (11)$$

$$f_1 = f \frac{1}{1+sT_i} \quad (12)$$

where f is the filter input value, f_1 is the filtered value and T_i is the time constant.

IV. THE GA-PSO ALGORITHM: DESCRIPTION

By studying the applications of different artificial intelligence algorithms, it has been determined that each of these algorithms has its strengths and weaknesses. A new approach to using these algorithms is to combine them to achieve a more efficient algorithm. For this purpose, by recognizing the strengths and weaknesses of these algorithms, they combine them in such a way that the strengths of these algorithms were used to eliminate and cover each other's weaknesses. Rapid convergence is one of the most significant issues with the PSO algorithm. As a result, the algorithm arrives at the best possible answer before examining the full answer space, increasing the chances of becoming stuck at the best local points. It should be noted that one of the most important things in designing a search algorithm is that the algorithm can navigate the answer space well, thus reducing the possibility of getting stuck in the optimal local points. In this paper, to solve the problem mentioned in the PSO algorithm, the genetic algorithm is used, which has a high search power and can perform an acceptable search in the answer space and escape from the local optimal points. After each iteration of the PSO algorithm, the proposed hybrid algorithm places the particles in the response space again and makes the response space more navigable by selecting half of the particle population that had inferior performance and utilizing the genetic algorithm operators. As a result, the chances of quick convergence and entrapment at local optimal spots are reduced. The steps of the hybrid algorithm used in this paper are shown in Figure 6, and the coding for this proposed algorithm is shown in Figure 7.

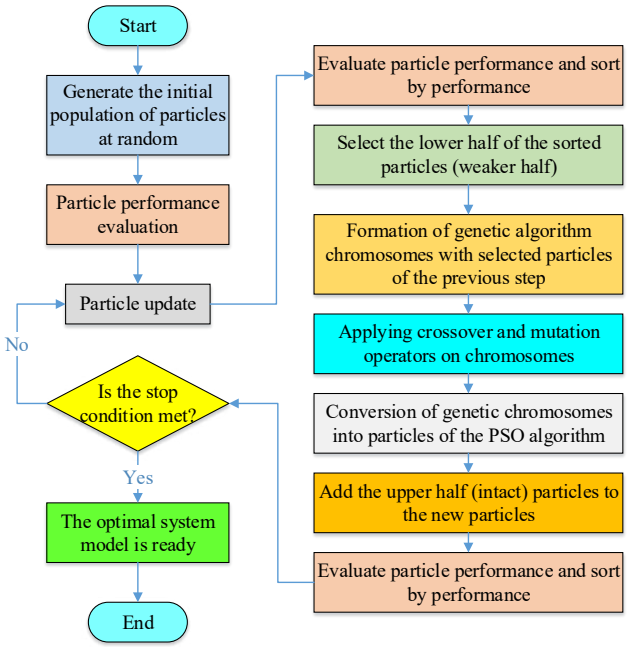

FIGURE 6. **Steps of the proposed hybrid algorithm.**

FIGURE 7. **Display of PSO particle coding.**

In this paper, microgrid stability is affected by four variables k_{pf}, k_{if}, k_{pv}, and k_{iv}, which are the input variables of the problem. It should be noted that each of these variables with a certain coefficient and slope, affect the stability of the microgrid. Here, microgrid stability refers to microgrid voltage and frequency control. To introduce how the particles are displayed, here we consider the microgrid stability as a particle or bird. Each particle is an array defined by the number of impact variables. Particle coding for the PSO algorithm is shown in Figure 7. It should be noted that all input variables are normalized their values are taken in the range of 0 to 1, and each particle is an answer to the coefficients of the regression Equation. If we assume that X_1, X_2, …, X_m are the variables affecting the microgrid stability and Y is the microgrid stability, then each particle of the answer to the problem is α_1, α_2, …, α_m in the Equation for maintaining the microgrid stability in Equation (13):

$$Y = \alpha_1 X_1 + \alpha_2 X_2 + \cdots + \alpha_m X_m \quad (13)$$

In fact, according to the coding of Figure 7, X_m is the variable that affects the stability of the microgrid and α_m is the effective coefficient of that variable, which ultimately determines the stability of the microgrid Y.

The purpose of microgrid stability in this study is for dispersed generation sources to be able to control output power to satisfy load demand while maintaining the microgrid's voltage and frequency at their nominal values. Therefore, considering the above control objectives, the objective function is defined as Equation (14) which is the result of the difference between the reference value and the controlled signal.

$$J_{obj} = \sum_{j=1}^{n_{DG}} \sum_{t=1}^{t_{end}} (|V_{rms} - V_a(k)| + |f_n - f(k)|) \quad (14)$$

The initial population formation stage is random. At this point, the algorithm randomly generates the initial solution (number of particles required) as much as N_{pop}. So that each answer in this step contains m numbers in the interval [0,1] and also the velocity of each particle (answer) is generated randomly. At this stage, birds or particles are allowed to move freely in the problem space and each shows a new answer to the problem. Our problem space (which is selected according to the affected variables) has four aspects, the particles are allowed to fly and select a point in space. This point in space gives us a new voltage and frequency according to the number of effective factors, which we calculate by comparing it with the actual amount of voltage and frequency at that point, the pattern error level. Now we have to evaluate the particles of the produced population. The fitness function used for this purpose is the mean square error (MSE) function, which is commonly used in the design of the forecasting system and is defined as follows:

$$MSE(C_j) = \frac{1}{N} \sum_{i=1}^{N} (Y_i - P_i)^2 \quad (15)$$

where C_j is the particle j^{th} of the population, Y_i is the output of the prediction system of the training set data i^{th}, P_i is the actual output of the training set data i^{th}, and N is the number of the training set data.

Finally, it is time to produce a new generation by operating the PSO algorithm and the genetic algorithm. In this section, the PSO algorithm is first implemented on the training data. At the end of each iteration of the algorithm, the crossover and mutation operators of the genetic algorithm act on the particles and move them further in the response space, thus the PSO algorithm performs a better general search in the response space with the help of the genetic algorithm. In other words, at this stage, after each iteration of the PSO algorithm, we take advantage of the genetic algorithm, given that it is possible to get stuck in local minima and the problem space may not be fully explored. By using powerful search engines, genetic algorithms, and random mutations, we force the particles to move to other parts of the multidimensional space of the problem. We continue this process in each iteration until the problem space is fully examined and finally, we reach the condition of stopping the problem (according to Figure 6). In other words, if the number of iterations is equal to the specified number, the process of executing the algorithm ends, otherwise, we go to the relevant step and repeat the above

process. At the end of the algorithm, the best particle in the last generation is considered the final answer of the system.

V. SIMULATION RESULTS

First, the proposed method is implemented on the three-phase VSI system model connected to the network in Figure 1, and all simulations are performed with MATLAB software. The system parameters are presented in Table 1.

TABLE 1: MICROGRID MODEL PARAMETERS.

Parameter	Value	Parameter	Value
k_p	12.656	L_s	6 mH
k_i	0.00215	R_s	0.01 Ω
Load	25 kW	C	1500 μF

TABLE 2: VALUES OF PI CONTROLLER PARAMETERS OBTAINED FROM PSO-GA ALGORITHM.

Parameter	Value
k_{pf}	2.98406421
k_{if}	4.00629538e-4
k_{pv}	-1.18647225
k_{iv}	0.00084279

In this simulation, a 75 kW DG is used. The constants k_p and k_i are the current control parameters. For SVPWM-based current controllers, the switching and sampling frequencies are 10 kHz and 500 kHz, respectively. The simulation is performed in two modes of voltage and frequency adjustment and load changes, which will be examined in the following subsections. As mentioned before, in the case of islands, it is a microgrid separated from the main network and independently provides load power. Unlike the grid-connected mode where the voltage and frequency were regulated by the grid, in this mode, the voltage and frequency of the two ends must be stabilized with proper microgrid control.

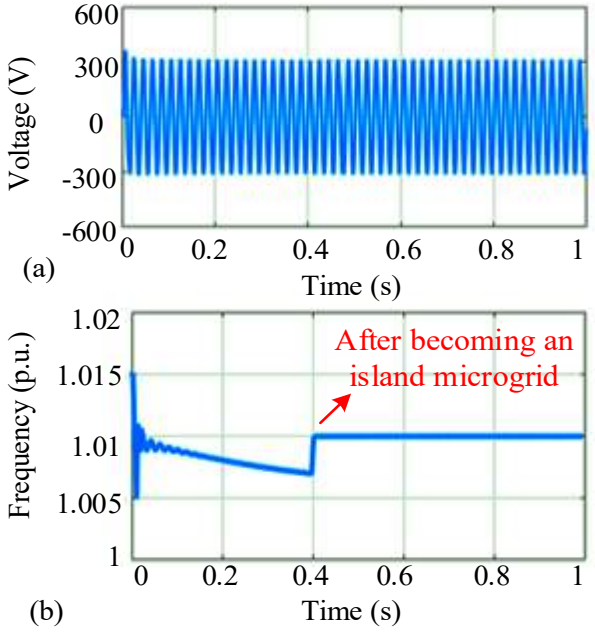

FIGURE 8. Voltage and (b) Frequency of system before and after islanding.

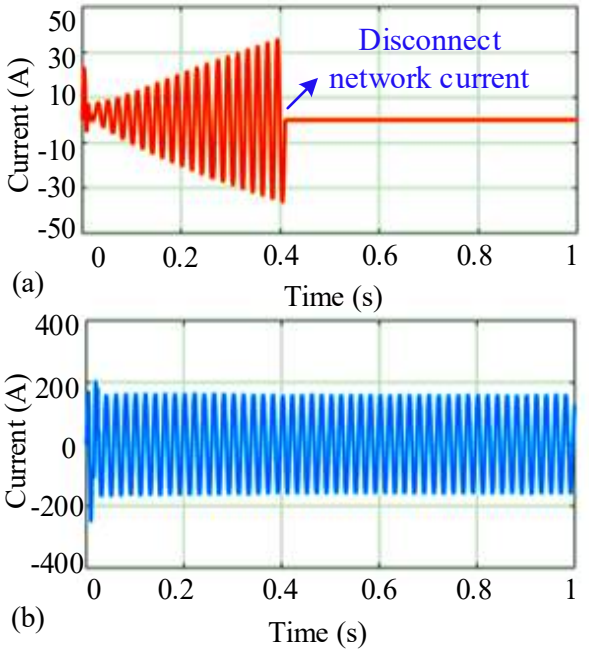

FIGURE 9. (a) Network current and (b) Microgrid current, before and after islanding.

A. ADJUST VOLTAGE AND FREQUENCY IN ISLAND MODE

In addition, the controller is built to analyze both dynamic and steady-state responses, As a result, the network adjusts the microgrid's voltage and frequency. At 0.4 s, it disconnects from the network and enters island mode. To avoid severe frequency deviation and voltage drop due to sudden load entry or starting island mode, DG enters VF control mode. According to Equation (9), V_{ref} is set at 310 V and f_{ref} at 50 Hz. Figure 8 shows the voltage and frequency adjusted using the control method. Which is the interaction of the control method and PSO-GA algorithm. Figure 8 shows that at 0.4 s it enters the island mode, and the controller maintains the system voltage and frequency at the desired value. During the simulation time, the PSO-GA algorithm adjusts the control parameters and during the process, the voltage and frequency values are in the acceptable range of 1 p.u limits. Figure 9 shows the injection current of the network and microgrid. As shown in Figure 9 (a), after starting the island mode, the load current is fully fed.

As mentioned, in the network-connected mode, the microgrid enters the PQ control mode, in which case it adjusts the active and reactive output power according to the system requirements. Figure 10 (a) shows the active injection power of the network. Power changes, in this case, indicate that the instantaneous power of the system is variable due to decreasing and increasing demand. On the other hand, Figure 10 (b) shows the microgrid active injection power that follows the changes in the active power in the network and controls the power injection according to the needs of the network.

According to Figures 10 (c) and (d), it can be seen that before starting the island mode, the reactive power required by

the network is provided by the microgrid, and after starting the island mode, the reactive power produced by the microgrid is zero due to the lack of non-ohmic load in the circuit.

According to the results of Figures 8 to 10, it can be said that the performance of the control system by applying the hybrid PSO-GA algorithm in the island mode was able to regulate the voltage and frequency in an acceptable range and the network-connected mode with QP control was able to active and reactive power sharing to meet network demand. Table 2 lists the settings of the PI controller optimized by the PSO-GA method. Figures 11 and 12 also show the convergence of the parameters and the goal function.

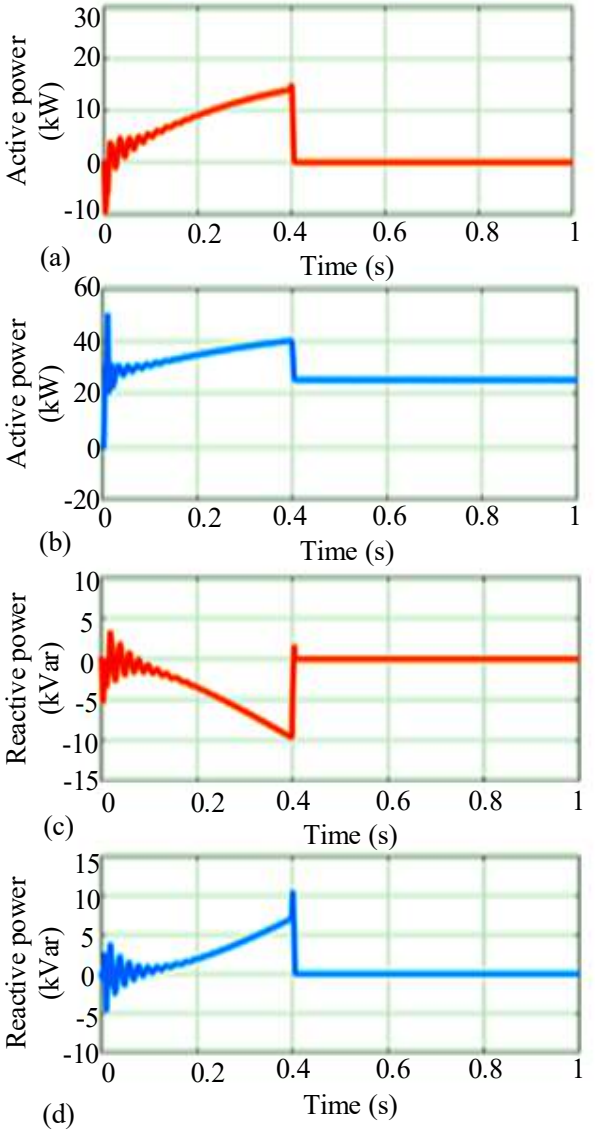

FIGURE 10. **(a) Network active power, (b) Microgrid active power, (c) Network reactive power, and (d) Microgrid reactive power before and after islanding.**

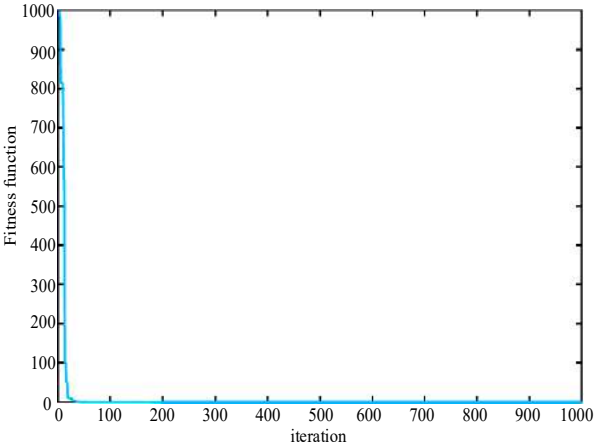

FIGURE 11. **Convergence curve of the objective function.**

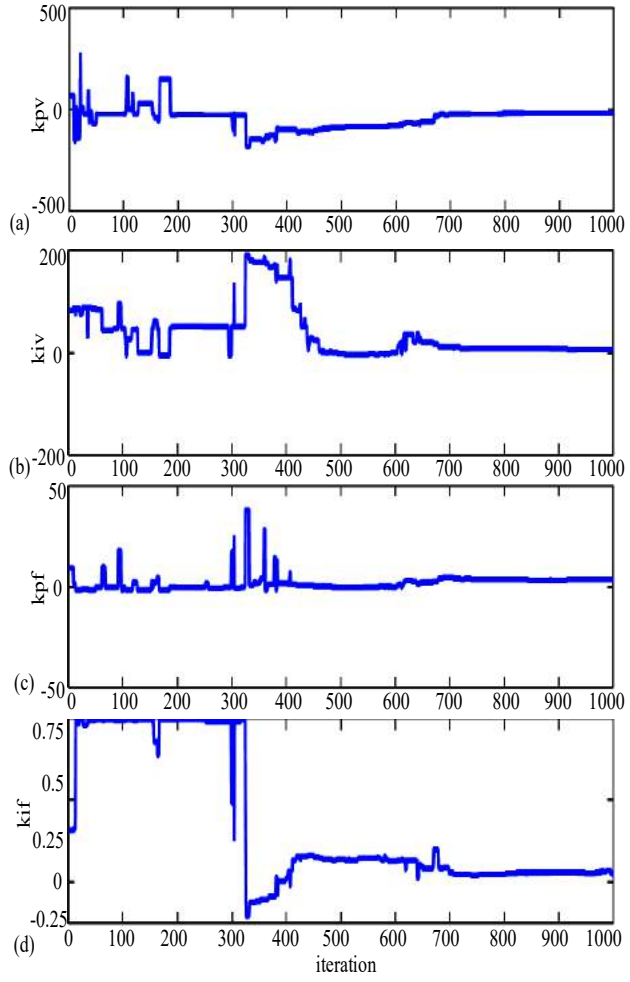

FIGURE 12. **Convergence diagram of controller parameters, (a) k_{pv} (b) k_{iv} (c) k_{pf} (d) k_{if}.**

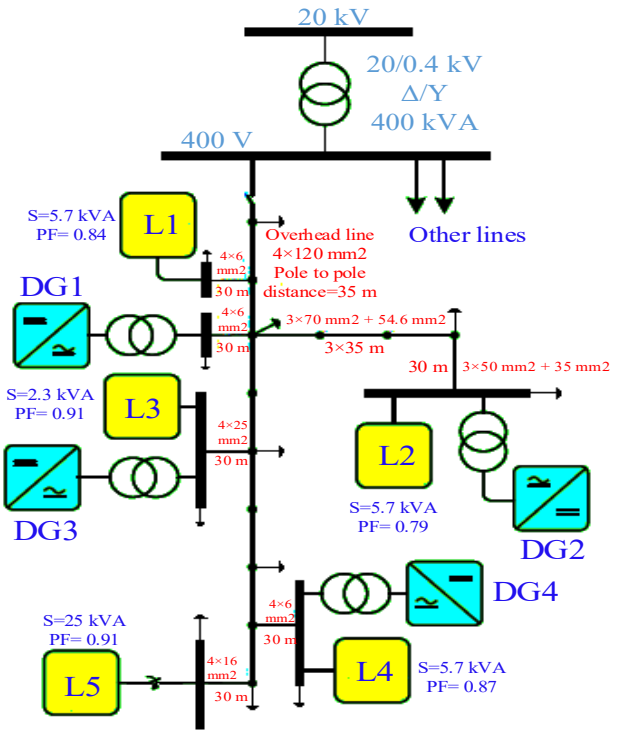

FIGURE 13. Single-line diagram of the microgrid understudy.

B. IMPLEMENT THE PROPOSED METHOD WITH THE PRESENCE OF SEVERAL DGS

In this part, the proposed method is implemented on a standard island microgrid including various loads and inverter-based DG. Figure 13 shows the single-line diagram of the studied microgrid [34]. The distributed generation units of this microgrid (DG1-DG4) with capacities equal to 12.5 kW are involved in the simulation process. Information about the loads and lines of this network are presented in the single-line diagram of Figure (13) and Table 3, and the controller specifications of the DG units are given in Table 4. Figure 14 shows the load power-sharing status between the units of this microgrid in different conditions. During the start-up of the microgrid, the level of participation of each unit in meeting the demand of loads will be based on the rules of common drop characteristics. Therefore, the active power output reaches the desired value, while the reactive power output of each unit has a different value depending on the size of its feeder impedance. In the next step, the load L5 is added to the microgrid at 1.25s and disconnected at 2.25s. It is observed that these changes are detected in all units and are responded to simultaneously and in a coordinated manner. Finally, in 3.5s, the DG4 unit exits the microgrid, and the simulation results confirm the efficiency of the proposed method in microgrid power control.

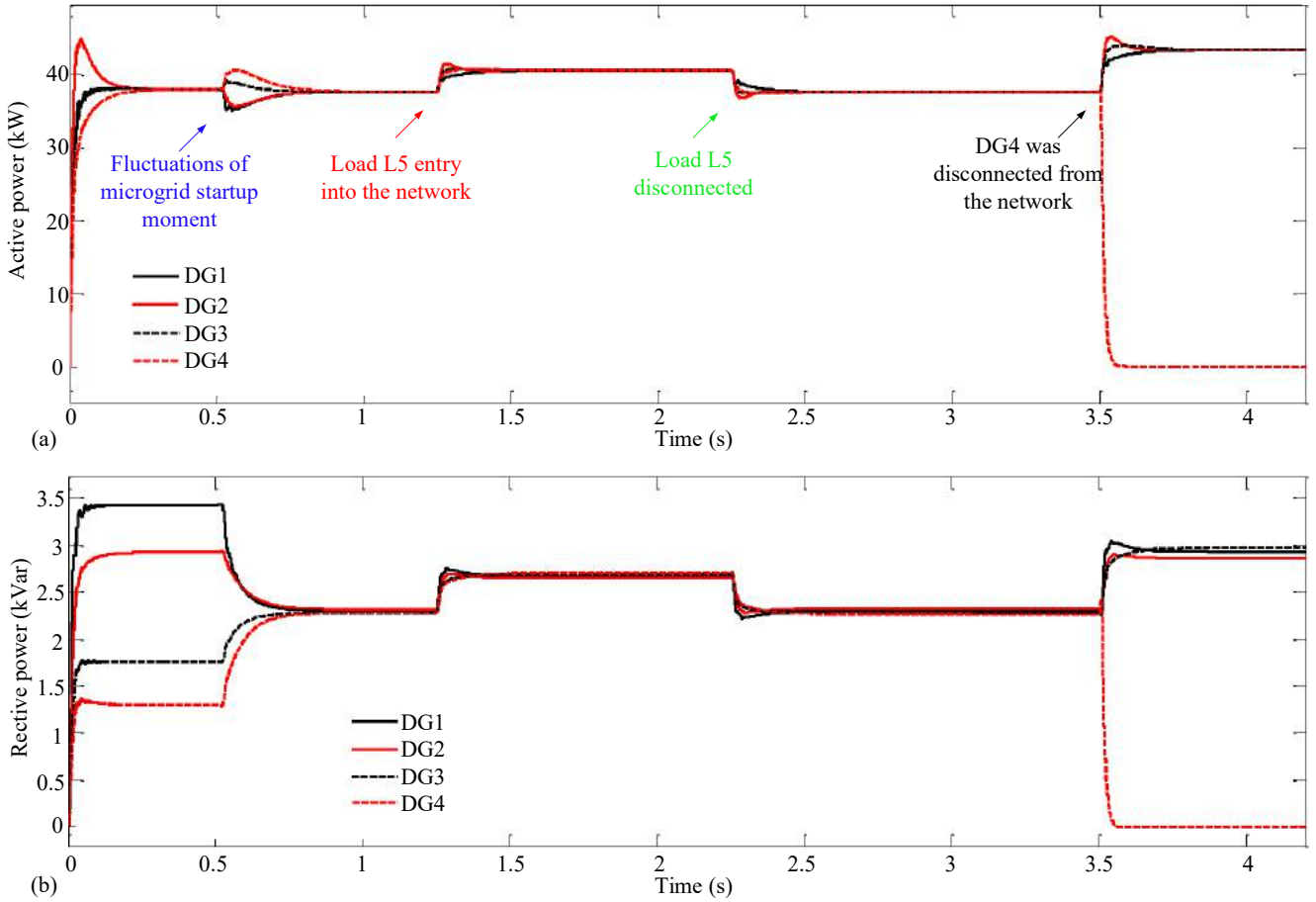

FIGURE 14. Production capacity of microgrid units (a) Active power and (b) Reactive power.

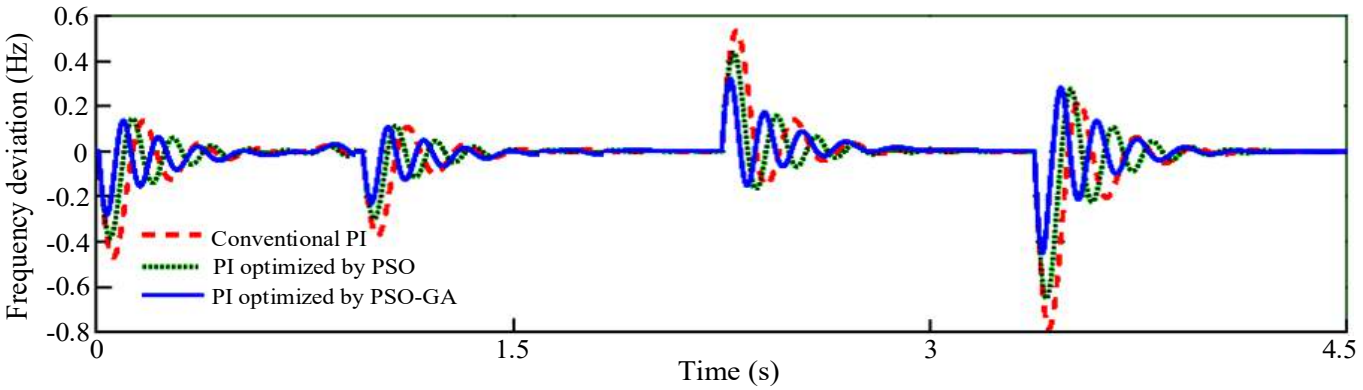

FIGURE 15. **Microgrid frequency deviation due to load and DG changes.**

TABLE 3: SPECIFICATIONS OF MICROGRID LINES UNDERSTUDY.

Line type	Z0 (Ω/km)	Z1 (Ω/km)
Overhead line, 4×120 mm2 AL XLPE	1.136 + j0.417	0.284 + j0.0825
Overhead line, 3×70 mm2 AL XLPE + 54.6 mm2 AAAC	2.387 + j0.447	0.497 + j0.0861
Cable, 3×50 mm2 AL XLPE + CU 35 mm2	2.04 + j0.421	0.462 + j0.0764
Cable, 4×25 mm2 CU	3.48 + j0.409	0.87 + j0.0805
Cable, 4×16 mm2 CU	5.52 + j0.418	1.38 + j0.0828
Cable, 4×6 mm2 CU	13.64 + j0.472	3.41 + j0.0963

TABLE 4: SPECIFICATIONS OF THE MICROGRID CONTROLLER UNDERSTUDY.

Parameter	Value
Nominal frequency fn	50 Hz
Filter capacitor Cf	100 μF
Filter inductance Lf	1 mH
Filter resistance Rf	0.01 Ω
Switching frequency f	4500 Hz
Maximum allowable frequency deviation Δf	0.3 Hz
Maximum allowable voltage deviation ΔV	0.05 p.u.

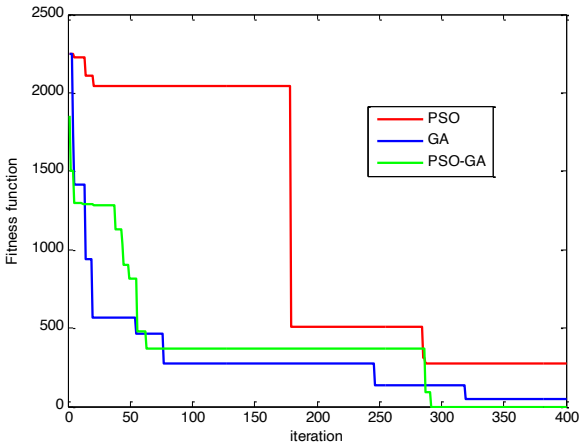

FIGURE 16. **Comparison of the convergence curve of the objective function.**

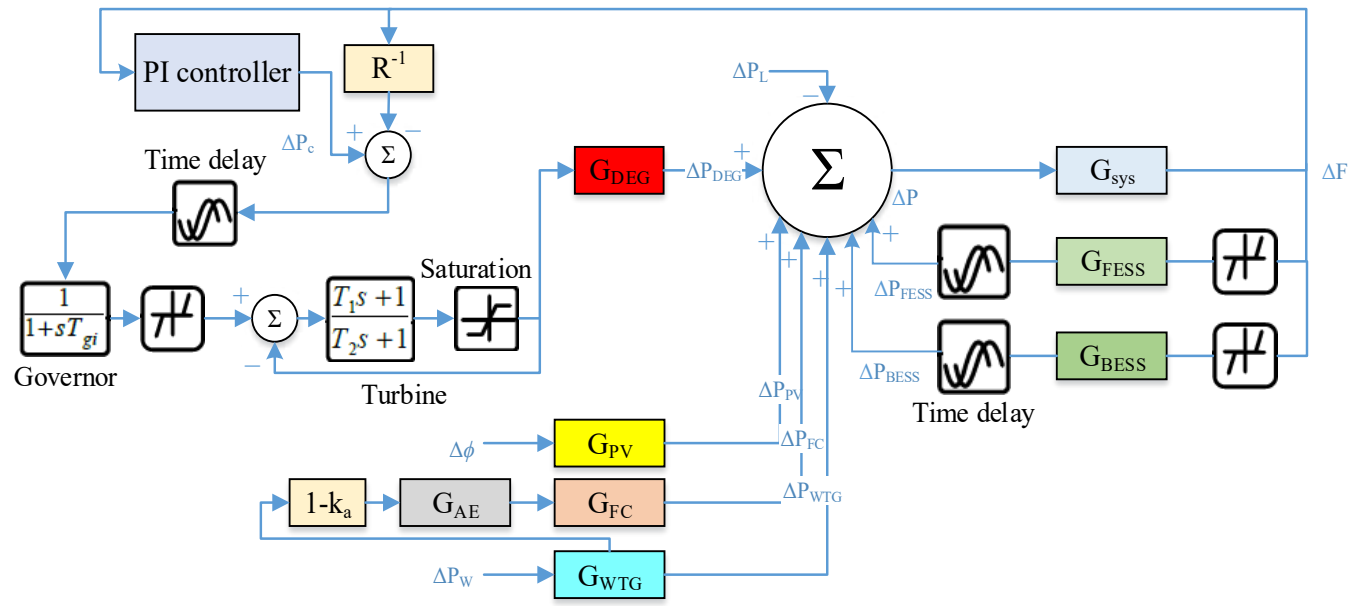

FIGURE 17. **Microgrid frequency model considering physical constraints**

Finally, Figure 15 shows the curve of changes in network frequency deviation due to these changes. When load L5 enters the network, the frequency decreases and with load L5 exiting the network, the frequency changes increase and at the moment DG4 exits the network, these frequency changes will be more intense, which can be seen in Figure 15. Where the proposed method is compared with conventional PI control methods and PI optimized by PSO [32]. As you can see, the proposed controller had a good response both in terms of minimizing the frequency changes and in terms of reducing the frequency recovery time. Figure 16 compares the performance of the PSO-GA algorithm with the GA and PSO algorithms. As you can see from the convergence curve of the fitness function, the combined method performed better.

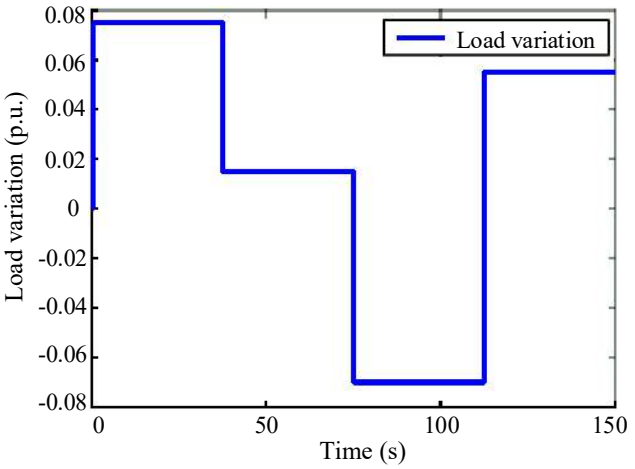

FIGURE 18. Sudden changes in increasing and decreasing load in the microgrid

C. SENSITIVITY ANALYSIS OF THE PROPOSED CONTROLLER FOR PARAMETERS UNCERTAINTY

In this section, the performance of the proposed controller has been evaluated for uncertainties in load changes, the presence of different DGs, and changes in the generation power of the units, and its results have been compared with other methods. The studied microgrid information is presented in reference [35]. In this microgrid, there are different types of DGs, including a photovoltaic (PV), and a wind turbine generator (WTG). Here, the microgrid is modeled through MATLAB software, to improve the model and get closer to the real response of the microgrid, a series of nonlinear elements, limiters, and time delays have been added to the microgrid model, as shown in Figure 17. In this evaluation, the results obtained in the presence of sudden decreasing and increasing changes in a load of consumers and changes in the generation power of WTG and PV in a reasonable range in the presence of non-linear factors such as dead bands and delays (with a delay of 50 milliseconds) have been examined. In this case, the proposed controller should be able to be robust in the presence of changes in atmospheric conditions such as wind speed and solar radiation. Here, because we have large load changes, WTG and PV power changes are also multiplied to be comparable to large load changes as disturbances.

Figure 18 shows the load changes in the form of steps, which according to the capacity of the units, step changes are created in such a way as to create significant frequency changes. Also, the random changes in WTG and PV power are shown in Figure 19. Considering that this figure shows the changes in generation power, it can be a negative number.

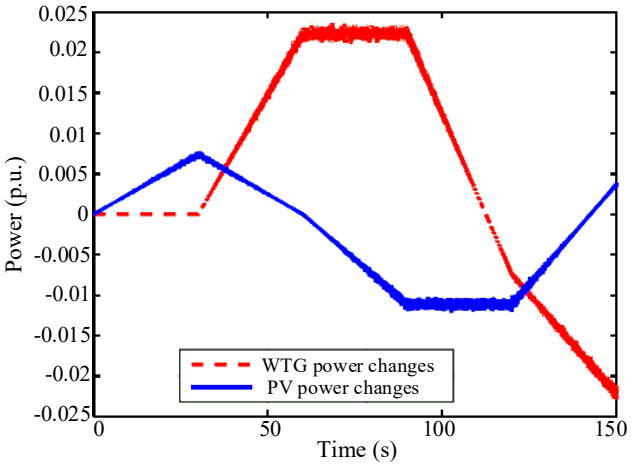

FIGURE 19. WTG and PV power changes

To compare the performance results of the controllers with each other in different states, a functional index is defined in the form of Equation (16). Which shows the integral amount of microgrid frequency deviation from its nominal amount (50 Hz) so that the lower the value, the better the controller performance. Figure 20 shows the changes in the functional index defined in Equation (16) for the proposed controller, IMPC [36], and MPC-PSO [35]. As it is known, the proposed controller has the lowest amount of functional index changes, which indicates its proper performance.

$$Functional\ index = \int \Delta f\, dt = \int |f - 50| dt \qquad (16)$$

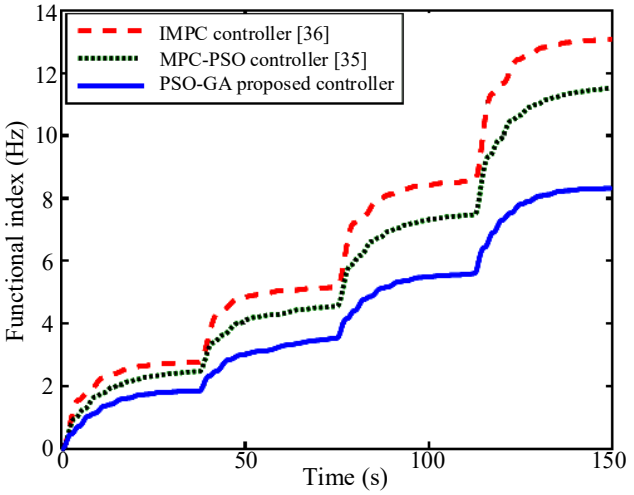

FIGURE 20. Functional index changes

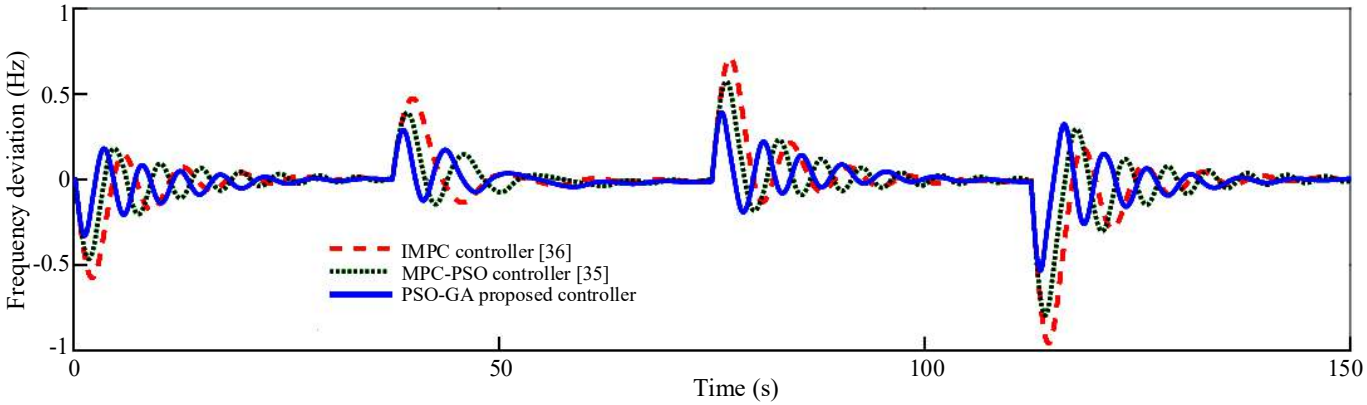

FIGURE 21. Microgrid frequency deviation curve for disturbances

TABLE 5: PERFORMANCE COMPARISON OF CONTROLLERS WITH DIFFERENT PARAMETERS.

Parameters	Controllers	Uncertainties		
		Normal	+30%	-30%
ISTSE	PSO-PID [37]	36.0223	39.6725	34.4608
	PSO-PIDF [38]	27.8301	34.2502	27.7341
	Fuzzy-PI [39]	10.2901	18.7536	12.2836
	PSO-GA	8.6802	8.7935	11.8886
Overshoot (Hz)	PSO-PID [37]	0.0693	0.0788	0.0531
	PSO-PIDF [38]	0.0223	0.0327	0.0041
	Fuzzy-PI [39]	0.0142	0.0231	0.0201
	PSO-GA	0.0021	0.0072	0.0033
Settling time (s)	PSO-PID [37]	10.7301	11.2346	9.9781
	PSO-PIDF [38]	10.6124	11.2337	8.2731
	Fuzzy-PI [39]	9.9216	12.3091	7.1741
	PSO-GA	5.1591	6.3201	4.0621

In reference [35], to improve the PI controller in the microgrid, model predictive control (MPC) is used to optimize the coefficients of the PI controller, and since its purpose is to control the frequency of the microgrid, the performance speed of MPC will be very important. To solve this problem, the PSO algorithm is used to improve the MPC controller both in terms of performance speed and accuracy. Following this issue, in reference [36], the improved MPC controller is used to improve the current control loop in the inverter. Finally, Figure 21 shows the curve of microgrid frequency changes according to the disturbances presented in Figure 18 and Figure 19. As you can see, the proposed controller has a more suitable response both in terms of reducing overshoot of frequency changes and in terms of reducing frequency settling time, compared to the two MPC-PSO [35] and IMPC [36] controllers.

A real microgrid contains different types of uncertainties due to microgrid load changes, system modeling errors, and microgrid structure changes. The simulation results for analyzing the frequency control performance of the studied microgrid show that the parameters are shown in Figure 17, such as T1, Tgi, etc., have a significant effect on the control performance of the system. Therefore, in this article, to reduce the settling time and frequency overshoot of the microgrid and the robust performance of the proposed controller, an integral square time square error (ISTSE) index in the form of Equation (17) has been used to evaluate the performance of the proposed controller.

$$ISTSE\ index = \int t^2 \Delta f^2\, dt \qquad (17)$$

Finally, TABLE 5 shows the amount of ISTSE, overshoot, and settling time obtained from the simulation results for normal and worst cases of uncertainty in the parameters, i.e. uncertainty of ±30% of the nominal value for different controllers. As you can see, according to the considered parameters, the proposed controller has been able to obtain better results.

VI. CONCLUSION

An effective power control method for VSI-based DG was researched in this paper to improve power quality in an island microgrid. An internal current control loop and a VF power control loop are part of the control approach. To implement the real-time auto-tuning method, the PSO-GA algorithm is inserted into the VF control loop. This technique is used to control voltage, frequency, and power-sharing when operating in island mode and while linked to the network. The controller is also designed to examine both dynamic and steady-state responses. According to the simulation results, the suggested controller has acceptable performance for controlling the microgrid's voltage and frequency, and its transient operating time is quite brief. This controller can therefore be used to control DG units in a microgrid while considering power-sharing. Even with these good results and perfect results, some limitations exist. The major of these limitations are related to the complex combination of the optimization application that will resolve the problem. Many parameters must be adapted and chosen and finding the best combination need to make more than testing and measuring. On the other side, this work must be applied in a real application for testing the real efficiency and demonstrating if the system will be stable or not. In future endeavors of this work, more than technic must be used and then compared. But verifying if this protocol is useful for a large charge amount of load must be made soon and try to be in connection with this work.

REFERENCES

[1] S. M. S. Hosseinimoghadam, M. Dashtdar, and M. Dashtdar, "Improving the sharing of reactive power in an islanded microgrid based on adaptive droop control with virtual impedance," *Autom. Contr. Comput. Sci.*, vol. 55, no. 2, pp. 155–166, 2021.

[2] M. Dashtdar, M. S. Nazir, S. M. S. Hosseinimoghadam, M. Bajaj, and S. Goud B, "Improving the sharing of active and reactive power of the islanded microgrid based on load voltage control," *Smart sci.*, vol. 10, no. 2, pp. 142–157, 2022.

[3] Z. Quan and Y. W. Li, "Impact of PWM schemes on the common-mode voltage of interleaved three-phase two-level voltage source converters," *IEEE Trans. Ind. Electron.*, vol. 66, no. 2, pp. 852–864, 2019.

[4] J. A. Riveros, J. Prieto, M. Rivera, S. Toledo, and R. Gregor, "A generalised multifrequency PWM strategy for dual three-phase voltage source converters," *Energies*, vol. 12, no. 7, p. 1398, 2019.

[5] U. Sultana, S. H. Qazi, N. Rasheed, and M. W. Mustafa, "Performance analysis of real-time PSO tuned PI controller for regulating voltage and frequency in an AC microgrid," *Int. J. Electr. Comput. Eng. (IJECE)*, vol. 11, no. 2, p. 1068, 2021.

[6] M. Castilla, M. Velasco, J. Miret, A. Borrell, and R. Guzman, "Control scheme for negative-sequence voltage compensation and current sharing in inverter-based grid-connected microgrids," *IEEE Trans. Power Electron.*, vol. 37, no. 6, pp. 6556–6567, 2022.

[7] S. M. S. Hosseinimoghadam, H. Roghanian, M. Dashtdar, and S. M. Razavi, "Power-sharing control in an islanded microgrid using virtual impedance," 2020.

[8] Y. Han *et al.*, "Reduced-order model for dynamic stability analysis of single-phase islanded microgrid with BPF-based droop control scheme," *IEEE Access*, vol. 7, pp. 157859–157872, 2019.

[9] M. Eskandari and A. V. Savkin, "A critical aspect of dynamic stability in autonomous microgrids: Interaction of droop controllers through the power network," *IEEE Trans. Industr. Inform.*, vol. 18, no. 5, pp. 3159–3170, 2022.

[10] M. Dashtdar and M. Dashtdar, "Power control in an islanded microgrid using virtual impedance," *Sci. Bull. Electr. Eng. Fac.*, vol. 20, no. 1, pp. 44–49, 2020.

[11] X. Hu, Z.-W. Liu, G. Wen, X. Yu, and C. Liu, "Voltage control for distribution networks via coordinated regulation of active and reactive power of DGs," *IEEE Trans. Smart Grid*, vol. 11, no. 5, pp. 4017–4031, 2020.

[12] M. Baharizadeh, H. R. Karshenas, and J. M. Guerrero, "An improved power control strategy for hybrid AC-DC microgrids," *Int. j. electr. power energy syst.*, vol. 95, pp. 364–373, 2018.

[13] Z. Liu, S. Miao, Z. Fan, J. Liu, and Q. Tu, "Improved power flow control strategy of the hybrid AC/DC microgrid based on VSM," *IET Gener. Transm. Distrib.*, vol. 13, no. 1, pp. 81–91, 2019.

[14] M. Gheisarnejad, H. Mohammadi-Moghadam, J. Boudjadar, and M. H. Khooban, "Active power sharing and frequency recovery control in an islanded microgrid with nonlinear load and nondispatchable DG," *IEEE Syst. J.*, vol. 14, no. 1, pp. 1058–1068, 2020.

[15] S. Iqbal *et al.*, "Aggregation of EVs for primary frequency control of an industrial microgrid by implementing grid regulation & charger controller," *IEEE Access*, vol. 8, pp. 141977–141989, 2020.

[16] M. Dashtdar and M. Dashtdar, "Voltage and Frequency Control of Islanded Micro-grid Based on Battery and MPPT Coordinated Control"," *IJECS*, vol. 2, no. 1, pp. 1–19, 2020.

[17] M. Jayachandran and G. Ravi, "Decentralized model predictive hierarchical control strategy for islanded AC microgrids," *Electric Power Syst. Res.*, vol. 170, pp. 92–100, 2019.

[18] M. Dashtdar and M. Dashtdar, "Voltage-frequency control (v-f) of islanded microgrid based on battery and MPPT control," *American Journal of Electrical and Computer Engineering*, vol. 4, no. 2, p. 35, 2020.

[19] P. Quintana-Barcia, T. Dragicevic, J. Garcia, J. Ribas, and J. Guerrero, "A distributed control strategy for islanded single-phase microgrids with hybrid energy storage systems based on power line signaling," *Energies*, vol. 12, no. 1, p. 85, 2018.

[20] A. Zafari, M. Mehrasa, K. Rouzbehi, M. S. Sadabadi, S. Bacha, and A. Hably, "DC-link voltage stability-based control strategy for grid-connected hybrid AC/DC microgrid," 2020.

[21] P. C. Sahu, S. Mishra, R. C. Prusty, and S. Panda, "Improved-salp swarm optimized type-II fuzzy controller in load frequency control of multi area islanded AC microgrid," *Sustain. Energy Grids Netw.*, vol. 16, pp. 380–392, 2018.

[22] Hosseinimoghadam, Seyed Mohammad Sadegh, Masoud Dashtdar, Majid Dashtdar, and Hamzeh Roghanian. "Security control of islanded micro-grid based on adaptive neuro-fuzzy inference system." Scientific Bulletin": Series C Electrical Engineering and Computer Science 1 (2020): 189-204.

[23] A. Naderipour, Z. Abdul-Malek, I. F. Davoodkhani, H. Kamyab, and R. R. Ali, "Load-frequency control in an islanded microgrid PV/WT/FC/ESS using an optimal self-tuning fractional-order fuzzy controller," *Environ. Sci. Pollut. Res. Int.*, 2021.

[24] T. Yao and R. Ayyanar, "Variable structure robust voltage regulator design for microgrid master-slave control," 2017.

[25] M. R. Khalghani, M. H. Khooban, E. Mahboubi-Moghaddam, N. Vafamand, and M. Goodarzi, "A self-tuning load frequency control strategy for microgrids: Human brain emotional learning," *Int. j. electr. power energy syst.*, vol. 75, pp. 311–319, 2016.

[26] M.-H. Khooban, T. Niknam, F. Blaabjerg, P. Davari, and T. Dragicevic, "A robust adaptive load frequency control for micro-grids," *ISA Trans.*, vol. 65, pp. 220–229, 2016.

[27] A. Abazari, M. G. Dozein, and H. Monsef, "A new load frequency control strategy for an AC micro-grid: PSO-based fuzzy logic controlling approach," 2018.

[28] A. Safari, F. Babaei, and M. Farrokhifar, "A load frequency control using a PSO-based ANN for micro-grids in the presence of electric vehicles," *Int. J. Ambient Energy*, vol. 42, no. 6, pp. 688–700, 2021.

[29] S. Kayalvizhi, "Load frequency control of an isolated microgrid using fuzzy adaptive model predictive control," *IEEE Access*, vol. 5, pp. 16241–16251, 2017.

[30] P. K. Ray and A. Mohanty, "A robust firefly–swarm hybrid optimization for frequency control in wind/PV/FC based microgrid," *Appl. Soft Comput.*, vol. 85, no. 105823, p. 105823, 2019.

[31] S. Mishra, P. C. Nayak, U. C. Prusty, and R. C. Prusty, "Implementation of a hybrid cuckoo search and pattern search algorithm for frequency control of the microgrid system," 2020.

[32] S. W. Waleed, D. Lachowicz, and O. Habibi, "Power quality improvement in autonomous microgrid operation using particle swarm optimization," in *2011 IEEE PES Innovative Smart Grid Technologies*, IEEE, 2011, pp. 1–6.

[33] A. Kahrobaeian and Y. A.-R. I. Mohamed, "Analysis and mitigation of low-frequency instabilities in autonomous medium-voltage converter-based microgrids with dynamic loads," *IEEE Trans. Ind. Electron.*, vol. 61, no. 4, pp. 1643–1658, 2014.

[34] M. S. Golsorkhi, "A control method for inverter-based islanded microgrids based on VI droop characteristics," *IEEE Transactions*, vol. 30, no. 3, pp. 1196–1204, 2014.

[35] M. Dashtdar, A. Flah, C. Z. El-Bayeh, M. Tostado-Véliz, A. A. Durra, and Z. M. Aleem, "Frequency control of the islanded microgrid based on optimized model predictive control by PSO," *IET Renewable Power Generation*, 2022.

[36] T. John and S. Ping Lam, "Voltage and frequency control during microgrid islanding in a multi-area multi-microgrid system," *IET Gener. Transm. Distrib.*, vol. 11, no. 6, pp. 1502–1512, 2017.

[37] D. Boopathi, S. Saravanan, K. Jagatheesan, and B. Anand, "Performance estimation of frequency regulation for a micro-grid power system using PSO-PID controller," *Int. J. Appl. Evol. Comput.*, vol. 12, no. 2, pp. 36–49, 2021.

[38] D. Mishra, P. Chandra Nayak, and R. C. Prusty, "PSO optimized PIDF controller for Load-frequency control of AC Multi-Islanded-Micro grid system," in *2020 International Conference on Renewable Energy Integration into Smart Grids: A Multidisciplinary Approach*

to Technology Modelling and Simulation (ICREISG), IEEE, 2020, pp. 116–121.

[39] A. Annamraju and S. Nandiraju, "Robust frequency control in an autonomous microgrid: A two-stage adaptive fuzzy approach," *Electr. Power Compon. Syst.*, vol. 46, no. 1, pp. 83–94, 2018.

MASOUD DASHTDAR was born in Bushehr, Iran, on September 20, 1986. He received an M.Sc. in power electrical engineering from Islamic Azad University of Bushehr, Iran, in 2013. He is holding a Ph.D. degree from Islamic Azad University, Bushehr, Iran, in 2020. He is an assistant professor and a faculty member of the Islamic Azad University, Bushehr Branch. He is a reviewer of ISI journals with the "Journal of Electrical Engineering & Technology (JEET)", "Artificial Intelligence Review", "Soft Computing", " Electrical Engineering", " Iranian Journal of Science and Technology, Transactions of Electrical Engineering", "Sustainable Energy, Grids and Networks", "International Transactions On Electrical Energy Systems", "Canadian Journal of Electrical and Computer Engineering", "IEEE Access" and "IEEE Transactions on Circuits and Systems II" cooperation. His research interests are distribution systems, including fault diagnosis in power systems, artificial neural network computing, power electronics, electric machines, renewable energy, microgrid, smart grids, harmonic analysis, power quality, optimization, and meta-heuristic algorithms.

FLAH AYMEN was born in Gabeès, Tunisia, in 1983. He received the bachelor's and M.Tech. degrees in electrical engineering from ENIG, Tunisia, in 2007 and 2009, respectively, and the Ph.D. degree from the Department of Electrical Engineering, in 2012. He has an academic experience of 11 years. He has published over 40 research articles in reputed journals, international conferences, and book chapters.

SEYED MOHAMMADSADEGH HOSSEINIMOGHADAM was born in Bushehr, Iran, on July 1, 1990. He holds a Bachelor's in power electrical engineering from the Islamic free university of Bushehr, Iran, in 2014. He holds M.Sc. from the science and research free university of Tehran, Iran in 2016, in power system engineering. He is holding a Ph.D. from the Islamic free university of Bushehr, Iran, in power systems. His research interests are Distribution systems, including fault diagnosis and Protection in power systems. Renewable Energy, Micro Grid, Harmonic analysis, Optimization Algorithms.

HOSSAM KOTB received his B.Sc., M.Sc., and Ph.D. degrees in Electrical Engineering from Alexandria University, Faculty of Engineering, Alexandria, Egypt, in 2009, 2013, and 2020, respectively. His Ph.D. research work is focused on the performance enhancement of renewable energy conversion systems. Currently, he is an Assistant Professor at the Electrical Power and Machines Department, Faculty of Engineering, Alexandria University. Dr. Kotb is an associate editor in Alexandria Engineering Journal (AEJ). His research interests include power system analysis, electrical drives, modern control techniques, smart grids, optimization, electric vehicles and renewable energy systems.

KAREEM M. ABORAS received his B.Sc., M.Sc., and Ph.D. degrees in Electrical Engineering from Alexandria University, Faculty of Engineering, Alexandria, Egypt, in 2010, 2015, and 2020, respectively. His Ph.D. research work is focused on the performance enhancement of renewable energy conversion systems. Currently, he is an Assistant Professor at the Electrical Power and Machines Department, Faculty of Engineering, Alexandria University. Mr. AboRas is a reviewer in IET journal. His research interests include power electronics, control, drives, power system, and renewable energy systems.

CH. RAMI REDDY (Member, IEEE) received the B.Tech. degree in electrical and electronics engineering and the M.Tech. degree in electrical machines and drives from Jawaharlal Nehru Technological University, Kakinada, Andhra Pradesh, India, in 2011 and 2014, respectively, and the Ph.D. degree in electrical and electronics engineering from K. L. University, Andhra Pradesh, in 2022. He is currently working as an Assistant Professor in electrical and electronics engineering with the Malla Reddy Engineering College (Autonomous), Secunderabad, Telangana, India. His current research interests include integrated renewable energy systems, distributed generation, FACTS devices, and power converters applications to energy systems. He is an Editorial Board Member and a Reviewer of various Web of Science and Scopus Indexed Journals. He is also a Guest Editor of Energies journal (MDPI) for a Special Issue ''Advancement in Renewable Energy Technologies and Smart Grid.''

EDSON C. BORTONI (Senior Member, IEEE) was born in Maringá, Brazil, in 1966. He received a bachelor's degree in electrical engineering from the Federal University of Itajubá (UNIFEI), Itajubá, Brazil, in 1990, and the M.Sc. degree in energy systems planning from the University of Campinas, Campinas, Brazil, in 1993, the D.Sc. degree in power systems from the Polytechnic School, University of São Paulo (USP), São Paulo, Brazil in 1998, and the Habilitation degree from USP, in 2012. He was a Professor with São Paulo State University, Guaratinguetá, Brazil. He was a Visiting Scholar with Montanuniversität Leoben, Austria, the École Polytechnique Fédérale de Lausanne, Switzerland, and the Politecnico di Torino, Italy. He is currently a Full Professor with UNIFEI. He is the Head of the EXCEN, the Excellence Center in Energy Efficiency. His research interests include electrical machine design, testing, and modeling, power generation, energy systems, sensors, and smart grids. He is a member of the EMC, WG-7 (IEEE STD. 115), WG-8 (IEEE STD. C50.13), WG10 (IEEE STD. 1110), of the EMC Grid Code Task Force. He is a Fellow Member of the International Hydropower Association and the International Society of Automation. He is the Chair of the Generator Subcommittee and the WG-4 (IEEE STD. C50.12), and several technical sessions in important conferences, including PowerTech, the IEEE PES General Meeting, IEMDC, and others. He is the President of the Brazilian Energy Planning Society. He is an Assistant Editor and a Subject Editor of the IET GTD Journal and an Assistant Editor of Flow Measurement and Instrumentation Journal. He is a Distinguished Lecturer of the PES IEEE.

energies

MDPI

Article

Experimental Investigation and Performance Characteristics of Francis Turbine with Different Guide Vane Openings in Hydro Distributed Generation Power Plants

Megavath Vijay Kumar [1,*], T. Subba Reddy [2], P. Sarala [3], P. Srinivasa Varma [4], Obbu Chandra Sekhar [5], Abdulrahman Babqi [6], Yasser Alharbi [6], Basem Alamri [6,*] and Ch. Rami Reddy [3,5]

1 Department of Mechanical Engineering, Malla Reddy Engineering College, Maisammaguda, Secunderabad 500100, India
2 Department of Mechanical Engineering, Andhra Loyola Institute of Engineering and Technology, Vijayawada 520008, India
3 Department of Electrical and Electronics Engineering, Malla Reddy Engineering College, Secunderabad 500100, India
4 Department of Electrical and Electronics Engineering, Koneru Lakshmaiah Education Foundation, Vaddeswaram 522502, India
5 Department of Electrical Engineering, National Institute of Technology, Srinagar 190006, India
6 Department of Electrical Engineering, College of Engineering, Taif University, P.O. Box 11099, Taif 21944, Saudi Arabia
* Correspondence: vijaykumar.084@mrec.ac.in (M.V.K.); b.alamri@tu.edu.sa (B.A.)

Abstract: This article presents a study on the performance characteristics of a Francis turbine operating with various guide vane openings to determine the best operating point based on unit quantities. The guide vane openings were specified based on the width between the vanes at their exit, i.e., 10 mm, 13 mm, 16 mm, and 19 mm. The performance characteristic curves of the Francis turbine—head versus speed, torque versus speed, discharge versus speed, and efficiency versus speed—were obtained at various input power and guide vane openings. From these data, unit curves were plotted and the corresponding best efficiency points were obtained. The highest efficiency of 50.25% was obtained at a guide vane opening of 19 mm. The values of head, discharge, speed, and output power at BEP were 7.84 m, 13.55 lps, 1250 rpm, and 524 W, respectively.

Keywords: renewable energy; Francis turbine; guide vane opening; performances & unit quantities

Citation: Vijay Kumar, M.; Reddy, T.S.; Sarala, P.; Varma, P.S.; Chandra Sekhar, O.; Babqi, A.; Alharbi, Y.; Alamri, B.; Reddy, C.R. Experimental Investigation and Performance Characteristics of Francis Turbine with Different Guide Vane Openings in Hydro Distributed Generation Power Plants. *Energies* **2022**, *15*, 6798. https://doi.org/10.3390/en15186798

Academic Editor: Chirag Trivedi

Received: 28 July 2022
Accepted: 10 September 2022
Published: 17 September 2022

1. Introduction

The motive energy found in water is known as hydropower. By using hydroelectric power plants, it can be transformed into electrical energy. All that is needed is a constant inflow of water and a height difference between the location where the water is found and the location where it can be released. The potential for hydropower is impressive. It is a free resource that is perpetually renewable and nonpolluting. Hydropower plays a significant role in the multipurpose use of water resources in many situations. The destructive forces of flood flows and the energy of normal flows are harnessed by hydropower projects to provide useful electrical energy. The economy of different power sources is reflected in the cost of electricity. Countries that have a large proportion of hydropower in their systems have the lowest tariffs. Upgrading existing hydropower plants is frequently more economical than building new ones. High initial investment-prone hydropower plants hold the substantial potential of uprating at the time of renovation, thereby making upgrading proposals cost-effective [1]. Due to the rising demand for electricity, hydropower plants are now more necessary than ever. Therefore, modernizing hydroelectric facilities is crucial to meeting public demand.

1.1. Selection of Turbines

The head under which a turbine is going to be operated gives guidance for the selection of the type of turbine. The range of operation of each type is shown concerning the head (H) and specific speed (ns) [2]. The total power to be installed must be known and the number of machines then are chosen by economic consideration of load factor, the extent of water storage, if any, cost of powerhouse, the convenience of operation, and maintenance. Once the output per machine has been decided, information must be obtained concerning the suitable speeds for which the generator can be constructed economically. From these data, the coupling power, effective head, and speed of the turbine are known. Hence, the specific speed is calculated. From the previous table, the suitable turbine is selected. Since the speed of the generator can generally be selected from several suitable numbers of pairs of poles, the appropriate specific speed is not limited to one value. In many cases, the overlap is considerably extended and the problem arises of selecting from two types of turbines, either of which could be used [3]. Here, knowledge of the advantages and disadvantages of each type will assist, especially concerning efficiency when running at part load. If the machine is required to operate for long periods of part loads, the Pelton turbine would be preferred to the Francis turbine. Similarly, if the choice lay between two Francis turbines, that with the lower specific speed would be more suitable, whereas if the choice lay between a Kaplan turbine or a propeller turbine or a Francis turbine with a high specific speed, the Kaplan turbine would be preferred. This is because of the flattest efficiency curve being obtained from the Kaplan turbine, followed by the Pelton turbine, the low-specific-speed Francis turbine, the high-specific-speed Francis turbine, and finally the propeller turbine, which has the most peaked form of the efficiency curve. It must not be assumed that the highest possible specific speed is always desirable [4,5].

1.2. Francis Turbine

Francis turbines can be built to handle a wide range of head and flow rates. This, combined with their high efficiency, has resulted in them being the most widely used turbine in the world. The Francis-type units have a head range of 20 m to 700 m, a specific speed of 60 to 400 rpm, and an output power ranging from a few kilowatts to one gigaton. Large Francis turbines are custom-built for each location to achieve the highest possible efficiency, typically exceeding 90% [6]. The water initially needs to enter the scroll (volute), which is an annular channel that surrounds the runner, and then flows between the stationary vanes and adjustable guide vanes, which provide the water with the best flow direction. It then enters the completely submerged runner, altering the momentum of the water and causing a reaction in the turbine. Water flows in a radial direction towards the center. The water is impinged upon by curved vanes on the runner. The guide vanes are configured in such a way that the energy of the water is largely converted into rotary motion, rather than being consumed by eddies and other undesirable flow phenomena that cause energy losses. The guide vanes are typically adjustable to provide some adaptability to variations in the water flow rate and turbine load. The Francis turbine's guide vanes are the elements that direct the flow of water [7]. The authors investigated flow parameters, such as flow angles at the runner's inlet and outlet, flow velocities, and guide vane angles, to derive flow characteristics. The goal was to analyze the pressure distribution and flow behavior to achieve the level of accuracy required for the concept design of a revitalized turbine. The obtained results are in good agreement with the on-site experiments, particularly for the characteristic curve [8].

For three different specific speed turbines, the authors predicted the accuracy and compared it to the model test results. It was demonstrated that the numerical model test presented in this investigation could predict important characteristics of the Francis turbine with high accuracy not only quantitatively but also qualitatively by comparing simulation results with model test results for pressure-fluctuation characteristics, efficiency characteristics, and cavitation characteristics. As a result, it was determined that numerical model testing would be a more realistic estimation tool for Francis turbine hydraulic

performance, contributing to cost reduction in the development of the Francis turbine [9]. The authors investigated Francis turbine guide vanes with pivoted support and an external control mechanism for converting pressure to kinetic energy and directing it to runner vanes. It has been discovered that increasing the clearance gap of the guide vane opening increases leakage, lowering energy conversion and turbine efficiency and resulting in a larger secondary vortex [10].

Many simulated results on hydroturbines have been conducted using various turbulence models to identify their performance parameters [11]. Three distinct turbulence models were explored in this work to measure the sensitivity of the model for the derivation of Francis hydroturbine performance characteristics. To evaluate the performance of the turbine, three different operating circumstances were chosen: part load, overload, and best efficiency point. The highest velocity fluctuation inside the Francis runner was anticipated by the model. The turbulence model can be used to capture the vortex rope that appears at the runner's output [12]. The influence of blade thickness on hydraulic performance was investigated numerically using six types of impellers with varied blade thicknesses that were integrated into the same pump to compare head and efficiency under design point [13]. The effect of clearance on the performance of a Francis turbine was investigated, and it was discovered that as transverse flow and loss increased, efficiency decreased significantly. When considering a specific degree of erosion, the pressure on both sides of the blade and at the outflow of the blade was precisely proportional to the erosion state [14–16]. The flow conditions in the runner inlet of a low-speed-number Francis turbine are found to be identical when a cascade with one guide vane between two flow channels is optimized [17].

Guide vane (GV) clearance gaps grow larger due to abrasive wear, which worsens the flow and reduces efficiency. In order to reduce potential consequences of an eroded guide vane on the performance of the turbine, this research evaluates several guide vane profiles. It is discovered that the pressure differential between the neighboring sides causes the clearance gap to create a leakage flow. A vortex filament is created when the leaky flow combines with the main flow and is forced within the runner [18]. The authors offer a methodology for the design, optimization, and additive manufacture of turbine blade rows and other components of highly stressed turbomachinery. The technique subsequently produces final geometries that have been suitably represented for additive manufacturing. A few aluminum prototypes of the newly improved turbine blade have been produced in order to undergo mechanical and fatigue testing [19]. The mechanical power turbine's torque varies with its size. With a peak value of 3249.7 Nm at pitch angle 17°, significant torque was obtained in the pitch angle range of 15–20°. As turbines grow in size and their pitch angle range increases, they will produce more power, reaching a maximum of 124,987.1 W or 125 kW [20]. The findings demonstrated that in operating conditions involving substantial flow rates, severe sand abrasion might be seen close to the blade head and outlet. In working conditions with low flow rates, there may be very minor abrasion found close to the blade flange. The runner is severely abraded and its effectiveness is lowered in proportion to the sediment concentration and sand diameter [21]. While the flow separation on the suction side close to the blade tip merges, the flow characteristics on the blade pressure side are often stable. The flow-separation phenomenon manifests itself more visibly with larger tip clearance. The tip leakage vortex, which is also a spatial three-dimensional spiral structure created by the entrainment effect of the tip leakage flow and main flow, becomes more pronounced as the tip clearance rises [22].

After detailed review of the literature, it was apparent that lots of research has been carried out on hydroturbines, but few studies have made an attempt at different guide vane openings and no literature was found on best operating point based on unit quantities. As such, the present work focuses the best operating point based on unit quantities by studying the performance characteristics of the Francis turbine at various input powers and guide vane openings.

2. Experimental Setup

2.1. Experimental Setup of Francis Turbine

The model Francis turbine available at Hydro Turbo Machines Lab was designed and built by Nilavalagan (1973) and was used for these experiments, as shown in Figures 1 and 2.

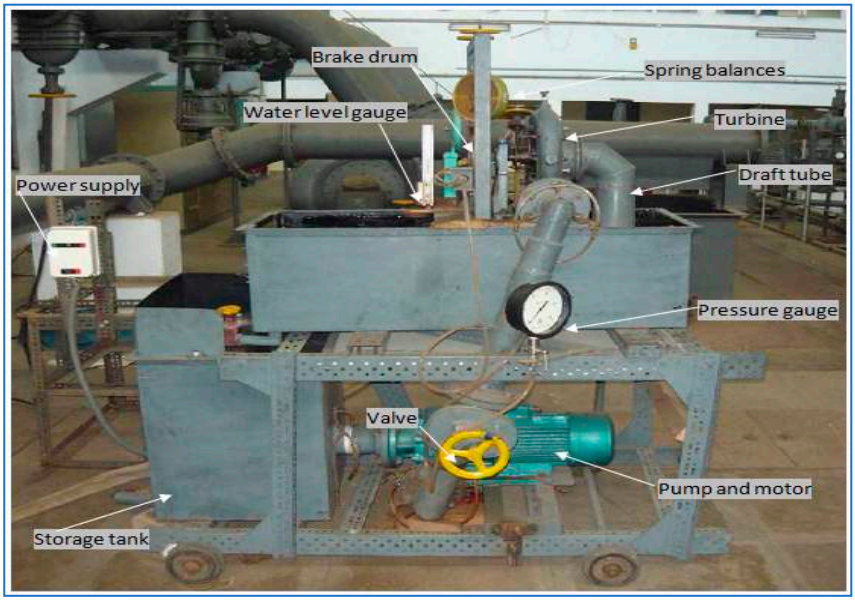

Figure 1. The Francis turbine test setup.

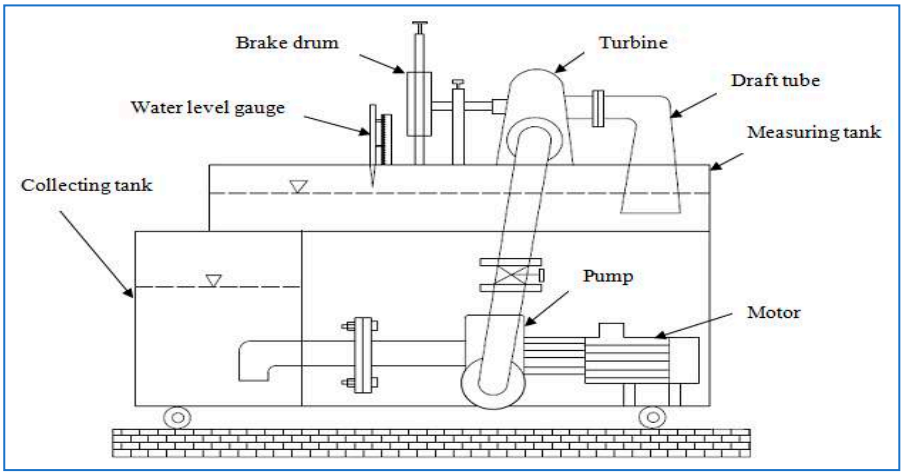

Figure 2. Schematic of Francis turbine test setup.

The Francis turbine is a machine that uses the energy of water and converts it into mechanical energy. Thus, it becomes the prime mover to run the electrical generators to produce electricity. The head is generated using a pump that draws water from the storage tank and supplies it to the inlet of the turbine. The torque generated by the turbine is measured using a brake drum. The water outlet flow of the turbine is sent to the measuring tank through the draft tube. The excess water from the measuring tank flows to the storage tank.

Four pressure tapings made near the inlet of the turbine were made to form a piezo-ring and were connected to a pressure gauge (range 0–2.5 kg/cm^2). The tachometer was used to measure the speed (N) of the turbine. The turbine was loaded with the help of a brake drum connected to a loading belt. The tension in the belt on both sides of the brake drum was measured with spring balances. The load on the turbines was altered with the help of hand wheels connected to balances. The diameter of the brake drum was 225 mm

and the thickness of the belt 5 mm. At the back of the turbine casing, there is a guiding vane mechanism. The distance between the two successive guide vanes can be altered by rotating a hand wheel. The maximum distance between one guide vane's tip to another was measured using a vernier caliper. It was found to be 19 mm maximum.

2.2. Specification of the Instruments Required for Measuring

(a) Discharge

The discharge measurement in this experiment was done using a rectangular notch, shown in Figure 3, fitted in the measuring tank. The discharge formula found by the Indian Standard (IS: 9108-1979) was used and is discussed below.

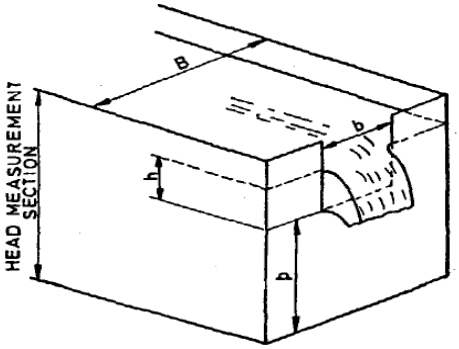

Figure 3. Rectangular notch.

The Kindsvater–Carter rectangular weir formula is

$$Q = C_e \frac{2}{3} \sqrt{2g} b_e h_e^{3/2} \quad (1)$$

where,

Q = discharge, m^3/sec

C_e = coefficient of discharge,

b_e = effective width, in mm, and

h_e = effective head in mm.

The coefficient of discharge was determined by experiment as a function of two variables from the formula:

$$C_e = f(\frac{b}{B}, \frac{h}{p}) \quad (2)$$

The effective width and head are defined by the equations:

$$b_e = b + k_b = b + 3.6 \quad (3)$$

$$h_e = h + k_h = h + 0.0012 \quad (4)$$

Which and are experimentally determined quantities, in meters, which compensates for the combined effects of viscosity and surface tension.

From the value of b/B, formula for C_e can be written as

$$(b/B = 0.6): = 0.593 + 0.018 \quad (5)$$

The water-level gauge was used to measure the height of the water level in a rectangular notch. This water-level gauge was fixed with the scale. This gauge mechanism has a rotating device for making adjustments.

(b) Speed

The digital tachometer was used to measure the speed of the turbine. Its range is 0–5000 rpm. This tachometer is kept at the back of the brake drum to find the speed of the turbine.

(c) *Pressure*

A Bourdon tube pressure gauge was used to find the pressure at the inlet of the turbine. The pressure gauge range was 0 to 2.5 kg/cm^2.

(d) *Load*

The spring balance was used to find the loads applied on the brake drum. The spring-balance range was 10 kg × 50 gm and 20 kg × 100 gm.

2.3. Experimental Methodology

- Connect the supply-pump motor unit to 3 ph, 440 V, 30 A, electrical supply, with neutral and earth connection and ensure the correct direction of pump motor unit. Keep the gate closed before the pump is on. Later, press the green button of the supply-pump starter and then release. The guide vane distance is maintained at 19 mm initially for fully open guide vane position and altered to 16 mm, 13 mm, and 10 mm distance with the help of a hand wheel. For each of the above guide vane openings, the speed of the turbine is maintained initially at 1000, 1500, 2000, and 2500 rpm by adjusting the pump outlet valve. Later, the load is applied in steps of 250 g till the lowest possible speed at which the turbine can run continuously. For each corresponding set of readings, the pressure at the inlet of the turbine, speed, load on the brake drum, and head over notch are noted. Then, the gate valve is closed and the supply-water pump switched off.
- The performances of the turbine were calculated, i.e., discharge, head, torque, input power, output, efficiency, and unit quantities. Later, the performance characteristics of the turbine were plotted.

3. Results and Discussion

The best efficiency point of the Francis laboratory scale was found by operating the water pump at different guide vane openings. The performance characteristics were plotted for these conditions. For each water supply, the reading was obtained and respective characteristics curves plotted for four different guide vane openings. The guide vane openings were specified based on the width between the vanes at their exit, i.e., 10 mm, 13 mm, 16 mm, and 19 mm. For each water supply and respective guide vane opening, an experiment was conducted as per the procedure indicated in Section 2.3. Each experiment was repeated and performance curves for discharge versus speed, head versus speed, torque versus speed, and efficiency versus speed were plotted.

A polynomial curve fit was done for the two individual sets of readings that were repeated for the same experimental condition to check repeatability. Then, the two individual experimental results were merged as one single set and fitted as a polynomial curve. The correlation coefficient was found to be not less than 0.98. The respective polynomial equation for each of torque, discharge, and head with speed were substituted in the efficiency formula and corresponding efficiency was calculated.

3.1. Performance Characteristics of Francis Turbine

The performance characteristics of discharge versus speed, head versus speed, torque versus speed, and efficiency versus speed for 10 mm guide vane opening are shown in Figures 4–11. At lower input power, few points could be obtained. The turbine came to a halt at higher loads, but starting the turbine at higher power enables taking a large number of readings. The discharge appears to be less at high speeds compared to low speeds; this may be because the machine is vibrating and fluctuating while it is functioning.

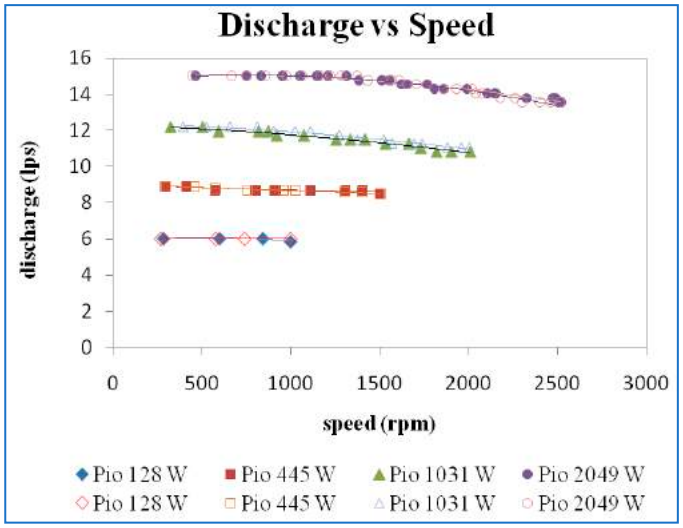

Figure 4. Discharge vs. speed at a guide vane opening of 10 mm.

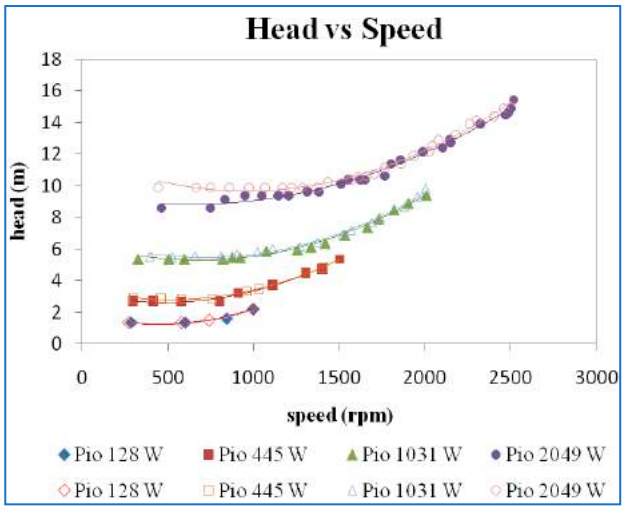

Figure 5. Head vs. speed at a guide vane opening of 10 mm.

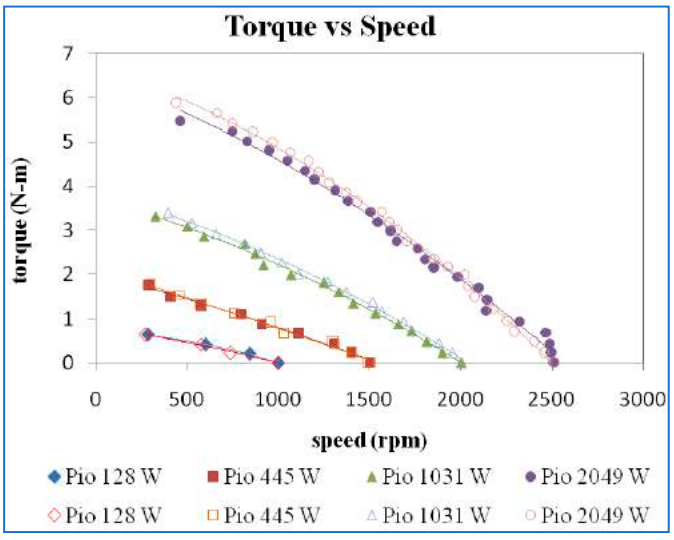

Figure 6. Torque vs. speed at a guide vane opening of 10 mm.

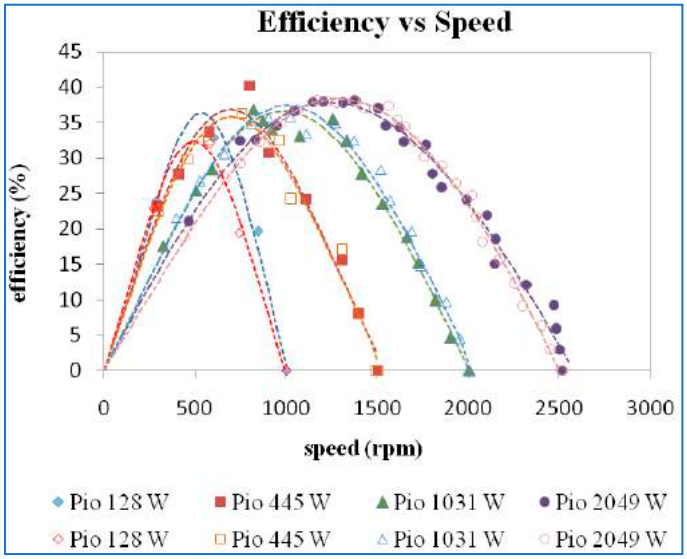

Figure 7. Efficiency vs. speed at a guide vane opening of 10 mm.

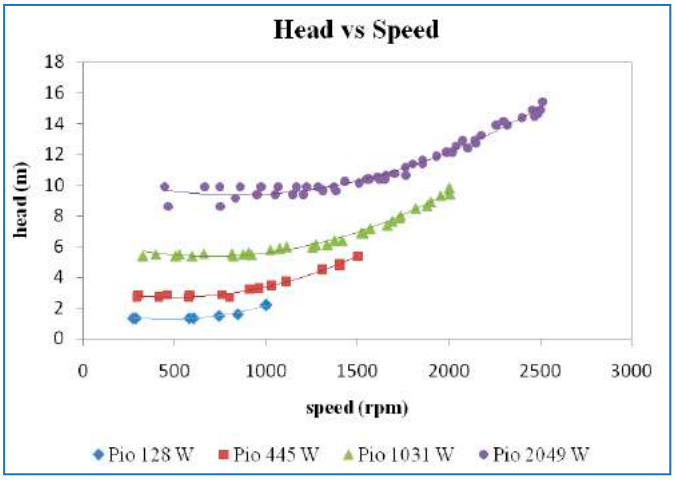

Figure 8. Head vs. speed at a guide vane opening of 10 mm.

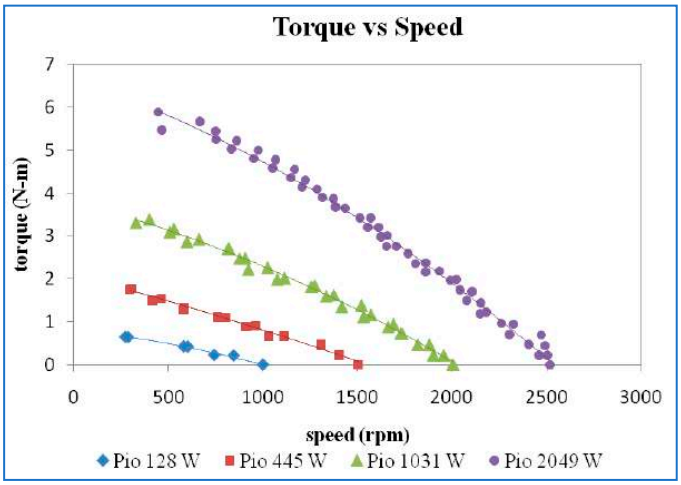

Figure 9. Torque vs. speed at a guide vane opening of 10 mm.

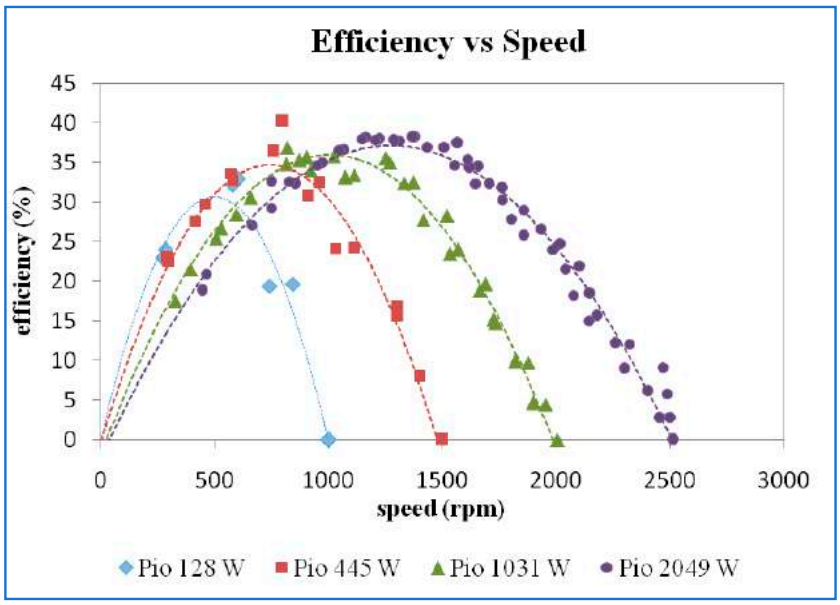

Figure 10. Efficiency vs. speed at a guide vane opening of 10 mm.

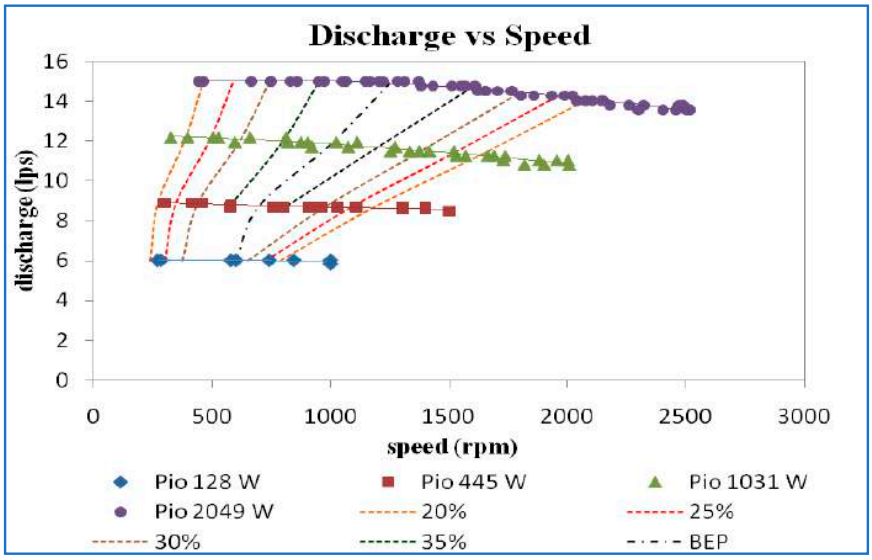

Figure 11. Discharge vs. speed and iso-efficiency line at 10 GVO.

Figure 5 shows the plot of the variation of the head concerning the speed for different power inputs. The head increases with an increase in the power inputs. The head is almost constant at lower speeds and then increases with speed. There is a slight increase in the head curves even during the lower speeds for the power input of 2049 (W). In this plot also, it may be observed that the repeatability of the readings is good.

A study of Figure 6 showing the plot of torque versus speed shows that at no load conditions, the speed of the turbine is about 2500 rpm for the power input of 2049 (W). This is the maximum speed that was achieved for the highest possible power input. The speed at no load came down to 2000 rpm, 1500 rpm, and 1000 rpm, respectively, as the input power was decreased. In fact, during the experiments, the input valve that changes the power input to the turbine was fixed based on the speed in the no-load condition. When a load is applied, the torque rises, increasing the frictional forces acting between the brake drum and the belt. This causes heat to be released, reducing speed. The repeatability of the readings can also be seen in the two sets plotted in Figure 6.

Efficiency versus speed for different power inputs is shown in Figure 7. It may be seen that higher maximum efficiency was obtained for higher inputs and efficiency increased

to a maximum then decreased as speed increased. This is because the output power is contributed by the torque and speed. The speed decreases with increases in torque; thereby, the overall output power increases, reaches a maximum, and then decreases. One can argue that the effect of input power may also contribute to the variation in efficiency. This is true, but only at higher speeds. The discharge and the head were almost constant at lower speeds, so the variation of input power becomes insignificant. That is the reason that the efficiency curves show the increasing and decreasing trend.

The two sets of points in Figures 4–7 indicate clearly that the results are repeatable and hence they were considered together and a single curve fitted for every value of input power.

Figure 8 shows the plot of the variation of the head concerning the speed for different power inputs. Trial 1 and trial 2 were combined and plotted as a single curve. It can be seen that head decreases with a decrease in the power inputs.

Figure 9 shows that when the load is applied, the torque increases the frictional forces acting between the brake drum and the belt increase and dissipate the energy in the form of heat; therefore, the speed comes down. The torque is increased by decreasing the speed.

The efficiency versus speed for different power inputs is shown in Figure 10. The higher maximum efficiency was obtained for higher input power. However, there is only a slight variation of maximum efficiency at 445 W, 1031 W, and 2049 W input power.

The iso-efficiency lines plotted on discharge versus speed curves are shown in Figure 11. From the efficiency curves, horizontal lines corresponding to efficiencies of 20%, 25%, 30%, 35%, and best efficiency point (BEP) were drawn and the speed and the discharge corresponding to the point where the efficiency curves intersect the horizontal iso-efficiency lines were noted and plotted, as shown in the above figure. It may be noted that the value of discharge and speed at maximum efficiency is 32%, 36%, 37%, and 38% at input power of 77 W, 243 W, 647 W, and 1414 W for guide vane opening of 10 mm.

The head versus speed curve shown in Figure 12 was obtained at a guide vane opening of 13 mm. The head is decreasing with decreasing the speed. When input power is more, the head seems to be more.

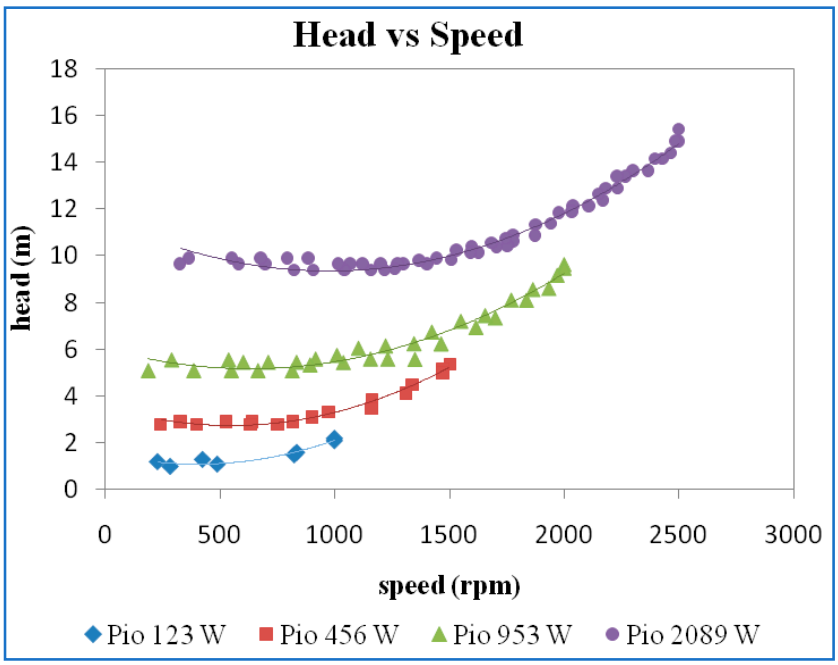

Figure 12. Head vs. speed at a guide vane opening of 13 mm.

From Figure 13, it may be seen that as speed decreases, the torque starts to increase when the load is applied to the brake drum. There is not much variation in these curves between guide vane openings of 13 mm and 10 mm, as seen in Figures 9 and 13.

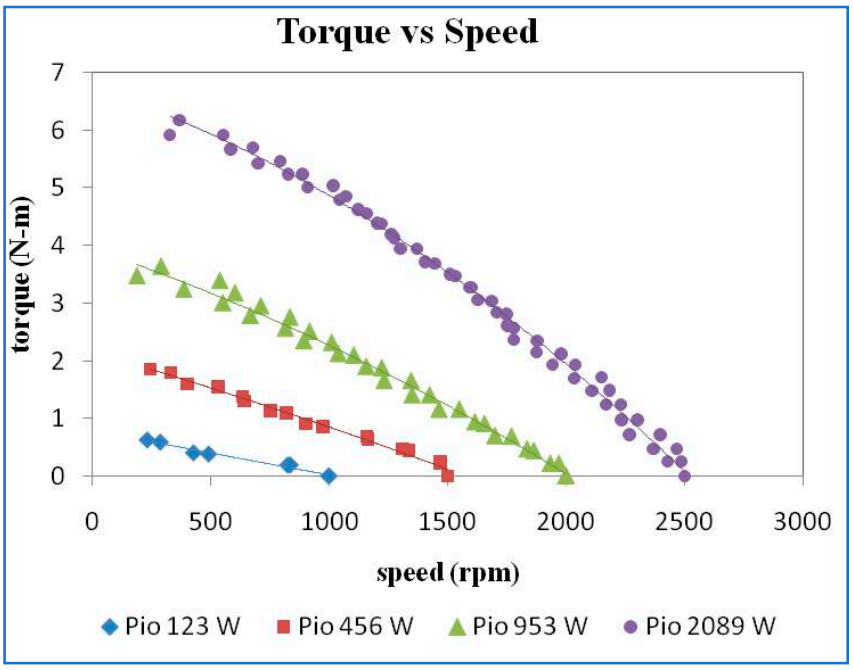

Figure 13. Torque vs. speed at a guide vane opening of 13 mm.

The maximum efficiency was observed at a power input of 953 W for a guide vane opening of 13 mm, as seen in Figure 14. At input power of 123 W, 456 W, and 953 W the maximum efficiency increases gradually, but at power input 2089 W it is decreased slightly due to the vibration, which leads to cavitations within the turbine.

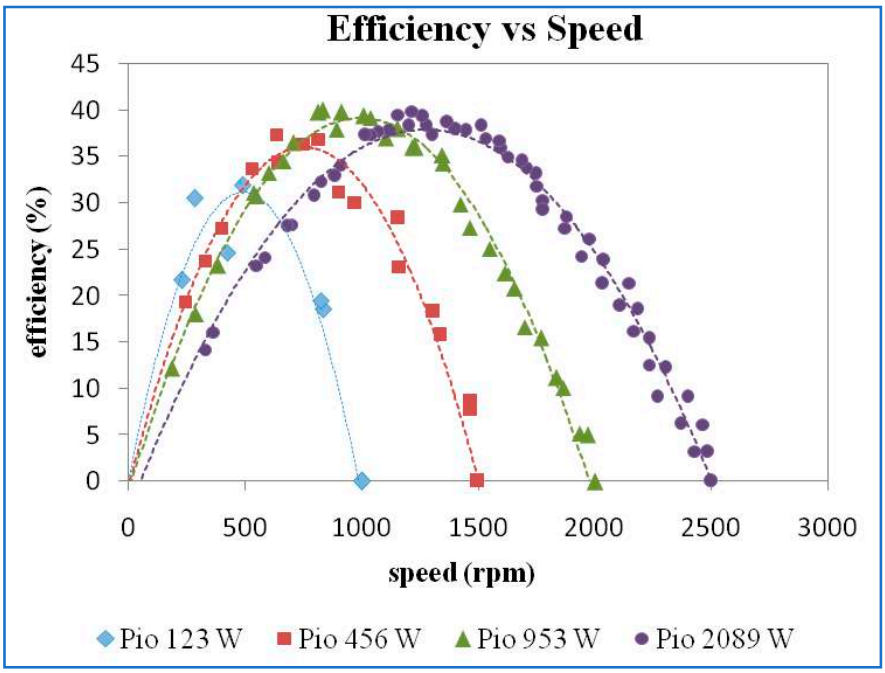

Figure 14. Efficiency vs. speed at a guide vane opening of 13 mm.

Figure 15 shows that the discharge is more or less constant at different input power. The iso-efficiency plot seems not much different between the guide vane openings of 10 mm and 13 mm. The values at best efficiency points are 33%, 37%, 40%, and 39%.

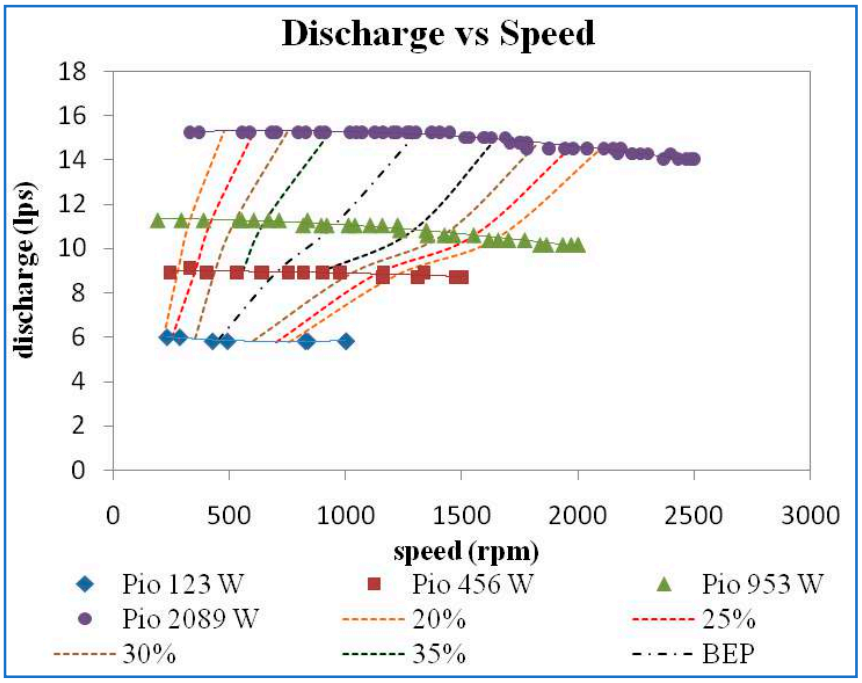

Figure 15. Discharge vs. speed and iso-efficiency line at 13 GVO.

The plot of the variation between the head and speed for different power input at 16 mm GVO is shown in Figure 16. The head decreases with decreasing power input. A notable variation may be observed at higher speeds.

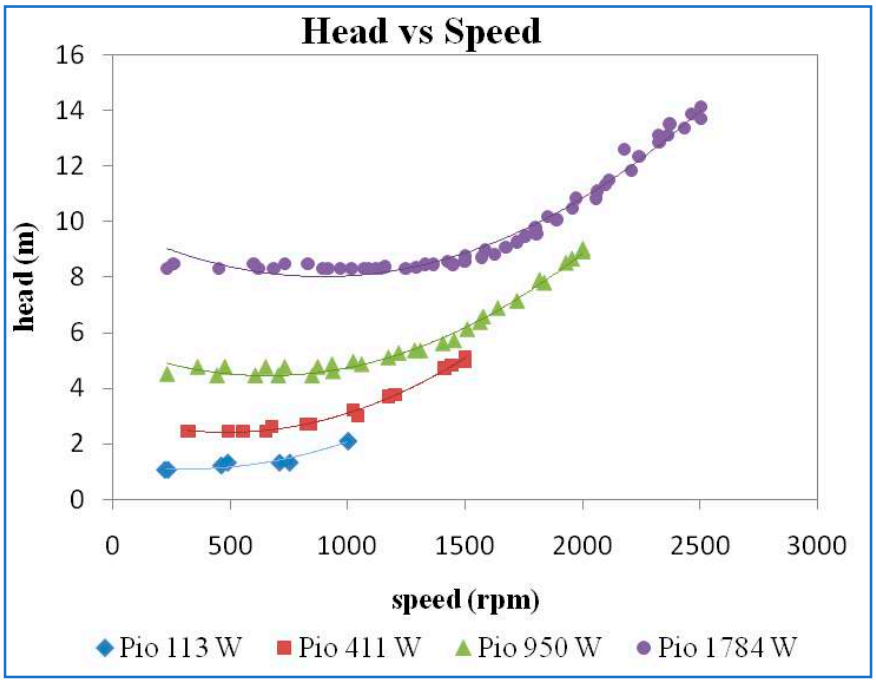

Figure 16. Head vs. speed at a guide vane opening of 16 mm.

From Figure 17, it may be concluded that at a GVO of 16 mm, when the torque increases the speed starts decreasing when the load is applied on the brake drum. There is not much variation from guide vane openings of 16 mm, 13 mm, and 10 mm.

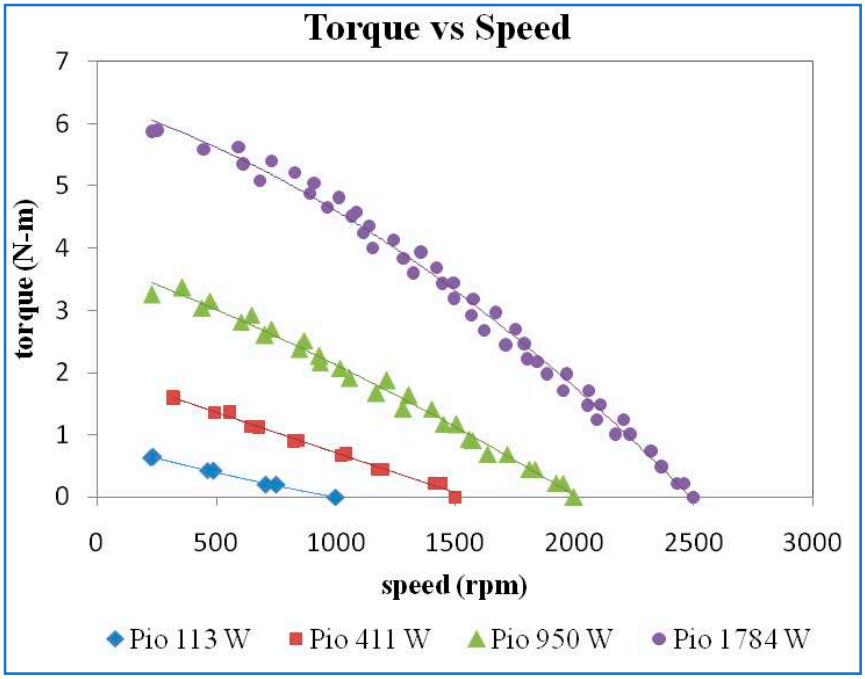

Figure 17. Torque vs. speed at a guide vane opening of 16 mm.

From Figure 18, it is observed that the maximum efficiency at 16 mm GVO was seen at a power input of 1784 W. The maximum efficiency decreases as input power is decreased. As there is an increase in guide vane opening, the efficiency improves compared to the low guide vane opening due to there being no impediment or vibration.

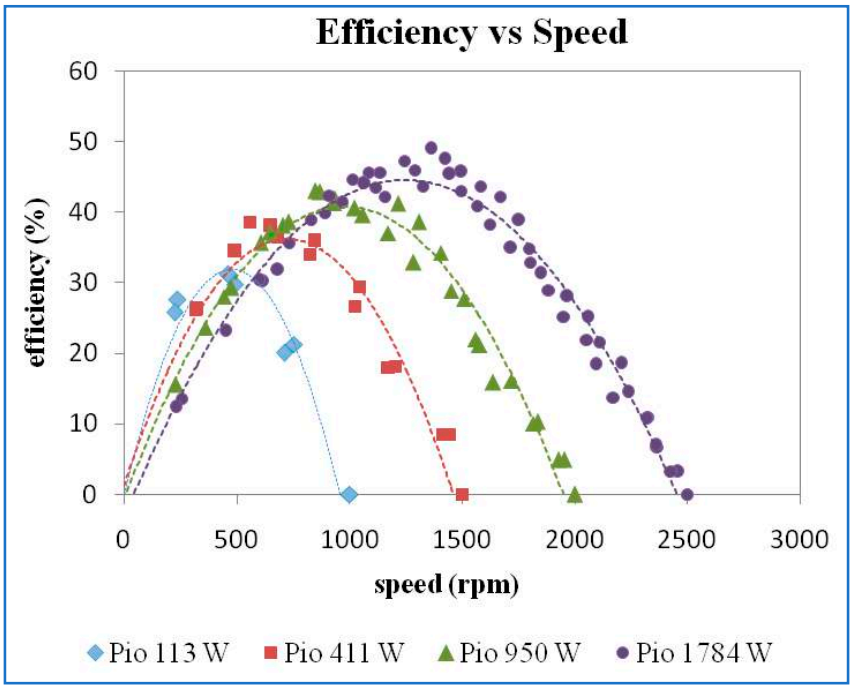

Figure 18. Efficiency vs. speed at a guide vane opening of 16 mm.

From Figure 19, it is seen that at 113 W power input, the discharge was constant. At other input power, the discharge was slightly decreased as speed increased at 16 mm GVO. The iso-efficiency lines plotted seem to be a straight line with different slopes. The discharge versus speed at BEP is 32%, 38%, 42%, and 46%.

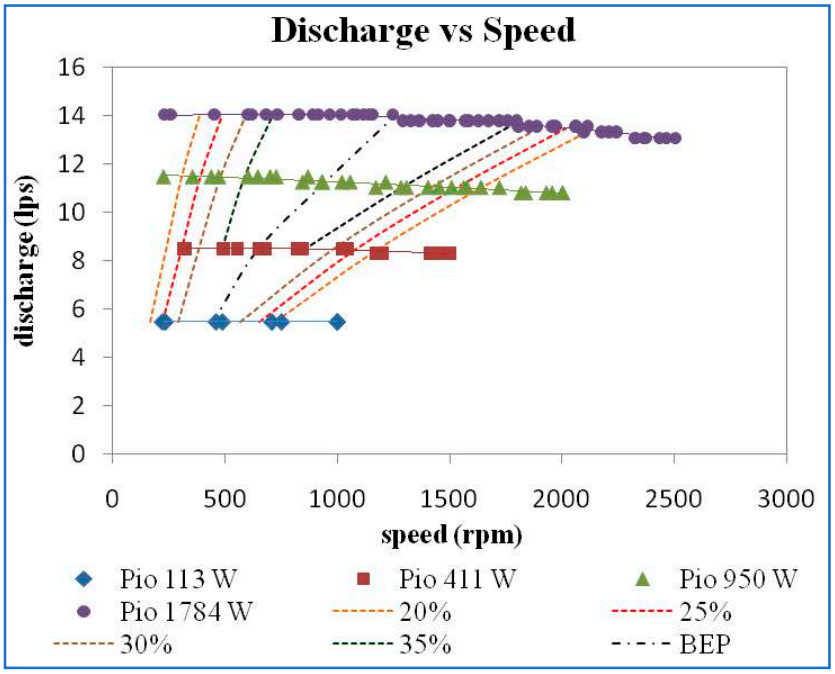

Figure 19. Discharge vs. speed and iso-efficiency line at 16 GVO.

Figure 20 shows the plot of the variation of head with respect to the speed for different power input at a GVO of 19 mm. The head increases with increase in the power input. There is a variation in the head curves at higher speed for all the four power inputs.

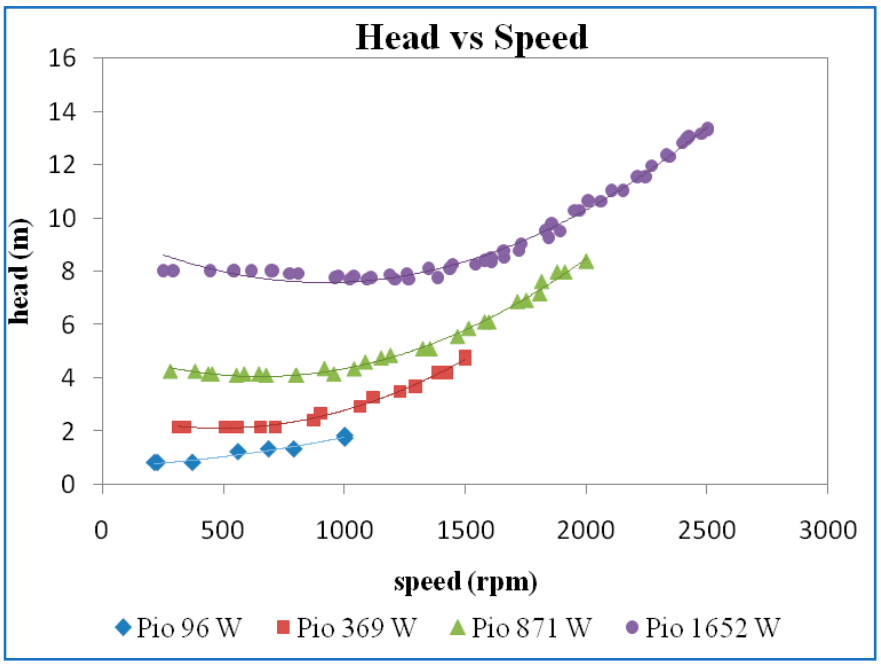

Figure 20. Head vs. speed at a guide vane opening of 19 mm.

According to Figure 21, when the load is applied the torque increases the frictional forces acting between the brake drum and the belt increases and dissipates the energy in the form of heat, and thus the speed comes down. The torque is increased with increased input power. There is a large variation in torque at 1652 W power input compared to other lower input power.

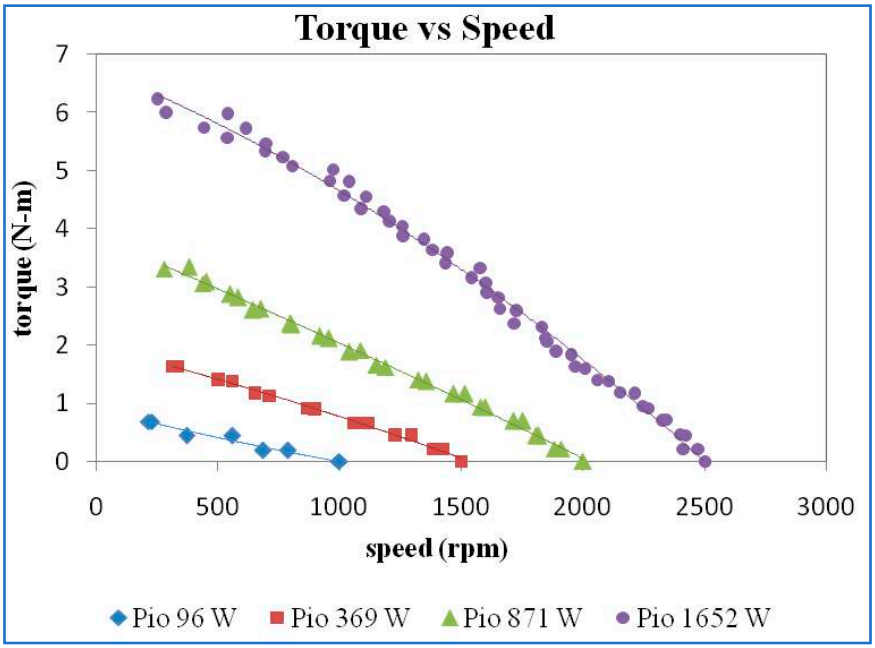

Figure 21. Torque vs. speed at a guide vane opening of 19 mm.

From Figure 22, maximum efficiency is observed at 1652 W. Maximum efficiency observed at 871 W was higher compared to the 96 W and 369 W power inputs. Compared to all other guide vane openings, the 19 mm guide vane opening showed the best efficiency due to no obstruction and vibration compared to low guide vane openings. As per the standard of this turbine, it could not achieve more efficiency at 19 mm guide vane opening due to some of the drawbacks, such as leakages between the blades and the casing and vibrations of the turbine.

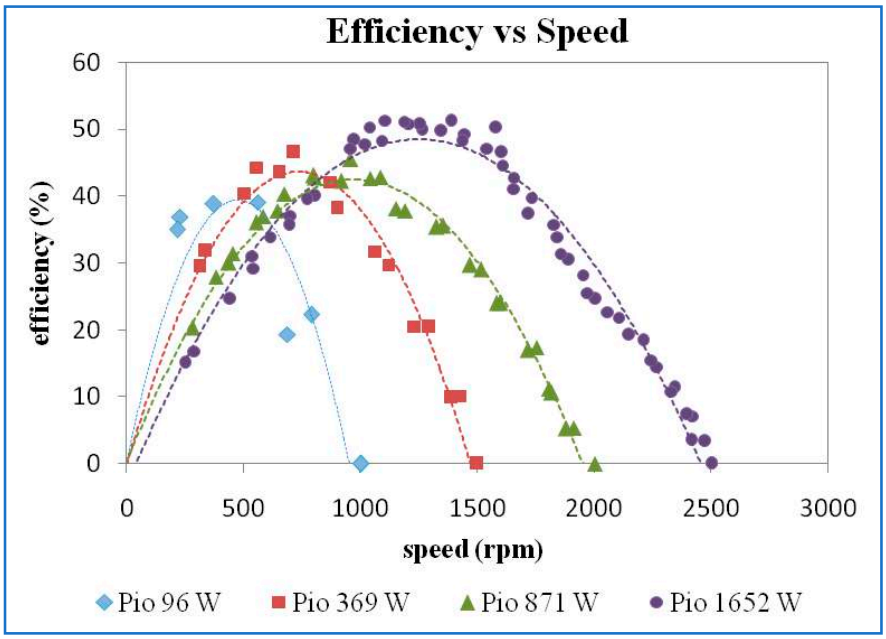

Figure 22. Efficiency vs. speed at a guide vane opening of 19 mm.

Discharge was found to be constant as speed was varied at different input powers, as shown in Figure 23 at a GVO of 19 mm. The iso-efficiency was plotted and seems not much different between guide vane openings of 10 mm, 13 mm, 16 mm and 19 mm. The bp values are 41%, 46%, 47% and 50%.

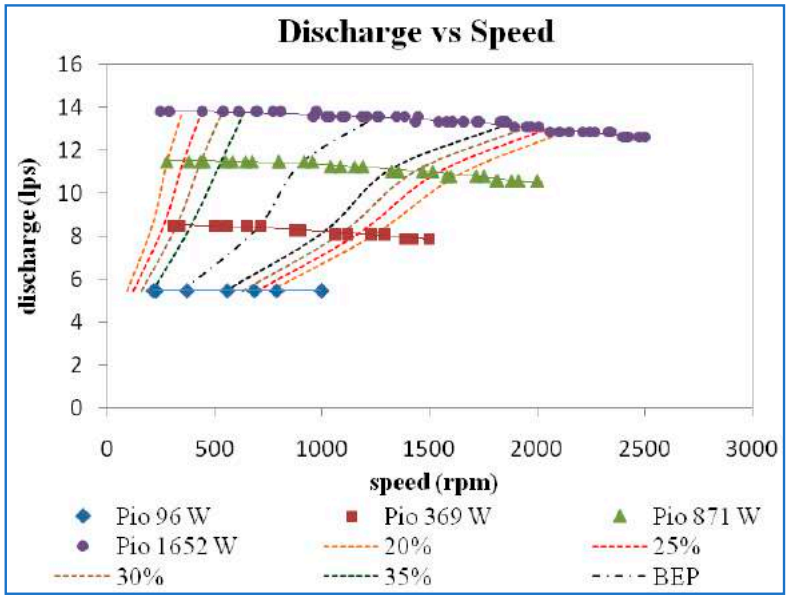

Figure 23. Discharge vs. speed and iso-efficiency line at 19 GVO.

3.2. Best Efficiency Point Curves

Figure 24 shows that all the best efficiency points with different guide vane openings are plotted in 10 mm guide vane opening. The four best efficiency points combined are intersecting at 930 speed and 11 discharge. They all split at higher discharge and lower discharge. All the discharge curves seem to be constant. As the guide vane opening was varied, there was a variation in the line of best efficiency, as shown in Figure 10. This plot indicates that all these lines merge at speed of 920 rpm.

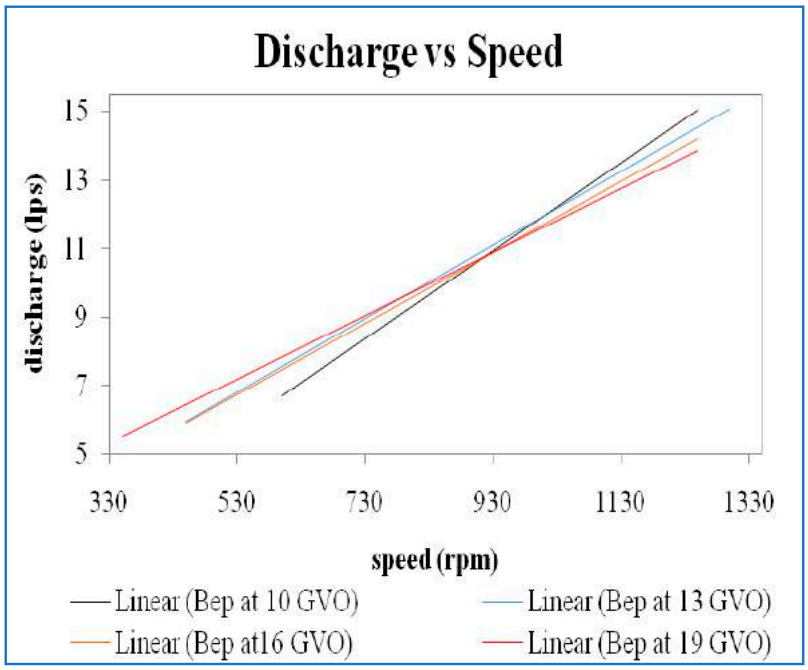

Figure 24. Discharge vs. speed for best efficiency point at 10 mm GVO.

3.3. Unit Curves

The unit discharge versus unit speed curve is shown in Figure 25. For all trial 1 and trial 2 readings at various input power, the points seem to coalesce, so one universal trend line was drawn for all the data indicating the variation of the unit discharge with respect to

unit speed. Compared to characteristic curves of discharge versus speed, the unit discharge decreases with increase in unit speed.

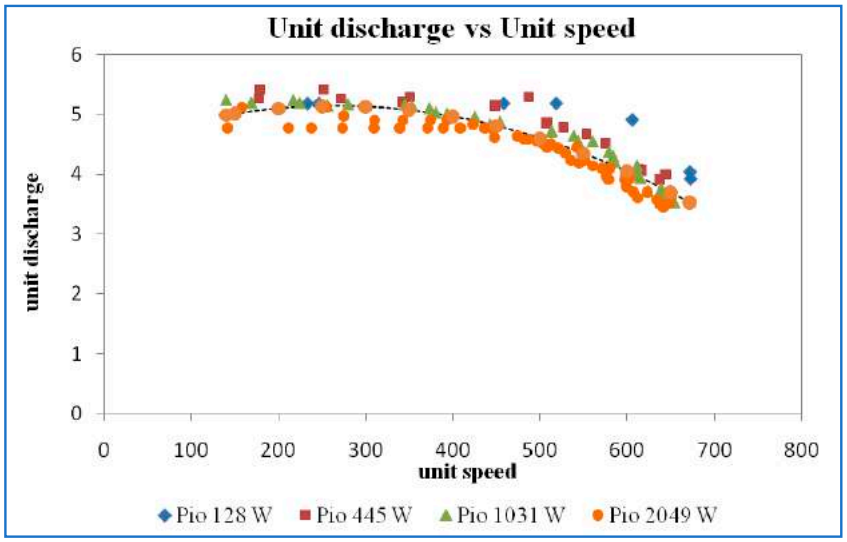

Figure 25. Unit discharge vs. unit speed at a guide vane opening of 10 mm.

The variation of output power versus unit speed operating at different power inputs is shown in Figure 26. These points form a second-order polynomial curve fit with correlation coefficients near one. The maximum unit output power is found at a unit speed of 396 rpm.

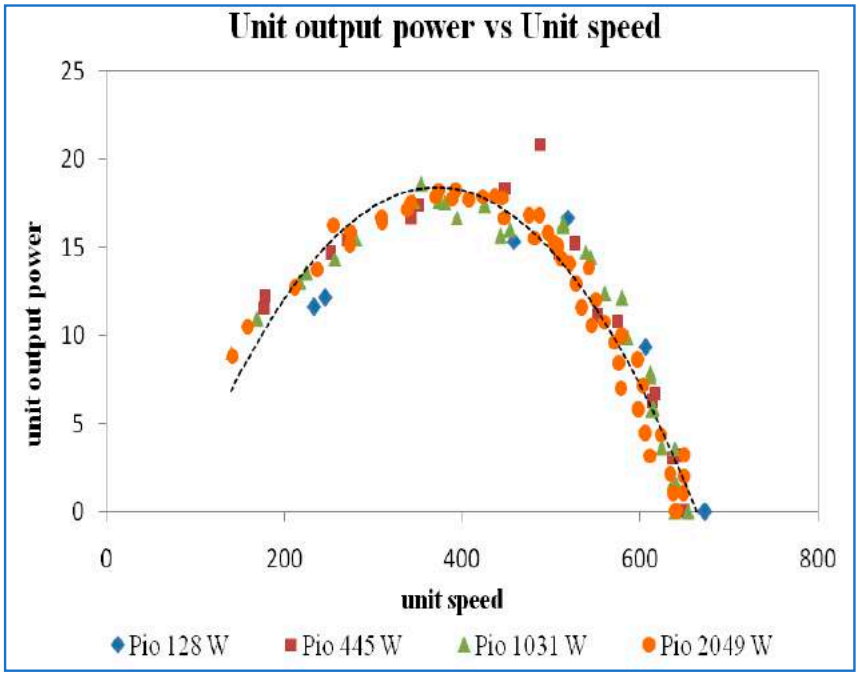

Figure 26. Unit output power vs. unit speed at a guide vane opening of 10 mm.

For the 10 mm guide vane opening, the maximum efficiency is obtained for unit speed of 400, as shown in Figure 27. The highest efficiency is about 38%.

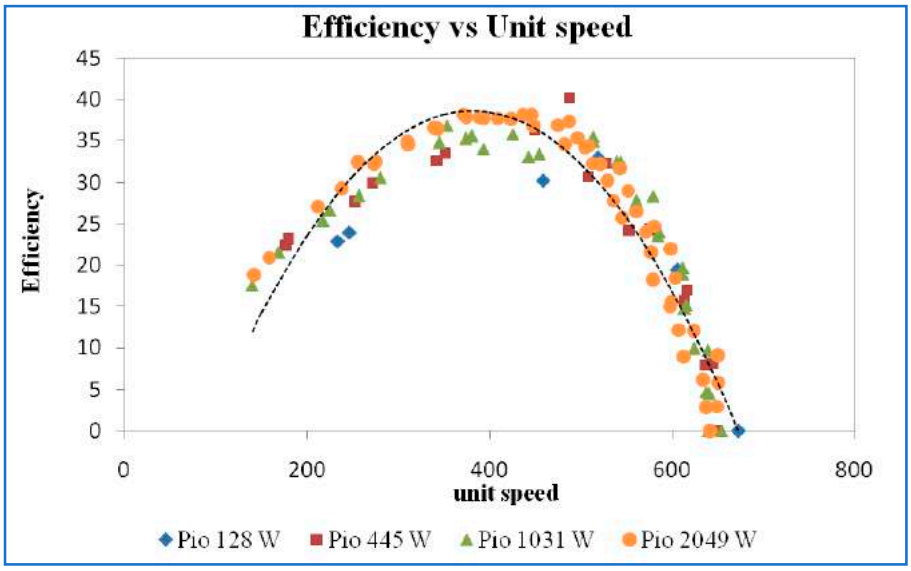

Figure 27. Efficiency vs. unit speed at a guide vane opening of 10 mm.

For a guide vane opening of 13 mm, the unit discharge versus unit speed curve is shown in Figure 28. The unit discharge decreases with increase in unit speed at this guide vane opening also. When compared to that for 10 mm, the unit discharge increases and decreases with increasing speed.

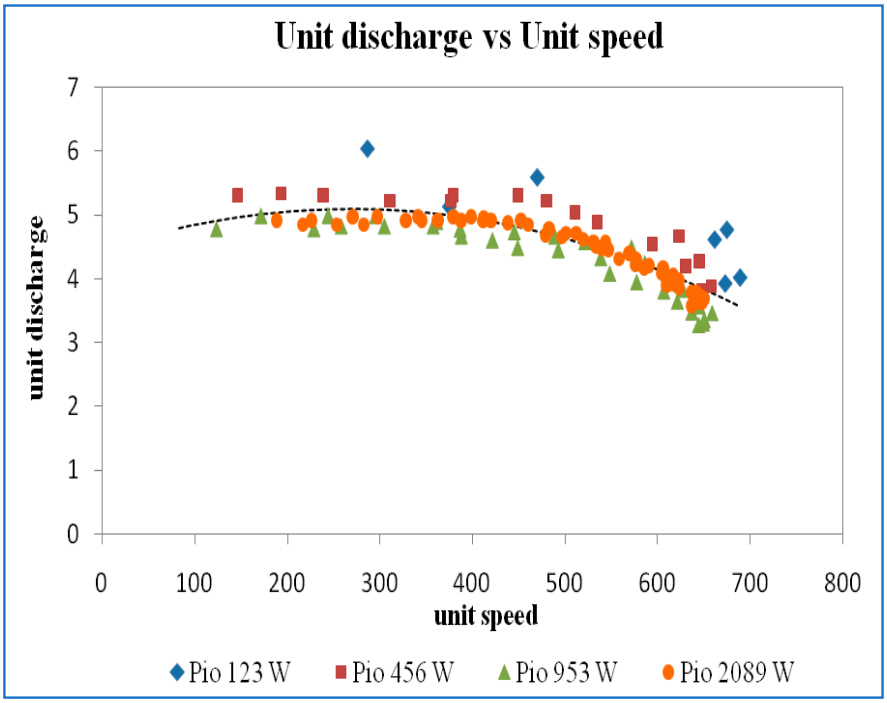

Figure 28. Unit discharge vs. unit Speed at a guide vane opening of 13 mm.

The variation in unit output power versus unit speed operating at different power inputs is shown in Figure 29. The maximum output power is found at a unit speed of 396 rpm, the same as that at a GVO of 10 mm.

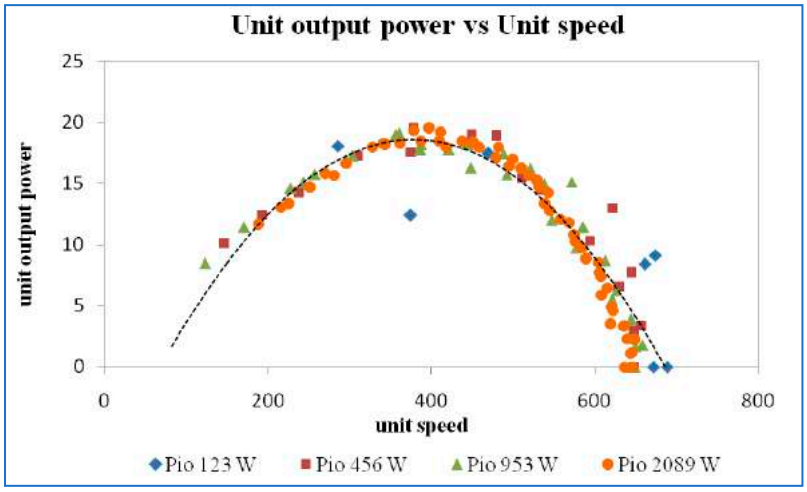

Figure 29. Unit output power vs. unit speed at a guide vane opening of 13 mm.

Variation in efficiency versus unit speed is shown in Figure 30. The efficiency gradually increases and decreases. The maximum efficiency is attained at a unit speed of 400 rpm.

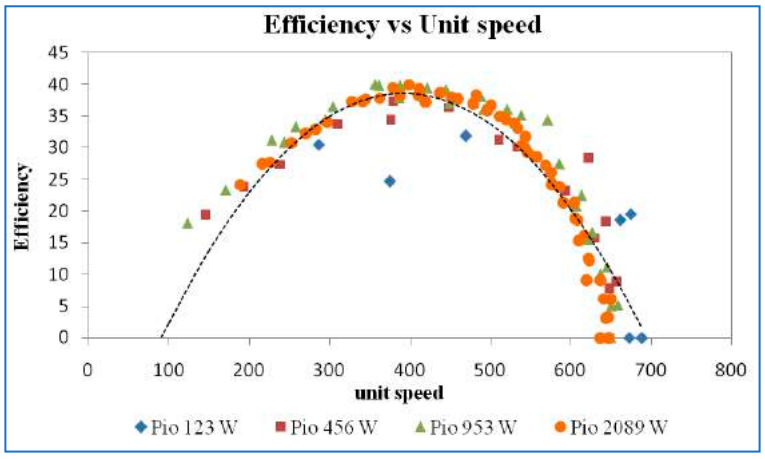

Figure 30. Efficiency vs. unit speed at a guide vane opening of 13 mm.

For a guide vane opening of 16 mm, the unit discharge versus unit speed curve is shown in Figure 31. The unit discharge decreases with an increase in unit speed.

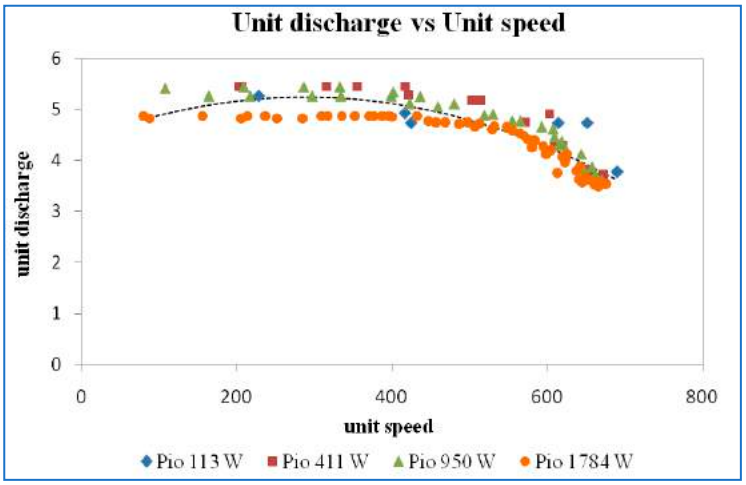

Figure 31. Unit discharge vs. unit speed at a guide vane opening of 16 mm.

The variation in unit output power versus unit speed operating at different power inputs is shown in Figure 32. The maximum output power is found at a unit speed of 396 rpm, the same as that at a GVO of 10 mm and 13 mm.

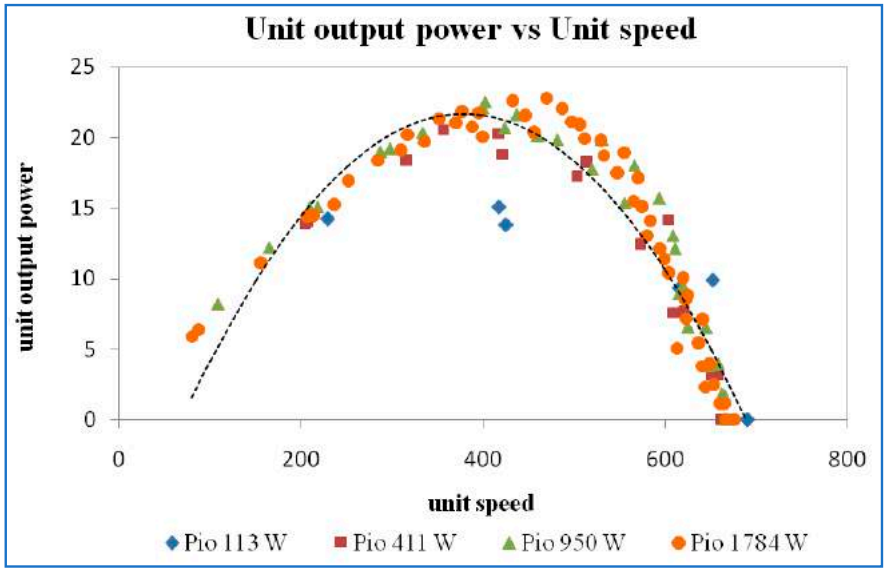

Figure 32. Unit output power vs. unit speed at a guide vane opening of 16 mm.

Figure 33 shows that a higher maximum efficiency is obtained at 45% with a guide vane opening of 16 mm. This curve at a unit speed value of 400 rpm attained maximum efficiency.

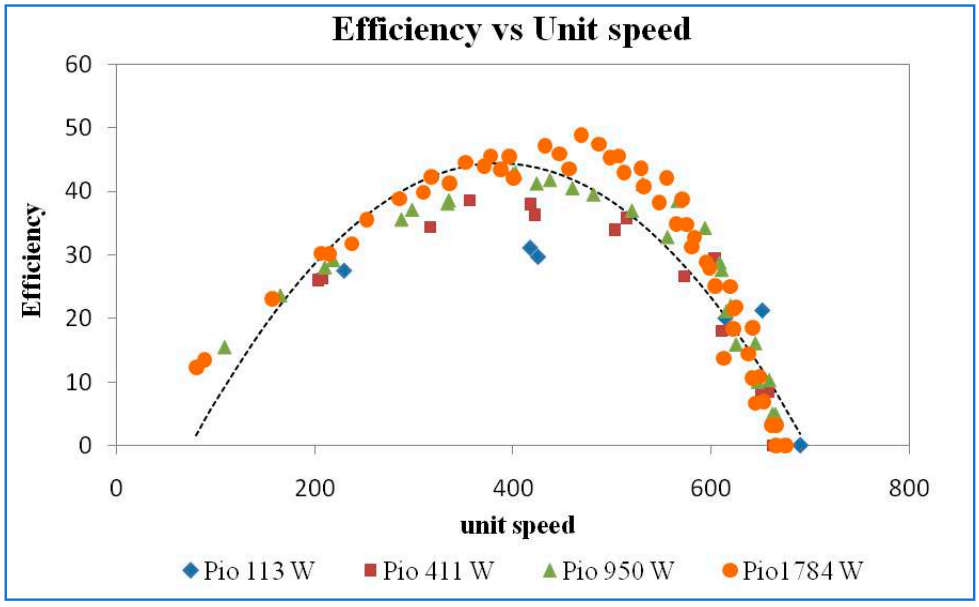

Figure 33. Efficiency vs. unit speed at a guide vane opening of 16 mm.

The unit discharge versus unit speed curve is shown in Figure 34. The unit discharge decreases with increasing unit speed. The unit discharge decreases with increasing unit speed. The unit discharge curve looks similar to GVO of 13 mm, 16 mm, and 19 mm.

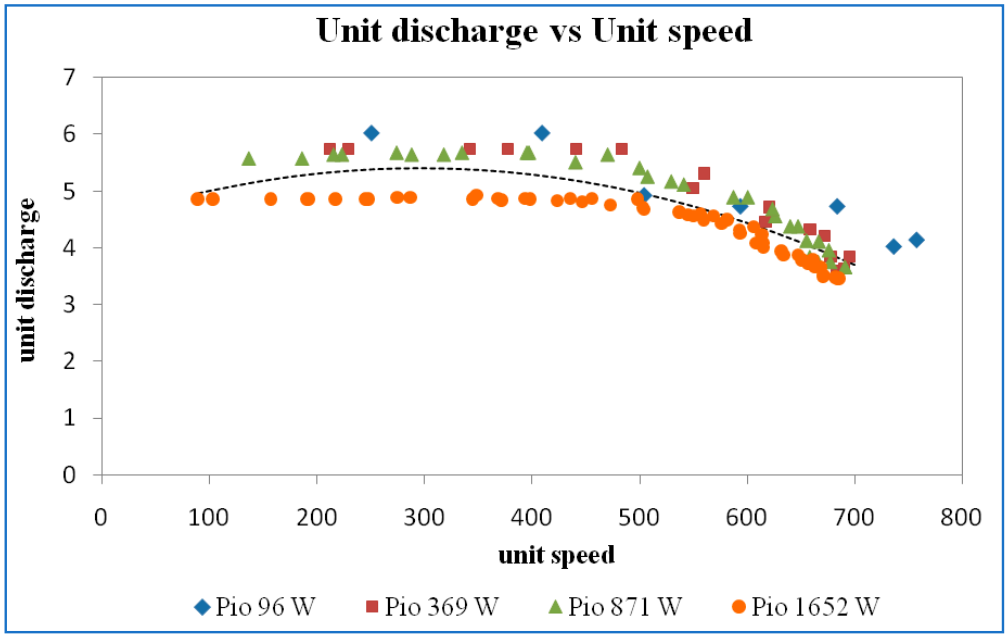

Figure 34. Unit discharge vs. unit speed at a guide vane opening of 19 mm.

The variation in unit output power versus unit speed operating at different power inputs is shown in Figure 35. The maximum output power is found at a unit speed of 400 rpm, the same as that at a GVO of 10 mm, 13 mm, and 19 mm.

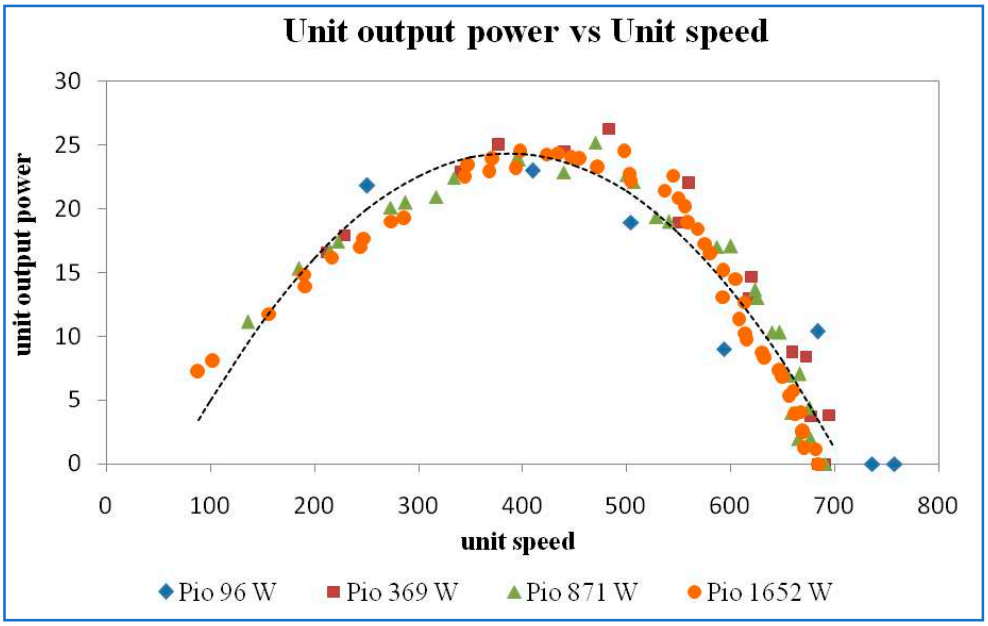

Figure 35. Unit output power vs. unit speed at a guide vane opening of 19 mm.

Figure 36 shows the variation in efficiency with unit speed for GVO of 19 mm. It shows that the unit speed at BEP is 400 rpm.

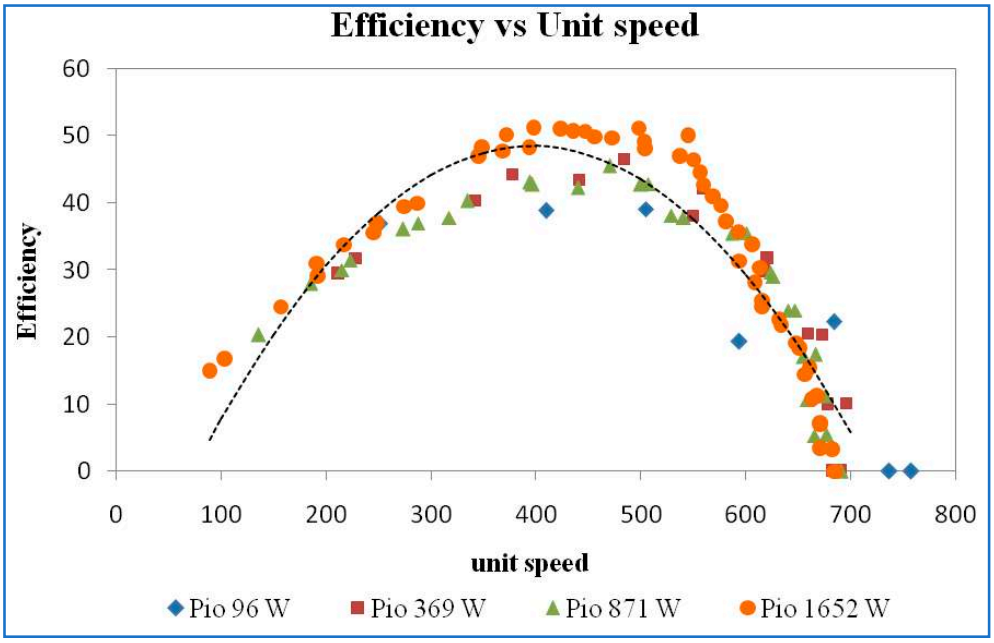

Figure 36. Efficiency vs. unit speed at a guide vane opening of 19 mm.

Using results obtained for other GVOs, as mentioned in Table 1, variations of unit quantities at the best efficiency point were plotted concerning GVO. The results presented in Figure 37 show the values to be more or less constant for all guide vane openings.

Table 1. Best efficiency points from characteristics of Francis turbine.

S. No	Guide Vane Opening GVO (mm)	Speed N (rpm)	Discharge Q (lps)	Head Given to Turbine H (m)	Brake Output Power (W)	Power Input to the Turbine (W)	Efficiency (%)
1	10	600	6.02	1.31	25.08	77.44	32.39
2		700	8.77	2.82	88.15	242.86	36.30
3		1000	11.83	5.58	239.34	647.33	36.97
4		1250	14.89	9.68	537.68	1414.14	38.02
5	13	450	5.86	1.09	20.90	62.89	33.24
6		700	8.92	2.81	92.36	245.79	37.58
7		950	11.06	5.39	236.09	584.55	40.39
8		1300	15.14	9.61	558.15	1427.69	39.09
9	16	450	5.47	1.14	20.57	61.33	33.54
10		650	8.49	2.47	78.64	205.51	38.27
11		950	11.29	4.67	220.64	517.26	42.66
12		1250	13.94	8.29	522.94	1134.04	46.11
13	19	350	5.47	0.91	19.99	48.89	40.88
14		700	8.40	2.25	85.26	185.57	45.94
15		900	11.38	4.19	209.13	468.15	44.67
16		**1250**	**13.55**	**7.84**	**524.00**	**1042.79**	**50.25**

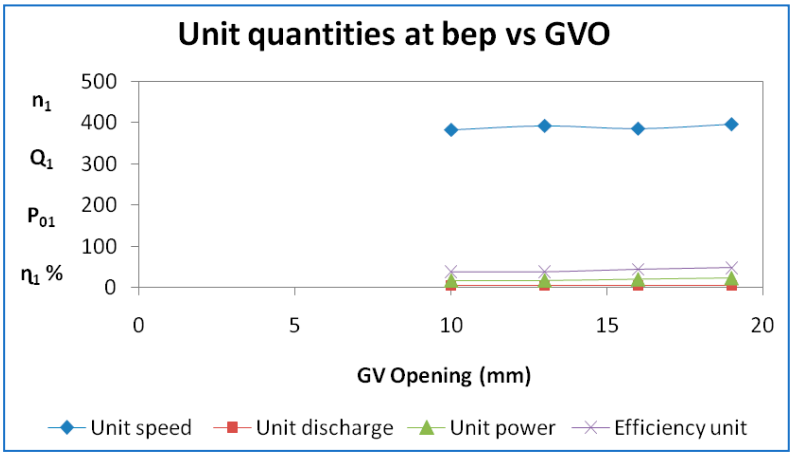

Figure 37. BEP unit quantities vs. GVO.

4. Conclusions

In the current work on the best operating point based on unit quantities by studying the performance characteristics of the Francis turbine at various input powers and guide vane openings, the important conclusions are revealed below.

The performance characteristic curves were plotted within the available range of variation of guide vane openings (10 mm to 19 mm) and input power (96 W to 2089 W). From these available data, unit curves were plotted and corresponding best efficiency points obtained. The highest efficiency of 50.25% was obtained at a guide vane opening of 19 mm. The values of head, discharge, speed, and output power at BEP were 7.84 m, 13.55 lps, 1250 rpm, and 524 W, respectively. As per the condition of this Francis turbine, the main reason for not obtaining more than the higher efficiency of 50.25% was leakage flow that passed through the clearance gap between the guide vanes' high-pressure and low-pressure sides. To determine how much leakage flow there is, finding the velocity vectors inside the gap can be used.

Author Contributions: Conceptualization, M.V.K., T.S.R. and P.S.; methodology, C.R.R., P.S.V. and O.C.S.; software, B.A., Y.A. and A.B.; validation, M.V.K., P.S.V. and C.R.R.; formal analysis, B.A. and Y.A.; investigation M.V.K. and A.B.; resources, M.V.K.; data curation, T.S.R.; writing—original draft preparation, M.V.K. and C.R.R.; writing—review and editing, M.V.K., T.S.R., C.R.R., P.S., P.S.V. and O.C.S.; visualization, Y.A.; supervision, C.R.R.; project administration, C.R.R.; funding acquisition, B.A. All authors have read and agreed to the published version of the manuscript.

Funding: The authors would like to acknowledge the financial support received from the Taif University Researchers Supporting Project (TURSP-2020/278), Taif University, Taif, Saudi Arabia.

Institutional Review Board Statement: Not applicable.

Informed Consent Statement: Not applicable.

Data Availability Statement: Not applicable.

Conflicts of Interest: The authors declare no conflict of interest.

References

1. Logan, E., Jr. *Turbomachinery: Basic Theory and Applications*; CRC Press: Boca Raton, FL, USA, 1993. Available online: https://books.google.co.in/books?hl=en&lr=&id=s4Qfa1AWGGkC&oi=fnd&pg=PR5&dq=1.%09Logan+Jr,+Earl.+Turbomachinery:+Basic+theory+and+applications (accessed on 25 June 2022).
2. Yannopoulos, S.I.; Lyberatos, G.; Theodossiou, N.; Li, W.; Valipour, M.; Tamburrino, A.; Angelakis, A.N. Evolution of Water Lifting Devices (Pumps) over the Centuries Worldwide. *Water* **2015**, *7*, 5031–5060. [CrossRef]
3. Reynolds, T.S. *Stronger than a Hundred Men: A History of the Vertical Water Wheel*; No. 7; JHU Press: Baltimore, MD, USA, 1983.
4. Pang, J.; Liu, H.; Liu, X.; Yang, H.; Peng, Y.; Zeng, Y.; Yu, Z. Study on sediment erosion of high head Francis turbine runner in Minjiang River basin. *Renew. Energy* **2022**, *192*, 849–858. [CrossRef]

5. Zhang, W.; Zhu, B.; Yu, Z.; Yang, C. Numerical study of pressure fluctuation in the whole flow passage of a low specific speed mixed-flow pump. *Adv. Mech. Eng.* **2017**, *9*, 1687814017707651. [CrossRef]
6. Gatte, M.T.; Rasim, A.K. Hydro Power. *Energy Conserv.* **2012**, *9*, 95–124. Available online: https://books.google.co.in/books?hl=en&lr=&id=DASaDwAAQBAJ&oi=fnd&pg=PA95&dq=Gatte,+Mohammed+Taih,+and+Rasim+Azeez+Kadhim.+%22Hydro+power (accessed on 30 June 2022).
7. Norquest, P.E. Ambient Pressure Water Turbine. U.S. Patent No. 4,416,584, 22 November 1983. Available online: https://patents.google.com/patent/US4416584A/en (accessed on 7 July 2022).
8. Choi, H.-J.; Zullah, M.A.; Roh, H.-W.; Ha, P.-S.; Oh, S.-Y.; Lee, Y.-H. CFD validation of performance improvement of a 500 kW Francis turbine. *Renew. Energy* **2013**, *54*, 111–123. [CrossRef]
9. Kurosawa, S.; Lim, S.M.; Enomoto, Y. Virtual model test for a Francis turbine. In *IOP Conference Series: Earth and Environmental Science*; IOP Publishing: Bristol, UK, 2010; Volume 12.
10. Sahu, R.K.; Gandhi, B.K. Erosive flow field investigation on guide vanes of Francis turbine—A systematic review. *Sustain. Energy Technol. Assess.* **2022**, *53*, 102491.
11. Li, G.; Ma, F.; Guo, J.; Zhao, H. Case Study of Roadway Deformation Failure Mechanisms: Field Investigation and Numerical Simulation. *Energies* **2021**, *14*, 1032. [CrossRef]
12. Kamal, M.; Abbas, A.; Prasad, V.; Kumar, R. A numerical study on the performance characteristics of low head Francis turbine with different turbulence models. *Mater. Today Proc.* **2021**, *49*, 349–353. [CrossRef]
13. Shigemitsu, T.; Fukutomi, J.; Kaji, K. Influence of Blade Outlet Angle and Blade Thickness on Performance and Internal Flow Conditions of Mini Centrifugal Pump. *Int. J. Fluid Mach. Syst.* **2011**, *4*, 317–323. [CrossRef]
14. Koirala, R.; Zhu, B.; Neopane, H.P. Effect of Guide Vane Clearance Gap on Francis Turbine Performance. *Energies* **2016**, *9*, 275. [CrossRef]
15. Koirala, R.; Thapa, B.; Neopane, H.P.; Zhu, B.; Chhetry, B. Sediment erosion in guide vanes of Francis turbine: A case study of Kaligandaki Hydropower Plant, Nepal. *Wear* **2016**, *362–363*, 53–60. [CrossRef]
16. Koirala, R.; Neopane, H.P.; Zhu, B.; Thapa, B. Effect of sediment erosion on flow around guide vanes of Francis turbine. *Renew. Energy* **2019**, *136*, 1022–1027. [CrossRef]
17. Thapa, B.S.; Trivedi, C.; Dahlhaug, O.G. Design and development of guide vane cascade for a low speed number Francis turbine. *J. Hydrodyn.* **2016**, *28*, 676–689. [CrossRef]
18. Chitrakar, S.; Dahlhaug, O.G.; Neopane, H.P. Numerical investigation of the effect of leakage flow through erosion-induced clearance gaps of guide vanes on the performance of Francis turbines. *Eng. Appl. Comput. Fluid Mech.* **2018**, *12*, 662–678. [CrossRef]
19. Amedei, A.; Meli, E.; Rindi, A.; Romani, B.; Pinelli, L.; Vanti, F.; Arnone, A.; Benvenuti, G.; Fabbrini, M.; Morganti, N. Innovative design, structural optimization and additive manufacturing of new-generation turbine blades. Turbo Expo: Power for Land, Sea, and Air. *Am. Soc. Mech. Eng.* **2020**, *84089*, V02CT35A004. [CrossRef]
20. Sosilo, A.K.; Hadi, H.; Soehartanto, T. Design of Hydro Power by Using Turbines Kaplan on The Discharge Channel Paiton 1 and 2. *E3S Web Conf.* **2018**, *42*, 01008. [CrossRef]
21. Weili, L.; Jinling, L.; Xingqi, L.; Yuan, L. Research on the cavitation characteristic of Kaplan turbine under sediment flow condition. *IOP Conf. Ser. Earth Environ. Sci.* **2010**, *12*, 012022. [CrossRef]
22. Ma, Y.; Qian, B.; Feng, Z.; Wang, X.; Shi, G.; Liu, Z.; Liu, X. Flow behaviors in a Kaplan turbine runner with different tip clearances. *Adv. Mech. Eng.* **2021**, *13*, 16878140211015879. [CrossRef]

Soft Computing
https://doi.org/10.1007/s00500-022-07561-3

APPLICATION OF SOFT COMPUTING

A deep CNN approach for islanding detection of integrated DG with time series data and scalogram

Ch. Rami Reddy[1,2] · K. Harinadha Reddy[3]

Accepted: 15 July 2022

Abstract
The ever increasing demand for electricity leads to the advancement of distributed generation (DG). Almost all DG sources are renewable nature. One of the major complications with the high penetration of DG sources is islanding. The islanding may damage the clients and their equipment. As per the IEEE 1547 DG interconnection standards, the islanding will be identified in two seconds and the DG must be turned off. In this paper, an advanced islanding detection process stands on a deep learning technique with continuous wavelet transforms and convolution neural networks implemented. This approach transforms the time series information into scalogram images, and later, the images are used to train and test the islanding and non-islanding events. The outcomes are correlated with the artificial neural networks and fuzzy logic methods. The comparison shows that the proposed deep learning approach efficiently detects the islanding and non-islanding events.

Keywords Distributed generation · Islanding detection · Scalogram · Time series data · CNN

1 Introduction

The high integration of DG systems makes the power system network further complex. One of the major complications as a result of such DG assimilation is islanding. It is a situation where DG feeds the regional loads after disconnecting from the utility grid (Reddy et al. 2022). It can be intentional or unintentional. The intentional islanding arises with the maintenance of utility. The unintentional islanding may cause due to utility grid failure or uncertainties in the power network (Cui et al. 2018). It not only damages the customer's appliances and personal but also makes the grid cumbersome (Raju et al. 2021). Considerable islanding detection approaches are recommended by the researchers. They are briefly described here.

The passive methods encounter the situation by regularly auditing the passive parameters at the point of common coupling (PCC) and comparing it with the predefined threshold value (Reigosa et al. 2017). The passive parameters are voltage, current, frequency, impedance, phase angle, etc. If the parameter exceeds the specified value, the method affirms the islanding (Rami et al. 2021). However, they have been suffering from massive non-detection zone (NDZ) and complexity in fixing threshold values (Salles et al. 2015; Rami and Harinadha Reddy 2019a). To overcome these demerits, active methods are suggested. In active methods, a low-frequency harmonic signal is continuously injected and the parameters at PCC are monitored (Rami and Harinadha Reddy 2019b). In grid-connected affair, the injected signal will not affect the monitored parameters, but in the islanding case, it leads to the discrepancy in the observed guidelines. The particular discrepancies have been used to find the islanding (Murugesan and Murali 2020; Sivadas and Vasudevan 2020). These recommendations have no NDZ, but they are degrading the quality of power (Rami and Harinadha Reddy 2018). To eliminate the drawbacks of active methods, hybrid methods are proposed. They are the aggregate of active and passive approaches (Kermany et al. 2017). When the passive method suspects the islanding case, the active approach

✉ Ch. Rami Reddy
crreddy229@gmail.com

[1] Department of Electrical Engineering, National Institute of Technology, Srinagar, India 190006

[2] Department of Electrical and Electronics Engineering, Malla Reddy Engineering College, Secunderabad 500100, India

[3] Department of Electrical and Electronics Engineering, Lakireddy Bali Reddy College of Engineering, Mylavaram, India

Published online: 12 October 2022

confirms it (Ch and Harinadha Reddy 2018). These methods have no NDZ and affect power quality less compared to active methods (Chen et al. 2019). The remote islanding approach finds the islanding by collecting data from utility and DG (Xu et al. 2007). Various signal processing approaches have been proposed by the researchers which reduce the NDZ and enhance the performance of the passive methods by extracting the hidden features from the passive parameters (Reddy et al. 2020; Reddy and Harinadha Reddy 2019; Do et al. 2016). Artificial intelligence learning models classify the islanding and non-islanding events without threshold settings efficiently (Khamis et al. 2018). They do not have NDZ, but large data are required for training the models (Kermany et al. 2017). It is compulsory to produce an accurate islanding detection technique due to advancements in smart grid technology and the complexity of the power system network in the future.

This paper presents a new IDM based on deep learning. This method uses CWT and CNN. First, the time series data obtained at PCC are transformed toward the scalogram illustrations with CWT which contain the data of various islanding and non-islanding events. Later the scalogram images will be used to train the proposed CNN model. This is the second attempt of applying image processing techniques for the classification of islanding cases. The remaining part of the paper is organized as per the following aspects. Segment 2 describes the practice of transforming time series input toward scalogram illustrations. Segment 3 describes the test system and data set preparation. In Sect. 4, the design and training of CNN are presented. The results and discussions are illustrated in Sect. 5. Section 6 presents the conclusion.

2 Time series data to Scalogram image conversion

This section presents the operation of transforming the time series signal toward the scalogram appearances. The signal data of (1) are used to prepare the basic scalogram image (Manikonda and Gaonkar 2019). It is one second duration composed of two different frequencies 10 Hz and 200 Hz near amplitudes 15 and 25, respectively. The amplitudes and frequencies are randomly selected for illustrating the explanation. This approach uses the wavelet transform of a signal.

$$f(t) = 15\sin(2\pi \times 10 \times t) + 25\sin(2\pi \times 200 \times t) \quad (1)$$

The wavelet transform of any signal $f(t)$ can be specified as:

$$X(u,s) = \int_{-\infty}^{+\infty} f(t)\frac{1}{\sqrt{s}}\psi^*\left(\frac{t-u}{s}\right)\mathrm{d}t \quad (2)$$

In wavelet transforms, the time frequency energy density of a signal is a scalogram. In simple words, a scalogram is an observable impersonation of the wavelet transform, to what end x, y and z axes produce the time, frequency and magnitude in color gradient, respectively (Sejdic et al. 2008). The scalogram of time series results represented in Eq. (1) is depicted in Fig. 1. It is obtained by applying the CWT with Morse wavelets. Figure 1 shows two frequencies 10 Hz and 200 Hz and two amplitudes 15 and 25, respectively. In this manner, any time series data can be converted into scalogram images. It is generally known that any supervised learning requires data set for training of the network and testing. In this paper, the data set is prepared with scalogram images of different time series events. The next section describes the test system and data set preparation for the training of CNN in detail.

3 Test system and data set preparation

Large training information is needed for testing any supervised learning methods. For problems related to image classifications, standard data sets are available. No such standard data sets are available for islanding detection methods. Hence, a standard test system is appropriate for developing a sufficient data set. A 100 KW grid integrated PV source shown in Fig. 2 is considered to create such a data set. This model has been adopted in such a way as to satisfy the proposed work. The simulations are born in the MATLAB/Simulink platform. At t = 0.4 s, by opening the

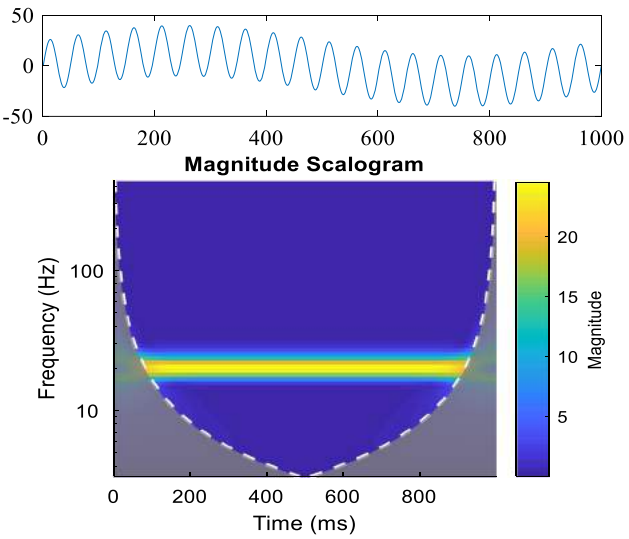

Fig. 1 Scalogram image of Eq. (1)

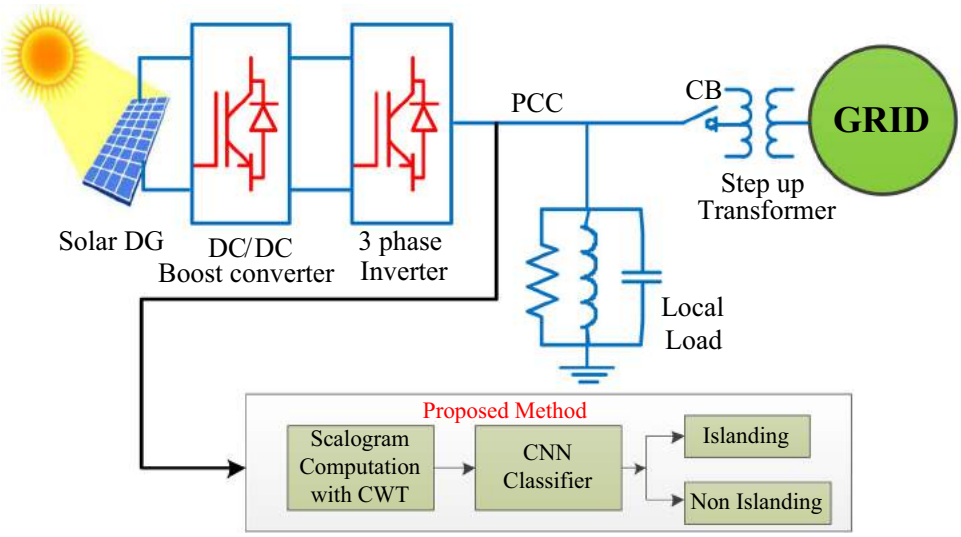

Fig. 2 Test system for implementation of the proposed method

CB (circuit breaker), the islanding event is created. The phase angle between the positive sequence component of voltage and current at PCC is acquired for 6 cycles at 1000 samples per second. A PC with an i5 processor, 8 GB RAM and Windows 10 operating system is used to get these simulations. For producing the image data set, different islanding and non-islanding events are validated and their results are recorded as time series plots.

CWT is applied to each time series data, for the generation of scalogram images. The scalogram of the phase angle between the positive sequence component of voltage and current at PCC for grid integrated and disconnected operations are shown in Fig. 3. It is observed against the

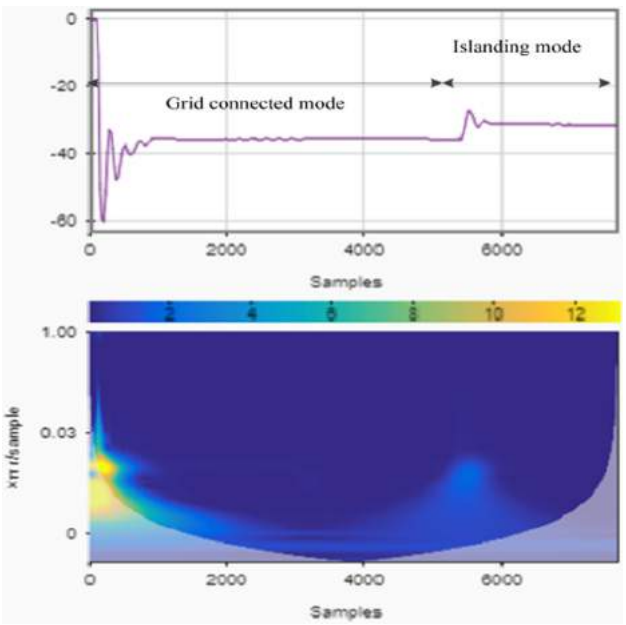

Fig. 3 Scalogram image variation for grid-connected and islanded data

scalogram illustrations that there is a good variation among the islanding and non-islanding images. The image classification technique is applied to these images for the detection of events. Most of the passive approaches are failed to detect the islanding cases when there is a zero or small power variation among the DG and the load in the islanding situation. This situation is taken into account, and different islanding capsules at nearly worst power mismatches are studied and included in the data set. The data set also includes several islanding cases and non-islanding cases such as switching of loads, capacitor banks, short-circuit faults and motor switching events. A total of 300 islanding and non-islanding are generated for data set creation, which include 150 islanding and 150 non-islanding events that are listed in Table 2.

4 Methodology and CNN design

This segment presents the methodology, architecture and training particulars of CNN. Figure 4 represents the steps in the proposed islanding detection process. The phase angle between the positive sequence component of voltage and current is acquired at PCC in time series form. This knowledge is transformed into scalogram pictures.

The scalogram pictures are given as input to the already experienced CNN for the classification of events. For any supervised learning method, feature extraction is crucial for workouts and examinations. The accuracy of the approach depends on these features. In deep learning, CNN naturally extracts these features from the input pictures. It has multiple layers, most of the layers are used for feature extraction and only the concluding minority layers are used for analysis. The general structure of CNN is depicted in

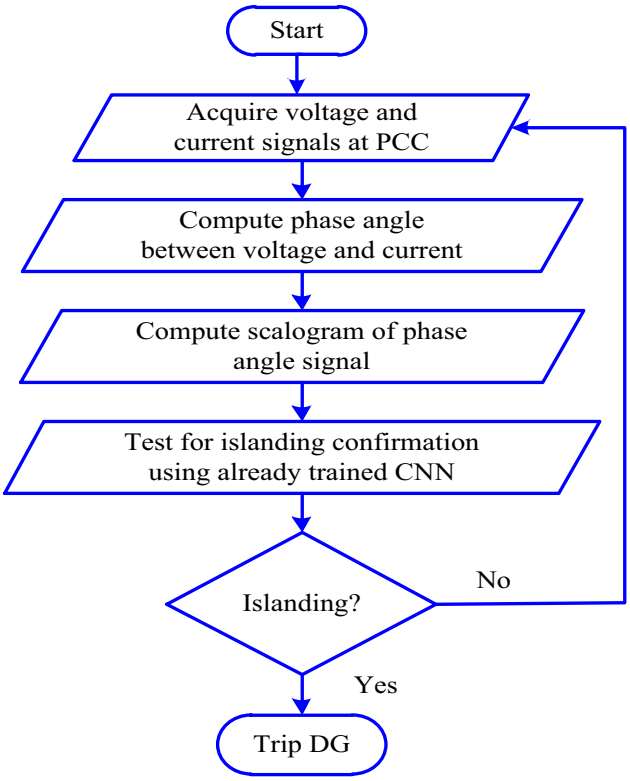

Fig. 4 Flowchart of the proposed method

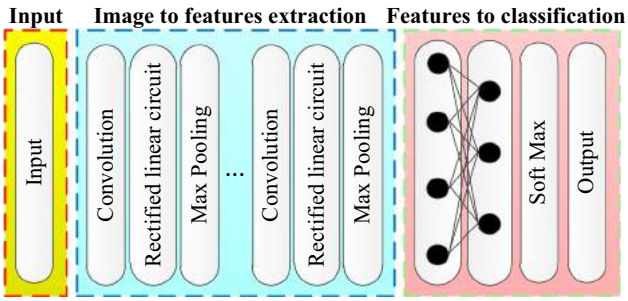

Fig. 5 Design structure of CNN

Fig. 5, and various slabs of CNN are shortly described here (Guo et al. 2018; Ker et al. 2018).

4.1 Convolution layer

In deep learning, convolution is a mathematical operation on two functions. Among the two functions, one function is an image in the form of pixels at the point on the picture and the other function is the kernel. Both are characterized as a cluster of numbers. The multiplication of these two arrays accords to the outcome. The filter is now moved to another position on the image which is decided through the stride duration. The convolution is continued as far as the total picture has been covered. The output of these computations is an activation map. Unlike the artificial neural networks where all input neurons are connected to all the output neurons, CNN has sparse connections, which means only the input neurons have only a few connections with the next layer neurons. The convolution activity is represented by the $*$ operator. Output $f(x)$ is characterized when the input $I(x)$ is convoluted with the kernel $K(x)$ as (3):

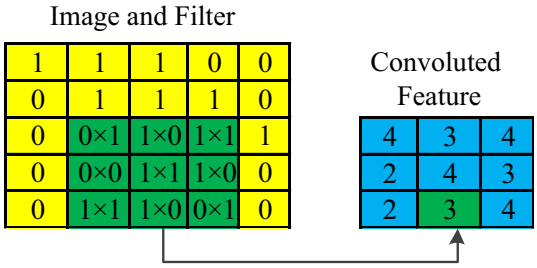

Fig. 6 Convolution operation in CNN

$$f(x) = (I * K)(x) \tag{3}$$

If x takes only integer attitudes, the discretized convolution can be defined as (4), which assumes the one-dimensional convolution

$$f(x) = \sum_{a} I(a) \cdot K(x - a) \tag{4}$$

The two-dimensional convolution with input $I(a, b)$ and filter $K(m, n)$ is illustrated as (5):

$$f(x) = \sum_{m} \sum_{n} I(m, n) \cdot K(a - m, b - n) \tag{5}$$

By commutative law, filter is flipped and Eq. (5) is corresponding to (6):

$$f(x) = \sum_{m} \sum_{n} I(a - m, b - n) \cdot K(m, n) \tag{6}$$

Neural networks appliance the cross-correlation operation, it is the same as the convolution operation without flipping the filter and the Eq. (6) changes to (7). Figure 6 shows the convolution operation in detail

$$f(x) = \sum_{m} \sum_{n} I(a + m, b + n) \cdot K(m, n) \tag{7}$$

4.2 Rectified liner unit (ReLu) layer

The activation function at the yield of the convolution lamination is linear naturally. The activations commonly happen through the ReLu unit, for getting the nonlinear transformation. There are different types of activation functions; a few among the familiar functions are tanh, sigmoid and rectified linear unit (ReLu). In this CNN architecture, ReLu activation function is used at the output of previous layers. It can be represented in Fig. 7.

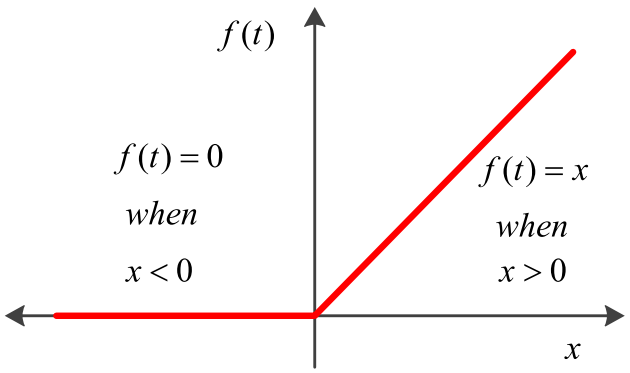

Fig. 7 ReLu activation function

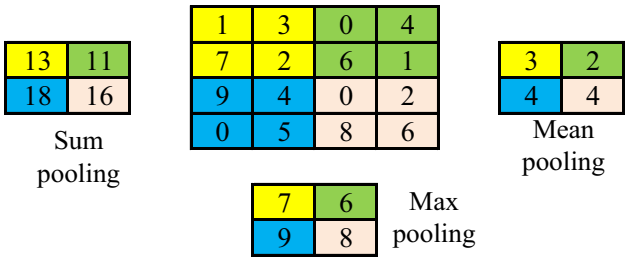

Fig. 8 Different pooling operations with 2 × 2 filter and stride 2

Here, x is the input to the neuron. It gives the output as zero if the input is negative and it gives the same output if the input is a positive value. This layer simplifies the calculations and accelerates the design, and it advises escaping the fading gradient problems.

4.3 Pooling layer

The pooling sheet lowers the resolution of the extractions. This layer produces the extractions strong counter to distortion and noise. Here are four types of pooling: They are max pooling, average pooling, L2 normalization and sum pooling. In these classifications, the input is separated into non-overlapping two-dimensional zones. For max pooling, the maximum value of zone values is considered as output. For average pooling, the average of zone values is considered as output, and for sum pooling, the sum of all values in the zone is considered. The proposed approach uses the max pooling layer (Fig. 8).

4.4 Softmax layer

Softmax layer provides the probabilities of all classes for n-dimensional input real numbers vector. These probabilities are used for classification. Mathematically, it can be represented as in Eq. (8):

Table 1 CNN design parameters

Training parameters	Design value
Optimizer	Stochastic gradient descent with momentum
Momentum	0.2
Learning rate	0.001
Maximum epochs	15
Mini batch size	10
Loss function	Cross entropy
Weight initialization	Random
Convolution layers	5
Kernals	3*3, 5*5, 11*11
Drop out	0.5
Stride	2
ReLu	5
Max pooling layers	5
Fully connected layer	3

Table 2 Different scalograms simulated for data set preparation

Events	Number of cases
Islanding	**110**
Near zero power loading	40
Large and medium loading	70
Non islanding	**148**
Capacitor switching (ON)	10
Capacitor switching (OFF)	10
Induction motor switching (ON)	10
Induction motor switching (OFF)	10
Load switching (ON)	10
Load switching (OFF)	10
Various types of fault switching	8
Grid connected (Out of islanding area)	80

$$x_i = \frac{e^{z_i}}{\sum_{j=1}^{n} e^{z_j}} \tag{8}$$

All the determined contingencies are in the dimension of zero and one. The importance of this function is that it can add the entire probabilities up to one.

4.5 Fully connected layer

These are the output layers of the CNN. This layer produces the output classification. Every neuron in a fully connected layer has a connection with all neurons in the last layers. All the features received from the previous layers are weighted together to produce the specific

Table 3 Customized CNN model generic details

Layer name	Type	Kernel Size	Output	Parameters
Input-1	Input Layer	–	256 × 256 × 3	0
conv2d-1	Convolution + ReLU	5 × 5	256 × 256 × 64	321
batch_norm-1	Batch normalization	–	256 × 256 × 64	256
max_pooling2d-1	Max Pooling	2 × 2	128, 128, 64	0
conv2d-2	Convolution + ReLU	5 × 5	128 × 128 × 128	9930
batch_norm-2	Batch normalization	–	128 × 128 × 128	512
max_pooling2d-2	Max Pooling	2 × 2	64 × 64 × 128	0
conv2d-3	Convolution + ReLU	5 × 5	64 × 64 × 256	36,234
batch_norm-3	Batch normalization	–	64 × 64 × 256	1024
max_pooling2d-3	Max Pooling	2 × 2	32 × 32 × 256	0
glob_ave_pool2d-1	Global Average pooling	–	256	0
Dropout-1	Dropout		256	0
Dense-1	Fully connected layer + softmax		2	524

Total params: 47,891

Trainable params: 46,905

Non-trainable params: 986

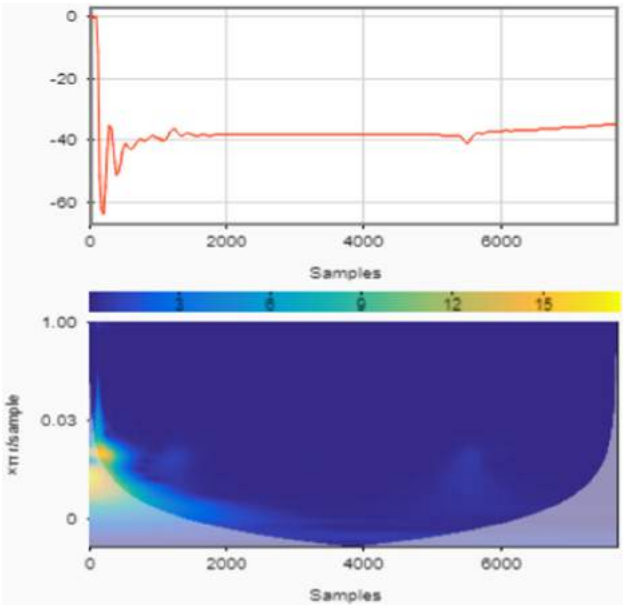

Fig. 9 Islanding case for 100% of load

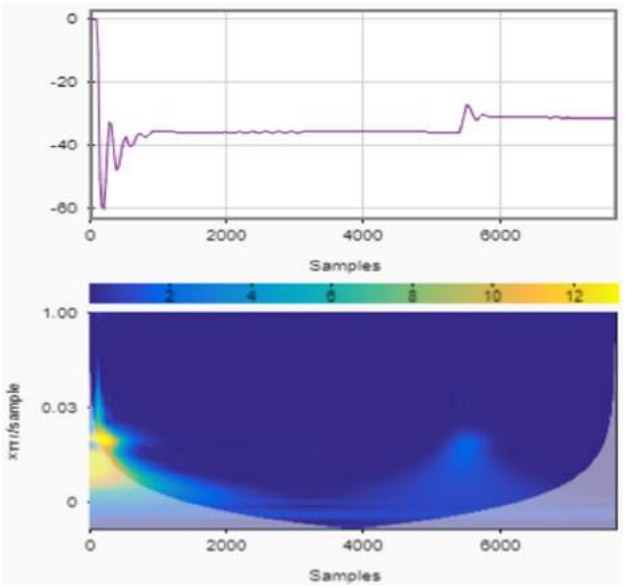

Fig. 10 Islanding case for 80% of load

classification output in this layer. The combination of these layers varies for different applications.

4.6 Design of CNN for islanding detection approach

In this paper, the CNN is constructed for the classification of different islanding and non-islanding events. Several aspects are taken into account while constructing the CNN. The subsequent steps are initially supported. During the training process, all the hyperparameters are uninterrupted initially. This will help in identifying the number of layers required for good efficiency. Once the statistics of slabs are identified, the variation of hyper parameters is identified for optimal values and they are fixed while designing CNN. It is initially started with a single layer. Every layer of CNN implements three operations such as convolution, ReLu activation and max pool operation. Once the CNN is designed and executed successfully for a single layer, the other layer is added and the same operations are repeated until it gets high accuracy. The response for the number of layers on accuracy found that eight layers architecture has good accuracy compared to five and seven layers. Hence,

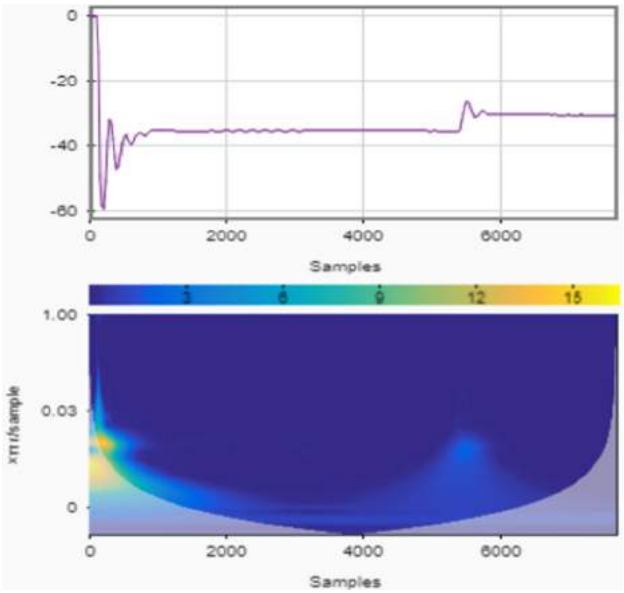

Fig. 11 Islanding case for 50% of load

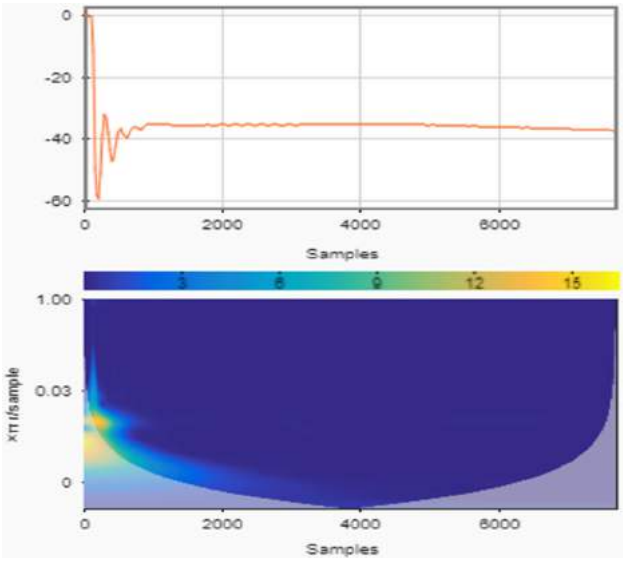

Fig. 12 Non-islanding case of capacitor switching

eight layers architecture is fixed for the CNN design for the classification of islanding and other events. Once it is fixed, the next step is the investigation of the size of the filters. It is found that 3×3 kernel has good output compared to 5×5 and 11×11 kernels. The variation of learning rate and momentum with stochastic gradient descent with the momentum method is verified. The learning rate of 0.001 accords good outputs in terms of accuracy and loss. The CNN design parameters and data set information and customized CNN parameters are listed in Tables 1, 2, 3, respectively.

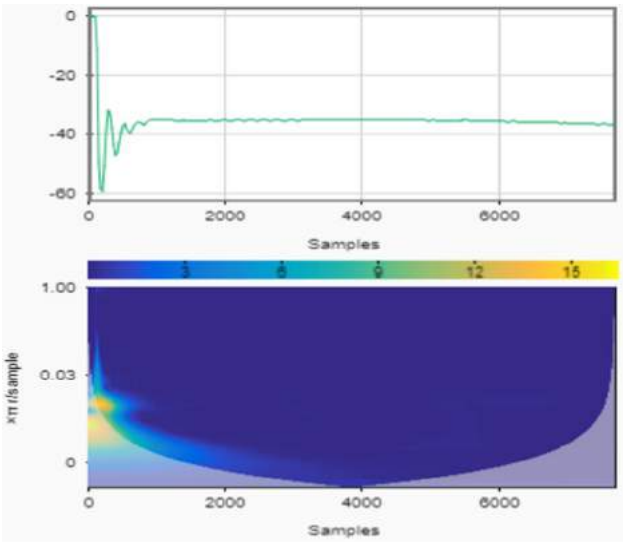

Fig. 13 Non-islanding case of induction motor switching

5 Results and discussion

The constructed structure is experienced with 75% of data and tested with 25% of data. 25% of data are completely unseen by the designed network. The data set contains the islanding events and various non-islanding events. The non-islanding events include load switching, capacitor switching, feeder switching, and fault switching for ON/OFF cases. In all these cases, the time series data are transformed into scalogram pictures. The voltage variations for islanding and non-islanding events are reflected as color gradients in the scalogram images. The few testing scalograms are depicted in Figs. 9, 10, 11, 12, 13. A total of 65 (25 islanding+ 40 non-islanding) cases are tested. Out of all the testing cases, only 3 cases are wrongly predicted. The accuracy and loss plots for training and validation are depicted in Fig. 14.

6 Conclusion

This paper presents a novel islanding detection method with CWT and CNN. The time series data of phase angle between positive sequence component of voltage and current obtained from Simulink are transformed into scalogram images. The data set is prepared with 258 events of islanding and non-islanding cases. 75% of the data set has been used for training the CNN, and the remaining 25% (65 cases) is used for testing. Out of tested 25 islanding and 40 non-islanding cases, only three non-islanding cases are wrongly predicted. This method has an accuracy 95.4%. It has been found that the deep learning-based CNN can

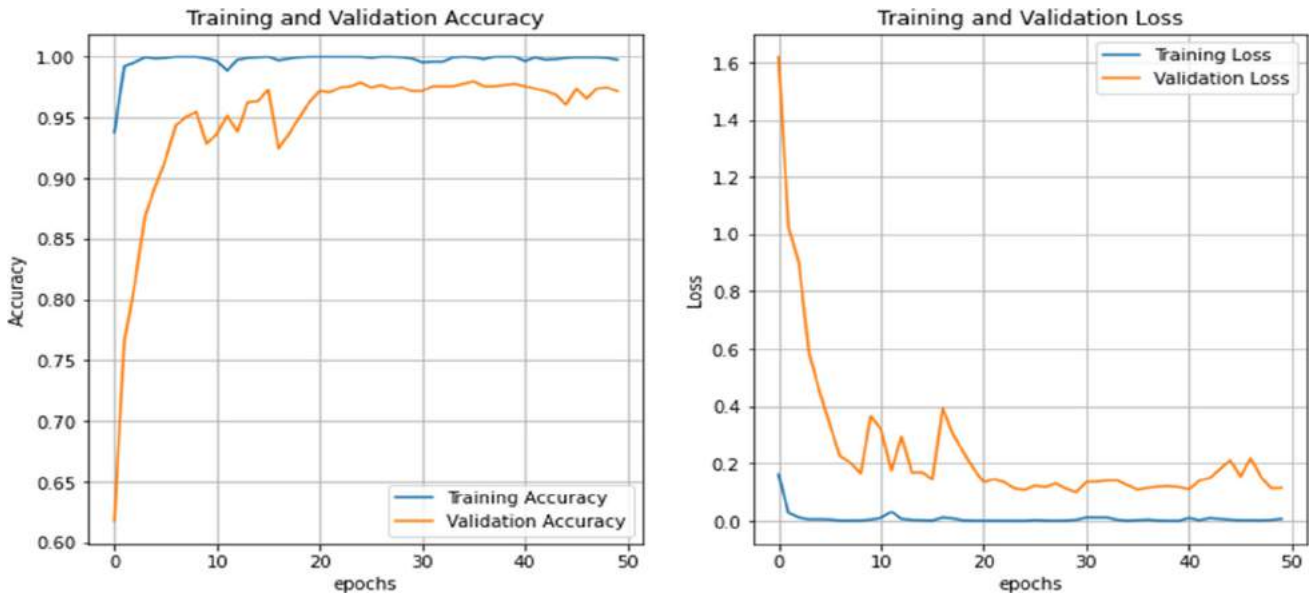

Fig. 14 Accuracy and loss plots for training and validation

detect the islanding classifications effectively compared to machine learning approaches.

Funding No funding received from external funding agencies.

Declaration

Conflict of interest The authors declare that they have no conflict of interest.

References

Chen X, Li Y, Crossley P (2019) A novel hybrid islanding detection method for grid-connected microgrids with multiple inverter-based distributed generators based on adaptive reactive power disturbance and passive criteria. IEEE Trans Power Electron 34(9):9342–9356

Cui Q, El-Arroudi K, Joós G (2018) Islanding detection of hybrid distributed generation under reduced non-detection zone. IEEE Trans Smart Grid 9(5):5027–5037

Do HT, Zhang X, Nguyen NV, Li SS, Chu TT (2016) Passive-islanding detection method using the wavelet packet transform in grid-connected photovoltaic systems. IEEE Trans Power Electron 31(10):6955–6967

Guo K et al (2018) Angel-eye: a complete design flow for mapping CNN onto embedded FPGA. IEEE Trans Comput Aided Des Integr Circuits Syst 37(1):35–47

Ker J, Wang L, Rao J, Lim T (2018) Deep learning applications in medical image analysis. IEEE Access 6:9375–9389

Kermany SD, Joorabian M, Deilami S, Masoum MAS (2017) Hybrid islanding detection in microgrid with multiple connection points to smart grids using fuzzy-neural network. IEEE Trans Power Syst 32(4):2640–2651

Khamis A, Xu Y, Dong ZY, Zhang R (2018) Faster detection of microgrid islanding events using an adaptive ensemble classifier. IEEE Trans Smart Grid 9(3):1889–1899

Manikonda SKG, Gaonkar DN (2019) IDM based on image classification with CNN. J Eng 2019(10):7256–7262

Murugesan S, Murali V (2020) Disturbance injection based decentralized identification of accidental islanding. IEEE Trans Ind Electron 67(5):3767–3775

Raju SG, Harinadha Reddy K, Reddy Ch (2021) Islanding detection parameters for integrated distributed generation. Recent Adv Electr Electron Eng 14(2):131–143

Reddy ChR, Harinadha Reddy K, Srikanth Goud B, Pakkiraiah B (2021) A Deep learning approach for Islanding Detection of Integrated DG with CWT and CNN. In: 2021 International Conference on Sustainable Energy and Future Electric Transportation (SEFET). IEEE, pp 1–7

Reddy ChR, Harinadha Reddy K (2018) Islanding detection for inverter based distributed generation with low frequency current harmonic injection through Q controller and ROCOF analysis. J Electr Syst 14(2):179–191

Reddy ChR, Harinadha Reddy K (2018) An efficient passive islanding detection method for integrated DG system with zero NDZ. Int J Renew Energy Res (IJRER) 8(4):1994–2002

Reddy CH, Harinadha Reddy K (2019) A new passive islanding detection technique for integrated distributed generation system using rate of change of regulator voltage over reactive power at balanced islanding. J Electr Eng Technol 14(2):527–534

Reddy ChR, Harinadha Reddy K (2019a) NDZ analysis of various passive islanding detection methods for integrated DG system over balanced Islanding. Int J Integr Eng 11(8):206–220

Reddy ChR, Harinadha Reddy K (2019b) Islanding detection techniques for grid integrated distributed generation—a review. Int J Renew Energy Res 9(2):960–977

Reddy JR, Pandian A, Reddy CR (2020) An efficient learning based RFMFA technique for islanding detection scheme in distributed generation systems. Appl Soft Comput 96:106638

Reddy R, Harinadha Reddy K, Aymen F, Goud BS, Bajaj M, Abdulaal MJ, Milyani AH (2022) Hybrid ROCOF relay for islanding detection. J Electr Eng Technol 17(1):51–60

Reigosa DD, Briz F, Blanco Charro C, Guerrero JM (2017) Passive islanding detection using inverter nonlinear effects. IEEE Trans Power Electron 32(11):8434–8445

Salles D, Freitas W, Vieira JCM, Venkatesh B (2015) A Practical method for non detection zone estimation of passive anti-islanding schemes applied to synchronous distributed generators. IEEE Trans Power Delivery 30(5):2066–2076

Sejdic E, Djurovic I, Stankovic L (2008) Quantitative performance analysis of scalogram as instantaneous frequency estimator. IEEE Trans Signal Process 56(8):3837–3845

Sivadas D, Vasudevan K (2020) An active islanding detection strategy with zero non detection zone for operation in single and multiple inverter mode using GPS synchronized pattern. IEEE Trans Ind Electron 67(7):5554–5564

Xu W, Zhang G, Li C, Wang W, Wang G, Kliber J (2007) A power line signaling based technique for anti-islanding protection of distributed generators—part I: Scheme and analysis. IEEE Trans Power Delivery 22(3):1758–1766

Sustainable Energy Technologies and Assessments 53 (2022) 102692

Contents lists available at ScienceDirect

Sustainable Energy Technologies and Assessments

journal homepage: www.elsevier.com/locate/seta

Challenges in achieving sustainable development goal 7: Affordable and clean energy in light of nascent technologies

M. Jayachandran [a,*], Ranjith Kumar Gatla [b], K. Prasada Rao [c], Gundala Srinivasa Rao [d], Salisu Mohammed [e], Ahmad H. Milyani [f,g], Abdullah Ahmed Azhari [h], C. Kalaiarasy [i], S. Geetha [j]

[a] Department of Electrical and Electronics Engineering, Sri Manakula Vinayagar Engineering College, Puducherry, India
[b] Department of Electrical and Electronics Engineering, Institute of Aeronautical Engineering, Hyderabad, India
[c] Department of Electrical and Electronics Engineering, Malla Reddy Engineering College, Secunderabad, India
[d] Department of Electrical and Electronics Engineering, CMR College of Engineering & Technology, Hyderabad, India
[e] Department of Maintenance, Instrumentation and Control Engineering, Nigerian National Petroleum Corporation, Kaduna, Nigeria
[f] Department of Electrical and Computer Engineering, King Abdulaziz University, Jeddah, Saudi Arabia
[g] Center of Research Excellence in Renewable Energy and Power Systems, King Abdulaziz University, Jeddah, Saudi Arabia
[h] The Applied College, King Abdulaziz University, Jeddah, Saudi Arabia
[i] Department of Computer Science Engineering, Puducherry Technological University, Puducherry, India
[j] Department of Humanities and Social Sciences, Puducherry Technological University, Puducherry, India

ARTICLE INFO

Keywords:
Energy transition
Clean energy
Green grid
Variable renewable energy systems
Transnational connectivity

ABSTRACT

The concerns about climate change mitigation, decarbonization in critical sectors, and environmental pollution reduction have instigated a global surge in the use of renewables. As distributed energy resources (DER) proliferate, the existing power grid may be transformed into a carbon-free power system, ensuring that everyone has access to affordable, reliable, sustainable, and modern energy. However, there are some practical impediments and challenges in the transition of the global energy system. Hence, the present study aims to examine the benefits, technological advancements, problems, and solutions for establishing a global sustainable green grid. This study also provides a comprehensive literature review of strategic research direction relating to energy transition in various sectors; identification of major issues and challenges in renewable power network; investment requirements in clean electricity generation; operational challenges of 100% renewable integration into the power grids; and power pool interconnection issues for building a renewable energy system on a global scale. Through reviewing several emerging low-carbon technologies, this article offers insights into the feasibility and sustainability assessment of transnational clean electricity networks for supplying power throughout the world. The findings of this study highlight the potential of adopting variable renewable energy (VRE) systems in the development of a global eco-friendly grid. It also confirms that solar PV systems on a global scale of 8519 gigawatts would reduce 4.9 Gt of greenhouse gas (GHG) emissions and fulfill 25% of global electricity demand by 2050. The review affirms that intercontinental solar power infrastructure can ensure solar power supply to solar power deficient countries, allowing the world to move toward a sustainable and clean energy future. Finally, this work suggests future research opportunities for the global clean energy system.

1. Introduction

Sustainable, practical, and efficient forms of energy are required to accelerate the green transition. Renewables are the only form of low carbon energy and play a big role in the energy future. Solar and wind energy technologies compete with the traditional sources of electricity. These facts are pushing the whole world to shift into a sustainable and clean energy revolution to mitigate climate change [1]. Theoretically, all of humanity's power needs can be met by solar power. Every 88 min, the sun emits 470 exajoules of energy to the earth's surface, enough to power the entire planet for one year. In a couple of hours,

* Corresponding author.
E-mail addresses: jayachandran.escet@pec.edu (M. Jayachandran), ranjith.gatla@gmail.com (R.K. Gatla), kpr879@gmail.com (K.P. Rao), drgundalasrinivasarao@gmail.com (G.S. Rao), salisu.mohammed3@nnpcgroup.com (S. Mohammed), ahmilyani@kau.edu.sa (A.H. Milyani), aaazhari@kau.edu.sa (A.A. Azhari), kalaidivi043@gmail.com (C. Kalaiarasy), geetha.s@ptuniv.edu.in (S. Geetha).

https://doi.org/10.1016/j.seta.2022.102692
Received 5 March 2022; Received in revised form 19 July 2022; Accepted 15 August 2022
Available online 13 September 2022

the earth receives more energy from the sun than all of the energy used by mankind in a year [2]. However, in practice, the conversion rate of the energy capture and distribution is extremely inefficient. So the conversion rate could improve the efficiency of solar panels using advanced materials [3]. Although identifying solar resource-rich countries is a big challenge, historical solar data will help to identify ideal locations to set up solar projects. Due to the intermittent nature of solar energy, energy storage is employed to store the energy for future use. However, long-term storage batteries are not affordable. As a result, multi-season storage is required to store hydro, wind, and solar energy for later consumption during a peak time [4]. Another technical challenge is to reduce transmission and distribution losses for a sustainable energy future [5].

The green energy revolution provides abundant, reliable, and low-cost electricity, allowing for the transit of economies and saving lives from climate change. Clean energy from solar and wind has become decisively cheaper than fossil fuels. By 2050, renewable energy will supply nearly half of the world's electricity, as the costs of wind, solar, and battery storage continue to plummet. However, creating and transporting clean energy is a challenge. Besides, a global clean electricity network is yet to be implemented [6,7].

Regarding the energy transition, rapid development and deployment of clean energy technologies are essential in achieving net-zero emissions [8]. A clean energy disruption by 2030 will herald the end of the current energy mix and the birth of cleaner power in every corner of the world. Solar energy, energy storage, and electric vehicles (EVs) are critical technologies that will disrupt all energy and transportation systems. However, the development of technology capable of capturing, storing, and exporting massive amounts of renewable energy has been difficult until now. The capacity to maintain a sufficient energy reserve over the long term when there is no wind or sunlight has historically been a concern for variable renewable energy sources, but the economics are changing in this sector [9].

In contrast to centralized power infrastructure, the proliferation of renewables allows end-users to generate their electricity, and in certain situations, surplus electricity may be transferred back to the grid. These areas are known as 'microgrids' [10]. A major concern is the regulation of this bidirectional power flow over massive transmission networks [11]. The patchwork technique is no more appropriate as more small generators join the network. One key aspect is to optimize the renewable sources, which are often located far from the final customer. Another difficult challenge is relocating the produced power onshore at a reasonable cost. Some electricity is lost during transmission as heat accumulates over long distances [12]. An additional benefit would be that renewables, if given transmission capacity, could power the dark side of the earth while the flipside is not sunshine. However, the cost of building this massive infrastructure would be enormous, and regulating it may require the involvement of several other international corporations [13].

From a technological perspective, it is completely feasible to power the entire world with renewable energy. The installation of long-distance transmission lines using HVDC submarine cables can help to transfer electricity over thousands of kilometers with minimal loss to the link between energy consumers and locations where renewable energy is most abundant [14]. In terms of technology advancement with HVDC in practice, global energy interconnection is feasible [15]. However, the electricity flow needs to be controlled precisely [16]. A crucial challenge is how to switch it from whenever it is most abundant and cheapest to wherever it is most needed with millisecond precision. The solution is "smart grids" that can control energy flows very precisely. So the combination of ultra-high voltage lines with smart grids and clean energy results in global energy interconnection [17]. If this vision is realized, it will be feasible to provide electricity across the world at any time of day or night. Electricity from solar hybrid mini-grids is still extremely expensive for many rural customers, and sectors suffer from a lack of investment [18]. A flexible, secure energy future should be a cost-effective, sustainable, and decarbonized energy system. Countries share their clean energy resources so that everyone gets a reliable supply of unlimited, cost-effective clean energy [19].

Considering global energy interconnection, each continent connects to a regional grid to trade renewable energy across borders [20]. Leaders in renewable energy can profit from interconnections and are frequently exporters [21]. This concept can provide greater energy security since it can import energy whether it is cloudy or windy. Although governments can only harness the massive potential, they require sufficient long-distance transmission lines to connect all the major consumption areas, cities, and factories with the greatest renewable energy locations. As a result, potential connections are being investigated all over the world [22]. Developing countries could quickly adopt the green grid concept, transforming the continent into a cutting-edge hub for renewable energy sharing and trade [23]. A mathematical model-based analysis for a 100% renewable power system is necessary for building the continental-scale grids and inter-regional grid connections [24–26]. This cross-border connectivity ensures universal access to modern energy and resolves the high cost of energy storage [27].

Due to a scarcity of critical reviews addressing knowledge gaps in research advancements pertaining to global clean energy systems, this review aims to present a comprehensive perspective on the sustainability and feasibility of global-scale renewable systems on the transcontinental grid while taking into consideration the nascent stages of contemporary technological breakthroughs. The following problems, issues, opportunities and developments for global renewable energy integration are addressed in this review paper:

- Policy framing, infrastructure, restructuring power systems, energy supply, energy efficiency, and energy security are all challenges in the energy transition.
- The integration of 100% renewable energy encounters issues such as power balance, inverter, stability, protection, unintentional islanding, and black start.
- Technological, market and economic, policy, regulatory, political, and social impediments hamper solar PV implementation.
- Net load change, the effect of high renewable energy penetration, curtailment of renewable energy, and managing power system forecasting errors are major operational concerns in large-scale renewable integration.
- The prospects of global renewable energy integration include enabling technologies, business models, market design, and system operation.
- Deployment policies, integrating policies, and enabling policies are essential to achieve a sustainable energy transition.

The number of documents identified from SCOPUS database dealing with SDG 7 has varied greatly in recent years. However, the period from 2015 to 2022 has been the most fruitful, as seen in Fig. 1. According to the data in Fig. 2, the majority of publications were in environmental science (24%), energy (16%), and social sciences (15%), accounting for more than half of total production. The extreme conditions impact the analysis and statistics is presented in Fig. 3. More than two-thirds (70%) of all published studies focused on extreme heat (33%), rainfall or flooding (20%), and drought (17%). According to the WMO Atlas of Mortality and Economic Losses from Weather, Climate, and Water Extremes, tropical cyclones accounted for 38%, while various types of floods accounted for 31% [28].

This study will primarily focus on green and low-carbon transcontinental grid connectivity as a solution to future energy demands, dependable and affordable energy access, energy security and self-sufficiency, energy decarbonization, and climate change. Moreover, challenges and opportunities in greening the grid on a global scale are the key focus of the study. Furthermore, this article highlights the energy transformation to a future of low carbon electricity at a reduced cost, with the greatest benefit of building a global clean energy network by 2050. High RE penetration in an interconnected electricity network

Table 1
Characteristics of this review based on Cooper's taxonomy.

Characteristic	Cooper's definition	Authors' selection
Focus	The material that is of central interest of the reviewer	Research methods, outcomes, and applications
Goal	What the author hopes the review will reveal	Integration and identification of central issues
Perspective	Reviewer point of view	Neutral
Coverage	The extent to which the reviewer includes the relevant works	Representative
Organization	Paper organization	Conceptual
Audience	Intended paper audience	Specialized researchers/policy maker

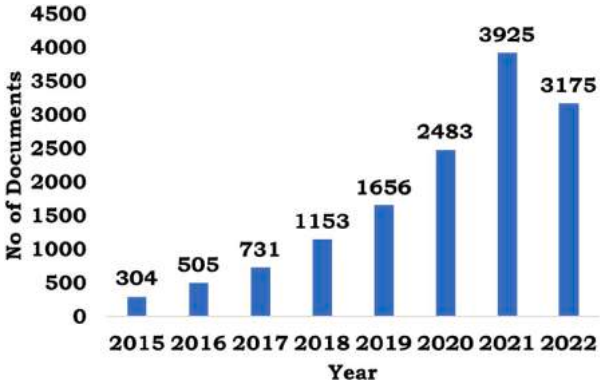

Fig. 1. Number of documents about SDG 7.

will eventually contribute to building a global clean energy system capable of meeting the estimated peak electricity demand by 2050. Table 1 summarizes this review using Cooper's taxonomy 1.

The rest of this study is organized as follows: Section 2 analyzes the importance of a global energy transition and highlights some key hurdles in various sectors from scenario analysis. Section 3 examines the necessity of a global energy transformation and highlights the challenges that have hindered achieving a 100% clean grid. The existing hindrances to accelerating solar PV deployment in the presence of contemporary technological solutions are investigated in Section 4. Then, the operational implications of RE integration for attaining a global green grid are analyzed in Section 5. Section 6 highlights the benefits, challenges, and roadmap of global renewable power grid connectivity. Finally, several unresolved scientific issues are addressed for future research to enable extensive solar PV deployment in various sectors, followed by some closing observations. Fig. 4 depicts the research flowchart of this investigation.

2. Global energy scenario and energy transformation rationale

Due to unprecedented uncertainties in the energy sector, energy consumption will continue to increase. Meeting future energy demand and supply will be a significant problem. The evolution and modernization of the energy sector are incredibly complicated. The World Energy Council (WEC) has estimated the energy scenario for the year 2050 as shown in Table 2. This energy scenario focuses on achieving energy access, affordability, and supply quality by utilizing the greatest available energy sources, environmental sustainability, and energy security. Moreover, population, GDP growth, technology support, climate policy, resources, and efficiency are all quantified in these scenarios.

Energy supply: Global primary energy consumption (equal to supply) will rise by 27%–61%, and it will be difficult to satisfy global demands [29]. The energy supply problem does not have a global solution. Instead, each part of the problem must be solved separately to achieve the global goal of a sustainable, affordable, and secure energy supply for all consumers. Besides, global electricity production is expected to increase by 47.9–53.6 billion TWh by 2050 [30].

Energy efficiency: Energy efficiency and conservation are critical in balancing demand and supply. Both involve a shift in client preferences and have cost implications across industries. As a result, capital is necessary to support energy-efficiency measures before they can pay off in terms of the initial investment [31].

The energy-mix: Although fossil fuels will dominate the energy mix in 2050, renewable energy sources will increase at the fastest rate. The energy generation, including installed capacity and investment requirements, is presented in the Table 3. The rapid decline in renewable energy costs supports the energy transition. Based on auction outcomes and continued technological improvements, renewable energy costs are expected to be reduced more in the future. By 2030, the cost of solar PV is projected to have dropped by half again. Surprisingly, VRE accounted for more than half of the electricity generated in Germany's eastern area. In addition, innovative solutions and life cycle thinking are required to meet the high energy needs of some power sectors, the excessive carbon emissions of some processes, and the high carbon content of certain products. In 2050, renewable energy will account for between 31% and 48% of total electricity generation [30].

2.1. Energy transition in critical sectors:

Integrating terawatts of clean energy resources into electric power systems can help to achieve decarbonization targets and combat global climate change. The reliability of integrating variable renewable generation will require electrification that will result in decarbonization in transportation, building, industry, and end-use sectors. Therefore, renewable energy should be expanded to fulfill the demands for electricity, heat, and transportation [32]. The energy transition analysis and insights from important sectors are presented in Table 4.

Transport: The transportation industry is currently dominated by fossil fuels, necessitating a significant shift. Although this industry contributes considerably to the electrification of passenger transportation, a cornerstone of the net-zero emission goal achievement of the transport sector is a hundred percent electrification. The net-zero goals hinge on solar deployment. By 2050, global liquid biofuel production will have surpassed 900 billion liters [33]. Another alternative is to use hydrogen as a transportation fuel for fuel cell cars. The transportation sector will require almost 14 trillion USD in total investment by 2050. The whole transportation sector is evolving as a result of modern energy resources combined with information and communication technology (ICT) [34].

Buildings: The consumption of electricity in the buildings is anticipated to rise by 70% by 2050 requiring a cumulative investment of 38 trillion USD [35]. Energy-efficient buildings can be made with renewables to meet the electricity demand. Bioenergy will continue to be the most common renewable fuel in buildings. Due to the high share of renewable power in the electricity supply, the transition in cooking technologies and energy-efficient heat pumps will promote renewables in green buildings. According to IRENA's report, the implementation of renewables in buildings would cost around USD 1.6 trillion and could meet over 56% of the sector's energy consumption [36].

Industry: The industrial sector is the second-largest emitter of greenhouse gases. It accounts for one-third of the global carbon emissions. Throughout the energy transition, biomass and renewable electricity will play an essential role in industries. By 2050, the industry must raise the renewable energy share in indirect applications and fuels to 48% [37]. Besides, hydrogen usage generated from renewables

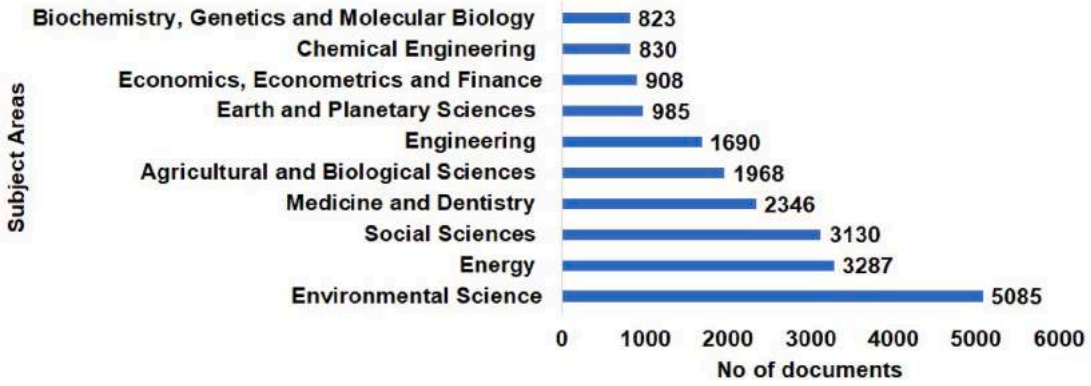

Fig. 2. Subject area distribution of papers on SDG 7.

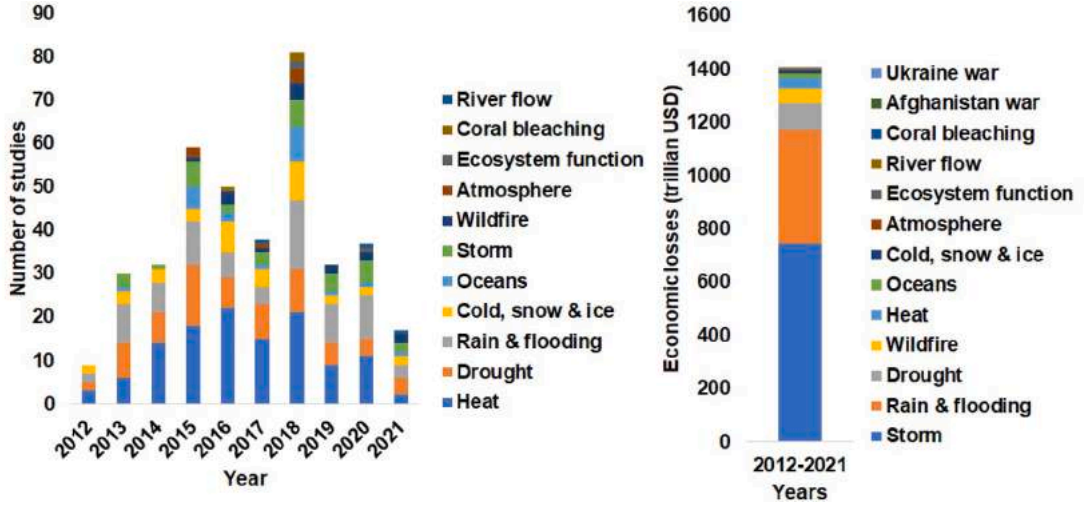

Fig. 3. Extreme condition impact on SDG 7.

Table 2
Global energy scenario: Creating an energy future in 2050 [29].

Parameters	Estimated value
Population (billion)	8.7–9.4
GDP per capita (USD)	18320–23140
Total primary energy supply (PWh)	193–244
Share of net imports in primary energy supply (%)	19.2–20.5
Share of renewable energy sources (%)	20–30
Global electricity generation (billion MWh)	47.9–53.6
Investment needed to meet globalelectricity demand (trillion USD)	19310–25720
Share of investment needed in renewable energy (%)	46–70
Degree of electrification (%)	30
Electricity consumption per capita increases globally (%)	78–111
People without access to electricity (billion)	0.319–0.530
Primary energy consumption (%)	45–48
CO_2 emissions (billion tones per annum)	19.1–44.1
Renewable electricity production (TWh/year)	16590–22800

will increase to 7 EJ by 2050. Furthermore, the industrial sector has significant potential to increase its efficiency. According to the IRENA analysis, using the best available technology could reduce industrial energy consumption by nearly a quarter.

Power: End-use sector consumption will rise to approximately 42,000 TWh over the next three decades [30]. However, the power sector's carbon intensity would be reduced by 85%. There should be no building of new coal-fired power plants and 95 percent of existing power plants should be decommissioned. In the power sector, the annual investment in green power production capacity is expected to rise to over USD 500 billion [30]. Moreover, decarbonizing the electrical grid will require an average of USD 1 trillion and renewable energy will provide over 85% of total power generation by 2050 [38].

2.2. Investment needs in electricity generation:

Although the energy revolution is certainly feasible and economically advantageous, it will need a significant increase in low-carbon technology investment over existing and planned policy. Table 5 shows the region-wise global energy generation, including investment requirements for the next three decades. A further 27 trillion USD investment will be required during the term. Between 2021 and 2050, a total investment of nearly USD 120 trillion in low-carbon technology is

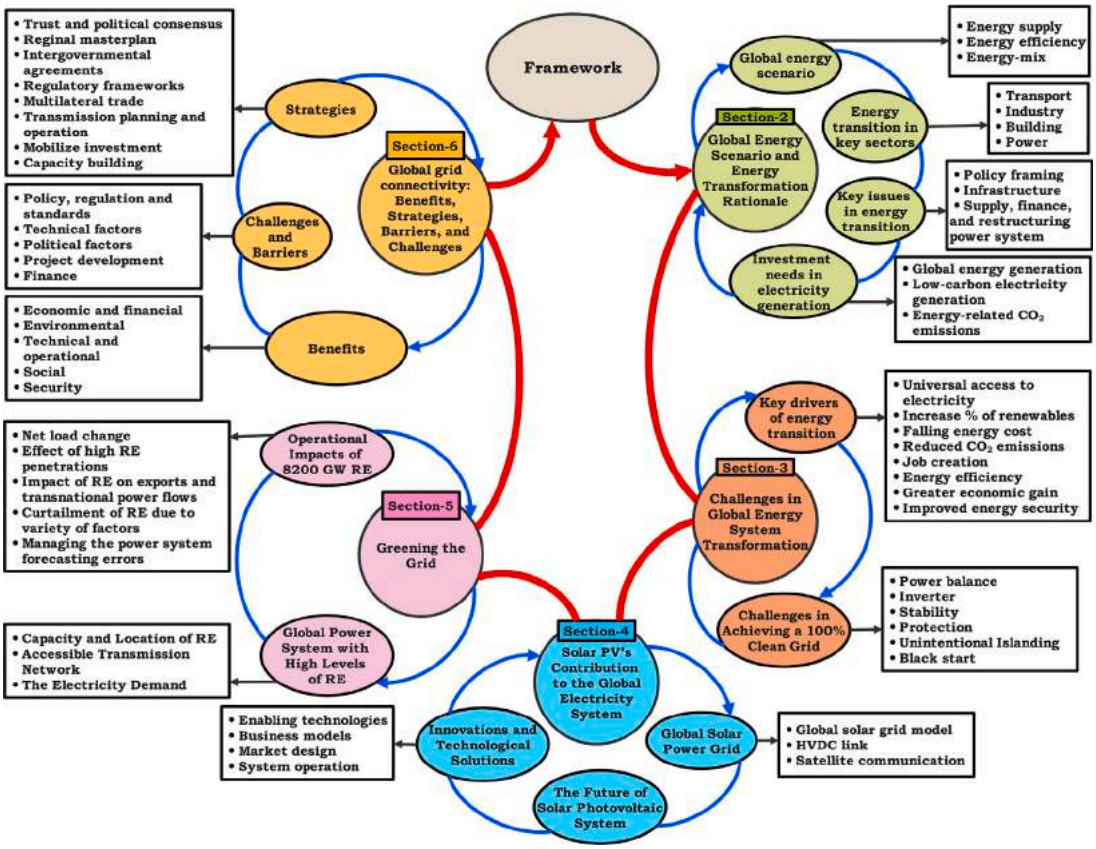

Fig. 4. Framework of this study.

Table 3
Global electricity production, generation capacity, and investment requirements in 2050 by fuel type [31].

Primary Energy	Global Electricity Production (TWh/y)	Global Installation in Electricity Generation Capacity (GW)	Investment Requirements in Electricity Generation (billion USD)
Coal (with CCS)	1007–7100	141–1006	200–1620
Coal	19272–1383	300–484	1660–6950
Oil	0	41	90
Gas (with CCS)	558–2505	178–603	140–490
Gas	12869–7012	2353–2036	1980–2050
Nuclear	3279–6950	421–884	1010–2020
Hydrogen	69–155	15–39	30–100
Hydro	5789–7701	1575–2161	1950–3520
Biomass	1913–1923	256–292	260–340
Biomass (with CCS)	441–800	78–141	240–440
Wind	4003–4513	1824–1654	2720–3280
Solar	2979–7741	1654–4439	2950–9660
Geothermal	654–949	102–141	520–720
Total	**47917–53648**	**11680–13881**	**19310–25720**

needed averaging about 2.0 percent of global GDP every year [33]. However, the cost reductions far exceed the rise in energy system expenses. Reduction in air pollution and carbon-related environmental harm will result less spending on healthcare. Massive investments in power generation between 19 trillion and 26 trillion dollars are required globally to meet future electricity demand [39]. Solar PV, hydro-power, and wind power capacities are all huge investment needs. Solar PV, in particular, is expected to grow by 230 times in 2050 and generate power of approximately 2980 and 7740 TWh/y. As a result, solar PV generates a significant amount of electricity around the world [40].

Low-carbon electricity generation: As a result of low-carbon energy generation, the global level of electrification will increase by more than 30% by 2050. Globally, electric power consumption per capita is anticipated to rise from 78% to 111%. However, the global economy would struggle to meet the 450 ppm target without a realistic carbon tax [41].

Energy-related CO_2 *emissions:* WEC's scenario show that CO_2 emissions will be between 19 and 44 billion tonnes per annum in 2050 [29]. Energy efficiency, together with renewable energy, is the main factor in lowering carbon emissions in the energy transformation. According to the government's goals and policies, total emissions will surpass the carbon budget to keep global warming below 2 degrees Celsius. By 2050, 470 Gt of emissions reductions will be necessary to keep global temperatures below 2 °C. Carbon emissions will increase each year until 2040, then decline somewhat by 2050 to nearly match the present levels. According to the IRENA study, widespread end-user electrification along with renewable energy and energy efficiency

Table 4
Energy transition analysis and insights from key sectors [32].

Indicators for energy use in Transport sector		Indicators for energy use in Industry sector		Indicators for energy use in Building sector	
(a) Cars	43076	(a) Iron & steel	3608	(a) Total building stock floor area (million m^2)	269
(b) 2/3 wheelers, Buses, & Rail	27493	(b) Cement	8889		
(c) Aviation (billion passenger km/yr)	21666	(c) Chemical	1079	(b) Number of households (billion)	3.2
(d) Freight (billion tone km/yr)	216500	(d) Aluminum	269		
		(e) Pulp & paper (Mt/yr)	822		
Renewable share	58%	Renewable share	63%	Renewable share	77%
Electricity share	33%	Electricity share	42%	Electricity share	56%
(a) Passenger vehicles	965	(a) Biomass heat	20.2	(a) Traditional cookstoves	0
(b) Buses & light duty vehicles	57	(b) Biomass feedstocks (EJ/yr)	10.5	(b) Modern cookstoves (million units)	867
(c) 2/3 wheelers (million)	2160			(c) Heat (EJ/yr)	7.6
(a) Battery storage (GWh)	12380	(a) Solar thermal (GWh)	134	(a) Solar thermal collector area (million m^2)	6299
		(b) Collector area (million m^2)	3450		
(a) Liquid biofuels (billion liters)	902	(a) Geothermal (EJ/yr)	4.11	(a) Geothermal (EJ/yr)	1.76
(b) Biomethane (billion m^3)	23	(b) Heat pumps (million units)	80	(b) Heat pumps (million units)	253
Energy related CO_2 emissions (Gt CO_2/yr)	3.1	Energy related CO_2 emissions (Gt CO_2/yr)	5.1	Energy related CO_2 emissions (Gt CO_2/yr)	2.3
Investment for decarbonization (trillion USD)	14.2	Investment for decarbonization (trillion USD)	5.0	Investment for decarbonization (trillion USD)	39.6
Stranded assets	–	Stranded assets (trillion USD)	0.75	Stranded assets	10.8

Table 5
Global electricity production and investment requirements in 2050 [29].

Region	Global Electricity Production (TWh/y)	Investment Requirements in Electricity Generation (billion USD)
North America	8024–8057	2770–4450
Latin America & The Caribbean	3221–3701	1330–1360
Europe	7961–8439	3260–4390
Sub-Saharan Africa	2836–3087	1260–1380
Middle East & North Africa	3314–3644	670–1410
South & Central Asia	6560–8429	3080–3460
Southeast Asia, Pacific	3398–4024	1820–1870
East Asia	12571–14298	5100–7400
Total	**47918–53646**	**19310–25720**

can account for more than 90% of emission reduction [35]. A low-carbon future requires renewable energy, carbon capture utilization and storage (CCUS), and behavioral changes in consumers to mitigate the uncertainties in climate change [42].

The practical energy transformation solutions are summarized in Table 6.

Thus, compromises and worldwide initiatives can help to balance energy security, energy equity, and environmental sustainability. Investments and regional integration are required for functioning energy markets. As a result, energy policy should ensure that the energy and carbon markets attract investment, foster regional integration, and supply electricity to all users. CC(U)S, solar, and wind, along with energy efficiency, will be the primary technologies driving change forward.

3. Challenges in global energy system transformation

Global energy development would be more advantageous in terms of economic, social, and environmental benefits than the existing energy plans and policies of nations. At present, carbon emissions are not on track to fulfill Paris Agreement goals. The CO_2 emissions need to be reduced by 70%. Low-carbon technologies must be scaled up rapidly to keep global warming below 2 °C. In particular, development of renewables in the energy sector would be more advantageous in terms of economic, social, and environmental benefits than the existing energy plans and policies of nations. As a consequence, a decarbonized energy sector dominated by renewables is critical to achieving a greener and more sustainable energy future [43].

Climate goals and the energy transition are built on two main pillars: renewable energy and energy efficiency. These should be expanded considerably across all sectors. The power sector has advanced significantly in recent years. However, development in industry, transport, and the building sectors has to be accelerated with renewables. Besides, significant energy efficiency improvements in energy intensity are needed with renewable energy accounting for two-thirds of total energy consumption. According to IRENA, end-use sectors would account for 40% of the increase in power demand by 2050 and hence all nations will have to significantly increase the renewable energy share in their total energy needs. [29,33,35]. The main drivers of energy transformation are depicted in Fig. 5.

Economically, the global energy transition makes sense. The financial system must be synchronized with sustainable development

Table 6
Summary of key issues and practical solutions for energy transition.

Elements	Challenges	Practical Solutions
Policy framing [29]	• Create and implement policy and regulatory framework. • Increase private-sector investment in long and short-term renewable energy projects. • Balancing short-term needs with long-term impacts in an uncertain global economic environment.	• Identify current and planned energy targets. • Reinforcing integration, enabling, structural, and deployment policies with market-pull and technology push mechanisms. • Deployment of modern decentralized and variable energy resources. • labor and social-protection policies must be tailored
Infrastructure including power systems and integration [42]	• Robust transmission and distribution system needed to ensure supply–demand balance • Network planning and operation. • Build the reliable, stable, and most efficient energy systems	• Substantial investment needs to flow into energy infrastructure to ensure a sustainable, climate-safe, and more resilient future. • Cross-border grid integration provide reliable and economic energy supplies throughout the year. • Digitalization and energy storage solutions manage demand, sector coupling, and ensure a stable electricity supply. • Effective and continuous planning based on robust data and stakeholder engagement. • Long-term plan to build the most resilient economic systems at regional and global levels.
Supply, finance and restructuring power system [33,39–41]	• International financial and technical support is required to develop flexible (interconnected and integrated markets) energy system. • Ensure energy supply meets growing demand. • Forecast and plan for secure supplies • Demand for energy efficiency is growing. • Balancing energy security, economic development, and climate concerns.	• Helping countries to develop and optimize low-carbon technologies. and specify their energy targets. • Analyzing the cost, benefit, and investment need in low-carbon technologies. • advanced biofuels, green hydrogen, and renewable energy supplies need to be considered in aviation, shipping, and heavy-duty transportation. • Government needs to accelerate deployment options to achieve sustainable development goals, disincentivize new investment in outdated technology, increase renewable procurement, support innovation and emerging technologies, and green taxation to enable the supply of clean energy. • These strategies must be accompanied by enabling national clean energy policies, and regulations, to scale-up private investments, supporting infrastructure
Demand, energy efficiency and energy security [31,36]	• Increase the renewables share in the growing demand for energy efficiency. • Increase energy efficiency in all sectors. • Inadequate energy infrastructure, demand management, regulatory systems, behavioral norms, and poor financial incentive structures for energy efficiency. • Building energy-efficient buildings	• Acceleration of energy efficiency needs to be implemented through cross-cutting, action-oriented efforts. • Increase renewable-based power capacity and emerging technology can deliver significant energy-efficiency benefits. • Use high efficient building materials, heating, cooling, and lighting systems, and smart energy management system. • Increase recycling of building materials will reduce emissions in the building sector. • Action to be taken in policies, regulation, information, incentives, aggregating demands, and investment in energy efficiency as part of energy sector transformation. • Develop international standards for energy-efficient buildings. • Lower the demand for primary resources by increasing circularity.
Transport [32–34]	• Concerns about global CO_2 emissions results in air pollution from aviation, shipping, and road transport. • Develop strategies to align sustainable development targets and carbon neutrality by 2050.	• Use of sustainable biofuels, clean hydrogen, efficiency improvements, and electrification in the transport sector can reduce carbon-related emissions. • Growth in EV charging stations and expansion of renewable energy can underpin the electrification of transport needs. • Government should adopt the 'avoid-shift-improve' approach and establish a plan of action in the transport sector.
Industry [37,38,42]	• Hard to impose national climate policy in the industry sector.	• Carbon capture utilization and storage (CCUS) may influence the direct emissions from energy use. • Long-term joint plan of hard-to-abate industries for decarbonization of their operations with government support. • With the support of cost-effective technology can accelerate decarbonization efforts.

goals. Compared to present policies and planned ones, a massive investment in low-carbon technologies will be necessary to mitigate climate change. By 2050, the energy transformation would have resulted in 11 million new jobs in the energy market. The global average Levelized cost of electricity (LCOE) from renewables has also dropped by 77%. A reduction in net energy subsidies might help to reduce healthcare expenses with the growing usage of renewables. As a consequence, there is a payback of at least 3 USD for every dollar invested in restructuring the global energy system between now and 2050 [45].

With the surge in usage of renewables, carbon emissions might be reduced by 70% compared to present levels, resulting in a decline in the public health crisis caused by air pollution. The global renewable energy infrastructure will not only improve air quality but also increase energy security and energy access for all. The transformation of the global energy system would also result in enormous socioeconomic gains, which are critical in influencing any political decisions [46].

3.1. Challenges in achieving a 100% clean grid

The term '100% renewable energy system' encompasses both variable and non-variable renewable energy sources. Hydro-power plants have been used for decades as non-variable renewable energy (NVRE). This power plant utilizes a synchronous machine to generate low-cost renewable energy. However, NVRE technologies are geographically

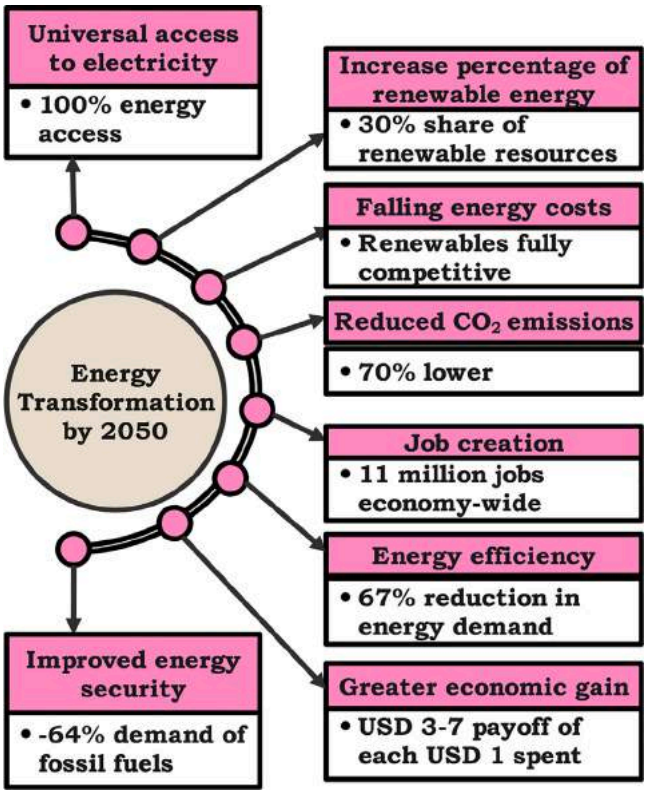

Fig. 5. The key drivers of energy transition to achieve sustainable development goals and net-zero emissions [44].

limited. Operating power transmission networks with extremely high levels of variable renewable energy (solar and wind) is an alternative cost-effective solution [47]. The existing electricity network is dominated by synchronous generators with high rotational inertia and fewer inverter-interfaced VRE sources. However, VRE systems have been vigorously installed recently in countries like Denmark, Germany, and Ireland, with annual penetrations of over 20%. When large-scale VRE with many more inverter-based generators are integrated into power networks, the future grid will be more distributed. As the number of inverter-based devices increases, conventional synchronous generators will be replaced with power semiconductor-based generating stations, energy storage, and controllable loads. If the future grid had a significant VRE penetration (more than 50%) of the rated power at any point in time, the system would be an inverter-dominated grid, as depicted in Fig. 6 [48].

3.1.1. The power balance challenge

In the 100% RE system, multiple timescales are involved in balancing demand and supply, including the shortest timescales (seconds to minutes), the diurnal cycle (minutes-to-hours-to-days), and the seasonal time frame.

The short-term variability problem: The main challenges in solar PV systems are the late-afternoon net load ramps and the short-term fluctuations. More accurate predictions, shorter scheduling intervals, and wider balancing regions in system operations can all aid in the resolution of resource uncertainty issues [49].

The diurnal mismatch problem: Power demand spikes 4 to 6 h after solar peaks, and wind tends to generate more power at night in many regions resulting in a diurnal mismatch. Due to the diurnal mismatch between demand patterns and VRE resources, the VRE capacity credit is limited and declining. The capacity credit is a measurement of a plant's contribution to ensuring reliable service [50]. The mix of higher VRE penetration and limited capacity credit has prompted the reliability of power system operation during low net demand. The integration, power flow, scenario, and stability studies have been conducted to explore cost-effective solutions for the diurnal demand/supply imbalance problem, which include the following:

(i) Shiftable load through responsive demand: Many electric vehicles are underutilized and unavailable during peak renewable production periods. Moreover, shifting new and current loads through responsive demand can alleviate the supply and demand mismatches. As a result, they may charge using low-value renewable energy or avoid charging during peak hours [51].

(ii) Transmission Network: Transmission improves access to potentially cost-effective renewable energy sources and minimizes net variability. However, installing a transmission network may be politically complicated in some countries.

(iii) Diurnal storage: Cost-effective multiple energy storage devices with 4–8-hour capacity are becoming available. However, rising penetrations diminish the capacity's marginal value. Despite Li-ion batteries having been widely deployed in recent years, other energy storage technologies typically have low marginal cost per unit. The electricity consumption from storage devices is often limited to specific locations. The diurnal storage could potentially be expensive for applications beyond 8–12 h [52].

(iv) Non-VRE: Regions with adequate resource quality and seasonal fluctuation are technically and economically viable for biomass, CSP with thermal storage, hydro, and geothermal technologies.

(v) VRE overbuild: Cost-effective deployment of VRE generators can result in lowering the price of energy even with higher curtailment rates. For instance, with a curtailment rate of 33%, delivered energy from PV and wind resources would be competitive by 2050 at $10 and $8/MWh, respectively.

According to studies, it is theoretically feasible to maintain supply/demand balance and appropriate operational reserves while dramatically increasing VRE deployment beyond 50% [53]. Thus, the diurnal mismatch issue might be solved cost-efficiently by prevailing technologies, providing yearly contributions of around 80% RE.

The seasonal balance problem: Wind, solar, and demand patterns have an enormous seasonal mismatch. Therefore, plant maintenance and outages are scheduled to ensure that electricity is available during high-demand periods. The seasonal mismatch in demand and supply is perhaps the most critical unresolved issue in addressing the balancing challenge at 100% RE. These issues include (1) An increase in the costs of RE deployment as a result of seasonal mismatches, (2) Seasonal balancing may need the use of technologies that have yet to be widely implemented, with uncertain costs and requirements, and (3) Reforms in the market design and policy are necessary to incentivize the proper resources [54]. Identifying renewables that can be accessible during extended periods of low solar production, biomass-fueled generators operating primarily as a capacity resource, and expanding the capacity of geothermal and hydropower generation during peak demand are all possible functions of peaking RE resources. Besides, Compressed air and hydro, power-to-gas technologies, and fuel cells are among the solutions for extremely long-term storage for solving the seasonal issue at 100% RE [55]. Although the challenges associated with the high renewable penetration in the power grid have been addressed, several solutions can provide the reliability needed to alleviate these issues.

(i) Geographic diversity: When locating VRE generators, adequate geographic diversity is used to smooth total VRE power production.

(ii) Expansion of transmission system: An expansion of the transmission infrastructure to transfer massive amounts of electricity more effectively from VRE power plants to load centers. Increased geographic variability of VRE generators and usage of transmission resources can be achieved by improved coordination across balancing authority regions and shorter interchange intervals.

(iii) Shifting of VRE: Energy storage technology permits for the temporal shifting of VRE. This intra- and inter-daily power shifting

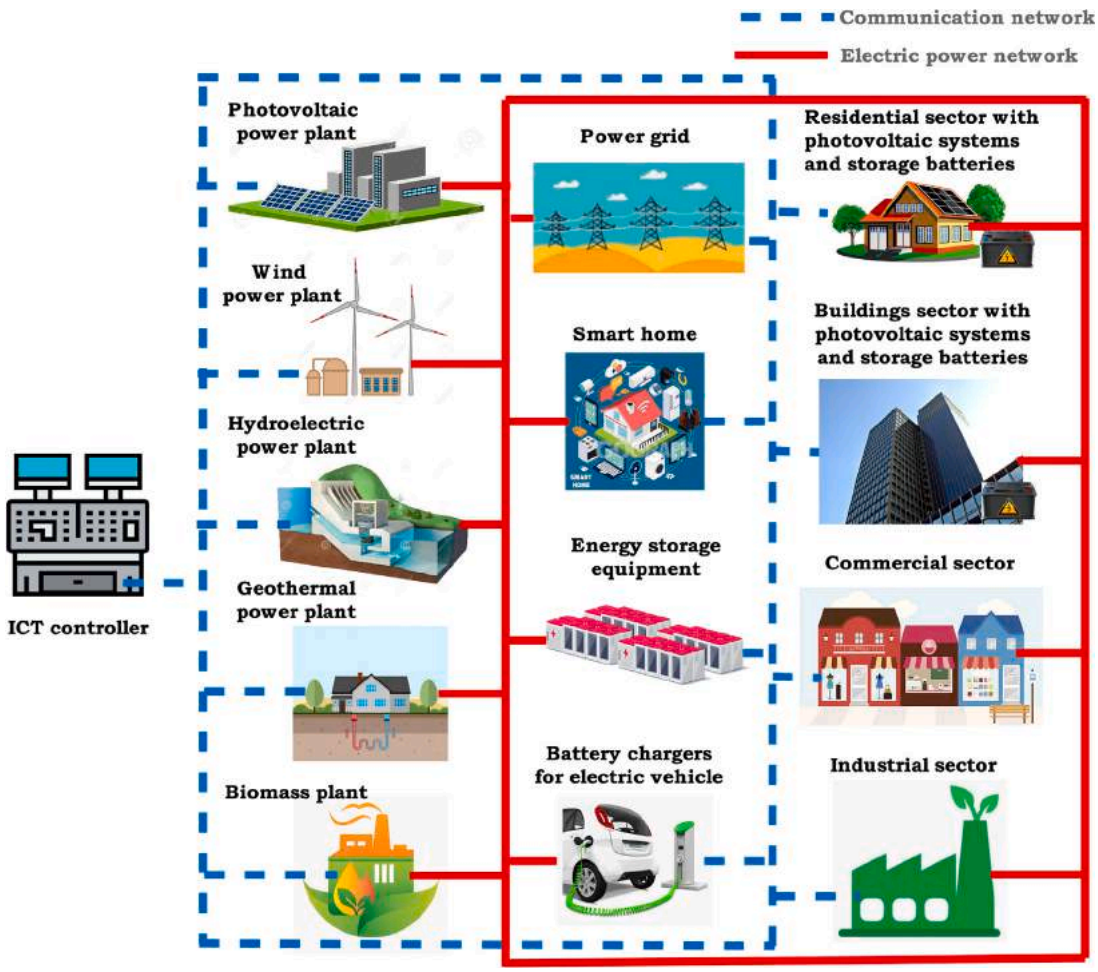

Fig. 6. Communication enabled future power system [48].

may be accomplished using several storage technologies, including battery technologies, compressed air energy storage systems, and pumped hydropower fleet.

(iv) Shifting of load demand: Demand-response technology can adjust load demand to match with VRE generation or reduce the remaining generating fleet's ramping requirements.

(v) Advanced RE and load forecasting: Advanced renewable energy and load forecasting are two other technologies that can help with the efficient utilization of flexible resources. As a result, minimizing the uncertainty in VRE output or load allows for more efficient use of the overall power system [56,57].

3.1.2. The inverter challenge

VRE systems that connect to the grid using power electronics converters are known as inverters. Inverters can control energy flow by manipulating semiconductor switching components in a shorter timeframe. Although wind energy systems employ several conversion stages before connecting to the grid, the inverter circuit is the focus since it interacts directly with the ac power system. Battery storage will play an essential role in controlling energy balance in high VRE systems. The inverter's response is entirely dependent on the particular control approach. Hence, inverters are referred to as "zero inertia systems". A closed-loop controller is necessary to govern power flow from the DC input, through the inverter, and finally to the AC grid, regardless of the VRE type. The combination of closed-loop controllers' instant responsiveness at each VRE system and slower-action centralized controllers can precisely regulate the system frequency and bus voltages. The inverter-based generators in power networks may exceed 50% of the rated power at any instant, thereby forming an inverter-dominated grid [58].

Grid following and grid forming converters are included in inverter controllers. The most common grid-connected PV and wind inverter control method is grid-following controllers. Grid-following inverters act like a voltage-following current source in that it follows the grid voltage. Grid-forming inverters are capable of managing v/f through local decentralized control to overcome the limitation of grid-following inverters [59]. Grid-forming inverter controllers have the following characteristics:

(i) Grid-forming units can function in the complete absence of synchronous machines to ensure that the infrastructure remains stable and reliable for the foreseeable future.

(ii) Large collections of geographically distributed units necessitate decentralized techniques that do not rely on communications [60].

(iii) Inverter controllers must be interoperable with existing systems and allow for a smooth transition between designs as the system grows. They use advanced control methods in addition to power controls to ensure the quality of power supply to loads [61].

Droop-controlled inverters achieve these objectives by establishing a linear relationship between real as well as reactive power and frequency as well as voltage. Nevertheless, they are prone to a sluggish response during transients. Alternatively, researchers have investigated techniques of emulating certain physical phenomena with inverters to create virtual inertia. The inertial response of the machine is programmed on the inverter controller in this type of application [62]. Furthermore, nonlinear oscillator dynamics have recently garnered attention in grid-forming inverters. These novel virtual oscillator controllers have been proven to have fast reaction times and are capable

of producing zero-inertia. According to the published road maps, extensive research and assessment will be required to verify that the 100% inverter-based grids may achieve the same degree of reliability as the present synchronous generators [63]. The following are some outstanding research topics:

Grid-forming inverters: Inverter controls with stored energy can emulate inertial response and provide rotor angle stability. However, this is not a concern in modern systems. More research is needed into inverter responsiveness to monitor and respond to frequency changes while preventing unintended tripping. To maximize their grid benefits, more study is needed to optimize the provision of services from inverter-based resources (IBRs), especially considering the many types of control used in grid-forming inverter variations. Grid-forming inverters have restricted overcurrent capabilities, resulting in lower system robustness. This may require the development of new inverter designs with overcurrent capabilities as well as new mechanisms to protect the system under fault circumstances. [64]

Modeling tools and capabilities: Existing power-flow tools must be modified to measure and interpret grid conditions based on the physics-based response of inverters. Improving electromagnetic transient models for inverters and testing their responsiveness to grid disruptions are primary concerns.

Understanding scale impacts: As IBRs become more prevalent in the electricity system, each inverter uses a unique control strategy, resulting in unknown stability issues under various grid configurations. Therefore, more research into coordinated responses and potential interactions in IBR-based systems, such as harmonics, oscillations, and resonances, is required.

Beyond frequency control: The frequency control mechanism is incompatible with grids that are entirely based on IBRs. Therefore, the coordinated control method must be developed for 100% IBR-based systems, that not only to monitors and regulates power-sharing among multiple generators but also maintains supply–demand balance and grid stability during transitions.

3.1.3. The stability challenge

Uncertain generation and fluctuating power demand levels are unpredictable in many power system conditions. Hence, an additional capacity known as "operational reserves" is made available throughout the dispatch process to maintain the frequency stability of the system during abrupt imbalances. Although wind and solar PV can provide any form of operational reserve, detailed resource forecasting across various periods is required to assure the availability of such reserves from VRE production. Furthermore, energy storage might be utilized to provide additional reserves and rectify imbalances caused by forecast inaccuracies [65].

Transient and small-signal stability: The absence of synchronous generators in 100% renewable power systems reduces system inertia and has an impact on transient and small-signal stability. Inverter-based generators with suitable controller designs are essential to provide both active and reactive power regulation. They offer a synthetic inertia-like response and fault ride-through performance like traditional synchronous generators. As a result, the overall power system reliability has improved.

Frequency stability: At all times, the electrical frequency of an interconnected power system must be kept near its nominal value. Frequency fluctuations can cause instability, load shedding, equipment damage, and blackouts. In recent years, there has been rising concern in the electricity sector about the falling inertia and primary frequency response in interconnected networks. Because of the rising penetration of inverter-coupled generation, this reduction is expected to persist. Well-designed prediction-based hierarchical converter controllers for VRE can outperform traditional generators with primary, secondary, and tertiary control levels due to the fast response time of the power electronics interfaces.

Voltage stability: Maintaining nominal voltages on all buses in a power network is crucial for guaranteeing reliable energy supply across the transmission network. Volt/VAR management and resource optimization are thus critical for providing required voltage support while minimizing the impact on renewable generators' capacity to produce active power.

3.1.4. Power system protection challenge

With the absence of synchronous generators from the grid, additional issues arise relating to protection systems and coordination. During a fault scenario, inverter-dominated systems typically provide additional output current. One potential option is to employ inverters with pre-programmed fault current. They can detect malfunction and stop generating current within one-fourth of a cycle and can respond to grid disruptions incredibly fast and may be able to detach from the grid. Another method for eliminating overcurrent is to employ synchronous condensers to provide the grid with both fault current and inertia. More advanced overcurrent protection solutions for detecting and clearing faults should also be developed and deployed. Besides, the controllers in frequency relays can assess the frequency deviation and identify the fault on the grid [66].

3.1.5. Unintentional islanding and black start

As grids become more distributed in the future, some parts of the grid may become weaker and form electrical islands during faults. Communication-based active anti-islanding solutions will be required to achieve overall grid stability at low penetrations.

Restarting a grid (black start) is critical to inverter-dominated system reliability. When the load is appropriately sized for its capabilities, synchronous generators will provide enough power to start electrical equipment with significant in-rush currents. Inverter-dominated systems must be capable of providing sufficient starting current [67].

In future, attaining 100% renewable electricity requires addressing supply–demand balance and inverter challenges, as summarized in Table 7.

Thus, the research is desired to ensure that the RE supply matches demand patterns at all time scales. As the electricity network shifts from synchronous generated dominated to inverter dominated, new inverter designs are essential to enhance grid stability under contingencies. Besides, additional grid services are necessary to improve operational stability. Thus, maintaining supply–demand balance economically and designing inverter-dominated reliable grids in light of technological advancements can result in cost-optimal decarbonized energy systems.

4. Solar PV's contribution to the global electricity system

Solar power will play a crucial role in facilitating the transition to a carbon-free future. However, solar panel installation may be expensive upfront, and the permitting process might take some time. This is a practical barrier that the solar industry must overcome to succeed on a global scale. As solar panel technology advances, the price of photovoltaics falls dramatically resulting in a surge in solar installations for both residential and utility-scale use. As a consequence, the price of solar energy has dropped from one of the most expensive to one of the most affordable. Although solar panels often generate excess electricity on most days, storing that energy for later use is not always a cost-effective solution. Thus, consumers typically rely on nonrenewable energy sources at night [68].

Utility-scale: Large-scale solar power plants that generate hundreds of megawatts of electricity and feed it into the grid are becoming the most cost-effective size for utility-scale operations [45]. However, it may be hard to find suitable land and transmission capacity. Several mid-size utility-scale installations are located closer to the load. As a result, utility-scale projects are essential for creating a diverse range of solar power options for different consumers.

Table 7
Summary of 100% renewable grid: challenges and solutions.

Challenge	Problem	Solutions
Power balance [49–57]	• Short-term resource variability and the late-afternoon netload ramps. • Diurnal mismatch • Seasonal mismatch	• Accurate forecasts of renewables and loads in shorter scheduling intervals can resolve uncertainty issues. • Shiftable load, demand response, and installing transmission network, diurnal storage, and non-VRE to match the diurnal supply/demand imbalance, • Shifting of VRE and load demand, advanced RE and load forecasting, expansion of the transmission system and geographic diversity are solving the seasonal issue.
Inverter [58–60,63,64]	• Low inertia • Power quality	• Inverter control with storage energy emulates virtual inertia to maintain frequency stability. • Droop-controlled inverter control active and reactive power.
Stability [65]	• Frequency instability • Transient and small-signal instability • Voltage instability	• Operational reserves such as solar, wind, and storage for the dispatch process. The prediction-based hierarchical converter controller designed for VRE to maintain the long-term frequency stability of the system. • Voltage source inverter with the suitable controller to provide both active and reactive power regulation • Volt/VAR management and resource optimization provides the required voltage.
Protection [66]	• Fault current/ over current	• Inverters with pre-programmed fault current, synchronous condensers and controllers in frequency, relays are more advanced protection schemes.
Unintentional Islanding and Black start [67]	• Intentional islanding during faults. • Restarting a grid	• Communication-based active anti-islanding solutions to achieve overall grid stability. • Voltage source inverter with the in-rush current.

Energy storage: However, these utility-scale plants cannot achieve their full potential without energy storage. Solar farms are capable of providing electricity on demand, not only when the sun is shining but also to compete with the reliability of fossil fuels. Lithium-ion batteries have traditionally been used for storage. Fortunately, the price of this technology is plummeting alongside the cost of solar panels. Both solar energy and battery storage systems are less expensive than a natural gas contract. However, lithium-ion batteries may not be considerably cheaper. Many experts predict that costs will eventually fall to approximately $70-$100 per kilowatt-hour. At current prices, Batteries will continue to be an affordable alternative for smoothing out hours-long gaps in solar production. However, they will not be a suitable choice for storing energy for weeks or months at a time, as this would massively increase consumers' electricity prices. Even though lithium-ion has made significant advances in technology, the way forward is to strive for even greater improvements. Researchers have recently been investigating flow batteries, which are liquid nickel-metal hydride batteries [69]. It is possible to operate a renewable-only system when roughly 20% of peak demand is available in storage devices. As prices drop and solar installation continues to rise, incentives and regulations encourage solar plant expansion.

4.1. Global solar power grid

Diverse geopolitical, market integration, and techno-economic considerations promote the need for higher voltage systems to be networked across nations and continents. Potential areas for renewable energy generation are scattered unevenly across the continent or around the world. Remote places have a high concentration of renewable energy potential. Local weather patterns also have a significant impact on renewable energy output. To efficiently utilize these resources, the existing power infrastructure must be improved to allow electricity to be transported to critical demand and storage centers. A more robust and flexible transmission system may be desirable for connecting distant power markets and leveraging the geographical and temporal complementary of low-carbon resources [70].

4.1.1. Global solar grid model

In general, if a power outage happens in one nation, the abrupt change in bus voltage and electric network frequency in the global grid could trigger a solar power generator in another country to compensate for the electricity shortfall. In this way, the global electricity grid concept ensures that all generated power must be consumed [22]. On the contrary, storing surplus energy would also prevent this issue. However, large-scale cost-effective energy storage is presently scarce. To optimize the utilization of available solar power generation capacity to meet global power demand, satellites are employed as a backup platform for data and communication exchange across electrical grids all over the world, as shown in Fig. 7. Satellite-based global grid power management can help with operations and maintenance while ensuring global grid stability.

4.1.2. HVDC link

All of the above factors may contribute to the development of a transcontinental high-capacity transmission system capable of transporting massive amounts of electricity over thousands of kilometers [71]. High voltage direct current (HVDC) technologies have the potential to be the foundations of such a global power system due to their lower losses and environmental effects. Bulk electricity export needs substantial reactive power support and a reliable link to the local grid. These criteria create a significant technological challenge in nations lacking a strong domestic power support infrastructure. Amid challenges in connectivity between power grids, HVDC technology allows energy operators to transfer power between grids and balance generation and consumption throughout the globe. A total of 100,000 km of HVDC power cable and 115 converter stations are required to build the global solar power grid. Therefore, high-capacity transmission lines need to be built to ease the exchange of more power across continents, as shown in Fig. 7 [72]. Due to the proliferation of carbon-free grids and the transfer of enormous amounts of power over great distances without substantial losses, high-rated 330MW HVDC converters with 1% conversion losses are installed at either end of the cable. SiC and GaN-based switching devices have recently been introduced for HVDC converters to reduce costs while increasing functionality [62]. Large-capacity circuit breakers with a short-circuit current of more than 60 kA should be developed for the HVDC transmission system to respond in milliseconds to detect faults. According to recent research, the superconducting

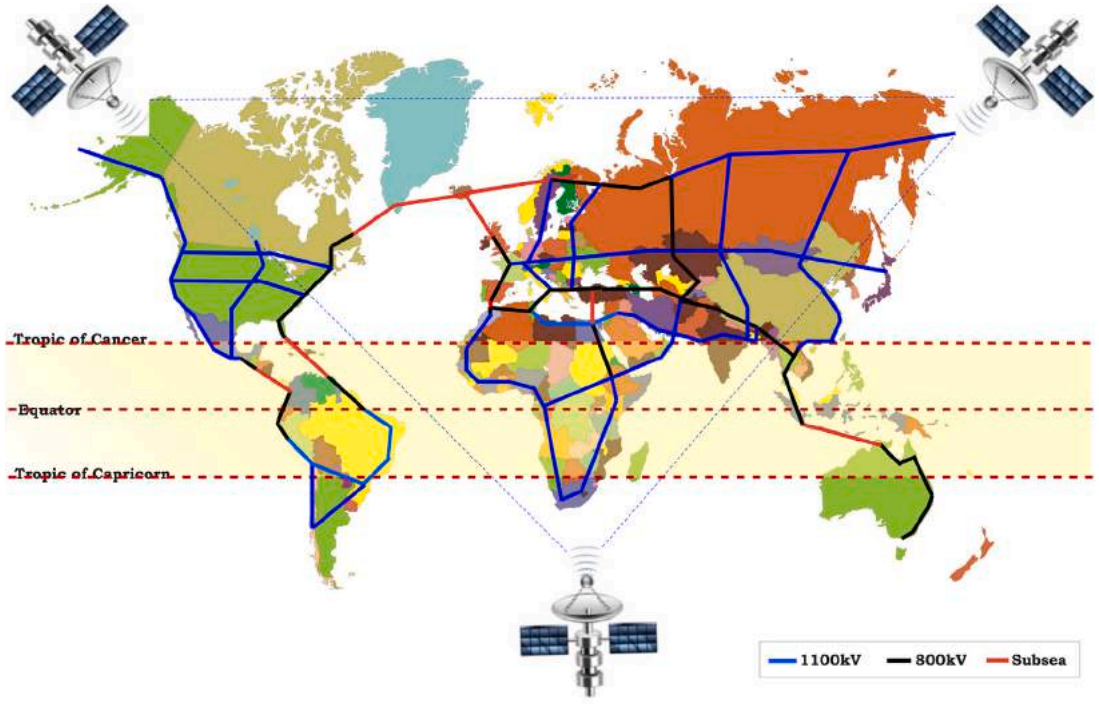

Fig. 7. The proposed interconnected transcontinental grid includes submarine HVDC power cable, and communication infrastructure. The sunny nations are highlighted in yellow.

cable can handle significantly higher voltage and power ratings with virtually no transmission losses, effectively replacing traditional copper or aluminum cable [73]. However, compared to conventional materials, these cables are more expensive. The feasibility and sustainability of an intercontinental green energy corridor that aims to synchronize the electricity produced by solar panels with conventional power stations on neighboring continents are being examined. An Ultra HVDC link in the voltage range of 800-1100-kV with a capacity of 3000–6400 MW is further required as a standardized system for the construction and integration of power transmission grids throughout the world. The techno-economic challenges for electricity trading through a submarine power cable should be investigated for the transcontinental electricity networks.

4.1.3. Satellite communication

An essential requirement for optimizing power flow between continents and successful power trading in energy markets is a high-speed communication service. Satellite communication is capable of managing solar grid operations in a dynamic environment and interactions with the world's main transcontinental grids with minimal latency. Using satellite time synchronization, the energy management system (EMS) at an electric utility control center manages the operations of the high voltage DC transmission grid to ensure that electricity is supplied to all continents at all times [74]. Grid conditions are monitored every few seconds at the EMS, and undesired circumstances are detected and communicated. Grid measurements must be visualized in real-time for successful grid operations. These real-time measurements have intelligently transformed into actionable information.

4.2. The future of solar photovoltaic system

A global solar electricity network is an ecosystem of interconnected renewable energy resources that are shared smoothly for global sustainability. This initiative aims to connect 200 countries through a common grid that will be used to transfer solar power. The sun is always present in some geographical regions, notwithstanding the motto "the sun never sets". The International Solar Alliance (ISA) was initiated in 2015 to meet climate change mitigation goals through "solarisation of the world". This launch aims to interconnect different regions, such as South-East Asia, the Middle East, Africa, South Asia, and other grids in the world to ensure steady and uninterrupted energy generation and transmission. ISA envisaged 121 sunny countries situated either completely or partly between the tropics of Cancer and Capricorn as its members as shown in Fig. 7. For this initiative, ISA is trying to help some member nations to install solar power. One of its initiatives is to deliver 1,000 GW of solar electricity to 1,000 million people by 2030 with a $1 billion investment [75]. In recent years, the solar PV industry has seen substantial growth with major milestones in cost reductions, off-grid installations, technology improvements, and the formation of solar energy organizations. Solar PV capacity expansions in leading countries have become more cost-effective due to R&D investment, deployment, and other government policies. As a result, solar photovoltaics will be one of the most rapidly expanding, mature, and cost-competitive renewable energy technology in the next decades. The estimations of solar PV deployment to meet Paris climate goals are shown in Table 8. Solar PV plants with a capacity of more than 8500 GW would be able to satisfy more than 25% of worldwide energy consumption by 2050. This power generation would minimize CO_2 emissions by 4.9 Gt, accounting for 21% of total emissions reductions in the energy sector. In 2030 and 2050, solar PV installations are expected to reach 2840 GW and 8519 GW, with annual solar PV additions of 270 GW and 372 GW, and the solar power share of global electricity

Table 8
Projected solar PV deployment to achieve Paris Climate targets [45].

Parameters	2030	2050
Total capacity to be installed (GW)	2480	8519
Total installation cost (USD/kW)	340–834	165–481
Levelized cost of electricity (USD/kWh)	0.02–0.08	0.01–0.05
Total power generation share (%)	13	25
Annual deployment (GW/yr)	270	372
Annual investment (USD billion/yr)	165	192
Employment	11.7	18.7
Energy related CO_2 emissions (Gt CO_2/yr)	24.9	9.8

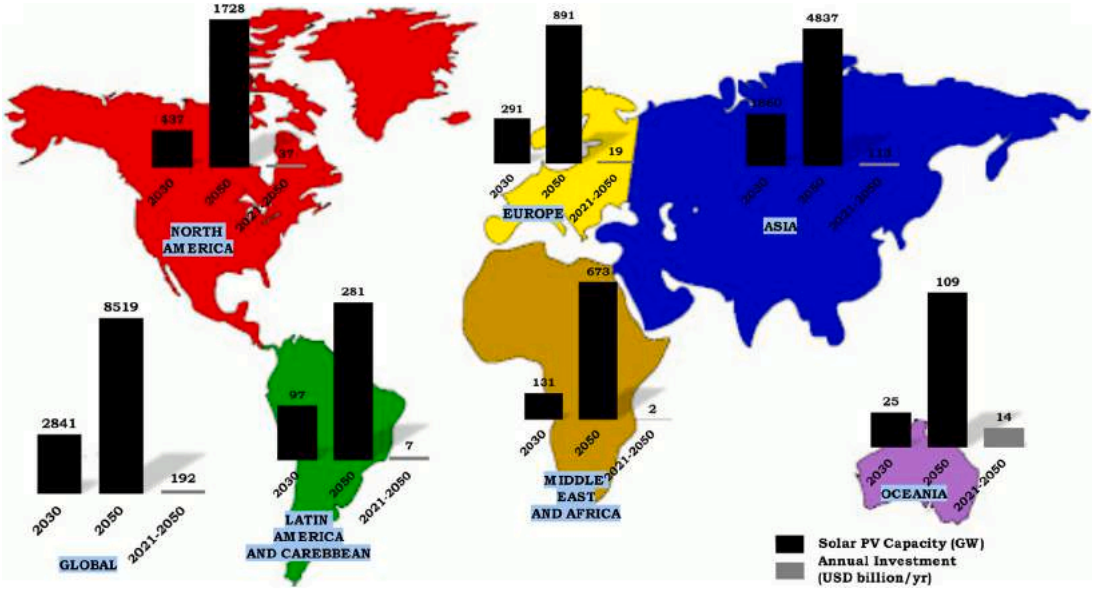

Fig. 8. Regional solar PV capacity (GW) installations with annual investments (USD billion/yr) [75].

generation to account for 13% and 25%, while installation costs fall to USD 834-340 per kW and USD 481–165 per kW, respectively. The dropping cost of technology has a significant impact on solar PV investment. Total expenditure of around USD 6.4 trillion and an annual investment of 192 billion per year will require for installing 8519 GW of solar PV as shown in Fig. 8. In terms of solar PV installations, Asia is anticipated to outperform the rest of the world, followed by North America and Europe. For a sustainable energy future, solar energy can meet a large part of the challenge of climate change, help displaces fossil fuels, and reduce carbon emissions [76].

4.3. Innovations and technological solutions

As the percentage of solar power approaches high levels in energy markets at the lowest cost, the fluctuating nature of solar resources will require significant modifications in the power system's operation. Adequate steps will be needed to guarantee the stability and reliability of the grid. Considering seasonal fluctuations in solar and wind power generation, changes to grid operation and management will be necessary on a minute-by-minute basis. According to IRENA, additional investments in transmission and distribution power systems, adequate power generation capacity, and flexibility mechanisms (such as storage) across the whole electrical network, amounting to USD 13 trillion by 2050 will be necessary to incorporate increased shares of variable renewable resources [39]. Batteries need to be integrated to ensure adequacy and flexibility in VRE systems. This comprises decentralized power generation with extra pumped hydropower capacity and battery storage, specialized utility-scale batteries, and EV batteries to support the grid via vehicle-to-grid (V2G) services. An estimated 14 TWh of electric vehicle batteries could be available to provide grid services [77]. Hydrogen is undoubtedly one of the developing technologies that have the potential to improve power system flexibility by functioning as seasonal storage and allowing high shares of variable renewables to be integrated. In total final energy consumption, there may be a worldwide economic potential for 19 EJ of hydrogen produced from clean energy. This would imply that by 2050, hydrogen production would account for 5% of total electricity consumption and 16% of total power production [78,79]. Incorporating a significant proportion of VRE into the power network, innovation is essential in all segments of the power sector. The optimal method for absorbing more VRE differs by country and environment. Solutions arising from the synergy between developments in all parts of the system would enable the creation of reliable and cost-effective power systems based on renewable energy. These developments offer a better solution that may be optimized to cut costs while enhancing system benefits. The innovation landscape for integrating high shares of VRE is presented in Fig. 9.

Enabling technologies such as battery storage, demand-side management, and digital technology are revolutionizing the power industry and paving the way for new applications that effectively improve flexibility. As a new market for renewables, end-use electrification is gaining traction. Innovative business models are essential for monetizing the additional value provided by these technologies. Numerous creative business models at the consumer level and innovative plans enable renewable energy distribution in off-grid or heavily inhabited areas. As the globe changes toward low-carbon power systems with large VRE shares, adapting market strategy to the evolving paradigm is critical for permitting value creation and suitable revenue streams. In addition, improvements in system operation are necessary with emerging technologies and sound market design in place. These developments include innovations that embrace uncertainty and novel system methods for incorporating DER [81].

4.3.1. Barriers and solutions to fostering solar PV deployment

The existing barriers at multiple levels, including technological, policy, economic, regulatory, and sociopolitical, may cause a slump in solar PV capacity expansion over the next three decades. It is essential to immediately mitigate these hurdles through several support policies and implementation approaches for boosting future deployment. To achieve a sustainable energy transition, deployment policies, integrating policies, and enabling policies must work together to eliminate the existing barriers [75,82].

Deployment policies: Long-term capacity mechanisms, support schemes, and adaptable policies are necessary to drive investment in solar PV technologies in response to changing market conditions. Renewable energy auctions are also employed to meet policy goals such as ensuring project completion on schedule, expanding solar PV capacity, and enabling a sustainable energy transition. For decarbonizing electricity generation, cost-effective PV deployment solutions are employed. Furthermore, renewable energy regulations help to overcome the challenges associated with increasing renewable energy investments. Third-party-owned pricing structures need to be created to promote residential solar PV growth. Through these models, consumers can invest in solar PV technology by acquiring or leasing a portion

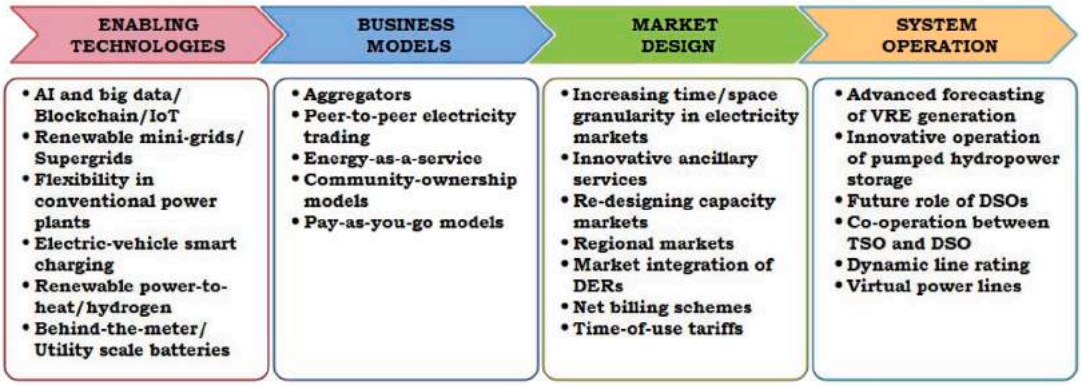

Fig. 9. High shares of VRE innovation scenario [80].

of a shared solar system. Companies should be permitted to further produce corporate renewable electricity for self-consumption and purchase options with energy suppliers so as to encourage corporate direct investment in solar PV installations [83].

Integrating policies The distributed energy resources at the consumer level should be deployed as roof-mounted solar PV, distributed energy storage, demand response, plug-in EVs, power-to-hydrogen, and power-to-heat systems, and should be supported by advanced digital technologies such as artificial intelligence, Internet of Things, blockchain, and big data mechanisms, and should be able to participate in wholesale electricity markets. Despite the unpredictability of solar PV generation, high voltage networks must be designed with an advanced weather forecasting system to generate and transmit power. They also strengthen the grid interconnections between countries, enhance energy access rates with renewable sources, and avoid renewable energy curtailment. To achieve rapid growth in future investment in solar PV deployment, the adverse social impacts that may occur during planning, construction, and operation and maintenance must be identified, examined, and mitigated well in advance. For maintaining the stability of investors and other stakeholders, installer training programs are needed to ensure the quality of solar PV installations. Community-based sustainable initiatives must also be incorporated from the beginning phases of solar PV development, operation, and equitable distribution. In future, PV systems can be included in the construction of new buildings to maximize installation space [84].

Enabling policies A transformation in enabling policies should drive the power industry to the forefront of the economy by promoting R&D funding in both public and private sectors and consumer awareness. Public investment should be targeted to stimulate the use of renewables, foster competitive conditions with lower energy prices, and create new jobs. Budgets should be reallocated and recycled to support universal healthcare, education, and other areas. Carbon tax revenue might be utilized for more job opportunities and alleviate the additional expenses on low-income households and small enterprises. Furthermore, technical development and training may equip the workforce with the essential skills while also assisting workers in reskilling from the petroleum industry to renewables, hence increasing local employment prospects [85].

In summary, existing impediments and potential solutions to expedite solar PV deployment are summarized in Table 9

Hence, total solar PV capacity is predicted to reach over 8519 GW globally by 2050, with capacity additions of 372 GW per year and an annual average investment of USD 192 billion per year. This would meet 25% of total power demands, making it a prominent generation source with an LCOE account of between USD 0.014 and 0.05/kWh. Among all low-carbon technological options, solar PV has the greatest potential to cut emissions by 4.9 Gt CO_2 in 2050 which accounts for 21% of carbon mitigation in the power sector. Competitive solar PV prizing and innovative business models are enabling the system price reductions. With sound policies, the transition can offer socio-economic benefits. As a result, harnessing the immense potential of solar PV is critical for meeting climate goals.

5. Greening the grid: Pathways to integrate RE into the electrical grid

For the transnational power system, VRE is expected to rise dramatically. According to the energy scenario, the world should achieve a global target of 8200 GW in installing renewable energy capacity by 2050 including 4439 GW of solar and 1654 GW of wind. Wind and solar energy can be incorporated into the grid at low levels successfully. However, they might pose some challenges to grid operations at higher levels due to the uncertainty of renewables [86]. The focus of this section is to assess strategies and operational challenges for high-RE systems. Furthermore, this section investigates the operational implications of attaining global RE targets and the steps required to integrate cost-effective VRE generation.

5.1. The global power system with high levels of RE at least cost

Forecasting strategies have been utilized for controlling demand variability and allowing the power system to operate efficiently. High-resolution meteorological data is used to capture the time- and location-specific characteristics of VRE generation. Using precise grid representations and RE inputs, the optimum scheduling and dispatch of available power reduce the overall production costs subject to physical, operational, and market constraints [87].

5.1.1. Capacity and location of the wind and solar

As weather determines the patterns and timing of VRE generation, it is impossible to predict the impacts of weather forecasting on load, wind, and solar generation at 15-minute time intervals for the whole year. Therefore, the typical approach is to base the future-year analysis on historical weather data. RE day-ahead forecasts will be used to make unit commitment decisions. RE forecasts are intended to be as precise as day-ahead forecasts in real life. With the knowledge of average wind speed and worldwide horizontal irradiation of the sun, a geospatial site suitability study with capacity estimation for utility-scale RE has been carried out. The best potential project sites have been identified from an existing RE pooling substation to locate suitable project sites. Several utility-scale solar, rooftop solar, and wind capacity expansions must be planned globally to achieve the global RE capacity targets [88].

5.1.2. Accessible transmission network

The Green Energy Corridor Project intends to synchronize VRE-generated electricity with conventional power plants in the grid. The power flow limits on transnational networks are estimated for the global study using total surge impedance loading limits. The linearized DC optimum power flow technique is used to compute power flows across continents [89].

Table 9
Summary of existing impediments and potential solutions to expedite solar PV deployment.

Existing Barriers	Solutions
(i) Technological Barriers [45,68]: • Inadequate capacity • Grid-flexibility problems • Grid-connection and integration issues • Architectural and spatial impediments	(i) Deployment Policies [83]: • Promote the expansion of the solar sector and market by implementing clear and well-designed incentive mechanisms. • Solar initiatives supported by the community
(ii) Market and Economic Barriers [62,73,75,76]: • Longer payback periods • Carbon-related emissions are not priced • Wholesale electricity is cheap in nations with limited irradiation	(ii) Integrating Policies [84]: (a) System Integration: • Enable DER to participate in established markets • Digital technologies • Advanced weather forecasting techniques (b) Social Integration: • Community engagement • Quality assurance mechanism (c) Urban Policies: • Spatial planning • Mandating solar installations in new buildings
(iii) Policy Barriers [54,75]: • Complex regulatory framework • Dearth of quality control mechanisms • Concerns regarding technological maturity and performance • Lack of long-term policy goals and a well-coordinated policy mix	(iii) Enabling Policies [85]: (a) Industrial: • Promote R&D strategies • Strengthen and maximize value creation (b) Financial: • Generate substantial income sources (c) Education and Skills: • Enhance support skills and supply chain development • Provide technical education and training • Promote workforce reskilling
(iv) Regulatory, Political, and Social Barriers [68,82]: • Scarcity of trained experts and experience • Inadequate standards and quality control methods • Lack of customer data on solar PV performance, cost competitiveness, and economics.	

5.1.3. The electricity demand

According to the World Energy Council, global power demand is expected to reach 193–244 petawatt hours (PWh) by 2050 [29]. The production cost model entails the simulation of a time series of loads at 15-minute intervals for the whole year 2050 based on the historical data for all countries. With an annual RE curtailment of 1.4 percent, this VRE capacity (4439 GW of solar and 1654 GW of wind) will meet 25% of the global power demand by 2050.

5.2. Operational impacts of 8200 GW RE

The annual energy flow on key corridors does not vary considerably, even though corridors usually transport electricity in both directions. Wind and solar energy contribute to overall generation. According to WES, the 6093 GW of solar and wind can generate 11.74 PWh of electricity annually resulting in a 25% penetration level of VRE (16.5% from solar and 8.5% from the wind).

5.2.1. Net load change

Steeper load ramps and lower overall generation levels during a period of high RE penetration are characterized as 'Netload'. The generator delivering the aggregate net load must be more flexible. Netload analysis can help in identifying periods that may be operationally challenging due to uncertain renewable profiles. To normalize the hourly net load ramps, the non-renewable capacity of all units is committed during the ramping period [90].

5.2.2. The effect of high RE penetrations on thermal power plant operations

The 6093 GW of solar and wind energy will displace 7.3 PWh of coal, representing an 84% decrease. Because of the reduction in coal generation, total annual CO_2 emissions will reach 19.1 Gt. As a consequence, CO_2 falls by 70% compared to the current level in the world energy scenario.

5.2.3. Impact of RE on exports and transnational power flows

Interstate energy exchange will decline in line with the trend of falling international imports and exports. However, with VRE, transnational energy interchange will become more common. The installation of 6093 GW VRE affects energy trade across continents. When compared to other nations, RE-rich countries have a huge volume of low variable-cost generation. Furthermore, the unpredictability of netload on a daily and hourly basis rises, increasing the importance of renewable energy interchange for balancing demand and generation across countries. In many instances, using the transmission system to transmit electricity to locations with higher-cost energy is the best option [91].

5.2.4. Curtailment of RE due to a variety of factors

RE curtailment can occur for several reasons, depending on the model objective of serving load at the lowest possible cost while complying with the system's physical and economic limits. The major factors in RE curtailment are transmission congestion, thermal and hydro inflexibility, start and stop costs, and trade barriers. To overcome this difficulty, experts employ a modeling technique called hurdle rates. A country with low-cost electricity generation can export energy to nearby countries if the difference is greater than the hurdle rate [92].

5.2.5. Managing the power system forecasting errors

When actual VRE generation varies from predicted generation, this is referred to as a forecasting error. Forecasting errors disrupt dispatch operations and force the power system to operate in real-time with limited resources to optimize electricity supply and demand. Underforecasting occurs when predicted generation is less than actual RE generation, whereas over-forecasting occurs when forecasted generation exceeds actual RE generation. Certain periods may cause reliability issues in a highly constrained system due to forecast errors. The planned generation fleet has sufficient capacity to manage RE forecast errors, fluctuations in net load (ramps), and low RE generation times of day and year. The reserve needs may benefit from being different according to the season or time of the day [93].

As a whole, the following strategies will significantly improve RE integration:

- The copper plate sensitivity is a representation of the projected transmission needs for the lowest-cost generator dispatch which results in peak power transfer and loop flows. It minimizes RE curtailment and production costs.
- Batteries can aid in the reduction of RE curtailment. However, due to inefficiencies, they have an insignificant impact on total generation costs and emissions.
- Operating large thermal plants at minimum generating levels is a key driver of RE curtailment reduction. Besides, changes in operational practice can reduce the power system's operational costs and minimize RE curtailment.
- If all renewable power plants utilize their inherent ramping capability, the ramp rate can be fulfilled.
- Hydroelectric generation's intrinsic flexibility helps to keep the system balanced.

Thus, power system balancing using VRE is possible with few integration issues, resulting in lower GHG emissions. Attaining present regulatory requirements for carbon flexibility, extending geographic and electrical balancing regions, expanding power transmission in important locations, and planning for future adaptability can enable the power system to operate efficiently and reliably in the future.

6. Global grid connectivity: Benefits, strategies, barriers, and challenges

The requirements for sustainable power provisions are energy transitions to low-carbon technologies, cost reductions in renewables, advancements in high-voltage transmission, and smart grid management. Although grid interconnection with renewable energy enables economic, environmental, and technical benefits, cross-border connectivity is fraught with difficulties in the areas of regulations, policies, standards, investment, energy security, information sharing, electricity trade, and technical and political factors [94].

6.1. Benefits in global power grid connectivity

Countries have a variety of energy resources, political systems, and market frameworks in place to enhance the environmental impacts of development, economic expansion, and energy security. The advantages of regional interconnected power networks are summarized in Fig. 10.

6.1.1. Environmental benefits

The Asia-Pacific region has diversified renewable energy resources, generation mixes, load profiles, and weather patterns. For instance, 750 GW of solar electricity from India, 240 GW of hydropower from ASEN, 32 GW of geothermal energy from Indonesia, 410 GW of wind energy, and 1150 GW of hydropower from South and South-West Asia are expected to satisfy the future power needs. Power export is enabled through cross-border power connectivity, which requires significant infrastructure support to increase the renewable energy share. Optimizing the energy mix and cross-border power trading can help to improve energy security by alleviating shortages and enhancing renewable energy access [96].

6.1.2. Technical and economical benefits

VRE cannot be scheduled to match instantaneous power demand due to its intermittency. Amid the development of renewables, the integration of non-dispatchable RE into power systems and compensation for stochastic fluctuations are two interrelated issues that need to be resolved to enhance reliable power supply. The output of VRE can be controllable to match the supply and demand across different timescales (minutes, days, and seasons). Transnational grid connectivity can enhance reliable electricity supply and minimize the economic value of renewable power curtailment. Robust grid connectivity and

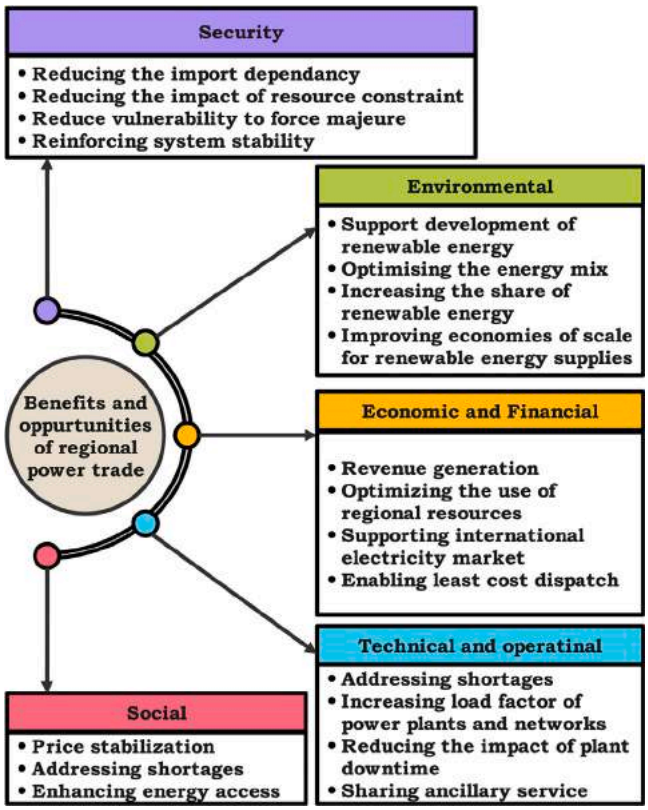

Fig. 10. Benefits of global power grid interconnection [95].

transnational electricity trade enable the least-cost power dispatch from generating units and ensure overall cost savings. Connected nations benefit from regional electricity trading and ancillary services. If one of the distributed generators fails, the spinning reserve refers to the generation capacity that is maintained in reserve yet prepared to respond immediately. Load diversification via interconnectivity greatly smoothes the entire network load profile. The reduced imbalances minimize the requirement for instant frequency responses and enable the distribution of spinning reserves among a broader range of customers lowering the service cost [97].

6.1.3. Energy security

Managing energy security concerns such as energy accessibility, self-sufficiency, supply dependability, demand and supply diversity, power continuity, price stability, and environmental effects necessitates the use of national and regional solutions. Besides, a more diversified generation mix enhances reliability by limiting supply outages. Higher diversity from geographic dispersion provides more security for renewable energy fluctuations. Sustainable energy development is also made possible via cross-border connectivity [98].

6.2. Challenges and barriers in global power grid connectivity

With environmental, social, economic, and energy security concerns, cross-border electricity trade necessarily requires infrastructure development, technical and regulatory standards harmonization, policy coordination, and information and data exchange, as seen in Fig. 11.

6.2.1. Policy, regulation and standards

Each country has its own set of power transmission regulations, standards, and grid codes. Diverse frameworks may impede the technical and financial coordination for cross-border connectivity. Therefore, gaps in standards, regulations, and policies must be identified and

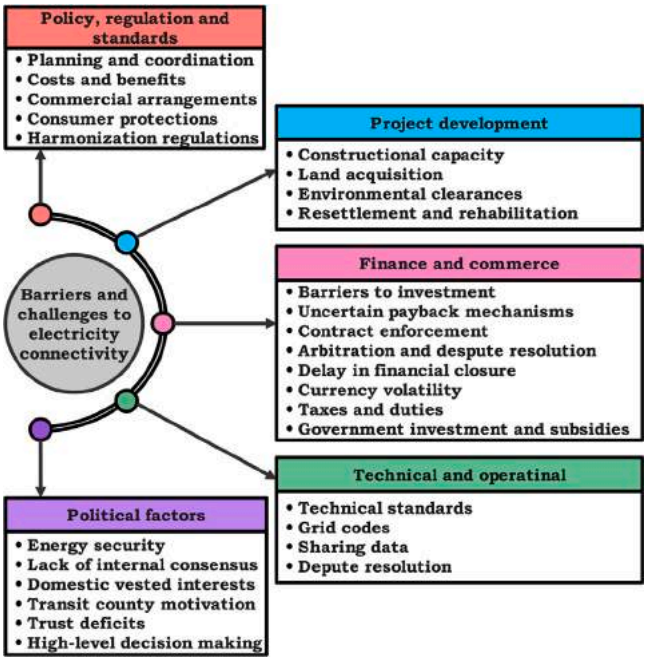

Fig. 11. Challenges and barriers to transcontinental grid connectivity [99,100].

rectified through extensive analysis of the interconnected transnational electricity network [101].

Planning and coordination: Transmission network infrastructure planning should be coordinated across nations, including technical specifications, financing, and scheduling in months or years.

Trade agreement: An integrated electricity market requires agreements on transmission service, power purchase, and secured payment mechanisms. Moreover, balanced, competitive, and transparent power markets with fair prizing procedures must be established for the electricity trade.

Costs, benefits, and risk: Develop methods for allocating costs, benefits, and risks between member nations.

Consumer protection: To appropriately distribute the benefits, a consumer protection policy must be devised and linked between protected customers and constituent nations.

Technical regulations and standards harmonization: For effective implementation of connectivity, energy producers, utilities, and system operators should harmonize international technical regulations and standards including alignment of metering codes, voltage, frequency, thermal limits, protection schemes, and ICT systems [102].

6.2.2. Technical factors

Technical standards like frequency and voltage, grid codes, and protective schemes are synchronized. Furthermore, data is shared promptly across member nations [103].

Alignment of standards and codes: Although the standards of frequencies may differ in member nations, frequency alignment (50/60 Hz) of the interconnected transmission system can be achieved to ensure interoperability or compatibility through either harmonization or conversion technique.

Strong electricity grid: Importing and exporting bulk electricity requires a robust transmission system with reactive power support, fault ride-through capabilities, contingency reserves, and system inertia.

Data sharing: Although certain countries have successfully adopted the smart grid, hybrid VRE power, and energy-saving projects, data is not managed globally. Intergovernmental organizations must maintain the member countries' available power sector information and update it regularly.

6.2.3. Political factors

Political instability, lack of trust and desire to collaborate among countries, and energy security concerns are major impediments in implementing regional interconnection initiatives [104].

Energy security: In an interconnected transmission network, technical faults or disruptions in one nation's grid cause grid failure in another country. Controlling the voltage and power flow in high-voltage DC transmission can alleviate this risk.

Internal disagreements: Low-cost renewable resources can be exported to countries with fewer renewable sources or retained for future domestic energy needs. However, large-scale energy storage is currently sparse. Estimates of the future energy demand and pricing result in varying weightings of the cost–benefit of energy trading.

Entrenched domestic interests: Regardless of the potential economic benefit of energy trading, politically powerful utilities may perceive an interconnection proposal as undermining their economic standing. Because of the risk of losing market share, power revenues, or strategic position, these organizations are likely to oppose grid interconnections across borders.

Motivation for transit nation: In many circumstances, electrical connectivity is not always confined to neighboring nations. Third-party nations may participate as "transit countries", offering right-of-way for transmission lines but not importing or exporting power. Due to a lack of political support, these partners do not perceive enough benefits from the initiative.

Deficits in trust: Because of a lack of trust among nations, there may be an absence of public and political support for power connectivity proposals to increase reliance on neighboring countries for substantial components of energy demands. However, with the successful integration of power networks in other parts of the globe, connectivity may be a helpful instrument for establishing trust and relationships among nations that expand to other regions of cooperation.

Decision-making at the highest levels: High-level decision-making on cross-border power connections is more challenging than many other difficulties, resulting in extended deadlines and project stalling.

Curbs in investment: Several nations have relaxed restrictions on foreign direct investment in electricity generation. However, investment in the transmission network is restricted to state-owned firms for expanding domestic transmission line. The overall economic situation of some countries makes obtaining competitive funding even more difficult because of uncertain payback mechanisms, contract law, resolving disputes, delays in financial closure, currency volatility, unfair taxes, and government interventions.

6.2.4. Project development

Beyond the technical, political, and investment considerations mentioned above, the green energy corridor project poses implementation challenges related to land acquisition and environmental clearance [105].

Land acquisition: With the influence on development timeframes, the framework, procedures, and expenses for acquiring land in nations may need to be accounted for in the project's cost–benefit analysis.

Environmental clearances, resettlement, and rehabilitation: In some nations, obtaining environmental permission, rehabilitation, and resettlement may be challenging. Before acquiring land for large-scale renewable deployment, social impact analyses may be required to determine the type of interest. Rehabilitation and resettlement might be significant in terms of the overall project budget.

6.3. Strategies of global grid connectivity

The roadmap for regional power system interconnection is presented in Fig. 12 for attaining the aim of SDG 7 to ensure reliable, affordable, and sustainable energy supply.

Trust and political consensus: Geopolitical problems and a lack of trust among many nations are critical impediments in strengthening cross-border connectivity and creating power trade. As a result, multinational

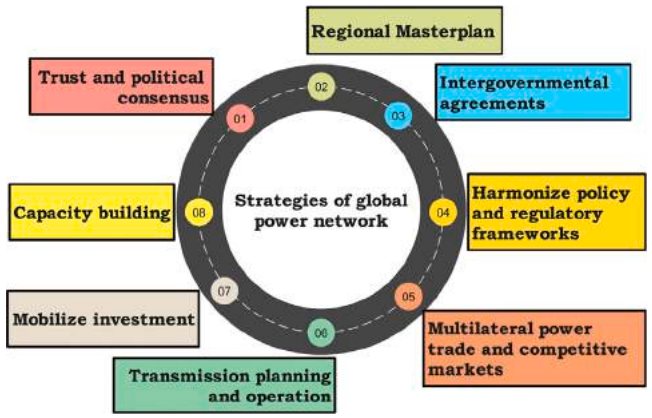

Fig. 12. Strategies of transnational grid interconnection [106].

corporations must make concerted action plans for integrated electricity networks on a global scale. Rebuilding trust for transcontinental power infrastructure should be sought by all nations, regardless of energy trade. This strategy is essential to raise awareness of the benefits across all segments of society and obtain support for the cross-border connectivity process [107].

Regional masterplan: Grid interconnection in some locations functions on a bilateral basis and is restricted in scope. To improve the connection for all locations throughout the world, it is essential to design and agree on a power network masterplan for the region's grid connectivity. The grid master plan should be created by the inclusion principle, considering stakeholders' concerns and demands [108].

Intergovernmental agreements: Multinational experiences of successful power pools exemplify the need for contracts among member nations to demonstrate each country's political commitment to fostering energy cooperation and integration within a defined time frame. If agreements are already in existence, member nations must ratify them and hasten their implementation [109].

Regulatory frameworks and harmonize policy: Policies, grid codes, standards, and regulations for electrical grids vary from country to country. It is critical to identify such gaps in each subregion through in-depth research and studies. Transparent and seamless electricity transactions necessitate a well-integrated market. Regulators in each subregion should create forums to facilitate regulatory harmonization, capacity-building, and information exchange. The electricity industry is to be tightly regulated to achieve grid stability. Synchronizing policies, regulations, and standards for intercontinental electricity trading are crucial [110].

Multilateral trade and competitive market: Shifting from bilateral to multilateral electricity trading is difficult in both countries. Moving this to a multilateral approach will assist nations in optimizing total regional power supplies, boosting economic growth, expanding renewable electricity generation, strengthening reliability, lowering prices, and contributing to the environmental sustainability of the power market. Furthermore, establishing attractive and transparent power purchase mechanisms with security procedures for a transit charge system for member nations will assist in accelerating cross-border connectivity and trade [111].

Transmission planning and operation: Transmission lines must be physically interconnected to allow electricity to be sent between several national grid networks. Grid codes such as metering codes, frequency and voltage standards, protection schemes, and thermal limitations must be harmonized to link two separate national power systems. To ensure a safe and reliable power flow, member nations and the technical institutions in each subregion must coordinate transmission planning, scheduling, metering connection, and protection schemes. Utility companies should design and build suitable power lines for energy transmission to support the cross-border connectivity projects, allowing developers unrestricted access to electricity [112].

Mobilize investment: Mobilizing investment is a challenge in the electricity sector since it is capital intensive with high risks and extended gestation periods. Most of the funding for cross-border electricity projects comes from IFIs, multinational banks, and state contributions. Therefore, it is critical to have investment-friendly regulations, standards, and frameworks to attract investment. These include removing impediments in the private sector and international investment, facilitating the land acquisition, relocation and resettlement processes, and obtaining planning permission [110].

Capacity building: Some nations have successfully implemented green power projects, smart grid initiatives, and energy efficiency projects. However, they have only limited capability for exchanging information and best practices through capacity-building. Intergovernmental organizations, multilateral financial institutions, and power utilities should develop capacity-building plans and share information. Leveraging expertise in new technologies, EV charging infrastructure, smart grid activities, massive solar power production, energy efficiency, and competitive bidding will enable to implement in all member countries [113].

6.4. Affordable and clean energy

Aspects of achieving SDG 7 from the perspective of energy access, including photovoltaic systems, wind farms, hydropower, lithium-ion batteries, electric vehicles, biodiesel, hydrogen fuel, microgrid, smart grid, energy efficiency, and internet of things, are taken into consideration [114–126]. The smart concepts of a planning tool, brown box, inertia controller, storage manager, and signaling framework can help power system operators in upgrading their traditional grids [127]. Forecasting, scheduling, and integrating renewables with Supervisory Control and Data Acquisition (SCADA) should be the focus of future interconnected intelligent electricity networks. Another promising area of study is to build a game-theoretic smart planning tool and a data-driven analysis for capacity planning, sizing, addition, and expansion of the network. Furthermore, several instances and case studies of mixed-energy systems should be investigated, with an emphasis being placed on the interaction between planning, operations, and cost of the cross-border electricity network [126].

Overall, the benefits, strategies, barriers, and challenges of global power grid connectivity are as follows:

- Despite the regional power trade (economic, environmental, and technical benefits), cross-border connectivity is plagued by issues such as regulations, policies, standards, investment, and energy security.
- Apart from the technical, political, and financial considerations, cross-border trade has implementation obstacles involving land acquisition and environmental clearance.
- Transnational grid interconnection ensures reliable, affordable, and sustainable energy supply.

Advancements in transnational electricity networks will provide more comprehensive advantages if they are connected with the sustainable development goals during the planning, implementation, and operational phases. Thus, the globally interconnected grid provides a reliable, affordable, and long-term electricity supply.

7. Discussion on future trends

In continuation of the above mentioned facts, it is evident that the development of renewables on a continental-scale will provide more than half of the world's power by 2050, because the costs of solar, wind, and energy storage will continue to decline [106,128,129]. Future research on the global clean energy system could focus on the following potential areas:

End-Use sector: Solar PV can help in the decarbonization of the building, transportation, and industrial sectors. Although temporary energy storage enables an extreme level of emission reduction, massive clean storage capacity is required to achieve global decarbonization in the power sector. Demand flexibility is crucial because it provides solid capacity while lowering the cost of decarbonization. More research is needed to breakthrough the barriers in optimizing solar PV, batteries, and load flexibility to achieve the corresponding private and grid advantages [130].

Building sector: Solar shingles, walls, windows, and rooftop-mounted PV continue to be a small niche market. More study is needed to increase the long-term sustainability of PV-integrated buildings and allied products such as PV coatings and glass. There is a need for research to identify techniques for dividing incentives to revitalize global PV markets. Further study on the pilot rate implementation of optimum retail tariffs for specific consumers, distributed resources, and rooftop solar PV technologies is needed [131].

Transportation sector: Coordination and control of an electric vehicle charging station with a photovoltaic power generation unit necessitate technological, business, and legislative solutions. One of the main topics in future research is to enable solar-to-EV-to-grid applications by withstanding more frequent charging and discharging cycles of batteries. Another prominent trend has been the combination of rapid charging technologies with solar power and storage. Thus, advanced technologies in the integration of electrolyzers with solar generation is one of the important directions in future research. The cost-competitive production of clean hydrogen will decrease the electrolysis investment costs, enhance efficiency, and reduce the solar electricity prices. One of the potential research areas to enable solar-to-FCEV-to-grid applications is the use of improved membrane and corrosion-resistant bipolar plate materials, reduction of platinum group metal catalysts, and improvement of control system schemes [132,133].

Industry sector: Industries must investigate several decarbonization strategies such as electrification, solar-powered fuels, and usage of carbon-free thermal energy. More studies might look at near-term cost reductions in a photoelectrochemical and thermochemical generation to develop innovative zero-carbon solar fuels. Furthermore, alternative energy sources such as ammonia for shipping, hydrogen, and synthetic hydrocarbons for aviation, as well as their distinct near- and long-term responsibilities, are mainstream developments. Further research into solar PV technology is required to solve social and political issues in polluting industries as well as tradeoffs in equity and environmental justice [134].

Utility-scale: One of the research trends is to realize terawatt-scale solar PV deployment on existing power infrastructure. Because of technology advancements, much of the deployment will take the form of large utility-scale power plants, as well as residential and business rooftop systems. Solar technology will enable the cost-effective deployment of buildings, water bodies, and agriculture. Further study should be conducted on the regional distribution of solar's resilience benefits, public benefits such as enhanced air quality and climate change mitigation, and electricity consumer benefits [135].

Technology advancements: Building continental-scale clean energy generation capacity and cross-border grid connections are critical challenges. Moreover, regulation of bidirectional power flow over power transmission networks is an important control challenge. Another technical challenge is optimizing the power flow from the most abundant and cheapest renewable energy to high energy consumption in real-time [136]. Therefore, the combination of clean energy interconnection, ultra-high voltage lines with protection devices, and advanced smart grid control is a future research area. One of the research trends is to identify the most cost-effective solution to operate the power system with more than 50% of VRE [137]. Uncertain power generation from VRE resources, low system inertia in inverter-based systems, and fluctuating load demand affect the stability of the power system. Therefore, the power balance between demand and supply, suitable control concepts in inverter-dominated systems, and power system stability should be the key focus of future research in clean energy networks. In addition, fault current and intentional islanding during a fault are major issues in renewable-dominated grid. Intelligent overcurrent protection schemes for detecting, as well as clearing faults and communication-based active anti-islanding methods, are potential areas for research [138,139].

Technical Development: Commercial crystalline silicon (c-si) wafer technology research aims to produce 400–550 W from 2.1–2.5 square meters with an efficiency of 19%–22%, to lower the cost of PV modules to around USD 0.17/W. The major tendency is to enhance efficiency in non-silicon-based thin-film technologies such as Perovskites, Copper Indium Gallium Selenide Cells, and Cadmium Telluride. To improve system output levels, further research should be focused on advanced cell architectures such as tandem, bifacial solar cells, half cells, multi-busbars, and solar shingles. Furthermore, Concentrating Solar Power (CSP) technology is another promising study option for meeting the aim of 50% net thermal-to-electrical efficiency and an LCOE of USD 50/MWh by 2030 [129,140].

8. Conclusion

The present review outlines the role of low-carbon technologies in the transformation of the global energy system to combat climate change. Developments in solar and other clean energy technologies have enabled a significant increase in deployment in the energy sector to decarbonize the global electricity system. Despite these advancements, many challenges have been addressed in this study for reaching 100% renewable electricity future. Conclusions and possible research directions can be formulated as follows:

- A global investment of up to 18 trillion USD in VRE technologies with a generating capacity of 6093 gigawatts is required to fulfill 25% of the total estimated electricity demand of 244 petawatt hours in 2050. This has been enabled through global renewable grid connections and breakthroughs in HVDC transmission technologies.
- Of all the low-carbon technology alternatives, solar PV has the highest potential to reduce emissions by 4.9 Gt CO2, accounting for 21% of the emission mitigation in the energy sector by 2050. From the findings of this study, cumulative solar deployment of 8519 GW would serve 25% of global electricity demand.
- Although the proposed global power grid connectivity has several impediments to solar PV development, innovations and technological solutions will foster the deployment of solar PV systems. Continued technological progress in solar is critical to achieving cost-effective and economy-wide grid decarbonization.
- Transcontinental grid connectivity would allow countries to not only trade electricity but also optimize the energy surpluses and deficits across the region based on future forecasts.
- For a sustainable energy future, unleashing the massive potential of solar PV can facilitate extensive decarbonization of the global electric grid to achieve sustainable development goals (affordable and clean energy) and climate targets by 2050 without raising expected electricity prices.
- Future studies should extend the precise approaches to accomplishing 100% emission reduction. SDG 7 achievement will catalyze measures to realize the Paris Climate Agreement.
- Future research directions include the interconnection of renewables with data centers, internet services, transportation, and cellular networks. Other essential aspects of a future renewable-supported intelligent electricity network include information security and user privacy.
- Maintaining resource adequacy, shifting net demand peaks, solar power curtailment, abatement costs and CO_2 emission implications, electricity pricing, energy storage, flexible demand, transmission, renewable capacity enhancement, extreme event analysis, and grid-integration issues are major future solar research directions.

CRediT authorship contribution statement

M. Jayachandran: Conception and design of study, Writing – original draft. **Ranjith Kumar Gatla:** Writing – review & editing. **K. Prasada Rao:** Writing – review & editing. **Gundala Srinivasa Rao:** Writing – review & editing. **Salisu Mohammed:** Writing – review & editing. **Ahmad H. Milyani:** Writing – review & editing. **Abdullah Ahmed Azhari:** Writing – review & editing. **C. Kalaiarasy:** Acquisition of data, Analysis and/or interpretation of data, Writing – original draft, Writing – review & editing. **S. Geetha:** Writing – review & editing.

Declaration of competing interest

The authors declare that they have no known competing financial interests or personal relationships that could have appeared to influence the work reported in this paper.

Data availability

No data was used for the research described in the article.

Acknowledgment

All authors approved the version of the manuscript to be published.

References

[1] Zou C, Zhao Q, Zhang G, Xiong B. Energy revolution: From a fossil energy era to a new energy era. Nat Gas Ind B 2016;3(1):1–11.
[2] Byrnes SJ, Blanchard R, Capasso F. Harvesting renewable energy from Earth's mid-infrared emissions. Proc Natl Acad Sci USA 2014;111:3927–32.
[3] Laratte B, Perminova T. New technology to improve the efficiency of photovoltaic cells for producing energy. Procedia Manuf 2017;7:358–63, International Conference on Sustainable Materials Processing and Manufacturing, SMPM 2017, 23-25 January 2017, Kruger.
[4] AL Shaqsi AZ, Sopian K, Al-Hinai A. Review of energy storage services, applications, limitations, and benefits. Energy Rep 2020;6:288–306, SI:Energy Storage - driving towards a clean energy future.
[5] Hamzaoglu A, Erduman A, Alçı M. Reduction of distribution system losses using solar energy cooperativity by home user. Ain Shams Eng J 2021;12(4):3737–45.
[6] Sørensen B. Chapter 26 - power transmission. In: Sørensen B, editor. Renewable energy conversion, transmission and storage. Burlington: Academic Press; 2007, p. 228–31.
[7] Hanna R, Victor DG. Marking the decarbonization revolutions. Nat Energy 2021;6(6):568–71.
[8] Williams JH, Jones RA, Torn MS. Observations on the transition to a net-zero energy system in the United States. Energy Clim Change 2021;2:100050.
[9] Blanco H, Faaij A. A review at the role of storage in energy systems with a focus on power to gas and long-term storage. Renew Sustain Energy Rev 2018;81:1049–86.
[10] Bhave VA, Rao AP, Mathur K. Micro-grid – generating green energy using renewable energy sources. In: 2019 Global conference for advancement in technology. 2019, p. 1–5.
[11] Monadi M, Rouzbehi K, Candela JI, Rodriguez P. Chapter 11 - DC distribution networks: A solution for integration of distributed generation systems. In: Gharehpetian G, Mousavi Agah SM, editors. Distributed generation systems. Butterworth-Heinemann; 2017, p. 509–61.
[12] Liu Z. Chapter 3 - characteristics of UHV DC transmission system. In: Liu Z, editor. Ultra-high voltage AC/DC grids. Boston: Academic Press; p. 95–132.
[13] Khalilpour KR. Chapter 6 - stranded renewable energies, beyond local security, toward export: A concept note on the design of future energy and chemical supply chains. In: Khalilpour KR, editor. Polygeneration with polystorage for chemical and energy hubs. Academic Press; 2019, p. 157–73.
[14] Zhao X, Liu Y, Wu J, Xiao J, Hou J, Gao J, et al. Technical and economic demands of HVDC submarine cable technology for global energy interconnection. Glob Energy Interconnect 2020;3(2):120–7.
[15] Chatzivasileiadis S, Ernst D, Andersson G. Chapter 12 - global power grids for harnessing world renewable energy. In: Jones LE, editor. Renewable energy integration. second ed.. Boston: Academic Press; 2017, p. 161–74.
[16] Rouzbehi K, Heidary Yazdi SS, Shariati Moghadam N. Power flow control in multi-terminal HVDC grids using a serial-parallel DC power flow controller. IEEE Access 2018;6:56934–44.
[17] Rafique SF, Shen P, Wang Z, Rafique R, Iqbal T, Ijaz S, et al. Global power grid interconnection for sustainable growth: concept, project and research direction. IET Gener, Transm Distrib 2018;12(13):3114–23.
[18] Come Zebra EI, van der Windt HJ, Nhumaio G, Faaij AP. A review of hybrid renewable energy systems in mini-grids for off-grid electrification in developing countries. Renew Sustain Energy Rev 2021;144:111036.
[19] Bogdanov D, Ram M, Aghahosseini A, Gulagi A, Oyewo AS, Child M, et al. Low-cost renewable electricity as the key driver of the global energy transition towards sustainability. Energy 2021;227:120467.
[20] Hua H, Qin Z, Dong N, Qin Y, Ye M, Wang Z, et al. Data-driven dynamical control for bottom-up energy internet system. IEEE Trans Sustain Energy 2022;13(1):315–27.
[21] Vakulchuk R, Overland I, Scholten D. Renewable energy and geopolitics: A review. Renew Sustain Energy Rev 2020;122:109547.
[22] Wu C, Zhang X-P, Sterling MJH. Global electricity interconnection with 100% renewable energy generation. IEEE Access 2021;9:113169–86.
[23] Mnisi J, Chowdhury SD, Ngoma L. Grid integration of solar PV for green energy. In: 2020 6th IEEE international energy conference. 2020, p. 782–6.
[24] Maruf MNI. Open model-based analysis of a 100% renewable and sector-coupled energy system–the case of Germany in 2050. Appl Energy 2021;288:116618.
[25] Gómez Sánchez M, Macia YM, Fernández Gil A, Castro C, Nuñez González SM, Pedrera Yanes J. A mathematical model for the optimization of renewable energy systems. Mathematics 2021;9(1).
[26] Aghahosseini A, Bogdanov D, Barbosa LS, Breyer C. Analysing the feasibility of powering the Americas with renewable energy and inter-regional grid interconnections by 2030. Renew Sustain Energy Rev 2019;105:187–205.
[27] Chatzivasileiadis S, Ernst D, Andersson G. The global grid. Renew Energy 2013;57:372–83.
[28] World Meteorological Association, et al. WMO atlas of mortality and economic losses from weather, climate and water extremes (1970–2019). Tech. rep., Technical Report; 2021.
[29] Frei C, Whitney R, Schiffer H-W, Rose K, Rieser DA, Al-Qahtani A, et al. World energy scenarios: Composing energy futures to 2050. In: Conseil Francais de L'Energie. 2013.
[30] Gielen D, Boshell F, Saygin D, Bazilian MD, Wagner N, Gorini R. The role of renewable energy in the global energy transformation. Energy Strategy Rev 2019;24:38–50.
[31] Ramirez-Sanchez E, Evangelista-Palma G, Gutierrez-Navarro D, Kammen DM, Castellanos S. Impacts and savings of energy efficiency measures: A case for Mexico's electrical grid. J Cleaner Prod 2022;340:130826.
[32] Bogdanov D, Gulagi A, Fasihi M, Breyer C. Full energy sector transition towards 100% renewable energy supply: Integrating power, heat, transport and industry sectors including desalination. Appl Energy 2021;283:116273.
[33] Dolf G, Ricardo G, Nicholas W, et al. Global energy transformation: A roadmap to 2050. International Renewable Energy Agency; 2019.
[34] García-Olivares A, Solé J, Osychenko O. Transportation in a 100% renewable energy system. Energy Convers Manage 2018;158:266–85.
[35] Dolf G, Ricardo G, Nicholas W, et al. Global energy transformation: A roadmap to 2050. International Renewable Energy Agency; 2018.
[36] Moghaddasi H, Culp C, Vanegas J. Net zero energy communities: Integrated power system, building and transport sectors. Energies 2021;14(21):7065.
[37] Widera B. Renewable hydrogen implementations for combined energy storage, transportation and stationary applications. Thermal Sci Eng Prog 2020;16:100460.
[38] Cozzi L, Gould T, Bouckart S, Crow D, Kim T, Mcglade C, et al. World energy outlook 2020, Vol. 2050. 2020, p. 1–461.
[39] Gielen D, Gorini R, Wagner N, Leme R, Prakash G, Ferroukhi R, et al. Global renewables outlook: Energy transformation 2050. Tech. Rep., Abu Dhabi, United Arab Emirates: Int. Renew. Energy Agency; 2020.
[40] Agency IE. World energy investment 2021. OECD Publishing; 2021.
[41] Sepulveda NA, Jenkins JD, de Sisternes FJ, Lester RK. The role of firm low-carbon electricity resources in deep decarbonization of power generation. Joule 2018;2(11):2403–20.
[42] Tarancon MA, Del Río P. Assessing energy-related CO2 emissions with sensitivity analysis and input-output techniques. Energy 2012;37(1):161–70, 7th Biennial International Workshop "Advances in Energy Studies".
[43] Gao Y, Gao X, Zhang X. The 2 °C global temperature target and the evolution of the long-term goal of addressing climate change—From the united nations framework convention on climate change to the Paris agreement. Engineering 2017;3(2):272–8.
[44] Bouckaert S, Pales AF, McGlade C, Remme U, Wanner B, Varro L, et al. Net zero by 2050: A roadmap for the global energy sector. 2021.
[45] Renewable power generation costs in 2019. Abu Dhabi: International Renewable Energy Agency; 2020.
[46] Garcia-Casals X, Ferroukhi R, Parajuli B. Measuring the socio-economic footprint of the energy transition. Energy Transit 2019;3:105–18.
[47] Denholm P, Arent DJ, Baldwin SF, Bilello DE, Brinkman GL, Cochran JM, et al. The challenges of achieving a 100% renewable electricity system in the United States. Joule 2021;5(6):1331–52.
[48] Kroposki B, Johnson B, Zhang Y, Gevorgian V, Denholm P, Hodge B-M, et al. Achieving a 100% renewable grid: Operating electric power systems with extremely high levels of variable renewable energy. IEEE Power Energy Mag 2017;15(2):61–73.

[49] Olauson J, Ayob MN, Bergkvist M, Carpman N, Castellucci V, Goude A, et al. Net load variability in nordic countries with a highly or fully renewable power system. Nat Energy 2016;1(12):1–8.
[50] Jain S, Kumar Jain N, Choudhary P, Vaughn W. Designing terawatt scale renewable electricity system: A dynamic analysis for India. Energy Strat Rev 2021;38:100753.
[51] Hansen J, Knudsen J, Kiani A, Annaswamy A, Stoustrup J. A dynamic market mechanism for markets with shiftable demand response. IFAC Proc Vol 2014;47(3):1873–8, 19th IFAC World Congress.
[52] Frazier AW, Cole W, Denholm P, Machen S, Gates N, Blair N. Storage futures Study: Economic potential of diurnal storage in the US power sector. Tech. rep., National Renewable Energy Lab.(NREL), Golden, CO (United States); 2021.
[53] Zeyringer M, Price J, Fais B, Li P-H, Sharp E. Designing low-carbon power systems for Great Britain in 2050 that are robust to the spatiotemporal and inter-annual variability of weather. Nat Energy 2018;3(5):395–403.
[54] Papaefthymiou G, Dragoon K. Towards 100% renewable energy systems: Uncapping power system flexibility. Energy Policy 2016;92:69–82.
[55] Dowling JA, Rinaldi KZ, Ruggles TH, Davis SJ, Yuan M, Tong F, et al. Role of long-duration energy storage in variable renewable electricity systems. Joule 2020;4(9):1907–28.
[56] Hasanuzzaman M, Kumar L. Chapter 4 - energy supply. In: Hasanuzzaman M, Rahim NA, editors. Energy for Sustainable Development. Academic Press; 2020, p. 89–104.
[57] Malik H, Fatema N, Iqbal A. Chapter 9 - intelligent data analytics for time-series load forecasting using fuzzy reinforcement learning (FRL). In: Malik H, Fatema N, Iqbal A, editors. Intelligent data-analytics for condition monitoring. Academic Press; 2021, p. 193–213.
[58] Song X, Cai H, Jiang T, Sennewald T, Kircheis J, Schlegel S, et al. Research on performance of real-time simulation based on inverter-dominated power grid. IEEE Access 2021;9:1137–53.
[59] Zuo Y, Yuan Z, Sossan F, Zecchino A, Cherkaoui R, Paolone M. Performance assessment of grid-forming and grid-following converter-interfaced battery energy storage systems on frequency regulation in low-inertia power grids. Sustain Energy, Grids Networks 2021;27:100496.
[60] Jayachandran M, Kalaiarasy C. Power-domain NOMA for massive connectivity in smart grid communication networks. In: Proceedings of international conference on power electronics and renewable energy systems. Springer; 2022, p. 205–12.
[61] Jayachandran M, Ravi G. MPC-based power quality solution using energy storage technology for PV based islanded microgrids. In: Recent advances in manufacturing, automation, design and energy technologies. Springer; 2022, p. 843–51.
[62] Jayachandran M, Reddy C, Padmanaban S, Milyani A, et al. Operational planning steps in smart electric power delivery system. Sci Rep 2021;11(1):1–21.
[63] Lin Y, Eto JH, Johnson BB, Flicker JD, Lasseter RH, Villegas Pico HN, et al. Research roadmap on grid-forming inverters. Tech. rep., National Renewable Energy Lab.(NREL), Golden, CO (United States); 2020.
[64] Buraimoh E, Davidson IE. Comparative analysis of the fault ride-through capabilities of the VSG methods of microgrid inverter control under faults. In: 2019 Southern African universities power engineering conference/robotics and mechatronics/pattern recognition association of South Africa. 2019, p. 400–5.
[65] Ela E, Milligan M, Kirby B. Operating reserves and variable generation. Tech. rep., Golden, CO (United States): National Renewable Energy Lab.(NREL); 2011.
[66] Li R, Booth C, Dyśko A, Roscoe A, Urdal H, Zhu J. Protection challenges in future converter dominated power systems: Demonstration through simulation and hardware tests. In: International conference on renewable power generation. 2015, p. 1–6.
[67] Kroposki B. Summarizing the technical challenges of high levels of inverter-based resources in power grids. Tech. rep., Golden, CO (United States): National Renewable Energy Lab.(NREL); 2019.
[68] Aly A, Moner-Girona M, Szabó S, Pedersen AB, Jensen SS. Barriers to large-scale solar power in Tanzania. Energy Sustain Dev 2019;48:43–58.
[69] Sánchez-Díez E, Ventosa E, Guarnieri M, Trovò A, Flox C, Marcilla R, et al. Redox flow batteries: Status and perspective towards sustainable stationary energy storage. J Power Sources 2021;481:228804.
[70] Ul-Haq A, Jalal M, Sindi HF, Ahmad S. Energy scenario in south Asia: Analytical assessment and policy implications. IEEE Access 2020;8:156190–207.
[71] Lew D, Bakke J, Bloom A, Brown P, Caspary J, Clack C, et al. Transmission planning for 100% clean electricity: Enabling clean, affordable, and reliable electricity. IEEE Power Energy Mag 2021;19(6):56–66.
[72] Sun J, Li M, Zhang Z, Xu T, He J, Wang H, et al. Renewable energy transmission by HVDC across the continent: system challenges and opportunities. CSEE J Power Energy Syst 2017;3(4):353–64.
[73] Thomas H, Marian A, Chervyakov A, Stückrad S, Salmieri D, Rubbia C. Superconducting transmission lines – sustainable electric energy transfer with higher public acceptance? Renew Sustain Energy Rev 2016;55:59–72.
[74] Ayiad M, Maggioli E, Leite H, Martins H. Communication requirements for a hybrid VSC based HVDC/AC transmission networks state estimation. Energies 2021;14(4):1087.
[75] IRENA–International Renewable Energy Agency. Future of solar photovoltaic: Deployment, investment, technology, grid integration and socio-economic aspects. United Arab Emirates: IRENA–International Renewable Energy Agency Abu Dhabi; 2019.
[76] Solaun K, Cerdá E. Climate change impacts on renewable energy generation. A review of quantitative projections. Renew Sustain Energy Rev 2019;116:109415.
[77] Anisie A, Boshell F, Mandatova P, Martinez M, Giordano V, Verwee P. Innovation outlook: Smart charging for electric vehicles. In: IRENA. 2019.
[78] Kakoulaki G, Kougias I, Taylor N, Dolci F, Moya J, Jäger-Waldau A. Green hydrogen in Europe –A regional assessment: Substituting existing production with electrolysis powered by renewables. Energy Convers Manage 2021;228:113649.
[79] Gielen D, Taibi E, Miranda R. Hydrogen: A renewable energy perspective. Abu Dhabi: International Renewable Energy Agency; 2019.
[80] Guerra K, Haro P, Gutiérrez R, Gómez-Barea A. Facing the high share of variable renewable energy in the power system: Flexibility and stability requirements. Appl Energy 2022;310:118561.
[81] Innovation landscape for a renewable-powered future. Abu Dhabi: International Renewable Energy Agency; 2019.
[82] Yu HJJ, Geoffron P. Chapter 13 - solar PV market and policies. In: Gorjian S, Shukla A, editors. Photovoltaic solar energy conversion. Academic Press; 2020, p. 413–37.
[83] Pitelis A, Vasilakos N, Chalvatzis K. Fostering innovation in renewable energy technologies: Choice of policy instruments and effectiveness. Renew Energy 2020;151:1163–72.
[84] Ozoegwu C, Mgbemene C, Ozor P. The status of solar energy integration and policy in Nigeria. Renew Sustain Energy Rev 2017;70:457–71.
[85] yin Mah DN, Wang G, Lo K, Leung MK, Hills P, Lo AY. Barriers and policy enablers for solar photovoltaics (PV) in cities: Perspectives of potential adopters in Hong Kong. Renew Sustain Energy Rev 2018;92:921–36.
[86] Impram S, Varbak Nese S, Oral B. Challenges of renewable energy penetration on power system flexibility: A survey. Energy Strategy Rev 2020;31:100539.
[87] Cole W, Gates N, Mai T. Exploring the cost implications of increased renewable energy for the U.S. power system. Electr J 2021;34(5):106957.
[88] Zappa W, van den Broek M. Analysing the potential of integrating wind and solar power in Europe using spatial optimisation under various scenarios. Renew Sustain Energy Rev 2018;94:1192–216.
[89] Ebeed M, Kamel S, Jurado F. Chapter 7 - optimal power flow using recent optimization techniques. In: Zobaa AF, Abdel Aleem SH, Abdelaziz AY, editors. Classical and recent aspects of power system optimization. Academic Press; 2018, p. 157–83.
[90] Mladenov V, Chobanov V, Georgiev A. Impact of renewable energy sources on power system flexibility requirements. Energies 2021;14(10):2813.
[91] DeSantis D, James BD, Houchins C, Saur G, Lyubovsky M. Cost of long-distance energy transmission by different carriers. IScience 2021;24(12):103495.
[92] Child M, Kemfert C, Bogdanov D, Breyer C. Flexible electricity generation, grid exchange and storage for the transition to a 100% renewable energy system in Europe. Renew Energy 2019;139:80–101.
[93] Chu Y, Pedro HT, Kaur A, Kleissl J, Coimbra CF. Net load forecasts for solar-integrated operational grid feeders. Sol Energy 2017;158:236–46.
[94] Burke MJ, Stephens JC. Political power and renewable energy futures: A critical review. Energy Res Soc Sci 2018;35:78–93, Energy and the Future.
[95] Brinkerink M, Gallachoir BO, Deane P. A comprehensive review on the benefits and challenges of global power grids and intercontinental interconnectors. Renew Sustain Energy Rev 2019;107:274–87.
[96] Chen F, Huang K, Hou Y, Ding T. Long-term cross-border electricity trading model under the background of global energy interconnection. Global Energy Interconnect 2019;2(2):122–9.
[97] Ismail AG, El-Dabah MA, Nassar IA. Enhancement of electrical distribution networks performance using the load management methodology. Energy Rep 2020;6:2066–74.
[98] Stroink A, Diestelmeier L, Hurink JL, Wawer T. Benefits of cross-border citizen energy communities at distribution system level. Energy Strategy Rev 2022;40:100821.
[99] Medeiros E, Ferreira R, Boijmans P, Verschelde N, Spisiak R, Skoniezki P, et al. Boosting cross-border regions through better cross-border transport services. The European case. Case Stud Transport Policy 2021;9(1):291–301.
[100] Christodoulou A, Christidis P. Bridges across borders: A clustering approach to support EU regional policy. J Transport Geogr 2020;83:102666.
[101] Nouri A, Khadem S, Mutule A, Papadimitriou C, Stanev R, Cabiati M, et al. Identification of gaps and barriers in regulations, standards, and network codes to energy citizen participation in the energy transition. Energies 2022;15(3):856.
[102] Surak JG. Chapter 20 - harmonization of international standards. In: Boisrobert CE, Stjepanovic A, Oh S, Lelieveld HL, editors. Ensuring Global Food Safety. San Diego: Academic Press; 2010, p. 339–51.
[103] Ul-Haq A, Hassan MS, Jalal M, Ahmad S, Anjum MA, Khalil IU, et al. Cross-border power trade and grid interconnection in SAARC region: Technical standardization and power pool model. IEEE Access 2019;7:178977–9001.
[104] Ralph N, Hancock L. Energy security, transnational politics, and renewable electricity exports in Australia and southeast Asia. Energy Res Soc Sci 2019;49:233–40.

[105] Mazzocchi C, Orsi L, Sali G. Environmental, climate and socio-economic factors in large-scale land acquisitions (LSLAs). Clim Risk Manag 2021;32:100316.
[106] ESCAP U. Electricity connectivity roadmap for Asia and the Pacific: Strategies towards interconnecting the region's grids. United Nations; 2019.
[107] Li S, Chang Y-C. Legal issues regarding energy market integration in northeast Asia. Energy Strategy Rev 2021;38:100700.
[108] Becker W, Domínguez-Torreiro M, Neves AR, Tacão Moura C, Saisana M. Exploring the link between Asia and europe connectivity and sustainable development. Res Glob 2021;3:100045.
[109] Glass LT, Schlachta CM, Hawel JD, Elnahas AI, Alkhamesi NA. Cross-border healthcare: A review and applicability to North America during COVID-19. Health Policy OPEN 2022;3:100064.
[110] West CD, Stokeld E, Campiglio E, Croft S, Detges A, Duranovic A, et al. Europe's cross-border trade, human security and financial connections: A climate risk perspective. Clim Risk Manag 2021;34:100382.
[111] Antweiler W. Cross-border trade in electricity. J Int Econ 2016;101:42–51.
[112] Chen Y-K, Koduvere H, Gunkel PA, Kirkerud JG, Skytte K, Ravn H, et al. The role of cross-border power transmission in a renewable-rich power system – A model analysis for Northwestern Europe. J Environ Manag 2020;261:110194.
[113] Bhagwat PC, Richstein JC, Chappin EJ, Iychettira KK, De Vries LJ. Cross-border effects of capacity mechanisms in interconnected power systems. Util Policy 2017;46:33–47.
[114] Hakimi SM, Hasankhani A, Shafie-khah M, Catalão JP. Demand response method for smart microgrids considering high renewable energies penetration. Sustain Energy, Grids Networks 2020;21:100325.
[115] Singh D, Sharma D, Soni S, Sharma S, Kumar Sharma P, Jhalani A. A review on feedstocks, production processes, and yield for different generations of biodiesel. Fuel 2020;262:116553.
[116] Elberry AM, Thakur J, Santasalo-Aarnio A, Larmi M. Large-scale compressed hydrogen storage as part of renewable electricity storage systems. Int J Hydrogen Energy 2021;46(29):15671–90.
[117] Faye O, Szpunar J, Eduok U. A critical review on the current technologies for the generation, storage, and transportation of hydrogen. Int J Hydrogen Energy 2022;47(29):13771–802.
[118] Hoelzen J, Silberhorn D, Zill T, Bensmann B, Hanke-Rauschenbach R. Hydrogen-powered aviation and its reliance on green hydrogen infrastructure – review and research gaps. Int J Hydrogen Energy 2022;47(5):3108–30, Hydrogen Energy and Fuel Cells.
[119] Gürsan C, de Gooyert V. The systemic impact of a transition fuel: Does natural gas help or hinder the energy transition? Renew Sustain Energy Rev 2021;138:110552.
[120] Fekete H, Kuramochi T, Roelfsema M, den Elzen M, Forsell N, Höhne N, et al. A review of successful climate change mitigation policies in major emitting economies and the potential of global replication. Renew Sustain Energy Rev 2021;137:110602.
[121] Wen W, Yang S, Zhou P, Gao S. Impacts of COVID-19 on the electric vehicle industry: Evidence from China. Renew Sustain Energy Rev 2021;144:111024.
[122] Jiang Z. Installation of offshore wind turbines: A technical review. Renew Sustain Energy Rev 2021;139:110576.
[123] Yue M, Lambert H, Pahon E, Roche R, Jemei S, Hissel D. Hydrogen energy systems: A critical review of technologies, applications, trends and challenges. Renew Sustain Energy Rev 2021;146:111180.
[124] Olabi A, Abdelkareem MA. Renewable energy and climate change. Renew Sustain Energy Rev 2022;158:112111.
[125] Kebede AA, Kalogiannis T, Van Mierlo J, Berecibar M. A comprehensive review of stationary energy storage devices for large scale renewable energy sources grid integration. Renew Sustain Energy Rev 2022;159:112213.
[126] Jayachandran M, Rao KP, Gatla RK, Kalaivani C, Kalaiarasy C, Logasabarirajan C. Operational concerns and solutions in smart electricity distribution systems. Util Policy 2022;74:101329.
[127] Raj BD, Kumar S, Padhi S, Sarkar A, Mondal A, Ramamritham K. Brownout based blackout avoidance strategies in smart grids. IEEE Trans Sustain Comput 2021;6(4):586–98.
[128] Henderson J, Sen A. The energy transition: Key challenges for incumbent and new players in the global energy system. Tech. rep., 2021, OIES Paper: ET.
[129] Jones-Albertus B. Solar futures study. U.S. Department of Energy; 2021.
[130] Jayachandran M, Ravi G. Predictive power management strategy for PV/battery hybrid unit based islanded AC microgrid. Int J Electr Power Energy Syst 2019;110:487–96.
[131] Biyik E, Araz M, Hepbasli A, Shahrestani M, Yao R, Shao L, et al. A key review of building integrated photovoltaic (BIPV) systems. Eng Sci Technol, Int J 2017;20(3):833–58.
[132] Ghotge R, van Wijk A, Lukszo Z. Off-grid solar charging of electric vehicles at long-term parking locations. Energy 2021;227:120356.
[133] Robledo CB, Oldenbroek V, Abbruzzese F, van Wijk AJ. Integrating a hydrogen fuel cell electric vehicle with vehicle-to-grid technology, photovoltaic power and a residential building. Appl Energy 2018;215:615–29.
[134] Gray N, McDonagh S, O'Shea R, Smyth B, Murphy JD. Decarbonising ships, planes and trucks: An analysis of suitable low-carbon fuels for the maritime, aviation and haulage sectors. Adv Appl Energy 2021;1:100008.
[135] Strbac G, Pudjianto D, Aunedi M, Papadaskalopoulos D, Djapic P, Ye Y, et al. Cost-effective decarbonization in a decentralized market: The benefits of using flexible technologies and resources. IEEE Power Energy Mag 2019;17(2):25–36.
[136] Jurasz J, Canales F, Kies A, Guezgouz M, Beluco A. A review on the complementarity of renewable energy sources: Concept, metrics, application and future research directions. Sol Energy 2020;195:703–24.
[137] Gils HC, Scholz Y, Pregger T, Luca de Tena D, Heide D. Integrated modelling of variable renewable energy-based power supply in Europe. Energy 2017;123:173–88.
[138] Usama M, Mokhlis H, Moghavvemi M, Mansor NN, Alotaibi MA, Muhammad MA, et al. A comprehensive review on protection strategies to mitigate the impact of renewable energy sources on interconnected distribution networks. IEEE Access 2021.
[139] Elshrief YA, Helmi DH, Abd-Elhaleem S, Abozalam BA, Asham AD. Fast and accurate islanding detection technique for microgrid connected to photovoltaic system. J Radiat Res Appl Sci 2021;14(1):210–21.
[140] Kuhn TE, Erban C, Heinrich M, Eisenlohr J, Ensslen F, Neuhaus DH. Review of technological design options for building integrated photovoltaics (BIPV). Energy Build 2021;231:110381.

Energy Reports 8 (2022) 13766–13779

Contents lists available at ScienceDirect

Energy Reports

journal homepage: www.elsevier.com/locate/egyr

Research paper

Solving the environmental/economic dispatch problem using the hybrid FA-GA multi-objective algorithm

Masoud Dashtdar [a], Aymen Flah [b,*], Seyed Mohammad Sadegh Hosseinimoghadam [a], Ch. Rami Reddy [c], Hossam Kotb [d], Kareem M. AboRas [d], Elżbieta Jasińska [e], Michał Jasiński [f]

[a] Electrical Engineering Department, Bushehr Branch, Islamic Azad University, Bushehr, Iran
[b] Processes, Energy, Environment, and Electrical Systems (code: LR18ES34), National Engineering School of Gabès, University of Gabès, Tunisia
[c] Electrical and Electronics Engineering, Malla Reddy Engineering College (A), Maisammaguda, Secunderabad 500100, India
[d] Department of Electrical Power and Machines, Faculty of Engineering, Alexandria University, Alexandria, Egypt
[e] Department of Operations Research and Business Intelligence, Wrocław University of Science and Technology, 50-370 Wroclaw, Poland
[f] Faculty of Electrical Engineering, Wroclaw University of Science and Technology, 50-370 Wroclaw, Poland

ARTICLE INFO

Article history:
Received 31 May 2022
Received in revised form 30 August 2022
Accepted 5 October 2022
Available online xxxx

Keywords:
Economic dispatch
Optimization
Operating costs
Emission of pollution
FA-GA algorithm

ABSTRACT

The emissions of polluting gases due to the consumption of fossil fuels in power plants have caused that in addition to operating costs, minimizing the amount of pollution in power plants is also given special attention. In this study, the hybrid firefly algorithm (FA) and genetic algorithm are used to solve the problem of environmental economic dispatch (EED) of power between thermal power plants in order to reduce operating costs and environmental pollution while accounting for the nonlinear constraints of power plants such as the effect of a steam valve, prohibited zones of generation, and generation change rate of plants (GA). Basing on the advantageous of these two optimization algorithms, the proposed application have make a combination between these algorithms and have concluded to have a hybrid FA-GA multi-objective algorithm, which can resolve this complicate optimization problem. The algorithm starts with a set of fireflies that are randomly distributed in the problem space, and these particles converge to the optimal solution of the problem during the evolutionary stages. Then a local search plan is presented and implemented as a way to search the neighborhood to improve the quality of the answers. This part of the algorithm is used to search for sparsely populated areas to find the dominant answers. To improve the algorithm, changes have been made in the criteria for determining the best global optimum for each firefly, as well as the best local optimum. The use of this method has increased the uniformity of the Pareto curve Finally, the suggested algorithm is applied on the 39-bus IEEE system by specifying the indices of losses, voltage stability, and emission of pollutants in the multi-objective problem and its results show its proper performance in comparison with other methods. Actually, the proposed control application have conducted to observe the minimum cost and gaz emission face five other conventional used algorithms.

1. Introduction

The economic dispatch (ED) of power is one of the most important issues in the operation of the power system. The purpose of this issue is to minimize the cost of fuel by optimally allocating the generation of each power plant in addition to providing the load required by the system. Fossil power plants, on the other hand, are one of the most important sources of environmental pollution and emit a wide range of pollutants from fossil fuels. The main gases produced in power plants include sulfur dioxide (SO_2), nitrogen oxides and their compounds (NO_x), carbon dioxide (CO_2), carbon monoxide (CO), suspended particles, and ozone. The first four are directly related to the consumption of fuel and ozone as chemical pollutants that are later formed in the air. Each of these gases is not only harmful to humans but also plants, animals, and the environment, causing adverse changes in the Earth's climate pattern. Given the limitations of the widespread use of clean energy sources for electricity generation, the use of fossil fuels, and the emission of pollutant gases from it, it seems inevitable. For this reason, it is necessary to reduce the emissions

* Corresponding author.
E-mail addresses: dashtdar.masoud@gmail.com (M. Dashtdar), aymen.flah@enig.u-gabes.tn (A. Flah), ms_hosseinimoghadam@yahoo.com (S.M.S. Hosseinimoghadam), crreddy229@mrec.ac.in (C.R. Reddy), hossam.kotb@alexu.edu.eg (H. Kotb), kareem.aboras@alexu.edu.eg (K.M. AboRas), elzbieta.jasinska@pwr.edu.pl (E. Jasińska), michal.jasinski@pwr.edu.pl (M. Jasiński).

https://doi.org/10.1016/j.egyr.2022.10.054

of these gases in fossil power plants, given the harms of these pollutants and the sensitivity of public opinion to their increase. The influence of gaz emission on the environment is remarquable and many scientific reports have given the related challenges for this decade (Thalassinos et al., 2022; Zhang et al., 2022; Li et al., 2022). There are various strategies to reduce the pollution of these power plants that can be divided into the following four categories (Li et al., 2022; Mutlaq, 2019; Dashtdar et al., 2020b; Ziane et al., 2017; Najafi et al., 2019; Bhattacharyya and Anusuya, 2022; Tian et al., 2017):

- Installation of equipment for cleaning or filtering pollutants at the site of power plants.
- Replacing old equipment with new and up-to-date equipment.
- Use of renewable sources including wind turbines and solar cells.
- Operation of power plants taking into account environmental pollutants.

The first three options require the installation of new equipment or the modification of the existing structure of power plants, which requires a high investment, so it is considered in long-term planning (Beigvand et al., 2017; Feng et al., 2021). However, introducing environmental considerations in the operation of power plants, which is presented in the form of ED of power taking into account environmental pollutants, is a short-term planning method in which, in addition to generation costs, the amount of pollutant emissions is also minimized (Benalcazar et al., 2019; Dashtdar et al., 2022; Espinosa-Juárez et al., 2019). There are various solutions to consider the pollution of power plants in the process of ED. This kind of environmental economic dispatch (EED) is called nonlinear multi-objective optimization.

In the past, most ED problems were solved in such a way that the main function was the cost of generators and the issue of pollutant emissions was considered a constraint. Today, attempts are made to solve such problems with the help of multi-objective problems, and various multi-objective methods have been proposed to solve these problems.

1.1. State of art

The EED solution method can be divided into classical and evolutionary categories. Analytical methods (Krishnamurthy et al., 2017; Liang et al., 2017), Lagrange (Chen et al., 2016; Wu et al., 2020; Marwan et al., 2021; Hosseinimoghadam et al., 2020; Narvaez et al., 2018), and Newton Raphson (Khan et al., 2016; Li et al., 2017; Xu et al., 2017) were among the first proposed methods to solve this problem that falls into the classical category. By more realistic modeling, the problem and taking into account the practical constraints of power plants increase the complexity of the problem so that it is not possible to achieve the desired answer using these methods. For this reason, in recent years, evolutionary methods have been used to solve this problem. Evolutionary methods such as genetic algorithm (Bora et al., 2019; Dashtdar et al., 2020a, 2021; Pattanaik et al., 2018; Ponciroli et al., 2020), particle swarm optimization (PSO) (Abbas et al., 2017a; Al Bahrani and Patra, 2017; Abbas et al., 2017b), artificial bee colony (ABC) (Sen and Mathur, 2016; Aydin et al., 2017), and differential evolution (Zou and Gong, 2022; Neto et al., 2017; Jena et al., 2016) have been proposed to solve the ED problem by considering pollution in terms of performance speed and the accuracy is different.

In traditional multi-objective methods based on analysis, they tried to find a set of insurmountable solutions using mathematical programming and turning the problem into a one-objective problem using nonlinear optimization to solve the problem. The disadvantage of these methods is that if all weights are positive, insurmountable solutions are obtained, but not all optimal solutions of the Pareto can be found unless all the objective functions, such as the acceptable region, are convex. In addition, many different sets of weights may produce the same solution and reduce efficiency. In methods based on metaheuristic algorithms, the goal is to improve the Pareto answer set. The most important difference between these algorithms is the modeling method and achieving the optimal solution set. Pareto answers here are the optimal combinations of power plants and their generation rate to achieve the minimum simultaneous objectives of the problem. The advantage of getting a Pareto answer set is that it does not focus on the optimization of a combination, because in practice it may not be possible to access a particular combination, but the Pareto answer set allows the central operator or decision-maker to use other options as well. Traditional methods, on the other hand, generally focus on single-objective economic modeling or tend to find the optimal point by using multi-objective optimization. One of the most common and widely used algorithms in solving nonlinear problems is the PSO algorithm, the main feature of which is the particle-free cooperation in which particles in a population exchange information among themselves.

1.2. Problematic and proposed solution

Since PSO cannot be used directly for multi-objective optimization, two issues need to be considered when using PSO in a multi-objective problem. The first issue is how to select the best local and global particles to guide the search for particles, and the second issue is how to maintain the appropriate points that have been found so far. A new way to solve this problem is to use the FA algorithm. This algorithm has two differences and advantages over the PSO algorithm: 1. Local attractions, 2. Automatic grouping. As the intensity of light decreases with distance, depending on the coefficient of gravity, the attraction among fireflies can be local or global, and thus all local, as well as global states, are examined.

By taking into account the criteria of the index of loss, voltage stability, and pollution in the transmission network, the issue of EED is given in this study as a combining cost and pollution functions of power plants. A novel combination approach employing the FA algorithm, GA algorithm, and local search is given and its implementation procedures are discussed in order to solve the associated multi-objective mathematical model using the advantageous of this combination for solving the knowed problems in relation to the PSO or FA unique.

1.3. Methodology

In the proposed method, in addition to the changes made to the FA algorithm, a new method is proposed to perform a local search around potential answers. In this method, we start with a potential answer, search around it based on a creative heuristic, and then move on to another potential answer. We do this until either the time limit for the local search is violated or get the answer is considered. To demonstrate and evaluate the efficiency of the proposed algorithm, the 39-bus IEEE system has been used and the results of solving the EED problem in different cases have been analyzed. The framework of the article is as follows: in the second part, the problem formulation and constraints are defined, in the third part the structure of the proposed hybrid algorithm for solving the problem is described, and in the fourth part the simulation results are presented and finally in the fifth part the conclusion the plan is expressed.

2. Formulation of the eed problem

In the problem of EED, the goal is to control the cost of fuel and pollution from power plants at the same time. This issue is presented as an optimization problem in which the objective function is obtained by combining the functions of fuel cost and pollution of power plants and various constraints are considered to solve it. In addition, to improve the problem, indexes such as losses, voltage stability, and pollution removal can be added to the problem. In the ED problem, the operating cost of each power plant is expressed in terms of its output power. Given that the cost of fuel is the most basic factor in the cost of power plants, usually, the operation cost function of power plants units is expressed based on the cost of fuel input, which in most cases is a quadratic function in terms of the active output power of the power plant unit; Therefore, the generation cost function of power plants is defined by Eq. (1):

$$F_C = \sum_{i=1}^{M} \left(a_i P_i^2 + b_i P_i + c_i\right) \tag{1}$$

Where M is the number of power plants in the system circuit, a_i, b_i, and c_i are the coefficients of the generation cost of the ith unit, P_i is the generation power of the ith unit and F_C is the generation cost ($). Considering the effect of steam valve position in power plant units causes the cost function to become a non-convex function. This effect is usually modeled as Eq. (2) by adding a sine sentence to the cost function.

$$F_C = \sum_{i=1}^{M} \left(a_i P_i^2 + b_i P_i + c_i + \left|e_i \sin\left(f_i\left(P_i^{min} - P_i\right)\right)\right|\right) \tag{2}$$

Where e_i, f_i is the recursive coefficient of the cost function for modeling the effect of the steam valve and P_i^{min} is the lower limit of ith unit generation. Fig. 1 shows the effect of the steam valve on the power plant generation curve. Because the main pollution of power plants is due to the production of NO_x and SO_2 gases, for this reason, it is necessary to reduce the pollution of power plants to minimize the emission of these gases. Studies show that the most important factor influencing the number of pollutant gases emitted from power plants is their active output power. The relationship between the pollution of a power plant and its active output power is a nonlinear relationship that can be modeled as a quadratic function of output power in Eq. (3).

$$F_E = \sum_{i=1}^{M} \left(A_i P_i^2 + B_i P_i + C_i\right) \tag{3}$$

Where A_i, B_i, and C_i are the pollution function coefficients ith unit and F_E is the total system pollution (kg). Finally, the objective function that should be minimized in the EED problem is obtained by combining the fuel cost function and the pollution function as Eq. (4):

$$F_T = w \times \sum_{i=1}^{M} \left(a_i P_i^2 + b_i P_i + c_i + \left|e_i \sin\left(f_i\left(P_i^{min} - P_i\right)\right)\right|\right) + (1-w) \times \sum_{i=1}^{M} h_i \left(A_i P_i^2 + B_i P_i + C_i\right) \tag{4}$$

Here, w is the reduction weight coefficient of the fuel cost, and h_i is the pollution penalty coefficient ith unit. The pollution penalty coefficient can have different values according to the operator's point of view and the value of pollution. In research, various methods have been proposed to define this coefficient, the most common of which is the pollution penalty coefficient for each generation unit is defined as the amount of fuel cost divided by the amount of pollution in the maximum output power of that unit as Eq. (5).

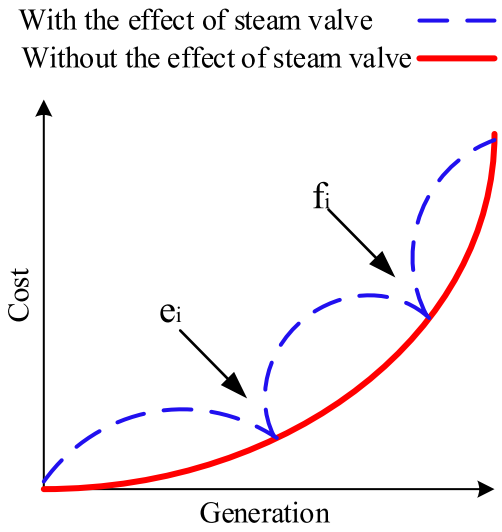

Fig. 1. Power plant generation curve.

$$h_i = \frac{a_i Pmax_i^2 + b_i P_i^{max} + c_i}{A_i Pmax_i^2 + B_i P_i^{max} + C_i}, \qquad \text{for } i = 1, \ldots, M \tag{5}$$

To improve the accuracy of the defined model and achieve better performance of the proposed method, indicators can be added to the problem. These indicators will include power losses, voltage stability, and pollution costs. After calculating the network power flow and obtaining the final values of voltages and currents, the active losses are calculated from Eq. (6):

$$P_{Loss} = \sum_{i=1}^{N_B} \sum_{j=1}^{N_B} Y_{ij} \left[V_i^2 + V_{i,j}^2 - 2V_i V_{i,j} \cos\left(\delta_i - \delta_j\right)\right] = \sum_{i=1}^{M} \sum_{j=1}^{M} P_i B_{ij} P_j + \sum_{i=1}^{M} B_{0i} P_i + B_{00} \tag{6}$$

Where N_B is the number of buses, V_i is the value of the bus voltage i, Y_{ij} is the value of ijth of the element of the admittance matrix, δ_i is the value of the angle of the phase voltage and δ_j is the angle value of the element ijth of the admittance matrix. B_{ij}, B_{oi}, and B_{00} are the coefficients of the network loss function that are obtained directly using the network impedance matrix.

The voltage stability index (VSI) is the ability of the system to maintain the voltage of the buses at an acceptable level. This feature controls the voltage and power when the normal load of the system increases and as a result, the active power injected into the network also increases. The voltage stability index is a numerical voltage between [0,1], which the closer this index is to one, indicates the stability of the network. To calculate the network voltage stability index, first using Eq. (7) this index is calculated for each bus, and finally, the minimum value of the index in the buses is considered as the system voltage stability index.

$$VSI_{m2} = |V_{m1}|^4 - \left\{4\left[P_{m2}X_i - Q_{m2}R_i\right]^2\right\} - \left\{4\left|V_{m1}\right|^2\left[P_{m2}R_i + Q_{m2}X_i\right]\right\} \tag{7}$$

Where i is the network line number, R_i and X_i are the resistance and reactance of line i, and V_{m1} is the bus voltage m1, respectively. In a two-bus system, as shown in Fig. 2, P_{m2} and Q_{m2} are the total active and reactive loads fed by the bus m_2, respectively.

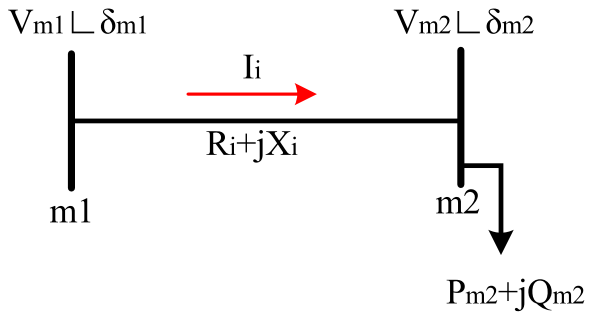

Fig. 2. Two-bus sample system.

To extend this relationship to wide area networks and calculate VSI_{m2}, which is the voltage stability index for bus m2 (m2 = 2,3,…, N), the active and reactive power of bus m2 will be changed so that: P_{m2} is equal to the sum of the total active load passing through the bus m2 (the sum of the active loads consumed in the bus after the bus m2 to the end of the line or lateral branch) and the active load consumed in the same bus. Q_{m2} is equal to the sum of the total reactive load passing through the bus m2 (the sum of the reactive loads consumed in the bus after the bus m2 to the end of the line or lateral branch) and the reactive load consumed in the same bus.

In addition, the cost of pollutant treatment (C_E) can be calculated through Equation (8).

$$C_E = \sum_{i=1}^{M} \sum_{k} C_k \gamma_k P_i \tag{8}$$

Here k is the type of pollutant emitted by the power plant (NO_x, SO_2), C_k is the cost of treatment of the type k pollutant per kg, and γ_k is the emission coefficient of type k pollutant. Now, the losses (P_{Loss}) and voltage stability (VSI) indices can be added to the problem with the coefficient w according to the dependence on the F_C function and the pollutant treatment cost (C_E) according to the dependence on the F_E function with the coefficient 1-w. In the following, the problem constraints, which are often the same constraints governing the power flow problem, are defined.

2.1. Problem constraints

To consider the real conditions in the power system, the balance of power in the system must be considered as a constraint. In this case, the total generation power of units is obtained through Equation (9). Where P_D is the system load demand.

$$\sum_{i=1}^{M} P_i = P_D + P_{Loss} \tag{9}$$

Restrictions on the generation of power plants include the limitation on the generation of the active power of generators, which is expressed in Eq. (10). Where P_i^{min} and P_i^{max} show the minimum and maximum active power output of each power plant unit, respectively.

$$P_i^{min} \le P_i \le P_i^{max} \tag{10}$$

The unequal constraint on the rate of increase or decrease in a generation is raised in more advanced models of the ED problem, but because classical methods are still applicable by applying this constraint, they can also be considered in the classical form of the problem. The power output of power plants cannot change abruptly for any value and cannot be increased or decreased immediately to another value. For this reason, for power plants, the amount of allowable changes in output power per time is determined and expressed as the generation rate. The rate of change in power output of units depends on their mechanical and thermodynamic characteristics. These constraints are given in Eq. (11) and Eq. (12) for the cases of increasing and decreasing generation, respectively.

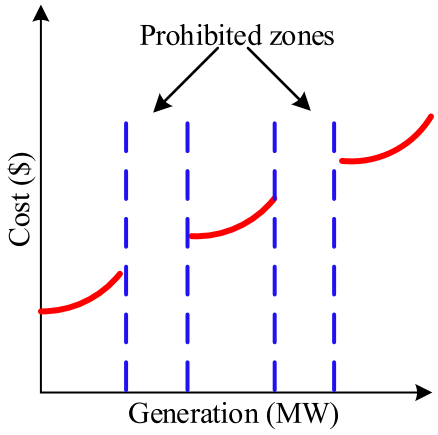

Fig. 3. The effect of prohibited zones on the fuel cost function of the power plant.

$$P_i - P_i^0 \le UR_i \tag{11}$$

$$P_i^0 - P_i \le DR_i \tag{12}$$

Where P_i^0 is the initial value of generation or its current state and UR_i and DR_i are the rate of increase and decrease of generation of unit *i*th, respectively. This constraint affects Eq. (10) and converts it to Eq. (13).

$$max\left(P_i^{min}, P_i^0 - DR_i\right) \le P_i \le min\left(P_i^{max}, P_i^0 + UR_i\right) \tag{13}$$

Another practical limitation of power plants is the prohibited zones. This performance is due to the technical operation of power plants (problems in accessories such as pumps and boilers) during generation. As a result, power plant units cannot generate power in all the ranges introduced in Eq. (10). Therefore, a generator has a non-continuous fuel cost curve for prohibited zones. This constraint is modeled by applying Eq. (14) to Eq. (16).

$$P_i^{min} \le P_i \le P_{i,1}^{LB}, \qquad i = 2, 3, \ldots, N_{PZi} \tag{14}$$

$$P_{i,k-1}^{UB} \le P_i \le P_{i,k}^{LB}, \qquad i = 2, 3, \ldots, N_{PZi} \tag{15}$$

$$P_{i,k}^{UB} \le P_i \le P_i^{max}, \qquad i = 1, 2, \ldots, N_{GPZ} \tag{16}$$

Where $P_{i,k}^{LB}$, and $P_{i,k}^{UB}$ are the upper and lower bounds of the prohibited zone *k*th of the generator *i*th, respectively, and N_{PZi} is the number of prohibited zones of generator *i*th and N_{GPZ} is the number of electric power generators within the prohibited operating zones. The non-continuous fuel cost curve of the generator to the prohibited operating zones is shown in Fig. 3.

Voltage limit in buses and power flow limit in network transmission lines are considered as network security constraints and are expressed as Eq. (17) and Eq. (18).

$$V_i^{min} \le V_i \le V_i^{max}, \qquad i = 1, 2, \ldots, N_B \tag{17}$$

$$LF_k \le LF_k^{max}, \qquad k = 1, 2, \ldots, N_L \tag{18}$$

Where V_i, V_i^{min}, V_i^{max}, and N_B are the bus voltage, the minimum and maximum voltage of each bus, and the number of network buses, respectively. LF is the power flow rate per transmission line, LF_k^{max} is the maximum transmission power per *k*th line and N_L is the number of transmission lines in the network.

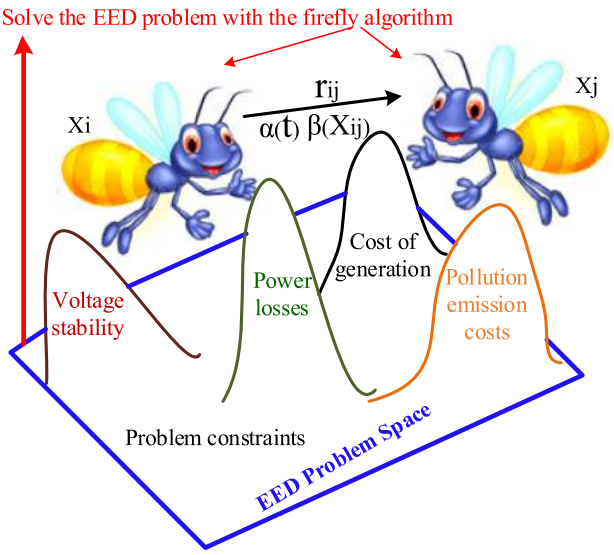

Fig. 4. The general space of the problem.

2.2. Multi-objective problem definition

In an optimization problem with objective O, the objective function of the problem can be defined as Eq. (19). In the case of the EED problem, these goals include reducing generation costs, pollution, and losses, and improving the voltage stability of the network.

$$\begin{cases} \min \vec{F}\left(\vec{x}\right) = \left[F_i\left(\vec{x}\right), i = 1, 2, \ldots, O\right] \\ Problem\ constraints: g_j\left(\vec{x}\right) \le 0, j = 1, 2, \ldots, J \end{cases} \tag{19}$$

Here, F(x) vector is the same as the functions defined in Section 2 of the article, and g_j is the same as the constraints presented in Section 2.1. Finally, the problem of multi-objective optimization leads to finding the vector x in such a way as to optimize F(x). Since the concept of optimal response in multi-objective optimization is different from single-objective optimization, the concept of Pareto dominance should be used to evaluate solutions, for which there are two definitions.

In the first definition, the concept of Pareto dominance is such that to optimize Eq. (19), the U_i vector overcomes the V_i vector, if and only if Eq. (20) holds.

$$\forall i \in \{i, \ldots, N\}, u_i \le v_i \Lambda \exists i \in \{i, \ldots, N\} : u_i \ll v_i \tag{20}$$

In the second definition, the concept of Pareto Optimality is that the solution u ∈ U is the Pareto optimal if and only if there is no other solution such as v ∈ U that the vector u is dominated by the vector v. In this case, the solution u is called the non-dominated solution. In this case, the non-dominated solution is said that improve the values produced by one or more objective functions of this problem to reduce the quality of the values produced by other objective functions of the same problem. The set of all non-dominated solutions obtains the optimal set of Pareto. Without additional information, all Pareto optimal solutions are equally good and considered equal.

According to the complete description of the dimensions of the defined problem, according to Fig. 4, we are faced with a multi-objective problem. In this paper, a combination of FA and GA algorithms is used to solve the problem, which the third part of the paper, the structure of the proposed algorithm will be presented.

3. The proposed algorithm to solve the multi-objective eed problem

Meta-heuristic algorithms are one the effective methods for solving complex problems that do not require the calculation of the gradient of the objective function and do not consider special assumptions such as linearity or continuity, and in most cases, provide acceptable answers. The firefly algorithm is one of the meta-heuristic algorithms with the group and collective approach that uses the lighting behavior of fireflies to solve optimization problems. The firefly algorithm like PSO is a population-based random search algorithm. If we put Xi = (x_{i1}, x_{i2},…, x_{iD}), where Xi is the ith firefly in the population, i = 1,2, .., N where N is the population and D is the dimension size. For both fireflies, i ≠ j, their attractiveness is calculated by Eq. (21).

$$\beta\left(r_{ij}\right) = \beta_0 e^{-\gamma r_{ij}^2} \tag{21}$$

Here β_0 is the attractiveness for $r = 0$ and γ is the coefficient for light absorption and r_{ij} is the distance between x_i and x_j and is calculated as Eq. (22).

$$r_{ij} = \left\|X_i - X_j\right\| = \sqrt{\sum_{d=1}^{D}\left(X_{id} - X_{jd}\right)^2} \tag{22}$$

For two different brightness fireflies, the lower brightness firefly moves to the brighter firefly. In standard FA this motion is defined as Eq. (23).

$$X_{id}\left(t+1\right) = X_{id}\left(t\right) + \beta_0 e^{-\gamma r_{ij}^2}\left(X_{jd}\left(t\right) - X_{id}\left(t\right)\right) + \alpha\left(rand - \frac{1}{2}\right) \tag{23}$$

Rand is a random number between 0 and 1 and α is between 0 and 1 and is called the randomization parameter. Firefly algorithm is a new method of optimizing collective intelligence that the efficiency of this method depends on its control parameter. There are different strategies for modulating the randomization parameter α, which are mentioned herein in four ways.

- In the standard FA algorithm, the values of α and β_0 are considered 0.5 and 1, respectively.
- In the Memetic Firefly Algorithm, the randomization parameter is automatically adjusted with increasing generation. In this algorithm, the parameters (0), γ, β_0, and β_{min} have values of 0.5, 1, 1, and 0.2, respectively. In this method, the α and β parameter values are obtained using Eq. (24) and Eq. (25).

$$\alpha\left(t+1\right) = \left(\frac{1}{9000}\right)^{\frac{1}{t}}\alpha\left(t\right) \tag{24}$$

$$\beta = \beta_{min} + \left(\beta_0 - \beta_{min}\right)e^{-\gamma r_{ij}^2} \tag{25}$$

- In the variable Step Size Firefly Algorithm, it was pointed out that a large α can create a new spatial search, and a small α can be useful for a limited search of a location. In this method, a dynamic model is designed to adjust the randomization parameter. In this algorithm, both values β_0 and γ are 1. The value of the α parameter is calculated from Eq. (26).

$$\alpha\left(t\right) = \frac{0.4}{1 + e^{\frac{t - G_{max}}{200}}} \tag{26}$$

- In the Adaptive control Parameters Firefly Algorithm, a consistent distance was defined based on the coefficient of attraction for perpetuating γ. In this method, (0) and β_0

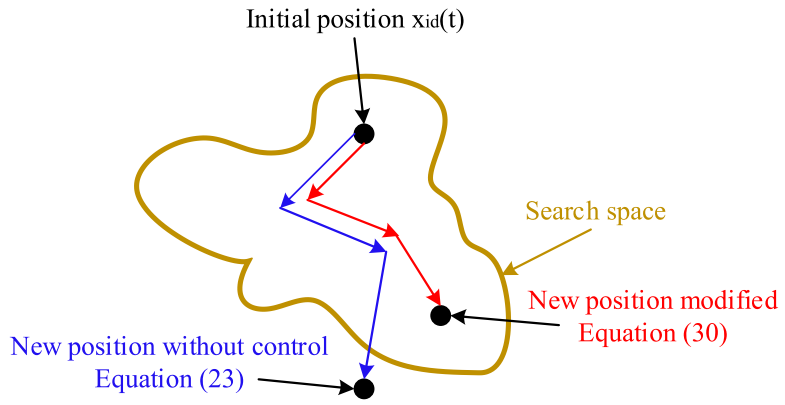

Fig. 5. Position of a firefly in search space.. (For interpretation of the references to color in this figure legend, the reader is referred to the web version of this article.)

are 0.5 and 1, respectively. Also, the α and β_0 values are obtained using Eq. (27) and Eq. (28):

$$\alpha\,(t+1) = \left(1 - \frac{t}{G_{max}}\right)\alpha\,(t) \tag{27}$$

$$\beta_0\,(t+1) = \begin{cases} rand_1\ if & rand_2 < 0.5 \\ \beta_0\ else \end{cases} \tag{28}$$

One of the disadvantages of Eq. (27) and Eq. (28) is that fireflies may leave the main search space of the problem and produce unacceptable answers. To solve this defect, a modified coefficient can be defined according to Eq. (29), and thus Eq. (23) can be converted to Eq. (30).

$$L = \frac{2}{\left|-2 - \tau - \sqrt{\tau^2 + \tau}\right|} \tag{29}$$

$$X_{id}\,(t+1) = X_{id}\,(t) + L\beta_0 e^{-\gamma r_{ij}^2}\left(X_{jd}\,(t) - X_{id}\,(t)\right) + \alpha\left(rand - \frac{1}{2}\right) \tag{30}$$

Eq. (30) can be used to calculate the new position of the firefly. Here τ represents the unacceptable longevity of the firefly. That is, for τ the new position of the firefly is calculated, and if the position of the firefly is out of the search space, the position is updated again. This process is repeated until the position of the firefly is corrected. To better understand the method, Fig. 5 shows the change in position of the firefly. Here the blue lines indicate the position of the firefly without the controller and the red lines indicate the position of the firefly with the modifier coefficient in the search space. As you can see, the modifier coefficient can prevent the production of unacceptable answers.

To improve the performance of fireflies in crossing the local minimum points, the features of the GA algorithm in the FA algorithm can be used. Two important features of the GA algorithm are mutation and crossover operators, which in standard GA algorithms usually consider mutation and crossover probabilities of constant, which means that even if the algorithm is repeated over and over again, better solutions (due to being in the local minimum points) are not obtained. In this paper, the feature of an adaptive genetic algorithm that can adjust the probability of mutations and crossovers adaptively and nonlinearly is used. In adaptive genetic algorithms, mutation and crossover probability regulation curves change slowly with f_{avg} (the average fitness), and the probability of mutation and crossover of genes whose fitness is largely close to the average fitness of the population increases. Usually, the increased range in the nonlinear adaptive genetic algorithm is more than linear adaptive genetic algorithm and other algorithms. Therefore, the probability of mutation (p_{m}) and crossover (p_{c}) based on the *sigmoid* function in Eq. (31) can be defined as Eq. (32) and Eq. (33):

$$f\,(x) = \frac{1}{1+exp(-ax)}a \geq 0 \tag{31}$$

$$p_c = \begin{cases} p_{c1} - \frac{p_{c1}-p_{c2}}{1+exp\left(-a\left(\frac{f-f_{avg}}{f_{max}-f_{avg}}\right)\right)} & f \geq f_{avg} \\ p_{c1} & f < f_{avg} \end{cases} \tag{32}$$

$$p_m = \begin{cases} p_{m1} - \frac{p_{m1}-p_{m2}}{1+exp\left(-a\left(\frac{f-f_{avg}}{f_{max}-f_{avg}}\right)\right)} & f \geq f_{avg} \\ p_{m1} & f < f_{avg} \end{cases} \tag{33}$$

To better understand the proposed technique, Fig. 6 shows the position of genes at different minimum points of the problem. The goal here is to take the genes out of the local minimum and to the minimum point of the problem, that is, to move the genes from position X1 to position X3. In this technique, the sigmoid transfer function is used to transfer genes from position X1 to position X2 and finally reach position X3. The probability of p_{m} and p_{c} based on the sigmoid function is designed to improve the performance of genes and get them out of the local minimum point. Therefore, in this design, after correcting the position of fireflies through Equation (30), at this stage, members of the FA algorithm population are considered as the initial population for the GA algorithm and by applying mutation and crossover operators on genes through Eq. (32) and Eq. (33) implement the process of the GA algorithm.

In Fig. 6, position X3 is a local minimum that is lower than all its neighbors, but higher than the global minimum, that is position XL. Therefore, in this scheme, a local search is applied to the algorithm so that it tends to search for sparsely populated areas in the optimal Pareto archive so that it can find more dominant answers. To understand local search, we consider the state space perspective, which has both location and height. Location is defined by state and height is defined by the value of the innovative cost function or the objective function. If the height corresponds to the cost, the goal is to reach the lowest global peak. So local search behaves using the current point (instead of multiple paths) and is passed only to the neighbors of that point, and instead of systematically examining paths from the starting state, evaluates and corrects one or more current states. In this algorithm, we first start with a point like Xm and a specific step length like ΔXi in different dimensions like i. Then k is the number of times this process must be repeated to get a better Xm answer. In the next step, the position of a point like Xi changes around the current point Xm to get point X'm with the conditions

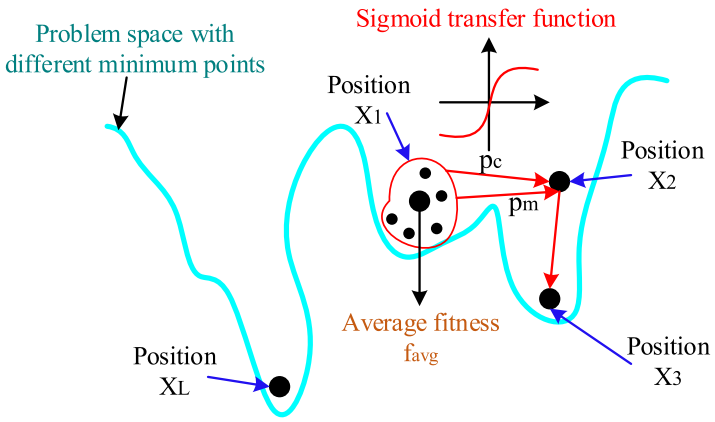

Fig. 6. The position of genes at different minimum points of the problem.

of Eq. (34):

$$X'_m = \begin{cases} X_m + \Delta X_i & if \quad f^+(0) > f \\ X_m - \Delta X_i & if \quad f^-(0) > \left(f(0)\, \Lambda f^+(0)\right) \\ X_m & if \quad f(0) > \left(f^+(0)\, \Lambda f^-(0)\right) \end{cases}$$
$$\forall i = 1, 2, \ldots, n \tag{34}$$

After performing multi-objective optimization and forming Pareto pages, fuzzy logic is used to select the best firefly as the optimal answer to the EED problem. In the fuzzy method, using the analysis of each of the objective functions and the results obtained by each firefly, the best result obtained from multi-objective optimization is selected. In this method, a linear membership function is formed for each of the objective functions. The membership function can be defined as Eq. (35). While $\mu_i^k = 0$ is the most undesirable and $\mu_i^k = 1$ is the most desirable result. Finally, for each non-dominated firefly, the normalized membership value is calculated using Eq. (36). Where N_O is the number of objective functions and N_K is the number of non-dominated fireflies. After calculating the normalized value of the membership function, the fireflies that have the highest value of the membership function are selected as the best firefly equivalent to the best answer to the EED problem.

$$\mu_i^k = \begin{cases} 1 & f_i^k \le f_i^{min} \\ \frac{f_i^{max} - f_i^k}{f_i^{max} - f_i^{min}} & f_i^{min} < f_i^k < f_i^{max} \\ 0 & f_i^{max} \le f_i^k \end{cases} \tag{35}$$

$$\mu^k = \frac{\sum_{i=1}^{N_O} \mu_i^k}{\sum_{k=1}^{N_k} \sum_{i=1}^{N_O} \mu_i^k} \tag{36}$$

Finally, in this research, three techniques have been used to improve the performance of the FA algorithm. In the first technique, the modifier coefficient is used to prevent the fireflies from leaving the problem space, in the second technique, the sigmoid transfer function in the structure of the GA algorithm is used to prevent fireflies from being located at local minimum points, and in third technique uses local search to find the global minimum point. Finally, the flowchart of the proposed method is shown in Fig. 7.

4. Simulation results

The test system used for the simulation is the 39-bus IEEE system with 10 generators shown in Fig. 8. Information related to the coefficients of a fuel cost function, pollution function, and practical limitations of power plants, including limitations in power generation, slope rate, and limitation of prohibited zones for the system are presented in the Zou and Gong (2022), Neto et al. (2017) and power demand for the sample system is 2000 MW. The minimum and maximum limits for the voltage of the buses connected to the network load are 0.95 and 1.05, respectively, and the maximum limit for the transmission power of the lines is 3.5 p.u. The simulation is done in two modes. In the first case, network stability indicators are not applied and the results of economic dispatch as well as bus voltage and line power that have exceeded their range are calculated in the test system. In the next case, the system stability indicators are applied to the objective function of the problem through the penalty function and the values exceeding the range for the bus voltage and line power are correct.

Table 1
Results of solving the EED problem in case 1.

Case 1	FA-GA	MOPSO (Dhifaoui et al., 2014)	NSGA-III (Bhesdadiya et al., 2016)
G1 (MW)	406.3746	380	395.1008
G2 (MW)	321.8524	341.8766	365.3285
G3 (MW)	320.1662	341.9057	315.7248
G4 (MW)	199.9304	203.5602	198.3176
G5 (MW)	235.6069	216.4019	219.5965
G6 (MW)	150	150	146.5141
G7 (MW)	125	124.1964	121.8342
G8 (MW)	90	90	87.7567
G9 (MW)	79.7180	80	79.0374
G10 (MW)	79.9336	79.6287	78.7628
Total losses (MW)	7.5266	7.5507	7.5823
Cost ($)	162600	162910	163200
Emission (kg)	32053	32373	33198

In this section, the simulation results of multi-objective problem solving with the proposed FA-GA hybrid algorithm are compared with algorithms of NSGA-III (Bhesdadiya et al., 2016) and MOPSO (Dhifaoui et al., 2014). Table 1 shows the results of case 1 of the simulation. As observed, the proposed FA-GA algorithm has a better fuel cost than other algorithms and at the same time has a lower pollution rate than other methods. According to Table 2, in case 2, after applying the network security constraints and defined indicators, the above multi-objective algorithm provides better results than in case 1. Fuel cost and pollution values obtained by the FA-GA algorithm have more optimal values than NSGA-III and MOPSO algorithms.

After simulation and according to Table 3, it was found that in case 1, lines 2, 15, and 38 have overload and power passing exceeding the allowable limit. In case 2, after applying the constraints and indicators, the mentioned lines are in normal loading,

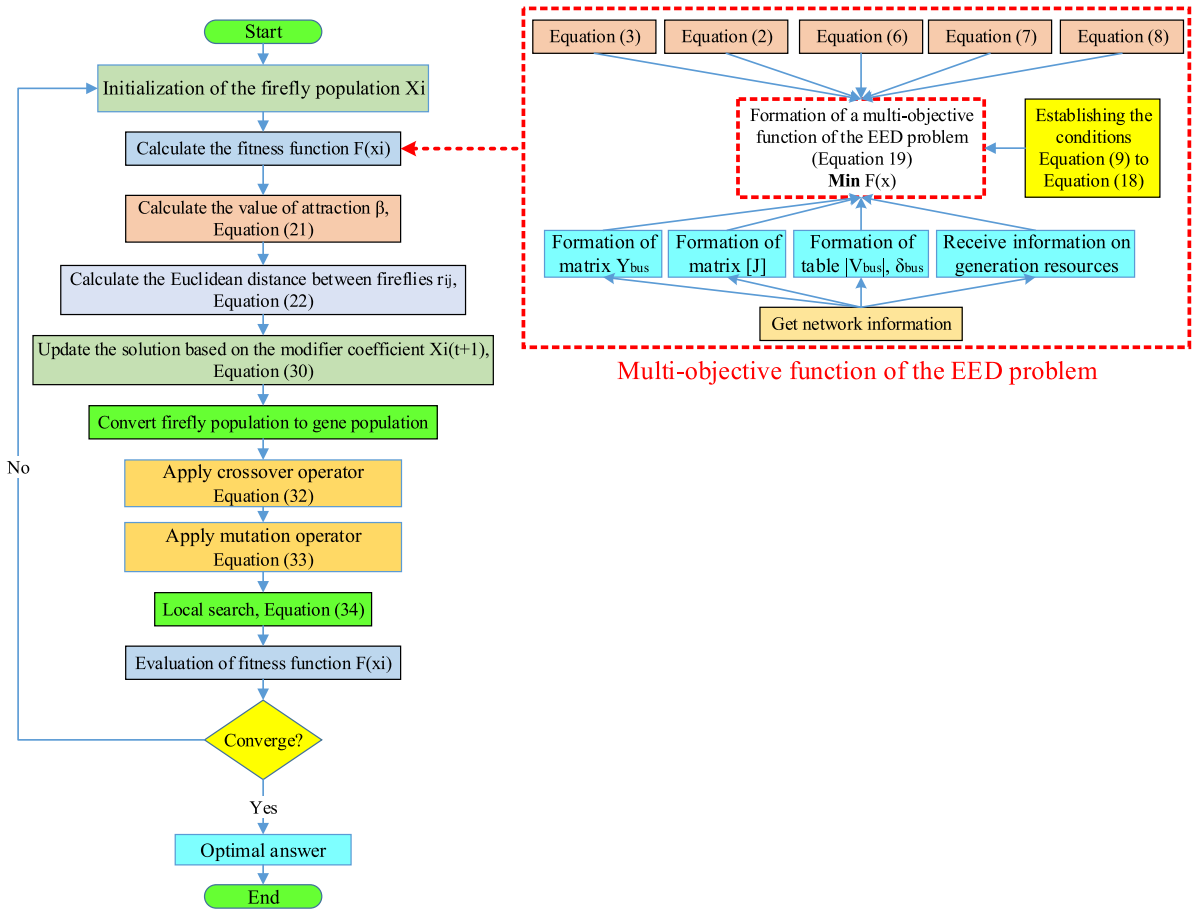

Fig. 7. Steps to implement the proposed method.

Table 2
Results of solving the EED problem in case 2.

Case 1	FA-GA	MOPSO (Dhifaoui et al., 2014)	NSGA-III (Bhesdadiya et al., 2016)
G1 (MW)	454.3521	455.1628	456.6693
G2 (MW)	284.7451	307.7589	305
G3 (MW)	290.8955	271.6853	279.1267
G4 (MW)	228.5	234.0171	229.8830
G5 (MW)	226.4588	223.5552	230
G6 (MW)	149.2502	146.6112	148.7274
G7 (MW)	124.6905	123.6045	117.5051
G8 (MW)	89.6450	89.2163	89.9525
G9 (MW)	80	78.3122	78.5703
G10 (MW)	79.929	78.1205	76.9762
Total losses (MW)	7.4806	7.4982	7.5137
Cost ($)	171820	173350	174820
Emission (kg)	32415	32723	33055

Table 3
Values exceeding the range for line power in case 1.

Line	Value (p.u.)
LF_2	4.0961
LF_{15}	3.7364
LF_{38}	3.5546

Table 4
Modified values of line power in case 2.

Line	Value (p.u.)
LF_2	3.4674
LF_{15}	3.1065
LF_{38}	3.4231

and their power is reduced, which is presented in Table 4. In both cases, the bus voltage is within the allowable range. The cost of fuel and the amount of pollution in the second case has increased compared to the previous case, which is due to the consideration of network security constraints.

Fig. 9 shows the performance curves of the two objective functions in case 2, which show the vertical axis of the pollution function values and the horizontal axis of the fuel cost function values. Where the performance of the proposed algorithm is compared with the two algorithms MOPSO and NSGA-III. As you can see from the results in Tables 1 to 4 and Fig. 9, the proposed algorithm performed better. Fig. 10 shows the Pareto page or non-dominant particles after applying the proposed algorithm for the EED problem in case 2. After applying the multi-objective algorithm and optimizing the objective functions, the best particle is selected as the most optimal response using the fuzzy method. In this network, the results of applying the proposed algorithm are compared with the results of MOPSO and NSGA-III algorithms, and the performance percentage of each method is compared.

Fig. 11 shows the performance of different algorithms in improving the indicators. The proposed algorithm for the loss index and voltage stability could improve by 66% compared to the initial conditions and the pollution index could improve by 69.95%. It also performed 31% better than the NSGA-III algorithm and 15% better than the MOPSO algorithm. Finally, Fig. 12 shows the output of the FAGA algorithm related to the introduced indicators.

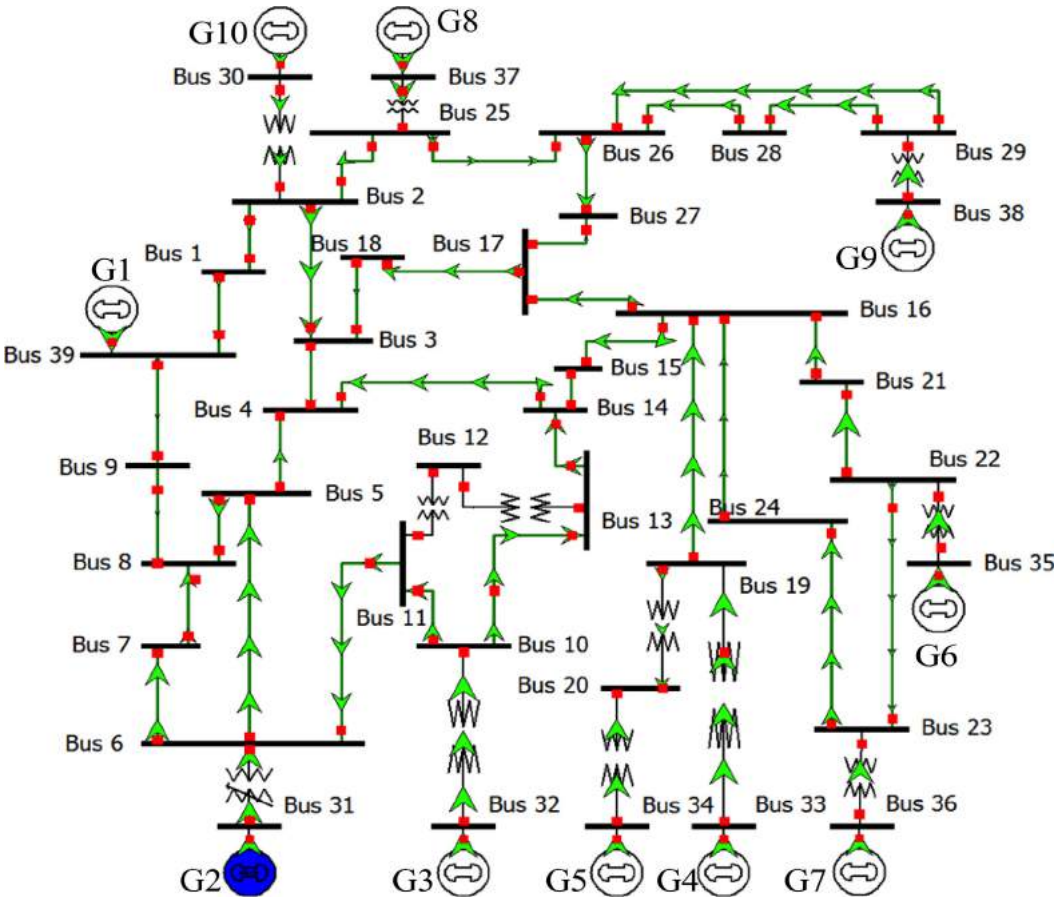

Fig. 8. 39-Bus IEEE system.

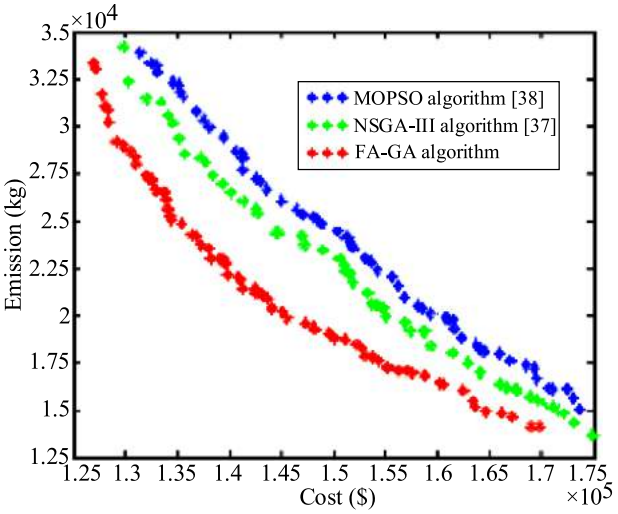

Fig. 9. The change curve of the objective functions in case 2.

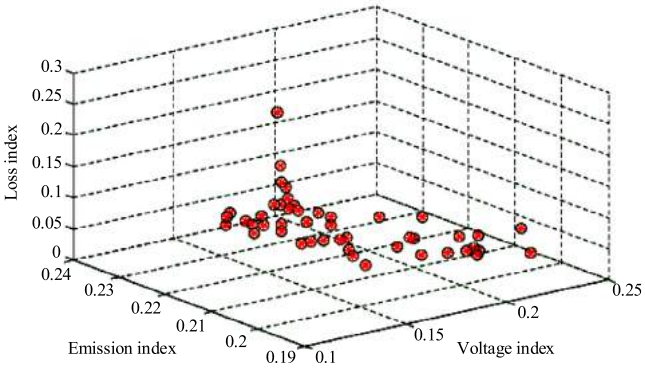

Fig. 10. Position of non-dominant answers on the Pareto page in case 2.

In the following, under case 3, the performance of the proposed algorithm is implemented on the IEEE 118-bus network, which is a larger network, and its results are compared with other algorithms. This network has 11 generation units, the information of which is presented in Balamurugan and Subramanian (2007), Uur and venccedil (2010). In case 3, the results of the best solution for the optimal generation of units at different load levels are obtained for 100 iterations of the algorithm. Fig. 13 and Fig. 14 respectively show the results of the implementation of the standard FA algorithm and the proposed algorithm on the function of Eq. (4). As you can see in Fig. 13, in the standard FA algorithm, the fireflies are still scattered after 100 iterations and do not fully match the Pareto curve. Also, these fireflies are not uniformly placed on Pareto optimal. While in the proposed algorithm according to the curve in Fig. 14, although the final firefly population has dispersion, this dispersion is relatively less and smoother and the fireflies are spread more evenly along the curve. As it is clear, the distance between the fireflies in Fig. 14 is less and the fireflies in this method are placed smoothly along the Pareto curve; which is a criterion for the optimality of the algorithm. Therefore, two criteria have been considered to calculate the error: 1. Pareto–Pareto distance, 2. Firefly–Pareto distance. In the first method, the error is calculated based on the average

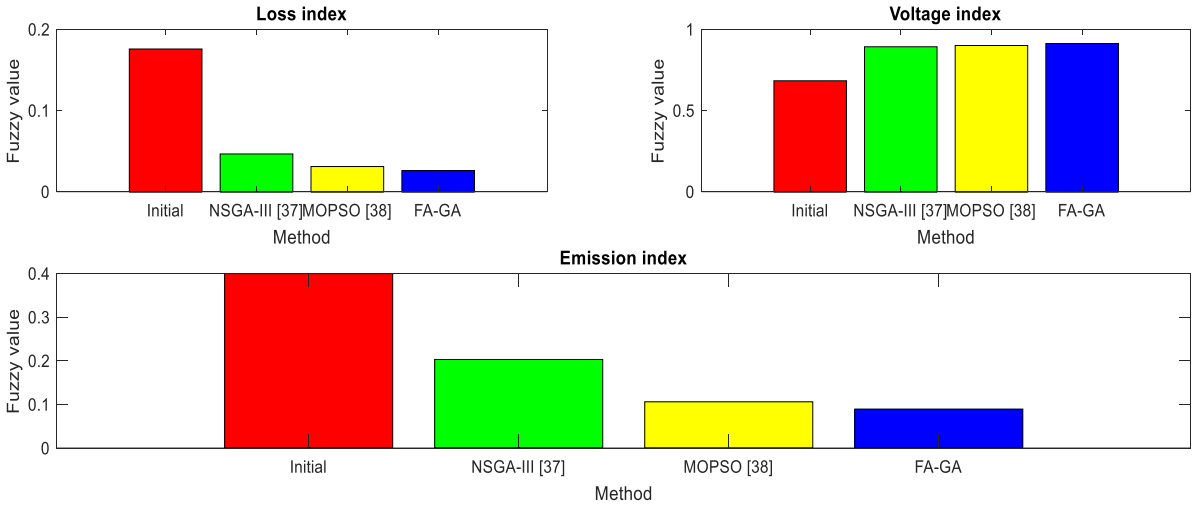

Fig. 11. Comparison of the improvement in the value of indicators for each algorithm.

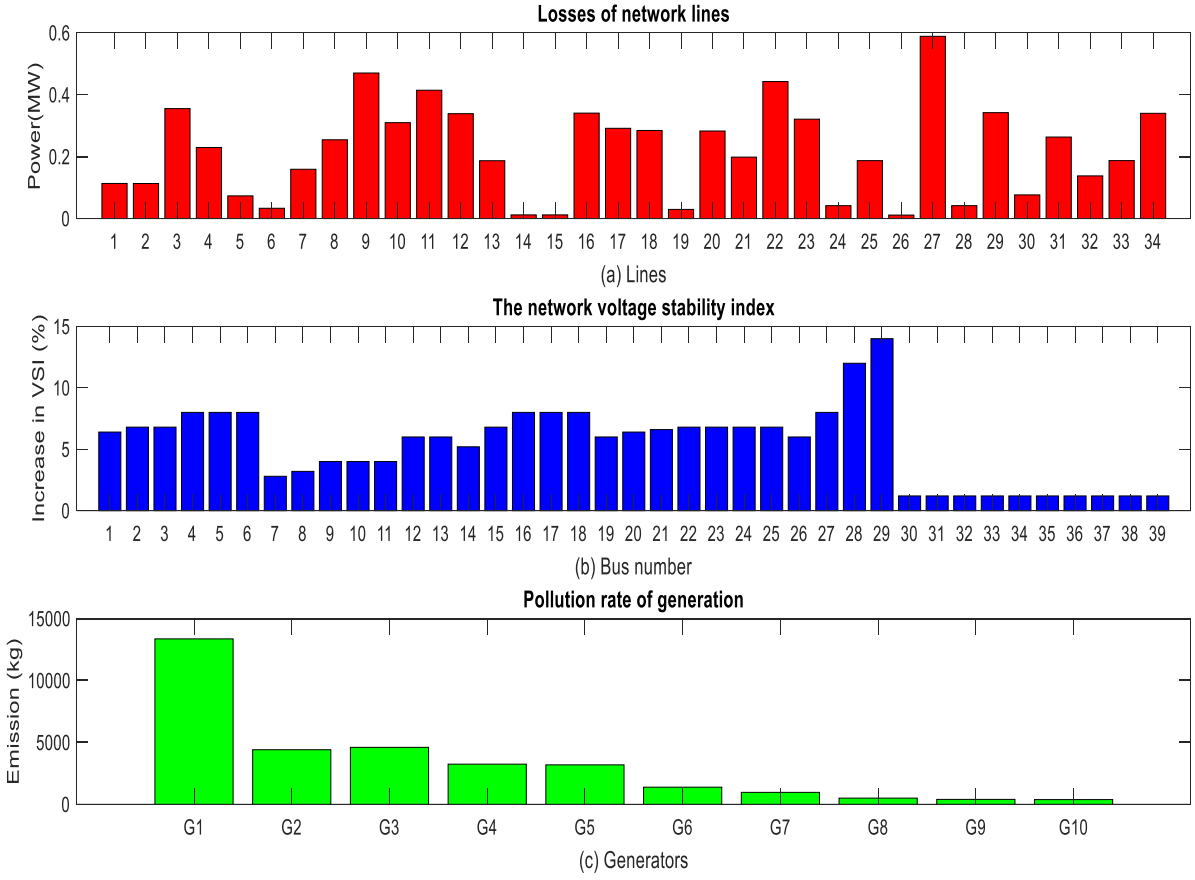

Fig. 12. Output of FA-GA algorithm, (a) Lines losses, (b) VSI index of buses, (c) generator emission rate.

distance between the optimal Pareto points (resulting from the applied algorithms) and the original Pareto of the function. In the second method, the error is calculated based on the average distance between the fireflies of the population (resulting from the applied algorithms) and the original Pareto of the function. The results related to the error of the standard FA algorithm and the proposed algorithm are shown in Table 5. Note that these errors are reported as averages. Table 6 shows the best solution of the proposed algorithm for the optimal generation of power plants at different load levels.

4.1. Discussion of the results

The important feature of the firefly algorithm, which distinguishes it from some similar optimization algorithms, is its very good performance in searching for optimal solutions related to "multimodality" problems and functions. Such an important feature in the firefly algorithm has made this algorithm an ideal choice for multimodal optimization applications. Another advantage of the firefly algorithm that distinguishes it from other conventional optimization algorithms is that different fireflies

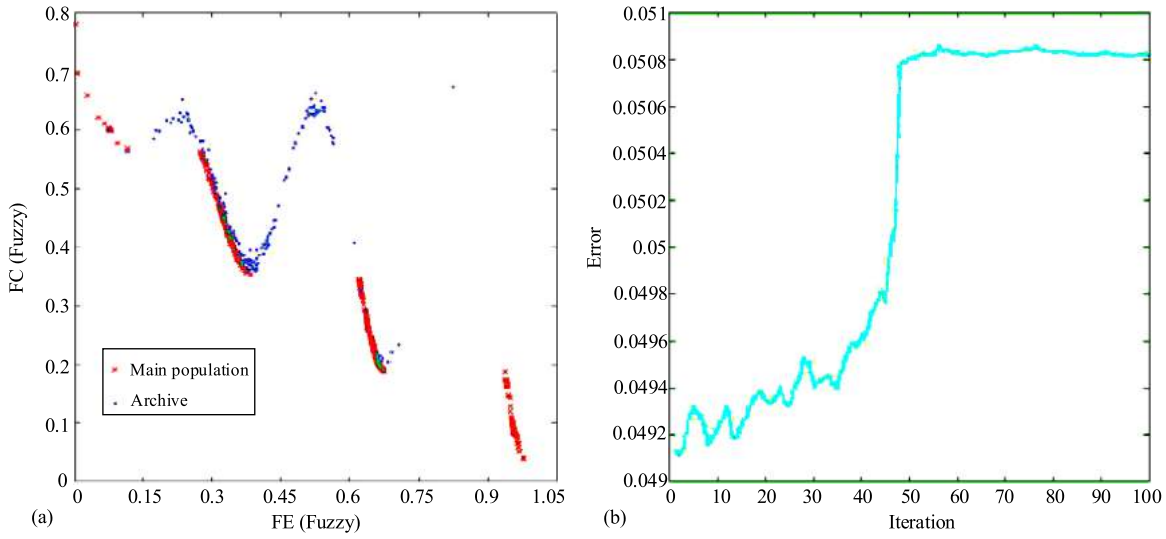

Fig. 13. The distribution pattern of 300 fireflies resulting from the implementation of the standard FA algorithm.

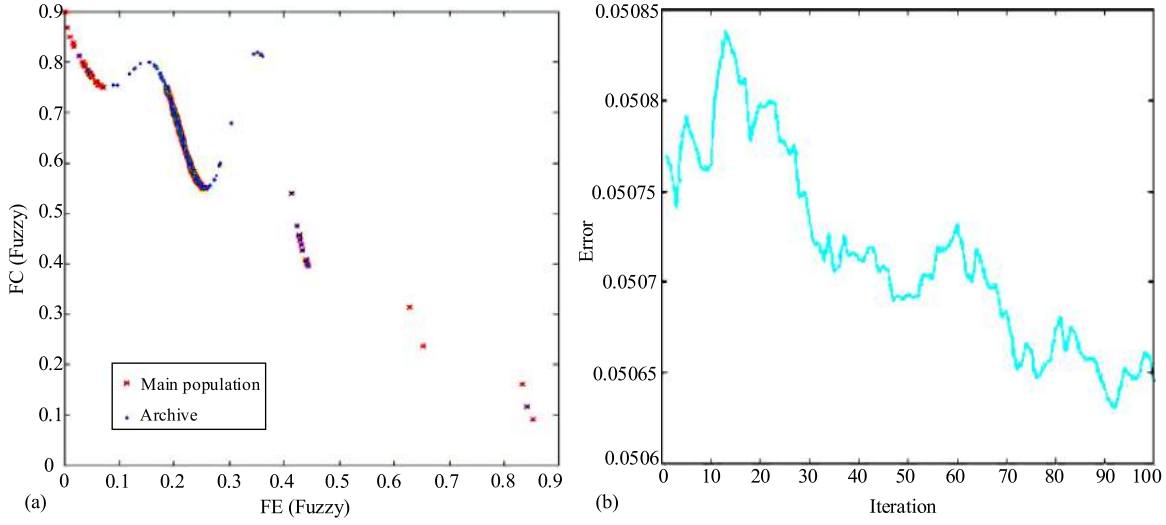

Fig. 14. The distribution pattern of 300 fireflies resulting from the implementation of the proposed algorithm.

Table 5
Comparison of average error of algorithms.

Error calculation method	Algorithms	Number of fireflies	Number of iterations	Average error
Method 1	Standard FA	100	100	0.0575
		200	100	0.06
		300	100	0.0573
	Proposed FA-GA	100	100	0.0565
		200	100	0.0559
		300	100	0.0558
Method 2	Standard FA	100	100	0.0604
		200	100	0.063
		300	100	0.0615
	Proposed FA-GA	100	100	0.0590
		200	100	0.0576
		300	100	0.0570

operate almost independently of each other. Such an important feature makes the firefly algorithm an ideal choice for "parallel implementations" of evolutionary algorithms. Also, since fireflies gather in a more compact form around the optimums in the problem search space, they perform better than the genetic algorithm and the particle swarm optimization algorithm. In the parallel implementation of the firefly algorithm, the interaction between "subregions" is minimized. One of the disadvantages of the standard firefly algorithm is the large changes in the solutions produced by the algorithm even as the fireflies approach the

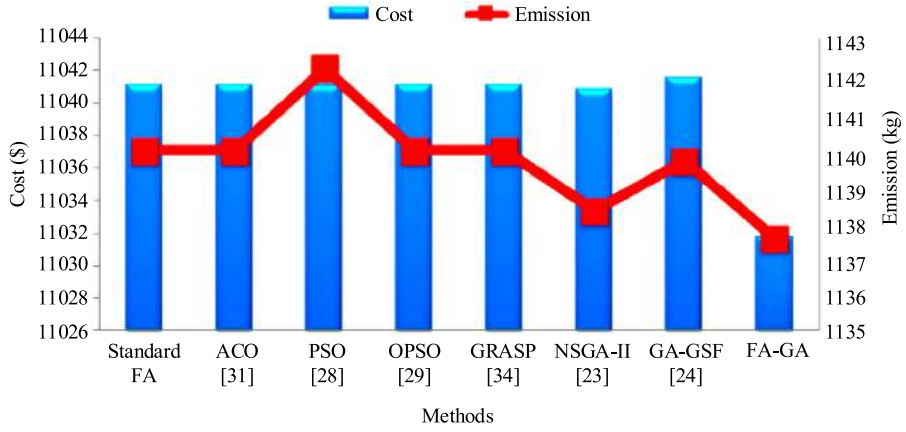

Fig. 15. Comparison of EED problem-solving results for different methods (1980 MW system load).

Table 6
Results of solving the EED problem in case 3.

Case 3	Different load levels (MW)				
	980	1230	1480	1730	1980
G1 (MW)	86.1521	93.8225	106.6611	113.09514	119.9993
G2 (MW)	77.1102	83.1432	86.7694	94.3871	101.0007
G3 (MW)	85.2329	96.1462	105.6188	114.2231	127.8091
G4 (MW)	73.8925	99.1742	128.8809	149.6791	173.6077
G5 (MW)	49.2009	64.7937	84.7151	95.05177	106.7558
G6 (MW)	81.0174	101.3011	124.1206	145.0959	171.1069
G7 (MW)	55.9083	63.0113	77.3169	98.7126	110.4231
G8 (MW)	131.6859	167.9122	215.5329	235.8803	276.0201
G9 (MW)	118.9132	160.6515	190.3161	223.3106	259.8412
G10 (MW)	120.5575	160.8216	192.7780	243.3792	284.7328
G11 (MW)	120.4319	159.3257	187.4007	237.2941	268.8139
Total losses (MW)	20.1028	20.1032	20.1076	20.1089	20.1106
Cost ($)	8498.53	9103.47	9729.93	10372.19	11031.72
Emission (kg)	205.101	340.006	539.997	805.919	1137.521

region containing the optimal solution. In the proposed algorithm, this problem is tried to be solved. Finally, in Fig. 15, the performance of the proposed algorithm in optimizing the fuel cost and the amount of emission from power plants is compared with the results of other algorithms. As you can see, using the proposed method has made a significant improvement in solving the problem.

The results obtained for the systems studied in the previous section were obtained by considering the equal weight coefficient for the problem. This is while the importance of the objectives of the problem may not be the same from the point of view of the system operator. In this section, to examine and analyze the sensitivity of the obtained results to the change of weight coefficient, the results of the generation cost and emission of power plants in the IEEE 118-bus network were calculated according to different coefficients and the obtained results are presented in Fig. 16. The obtained results show that by increasing the weight coefficient, the effect of cost in the objective function increases, and the generation costs decrease. This is while the importance of the production of emission in the objective function is reduced and the amount of emission increases.

Finally, a comparison between some methods presented so far to solve the EED problem is shown in Table 7. In this table, a series of criteria are defined and the performance percentage of each method in reducing the cost of the objective function is shown. Here, the innovation of each method is introduced under the feature factor and the indicators of each method are stated. One of the important factors in solving the EED problem is how to formulate the problem in the form of linear or non-linear problems, which are introduced here under DC-OPF and AC-OPF. The next factor is the type of network, it has a great impact on the performance percentage of the algorithm. Now, with these interpretations, you can see that the proposed algorithm has a better performance percentage.

5. Conclusions

In this paper, the problem of economic dispatch of power plants along with environmental dispatch by considering the indicators of losses, voltage stability, and emission of pollution was investigated. To be closer to reality and increase accuracy, the fuel cost function of power plants was considered as the third degree and all practical constraints of power plants. The above complicates the problem and necessitates the use of effective optimization algorithms. Here, a combination of multi-objective firefly algorithms and genetic algorithms are used to optimize the objective functions. Three techniques have been used to improve the firefly algorithm so that it does not locate in the local minimum points, and then the fuzzy method is used to select the best particle from the Pareto page. Finally, the proposed method is compared with two other advanced optimization methods, which show that the proposed algorithm offers better answers compared to the other two algorithms. These answers further reduce fuel costs and emissions of pollution compared to the answers of other algorithms. Even these positive results which show the benefit of the proposed control loop, the weaknesses cannot be hided, especially if we concentrate on the enorm parameters of algorithms that must be fixed and adjusted to find the best combination. But from the other side, the robustness of the proposed approach must be tested on a more complicate Bus system. It is important to test if the good results will appear even hundred of buses come online. Therefore, some of the future endeavors of this work is to test if the proposed approach performances decrease if the buses number increase more. Even, a practical application seems important to test the real efficiency of this approach as the calculators performances can make a negative effect on the global yield and on the system stability. Also it is possible to extend this work and give more comparison between multiobectives algorithms and try to make a serious discussion between challenges of each method.

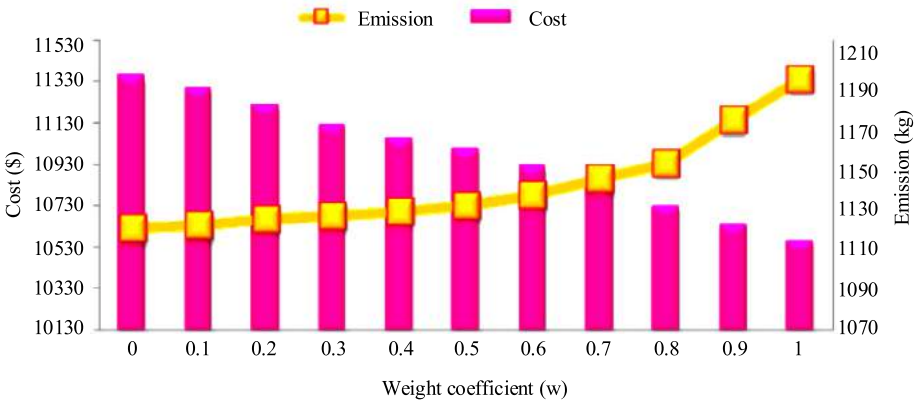

Fig. 16. The effect of changing the weight coefficient on the EED problem.

Table 7
Comparison of different methods for solving the EED problem.

Method provider	Methods	Features	Objective function	Indexes	OPF type	Network type	Reduction percentage
Zaman et al. (2015)	GA Algorithm	Non-uniform mutation	Dynamic economic dispatch (DED)	P_{Loss}	AC	59-bus IEEE system	36.90%
Wang et al. (2016)	ADMM approach	Smart grid with a new communication strategy	Economic dispatch (ED)	Demand response	DC	118-bus IEEE system	43.75%
Jin and Xu (2017)	MIQP program	Using FACTS devices	Economic dispatch (ED)	–	DC	118-bus IEEE system	51.43
Liang et al. (2017)	Bat algorithm	The usage of weighted sum method	Environmental economic dispatch (EED)	–	AC	39-bus IEEE system	25.67%
Benalcazar et al. (2019)	Fuzzy inference systems	Energy storage devices, Plug-in electric vehicles (PEV)	Short-term economic dispatch (ED)	–	DC	Test feeder IEEE 13N	35.67%
Bora et al. (2019)	NSGA-II algorithm	Incorporating a parameter-free self-tuning by reinforcement learning technique	Environmental economic dispatch (EED)	P_{Loss}	AC	30-bus IEEE system	45.89%
Li et al. (2020)	MOMFO algorithm	Including Hybrid Renewable in the problem with the efficient heuristic dynamic relaxation approach	Dynamic environmental economic dispatch (DEED)	P_{Loss}	AC	39-bus IEEE system	49.73%
Presented	FA-GA Algorithm	A new setting of the α and β parameter values, mutation (pm) and crossover (pc) based on the sigmoid function, local search	Environmental economic dispatch (EED)	P_{Loss}, VSI, C_E	AC	39-118-bus IEEE system	69.95%

CRediT authorship contribution statement

Masoud Dashtdar: Conceptualization, Methodology, Investigation, Supervision, Validation, Writing – original draft, Writing – review & editing. **Aymen Flah:** Methodology, Resources, Formal analysis, Writing – review & editing. **Seyed Mohammad Sadegh Hosseinimoghadam:** Software, Resources, Visualization. **Ch. Rami Reddy:** Software, Resources, Visualization. **Hossam Kotb:** Methodology, Resources, Writing – review and editing. **Kareem M. AboRas:** Data curation, Validation, Writing – review & editing. **Elżbieta Jasińska:** Formal analysis, Funding acquisition, Validation. **Michał Jasiński:** Supervision, Project administration, Validation.

Declaration of competing interest

The authors declare that they have no known competing financial interests or personal relationships that could have appeared to influence the work reported in this paper.

Data availability

Data will be made available on request.

Human and animal rights

This article does not contain any studies with animals performed by any of the authors.

Informed consent

Informed consent was obtained from all individual participants included in the study.

References

Abbas, Ghulam, Gu, Jason, Farooq, Umar, Asad, Muhammad Usman, El-Hawary, Mohamed, El-Hawary, Mohamed, 2017a. Solution of an economic dispatch problem through particle swarm optimization: A detailed survey-Part I. IEEE Access 5, 15105–15141.

Abbas, Ghulam, Gu, Jason, Farooq, Umar, Raza, Ali, Asad, Muhammad Usman, El-Hawary, Mohamed E., 2017b. Solution of an economic dispatch problem through particle swarm optimization: A detailed survey–Part II. IEEE Access 5, 24426–24445.

Al Bahrani, Loau Tawfak, Patra, Jagdish Chandra, 2017. Orthogonal PSO algorithm for economic dispatch of thermal generating units under various power constraints in smart power grid. Appl. Soft Comput. 58, 401–426.

Aydin, Doğan, Yavuz, Gürcan, Özyön, Serdar, Yaşar, Celal, Stützle, Thomas, 2017. Artificial bee colony framework to non-convex economic dispatch problem with valve point effects: A case study. In: Proceedings of the Genetic and Evolutionary Computation Conference Companion. pp. 1311–1318.

Balamurugan, R., Subramanian, S., 2007. A simplified recursive approach to combined economic emission dispatch. Electr. Power Compon. Syst. 36 (1), 17–27.

Beigvand, Soheil Derafshi, Abdi, Hamdi, Scala, Massimo La, 2017. Economic dispatch of multiple energy carriers. Energy 138, 861–872.

Benalcazar, Patricio, Samper, Mauricio E., Vargas, Alberto, 2019. Short-term economic dispatch of smart distribution grids considering the active role of plug-in electric vehicles. Electr. Power Syst. Res. 177, 105932.

Bhattacharyya, Supratik Sekhar, Anusuya, B., 2022. Multiobjective optimization of economic-environmental dispatch (EED) problems including CO 2 emission. In: 2022 International Conference for Advancement in Technology. ICONAT, IEEE, pp. 1–9.

Bhesdadiya, Rajnikant H., Trivedi, Indrajit N., Jangir, Pradeep, Jangir, Narottam, Kumar, Arvind, 2016. An NSGA-III algorithm for solving multi-objective economic/environmental dispatch problem. Cogent Eng. 3 (1), 1269383.

Bora, Teodoro Cardoso, Mariani, Viviana Cocco, dos Santos Coelho, Leandro, 2019. Multi-objective optimization of the environmental-economic dispatch with reinforcement learning based on non-dominated sorting genetic algorithm. Appl. Therm. Eng. 146, 688–700.

Chen, Guo, Li, Chaojie, Dong, Zhaoyang, 2016. Parallel and distributed computation for dynamical economic dispatch. IEEE Trans. Smart Grid 8 (2), 1026–1027.

Dashtdar, Masoud, Flah, Aymen, Hosseinimoghadam, Seyed Mohammad Sadegh, Fard, Mohammad Zangoui, Dashtdar, Majid, 2022. Optimization of microgrid operation based on two-level probabilistic scheduling with benders decomposition. Electr. Eng. 1–15.

Dashtdar, Masoud, Najafi, Mojtaba, Esmaeilbeig, Mostafa, 2020a. Calculating the locational marginal price and solving optimal power flow problem based on congestion management using GA-GSF algorithm. Electr. Eng. 102 (3), 1549–1566.

Dashtdar, Masoud, Najafi, Mojtaba, Esmaeilbeig, Mostafa, 2020b. Probabilistic planning for participation of virtual power plants in the presence of the thermal power plants in energy and reserve markets. Sādhanā 45 (1), 1–9.

Dashtdar, Masoud, Najafi, Mojtaba, Esmaeilbeig, Mostafa, 2021. Reducing LMP and resolving the congestion of the lines based on placement and optimal size of DG in the power network using the GA-GSF algorithm. Electr. Eng. 103 (2), 1279–1306.

Dhifaoui, Chefai, Guesmi, Tawfik, Abdallah, Hsan Hadj, 2014. Application of multi-objective PSO algorithm for economic dispatch (ED) through unit commitment problems (UCP). In: 2014 15th International Conference on Sciences and Techniques of Automatic Control and Computer Engineering. STA, IEEE, pp. 704–710.

Espinosa-Juárez, Elisa, Solano-Gallegos, Jorge Luis, Ornelas-Tellez, Fernando, 2019. Economic dispatch for power system with short-term solar power forecast. In: 2019 International Conference on Computational Science and Computational Intelligence. CSCI, IEEE, pp. 499–504.

Feng, Chenjia, Shao, Chengcheng, Wang, Xifan, 2021. A fast solution method to economic dispatch type problem. J. Mod. Power Syst. Clean Energy 9 (5), 1227–1232.

Hosseinimoghadam, Seyed Mohammad Sadegh, Roghanian, Hamzeh, Dashtdar, Masoud, Razav, Seyed Mohammad, 2020. Power-sharing control in an islanded microgrid using virtual impedance. In: 2020 8th International Conference on Smart Grid. IcSmartGrid, IEEE, pp. 73–77.

Jena, C., Basu, Mousumi, Panigrahi, C.K., 2016. Differential evolution with Gaussian mutation for combined heat and power economic dispatch. Soft Comput. 20 (2), 681–688.

Jin, Jiangliang, Xu, Yunjian, 2017. A flow direction enforcing approach for economic dispatch with adjustable line impedance. In: 2017 IEEE Power & Energy Society General Meeting. IEEE, pp. 1–5.

Khan, Naveed Ahmed, Sidhu, Guftaar Ahmad Sardar, Gao, Feifei, 2016. Optimizing combined emission economic dispatch for solar integrated power systems. IEEE Access 4, 3340–3348.

Krishnamurthy, Senthil, Tzoneva, Raynitchka, Apostolov, Alexander, 2017. Method for a parallel solution of a combined economic emission dispatch problem. Electr. Power Compon. Syst. 45 (4), 393–409.

Li, Xueping, Fang, Liangxing, Lu, Zhigang, Zhang, Jiangfeng, Zhao, Hao, 2017. A line flow granular computing approach for economic dispatch with line constraints. IEEE Trans. Power Syst. 32 (6), 4832–4842.

Li, Xiaozhu, Wang, Weiqing, Wang, Haiyun, Wu, Jiahui, Fan, Xiaochao, Xu, Qidan, 2020. Dynamic environmental economic dispatch of hybrid renewable energy systems based on tradable green certificates. Energy 193, 116699.

Li, K., Xiong, P., Wu, Y., Dong, Y., 2022. Forecasting greenhouse gas emissions with the new information priority generalized accumulative grey model. Sci. Total Environ. 807, 150859.

Liang, Huijun, Liu, Yungang, Shen, Yanjun, Li, Fengzhong, 2017. A multiobjective chaotic bat algorithm for economic and emission dispatch. In: 2017 Chinese Automation Congress. CAC, IEEE, pp. 4684–4689.

Marwan, Marwan, Marwan, Muhammad Dihyah, Anshar, Muhammad, Jamal, Jamal, Aksan, Aksan, Apollo, Apollo, 2021. Optimal economic dispatch for power generation under the lagrange method. In: 2021 International Conference on Artificial Intelligence and Mechatronics Systems. AIMS, IEEE, pp. 1–5.

Mutlaq, Mohammed, 2019. Environmental economic dispatch of thermal power plants in Saudi Arabia: A case study. In: 2019 Industrial & Systems Engineering Conference. (ISEC), IEEE, pp. 1–5.

Najafi, Mojtaba, Ahmadi, Samaneh, Dashtdar, Masoud, 2019. Simultaneous energy and reserve market clearing with consideration of interruptible loads as one of demand response resources and different reliability requirements of consumers. Int. J. Emerg. Electr. Power Syst. 20 (5).

Narvaez, D.M. Devia, Vélez, Germán Correa, Narvaez, DF Devia, 2018. Application of the gradient method in the economic dispatch. Contemprary Eng Sci 11 (96), 4761–4768.

Neto, Júlio Xavier Viann, Reynoso-Meza, Gilberto, Ruppel, Thiago Hauer, Mariani, Viviana Cocco, dos Santos Coelho, Leandro, 2017. Solving non-smooth economic dispatch by a new combination of continuous GRASP algorithm and differential evolution. Int. J. Electr. Power Energy Syst. 84, 13–24.

Pattanaik, Jagat Kishore, Basu, Mousumi, Dash, Deba Prasad, 2018. Improved real coded genetic algorithm for dynamic economic dispatch. J. Electr. Syst. Inform. Technol. 5 (3), 349–362.

Ponciroli, Roberto, Stauff, Nicolas E., Ramsey, Jackson, Ganda, Francesco, Vilim, Richard B., 2020. An improved genetic algorithm approach to the unit commitment/economic dispatch problem. IEEE Trans. Power Syst. 35 (5), 4005–4013.

Sen, Tanuj, Mathur, Hitesh Datt, 2016. A new approach to solve economic dispatch problem using a hybrid ACO–ABC–HS optimization algorithm. Int. J. Electr. Power Energy Syst. 78, 735–744.

Thalassinos, E., Kadłubek, M., Thong, L.M., Hiep, T.V., Ugurlu, E., 2022. Managerial issues regarding the role of natural gas in the transition of energy and the impact of natural gas consumption on the GDP of selected countries. Resources 11, 42. http://dx.doi.org/10.3390/resources11050042.

Tian, Yuting, Bera, Atri, Benidris, Mohammed, Mitra, Joydeep, 2017. Reliability and environmental benefits of energy storage systems in firming up wind generation. In: 2017 North American Power Symposium. NAPS, IEEE, pp. 1–6.

Uur, Guuml, venccedil, 2010. Combined economic emission dispatch solution using genetic algorithm based on similarity crossover. Sci. Res. Essays 5 (17), 2451–2456.

Wang, Yamin, Wu, Lei, Wang, Shouxiang, 2016. A fully-decentralized consensus-based ADMM approach for DC-OPF with demand response. IEEE Trans. Smart Grid 8 (6), 2637–2647.

Wu, Kunming, Li, Qiang, Lin, Jiayang, Yi, Yongli, Chen, Ziyu, Chen, Minyou, 2020. Fast distributed Lagrange dual method based on accelerated gradients for economic dispatch of microgrids. Energy Rep. 6, 640–648.

Xu, Tong, Wu, Wenchuan, Zheng, Weiye, Sun, Hongbin, Wang, Liming, 2017. Fully distributed quasi-Newton multi-area dynamic economic dispatch method for active distribution networks. IEEE Trans. Power Syst. 33 (4), 4253–4263.

Zaman, M.F., Elsayed, Saber M., Ray, Tapabrata, Sarker, Ruhul A., 2015. Evolutionary algorithms for dynamic economic dispatch problems. IEEE Trans. Power Syst. 31 (2), 1486–1495.

Zhang, X., Qian, H., Hua, K., Chen, H., Deng, A., Song, Z., Zhang, J., Raheem, A., Danso, F., Wang, D., et al., 2022. Organic amendments increase crop yield while mitigating greenhouse gas emissions from the perspective of carbon fees in a soybean-wheat system. Agric. Ecosyst. Environ. 325, 107736.

Ziane, Ismail, Benhamida, Farid, Graa, Amel, 2017. Simulated annealing algorithm for combined economic and emission power dispatch using max/max price penalty factor. Neural Comput. Appl. 28 (1), 197–205.

Zou, Dexuan, Gong, Dunwei, 2022. Differential evolution based on migrating variables for the combined heat and power dynamic economic dispatch. Energy 238, 121664.

Further reading

Chowdhury, A.F.M. Kamal, Kern, Jordan, Thanh, Dang Duc, Galelli, Stefano, 2020. PowNet: A network-constrained unit commitment/economic dispatch model for large-scale power systems analysis. J. Open Res. Softw. 8 (1).

Journal of Ambient Intelligence and Humanized Computing
https://doi.org/10.1007/s12652-021-03681-0

ORIGINAL RESEARCH

MRI de-noising using improved unbiased NLM filter

S. Sahu[1] · A. Anand[2] · A. K. Singh[3] · A. K. Agrawal[4] · M. P. Singh[3]

Received: 16 July 2021 / Accepted: 15 December 2021

Abstract
The magnetic resonance images focus on soft tissues, and it is often necessary for healthcare professionals to reach the final conclusion in clinical diagnosis. However, these images are often affected by random noise, which decreases the visual quality and reliability of the images. This paper presents an improved unbiased non-local mean (NLM) filter to solve the de-noising issue in the MRI images. Local statistics of the noise is combined with the NLM filter to design an unbiased NLM filter. First of all, the Gaussian noise information is extracted from the noisy image by performing the wavelet decomposition, statistically modeling the diagonal sub-band wavelet coefficients, and estimating the noise variance by applying the median absolute deviation (MAD) estimator. Next, the Rician noise is removed by applying a NLM filter which averages the noisy pixels by a Gaussian weight factor. Finally, the NLM filtered output pixels are unbiased by applying the noise bias subtraction method for recovering the original pixel values. Our experiments on real MRI and synthetic images demonstrate that promising results that can be obtained much superior than results estimated using existing non-local mean filtering schemes.

Keywords MRI image · Non-local mean (NLM) filter · MAD estimator · Wavelet decomposition

1 Introduction

Magnetic resonance imaging (MRI) is a medical image modality employed in health care system that provides images of internal tissues and organs in the subject body for demonstrating the physiological or pathological anomalies (Heo et al. 2020). Medical image processing plays an important role in healthcare sector. Noise may result inaccurate diagnosis which leads to loss of human life. This motivates to develop a methodology that removes the noise and results accurate diagnosis. Now a day the MRI has widespread use in healthcare systems for biomedical research and diagnostic medicine but it also covers a broad area of applications in different sectors such as pharmaceutical applications (Richardson et al. 2005), forensic imaging, study of internal body structure of animal species, study of anatomy of plants and structure of fossils etc., as shown in Fig. 1.

MRI can capture 2D and 3D images and is a non-invasive and non-destructive in nature. MR imaging method has basically two functional blocks: acquisition and reconstruction. Following Fig. 2 shows the MR imaging process. The acquisition block acquires the RF signals from the subject's body, digitizes and stores the digitized data in K space (a memory configuration). The reconstruction block reconstructs the MR image from the acquired signal. The number of rows and columns (size) of the K space depends upon the image details requirements.

An important drawback of MR image is the limited acquisition time, made for patient's comfort that affects visual quality and results decrease in signal-to-noise ratio (SNR) (Hanchate and Joshi 2020a). MRI acquisition process results high Gaussian density noise and affects the disease diagnosis

✉ A. K. Singh
amit.singh@nitp.ac.in

S. Sahu
simahal@mrec.ac.in

A. Anand
ashima1795@gmail.com; ashima.anand@thapar.edu

A. K. Agrawal
agrawal.amrit4@gmail.com

M. P. Singh
mps@nitp.ac.in

[1] Department of ECE, Malla Reddy Engineering College (Autonomous), Maisammaguda, Hyderabad, Telangana, India

[2] Department of CSE, Thapar Institute of Engineering and Technology, Patiala, Punjab, India

[3] Department of Computer Science and Engineering, NIT Patna, Patna, India

[4] Department of CSE, Galgotias College of Engineering and Technology, Greater Noida, India

Published online: 08 January 2022

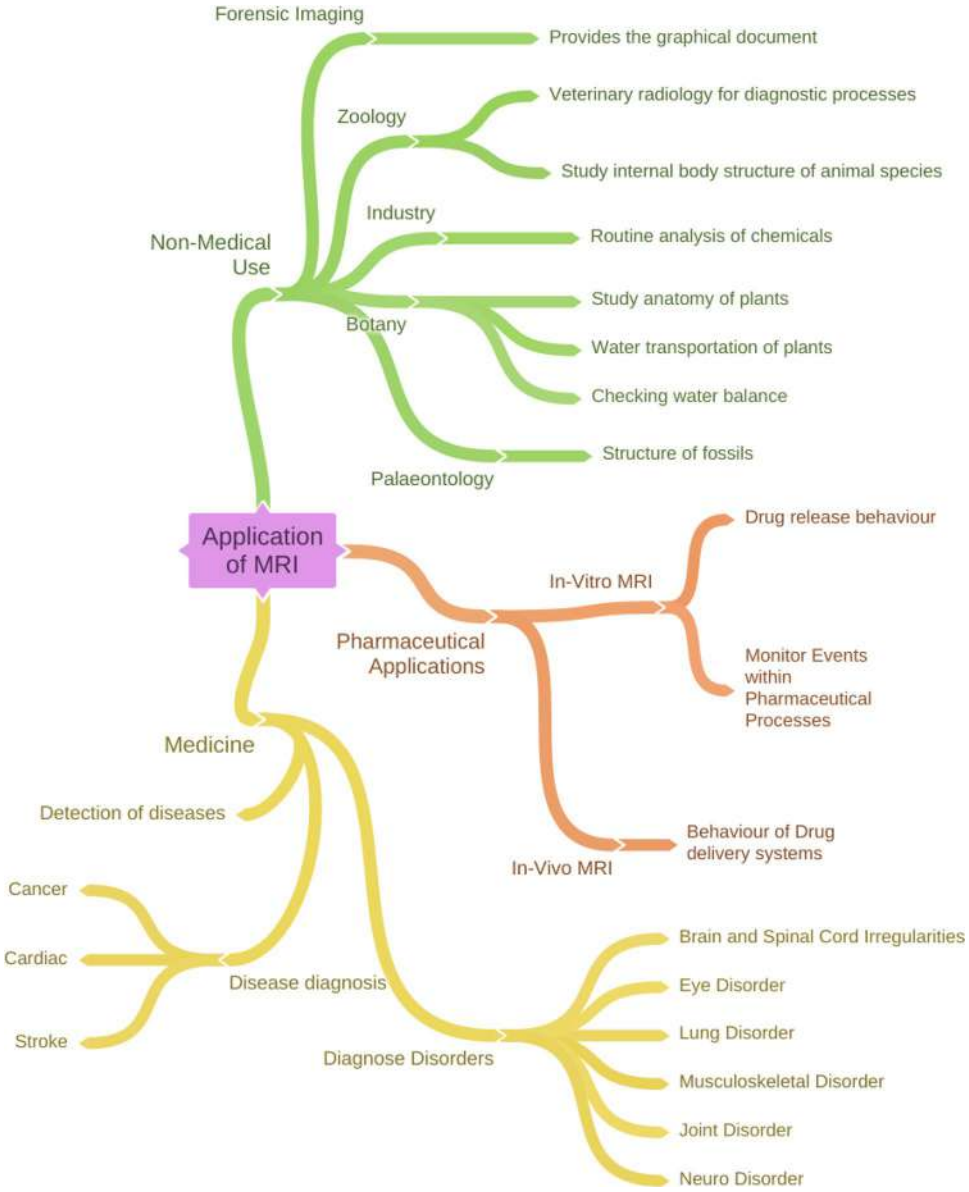

Fig. 1 Applications of MRI in different areas

and management process (Redpath 1998). The main reason of noise in MRI is artifacts during image acquisition and reconstruction process and results image degradation. One of the factors which degrades the MR images and also affect the quantitative measurements extracted from the image is the thermal noise (Zhu et al. 2009). During the reconstruction process of MR image, the main sources of artifacts are: magnetic susceptibility of scanned object, pulse sequence design, radio frequency coil and motions (rigid and non-rigid) (Macovski 1996). Based on the acquisition system, the random noise in MRI may be Rician or Gaussian noise. Single coil acquisition technique results Rician noise while parallel coil acquisition technique results Gaussian noise with zero mean (Sijbers et al. 1998). High SNR is highly required for true interpretation of MR image data (Kanoun et al. 2020) and this necessitates the de-noising of MR images.

An improved de-noising methodology is presented in this paper motivated by the work of Manjón et al. (2008) that utilizes the non-local features of the NLM method. A noise estimation method based on non-local mean was proposed by them for removing Gaussian and Rician noise from MRI. In our paper special attention is given for finding the accurate noise variance which Manjón et al. (2008) failed to explain.

In this paper, we develop a robust de-noising mechanism to recover MR images degraded by Gaussian and Rician noise. Here, multi-resolution approach is combined with the non-local mean (NLM) filter to design an unbiased NLM filter. The noise variance is calculated from the complex

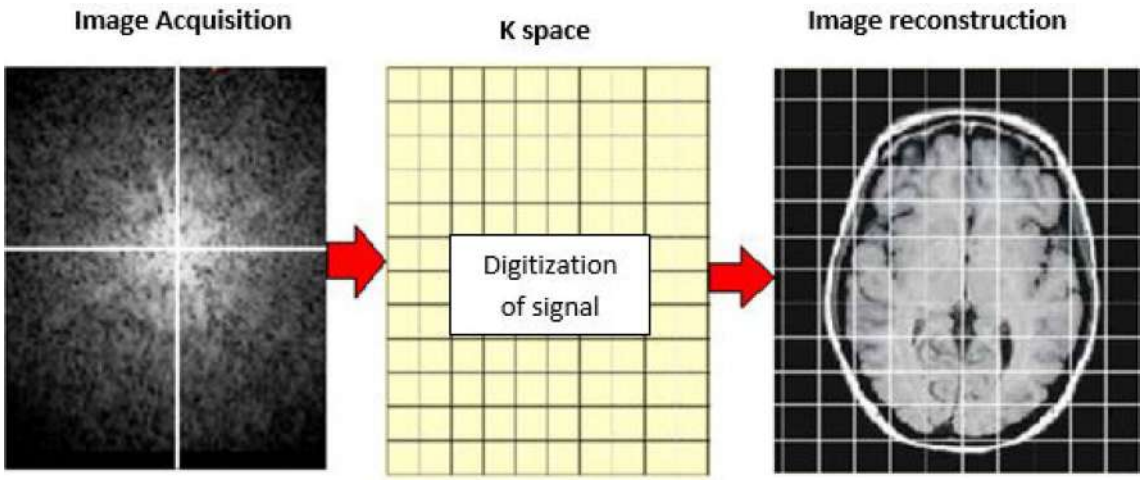

Fig. 2 MR imaging process

dataset assuming the noise is distributed in Gaussian nature. The simulated results demonstrate that the proposed mechanism performed more efficiently than the other traditional schemes. It indicates a considerable improvement of 25.32%, 11.26%, 19.93%, 28.31% and 30.81% in Peak Signal to Noise Ratio (PSNR), Correlation of coefficient (CoC), Pratt's Figure of Merit (FOM), Mean Structural Similarity Index (MSSIM), and Edge Preservation Index (EPI) performance parameters, respectively over the existing Unbiased NLM filters.

The rest of the paper is arranged like below. Section 2 includes the relevant works. Section 3 introduces our proposed filter for noisy MR images. Section 4 gives the experimental results and discussion, followed by the conclusions along with future scope in the Sect. 5.

2 Related work

To date, a variety of de-noising schemes for MRI images have been widely concerned by many scholars and researchers. Therefore, we review them separately. During MR image acquisition the most common approach to reduce the random noise is increasing the count of signal averages and speed is the main disadvantage of this method (Sahu et al. 2019c). This limitation can be overcome by applying algorithmic approached de-noising methods likely; filtering approached methods, transform based methods and statistical approached methods.

Filtering approached methods can be categorized as spatial, temporal, frequency-domain (McVeigh et al. 1985), NLM (Manjon et al. 2007), Bilateral (Hamarneh and Hradsky 2007) and anisotropic diffusion (Krissian and Aja-Fernández 2009). An MRI de-noising method was proposed by Hong et al. (2020) for Rician noise removal. The author developed a network called feature fusion and attention network (FFA-DMRI), which consists of three blocks namely feature block, fusion block and attention block for separating noise from MR data. A hybrid noise removal methodology for MRI was developed by Romdhane et al. (2021). Their approach was based on anisotropic diffusion filter and NLM filter. They validated the method on In-Vivo data. Xie et al. (2020) developed a machine learning based de-noising method for MRI image of low SNR. In NLM filtering method the image pixels of similar value are averaged based on their intensity distance. Based on this principle, bilateral filter is designed. The difference between these filters and NLM filter is that, NLM filter supports the comparison of regions than pixel comparison. The original NLM filter utilizes Euclidean distance for similarity measurement (Buades et al. 2005). Further this approach was improved by Rajan et al. (2014). They proposed KS distance for similarity measurement. He and Greenshields (2008) proposed a Non Local Maximum Likelihood Estimation (NLML) algorithm for de-noising MR image affected by Rician noise. They developed a non-local maximum likelihood estimator that estimates the level of redundancy in an MR image. An MRI de-noising technique was presented by Chen et al. (2020) which utilized the principle of NLM filter. They combined adaptive NLM filter with Fuzzy C-Means algorithm to remove Rician noise. An improved non local correction patch based de-noising technique was proposed by Sarkar et al. (2020), to de-noise brain MRI. Their proposed method was based on NLM filtering technique. The input image was divided into smooth component and periodic component by utilizing a Fast Fourier Transform (FFT) algorithm. Further non local based averaging was used to de-noise both the components. A de-noising algorithm based on Shearlet transform was developed by Sharma and

Chaurasia (2021). They designed a NLM filter by combining Shearlet filter and non-sub-sampled pyramid filter.

A non local (NL) based MRI de-noising method was proposed by Leal et al. (2020) for removing noise from MR image. Their method was based on sparse representation by using NL single value decomposition algorithm.

Transform based methods are preferred than the filtering approached methods commonly Wavelet transform due to its multiresolution and multiscale property. In transform based methods, the noisy image is converted to transform coefficients by applying mathematical based transforms such as Wavelet (Kagoiya and Mwangi 2017), contourlet (Anila et al. 2017) and Curvelet (Bhadauria and Dewal 2013) transforms. Further the transform coefficients are threshold and the image is recovered by applying inverse transformation method. A transform based gamma correction methodology was developed by Kollem et al. (2020) to de-noise brain MRI. In this method the noisy pixels were threshold by a generalized cross-validation method. Combining Wavelet transform and Laplace transform a de-noising method was proposed by Upadhyay et al. (2021) for removing noise from MR image. Hanchate and Joshi (2020b) developed a noise removal methodology by grouping Wavelet shrinkage and 3D Discrete Wavelet Transform (DWT) for de-noising MRI. The threshold value was decided by implementing a noise validation de-noising technique.

The transform based de-noising methods heavily depend upon the threshold value selection. A correct estimation of the threshold value is required to remove the noise effectively. This problem is solved by applying statistical models and estimators which utilizes the local statistics of the data distribution to find the threshold value (Sahu et al. 2020a). Das et al. (2020) presented de-noising methodology for removing noise and preserving edge and details of MR image. They utilized an estimator (local variance based) to estimate the noise and, statistical edge stopping function for image details preservation. A statistical based de-noising method was presented by Sahu et al. (2020b) for MR images. In this method wavelet coefficient data distribution was fitted to a Normal Inverse Gaussian (NIG) density function to extract the noise-free pixels and noise variance was estimated by MAD estimator.

The MR noise reduction algorithm based on NLM filter is an excellent methodology to remove noise and enhance the diagnostic accuracy due to its non-local self-similarity nature (Heo et al. 2020). In other filtering methods there is a chance of loss of inherent information which is minimized by applying the improved unbiased NLM filter that utilizes a MAD estimator for effective noise calculation and so preserves the edge and details information.

3 Proposed algorithm

In this section, we concentrate on the proposed model to recover MR images degraded by Gaussian and Rician noise. First of all, the Gaussian noise information is extracted from the noisy image by performing the wavelet decomposition, statistically modeling the diagonal sub-band wavelet coefficients, and estimating the noise variance by applying the MAD estimator. Next, the Rician noise is removed by applying a NLM filter which averages the noisy pixels by a Gaussian weight factor. Finally, the NLM filtered output pixels are unbiased by applying the noise bias subtraction method for recovering the original pixel values. Figure 3 presents the basic process of our de-noising scheme, and the details are as follows.

Step 1. Wavelet decomposition of the input image.

The wavelet decomposition of an image of size A × B number can be defined mathematically as Gonzalez and Woods (2002), Sahu et al. (2018, 2019a, b):

$$W(a,b) = \frac{1}{\sqrt{AB}} \sum_{p=1}^{A} \sum_{q=1}^{B} f_M^A(p,q) \varphi_M^A(a,b,p,q) + \sum_{m=1}^{M} \sum_{N \epsilon H,V,D} \sum_{p=1}^{A} \sum_{q=1}^{B} f_m^N(p,q) \Psi_m^N(a,b,p,q) \tag{1}$$

where $\varphi(.)$ and $\Psi(.)$ are scaling and wavelet functions respectively. Nϵ H,V,D represents horizontal, vertical and diagonal sub-bands respectively and a, b, p and q are the variables. f_M^A (p,q), φ_M^A (a,b,p,q), f_m^N (p,q), and Ψ_m^N (a,b,p,q) are M level approximation coefficients, 2D scaling coefficients, detailed coefficients and 2D wavelet coefficients respectively. The 2D scaling and wavelet functions are defined as follows:

$$\varphi_M^A(a,b,p,q) = 2^{\frac{M}{2}} \varphi\left(2^M a - p\right) \varphi\left(2^M b - q\right) \tag{2}$$

$$\Psi_M^H(a,b,p,q) = 2^{\frac{M}{2}} \psi\left(2^M a - p\right) \varphi\left(2^M b - q\right) \tag{3}$$

$$\Psi_M^V(a,b,p,q) = 2^{\frac{M}{2}} \varphi\left(2^M a - p\right) \psi\left(2^M b - q\right) \tag{4}$$

$$\Psi_M^D(a,b,p,q) = 2^{\frac{M}{2}} \psi\left(2^M a - p\right) \psi\left(2^M b - q\right) \tag{5}$$

Step 2. Noise variance estimation using the MAD Estimator.

An MAD estimator is applied in first level of diagonal detailed Sub-band (HH1) to find the variance of the Gaussian

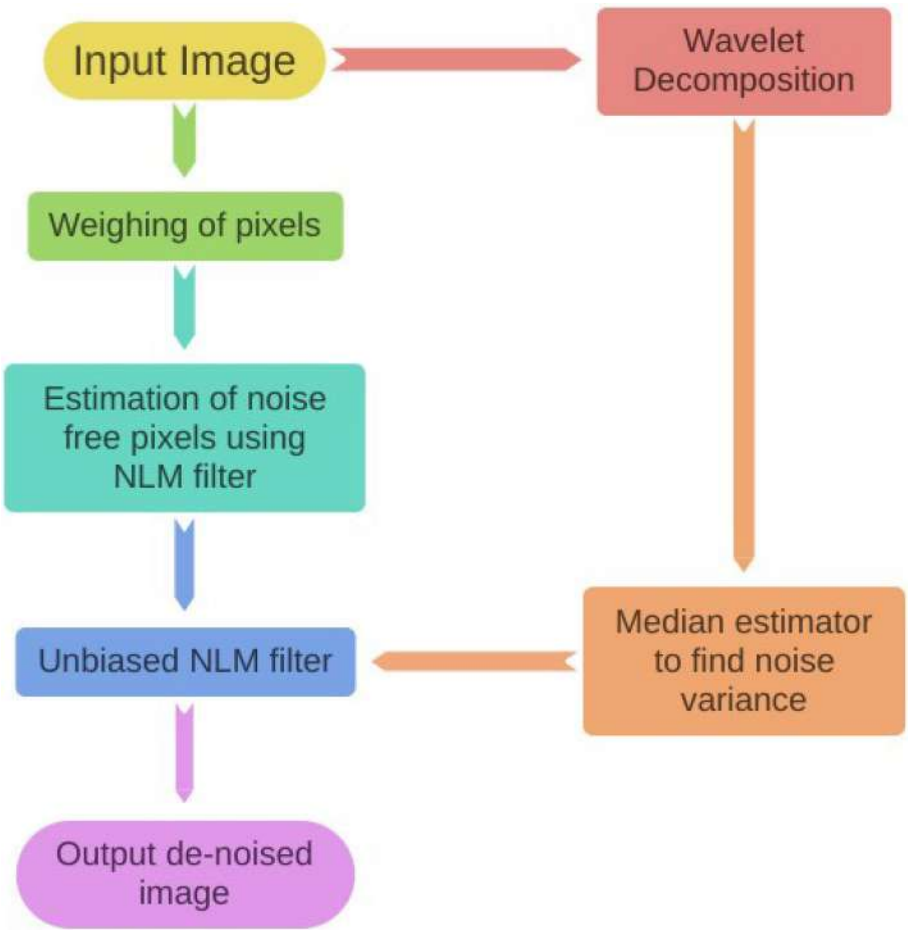

Fig. 3 Flow chart of proposed de-noising scheme

noise. The diagonal detailed sub-band contains most of the noise information. The noise variance σ_n^2 is given by:

$$\hat{\sigma}_{\eta}^2 = \left(\frac{median(|HH1|)}{0.6745}\right)^2 \tag{6}$$

The wavelet transform of the Gaussian noise is also Gaussian in nature. So a Normal PDF is used to model the diagonal detailed wavelet coefficients. The density distribution of wavelet coefficients of HH1 sub-band is shown in Fig. 4. The goodness-of-fit of HH1 sub-band with Normal PDF and CDF are shown in Figs. 5 and 6 respectively. It can be seen that the Gaussian PDF and CDF fits well with the HH1 sub-band data.

Step 3. Calculation of weighing coefficients.

Let W(c,d,a,b) be the weighing Coefficient where,

$$\sum_{a=0}^{A-1}\sum_{b=0}^{B-1} W(c,d,a,b) = 1.$$

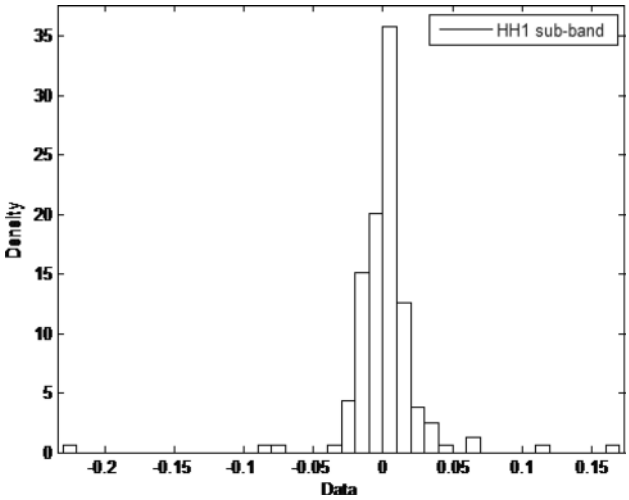

Fig. 4 Distribution of wavelet coefficients in HH1 sub-band for MR image

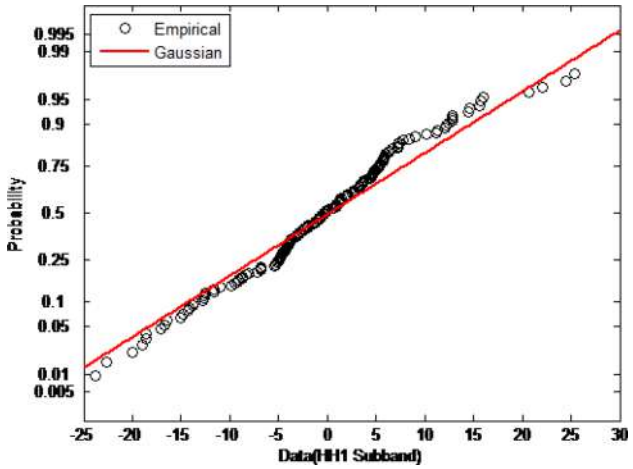

Fig. 5 Goodness-of-fit graph of HH1 sub-band: PDF plot

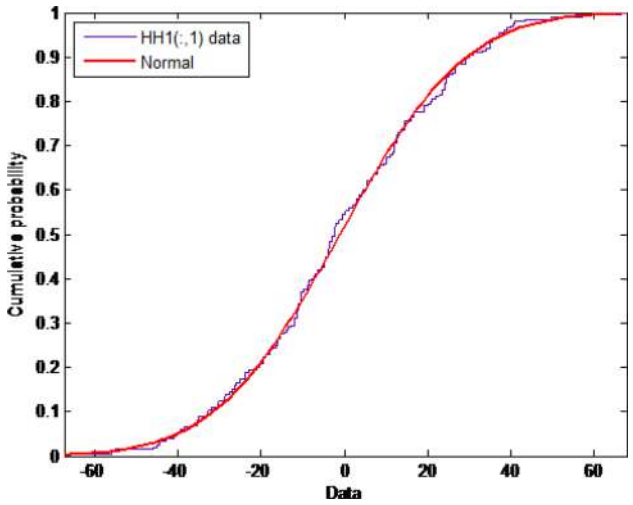

Fig. 6 Goodness of fit graph of HH1 sub-band: CDF plot

The weighing coefficient for the image of size A × B can be defined as:

$$W(c,d,a,b) = \frac{1}{Z(c,d)} e^{\frac{-G_\sigma ||g(N_{cd}) - g(N_{ab})||^2}{h^2}} \tag{7}$$

where c, d, b, and a are the variables and G_σ = Gaussian weighing function with unity standard deviation and zero mean. The parameter h is defined as smoothing parameter, set depending on the value of noise standard deviation and $\|\cdot\|^2$ is the Euclidean distance (Gaussian weighted). Z(c,d) is the normalizing constant defined as:

$$Z(c,d) = \sum_{a=0}^{A-1} \sum_{b=0}^{B-1} e^{\frac{G_\sigma ||g(N_{cd}) - g(N_{ab})||^2}{h^2}} \tag{8}$$

Step 4. Averaging the weighing sum of pixel of intensities and generation of noise-free pixels by using NLM filter.

Let g(a,b) is the input noisy image of size A and the NLM filtered output of the noisy image is defined as Manjón et al. (2008):

$$G(c,d) = \sum_{a=0}^{A-1} \sum_{b=0}^{B-1} W(c,d,a,b) g(a,b) \tag{9}$$

Step 5. Removal of noise bias and obtaining noise free image.

Noise in MRI follows a Rician distribution which results Rayleigh distribution in low intensity region and for higher intensity region results Gaussian distribution. This results the decrease in image contrast. This problem can be overcome by subtracting the noise bias from the square of the MRI magnitude image (Sharma and Chaurasia 2021). So the noise bias can be easily removed from the NLM filtered image as it is signal independent. The unbiased non local mean filter can be found out by Nowak (1999):

$$UNLM[G(c,d)] = \sqrt{G(c,d)^2 - 2\sigma_\eta^2} \tag{10}$$

where $2\sigma_n^2$ =noise bias and σ_n is the standard deviation of the noise and is calculated by using equation (6).

4 Simulation results

In this section we present experimental results to demonstrate the validity of the proposed filter. Firstly, dataset information along with experimental setting is discussed. Next, evaluation metric followed by detail results are also given.

4.1 Dataset and experimental settings

Two kinds of datasets for different noise variances: 0.1, 0.3 and 0.5, are simulated in MATLAB environment.The first kind of dataset is real MR images collected from OSIRIX DICOM (Digital Imaging and Communications in Medicine) image library (Osirix 2014). A total of 100 MRI images were collected and resize to 400 × 400. The second dataset are synthetic images: the self-generated image and the head phantom Image. The generated image with the size (173 × 184), consists of circles and rectangles of various intensities. The head phantom image with the size 256 × 256 was generated in MATLAB environment. Simulation work is performed in MATLAB R2019a environment and the same is used for comparison with existing methods. Wavelet decomposition is performed by using Daubechies 8 (db8), Discrete Wavelet Transform (DWT) and it is preferred due to its orthogonality property (Sahu et al. 2019a, c).

Quantitative comparison is performed through image quality and performance indexes likely Peak Signal to Noise Ratio (PSNR), Correlation of coefficient (COC), Pratt's Figure of Merit (FOM), Mean Structural Similarity Index (MSSIM) and Edge Preservation Index (EPI) (Kanoun et al. 2020; Sahu et al. 2018, 2019a, 2020b). PSNR Measures the quality of reconstructed image and provides the ratio between the original data and the noise introduced. COC determines the interdependence between the reconstructed and original images. FOM measures the dislocated or misplaced edge pixels during reconstruction process. EPI measures the extent of edge preservation in reconstructed image. MSSIM is a quality assessment index that measures the similarity between original and reconstructed images.

4.2 Results and discussion

The ability of the proposed method on removing the noise and preserving the original image properties is proved by comparison with the widely known existing methods, are Unbiased NLM filter (Manjón et al. 2008), KS-NLM method (Rajan et al. 2014), and NLML method (He and Greenshields 2008).The qualitative comparison of the denoising schemes is performed through visual inspection. Figure 7 shows the visual comparison between the existing and proposed methods. First row shows the simulation results of real Brain MRI. Second row shows the simulation results for real spine MRI. And the third row shows the experimental results of real Sagittal T1 Brain MRI. Better evaluation of filter performance can be done by selecting a small area and applying the filter methods. Figure 8 shows the visual image quality comparison for the small selected area marked as red box. It is seen that the contrast and visual quality of the proposed method is superior to other methods. Qualitative assessment for filtering methods is shown in Fig. 9 for synthetic images. First row shows the simulation result for self-generated synthetic image and the second row shows for head phantom synthetic image.

Proposed method's efficiency on noise removal and edge and details preservation can be confirmed by the performance parameters values. The performance and quality parameters comparison for non-local methods for self-generated synthetic image are discussed in Tables 1, 2, 3, 4 and 5 and for real brain MR image is discussed in Table 6. In

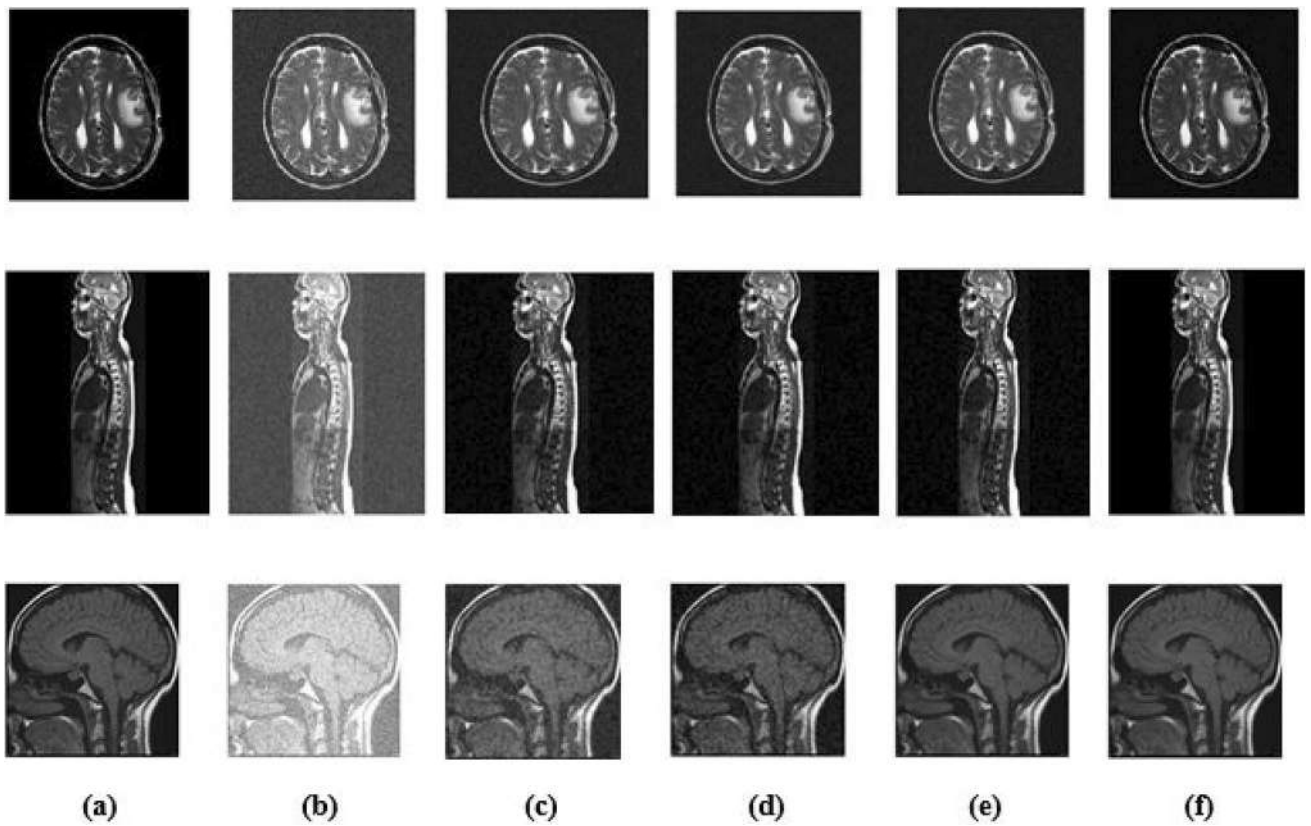

Fig. 7 De-noising Performance result of MR Images (a) Real MR images (b) Degraded by White Gaussian Noise (first row, second row and third row by standard deviations 0.1, 0.3 and 0.5 respectively) (c) NLML (d) KS-NLM (e) UNLM (f) Proposed Method

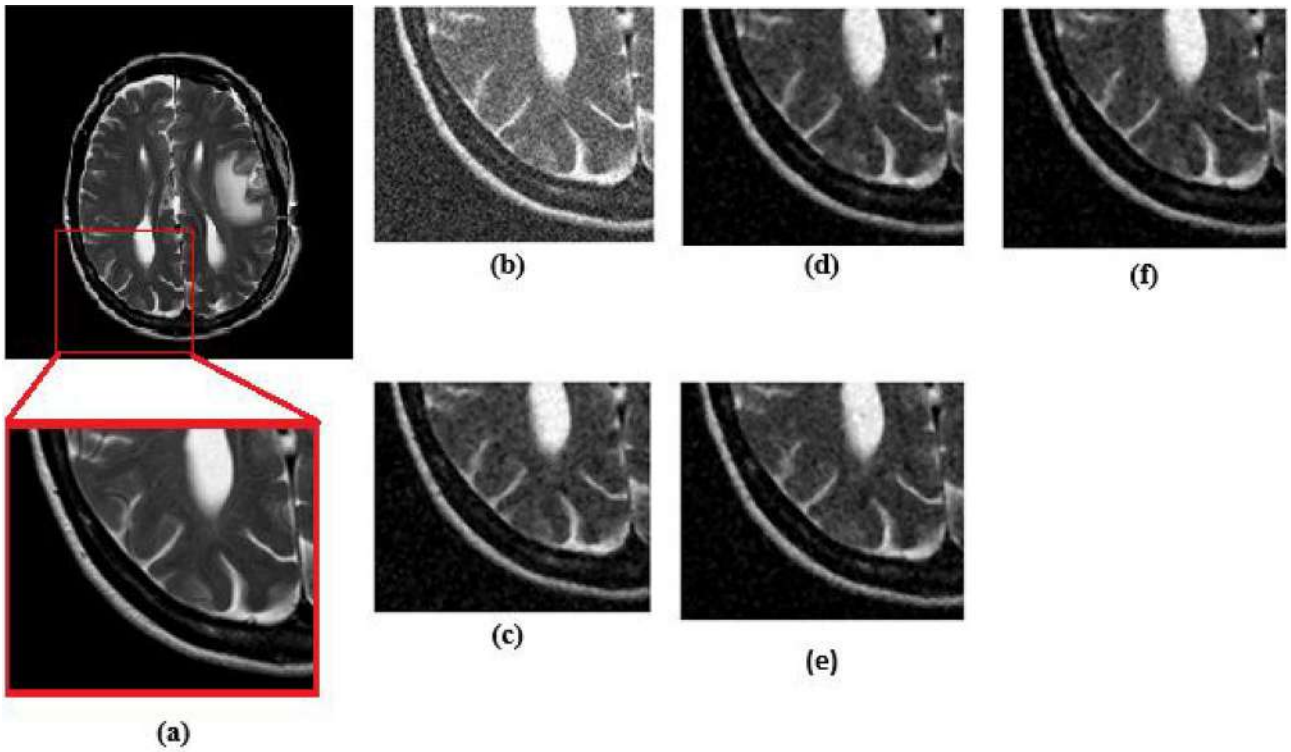

Fig. 8 De-noising performance result of a Zoomed view of a small selected area, **a** real MR image, **b** noisy Image degraded by Gaussian noise of $\sigma_n^2 = 0.3$ **c** NLML **d** KS-NLM **e** UNLM **f** proposed method

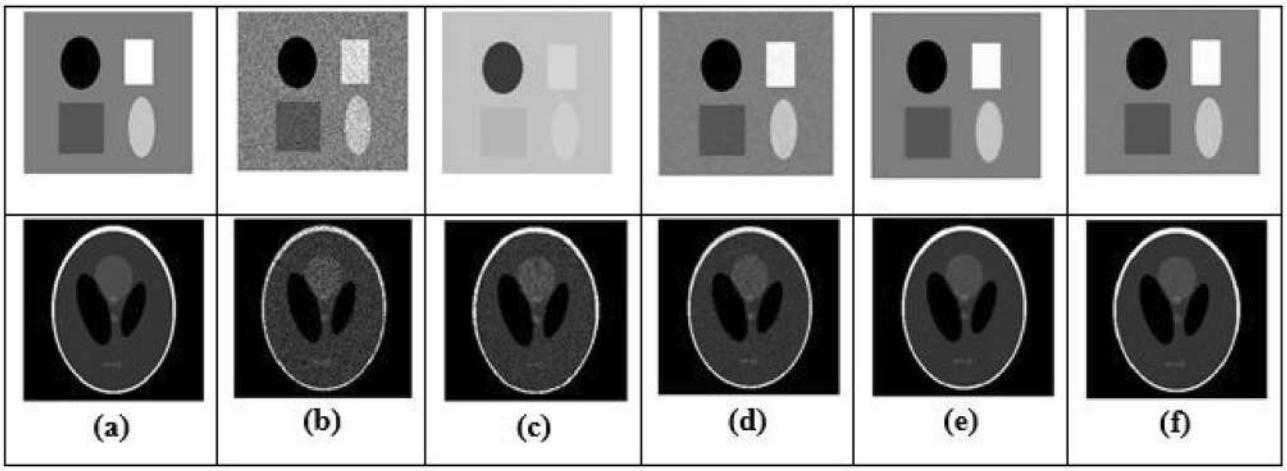

Fig. 9 De-noising performance result of synthetic images **a** original image **b** noisy synthetic Image (Gaussian Noise of $\sigma_n^2 = 0.2$) **c** NLML **d** KS-NLM **e** UNLM **f** proposed method

Table 1, we compare our proposed filter in terms of PSNR with compared methods (Manjón et al. 2008; Rajan et al. 2014) and He and Greenshields (2008) by using synthetic image with three different noise variances. If we set value of $\sigma_n^2 = 0.1$, the PSNR (in dB) score is 33.66. If we set value of $\sigma_n^2 = 0.3$, the PSNR (in dB) score is 32.43. If we set value of $\sigma_n^2 = 0.5$, the PSNR(in dB) score is 30.09. This Table shows that value of PSNR as obtained by our scheme is

Table 1 PSNR (dB) values for different techniques

Techniques	Noise variances		
	0.1	0.3	0.5
Noisy	19.26	14.15	12.59
Unbiased NLM (Manjón et al. 2008)	31.41	30.29	28.25
KS-NLM (Rajan et al. 2014)	30.35	27.68	25.33
NLML (He and Greenshields 2008)	27.89	26.29	22.47
Proposed	33.66	32.43	30.09

always greater than 30.09. The best improvements of our suggested scheme on PSNR score compared with the scheme in Manjón et al. (2008), Rajan et al. (2014) and He and Greenshields (2008) are 6.68% (for $\sigma_n^2 = 0.1$), 15.81% (for $\sigma_n^2 = 0.5$), and 25.32% (for $\sigma_n^2 = 0.5$), respectively. In Table 2, we compare our proposed filter in terms of CoC with compared methods (Manjón et al. 2008; Rajan et al. 2014), and He and Greenshields (2008) by using synthetic image with three different noise variances. If we set value of $\sigma_n^2 = 0.1$, the CoC score is 0.989. If we set value of $\sigma_n^2 = 0.3$, the CoC score is 0.974. If we set value of $\sigma_n^2 = 0.5$, the CoC score is 0.957. This Table shows that value of CoC as obtained by our scheme is always greater than 0.957.The best improvements of our suggested scheme on CoC score compared with the scheme in Manjón et al. (2008), Rajan et al. (2014) and He and Greenshields (2008) are 4.07% (for $\sigma_n^2 = 0.5$), 6.68% (for $\sigma_n^2 = 0.5$), and 11.26% (for $\sigma_n^2 = 0.3$) respectively. In Table 3, we compare our proposed filter in terms of FOM with compared methods (Manjón et al. 2008; Rajan et al. 2014), and He and Greenshields (2008) by using synthetic image with three different noise variances. If we set value of $\sigma_n^2 = 0.1$, the FOM score is 0.968. If we set value of $\sigma_n^2 = 0.3$, the FOM score is 0.953. If we set value of $\sigma_n^2 = 0.5$, the FOM score is 0.89. This Table shows that value of FOM as obtained by our scheme is always greater than 0.953.The best improvements of our suggested scheme on FOM score compared with the scheme in Manjón et al. (2008), Rajan et al. (2014) and He and Greenshields (2008) are 3.88% (for $\sigma_n^2 = 0.3$), 15.61% (for $\sigma_n^2 = 0.5$), and 19.93% (for $\sigma_n^2 = 0.3$), respectively. In Table 4, we compare our proposed filter in terms of MSSIM with compared methods (Manjón et al. 2008; Rajan et al. 2014), and He and Greenshields (2008) by using synthetic image with three different noise variances. If we set value of $\sigma_n^2 = 0.1$, the MSSIM score is 0.877. If we set value of $\sigma_n^2 = 0.3$, the MSSIM score is 0.851. If we set value of $\sigma_n^2 = 0.5$, the MSSIM score is 0.825. This Table shows that value of MSSIM as obtained by our scheme is always greater than 0.825. The best improvements of our suggested scheme on MSSIM score compared with the

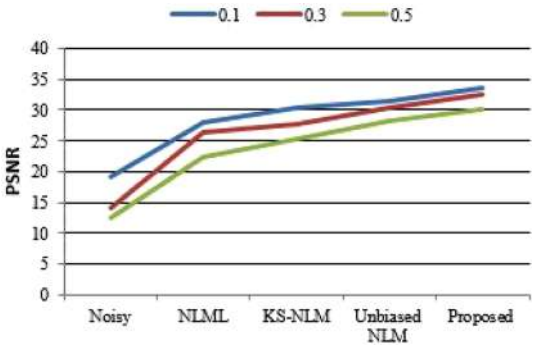

Fig. 10 Graphical comparison of schemes in terms of PSNR

Table 2 CoC results for different techniques

Techniques	Noise variances		
	0.1	0.3	0.5
Noisy	0.823	0.766	0.635
Unbiased NLM (Manjón et al. 2008)	0.971	0.959	0.918
KS-NLM (Rajan et al. 2014)	0.921	0.915	0.893
NLML (He and Greenshields 2008)	0.895	0.866	0.858
Proposed	0.989	0.974	0.957

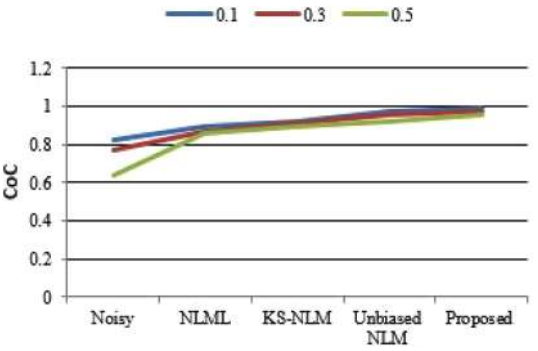

Fig. 11 Graphical comparison of schemes in terms of CoC

Table 3 FOM results for different techniques

Techniques	Noise variances		
	0.1	0.3	0.5
Noisy	0.711	0.623	0.605
Unbiased NLM (Manjón et al. 2008)	0.935	0.916	0.863
KS-NLM (Rajan et al. 2014)	0.850	0.831	0.751
NLML (He and Greenshields 2008)	0.832	0.763	0.720
Proposed	0.968	0.953	0.890

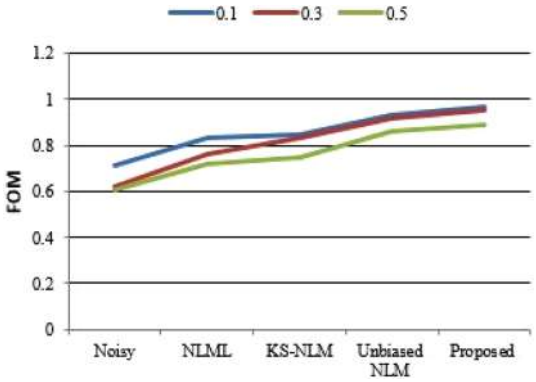

Fig. 12 Graphical comparison of schemes in terms of FOM

Table 4 MSSIM results for different techniques

Techniques	Noise variances		
	0.1	0.3	0.5
Noisy	0.638	0.599	0.454
Unbiased NLM (Manjón et al. 2008)	0.844	0.827	0.809
KS-NLM (Rajan et al. 2014)	0.755	0.728	0.684
NLML (He and Greenshields 2008)	0.735	0.61	0.592
Proposed	0.877	0.851	0.825

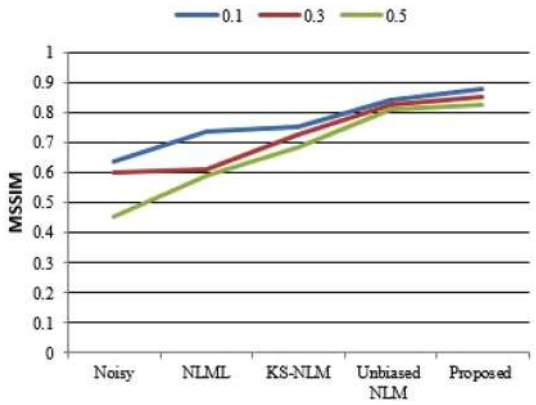

Fig. 13 Graphical comparison of schemes in terms of MSSIM

scheme in Manjón et al. (2008), Rajan et al. (2014) and He and Greenshields (2008) are 3.71% (for $\sigma_n^2 = 0.1$),17.09%(for $\sigma_n^2 = 0.5$), and 28.31%(for $\sigma_n^2 = 0.3$), respectively. In Table 5, we compare our proposed filter in terms of MSSIM with compared methods (Manjón et al. 2008; Rajan et al. 2014), and He and Greenshields (2008) by using synthetic image with three different noise variances. If we set value of $\sigma_n^2 = 0.1$, the EPI score is 0.788. If we set value of $\sigma_n^2 = 0.3$, the

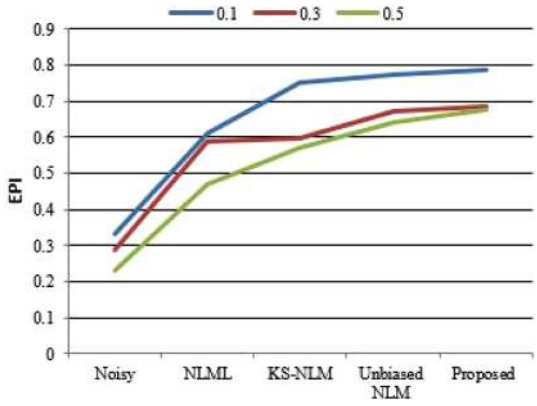

Fig. 14 Graphical comparison of filters in terms of EPI

EPI score is 0.685. If we set value of $\sigma_n^2 = 0.5$, the EPI score is 0.675. This Table shows that value of EPI as obtained by our scheme is always greater than 0.675. The best improvements of our suggested scheme on EPI score compared with the scheme in Manjón et al. (2008), Rajan et al. (2014) and He and Greenshields (2008) are 7.24% (for $\sigma_n^2 = 0.5$), 15.4% (for $\sigma_n^2 = 0.5$), and 30.81% (for $\sigma_n^2 = 0.5$), respectively.

Table 6 shows the comparison of Non Local filters with the proposed filter for real image in terms of the performance parameters. The proposed methodology performed well in terms of edge and structure preservation and noise reduction. The proposed methodology improved 6.35%in terms of PSNR, 2.22% in terms of CoC, 2.91% in terms of FOM, 11.9% in terms of MSSIM and 5.76% in terms of EPI over Unbiased NLM method (Manjón et al. 2008), the next best method. The graphical comparison of performance indexes for all Non Local filters and proposed method for self-generated synthetic image are shown in Figs. 10, 11, 12, 13 and 14, for noise variances 0.1 (Green color), 0.3 (Red color) and 0.5 (Blue color). Performance indexes comparison for real Brain MRI is shown in Fig. 15. All the parameter values are plotted as a function of noise variance. It is seen that the proposed filtering method performs better than the compared schemes.

5 Conclusion

In this paper, we have suggested an improved unbiased-NLM filter to solve the de-noising issue in the MRI images. An unbiased NLM filter is designed by combining the features of NLM filter and the local statistics of the noise.The noise variance is calculated from the complex dataset assuming the noise is distributed in Gaussian nature.Compared

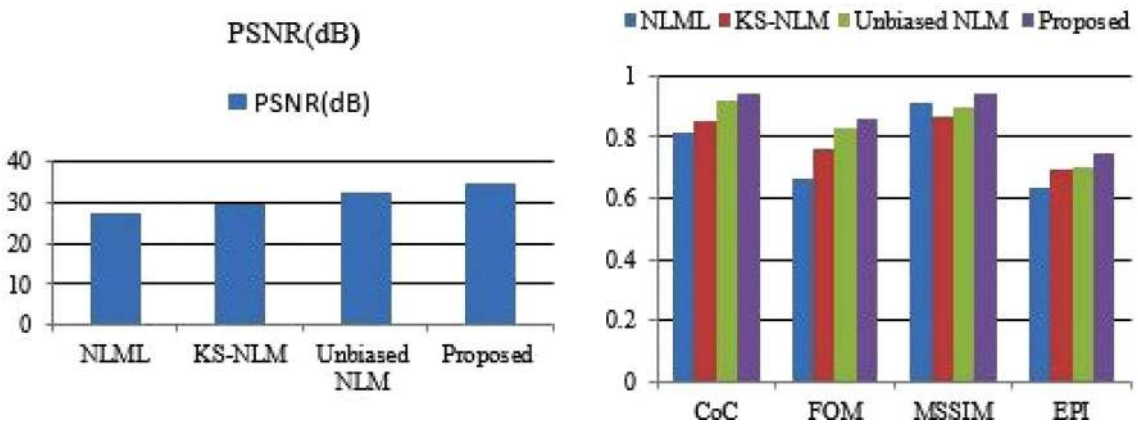

Fig. 15 Graphical comparison of filters in terms of Performance Index for Real brain MR Image

Table 5 EPI results for different techniques

Techniques	Noise variances		
	0.1	0.3	0.5
Noisy	0.334	0.287	0.231
Unbiased NLM (Manjón et al. 2008)	0.775	0.673	0.642
KS-NLM (Rajan et al. 2014)	0.75	0.597	0.571
NLML (He and Greenshields 2008)	0.612	0.589	0.467
Proposed	0.788	0.685	0.675

with the traditional existing non-local mean filtering technology, this proposed filter has the following advantages: (1) Through statistically modeling the wavelet coefficients, accurate noise variance is computed to remove the Gaussian and Rician noise from MR-image (2) By using the accurate estimation of noise bias by statistically modeling the diagonal detail wavelet coefficients, the strength of our proposed de-noising mechanism is further improved.Our experiments on OSIRIX DICOM MRI dataset and some self-generated synthetic images demonstrate that promising results against attacks. Comparison with the non-local mean filtering technology algorithms, the proposed filter has more excellent results.In future the de-noising results may be improved by modeling the wavelet coefficient by Rayleigh distribution to find the Rician noise information.

Table 6 Parameter values for Different Non Local Methods for Real brain MR Image

Techniques	Performance parameters				
	PSNR (dB)	CoC	FOM	MSSIM	EPI
Unbiased NLM (Manjón et al. 2008)	32.56	0.921	0.833	0.901	0.703
KS-NLM (Rajan et al. 2014)	29.69	0.854	0.765	0.866	0.696
NLML (He and Greenshields 2008)	27.38	0.812	0.667	0.911	0.636
Proposed	34.77	0.942	0.858	0.946	0.746

Data availability No data were used to support this study.

References

Anila S, Sivaraju S, Devarajan N (2017) A new contourlet based multiresolution approximation for MRI image noise removal. Natl Acad Sci Lett 40(1):39–41

Bhadauria H, Dewal M (2013) Medical image denoising using adaptive fusion of curvelet transform and total variation. Comput Electric Eng 39(5):1451–1460

Buades A, Coll B, Morel JM (2005) A non-local algorithm for image denoising. In: 2005 IEEE Computer Society Conference on computer vision and pattern recognition (CVPR'05), IEEE, vol 2, pp 60–65

Chen K, Lin X, Hu X, Wang J, Zhong H, Jiang L (2020) An enhanced adaptive non-local means algorithm for Rician noise reduction in magnetic resonance brain images. BMC Med Imaging 20(1):1–9

Das P, Pal C, Chakrabarti A, Acharyya A, Basu S (2020) Adaptive denoising of 3d volumetric MR images using local variance based estimator. Biomed Signal Process Control 59:101901

Gonzalez R, Woods R (2002) Digital image processing, 2nd edn. Prentice Hall, Upper Saddle River

Hamarneh G, Hradsky J (2007) Bilateral filtering of diffusion tensor magnetic resonance images. IEEE Trans Image Process 16(10):2463–2475

Hanchate V, Joshi K (2020a) Denoising of MRI images using fast NLM. J Electric Eng Comput Sci (IJEECS) 18(1):135–141

Hanchate V, Joshi K (2020b) MRI denoising using bm3d equipped with noise invalidation denoising technique and VST for improved contrast. SN Appl Sci 2(2):1–8

He L, Greenshields IR (2008) A nonlocal maximum likelihood estimation method for Rician noise reduction in MR images. IEEE Trans Med Imaging 28(2):165–172

Heo YC, Kim K, Lee Y (2020) Image denoising using non-local means (NLM) approach in magnetic resonance (MR) imaging: a systematic review. Appl Sci 10(20):7028

Hong D, Huang C, Yang C, Li J, Qian Y, Cai C (2020) FFA-DMRI: a network based on feature fusion and attention mechanism for brain MRI denoising. Front Neurosci 14:934

Kagoiya K, Mwangi E (2017) A hybrid and adaptive non-local means wavelet based MRI denoising method with bilateral filter enhancement. Int J Comput Appl 166:1–7

Kanoun B, Ambrosanio M, Baselice F, Ferraioli G, Pascazio V, Gómez L (2020) Anisotropic weighted KS-NLM filter for noise reduction in MRI. IEEE Access 8:184866–184884

Kollem S, Rama Linga Reddy K, Srinivasa Rao D (2020) Modified transform-based gamma correction for MRI tumor image denoising and segmentation by optimized Histon-based elephant herding algorithm. Int J Imaging Syst Technol 30(4):1271–1293

Krissian K, Aja-Fernández S (2009) Noise-driven anisotropic diffusion filtering of MRI. IEEE Trans Image Process 18(10):2265–2274

Leal N, Zurek E, Leal E (2020) Non-local SVD denoising of MRI based on sparse representations. Sensors 20(5):1536

Macovski A (1996) Noise in MRI. Magn Reson Med 36(3):494–497

Manjon J, Robles M, Thacker N (2007) Multispectral MRI de-noising using non-local means. Med Image Underst Anal (MIUA), pp 41–46

Manjón JV, Carbonell-Caballero J, Lull JJ, García-Martí G, Martí-Bonmatí L, Robles M (2008) MRI denoising using non-local means. Med Image Anal 12(4):514–523

McVeigh E, Henkelman R, Bronskill M (1985) Noise and filtration in magnetic resonance imaging. Med Phys 12(5):586–591

Nowak RD (1999) Wavelet-based Rician noise removal for magnetic resonance imaging. IEEE Trans Image Process 8(10):1408–1419

Osirix (2014) Osirix dicom image. http://www.osirix-viewercom/resources/diacom-image-library/. Accessed 13 Mar 2021

Rajan J, Arnold J, Sijbers J (2014) A new non-local maximum likelihood estimation method for Rician noise reduction in magnetic resonance images using the Kolmogorov-Smirnov test. Signal Process 103:16–23

Redpath TW (1998) Signal-to-noise ratio in MRI. Br J Radiol 71(847):704–707

Richardson JC, Bowtell RW, Mäder K, Melia CD (2005) Pharmaceutical applications of magnetic resonance imaging (MRI). Adv Drug Deliv Rev 57(8):1191–1209

Romdhane F, Villano D, Irrera P, Consolino L, Longo DL (2021) Evaluation of a similarity anisotropic diffusion denoising approach for improving in vivo CEST-MRI tumor pH imaging. Magn Reson Med 85(6):3479–3496

Sahu S, Singh HV, Kumar B, Singh A (2018) Statistical modeling and Gaussianization procedure based de-speckling algorithm for retinal oct images. J Ambient Intell Human Comput. https://doi.org/10.1007/s12652-018-0823-2

Sahu S, Singh HV, Kumar B, Singh AK (2019a) De-noising of ultrasound image using Bayesian approached heavy-tailed Cauchy distribution. Multimed Tools Appl 78(4):4089–4106

Sahu S, Singh HV, Kumar B, Singh AK, Kumar P (2019b) Enhancement and de-noising of oct image by adaptive wavelet thresholding method. In: Singh AK, Mohan A (eds) Handbook of multimedia information security: techniques and applications. Springer, pp 449–471

Sahu S, Singh HV, Kumar B, Singh AK, Kumar P (2019c) Image processing based automated glaucoma detection techniques and role of de-noising: a technical survey. In: Singh AK, Mohan A (eds) Handbook of multimedia information security: techniques and applications. Springer, pp 359–375

Sahu S, Singh HV, Kumar B, Singh AK (2020a) A Bayesian multiresolution approach for noise removal in medical magnetic resonance images. J Intell Syst 29(1):189–201

Sahu S, Singh HV, Singh AK, Kumar B (2020b) Mr image denoising using adaptive wavelet soft thresholding. In: Dutta D, Kar H, Kumar C, Bhadauria V (eds) Advances in VLSI, communication, and signal processing. Springer, pp 775–785

Sarkar S, Tripathi PC, Bag S (2020) An improved non-local means denoising technique for brain MRI. In: Das AK, Nayak J, Naik B, Pati SK, Pelusi D (eds) Computational intelligence in pattern recognition. Springer, pp 765–773

Sharma A, Chaurasia V (2021) Mri denoising using advanced NLM filtering with non-subsampled Shearlet transform. Signal Image Video Process 15:1–9

Sijbers J, den Dekker AJ, Van Audekerke J, Verhoye M, Van Dyck D (1998) Estimation of the noise in magnitude MR images. Magn Reson Imaging 16(1):87–90

Upadhyay P, Upadhyay S, Shukla K (2021) Magnetic resonance images denoising using a wavelet solution to Laplace equation associated with a new variational model. Appl Math Comput 400:126083

Xie D, Li Y, Yang H, Bai L, Wang T, Zhou F, Zhang L, Wang Z (2020) Denoising arterial spin labeling perfusion MRI with deep machine learning. Magn Reson Imaging 68:95–105

Zhu H, Li Y, Ibrahim JG, Shi X, An H, Chen Y, Gao W, Lin W, Rowe DB, Peterson BS (2009) Regression models for identifying noise sources in magnetic resonance images. J Am Stat Assoc 104(486):623–637

Journal of Information Security and Applications 66 (2022) 103147

Contents lists available at ScienceDirect

Journal of Information Security and Applications

journal homepage: www.elsevier.com/locate/jisa

Enhanced security to MANETs using digital codes

Syed Jalal Ahmad [a,*], Ishrath Unissa [b], M. Shoukath Ali [c], Abhay Kumar [d]

[a] Malla Reddy Engineering College (main Campus) Secundrabad, India
[b] CMR Technical Campus Secunderadad, India
[c] Geetanjali College of Engineering & Technology, Hyderabad, India
[d] J B. Institute of Engineering and Technology

ARTICLE INFO

Keywords:
MANET
Multi-hop
Security
Hamming positions, Equal weighted hex code

ABSTRACT

A Mobile Ad-hoc Network (MANET) is a multi-hop, distributed routing network of dynamic nodes without any base structure. Mobile nodes can enter and exit the network at any point, which causes various security threats in MANETs. State-of-the-art approaches resolve this issue mainly by distributing keys and designing the models based on energy parameters. However, key distribution among the nodes is difficult due to the absence of central synchronization and also nodes enter the network with different energies to match the energies of the active node. In this paper, an improved multi-level security (or trust) support for MANETs using Equal Weighted Hex code Cyclic Division Method and Hamming bit positions is presented. The initial security code is generated using the cyclic code division method and the security at each hop is improvised using hamming bits. Our model handles various attacks at network, transport, and application layers. We also discuss simulation experiments that demonstrate the viability of the proposed security model.

Respected Sir,

1. Introduction

Mobile Ad-hoc Networks (MANETs) are temporarily established, self-organized, and maintained networks used for communication from source to the destination node. The data transfer may be in a single hop from source to destination or in multiple hops by using intermediate nodes as routers until the destination node is reached. MANETs are widely used in wireless systems as they are simple and cost-effective. However, there are certain issues incorporated with MANETs such as lack of central authority and association, limited bandwidth, and power, which may cause security challenges in the network [1].

In the current literature, the research community proposed several approaches for improving the security of MANETs by providing keys. Key management uses two main algorithms namely symmetric key algorithm and asymmetric key algorithm [2, 3]. In the symmetric key algorithm, a common key is used for both encryption and decryption. Hence one can know the information that is sent and what is received only with a single key. If any of the active nodes have compromised the key to the attacker node of which the sender is unaware, it can share the information with the attacker node. Moreover, the keys are created using complex mathematical calculations. The asymmetric algorithm consists of two keys, private and public. The public key is common to all the nodes but the private key is unique for each node. Therefore for a multi-node network, it has to generate several keys to provide node authentication. This may not be efficient as key generation depends on complex mathematical problems and once the key is compromised the network is exposed to security attacks [4]. The security can also be improved by considering node energy [5]. However, this may not be valid as the nodes in MANETs have different energies and the network is susceptible to malicious attacks.

In this paper, we improve security by enabling multi-level security using hamming bits. Hamming code is widely used in wireless communication as it is simple and cost-effective. It has a set of binary bits used to detect and correct errors in a communication system. Hamming code adds parity bits to the data, which are at powers of 2 locations in the codeword. Instead of simply considering any digital code, the initial codeword in the presented approach is generated by using the equal-weighted binary hex code as this code is not a continuous series to be judged. Hex-code has been used in [32] but in this paper cyclic division is performed in addition (on the hex-code) to improve the authentication of the node and make it difficult for the attacker node to crack it. The generation of code is simple and reduces mathematical and hardware complexity which in turn increases the

* Corresponding author.
E-mail address: jalalkashmire@gmail.com (S.J. Ahmad).

https://doi.org/10.1016/j.jisa.2022.103147

Available online 4 March 2022

efficiency of a system (node).

To avoid the attacks present at different layers of the network, we develop a multi-level security model. The first security level is developed to overcome the attacks in the network layer (e.g., wormhole attack, byzantine attack, black hole attack, etc.). The attack in the transport layer (e.g., session hijack attack) can be avoided by the second level of security and the attack associated with the application layer (repudiation) can be solved at the third security level The term multi-level security indicates that the node is trusted multiple times (as three checks of security are performed on it) to decide either the node is active or attacker node. It is the authentication given to the node at each layer (i.e. network, transport, and application layers) to access the data being transferred from source to destination depending upon the security codes being matched at every layer.

In this work, we address security to MANETs based on Software-Defined Networking (SDN). SDN is gaining importance in the research community, as this field of networking minimizes time and gives innovative ideas in the communication field and we use the IPV4 header to analyze the security. The introduction of SDN induces the control and architectural modifications in the network [6, 7], and hence the SDN in combination with the proposed model will improve the performance of the network.

The rest of the paper is organized as follows: In Section 2, we present the related work. Background and motivation are described in Section 3, and the proposed approach is given in Section 4. Simulation results are given in Section 5. Discussion and Conclusion are given in Sections 6 and 7 respectively.

2. Related work

MANETs are exposed to various security threats. Sharma et al [8] proposed an approach based on waiting time to get repeat requests from intermediate nodes to the source node for black hole attack avoidance. Mamatha and Sharma [9] present a highly secured network to detect several attacks in MANETs, preventing the drop of packets and tampering of a message caused by the malicious node. However, this approach increases the complexity of the network, and also may not be valid for multi-hop MANETs. The model presented by Hu et al [10] prevents routing attacks and various DoS attacks using an on-demand source network. However, this technique does not give authorization to routing nodes of the networks. So the attacker node may enter the network and degrade its performance.

Lu et al [11] proposed *Secure on-demand Distance Vector* routing (SAODV) by recognizing few security issues in AODV and can hold better for black hole attack avoidance. However, it may not give complete security against blackhole attacks. The approach given by Deswal and Singh [12] is an improvised version of AODV, by allocating a password to each intermediate node acting as a router in the network. The main short come of this approach is that it may fail when new nodes enter the network. The model proposed by Chandrakant [13] distributes specific identification numbers and energy levels to the nodes of the network to improve security. However, it may not be valid as the nodes enter the network with different energy values.

Xiong and Gong [14] presented a three-level management technique by using cryptography, due to complex mathematics the overhead increases, and the model may not be valid for the miscellaneous networks. Celestin et al [15] present an elliptic curve cryptography (ECC) based model to enhance security. But, this becomes complex because of encryption and decryption of the message. Sun and Yu [16] proposed cost-effective three-layer key management architecture and analyze its efficiency. Michiardi [17] proposed a generic methodology based on reputation and cooperation among the nodes present in the network to avoid selfish nodes. But, this causes an impact on the protocols when implemented on basic network functionality. In [18], the author improves security to the network based on trust and reputation by which the nodes are authorized in the routing process. However, it may be difficult to authenticate the mobile node in the network.

Balakrishnan et al [19] proposed secure MANET routing with trust intrigue (SMRTI) which prevents the network from flooding and packet drop threats. The approach presented by Jay and Hasbi [20] represents a fragmentation scheme to protect the data packets loss by providing sequence numbers to the packets. However, it may be difficult to arrange the packets in sequence order and causes overhead with more packet delivery ratio (PDR). Ahmed et al [21] present *trust and energy-aware routing protocol* (TERP) to detect the malicious node, breaks in the link of the networks, and provide a smaller path for data transfer. This approach may fail to identify the attacker node by taking energy to constrain as nodes with different energies are free to enter and leave the network. Deepika et al [22] proposed a scheme to detect the misbehaving node in MANETs by considering the power factor. However, this approach may not hold well as compromised heterogeneous nodes can enter the network.

Todd and Alec [23] compared various security methods related to MANETs based on energy parameters. Li et al [24] proposed a model in which the key is shared by a local group of nodes called a distributed verifiable key for enhancing security. Tejpreet et al [25] proposed an approach based on routing protocol which is energy efficient. Scott et al [26] presents security issues in SDN and illustrate approaches for improving security in SDN. However, this approach is restricted in the extent to face the current innovations in SDN security. In SDN, the checker is shoveling instructions in an appropriate time to the system fundamentals, to reduce the delay and improves the quality of service. As the software is on top of hardware, so software level can be used to exploit and organize heterogeneous network resources [27]. Ahmad et al [28] presented a survey that exploits the security issues and challenges in SDN. In [29] the author discussed different security methods to authenticate the nodes and prevent security attacks in wireless sensor networks. Yang. J et al [30] represented an approach in which security is given to the network using a chain of blocks and a reinforcement adaptive method that sums the delay of the nodes from source to destination. However, this method may be complex practically and decrease the efficiency of the network. Syed Jalal Ahmad and P. R. Krishna [31] presented an approach to provide security to MANETs using binary hex code and residue technique. But this method becomes complex as the number of nodes increases in the network.

In our approach, we use the Equal Weighted Hex code Cyclic Division Model and Hamming bits to provide multi-level authentication and enhance trust by tackling the attacks present in different network layers.

3. Background and motivation

Ad-hoc networks are widely used in wireless communication as they are easy to build and don't require infrastructure. It is an open network with mobile nodes and no central synchronization is needed. Security attacks in MANETs can be classified as active and passive attacks. Passive attacks snoop the information exchanged between the nodes without changing them. Active attacks degrade the network performance. There are two types of active attacks: internal attack – where the attacker node is present in the network, external attack – the attacker node is present outside the network. Active attacks present in different internet protocol layers are given below [32].

3.1. Attacks in network layer

3.1.1. Wormhole attack

The attacker node takes the packets from the network and passes them to another location of the network from where they can be resent. The proper mechanism should be developed to detect the wormhole attack.

3.1.2. Blackhole attack

In this attack, the attacker node exhibits the most favorable

Table 1.
Security levels that deal with the attacks at different layers

Security level	*Name of the Layer*	*Attacks*
Level 1	Network Layer	a) Wormhole attack b) Blackhole attack c) Byzantine attack d) Information disclosure e) Resource consumption attack f) Routing attacks
Level 2	Transport layer	a) Session hijacking
Level 3	Application layer	a) Repudiation

characteristics of the router in the route finding process. This may degrade the function of the network and interrupt the data transmission process.

3.1.3. Byzantine attack

The main purpose of this attack is to mislead the routing process and cause a drop of packets, non-optimal routing by a single or group of attacker nodes working cooperatively in a network.

3.1.4. Information disclosure

Here the attacker node discloses the authorized information such as network topology, the location of the nodes, and authenticated routing of nodes in the network to the unauthorized node.

3.1.5. Resource consumption attack

In ad-hoc networks, the nodes have limited computational power, battery, and bandwidth. The attacker node tries to degrade the node performance by sending unnecessary routing requests, generate warning packets, and always keep the network node occupied.

3.1.6. Routing attacks

There are various routing attacks such as routing table overflow, packet replication, rushing attacks, etc which interrupt the network performance.

3.2. Attack in transport layer

Session hijacking: the attacker node takes over the session of two nodes in this attack. The most authorized operations are performed at the beginning of the session. Once the session is established the attacker node, disguise as one of the routing nodes and hijack the session. This attack can be avoided by the data encryption process.

3.3. Attack in application layer

Repudiation: it means the node denies its participation in the entire or partial data transfer process. Non-repudiation is one of the important parameters of security assurance in any network.

Most of the existing security models focused either by giving a key or by considering the energy factor which may not be appropriate to provide security to MANETs due to their complexity. In this work, we developed a model based on simple binary codes to improve the security at different layers in three levels Table 1. represents the three security levels at internet protocol layers and respective attacks associated with them. Security level 1 is provided to the network layer to overcome the attacks such as wormhole attacks, black hole attacks, byzantine attacks, information disclosure, resource consumption attack, and routing attacks. These attacks may degrade the network performance. Prevention of session hijack attack in transport level can be given by security level 2 and repudiation can be avoided in security level 3. The authors in [33–37] discussed the detection and prevention of various attacks in MANETs using piece-wise keys and different routing protocols to secure the network. However, these methods may not be efficient as they have to produce keys as well as maintain the routing table of the network.

3.4. Analysis of the proposed model under different attacks

In the presented approach, the first level of security is given to the network layer with the matrix of digital code. A series of mathematical operations are performed to generate this matrix (see equation "(7-11)") and this information can be accessed by the active node of the network (as the information is already stored in the node header). To take part in the routing a node has to match the matrix code and hence the attacks in the network layer can be prevented.

In the transport layer attack can be avoided as such it (attacker node) hijacks the session after some time as it assumes that all the authentication processes will take place at the beginning (i.e. at security level 1 check). However, in security level 2 check it cannot match with the code generated so it can be easily detected as an attacker node. In the application layer, the attacker node intrudes into the system and will manipulate the information. But for the intrusion, has to match with the security level 3 code, and therefore this attack can be avoided.

At each every hop the security code of level 2 and level 3 changes based on mathematical and logical operations which makes the proposed node authentication process even more efficient and reliable. At last, the PDR monitoring of the node makes this process even stronger. The PDR is directly proportional to the energy of the node and the energy of the node can be calculated by the formula given in [38]. Therefore monitoring of energy and PDR enable this approach to eliminate the node with less energy and PDR. If the node is active and has less energy and PDR it may not be efficient for the node to take part in routing, in the proposed approach such node will be considered as attacker node and will not take part in information transfer.

4. Proposed approach

4.1. Generation of initial code matrix

Initially consider equal-weighted Hex code from 0 - 15 (i.e., 3, 5, 6, 9, 10, and 12) are considered as these codes are orthogonal and can be generated using mathematical equations. These decimal numbers are converted into their equivalent binary hex codes as 0011, 0101, 0110, 1001, 1010, and 1100. The decimal numbers which are divisible by 3 as dividend 'B_x' and can be represented as,

$$B_x = \prod_{i=1}^{M} Yi1 \ \ \leq M \leq 4 \text{and} Y = 3 \tag{1}$$

The remaining decimal numbers in the concatenation series can be considered as divisor 'Qx' and are represented in equations "(2)" and "(3)" respectively.

$$\mathrm{F_{MDN}} \ = \frac{F_D + L_D}{F_D} \tag{2}$$

Here, 'F_{MDN}'is the first missing decimal number (i.e. 5) in the concatenation series, 'F_D'=3 is the first decimal value of the concatenation series of 'B_x' and'L_D'=12 is the last decimal value of the concatenation series 'B_x'.

The Second missing decimal number (i.e. 10) in the series can be represented as,

$$S_{MDN} = 2F_{MDN} \tag{3}$$

However, the hex value of the decimal digit 5 starts with zero (0101), so we start with hex code of decimal number '10'(1010) and append hex value of decimal number '5' to it as,

$$Q_x = S_{MDN}\mathrm{F_{MDN}} \tag{4}$$

$$R_x = \frac{B_x}{Q_x} \tag{5}$$

where 'R_x' is the remainder.'R_x' is EX-OR with 'B_x' from LSB to MSB

Table 2.
Level 1 Security Matrix of Proposed Approach

1	2	3	4	5	6	7	8	9	10	11	12	13	14	15	16
H_1	H_2		H_3				H_4								H_5
0	0	1	1	0	1	1	0	1	1	1	1	1	0	1	0
0	M_{22}	M_{23}	M_{24}	-	-	-	-	-	-	-	-	-	-	-	M_{2n}
1	M_{32}	S_{33}	M_{34}	-	-	-	-	-	-	-	-	-	-	-	M_{3n}
1	-	-	-	-	-	-	-	-	-	-	-	-	-	-	-
0	-	-	-	-	-	-	-	-	-	-	-	-	-	-	-
1	-	-	-	-	-	-	-	-	-	-	-	-	-	-	-
1	-	-	-	-	-	-	-	-	-	-	-	-	-	-	-
0	-	-	-	-	-	-	-	-	-	-	-	-	-	-	-
1	-	-	-	-	-	-	-	-	-	-	-	-	-	-	-
1	-	-	-	-	-	-	-	-	-	-	-	-	-	-	-
1	-	-	-	-	-	-	-	-	-	-	-	-	-	-	-
1	-	-	-	-	-	-	-	-	-	-	-	-	-	-	-
1	-	-	-	-	-	-	-	-	-	-	-	-	-	-	-
0	-	-	-	-	-	-	-	-	-	-	-	-	-	-	-
1	-	-	-	-	-	-	-	-	-	-	-	-	-	-	-
0	M_{n2}	M_{n3}	-	-	-	-	-	-	-	-	-	-	-	$M_{n(n-1)}$	M_{nn}

direction of the series to

$$I_{Sec} = B_x \oplus R_x \tag{6}$$

generate the initial security code:

By the use of 'I_{Sec}', we are generating the first row and first column of the N x N security matrix (see Table 2) and the remaining bits of the matrix can be calculated as

$$M_{22} = M_{12} \oplus M_{21} \tag{7}$$

$$M_{23} = M_{21} \oplus M_{13} \tag{8}$$

••••
••••

$$M_{2n=}M_{21} \oplus M_{1n} \tag{9}$$

Generalizing the above, we get,

$$M_{n(n-1)} = M_{n1} \oplus M_{1(n-1)} \tag{10}$$

and,

$$M_{nn} = M_{n1} \oplus M_{1n} \tag{11}$$

Our approach provides security at three levels, and at the same time, we continuously monitor the PDR of the receiving node Table 2. represents the matrix code block that is used to check the first level of security to the MANET. In this approach at hop 1, the matrix block will remain the same as represented in Table 2.

The steps from the equation "(5)-(11)" are performed to make the generation of initial code a difficult task to understand by the attacker node, codes of fewer lengths can be easily hacked but if the length is increased (256 bits) and the bits are generated performing sequence of operations then it may be difficult to decode it. At each layer and hop, the code is modified using hamming bits and performing mathematical operations to detect the attacker nodes.

At hop 1, the second level of security is being provided by the use of security bits H_1, H_2, H_3, H_4, and H_5 which are changed at security level 2 and security level 3 of every hop. Here digital codes which satisfy the hamming rule are used to authenticate the nodes as one of the security criteria. At security level 2, we are directly taking security bits from the equation "(6)" (such as 00100) and complimenting odd terms of the security code (i.e., the complement of H_1, H_3, and H_5), so the final security code word at level two of hop 1 can be represented as '10001'. In terms of the polynomial, it can be shown as

$$P(x) = x^4 + 1 \tag{12}$$

To show the actual length of the codeword, we represent the codes at security level two and three in terms of the polynomial. Instead of transmitting the sequence of 0's and 1's, to reduce the memory space a polynomial can be sent as a security code. At the receiver end i.e. the active node can retrieve the digital security code. To convert digital code to polynomials the following property has been considered and these properties are known to the active nodes.

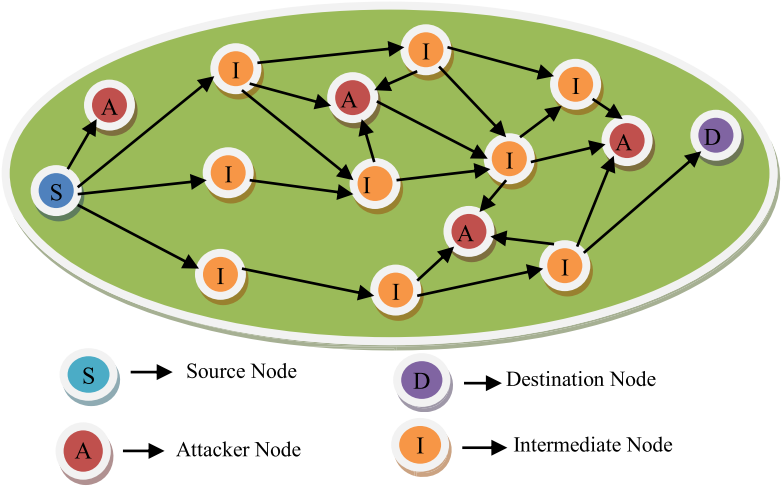

Fig. 1. Sample Multi-hop MANET with Attacker Nodes

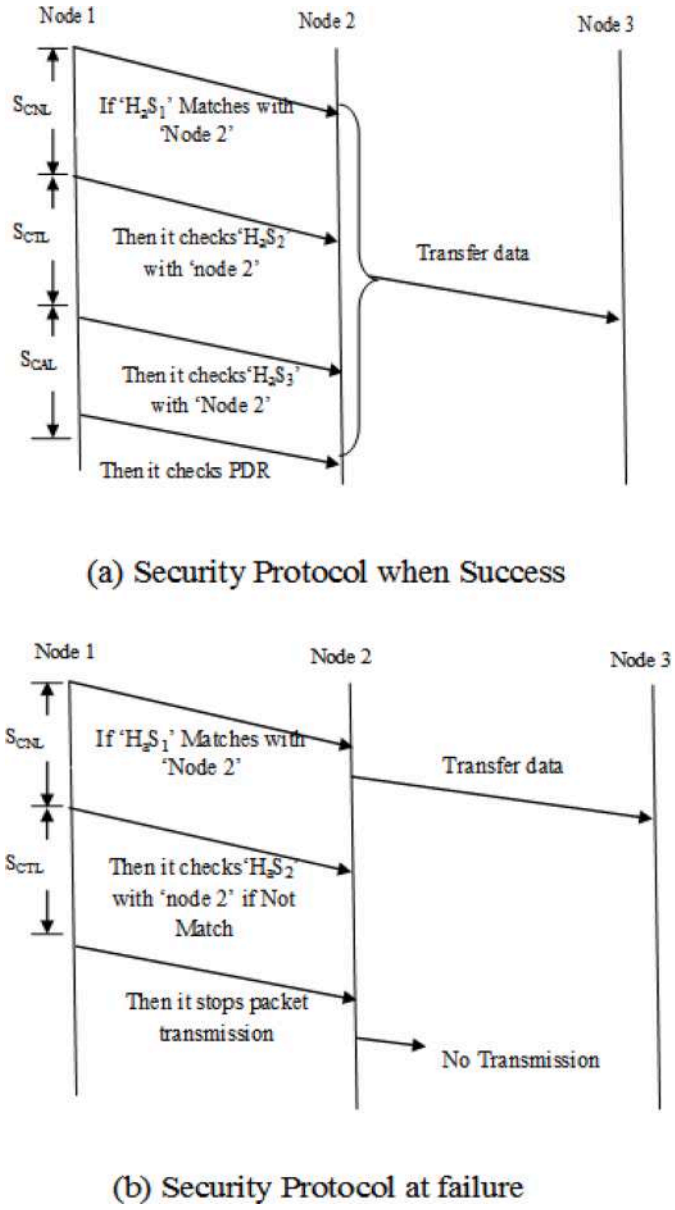

Fig. 2.. Security protocol at various layers

4.2. Property

If LSB and MSB of the code bits are 0 then complement the code, and if either of the MSB or LSB is 0, MSB or LSB is EX-OR with 1 as shown in "(13)":

$$X = \begin{cases} \overline{X} \forall MSB = LSB = 0 \\ MSB \oplus 1 \forall MSB = 0 \\ LSB \oplus 1 \forall LSB = 0 \end{cases} \tag{13}$$

where

X is the security codeword at level 2 & 3.

Hop 1 security level three has been given to the node by proving left shift property to the security code obtained at security level two (shift is user-defined) as,

$$N_S = \sum_{k=0}^{n} (k+1) \tag{14}$$

where 'N_S' is the number of shifts. That is, we are giving one shift for hop 1 and two shifts for hop 2, and this process of shifting continues till the destination node. Note that one can also use the right shift method, it depends on the user. However, security can be provided by changing the operation based on the requirement of the network.

4.3. Node matching process

Consider a multi-hop mobile ad-hoc network (MANET) along with the attacker nodes as shown in Fig. 1. The source node '*S*' wants to communicate with the destination node '*D*' through intermediate nodes. Initially, the source node transmits the data to all its neighbors. The nodes that satisfy the security criteria can access the data otherwise, the node will be treated as an attacker node. Fig. 2 represents the security protocol of the proposed approach. Here, S_{CNL} is a security check at the network layer, S_{CTL} is a security check at the transport layer and S_{CAL} is a security check at the application layer.

Node 1 transmits the information to node 2 if security level 1 is matched in the network layer. While transferring the data, simultaneously it will check security level 2 at the transport layer and security level 3 at the application layer, if security matches at both the levels it will transfer the data to node 3 as shown in Fig. 2(a). At level 2 and 3, if the security is unmatched then the packets are not transferred further as represented in Fig. 2(b) which reduces the delay in this approach. This process of node matching continues till the destination node. Here, for simplicity, we take four hops to validate the security model of the proposed approach. In this security model, we authenticate each hop by three levels of security and investigate the PDR at every intermediate node. Though it appears to be step by step process, it is a pipeline process such that the security checks are carried out simultaneously. At the first node, there may be some delay to initiate the process but after the first security check of node 1, a simultaneous check of security level 2 of node 1 and security level 1 of node 2 is carried out.

The security check levels for the number of hops can be represented as,

$$H_a S_b \tag{15}$$

where H_a is the hop count such that, $1 \leq a \leq j$ and S_b is the level of security $1 \leq b \leq 3$.

4.4. Levels of security at Hop 1

At this level of security check, the intermediate node, which is one hop away from the source node should generate the matrix block is represented in Table 2.

H_1S_1 = matrixblock

In the second check of security level at hop 1, the node will check the complement of the odd positions such as 1, 3, and 5 of the security bits (i.e. H_1,H_2,H_3,H_4,H_5). Then it will also check the polynomial equation of the complimented security code.

$$\begin{aligned} &H_1H_2H_3H_4H_5 = 00100 \\ &H_1S_2 = \overline{H}_1H_2\overline{H}_3H_4\overline{H}_5 = 10001 \\ &P_{12} = x^4 + 1 \end{aligned} \tag{16}$$

Here,'P_{uv}'represents the polynomial equation of u^{th} hop and v^{th} security level, in "(16)", u=1 and v =2.

Hop 1, a third security check is a code obtained by giving one shift (user-defined) to H_1S_2 code,

H_1S_2(After one shift) =

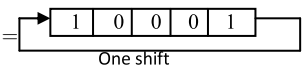

Therefore, after one shift H_1S_2= 1 1 0 0 0, but LSB is having value zero so by the use of property, the security code at level three will be,

$H_1S_3 = 11001$

So the security code at level three is represented in terms of the polynomial equation as,

$$P_{13} = x^4 + x^3 + 1 \tag{17}$$

Hence, at this level of security check, the node should match both H_1S_3 and "(17)".

After matching all the levels of security, the PDR of the node is checked. If the PDR is below the threshold limit, then the node can access the data. The PDR factor is considered to detect the node, which enters the network as an active node, and after a certain interval of time, it becomes an attacker node.

The security code and the polynomial at this level three is also the same for the third level security of the hops represented in '(18)" as,

$$h_{num} = \begin{cases} 10q + 1 & \text{oddterms} \\ 10q + 1 & \text{eventerms} \end{cases} \tag{18}$$

i.e. for hops 1, 3, 11, 13, 21, 23……. where p = 0, 1, 2, 3, …, and h_{num} are hop numbers.

4.5. Levels of security at hop 2

The first security level of hop 2 checks the matrix developed in the similar manner of Table 2 by replacing security bits of "(6)" (i.e., bits H_1, H_2, H_3, $H_4$and H_5) with the code bits of H_1S_2.I_{Sec} = 0011011011111010 (from "(6)")

I_{Sec} after replacing its security bits with code bits 1 0 0 0 1 (H_1S_2):

$$I_{Sec.h2} = 1010011011111011$$

where

$I_{Sec.hs}$ represents initial security code at hop s, here s = 2.

Therefore,H_2S_1= matrix N × N generated by taking $I_{Sec.h2}$as first row and first column as in Table 2 and remaining bits of the matrix are generated in the same way of equations"(7)" to "(11)".

H_2S_2 code is given by taking security bits of $I_{Sec.h2}$ and complementing its even terms and writing polynomial equation as in "(19)".

Security bits of $I_{Sec.h2}$ are $H_1H_2H_3H_4H_5 = 10001$

$$\begin{aligned} H_2S_2 &= H_1\overline{H}_2H_3\overline{H}_4H_5 = 11011 \\ P_{22} &= x^4 + x^3 + x + 1 \end{aligned} \tag{19}$$

H_2S_3 is the code and polynomial equation obtained after giving two shifts to H_2S_2

H_2S_2 after two shifts =

After giving shifts the LSB value is '0', by use of property, we get H_2S_3 and also its polynomial expression as,

$$\begin{aligned} H_2S_3 &= 11111 \\ P_{23} &= x^4 + x^3 + x^2 + x + 1 \end{aligned} \tag{20}$$

As per the analysis of the code in H_2S_3 and "(20)" remain same to the security level three at hops represented as,

$$h_{num} = \begin{cases} 10p + 2 & \text{oddterms} \\ 10q - 2 & \text{eventerms} \end{cases} \tag{21}$$

i.e. for hops 2, 8, 12, 18, 22, 28…… where p = {0, 1, 2, 3, ….} and q = {1, 2, 3, 4, ……}.

4.6. Levels of security at hop 3

At first security level check of hop 3, we substitute the code bits of H_2S_2in the initial security code (i.e.,I_{Sec}) at hamming bit positions and generating matrix block in similar procedure of Table 2

$$I_{Sec} = 0011011011111010$$

I_{Sec} after substituting code bits of H_2S_2at hamming bit positions, we get,

$$I_{Sec.h3} = 111001111111101$$

By taking $I_{Sec.h3}$ as first row and first column we develop matrix block code which will become the first check of hop 3(H_3S_1).

H_3S_2 is calculated by complementing odd terms of security bits in $I_{Sec.h3}$and its polynomial equation.

$H_1H_2H_3H_4H_5$of $I_{Sec.h3} = 11011$

Complementing odd terms (i.e., $\overline{H_1}H_2\overline{H_3}H_4\overline{H_5}$) = 0 1 1 1 0.

Note that the LSB and MSB are having '0', so we get the polynomial equation as

$$\begin{aligned} H_3S_2 &= 10001 \\ P_{32} &= x^4 + 1 \end{aligned} \tag{22}$$

H_3S_3can be evaluated by shifting three bits of security in $H_3S_2$and obtaining code along with its polynomial equation.

H_3S_2 after three = 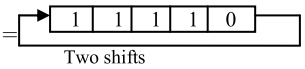

As the value of MSB=LSB=0, we obtain the polynomial equation as,

$$\begin{aligned} H_3S_3 &= 11001 \\ P_{33} &= x^4 + x^3 + 1 \end{aligned} \tag{23}$$

4.7. Levels of security at hop 4

For hop 4 security level check 1, consider the initial security code after inserting the bits of H_3S_2, in the parity bit position. A new code is generated which is used to develop a matrix code block.

$$I_{Sec} = 0011011011111010$$

After inserting bits of H_3S_2, the new code is

$$I_{Sec.h3} = 1010011011111011$$

H_4S_1 is the Matrix N × N which is developed by taking $I_{Sec.h3}$as the first row and first column (similar to Table 2).

H_4S_2 is given by complementing even terms of the security code obtained at $H_4S_1$and its polynomial equation:

Security bits of $I_{Sec.h3}$ are$H_1H_2H_3H_4H_5 = 10001$

$$\begin{aligned} &H_4S_2 = \\ &H_1\overline{H_2}H_3\ \overline{H_4}H_5 = 11011 \\ &P_{42} = x^4 + x^3 + x + 1 \end{aligned} \tag{24}$$

H_4S_3 are the code bits obtained after giving four bits shift toH_4S_2. and writing its polynomial equation:

H_4S_2. after 4-bit shift = 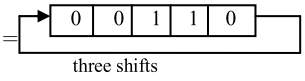

$$\begin{aligned} H_4S_3 &= 10111 \\ P_{43} &= x^4 + x^2 + x + 1 \end{aligned} \tag{25}$$

The binary code ofH_4S_3. and "(25)" validates security and are same for the hops, obtained as,

$$h_{num} = 10q - 6 \tag{26}$$

where q= {1, 2, 3, ...} .

4.8. Observations from node analysis process

From the above evaluations of the four-hop network, we can make the following oervations:

(a) Hop number is equal to the number of shifts given in the third level of security check.
(b) For odd hops, we are complementing odd terms and for even hops, we complement even terms at level 2 security (that is, for hop 1, hop 3, hop 5 so on, we complement odd terms and for hop 2, hop 4, and so on, we complement even terms).
(c) Avel 2 security, we notice that equations "(16)" and "(22)", and equations "(19)" and "(24)" are equal.

Table 3.
Parameters for Simulation

Network Parameters	Values
Total Simulation Time	15 min
Number of nodes	2 to 200
Maximum number of hops	12
Link Layer Type	Logical Link (LL)
MAC type	IEEE 802.11
Radio Propagation Model	Two-Ray Ground
Queue Type	Drop-Tail
Antenna	Omni antenna
Traffic	Video (VBR)
Network Area	1000m x 1000m
Node Mobility Speed	2, 5, 8, 10, 12 m/sec
Packet Size	512 bytes
Routing Protocol	LAEERP

Trefore, we can generalize the level 2 of security check for multiple hops as,

$$H_1S_2 = H_3S_2 = H_5S_2 = H_{2n+1}S_2 \tag{27}$$

where n= {0, 1, 2 …}

$$H_2S_2 = H_4S_2 = H_6S_2 = H_{2m}S_2 \tag{28}$$

where m= {1, 2, 3….}

(a) In multi hop network assuming n hops from source to destination, we get different binary codes and polynomial equations at security level three. Various cases are noticed at this security level as represented below:

Case 1:

binary code 1 0 0 0 1 and polynomial expressionP_{53}= x^4 +1 will remain same at hops obtained by "(29)":

$$h_{num} = 10q - 5 \tag{29}$$

where q = {1, 2, 3, 4, ……}

Case 2

The binary code 1 1 1 0 1 and polynomial expression P_{63}= x^4+x^3 +x^2+1 will remain same at hops obtained by "(30)":

$$h_{num} = 10q - 4 \tag{30}$$

where q = {1, 2, 3, 4, ……}

Case 3:

The binary code 1 0 0 1 1 and polynomial expression P_{73}. = x^4+x+1 will remain the same at hops obtained by "(31)"

$$h_{num} = \begin{cases} 10q - 3 & \text{oddterms} \\ 10q - 1 & \text{eventerms} \end{cases} \tag{31}$$

e q = {1, 2, 3, 4, ……}.

Case 4:

The binary code 1 1 0 1 1 and polynomial expression $P_{10.3}$. = x^4+x^3+x+1 validates security at hops obtained by "(32)"

$$h_{num} = 10q. \tag{32}$$

where q = {1, 2, 3, 4, ……}.

Note that Hamming code circuitry is a commonly available infrastructure in communication systems as part of error-correcting code. So, additional infrastructure/mechanisms are not needed to implement the Hamming code. Further, our approach minimizes the complexity of the algorithm as we represented the number of hops with simple mathematical equations, and thus the model is applicable for huge networks with multiple hops as well.

5. Simulation experiments

Different parameters required for simulation are shown in Table 3. A multi-hop network is being considered to transmit data between end nodes. Intermediate nodes take the data from the source node and transfer it to the destination node. For simulation, we consider total simulation time as 15 minutes to get the appropriate working of the proposed method the number of nodes varies between 2 to 200 for the occurrence of most of the attacks simultaneously, and to examine the network behavior number of hops are considered to be 12 (one can

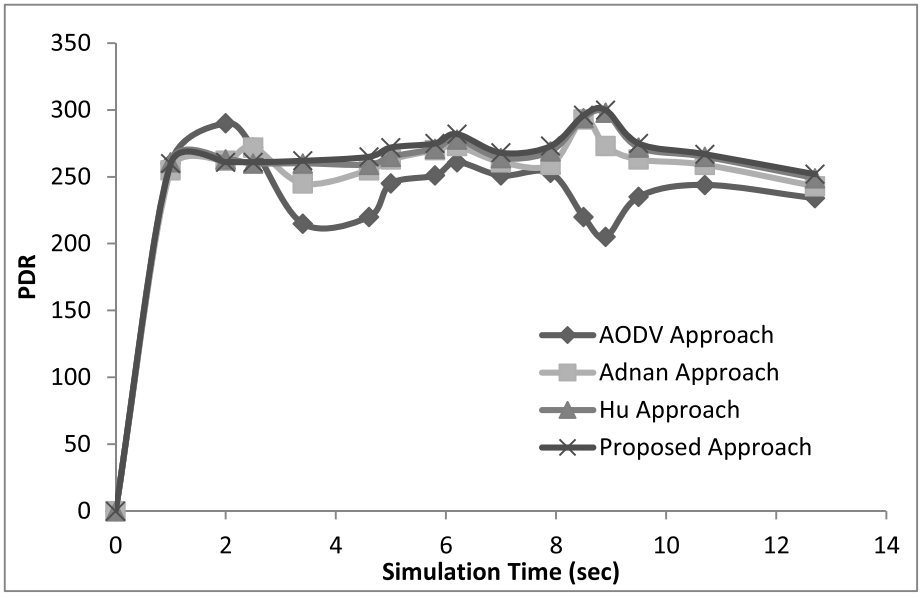

Fig. 3. Variation of PDR with simulation time

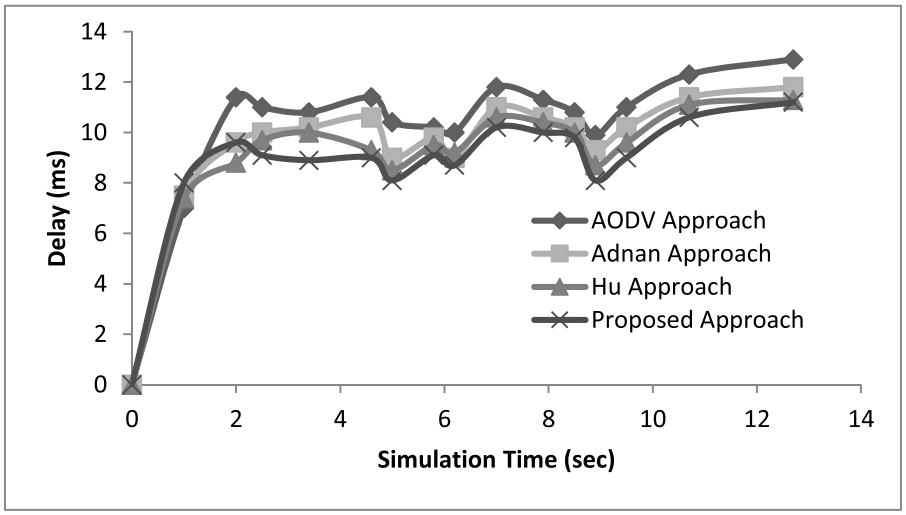

Fig. 4. Variation of delay with simulation time

increase or decrease it depending on one's desired precision). To maintain the mobility nature of the network, we monitor several mobility speeds of the node (i.e. 2, 5, 8, etc.). We use video traffic (i.e., VBR), which provides different frame sizes. To enhance the Quality of Service, the transmission of packets should be in sequential order. To synchronize input data rate with output, we consider constant packet size which is 512 bytes. However, one can change the size of the packet by giving an extra circuit to synchronize the end user. A simulation area of 1000m x 1000m is considered and an omnidirectional antenna is used to improve the directivity and beamforming. The routing protocol used is Location-aware and energy-efficient routing protocol (LAEERP) [38].

The number of nodes is varied i.e. 40, 60, 90, and 150 to observe the behavior of the network while running the script of different attacks. The experiment is repeated 4 times considering the different source and destination nodes and the average result is taken to calculate different parameters such as PDR, delay, packet loss, and overhead using AWK scripts. All the attacks are intended in the Transaction Control Language (TCL) scripts and class files for some specified nodes of the network. When these scripts are run with the command of "ns name of the attack_nodes.tcl" (.tcl is an extension) and two files namely 'trace' and 'nam' files are generated. Note that all the attacks are given in the same network and if any of the attack occurs at any of the layer the program will declare it as attacker node. It will not differentiate that which attack has been occurred and at which layer. The attacker node is mostly placed in the middle to make the attack success and mesh topology is used in the design of the network to connect different sources and destination nodes. Different time frames are given for different attacks on the TCL code if the attacks are true. The parameters such as PDR and delay through the nodes are inspected and graphically represented in the figures of this section. The proposed approach outperforms the existing approaches as the attacks are mostly avoided by the network using digital security codes

Fig. 3 represents the PDR versus simulation time. It is observed from the figure that initially all the existing approaches (i.e. AODV, Adnan, and Hu) demonstrate better results when compared to the proposed approach. This is because initially, attacker nodes (here the attacker node indicates the node with any attack in any layer mentioned in Section 3 as the network as a whole is considered for simulation) enter with static energy into the network so can be easily judged and removed from the path. However over time, attacker nodes come with different energies and take part in the network, so cannot be judged and eliminated from the path. But our approach still performs better which shows the validity of our approach.

Fig. 4 demonstrates the variation of delay versus simulation time. It is obvious from the figure that the delay of the proposed approach is less in comparison with the existing approaches. However, initially, the delay of the AODV and Hu approach is better, this is because time management at initial hops is pleasantly maintained by AODV and Hu.

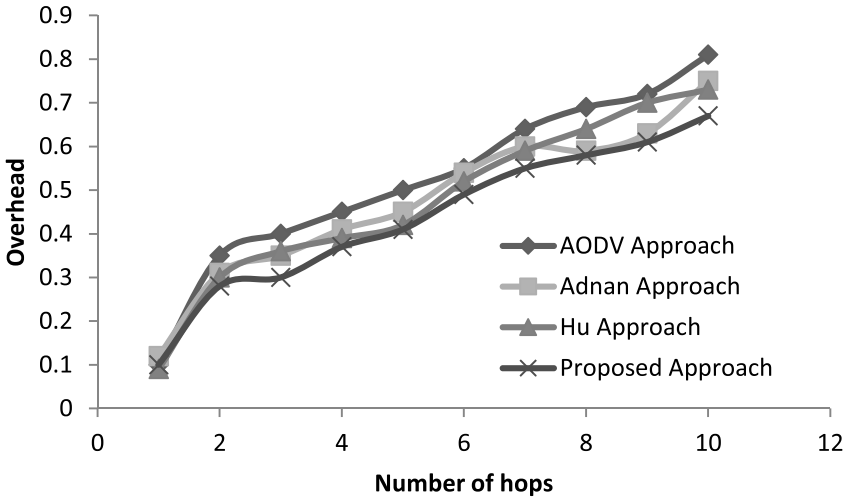

Fig. 5. Variation of overhead with number of hops

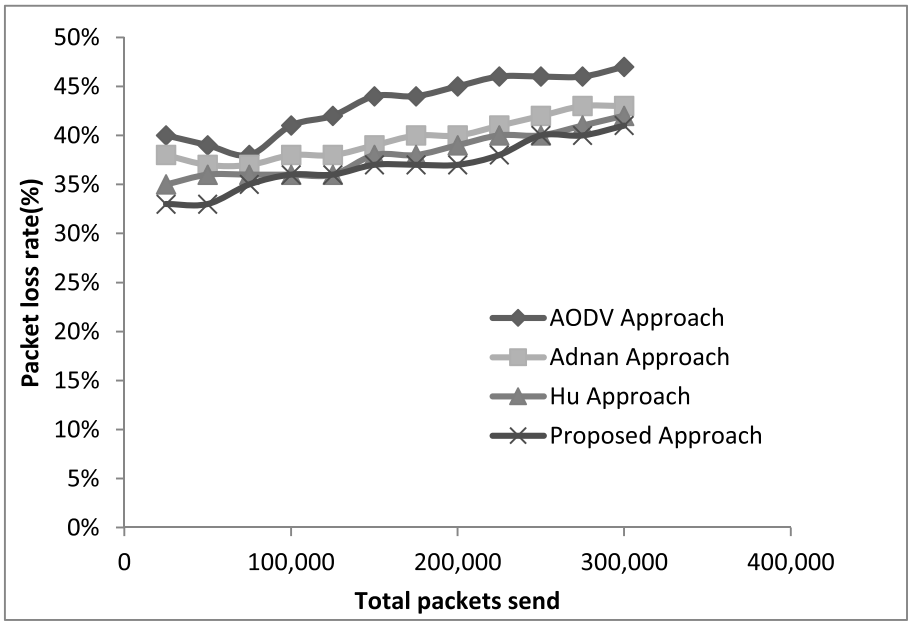

Fig. 6. Total packets send vs Packet loss rate between end nodes

But when hops increase they could not give the optimum path between end-users and increased the delay. Fig. 5 represents the variation of overhead versus the number of hops. Our approach reduces the overhead as it did not allow the attacker node to drop the packets and saves the data packets, so increases the PDR.

Fig. 6 shows the variation of total packets sent to packet loss ratio between end nodes. From the figure it is clear that the drop percentage of packets is less in our when compared to the existing approaches, reason behind this is our approach not only reduces the overhead but also reduces the delay. Delay and overhead are the main constraints for reducing packet loss at any interval of time.

From all the figures, the proposed approach outperforms the existing approaches. As the differentiation of nodes (i.e. active or attacker) is better for the proposed approach, node authentication becomes easier. Hence, there is less scope of packet loss and delay as none of the node is misguided.

6. Discussion

The presented approach is efficient based on simple mathematical logics (such as cyclic division, X-OR operation, even and odd complements, and shifting of binary numbers) which reduces the power consumption and complexity. The techniques of Equal weighted hex code and hamming bit positions have the feasibility to satisfy orthogonality property and can be used in communication models.

In this paper, we compared the presented approach with three existing approaches (i.e. AODV, Adnan, and Hu). This approach finds better utility in communication networks particularly in ad-hoc networks, gives a simplex mode of security, and simultaneously authenticates the security at different layers. It can be used in military communication where multiple frequencies are used for radio communication. Where it can easily and dynamically provide security to all the radio sets which act (here) as a mobile node and increases the performance of the network.

7. Conclusion

In this paper, we presented a multi-level trust model to enhance the security in MANETs. We generated various levels of security at each intermediate node using equal-weighted hex coding matrix and hamming code techniques. In our approach, the security changes for the number of hops count so cannot be easily compromised. To validate nodes at different hops, we used different levels of security to improve the security of the nodes within the network. Also, our approach facilitates less overhead. We compared our approach with AODV, Adnan, and Hu's approach and the results show the applicability of our approach.

Author statement

The paper has been revised as per the reviewer comments to best of our knowledge, wherever there was a necessity to change or to modify the sentence it is incorporated in the revised manuscript. All comments are addressed and inserted in the manuscript as per the requirement.

In support of this statement, please see the Response to the reviewer document.

Thanks and Regards
Syed Jalal Ahmad.
To
The Editor,
Journal of Information Security and Applications.
Subject: Submission of the research paper regd.

I Syed Jalal Ahmed is submitting the original research manuscript to your esteemed journal titled as "**Enhanced Security to MANETs using Digital Codes**". We don't have any conflict of interest

I kindly request you to accept the manuscript for review process.
Thanks and Regards
Syed Jalal Ahmad
(Corresponding Author)

Declaration of Competing Interest

None

References

[1] Kumar Mohit, Mishra Rashmi. An overview of MANET: history, challenges, and applications. Indian J Comput Sci Eng (IJCSE) Feb-Mar 2012;3 No(1).
[2] Kaur Inderpreet, Rao ALN. A Framework to Improve the Network Security with Less Mobility in MANET'. Int J Comput Applica June 2017;167(10):0975–8887. No.

[3] Yang Yang. Broadcast encryption-based non-interactive key distribution in MANETs. J Comput System Sci 2014;80(3):533–45.
[4] Singh Pooja, Gill Nasib Singh. A survey on key management schemes in wireless Ad Hoc networks. Int J Appl Eng Res 2018;13(Number 1):268–72. pp.
[5] Muthurajkumar S, Ganapathy S, Vijayalakshmi M, et al. An intelligent secured and energy efficient routing algorithm for MANETs. Wirel Pers Commun 2017;96:1753–69.
[6] **MahaAlqallaf**. Software Defined Secure Ad Hoc Wireless Networks. Wright State University; 2016. p. 1–177.
[7] Dajun Zhang, 'Software-defined Mobile Ad Hoc Networks with Trust Management'. Carleton University, pp: 1-105, 2016.
[8] Sharma VC, Gupta A, Dimri V. Detection of Black Hole Attack in MANET under AODV Routing Protocol. Int J Adv Res Comput Sci Softw Eng 2013;3(6):438–43.
[9] Mamatha GS, Sharma SC. A highly secured approach against attacks in MANETS. Int J Comput Theor Eng 2010;2:815–9.
[10] Hu YC, Perrig A, Johnson DB. Aridane: a secure on-demand routing protocol for Adhoc networks. Wirel Netw 2005;11:21–38.
[11] Lu S, Li L, Lem KY, Jia L. SAODV: A MANET Routing Protocol that can withstand Black Hole Attack. In: Proc. of the 2009 International Conference on Computational Intelligence and Security (CIS 2009)2; 2009. p. 421–5.
[12] Deswal S, Sing S. Implementation of routing security aspects in AODV. Int J Comput Theor Eng 2010;2(1):135–8.
[13] Chandrakant N. Self protecting nodes for secured data transmission in energy efficient MANETs. Int J Adv Res Comput Sci Softw Eng 2013;3(6):673–5.
[14] Xiong WA, Gong YH. Secure and highly efficient three level key management scheme for MANET. Proc WSEAS Trans Comput 2011;10:6–15.
[15] Celestin M, Vigila S, Muneeswaran K. Implementation of text-based cryptosystem using Elliptic Curve Cryptography. Prof 1st Int Conf Adv Comput 2009;9:82–5.
[16] Sun B, Yu B. The three-layered group key management architecture for MANET. Proc 11th Int Conf Adv Commun Technol 2009;2:1378–81.
[17] Michiardi P, Molva R. Core: a collaborative reputation mechanism to enforce node cooperation in mobile Adhoc networks. In: Proc. of 6th IFIP Communications and Multimedia Security Conference; 2002. p. 107–21.
[18] Lindsay SY, Wei Y, Zhu H, Liu KJR. Information-theoretic framework of trust modeling and evaluation for AdHoc networks. IEEE J Sel Ar Commun 2006;24(2):305–17.
[19] Balakrishnan V, Varadharajan V, Tupakula UK, Lucas P. Trust integrated cooperation architecture for mobile Ad-hoc networks. In: Proc. of 4th IEEE International Symposium on Wireless Communication Systems (ISWCS 2007); 2007. Trondheim, Norway.
[20] Jay SEI, Hasbi A. Security in MANETs and WSNs. Int J Comput Sci Netw Secur 2016;16(9):118–22.
[21] Ahmed A, Bakar KA, Channa ML, Haseeb K, Khan AW. A trust-aware routing protocol for energy constraint wireless sensor networks. Telecommun Syst 2016;61(1):123–40.
[22] Deepika K, Dhurandher S K, Reddy B V R. Power-aware malicious nodes detection for securing MANETs against packet forwarding misbehavior attack. J Amb Intell Human Comput 2017:1–16.
[23] Todd AR, Alec Y. Surveying security analysis techniques in MANET routing protocols. IEEE Commun Surv Tutor 2007;9:70–84.
[24] Li J, Cui G, Fu X, Liu Z, Su L. A secure group key management scheme in Ad Hoc networks. In: Proc. of 2005 International Conference Wireless Communications, Networking And Mobile Computing; 2005.
[25] Singh T, Singh J, Sharma S. Energy Efficient Secured Routing Protocol for MANETs. Wireless Networks Journal, 23. Springer; May 2017. p. 1001–9.
[26] Scott-Hayward S, O'Callaghan G, Sezer S. SDN security: a survey. Proc. IEEE SDN4FNS 2013:1–7.
[27] Namal S, Ahmad I, Saud S, Jokinen M, Gurtov A. Implementation of open flow-based cognitive radio network architecture: SDN&R. Wireless Networks. New York, NY, USA: Springer; 2015. p. 1–15.
[28] Ahmad I, Namal S, Ylianttila M. Security in software defined networks: a survey. IEEE Commun Surv Tutor 2015;17(4):2317–46.
[29] Sirohi Ankur, Agarwal Amit K. Security in wireless sensor network (WSN): a detailed survey. Int J Adv Sci Technol 2020;29(Special Issue). No5s: Vol 29 No 5s.
[30] Yang J, He S, Xu Y, Chen L, Ren J. A trusted routing scheme using blockchain and reinforcement learning for wireless sensor networks. Sensors 2019;19:970.
[31] Ahmad Syed Jalal, Krishna; PR. BHQRSM: binary hex quadratic residue security model to enhance the trust in MANETs. Wirel Person Commun 2018;101:661–76.
[32] Siva Ram Murthy C, S Manoj B. Ad Hoc Wireless Networks: Architectures and Protocols. Pearson Education India; 2006.
[33] Ramesh Babu A, Nagendranath M V S S. Adverse effect of Blackhole and Wormhole attacks on MANETs. Int J Appl Eng Res 2017;12:9245–52. Number 20.
[34] Yu M, Zhou M, Su W. A Secure Routing Protocol Against Byzantine Attacks for MANETs in Adversarial Environments. IEEE Trans Veh Technol Jan. 2009;58(1):449–60.
[35] Harmeet Singh Dr JK. DDoS attack detection and prevention in MANETs. Int J Adv Sci Technol 2020;29(3):2402–7.
[36] Kuyoro Shade, Okolie O, Aduragbemi Oyebode. Session hijacking in mobile Ad-hoc networks: trends, challenges, and future. Res J Math Comput Sci 2017. https://doi.org/10.28933/rjmcs-2017-10-3001.
[37] Ahmad SJ, Reddy VSK, Damodaram A, Krishna PR. An improved QoS and ranking paths for multimedia traffic over MANETs. In: 2014 International Conference on Information Technology; 2014. p. 41–6.
[38] Jalal Ahmad Syed, Reddy VSK, Damodaram A, Pisipati Radha Krishna. Location-aware and energy-efficient routing protocol for long-distance MANETs. Int J Network Virt Organ 2013;13:327. https://doi.org/10.1504/IJNVO.2013.064461.

Hindawi
International Journal of Photoenergy
Volume 2022, Article ID 7797488, 7 pages
https://doi.org/10.1155/2022/7797488

Research Article

Forecasting Solar Energy Production Using Machine Learning

C. Vennila,[1] Anita Titus,[2] T. Sri Sudha,[3] U. Sreenivasulu,[4] N. Pandu Ranga Reddy,[3] K. Jamal,[5] Dayadi Lakshmaiah,[6] P. Jagadeesh,[7] and Assefa Belay[8]

[1]*Department of Electrical and Electronics Engineering, Alagappa Chettiar Government College of Engineering and Technology, Karaikudi, 630003 Tamil Nadu, India*
[2]*Department of Electronics and Communication Engineering, Jeppiaar Engineering College, Semmenchery Raghiv Gandhi Salai OMR, Chennai, 600119 Tamil Nadu, India*
[3]*Department of Electronics and Communication Engineering, Malla Reddy Engineering College, (A) Hyderabad 500100, India*
[4]*.Department of Electronics and Communication Engineering, NBKR Institute of Science and Technology, Vidyanagar, Andhra Pradesh 524413, India*
[5]*Department of Electronics and Communication Engineering, GRIET Gokaraju Rangaraju Institute of Engineering and Technology, Bachupally, Hyderabad 500090, India*
[6]*Department of Electronics and Communication Engineering, Sri Indu Institute of Engineering and Technology, Hyderabad 501510, India*
[7]*Department of Electronics and Communication Engineering, Saveetha School of Engineering, (SIMATS) Chennai, 602105 Tamil Nadu, India*
[8]*Department of Mechanical Engineering, Mizan Tepi University, Ethiopia*

Correspondence should be addressed to Assefa Belay; assefa@mtu.edu.et

Received 8 February 2022; Accepted 24 March 2022; Published 30 April 2022

Academic Editor: V. Mohanavel

When it comes to large-scale renewable energy plants, the future of solar power forecasting is vital to their success. For reliable predictions of solar electricity generation, one must take into consideration changes in weather patterns over time. In this paper, a hybrid model that integrates machine learning and statistical approaches is suggested for predicting future solar energy generation. In order to improve the accuracy of the suggested model, an ensemble of machine learning models was used in this study. The results of the simulation show that the proposed method has reduced placement cost, when compared with existing methods. When comparing the performance of an ensemble model that integrates all of the combination strategies to standard individual models, the suggested ensemble model outperformed the conventional individual models. According to the findings, a hybrid model that made use of both machine learning and statistics outperformed a model that made sole use of machine learning in its performance.

1. Introduction

Machine learning approaches have been increasingly popular across a wide range of businesses where data-driven difficulties have been common in recent decades. Machine learning encompasses a wide range of disciplines, including data mining, optimization, and artificial intelligence, to name a few of the more prominent. Machine learning approaches seek to discover connections between input data and output data, whether or not they make use of mathematical models in the process. Following training with the training dataset, the forecasting input data can be fed into the well-trained machine learning models, which can then be used to make predictions [1, 2]. This stage is crucial to machine learning since it has the ability to improve the performance and speed of the algorithm.

Generalizations aside, machine learning relies on three forms of training: supervised training, unsupervised training, and reinforcement training. Clustering criteria are used, and the number of clusters can change depending on the situation.

Figure 1: Fossil fuels.

In order to maximize the intended benefits of reinforcement learning, the learner must interact with their environment in order to obtain feedback from it. This is known as interactivity.

There have been a variety of theories and implementations presented that are based on the three fundamental learning principles [3]. As a result, deep learning is capable of achieving characteristic nonlinear features and invariant high-level data configurations, and as a result, it has been applied in a variety of diverse fields with good results.

According to some studies, a single machine learning model has also been used to anticipate the availability of renewable energy sources [4]. Because of the large range of datasets and time steps, prediction ranges, settings, and performance measurements, a single machine learning model cannot improve forecasting performance on a single dataset or time step. There have been a number of studies in renewable energy forecasting that have resulted in hybrid machine learning models or overall prediction methodologies that are intended to improve prediction performance. Significant attention has lately been drawn to support vector machines (SVMs) and deep learning algorithms [5].

In addition to hastening the depletion of fossil fuel reserves as in Figure 1, overconsumption of fossil fuels has a negative influence on the environment as a whole. Increased health risks as well as climate change threats will result as a result of these issues. Renewable energy, which includes both nuclear power and fossil fuels, is the energy source, surpassing both.

Renewable energy has recently received a great deal of attention as a result of its long-term viability and minimal impact on the surrounding environment. In the near future, the provision of renewable energy will be one of the most critical challenges to be addressed. Alternative terminology: the inclusion of renewable energy sources into current or future electric power generation systems.

Existing energy challenges, such as increasing supply stability and alleviating regional power shortages, can be solved through the evolution of renewable energy technologies. This creation of diverse energy sources, on the other hand, is interrupted and chaotic as a result of the volatility of the energy market as well as the unpredictable and intermittent renewable energy. Dealing with renewable energy fluctuation in an accurate way prevails as a challenge. The energy system efficiency is improved via energy monitoring with high precision. The application of energy forecasting technologies can assist in the creation, management, and formulation of energy policy at all levels of government. As renewable energy sources become more generally available, it is vital to create cutting-edge technologies for storing this energy [6]–[7].

Several studies have discovered that a variety of machine learning algorithms have been employed to estimate the output of renewable energy resources. With the help of data-driven models, it is possible to make more accurate predictions about renewable energy. With the use of hybrid machine learning algorithms, projections for renewable energy sources have also been enhanced. In order to effectively predict the availability of renewable energy sources, it was required to use a number of time intervals. When it comes to renewable energy forecasting, these criteria have been widely used to evaluate the accuracy and efficiency of machine learning algorithms [8].

2. Related Works

Wang et al. [9] investigated deep learning-based renewable energy forecast algorithms in their research. There were four kinds of approaches: stack autoencoder, deep belief networks, recurrent neural networks, and other approaches are lumped together. Certain data processing is employed in order for performance improvement of the predicted results even further.

When it comes to dependability and estimating energy, Bermejo et al. [10] proposed a model using ANN. In this inquiry, potential sources of energy such as solar, hydraulic, and wind power were all taken into consideration. A number of examples are developed to demonstrate the advantages of ANN in the prediction of energy and trustworthiness, among other things. In their study, Mosavi et al. [11] looked at the analysis and classification of ML algorithms used in energy systems. According to the findings of the study, hybrid models outperform standard ML models in energy systems.

According to Ahmed and Khalid [12], they investigated the reliability of renewable power generation systems and optimal reserve capacity in order to better understand forecasting models for renewable power production systems. According to the power industry, this review gave current trends and forecasts for future improvements in system design and operation. In the field of solar and wind energy forecasting, Zendehboudi et al. [13] discovered that support vector machine (SVM) outperformed others. Furthermore, when it comes to forecasting accuracy, hybrid SVM models outperforms single SVM models.

Das et al. [14] conducted an investigation and evaluation of the forecasting methodologies utilized in solar photovoltaic

electricity generation. According to the findings of this study, artificial neural networks and the support vector machine model were found to be particularly prevalent in this field. In their paper, the scientists noted that weather conditions have an impact on the accuracy of solar power forecasts.

Due to the fact that solar radiation is a key source of solar energy, Voyant et al. [15] investigated the application of machine learning algorithms in forecasting solar radiation. Several strategies for forecasting solar radiation have been described. Perez-Ortiz et al. [16] conducted an evaluation of categorization approaches for problems of renewable energy and provided insights for both academics and industry practitioners in this field. In this study, we employed evolutionary approaches and game theory to investigate the feasibility of hybrid renewable energy systems and the obstacles associated with them.

To give a comprehensive survey [17]–[18] of current developments in the field, this paper examines data pretreatment methodologies, machine learning algorithms, parameter selection, and performance assessments of machine learning models in renewable energy projections.

3. Proposed Method

In this section, we validate the forecasting made by the ensemble model for optimal prediction of power generation using PV plants. The study considers two case studies, where the former is simulated for smaller PV farms of 1000 PV cells and larger PV farms of 100000 PV cells. The illustration of training the ensemble model is given in Figure 2. In these proposed methods, the data is classified into a single classifier and another set will act as a training data from which we will classify the samples, classifier, Aggregation was done once it was completed. It will be moved to performance metric evaluation with several comparison techniques.

3.1. Feature Selection. The sun delivers solar energy in the form of solar radiation, which is produced by the photovoltaic effect. Sunlight intensity is the most important factor influencing the output of photovoltaic (PV) solar panels. A PV system output can be affected by a variety of different environmental variables among others. Identifying which parts of PV are valuable and which aspects are not is also essential so that a suitable feature subset may be selected as an input to the model. We propose a hybrid method for feature variable selection that comprises two basic processes, namely, the filter stage and the wrapper stage, as depicted in Figure 3.

Prior to begin the learning process, the filter technique analyzes features based on the inherent attributes of each one of the features. Filter criteria are used to select a subset of features from a dataset based on their relevance.

Because of the characteristics of PV data, the Pearson correlation coefficient (PCC) is employed to assess the relationship between input factors and the target variable. A PCC is a statistical metric that is used to determine the linear correlation between two variables, $\boldsymbol{X}$ and $\boldsymbol{Y}$, in a dataset. Data from time series analysis captures the degree to which a target variable $\boldsymbol{Y}$ correlates with an input variable $\boldsymbol{X}$ over the course of an observation period. When calculating the correlation between two variables, the time series data at

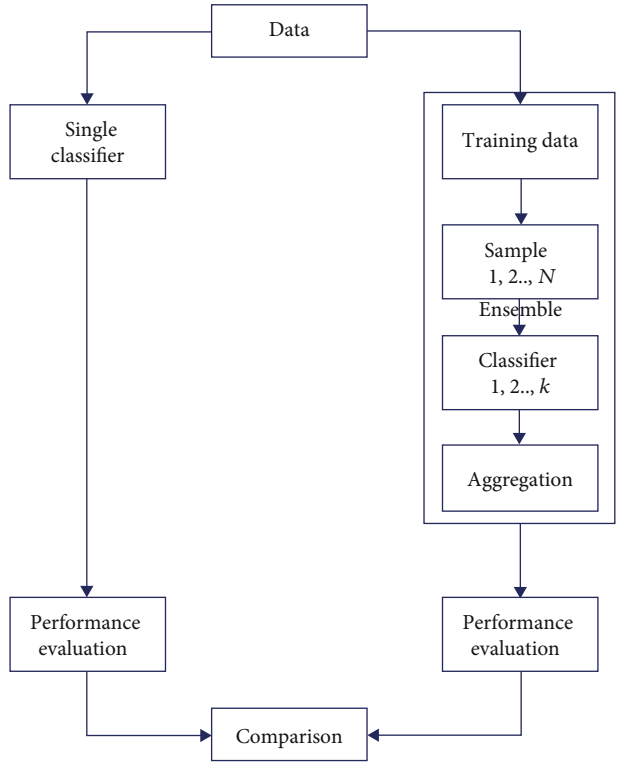

Figure 2: Proposed model.

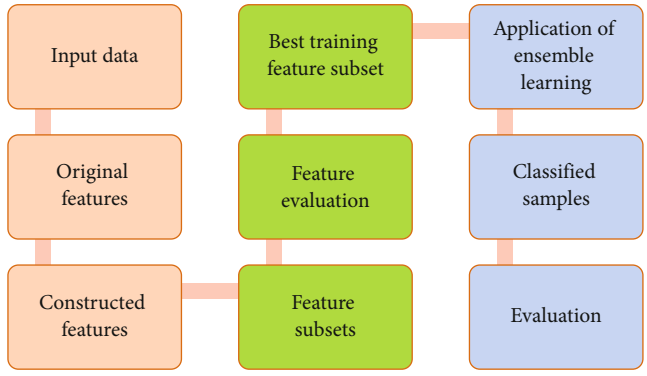

Figure 3: Feature selection.

the points $\boldsymbol{t}$ and $\boldsymbol{t1}$ of the variable are not used. In our example, the meteorological factors that have an impact on PVPG are represented by the letters $\boldsymbol{Y}$ and $\boldsymbol{X}$, respectively. As a result, the PCC may be expressed mathematically as

$$\rho(X, Y) = \frac{\sum_{i=1}^{N}(x_i - \bar{x})(y_i - \bar{y})}{\sqrt{\sum_{i=1}^{N}(x_i - \bar{x})^2}\sqrt{\sum_{i=1}^{N}(y_i - \bar{y})^2}}, \quad (1)$$

where PCC is the value that lies between +1 and -1. PCC is one of the most commonly used criteria for describing the relationship between variables in practice, and it is also one of the most widely studied.

The wrapper approach is utilized to analyze each subset that has been selected. The learning algorithm is integrated into the feature selection process, which in turn makes use

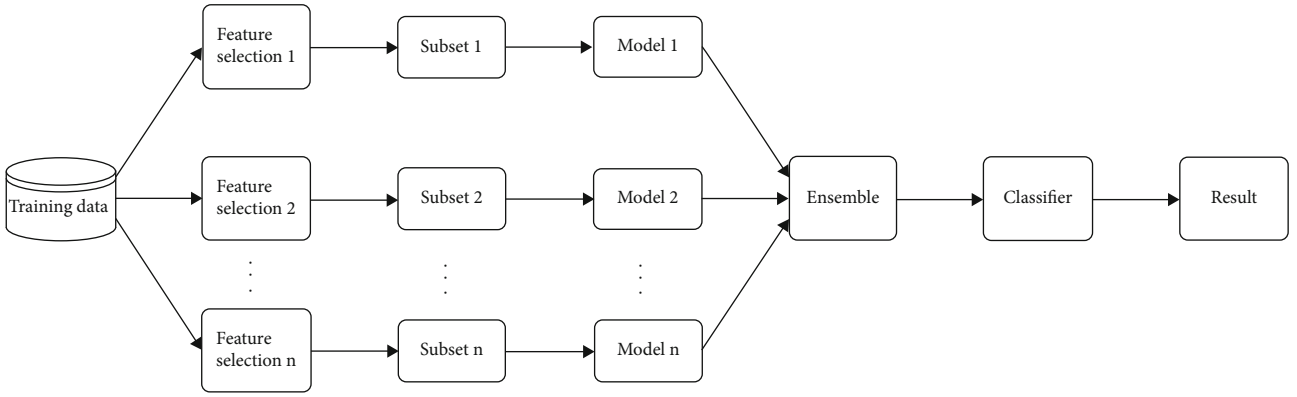

Figure 4: Classification [19].

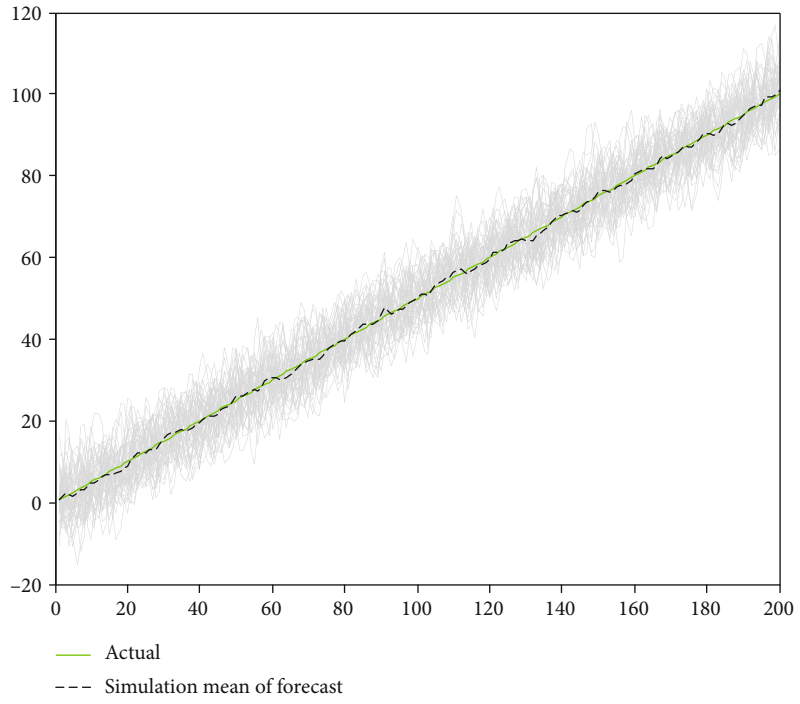

Figure 5: Observations from ensemble model for smaller PV farms.

of the error of a given model to determine which feature subset is most important to the user. It was decided to employ the traditional LSTM model for the analysis of feature subsets in this study because of its capacity to address time series forecasting issues. As a result, the optimal subset of training characteristics may be determined from among all of the subsets that have been investigated.

Through the use of a hybrid approach, the proposed feature selection attempts to integrate the best aspects of wrapper and filter methods into a single method. After examining the correlations between variables using filter criteria, appropriate thresholds are determined in order to reduce the number of feature variables that can be evaluated. The filter technique, in contrast to other learning algorithms, is univariate in nature.

This results in it being significantly more efficient and faster to compute than the wrapper technique, and it is capable of dealing with massive datasets with ease. No consideration is currently given to how features interact with one another or with the learning algorithms, which is a problem. In this case, the wrapper technique is required because coupled features in the single feature evaluation. In order to effectively use an individual wrapper strategy, a significant amount of computer power is required. This is owing to the learning methods used and the enormous number of feature subsets that must be analyzed. Despite this, when the correlation results of the filter approach are utilized as a guide, fewer feature subsets are generated and analyzed than would otherwise be the case. As a result, the hybrid method that has been proposed has the potential to improve the effectiveness of the feature selection.

3.2. Ensemble Feature Classification. In this study, we employed an approach known as multimodel ensemble feature selection, which is an alternative to the methods that have been previously explored. Initially, the training data is

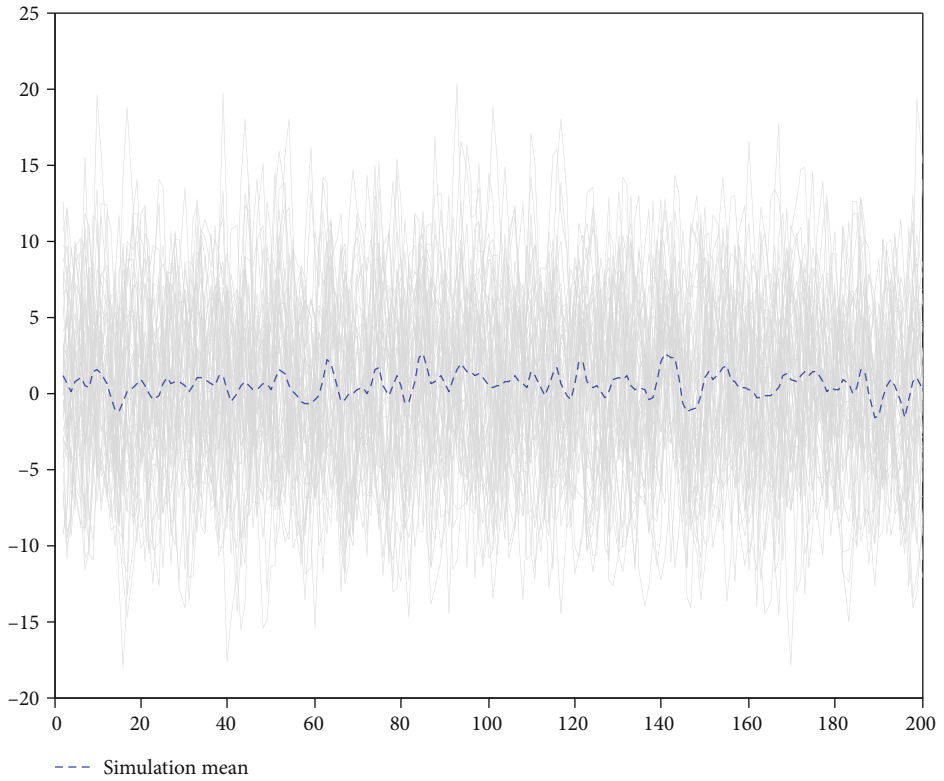

Figure 6: Difference between the smaller and larger PV farms using ensemble model.

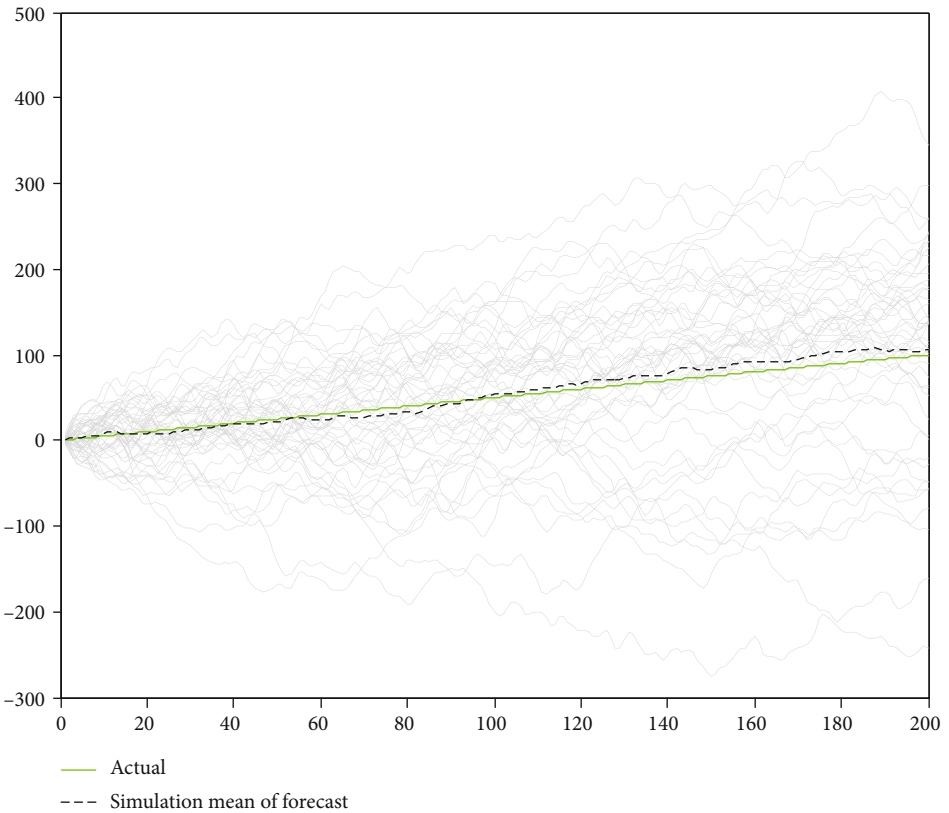

Figure 7: Observations from ensemble model for larger PV farms.

analyzed using a number of feature selection algorithms, each of which generates a subset of the total data. Second, a model is trained using a single subset of data that was previously acquired, as described above. Finally, we compile the results of all of the simulations that we have conducted. Figure 4 depicts the process of selecting ensemble features from a large number of candidates.

4. Results and Discussions

During the experiment, a total of 10 MW of capacity was achieved through the use of polycrystalline solar panels (Poly-SI) and thin-film solar cells (TFSC). The time series dataset can be accessed in a number of different formats. For our research, we used data with a five-minute resolution.

Low-bias machine learning models also reveal that estimates for energy generation are pretty close to the reality. According to the example studies depicted in Figure 5, clear weather conditions outperformed overcast and partly cloudy conditions for each ML model. When the weather is clear, the shift in cloud cover is gradual, which allows for more accurate power predictions. The RMSE of the power forecast for a gloomy day is slightly higher than that of the power forecast for a clear day. It is the actual and forecasted of the predicted power for the partly cloudy day that are particularly bad. The error in a forecast is influenced by the variety of the forecast. It is mostly owing to the greater unpredictability associated with partially cloudy conditions that the abovementioned discrepancies in forecast errors exist. In contrast to the findings in Figure 6, the results in Figure 7 appear to be contradictory.

It is obvious from this dataset that the ensemble model is capable of producing accurate estimates. It is possible that a generalized ML model that can be applied to any PV plant will never be developed. It is possible that the ensemble model, despite its excellent performance in this study, will perform even better on a different dataset. The location and construction of the power plant may have an impact on the weather conditions and the amount of electricity that is generated. Clear data is more abundant in the dataset than cloudy data, which indicates that the data is more reliable. Because the dataset has a higher proportion of clear data than other models for polar regions, the ML model overall performance is superior to that of other models for polar regions.

5. Conclusions

An integrated machine learning model and the statistical approach are used to anticipate future solar power generation from renewable energy plants. This hybrid model improves accuracy by integrating machine learning methods and the statistical method. In order to improve the accuracy of the suggested model, an ensemble of machine learning models was used in this study. When comparing the performance of an ensemble model that integrates all of the combination strategies to standard individual models, the suggested ensemble model outperformed the conventional individual models. According to the findings, a hybrid model that made use of both machine learning and statistics outperformed a model that made sole use of machine learning in its performance. In future work, the proposed method can improvise the performance, accuracy, and the other metrics using several deep learning mechanisms.

Data Availability

The data used to support the findings of this study are included within the article. Further data or information is available from the corresponding author upon request.

Conflicts of Interest

The authors declare that there is no conflict of interest regarding the publication of this paper.

Acknowledgments

The authors thanks to Mizan Tepi University, Ethiopia, for providing help during the research and preparation of the manuscript.

References

[1] I. Jebli, F. Z. Belouadha, M. I. Kabbaj, and A. Tilioua, "Prediction of solar energy guided by Pearson correlation using machine learning," *Energy*, vol. 224, article 120109, 2021.

[2] G. Narvaez, L. F. Giraldo, M. Bressan, and A. Pantoja, "Machine learning for site-adaptation and solar radiation forecasting," *Renewable Energy*, vol. 167, pp. 333–342, 2021.

[3] S. Park, Y. Kim, N. J. Ferrier, S. M. Collis, R. Sankaran, and P. H. Beckman, "Prediction of solar irradiance and photovoltaic solar energy product based on cloud coverage estimation using machine learning methods," *Atmosphere*, vol. 12, no. 3, p. 395, 2021.

[4] K. Mahmud, S. Azam, A. Karim, S. Zobaed, B. Shanmugam, and D. Mathur, "Machine learning based PV power generation forecasting in Alice Springs," *IEEE Access*, vol. 9, pp. 46117–46128, 2021.

[5] A. Nespoli, A. Niccolai, E. Ogliari, G. Perego, E. Collino, and D. Ronzio, "Machine learning techniques for solar irradiation nowcasting: cloud type classification forecast through satellite data and imagery," *Applied Energy*, vol. 305, article 117834, 2022.

[6] F. Rodríguez, F. Martín, L. Fontán, and A. Galarza, "Ensemble of machine learning and spatiotemporal parameters to forecast very short term solar irradiation to compute photovoltaic generators output power," *Energy*, vol. 229, article 120647, 2021.

[7] H. Musbah, H. H. Aly, and T. A. Little, "Energy management of hybrid energy system sources based on machine learning classification algorithms," *Electric Power Systems Research*, vol. 199, article 107436, 2021.

[8] U. Singh, M. Rizwan, M. Alaraj, and I. Alsaidan, "A machine learning-based gradient boosting regression approach for wind power production forecasting: a step towards smart grid environments," *Energies*, vol. 14, no. 16, article 5196, 2021.

[9] H. Wang, Z. Lei, X. Zhang, B. Zhou, and J. Peng, "A review of deep learning for renewable energy forecasting," *Energy Conversion and Management*, vol. 198, article 111799, 2019.

[10] J. Ferrero Bermejo, J. F. Gomez Fernandez, F. Olivencia Polo, and A. Crespo Márquez, "A review of the use of artificial neural network models for energy and reliability prediction A

study of the solar PV hydraulic and wind energy sources," *Applied Sciences*, vol. 9, no. 9, article 1844, 2019.

[11] A. Mosavi, M. Salimi, S. Faizollahzadeh Ardabili, T. Rabczuk, S. Shamshirband, and A. R. Varkonyi-Koczy, "State of the art of machine learning models in energy systems, a systematic review," *Energies*, vol. 12, no. 7, article 1301, 2019.

[12] A. Ahmed and M. Khalid, "A review on the selected applications of forecasting models in renewable power systems," *Renewable and Sustainable Energy Reviews*, vol. 100, pp. 9–21, 2019.

[13] A. Zendehboudi, M. A. Baseer, and R. Saidur, "Application of support vector machine models for forecasting solar and wind energy resources: a review," *Journal of Cleaner Production*, vol. 199, pp. 272–285, 2018.

[14] U. K. Das, K. S. Tey, M. Seyedmahmoudian et al., "Forecasting of photovoltaic power generation and model optimization: a review," *Renewable and Sustainable Energy Reviews*, vol. 81, pp. 912–928, 2018.

[15] C. Voyant, G. Notton, S. Kalogirou et al., "Machine learning methods for solar radiation forecasting: a review," *Renewable Energy*, vol. 105, pp. 569–582, 2017.

[16] M. Pérez-Ortiz, S. Jiménez-Fernández, P. A. Gutiérrez, E. Alexandre, C. Hervás-Martínez, and S. Salcedo-Sanz, "A review of classification problems and algorithms in renewable energy applications," *Energies*, vol. 9, no. 8, article 607, 2016.

[17] S. F. Stefenon, M. H. D. M. Ribeiro, A. Nied et al., "Time series forecasting using ensemble learning methods for emergency prevention in hydroelectric power plants with dam," *Electric Power Systems Research*, vol. 202, article 107584, 2022.

[18] K. Lingelbach, Y. Lingelbach, S. Otte, M. Bui, T. Künzell, and M. Peissner, "Demand forecasting using ensemble learning for effective scheduling of logistic orders," in *In International Conference on Applied Human Factors and Ergonomics*, pp. 313–321, Springer, Cham, 2021.

[19] S. Zhao, Y. Zhang, H. Xu, and T. Han, "Ensemble classification based on feature selection for environmental sound recognition," *Mathematical Problems in Engineering*, vol. 2019, 7 pages, 2019.

Computer Systems Science & Engineering
DOI: 10.32604/csse.2023.027744
Article

Tech Science Press

An Optimized Deep-Learning-Based Low Power Approximate Multiplier Design

M. Usharani[1,*], B. Sakthivel[2], S. Gayathri Priya[3], T. Nagalakshmi[4] and J. Shirisha[5]

[1]Department of Electronics and Communication Engineering, Er.Perunal Manimekalai College of Engineering, Konneripalli, Hosur, 635117, India
[2]Department of Electronics and Communication Engineering, Pandian Saraswathi Yadav Engineering College, Sivagangai, Tamilnadu, 630561, India
[3]Department of Electronics and Communication Engineering, R.M.D Engineering College, Gummidipundi, Tamilnadu, 601206, India
[4]Department of Computer Science and Engineering, Koneru Lakshmaiah Education Foundation, Vaddeswaram, Guntur, 522502, India
[5]Department of Electronics and Communication Engineering, Malla Reddy Engineering College, Hyderabad, Telangana, 500015, India
*Corresponding Author: M. Usharani. Email: usharaniphd@gmail.com
Received: 24 January 2022; Accepted: 27 February 2022

Abstract: Approximate computing is a popular field for low power consumption that is used in several applications like image processing, video processing, multimedia and data mining. This Approximate computing is majorly performed with an arithmetic circuit particular with a multiplier. The multiplier is the most essential element used for approximate computing where the power consumption is majorly based on its performance. There are several researchers are worked on the approximate multiplier for power reduction for a few decades, but the design of low power approximate multiplier is not so easy. This seems a bigger challenge for digital industries to design an approximate multiplier with low power and minimum error rate with higher accuracy. To overcome these issues, the digital circuits are applied to the Deep Learning (DL) approaches for higher accuracy. In recent times, DL is the method that is used for higher learning and prediction accuracy in several fields. Therefore, the Long Short-Term Memory (LSTM) is a popular time series DL method is used in this work for approximate computing. To provide an optimal solution, the LSTM is combined with a meta-heuristics Jellyfish search optimisation technique to design an input aware deep learning-based approximate multiplier (DLAM). In this work, the jelly optimised LSTM model is used to enhance the error metrics performance of the Approximate multiplier. The optimal hyperparameters of the LSTM model are identified by jelly search optimisation. This fine-tuning is used to obtain an optimal solution to perform an LSTM with higher accuracy. The proposed pre-trained LSTM model is used to generate approximate design libraries for the different truncation levels as a function of area, delay, power and error metrics. The experimental results on an 8-bit multiplier with an image processing application shows that the proposed approximate computing multiplier achieved a superior area and power reduction with very good results on error rates.

Keywords: Deep learning; approximate multiplier; LSTM; jellyfish

1 Introduction

Recently, approximate computing is an emerging approach to reduce the power consumption for several applications like video processing, multimedia, image processing and data mining etc. The approximate computing technique is performed by regulating the inexact calculation with a tolerable error in terms of reducing power and increasing an operational frequency. These errors have not affected the operations of computing and its performances [1]. The performance of approximate computing is based on multiplication and additions. The function of multiplier or adder is truncated with some error compensation which consumes a low power than exact circuits. This inexact or approximate design of adder or multiplier will not affect a system's output and it also improved energy efficiency with a good performance.

The Multipliers are the primary component in Approximate computing which is utilized for many applications like digital signal processors, microprocessors and embedded systems [2]. Also, multiplier requires high energy consumption and also design complexity. It becomes a greater challenge to design a low power multiplier in digital circuits. On designing approximate multipliers, performance in terms of energy consumption and hardware complexity is reduced. Thus the approximate multiplier application achieved higher success in research and also enhanced the quality and performance of systems. Though it is also more challenging to work for researchers in minimum power, the field is searching for a few implementations with a higher training of input dependent or input aware techniques.

The DL is an advanced learning technique for solving a complex issue and highly predictable than any other method. The DL model of Long Short-Term Memory (LSTM) model is used which is highly efficient in classifying, predicting and processing the data in time series [3]. The main contribution of the proposed work is to introduce a new DL model-based approximate multiplier with the awareness of prediction in area, delay and power for the corresponding truncation levels.

To enhance the optimal Accuracy in approximate computing, the LSTM is combined with a Meta-heuristics algorithm like the jellyfish Search Optimization algorithm. The jellyfish Search Optimization is based on swarm Meta-heuristics that is developed by its food searching behaviour in an ocean current. In this work, the novel input aware approximate multiplier design technique is presented. The input awareness is done by using a novel Jelly optimised LSTM technique that is used to pre-train the input data of the Approximate multiplier. This Approximate multiplier is highly trained with an optimal result and stored in a library. As a result, by implementing this input aware approximate multiplier, the performance of approximate computing is more efficient in terms of area, power and delay than the previous techniques.

The rest of the work is contributed as: Section 2 described the related literature based on approximate computing by using various DL methods. Section 3 explores preliminaries of a proposed method where the clear view of the LSTM model is explained in it. Next, the proposed methodology is discussed with an input aware jelly optimised LSTM technique in Section 4. Then the result and discussion of proposed and previous methods are evaluated in Section 5. Finally, the summary of the entire work is concluded in Section 6.

2 Related Works

There are several experts are developed numerous novel approximate computing in terms of error and power reduction. In some cases, the literature is explored with a DL based approximate computing which is discussed below.

Jiang et al. [4] presented a survey and an approximate arithmetic circuit evaluation for various design constraints. This method is improved the system performance quality and obtained a minimum power consumption. Jo et al. [5] explored a neural processing element based on approximate adders. This method used a fault tolerance property of DL algorithms that reduced resource usage without modifying accuracy. Next, the tiny two-class precision (high and low) controller model is designed by Hammad

et al. [6] to improve the multiplier performance. This hybrid of high and low achieved a maximum gain with a low error rate than a single-precision controller technique.

Nourazar et al. [7] developed a mixed-signal memristor design to multiply floating-point signed complex numbers. This multiplier is used to stimulate a CNN and lastly integrated with a generic pipeline ×86 processor. This method achieved a high computational speed and low error tolerance. Next, the Stochastic Computing techniques are explored by Lammie et al. [8] that performed training in terms of fixed-point weights and biases. The FPGA implementation is experimented with using this method by achieving minimum power consumption than GPU counterparts. Siddique et al. [9] designed an Evoapprox8b signed multipliers which is energy efficient with bit-wise fault resilience and extensive layer-wise. The result shows that the energy efficiency obtained a fault resilience was orthogonal.

Also, an efficient approximation is designed using DNN accelerators by Mrazek et al. [10]. The DNN accelerators based computational path avoided the retraining process to save power consumption. The pruning techniques in digital circuits are designed using Machine Learning (ML) by Sakthivel et al. [11]. The Random forest method is applied to prune the selected gates according to an input. This result obtained a minimum error rate with higher accuracy by Pruning nodes prediction. Chou et al. [12] explored a jellyfish Search optimization that is based on jellyfish searching food behaviour in an ocean current. This model also included a time control mechanism to control its movements between the swarm and inside the swarm. Chandrasekaran et al. [13] applied a dragonfly and lion optimization based algortihms to solve the optimization problems in test scheduling of system on chips.

3 Preliminaries

Based on the novel jelly optimised LSTM model, the preliminary of the proposed work is discussed in this section. In the proposed work, the LSTM model is majorly contributed in it that is explained with its working operation below.

LSTM model

The LSTM is the most popular DL model in recent times which is applied for sequential modelling. The LSTM is followed by a time series model of Recurrent Neural Network (RNN) which is also efficient in non-linear function. But the RNN, it is faced a few issues like gradient vanishing which can be store limited data in the memory. These issues are rectified by using an LSTM model.

The LSTM structure is shown in Fig. 1 which consists of three gates and a cell state. The cell state is used to flow the relevant units by permitting a few linear functions. The three gates are input, forget and output gates. The Input gate is used to fetch the data from the dataset. Next, the forget gate is used for data storage where the long term information is stored in it. This gate also stored hidden data of previous states which is useful for long term execution. Last an output gate is decided to write the data and also passed it to the next hidden layer. All these gates are performed by controlling a gate's valve opening and closing i.e., 0 and 1 respectively.

The mathematical derivation of forget state based on X_t (input) and h_t (hidden layer activation functions) is expressed as follow,

$$F_t = \sigma(\mathrm{W_f}[h_t - 1\ ,\ x_t] + b_f \tag{1}$$

where
$\sigma \rightarrow$ Sigmoid activation function,
$\mathrm{W} \rightarrow$ weight matrices
$b \rightarrow$ threshold bias

$$\sigma(\mathrm{X}) = \frac{1}{1 - e^{-x}} \tag{2}$$

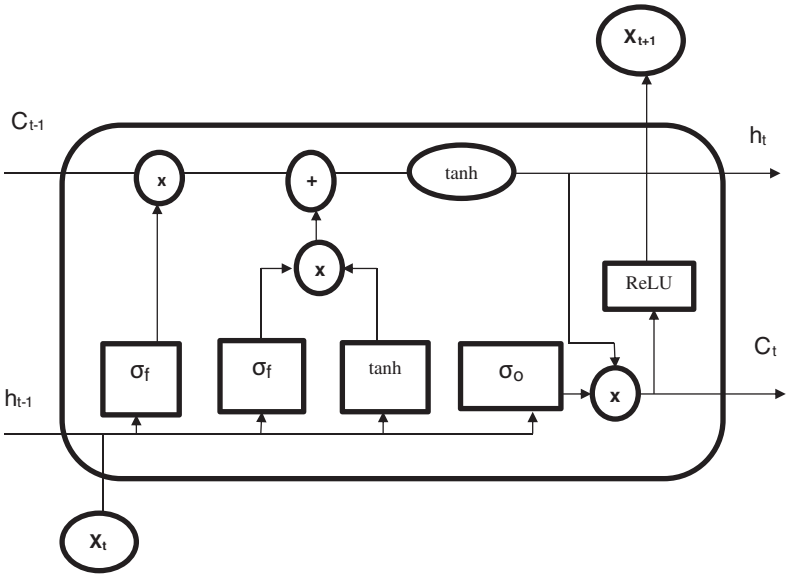

Figure 1: LSTM model

The Input Gate and output gates are activated to obtain a hidden cell state Ct. The hidden cell state is used to move the information into a new hidden cell state. Both the gates are performed by using a sigmoid (σ) and hyperbolic tangent function (tanh) activation function. Thus, the input gate (i_t) and an output gate with a new hidden cell state (o_t) that is expressed in the following.

$$i_t = \sigma(\mathrm{w_i}[h_{t-1},\ x_t] + b_i \tag{3}$$

$$o_t = \tanh w_o[h_{t-1},\ x_t] + b_o \tag{4}$$

$$\tanh(X) = \frac{e^{x'} - e^{-x'}}{e^{x'} + e^{-x'}},\ \text{between}\ -1\ \text{to}\ 1 \tag{5}$$

Objective Function

The objective function is defined by fine-tuning the weights and threshold bias of the LSTM hyperparameter. The fine-tuning is done by using the JellyFish search optimization which is obtained an optimal result. Based on this function, the approximate computing multiplier is trained by optimised LSTM to provide a pre-defined library function. This predefined library can be achieved an error rate reduction and high computational speed in approximate computing. Thus, the Mean Square Errors (*MSE*) can be formulated in terms of desired output of the approximate multiplier (D_i) and a predicted output of Approximate multiplier (P_i) in below.

$$MSE = minimum\left(\frac{\sum_{i=1}^{N}(D_i - P_i)^2}{N}\right) \tag{6}$$

Based on the MSE value, the fine-tuning is performed by the novel jelly optimised LSTM algorithm in terms of weight and biases respectively.

4 Proposed Methodology

In this section, the proposed approximate multiplier based DL based library generation. This proposed approximate multiplier is aimed to reduce the power and area with improved error rate performance. The overall architecture of proposed approximate computing is shown in Fig. 2. The proposed Approximate Computing architecture comprises an input module, Approximate multiplier, Novel Jelly optimised LSTM model, Optimised Pre-trained Library and output module.

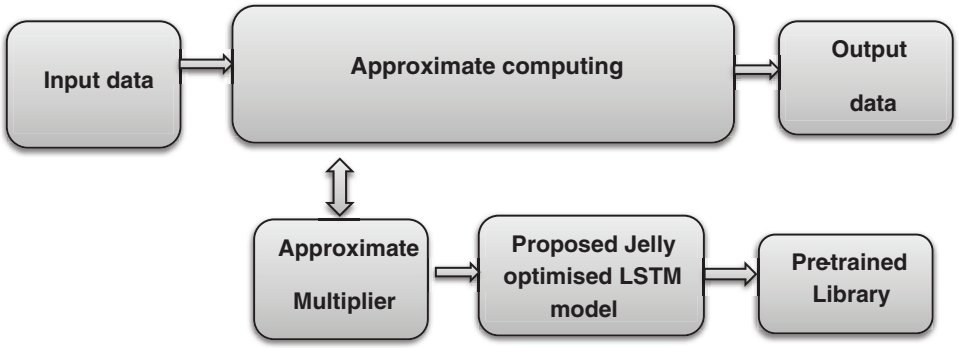

Figure 2: Novel approximate computing

From Fig. 2, the input module is used to fetch the data for computing that is sent to perform an approximate multiplier. The Approximate multiplier has two main processes namely Jelly optimised LSTM and pre-trained library. Initially, to provide an optimal solution with higher accuracy, the Jelly optimised LSTM is performed. This model has applied all the functional possibilities of an approximate multiplier. Then all these optimised values are stored in a library. The optimised pre-trained library is the memory block that is stored a maximum amount of data after jelly optimised LSTM is performed. Based on the input data, the approximate multiplier provides a corresponding output value to the output module. Finally, the output of the approximate computing is obtained with a minimum error rate, low power dissipation and high accuracy.

Therefore, the proposed Approximate computing has resulted in higher merits based on the Novel Jelly Optimised LSTM model (discussed below)

Proposed Novel Jelly Optimised LSTM

The Novel Jelly Optimised LSTM is proposed that is used to fine-tune the LSTM hyperparameters using JellyFish search optimization. The weight and threshold biases are the main hyperparameters of LSTM. These parameters are fine-tuned by JellyFish Search optimization to determine its objective function. This objective function is evaluated to provide the best optimal result. Later, the LSTM model is performed with a classification in approximate computing multiplier. Thus the optimal input awareness of approximate computing is achieved with greater accuracy by using a pre-trained Optimised LSTM. Therefore the JellyFish Search optimization is discussed in the following.

Jellyfish optimizer

Jellyfish is a very famous and well-known fish in an entire world which is lived from surface waters to the deep sea. It is structured as a soft body bell-shaped and long, harsh tentacles with various colours, shapes and sizes. The tentacles are used to attack and paralyze the prey by its venom. It has a special feature of allowing controlling its own movements. It is formed an umbrella structure to move forward by pushing water. Based on currents and tides, it is mostly drifting in the water. At a time of favourable condition, the jellyfish used to make a swarm to show its mass named as Jellyfish bloom. To form a jellyfish swarm,

there are several parameters measured such as ocean currents, oxygen availability, available nutrients, predation, and temperature. The swarm formations are obtained with this parameter where ocean currents are the most significant factor for a swarm. Thus the Jellyfish Search algorithm is inspired by its searching characteristic and ocean movement. These fishes are made actions in three possible ways namely,

1. It is lived either in an ocean current or towards the swarm; it has a "time control process that carried between these movement types.
2. It is searched for food in the ocean and attracted to the location of maximum little fish prey or quantity is presented.
3. Once the prey's location is identified location and its objective function is evaluated.

The Jellyfish behaviour based on search food in the ocean is shown in Fig. 3.

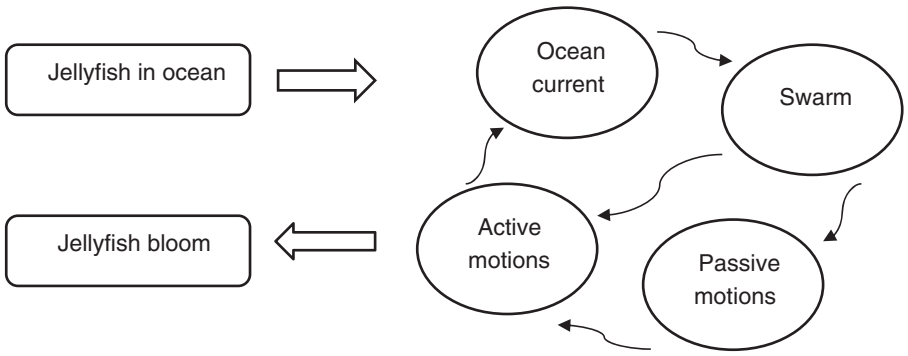

Figure 3: Jellyfish behaviour in the ocean

Ocean current

The ocean current with numerous nutrients is attracted by jellyfish. The ocean current direction (trend) is expressed in Eq. (1).

$$\overrightarrow{trend} = X^* - \beta * random(0,\ 1) * \mu, \tag{7}$$

where $X^* \rightarrow$ current best position of jellyfish which is the mean value of every jellyfish location; $\beta > 0$ represents a coefficient of distribution towards trend length.

The position update of jellyfish is formulated in the following.

$$X_i(t+1) = X_i(t) + randon(0.1) * \overrightarrow{trend} \tag{8}$$

Jellyfish swarm

A swarm is the collection of jellyfish in large quantities. It is moved in its original position known as passive motion, type A or a new position known as active motion, type B.

Thus, the Type A motion is expressed by updating its own position by using the following equation

$$X_i(t+1) = X_i(t) + \gamma * randon(0.1) * (UB - LB) \tag{9}$$

where, $UB \rightarrow$ upper bound of search space, $LB \rightarrow$ lower bound of search space and $\gamma \rightarrow$ motion coefficient.

Thus the coefficient with the motion's length is updated and considered as $\gamma = 0.1$

In Eq. (9), the type B movement is simulated. The jellyfish (j) is selected randomly to evaluate the movement direction. The jellyfish vector is chosen with an interest (i) to the selected jellyfish (j). If the preys are predicted at the location of chosen jellyfish (j) exceeds that jellyfish position of interest (i), then again moves to the first. When the prey is available for the selected jellyfish (j) is minimum than the jellyfish position of interest (i), then it will move away directly from the location Therefore every jellyfish is moved to determine better positions for prey by updated jellyfish position.

$$\overrightarrow{step}\ simulated\ random\ (0,\ 1)\overrightarrow{Dir} \tag{10}$$

$$\overrightarrow{Dir} = \begin{cases} X_j(t) - X_i(t) & if\ f(X_i) \geq f(X_j) \\ X_j(t) - X_j(t) & if\ f(X_i) \geq f(X_j) \end{cases} \tag{11}$$

$$X_i(t+1) = -X_i(t) + \overrightarrow{step} \tag{12}$$

where f represents an objective function of position X

To evaluate the motion types over time, a time control mechanism is presented. This control mechanism controlled an overall swarm type A and type B motions and also a jellyfish movement toward an ocean current. Thus the time control mechanism is explained in the following.

Time control mechanism

In this mechanism, the Jellyfish are often attracted to an ocean current because of its numerous nutritious plants. Frequently the temperature, wind and other atmospheric changes are carried in an ocean current. Then the jellyfish swarm migrated to another ocean current and form a new swarm in a new ocean current. The Jellyfish can be moved inside a swarm among type A and type B motion. Initially type A is selected for many overtimes, then type B is preferred gradually. To control the jellyfish movement between ocean current and between swarm, the Time control mechanism c(t) is expressed below.

$$c(t) = \left| 1 - \frac{1}{Max_{iter}} * (2 * random(0,\ 1) - 1) \right| \tag{13}$$

where t represents a number of iterations in a specified time and Max_{iter} represents a maximum number of iterations. Therefore, jellyfish Search Optimization is discussed in algorithm 1.

Algorithm 1: proposed Jelly Optimised LSTM

Input: LSTM Hyper-parameter population (n_{pop}), Max_{iter}

Output: Optimal Result

Begin

Initialize LSTM Hyper-parameter population X_i, i = 1, 2,.., n_{pop} and Max_{iter}

Evaluate prey at X_i and $f(X_i)$

Determine present position jellyfish at X*

Initialize t = 1

For i = 1: n_{pop} do

Estimate c(t)

If $c(t) \geq 0.5$

Evaluate Ocean current

Update new jellyfish position

(Continued)

Algorithm 1: (continued)

Else movement inside the swarm

If random (0, 1)>(1-c(t)): type A motion exhibits

Update New position

Else type B motion exhibits

Evaluate Jellyfish Direction

Update new position

End if

End if

Verify boundary and new location prey's quantity

Update X_i and X_i with most prey X*

End for if

Generate time: t = t + 1

Until $t > Max_{int}$

Obtain optimal solution

End

Approximate multiplier design

The proposed jelly optimized LSTM model is trained with all possible combinations of multiplier inputs by varying truncation levels. The pretrained clusters are formed by the LSTM model to design an approximate multiplier with an optimal error rate. The knowledge about error rate and power consumption leads to improving the approximate performance of the proposed multiplier.

5 Performance Evaluation

The proposed multiplier is coded in Verilog and simulated using a synopsis compiler. The proposed multiplier compared with other conventional approximate multipliers like Under Designed Multiplier (UDM) [14] , Partial product perforation (PPP) [15], Static Segment Multiplier (SSM) [16] , Approximate compressor-based multiplier (ACM) [17] and Machine Learning based Approximate Multiplier(MLAM) in terms of area, delay, power mean relative error (MRE) and normalized error distance (NRE). In image processing applications, a geometric mean filter (GMF) is used to the smoothen image by removing unwanted noise. It performs geometric mean operations of pixels to enhance the image visual effects. The output image after performing GMF is given by

$$GMF(x,\ y) = \left[\prod I(i;\ j) \right]^{1/mn} \tag{14}$$

where I denote the original image. Each pixel of the GMF processed image at point (x, y) is specified by the product of the pixels within the geometric mean mask raised to the power of 1/mn. To evaluate the efficiency of the proposed DL based multiplier, two 8-bits per pixel greyscale images with Gaussian noise are considered. The noisy images are filtered by applying a 3*3 mean filter with neighbouring pixels centred around them. The workflow of the proposed Peak signal-to-noise ratio (PSNR) and energy requirement is shown in Fig. 4. The performance of the proposed multiplier is given in Tab. 1. PSNR is the proportion

among the extreme possible power of an image and the power of corrupting noise that disturbs the quality of its illustration. To calculate the PSNR, it is required to correlate that image to an ideal original image with the maximum possible power.

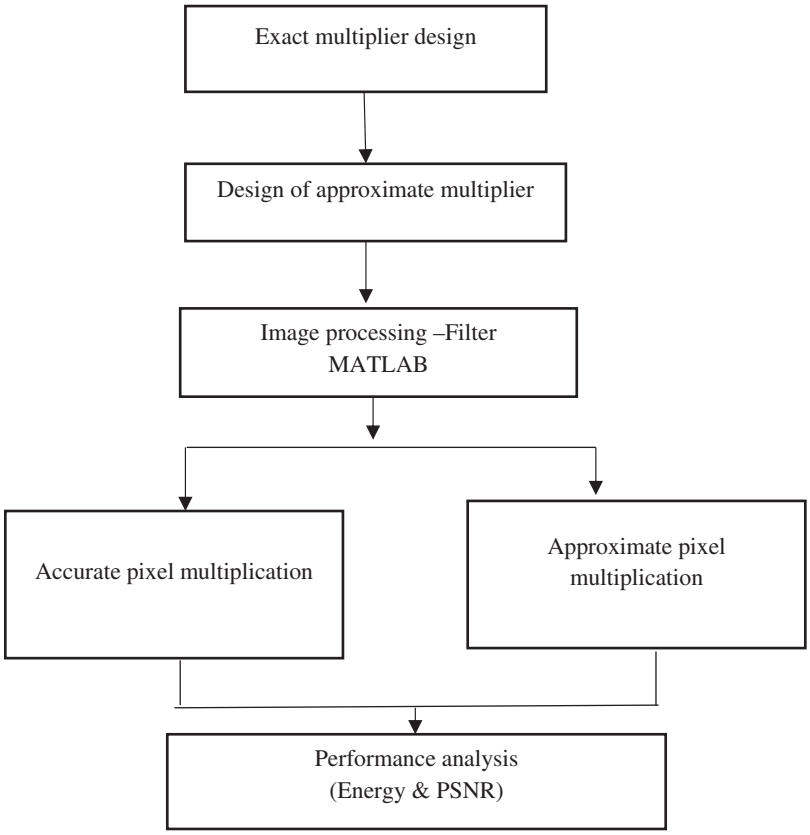

Figure 4: Proposed image processing performance analysis

Table 1: Area, power and delay analysis of proposed multiplier

TYPE	AREA	POWER	DELAY
Multiplier without approximation	2412.6	872.19	0.34
DLAM	853.19	151.51	0.21
MLAM	913.66	167.69	0.22
AM [18]	1079.14	251.3	0.23
ACM	1365.56	219.22	0.2
SSM	1977.51	630.49	0.345
PPP	2270.37	786.43	0.32
UDM	1970.3	662.44	0.33

In the proposed DL multiplier model, the approximated library is generated for all combinations of inputs. The truncation level of outputs with the corresponding area, energy, and error metrics are trained to the model to identify the best truncation bits and error compensation values. For 8-bit multiplier, 2^{16} combinations of inputs and error metric for various truncation and error compensation values trained to LSTM model for selection best multiplication with the awareness of inputs.

Compared to other approximate multipliers, the proposed DL multiplier outperforms in terms of area, power and delay. Tab. 2 gives an error metric comparison of a proposed multiplier. From the results observed that the lower values of MRE and NRE prove the better suitability of the proposed multiplier in high power savings with more error tolerance applications.

Table 2: MRE and NRE analysis of proposed multiplier

TYPE	MRE	NRE
DLAM	0.187	0.003
MLAM	0.296	0.003
AM	0.305	0.005
ACM	0.376	0.006
SSM	0.319	0.006
PPP	0.452	0.007
UDM	0.332	0.007

The PSNR and energy savings of noisy images with resultant geometric mean filtered images are given in Tab. 3. The energy requirement of ML and DL based approximate multiplier is 1.90 and 1.34 μJ respectively**.** PSNR outputs of ML and DL based approximate multiplier is 71.5 and 74.9 respectively**.**

Table 3: PSNR and average energy required for filtering

Benchmark	MLAM (PSNR)	DLAM (PSNR)	DLAM (Energy-μJ)	DLAM (Energy-μJ)
Lena	67.2	73.5	1.90	1.34
Airplane	74	76.81	2.06	1.89
Baboon	69.5	72.5	1.10	0.94
Peppers	53	56.4	0.98	0.54
Cameraman	71.5	74.9	1.89	1.71
Moon surface	63	72.4	1.13	0.82

6 Conclusion

Approximate computing or inexact computing is used in numerous applications. Several researchers are worked on the low power approximate multiplier to improve the performance of Approximate computing. In this work, the novel Jelly optimised LSTM techniques are presented for an approximate multiplier. The approximate multiplier is obtained a highly optimised pre-trained input data using Jelly optimised LSTM techniques. The proposed technique is performed by fine-tuning the LSTM hyperparameters using jellyfish search optimisation. Based on the input aware knowledge of the pre-trained library, the performance of Approximate computing is increased. Therefore, the proposed Approximate computing is

obtained a low power and minimum error rate than the previous model. Further, the performance of the proposed work is evaluated in terms of area, power and accuracy with the previous techniques. As a result, the proposed work is achieved a higher performance in all metrics than existing.

Funding Statement: The authors received no specific funding for this study.

Conflicts of Interest: The authors declare that they have no conflicts of interest to report regarding the present study.

References

[1] S. Ullah, S. Rehman, M. Shafique and A. Kumar, "High-performance accurate and approximate multipliers for FPGA-based hardware accelerators," *IEEE Transactions on Computer-Aided Design of Integrated Circuits and Systems*, vol. 41, no. 2, pp. 211–224, 2022.

[2] I. Hammad and K. El-Sankary, "Impact of approximate multipliers on VGG deep learning network," *IEEE Access*, vol. 6, no. 1, pp. 60439–60444, 2018.

[3] S. Sen and A. Raghunathan, "Approximate computing for long short term memory (LSTM) neural networks," *IEEE Transactions on Computer-Aided Design of Integrated Circuits and Systems*, vol. 37, no. 11, pp. 2266–2276, 2018.

[4] H. Jiang, F. J. H. Santiago, H. Mo, L. Liu and J. Han, "Approximate arithmetic circuits: A survey, characterization, and recent applications," in *Proc. of the IEEE*, Shanghai, China, vol. 108, no. 12, pp. 2108–2135, 2020.

[5] C. Jo and K. Lee, "Bit-serial multiplier based neural processing element with approximate adder tree," in *2020 Int. SoC Design Conf. (ISOCC)*, Yeosu, Korea, pp. 286–287, 2020.

[6] I. Hammad, L. Li, K. El-Sankary and W. M. Snelgrove, "CNN inference using a preprocessing precision controller and approximate multipliers with various precisions," *IEEE Access*, vol. 9, pp. 7220–7232, 2021.

[7] M. Nourazar, V. Rashtchi, A. Azarpeyvand and F. Merrikh-Bayat, "Code acceleration using memristor-based approximate matrix multiplier: Application to convolutional neural networks," *IEEE Transactions on Very Large Scale Integration (VLSI) Systems*, vol. 26, no. 12, pp. 2684–2695, 2018.

[8] C. Lammie and M. R. Azghadi, "Stochastic computing for low-power and high-speed deep learning on FPGA," in *2019 IEEE Int. Symp. on Circuits and Systems (ISCAS)*, Sapporo, Japan, pp. 1–5, 2019.

[9] A. Siddique, K. Basu and K. A. Hoque, "Exploring fault-energy trade-offs in approximate dnn hardware accelerators," in *2021 22nd Int. Symp. on Quality Electronic Design (ISQED)*, Santa Clara, CA, USA, pp. 343–348, 2021.

[10] V. Mrazek, Z. Vasicek and L. Sekanina, "ALWANN: Automatic layer-wise approximation of deep neural network accelerators without retraining," in *2019 IEEE/ACM Int. Conf. on Computer-Aided Design (ICCAD)*, Westminster, CO, USA, pp. 1–8, 2019.

[11] B. Sakthivel, K. Jayaram and N. Devarajan, " "Machine learning-based pruning technique for low power approximate computing," *Computer Systems Science and Engineering*, vol. 42, no. 1, pp. 397–406, 2022.

[12] J. S. Chou and D. N. Truong, " "A novel metaheuristic optimizer inspired by behavior of jellyfish in ocean," *Applied Mathematics and Computation*, vol. 389, no. 6, pp. 125535–125542, 2021.

[13] J. Chandrasekaran and R. Gokul, "Test scheduling of system-on-chip using dragonfly and ant lion optimization algorithms," *Journal of Intelligent & Fuzzy Systems*, vol. 40, no. 3, pp. 4905–4917, 2021.

[14] P. Kulkarni, P. Gupta, and M. D. Ercegovac, "Trading accuracy for power in a multiplier architecture," *Journal of Low Power Electron*, vol. 7, no. 4, pp. 490–501, 2011.

[15] G. Zervakis, K. Tsoumanis and S. Xydis, "Design-efficient approximate multiplication circuits through partial product perforation," *IEEE Transaction on. Very Large Scale Integr. (VLSI) System.*, vol. 24, no. 10, pp. 3105–3117, 2016.

[16] H. A. Narayanamoorthy, Z. Moghaddam and T. Liu, "Energy-efficient approximate multiplication for digital signal processing and classification applications," *IEEE Transaction on Very Large Scale Integr. (VLSI) Sysem.*, vol. 23, no. 6, pp. 1180–1184, 2015.

[17] A. Momeni, J. Han and P. Montuschi, "Design and analysis of approximate compressors for multiplication," *IEEE Transaction. Computers*, vol. 64, no. 4, pp. 984–994, 2015.

[18] S. Venkatachalam and S. B. Ko, "Design of power and area efficient approximate multipliers," *IEEE Transactions on Very Large Scale Integration (VLSI) Systems*, vol. 25, no. 5, pp. 1782–1786, 2017.

Hindawi
Journal of Nanomaterials
Volume 2022, Article ID 4435591, 12 pages
https://doi.org/10.1155/2022/4435591

Research Article

Design and Implementation of Smart Hydroponics Farming Using IoT-Based AI Controller with Mobile Application System

S. V. S. Ramakrishnam Raju[1], **Bhasker Dappuri**[2], **P. Ravi Kiran Varma**[3], **Murali Yachamaneni**[4], **D. Marlene Grace Verghese**[5] and **Manoj Kumar Mishra**[6]

[1]*Professor and Dean Academics, Department of Electronics and Communication Engineering, St. Martin's Engineering College, Dulapally, Secunderabad, Telangana, India*
[2]*Department of Electronics and Communication Engineering, CMR Engineering College, Kandlakoya, Secunderabad, Telangana, India*
[3]*Department of Computer Science and Engineering, Maharaj Vijayaram Gajapathi Raj College of Engineering, Vizianagaram, 535005 Andhra Pradesh, India*
[4]*Malla Reddy Engineering College (Autonomous), Secunderabad, Telangana, India*
[5]*Department of Information Technology, Vidya Jyothi Institute of Technology (Autonomous), Aziz Nagar, C. B Post, Hyderabad, 500075 Telangana, India*
[6]*Salale University, Fitche, Ethiopia*

Correspondence should be addressed to Manoj Kumar Mishra; mkmishra@slu.edu.et

Received 31 May 2022; Accepted 30 June 2022; Published 12 July 2022

Academic Editor: Samson Jerold Samuel Chelladurai

Hydroponics is the soil less agriculture farming, which consumes less water and other resources as compared to the traditional soil-based agriculture systems. However, monitoring of hydroponics farming is a challenging task due to the simultaneous supervising of numerous parameters, nutrition suggestion, and plant diagnosis system. But the recent technological developments are quite useful to solve these problems by adopting the artificial intelligence-based controlling algorithms in agriculture sector. Therefore, this article focuses on implementation of mobile application integrated artificial intelligence based smart hydroponics expert system, hereafter referred as AI-SHES with Internet of Things (IoT) environment. The proposed AI-SHES with IoT consists of three phases, where the first phase implements hardware environment equipped with real-time sensors such as NPK soil, sunlight, turbidity, pH, temperature, water level, and camera module which are controlled by Raspberry Pi processor. The second phase implements deep learning convolutional neural network (DLCNN) model for best nutrient level prediction and plant disease detection and classification. In third phase, farmers can monitor the sensor data and plant leaf disease status using an Android-based mobile application, which is connected over IoT environment. In this manner, the farmer can continuously track the status of his field using the mobile app. In addition, the proposed AI-SHES also develops the automated mode, which makes the complete environment in automatic control manner and takes the necessary actions in hydroponics field to increase the productivity. The obtained simulation results on disease detection and classification using proposed AI-SHES with IoT disclose superior performance in terms of accuracy, F-measure with 99.29%, and 99.23%, respectively.

1. Introduction

IoT in agriculture might be a game changer for humans and the whole planet [1]. We are now seeing how harsh weather, eroding soil, drying areas, and collapsing ecosystems make food production more difficult and costly. Meanwhile, we are not getting any fewer. According to a well-known forecast, there would be more than 9 billion people in 2050. Fortunately, owing to quickly emerging technology and IoT applications [2] for smart farming, there is still hope. According to

analysts, this industry will reach 23.14 billion US dollars by 2022, with 75 million IoT devices implemented for agricultural applications in the following several years. The Internet of Objects is all about making "dumb" things "smart" by linking them to one another and to the Internet. It permits the remote sensing and control of physical things, allowing for more direct integration of the real world with computer-based systems [3, 4]. IoT allows devices equipped with sensors to communicate and interact with one another via the Internet. Pumps, barns, and tractors, as well as weather stations and computers, may all be remotely monitored and operated in real time. Agriculture is the only source for food production in many countries including Ethiopia, India. It is a wealthy industry, but over the years, people and work force involved in this industry are reducing drastically. The traditional farming face lots of challenges for increasing the productivity [5]. Some of the challenges in rural areas are the global climate changes, pollutions, loosing soil integrity to grow the crops, rapid increment in urbanization, and agricultural land sacristy etc.. Therefore, farmers need to employ smart farming as shown in Figure 1, which can help in increasing the food yield production [6]. In addition, these new methods of farming along with traditional farming methods need some technological backing to counter global food crisis. To meet these challenges, it is necessary to adopt new technologies in farming like hydroponics, vertical forming, and polyhouse. Among those, the hydroponics is the best farming method, which directly involves with the technological requirements.

Some of the problems presented in the hydroponics are seedling (wilting, dead roots), system clogging, infestation (algae, pest), and nutrient deficiencies [7]. Because seedlings are susceptible to issues when they are in the beginning stages of their development, one of the most difficult tasks in the process of producing plants in hydroponics is cultivating healthy seedlings. Wilting occurs when a plant loses its stiffness, and its leaves begin to dry up. Wilting may be caused by a number of circumstances, including insufficient watering or extreme temperature [8]. There are a variety of factors that may contribute to dead roots, including the water's high temperature, a very high or extremely low EC, and over watering in thick substrates. Roots that have died might be an indication that a root rot pathogen is present in the system. It is generally agreed that clogging is the issue that arises most commonly in hydroponic systems, and this is particularly true for drip-style systems. The majority of the time, the tubes get clogged as a result of fragments of the growth media that become lodged inside of them. The circulation of the whole system is disrupted when there is clogging, which may cause significant harm to your crops. There is no way for producers to completely eliminate the risk of infection in hydroponic farms, no matter how well they manage their operations. During the early stages of an infestation, there are a few actions that you may do to combat the problem. In most cases, a grower will be able to identify a specific nutrient deficit by evaluating the symptoms, but this method is not fool proof and may occasionally lead to incorrect conclusions [9]. Checking the water temperature, pH of the nutrient solution, and electrical conductivity of the solution should come first before determining whether or not there is an issue.

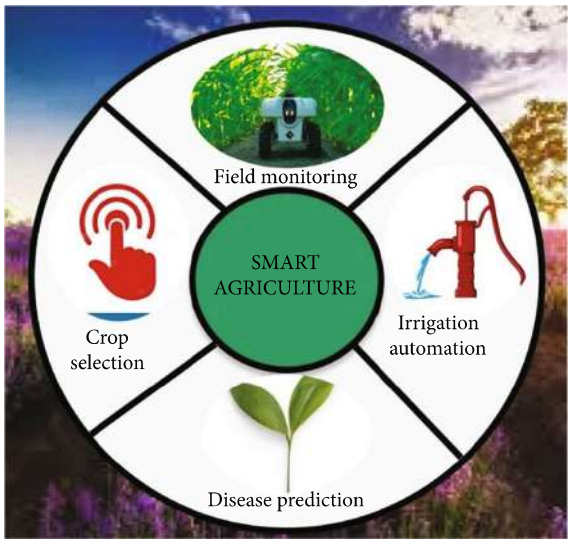

Figure 1: Sample illustration of smart farming.

Recently, AI-based autonomous robots with a variety of hardware controllers and industrial robots are playing the key role in hydroponics for minoring of plants [10]. However, they are failed to monitor the multiple sensors at the same time to solve the above-mentioned problems. Another major challenge presented in the traditional farming and hydroponics is the plant diseases, which affect the growth of plants and thereby reduce the productivity. Traditionally, either farmers are manually classifying the diseases or pathologist are identifying the disease through lab experiments. However, the performance of traditional systems is purely depending on their experience, and it also a time-consuming task [11, 12]. Further, the early detection and prevention of plant diseases can improve the hydroponics performance. Therefore, recently, image processing-based computer aided methods are widely developed for benefit of the farmers. Thus, image processing technologies for early detection and diagnosis is preferred [13], which is done by using color feature extraction, texture extraction, and shape feature extraction. To overcome these problems, the major contributions of these works are illustrated as follows:

(i) Design and implementation of AI-SHES by integrating Raspberry Pi controller, IoT environment with mobile application

(ii) Implementation of user-friendly environment for farmers using Agri-Hydroponic application, which provides hybrid monitoring and controlling of hydroponics farm field

(iii) Development of IoT based cloud environment for global monitoring of sensor data

(iv) In addition, an AI framework is implemented for alerting, and predictive analytics of sensor data, and plant diseases

Rest of the article is organized as follows: Section 2 deals with the literature survey with problems. Section 3 deals

with the detailed implementation of proposed AI-SHES. Section 4 deals with the detailed analysis of experimental results. Section 5 deals with the conclusion and future scope.

2. Literature Review

This section deals with the detailed analysis of existing methods with the drawbacks. In [14], the authors developed the Internet of Everything (IoE), which is considered a modern platform for advancement of IoT. This system considered the advanced soil sensors for monitoring the crop field. However, the proposed system conserves higher energy and decreases the efficiency, while calculating the heat index of the parameters to observe the surrounding for growth of crops. Further, efficient management of irrigation system (EFIS) [15] is developed for automatic water controlling to avoid the water sacristy problems in Ethiopia, Kenya, and South Africa countries. This work jointly monitors the soil conditions with water levels. However, this system reduces the current intake of the parameters and reduces the data transmission range of the system. Further, a machine learning model known as support vector machine (SVM) [16] is developed for plant disease classification along with the sensor data. In this model, a camera model equipped controller is designed with moisture, color, texture, humidity, and temperature of the leaf. However, this method suffers with the high computational complexity. In [17], authors focused on implementation of calculational intelligence technique for prediction and utilization of nitrogen in wheat crops. The calculation depends on the analysis of image of crops, which are captured the image in the real time field with different time samples and different lighting conditions. Further, artificial neural network with genetic algorithm (ANN-GA) is used to classify the plant diseases. However, this method suffers with the low classification accuracies. Further, MicConvNet [18] classifier is developed for red palm weevil larvae detection in initial stage for protection of date trees. This detection system consists of based on a modified mixed depth wise convolution network. Anyhow, this method did not implement the IoT environment due to complexity issues. Further, hybrid convolutional neural network (HCNN) [19] is trained with dual image database. The database consists of previously infected images, which is used for training the database for such diseases. Secondly, texture, color, and morphology features are extracted from image. However, this method consumed higher training time for feature training.

In [20], the authors integrated the deep learning with IoT for automatic disease identification from plants. The IoT is used for remote sensing of field parameters storage, with modified ResNET51 model which was used on the cloud for purpose of building smart disease detection. This method suffers with the low classification performance. In [21], the authors developed the mobile application, which displays the sensor values in efficient manner by administrating the field. Further, IoT is used to store the disease affected region with specific classes. Further, DeepLens [22] variations are introduced for continuous monitoring of data with ubiquitous access and reliability, which is accessed by cloud data integrating with recursive CNN classification. The RCNN is used to identify the condition of leaves of fruit trees and vegetable plan. However, this method is not useful for diagnosis of hand full of plants and trees diseases detection. In addition, AI and IoT enabled smart agriculture technologies' [23] system is developed with decision tree classification. The data from the hardware is processed by AI, which contains valuable data for prediction of the all the parameters of crop. However, this method suffering with power related issues in real time environment. In [24], the authors implemented the AI-based agriculture system with IoT environment, and this method gives the feedback to farmer for ideal maintaining of the crop production. The AI system utilizes fuzzy logic for predicting types of crop type, soil integration and weather conditions. In [25], the authors implemented the hydroponic automation system for plant growth analysis from seed stage to yield stage. Further, ESP32 microcontroller is used for controlling of different sensors and actuators. Further, LOTUS mobile application was updated with humidity, irrigation, and temperature monitoring. However, this method is a high computational complexity. In [26], the authors implemented the hybrid system with multiple monitoring parameters such as nutrient level, pH, and temperature of the water. Further, K-Nearest Neighbor– (KNN–) based machine learning approach is used to automate these parameters according to reference water levels generated by nutrient film technique. However, this method has low reliability and efficiency as compared to deep learning models.

3. Proposed Methodology

This section gives the detailed implementation analysis of AI-SHES, which is developed by integrating the Raspberry Pi, IoT environment with mobile application. Figure 2 shows the architecture of proposed AI-SHES. An AI-SHES is developed with the user-friendly environment for farmers using Raspberry Pi controller, IoT environment with Agri-Hydroponic application. The farmers monitor and control their hydroponics farm field using Agri-Hydroponic application with manual and automatic controlling modes of operation. The Raspberry Pi controller-based hardware system is placed in hydroponics farm field, which monitors the statics of plants using different sensors. Further, all these sensors' data is uploaded into cloud based IoT environment. An artificial intelligence system is placed across the cloud served with DLCNN, which continuously monitors the sensor data and plant disease status and sends the necessary alerts to the farmers using Agri-Hydroponic application. Finally, the farmer controls his hydroponics farm field during manual mode, so nutrients are supplied to plants as per farmer mentioned levels. In addition, the nutrients are applied to plants with standard reference levels during automated mode of operation.

3.1. Hardware Environment. The proposed AI-SHES implemented with the Raspberry Pi controller with the different types of sensors. Figure 3 shows the hardware environment of proposed AI-SHES. This environment uses different

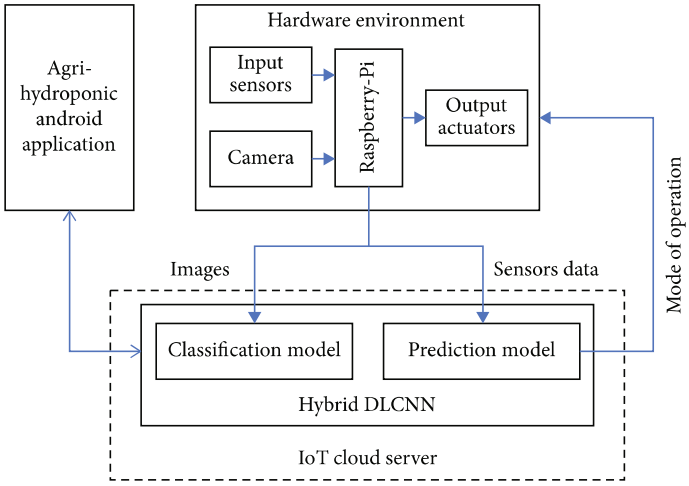

Figure 2: Proposed architecture of AI-SHES with IoT.

sensor for analysis of different parameters in the hydroponics farming methods. The proposed AI-SHES controls the parameters such as temperature, water level, water with nutrient considered fresh water, excessive sunlight, drain water, and cooler for temperature reduction.

Further, sensor values are continuously updated in IoT-based cloud environment. Here, the grove sunlight sensor is used for analysis of sunlight, which generates the parameters of light in the sun rays such as IR rays, UV rays, and visible rays. These sensor parameters can used to determine the amount of photosynthesis taking place inside the leaf of the plant. The SHT-20 sensor is used for parameters such as temperature and humidity of atmosphere. In hydroponics farming, it is important to measure the minerals present in water continuously, because the nutrients are supplied to the plant's trough the water only. Therefore, the hardware environment of hydroponic system requires the greater number of water sensors. The DS18B20 waterproof probe sensor is used to measure the water temperature. Further, SEN0161 water sensor also used for extracting the P_H levels such as acidic and basic nature of the water. Then, WQ730 turbidity sensor is used to extract the turbidity of water. Further, NPK sensor is used to measure the amount of nitrogen, phosphorus, and potassium levels present in water, which acts as an alternative to soil moisture sensor. In addition, hydrostatic pressure level sensor also used for measuring the different water levels. Additionally, camera modules capture the images of plants with the specified time scale.

Finally, the Raspberry Pi receives all sensor values and images and sends these data to the DLCNN model of cloud server. Here, the Prediction-DLCNN model is effectively used to identify the nutrient deficiency of plants, which predicts the standard nutrient levels through comparison with trained reference levels. The plants also suffer with the different types of diseases due to nutrient's deficiency, so it is necessary to identify the plant diseases in early stage. Therefore, the Classification-DLCNN model is used to identify the different types of plant diseases form the camera captured images. Finally, the DLCNN model sends this information to the Agri-Hydroponic application, where the farmer selects the mode of operation. Finally, the farmer controllers his hydroponics farm field during manual mode, so nutrients are supplied to plants as per farmer mentioned levels. In addition, the nutrients are applied to plants with standard reference levels during automated mode of operation. Further, the Raspberry Pi controllers control the output actuators (devices) based on the mode of operation generated by DLCNN environment. Therefore, the output devices such as motor and pump are controlled by this mode of operation directly from the mobile application. Here, two different pumps are used for pumping nutrient water and normal water, and they are supply water to plants till all the minerals and nutrients are observed. Further, heater output device is used to control water and air temperature inside the hydroponics structure. In addition, motors are used to regulate the sunlight intensity by controlling the outer environment of farm field.

3.2. AI-Based IoT Cloud Server. The AI-SHES system contains two DLCNN models named as Prediction-DLCNN and Classification-DLCNN, which are placed at the cloud server. Here, the Prediction-DLCNN model is used to estimate the perfect nutrient levels based on reference values. Further, the Classification-DLCNN model is used to identify the different types of plant diseases. In addition, the operation of both models was performed in a parallel manner and updates the values to the farmer through mobile application. Figure 4 presents the architecture of Prediction-DLCNN. Here, input feature matrix is generated by concatenating the sensor data. Initially, the sensor data is monitored in the hydroponics filed during different environment conditions. Then, the Raspberry Pi controller controls this data and transfers to IoT cloud. Then, the Prediction-DLCNN models take these sensor data as test input. The DLCNN model is trained with the reference nutrient dataset, where the dataset contains the perfect nutrient levels according to the different sensor conditions. The dataset is formed in different environmental conditions, so the Prediction-DLCNN model perfectly estimates the new nutrient values for every combination of sensor data in all atmospheric conditions.

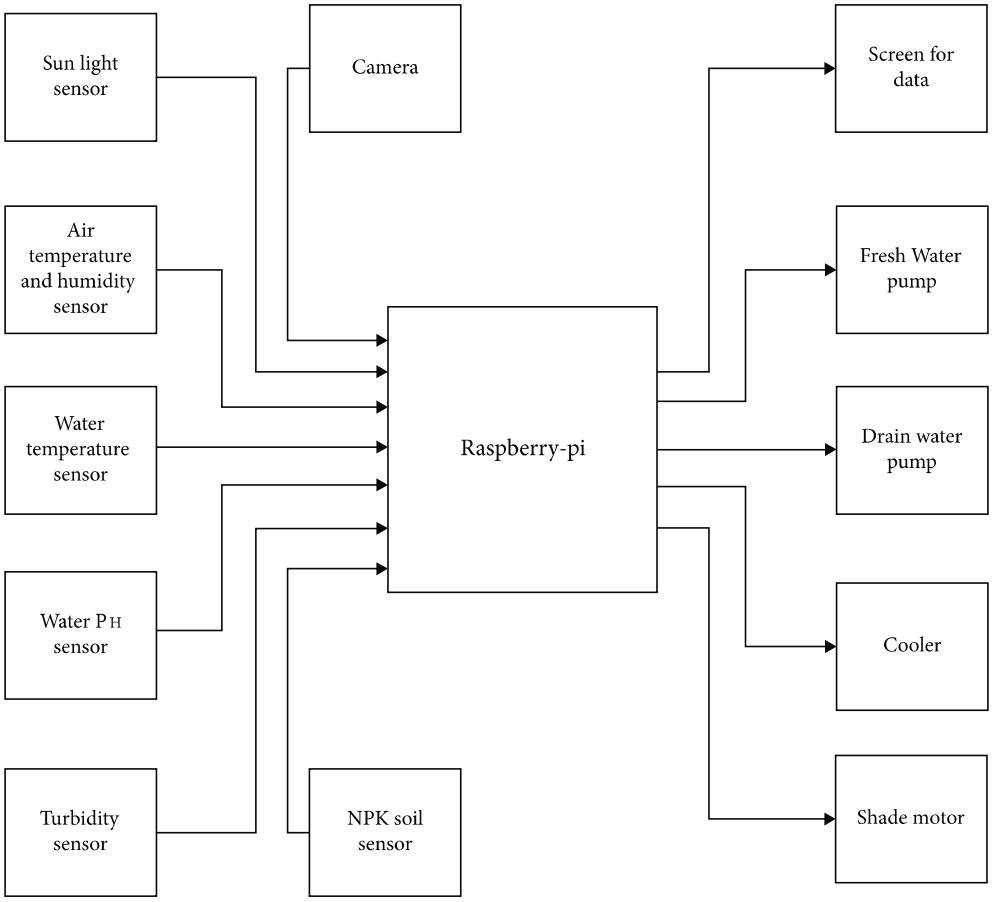

Figure 3: Hardware environment of AI-SHES system.

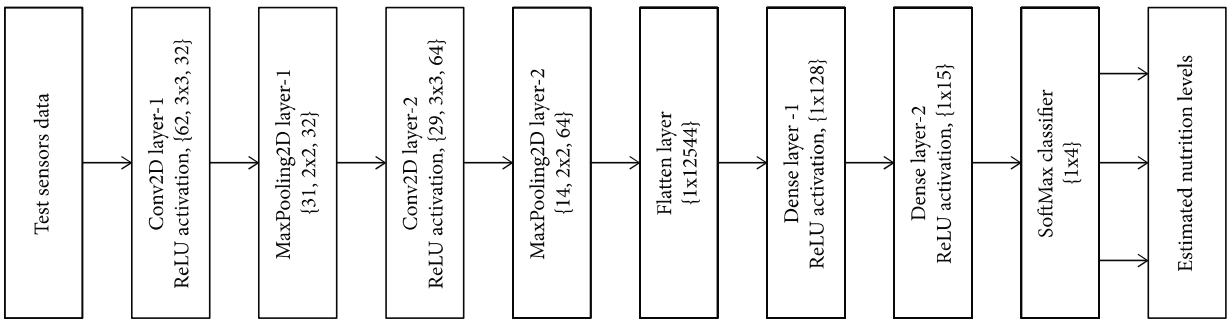

Figure 4: Architecture of Prediction-DLCNN model.

Figure 5 shows the architecture of Classification-DLCNN model, and Table 1 lists the description of layers employed in this architecture. The images captured in hydroponics filed are updated into IoT cloud through Raspberry Pi controller, and the same images are applied as input Classification-DLCNN model. The plants are suffering with different types of diseases due to nutrient deficiencies and disease attacks. Therefore, the proposed Classification-DLCNN model is capable of identifying the different types of diseases presented in plant images. Further, these disease classes and sensors' data monitored during test image captured time are applied as input to the Prediction-DLCNN model. Now, the Prediction-DLCNN model estimates the new nutrient values based on input data. Finally, these information transfer to the farmer through Agri-Hydroponic application.

3.3. Agri-Hydroponic Application. The farmers monitor the sensor data and plant images continuously through the Agri-Hydroponic application. Further, the farmers can control the different types of motors, actuators, and output devices placed in the hydroponic farm field using Agri-Hydroponic application as shown in Figure 6. In order to provide the security to the famers data, the application is

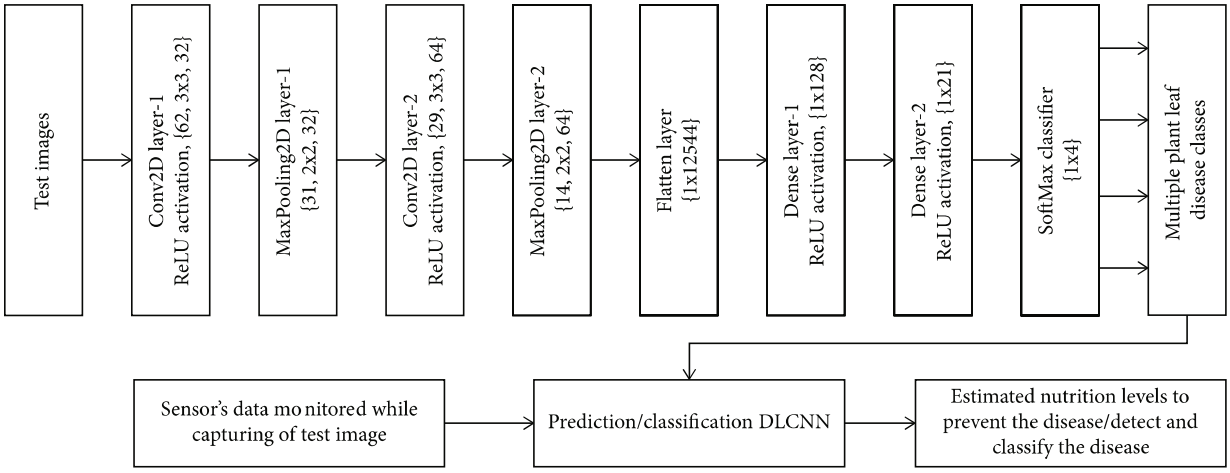

Figure 5: Proposed Classification-DLCNN model.

Table 1: Layer-wise analysis of Prediction-DLCNN and Classification-DLCNN models.

Layer name	No. of filters	Filter size	Feature size
Conv2D-1	32	3x3	62x62
MaxPooling2D-1	32	2x2	31x31
Conv2D-2	64	3x3	29x29
MaxPooling2D-2	64	2x2	14x14
Flatten	—	—	1x12544
Dense-1	—	—	1x128
Dense-2	—	—	1x15
SoftMax	—	—	1x4

developed with login page as shown in Figure 6(a). Therefore, intruders cannot control the field and cannot access the application. The RSA- and SHA-based hybrid security protocols are used in the application for maximum security. After successful login, the farmer can monitor and control the field using "plant disease prediction," "farm sensor data," and "farm controlling" buttons as shown in Figure 6(b). In the "farm sensor data" page, the different types of sensor data (water level, water turbidity, water pH UV light, visible light, IR light, air temperature, and water temperature, nitrogen, phosphorus, and potassium levels) are displayed as shown in Figure 6(c). The farmers can select the zone of hydroponics farm, which is divided into many sectors according to plantations. Therefore, the data is displayed based on average of all zones, whereas the farmer can also monitor individual zone-specific information. Further, the "farm controlling" operation is performed in two modes of operation such as automatic and manual modes as shown in Figure 6(d).

The farmers can control the devices presented in hydroponic filed during manual mode through Raspberry Pi controller as shown in Figure 6(e). Here, UV light, visible light, and IR light-based sunlight parameters are improper; then, the motors control the poly-cloth placed at the hydroponic farm. So the poly-cloth will regulate the light intensity by multiple layers. Further, air conditioner is manually controlled from the application based on air and water temperature levels. In addition, moisture inside the farm field also controlled based on humidity of the atmosphere. Moreover, the nutrient water supplied to plants also controlled by the drain water and freshwater motors based on nitrogen, phosphorus, and potassium mineral levels. All these input sensor data are monitored, and output devices are controlled automatically by Raspberry Pi controller during the automatic mode selection by the farmer in the application as shown in Figure 6(f). The farmers can also monitor the diseases presented in the plants during "plant disease classification page." The Classification-DLCNN model classifies the type of plant diseases and transfers to the "plant disease classification page" as shown in Figure 6(g). Here, the farmer can manually capture the images by his own, and Classification-DLCNN model identifies the disease. Finally, the selected action (mode) of farmers is sent to the Raspberry Pi controller to control output devices though IoT cloud server.

4. Results and Discussion

This section gives the experimental and simulation results of proposed AI-SHES with IoT system. In addition, it also provides the performance of proposed Prediction-DLCNN and Classification-DLCNN models compared to the state-of-the art approaches using standard nutrition and plant leaf datasets.

4.1. Dataset Description

4.1.1. NUOnet (Nutrient Use and Outcome Network). This dataset is collected by Agricultural Collaborative Research Outcomes System (AgCROS), which is a publicly available dataset. The most effective methods of nutrient management are very necessary for ensuring successful economic returns, preserving greater yields, minimizing negative effects on the environment, maximizing nutritional quality, and delivering

Figure 6: Continued.

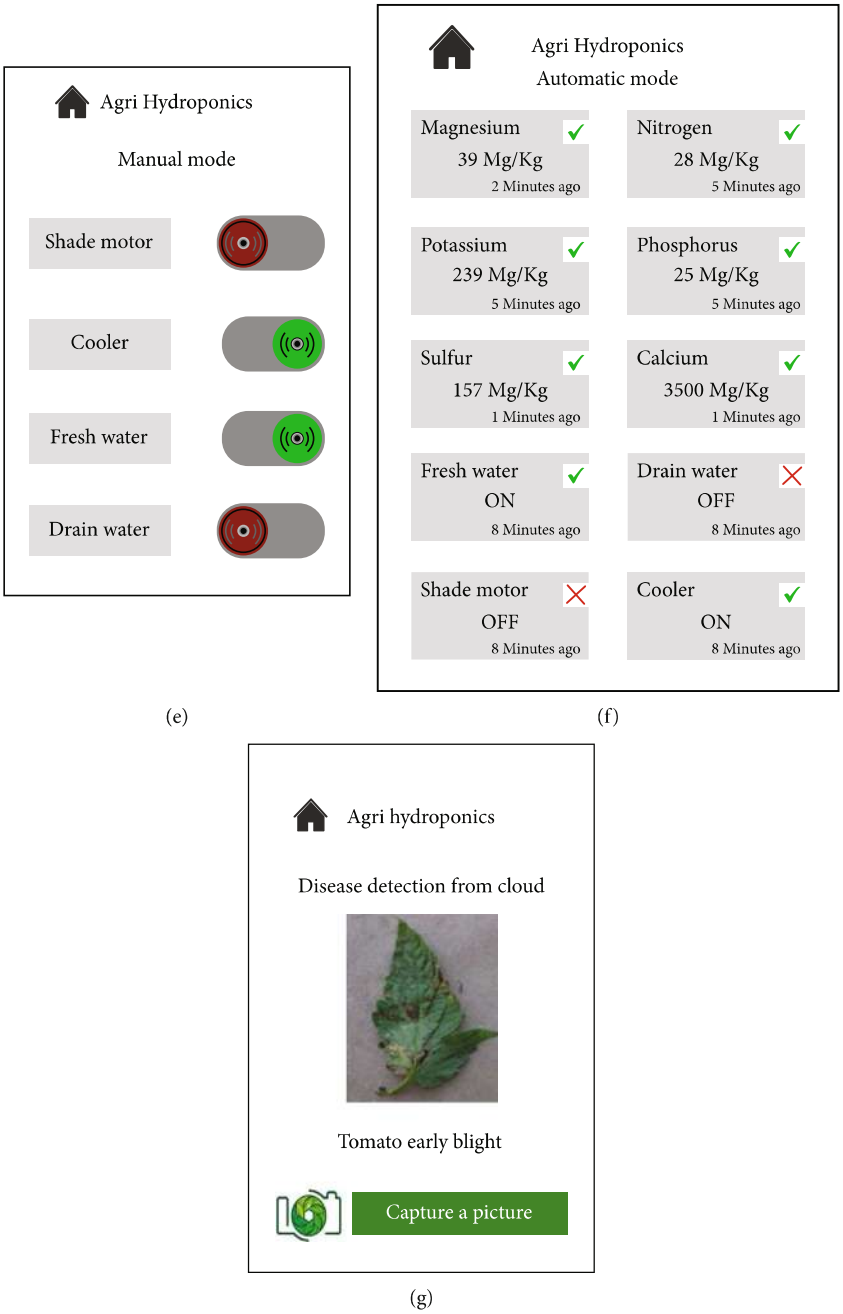

Figure 6: Agri-Hydroponic application options. (a) Login page. (b) User-access menu. (c) Sensor data. (d) Modes of operation. (e) Manual mode controlling. (f) Automatic mode controlling. (g) Plant disease classification page.

ecosystem services. Nutrient losses from agricultural systems may be reduced by using best management practices, which are techniques that increase the efficiency with which nutrients are used. This collection includes crop composition data derived from investigations that were carried out over the course of a number of years in sites all over the globe. The information that it carries offers some understanding of the inherent variation that exists in the nutritional profile of hydroponic crops.

4.1.2. PlantVillage Dataset. PlantVillage is a well-known and extensively used database that can be accessed without cost and is used for the training and testing of CNN models. Additionally, the database is frequently utilized. The PlantVillage collection has 20798 color leaf photos with a constant background. Additionally, the collection contains 19 crop-disease pairs. To accomplish the prediction and classification objective of this study, the given dataset is partitioned into train, test, and validation subsets using an 80-10-10 splitting ratio. As a result, there are a total of 16638 images in the training set (i.e., 80% of available dataset), 2130 images for training (i.e., 10% of total dataset), and another 10% for validation. Normalization was considered by dividing the pixel values by 255. This was done to make

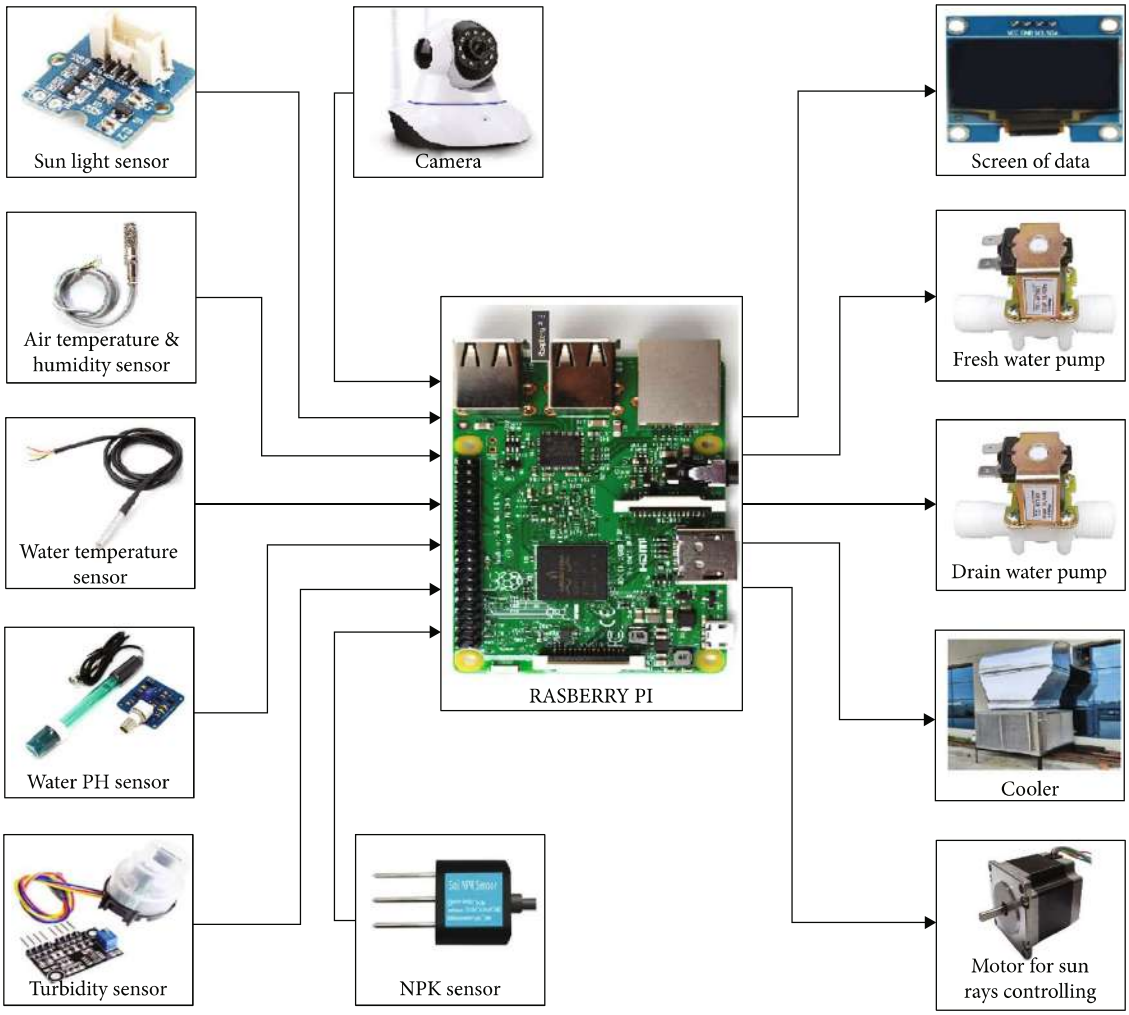

Figure 7: Hardware setup.

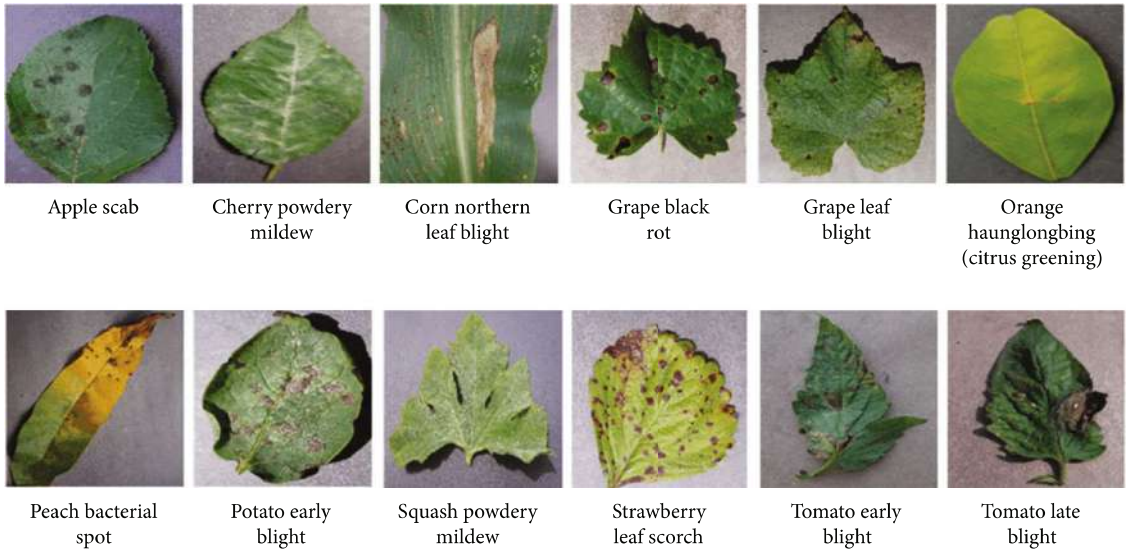

Figure 8: Classified plant diseases using DLCNN.

Table 2: Prediction-DLCNN response.

	Devices	Sample 1	Sample 2	Sample 3
Sensor data	Sunlight	HIGH	LOW	LOW
	Air temperature (°C)	38	30	28
	Water temperature (°C)	32	28	30`
	pH	6	8	7
	Turbidity (%)	80	30	40
	NPK	72	65	80
Predicted nutrients	Nitrogen (mg/kg)	25	26	31
	Phosphorus (mg/kg)	39	40	42
	Potassium (mg/kg)	41	50	36
	Magnesium (mg/kg)	157	142	138
	Sulphur (mg/kg)	3500	3150	3420
	Calcium (mg/kg)	ON	OFF	OFF
Output actuator action during automatic mode	Fresh water pump	OFF	ON	ON
	Drain water pump	ON	OFF	OFF
	Cooler	ON	ON	OFF
	Motor	HIGH	LOW	LOW

Table 3: Performance estimation of Prediction-DLCNN model.

Method	Accuracy (in %)	Precision (in %)	Recall (in %)	F-measure
EFIS [15]	90.898	92.514	90.355	91.673
SVM [16]	92.960	94.117	91.518	93.234
MicConvNet [18]	93.264	95.515	92.885	94.596
RCNN [23]	94.599	96.889	93.614	95.845
Prediction-DLCNN	99.82	98.64	99.937	99.283

Table 4: Performance estimation of Classification-DLCNN.

Method	Accuracy (in %)	Precision (in %)	Recall (in %)	F-measure
KNN [13]	89.28	88.384	88.24	83.484
ANN-GA [17]	90.898	92.514	90.355	91.673
HCNN [19]	92.960	94.117	91.518	93.234
ResNET51 [20]	93.264	95.515	92.885	94.596
Prediction-DLCNN	99.297	99.382	98.58	99.237

the images more acceptable for the beginning values of the models, which was accomplished by dividing the pixel values by 255. The images were resized to a size of $224 \times 224 \times 3$ pixels, and their dimensions were changed to reflect this. Rice brown spot, rice healthy, rice leaf blast, rice leaf blight, pepper bell healthy, and pepper bell bacterial spot are all included in this dataset. Tomatoes may be susceptible to a variety of pests and diseases, including the tomato healthy disease, the tomato mosaic disease, the tomato yellow leaf curl disease, and the tomato target spot disease.

4.2. Hardware Setup. Figure 7 shows the hardware setup of proposed AI-SHES with IoT, which is working model and integrated with Raspberry Pi controller with sensors, cloud server, and Agri-Hydroponic application. Here, the sensors placed in different zones of field are controlled by Raspberry Pi; then, these data are transferred to the laptop equipped cloud server. Magnesium and calcium are measured according to crop requirement, and we place magnesium and calcium probes in water/soil to measure these. For example, spinach has high volume of magnesium, hence we will provide magnesium raw materials in water. This will be similar with even calcium as well. For sulfur, we have sulfur gas sensor, and we can measure by boiling small amount of water and measure the contents of sulfur in water. Further, the farmers monitor and control the field using Agri-Hydroponic application through

electronic devices like mobile phones and tablets. It also shows the output devices like water motors controlling the supply of water in hydroponics field.

4.3. Results of AI-Based IoT Cloud Server. Figure 8 shows the classified plant diseases using DLCNN model. The proposed model accurately classified the apple scab, cherry powdery mildew, corn northern leaf blight, grape black rot, grape leaf blight, orange disease, peach bacterial spot, potato early blight, squash powdery mildew, strawberry leaf scorch, tomato early blight, and tomato late blight diseases.

Table 2 presents the Prediction-DLCNN response for three samples of sensor data. Here, sample-1 data is considered during rainy season, sample-2 data is considered during winter season, and sample-3 data is considered during summer season. The Prediction-DLCNN analyzed these sensor data and resulted in the perfect predicted nutrients. Further, Table 2 also presents the output action of actuators during automatic mode of operation.

Table 3 shows that the proposed Prediction-DLCNN model accurately estimated the nutrient values as compared to state-of-art approaches like EFIS [15], SVM [16], MicConvNet [18], and RCNN [23]. These conventional methods considered the reference data during perfect atmospheric conditions, so they failed to result in the best prediction for all environmental situations. In addition, these conventional methods considered a smaller number of input sensors as compared to proposed system, which is also impacted the nutrition prediction performance.

Table 4 shows the disease detection and classification performance of proposed Classification-DLCNN. Here, the proposed method resulted in superior performance as compared to conventional methods like KNN [13], ANN-GA [17], HCNN [19], and ResNET51 [20] for all performance metrics.

5. Conclusion

This article presented the design and implementations of AI-SHES with IoT, which is developed by integrating the Raspberry Pi, IoT environment with mobile application. The farmer observes and manages his hydroponics farm field using the Agri-Hydroponic program, which has manual and automated control modes. A Raspberry Pi controller-based hardware design is installed in a hydroponics farm field to monitor plant statics using various sensors. Furthermore, the data from these sensors is transferred to a cloud-based IoT system. An AI system is deployed in the cloud serviced by DLCNN, which continually analyzes sensor data, plants disease condition, and gives alerts to farmers via the Agri-Hydroponic application. Finally, the farmer operates his hydroponics farm field in manual mode, ensuring that nutrients are provided to plants at the amounts specified by the farmer. Furthermore, nutrients are applied to plants at specified reference levels during automated mode of operation. This system can be extended with hybrid deep learning architectures and optimization methods.

Data Availability

The data used to support the findings of this study are included within the article.

Disclosure

It was performed as a part of the Employment of Salale University, Ethiopia.

Conflicts of Interest

Authors declared that there is no conflict of interest in publication.

References

[1] W. Tao, L. Zhao, G. Wang, and R. Liang, "Review of the internet of things communication technologies in smart agriculture and challenges," *Computers and Electronics in Agriculture*, vol. 189, article 106352, 2021.

[2] S. Qazi, B. A. Khawaja, and Q. U. Farooq, "IoT-equipped and AI-enabled next generation smart agriculture: a critical review, current challenges and future trends," *IEEE Access*, vol. 10, pp. 21219–21235, 2022.

[3] D. Das, J. Sahoo, M. B. Raza, M. Barman, and R. Das, "Ongoing soil potassium depletion under intensive cropping in India and probable mitigation strategies. A review," *Agronomy for Sustainable Development*, vol. 42, no. 1, pp. 1–26, 2022.

[4] M. O. H. D. B. K. Putra and N. Nopriadi, "IOT based SMART agriculture using fuzzy logic," *Computer and Science Industrial Engineering (COMASIE)*, vol. 6, no. 2, pp. 52–61, 2022.

[5] K. Lova Raju and V. Vijayaraghavan, "A self-powered, real-time, NRF24L01 IoT-based cloud-enabled service for smart agriculture decision-making system," *Wireless Personal Communications*, pp. 1–30, 2022.

[6] E. S. Mohameda, A. A. Belal, S. K. Abd-Elmabod, M. A. El-Shirbeny, A. Gad, and M. B. Zahrana, "Smart farming for improving agricultural management," *The Egyptian Journal of Remote Sensing and Space Science*, vol. 24, no. 3, pp. 971–981, 2021.

[7] E. Nigussie, T. Olwal, G. Musumba, T. Tegegne, A. Lemma, and F. Mekuria, "IoT-based irrigation management for smallholder farmers in rural sub-Saharan Africa," *Procedia Computer Science.*.

[8] A. Sharma, M. Georgi, M. Tregubenko, A. Tselykh, and A. Tselykh, "Enabling smart agriculture by implementing artificial intelligence and embedded sensing," *Computers & Industrial Engineering*, vol. 165, article 107936, 2022.

[9] M. E. Karar, A. H. Abdel-Aty, F. Algarni, M. F. Hassan, M. A. Abdou, and O. Reyad, "Smart IoT-based system for detecting RPW larvae in date palms using mixed depthwise convolutional networks," *Alexandria Engineering Journal*, vol. 61, no. 7, pp. 5309–5319, 2022.

[10] H. Pang, Z. Zheng, T. Zhen, and A. Sharma, "Smart Farming," *International Journal of Agricultural and Environmental Information Systems (IJAEIS)*, vol. 12, no. 1, pp. 55–67, 2021.

[11] A. Khan, U. Nawaz, A. Ulhaq, and R. W. Robinson, "Real-time plant health assessment via implementing cloud-based scalable transfer learning on AWS DeepLens," *PLoS One*, vol. 15, no. 12, p. e0243243.

[12] F. Sabrina, S. Sohail, F. Farid, S. Jahan, F. Ahamed, and S. Gordon, "An interpretable artificial intelligence based smart agriculture system," *Computers, Materials & Continua*, vol. 72, no. 2, pp. 3777–3797, 2022.

[13] D. Adidrana, A. R. Iskandar, A. Nurhayati et al., "Simultaneous hydroponic nutrient control automation system based on Internet of Things," *JOIV: International Journal on Informatics Visualization*, vol. 6, no. 1, pp. 124–129, 2022.

[14] V. Bhatnagar and R. C. Poonia, ""sustainable development in agriculture: past and present scenario of Indian agriculture." research anthology on strategies for achieving agricultural sustainability," *IGI Global*, pp. 1342–1364, 2022.

[15] N. G. Rezk, E. E.-D. Hemdan, A.-F. Attia, A. El-Sayed, and M. A. El-Rashidy, "An efficient IoT based smart farming system using machine learning algorithms," *Multimedia Tools and Applications*, vol. 80, no. 1, pp. 773–797, 2021.

[16] P. Wang, B. A. Hafshejani, and D. Wang, "An improved multilayer perceptron approach for detecting sugarcane yield production in IoT based smart agriculture," *Microprocessors and Microsystems*, vol. 82, article 103822, 2021.

[17] Z. Khan, M. Zahid Khan, S. Ali et al., "Internet of things-based smart farming monitoring system for bolting reduction in onion farms," *Scientific Programming*, vol. 2021, 15 pages, 2021.

[18] E. T. Bouali, M. R. Abid, E. M. Boufounas, T. A. Hamed, and D. Benhaddou, "Renewable energy integration into cloud & IoT-based smart agriculture," *IEEE Access*, vol. 10, pp. 1175–1191, 2022.

[19] J. Arshad, M. Aziz, A. A. Al-Huqail et al., "Implementation of a LoRaWAN based smart agriculture decision support system for optimum crop yield," *Sustainability*, vol. 14, no. 2, p. 827, 2022.

[20] M. Cicioğlu and A. Çalhan, "Smart agriculture with internet of things in cornfields," *Computers and Electrical Engineering*, vol. 90, article 106982, 2021.

[21] D. Manikandan, S. Prabhu, P. Chakraborty, T. Manthra, and M. Kumaravel, "IoT-Based Smart Irrigation and Monitoring System in Smart Agriculture," in *Futuristic Communication and Network Technologies*, pp. 45–56, Springer, Singapore, 2022.

[22] H. N. Saha, R. Roy, M. Chakraborty, and C. Sarkar, "Development of IoT-based smart security and monitoring devices for agriculture," *Agricultural informatics: automation using the IoT and machine learning*, pp. 147–169, 2021.

[23] P. S. Chatterjee, N. K. Ray, and S. P. Mohanty, "LiveCare: an IoT-based healthcare framework for livestock in smart agriculture," *IEEE Transactions on Consumer Electronics*, vol. 67, no. 4, pp. 257–265, 2021.

[24] S. Biswas, L. K. Sharma, R. Ranjan, S. Saha, A. Chakraborty, and J. S. Banerjee, "Smart farming and water saving-based intelligent irrigation system implementation using the internet of things," in *Recent Trends in Computational Intelligence Enabled Research*, pp. 339–354, Academic Press, 2021.

[25] I. L. Maldonado, J. M. M. Reyes, H. F. Breceda, H. R. Fuentes, J. A. V. Contreras, and U. L. Maldonado, "Automation and Robotics Used in Hydroponic System," in *Urban Horticulture - Necessity of the Future*, Open, London, United Kingdom, 2019.

sustainability

MDPI

Article

Impact of a Thermal Barrier Coating in Low Heat Rejection Environment Area of a Diesel Engine

Megavath Vijay Kumar [1,*], Thumu Srinivas Reddy [2], Ch. Rami Reddy [3,*], S. Venkata Rami Reddy [4], Mohammad Alsharef [5], Yasser Alharbi [5] and Basem Alamri [5]

[1] Department of Mechanical Engineering, Malla Reddy Engineering College, Secunderabad 500100, India
[2] Department of Electronics and Communication Engineering, Malla Reddy Engineering College, Secunderabad 500100, India
[3] Department of Electrical and Electronics Engineering, Malla Reddy Engineering College, Secunderabad 500100, India
[4] Department of Electrical and Electronics Engineering, JNTUA College of Engineering, Pulivendula 516390, India
[5] Department of Electrical Engineering, College of Engineering, Taif University, P.O. Box 11099, Taif 21944, Saudi Arabia
* Correspondence: vijaykumar.084@mrec.ac.in (M.V.K.); crreddy229@mrec.ac.in (C.R.R.)

Abstract: The most recent developments in Thermal Barrier Coating (TBC) relate to engine performance, manufacturing and other related challenges. TBC on the piston crown and valves to enhance engine characteristics while using diesel and Mahua Methyl Ester (MME) as a petroleum fuel has a great sustainable development. For this utility, a Direct Injection (DI) conventional diesel engine was renewed to an LHR engine by applying 0.5 mm thickness of $3Al_2O_3$-$2SiO_2$ (as TBC) onto the piston crown and valves. The MME is used in the LHR (Low Heat Rejection) engine. For examination, the fuel injector pressure is set at 200 bar. Compared to a standard DI diesel engine, the results demonstrate that the application of TBC boosts brake thermal efficiency to 13.65% at 25% load. The LHR engine's SFC and BTE significantly improved at full load while using MME fuel. The lower temperature of exhaust gases is achieved by combining MME and diesel fuels with TBC. It was observed that both MME with and without TBC significantly reduced the smoke density. In addition, it was exposed that using MME fuel with TBC very slightly reduced carbon monoxide emissions under all loads. It was also shown that MME with TBC significantly reduced environmental hydrocarbon emissions at all loads.

Keywords: mahua methyl ester biodiesel; diesel fuel; thermal barrier coating; low heat rejection engine; environment; renewable energy

Citation: Vijay Kumar, M.; Srinivas Reddy, T.; Rami Reddy, C.; Rami Reddy, S.V.; Alsharef, M.; Alharbi, Y.; Alamri, B. Impact of a Thermal Barrier Coating in Low Heat Rejection Environment Area of a Diesel Engine. *Sustainability* **2022**, *14*, 15801. https://doi.org/10.3390/su142315801

Academic Editor: Jacopo Bacenetti

Received: 13 October 2022
Accepted: 23 November 2022
Published: 28 November 2022

1. Introduction

In India, the production of inedible oil is poor, leading to some development work undertaken by the Government of India for the production of alternative fuel to inedible oils, such as Jatropha, Mahua, Karanja, Linseed, Cotton, Mustard, Neem, etc. In India, most of the states are tribal regions where Mahua seeds are found in abundance [1,2]. The Mahua tree can provide sources from the seventh year of the plantation onward. Mahua seed oil is a common ingredient of Indian hydrogenated fat. The Mahua raw oil is extracted from the seed kernels and its oil appears similarly to semi-solid fat at room temperature, pale yellow due to the high viscosity in oil. Mahua crude oil contains 30 to 40% free acids. During biodiesel production, the manufacturer can produce various products from glycerin [3,4]. Generally, the raw Mahua Oil (MO) has a high percentage of Free Fatty Acids (FFA) and the change in FFA to biodiesel is very much essential in employing the transesterification or esterification process [5,6]. It is also observed that MO's properties and chemical composition are approximately similar to other inedible oil such as Cotton, Neem, Karanja, etc.,

but the Mahua has a high content of viscosity and FFA. Some renowned processes such as transesterification, esterification, dilution, microemulsion and pyrolysis are utilized to reduce the viscosity in order to produce biodiesel. However, transesterification is one of the best processes for obtaining maximum yield with some effective properties compared to diesel properties [7,8]. The impact of n-butanol/diesel blended fuels on the performance and emissions of heavy-duty diesel engines was investigated. The results showed that the engine performed better when 10% n-butanol was combined with diesel [9]. The effect of n-butanol/diesel fuel on engine performance and emission parameters was investigated and the results revealed that n-butanol at 2% and 4% in the blended fuel reduced emission levels [10]. The impact of n-butanol blended fuels on Euro VI diesel engines was investigated. The findings revealed that diesel/n-butanol mixed fuels increased CO and HC emissions while having no influence on NOx emissions [11]. The combustion and exhaust characteristics of an n-butanol/diesel fuel blend were investigated. The results revealed that the 20% n-butanol/diesel blend reduced soot, NOx, and CO emissions by 56.52%, 17.19%, and 30.43%, respectively, when compared to diesel [12]. The combustion and exhaust characteristics of a blended n-butanol/diesel fuel engine were investigated. The results revealed that n-butanol reduced CO and soot emissions while increasing NOx emissions in n-butanol/diesel fuel [13]. Particulate matter emissions from vehicles can be produced directly throughout fuel combustion or through condensation in the air and nucleation during the dilution and cooling of hot tailpipe exhaust [14]. The majority of particles produced by engine combustion are graphitic carbon, with minor amounts of metallic ash, sulfur compounds, and hydrocarbons [15]. Particle number size distributions (PNSDs) and PM emissions from vehicles are influenced by several factors, including engine type such as SI or CI Engines, type of fuel and engine specifications, vehicle operating conditions, particulate filter technology, and atmospheric conditions (temperature, wind speed, and humidity) [16,17]. One of the physical methods for using vegetable oil in a diesel engine that does not require any chemical treatment is microemulsion [18]. Microemulsions are made by combining esters and dispersants (solvents) with or without diesel fuel to form clear, thermodynamically stable oil-surfactant dispersion [19]. As a result of their higher alcohol content, microemulsions have a lower calorific value than diesel; however, these alcohols have a higher latent heat property and can cool the combustion chamber, reducing nozzle coking. The effects of microemulsification and transesterification on the performance of vegetable oil engines using methanol were examined. The effectiveness of methanol/vegetable oil microemulsions is based on employing methanol-based biodiesel as a surfactant. Previous research focused on the impact of co-surfactants and the effect of catalysts in water oil microemulsions produced from various refined and high-free fatty acid (FFA) oils [20,21]. A few thermos-chemical liquefication studies have focused on using waste sludge mixed with various co-surfactants to develop diesel fuel via microemulsion in enhancing its use and the physicochemical properties of the emulsified fuel. However, due to the high carbon waste and low efficiency, more research is required to enhance this technology for large-scale use [22,23]. As per the authors view, during the combustion of IC engines it was noticed that heat loss is one of the major problems and plays a vital role in all aspects of engine operation such as engine efficiency, fuel consumption, and emissions. Due to the loss of heat energy, the engine's performance and efficiency will be reduced. When the combustion gases take place inside the combustion chamber, the heat energy will be rejected to the atmosphere and pass through the other heat transfer modes. The gas temperature and pressure will be lost due to the engine output.

According to the Global Energy Statistical Yearbook 2020, India consumed 1230 TWh of energy in 2019. In comparison to 2018, global consumption increased by 0.7%. Global energy consumption is expected to skyrocket in the coming century. New industrial power generation equipment materials have resulted in more efficient and long-lasting engines to meet increasing energy demands [24]. Turbines generate energy over a long period. Gas turbines are widely used in energy generation and transportation. The material used in turbine engines has a longevity of over 50,000 h when operated at temperatures ranging

from 900 to 1100 °C. The materials will oxidize regardless of how good they are. Protective coatings are commonly used to keep the fabric from further oxidation and corrosion. Surface modification aims to improve or enhance surface properties that aid in corrosion and oxidation resistance. Coatings have become more resistant to deterioration under operational conditions in recent years [25].

Thermal barrier coatings act as heat barriers, preventing heat from spreading throughout the material. TBC plays an important role in safeguarding parts of gas turbines, internal combustion engines, and other high-temperature machines. TBC is a patterned framework that is layered over metallic segments, such as gas turbine blades. TBCs are distinguished by their low heat conductivity; the coating withstands extremely high temperatures when subjected to a heat stream [26,27]. The need for a higher working temperature in today's gas turbines is an ever-increasing process to improve their work productivity. As a result, the extended working temperatures exceed the melting point of nickel-based super alloys, which is deleterious to the chemical and heat-resistant properties of these composites. As a result, it is critical to protect these substrate materials from high operating temperature levels by providing heat protection via TBC's. Many years ago, ceramics were used before the LHR Engines. Cerium is also used in a thermal barrier coating with a high melting point that is spattered on the outside of alloy parts and has a thickness of 120–400 µm. Ceramic materials have a lower heat conduction coefficient and weight than the other materials used in conventional methods [28]. Nowadays, it is observed that ceramic materials have grown to achieve a better performance in diesel engines [29,30]. Lanthanum zirconate (LaZrO) is well-known in aircraft engines for its high melting point and good thermal stability. The thermal properties and failure mechanisms of these advanced TBCs remain difficult to understand [31]. Due to TBC's capacity to shield, which permits greater working temperatures and lowers the cost of cooling systems, this trend will undoubtedly continue, improving component efficiency overall [32]. The significant lengthening of YSZ TBC lifetime with the application of particular transient regimes with medium cooling/heating rates. This would enable the usage of YSZ at surface temperatures much higher than 1200 °C [33,34]. This paper examines the current state of TBCs, including the most recent developments in terms of their performance and manufacture, associated difficulties, and suggestions for their potential usage in severe settings such as diesel engines, aerospace, nuclear, high-temperature, or other.

Consequently, the loss of heat transfer energy in the engine decreases the overall performance. Many experimental studies have been conducted to gain a better understanding of the mechanisms that affect heat transfer within the combustion chamber. Each of these fundamental studies has contributed to understanding heat transfer in the IC engine, with the ultimate goal of improved engine performance and efficiency. Thus, many have demonstrated that the most essential factors affecting heat transfer include engine load, speed, compression ratio, ignition timing, fuel pressure variation, and equivalence ratio. By applying TBC onto the piston crown and valve, the direct injection (DI) conventional diesel engine is transformed into an LHR engine to reduce heat loss [24]. Enhancing the LHR engine with effective TBC promises lower fuel consumption, higher thermal efficiency, lowering emissions and elimination of the cooling system [25]. Several ceramic coatings such as Mullite, AL_2O_3, TiO_2, CaO/MgO–ZrO_2 and Yttria-stabilized Zirconia (YSZ), have been used in several engine applications [26,27].The key contributions of this paper are summarized as follows:

- The system was designed to improve the diesel engine with certain modified parameters such as Thermal Barrier Coating on the piston crown and valve surface based on a thorough literature review;
- The conventional diesel engine was aimed renewed to an LHR engine by applying 0.5 mm thickness of $3Al_2O_3$-$2SiO_2$ (as TBC) onto the piston crown and valves;
- In addition, an alternative fuel was used to reduce emissions with a low heat rejection system;

- Mahua oil was selected for investigation with TBC due to more O_2 content present in Mahua oil.

As per the literature survey, further criteria are discussed in choosing the TBC for diesel engines and the Mullite material characteristics are covered in Section 2. The transesterification procedure for creating Mahua Methyl Ester from its raw oil is described in Section 3. The comparison of the various fuel attributes is discussed in Section 4, along with an analysis. The experimental photography and the engine parameters are described in Section 5, alongside their specifications.

2. Low Heat Rejection Engine

Selection of TBC Material for IC Engines

To fulfill the requirement of a suitable TBC, we have to find an appropriate TBC with a good attachment of coating materials that can resist rigorous conditions in the diesel combustion chamber. The essential requirements for an excellent quality TBC are outlined below.

- Chemical inertness;
- Good adherence capability with a metallic substrate;
- Higher melting point of a material;
- Lower thermal conductivity of a material;
- At room temperature, no phase changes take place;
- Same thermal expansion coefficient with the metallic substrate [35,36].

Even though numerous ceramic materials are used as TBC in diesel engines, the physical properties of Mullite, such as thermal conductivity, high corrosion resistance, high hardness, good thermal shock resistance below 1273 K, etc., are promising. There are some physical properties of Mullite as TBC as shown in the below Table 1. From the below table, we can expect that a quality outside layering material is quite suitable for an internal combustion engine's purpose.

Table 1. Properties of Mullite.

Name	Properties				
Mullite ($3Al_2O_3$-$2SiO_2$)	Melting Point	Poisson's Ratio	Thermal Conductivity (λ)	Young's Modulus (E)	Thermal Expansion Coefficient (α)
	2123 K	0.25	3.3 W/mk (1400 K)	127 GPa (293 K)	5.3×10^{-6} (293–1273 K)

The conventional engine was converted into an LHR engine with a Mullite coating in order to improve the engine. For this purpose, one bore diesel engine is transformed into LHR engine by applying the Mullite of 0.5 mm thickness onto the valves and piston crown as shown in Figure 1.Later, experimental work was carried out with standard diesel and biodiesel with and without TBC to analyze the performance and emission characteristics.

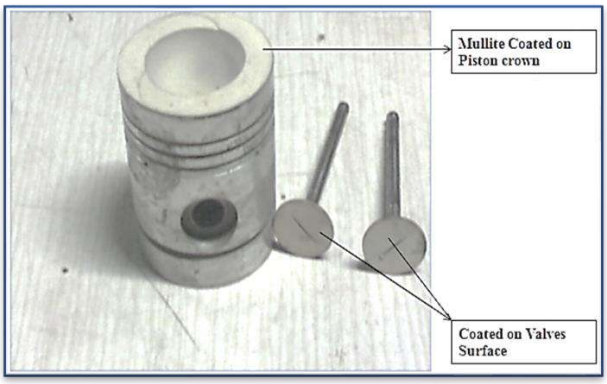

Figure 1. Mullite coated to Piston crown and valves surface.

3. Transesterification Process

In this section, the transesterification process is presented. Initially, the Mahua oil is preheated at 65 °C to 70 °C for 30 min to remove the moisture content. After the preheating process, 1000 mL of Mahua oil is taken with 14 g of potassium hydroxide and 300 mL of methanol. The potassium hydroxide and methanol are added to 1000 mL of Mahua oil, then it is heated at 55 °C and simultaneously the solution has to be stirred for 60 min. During the process, the chemicals react with the Mahua oil and produce the MME. After finishing the process, the mixture is allowed to settle down in a separating flask for 24 h. Once the reaction process is completed, the glycerin must be settled down and the methyl ester should be separated in a separate container. After the separation, the MME should be washed with distilled warm water. The distilled water is heated at 45 °C; then, the heated distilled water is mixed with MME and after mixing the solution, it must be shaken gently to remove residual catalyst or soap content. Then, the distilled water is removed. The MME is then heated at 100 °C for 30 min to remove the trace of water left over in it. Finally, the Mahua biodiesel was obtained as per the methodology of the reference article [37] as shown in Figure 2.

Figure 2. Final Product of Pure Mahua Biodiesel.

4. Fuel Properties

Various physical properties of diesel and MME fuels are mentioned in Table 2. Some of the physical properties, such as density, specific gravity, kinematic viscosity, calorific value, flash point, fire point, Cloud point, pour point and colour, were tested in the fuel laboratory of Malla Reddy Engineering College, India and the rest of the properties were cited [38]. The properties of the MME fuel are within the standard of ASTM D 6751 and EN 14214.

Table 2. Properties of the Fuels.

Properties	Diesel	MME	Test-Method	Instruments Used
Density(15 °C), kg/m^3	835	872	EN ISO 3675/EN ISO 12185	Hydrometer
Specific gravity	0.850	0.916	ASTM D792	Hydrometer
Kinematic viscosity at 40 °C, mm^2/s	2.4	4.0	EN ISO 3104/EN 14105	Redwood Viscometer
Calorific value (KJ/kg)	42,930	39,400	ASTM D240	Bomb Calorimeter
FlashPoint °C	70	127	EN ISO 2719/EN ISO 3679	Pensky-Martens
FirePoint °C	76	136	EN ISO 2719/EN ISO 3679	Pensky-Martens
Cloud point °C	−10 to −15	6	ASTM D2500	Cloud Point
Pour point °C	−35 to −15	1	ASTM D97	Pour Point
Colour	Light brown	Dark yellow	NM	Based on eye visibility
Cetane number	51	46	EN ISO 5165	[38]
Aniline point °C	69	63	EN 14111	[38]
Iodine value	NM	60	ASTM D1959-97	[38]
Diesel index	150	145	NM	[38]

Note: NM = Not measured.

5. Experimental Setup Description

5.1. Engine Test

A 3.5 kW single bore diesel engine (Table 3) with a fixed speed 1500 rpm water cooled is used for the investigation to progress the performance and to diminish the harmful emissions. The layout of the experimentation setup has been depicted in Figure 3. For loading the engine, the eddy current dynamometer has been used for investigation.

Table 3. Engine Specifications.

Name of the Specifications	Values
Name of Engine	Kirloskar
Stroke	4
Type of cooling	Water Cooled
Loading Type	Eddy Current Dynamometer
BHP	5
Stroke length	110 mm
Bore	80 mm
No. of Cylinder	1
Compression Ratio	16.5:1
Speed	1500 rpm
Fuel Injection Pressure	200 bar
Rated output	3.68 kw (5.0 hp)
Connecting Rod Length	230.0 mm
Exhaust Valve Open	20° BBDC [39]
Exhaust Valve Closes	20° ATDC [39]
Inlet Valve Open	20°BTDC [39]
Inlet Valve Close	25° ATDC [39]
Injection Advance	27° BTDC

The fuel has been injected into a cylinder with a pressure of 200 bar. The timing made for valve opening and closing is the exhaust valve opens at 20° BBDC, the exhaust valve closes at 20° ATDC, the inlet valve opens at 20° BTDC and the inlet valve closes at 25° ATDC. The fuel injection timing was maintained at 27° before Top Dead Center. Emission gas analyzers and smoke analyzers were used to find the content of HC, CO, NO_x, and smoke opacity.

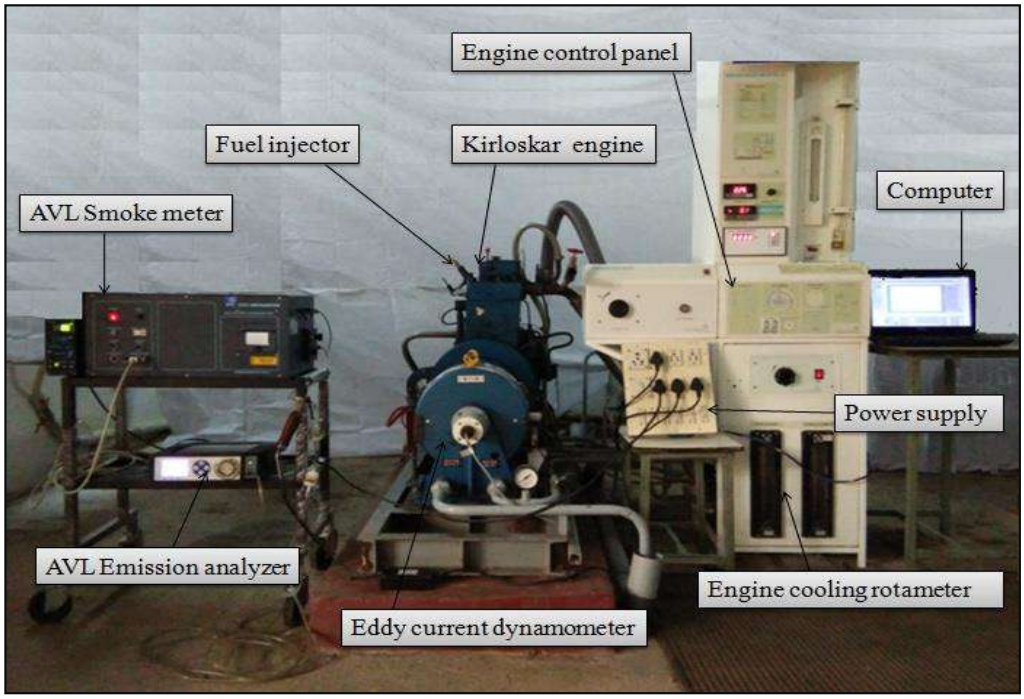

Figure 3. Photograph view of an experimental setup.

5.2. AVL 444 Gas Analyzer

This procedure must be performed on gas analyzers after they have been field-commissioned and for subsequent calibration. The accuracy and measuring ranges are presented in Tables 4 and 5.

Table 4. Gas Analyzer Measuring Range.

S. No.	Measured Parameter	Specification
1	Oxygen	0–22% vol.
2	Carbon monoxide	0–10% vol.
3	Carbon dioxide	0–20% vol.
4	Hydro carbon	0–20,000 ppm
5	Nitrogen oxide	0–5000 ppm
6	Engine speed	400–6000 rpm
7	Oil temperature	30–125 °C
8	Lambda	0 to 9.999

Table 5. Gas Analyser Accuracy.

S. No.	Measured Parameter	Specification
1	Oxygen	<2% vol.: ±0.1% vol. >2% vol.: ±1% vol.
2	Carbon monoxide	<0.6% vol.: ±0.03% vol. >0.6% vol.: ±5% vol.
3	Carbon dioxide	<10% vol.: ±0.5% vol. >10% vol.: ±5% vol.
4	Hydro carbon	<200 ppm: ±10 ppm >200 ppm ±5% of ind. value
5	Nitrogen oxide	<5000 ppm: ±50 ppm
6	Engine speed	±1% of ind. value
7	Oil temperature	±4 °C

The test procedure for gas analyzers is as follows:

- Ensure that the power supply meets the manufacturer's specifications and that the electrical earthing is correct;
- Ensure that all of the accessories specified by the manufacturer are present and functional;
- Validate the span and zero calibration with suitable CO and HC sample gases;
- Examine the electrical calibration;
- Ensure that the sampling system is leak-free;
- The printer is operational, and the printout details are correct;
- Using this analyzer, check one vehicle for idling emission measurement.

5.3. Specification of AVL Smoke Meter and its Operating Conditions

The specifications of AVL smoke meter are presented in Table 6. Operating conditions:

- Warm-up time:20 min (max.) at 220 V Supply;
- Operating temperature:0–50 °C;
- Relative humidity:90% at 50 °C relative humidity (non condensing).

Table 6. Specification of AVL smoke meter.

Type	Values/Model
Make and Model	AVL 437C Smoke meter
Sampling type	Partial flow
Light source	Halogen Lamp, 12 V/5 W
Range	0–100% opacity, 0–99.99 m^{-1} absorption
RPM	400–6000 in

5.4. Percentage Uncertainties of Calculated Parameters

The uncertenities of calculated parameters are shown in Table 7.

Table 7. Uncertainties for Calculated parameters.

Parameters	Percentage Uncertainties
Brake power	±0.5
Brake specific fuel consumption	±1.5
Brake thermal efficiency	±1.0

6. Results and Discussion

At different loadings, the LHR engine was investigated for different diesel and biodiesel with TBC and without TBC. The result was analyzed and is presented in the following sections.

6.1. Performance and Emission Parameters

6.1.1. Brake Specific Fuel Consumption

The variation of brake specific fuel consumption (BSFC) with a load at 200 bar pressure, which shows the results both with and without TBC for different fuels, is presented in Figure 4. Here, the fuel consumption of diesel is lower when compared to biodiesel. The BSFC without TBC of diesel at full load is 0.40 kg/kWh and for biodiesel is 0.44 kg/kWh. The comparison of TBC of diesel at full load is 0.37 kg/kWh and for biodiesel is 0.42 kg/kWh. At 25% load diesel with TBC, fuel consumption was found to be lower. The use of with and without TBC increases biodiesel fuel consumption because of its lower calorific value.

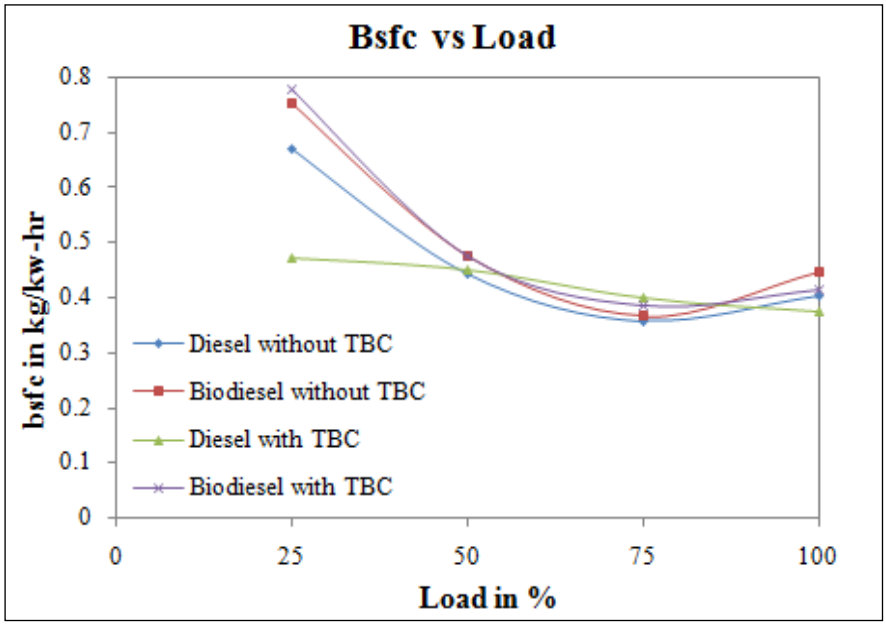

Figure 4. BSFC vs. Load.

6.1.2. Brake Thermal Efficiency

The Figure 5 shows the variation of brake thermal efficiency (BTE) with load at 200 bar pressure. The experiment was conducted with and without TBC for different fuels. At 25% load condition, diesel with TBC was found to be improved. At full load conditions, not much remarkable improvement was observed because higher viscosity leads to poor atomization, fuel vaporization and combustion. Hence, there was not much improvement in thermal efficiency.

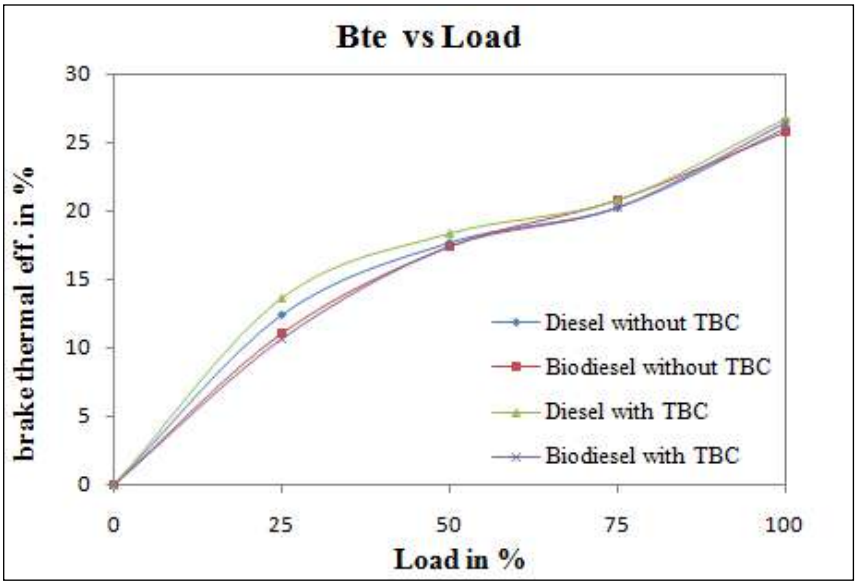

Figure 5. BTE vs. Load.

6.1.3. Exhaust Gas Temperature

Figure 6 shows the variation of exhaust gas temperature with a load at 200 bar injection pressure. The results showed that, in all cases, the exhaust gas temperature increased with the increase in load. For the diesel and biodiesel fueled without TBC, the biodiesel was the highest value of exhaust gas temperature of 265 °C, whereas the corresponding value with diesel was found to be 255 °C; for biodiesel with TBC, the highest value of exhaust gas temperature

was 427 °C, whereas the corresponding value with diesel was found to be 337 °C only. The exhaust temperature having a higher percentage of biodiesel was found to be higher at the entire load in comparison to diesel oil with TBC. The MME and diesel without TBC were found to lower exhaust gas temperature compared to others with TBC. This may be due to the higher combustion temperature of TBC, which gains more heat during the combustion process, and the presence of more oxygen in biodiesel, resulting in a higher peak combustion temperature; this, therefore, increases the exhaust gas temperature for biodiesel at full load.

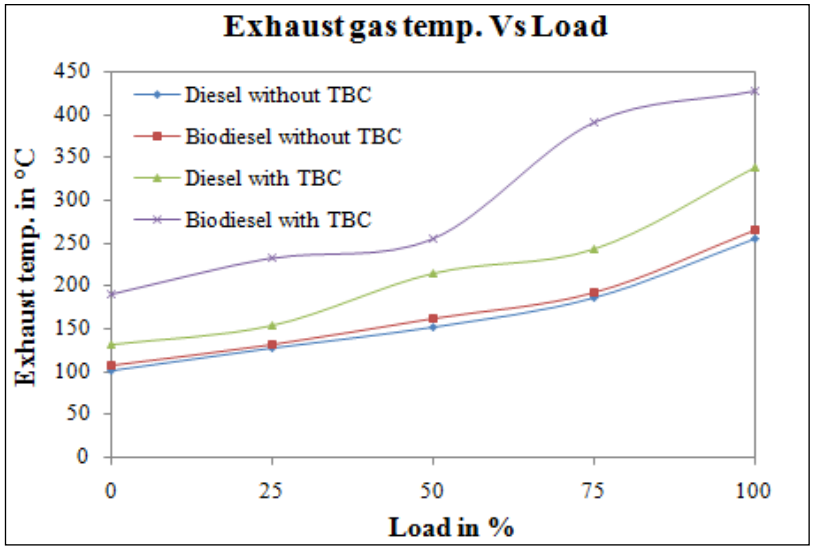

Figure 6. Exhaust Gas Temperature vs. Load.

6.1.4. Smoke Density

The variation of smoke density with load is shown in Figure 7. The smoke density of biodiesel with and without TBC was found significantly reduced compared to diesel with TBC and without TBC. This is because biodiesel has a better vaporization effect at higher combustion temperatures, and there is more oxygen in biodiesel. In comparison to all other trends, the particulate matter has been reduced for biodiesel with TBC because TBC has the ability to resist heat in the combustion chamber, which has aided in the burning of smoke particles.

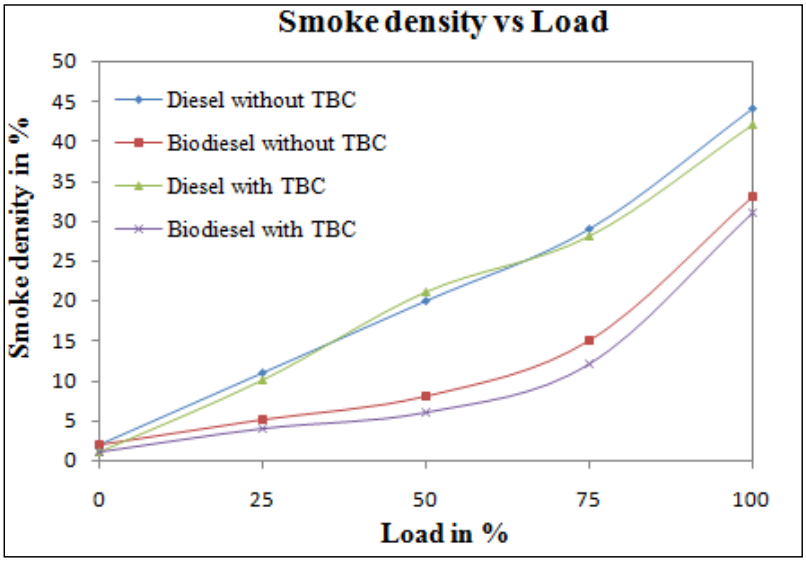

Figure 7. Smoke Density vs. Load.

6.1.5. CO Emissions

Figure 8 shows the variation of carbon monoxide emission with load at 200 bar injection pressure. The results were compared with and without TBC which was fueled with diesel and biodiesel. At 100% load condition, the results were found to increase the CO emissions compared to the different loads such as 0%, 25%, 50% and 75%. At 1% to 75% load, the CO emission was found to be lower because of improvements in combustion and because more oxygen molecules are contained in biodiesel [40]. At all load conditions, the flow rate of the air will be constant, but the fuel flow rate will vary as the load varies. So, as the fuel flow rate increases, the mixture keeps becoming rich. However, in the case of high load, with more amount of fuel and a lower amount of air present, and also as a result of the improper mixing, more carbon monoxide will be released.

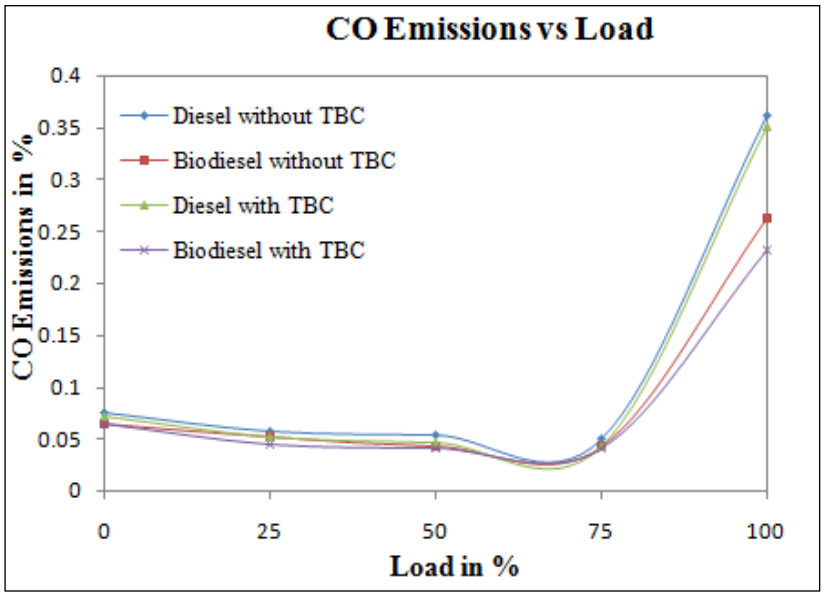

Figure 8. CO Emissions vs. Load.

6.1.6. HC Emissions

The comparisons of hydrocarbon emissions of diesel and biodiesel at 200 bar injection pressure with and without TBC are shown in Figure 9. Biodiesel was found to emit much fewer HC emissions compared to the baseline fuel. At maximum load without TBC, the HC emissions are 90 (PPM) for diesel and for biodiesel 47 (PPM). At 100% load without TBC, biodiesel emits much fewer CO emissions compared to diesel. At maximum load, there was a remarkable reduction in HC emissions: 63 (PPM) for diesel and 45 (PPM) for biodiesel with TBC. The use of thermal barrier coating inside the cylinder resists the high temperature at the surface of the cylinder due to the high temperature, the formation of hydrocarbon will reduce. Additionally, the use of biodiesel with TBC enhances in the reduction in HC due to the oxygen present in biodiesel. This may be owing to an increase in combustion gas temperature as a result of a decline in heat losses.

6.1.7. NOx Emissions

The variation of oxide of nitrogen (NOx) with load at 200 bar pressure, which is shown with and without TBC for diesel and biodiesel fuels, is presented in Figure 10. NOx is formed by oxidizing nitrogen in the atmosphere at a sufficiently high temperature, depending on the number of oxygen ions present. It was well noted that the biodiesel with and without TBC causes more NOx emissions because more O_2 levels are present in biodiesel which helps in better combustion and results in increasing the temperature. The diesel without TBC was found to lower NOx emissions.

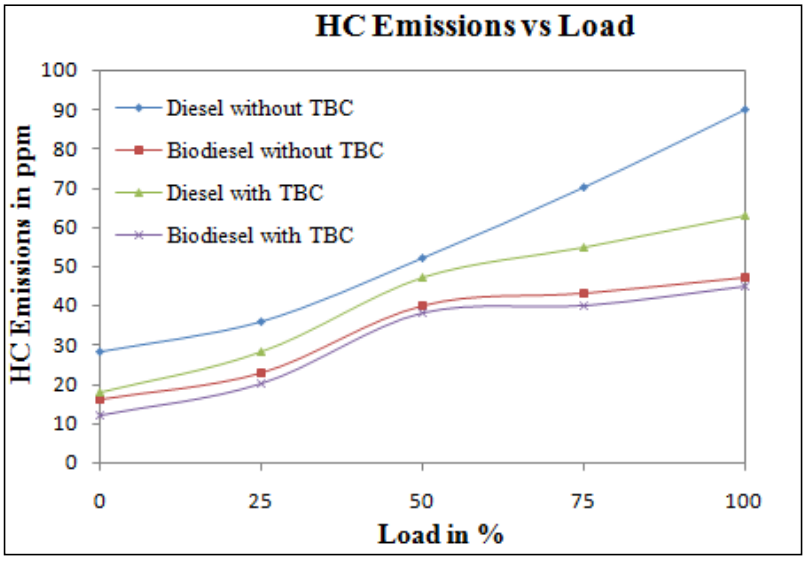

Figure 9. HC Emissions vs. Load.

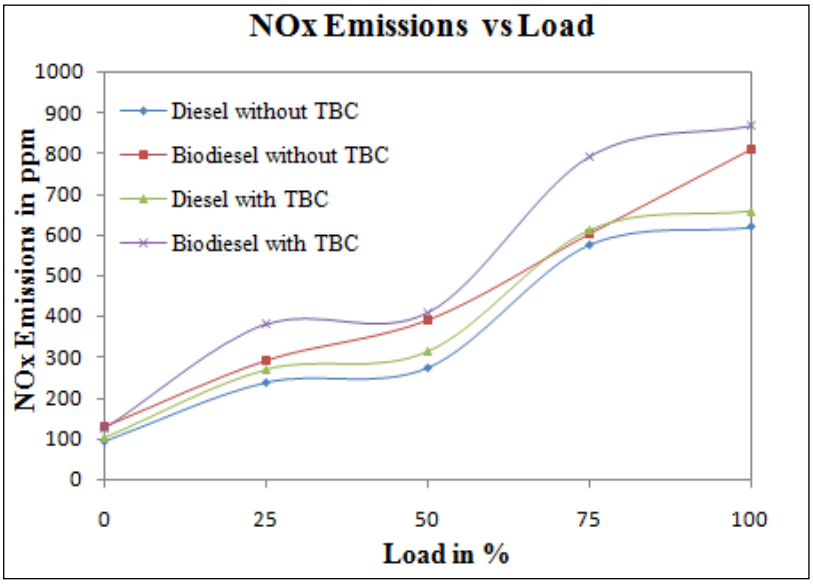

Figure 10. NOx vs. Load.

7. Conclusions

In the current work, to improve engine performance with Mahua biodiesel in CI engines, different technologies with and without TBC have been studied and compared with baseline fuel. Here, experiments were conducted with biodiesel and TBC technologies and have been studied extensively through performance and emissions. The experiments were demonstrated with constant fuel injector pressure of 200 bar and at a constant speed of 1500 rpm. Now that we have conducted the investigation and analysis of the LHR engine, we reveal the important conclusions below.

The Mahua methyl ester properties of density, fire point, flash point, and kinematic viscosity were observed to be within the limits of ASTM D 6751 and EN 14214 specifications. The property value is observed to be sealed and higher than the diesel. The calorific value (CV) of the alternative fuel is seen to be lower than diesel. This will cause an increase in ignition delay during the combustion process in LHR engine.

DI diesel engine was transformed to an LHR engine with the modification of 0.5 mm thickness of $3Al_2O_3$-$2SiO_2$ as TBC onto the piston crown and valves. Later, the engine characteristics were investigated and analyzed.

The fuel consumption of diesel is lower when compared to MME biodiesel. Due to the low calorific value, using and not using the TBC will increase the fuel consumption of biodiesel.

A significant increase in brake thermal efficiency at 25% load condition diesel with TBC was found to be improved due to the TBC.

Using TBC, good results for exhaust gas temperature with diesel and MME were obtained at all loads. The use of thermal barrier coating inside the cylinder resists the high temperature at the surface of the cylinder due to this more heat is attained during combustion by the TBC. A temperature of 427 °C was achieved by biodiesel with TBC high load and 337 °C by diesel with TBC at a high load. The smoke density of MME with and without TBC was found significantly reduced due to the greater amount of O_2 atoms present in the biodiesel and as well as the use of thermal barrier coating inside the cylinder resist the high temperature at the surface.

CO emissions were observed to decrease with the combination of biodiesel and TBC at all loads. This was due to the resistance of heat in a combustion chamber, as well as the biodiesel being given an extra dose of oxygen content in burning. At all loads, MME biodiesel with TBC was found a remarkable reduction in HC emissions. At maximum load, there was a remarkable reduction in HC emissions: 63 (PPM) for diesel and 45 (PPM) for biodiesel with TBC. This happened due to the O_2 molecules present in the MME oil.

It is observed that biodiesel with and without TBC causes more NOx emissions, and that biodiesel with TBC has increased to 870 ppm of NOx emission at high load conditions. High-temperature fuel combustion occurs when a fuel is burned at a temperature high enough (over 1300 °C or 2370 °F) to cause some of the nitrogen in the air to oxidize and produce NOx emissions. The diesel without TBC was found to lower NOx emissions.

As a result, MME biodiesel can be used as a substitute fuel for diesel engines, rather than modified and unmodified diesel fuel. For added benefit, the TBC can be used as a diesel engine substitute fuel.In future works, we can go to further enhance the engine with different alternative fuels and fuel additives. Moreover, to reduce the NOx, it can be investigated with the exhaust gas recirculation system.

Author Contributions: Conceptualization M.V.K., C.R.R.; methodology, S.V.R.R., M.V.K.; software, M.V.K., C.R.R.; validation M.A., Y.A. and B.A.; formal analysis, M.V.K.; investigation, M.V.K. and C.R.R.; resources, M.V.K.; data curation, C.R.R. and T.S.R.; writing—original draft preparation, M.V.K.; writing—review and editing, C.R.R., S.V.R.R., T.S.R., M.A., Y.A. and B.A.; visualization, B.A.; supervision, C.R.R. and T.S.R.; project administration, M.V.K.; funding acquisition, B.A. All authors have read and agreed to the published version of the manuscript.

Funding: The authors would like to acknowledge the financial support received from Taif University Researchers Supporting Project Number (TURSP-2020/278), Taif University, Taif, Saudi Arabia.

Institutional Review Board Statement: Not applicable.

Informed Consent Statement: Not applicable.

Data Availability Statement: Not applicable.

Conflicts of Interest: The authors declare no conflict of interest.

References

1. Nandi, S. Performance of CI engine by using biodiesel-mahua oil. *Am. J. Eng. Res.* **2013**, *2*, 22–47.
2. Padhi, S.K.; Singh, R.K. Optimization of esterification and transesterification of Mahua (Madhuca Indica) oil for production of biodiesel. *J. Chem. Pharm. Res.* **2010**, *2*, 599–608.
3. Agarwal, A.; Das, L.M. Biodiesel Development and Characterization for Use as a Fuel in Compression Ignition Engines. *J. Eng. Gas Turbines Power* **2001**, *123*, 440–447. [CrossRef]
4. Padhi, S.K.; Singh, R.K. Non-edible oils as the potential source for the production of biodiesel in India: A re-view. *J. Chem. Pharm. Res.* **2011**, *3*, 39–49.
5. Vijay Kumar, M.; Veeresh Babu, A.; Ravi Kumar, P. Producing biodiesel from crude Mahua oil by two steps of trans-esterification process. *Aust. J. Mech. Eng.* **2019**, *17*, 2–7. [CrossRef]
6. Azam, M.M.; Waris, A.; Nahar, N. Prospects and potential of fatty acid methyl esters of some non-traditional seed oils for use as biodiesel in India. *Biomass Bioenergy* **2005**, *29*, 293–302. [CrossRef]

7. Chauhan, P.S.; Chhibber, V.K. Non-edible oil as a source of bio-lubricant for industrial applications: A re-view. *Int. J. Eng. Sci. Innov. Technol.* **2013**, *2*, 299–305.
8. Sirurmath, S.; Vikram, P.M.; Das, G. Transesterification of Fish Oil and Performance Study on 4-Stroke CI Engine with Blends of Fish Biodiesel. *IJRET Int. J. Res. Eng. Technol.* **2014**, *3*, 608–612.
9. Tipanluisa, L.; Fonseca, N.; Casanova, J.; López, J.-M. Effect of n-butanol/diesel blends on performance and emissions of a heavy-duty diesel engine tested under the World Harmonised Steady-State cycle. *Fuel* **2021**, *302*, 121204. [CrossRef]
10. Şahin, Z.; Aksu, O.N. Experimental investigation of the effects of using low ratio n-butanol/diesel fuel blends on engine performance and exhaust emissions in a turbocharged DI diesel engine. *Renew. Energy* **2015**, *77*, 279–290. [CrossRef]
11. Lapuerta, M.; Hernández, J.J.; Rodríguez-Fernández, J.; Barba, J.; Ramos, A.; Fernández-Rodríguez, D. Emission benefits from the use of n-butanol blends in a Euro 6 diesel engine. *Int. J. Engine Res.* **2018**, *19*, 1099–1112. [CrossRef]
12. Nayyar, A.; Sharma, D.; Soni, S.L.; Mathur, A. Experimental investigation of performance and emissions of a VCR diesel engine fuelled with n-butanol diesel blends under varying engine parameters. *Environ. Sci. Pollut. Res.* **2017**, *24*, 20315–20329. [CrossRef] [PubMed]
13. Siwale, L.; Kristóf, L.; Adam, T.; Bereczky, A.; Mbarawa, M.; Penninger, A.; Kolesnikov, A. Combustion and emission characteristics of n-butanol/diesel fuel blend in a turbo-charged compres-sion ignition engine. *Fuel* **2013**, *107*, 409–418. [CrossRef]
14. Maricq, M.; Chase, R.; Podsiadlik, D.; Vogt, R. Vehicle exhaust particle size distributions: A comparison of tailpipe and dilution tunnel measure-ments. *SAE Trans.* **1999**, *108*, 721–732.
15. Shi, J.P.; Mark, D.; Harrison, R.M. Characterization of Particles from a Current Technology Heavy-Duty Diesel Engine. *Environ. Sci. Technol.* **2000**, *34*, 748–755. [CrossRef]
16. Myung, C.L.; Park, S. Exhaust nanoparticle emissions from internal combustion engines: A review. *Int. J. Automot. Technol.* **2011**, *13*, 9–22. [CrossRef]
17. Vu, T.V.; Delgado-Saborit, J.M.; Harrison, R.M. Review: Particle number size distributions from seven major sources and implications for source apportionment studies. *Atmos. Environ.* **2015**, *122*, 114–132. [CrossRef]
18. Fangrui, M.; Hanna, M.A. Biodiesel production: A review. *Bioresour. Technol.* **1999**, *70*, 1–15.
19. Yusuf, N.; Kamarudin, S.; Yaakub, Z. Overview on the current trends in biodiesel production. *Energy Convers. Manag.* **2011**, *52*, 2741–2751. [CrossRef]
20. Wellert, S.; Karg, M.; Imhof, H.; Steppin, A.; Altmann, H.J.; Dolle, M.; Richardt, A.; Tiersch, B.; Koetz, J.; Lapp, A.; et al. Structure of biodiesel based bicontinuous microemulsions for environmentally compatible decontamina-tion: A small angle neutron scattering and freeze fracture electron microscopy study. *J. Colloid Interface Sci.* **2008**, *325*, 250–258. [CrossRef]
21. de Jesus, A.; Silva, M.M.; Vale, M.G.R. The use of microemulsion for determination of sodium and potassium in biodiesel by flame atomic absorption spectrometry. *Talanta* **2008**, *74*, 1378–1384. [CrossRef] [PubMed]
22. Ding, X.; Yuan, X.; Leng, L.; Huang, H.; Wang, H.; Shao, J.; Jiang, L.; Chen, X.; Zeng, G. Upgrading Sewage Sludge Liquefaction Bio-Oil by Microemulsification: The Effect of Ethanol as Polar Phase on Solubilization Performance and Fuel Properties. *Energy Fuels* **2017**, *31*, 1574–1582. [CrossRef]
23. Leng, L.; Han, P.; Yuan, X.; Li, J.; Zhou, W. Biodiesel microemulsion upgrading and thermogravimetric study of bio-oil produced by liquefaction of different sludges. *Energy* **2018**, *153*, 1061–1072. [CrossRef]
24. Karaoglanli, A.C.; Dikici, H.; Kucuk, Y. Effects of heat treatment on adhesion strength of thermal barrier coating systems. *Eng. Fail. Anal.* **2013**, *32*, 16–22. [CrossRef]
25. Buyukkaya, E.; Cerit, M. Experimental study of NOx emissions and injection timing of a low heat rejection diesel engine. *Int. J. Therm. Sci.* **2008**, *47*, 1096–1106. [CrossRef]
26. Cao, X.Q.; Vassen, R.; Stoever, D. Ceramic materials for thermal barrier coatings. *J. Eur. Ceram. Soc.* **2004**, *24*, 1–10. [CrossRef]
27. MohamedMusthafa, M.; Sivapirakasam, S.; Udayakumar, M. Comparative studies on fly ash coated low heat rejection diesel engine on performance and emission characteristics fueled by rice bran and pongamia methyl ester and their blend with diesel. *Energy* **2011**, *36*, 2343–2351. [CrossRef]
28. Jia, L.; Wen, T.; Tian, C.; Liu, Z.; Yu, J.; Yuan, L. Preparation and thermophysical properties of RE2CrTaO7 (Y, Sm, Dy, Yb) ceramics for thermal barrier coating applications. *Ceram. Int.* **2022**, *48*, 23814–23820. [CrossRef]
29. Lima, C.; Guilemany, J. Adhesion improvements of Thermal Barrier Coatings with HVOF thermally sprayed bond coats. *Surf. Coatings Technol.* **2007**, *201*, 4694–4701. [CrossRef]
30. Gatowski, J.A. Evaluation of a selectively-cooled single-cylinder 0.5-l Diesel engine. *SAE Trans.* **1990**, *99*, 1580–1591.
31. Shen, Z.; Liu, G.; Dai, J.; He, L.; Mu, R. LaNdZrO thermal barrier coatings by electron beam physical vapor deposition: Morphology, thermal property and failure mechanism. *Chem. Eng. J. Adv.* **2022**, *11*, 100328. [CrossRef]
32. Mondal, K.; Nuñez, L., III; Downey, C.M.; van Rooyen, I.J. Recent advances in the thermal barrier coatings for extreme environments. *Mater. Sci. Energy Technol.* **2021**, *4*, 208–210. [CrossRef]
33. Vaßen, R.; Bakan, E.; Mack, D.E.; Guillon, O. A Perspective on Thermally Sprayed Thermal Barrier Coatings: Current Status and Trends. *J. Therm. Spray Technol.* **2022**, *31*, 685–698. [CrossRef]
34. Mondal, K.; Nuñez, L., III; Downey, C.M.; Van Rooyen, I.J. Thermal barrier coatings overview: Design, manufacturing, and applications in high-temperature industries. *Ind. Eng. Chem. Res.* **2021**, *60*, 6061–6077. [CrossRef]
35. Kamo, R.; Assanis, D.N.; Bryzik, W. Thin Thermal Barrier Coatings for Engines. *SAE Trans.* **1989**, *98*, 131–136. [CrossRef]
36. Abedin, M.J.; Masjuki, H.H.; Kalam, M.A.; Sanjid, A.; Ashraful, A.M. Combustion, performance, and emission characteristics of low heat rejection engine operating on various biodiesels and vegetable oils. *Energy Convers. Manag.* **2014**, *85*, 173–189. [CrossRef]

37. Kumar, M.V.; Veeresh Babu, A.; Ravi Kumar, P. Experimental investigation on mahua methyl ester blended with diesel fuel in a compression ignition diesel engine. *Int. J. Ambient. Energy* **2019**, *40*, 304–316. [CrossRef]
38. Vijay Kumar, M.; Babu, A.V.; Kumar, P.R.; Reddy, S.S. Experimental investigation of the combustion characteristics of Mahua oil biodiesel-diesel blend using a DI diesel engine modified with EGR and nozzle hole orifice diameter. *Biofuel Res. J.* **2018**, *5*, 863–871. [CrossRef]
39. Basaran, H.U.; Ozsoysal, O.A. Effects of application of variable valve timing on the exhaust gas tem-perature improvement in a low-loaded diesel engine. *Appl. Therm. Eng.* **2017**, *122*, 758–767. [CrossRef]
40. Hegab, A.; Dahuwa, K.; Islam, R.; Cairns, A.; Khurana, A.; Shrestha, S.; Francis, R. Plasma electrolytic oxidation thermal barrier coating for reduced heat losses in IC engines. *Appl. Therm. Eng.* **2021**, *196*, 117316. [CrossRef]

TELEMATIQUE Volume 21 Issue 1, 2022
ISSN: 1856-4194 4816– 4831

A New Framework for Simulating and Modeling Cloud Computing Infrastructures and Services is Cloudsim

Ms. Aenugu Rasagnya[1], Dr. R. Kavitha[2], Dr. Kunchala Little Flower[3], Mrs Veena Rani[4]

[1]Assistant Professor, Department of CSE, Malla Reddy Engineering College(A), Maisammaguda, Hyderabad, Telangana, India
[2]Associate Professor, Department of CSE, Siddhartha Institute of Engineering and Technology, Ibrahim Patnam, Hyderabad, Telangana, India
[3]Professor, Department of CSE-AIML, School of Engineering, Malla Reddy University, Hyderabad, Telangana, India
[4]Professor, Department of CSE-AIML, School of Engineering, Malla Reddy University, Hyderabad, Telangana, India

Email id: [1]nishithareddyaenugu.ajr@gmail.com, [2]kavitha161731@gmail.com, [3]littleflower@mallareddyuniversity.ac.in, [4]veena@mallareddyuniversity.ac.in

Received 16/08/2022; **Accepted** 08/09/2022

Abstract:
Among cloud computing's key aims is the provision of frameworks for the dependable, secure, fault-tolerant, practically applicable, and adaptable hosting of web-based application services via the Internet. Each of these applications has its own own design, style, and organisation needs. It is a challenging task to optimise the scheduling and distribution of resources on a Cloud infrastructure (equipment, software, services) for different application and service models with varying loads, energy use (power utilisation, heat dispersion), and overall framework size. In this article, we suggest CloudSim, a simulation tool that may help with this loop: a new summed up and extensiblereproduction system that empowers consistent displaying, reproduction, and trial and error of arising Cloudfiguring foundations and the executives administrations. The new features of the reenactment system are (I)help with showing and launching on a massive scale Architecture for decentralised computation, remembering server farms fora solitary actual figuring hub and java virtualmachine; (ii) an independent stage for displaying informationfocuses, administration representatives, booking, and portionsarrangements; (iii) In addition to (iii), switching from space-shared and time-shared portions of data centres to virtualized Services; and (iv) access to a virtualization motor that facilitates the creation and maintenance of many free and co-facilitated virtualized administrations on a server farm hub.

Keywords: Cloud computing, CloudSim, virtualized Services, Server

1. INTRODUCTION

Using a membership-based, pay-as-you-go pricing model, clients of distributed computing may access the framework, platform, and software (application) as services. Common abbreviations for these kinds of business services include "IaaS" (Infrastructure as a Service), "PaaS" (Platform as a Service), and "SaaS" (Software as a Service) (SaaS). This long-held concept of computing as a service, distributed computing, might potentially transform a huge piece of the IT sector, making programming much more desirable as an assist, as stated by

Professor Patterson et al. in a Berkeley Report [11] published in February 2009Quality of Service (QoS) enables customers to receive and submit applications on demand from anywhere in the globe at reasonable prices. Mists [10] plan to control the present data focuses by planning them as an organisation of virtual administrations (equipment, data base, UI, application rationale). If a designer comes up with a novel idea for an online service, they often won't have to invest a lot of money up front in infrastructure like servers and databases, or in labour costs like maintaining and updating the system [11]. It's a major boon to IT departments since it frees them up to focus less on mundane tasks like setting up servers and more on strategic initiatives like developing products and services that customers really want.

A portion of the customary and arising Cloud-based applications incorporate long range informal communication, web facilitating, content conveyance, and constant instrumented information handling. Every one of these application types has unique arrangement, design, and sending necessities. It is an interesting challenge to investigate how different application and administration models are affected by the presentation of a planning and allotment strategy on Cloud frameworks (equipment, programming, administrations) based on load, energy execution (power utilisation, heat dispersion), and framework size. Using real test environments like Amazon EC2 restricts experiments to the size of the testbed and makes reproducing findings very challenging since the analyzer has no control over the variables that affect performance under Internet-based settings. Using simulation tools that allow for the replication of test conditions before the development of the corresponding software is another viable alternative. Particularly in the context of Cloud processing, where access to the system results in real-money payments, recreation-based approaches offer substantial advantages, as they permit Cloud clients to test their services in a repeatable and controllable environment at no cost, and to tune the exhibition bottlenecks before delivering on genuine Clouds. For the service provider, the presence of recreational options allows for the calculation of allotted cash and the examination of a variety of asset rental scenarios under varied loads. Providers may profit from such probes if they are conducted with a focus on lowering the costs of gaining access to assets while expanding their benefits. Without such entertainment hubs, Cloud users and service providers are forced to rely on their own intuition, which may lead to poor decisions, or to fumble their way through ineffective help desk support and revenue generating. We offer CloudSim, a new unified and extendable reenactment structure that allows for standardised demonstration, recreation, and experimentation with future Distributed computing frameworks and application administrations. This is essential since no current distributed framework test systems [4][7][9] provide an environment that can be used directly by the Cloud processing neighbourhood. Without worrying about the nitty-gritty details of Cloud-based systems and services, analysts and industry-based engineers may utilise CloudSim to zero in on certain framework configuration variables of interest. CloudSim's unique features are its I ability to simulate and replicate a Cloud computing infrastructure of massive scale, down to the level of individual servers and data centres, and (ii) standalone platform for simulating such infrastructure components as server farms, administration representatives, planning, and designations arrangements. The distinctive features of CloudSim are I its ability to switch between spaceshared and timeshared distribution of handling centres to virtualized administrations, and (ii) the availability of a virtualization motor that facilitates the development and the administration of a range of free and co-facilitated virtualized administrations on a data centre node. These alluring aspects of CloudSim would hasten the creation of new Cloud figure calculations, techniques, and standards, which in turn would aid in the extension of our worldview more quickly.

Distributed computing is a "as-a-service" approach that provides infrastructure (IaaS), platforms (PaaS), and applications (SaaS) to customers on a "as-needed" basis. Through computational dispersion, server farms' features as business virtual services were unmasked, which may involve configuring hardware, software, and a database and user interface. Online application submission and receipt is now an option for customers, albeit its usefulness will rely on their specific requirements and the level of service provided. The notion of Cloud registration is still in its infancy, therefore researchers and framework engineers are hard at work refining it to improve transmission on handling, quality, and cost. However, most studies concentrate on bettering the presentation of provisioning arrangements, and it is difficult to put these studies to the test in a production cloud environment like Amazon EC2, Microsoft Azure, or Google App Engine, using different types of applications and real-world constraints. Mists display changing requests, supply designs, framework sizes, and assets (equipment, programming, and organization).

In terms of quality of service (QoS), customers have varying, ever-changing, and often conflicting needs. The requirements for executing, managing, and growing applications are always evolving. Since real public cloud frameworks like Google Cloud, Microsoft Azure, etc. are multi-tenant and need factor responsibility fulfilment, it is not fair to benchmark application performance on these platforms. Similarly, a client/scientist is unlikely to alter many settings at the administrator level. As a consequence, it becomes very challenging to spread reliable findings. As an added note, whether we do it or not, redesigning benchmarking boundaries over a broad scope Cloud processing framework throughout several trials is a tedious and time-consuming effort. Accordingly, it is incomprehensible on genuine public Cloud frameworks to attempt benchmarking ordered trials as repeatable, trustworthy, and adaptable conditions. As a consequence, the possibility of using replication tool(s) to assess/benchmark test tasks in a controlled and completely programmed environment that can replicate outcomes for analysis across multiple focus levels develops. Benefits may vary depending on the researcher's location, since this reproduction-based strategy allows them to: Tests given in an environment where results may be reliably reproduced and manipulated. Before releasing actual clouds, it's important to tune the system's bottlenecks (execution difficulties). To create, test, and distribute flexible application provisioning techniques, it is necessary to simulate the necessary infrastructure (of any size). This article is meant to serve as a guide for beginners to cloudsim reproduction tool stash and to help them learn how its many components function.

HIGHLIGHTS OF CLOUDSIM SIMULATION TOOLKIT

It aids in modelling and visualising large-scale Cloud processing environments, such as server farms, on a single physical computer node (could be a work area, PC, or server machine). An independent stage for displaying Clouds, administration dealers, provisioning, and distribution strategies.Works with the reproduction of organization associations across the recreated framework components. An essential part of Cloudbursts and automated application scaling research is an office for recreating a unified Cloud environment that combines network resources from different locations. A virtualization engine that enables many autonomous and cooperatively-facilitated virtualized administrations to be developed and managed on a single server farm infrastructure. Facilitates a simple shift to virtual data centres from those located in different physical locations. This multitude of aspects would aid in speeding up the creation, testing, and organisation of potential asset/application provisioning approaches/calculations for Cloud Computing based frameworks. CloudSim Simulation Toolkit has a multi-tiered structure, as seen in the following diagram. Support for

demonstrating and recreating virtualized Cloud-based server farm conditions is provided by the CloudSim Core reenactment motor. This includes the scheduling and management of events, the creation of cloud framework elements (such as server farm, have, virtual machines, representatives, services, etc.), and the management of communication between components. Administrators of Virtual Machines, data storage, and data transfer may all make use of the specialised APIs provided by theCloudSim layer. For the most part, it takes care of the basics, such as providing hosts for Virtual Machines, keeping checks on how applications are doing, and tracking the health of a reliable infrastructure (including network topology, sensors, capacity characteristics, etc.). Users may reinvent the engaging setting in light of audit results by coding their own solutions in the User Code layer.

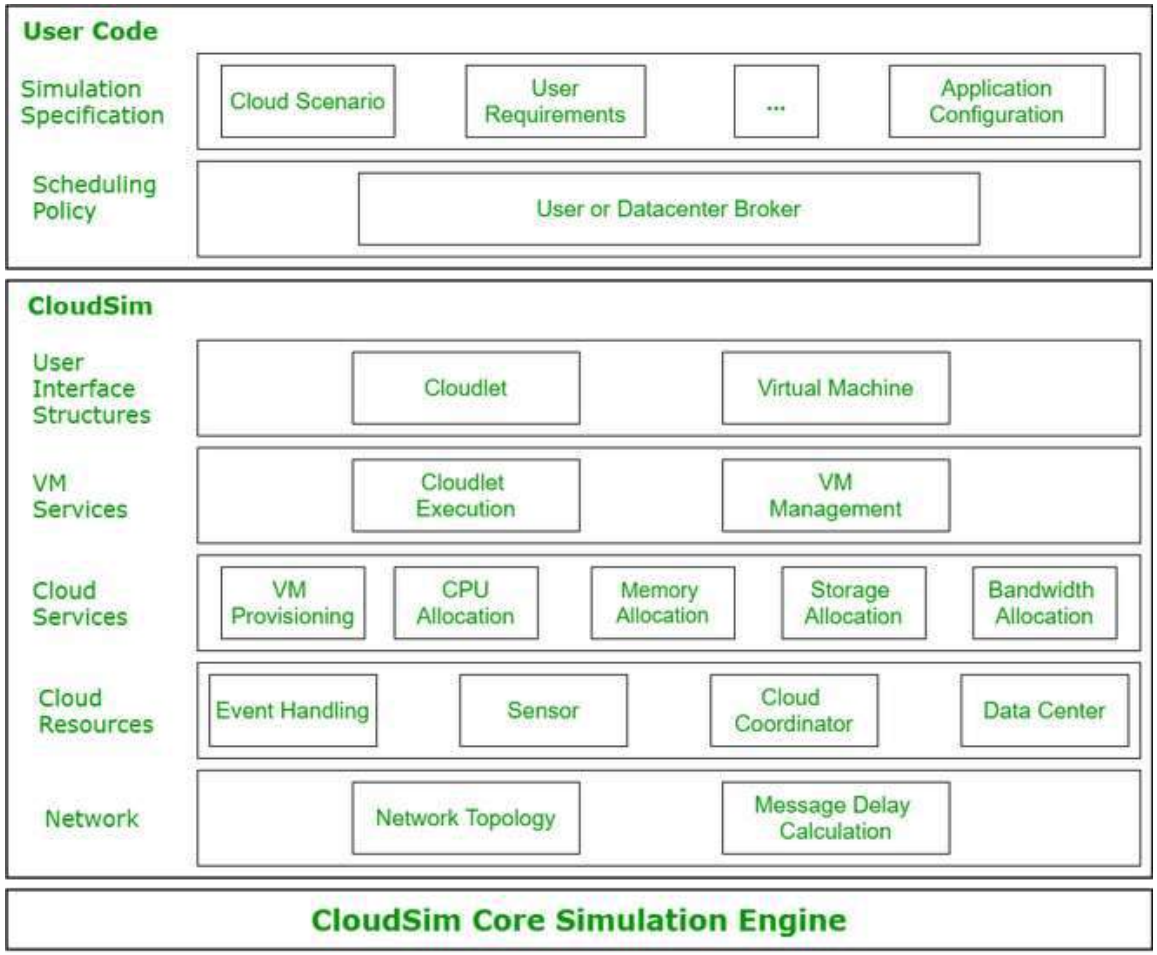

Figure 1: CloudSim Architecture

2.1 Simulation

In the previous 10 years, Grids [5] have advanced as the foundation for conveying superior execution administration for figure and information concentrated logical applications. GridSim [9], SimGrid [7], and GangSim [4] are only a few examples of the Grid test systems that have been suggested to facilitate the development of novel Grid components, tactics, and middleware. When it comes to simulating networked applications, SimGrid is the gold standard. To aid with showcasing Grid-based virtual connections and resources, GangSim is a Grid reenactment tool cache. GridSim, on the other hand, is a heterogeneous Grid assets reproduction toolkit driven by events. It bolsters the visibility of infrastructure components, users, devices, and infrastructure, as well as data flow. Albeit the previously mentioned tool

stash are able to do demonstrating and recreating the Grid application ways of behaving (execution, planning, designation, and checking) in a appropriated climate comprising of numerous Grid associations, none of these can uphold the foundation and application-level necessities emerging from Cloud processing worldview. In particular, there is a lack of help for showcasing virtualized assets and apps in the cloud in the containers used for Grid reenactment today. In addition, Clouds guarantee to provide services to Cloud clients on a subscription basis with a pay-more-as-you-go pricing model. Thus, Cloud foundation isplaying and reenactment tool compartments should offer help for monetary elements, for example, Cloud representatives and Cloud trade for empowering ongoing exchanging of administrations among clients and suppliers. Only GridSim has support for financially motivated asset the executives and application booking recreation, making it unique among the currently available test systems discussed in this research. The fact that pioneering work is still in its infancy in Cloud computing frameworks, apps, and services is another factor related to Clouds that deserves consideration. There are various significant issues that need nitty gritty examination along the Cloud programming stack. Subjects important to Cloud designers incorporate monetary methodologies for provisioning of virtualized assets to approaching client's solicitations, booking of utilizations, assets revelation, between cloud dealings, and alliance of mists, etc. To help and speed up the exploration connected with Cloud figuring frameworks, applications and administrations it is critical that the essential programming instruments are planned and created to help specialists and engineers.

CLOUDSIM DESIGN AND IMPLEMENTATION

In this paper, we expand upon the fundamental classes of CloudSim Simulation Toolkit(Version 3.0.3), which provide the backbone of the test environment. CloudSim's overall class configuration layout is as (to learn more, see the "Manual for CloudsimExample1.java reenactment work process"):

VM Distribution Demonstration The massive distribution of virtualization technologies and infrastructure is a major feature that differentiates Cloud computing from Grid computing. Consequently, In contrast to Grids, Clouds include an additional layer (the virtualization) that serves as the execution and enabling environment for Cloud-based application services. Therefore, typical application planning approaches that restrict individual application components to registration hubs are not necessarily well suited to manage the computational reflection that is commonly associated with the Clouds. For model, consider an actual server farm have that has single handling center, and there is a prerequisite of simultaneously starting up two VMs on that center. Though the two virtual machines (VMs) may seem to behave differently (in terms of the application execution settings they use), The amount of power available to each VM is ultimately determined by the host's overall computing power. Keep this basic variable in mind both during application execution and the designation phase to prevent establishing a VM that needs more processing power than is available in the host, since the task units in each VM share time slices of a comparable processing centre. CloudSim allows virtual machine planning at both the host and VM levels. Because of this, it's possible to replicate a wide range of methods while keeping their implementation strictly compartmentalised. At first, you may estimate how much of a host's overall processing power will be allotted to each VM's individual core. The VMs, at a higher level, allocate a certain portion of the available handling capacity to the individual tasks that are supported by its execution motor.

CloudSim uses both the time-shared and space-shared asset chunk techniques in all of its simulation layers. To clarify the distinction between these options and their impact on the program's actual implementation, we illustrate a simplified planning scenario in Figure 3. In the illustration, a host with just two CPU cores is working overtime to maintain four separate virtual machines (VMs), with VM1 handling tasks t1, t2, t3, and t4 and VM2 handling tasks t5, t6, t7, and t8. offers a way for the two virtual machines to share the same host computer. Since each virtual machine (VM) requires two datacenters, only one VM may be operational at any one time. This is where task units come in. When VM1 finishes carrying out the units of work, VM2 must be moved to the core. In a similar vein, two task units execute simultaneously inside the VM since each requires just a single core, while the other two wait in line until the completion of the first set of task units. VMs are designated using a space-shared method, whereas individual assignment units inside a VM are designated with a time-shared method. All tasks assigned to a VM will run in the background throughout its lifespan until it is shut down. Using this method of distribution, errandunits may be reserved ahead of time, but the completion season of leading-line undertakingunits is still impacted. Virtual machines use shared planning over a period of time, whereas task units use shared planning over a geographical area. In this setup, workstations on a shared physical infrastructure distribute processing core allocations to virtual machines (VMs) for a certain time period. In a shared data centre, the VM has less access to resources than in the aforementioned scenarios. Since the errand unit's work requires the use of shared facilities, only one errand at a time may be sent to a given centre before the others are placed in a queue for review. The last common component between VMs and task units is shown in Figure 3(d). When the processing power is shared across the VMs, the parts of each VM are divided proportionately among the number of tasks allocated to each VM. In this setup, VMs and TUs use the same communications infrastructure.

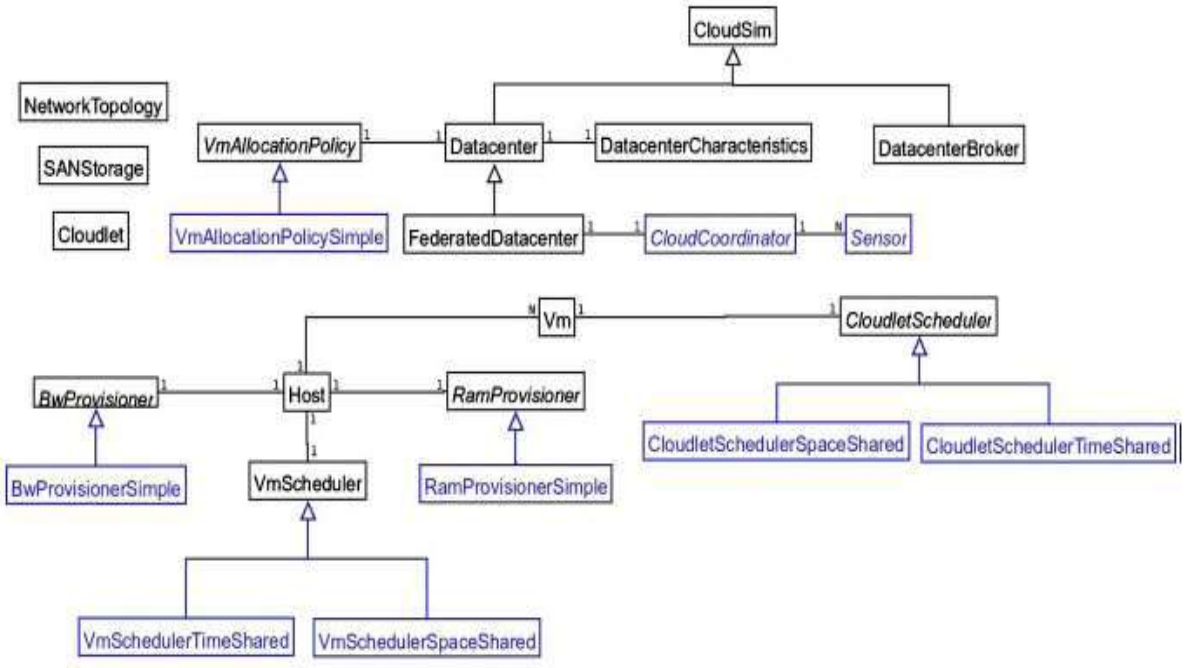

Figure 3: CloudSim Class design diagram

The depiction of the relative multitude of significant classes referenced in the class graph above is portrayed underneath:

Cloudlet: Application management (programming-based duties) on the cloud, including content distribution, long-distance communication, etc. are modelled using this class (define specific parameters like duration of guidance, input/yield filesize, number of processor necessary, etc.). Any application's computational complexity may be simulated using CloudSim. As designers, we are aware that any executable application/administration duty must adhere to a predefined set of guidelines during the course of its life cycle and must include a unique set of organisational data streams (both before and post brings). This category makes it possible to present all of the aforementioned conditions
CloudletScheduler: This component is in charge of executing the various methods used to partition CPU resources inside a VM's Cloudlets. Through the CloudetSchedulerSpaceShared class, we encourage both time-shared and space-shared provisioning strategies (utilizing CloudletSchedulerTimeShared class).

Datacenter: Services at this level mirror the fundamental infrastructure provided by Cloud service providers, such as hardware (Amazon, Azure, and App Engine). It represents a collection of hosts(such as a server machine model) that may or may not have similar hardware configurations (memory, centers, limit, and capacity). Similarly, every Datacenter component manages consolidated application provisioning, which employs a variety of methodologies for allocating transfer rates, memory, and storage to a Datacenter's VMs.

DatacenterBroker or Cloud Broker: This abstract factory class represents the role of an intermediary responsible for facilitating transactions between SaaS and Cloud providers, with the underlying motivation being the need for quality of service. In order to reap the benefits of using agents, it is important to learn from their exemplary practises. It does a great job of probing the CIS for relevant assets/benefits and welcoming trades for the allocation of assets/benefits that can meet the QoS requirements of the application. This group needs more time to evaluate and play with different unique handling strategies.

DatacenterCharacteristics: Information about the server farm's assets, such as the list of available hosts, the fine-grained cost for each asset type, and so on, are stored in this class's configuration data.

Have: This class model an actual asset like a PC or capacity server. It contains crucial information including the amount of storage space available, the number of processing cores, available types of processors (if the host is a multi-core computer), and the provisioning strategy for the host's virtual machines (VMs), among other things.

NetworkTopology: The reproduction network behaviour (latency data) is stored in this class. This database is used to save the geography information that is generated by the BRITE geography generator.

RamProvisioner: The allocation of physical RAM to Virtual Machines is discussed in depth in this theoretical course. As soon as the RamProvisioner subcomponent determines that there is sufficient RAM available on the host, the VM may be launched and configured there. The

RamProvisionerSimple doesn't put a limit on how much RAM a virtual machine may request. If the requested RAM assets exceed the available amount, the request will be denied.

BwProvisioner: Accepting the distribution of network resources between many competing VMs located in different parts of the data centre is the major duty of this section. To better meet the needs of their applications, cloud framework architects and researchers might broaden this category with their own methods (need, QoS).

Vm: Each instance of this class represents a simulated computer, known as a virtual machine (VM), that exists in a cloud environment. Each VM component exchanges data with a storage component that monitors the VM's auxiliary properties, such as memory, processing speed, storage capacity, and the VM's internal provisioning strategy, which is expanded from a theoretical class called the CloudletScheduler.
VmAllocationPolicy: This is a theoretical class on a provisioning approach that VM Monitor may employ for virtual machine preparation. Choosing the most suitable have in a server farm that satisfies the memory, storage, and accessibility need for VM organisation design is a crucial task.

VmScheduler: A theoretical class, run by the Host component, that simulates the policies for allocating CPU cores to Virtual Machines (space-shared, time-shared). In order to accommodate processor sharing schemes that are application-specific, the class utility may be used to describe a different set of provisioning rules.

CloudSim: The best of the best, this group is responsible for managing the timeliness and order in which reenactment events are performed. At runtime, the CloudSim content generates events, which are then saved in a line labelled future events. These events are queued into the future line according to their time constraints. When the reenactment is complete, the events that were scheduled are transferred from the "future events" line to the "confirmed events" line. After this, an event handling strategy is called for each component, which chooses events from the authorised event queue and does the necessary operations. Such a group enables flexible leisure management and bestows the following formidable abilities:
Deactivation (hold/stop) of substances.
Setting exchanging of substances between various states (for example holding up to dynamic). Disruption and pick up where you left off with your leisure activity.
The creation of new components in real time.
Terminating a pregnancy and beginning a new one midstream.
FutureQueue: This class acts as a prepared line to the reenactment motor, executing the future event line obtained by CloudSim.
DeferredQueue: This class executes the conceded occasion line utilized by CloudSim and hold such occasions which are fizzled or stopped. It goes about as a stand by line of the reenactment motor, where seized asset demands are kept.
CloudInformationService: A CIS is a substance that gives asset enlistment, ordering, and finding capacities. CIS upholds two fundamental natives:
distribute(), used at the start of a game, lets components sign up with CIS search(), used by Brokers to learn about the health of their assets and where they'll eventually be used. This element likewise goes about as a warning support of different substances about the finish of the reenactment.

SimEntity: This theoretical category describes a reenactment material (similar to DataCenter, DatacenterBroker, etc.) that can send and receive messages, reuse received messages, and trigger and react to events. The SimEntity class enables the scheduling of future events and the communication with other components; in this case, the BRITE model governs the scheduling lag. Once manufactured, chemicals will spontaneously log into CIS. These three core methods should be eliminated and the class expanded to include all possible parts.
startEntity(), which characterize activities for substance introduction.
activities' treatment of each called event(s) related to the substance is characterised by processEvent().
shutdown Entity(), which defines substance-eradicating actions.

CloudSimTags. When receiving or sending events, CloudSim substances may refer to the various static occasion/order labels included in this class to determine what kind of action to take.
SimEvent: This item discusses a shared recreational experience involving at least two parties. Information related to an event is saved in SimEvent, including:

- type,
- init time,
- the expected time of occurrence,
- In the finish,
- the epoch at which the event's objective essence should be communicated,
- Identification numbers for both the subject and the subject of the investigation,
- the event's official hashtag and
- Details that must be communicated to the material at hand.
-

CloudSimShutdown: This content type waits for all submitted cloudlets (tasks) and expert elements events to complete before signalling the end of play to CIS.
The following exhibits the class hierarchy that, when followed, allows the CloudSim Simulation Toolkit to mimic the distributed computing environment:

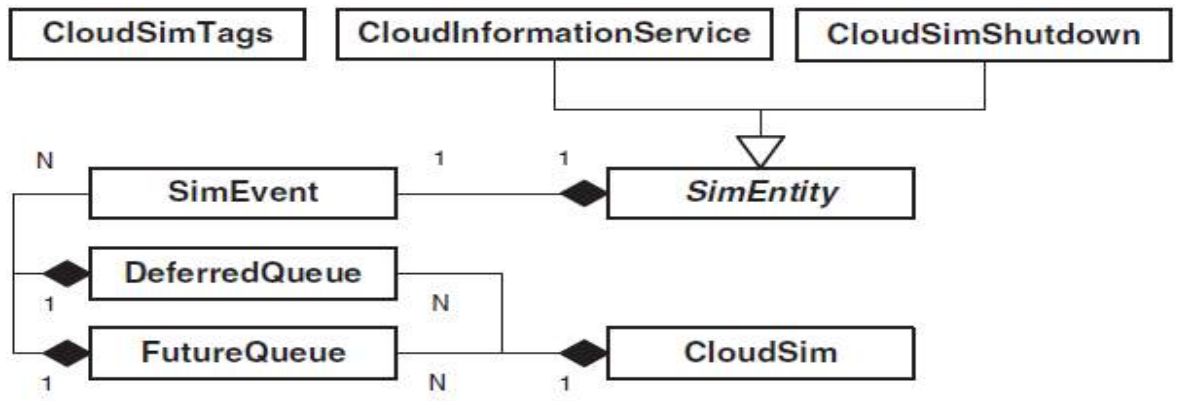

Figure 3: the class-calling structure that makes the CloudSim Simulation Toolkit possible

When and where can I download Cloudsim?

Cloudsim's GitHub page (https://github.com/Cloudslab/cloudsim) has the project's source code in addition to documentation for the built containers. The website also features essential project and distribution specifics, such as the source code(based on expert form equipment) of the current delivery, version 5.0. (beta). Presently in the event that you are keen on utilizing the past forms of this task, you have click on discharges connect choice accessible on project primary page etc., you might get to it straightforwardly from the accompanying connections:
Version 5.0, Version 4.0, Version 3.0.3, Version 3.0.2, Version 3.0.1, Version 3.0, Version 2.1.1, Version 2.1
Each adaptation with the exception of 5.0(still being worked on) contains 4 resource documents model depiction for every resource record is as per the following:
cloudsim-4.0.tar.gz: If you have a good cause to make changes to the source code of the cloudsim reproduction motor, you may import the modified code into your own custom reenactment right from this page, which provides the compiled JAR file for doing so. That's a Linux-specific adaption right there.
cloudsim-4.0.zip: The main difference from over here is that this one is windows explicit.
Source code(zip): The whole cloudsimreenactment structure project's source code is provided here. Since cloudsim is a DevOps tool, it must use the expert form instrument. Accordingly, you should choose an IDE that supports expert undertaking imports to build up this project. If it's an expert-based endeavour, how would you tell? The "pom.xml" file may be found in the project's root directory. This is a Windows-only compression file.
Source code(tar.gz): This file follows a structure similar to that described above, except it is designed for use on Linux.
It's highly recommended that you check out the following link for further information on how to set up CloudSim: cloud-sim setup with shroud/.The steps necessary to set up the Cloudsim 3.0.3 version are all outlined in detail in the linked document. If you're just getting started with cloudsim, we recommend starting with version 3.0.3; after you've mastered the basics, you may upgrade to the most current release.

cloudsim working

Cloudsim's capacity to display and simulate the cloud framework's components has been mentioned, thus its designers have arranged classes in various ways to support this function. Datacenter.java, a class in org.cloudbus.cloudsimbundle, may be used to recreate the regions and data centres. The org.cloudbus.cloudsim package includes a class called "Cloudlet.java" that may be used to simulate cloud-based workloads. DatacenterBroker.java, CloudletScheduler.java, VmAllocationPolicy.java, and so on can be found in the org.cloudbus.cloudsim bundle and may be used to simulate the heap adjustment and strategy related execution.

To ensure that all the different replicated equipment models are communicating with one another and updating the replication work, Among the various duplicated cloud components, cloudsim utilises a discrete event reenactment motor to monitor and record all tasks. The articles "CloudSim Simulation Toolkit: An Introduction" and "Fledglings Guide to Cloudsim Project Structure" might provide further detail about the architecture.

Run my first cloudsim reproduction situation

Once you get your cloudsim up and running and have a handle on its fundamentals, the next step is to put your own unique scenario into action. The following enhancements will be applied to any recreation:

In addition to re-establishing the core Cloud Information Service, introducing the CloudSim with the current time will do so as well.

Construct a Datacenter(s), since these facilities serve as CloudSim's "asset providers." One day, we want to have one of them function as a fully functional CloudSim copy.

Broker should be asked to recreate the client's booking and virtual machine assignment and arrangements. Make a virtual computer (or computers), then send them to the middleman, who will distribute them to the many data centres where they will be placed and used to run the reproduction process's executives. Create one or more cloudlets, and brief the representative on their purpose and intended use before the reenactment run, so that further tasks may be planned on the moving target virtual computers. Launches the reenactment, kicking off the process by putting into action the many components and pieces created in preparation for it. Before ending a reenactment run, it is important to halt the simulation, shut off the replication, and cleanse all of the chemicals and components. When the replica is complete, you should print the findings, which should include information on which cloudlet was performed on which virtual machine, for how long, and when the reproduction began and ended. The article "Manual for CloudsimExample1.java reenactment work procedure" provides a step-by-step description of the whole process.

- Typically used for what, though?
- Fair distribution of resources and duties
- The sequencing and planning of actions involved in a task
- Enhancing Virtual Machine Allocation and Placement Strategies
- Virtual Machine Consolidations and Migrations with Energy Efficiency in Mind
- Adding additional specifics to the improvement plans for network latency in various cloud scenarios.

Different test systems in light of cloudsim

Since the Cloudsim 3.x.x version served as the basis for the great majority of later modifications, it continues to support just a subset of use cases to this day.

CloudSimEx, EdgeCloudSim, WorkflowSim, CloudReports, CloudAnalyst, iFogSim, Cloudsim Plus

Correspondence among Entities

Correspondence among centerCloudSim compounds is shown graphically in Figure 5. EveryDatacenter component begins its replication by signing up for the CIS (CloudData Service) Registry. Matchmaking services at the database level are made available by CIS in order to help customers choose reliable Cloud service providers to meet their needs. Agents that follow up with customers advise the CIS administration on a list of Clouds that provide foundation services suitable for customers' applications. If a good fit can be found between the CIS's suggested Cloud and the application, the intermediate will make the connection.

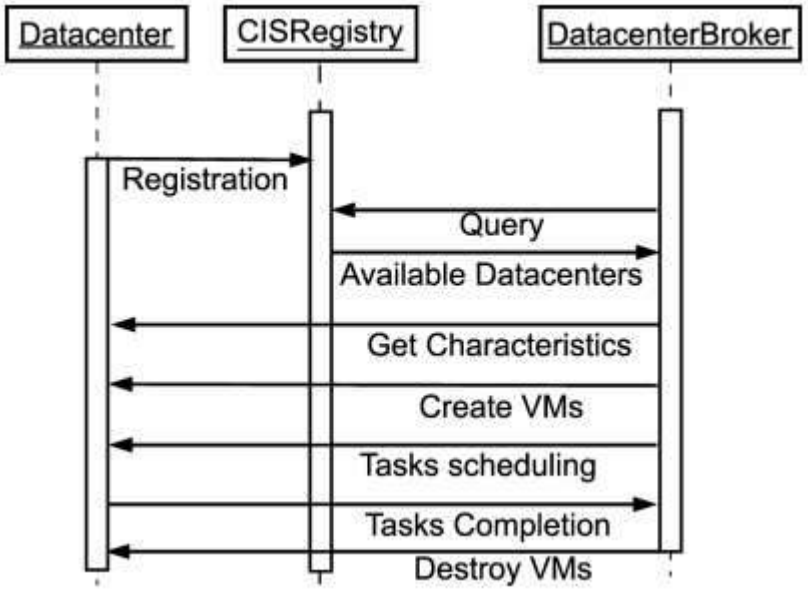

Figure 4: Simulation data flow.

In a reenacted exam, the depicted correspondence stream links up with the fundamental stream. There might be a few distinct forms of this stream, depending on how you go about it. For instance, Brokers and Datacenters may agree on a limit number of VMs a client is allowed to create ahead of time, or Brokers may request confirmation from a Datacenter component before proceeding with an operation.

Tests and Evaluation

The assessments and tests we conducted to test how well CloudSimin simulated Cloud infrastructures are described in this article. We used the preinstalled versions of Ubuntu Linux 8.04 and JDK 1.6 on a 1.86GHz Celeron machine with 1MB of L2 storage and 1 GB of RAM to run the tests.

We conducted a battery of tests to evaluate the aforementioned in the context of developing a reconstructed Cloudregistering environment with a single information focus, a dealer, and a customer. The data center's server count was boosted from 100 to 100,000. Due to the nature of these assessments—determining how much energy would be needed to register the Cloud reproduction foundation—the service provider bore the whole weight of responsibility. As part of our memory test, we profile the total RAM consumed by the hosting PC (a Celeron machine) when it boots up and loads the CloudSim environment. The time it takes for the game world to load depends on two factors: I how long it takes for the runtime environment (java virtual machine) to be configured to stack the CloudSim programme, and (ii) how long it takes for all of CloudSim's components and parts to be introduced and ready to handle events. Increasing the number of hosts in a server farm increases the startup time and memory requirements for thetry, as shown in Figures 6 and 7, respectively. A experiment with one hundred thousand machines required seventy-five megabytes of RAM, and this resulted in a direct increase in memory consumption (see Fig. 7). Since CloudSim's memory requirements, at least for larger simulated situations, can be efficiently provided by even low-end personal computers with directed handling capability, this makes our replication suitable for running on such systems.

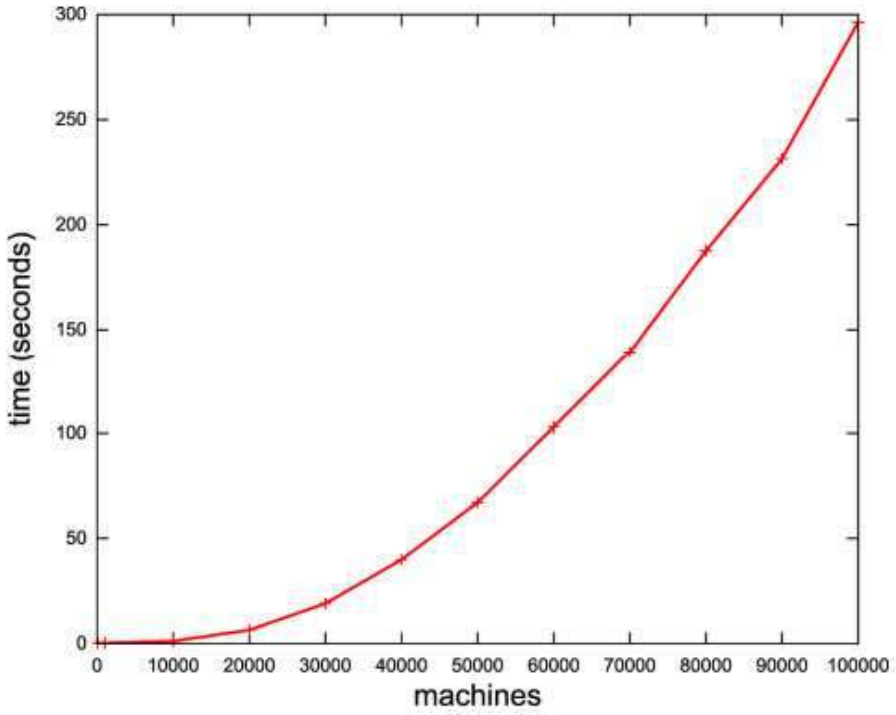

Figure 5: Time to simulation instantiation.

With respect to above connected with reenactmentlaunch, the development as far as time developsdramatically with the quantity of hosts/machines. Given the massive scope of the experiment, it seems sense that the time required to power on 100,000 devices is less than five minutes. We are currently investigating the root cause of this behaviour with the goal of eliminating it from future iterations of CloudSim. This test was developed to determine how well CloudSim's foundational elements fared when subjected to heavy demand from clientjobs such VM creation and task unit execution. It was shown that each of the 100,000 hosts in the production environment included one CPU (1000MIPS), one gigabyte of random access memory (RAM), and two terabytes of storage space. In a Space-shared model, only one virtual machine could run in a particular host at any one moment. We demonstrated to the client that they could acquire 50 virtual machines (VMs) with 512MB of RAM, 1 CPU core, and 1GB of storage using DatacenterBroker. It was shown that 1200000 million recommendations (20 minutes in the reproduced has) are required to carry out a single job unit in the programme on a host. The taskunits only required 300kB of data transfer to and from the data centre since they didn't have to deal with systems administration.

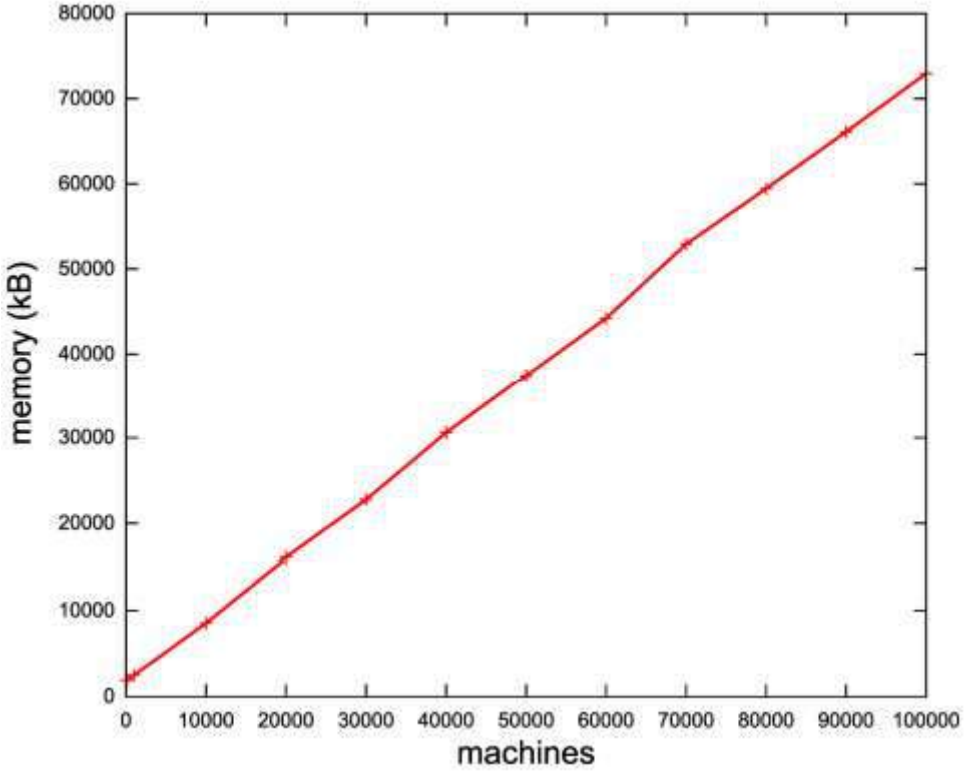

Figure: Instances of resources and their associated memory use

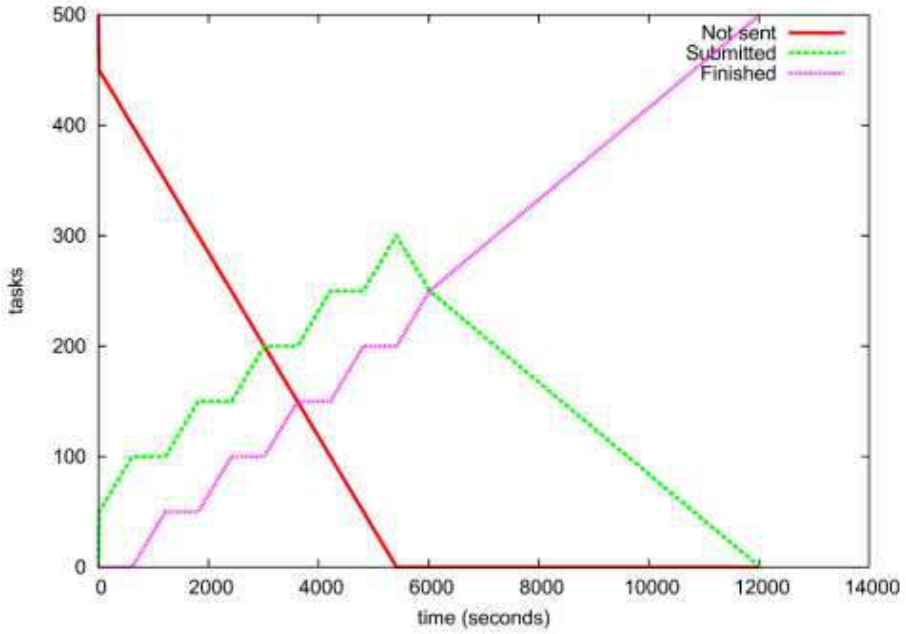

Figure6: Tasks execution with space-shared scheduling of tasks

2. CONCLUSSION

Characterizing fresh tactics, methodologies, and systems for efficiently supervising Cloud infrastructures is at the heart of the latest efforts to design and develop Cloudadvancements. In order to put these freshly devised methods and arrangements through their paces, experts

need tools that allow them to assess the theory before real arrangement in a context where testing may be repeated. In the context of distributed computing, where access to the foundation causes actual monetary installations, the ability to test the performance of provisioning and administration conveyance arrangements in a repeatable and controllable environment for no cost and to tune the exhibition bottlenecks before delivering on real Clouds is a major benefit of reenactment based approaches. In order to do this, we nurtured the CloudSim framework, a futureMists demonstration and replication apparatus. As a flexible tool, it allows for the expansion and interpretation of arrangements throughout the whole product stack, making it a practical testing apparatus capable of handling the complexities arising from simulated environments. Our long-term goal is to have CloudSim's built-in aid for recreating currently available Clouds be a set of innovative estimation and provisioning methodologies. In addition, we want to provide assistance for simulating unified mist organisation, with an emphasis on the development and testing of flexible Cloud applications.

3. REFERENCES

[1]. R. Buyya, C. S. Yeo, and S. Venugopal. Marketoriented cloud computing: Vision, hype, and reality for delivering IT services as computing utilities. In Proceedings of the 10th IEEE International Conference on High Performance Computing and Communications, 2008.

[2]. D. Chappell. Introducing the Azure services platform. White paper, Oct. 2008.

[3]. X. Chu et al. Aneka: Next-generation enterprise grid platform for e-science and e-business applications. In Proceedings of the 3rd IEEE International Conference on e-Science and Grid Computing, 2007.

[4]. C. L. Dumitrescu and I. Foster. GangSim: a simulator for grid scheduling studies. In Proceedings of the IEEE International Symposium on Cluster Computing and the Grid, 2005.

[5]. I. Foster and C. Kesselman (editors). The Grid: Blueprint for a New Computing Infrastructure. Morgan Kaufmann, 1999.

[6]. F. Howell and R. Mcnab. SimJava: A discrete event simulation library for java. In Proceedings of the first International Conference on Web-Based Modeling and Simulation, 1998.

[7]. A. Legrand, L. Marchal, and H. Casanova. Scheduling distributed applications: the SimGrid simulation framework. In Proceedings of the 3rd IEEE/ACM International Symposium on Cluster Computing and the Grid, 2003.

[8]. J. E. Smith and R. Nair. Virtual Machines: Versatile platforms for systems and processes. Morgan Kauffmann, 2005.

[9]. R. Buyya and M. Murshed, GridSim: A Toolkit for the Modeling and Simulation of Distributed Resource Management and Scheduling for Grid Computing, The Journal of Concurrency and Computation: Practice and Experience (CCPE), Volume 14, Issue 13-15, Wiley Press, Nov.-Dec., 2002. [10]A. Weiss. Computing in the clouds. NetWorker, 11(4):16–25, Dec. 2007.

[10]. M. Armbrust, A. Fox, R. Griffith, A. Joseph, R. Katz, A. Konwinski, G. Lee, D. Patterson, A. Rabkin, I. Stoica, M. Zaharia. Above the Clouds: A Berkeley View of Cloud computing. Technical Report No. UCB/EECS-2009-28, University of California at Berkley, USA, Feb. 10, 2009.

[11]. https://www.cloudsimtutorials.online/cloudsim-simulation-toolkit-an-introduction/

[12]. https://www.cloudsimtutorials.online/category/introduction/
[13]. Rodrigo N. Calheiros, Rajiv Ranjan , César A. F. De Rose , and Rajkumar Buyya "CloudSim: A Novel Framework for Modeling and Simulation of Cloud Computing Infrastructures and Services".

A Study on Inside Views of Cloud Computing Tools

Published: Aug 24, 2022

Keywords:
CloudAnalyst, CloudReports, CloudExp, GreenCloud, and iCanCloud, CloudSim

Dr. A. Ramaswami Reddy, Dr. Arun Kumar Kandru, Dr. Vasavi Bande

Abstract

Distributed computing instruments can be isolated into different classifications as demonstrated by their features. Around here, we have made a broad examination with different classes based on the accompanying boundaries like expanding, connection and characterization. In this study, we compare and evaluate many notable open-source Cloud devices for greater efficiency. Particularly helpful would be the development of new calculations for all customers related with the various cycles and its design, which would allow for the improvement of codes in the finer details. Different test frameworks, such as the five open-source Cloud registration apparatuses (CloudSim, Cloud Analyst, Cloud Reports, , iCanCloud, EMUSIM, GroudSim, DCSim and Green Cloud), have different engineering configurations, showing components, reproduction processes, execution measures, and degrees of adaptability. The commercial vendors of these products often advertise them as having standard characteristics, notably with regards to layout, diagrams of components, and the method of multiplication. Some of the key characteristics that may be utilised to zero in on the benefits of these tools include a laser-like focus on a variety of layers and the ability to make accurate predictions about how well they will perform. A few gaming tools have been developed with distributed computing in mind. Simulation develops a virtual environment for testing and validating research trials in quest of effective and superior application-specific solutions. Making a model or real-time system is a scientific approach. As a result, it removes the requirement for and cost of computational facilities for performance assessment and modelling of the research solution. The Cloud Sim simulation is the primary emphasis of this guidebook instrument and its advantages for researchers.

Issue

Vol. 12 No. 1 (2022) (https://www.e-csac.org/index.php/journal/issue/view/9)

Section

Articles

Home (http://e-csac.org/index.php/journal)
Aims and Scope (http://e-csac.org/index.php/journal/aims_and_scope)
Instructions for Authors (http://e-csac.org/index.php/journal/instructions_for_authors)
Editorial Board (http://e-csac.org/index.php/journal/about/editorialTeam)
Archive (http://e-csac.org/index.php/journal/issue/archive)
Download (http://e-csac.org/index.php/journal/downloads)
Ethics & Policies (http://e-csac.org/index.php/journal/ethics_and_policies)
Publication Ethics and Publication Malpractice Statement (http://e-csac.org/index.php/journal/publication_ethics)
Peer Review Policy (http://e-csac.org/index.php/journal/peer_review_policy)
Plagiarism Policy (http://e-csac.org/index.php/journal/plagiarism_policy)
Copyright, Grants and Ownership Declaration (http://e-csac.org/index.php/journal/copyright_grants_ownership_declaration)
Refund Policy (http://e-csac.org/index.php/journal/refund_policy)
Open Access Overview (http://e-csac.org/index.php/journal/open_access_overview)
Open Access License (http://e-csac.org/index.php/journal/open_access_license)
Permissions (http://e-csac.org/index.php/journal/permissions)

Copyright Transfer Form (http://e-csac.org/downloads/copyright_form.pdf)
Paper Template (http://e-csac.org/downloads/paper_template.docx)

Computers, Materials & Continua
DOI: 10.32604/cmc.2022.030267
Article

Tech Science Press

Wind Driven Optimization-Based Medical Image Encryption for Blockchain-Enabled Internet of Things Environment

C. S. S. Anupama[1], Raed Alsini[2], N. Supriya[3], E. Laxmi Lydia[4], Seifedine Kadry[5], Sang-Soo Yeo[6] and Yongsung Kim[7,*]

[1]Department of Electronics & Instrumentation Engineering, V. R. Siddhartha Engineering College, Vijayawada, 520007, India
[2]Department of Information Systems, Faculty of Computing and Information Technology, King Abdulaziz University, Jeddah, Saudi Arabia
[3]Department of Computer Science and Engineering, Malla Reddy Engineering College(A), Hyderabad, 500100, India
[4]Department of Computer Science and Engineering, Vignan's Institute of Information Technology, Visakhapatnam, 530049, India
[5]Department of Applied Data Science, Noroff University College, 4612, Kristiansand, Norway
[6]Department of Computer Engineering, Mokwon University, Daejeon, 35349, Korea
[7]Department of Technology Education, Chungnam National University 99, Daehak-ro, Yuseong-gu, Daejeon, 34134, Korea
*Corresponding Author: Yongsung Kim. Email: kys1001@cnu.ac.kr
Received: 22 March 2022; Accepted: 04 May 2022

Abstract: Internet of Things (IoT) and blockchain receive significant interest owing to their applicability in different application areas such as healthcare, finance, transportation, etc. Medical image security and privacy become a critical part of the healthcare sector where digital images and related patient details are communicated over the public networks. This paper presents a new wind driven optimization algorithm based medical image encryption (WDOA-MIE) technique for blockchain enabled IoT environments. The WDOA-MIE model involves three major processes namely data collection, image encryption, optimal key generation, and data transmission. Initially, the medical images were captured from the patient using IoT devices. Then, the captured images are encrypted using signcryption technique. In addition, for improving the performance of the signcryption technique, the optimal key generation procedure was applied by WDOA algorithm. The goal of the WDOA-MIE algorithm is to derive a fitness function dependent upon peak signal to noise ratio (PSNR). Upon successful encryption of images, the IoT devices transmit to the closest server for storing it in the blockchain securely. The performance of the presented method was analyzed utilizing the benchmark medical image dataset. The security and the performance analysis determine that the presented technique offers better security with maximum PSNR of 60.7036 dB.

Keywords: Internet of things; image security; medical images; encryption; optimal key generation; blockchain

1 Introduction

With the fast advancement in medical innovation, it became normal to analyze different sicknesses utilizing medical images. Medical images are communicated through various organizations; hence, getting these images turned into a fundamental theme lately [1]. Safe transmission of medical images requires secrecy, trustworthiness, and validation. Unapproved use of such images might prompt loss of security of patients' information [2]. The Internet of Things (IoT) characterizes the idea of associated gadgets and objects of numerous types over the web, remote, or wired. For example, the most recent movements from 1G to 5G organizations assume a significant part in the IoT applications and frameworks. This idea draws in scientists' interest and consideration about the conceivable protection and security chances, especially with high transmission capacity and recurrence [3]. The short frequency is probably going to change the framework, making a requirement for more base stations serving a similar area covered by the other remote system [4]. The absence of gadget refreshes, oblivious utilization of the gadgets without understanding the related outcomes, and change of passwords have expanded the cybersecurity access and dangers to malignant uses of touchy information on IoT frameworks [5]. The unseemly security components increment the chance of an information break, among different dangers. Additional, one of the security specialists consider that IoT gadgets give weak focus to digital assaults due to powerless security strategies and conventions [6]. Notwithstanding the few security systems that have been created and set up to safeguard IoT gadgets from digital assaults, rules on arising security challenges are satisfactorily recorded. This implies that the end-client can't utilize defensive measures to turn away the assaults on information. Overseeing IoT-empowered security thinks about three contemplations.

To start with, perceive the gadgets as associated with an organization. Second, decide and uphold what different frameworks, applications, and devices convey [7]. In conclusion, guarantee that these IoT gadgets have disrupted different gadgets in the organization or the associations assuming something turns out badly. The openness of IoT applications permits to make a finding, make duplicates, information, and recover an enormous number of advanced images all over the planet. It regularly brings about the creation of ill-conceived duplicates or unapproved use in concern [8]. In this manner, to safeguard images, numerous scientists have zeroed in on creating procedures for image security in IoT applications [9]. To get each kind of image, for instance, medical images, numerous innovations have been grown up until this point. Encryption is among these innovations the most unconstrained and proficient method for changing images into unnoticed examples. Just with the upholding right (secret) key, would the first image be able to be recuperated productively [10]. A few image encryptions plans have as of late been proposed which can be utilized to safeguard high-security medical images.

This paper presents a new wind driven optimization algorithm based medical image encryption (WDOA-MIE) technique for blockchain enabled IoT environments. The WDOA-MIE model involves three major processes namely data collection, image encryption, optimal key generation, and data transmission. Initially, the medical images are captured from the patient using IoT devices. Then, the captured images are encrypted using signcryption technique. Moreover, for improving the performance of the signcryption technique, the optimal key generation process was applied by WDOA algorithm. The performance of the presented algorithm was examined using the benchmark medical image dataset.

2 Related Works

Alqaralleh et al. [11] designed deep learning (DL) using blockchain-aided secured image communication and diagnoses method for the IoT setting. Mainly, elliptic curve cryptography (ECC) is exploited, also the optimum key generation of ECC occurs by hybridizing grasshopper using fruit-fly optimization (GO-FFO) approach. Next, the neighborhood indexing sequence (NIS) using burrow wheeler transform (BWT), named NIS-BWT was applied for encrypting the hash value. In conclusion, a DBN was employed as the classifier method for diagnosing the presence of disease. Khasawneh et al. [12] examine the parallel technique of image encryption on a massive amount of remotely sensed image from Hadoop. The Hadoop file visit technique is improved thus it could process the whole Tiff files as an individual unit. Moreover, the file setup is expanded to support Hadoop for supporting GeoTiff in Hadoop. The outcomes of the experiment show that the presented approach is scalable and effective to a massive amount of images in comparison with other familiar techniques.

Bharadwaj et al. [13] presented a simple security architecture for ensuring the secrecy of medicinal information in the transmission among IoT hops. The presented architecture employs the idea of encryption to guarantee safety. In [14], presented a V-net convolution neural network (CNN) based 4D hyperchaotic scheme for medicinal image encryption. Initially, the plaintext medicinal image is processed into 4D hyperchaotic sequential image, involving pseudorandom sequence generation, image segmentation, and chaotic system processing. Jan et al. [15] proposed an Image Encryption architecture based on Hessenberg transform and Chaotic encryption (IEFHAC), for reducing computation time and enlightening privacy when encrypting patient information. IEFHAC employs 2 1D-chaotic maps: Sine and Logistic maps for the data confusion, whereas diffusion was accomplished by employing the Hessenberg household transform. The Logistic and Sin maps were utilized for regeneration affecting output, as dynamically changes the primary parameter. Some other models are available in the literature [16–25].

3 The Proposed Model

In this article, a new WDOA-MIE technique has been developed for blockchain enabled IoT environment. The WDOA-MIE model enables the acquisition of medical images from the patient via IoT devices. Followed by, the acquired images are coded by the use of signcryption technique. For enhancing the efficacy of the signcryption technique, the optimal key generation process was applied by WDOA algorithm.

3.1 Level I: Image Encryption

At this stage, the acquired images are coded by the use of signcryption technique [26]. Signcryption is determined by a public-key primitive that performs the use of encryption and digital signature. The digital signature and encryption are considered important cryptographic tool that ensures redundancy, privacy, and reliability. However, it can be constraint with two potential objectives namely maximum processing cost and minimum efficiency. The signcryption is determined by an expanded method of cryptographic framework that is applied for implementing encryption and digital signature in a single logical stage and to limit the transmission overhead and assessment cost. A signcryption includes digital signature and encryption methods which are appropriate rather than encryption and individual signature. Assume the hybrid encryption was employed rather than utilizing easier encryption, the single session-key was treated in various encryption for achieving optimal signature-encryption in comparison to signcryption method.

The signcryption indicates the public-key primitive that constituted 2 indispensable cryptographic tool that is capable of ensuring honesty, non-repudiation, and privacy. The initialized technique initialized the prime number, hash function (HF) with key. It develops the public and private keys to the sender and receiver. To increase the information security, the presented method uses the perfect private key by enhanced method.

Initialization:- L_P denotes the massive prime numbers, L_f denotes the prime factor, I signifies the integer with order L_f modulo L_P, some randomly in $[1, \ldots; L_P - 1]$, Hash One way HF, that result is a minimal 128 bit, L_P Keyed one way HF D Value, arbitrarily selected $\left[1, \ldots; L_f - 1\right]$.

Sender Key pair $((M_{k1}, N_{k1}))$

$$M_{k1} = Q^{A_{k1}} \bmod L_P \tag{1}$$

Receiver key pairs (M_{k2}, N_{k2})

$$N_{k2} = Q^{A_{k2}} \bmod L_P \tag{2}$$

3.2 Level II: Optimal Key Generation Using WDOA

For enhancing the efficacy of the signcryption technique, the optimal key generation procedure is carried out by WDOA algorithm [27]. The stimulus of the presented WDOA develops in the atmosphere. During the atmosphere, wind blows from try for balancing the imbalance of pressures. It flows in maximal pressure regions for minimal regions at a velocity. The initial point of WDOA technique was Newton's second law of motion that was utilized for providing accurate outcomes for investigation of atmospheric motion from the Lagrangian description

$$\rho\vec{\alpha} = \sum \vec{F}_i, \tag{3}$$

whereas $\vec{\alpha}$ implies the acceleration, ρ refers the air density to infinitesimal air parcel, and $\vec{F}$ are every force performing on the air parcel. For assuming air pressure introduce the formula connection with air parcel density and temperature, the ideal gas law was provided as:

$$P = \rho RT, \tag{4}$$

In which P refers to the pressures, R signifies the universal gas constants, and T denotes the temperature. The reason for air movements are because of the integration of several forces mostly containing gravitational force $(\vec{F}_G)$, pressure gradient force $(\vec{F}_{PG})$, Coriolis force $(\vec{F}_C)$, and friction force $(\vec{F}_F)$. The physical formulas of aforementioned force are as follows:

$$\begin{aligned} \vec{F}_G &= \rho\delta V\vec{g}, \\ \vec{F}_{PG} &= -\nabla P\delta V, \\ \vec{F}_C &= -2\Omega \times \vec{u}, \\ \vec{F}_F &= -\rho\alpha\vec{u}, \end{aligned} \tag{5}$$

In which δV refers the finite volume of air, $\vec{g}$ stands for the gravitational acceleration, ∇P denotes the pressure gradients, Ω refers the rotation of Earth, $\vec{u}$ signifies the velocity vector of winds, and α refers the friction co-efficient. The force aforementioned was added to (3). The formula is explained as

$$\rho\frac{\Delta\vec{u}}{\Delta t} = \left(\rho\delta V\vec{g}\right) + \left(-\nabla P\delta V\right) + \left(-2\Omega \times \vec{u}\right) + \left(-\rho\alpha\vec{u}\right), \tag{6}$$

whereas the acceleration $\vec{\alpha}$ in (3) is modified as $\vec{\alpha} = \vec{u}/t$; to simplicity set $\Delta t = 1$; to an infinitesimal air parcel, set $\delta V = 1$ that make simpler (6) to

$$\rho \Delta \vec{u} = \left(\rho \vec{g}\right) + \left(-\nabla P\right) + \left(-2\Omega \times \vec{u}\right) + \left(-\rho \alpha \vec{u}\right). \tag{7}$$

At the beginning of (2), the density ρ is expressed with respect to the pressure; therefore (7) is modified as;

$$\Delta \vec{u} = \vec{g} + \left(-\nabla P \frac{RT}{P_{cur}}\right) + \left(\frac{-2\Omega \times \vec{u} RT}{P_{cur}}\right) + \left(-\alpha \vec{u}\right), \tag{8}$$

In which P_{cur} refers the pressure of existing place. It can be considered in the WDOA technique which velocity as well as position of air parcels were altered at all the iterations. Therefore, $\Delta \vec{u}$ is formulated as $\Delta \vec{u} = \vec{u}_{new} - \vec{u}_{cur}$, whereas $\vec{u}$ signifies the velocity in next iterations and $\vec{u}$ refers the velocity at existing iterations. $\vec{g}$ and ∇P are vectors, it could be broken down from direction and magnitude as $\vec{g} = |g|(0 - x_{cur})$, $-\nabla P = \left|P_{opt} - P_{cur}\right| \left(x_{opt} - x_{cur}\right)$, P_{opt} refers the optimal pressure point which is establish so far, x_{opt} signifies the optimal place which is established so far, and x_{cur} refers the existing place; update (8) with the novel formula, (8) is altered as:

$$\vec{u}_{new} = (1 - \alpha)\, \vec{u}_{cur} - g x_{cur} + \left(\frac{RT}{P_{cur}} \left|P_{opt} - P_{cur}\right| \left(x_{opt} - x_{cur}\right)\right) + \left(\frac{-2\Omega \times \vec{u} RT}{P_{cur}}\right). \tag{9}$$

The formula of updating the place was explained as in (11):

$$\vec{u}_{new} = (1 - \alpha)\, \vec{u}_{cur} - g x_{cur} + \left(RT \left|1 - \frac{1}{i}\right| \left(x_{opt} - x_{cur}\right)\right) + \left(\frac{c\vec{u}_{cur}^{other\ dim}}{i}\right) \tag{10}$$

$$\vec{x}_{new} = \vec{x}_{cur} + \left(\vec{u}_{new} \times \Delta t\right), \tag{11}$$

whereas i refers the ranking amongst every air parcel and $\vec{x}_{new}$ signifies the novel place to the next iterations. WDOA is related to other nature-inspired optimized techniques, however, related to other optimized techniques, the code of WDOA is very easy and simple for implementing; it is lesser some control variables which require change.

The WDOA derived a fitness function for optimum key generation procedure, as follows.

$$fitness\ function = \max\{PSNR\} \tag{12}$$

The purpose of the WDOA is to choose the optimum key for the signcryption method that the peak signal to noise ratio (PSNR) is increased. Fig. 1 depicts the flowchart of WDOA.

3.3 Level III: Blockchain Enabled Secure Transmission

The recognized field of Blockchain is a Bitcoin Blockchain that can be determined as a ledger established to provide economic transactions via Bitcoin cryptocurrency [28]. The miners are appropriate in confirming the operation and gathering into block; miners are appropriate in solving exclusive cryptographic puzzles termed "proof-of-work," wherein a determined hash value is associated with concluding blocks. In recent times, alternative class of Blockchain model has been organized.

For example, Ethereum Blockchain Buterin provides a standardized technique by using "smart contracts" which allows the program to implement the Blockchain and implements retrieval and storage operation. Furthermore, the information is stored in inner state parameter and describes the convention procedure to alter the real state. The procedure implemented in current contracts is transmitted in transaction that is universally progressive. Such techniques are validated and measurable by miners in Ethereum Blockchain and guarantee legitimacy. This feature develops Blockchain

model in healthcare field and thus, developer enhances the healthcare prediction. Fig. 2 depicts the framework of blockchain.

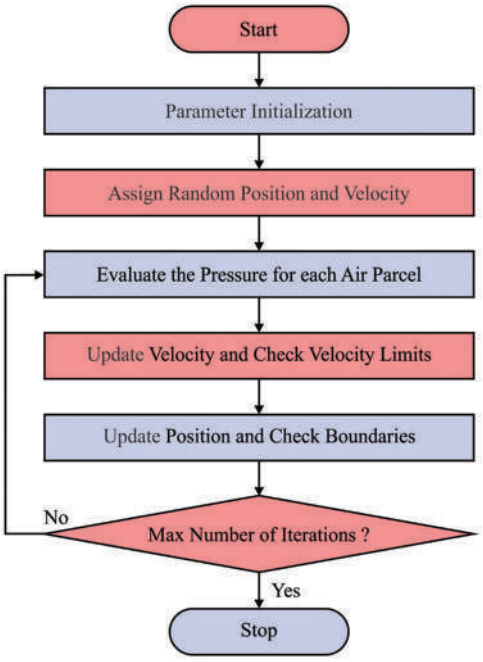

Figure 1: Flowchart of WDO algorithm

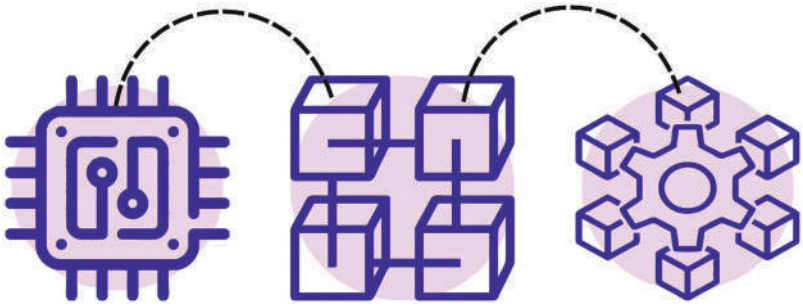

Figure 2: Structure of blockchain

4 Experimental Validation

This section portrays the results offered by the WDOA-MIE model on benchmark medical images. Fig. 3 shows the sample set of test medical images. Besides, Fig. 4 illustrates the histogram of the input and encrypted images.

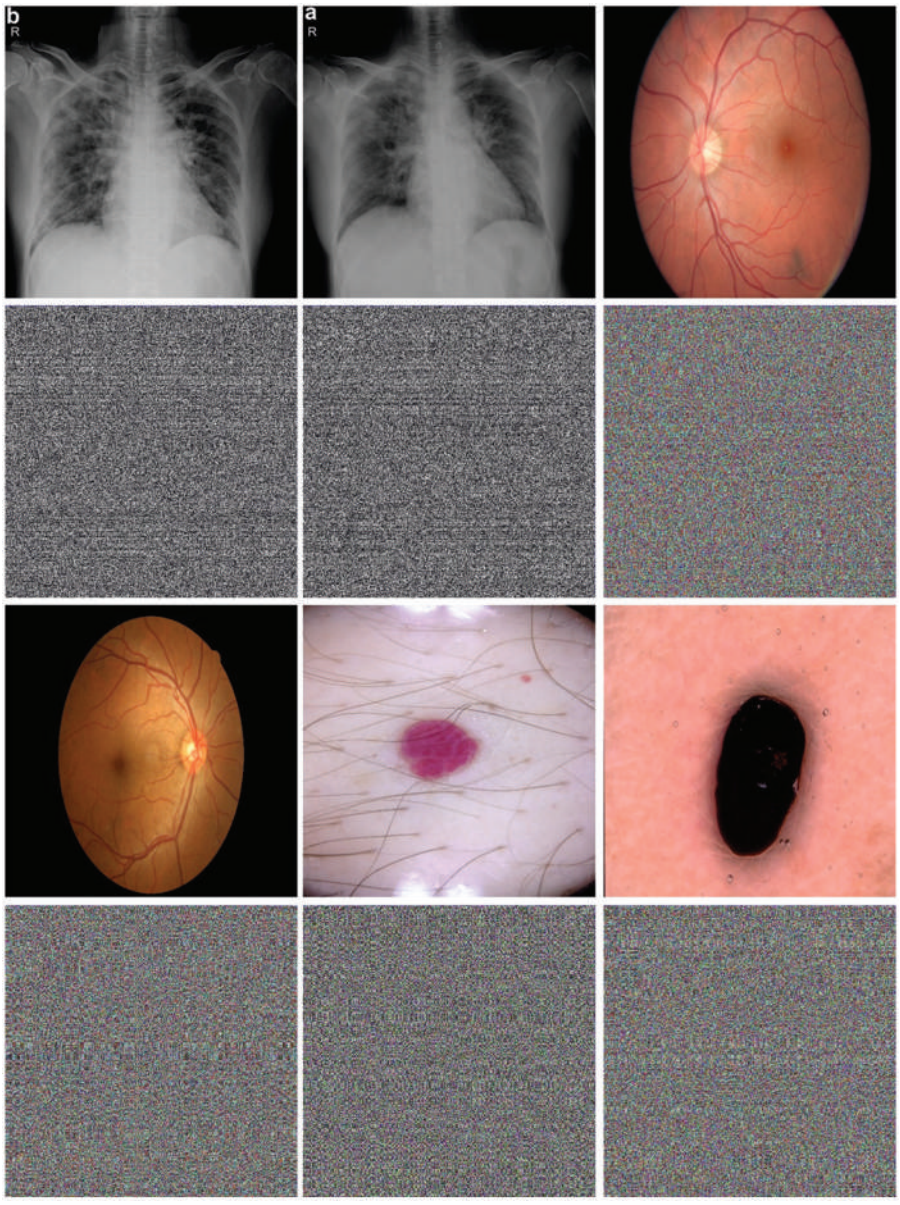

Figure 3: Sample medical images

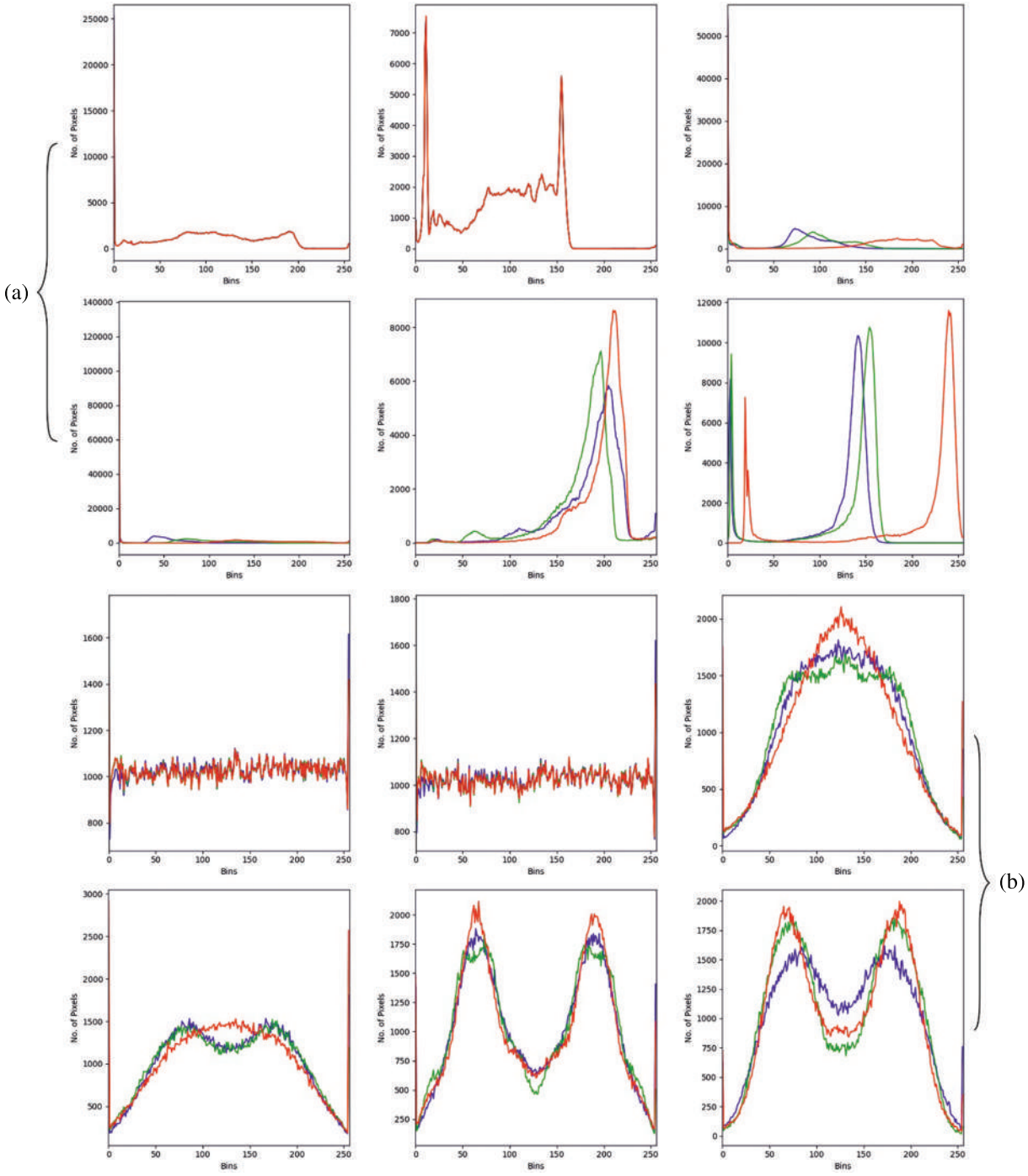

Figure 4: Histogram analysis (a) histogram of original images (b) histogram of encrypted images

Tab. 1 reports the overall results offered by the WDOA-MIE model on six test images. The experimental values implied that the WDOA-MIE model has obtained minimal values of MSE and RMSE with maximum values of PSNR and structural similarity (SSIM). For instance, on image-1, the WDOA-MIE method has gained mean square error (MSE) of 0.0713, root mean square error (RMSE)

of 0.2670, PSNR of 59.5999 dB, and SSIM of 0.9999. Besides, on image-2, the WDOA-MIE model has obtained MSE of 0.1021, RMSE of 0.3195, PSNR of 58.0405 dB, and SSIM of 0.9992. At last, on image-6, the WDOA-MIE model has resulted in MSE of 0.0553, RMSE of 0.2352, PSNR of 60.7036 dB, and SSIM of 0.9993.

Table 1: Result analysis of WDOA-MIE model under distinct test images

Image No.	MSE	RMSE	PSNR (dB)	SSIM
Image-1	0.0713	0.2670	59.5999	0.9999
Image-2	0.1021	0.3195	58.0405	0.9992
Image-3	0.1060	0.3256	57.8777	1.0000
Image-4	0.0748	0.2735	59.3918	0.9994
Image-5	0.1075	0.3279	57.8167	0.9999
Image-6	0.0553	0.2352	60.7036	0.9993

Tab. 2 and Fig. 5 illustrate a comparative MSE examination of the WDOA-MIE model with other encryption models. The results signified the betterment of the WDOA-MIE model with least values of MSE. For instance, with Image-1, the WDOA-MIE model has gained lower MSE of 0.0713 while the RSA, ECC, cuckoo search (CS), and particle swarm optimization (PSO) approaches have achieved superior MSE of 0.3379, 0.2446, 0.1792, and 0.1680 respectively. Moreover, with Image-4, the WDOA-MIE model has gained lower MSE of 0.0748 while the RSA, ECC, CS, and PSO models have reached increased MSE of 0.3449, 0.2140, 0.1865, and 0.1747 respectively. Furthermore, with Image-5, the WDOA-MIE model has resulted in least MSE of 0.0553 but the RSA, ECC, CS, and PSO models have accomplished increased MSE of 0.3225, 0.2398, 0.1744, and 0.1245 respectively.

Table 2: MSE examination of WDOA-MIE with existing models

Mean Square Error					
Image No.	RSA	ECC	CS	PSO	WDOA-MIE
Image-1	0.3379	0.2446	0.1792	0.1680	0.0713
Image-2	0.3364	0.2419	0.1751	0.1450	0.1021
Image-3	0.3418	0.2438	0.1987	0.1409	0.1060
Image-4	0.3449	0.2140	0.1865	0.1747	0.0748
Image-5	0.3258	0.2151	0.1681	0.1440	0.1075
Image-6	0.3225	0.2398	0.1744	0.1245	0.0553

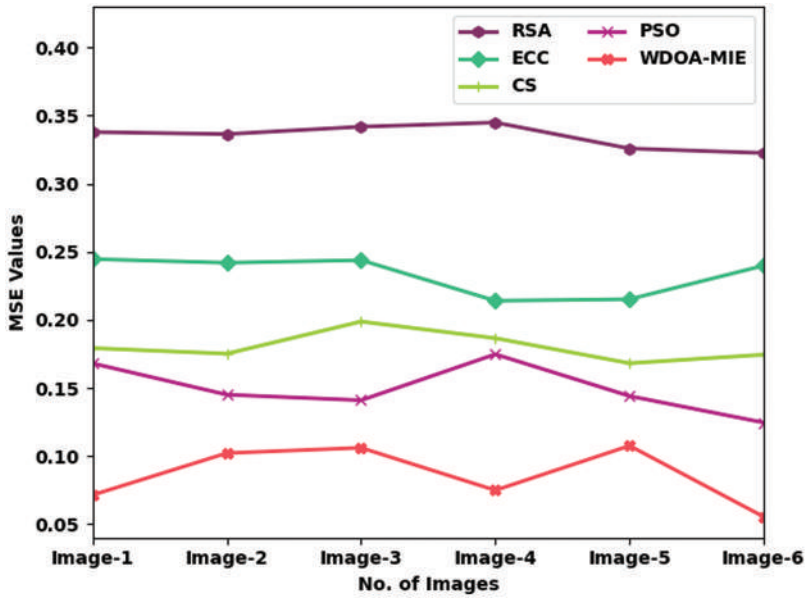

Figure 5: Comparative MSE examination of WDOA-MIE with existing models

A comprehensive PSNR investigation of the WDOA-MIE model with recent models is made in Tab. 3 and Fig. 6. The obtained values implied that the WDOAMIE model has accomplished effectual outcomes with increased PSNR values under all images. For instance, with image1, the WDOAMIE approach has provided maximum PSNR of 59.60 dB but the RSA, ECC, CS, and PSO models have resulted to lower PSNR of 52.84, 54.25, 55.60, and 55.88 dB respectively. Simultaneously, with image5, the WDOAMIE model has delivered enhanced PSNR of 57.82 dB whereas the RSA, ECC, CS, and PSO models have accomplished reduced PSNR of 53, 54.80, 55.88, and 56.55 dB respectively.

Table 3: PSNR examination of WDOA-MIE with existing models

PSNR (dB)					
Image No.	RSA	ECC	CS	PSO	WDOA-MIE
Image-1	52.84	54.25	55.60	55.88	59.60
Image-2	52.86	54.29	55.70	56.52	58.04
Image-3	52.79	54.26	55.15	56.64	57.88
Image-4	52.75	54.83	55.42	55.71	59.39
Image-5	53.00	54.80	55.88	56.55	57.82
Image-6	53.05	54.33	55.72	57.18	60.70

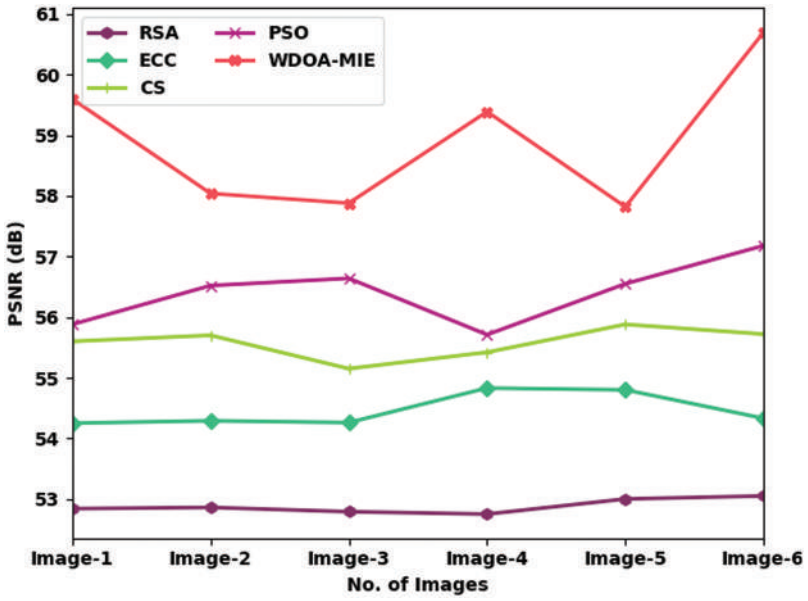

Figure 6: Comparative PSNR examination of WDOA-MIE with existing models

A comprehensive SSIM investigation of the WDOAMIE model with existing models is made in Tab. 4 and Fig. 7. The achieved values implied that the WDOAMIE model has accomplished effectual outcomes with increased SSIM values under all images. For instance, with Image-1, the WDOAMIE method has provided superior SSIM of 0.9989 while the RSA, ECC, CS, and PSO models have resulted to lower SSIM 0.9600, 0.9706, 0.9782, and 0.9836 respectively. Simultaneously, with Image-5, the WDOAMIE model has delivered enhanced SSIM of 0.9949 whereas the RSA, ECC, CS, and PSO models have accomplished reduced SSIM of 0.9260, 0.9700, 0.9707, and 0.9825 respectively.

Table 4: SSIM examination of WDOA-MIE with existing models

SSIM					
Image No.	RSA	ECC	CS	PSO	WDOA-MIE
Image-1	0.9600	0.9706	0.9782	0.9836	0.9989
Image-2	0.9364	0.9673	0.9857	0.9931	0.9968
Image-3	0.9209	0.9675	0.9855	0.9953	0.9991
Image-4	0.9007	0.9707	0.9763	0.9952	0.9994
Image-5	0.9260	0.9700	0.9707	0.9825	0.9949
Image-6	0.9551	0.9622	0.9851	0.9944	0.9983

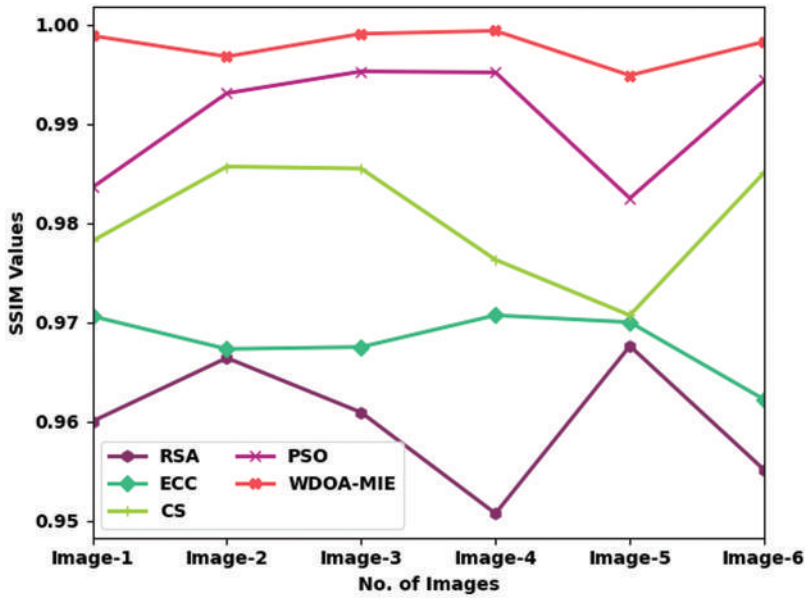

Figure 7: Comparative SSIM examination of WDOA-MIE with existing models

Tab. 5 and Fig. 8 exemplify a comparative computation time (CT) investigation of the WDOA-MIE model with other encryption models [29]. The results indicated the improvement of the WDOA-MIE model with minimum values of CT. For instance, with Image-1, the WDOA-MIE model has gained lower CT of 72.60 s whereas the RSA, ECC, CS, and PSO models have obtained higher CT 106.56, 122.76, 110.22, and 104.10 s respectively. Also, with Image-4, the WDOA-MIE model has gained lower CT of 66.90 s whereas the RSA, ECC, CS, and PSO models have obtained higher CT of 124.62, 80.88, 81.78, 132 s, respectively. In addition, with Image-6, the WDOA-MIE model has resulted in least CT of 42.60 s whereas the RSA, ECC, CS, and PSO models have accomplished increased CT of 128.04, 113.88, 52.38, and 54.66 s respectively.

Table 5: CT examination of WDOA-MIE with existing models

Computation Time (s)					
Image No.	RSA	ECC	CS	PSO	WDOA-MIE
Image-1	106.56	122.76	110.22	104.10	72.60
Image-2	142.62	99.06	107.16	96.00	70.20
Image-3	111.78	108.18	108.36	80.10	60.00
Image-4	124.62	80.88	81.78	132.00	66.90
Image-5	77.88	52.02	109.74	95.46	41.34
Image-6	128.04	113.88	52.38	54.66	42.60

From the comprehensive results and discussion, it can be evident that the WDOA-MIE model has gained effectual encryption performance over the other methods.

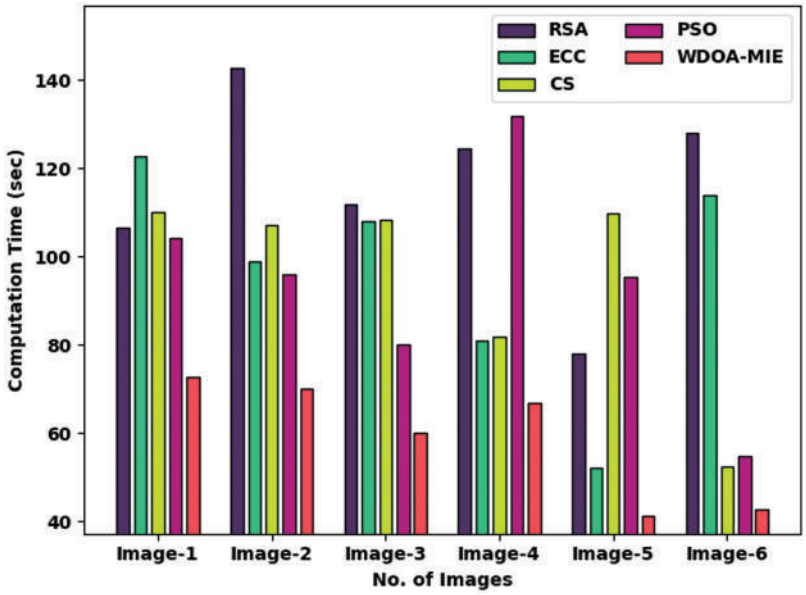

Figure 8: Comparative CT examination of WDOA-MIE with existing models

5 Conclusion

In this article, a new WDOA-MIE technique was established for blockchain enabled IoT environment. The WDOA-MIE model enables the acquisition of medical images from the patient via IoT devices. Followed by, the acquired images are coded by the use of signcryption technique. For enhancing the efficacy of the signcryption technique, the optimal key generation procedure was executed by WDOA algorithm. The goal of the WDOA-MIE algorithm is to derive a fitness function based on PSNR. Upon successful encryption of images, the IoT devices transmit to the closest server for storing it in the blockchain securely. The performance of the presented approach was analyzed utilizing the benchmark medical image dataset. The security and the performance analysis establish that the presented method offers better security with increased PSNR of 60.7036 dB. In future, hybrid metaheuristic optimization algorithms can be designed to further enhance security performance. In addition, lightweight cryptographic techniques can be involved to ensure security.

Acknowledgement: This work was supported by the National Research Foundation of Korea (NRF) grant funded by the Korea government (MSIT) (No. 2020R1G1A1099559).

Funding Statement: The authors received no specific funding for this study.

Conflicts of Interest: The authors declare that they have no conflicts of interest to report regarding the present study.

References

[1] M. K. Hasan, S. Islam, R. Sulaimanm, S. Khan, A. H. A. Hashim *et al.,* "Lightweight encryption technique to enhance medical image security on internet of medical things applications," *IEEE Access*, vol. 9, pp. 47731–47742, 2021.

[2] M. H. Kashani, M. Madanipour, M. Nikravan, P. Asghari and E. Mahdipour, "A systematic review of IoT in healthcare: Applications, techniques, and trends," *Journal of Network and Computer Applications*, vol. 192, p. 103164, 2021.
[3] S. T. Kamal, K. M. Hosny, T. M. Elgindy, M. M. Darwish and M. M. Fouda, "A new image encryption algorithm for grey and color medical images," *IEEE Access*, vol. 9, pp. 37855–37865, 2021.
[4] J. Jain and A. Jain, "Securing e-healthcare images using an efficient image encryption model," *Scientific Programming*, vol. 2022, pp. 1–11, 2022.
[5] J. Deepika, C. Rajan and T. Senthil, "Security and privacy of cloud- and IoT-based medical image diagnosis using fuzzy convolutional neural network," *Computational Intelligence and Neuroscience*, vol. 2021, pp. 1–17, 2021.
[6] P. Sarosh, S. A. Parah and G. M. Bhat, "An efficient image encryption scheme for healthcare applications," *Multimedia Tools and Applications*, vol. 81, no. 5, pp. 7253–7270, 2022.
[7] M. Gupta, K. K. Gupta, M. R. Khosravi, P. K. Shukla, S. Kautish *et al.,* "An intelligent session key-based hybrid lightweight image encryption algorithm using logistic-tent map and crossover operator for internet of multimedia things," *Wireless Personal Communications*, vol. 121, no. 3, pp. 1857–1878, 2021.
[8] W. E. Shafai, F. Khallaf, E. E. Rabaie and F. E. Samie, "Robust medical image encryption based on DNA-chaos cryptosystem for secure telemedicine and healthcare applications," *Journal of Ambient Intelligence and Humanized Computing*, vol. 12, no. 10, pp. 9007–9035, 2021.
[9] S. Doss, J. Paranthaman, S. Gopalakrishnan, A. Duraisamy, S. Pal *et al.,* "Memetic optimization with cryptographic encryption for secure medical data transmission in IoT-based distributed systems," *Computers, Materials & Continua*, vol. 66, no. 2, pp. 1577–1594, 2021.
[10] S. Jeevitha and N. A. Prabha, "Novel medical image encryption using DWT block-based scrambling and edge maps," *Journal of Ambient Intelligence and Humanized Computing*, vol. 12, no. 3, pp. 3373–3388, 2021.
[11] B. A. Y. Alqaralleh, T. Vaiyapuri, V. S. Parvathy, D. Gupta, A. Khanna *et al.,* "Blockchain-assisted secure image transmission and diagnosis model on internet of medical things environment," *Personal and Ubiquitous Computing*, vol. 19, no. 2, p. 326, 2021.
[12] M. A. A. Khasawneh, I. Uddin, S. A. A. Shah, A. M. Khasawneh, L. Abualigah *et al.,* "An improved chaotic image encryption algorithm using Hadoop-based MapReduce framework for massive remote sensed images in parallel IoT applications," *Cluster Computing*, vol. 25, no. 2, pp. 999–1013, 2022.
[13] V. Bharadwaj, A. Lakshman, G. Bhatnagar and C. Chattopadhyay, "A novel security framework for medical data in IoT ecosystem," *IEEE MultiMedia*, pp. 1–1, 2022.
[14] X. Wang, S. Yin, M. Shafiq, A. A. Laghari, S. Karim *et al.,* "A new V-net convolutional neural network based on four-dimensional hyperchaotic system for medical image encryption," *Security and Communication Networks*, vol. 2022, no. 1, pp. 1–14, 2022.
[15] A. Jan, S. Parah and B. Malik, "IEFHAC: Image encryption framework based on Hessenberg transform and chaotic theory for smart health," *Multimedia Tools and Applications*, vol. 78, no. 1, pp. 27569, 2022.
[16] J. Arif, M. A. Khan, B. Ghaleb, J. Ahmad, A. Munir *et al.,* "A novel chaotic permutation-substitution image encryption scheme based on logistic map and random substitution," *IEEE Access*, vol. 10, pp. 12966–12982, 2022.
[17] F. Masood, J. Masood, L. Zhang, S. S. Jamal, W. Boulila *et al.,* "A new color image encryption technique using DNA computing and chaos-based substitution box," *Soft Computing*, vol. 266, no. 5187, pp. 1021, 2021.
[18] F. Masood, J. Ahmad, S. A. Shah, S. S. Jamal and I. Hussain, "A novel hybrid secure image encryption based on Julia set of fractals and 3D Lorenz chaotic map," *Entropy*, vol. 22, no. 3, p. 274, 2020.
[19] F. A. Khan, J. Ahmed, J. S. Khan, J. Ahmad and M. A. Khan, "A novel image encryption based on Lorenz equation, Gingerbreadman chaotic map and S8 permutation," *Journal of Intelligent & Fuzzy Systems*, vol. 33, no. 6, pp. 3753–3765, 2017.
[20] J. S. Khan and J. Ahmad, "Chaos based efficient selective image encryption," *Multidimensional Systems and Signal Processing*, vol. 30, no. 2, pp. 943–961, 2019.

[21] J. Ahmad and S. O. Hwang, "Chaos-based diffusion for highly autocorrelated data in encryption algorithms," *Nonlinear Dynamics*, vol. 82, no. 4, pp. 1839–1850, 2015.
[22] X. R. Zhang, X. Chen, W. Sun and X. Z. He, "Vehicle re-identification model based on optimized densenet121 with joint loss," *Computers, Materials & Continua*, vol. 67, no. 3, pp. 3933–3948, 2021.
[23] M. Wang, Z. Zhou and C. Ding, "Blockchain-based decentralized reputation management system for internet of everything in 6G-enabled cybertwin architecture," *Journal of New Media*, vol. 3, no. 4, pp. 137–150, 2021.
[24] H. M. Waseem, M. Khan and T. Shah, "Image privacy scheme using quantum spinning and rotation," *Journal of Electronic Imaging*, vol. 27, no. 6, p. 1, 2018.
[25] M. Khan, F. Masood, A. Alghafis, M. Amin and S. I. Batool Naqvi, "A novel image encryption technique using hybrid method of discrete dynamical chaotic maps and Brownian motion," *PLoS ONE*, vol. 14, no. 12, p. e0225031, 2019.
[26] T. S. Ali and R. Ali, "A novel medical image signcryption scheme using TLTS and Henon chaotic map," *IEEE Access*, vol. 8, pp. 71974–71992, 2020.
[27] O. Abdalla, H. Rezk and E. M. Ahmed, "Wind driven optimization algorithm based global MPPT for PV system under non-uniform solar irradiance," *Solar Energy*, vol. 180, no. 5, pp. 429–444, 2019.
[28] D. Berdik, S. Otoum, N. Schmidt, D. Porter and Y. Jararweh, "A survey on blockchain for information systems management and security," *Information Processing & Management*, vol. 58, no. 1, p. 102397, 2021.
[29] M. Elhoseny, K. Shankar, S. Lakshmanaprabu, A. Maseleno and N. Arunkumar, "Hybrid optimization with cryptography encryption for medical image security in internet of things," *Neural Computing and Applications*, vol. 32, no. 15, pp. 10979–10993, 2018.

How to Cite:
Supriya, N., Vidyasri, P., Shivaprasad, S., Murali, G., & Kumari, M. K. (2022). IoT for analyzing and investigating digital forensics tools using cloud computing. *International Journal of Health Sciences*, *6*(S3), 1934–1955. https://doi.org/10.53730/ijhs.v6nS3.5903

IOT for analyzing and investigating digital forensics tools using cloud computing

N. Supriya
Associate Professor, Department of Computer Science and Engineering, Malla Reddy Engineering College (A), Hyderabad, Telangana

P. Vidyasri
Assistant Professor, Department of Computer Science and Engineering, SRM Institute of Science and Technology, Ramapuram Campus, Chennai

S. Shivaprasad
Professor, Department of Computer Science and Engineering (data science), Malla Reddy Engineering College, Secunderabad

Gudipati Murali
Professor, Department of Computer Science and Engineering, KKR & KSR Institute of Technology and Science, Guntur, Andhrapradesh

Matta Krishna Kumari
Assistant Professor, Department of Computer Science and Engineering, VFSTR (Deemed to be University), Guntur, Andhra Pradesh

Abstract---One of these articles examines how cloud computing affects standard digital proof methodologies and offers some suggestions on how to improve digital proof reviews in the cloud. As Cloud-Computing gains traction as an IT business solution, it is attracting the attention of an increasing number of companies as a viable migrations path for their IT infrastructures and business strategy. The criminal's element among has made aware of the centralization of data stored in clouds. Then Data Centers and Clouds Service providers are becoming targeted for assault. Inside the coming years, implementing a Forensics-as-a-Service (FaaS) solution may be the only viable option, but until it is consented upon as a guideline and executed by service suppliers, participants are completely reliant on clients receiving a few assurances in their service level agreements to allow the retrieval of users and the systems logs on supply.

Keywords---forensics-as-a-service, cloud computing, virtualization storage management, security, business model.

International Journal of Health Sciences ISSN 2550-6978 E-ISSN 2550-696X © 2022.
Corresponding author: *Supriya, N.*
Manuscript submitted: 18 Nov 2021, Manuscript revised: 09 Feb 2022, Accepted for publication: 27 March 2022

Introduction

As seen by the rise in the global acceptance of the products it delivers, clouds computing is a constantly developing technology solution and business plan. Although clouds computing has roots in mainframes computing which has

International Journal of COMMUNICATION systems

RESEARCH ARTICLE

Dynamic resource allocation in cloud infrastructure using ant lion-based auto-regression model

Jaggannagari Kavitha, Komati Thirupathi Rao

First published: 04 January 2022
https://doi.org/10.1002/dac.5071

Summary

Cloud computing provides a quick, simple, and gainful means for configuring and assigning the resources for a web-based appliance, like medical records systems, smart grid applications, and security management infrastructures. The optimization of resource allocation in the cloud is a major task for meeting customer demands and maximizing profit. This paper devises an optimization method for allocating resources in cloud infrastructures. The main contribution is to provide a framework for allocating the available resource to the deserving tasks. Here, the dynamic resource allocation is performed to allocate the resources dynamically as requested by users without affecting the system performance. Here, the ant lion-based auto-regressive optimization (ALAO) strategy is employed to allocate the cloud resources. ALAO is designed by integrating Ant Lion Optimizer (ALO) in auto-regression model for further enhancing the allocation of resources, and a new fitness function is adapted, which considers certain parameters, such as cost, speed, and load. The results proved that the proposed ALAO algorithm attained enhanced performance with a maximal profit of 0.153, a minimum load of 0.028, and a minimal task assignment cost of 0.094.

Open Research

DATA AVAILABILITY STATEMENT

The data generated for the study are purely based on the simulation.

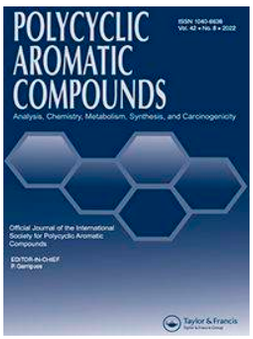

Polycyclic Aromatic Compounds

ISSN: (Print) (Online) Journal homepage: https://www.tandfonline.com/loi/gpol20

Electronic Spectra (Experimental and Simulated), and DFT Investigation of NLO, FMO, NBO, and MESP Characteristics of Some Biphenylcarboxaldehydes

K. Srishailam, L. Ravindranath, B. Venkatram Reddy & G. Ramana Rao

To cite this article: K. Srishailam, L. Ravindranath, B. Venkatram Reddy & G. Ramana Rao (2022): Electronic Spectra (Experimental and Simulated), and DFT Investigation of NLO, FMO, NBO, and MESP Characteristics of Some Biphenylcarboxaldehydes, Polycyclic Aromatic Compounds, DOI: 10.1080/10406638.2022.2130376

To link to this article: https://doi.org/10.1080/10406638.2022.2130376

POLYCYCLIC AROMATIC COMPOUNDS
https://doi.org/10.1080/10406638.2022.2130376

Taylor & Francis
Taylor & Francis Group

Electronic Spectra (Experimental and Simulated), and DFT Investigation of NLO, FMO, NBO, and MESP Characteristics of Some Biphenylcarboxaldehydes

K. Srishailam[a,b], L. Ravindranath[b,c], B. Venkatram Reddy[b], and G. Ramana Rao[b]

[a]Department of Physics, SR University Warangal, Warangal, India; [b]Department of Physics, Kakatiya University, Warangal, India; [c]Department of Physics, Malla Reddy Engineering College, Hyderabad, India

ABSTRACT

Experimental UV–Visible spectral data for biphenyl-4-carboxaldehyde (B4A), biphenyl-3-carboxaldehyde (B3A), and biphenyl-2-carboxaldehyde (B2A) were obtained in the spectral space 200–400 nm in a solution of $CDCl_3$. In order to substantiate the experimental data, theoretical quantum chemical calculations were made using time-dependent DFT (TD-DFT) formalism employing B3LYP functional in combination with 6–311++G(d,p) for the three molecules in $CDCl_3$ solution phase. Certain global reactivity descriptors were evaluated with the highest occupied molecular orbital (HOMO) and lowest unoccupied molecular orbital (LUMO) (FMOs) analysis, with in the frame work of DFT/B3LYP/6–311++G(d,p) method for the three molecules being investigated. The non-linear optical (NLO) material profiles of the three molecules consisting of their static NLO parameters were theoretically investigated to find their utility for NLO applications. Hyperconjugative interactions, as revealed by natural bond orbital (NBO) analysis, helped to explain NLO behavior of the molecules in terms of intramolecular charge transfer (ICT). The reactive sites of B4A, B3A, and B2A molecules were probed by MESP surface analysis.

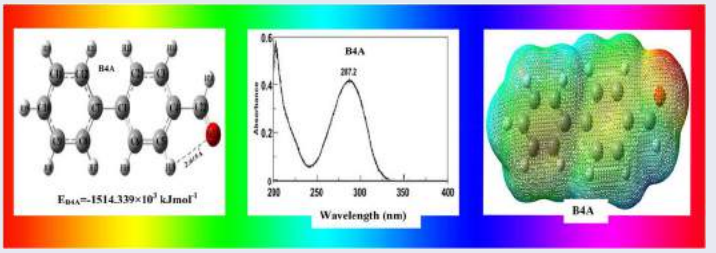

ARTICLE HISTORY
Received 1 July 2022
Accepted 25 September 2022

KEYWORDS
Biphenylcarboxaldehyde; electronic spectra; NLO; FMO; NBO; MESP; DFT

HIGHLIGHTS

- Experimental and simulated electronic absorption maxima agree well for, B4A, B3A, and B2A.
- Highest occupied molecular orbital (HOMO) and lowest unoccupied molecular orbital (LUMO) orbitals are used to understand $\pi \rightarrow \pi^*$ UV–Visible transitions in the three molecules.
- The molecules are highly reactive and stable.
- B4A and B3A are good for developing NLO materials.
- Space around oxygen atom of the aldehyde moiety of the molecules is the most favorable site, for electrophilic attack.

CONTACT B. Venkatram Reddy bvreddy67@yahoo.com Department of Physics, Kakatiya University, Warangal 506009, Telangana, India

Supplemental data for this article can be accessed online at https://doi.org/10.1080/10406638.2022.2130376

1. Introduction

Substituted Biphenyls (BP) are known for their importance in commercial applications of liquid crystals,[1] in pharmaceutical research for obtaining high success rates[2] (e.g. sartan family of drugs used to treat hypertension[3]) as industrial flame retardants and plasticizers[4] (e.g. polychlorinated BP and polybromonated BP), and in asymmetric synthesis[5] of vital chiral ligands[6,7] (e.g. BINAP and Meo-BIPHEP). Further, the biphenyl moiety plays a pivotal role in imparting biological activity to numerous natural products[8,9] (e.g. michellamine, steganon, and vancomycin). Moreover, there is an interesting aspect of structure of biphenyl derivatives. The torsional angle around C–C inter-ring bond, associated barrier to internal rotation, and consequent conformer are dictated by two opposing interactions: the π–electron conjugation (i.e. delocalization of π–electrons) between the two phenyl rings favoring a coplanar structure, whereas the repulsion between ortho atoms favoring a non-coplanar conformer. This stimulated intense experimental and theoretical research activity of biphenyl derivatives in order to understand their equilibrium geometries, vibrational frequencies, molecular force field, chemical reactivity, barrier to internal rotation around inter-ring C–C bond, electronic structure, laser-induced flouroscence spectra, and electronic spectra. However, these studies are mainly restricted to methyl-,[10] flouro-,[11,12] chloro-,[13,14] bromo-,[14] amino-,[15] cyano-,[16] and hydroxyl-,[13] substituted BP. Hence in an earlier article we reported results of our investigation of biphenyl-4-carboxaldehyde (B4A), biphenyl-3-carboxaldehyde (B3A), and biphenyl-2-carboxaldehyde (B2A) involving their torsional potentials, hindered rotation, molecular structure and vibrational properties.[17] As a continuation of this work we report results of our work on B4A, B3A, and B2A covering their UV–Vis spectra (both experimental and simulated), frontier molecular orbital (FMO) characteristics, non-linear optical (NLO) properties, natural bond orbital (NBO) behavior, and molecular electrostatic potentials (MEP). In a recent article, we reported results of such investigations on a couple of thiosemicarbazones.[18] This work is of current interest, as several research articles are published in the immediate recent past, that deal with subject matter of this article, for a good number of other molecular systems.[19–22]

2. Measurement of spectra

High purity samples of B4A (solid) and B3A (liquid) were purchased from Tokyo Kasei Kogyo Co., Ltd, Tokyo, Japan, whereas B2A (liquid) was procured from Aldrich Chemical Company, St. Louis, MO. They were used as such, without further purification for recording the spectra.

UV–Vis spectra of the three compounds were measured, in a solution of Deuterated Chloroform ($CDCl_3$), employing Perkin-Elmer UV–Vis LAMBDA-25 double beam spectrometer, in the spectral range 200–400 nm, at room temperature.

3. Computational aspects

In order to evaluate various molecular properties related to electronic transitions, FMO behavior, nonlinear optical parameters, NBO characteristics, and MESPs of B4A, B3A, and B2A, we used *ab initio* quantum chemical calculations modified to include density functional theory (DFT) formalism as available in Gaussian 09/DFT program package.[23] The level of theoretical formalism used consisted of three essential components: (i) Beck's non-local gradient three parameter hybrid exchange functional (B3),[24] (ii) Lee–Yang–Parr gradient corrected correlation functional (LYP),[25] and (iii) split valence triple zeta basis set, 6–311++G(d,p). We call this B3LYP/6–311++G(d,p) formalism or method.

Time dependent-DFT (TD-DFT) was employed, using the formalism mentioned in the preceding paragraph, to compute electronic absorption spectra of B4A, B3A, and B2A in a solution of $CDCl_3$ (this is the solvent used to measure experimental spectra).[26–28]

Orbital energy gap (ΔE), ionization potential (I), electron affinity (A), global chemical hardness (η), global chemical softness (ζ), electronegativity (χ) chemical potential (μ), global electrophilicity index (ω), and maximum charge transfer index (ΔN_{max}) are chemically important parameters. Following common practice, we evaluated ΔE, I, A, η, ζ μ, ω, and ΔN_{max} for B4A, B3A and B2A, using the highest occupied molecular orbital (HOMO) and lowest unoccupied molecular orbital (LUMO) energies E_{HOMO} and E_{LUMO}, respectively. HOMO and LUMO are called FMOs. Relevant expressions required for calculating above parameters using DFT were taken from literature.[22,29–31]

Nonlinear optical behavior of a given compound is usually analyzed in terms of its total molecular dipole moment (μ_t) and its components, total molecular polarizability (α_t) and its components, anisotropy of polarizability ($\Delta\alpha$), and first-order static hyperpolarizability (β_t). Their values were found, for B4A, B3A, and B2A, utilizing DFT in conjunction with Buckingham's definitions[32] based on finite field approach (see[21] also for fundamental equations of NLO).

A major structural aspect of B4A, B3A, and B2A is the π-electron conjugation (i.e. delocalization or hyper conjugation) between the two phenyl rings as stated earlier in the introduction. It is essential to quantify this aspect in the three molecules under investigation. This leads to an understanding of several second-order interactions involving occupied orbitals of one subsystem and vacant orbitals of another subsystem. This is achieved by evaluating donor–acceptor interactions for each of the three molecules B4A, B3A, and B2A by subjecting their Fock matrices in NBO basis to second-order pertbation analysis. These interactions reveal themselves as a loss of occupancy from the localized NBO of the idealized Lewis structure into an empty non-Lewis orbital. We used NBO version 3.1 computer program (Madison, UK)[33] which is a part of the Gaussian 09/DFT suit of programs.

MESP $V(\mathbf{r})$ at any point $\mathbf{r}$ (x, y, z) is given exactly by the following expression.[21,34]

$$V(\mathbf{r}) = \sum_A \frac{Z_A}{|\mathbf{R}_A - \mathbf{r}|} - \int \frac{\rho(\mathbf{r}')d\mathbf{r}'}{|\mathbf{r}' - \mathbf{r}|}$$

where $\mathbf{Z_A}$, $\mathbf{R_A}$, $\mathbf{r}'$, $\mathbf{r}$ and $\rho(\mathbf{r}')$ are

Nuclear charge on the nucleus A, position of nucleus A, position of an electron in the molecule, position of a point where $V(\mathbf{r})$ is required in the surroundings of the molecule, and $\rho(\mathbf{r}')$ is electron density (ED) function at the point $\mathbf{r}'$, respectively. $\mathbf{R_A}$, $\mathbf{r}'$, and $\mathbf{r}$ are measured from an arbitrary origin.

The first term on the right-hand side of the above equation represents nuclear contribution to the potential, which is responsible for the positive interaction energy. This arises from the interaction of nuclei belonging to the molecule with a positive test charge situated at $\mathbf{r}$. The second term in the equation is due to electrons, which is the origin of the negative interaction energy. This energy originates from the interaction of electrons with the same test charge used above at $\mathbf{r}$. To evaluate MESP, we mapped MESP $_{V(\mathbf{r})}$ onto iso-ED surface. MESP surfaces of B4A, B3A, and B2A are evaluated, along with total ED, using DFT/B3LYP/6–311++G(d,p) level of theory, by mapping MESP onto iso-ED surfaces.

4. Results and discussion

4.1. Frontier molecular orbital (FMO) characteristics

In this section, we wish to present FMOs (i.e. HOMO and LUMO) and their utility to understand UV–Visible spectra and chemical reactivity. FMOs are very important in quantum chemistry for

determination, understanding, and interpretation of a host of molecular electronic and electrical parameters, electronic transitions responsible for absorption bands in UV–Visible region, chemical reactivity of conjugated molecules at molecular level and charge transfer within molecular systems.[21,22,30,31,35–39]

HOMO can be thought of as an electron donor, whereas LUMO can be considered as an electron acceptor.

4.1.1. UV–Visible spectrum

It is a common practice to employ UV–Visible absorption spectra for quantitative analysis of organic compounds in a solution. But it is almost impossible to avoid impurities in the solution in an organic synthesis. Two methods are available to make quantitative analysis of such a solution possible. The first method requires separation of various impurities present in the solution, whereas the second procedure needs re-synthesis of the impurities separately. Both procedures require considerable time, in addition to being financially taxing. Hence, one should look for an alternative method that can address this problem effectively. The answer is available in numerous theoretical methods, that have the common purpose of simulating UV–Visible spectra. Recently Parrish et al.[40] reviewed these methods alongwith DFT, wherein they extended variational quantum eigensolver method for calculating electronic transitions. We prefer to use time-dependent DFT (TD-DFT) for this purpose, as it was established that TD-DFT simulates UV–Visible spectra with fair degree of accuracy.[26–28] Further, such usage conforms to the general purpose of this article.

It is customary to use a three-step procedure[41,42] to generate UV–Visible spectra theoretically. In the first step, the ground state geometry is optimized until the default convergence limit (i.e. the root-mean-square of forces is less than 3.0×10^{-4} a.u) is reached. This is followed by the second step, wherein vibrational wave numbers are determined analytically to check for the absence of negative frequencies in order to ensure that the structure corresponds to an actual minimum. In the final step vertical transitions to valence excited states are calculated. In the first two steps, the DFT formalism is employed, while the last step is implemented with its time-dependent variant, i.e. TD-DFT. Optimized molecular geometry of B4A, B3A, and B2A as obtained by implementing the first two steps and reported in our earlier publication,[17] is shown in Figure 1, since the geometry is essential for the computations reported in this article.

Quantum theoretical formalisms described above give rise to a line spectrum for the UV–Visible transitions. This needs to be modified as the corresponding experimental spectrum has a broad shape due to line-broadening effects such as natural line width, Doppler effect, pressure broadening, and thermal excitement. Therefore, each computed line has to be widened to have a Gaussian shape.[43,44] To realize this, computation of UV–Visible transitions has to be made following an integrated approach.[45] The input in this process is the electronic transitions generated by TD-DFT. Then, each line spectrum is modified into a Gaussian function making independent optimization by using a convenient value for full width at half maximum (FWHM). This process leads to improved agreement between measured and computed spectra.[45] It is important to note that there should be certain amount of deviation between the observed and computed values of UV–Visible spectra as it is not possible to incorporate line-broadening effects exactly using present theoretical methods.

Simulated electronic absorption spectral parameters were obtained for B4A, B3A, and B2A in a solution of $CDCl_3$ using foregoing quantum chemical methods. Solvent effects were addressed by means of polarizable continuum model (PCM). For this, we employed a variant of integrated equation formalism (IEF-PCM),[46] incorporated into Gaussian version 09 program package.

Measured UV–Visible absorption bands caused by electronic transitions are made available in Figure 2, for B4A, B3A, and B2A. Comparison of these transitions with their corresponding computed parameters can be found in Table 1.

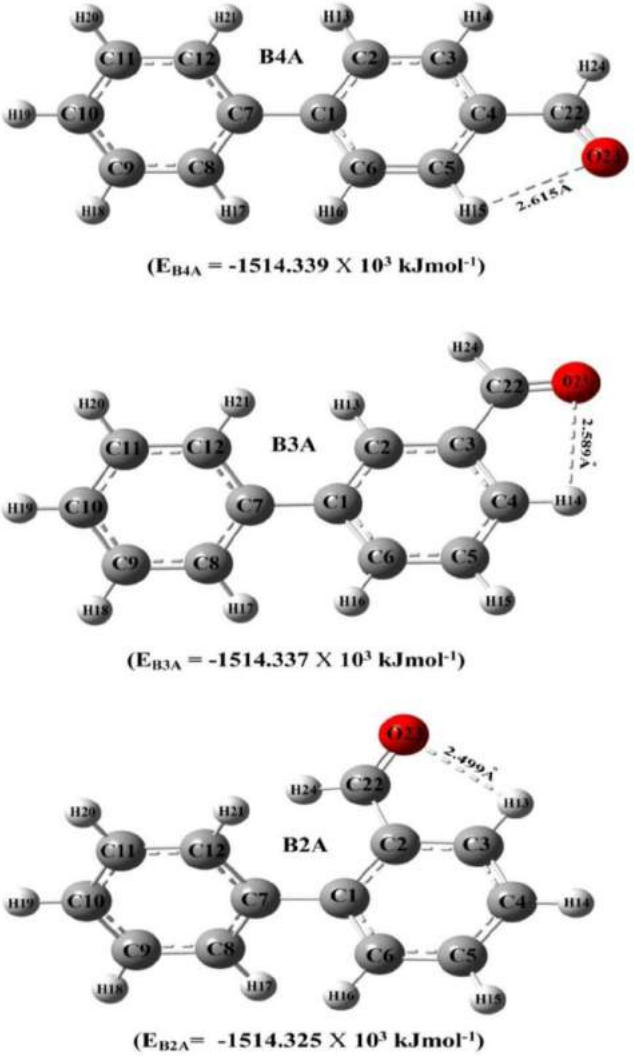

Figure 1. Optimized molecular structure of B4A, B3A, and B2A monomers along with numbering of atoms and intramolecular hydrogen bonding.

According to our calculations B4A, B3A, and B2A should have one electronic transition each, at λ_{max}= 308.2, 315.8, and 302.4 nm, respectively, with corresponding oscillator strength 0.670, 0.031, and 0.103. These are in good agreement with observed electronic transitions near 287.2, 303.1, and 299.9 nm, for B4A, B3A, and B2A, respectively. Prominent HOMO–LUMO and their neighboring molecular orbitals in various electronic transitions are shown in Figure 3, for B4A, B3A, and B2A. Our simulations establish that the experimental bands mentioned in the foregoing paragraph, arise mainly due to H→L transitions (H and L denote HOMO and LUMO, respectively). The percentage contribution of H→L transition is 98%, 88%, and 56% in B4A, B3A, and B2A, respectively. We can attribute H→L electronic transition to $\pi \rightarrow \pi^*$ excitation.

4.1.2. Chemical reactivity

FMO parameters (or global reactive descriptors), such $\Delta E=(E_{HOMO}-E_{LUMO})$, $I= -E_{HOMO}$, $A= -E_{LUMO}$, $\eta=(I-A)/2$, $\zeta= 1/2\eta$, $\chi =(I+A)/2$, $\mu = -(I+A)/2$, $\omega = \mu^2/2\eta$, and $\Delta N_{max} = -\mu/\eta$,

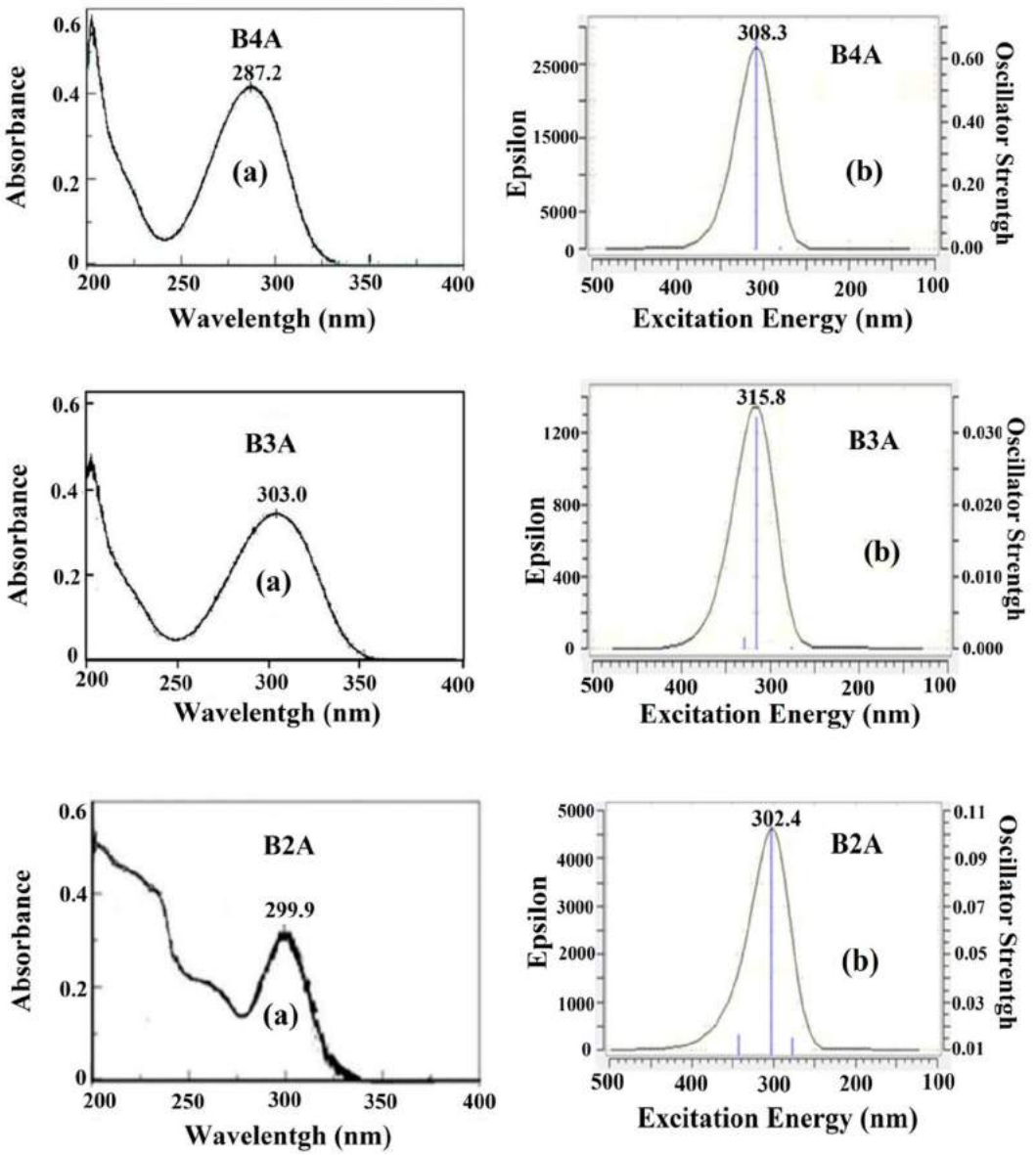

Figure 2. UV–Vis Spectra of B4A, B3A, and B2A: (a) Experimental (b) Simulated with TD-DFT/B3LYP 6–311++G(d,p) formalism.

Table 1. Electronic absorption parameters for B4A, B3A, and B2A as evaluated by TD-DFT/B3LYP/6-311++G(d,p) formalism.

	Absorption maximum λ_{max} (nm)					
Molecule	Calculated	Experimental	Excitation energy (eV)	Oscillator strength (f)	Major contribution (≥10%)	Transit-ion
B4A	308.3	287.2	4.02	0.670	Hz→L (98%)	$\pi \rightarrow \pi^*$
B3A	315.8	303.0	3.92	0.031	H→L (88%)	$\pi \rightarrow \pi^*$
B2A	302.4	299.9	4.10	0.103	H→L (56%) H-1→L (15%) H-2→L (22%)	$\pi \rightarrow \pi^*$

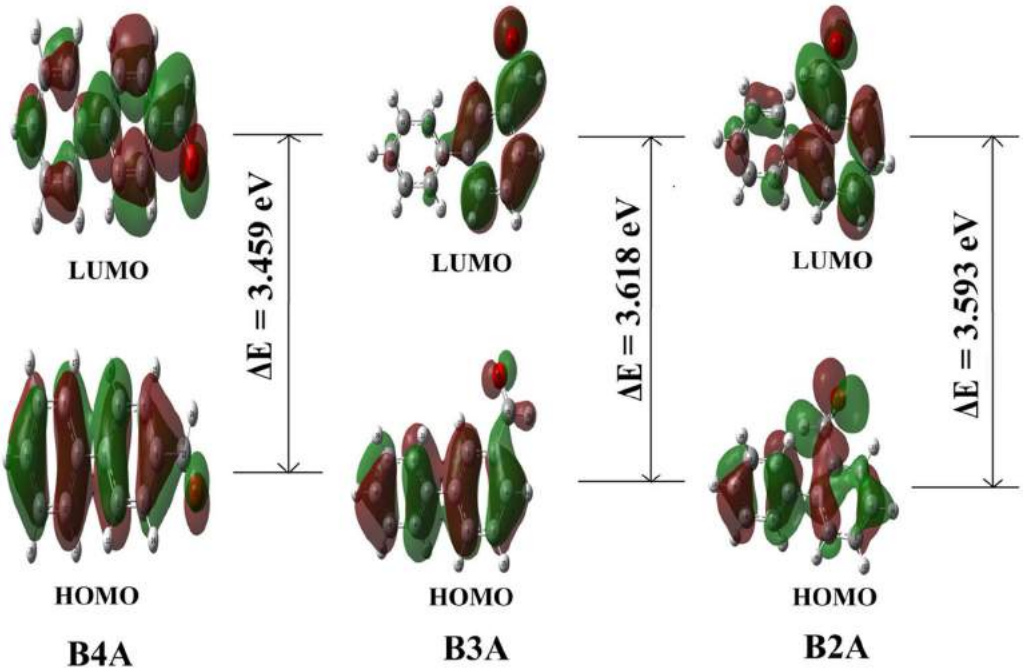

Figure 3. Frontier molecular orbitals of (a) B4A, (b) B3A, and (c) B2A as obtained using DFT/B3LYP/6–311++G(d,p) formalism.

Table 2. Frontier molecular orbital parameters of B4A, B3A, and B2A by DFT/B3LYP/6-311++G(d,p) method.

	Value (eV)		
Frontier molecular orbital parameter	B4A	B3A	B2A
HOMO energy	−9.781	−9.780	−9.795
LUMO energy	−6.322	−6.161	−6.200
Frontier molecular orbital energy gap	3.459	3.618	3.594
Ionization energy (I)	9.781	9.780	9.795
Electron affinity (A)	6.322	6.161	6.200
Global chemical hardness (η)	1.729	1.809	1.797
Global chemical softness (ζ)	0.289	0.276	0.278
Electronegativity (χ)	80.51	7.970	7.997
Chemical potential (μ)	−8.051	−7.970	−7.997
Global electrophilicity index (ω)	18.739	17.555	17.792
Maximum charge transfer index (ΔN_{max})[a]	4.656	4.406	4.450

[a]ΔN_{max} has no units as it is ratio of similar quantities

where estimated for B4A, B3A, and B2A on the basis of DFT/B3LYP/6-311++G(d,p) formalism.[22,29–31] These are presented in Table 2. The primary quantity that can be obtained from these parameters is the energy gap, which is equal to the difference between orbital energies of HOMO and LUMO. This parameter, for B4A, B3A, and B2A, is calculated at 3.459, 3.619, and 3.595 eV, respectively, using the data from Table 2. These values are relatively small. This is a characteristics feature of conjugated molecules, and is an indicator of high chemical reactivity of B4A, B3A, and B2A. Low value of frontier orbital energy gap creates energetically favorable situation wherein it is easy to excite electrons from low-lying HOMO to high-lying LUMO leading to accumulation of electrons in the LUMO, polarizing the molecule. Thus a molecule having low energy gap is easily polarizable, has high chemical reactivity and exhibits low kinetic stability.[47–49] From Table 2, we note that the

chemical potential (μ) for the three molecules under investigation is negative. This indicates that the molecules are stable under normal conditions.[50]

4.2. Non-linear optical (NLO) properties

An electromagnetic wave, in its passage through a NLO material, experiences changes in its propagation characteristics, such as amplitude, frequency, or phase, due to its interaction with the material, generating new fields.[51,52] If such modifications are sufficiently high, then the NLO material becomes useful for NLO applications, such as frequency shifting, optical logic, optical memory, and optical switching, in the fields of telecommucations, signal processing, and optical inter-connections.[22,50,52–56] First-order hyperpolarizability (β_t) plays a pivotal role in deciding the NLO behavior of a given material. Consequently, density functional formalism was extensively employed to investigate organic NLO materials.[50–52,57–60]

The NLO quantities calculated for B4A, B3A, and B2A are collected in Table 3. Following usual practice one compares total molecular dipolemoment (μ_t) and total first-order hyperpolarizability (β_t) of a given material with values of corresponding quantities of urea, in order to evaluate NLO behavior of the material under consideration. For Urea μ_t and β_t are 1.3732 Debye and 372.8 × 10–33 cm^5/esu, respectively. For B4A, the values of μ_t and β_t are 1.944 Debye and $4095.0427 \times 10^{-33}$ cm^5/esu, whereas the corresponding values for B3A are 1.674 Debye and 959.379×10^{-33} cm^5/esu, while they are 1.445 Debye and 131.227×10^{-33} cm^5/esu, for B2A. Thus, μ_t and β_t for B4A are 1.42 and 10.98 times of that of corresponding values for Urea.

Corresponding figures for B3A are 1.23 and 2.57, whereas they are 1.05 and 0.35 for B2A. Hence, B4A and B3A are very useful for NLO applications, whereas B2A is not useful for this purpose. The value of hyperpolarizability of a given material is a measure of NLO activity. Its origin is in the intramolecular charge transfer (ICT), which has its roots in electron cloud

Table 3. Values of dipole moment, μ_t (in Debye); polarizability, α_t (in 1.4818×10^{-25} cm^3); and first-order hyperpolarizability, β_t (in 8.641×10^{-33} cm^5/e.s.u) of B4A, B3A, and B2A.

	Value with B3LYP/6 − 311++G(d,p)		
Type of component	B4A	B3A	B2A
μ_x	1.766	−0.507	−0.592
μ_y	0.769	1.573	−1.313
μz	0.256	−0.264	0.108
μ_t	**1.944**	**1.674**	**1.445**
α_{xx}	325.930	275.444	209.787
α_{xy}	1.337	3.564	−5.408
α_{yy}	187.816	210.075	156.733
α_{xz}	−0.271	−4.720	3.764
α_{yz}	1.266	6.558	7.047
α_{zz}	108.889	111.662	100.801
α_t	**207.545**	**199.060**	**155.774**
Δα	**190.278**	**142.798**	**94.394**
β_{xxx}	3886.314	630.762	146.142
β_{xxy}	125.307	−137.748	10.602
β_{xyy}	96.116	342.199	−68.437
β_{yyy}	109.183	−100.590	121.623
β_{xxz}	34.604	18.267	−16.502
β_{xyz}	38.461	−34.277	22.432
β_{yyz}	21.761	58.999	−55.422
β_{xzz}	103.982	−33.373	−7.823
β_{yzz}	20.648	50.142	−36.724
β_{zzz}	17.806	−30.739	15.208
β_t	**4095.0427**	**959.379**	**131.227**

association through π-conjugated structure of electrons. The components of hyperpolarizability decide charge delocalization in the molecule. In the case of B4A, B3A, and B2A, the direction along which maximum charge delocalization takes place is β_{xxx} direction.

4.3. Natural bond orbital (NBO) analysis

Results of important hyperconjugative interactions obtained with second-order pertbation theory analysis of Fock matrix in NBO basis using DFT/B3LYP/6-311++G(d,p) computational level for B4A, B3A, and B2A are summarized in Tables ST1, ST2, and ST3, respectively, which can be found in Supplementary information.

NBO method is a mathematical tool to construct orbitals so as to include maximum possible percentage of the ED. As a result, they are helpful in providing clear understanding of:

i. ICT,
ii. intra and intermolecular bonding interactions, and
iii. hyperconjugative interactions between donor (i) and acceptor (j) groups within a given electronic structure.

To drive this point home let us consider the stabilization energy E(2), associated with donor (i)→acceptor(j) electron delocalization, as estimated using the equation[19,61]

$$E(2) = -q_i \frac{F_{ij}^2}{\Delta E} = -q_i \frac{\langle i|F|j\rangle^2}{\varepsilon_j - \varepsilon_i}$$

where q_i is the donor orbital occupancy, $\mathfrak{E}_i$ and $\mathfrak{E}_j$ are energies of ith and jth orbitals (diagonalelements), respectively, and F_{ij} is the off diagonal NBO Fock matrix element.

Significant value of stabilization energy $E(2)$ indicates strong interaction between the electron donors and electron acceptors resulting in greater extent of conjugation of the entire structure. The delocalization of ED, between occupied Lewis-type (bonding or lone pair) NBO orbitals and empty non-Lewis (anti-bonding or Rydberg) NBO orbitals implies stabilization of donor–acceptor interaction. Intramolecular hyper conjugative interactions arise due to overlap between the bonding π-orbitals and anti-bonding π^*-orbitals. This leads to ICT stabilizing the system. This type of interactions reveal themselves as enhancement in the ED in biphenyl C1–C6, C2–C3, C4–C5, C7–C12, C8–C9, and C10–C11 anti-bonding orbitals. They reduce strength of the corresponding bonds. The ED, for B4A at the conjugated π-bonds of the biphenyl ring is between 1.6159 and 1.6663, as can been seen from Table ST1, whereas the corresponding values, for π^*-anti-bonds are in the range 0.2688–0.3799. Consequent to this intense charge delocalization the molecule generates total stabilization energy 261.29 kcal mol^{-1} from the biphenyl ring alone. The interactions π (C1–C6)→π^* (C2–C3 and C4–C5); π (C2–C3)→π^* (C1–C6 and C4–C5); π (C4–C5)→π^* (C1–C6, C2–C3, and C22–O23); π (C7–C12)→π^* (C8–C9 and C10–C11); π (C8–C9)→ π^* (C7–C12 and C10–C11); π (C10–C11)→π^* (C7–C12 and C8–C9); LP(2) O23→π^*(C4–C22) possess large stabilization energies in the range 17.68–24.12 kcal mol$^{-1,}$ according to NBO analysis. As a result ICT, i.e. of π- electron movement from donor to acceptor (i.e. ICT) the molecule becomes more polarized. On the basis of this observation, it can be stated that the NLO properties of B4A originate from ICT. This statement substantiates the conclusion arrived at in Section Non-linear optical (NLO) properties on NLO properties, regarding the usefulness of the molecule for NLO applications. Corresponding conclusions can be arrived at for B3A and B2A from the data presented in Tables ST2 and ST3, respectively.

4.4. Molecular electrostatic potentials (MESP)

MESP is an established tool to understand molecular reactivity properties, by identifying electrophilic and nucleophilic regions, in addition to hydrogen bond interactions, in a molecule.[62–64] The role of MESP extends to revealing nature of biological recognition processes. It also facilitates visual representation of relative polarities of a molecule. It is to be noted that MESP is a real physical quantity that can be measured with the help of diffraction experiments.[65,66] This is an important aspect of MESP that distinguishes it from other reactivity indices like atomic charges that are mere defined properties, which do not correspond to anything real directly.

MESP maps obtained according to the formalism mentioned in Section Computational aspects, are available in Figure 4, for B4A, B3A, and B2A. It is customary to use color grading[67] to indicate regions of varying ED in the molecule. According to the color scheme, red indicates electron-rich region (partial negative charge); blue denotes electron deficient portion (partial positive charge); orange (light blue) gets associated with slightly electron deficient part (slightly less partial positive charge), yellow stands for slightly electron rich location (slightly less partial negative charge) and green identifies neutral area[61] in a molecule. Hence the color grading from the most

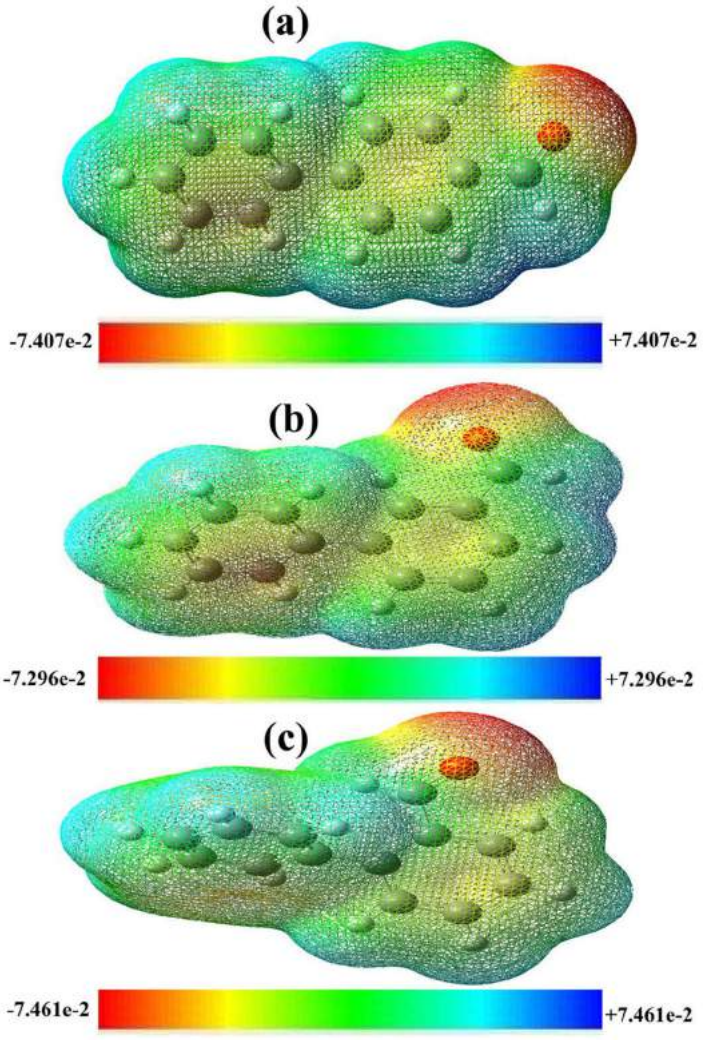

Figure 4. Total electron density mapped with electrostatic potential surface of (a) B4A, (b) B3A, and (c) B2A.

negative region to the highest positive region follows the order red > yellow > green > orange > blue. From Figure 4, it is clear that the highest electron-rich region in B4A contains oxygen atom of the aldehyde group. Hence, oxygen atom is the most reactive site in B4A. This is substantiated by the fact that this oxygen atom is involved in intermolecular hydrogen bond formation in B4A.[17] These statements pertaining to B4A are equally true of B3A and B2A, as can be seen from Figure 4.

5. Conclusions

Theoretically simulated electronic transitions, one each for B4A, B3A, and B2A, at TD-DFT/B3LYP/6–311++G(d,p) level showed good agreement with their experimentally measured counterparts in a solution of $CDCl_3$ using IEF-PCM solution model. Their origin is in the $\pi \rightarrow \pi^*$ transitions in these molecules, as revealed by FMO (HOMO, LUMO) analysis. Global reactivity descriptors, such as energy gap (ΔE) and chemical potential (μ), evaluated through HOMO and LUMO analysis proved that the molecules are highly reactive attributable to relatively small value of corresponding energy gap, which is around 4 eV. Further, the negative value of related chemical potentials ascertained that the molecules were stable under normal conditions. The theoretical static NLO parameters μ_t and $\boldsymbol{\beta_t}$ of these molecules, on comparison with corresponding values of Urea, suggested that B4A and B3A were good for use in NLO industry, whereas such was not the case with B2A. Hyperconjugative interactions, as obtained from NBO, analysis, helped to explain NLO behavior of the molecules in terms of ICT. On the basis of MESP surface analysis by DFT, it was calculated that the most reactive site is located around the oxygen atom of aldehyde moiety in B4A, B3A, and B2A.

Acknowledgments

The authors sincerely acknowledge financial support, under SAP-DRS-II, extended by the University Grants Commission, New Delhi, India through their Lr.No.F.530/24/DRS-II, 2015 (SAP). They are also grateful to NIPER, Hyderabad for recording UV–Visible spectra. The first author (KSS) is grateful to the management of SR University, Warangal, India, for permitting him to undertake the reported investigations.

Disclosure statement

No potential conflict of interest was reported by the authors.

Funding

This work was supported under SAP-DRS-II, extended by the University Grants Commission, New Delhi, India through their Lr.No.F.530/24/DRS-II, 2015 (SAP).

ORCID

B. Venkatram Reddy http://orcid.org/0000-0001-6516-7731

References

1. P. J. Collings, and M. Hird, *Introduction to Liquid Crystals Chemistry and Physics* (London: Taylor & Francis, 1997), 314. doi: 10.1201/9781315272801.
2. A. A. Patchett, and R. P. Nargund, "Chapter 26. Privileged Structures — an Update," *Annual Reports in Medicinal Chemistry* 35 (2000): 289–98.

3. H. Ji, M. Leung, Y. Zhang, K. J. Catt, and K. Sandberg, "Differential Structural Requirements for Specific Binding of Nonpeptide and Peptide Antagonists to the AT1 Angiotensin Receptor. Identification of Amino Acid Residues That Determine Binding of the Antihypertensive Drug Losartan," *Journal of Biological Chemistry* 269, no. 24 (1994): 16533–6.
4. W. J. Trotter, "Confirming Low Levels of Hexabromobiphenyl by Gasliquidchromatographyof Photolysis Products," *Bulletin of Environmental Contamination and Toxicology* 18, no. 6 (1977): 726–33.
5. R. Noyori, "Asymmetric Catalysis by Chiral Metal Complexes," *Chemtech (American Chemical Society)* 22, no. 6 (1992): 360–7.
6. C. Rosini, L. Franzini, A. Raffaelli, and P. Salvadori, "Synthesis and Applications of Binaphthylic C2-Symmetry Derivatives as Chiral Auxiliaries in Enantioselective Reactions," *Synthesis* 1992, no. 06 (1992): 503–17.
7. R. Schmid, J. Foricher, M. Cereghetti, and P. Schönholzer, "Axially Dissymmetric Diphosphines in the Biphenyl Series: Synthesis of (6,6′-Dimethoxybiphenyl-2,2′-Diyl)Bis(Diphenylphosphine)('MeO-BIPHEP') and Analogues via an ortho-Lithiation/Iodination Ullmann-Reaction Approach," *Helvetica Chimica Acta* 74, no. 2 (1991): 370–89.
8. F. P. GerhardBringmann, "Chapter 4 the Naphthylisoquinoline Alkaloids," *The Alkaloids: Chemistry and Pharmacology* 46 (1995): 127–271. doi: 10.1016/S0099-9598(08)60288-6.
9. D. H. Williams, and B. Bardsley, "The Vancomycin Group of Antibiotics and the Fight against Resistant Bacteria," *Angewandte Chemie International Edition* 38, no. 9 (1999): 1172–93. doi: 10.1002/(SICI)1521-3773(19990503)38:9 < 1172::AID-ANIE1172 > 3.0.CO;2-C.
10. P. J. Wagner, and B. J. Scheve, "Triplet Energy Transfer. 11. Steric Effects in the Singlet-Triplet Transitions of Methyl- and Chlorobiphenyls," *Journal of the American Chemical Society* 99, no. 9 (1977): 2888–92.
11. R. J. Pulham, and D. Steele, "Vibrational Spectra of 4, 4′-Difluorobiphenyl-d8 and the Structure of Biphenyls in Solution," *Journal of Raman Spectroscopy* 15, no. 4 (1984): 217–23. doi: 10.1002/jrs.1250150403.
12. X. Zhang, R. Xi, J. Liu, J. Jiang, G. Wang, and Q. Zeng, " "Molecular and Electronic Structures as Well as Vibrational Spectra Assignment of Biphenyl, 2,2′- and 4,4′-Dichlorobiphenyl from Density Functional Calculations," *Journal of Molecular Structure: Theochem* 763, no. 1–3 (2006): 67–73. doi: 10.1016/j.theochem.2006.01.025.
13. Y. Takei, T. Yamaguchi, Y. Osamura, K. Fuke, and K. Kaya, "Electronic Spectra and Molecular Structure of Biphenyl and Para-Substituted Biphenyls in a Supersonic Jet," *The Journal of Physical Chemistry* 92, no. 3 (1988): 577–81. doi: 10.1021/j100314a003.
14. C. W. Lee, D. Pan, L. C. T. Shoute, and D. Lee Phillips, "Transient Resonance Raman Spectroscopic and ab Initio MO Investigation of Substituent Effects on the T1 Triplet States of Halobiphenyls," *Journal of Raman Spectroscopy* 32, no. 6–7 (2001): 461–70. doi: 10.1002/jrs.720.
15. M. K. Subramanian, P. M. Anbarasan, V. Ilangovan, and N. Sundaraganesan, "FT-IR, FT-Raman Spectra and DFT Vibrational Analysis of 2-Aminobiphenyl," *Molecular Simulation* 34, no. 3 (2008): 277–87. doi: 10.1080/08927020701829856.
16. K. Merkel, R. W. Rzalik, and A. Kocot, "Calculation of Vibrational Spectra for Cyanobiphenyl Liquid Crystals," *Journal of Molecular Structure* 563–564 (2001): 477–90. doi: 10.1016/S0022-2860(00)00891-7.
17. K. Srishailam, B. V. Reddy, and G. R. Rao, "Investigation of Torsional Potentials, Hindered Rotation, Molecular Structure and Vibrational Properties of Some Biphenyl Carboxaldehydes Using Spectroscopic Techniques and Density Functional Formalism," *Journal of Molecular Structure* 1196 (2019): 139–61. doi: 10.1016/j.molstruc.2019.06.064.
18. K. Srishailam, K. Ramaiah, K. Laxma Reddy, B. V. Reddy, and G. R. Rao, "Synthesis and Evaluation of Molecular Structure from Torsional Scans, Study of Molecular Characteristics Using Spectroscopic and DFT Methods of Some Thiosemicarbazones, and Investigation of their Anticancer Activity," *Chemical Papers* 75, no. 7 (2021): 3635–47. doi: 10.1016/j.molstruc.2008.06.031.
19. H. Gökce, S. Ceylan, N. Öztürk, and Y. Sert, "Tautomeric, Spectroscopic, Electronic and NLO Analyses of Purpald (4-Amino-3-Hydrazino-5-Mercapto-1,2,4-Triazole," *Materials Today Communications* 32 (2022): 103862. doi: 10.1016/j.mtcomm.2022.103862.
20. G. A. El-Hitih, S. Q. Makki, Y. Sert, F. Ucun, M. B. Alshammari, P. Thordarson, and G. A. El-Hiti, "Synthesis, Spectrophotometric and DFT Studies of New Triazole Schiff Bases as Selective Naked-Eye Sensors for Acetate Anion," *Supramolecular Chemistry* 32 (2020): 519–26. doi: 10.1080/10610278.2020.1808217.
21. N. Dege, H. Gökce, O. E. Doğan, G. Alpaslan, T. Ağar, S. Muthu, and Y. Sert, "Quantum Computational, Spectroscopic Investigations on N-(2-((2-Chloro-4,5-Dicyanophenyl)Amino)Ethyl)-4-Methylbenzenesulfonamideby DFT/TD-DFT with Different Solvents, Molecular Docking and Drug-Likeness Researches," *Colloids and Surfaces A: Physicochemical and Engineering Aspects* 638 (2022): 128311. doi: 10.1016/j.colsurfa.2022.128311.

22. H. Gökce, Y. Sert, G. Alpaslan, A. S. El-Azab, M. M. Alanazi, M. H. M. Al-Agamy, and A. A.-M. Abdel-Aziz, "Hirshfeld Surface, Molecular Docking Study, Spectroscopic Characterization and NLO Profile of 2-Methoxy-4,6-Diphenylnicotinonitrile," *ChemistrySelect* 4 (2019): 9857–70. doi: 10.1002/slct.201902391.
23. M. J. Frisch, Gaussian 09 *Revision B.01* (Wallingford CT: Gaussian, Inc, 2010).
24. A. D. Becke, "Density-Functional Thermochemistry. III. The Role of Exact Exchange," *The Journal of Chemical Physics* 98, no. 7 (1993): 5648–52.
25. C. Lee, W. Yang, and R. G. Parr, "Development of the Colle-Salvetti Correlation-Energy Formula into a Functional of the Electron Density," *Physical Review. B, Condensed Matter* 37, no. 2 (1988): 785–9.
26. D. Jacquemin, E. A. Perpète, I. Ciofini, and C. Adamo, "Accurate Simulation of Optical Properties in Dyes," *Accounts of Chemical Research* 42, no. 2 (2009): 326–34.
27. D. Jacquemin, J. Preat, V. Wathelet, M. Fontaine, and E. A. Perpète, "Thioindigo Dyes: Highly Accurate Visible Spectra with TD-DFT," *Journal of the American Chemical Society* 128, no. 6 (2006): 2072–83.
28. I. Ciofini, and C. Adamo, "Accurate Evaluation of Valence and Low-Lying Rydberg States with Standard Time-Dependent Density Functional Theory," *The Journal of Physical Chemistry A* 111, no. 25 (2007): 5549–56.
29. G. Gece, "The Use of Quantum Chemical Methods in Corrosion Inhibitor Studies," *Corrosion Science* 50, no. 11 (2008): 2981–92. doi: 10.1016/j.corsci.2008.08.043.
30. K. Fukui, "Role of Frontier Orbitals in Chemical Reactions," *Science (New York, NY)* 218, no. 4574 (1982): 747–54.
31. R. G. Parr, L. V. Szentpály, and S. Liu, "Electrophilicity Index," *Journal of the American Chemical Society* 121, no. 9 (1999): 1922–4.
32. A. D. Buckingham, "Permanent and Induced Molecular Momentsand Long-Range Intermolecular Forces," *Advances in Chemical Physics* 12 (1967): 107–40. doi: 10.1002/9780470143582.ch2.
33. E. D. Glendening, A. E. Reed, J. E. Carpenter, and F. Weinhold, *NBO Version 3.1* (Madison, WI: University of Wisconsin, 1998).
34. P. Politzer, P. R. Laurence, and K. Jayasuriya, "Structure-Activity Correlation in Mechanism Studies and Predictive Toxicology," *Environmental Health Perspectives* 61 (1985): 191–202.
35. C. Ho Choi, and M. Kertesz, "Conformational Information from Vibrational Spectra of Styrene, trans-Stilbene, and cis-Stilbene," *The Journal of Physical Chemistry A* 101, no. 20 (1997): 3823–31. no
36. R. G. Pearson, "Absolute Electronegativity and Hardness: Applications to Organic Chemistry," *The Journal of Organic Chemistry* 54, no. 6 (1989): 1423–30.
37. R. G. Parr, and R. G. Pearson, "Absolute Hardness: Companion Parameter to Absolute Electronegativity," *Journal of the American Chemical Society* 105, no. 26 (1983): 7512–6.
38. P. Geerlings, F. De. Proft, and W. Langenaeker, "Conceptual Density Functional Theory," *Chemical Reviews* 103, no. 5 (2003): 1793–8731873.
39. C. G. Zhan, J. A. Nichols, and D. A. Dixon, "Ionization Potential, Electron Affinity, Electronegativity, Hardness, and Electron Excitation Energy: Molecular Properties from Density Functional Theory Orbital Energies," *The Journal of Physical Chemistry A* 107, no. 20 (2003): 4184–95.
40. R. M. Parrish, E. G. Hohenstein, P. L. McMahon, and T. J. Martínez, "Quantum Computation of Electronic Transitions Using a Variational Quantum Eigensolver," *Physical Review Letters* 122, no. 23 (2019): 230401.
41. D. Jacquemin, and E. A. Perpète, "Ab Initio Calculations of the Colour of Closed-Ring Diarylethenes: TD-DFT Estimates for Molecular Switches," *Chemical Physics Letters* 429, no. 1–3 (2006): 147–52. doi: 10.1016/j.cplett.2006.08.028.
42. J. Preat, C. Michaux, A. Lewalle, E. A. Perpète, and D. Jacquemin, "Delocalisation in Conjugated Triazene Chromophores: Insights from Theory," *Chemical Physics Letters* 451, no. 1–3 (2008): 37–42. doi: 10.1016/j.cplett.2007.11.056.
43. D. Maric, and J. P. Burrows, "Application of a Gaussian Distribution Function to Describe Molecular UV-Visible Absorption Continua.1. Theory," *The Journal of Physical Chemistry* 100, no. 21 (1996): 8645–59.
44. D. Marić, J. N. Crowley, and J. P. Burrows, "Application of a Gaussian Distribution Function to Describe Molecular UV – Visible Absorption Continua. 2. The UV Spectra of RO2• Radicals," *The Journal of Physical Chemistry A* 101, no. 14 (1997): 2561–7.
45. É. A. G. Brémond, J. Kieffer, and C. Adamo, "A Reliable Method for Fitting TD-DFT Transitions to Experimental UV–Visible Spectra," *Journal of Molecular Structure: Theochem* 954, no. 1–3 (2010): 52–6. doi: 10.1016/j.theochem.2010.04.038.
46. G. Scalmani, and M. J. Frisch, "Continuous Surface Charge Polarizable Continuum Models of Solvation. I. General Formalism," *The Journal of Chemical Physics* 132, no. 11 (2010): 114110.
47. L. Sinha, O. Prasad, V. Narayan, and S. R. Shukla, "Raman, FT-IR Spectroscopic Analysis and First-Order Hyperpolarisability of 3-Benzoyl-5-Chlorouracil by First Principles," *Molecular Simulation* 37, no. 2 (2011): 153–63. doi: 10.1080/08927022.2010.533273.

48. D. F. V. Lewis, C. Ioannides, and D. V. Parke, "Interaction of a Series of Nitriles with the Alcohol-Inducible Isoform of P450: Computer Analysis of Structure—Activity Relationships," *Xenobiotica* 24, no. 5 (1994): 401–408.
49. B. Kosar, and C. Albayrak, "Spectroscopic Investigations and Quantum Chemical Computational Study of (E)-4-Methoxy-2-[(p-Tolylimino)Methyl]Phenol," *Spectrochimica Acta. Part A, Molecular and Biomolecular Spectroscopy* 78, no. 1 (2011): 160–7.
50. M. Nakano, H. Fujita, M. Takahata, and K. Yamaguchi, "Theoretical Study on Second Hyperpolarizabilities of Phenylacetylene Dendrimer: Toward an Understanding of Structure − Property Relation in NLO Responses of Fractal Antenna Dendrimers," *Journal of the American Chemical Society* 124, no. 32 (2002): 9648–55.
51. Y. X. Sun, Q. L. Hao, W. X. Wei, Z. X. Yu, L. D. Lu, X. Wang, and Y. S. Wang, "Experimental and Density Functional Studies on 4-(3,4-Dihydroxybenzylideneamino)Antipyrine,and 4-(2,3,4-Trihydroxybenzylideneamino) Antipyrine," *Journal of Molecular Structure: Theochem* 904, no. 1–3 (2009): 74–82. doi: 10.1016/j.theochem.2009.02.036.
52. Y. X. Sun, Q. L. Hao, W. X. Wei, Z. XueYu, L. D. Lu, X. Wang, and Y. S. Wang, "Experimental and Density Functional Studies on 4-(4-Cyanobenzylideneamino)Antipyrine," *Molecular Physics* 107, no. 3 (2009): 223–35.
53. C. Andraud, T. Brotin, C. Garcia, F. Pelle, P. Goldner, B. Bigot, and A. Collet, "Theoretical and Experimental Investigations of the Nonlinear Optical Properties of Vanillin, Polyenovanillin, and Bisvanillin Derivatives," *Journal of the American Chemical Society* 116, no. 5 (1994): 2094–102. no
54. V. M. Geskin, C. Lambert, and J. L. Brédas, "Origin of High Second- and Third-Order Nonlinear Optical Response in Ammonio/Borato Diphenylpolyene Zwitterions: The Remarkable Role of Polarized Aromatic Groups," *Journal of the American Chemical Society* 125, no. 50 (2003): 15651–8.
55. D. Sajan, H. Joe, V. S. Jayakumar, and J. Zaleski, "Structural and Electronic Contributions to Hyperpolarizability in Methyl p-Hydroxy Benzoate," *Journal of Molecular Structure* 785, no. 1–3 (2006): 43–53. doi: 10.1016/j.molstruc.2005.09.041.
56. H. S. Nalwa, and S. Miyata, *Nonlinear Optics of Organic Molecules andPolymers* (Boca Raton, FL: CRC Press, 1997).
57. A. B. Ahmed, H. Feki, Y. Abid, H. Boughzala, C. Minot, and A. Mlayah, "Crystal Structure, Vibrational Spectra and Theoretical Studies of L-Histidinium Dihydrogen Phosphate-Phosphoric Acid," *Journal of Molecular Structure* 920, no. 1–3 (2009): 1–7.
58. J. P. Abraham, D. Sajan, V. Shettigar, S. M. Dharmaprakash, I. Němec, I. Hubert Joe, and V. S. Jayakumar, "Efficient π-Electron Conjugated Push-Pull Nonlinear Optical Chromophore 1-(4-Methoxyphenyl)-3-(3,4-Dimethoxyphenyl)-2-Propen-1-One: A Vibrational Spectral Study," *Journal of Molecular Structure* 917, no. 1 (2009): 27–36. doi: 10.1016/j.molstruc.2008.06.031.
59. S. G. Sagdinc, and A. Esme, "Theoretical and Vibrational Studies of 4,5-Diphenyl-2-2 Oxazole Propionic Acid (Oxaprozin)," *Spectrochimica Acta Part A, Molecular and Biomolecular Spectroscopy* 75, no. 4 (2010): 1370–6. no
60. A. Ben Ahmed, H. Feki, Y. Abid, H. Boughzala, and C. Minot, "Crystal Studies, Vibrational Spectra and Non-Linear Optical Properties of l-Histidine Chloride Monohydrate," *Spectrochimica Acta Part A, Molecular and Biomolecular Spectroscopy* 75, no. 1 (2010): 293–8.
61. F. Wienhold, and C. R. Landis, *Valency and Bonding-A Natural Bond Orbital Donor-Acceptor Perspective* (New York, NY: Cambridge University Press, 2005).
62. P. Politzer, and J. S. Murray, "The Fundamental Nature and Role of the Electrostatic Potential in Atoms and Molecules," *Theoretical Chemistry Accounts* 108, no. 3 (2002): 134–42.
63. L. F. Javier, L. J. Maria, and M. Orozco, "Electrostatic Interactions of a Solute with a Continuum. A Direct Utilization of ab Initio Molecular Potentials for the Prevision of Solvent Effects," *Theoretical Chemistry Accounts* 103 (2000): 343–5. doi: 10.1007/s002149900013.
64. I. V. Kochikov, Yu I. Tarasov, V. P. Spiridonov, G. M. Kuramshina, D. W. H. Rankin, A. S. Saakjan, and A. G. Yagola, "The Equilibrium Structure of Thiophene by the Combined Use of Electron Diffraction, Vibrational Spectroscopy and Microwave Spectroscopy Guided by Theoretical Calculations," *Journal of Molecular Structure* 567–568 (2001): 29–40.
65. J. Bentley, "Determination of Electronic Energies from Experimental Electron Densities," *The Journal of Chemical Physics* 70, no. 1 (1979): 159.
66. M. Fink, and R. A. Bonhan, "Electrostatic Potential of Free Molecules Derived from Electron Diffraction Results," *Chemical Applications of Atomic and Molecular Potentials* (1981): 93–122.
67. R. G. Pearson, "Absolute Electronegativity and Hardness Correlated with Molecular Orbital Theory," *Proceedings of the National Academy of Sciences of the United States of America* 83, no. 22 (1986): 8440–1.

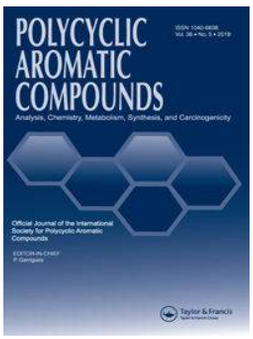

Polycyclic Aromatic Compounds

ISSN: (Print) (Online) Journal homepage: https://www.tandfonline.com/loi/gpol20

Experimental and DFT Quantum Chemical Studies on Structural, Vibrational and Molecular Properties of Some Substituted 4-Phenylphenols

L. Ravindranath, K. Srishailam & B. Venkatram Reddy

To cite this article: L. Ravindranath, K. Srishailam & B. Venkatram Reddy (2022): Experimental and DFT Quantum Chemical Studies on Structural, Vibrational and Molecular Properties of Some Substituted 4-Phenylphenols, Polycyclic Aromatic Compounds, DOI: 10.1080/10406638.2022.2161584

To link to this article: https://doi.org/10.1080/10406638.2022.2161584

POLYCYCLIC AROMATIC COMPOUNDS
https://doi.org/10.1080/10406638.2022.2161584

Taylor & Francis
Taylor & Francis Group

Experimental and DFT Quantum Chemical Studies on Structural, Vibrational and Molecular Properties of Some Substituted 4-Phenylphenols

L. Ravindranath[a,b], K. Srishailam[c], and B. Venkatram Reddy[b]

[a]Department of Physics, Malla Reddy Engineering College(a), Hyderabad, India; [b]Department of Physics, Kakatiya University, Warangal, India; [c]Department of Physics, SR University, Warangal, India

ABSTRACT

Fourier Transform infrared spectra (4000–400 cm^{-1}) and Fourier Transform Raman spectra (4000–50 cm^{-1}) were recorded for 2-chloro-4-phenylphenol (CP); 2-nitro-4-phenylphenol (NP); and 2-amino-4-phenylphenol (AP). ^{1}H and ^{13}C NMR spectra, along with UV-Vis spectra of the three samples were also measured. Quantum chemical calculations, at the level of DFT/B3LYP/6-311++G(d,p) theory were implemented to study their ground state geometry, vibrational wave numbers, infrared and Raman intensities, ^{1}H and ^{13}C NMR spectra, frontier molecular orbital parameters, NLO behavior, NBO properties, thermodynamic quantities, rotational constants and MESP behavior. TD-DFT variant was employed to simulate electronic transitions of these molecules. Observed and calculated vibrational frequencies agreed with an rms error 7.44, 8.98 and 6.97 cm^{-1}, the corresponding RMSD values being 7.09, 9.39 and 6.59 cm^{-1} for CP, NP and AP, respectively. Experimental chemical shifts concurred, with their theoretical counterparts, with RMSD value, 0.19, 0.29 and 0.56 ppm for ^{1}H NMR; and 6.34, 6.28 and 5.39 ppm for ^{13}C NMR, respectively, in CP, NP and AP. This kind of agreement was also true for absorption maxima (λ_{max}) of their electronic transitions in solution form. Frontier molecular orbitals were found useful to understand origin of electronic transition maxima and chemical reactivity of the three molecules which was supported by NBO analyses. The computations showed that the three molecules were potentially good for developing NLO materials. MESP investigations showed that the most reactive sites are at oxygen atoms in the three molecules. Moreover, we also made an attempt to understand the effect of deactivating (Cl, NO_2) and activating (NH_2) groups on certain properties of the three molecules. Presence of intra-molecular hydrogen bond was predicted in CP, NP and AP.

ARTICLE HISTORY
Received 27 September 2022
Accepted 16 December 2022

KEYWORDS
4-Phenylphenol; DFT; vibrational spectra; NMR spectra; NBO analysis

CONTACT B. Venkatram Reddy bvreddy67@yahoo.com Department of Physics, Kakatiya University, Warangal, Telangana 506009, India

Supplemental data for this article can be accessed online at https://doi.org/10.1080/10406638.2022.2161584

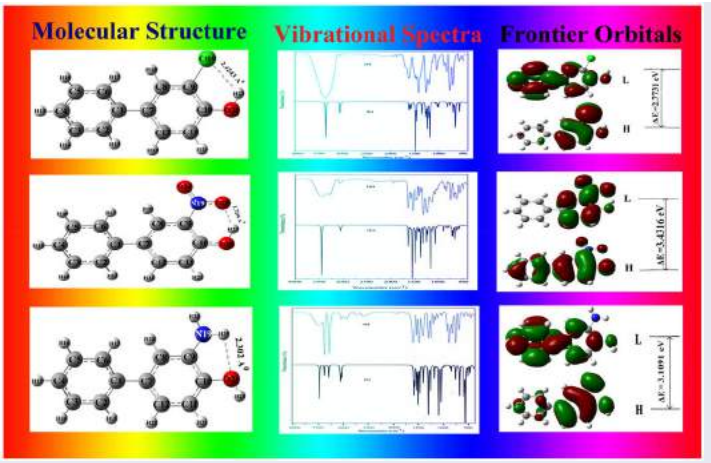

HIGHLIGHTS

- Structure parameters for CP, NP and AP agree well with their experimental counterparts.
- Computed and measured frequencies, chemical shifts and electronic transitions agree acceptably.
- Effect of activating and deactivating groups is studied.
- CP, NP and AP are potential NLO materials.
- Intra-molecular charge transfer (ICT) is demonstrated using NBO analysis.

1. Introduction

We know that 4-phenylphenol or 4-hydroxyphenyl, a derivative of the representative molecule biphenyl (BP) can be considered as a basic unit for its chloro-, nitro-, and amino derivatives. In this article we considered three such substituted hydroxybiphenyls. These are 2-chloro-4-phenylphenol (CP); 2-nitro-4-phenylphenol (NP); and 2-amino-4-phenylphenol (AP). Nitrophenylphenols were known for their herbicidal activity, which showed significant increase with progressive substitution of nitro groups on non-phenolic ring.[1] Extension of these investigations to chlorophenylphenols revealed that the herbicidal characteristics were influenced remarkably with increasing number of chlorine atoms on the phenylphenol ring.[2] Further, chloro derivatives of 4-phenylphenol along with their basic value were found highly effective fungistatic agents against *Aspergillus niger* and *Piricularia oryzae*, arising from their reactivity, steric repulsion, permeability and metabolic simulation.[3] Miticidal activity of phenylphenols was correlated with their molecular structure,[4] which was found sensitive to the position of substitution and number of substituents such as chlorine atoms, nitro groups and amino moieties.[5–7] Several antimicrobial agents found in biosolids were identified as derivatives of chlorinated phenylphenols.[8] X-ray structure of 4-hydroxybiphenyl is also available.[9] From existing literature we find that the earlier studies were confined mainly to exploring biological activity, comprising of antimicrobial,[10,11] antiproliferative,[12] estrogenic,[13] antioxidant,[14] metabolic[15,16] and antimalarial[17] properties, of CP, NP, AP and their derivatives. Molecular structure, either experimental or theoretical, is not reported in literature for CP, NP and AP. This is also the case with normal coordinate analysis and other important molecular parameters for the three molecules. Against this backdrop we undertook the work reported in this article with the objectives: (i) to investigate molecular structure of CP, NP and AP in gas phase by employing DFT/B3LYP/6-311++G(d,p) formalism, (ii) to perform normal coordinate analysis making use of measured infrared and Raman spectra, evaluating general valence force field in the process, in order to assign all

observed vibrational fundamentals unambiguously, (iii) to record ^{1}H and ^{13}C NMR spectra and compare them with corresponding theoretical counterparts, (iv) to use frontier molecular orbitals to help assign observed electronic spectra and to gain some insight into chemical reactivity, (v) to evaluate nonlinear optical (NLO) parameters, in order to examine utility of the compounds for nonlinear applications, (vi) to make natural bond orbital analyses, so as to understand origin of the stabilizing energy, (vii) to compute molecular electrostatic surface potentials, in order to identify reactive sites, and (viii) to estimate thermodynamic quantities for future use. Further, we wish to examine the effect of presence of activating or electron donating (NH_2) and deactivating or electron withdrawing (NO_2 and Cl) groups on the phenolic ring of 4-phenylphenol on certain properties of CP, NP and AP. It is to be stated that the effect of activating and deactivating moieties on molecular properties was reported earlier by Castillo et al.,[18] for a different molecule. In this way, this article constitutes a significant addition to the existing knowledge regarding CP, NP and AP.

2. Experimental methods

Samples of CP and AP were purchased from TCI chemical company, Japan, whereas NP was obtained from Sigma Aldrich Chemical Company, USA as high purity chemicals. Hence, they were used as received, without further purification, for spectral measurements. The samples were solids at room temperature. Therefore, their FTIR spectra were measured by diluting the samples in KBr pellet, using JASCO FTIR-4200 Model spectrometer in the 4000–400 cm^{-1} region with resolution ±0.5 cm^{-1}. The FT Raman spectra of the three compounds were recorded employing BRUKER RFS27 model interferometer accessory in the 4000–50 cm^{-1} strokes region with ±2 cm^{-1} resolution using with the exciting radiation at 1064 nm provided by Nd-YAG laser operating at 200 mW power. ^{1}H and ^{13}C NMR spectra were obtained with the help of Bruker's AV NEO Spectrometer at 400 MHz in solution of deuterated chloroform ($CDCl_3$) for CP and NP; and dimethylsulfoxide-d_6 (DMSO-d_6) was the solvent for AP. The chemical shifts were obtained in ppm units using TMS as internal standard. The UV-Visible spectra of the three samples were measured with Jasco UV-670 spectrophotometer in the range 500–190 nm using quartz cell of 1 cm path length in a solution of $CDCl_3$ for CP and NP, whereas the same measurement for AP was made in solution of DMSO-d_6. Purity of all chemicals and reagents was of spectro grade. All spectral measurements were made at room temperature.

3. Computational considerations

Quantum chemical calculations were carried out by make use of density functional theory (DFT) method. Becke's non-local gradient approach with three parameter hybrid density exchange functional (B3)[19] in association with Lee, Young and Parr gradient corrected correlation functional (LYP)[20] in combination with triple zeta split-valence basis set, 6-311++G(d,p) was employed for computations using Gaussian 09 software.[21] The geometry optimization is generally done by initiating the starting structure of a given molecule. But both experimental and theoretical structures are not available for CP, NP and AP. In such cases, it is customary to use Gauss view[22] to generate an initial structure of the given molecule. Hence, the initial structure parameters, viz, bond lengths, bond angles and dihedral angles for CP, NP and AP were borrowed from Gauss view[22] library, except the dihedral angles associated with C–C inter-ring bond, phenolic C–O bond in the three molecules, and C–N carbon-nitrogen bond in NP and AP, as the database available with gauss view[22] is not sufficient to provide reliable values for these dihedrals. For instance, according to gauss view,[22] dihedral angle around C–C inter-ring bond is 0° for the three molecules, whereas its experimental value for the representative molecule, biphenyl is 44.4°, as determined from electron diffraction experiments.[23] Hence, the torsion angle around C–C inter-ring bond was taken from biphenyl[23] for the three molecules, whereas that associated with phenolic

C–O bond was transferred from experimental value reported for 4-methoxy-3-nitrobiphenyl.[24] Similarly, the torsion angle for C–N bond in AP was borrowed from experimental value available for 3, 3′, 4, 4′-tetraaminobiphenyl,[25] while that corresponding to the C–N bond was taken from 4-methoxy-3-nitrobiphenyl.[24] The initial structures obtained in this way were subjected to rigorous geometry optimization by relaxing all structure parameters simultaneously; allowing the process to get terminated on achieving default convergence criterion as defined in Gaussian 09 program suit.[21] This procedure resulted in non-planar structure of C_1 symmetry for CP, NP and AP. Absence of negative frequencies stands as testimony for the reliability of above result for the optimized structures. It is to be noted that the calculations were performed on a single molecule, each of CP, NP and AP, in the gas phase.

Using C_1 structure as equilibrium geometry for CP, NP and AP, the harmonic vibrational frequencies, cartesian force constants and dipole moment along with its derivatives were evaluated. Further computations were carried out using the equilibrium geometry and resultant final force constants. Employing MOLVIB 7.0 Program,[26,27] the force constants were transformed into a non-redundant set of 63, 69 and 69 natural internal coordinates for CP, NP and AP, respectively. These were constructed from redundant internal coordinates following the procedure suggested by Fogarasi et al.[28] Scaling of force constants was made using least-square refinement procedure suggested by Pulay and Fogarasi[29] and Arenas et al.[30] so as to achieve the best possible fit between observed and calculated wave numbers for these molecules. In order to characterize the normal modes of vibration, the fundamental frequencies, corresponding eigenvectors, potential energy distribution (PED), relative IR absorption intensities[31] and relative Raman scattering intensities[32,33] were computed. To compare experimental IR and Raman spectra with their theoretical counterparts for CP, NP and AP, pure Lorentzian band shape with full width at half maximum (FWHM) of 10 cm^{-1} was used in the simulation process.

NMR spectra (^1H and ^{13}C Chemical shifts) were computed employing gauge-independent or gauge-including atomic orbital (GIAO) approach[34] with DFT/B3LYP/6-311++G(d,p) method. Resulting simulated NMR spectra of the three molecules were compared with corresponding observed spectra by making linear regression plots. To simulate electronic absorption spectra of CP, NP and AP, time-dependent density functional theory (TD-DFT) was used employing B3LYP/6-311++G(d,p) formalism. Calculated values of absorption maxima (λ_{max}) were identified with their corresponding observed values in UV–Vis spectra. Solvent effects, in both NMR and UV-Vis spectra were taken care of by the Polarizable Continuum Model (PCM) using the integral equation formalism (IEF-PCM) variant[35] integrated into Gaussian 09 software package.

Using frontier molecular orbital energies, comprising of the highest occupied molecular orbital (HOMO) and the lowest unoccupied molecular orbital (LUMO), the values for molecular electronic properties of CP, NP and AP such as ionization potential (I), electron affinity (A), global hardness (η), chemical potential (μ), and global electrophilicity power (ω) were determined using well-known expressions.[36–38]

NLO behavior of the molecules CP, NP and AP was studied by computing the total molecular dipole moment (μ_t) and its components, total molecular polarizability (α_t) and its components, anisotropy of polarizability ($\Delta\alpha$), and first order static hyperpolarizability (β_t) using density functional theory following Buckingham's definitions[39] and DFT/B3LYP/6-311++G(d,p) level of theory. Similarly, thermodynamic parameters and rotational constants were determined and the molecular electrostatic surface potential (MESP) was investigated by mapping of molecular electrostatic potential.

Natural bond orbital (NBO) analysis was performed using NBO 3.1 program[40] as implemented in the Gaussian 09 package with the 6-311++G(d,p) basis set, in order to understand various second order interactions between the filled orbitals of one subsystem and vacant orbitals of another subsystem using second-order perturbation theory as revealed by Fock matrix analysis. The stabilization energy associated with the hyper conjugation is evaluated using the equation given by Glendening et al.[40]

4. Results and discussion

4.1. Molecular geometry in the ground state and intra-molecular hydrogen bond

Ground state molecular geometry of CP, NP and AP is dictated by two opposing effects. These are:

1. The π-electron delocalization between the two phenyl rings favors a co-planar structure. This is further strengthened by participation of lone pair electrons from oxygen atom of activating OH moiety in the three molecules. In addition, lone pairs from deactivating chlorine atom in CP; corresponding pairs from two oxygen atoms and one nitrogen atom from deactivating nitro group in NP, along with similar electrons associated with nitrogen atom in activating amino moiety in AP take part in stabilizing the planar structure, and
2. The steric repulsion of
   - two pairs of ortho hydrogens, neighboring the inter-ring C–C bond;
   - ortho hydrogen and hydroxyl group,
   - ortho hydrogen on X, where X is Cl, NO_2 and NH_2 in CP, NP and AP, respectively, and
   - ortho hydroxyl moiety and hence X,

favors a non-planar structure, in order to minimize steric effects. The most stable rotamer of either CP or NP or AP is a result of equilibrium between these two opposing effects. Relative contributions of the above effects determine the dihedral angle around inter-ring C–C bond / phenolic C–O bond / nitro C–N bond / amino C–N bond. This sensitive balance is greatly influenced by two factors:

i. the amount of correlation energy that the theoretical formalism can accommodate, and
ii. The size of basis set used for the computations.[41–43]

Initial values of dihedral angles associated with inter-ring C–C bond, phenolic C–O bond, nitro C–N bond and amino C–N bond were transferred from related molecules[23–25] as already stated. These were (44.4° and 178.07°) for CP (note that there is no C–N bond in CP); (44.4°, 178.07° and 27.5°) for NP; and (44.4°, 178.07° and 26°) for AP. They were refined to (40.56°, and 0.093°) for CP; (39.720°, 0.520° and 0.951°) for NP and (40.29°, 176.71° and 26.74°) for AP, on optimization.

The torsional angles of C–C inter-ring bond at 40.56°, 39.72° and 40.29° for CP, NP and AP, respectively, are close to their initial value borrowed from BP at 44.4° determined from electron diffraction experiments.[23] They also agree well with that of BP at 42° obtained from DFT/B3LYP/6-311++G(d,p) calculations,[44] which is the same formalism used in the present article. This is expected as the steric repulsion arises from the same set of two pairs of ortho hydrogens neighboring the C–C inter-ring bond in the four molecules BP, CP, NP and AP. Further, occurrence of twist angles of C–C inter-ring bond at lower values in comparison with that of BP should be attributed to the presence of activating OH and NH_2 groups and deactivating Cl and NO_2 species in the molecules under consideration. The difference between twist angles of C–C inter-ring bond for CP and NP is the difference between 40.56° and 39.72°, which is 0.84°. Justification of this difference is not attempted, as it is significantly less than the RMSD value for dihedral angles reported in this article around 2° (see Table 1). The same explanation applies equally well for similar difference between same quantities for CP and AP; and NP and AP. Optimized values of torsion angles around phenolic C–O bond are near 0.093°, 0.520° and 176.71° for CP, NP and AP, respectively. We assumed *trans* position for hydrogen atom of hydroxyl moiety with respect to amino group nitrogen atom in AP, initially (see Figure 1). If we were to start with *cis* position for the hydrogen atom, the separation between this atom and the nearest amino hydrogen atom

Table 1. Experimental and DFT/B3LYP/6-311 ++ G(d,p) optimized geometric parameters of CP, NP and AP.

	Calculated value			Experimental value	
Geometric parameter	CP	NP	AP	Ref.[9]	Ref.[24]
Bond lengths (in Å)					
C1–C2	1.403	1.403	1.403	1.389	1.381
C2–C3	1.392	1.392	1.392	1.392	1.376
C3–C4	1.394	1.394	1.394	1.374	1.358
C4–C5	1.394	1.394	1.394	1.359	1.363
C5–C6	1.392	1.392	1.392	1.387	1.377
C6–C1	1.403	1.402	1.403	1.389	1.383
C1–C7	1.485	1.484	1.485	1.488	1.473
C7–C8	1.400	1.388	1.402	1.399	1.387
C8–C9	1.388	1.400	1.396	1.386	1.370
C9–C10	1.398	1.414	1.407	1.369	1.398
C10–C11	1.396	1.403	1.387	1.359	1.385
C11–C12	1.387	1.380	1.394	1.386	1.370
C12–C7	1.404	1.413	1.399	1.383	1.384
C2–H13	1.084	1.084	1.084	*	0.930
C3–H14	1.084	1.084	1.085	*	0.930
C4–H15	1.084	1.084	1.084	*	0.930
C5–H16	1.084	1.084	1.085	*	0.930
C6–H17	1.084	1.084	1.084	*	0.930
C8–H18	1.082	1.081	1.085	*	0.930
C9–Cl19	1.766	–	–	1.401[a]	–
C9–N19	–	1.453	–	*	1.459
C9–N19	–	–	1.394	*	1.40[b]
C10–O20	1.357	1.337	1.378	1.385	1.336
C11–H21	1.083	1.083	1.086	*	0.930
C12–H22	1.083	1.084	1.083	*	0.930
O20–H23	0.967	0.982	0.962	0.968[a]	–
N19–O24	–	1.219	–	*	1.209
N19–O25	–	1.248	–	*	1.215
N19–H24	–	–	1.009	0.9[b]	–
N19–H25	–	–	1.009	0.9[b]	–
RMSD	0.094	0.088	0.094		
Bond angle (in °)					
C1–C2–C3	120.91	120.84	121.03	121.4	121.3
C2–C3–C4	120.28	120.24	120.30	120.7	120.8
C3–C4–C5	119.44	119.51	119.36	118.7	119.1
C4–C5–C6	120.27	120.26	120.30	120.9	120.7
C5–C6–C1	120.92	120.82	121.03	121.8	121.1
C6–C1–C2	118.17	118.32	117.99	116.4	117.07
C7–C8–C9	120.43	121.03	122.09	121.3	120.92
C8–C9–C10	121.69	121.37	120.50	120.4	121.36
C9–C10–C11	117.96	117.17	118.14	119.7	116.20
C10–C11–C12	120.58	120.99	120.57	119.9	121.33
C11–C12–C7	121.53	122.01	120.25	121.8	122.37
C12–C7–C8	117.80	117.42	118.43	116.8	116.83
C2–C1–C7	120.82	120.77	120.94	*	120.93
C6–C1–C7	121.00	120.90	121.07	*	121.99
C8–C7–C1	120.78	121.36	120.55	*	121.15
C12–C7–C1	121.41	121.22	121.01	*	122.02
C1–C2–H13	119.53	119.70	119.37	*	119.4
C3–C2–H13	119.54	119.43	119.58	*	119.4
C2–C3–H14	119.65	119.67	119.65	*	119.6
C4–C3–H14	120.06	120.09	120.04	*	119.6
C3–C4–H15	120.28	120.24	120.32	*	120.5
C5–C4–H15	120.28	120.24	120.31	*	120.5
C4–C5–H16	120.07	120.09	120.04	*	119.7
C6–C5–H16	119.66	119.65	119.67	*	119.7
C5–C6–H17	119.52	119.53	119.54	*	119.4
C1–C6–H17	119.54	119.63	119.40	*	119.4
C7–C8–H18	120.50	121.17	119.47	*	119.5
C9–C8–H18	119.05	117.79	118.42	*	119.5

(*continued*)

Table 1. Continued.

	Calculated value			Experimental value	
Geometric parameter	CP	NP	AP	Ref.[9]	Ref.[24]
C8–C9–Cl19	119.97	–	–	119.50[a]	–
C10–C9–Cl19	118.34	–	–	119.10[a]	–
C8–C9–N19	–	117.89	122.38	–	116.53
C10–C9–N19	–	120.73	119.48	–	121.11
C9–C10–O20	123.45	124.83	115.94	*	124.48
C11–C10–O20	118.58	117.99	123.56	*	119.30
C10–C11–H21	118.21	117.65	119.45	*	119.3
C12–C11–H21	121.20	121.36	119.97	*	119.3
C11–C12–H22	118.97	118.79	119.51	*	118.8
C7–C12–H22	119.48	119.18	120.20	*	118.8
C10–O20–H23	109.27	107.30	109.82	*	–
C9–N19–O24	–	119.37	–	*	119.17
C9–N19–O25	–	117.88	–	*	117.51
C9–N19–H24	–	–	115.76	109.9[b]	–
C9–N19–H25	–	–	114.94	104.3[b]	–
RMSD	0.722	0.786	0.823		
Dihedral angle (in °)					
C1 – C2 – C3 – C4	−0.147	−0.024	−0.157	*	−0.3
C2 – C3 – C4 – C5	0.075	0.019	0.095	*	1.0
C3 – C4 – C5 – C6	0.065	0.038	0.057	*	1.6
C4 – C5 – C6 – C1	−0.135	−0.092	−0.150	*	−1.0
C5 – C6 – C1 – C2	0.063	0.086	0.089	*	0.3
C6 – C1 – C2 – C3	0.077	0.029	0.065	*	0.9
C7 – C8 – C9 – C10	−0.188	−0.437	−0.016	*	−0.7
C8 – C9 – C10 – C11	0.177	0.421	0.128	*	0.7
C9 – C10 – C11 – C12	−0.101	−0.190	−0.188	*	−0.3
C10 – C11 – C12 – C7	0.039	0.033	0.099	*	0.0
C11 – C12 – C7 – C8	−0.045	−0.033	−0.044	*	0.0
C12 – C7 – C8 – C9	0.117	0.198	0.102	*	0.4
C12 – C7 – C1 – C6	−139.44	−140.33	−139.46	*	−144.19
C8 – C7 – C1 – C6	40.56	39.72	40.29	44.4[b]	36.2
C12 – C7 – C1 – C2	40.53	39.67	40.61	*	36.6
C8 – C7 – C1 – C2	−139.46	−140.28	−139.78	*	−143.06
C6 – C1 – C2 – H13	−178.42	−178.43	−178.48	*	*
C4 – C3 – C2 – H13	178.35	178.38	178.39	*	*
C1 – C2 – C3 – H14	−179.51	−179.42	−179.53	*	*
C5 – C4 – C3 – H14	179.43	179.41	179.47	*	*
C2 – C3 – C4 – H15	179.95	179.98	179.92	*	*
C6 – C5 – C4 – H15	−179.91	−179.92	−179.93	*	*
C3 – C4 – C5 – H16	179.44	179.47	179.40	*	*
C1 – C6 – C5 – H16	−179.51	−179.53	−179.49	*	*
C4 – C5 – C6 – H17	178.33	178.46	178.30	*	*
C2 – C1 – C6 – H17	−178.40	−178.46	−178.36	*	*
C12 – C7 – C8 – H18	−178.40	−178.58	−178.69	*	*
C10 – C9 – C8 – H18	178.35	178.39	178.62	*	*
C7 – C8 – C9 – Cl19	−179.50	–	–	*	*
C11 – C10 – C9 – Cl19	179.50	–	–	*	*
C7 – C8 – C9 – N19	–	−179.75	−177.92	*	−179.67
C11 – C10 – C9 – N19	–	179.71	177.84	*	179.73
C8 – C9 – C10 – O20	−179.90	−179.81	−179.41	*	*
C12 – C11 – C10 – O20	179.98	179.97	179.31	*	*
C9 – C10 – C11 – H21	179.26	179.18	179.36	*	*
C7 – C12 – C11 – H21	−179.31	−179.38	−179.45	*	*
C10 – C11 – C12 – H22	178.54	178.69	178.37	*	*
C8 – C7 – C12 – H22	−178.54	−178.69	178.21	*	*
C8 – C9 – N19 – O24	–	0.951	–	*	27.5
C10 – C9 – N19 – O24	–	−179.73	–		−152.12
C8 – C9 – N19 – O25	–	−179.20	–	*	−149.80
C10 – C9 – N19 – O25	–	0.115	–		30.6
C8 – C9 – N19 – H24	–	–	26.74	26.9[b]	*
C10 – C9 – N19 – H24			155.37		*

(*continued*)

Table 1. Continued.

	Calculated value			Experimental value	
Geometric parameter	CP	NP	AP	Ref.[9]	Ref.[24]
C8 – C9 – N19 – H25	–	–	161.85	*	*
C10 – C9 – N19 – H25			20.27	*	*
C9 – C10 – O20 – H23[c]	0.093	0.520	176.71	*	178.07
C11 – C10 – O20 – H23[d]	179.99	179.71	2.81	*	*
RMSD	2.108	1.815	2.086		

Bifurcated intramolecular hydrogen bond geometry (bond length in Ð; bond and dihedral angles in degrees) for CP, NP, and AP

Molecule	DH···A	D—H	H···A	D···A	∠D—H···A	∠D—H···A—X[e]
CP	O20–H23···Cl19	0.967	2.424	3.014	119.04	0.50
NP	O20–H23···O25	0.982	1.725	2.575	142.71	0.53
AP	N19–H25···O20	1.010	2.302	2.695	101.64	165.82

–: Not relevant; *: Not available. a: from reference 44. b: Experimental value from reference 25. c: *cis* angle in (CP and NP) and trans angle in AP. d: *trans* angle in (CP and NP) and cis angle in CP. e: X = C9 in CP, N19 in NP, and H23 in AP.

being short at 1.5 Å could have pushed hydroxyl hydrogen atom into the trans position due to strong steric repulsion between the hydrogen atoms under consideration. In fact geometry optimization confirmed our assumption. This explains the agreement of initial value at 178.07° and final value near 176.71° for AP. However, the corresponding values, 0.093° and 0.520° for CP and NP, respectively are not comparable to their initial value at 178.07°, which is transferred from 4-methoxy-3-nitrobiphenyl.[24] During the optimization it was assumed that the hydrogen atom of hydroxyl moiety is in *trans* position with respect to the nitrogen atom of the nitro group in NP, and with respect to the chlorine atom in CP as in AP. In this position the separation between the hydrogen atom of hydroxyl group and the nearest hydrogen atom of the phenyl ring is 2.05 Å and 2.14 Å in NP and CP, respectively. Steric repulsion, being strong enough to negate attraction due to formation of intra-molecular hydrogen bond between these hydrogen pairs pushes the hydrogen atom of the hydroxyl moiety into the *cis* position in both the molecules NP and CP (see Figure 1). It is to be noted, that the *trans* dihedral angle and the *cis* dihedral angle for a given bond in a molecule are mutually supplementary. Hence, initial value for dihedral angle for NP and CP can be obtained by subtracting *trans* dihedral angle 178.07°, taken from reference number 24, from 180°. This comes out to be 1.93°, which compares reasonably well with final values at 0.520° and 0.093° for NP and CP, respectively. Thus, the seemingly absurd values can be explained. The optimized value of torsion angle around nitro C–N bond in NP is at 0.951°, whereas its initial value borrowed from 4-methoxy-3-nitrobiphenyl[24] is 27.5°. Steric repulsion is the cause for this significant difference between the initial and optimized value. The steric repulsion exerted by the bulky methoxy group on the adjacent nitro moiety in 4-methoxy-3-nitrobiphenyl is considerably higher than that exerted by relatively small hydroxyl molecular fragment on the nitro group in NP, making the dihedral angle in the former molecule is significantly greater than the corresponding angle in the latter molecule. Initial value of amino C–N bond at 26° taken from 3,3′,4,4′-tetra amino biphenyl[25] in AP agrees nicely with its optimized value near 26.74°.

Optimized molecular geometries generated as a result of solving self-consistent field equations for CP, NP and AP are shown in Figure 1, along with numbering of atoms. Corresponding structure data consisting of bond lengths, bond angles and dihedral angles for the molecules are presented in Table 1. This table also contains information about intra-molecular hydrogen bond present in CP, NP and AP. The data regarding structure parameters are compared with corresponding experimental values for 4-hydroxybiphenyl[9] and 4-methoxy-3-nitrobiphenyl[24] in the same table, as experimental structure is not available for CP, NP and AP. It can be seen from Table 1 that the RMSD values for bond lengths, bond angles and dihedral angles are (0.094 Å,

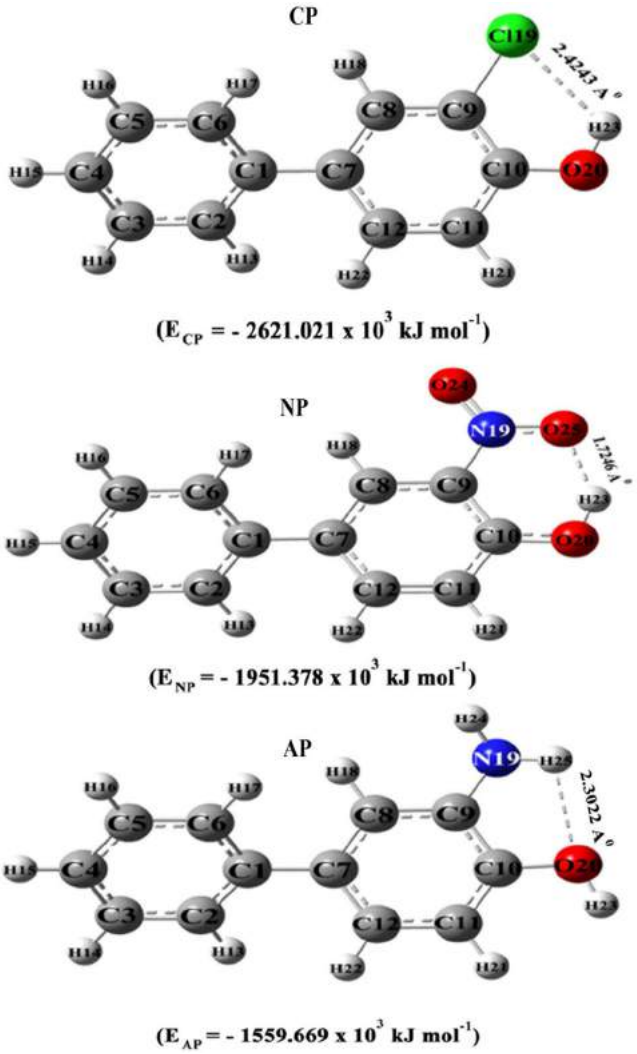

Figure 1. Optimized molecular structure of CP, NP and AP along with numbering of atoms and minimum energy.

0.088 Å and 0.094 Å); (0.722°, 0.786° and 0.823°) and (2.108°, 1.815° and 2.086°) for CP, NP and AP, respectively. From Table 1, it is evident that the theoretical structure parameters for CP, NP and AP are close to their corresponding experimental values in related molecules.[9,24,25,44] For example, as per the calculations made for NP, the average value of intra-ring C–C bond length is 1.396 Å; the mean value of nitro N–O bond is 1.235 Å; inter-ring C–C bond measures 1.484 Å; phenolic C–O bond spans 1.337 Å; and nitro C–N bond is estimated at 1.453 Å. They concur nicely with their corresponding x-ray values for 4-methoxy-3-nitrobiphenyl[24] near 1.378 Å; 1.212 Å; 1.473 Å; 1.336 Å; and 1.459 Å, respectively. Theoretical value for each C–H bond length is invariably less than their corresponding experimental x-ray values, as listed in Table 1. This systematic deviation is attributable to the inherent inability of x-ray methods to locate exact position of the hydrogen atoms. The reason is, the electron cloud surrounding the hydrogen atom responsible for x-ray scattering is diffuse, as it mainly arises from the sole valence electron of the hydrogen atom resulting in poor scattering and consequent uncertainty in the position of hydrogen atom.

From Table 1, we see that the amino C–N bond length in AP at 1.394 Å is considerably smaller than that of nitro C–N bond length in NP near 1.453 Å. Since, the nitro group, being a deactivating moiety, withdraws electron charge from the ring system, accumulating it across its C–N bond, there by weakening it due to increased repulsion between the existing electronic charge and presently accumulated negative charge with consequent lengthening of the bond, whereas the amino group, being an activating species, donates lone pair on its nitrogen atom to the ring system decreasing electron density across its C–N bond, which manifests itself in strengthening it, with subsequent shortening of the C–N bond.

There are three angles around carbon atom where nitro group is substituted and three more angles around carbon atom to which hydroxyl moiety is attached, which need to be mentioned here, in NP. These are: ∠C8C9C10, ∠C8C9N19, ∠C10C9N19, ∠C9C10C11, ∠C9C10O20, and ∠C11C10O20 having theoretical values at 121.37°, 117.89°, 120.73°, 117.17°, 124.83°, and 117.99°, respectively (see Figure 1 and Table 1). The experimental x-ray values for their corresponding angles in 4-methoxy-3-nitrobiphenyl are near 121.36°, 116.53°, 121.11°, 116.20°, 124.48°, and 119.30°, respectively. Hence, the theoretical values obtained in the investigation can be considered as in good agreement with experimental values.

Further, the chlorine atom of CN is located in the plane of phenolic ring, whereas deviation of the nitro group of NP from coplanarity with the phenolic ring is insignificant, while the non-coplanarity of the amino group of AP from the phenolic ring plane is significant. This variation resulted is due to the steric repulsion. The amount of steric repulsion exerted on chlorine atom of CP, nitro group of NP, and amino group of AP is the same, as it arises from the same set of nearest hydrogen atom (H18, see Figure 1) and the hydroxyl moiety in the three molecules. This steric repulsive force is perfectly balanced by the chlorine atom of CP, due to its considerable mass, retaining its position in the phenolic ring plane, whereas the nitro group of NP being less in mass in comparison with that of chlorine atom of CP gets slightly displaced from the phenolic ring plane, while the amino group being the lightest of the three substituents (–Cl, $–NO_2$ and $–NH_2$) undergoes significant twist around amino C–N bond in an effort to confer the steric effect effectively.

Present calculations predict formation of intra-molecular hydrogen bond in CP, NP and AP. This bond is manifested between chlorine atom and hydroxyl hydrogen atom in CP; between oxygen atom of the nitro group and adjacent hydroxyl hydrogen atom in NP; and hydroxyl oxygen atom and the nearest hydrogen atom of the amino moiety. The relevant hydrogen bonds are H23···Cl19, H23···O25, and H25···O20 having lengths 2.424 Å, 1.725 Å, and 2.302 Å in CP, NP, and AP, respectively.

4.2. Vibrational assignments

Geometry optimization described in Section 3 showed that the molecules of CP, NP and AP were non-planar with C_1 symmetry in the ground state. CP consists of 23 atoms, whereas this number is 25 for NP and AP. Hence, the number of vibrational fundamentals for CP is 63, whereas the same parameter for NP and AP is 69 each, according to the formula (3N-6) for a nonlinear molecule, where N is the number of atoms in the molecule. All these fundamental vibrations in the three molecules with C_1 symmetry belong to a-species and are active in both infrared and Raman spectra.

Observed infrared and Raman frequencies, corresponding un-scaled and scaled frequencies computed by theory, predicated IR and Raman intensities, potential energy distribution (PED) and vibrational assignments for CP, NP and AP are listed in Tables 2–4, respectively. Modes originating from the aromatic nucleus are designated using Wilson's notation,[45] for the phenolic ring substituted with either chlorine atom or nitro group or amino moiety, considering it as a tri-substituted benzene[46] and with a prime (′) on the mode for the non-phenolic ring, treating it as a

Table 2. Observed, calculated frequencies (in cm^{-1}) with DFT/6-311++G(d,p) and vibrational assignment of CP.

	Obs. freq. (cm^{-1})		Cal. freq. (cm^{-1})		Intensity[a]			
S. no	IR	Raman	Un-scaled	Scaled	IR (I_i)	Raman (S_i)	Vibrational assignment[b]	Mode identification[c]
(i) Vibrations of aromatic (biphenyl) unit								
1	–	3065	3191	3066	0.921	54.893	98(2′)	ν(C–H)2′
2	–	3065	3199	3060	4.368	55.118	99(2)	ν(C–H)2
3	–	3065	3181	3058	3.091	12.984	96(20a)	ν(C–H)20a
4	–	3065	3176	3057	9.991	6.529	96(20a′)	ν(C–H)20a′
5	–	3065	3167	3052	2.707	15.464	95(7b′)	ν(C–H)7b′
6	3030	–	3183	3043	4.228	7.385	94(20b′)	ν(C–H)20b′
7	3030	–	3197	3041	0.373	27.180	95(20b)	ν(C–H)20b
8	3030	–	3161	3037	1.969	4.120	97(7a′)	ν(C–H)7a′
9	–	1608	1645	1610	7.095	34.604	67(8b)+14(18a)+9(6b)	ν(C–C)8b
10	–	1598	1640	1598	9.135	100.00	63(8a′)+17(18b′)+11(12′)	ν(C–C)8a′
11	–	1598	1604	1589	1.162	1.301	42(8a)+19(8a′)+12(18b′)+7(12)	ν(C–C)8a
12	1590	–	1620	1582	4.478	0.506	41(8b′)+19(8b)+7(18b′)+6(6b′)	ν(C–C)8b′
13	1480	–	1539	1464	70.981	12.449	39(18a)+37(19b)+6(18a′)+6(13)	ν(C–C)19b
14	1446	–	1514	1445	20.461	5.368	52(18a′)+33(19a′)+7(18a)+6(19a)	ν(C–C)19a′
15	1411	–	1480	1416	1.292	1.090	38(18a′)+31(19b′)+13(19b)+5(15′)+5(18a)	ν(C–C)19b′
16	1367	–	1430	1379	1.631	0.867	48(19a)+17(18a)+13(18a′)+12(19a′)	ν(C–C)19a
17	–	–	1367	1325	9.543	1.045	68(14)+17[β(OH)] + 6(3)	ν(C–C)14
18	–	1284	1352	1289	0.512	0.882	72(14′)+25(3′)	ν(C–C)14′
19	1273	–	1322	1267	2.880	0.282	40(3′)+23(14′)+14(3)+8[β(OH)] + 6(14)	β(CH)3′
20	–	–	1311	1247	9.053	0.485	33(3)+30(14)+18(14′)+12(3′)	β(CH)3
21	1225	–	1297	1218	32.617	15.767	31(7a)+26(14)+12(12′)+8(14′)+6[β(OH)] + 6(18a′)	ν(C–O)7a
22	–	1183	1268	1183	4.138	75.969	43(18a)+16(14′)+15(14)+10(12)+7(13)	β(CH)18a
23	1146	–	1205	1143	1.813	1.323	82(9a′)+17(14′)	β(CH)9a′
24	–	–	1183	1119	0.090	1.323	84(9b′)+12(14′)	β(CH)9b′
25	–	–	1157	1114	2.569	2.908	53(18b)+28(14)	β(CH)18b
26	1056	–	1104	1058	2.303	0.044	48(18b′)+47(19a′)	β(CH)18b′
27	–	1046	1066	1044	1.931	2.351	48(12′)+32(1)+19(18b)	β(CCC)12′
28	–	1023	1058	1023	2.562	0.722	43(1′)+27(18a′)+25(12′)	ν(C–C)1′
29	–	–	979	1004	5.683	8.042	52(12)+28(1′)+13(1)+10(18a′)	β(CH)18a′
30	–	–	1015	979	5.358	14.793	52(12)+28(1′)+13(1)+10(18a′)	β(CCC)12
31	880	–	1003	876	0.013	0.046	85(5′)+15(16b′)	π(CH)5′
32	–	861	984	867	0.276	0.490	80(17a′)+8(16a′)+7(5)	π(CH)17a′
33	–	861	967	865	0.052	0.203	57(5)+21(4)+9(10b)+8(5′)	π(CH)5
34	–	–	891	834	2.124	0.258	49(17b)+15(17b′)+14(4)+12(10b)+5(4′)	π(CH)17b
35	–	–	932	812	5.704	3.702	66 (17b′)+16(17b)+7(4)+5(4′)	π(CH)17b′
36	–	–	868	792	4.021	0.371	30(12)+27(7a)+26(1)	ν(C–C)1
37	758	–	855	762	5.228	1.115	99(11′)	π(CH)11′
38	758	–	840	758	0.020	1.428	75(11)+11(16a)+7(10a)	π(CH)11

(*continued*)

Table 2. Continued.

S. no	Obs. freq. (cm^{-1}) IR	Obs. freq. (cm^{-1}) Raman	Cal. freq. (cm^{-1}) Un-scaled	Cal. freq. (cm^{-1}) Scaled	Intensity[a] IR (I_i)	Intensity[a] Raman (S_i)	Vibrational assignment[b]	Mode identification[c]
39	–	712	777	713	7.845	4.055	60(4′)+16(10a′)+10(10b′)+6(11)	π(CH)10a′
40	–	712	748	701	20.555	0.489	50(6b′)+11(13)+10(6b)+9(7a)+8(1)+5(18a′)	ν(C–C7)13
41	694	687	708	694	6.451	0.060	48(4)+16(4′)+12(10a)+10(10b)	τ(CCCC)4
42	–	–	712	658	13.452	0.067	72(17b′)+17(4′)+5(4)	τ(CCCC)4′
43	–	–	635	643	0.768	1.027	73(6b′)+8(6b)	β(CCC)6b′
44	–	622	694	626	18.550	1.548	65(6b)+10(6b′)+6(7b)+6(1)	β(CCC)6b
45	–	–	601	581	0.611	0.071	34(16b)+24(10a)+16(17a)+10(10a′)+9(10b)	τ(CCCC)16b
46	580	–	595	562	10.266	1.074	42(6a)+25(6a′)+11(7a)	β(CCC)6a
47	–	–	543	494	1.548	0.348	30(16b′)+18(10b′)+17(15)+9(5)+7(6a)	τ(CCCC)16b′
48	–	446	450	438	2.127	0.241	59(16a)+17(17a)+8(17a′)	τ(CCCC)16a
49	–	411	494	423	4.959	1.076	32(16a)+15(16a′)+12(9b)+10(10a)+9(7b)+5(10b′)	β(CO)9b
50	–	–	417	405	0.254	0.807	83(16a′)+16(17b′)	τ(CCCC)16a′
51	–	–	433	380	20.709	0.145	20(9b)+17(6b)+15(10a)+9(15′)	π(CO)10a
52	–	301	368	308	1.076	0.512	35(16a′)+10(7b)+9(9b)+8(15)+6(16a)+5(10a)	β(C–C7)15
53	–	247	265	253	0.159	0.326	30(6a′)+28(13)+12(6a)+6(1)	β(CCC)6a′
54	–	–	302	224	0.565	0.650	65(7b)+6(15)+5(9b)	ν(C–Cl)7b
55	–	–	237	214	0.040	0.678	22(17a)+15(16a)+12(15′)+8(16a′)+8(9a)+8(11)	β(C7–C)15′
56	–	180	214	181	0.777	0.204	55(9a)+9(16a′)+7(17a)	β(CCl)9a
57	–	150	162	155	0.089	0.640	53(16a)+16(17a)+6(10b)+6[τ(C–C7)]	π(CCl)17a
58	–	–	94	89	0.005	0.325	27(15)+22(15′)+21(16a)+8(9a)+6(10b′)	π(C–C7)10b′
59	–	74	71	69	0.075	0.547	37(10b′)+22(16a)+14(10b)+8(17b)	π(C7–C)10b
60	–	–	51	44	0.009	1.773	85[τ(C–C7)] + 5(16a)	τ(C–C7)
(ii) Vibrations of OH moiety								
61	3346	–	3767	3346	49.318	21.074	100[ν(OH)]	ν(OH)
62	–	1158	1208	1156	100.00	13.154	36[β(OH)] + 27(19b)+18(7a)+12(18a′)	β(OH)
63	–	370	409	370	24.668	0.328	86[τ(OH)] + 6(16a)	τ(OH)
RMSD				7.09				

–: Not observed. a: Relative infrared and Raman intensities are normalized to 100. b: Number before the parenthesis is % of PED. Number in the parenthesis is vibrational mode. PED less than 5% is not shown. c: Mode in Wilson's notation,[45] for phenolic ringprime (′) on the mode (in Wilson's notation) refers to the modes associated with the non-phenolic ring and ν, stretching; β, in-plane bending; π, out-of-plane bending; τ, torsion.

Table 3. Observed, calculated frequencies (in cm^{-1}) with DFT/6-311++G(d,p) and vibrational assignment of NP.

	Obs. freq. (cm^{-1})		Cal. freq. (cm^{-1})		Intensity[a]			
S. no	IR	Raman	Un-scaled	Scaled	IR(I_i)	Raman(S_i)	Vibrational assignment[b]	Mode identification[c]
(i) Vibrations of aromatic (biphenyl) unit								
1	3069	3061	3193	3071	4.432	82.715	99(2′)	ν(C–H)2′
2	3069	3061	3219	3065	0.676	4.995	98(2)	ν(C–H)2
3	3069	3061	3177	3062	8.812	7.121	96(20a′)	ν(C–H)20a′
4	3069	3061	3168	3055	3.732	18.659	97(7b′)	ν(C–H)7b′
5	3069	3061	3281	3048	0.254	39.627	98(20a)	ν(C–H)20a
6	3035	–	3184	3047	0.254	15.950	96(20b′)	ν(C–H)20b′
7	3035	–	3163	3042	1.205	3.613	98(7a′)	ν(C–H)7a′
8	3035	–	3201	3026	1.518	11.789	98(20b)	ν(C–H)20b
9	1630	1634	1667	1640	30.608	33.497	63(8b)+14(18a)+9(6b)	ν(C–C)8b
10	–	1582	1642	1606	5.540	83.915	65(8a′)+20(18b′)+10(12′)	ν(C–C)8a′
11	1577	–	1620	1585	2.690	4.596	62(8b′)+16(18b′)+9(12′)+7(8b)	ν(C–C)8b′
12	–	1582	1609	1566	1.907	12.001	55(8a)+ 9[$\nu_{as}(NO_2)$] + 8(18a)+7(6b)+6(8a′)	ν(C–C)8a
13	–	1499	1514	1494	43.059	19.848	31(19b)+29(18a)+12(7a)+9(18a′)+6(19b′)	ν(C–C)19b
14	1475	–	1536	1476	33.350	1.635	52(18a′)+28(19b′)+8(18a)+7(19b)	ν(C–C)19b′
15	1450	1449	1481	1437	9.594	1.584	46(18b′)+32(19a′)+7(19a)	ν(C–C)19a′
16	1408	1408	1443	1408	8.799	7.249	57(19a)+15(18a)+7(18a′)+6(19a′)	ν(C–C)19a
17	1322	–	1360	1324	59.213	4.417	25(14′)+16(14)+16[$\nu_s(NO_2)$] + 14(3)+11(7a)	ν(C–C)14
18	1322	–	1349	1321	7.987	1.057	46(14′)+46(3′)	ν(C–C)14′
19	–	1283	1323	1287	10.088	1.629	50(14′)+28(3′)+7(14)	β(CH)3′
20	–	1283	1306	1272	45.366	17.024	38(3)+23[β(OH)] + 9[$\nu_s(NO_2)$] + 7(7b)+6(14)	β(CH)3
21	1247	–	1273	1249	63.073	17.038	27(18a)+23(7a)+18[$\nu_s(NO_2)$] + 7(18a)	ν(C–O)7a
22	–	1230	1304	1226	13.143	100.00	32(13)+17(18a)+9(12)+8(14′)+8(12′)+7(7b)	β(CH)18a
23	–	1154	1207	1170	11.785	1.713	66(9a′)+16(14′)+9(18a)	β(CH)9a′
24	–	1132	1184	1148	0.075	1.226	84(9b′)+16(14′)	β(CH)9b′
25	1136	–	1162	1135	15.313	6.206	40(18b)+23(14)+14(7b)+5[β(OH)]	β(CH)18b
26	1076	–	1101	1077	2.953	2.209	23(12)+18(19b)+12(7b)+9(19b′)+8(18b)	ν(C–N)7b
27	1076	–	1106	1073	0.763	0.427	42(19b′)+33(18b′)+6(12)+6(19b)	β(CH)18b′
28	–	1044	1067	1046	1.576	3.696	35(1)+22(1′)+17(18a)+12(18a′)+10(12′)	ν(C–C)1
29	1037	–	1041	1024	1.358	0.539	41(12′)+39(1′)+13(18a′)	β(CCC)12′
30	–	995	1015	1000	0.030	21.686	60(1′)+35(12′)	ν(C–C)1′
31	919	–	989	911	0.249	0.639	84(5)+14(16b)	π(CH)5
32	919	–	1005	905	0.007	0.027	87(5′)+13(16a′)	π(CH)5′
33	–	–	985	897	0.082	0.167	90(17a′)+9(4′)	π(CH)17a′
34	888	–	912	888	1.489	0.994	39(12)+20[$\delta(NO_2)$] + 9[$\nu_s(NO_2)$] + 6(1′)+6(7b)	β(CCC)12
35	860	–	919	862	1.275	0.028	40(17b)+25(17b′)+17(16b)+7(16b′)+5(10b)	π(CH)17b
36	860	–	938	846	2.092	0.208	48(17b′)+33(17b)+11(4)+5(4′)	π(CH)17b′
37	–	–	856	793	0.081	2.168	99(11′)	π(CH)11′
38	–	–	852	786	2.353	0.886	67(11)+11(16a)+8(10b)+6(16a′)	π(CH)11

(*continued*)

Table 3. Continued.

S. no	Obs. freq. (cm^{-1}) IR	Obs. freq. (cm^{-1}) Raman	Cal. freq. (cm^{-1}) Un-scaled	Cal. freq. (cm^{-1}) Scaled	Intensity[a] IR(I_i)	Intensity[a] Raman(S_i)	Vibrational assignment[b]	Mode identification[c]
39	763	–	779	760	3.072	0.272	64(16a′)+17(10a′)+11(17a′)	π(CH)10a′
40	–	740	753	728	2.371	2.958	20(12′)+14(12)+10[$\delta(NO_2)$] + 10(13)	ν(C–C7)13
41	–	–	740	722	17.852	0.230	64(4)+11(11)+10(10a)+5(10b)	τ(CCCC)4
42	–	–	711	689	12.669	0.127	68(17b′)+19(4′)	τ(CCCC)4′
43	698	–	695	674	6.217	0.793	35 (12)+22(12′)+ 12(18a′)	β(CH)18a′
44	–	617	634	628	0.152	1.016	86(6b′)+6(1′)+5(18a′)	β(CCC)6b′
45	–	–	601	421	5.544	1.022	28(6b)+27(9b)+15(7b)+6(16b′)	β(CCC)6b
46	–	–	586	541	1.879	0.269	22(16b)+20(16b′)+14(10b′)+11(10b)+8(17a′)+8(10a)	τ(CCCC)16b′
47	500	–	512	493	6.971	0.144	29(16b)+17(16b′)+14(10a)+7(10b)+7(10b′)	τ(CCCC)16b
48	–	424	437	424	0.169	0.744	72(16a)+19(17a)+8(11)	τ(CCCC)16a
49	575	–	429	573	0.124	1.214	48(6a)+30(6a′)	β(CCC)6a
50	–	402	415	406	0.125	0.921	81(16a′)+16(17a′)	τ(CCCC)16a′
51	–	–	438	399	1.744	0.484	17(9b)+16(16a)+14(10a)+10(15)+10(15′)	β(CO)9b
52	–	325	370	340	1.487	0.268	28(10a)+20(9b)+10(16a)+8(16a′)+8(15′)+7(6a)	β(C7–C)15′
53	–	292	336	301	1.047	0.510	30(16a′)+13(9b)+13(10a)+11(15)+6(9a)	β(C–C7)15
54	–	–	285	267	0.006	0.428	30(6a)+30(13)+16(6a′)+8(19b)+5(19b′)	β(CCC)6a′
55	–	–	208	204	0.601	0.387	21(10a)+17(10b)+15(15′)+13(16a)+11(9a)+6(11)	π(C–O)10a
56	–	178	246	177	0.922	0.445	61(9a)+11(16a′)	β(CN)9a
57	–	–	151	143	0.067	1.070	45(17a)+22[τ(OH)] + 14(16a)+7[τ(C–C7)]	π(C–N)17a
58	–	70	84	78	0.162	0.239	21(15)+19[$\tau(NO_2)$] + 17(10b′)+12(9a)+5(16a′)	π(C7–C)10b′
59	–	–	58	57	0.008	0.325	49[$\tau(NO_2)$] + 17(16a)+10[τ(OH)] + 9(10b)+5(10b′)	π(C–C7)10b
60	–	–	48	46	0.098	1.682	70[τ(C–C7)] + 12[$\tau(NO_2)$] + 6(16a)	τ(C–C7)
(ii) Vibrations of OH moiety								
61	3450	–	3472	3450	90.490	38.663	100[ν(OH)]	ν(OH)
62	1170	–	1230	1177	53.823	5.743	41(18a)+21[β(OH)] + 12(19b)+11(18a′)	β(OH)
63	668	–	703	669	33.657	0.167	63[τ(OH)] + 19(16b)+8(11′)+5(10b)	τ(OH)
(iii) Vibrations of nitro group								
64	1538	1541	1578	1540	100.00	14.537	55[$\nu_{as}(NO_2)$] + 17(19a)+6[$\gamma(NO_2)$]	$\nu_{as}(NO_2)$
65	1371	–	1410	1372	30.596	33.895	53(19b)+13[β(OH)] + 10[$\nu_s(NO_2)$] + 10(7b)	$\nu_s(NO_2)$
66	–	822	840	825	2.148	10.687	32[$\delta(NO_2)$] + 29(1)+16(12)+11(7a)	$\delta(NO_2)$
67	639	–	714	639	3.786	0.129	57[$\omega(NO_2)$] + 10(17a)+16(4)	$\omega(NO_2)$
68	560	–	576	557	2.346	1.056	53[$\gamma(NO_2)$] + 11(1)+10(9b)+7(9a)	$\gamma(NO_2)$
69	–	–	93	87	0.117	0.134	34[$\tau(NO_2)$] + 15[τ(OH)] + 12(10b)+1(15′)+6(15)	$\tau(NO_2)$
RMSD				9.39				

–: Not observed. a: Relative infrared and Raman intensities are normalized to 100. b: Number before the parenthesis is % of PED. Number in the parenthesis is vibrational mode. PED less than 5% is not shown. c: Mode in Wilson's notation,[45] for phenolic ring prime(′) on the mode (in Wilson's notation) refers to the modes associated with the non-phenolic ring and ν, stretching; β, in-plane bending; π, out-of-plane bending; δ, scissoring; γ, rocking; ω, wagging; τ, torsion; s, symmetric; as, asymmetric.

Table 4. Observed, calculated frequencies (in cm^{-1}) with DFT/6-311++G(d,p) and vibrational assignment of AP.

	Obs. freq. (cm^{-1})		Cal. freq. (cm^{-1})		Intensity[a]			
S. no	IR	Raman	Un-scaled	Scaled	IR (I_i)	Raman (S_i)	Vibrational assignment[b]	Mode identification[c]
(i) Vibrations of aromatic (biphenyl) unit								
1	–	3059	3188	3070	2.509	15.344	97(2)	ν(C–H)2
2	–	3059	3190	3063	7.682	58.836	98(2′)	ν(C–H)2′
3	–	3059	3176	3055	15.754	3.433	96(20a′)	ν(C–H)20a′
4	–	3059	3166	3050	4.547	8.670	97(7b′)	ν(C–H)7b′
5	–	3059	3147	3046	5.149	8.494	98(20a)	ν(C–H)20a
6	3030	–	3181	3039	2.059	19.940	96(20b′)	ν(C–H)20b′
7	3030	–	3159	3032	9.596	21.320	98(7a′)	ν(C–H)7a′
8	3030	–	3163	3030	5.368	3.987	98(20b)	ν(C–H)20b
9	–	1599	1642	1596	12.044	0.891	68(8b′)+18(18b′)+11(12′)	ν(C–C)8b′
10	–	1599	1638	1587	40.492	100.00	70(8a′)+17(18b′)+10(12′)	ν(C–C)8a′
11	1525	1528	1612	1536	0.847	3.146	59(8b)+15(18a)+11(6b)	ν(C–C)8b
12	1525	1528	1633	1526	26.158	4.969	52(8a)+9(6b)+6(18a)	ν(C–C)8a
13	–	1494	1552	1486	65.771	16.598	34(18a′)+27(19b′)+12(19b)+12(13)+8(18a)	ν(C–C)19b′
14	1476	1461	1522	1461	73.360	3.461	30(19b)+26(18a)+17(18a′)+10(19b′)+8(7a)	ν(C–C)19b
15	–	1413	1485	1420	8.701	8.302	43(18b′)+31(19a′)+9(19a)	ν(C–C)19a′
16	1400	–	1456	1393	9.288	3.587	30(19a)+15(18a′)+14(19a′)+10(18a)+8(7b)	ν(C–C)19a
17	–	1312	1351	1316	43.817	20.169	76(14′)+16(3′)	ν(C–C)14′
18	1301	–	1372	1300	7.881	5.128	32(14)+22(3)+9[β(OH)] + 8(13)+8(7a)+7(7b)	ν(C–C)14
19	–	–	1339	1277	11.873	13.257	27(3′)+14(14)+13(14′)+10[γ(NH_2)] + 10(3)+6(13)	β(CH)3′
20	–	–	1333	1272	13.185	5.253	40(14)+30(3)+10[β(OH)] + 6(13)+6(3′)	β(CH)3
21	1251	1250	1277	1254	13.185	5.253	21(19b′)+17(18a)+16(18a′)+16(19b)+10(7a)	ν(C–O)7a
22	–	–	1302	1234	11.663	2.984	31(14)+25(18a)+19(7a)+7(13)	β(CH)18a
23	1194	–	1242	1201	9.729	3.018	23(7b)+22(18a)+11(7a)+11(12)+9(13)+5[β(OH)]	ν(C–N)7b
24	1155	1159	1204	1159	0.029	1.975	83(9a′)+16(14′)	β(CH)9a′
25	–	–	1181	1135	0.013	1.051	88(9b′)+12(14′)	β(CH)9b′
26	1067	–	1100	1063	3.121	0.008	50(19b′)+44(18b′)	β(CH)18b′
27	–	1041	1104	1050	81.161	0.141	30(14)+21(18b)+13[γ(NH_2)] + 8(12)+5[β(OH)]	β(CH)18b
28	1032	–	1060	1033	0.032	7.349	55(1′)+28(18a′)+13(12′)	β(CH)18a′
29	–	–	1040	1019	3.680	1.774	66(12′)+19(1′)+7(1)	β(CCC)12′
30	–	997	1015	994	1.267	9.671	39(1′)+38(1)+10(18a′)+8[γ(NH_2)]	ν(C–C)1′
31	–	974	1000	968	0.239	0.068	80(5′)+20(16b′)	π(CH)5′
32	927	–	983	945	0.090	0.344	90(17a′)+9(4′)	π(CH)17a′
33	–	917	933	916	1.423	0.179	56(17b′)+20(16b′)+12(10b′)	π(CH)17b′
34	884	–	921	876	2.911	2.312	43(12)+11(1′)+9(1)+8(7b)+7(17b′)+6(13)	β(CCC)12
35	–	839	918	841	0.493	0.183	78(5)+16(16a)	π(CH)5
36	–	–	855	827	7.166	0.206	99(11′)	π(CH)11′
37	821	–	878	823	0.012	0.976	33(17b)+17(4)+14(4′)+14(17b′)+10(10b)+9(10b′)	π(CH)17b
38	–	–	809	790	2.816	1.029	41(17b)+17(16a′)+14(16a)+9(10a′)+8(10b′)	π(CH)10a′

(*continued*)

Table 4. Continued.

S. no	Obs. freq. (cm^{-1}) IR	Obs. freq. (cm^{-1}) Raman	Cal. freq. (cm^{-1}) Un-scaled	Cal. freq. (cm^{-1}) Scaled	Intensity[a] IR (I_i)	Intensity[a] Raman (S_i)	Vibrational assignment[b]	Mode identification[c]
39	758	–	788	748	2.732	5.993	33 (1)+19(11)+12(7a)+10(16a)+10(12)+6(10b)	ν(C–C)1
40	–	–	771	741	34.030	0.762	46(11)+19(16a′)+9(16a)+8(1)+6(10b)	π(CH)11
41	–	728	736	719	8.011	0.190	48(4)+18(11)+9(10a)+9(4′)+7(17b)	τ(CCCC)4
42	–	706	711	709	0.987	2.061	49(17b′)+23(4)+17(4′)	τ(CCCC)4′
43	696	–	721	700	20.349	0.135	45(12′)+22(12)+8(1)+7(13)+7(1′)	ν(C–C7)13
44	625	–	649	636	0.148	0.641	87(6b′)+5(18a′)	β(CCC)6b′
45	–	600	631	601	10.941	0.073	26(16b)+16(17a)+13(16b′)+11(17a′)+10(10b)	τ(CCCC)16b
46	584	–	585	577	16.502	0.765	51(6a)+28(6a′)+6(1)	β(CCC)6a
47	–	–	591	562	10.882	0.994	21(16b)+12(17a)+10(10a)+9(15)+8(9b)+8(16b′)	β(CO)9b
48	–	–	529	538	22.347	0.081	51[ω(NH_2)] + 10(6a)+10(16b′)+6(10b′)	τ(CCCC)16b′
49	452	–	490	452	8.056	0.298	32(16b)+17(6b)+10(17a)+7(16a′)+7(9a)+5(15)	β(CCC)6b
50	428	–	450	437	5.489	0.079	34(16a)+31(16a′)+6(17a)	τ(CCCC)16a
51	428	–	417	434	0.105	0.481	60(16a′)+18(16a)+6(17b′)	τ(CCCC)16a′
52	–	–	395	325	5.727	0.320	34[τ(NH_2)] + 22(10a)+8(15′)+5(15)	π(CO)10a
53	–	–	306	298	1.841	0.317	34(9a)+25(16a′)+10(15)+7(1)	β(C–C7)15
54	–	–	321	291	9.083	0.081	29(9a)+25(6a)+10(9b)+8(16a′)	β(CN)9a
55	–	270	278	265	2.859	0.989	18(9a)+18(13)+16(6a)+13(6a′)+12(1)+5(16a′)	β(CCC)6a′
56	–	–	236	218	15.112	0.474	26(17a)+24(16a)+12[τ(OH)] + 12(17b)+8(16a′)+ 6(10a)	π(C–N)17a
57	–	171	182	172	0.579	0.332	53(16a)+11(16a′)+10(15′)+6(10a)	β(C7–C)15′
58	–	87	102	93	0.133	0.428	33(15′)+20(15)+16(16a′)+15(10b′)	π(C–C7)10b′
59	–	–	72	69	0.656	0.145	27(15′)+24(16a)+23(10b)+910(10b′)+9(17b)	π(C7–C)10b
60	–	–	56	54	0.063	1.465	85[τ(C–C7)] + 5(16a)	τ(C–C7)
(ii) Vibrations of OH moiety								
61	3469	–	3847	3469	48.282	28.274	100[ν(OH)]	ν(OH)
62	1106	–	1183	1114	29.314	0.347	50(18b)+22(19b)+20[β(OH)]	β(OH)
63	–	–	260	254	43.532	0.098	77 [τ(OH)]	τ(OH)
(iii) Vibrations of amino group								
64	3373	–	3672	3373	14.605	8.003	100[ν_{as}(NH_2)]	ν_{as}(NH_2)
65	3287	–	3570	3287	16.983	36.465	100 [ν_s(NH_2)]	ν_s(NH_2)
66	1602	–	1659	1601	56.310	2.926	88[δ(NH_2)] + 7(7b)	δ(NH_2)
67	–	1101	1146	1089	2.457	0.517	32(14)+27[β(OH)] + 25[γ(NH_2)] + 9(18b)	γ(NH_2)
68	511	–	564	509	100.00	0.615	27[ω(NH_2)] + 14(6a)+11(16b)+9(7b)+9(16b′)+7(10a)	ω(NH_2)
69	–	344	342	346	9.082	0.477	47 [τ(NH_2)] + 23(10a)+7(16a)+5(16a′)+5(17a)	τ(NH_2)
RMSD				6.59				

–: Not observed. a: Relative infrared and Raman intensities are normalized to 100. b: Number before the parenthesis is % of PED. Number in the parenthesis is vibrational mode. PED less than 5% is not shown. c: Mode in Wilson's notation,[45] for phenolic ring prime(′) on the mode (in Wilson's notation) refers to the modes associated with the non-phenolic ring and ν, stretching; β, in-plane bending; π, out-of-plane bending; δ, scissoring; γ, rocking; ω, wagging; τ, torsion; s, symmetric; as, asymmetric.

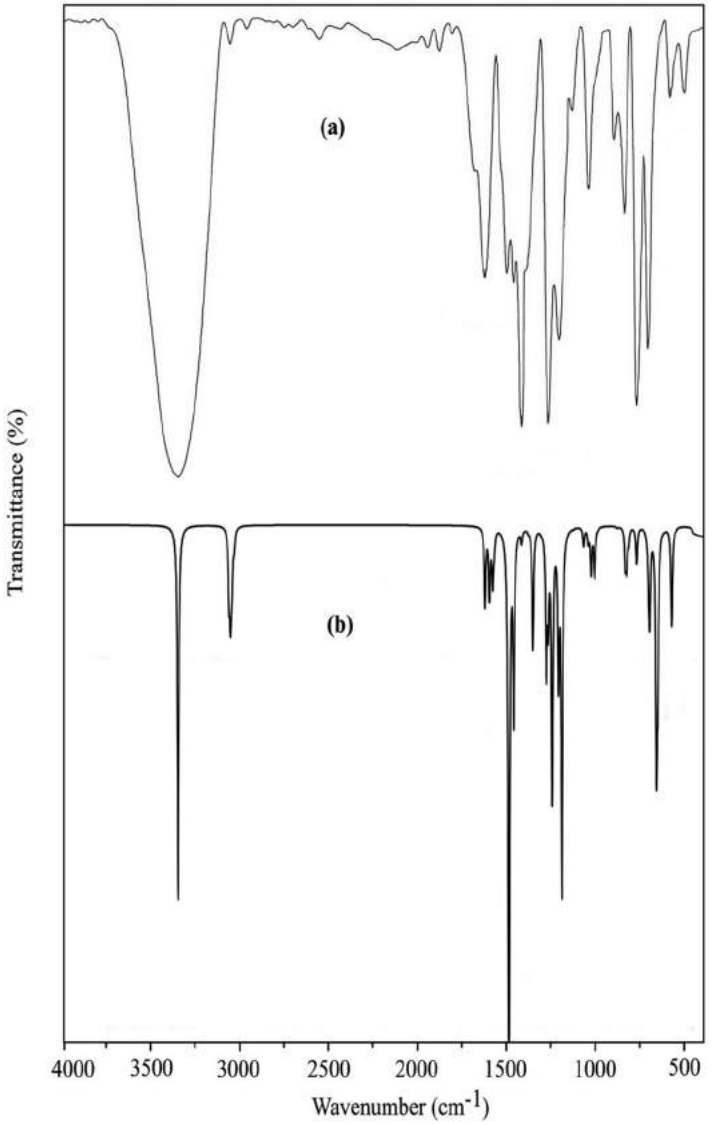

Figure 2. FT-IR spectra of CP (a) experimental and (b) simulated with DFT/B3LYP/6-311++G(d,p) formalism.

mono-substituted benzene.[46] A comparison of FT-IR spectra, both experimental and simulated, is made in Figures 2, 4 and 6, for CP, NP and AP, whereas comparison for their Raman counterpart is made in Figure 3, 5 and 7.

The rms error, for CP, NP and AP is 7.44, 8.98 and 6.97 cm^{-1}, between measured and scaled fundamentals, respectively, whereas the corresponding RMSD values are 7.09, 9.39 and 6.59 cm^{-1}. Further, observed IR and Raman fundamentals exhibit good agreement with their corresponding computed values, as evident from Tables 2–4 and Figures 2–7 for CP, NP and AP. Hence, reliable vibrational assignments can be proposed for CP, NP and AP, on the basis of present calculations, with emphasis on dominant PED contributions.

The results available in Tables 2–4 are self-explanatory. Hence, the discussion of vibrational assignments is mainly confined to the fundamentals originating from the phenolic ring and its substituents.

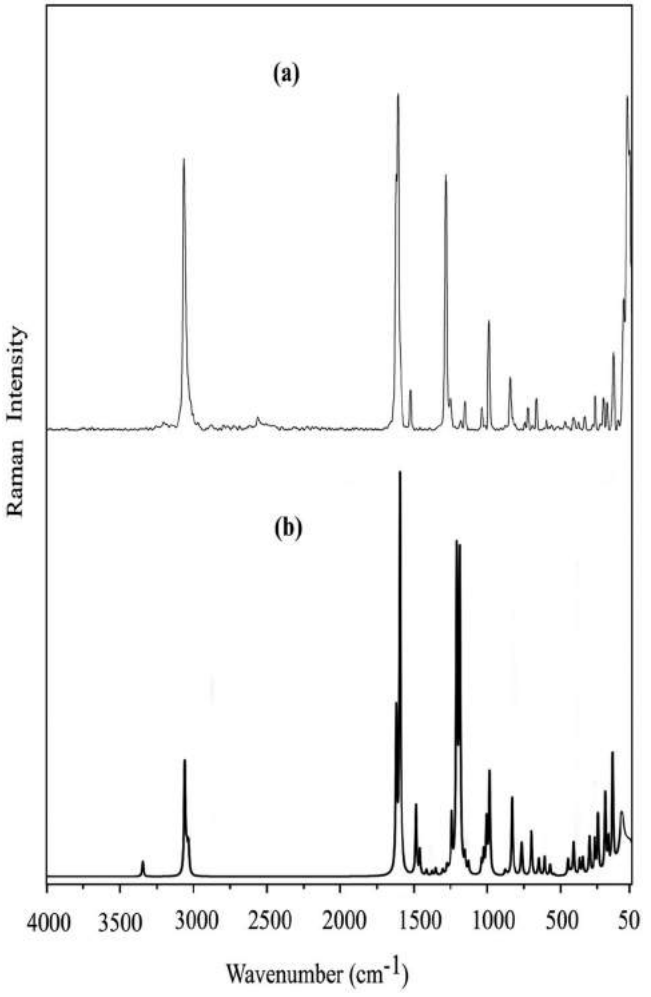

Figure 3. FT Raman spectra of CP (a) experimental and (b) simulated with DFT/B3LYP/6-311++G(d,p) formalism.

4.2.1. Vibrations of the phenolic ring

4.2.1.1. C–C Stretching vibrations:. In CP, NP and AP, modes 8a and 8b are expected in the frequency range 1500–1600 cm^{-1}. The higher frequency (scaled value) is a C–C stretching mode to the extent of 59 to 67% in the three molecules. It mixes with C–H in plane bending mode 18a and ∠CCC bending vibration 6b uniformly in the molecules under consideration. The lower frequency exhibits considerable C–C stretching character ranging from 42 to 55%. It mixes with C–H in-plane bending fundamental 18a and ∠CCC bending mode 6b in NP and AP to a small extent. It is interesting to note that contributions from 18a and 6b in NP and AP, are replaced by that from mode 18b' (C–H in-plane bending of benzene ring connected to phenolic ring) and ∠CCC ring bending vibration 12 in CP. It is to be noted that C–C stretching fundamental 8a' of the monosubstituted benzene ring makes a PED contribution of 19% in CP, whereas this component decreases to 6% in NP, while such contribution disappears in AP. There is an additional contribution to this mode from asymmetric stretching vibration of the nitro group in NP. Present computation reveal that the frequency of mode 8b should be higher than that of vibration 8a, which does not agree with that for biphenylcarboxaldehydes, wherein 8a is greater than 8b.[47] Hence, Raman shifts at 1598 and 1582 cm^{-1} in CP and NP, respectively, along with IR absorption

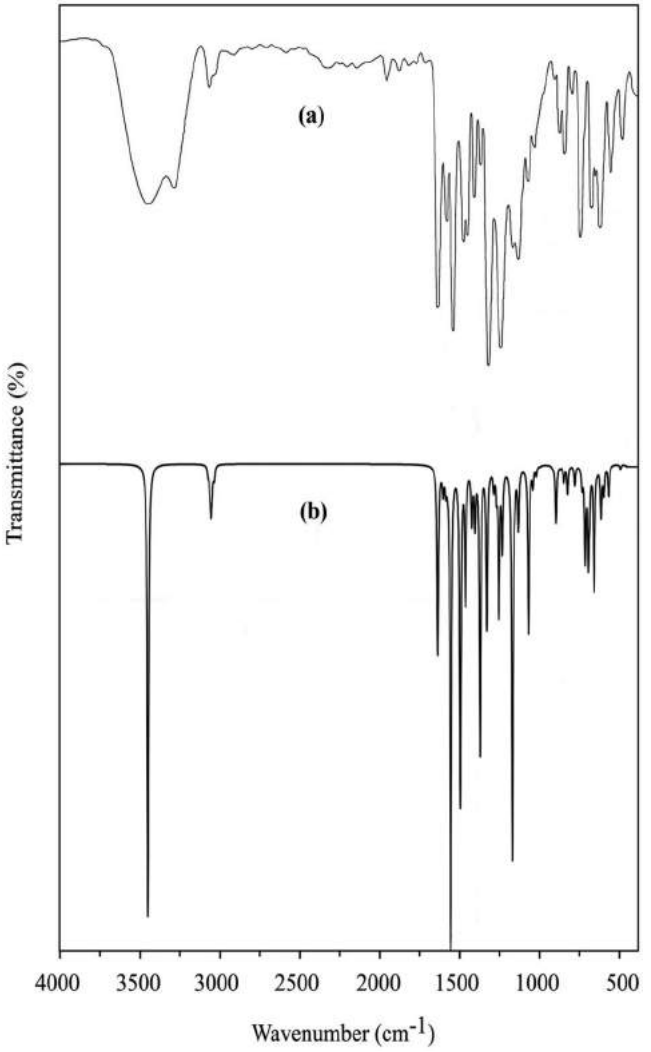

Figure 4. FT-IR spectra of NP (a) experimental and (b) simulated with DFT/B3LYP/6-311++G(d,p) formalism.

near 1525 cm^{-1} are assigned to mode 8a, whereas those around 1608 R (R indicates Raman shift), 1630, and 1525 cm^{-1} are ascribed to vibration 8b in CP, NP and AP, respectively.

Modes 19a and 19b normally appear in the spectral region 1400–1500 cm^{-1} in benzene derivatives. The C–C stretching character of the higher fundamental falls in the range 30–37% in CP, NP and AP. It mixes strongly with C–H in-plane bending normal frequency in the three molecules. This mode also combines with C–H in-plane bending vibration 18a' in the three molecules. Mixing with other modes can be identified in Tables 2–4 for CP, NP and AP, respectively. Lower frequency exhibits C–C stretching nature to the extent of 30–57%. It mixes with C–H in-plane bending vibration 18a and its counterpart 18a' of the monosubstituted benzene ring. Other minor contributions are available in Tables 2–4 for this mode. According to the present calculations frequency of vibration 19b should be greater than that of mode 19a, which is in direct contradiction with that obtained for biphenylcarboxaldehydes, wherein frequency of 19a is greater than that of 19b.[47] Thus, the IR bands around 1367, 1408 and 1400 cm^{-1} are attributed to mode 19a, whereas

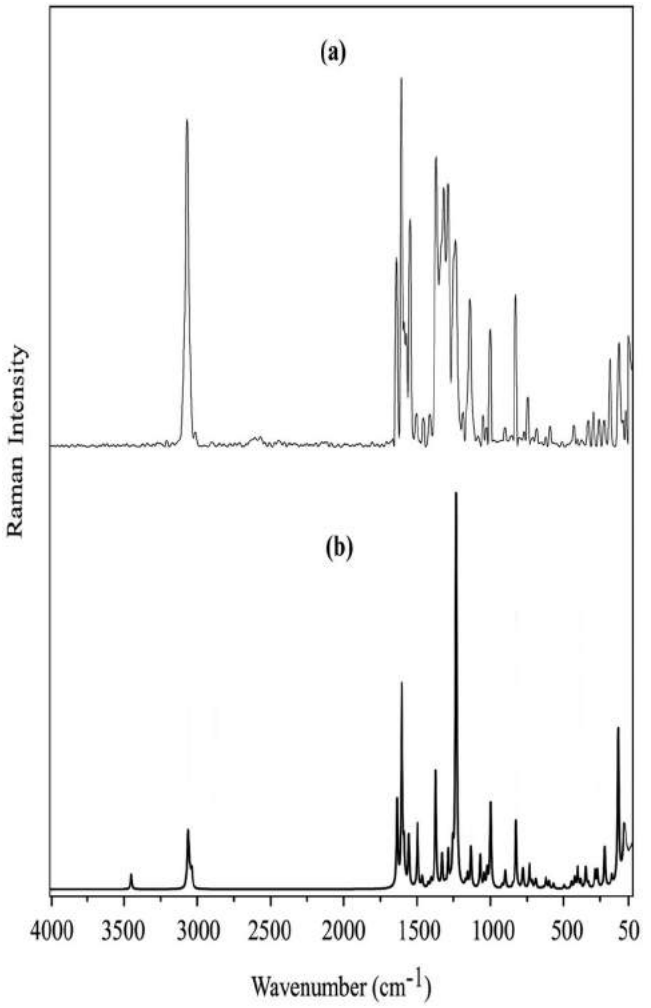

Figure 5. FT Raman spectra of NP (a) experimental and (b) simulated with DFT/B3LYP/6-311++G(d,p) formalism.

those near 1480, 1499 R and 1476 cm^{-1} are assigned to vibration 19b in CP, NP and AP, respectively.

Characteristic feature of vibration 14 is that the alternate carbon bonds of the ring either increase or decrease. It appears at 1325 C (C indicates calculated scaled value), 1322 and 1301 cm^{-1} in CP, NP and AP, respectively, wherein the C–C stretching character varies from 16% to 68%. It is known that this vibration shows strong mixing with C–H in-plane bending mode 3 in many substituted benzenes. However, this is not valid for present molecules as the corresponding PED contribution from mode 3 is 6% in CP, 14% in NP and 22% in AP. This result is identical with that obtained for biphenylcarboxaldehydes.[47] A note-worthy point is that this fundamental mixes with symmetric stretching of nitro group in NP.

4.2.1.2. C–H in-plane bending vibrations. According to the present computations, the bands in the vicinity of 1247 C, 1283 R and 1272 C cm^{-1} essentially originate from C–H in-plane bending mode 3, as it draws PED to the extent of 33%, 38% and 30% from its own coordinate in CP, NP and AP, respectively. It exhibits significant mixing with C–C stretching vibration 14 in CP and

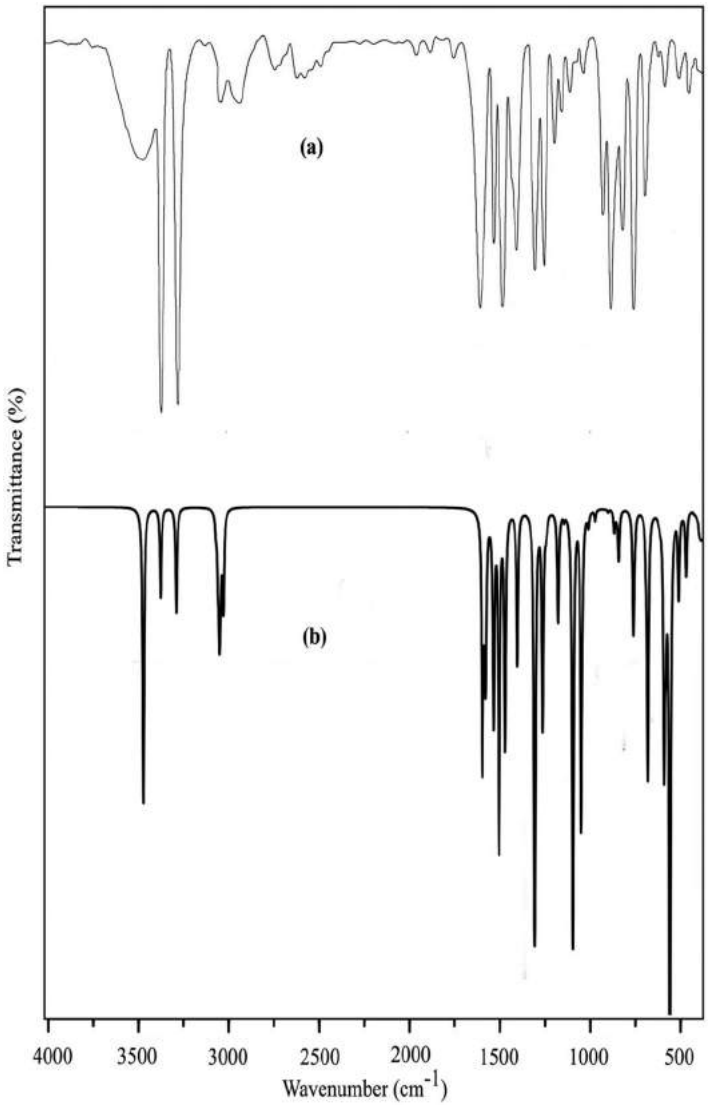

Figure 6. FT-IR spectra of AP (a) experimental and (b) simulated with DFT/B3LYP/6-311++G(d,p) formalism.

AP, whereas this mixing is of no significance in NP, as it is very low. This mixing in CP and AP agrees with that for the corresponding vibration in biphenylcarboxaldehydes.[47]

Raman shifts around 1183 and 1230 cm^{-1} in CP and NP, along with scaled value near 1234 cm^{-1} in AP are attributed to mode 18a, considering their PED, which is 43%, 17% and 25% in CP, NP and AP, respectively. Strong mixing of this mode with vibrations 13 and 14 in NP and AP, respectively, to the extent of 32% and 31%, is note-worthy, whereas the same mixing drops to 15% in CP. It is important to note that, this vibration mixes with C–O stretching mode 7a with 19% PED in AP. Vibration 18b is predicated at 1114 C, 1136 and 1041 R cm^{-1} in CP, NP and AP, respectively, according to the computations. This vibration has strong mixing with mode 14 in the three molecules. Further, its mixing with C–N stretching mode 7b in NP, and the rocking vibration of amino group in AP are important.

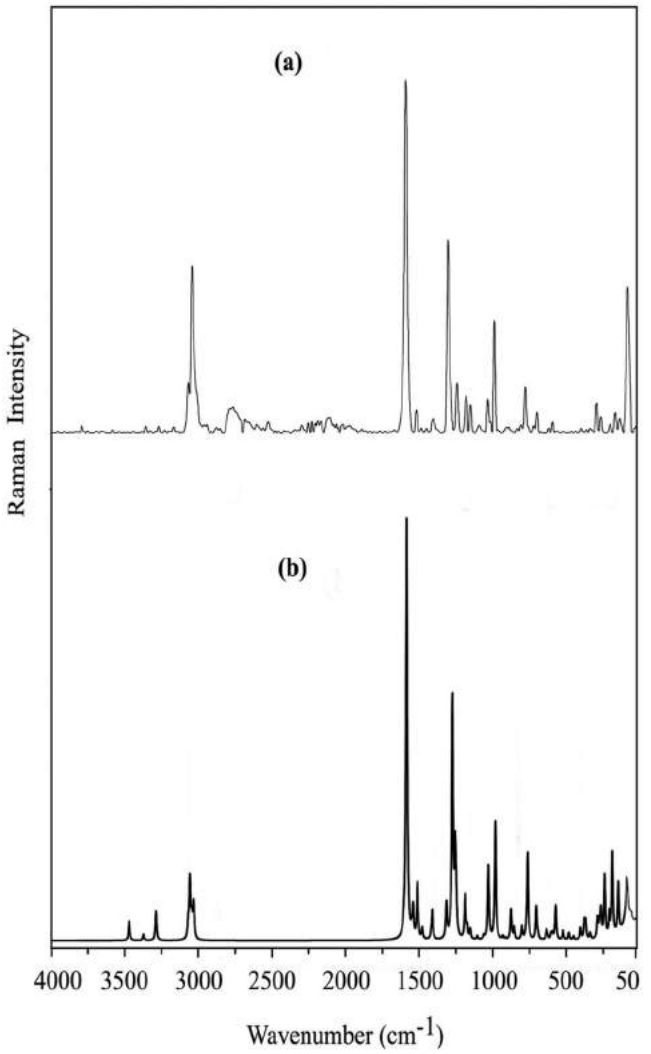

Figure 7. FT Raman spectra of AP (a) experimental and (b) simulated with DFT/B3LYP/6-311++G(d,p) formalism.

4.2.1.3. Ring or substituent sensitive modes. Vibrations 1, 6a, 6b and 12 are known as ring modes or substituent sensitive modes, as their frequency value varies from molecule to molecule. Further, they are known to mix with several other vibrations of the ring system and substituent group vibrations that share the same complicated region of spectral space. Hence, it is essential to use their characteristic eigenvector distribution carefully, for their correct identification and assignment, as proposed by Patel et al.,[48] and successfully implemented by us for a host of substituted benzenes (for instance see reference47). We employed local symmetry coordinates constructed in terms of primitive internal coordinates for vibrations 6a, 6b and 12. Therefore, it is expected that for a given vibration say 12, the corresponding eigenvector element should have a relatively prominent magnitude with respect to the elements of the other two normal frequencies. This is, in fact, found true for the mode 12, wherein the corresponding elements 0.512, 0.639 and 0.602, for CP, NP and AP, respectively, dominate the other two elements ranging from −0.005 to 0.239. Thus the frequencies at 979 C, 888 and 884 cm^{-1} are assigned to vibration 12 in CP, NP and AP, respectively, with PED 52%, 39% and 43%, from its own corresponding coordinate. It

mixes with several other normal modes in these molecules. The details can be found in Tables 2–4.

The vibrational modes, 6a and 6b were identified and assigned from careful consideration of their characteristic eigenvector distribution. The C–C–C angles change in the ratio +2, −1, −1, +2, −1, −1 in mode 6a, whereas they change in the ratio 0, +2, −2, 0, +2, −2 in mode 6b. Significant PED contribution comes from the corresponding ∠CCC bending modes to these vibrations. For instance, the IR band at 580 cm^{-1} gets 42% PED from mode 6a, whereas the Raman shift around 622 cm^{-1} has 65% PED from mode 6b, in CP. Bands that can be considered 6a and 6b in NP and AP can be read from Tables 3 and 4, respectively.

A characteristic feature of mode 1 is that all ring C–C bonds, either increase or decrease at the same time. In benzene this frequency is a pure C–C stretching fundamental as it is totally symmetric and occurs in a spectral region that is far away from C–H stretching region. As these restrictions are removed from the present set of molecules, mode 1 can mix with several bending modes and in particular with lower frequencies of substituent stretching vibrations. As a result, mode 1 cannot maintain its purity, in the present set molecules, as in benzene. Based on the present calculations, the bands near 792 C, 1044 and 758 cm^{-1} are attributed to mode 1 in CP, NP and AP, respectively. Tables 2–4, reveal its mixing with other normal modes.

4.2.1.4. C–H out-of-plane bending modes. Another name for these vibrations is C–H wagging modes. They are labeled 5, 11 and 17b in the present set of molecules. There is no difficulty in identifying the bands around 861 R, 919 and 839 R cm^{-1} with mode 5, in CP, NP and AP, respectively, as significant PED comes from the corresponding C–H wagging coordinate, which falls in the range 57 to 84%. In the same way, it is easy to ascribe the normal modes at 758, 786 C and 741 C cm^{-1} to fundamental 11, based on high PED contribution from related C–H wagging coordinate, which varies from 46 to 75%, in CP, NP and AP, respectively. Similarly, there is no problem in associating the fundamentals near 834 C, 860 and 821 cm^{-1} with vibration 17b due to dominant PED drawn from relevant C–H wagging coordinate, which is in the range 33 to 49%, in CP, NP and AP, respectively. It is to be noted that the attribution of IR absorption in the vicinity of 919, 786 C and 860 cm^{-1} in NP to mode 5, 11 and 17b compare nicely with those of the corresponding bands in 2,5-dihydroxytoluene in the neighborhood of 933, 819 and 878 cm^{-1}, respectively.[49]

4.2.1.5. Ring torsions. Normal modes 4, 16a and 16b are called the ring torsions in benzene and its derivatives. Vibration 4 is identified at 694, 722 C and 728 R cm^{-1} in CP, NP and AP, respectively. It essentially results from mixing of mode 4 with normal frequencies 4′, 10a and 10b; 11, 10a and 10b; and 11, 10a, 4′ and 17b in CP, NP and AP, respectively. Vibration 16a is assigned to the Raman shifts near 446 and 424 cm^{-1} in CP and NP, respectively, whereas it is located around 428 cm^{-1} in IR absorption, in AP. Similarly, vibration 16b is ascribed to 581 C, 500 and 600 R cm^{-1} in CP, NP and AP, respectively. Mixed nature of 16a and 16b can be understood from Tables 2–4.

4.2.1.6. Vibrations associated with the bonds linking phenyl ring to the substituent groups:. These are inter-ring C–C bond, phenolic C–O bond, C–Cl bond and nitro and amino C–N bonds.

4.2.1.6.1. Vibrations of the inter-ring C–C bond. There are four vibrations associated with C–C inter-ring bond that are to be considered here. These are ν(C–C7)13, β(C–C7)15, π(C7–C)10b and τ(C–C7). As predicted by the present computations, the Raman shifts at 712, 301, 74 and scaled value near 44 cm^{-1} are assigned to the inter-ring C–C bond stretching vibration 13, its associated in-plane bending mode 15, related wagging fundamental 10b and relevant torsion frequency in CP, respectively. In NP, the Raman shifts around 740, 292, 70, along with scaled value at 46 cm^{-1} are due to the vibrations 13, 15, 10b and torsion of inter-ring C–C bond, respectively.

Similarly in AP, the IR absorptions near 696, 298 C, 69 C and 54 C cm^{-1} are identified with normal modes 13, 15, 10b and τ(C–C7), respectively. However, it is important to bear in mind that the former three vibrations are a result of mixing of several fundamentals, whereas the last one is predominantly torsion mode of the inter-ring C–C bond. The details can be read from Tables 2–4. These assignments for modes 13, 15 and inter-ring torsion in the three molecules coincide to a good degree of accuracy with those of corresponding bands in biphenyl-2-carboxaldehyde at 731, 277 C and 45 C cm^{-1}, respectively.[47] Obviously, same degree of coincidence cannot be expected for the wagging mode, due to mass differences involved in the substituted phenyl ring part of the biphenyl ring.[47]

4.2.1.6.2. Vibrations of the phenolic C–O bond. These are ν(C–O)7a, β(C–O)9b and π(C–O)10a, that are common to the three molecules CP, NP and AP. On the basis of present computations the fundamentals at 1225, 1247 and 1251 cm^{-1}; 411 R, 399 C and 562 C cm^{-1}; and 380 C, 204 C and 325 C cm^{-1} are ascribed to modes 7a, 9b and 10a, respectively, in CP, NP and AP. As can see from Tables 2–4, these vibrations are mixed normal modes.

4.2.1.6.3. Vibrations of the C–Cl bond. Stretching, in-plane and out-of-plane bending vibrations having their origin in the C–Cl bond, in CP, are designated 7b, 9a and 17a, respectively. Raman shifts near 180 and 150 cm^{-1} are identified with β(C–Cl)9a and π(C–Cl)17a, whereas that predicted at 224 cm^{-1} is attributed to ν(C–Cl)7b. Mode 7b is C–Cl stretch to the extent of 65%, whereas vibration 9a exhibits 55% C–Cl in-plane bending nature.

4.2.1.6.4. Vibrations of the nitro and amino (C–N) bonds. C–N bond is present in both NP and AP, each being responsible for three vibrations associated with the C–N bond. The IR absorption at 1076 cm^{-1} in NP is a mixed mode of vibrations 12, 19b, 7b, 19b' and 18b with PED 23%, 18%, 12%, 9% and 8%, respectively. Similarly, the IR band around 1194 cm^{-1} in AP is also a mixed vibration of modes 7b, 18a, 7a, 12, 13 and β(OH) having PED contribution 23%, 22%, 11%, 11%, 9% and 5%, respectively, in AP. We find that the stretching frequency of amino C–N bond near 1194 cm^{-1} is higher than that of nitro C–N bond stretching around 1076 cm^{-1}. This result is consistent with higher bond length of nitro C–N bond (1.453 Å); in comparison with that of amino C–N bond (1.394 Å). This is further supported by the lower value of nitro C–N stretching force constant, which is 5.080 mdyne $Å^{-1}$, in comparison with that for amino C–N bond at 6.119 mdyne $Å^{-1}$. These results are a consequence of deactivating nitro group in NP and activating amino group in AP, to certain extent only. Because the systematics shown by C–N stretching frequencies and associated force constants of NP and AP cannot be attributed entirely to the movement of electron charge alone, as they are known to depend, to a significant extent, on the effective mass of NP and AP in general, and that of nitro and amino moieties in particular. There is no difficulty in assigning Raman shift near 178 cm^{-1}, with 61% PED from vibration 9a, and the scaled value at 143 cm^{-1} with 45% PED from mode 17a, in NP, to the normal modes β(C–N)9a and π(C–N)17a, respectively. The scaled values around 291 and 218 cm^{-1}, attributable to modes 9a and 17a, in AP, are in fact arise due to participation of several vibrations as evident from Table 4.

4.2.1.7. Vibrations of the substituent groups.

4.2.1.7.1. Vibrations of the nitro group. These comprise of six vibrations $\nu_{as}(NO_2)$, $\nu_s(NO_2)$, $\delta(NO_2)$, $\omega(NO_2)$, $\gamma(NO_2)$ and $\tau(NO_2)$, which are present in NP only. The absorptions near 1538, 1371, 822R, 639, 560 and 87 C cm^{-1} are attributed to the above vibrations in NP, respectively. It is to be noted that significant PED contribution, ranging from 32% to 57% comes from the corresponding mode of the nitro group except $\nu_{as}(NO_2)$. As these vibrations are situated in a complex region of vibrational space, they are expected to mix with several other frequencies that fall in the same region. This is, indeed, found true in Table 3. These assignments for asymmetric stretching,

symmetric stretching, in-plane deformation and rocking vibrations of the nitro group in NP, agree well with those of corresponding modes in monohalogenated nitrobenzenes,[50] in the vicinity of 1520, 1350, 860 and 540 cm^{-1}. This is also true of scaled value for torsion mode of the nitro group at 87 cm^{-1}, as it is close to corresponding observed mode near 80–90 cm^{-1} in several monohalogenated nitrobenzenes.[50]

4.2.1.7.2. Vibrations of the amino group. These are relevant for AP only. The symmetric and asymmetric stretching vibrations of the amino group occur at 3373 and 3287 cm^{-1} in the solid phase. Both of them are pure as PED contribution from their corresponding coordinates is 100%. In-plane deformation of the amino group is identified with infrared absorption near 1602 cm^{-1}. This is almost a pure mode, as it gets 88% PED from its own coordinate, with a minor contribution (7%) from amino C–N stretching vibration. Rocking mode of the amino group is assigned to the Raman shift near 1101 cm^{-1}, having 25% PED from its own coordinate and mixing with mode 14 (32%), in-plane bending of OH moiety (27%) and 18b (9%). Similarly, IR absorption in the neighborhood of 511 cm^{-1} with 27% PED, and Raman shift in the vicinity of 344 cm^{-1} with 47% PED, from wagging and torsion vibration of the amino group are ascribed to $\omega(NH_2)$ and $\tau(NH_2)$, respectively. Obviously, they cannot be pure modes (see Table 4). The assignments for in-phase vibrations of the amino moiety $\nu_{as}(NH_2)$, $\nu_s(NH_2)$, $\delta(NH_2)$ and$\gamma(NH_2)$ agree reasonably well with those of the corresponding IR absorptions around 3395, 3204, 1600 and 1048 cm^{-1}, in 2-((2-aminopyridin-3-yl) methylene) hydrazinecarbothioamide[51] and its N-ethyl variant at 3362, 3197, 1584 and 1028 C,[52] respectively, obtained with same level of theory as in the present case.

4.2.1.7.3. Vibrations of the hydroxyl moiety. The three vibrations ν(OH), β(OH) and τ(OH) (the twist is around C–O bond of COH moiety, hence, it can also be designated τ(C–O)) belong to this category. The IR absorptions at 3346, 3450 and 3469 cm^{-1}, in CP, NP and AP, respectively, are pure and assignable to OH stretching vibrations, as the corresponding coordinate contributes 100% PED to them. Raman shift at 1158 cm^{-1} in CP, along with IR absorptions near 1170 and 1106 cm^{-1}, in NP and AP, respectively, are attributed to in-plane bending mode of the OH moiety. It gets 36%, 21% and 20% PED from its own coordinate in CP, NP and AP, respectively. There are several other vibrations that take part in this normal mode, as it appears in a complicated region of vibrational spectrum in these molecules (see Tables 2–4). The torsion vibration of OH group is identified with the bands around 370 R, 668 and 254 C in CP. NP and AP, wherein the PED from the corresponding coordinate varies from 63 to 86%. It shows considerable mixing with ring torsion 16a in NP, whereas in CP and AP, this vibration does not exhibit any such mixing with other vibrations. The assignments for ν(OH) and β(OH) in CP, NP and AP are acceptable, when compared to the attribution of corresponding vibrations for one of the hydroxyl fragment in 2,6-dihydroxytolune.[49]

Discussion of attribution of C–H stretching vibrations in detail is not required as all of them are pure having 94–100% PED from corresponding C–H stretching coordinate. Further, the assignment of vibrations originating from the non-phenolic ring of CP, NP and AP, can be understood with the help of PED in Tables 2–4.

4.3. NMR spectral analysis

The NMR serves as a great resource in determining the structure of an organic compound by revealing its hydrogen and carbon skeleton. In order to make a definite assignment and analysis of ^{13}C and ^{1}H NMR spectra, theoretical calculations on chemical shifts of CP, NP and AP are undertaken, as explained in Section 3 dealing with computational aspects. Chemical shifts measured for CP and NP, in a solution of $CDCl_3$, and those obtained for AP in a solution of DMSO-d_6, employing TMS as internal standard are depicted in Figure SF1 (^{1}H spectra) and Figure SF2 (^{13}C spectra) (see supplementary information).

Table 5. Experimental and calculated ^{1}H and ^{13}C NMR chemical shifts δ (ppm) of CP, NP and AP.

	CP		NP		AP	
Atom	Experimental	Calculated	Experimental	Calculated	Experimental	Calculated
H13	7.635	7.707	7.842	7.732	7.496	7.705
H14	7.409	7.548	7.413	7.603	7.262	7.590
H15	7.427	7.565	7.580	7.646	7.226	7.559
H16	7.584	7.685	7.864	7.778	7.372	7.641
H17	7.390	7.533	7.489	7.629	7.399	7.653
H18	7.488	7.622	8.544	8.498	6.946	7.071
H21	7.166	7.281	7.267	7.438	6.751	6.899
H22	7.283	7.478	8.337	8.005	6.748	6.840
H23	5.734	5.309	10.607	11.353	9.234	9.125
H24	–	–	–	–	4.959	3.577
H25	–	–	–	–	4.959	3.929
RMSD	0.19		0.29		0.56	
C1	139.603	147.550	138.239	145.771	144.723	149.507
C2	127.202	132.467	126.695	132.262	126.582	132.285
C3	128.866	133.562	129.123	133.838	129.105	133.304
C4	120.375	131.594	127.992	132.582	126.125	130.808
C5	128.950	133.710	129.145	134.177	129.129	133.378
C6	126.785	131.890	126.689	132.076	126.350	132.070
C7	135.054	142.582	133.871	141.137	136.645	142.884
C8	127.342	132.714	122.812	128.914	115.226	117.816
C9	126.760	131.887	133.792	140.218	132.106	140.676
C10	150.801	157.160	154.356	162.872	141.487	148.418
C11	116.626	120.375	120.425	124.681	113.500	117.388
C12	127.588	132.923	136.278	144.358	115.854	120.419
RMSD	6.34		6.28		5.39	

–: Not relevant.

Observed and calculated chemical shifts are summarized in Table 5 for both ^{1}H and ^{13}C NMR signals. The RMSD value for ^{1}H NMR, between the experimental and computed chemical shifts is 0.19, 0.29 and 0.56 ppm, whereas the same quantity for ^{13}C NMR is 6.34, 6.28 and 5.39 ppm, for CP, NP and AP, respectively. These are acceptable, as they are small. The linear regression between the experimental and calculated chemical shifts obtained by DFT method for ^{1}H and ^{13}C are plotted in Figure FS3 and Figure FS4, for CP, NP and AP, respectively. The correlation coefficients for proton chemical shifts are 0.990, 0.955 and 0.989, whereas those for carbon-13 chemical shifts are 0.945, 0.982 and 0.984, respectively, for CP, NP and AP. As these are close to unity the assignments made for NMR signals are reliable.

The chemical shifts, both experimental and theoretical, for the ^{1}H atoms on the biphenyl ring appear in the range 6.748–8.544 ppm in the titled molecules. They are assigned for five hydrogen atoms on the phenyl ring, attached to the phenolic ring below.

CP: ^{1}H NMR ($CDCl_3$, 400 MHz): δ (ppm) = 7.64 (d, J = 2.1 Hz, 1H), 7.61–7.46 (m, 5H), 7.40 (dd, J = 13.5, 6.2 Hz, 1H), 7.17 (d, J = 8.4 Hz, 1H) and 5.73 (s, 1H, –OH).

NP: ^{1}H NMR ($CDCl_3$, 400 MHz): δ (ppm) = 10.61 (s, 1H, –OH), 8.34 (d, J = 2.3 Hz, 1H), 7.85 (dd, J = 8.7, 2.3 Hz, 1H), 7.60–7.39 (m, 5H) and 7.28 (d, J = 4.40 Hz, 1H).

AP: ^{1}H NMR (DMSO-d_6, 400 MHz): δ (ppm) = 9.23 (s, 1H, –OH), 7.52–7.22 (m, 5H), 6.95 (d, J = 2.34 Hz, 1H), 6.76 (dd, J = 0.96, 5.77 Hz, 1H), 6.74 (d, J = 4.20 Hz, 1H), and 4.96 (s, 2H, –NH2).

The ^{13}C NMR chemical shifts for an organic compound are usually greater than 100 ppm.[53,54] In the present investigation also, ^{13}C NMR chemical shifts are greater than 100 ppm. They vary from 117.388 to 162.872 ppm for carbons, as per present calculations for CP, NP and AP. The variation of chemical shifts depends on the decrease in electron donating or shielding ability of the attached atoms.[55] The molecules CP, NP and AP consist of twelve carbon atoms each, and all of them are aromatic carbons associated with biphenyl unit shown in Figure 1. As expected we find twelve ^{13}C chemical shifts in NMR spectra of CP, NP and AP, each.

They are assigned below.

CP: ^{13}C NMR ($CDCl_3$, 400 MHz): δ (ppm) = 150.801 139.603, 135.054, 128.950, 128.866, 127.588, 127.342, 127.202, 126.785, 126.760, 120.375 and 116.626.

NP: ^{13}C NMR ($CDCl_3$, 400 MHz): δ (ppm) = 154.356, 138.239, 136.278, 133.871, 133.792, 129.145, 129.123, 127.992, 126.695, 126.689, 122.812 and 120.425.

AP: ^{13}C NMR (DMSO-d_6, 400 MHz): δ (ppm) = 144.723, 141.487, 136.645, 132.106, 129.129, 129.105, 126.582, 126.350, 126.125, 115.854, 115.226 and 113.500.

4.4. Frontier molecular orbitals

Frontier molecular orbitals facilitate proper understanding of the electronic transitions. They have significant role in quantum chemistry for determining the molecular reactivity of conjugated systems[56] and capability of a molecule to absorb electromagnetic radiation. HOMO plays the role of an electron donor, whereas LUMO acts as the electron acceptor.[36,37]

4.4.1. Analysis of UV-Vis spectra

The electronic absorption spectra of CP, NP and AP were computed with the help of calculations using TD-DFT/B3LYP/6-311++G(d,p) method using the Polarizable Continuum Model (PCM) through the integrated equation formalism (IEF-PCM), to take care of solvent effects,[35] as already mentioned in Section 3. The observed and simulated UV-Vis spectra of the molecules CP, NP and AP are shown in Figure FS5, and corresponding spectral values are presented in Table ST1 (see supplementary information).

The experimental UV-Vis spectra, in solution, show two absorption bands (λ_{max}) at 305 and 250 nm in CP; 455 and 306 nm in NP; and 305 and 260 nm in AP. In simulated UV-Vis spectra the absorption bands at 271.60, 264.24 and 255.95 nm for CP; 436.55, 343.79 and 315.01 nm for NP; and 301.16, 278.71 and 268.75 nm for AP, with associated oscillator strengths $f = 0.2751$, 0.3419 and 0.0041 for CP; 0.0495, 0.0002 and 0.0150 for NP; and 0.2122, 0.0012 and 0.0481 for AP, respectively, are predicated as in Table ST1. Calculations show that the higher of the two observed absorptions is a $n \rightarrow \pi^*$ transition, whereas the lower one is a $\pi \rightarrow \pi^*$ transition. Further, the major contribution of molecular orbitals for the maximum absorption wavelength corresponds to the electronic transition from the H→L (57%) and H-1→L + 1 (34%) for CP; H→L (98%) for NP; and H→L (92%) for AP. The other remaining electronic transitions are available in Table ST1. These transitions, along with their corresponding energy gaps are shown in Figure 8.

4.4.2. Chemical reactivity descriptors

Frontier molecular orbitals (HOMO and LUMO) and their properties, such as energies, play a vital role in chemical reactions. The frontier orbital energy gap between HOMO and LUMO helps to characterize the chemical reactivity, kinetic stability and polarizability of a molecule.[57] A small HOMO-LUMO energy gap implies low kinetic stability and high chemical reactivity since it is energetically favorable to accumulate electrons in high-lying LUMO by exciting electrons from low-lying HOMO.[58–61] Large energy gap between two frontier orbitals is a reflection of greater hardness of the molecule. Chemical hardness is a useful concept for understanding the behavior of chemical systems. It is known that soft molecules have small energy gap and hence are more polarizable making them chemically more reactive than hard molecules.[62] The electrophilicity index is an indicator of electron flow between a donor and an acceptor.[63]

The energies of HOMO-LUMO orbitals, and various indicative parameters of chemical reactivity, obtained as a result of computations at B3LYP/6-311++G(d,p) level for CP, NP and AP are presented in Table ST2 (see Figure 8 also). It is seen from Table ST2, the difference between the

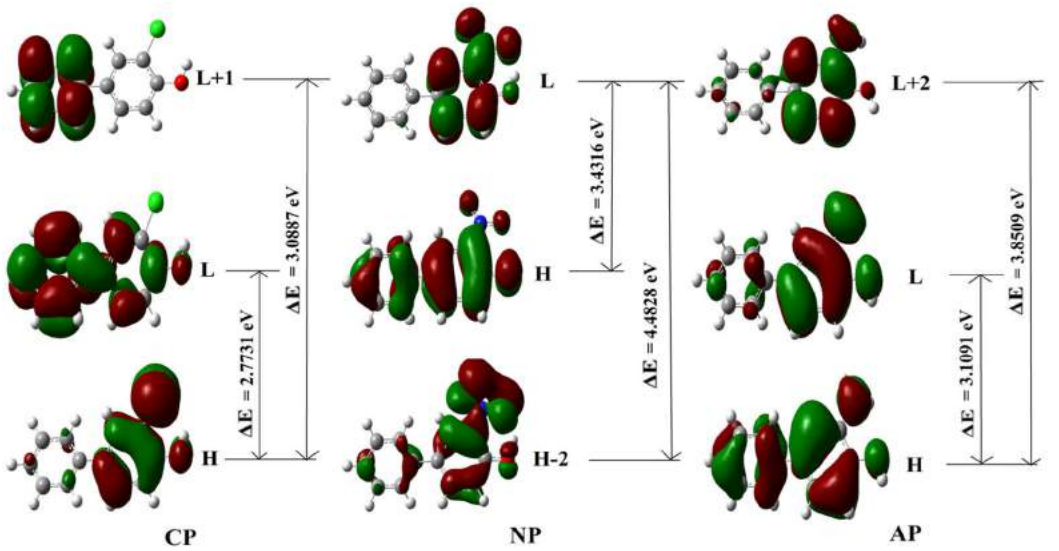

Figure 8. Frontier molecular orbitals of CP, NP and AP.

HOMO and LUMO orbital energies is 2.7731, 3.4316 and 3.1091 eV in CP, NP and AP, respectively. The values of chemical hardness and softness are 1.3865 and 0.3606 eV for CP; 1.7158 and 0.2914 eV for NP; and 1.5545 and 0.3216 eV for AP, respectively. It can also be seen from Table ST2 (depicted as supplementary information), the value of electrophilicity power (ω) of the three molecules is larger which indicates that these molecules are strong electrophilic due to small value of chemical potential.[64] The electrophilicity power of a given molecule can also be used to study the biological activity and toxicity of that molecule.[65,66]

4.5. Non-linear optical (NLO) characteristics

Organic NLO materials are being investigated widely by means of DFT,[67–70] due to their potential applications for optical logic, optical switching, optical memory and frequency shifting.[71–74]

The values of total molecular dipole moment (μ_t) and its components, total molecular polarizability (α_t) and its components; and first order hyperpolarizability (β_t) and its components of CP, NP and AP are computed with DFT employing B3LYP/6-311++G(d,p) level of theory using Gaussian 09 program. The results are summarized in Table ST3 (see supplementary information).

The NLO behavior of a molecular system is usually evaluated by comparing its total molecular dipole moment (μ_t) and the mean first order hyperpolarizability (β_t) with corresponding parameters of a prototypical molecule like Urea. Since, Urea is often considered to be a standard NLO material due to the combination of non-centrosymmetric crystal packing and capacity for intramolecular charge transfer. It is one of the standards among second-order NLO materials which demonstrate the electrooptic effect by which an external field changes the refractive index and second harmonic generation (SHG), where the material scatters the light at twice the frequency of the incident light. The efficiency of both NLO processes is determined by the second-order susceptibility, which vanishes in centrosymmetric media. Therefore, the possibility to design photonic devices at smaller scale critically depends on new non-centrosymmetric materials with high nonlinear susceptibility.[75] Moreover, Urea does not exhibit a large nonlinearity compared to visible absorbing molecules. Its second order nonlinearity is substanially larger than that of other organic molecules, such as fluorobenzene, aniline, nitrobenzene, p-nitroaniline and merocyanine

with comparable UV transparency.[76] Hence, Urea is considered as standard molecule to study the NLO behavior of a molecule.

The values of μ_t and β_t for Urea are 1.3732 Debye and 372.8×10^{-33} cm^5/esu, respectively, which are used frequently as threshold values. μ_t is estimated at 0.4306, 1.6847 and 0.5590 Debye, respectively, for CP, NP and AP, whereas β_t for them is predicted near 876.7213×10^{-33}; 562.4747×10^{-33} and $1247.6376 \times 10^{-33}$ cm^5/esu. Thus, we find that the value of μ_t for NP is higher, and those for CP and AP are lower than the threshold value of Urea, whereas value of β_t for CP, NP and AP is 2.35, 1.51 and 3.35 times higher than the threshold value of Urea. Hence, due to this relatively higher value of hyperpolarizability for CP, NP and AP, with respect to corresponding parameter for Urea, they are potential candidates for NLO applications. Hyperpolarizability of a molecule is caused by movement of electron cloud through π-conjugated structure of electrons.[77] The charge delocalization in the molecule can be understood from the components of hyperpolarizability. The maximum charge delocalization occurs along β_{xxx} in the molecules CP and AP, and β_{xxy} in NP, as evidenced from Table ST3 (see supplementary information).

4.6. Thermodynamic parameters and rotational constants

Various calculated thermodynamic parameters and rotational constants for CP, NP and AP are collected in Table ST4 (see supplementary information). The standard thermodynamic functions such as SCF energy, specific heat capacity at constant volume (C_v), entropy (S), vibrational energy (E_{vib}), zero-point energy (E_0) and rotational constants (A, B and C) are evaluated employing rigid rotor harmonic oscillator approximation employing standard expressions,[78–80] using DFT/B3LYP/6-311++G(d,p) level of theory. The rotational constants A, B and C are calculated at 1499, 306 and 262 MHz for CP; 1259, 283 and 237 MHz for NP; and 1999, 351 and 309 MHz for AP, respectively. Calculation of thermodynamic parameters is performed in gas phase and pertains to one mole of ideal gas at one atm pressure. As per the second law of thermodynamics in thermo chemical field,[81] the results of present calculations can be used to compute the other thermodynamic energies and help to estimate the direction of chemical reactions.

4.7. Natural bond orbital (NBO) analysis

The NBO analysis provides a description of the structure of a conformer by a set of localized bond and antibond orbitals; and Rydberg extra valence orbitals. It tells about the interaction between the bond orbitals, electron delocalization, bond bending effect, intra-molecular charge transfer (ICT) and identification of hydrogen bonding.[82] In the NBO analysis,[40,83,84] the electron wave functions are interpreted in terms of a set of occupied Lewis-type (bond or lone pair) and a set of unoccupied non-Lewis-type (anti-bond or Rydberg) localized NBO orbitals. The delocalization of electron density (ED) among these orbitals causes a stabilizing donor-acceptor interaction. The stabilization energies of all possible interactions between donor and acceptor orbitals in the NBO basis can be evaluated using the second order perturbation theory. The interaction yields in a loss of occupancy from the localized NBO of the idealized Lewis structure into an empty non-Lewis orbital. The delocalization effects (or donor-acceptor charge transfers) can be estimated from the off-diagonal elements of the Fock matrix in the NBO basis. So, the natural bond orbital (NBO) computations are made using NBO 3.1 program[85] as implemented in the Gaussian 09 W software at the DFT/B3LYP level using 6-311++G(d,p) basis set, in order to understand various second-order interactions between the filled orbitals of one subsystem and vacant orbitals of another subsystem. The output obtained by second-order perturbation theory is used for identifying the significant delocalization effects. The strength of these delocalization interactions E(2) is evaluated by the method reported by A. E. Reed et al.[40]

The larger the E(2) value, the stronger is the interaction between electron donors and acceptors, i.e. the more electron donating tendency from electron donors to acceptors and greater the extent of conjugation of the whole system. The dominant contributors, to the stabilization energies, that emerge from NBO analysis for CP, NP and AP are presented in Tables ST5, ST6 and ST7, respectively. The molecular interaction is formed by the orbital overlap between σ(C–C) and σ^*(C–C) bond orbitals, which results in intra-molecular charge transfer (ICT) causing stabilization of the molecule. Large value of interaction energy indicates weakening of the corresponding bonds. The intra-molecular hyper conjugative energy between σ and σ^* electrons of aromatic ring is found at 4.88 kcal mol^{-1} due to interactions σ(C10–C11) $\rightarrow$ σ^*(C9–C10) in CP, whereas 4.54 kcal mol^{-1} for the interaction of σ(C9–C10) $\rightarrow$ σ^*(C8–C9) in NP; while it is 4.56 kcal mol^{-1} for the interaction of σ(C10–C11) $\rightarrow$ σ^*(C9–C10) in AP.

The electron density at the conjugated π-bonds of the biphenyl unit is in the range 1.6405–1.7007, 1.6150–1.7044 and 1.6369–1.7030 in CP, NP and AP, respectively, whereas that for π^*-antibonds are in the range between 0.3234–0.4481, 0.3057–0.4525 and 0.3258–0.3960.

According to NBO analysis, the interactions π(C1–C6) $\rightarrow$ π^*(C4–C5); π(C2–C3) $\rightarrow$ π^*(C1–C6); π(C4–C5) $\rightarrow$ π^*(C2–C3); π(C7–C8) $\rightarrow$ π^*(C11–C12); π(C9–C10) $\rightarrow$ π^*(C7–C8); π(C11–C12) $\rightarrow$ π^*(C9–C10) and LP(2)O20 $\rightarrow$ π^*(C9–C10) have high stabilization energy in the range 20.56–31.15 kcal mol^{-1}, respectively, in CP; the interactions π(C1–C2) $\rightarrow$ π^*(C3–C4); π(C3–C4) $\rightarrow$ π^*(C1–C2, C5–C6); π(C5–C6) $\rightarrow$ π^*(C1–C2, C3–C4); π(C7–C8) $\rightarrow$ π^*(C11–C12); π(C9–C10) $\rightarrow$ π^*(C7–C8, N19–O24); π(C11–C12) $\rightarrow$ π^*(C9–C10), LP(2)O20 $\rightarrow$ π^*(C9–C10) and LP(3)O25 $\rightarrow$ π^*(N19–O24) have high stabilization energy in the range 20.03–126.90 kcal mol^{-1}, respectively in NP; and π(C1–C6) $\rightarrow$ π^*(C4–C5); π(C2–C3) $\rightarrow$ π^*(C1–C6); π(C4–C5) $\rightarrow$ π^*(C2–C3); π(C7–C12) $\rightarrow$ π^*(C10–C11); π(C8–C9) $\rightarrow$ π^*(C7–C12) and LP(2)O20 $\rightarrow$ π^*(C10–C11) interactions have high stabilization energy in the range 20.48–24.09 kcal mol^{-1}, respectively, in AP. Due to movement of π-electron cloud from donor to acceptor (i.e, ICT), the molecules get more polarized. This leads us to the inference that the NLO properties of CP, NP and AP arise from ICT. This result is in supports of our earlier observation that the three materials are good for nonlinear applications, made in the section on NLO properties. As a consequence of this charge delocalization, the molecule gains total stabilization energy 258.03, 254.67 and 254.81 kcal mol^{-1} in CP, NP and AP, respectively from the biphenyl unit alone. The stabilization energies due to charge transfer from lone pairs of oxygen, nitrogen and chlorine atoms to various other bonds that weaken and elongate the bonds in the three molecules under investigation can be found in Tables ST5–ST7.

4.8. Analysis of molecular electrostatic surface potential (MESP)

The molecular electrostatic surface potential (MESP) is the net electrostatic effect of a molecule in the surrounding space and is well defined by the total charge distribution (nuclei and electrons). The MESP correlates with the partial charges, dipole moment, electronegativity and chemical reactivity of a given molecule,[86–88] non-covalent interactions, particularly, hydrogen bonds[89–91] and molecular aggregation,[92,93] lone pair–π interactions,[94,95] aromaticity and reaction mechanisms.[96,97] Molecular electrostatic surface potential has been plotted for CP, NP and AP molecules with DFT/B3LYP/6-311++G(d,p) formalism. The negative (electron rich) regions, represented by red color, in the MESP diagram are related to electrophilic reactivity while the positive (electron deficient) regions, represented by the blue region, are related to nucleophilic reactivity. MESP plots are shown, in Figure SF6, for the molecules under investigation. It can be seen from this figure that the maximum negative electrostatic potential region is located over the oxygen atoms, which are prone to the electrophilic reactions, whereas regions having the positive electrostatic potential are around the hydrogen atoms, which are preferentially nucleophilic reaction sites, in the three molecules under investigation.

5. Conclusions

Geometry optimization of structures revealed that the three molecules investigated are stabilized in the ground state with lowest energy in a non-planar structure belonging to C_1 point group symmetry, forming intra-molecular hydrogen bond in three molecules. Conformational studies demonstrated that the hydrogen atom of hydroxyl moiety assumes *cis* position with respect to chlorine atom in CP, and nitrogen atom of nitro group in NP, whereas it prefers *trans* position with respect to nitrogen atom of amino group in AP. The steric repulsion of nitrogen atom of amino group in AP influences the C–N bond to be twisted since this group is more compact and light, whereas, chlorine atom and nitrogen atom, respectively in CP and NP retains in the same plane of phenolic ring due to their heavy mass. Evaluated geometry parameters obtained in DFT computations show good agreement with available experimental data. Proposed vibrational assignments exhibit reasonably good accordance with those of corresponding bands in related molecules. Deactivating nature of the nitro group in NP and activating property of amino moiety in AP are well manifested in C–N bond lengths at 1.453 Å and 1.394 Å, respectively. This result is substantiated by lower values of nitro C–N bond stretching frequency near 1076 cm^{-1} and its associated C–N stretching force constant at 5.080 mdyne $Å^{-1}$, in comparison with those of corresponding parameters around 1194 cm^{-1} and 6.119 mdyne $Å^{-1}$ for amino C–N bond. Measured ^{1}H and ^{13}C NMR chemical shifts and electronic spectra concur satisfactorily with their simulated counterparts for the three molecules. FMO investigations showed that the studied molecules are highly reactive as the energy gap for them was comparatively small, and helped in the assignment of observed UV-Vis spectral bands. It was concluded on the basis of computed NLO parameters that CP, NP and AP were potentially good for NLO applications. It was found using NBO studies that intra-molecular charge transfer (ICT) imparts NLO properties to these molecules. The evaluated molecular electrostatic potentials proved that the most reactive site is in the vicinity of oxygen atoms in the three molecules investigated here.

Acknowledgements

The authors sincerely acknowledge to Central Analytical Laboratory (CAL), BITS Pilani, Hyderabad, India (IR, NMR and UV-Vis) and Sophisticated Analytical Instruments Facility (SAIF) IIT-Madras, India for measurement of Raman spectra. The second author (KSS) is grateful to the management of SR University Warangal, India, for permitting him to undertake the reported investigations.

Disclosure statement

No potential conflict of interest was reported by the author(s).

ORCID

B. Venkatram Reddy http://orcid.org/0000-0001-6516-7731

References

1. Hong-Ming Cheng, Morifusa Eto, Shozo Kuwatsuka, and Yasuyoshi Oshima, "Studies on the Phenylphenol Derivatives with Biological Activity. Part I. Herbicidal Activity of Nitro-Substituted Phenylphenols," *Agricultural and Biological Chemistry* 32, no. 3 (1968): 345–52. doi:10.1080/00021369.1968.10859062
2. Hong-Ming Cheng, Morifusa Eto, Shozo Kuwatsuka, and Yasuyoshi Oshima, "Studies on the Phenylphenol Derivatives with Biological Activity. Part II. The Herbicidal Activity of Chloro-Substituted Phenylphenols," *Agricultural and Biological Chemistry* 32, no. 3 (1968): 353–8. doi:10.1080/00021369.1968.10859062
3. Hong-Ming Cheng, Morifusa Eto, Kanji Nakamura, Shozo Kuwatsuka, Yasuyoshi Oshima, and Masaru Kado, "Studies on the Phenylphenol Derivatives with Biological Activity. Part III. Fungistatic Activity of

Phenylphenol Derivatives," *Agricultural and Biological Chemistry* 32, no. 9 (1968): 1162–74. doi:10.1080/00021369.1968.10859205
4. Hong-Ming Cheng, Morifusa Eto, Eiji Taniguchi, Shozo Kuwatsuka, Yasuyoshi Oshima, and Masaru Kado, "Studies on Phenylphenol Derivatives with Biological Activity. Part V. Miticidal Activity and Effect on Oxidative Phosphorylation," *Botyu-Kagaku* 34, no. 176 (1969): 176–82.
5. Cora May Segura Savoy, and John Leo Abernethy, "The Halogenation of Certain Esters in the Biphenyl Series. II. The Chlorination of 4-Phenylphenyl Benzoate and 4-Phenylphenyl Benzenesulfonate," *Journal of the American Chemical Society* 64, no. 9 (1942): 2219–21. doi:10.1021/ja01263a057
6. Cora May Segura Savoy, and John Leo Abernethy, "The Halogenation of Certain Esters in the Biphenyl Series. I. The Chlorination of 4-Phenylphenyl Acetate," *Journal of the American Chemical Society* 64, no. 11 (1942): 2719–20. doi:10.1021/ja01261a052
7. Cora May Segura Savoy, and John Leo Abernethy, "Studies in the Biphenyl Series. III. The Attempted Chlorination of the Acetate, Benzoate and Benzenesulfonate of 4-(4-Chlorophenyl)-Phenol: 2-Chloro-4-(4-Chlorophenyl)-Phenol," *Journal of the American Chemical Society* 65, no. 8 (1943): 1464–5. doi:10.1021/ja01248a007
8. R. M. Holzem, H. M. Stapleton, and C. K. Gunsch, "Determining the Ecological Impacts of Organic Contaminants in Biosolids Using a High-Throughput Colorimetric Denitrification Assay: A Case Study with Antimicrobial Agents," *Environmental Science & Technology* 48, no. 3 (2014): 1646–55. doi:10.1021/es404431k
9. Carolyn Pratt Brock, and Kurt L. Haller, "Two Crystal Modifications of 4-Hydroxybiphenyl: The Biphenyl Structure without an Inversion Center and a Fully Ordered Structure Containing Nearly Planar Molecules," *The Journal of Physical Chemistry* 88, no. 16 (1984): 3570–4. doi:10.1021/j150660a039
10. Kihwan Bae, Sunghyen Koo, and Wonjun Seo, "Antimicrobial Activities of Hydroxybiphenyl Derivatives," *Korean Journal of Pharmacognosy* 17, no. 1 (1986): 85–90.
11. Wonjun Seo, Sunghyen Koo, and Kihwan Bae, "Antimicrobial Activities of Hydroxybiphenyl Derivatives (II). Synthesis and Antibacterial Activities of Allylhydroxybiphenyl Compounds against a Cariogenic Bacterium *Streptococcus mutans* ATCC OMZ176," *Archives of Pharmacal Research* 9, no. 3 (1986): 127–30. doi:10.1007/BF02899995
12. Nikola Basarić, Nikola Cindro, Damir Bobinac, Kata Mlinarić-Majerski, Lidija Uzelac, Marijeta Kralj, and Peter Wan, "Sterically Congested Quinone Methides in Photodehydration Reactions of 4-Hydroxybiphenyl Derivatives and Investigation of Their Antiproliferative Activity," *Photochemical & Photobiological Sciences* 10, no. 12 (2011): 1910–25. doi:10.1039/c1pp05182b
13. Edwin J. Routledge, and John P. Sumpter, "Structural Features of Alkylphenolic Chemicals Associated with Estrogenic Activity," *The Journal of Biological Chemistry* 272, no. 6 (1997): 3280–8. doi:10.1074/jbc.272.6.3280
14. A. H. Filbey, Jr. H. G. Braxton, and B. R. Meltsner, "Process for Preparing Benzyl Substituted Phenols, Dibenzyl Phenolic Compounds, and the Antioxidant Use of Such Phenols" (European Patent 0186255, filed February 28 1985, and issued July 02, 1986).
15. G. Powis, D. C. Melder, and T. J. Wilke, "Human and Dog, but Not Rat, Isolated Hepatocytes Have Decreased Foreign Compound-Metabolizing Activity Compared to Liver Slices," *Drug Metabolism and Disposition* 17, no. 5 (1989): 526–31.
16. G. Powis, D. J. Moore, T. J. Wilke, and K. S. Santone, "A High-Performance Liquid Chromatography Assay for Measuring Integrated Biphenyl Metabolism by Intact Cells: Its Use with Rat Liver and Human Liver and Kidney," *Analytical Biochemistry* 167, no. 1 (1987): 191–8. doi:10.1016/0003-2697(87)90151-5
17. J. H. Burckhalter, F. H. Tendick, E. M. Jones, P. A. Jones, W. F. Holcomb, and A. L. Rawlins, "Aminoalkylphenols as Antimalarials. II. (Heterocyclic-Amino)-α-Amino-o-Cresols. The Synthesis of Camoquin," *Journal of the American Chemical Society* 70, no. 4 (1948): 1363–73. doi:10.1021/ja01184a023
18. María V. Castillo, Roxana A. Rudyk, Lilian Davies, and Silvia Antonia Brandán, "Analysis of the Structure and the FT-IR and Raman Spectra of 2-(4-Nitrophenyl)-4H-3,1-Benzoxazin-4-One. Comparisons with the Chlorinated and Methylated Derivatives," *Journal of Molecular Structure* 1140 (2017): 2–11. doi:10.1016/j.molstruc.2016.08.070
19. Axel D. Becke, "Density-Functional Thermochemistry. III. The Role of Exact Exchange," *The Journal of Chemical Physics* 98, no. 7 (1993): 5648–52. doi:10.1063/1.464913
20. C. Lee, W. Yang, and R. G. Parr, "Development of the Colle-Salvetti Correlation-Energy Formula into a Functional of the Electron Density," *Physical Review. B, Condensed Matter* 37, no. 2 (1988): 785–9. doi:10.1103/physrevb.37.785
21. M. J. Frisch, et al, *Gaussian 09, Revision B.01* (Wallingford, CT: Gaussian, Inc., 2010).
22. R. Dennington, T. Keith, and J. Millam, *Gauss View, Version 5.0. 9* (Shawnee Mission: Semichem Inc., 2009).

23. Arne Almenningen, Otto Bastiansen, Liv Fernholt, Bjørg N. Cyvin, Sven J. Cyvin, and Svein Samdal, "Structure and Barrier of Internal Rotation of Biphenyl Derivatives in the Gaseous State," *Journal of Molecular Structure* 128, no. 1–3 (1985): 59–76. doi:10.1016/0022-2860(85)85041-9
24. Xuqiang Chao, Xiuqin Zhang, Kai Wang, and Jun Ji, Qiang Chen, "4-Methoxy-3-Nitrobiphenyl," *Acta Crystallographica. Section E, Structure Reports Online* 68, no. Pt 1 (2012): o114. doi:10.1107/S1600536811052846
25. Hui-Fen Qian, and Wei Huang, "Biphenyl-3,3′,4,4′-Tetraamine," *Acta Crystallographica. Section E, Structure Reports Online* 66, no. Pt 5 (2010): o1060. doi:10.1107/S1600536810012511
26. T. Sundius, "Molvib – A Flexible Program for Force Field Calculations," *Journal of Molecular Structure* 218 (1990): 321–6. doi:10.1016/0022-2860(90)80287-T
27. T. Sundius, "Scaling of ab Initio Force Fields by MOLVIB," *Vibrational Spectroscopy* 29, no. 1–2 (2002): 89–95. doi:10.1016/S0924-2031(01)00189-8
28. Geza Fogarasi, Xuefeng Zhou, Patterson W. Taylor, and Peter Pulay, "The Calculation of ab Initio Molecular Geometries: efficient Optimization by Natural Internal Coordinates and Empirical Correction by Offset Forces," *Journal of the American Chemical Society* 114, no. 21 (1992): 8191–201. doi:10.1021/ja00047a032
29. Peter Pulay, Geza Fogarasi, Gabor Pongor, James E. Boggs, and Anna Vargh, "Combination of Theoretical ab Initio and Experimental Information to Obtain Reliable Harmonic Force Constants. Scaled Quantum Mechanical (QM) Force Fields for Glyoxal, Acrolein, Butadiene, Formaldehyde, and Ethylene," *Journal of the American Chemical Society* 105, no. 24 (1983): 7037–47. doi:10.1021/ja00362a005
30. J. F. Arenas, I. López Tocón, J. C. Otero, and J. I. Marcos, "Vibrational Spectra of Methylpyridines," *Journal of Molecular Structure* 476, no. 1–3 (1999): 139–50. doi:10.1016/S0022-2860(98)00541-9
31. Z. Latajka, W. B. Person, and K. Morokuma, "An Ab Initio Calculation of the Infrared Spectrum and Tautomerism of Guanine," *Journal of Molecular Structure: THEOCHEM* 135 (1986): 253–66. doi:10.1016/0166-1280(86)80063-X
32. G. Keresztury, S. Holly, G. Besenyei, J. Varga, Aiying Wang, and J. R. Durig, "Vibrational Spectra of Monothiocarbamates-II. IR and Raman Spectra, Vibrational Assignment, Conformational Analysis and Ab Initio Calculations of S-methyl-N,N-Diethyldithiocarbamate," *Spectrochimica Acta Part A: Molecular Spectroscopy* 49, no. 13-14 (1993): 2007–26. doi:10.1016/S0584-8539(09)91012-1
33. Gábor Keresztury, "Raman Spectroscopy: Theory," in *Hand Book of Vibrational Spectroscopy*, edited by John M. Chalmers and Peter R. Griffiths (New York: John Wiley and Sons Ltd., 2006), 71–87.
34. Krzysztof Wolinski, Robert Haacke, James F. Hinton, and Peter Pulay, "Methods for Parallel Computation of SCF NMR Chemical Shifts by GIAO Method: Efficient Integral Calculation, multi-Fock Algorithm, and Pseudodiagonalization," *Journal of Computational Chemistry* 18, no. 6 (1997): 816–25. doi:10.1002/(SICI)1096-987X(19970430)18:6<816::AID-JCC7>3.0.CO;2-V
35. Giovanni Scalmani, and Michael J. Frisch, "Continuous Surface Charge Polarizable Continuum Models of Solvation. I. General Formalism," *The Journal of Chemical Physics* 132, no. 11 (2010): 114110. doi:10.1063/1.3359469
36. Kenichi Fukui, "Role of Frontier Orbitals in Chemical Reactions," *Science* 218, no. 4574 (1982): 747–54. doi:10.1126/science.218.4574.747
37. Tjalling Charles Koopmans, "Ordering of Wave Functions and Eigenenergies to the Individual Electrons of an Atom," *Physica* 1 (1933): 104–13. doi:10.1016/S0031-8914(34)90011-2.
38. Robert G. Parr, László V. Szentpály, and Shubin Liu, "Electrophilicity Index," *Journal of the American Chemical Society* 121, no. 9 (1999): 1922–4. doi:10.1021/ja983494x
39. Amyand David Buckingham, "Permanent and Induced Molecular Moments and Long-Range Intermolecular Forces," *Advances in Chemical Physics* 12 (1967): 107–42. doi:10.1080/00268979600100491
40. Alan E. Reed, Larry A. Curtiss, and Frank Weinhold, "Intermolecular Interactions from a Natural Bond Orbital, Donor-Acceptor Viewpoint," *Chemical Reviews* 88, no. 6 (1988): 899–926. doi:10.1021/cr00088a005
41. Seiji Tsuzuki, Tadafumi Uchimaru, Kazunari Matsumura, Masuhiro Mikami, and Kazutoshi Tanabe, "Torsional Potential of Biphenyl: Ab Initio Calculations with the Dunning Correlation Consisted Basis Sets," *The Journal of Chemical Physics* 110, no. 6 (1999): 2858–61. doi:10.1063/1.477928
42. J. C. Sancho-García, and A. J. Pérez-Jiménez, "A Theoretical Study of the Molecular Structure and Torsional Potential of Styrene," *Journal of Physics B: Atomic, Molecular and Optical Physics* 35, no. 6 (2002): 1509–23. doi:10.1088/0953-4075/35/6/308
43. J. C. Sancho-García, and, and A. J. Pérez-Jiménez, "Nitrobenzene Rotational Energy Barrier: A Survey of Several ab Initio Methods," *The Journal of Chemical Physics* 119, no. 10 (2003): 5121–7. doi:10.1063/1.1597632
44. Alfred Karpfen, Cheol Ho Choi, and Miklos Kertesz, "Single-Bond Torsional Potentials in Conjugated Systems: A Comparison of ab Initio and Density Functional Results," *The Journal of Physical Chemistry A* 101, no. 40 (1997): 7426–33. doi:10.1021/jp971606l

45. E. Bright Wilson, Jr., "The Normal Modes and Frequencies of Vibration of the Regular Plane Hexagon Model of the Benzene Molecule," *Physical Review* 45, no. 10 (1934): 706–14. doi:10.1103/PhysRev.45.706
46. G. Varsanyi, *Assignments for Vibrational Spectra of Seven Hundred Benzene Derivatives*, Vol. 1:27 (London: Adam Hilger, 1974), 322–3.
47. K. Srishailam, B. Venkatram Reddy, and G. Ramana Rao, "Investigation of Torsional Potentials, Hindered Rotation, Molecular Structure and Vibrational Properties of Some Biphenyl Carboxaldehydes Using Spectroscopic Techniques and Density Functional Formalism," *Journal of Molecular Structure* 1196 (2019): 139–61. doi:10.1016/j.molstruc.2019.06.064
48. N. D. Patel, V. B. Kartha, and N. A. Narasimham, "Vibrational Spectra Dihalogenated Benzenes. I. In-Plane Vibrations," *Journal of Molecular Spectroscopy* 48, no. 2 (1973): 185–201. doi:10.1016/0022-2852(73)90185-9
49. P. Venkata Ramana Rao, K. Srishailam, B. Venkatram Reddy, and G. Ramana Rao, "Theoretical (DFT) and Experimental (FT-IR & FT Raman) Approach to Investigate the Molecular Geometry and Vibrational Properties of 2,5- and 2,6-Dihydroxytoluenes," *Journal of Molecular Structure* 1240 (2021): 130617. doi:10.1016/j.molstruc.2021.130617
50. P. Muralidhar Rao, and G. Ramana Rao, "Vibrational Spectra and Normal Coordinate Analysis of Monohalogenated Nitrobenzenes," *Journal of Raman Spectroscopy* 20, no. 8 (1989): 529–40. doi:10.1002/jrs.1250200809
51. K. Srishailam, K. Ramaiah, K. Laxma Reddy, B. Venkatram Reddy, and G. Ramana Rao, "DFT Simulation of Barrier Heights, Infrared and Raman Spectra, and Investigation of Vibrational Characteristics of 2-((2-Aminopyridin-3-yl) Methylene) Hydrazinecarbothioamide and Its *N*-Methyl Variant," *Molecular Simulation* 48, no. 15 (2022): 1315–29. doi:10.1080/08927022.2022.2086277
52. K. Ramaiah, K. Srishailam, K. Laxma Reddy, B. Venkatram Reddy, and G. Ramana Rao, "Synthesis, Crystal and Molecular Structure, and Characterization of 2-((2-Aminopyridin-3-yl)Methylene)-N-Ethylhydrazinecarbothioamide Using Spectroscopic (1H and 13C NMR, FT-IR, FT-Raman, UV-Vis) and DFT Methods and Evaluation of Its Anticancer Activity," *Journal of Molecular Structure* 1184 (2019): 405–17. doi:10.1016/j.molstruc.2019.02.060
53. Hans-Otto Kalinowski, Stefan Berger, and Siegmar Braun, *Carbon13 NMR Spectroscopy* (London: John Wiley & Sons, 1991), 792.
54. Kalevi Pihlaja, and Erich Kleinpeter, *Carbon-13 NMR Chemical Shifts in Structural and Spectrochemical Analysis* (New York: VCH Publishers, 1994).
55. P. S. Kalsi, *Spectroscopy of Organic Compounds* (New Delhi: New Age International Publishers, 2004.).
56. Cheol Ho Choi, and Miklos Kertesz, "Conformational Information from Vibrational Spectra of Styrene, Trans-Stilbene, and Cis-Stilbene," *The Journal of Physical Chemistry A* 101, no. 20 (1997): 3823–31. doi:10.1021/jp970620v
57. I. Fleming, *Frontier Orbitals and Organic Chemical Reactions* (London: John Wiley, 1976).
58. Serap Yazıcı, Ciğdem Albayrak, Ismail Erdem Gümrükçüoğlu, Ismet Senel, and Orhan Büyükgüngör, "Experimental and Quantum Chemical Computational Study of (E)-1-[5-(3,4-Dimethylphenyldiazenyl)-2-Hydroxyphenyl]Ethanone," *Spectrochimica Acta. Part A, Molecular and Biomolecular Spectroscopy* 93 (2012): 208–13. doi:10.1016/j.saa.2012.02.092
59. Michael D. Diener, and John M. Alford, "Isolation and Properties of Small-Bandgap Fullerenes," *Nature* 393, no. 6686 (1998): 668–71. doi:10.1038/31435
60. S. H. Yang, C. L. Pettiette, J. Conceicao, O. Cheshnovsky, and R. E. Smalley, "Ups of Buckminsterfullerene and Other Large Clusters of Carbon," *Chemical Physics Letters* 139, no. 3–4 (1987): 233–8. doi:10.1016/0009-2614(87)80548-1
61. H. Handschuh, G. Ganteför, B. Kessler, P. S. Bechthold, and W. Eberhardt, "Stable Configurations of Carbon Clusters: Chains, Rings, and Fullerenes," *Physical Review Letters* 74, no. 7 (1995): 1095–8. doi:10.1103/PhysRevLett.74.1095
62. Ralph G. Pearson, "Absolute Electronegativity and Hardness Correlated with Molecular Orbital Theory," *Proceedings of the National Academy of Sciences of the United States of America* 83, no. 22 (1986): 8440–1. doi:10.1073/pnas.83.22.8440
63. Zeynep Demircioğlu, Çiğdem Albayrak Kaştaş, and Orhan Büyükgüngör, "The Spectroscopic (FT-IR, UV–Vis), Fukui Function, NLO, NBO, NPA and Tautomerism Effect Analysis of (E)-2-[(2-Hydroxy-6-Methoxybenzylidene)Amino]Benzonitrile," *Spectrochimica Acta. Part A, Molecular and Biomolecular Spectroscopy* 139 (2015): 539–48. doi:10.1016/j.saa.2014.11.078
64. G. Ramesh, and B. Venkatram Reddy, "Barrier Potential, Structure (Monomer and Dimer), Inter- and Intra-Molecular Interactions, Vibrational Analysis, Fukui Functions, MESP, NBO, UV and NMR Analysis of Pyridine-3-Carboxylic Acid Using Spectroscopic and DFT Approach," *Polycyclic Aromatic Compounds* (2022): 1–18. doi:10.1080/10406638.2022.2046614
65. S. Renuga, M. Karthikesan, and S. Muthu, "FTIR and Raman Spectra, Electronic Spectra and Normal Coordinate Analysis of N,N-Dimethyl-3-Phenyl-3-Pyridin-2-yl-Propan-1-Amine by DFT Method,"

Spectrochimica Acta. Part A, Molecular and Biomolecular Spectroscopy 127 (2014): 439–53. doi:10.1016/j.saa.2014.02.068

66. R. Shahidha, A. Abdulaziz Al-Saadi, and S. Muthu, "Vibrational Spectroscopic Studies, Normal Co-Ordinate Analysis, First Order Hyperpolarizability, HOMO–LUMO of Midodrine by Using Density Functional Methods," *Spectrochimica Acta. Part A, Molecular and Biomolecular Spectroscopy* 134 (2015): 127–42. doi:10.1016/j.saa.2014.06.033
67. Yu-Xi Sun, Qing-Li Hao, Wen-Xian Wei, Zong-Xue Yu, Lu-De Lu, Xin Wang, and Yi-Shi Wang, "Experimental and Density Functional Studies on 4-(4-Cyanobenzylideneamino)Antipyrine," *Molecular Physics* 107, no. 3 (2009): 223–35. doi:10.1080/00268970902769471
68. Ali Ben Ahmed, Habib Feki, Younes Abid, Habib Boughzala, C. Minot, and Adnen Mlayah, "Crystal Structure, Vibrational Spectra and Theoretical Studies of L-Histidinium Dihydrogen Phosphate-Phosphoric Acid," *Journal of Molecular Structure* 920, no. 1-3 (2009): 1–7. doi:10.1016/j.molstruc.2008.09.029
69. Jose P. Abraham, D. Sajan, Venkataraya Shettigar, S. M. Dharmaprakash, I. Němec, I. Hubert Joe, and V. S. Jayakumar, "Efficient π-Electron Conjugated Push-Pull Nonlinear Optical Chromophore 1-(4-Methoxyphenyl)-3-(3,4-Dimethoxyphenyl)-2-Propen-1-One: A Vibrational Spectral Study," *Journal of Molecular Structure* 917, no. 1 (2009): 27–36. doi:10.1016/j.molstruc.2008.06.031
70. Seda G. Sagdinc, and Aslı Esme, "Theoretical and Vibrational Studies of 4,5-Diphenyl-2-2 Oxazole Propionic Acid (Oxaprozin)," *Spectrochimica Acta. Part A, Molecular and Biomolecular Spectroscopy* 75, no. 4 (2010): 1370–6. doi:10.1016/j.saa.2010.01.004
71. Chantal Andraud, Thierry Brotin, Chantal Garcia, Fabrienne Pelle, Philippe Goldner, Bernard Bigot, and Andre Collet, "Theoretical and Experimental Investigations of the Nonlinear Optical Properties of Vanillin, Polyenovanillin, and Bisvanillin Derivatives," *Journal of the American Chemical Society* 116, no. 5 (1994): 2094–102. doi:10.1021/ja00084a055
72. Victor M. Geskin, Christoph Lambert, and Jean-Luc Brédas, "Origin of High Second- and Third-Order Nonlinear Optical Response in Ammonio/Borato Diphenylpolyene Zwitterions: The Remarkable Role of Polarized Aromatic Groups," *Journal of the American Chemical Society* 125, no. 50 (2003): 15651–8. doi:10.1021/ja035862p
73. Masayoshi Nakano, Harunori Fujita, Masahiro Takahata, and Kizashi Yamaguchi, "Theoretical Study on Second Hyperpolarizabilities of Phenylacetylene Dendrimer: Toward an Understanding of Structure − Property Relation in NLO Responses of Fractal Antenna Dendrimers," *Journal of the American Chemical Society* 124, no. 32 (2002): 9648–55. doi:10.1021/ja0115969
74. D. Sajan, H. Joe, V. S. Jayakumar, and J. Zaleski, "Structural and Electronic Contributions to Hyperpolarizability in Methyl p-Hydroxy Benzoate," *Journal of Molecular Structure* 785, no. 1–3 (2006): 43–53. doi:10.1016/j.molstruc.2005.09.041
75. E. Artëm Masunov, Arman Tannu, A. Alexander Dyakov, D. Anastasia Matveeva, Alexandra Ya Freidzon, V. Alexey Odinokov, and A. Alexander Bagaturyants, "First Principles Crystal Engineering of Nonlinear Optical Materials. I. Prototypical Case of Urea," *The Journal of Chemical Physics* 146, no. 24 (2017): 244104. doi:10.1063/1.4986793
76. C. Cassidy, J. M. Halbout, W. Donaldson, and C. L. Tang, "Nonlinear Optical Properties of Urea," *Optics Communications* 29, no. 2 (1979): 243–6. doi:10.1016/0030-4018(79)90027-0
77. M. Arivazhagan, and S. Jeyavijayan, "Vibrational Spectroscopic, First-Order Hyperpolarizability and HOMO, LUMO Studies of 1,2-Dichloro-4-Nitrobenzene Based on Hartree–Fock and DFT Calculations," *Spectrochimica Acta. Part A, Molecular and Biomolecular Spectroscopy* 79, no. 2 (2011): 376–83. doi:10.1016/j.saa.2011.03.036
78. Gerhard Herzberg, *Infrared and Raman Spectra of Polyatomic Molecules, Vol. 2, Molecular Spectra and Molecular Structure*, 1st ed. (New York: D. Van Nostrand Company, 1945).
79. Kenneth S. Pitzer, *Molecular Structure and Statistical Thermodynamics, Vol. 1, World Scientific Series in 20th Century Chemistry* (Singapore: World Scientific, 1993).
80. Mohammad M. Ghahremanpour, Paul J. van Maaren, Jonas C. Ditz, Roland Lindh, and David van der Spoel, "Large-Scale Calculations of Gas Phase Thermochemistry: Enthalpy of Formation, Standard Entropy, and Heat Capacity," *The Journal of Chemical Physics* 145, no. 11 (2016): 114305. doi:10.1063/1.4962627
81. V. Balachandran, and V. Karunakaran, "Quantum Mechanical Study of the Structure and Vibrational Spectroscopic (FT-IR and FT-Raman), First-Order Hyperpolarizability, NBO and HOMO − LUMO Studies of 4-Bromo-3-Nitroanisole," *Spectrochimica Acta. Part A, Molecular and Biomolecular Spectroscopy* 106 (2013): 284–98. doi:10.1016/j.saa.2012.12.070
82. Leena Rajith, A. K. Jissy, Krishnapillai Girish Kumar, and Ayan Datta, "Mechanistic Study for the Facile Oxidation of Trimethoprim on a Manganese Porphyrin Incorporated Glassy Carbon Electrode," *The Journal of Physical Chemistry C* 115, no. 44 (2011): 21858–64. doi:10.1021/jp208027s
83. J. P. Foster, and F. Weinhold, "Natural Hybrid Orbitals," *Journal of the American Chemical Society* 102, no. 24 (1980): 7211–8. doi:10.1021/ja00544a007

84. Jana Chocholoušová, Vladimír Špirko, and Pavel Hobza, "First Local Minimum of the Formic Acid Dimer Exhibits Simultaneously Red-Shifted O–H···O and Improper Blue-Shifted C–H···O Hydrogen Bonds," *Physical Chemistry Chemical Physics* 6, no. 1 (2004): 37–41. doi:10.1039/B314148A
85. E. D. Glendening, A. E. Reed, J. E. Carpenter, and F. Weinhold, *NBO Version 3.1* (Madison, WI: TCI, University of Wisconsin, 1998).
86. M. Suhasini, E. Sailatha, S. Gunasekaran, and G. R. Ramkuma, "Vibrational and Electronic Investigations, Thermodynamic Parameters, HOMO and LUMO Analysis on Lornoxicam by Density Functional Theory," *Journal of Molecular Structure* 1100 (2015): 116–28. doi:10.1016/j.molstruc.2015.07.003
87. M. Govindarajan, M. Karabacak, S. Periandy, and S. Xavier, "Vibrational Spectroscopic Studies, NLO, HOMO–LUMO and Electronic Structure Calculations of α,α,α-Trichlorotoluene Using HF and DFT," *Spectrochimica Acta. Part A, Molecular and Biomolecular Spectroscopy* 94 (2012): 53–64. doi:10.1016/j.saa.2012.03.074
88. C. Muñoz-Caro, A. Niño, M. L. Senent, J. M. Leal, and S. Ibeas, "Modeling of Protonation Processes in Acetohydroxamic Acid," *The Journal of Organic Chemistry* 65, no. 2 (2000): 405–10. doi:10.1021/jo991251x
89. Eolo Scrocco, and Jacopo Tomasi, "Electronic Molecular Structure, reactivity and intermolecular Forces: An Euristic Interpretation by Means of Electrostatic Molecular Potentials," *Advances in Quantum Chemistry* 11 (1979): 115–93. doi:10.1016/S0065-3276(08)60236-1
90. F. Javier Luque, Josep Maria López, and Modesto Orozco, "Perspective on "Electrostatic Interactions of a Solute with a Continuum. A Direct Utilization of ab Initio Molecular Potentials for the Prevision of Solvent Effects," *Theoretical Chemistry Accounts* 103, no. 3–4 (2000): 343–5. doi:10.1007/s002149900013
91. Nora Okulik, and Alicia H. Jubert, "Theoretical Analysis of the Reactive Sites of Non–Steroidal anti–Inflammatory Drugs," *Internet Electronic Journal of Molecular Design* 4 (2005): 17–30. BioChem Press).
92. Subhash S. Pingale, Shridhar R. Gadre, and Libero J. Bartolotti, "Electrostatic Insights into the Molecular Hydration Process: A Case Study of Crown Ethers," *The Journal of Physical Chemistry A* 102, no. 49 (1998): 9987–92. doi:10.1021/jp982444b
93. K. V. Jovan Jose, and Shridhar R. Gadre, "An ab Initio Investigation on $(CO_2)_n$ and $CO_2(Ar)_m$ Clusters: Geometries and IR Spectra," *The Journal of Chemical Physics* 128, no. 12 (2008): 124310. doi:10.1063/1.2838202
94. Neetha Mohan, Cherumuttathu H. Suresh, Anmol Kumar, and Shridhar R. Gadre, "Molecular Electrostatics for Probing Lone Pair–π Interactions," *Physical Chemistry Chemical Physics* 15, no. 42 (2013): 18401–9. doi:10.1039/c3cp53379d
95. Neetha Mohan, and Cherumuttathu H. Suresh, "Anion Receptors Based on Highly Fluorinated Aromatic Scaffolds," *The Journal of Physical Chemistry. A* 118, no. 24 (2014): 4315–24. doi:10.1021/jp5019422
96. C. H. Suresh, and Shridhar R. Gadre, "Clar's Aromatic Sextet Theory Revisited via Molecular Electrostatic Potential Topography," *The Journal of Organic Chemistry* 64, no. 7 (1999): 2505–12. doi:10.1021/jo990050q
97. Puthannur K. Anjalikrishna, Cherumuttathu H. Suresh, and Shridhar R. Gadre, "Electrostatic Topographical Viewpoint of π-Conjugation and Aromaticity of Hydrocarbons," *The Journal of Physical Chemistry. A* 123, no. 46 (2019): 10139–51. doi:10.1021/acs.jpca.9b09056

Solid State Communications 351 (2022) 114790

Contents lists available at ScienceDirect

Solid State Communications

journal homepage: www.elsevier.com/locate/ssc

$Ni_{0.48}Cu_{0.12}Zn_{0.4}Fe_2O_4$+ paraformaldehyde nanocomposites as microwave absorbent dominant materials

P. Raju [a], A. Thirupathi [b], P. Neelima [c], M. Kanakadurga [a,*]

[a] Geethanjali College of Engineering and Technology, Cheeryal, Hyderabad, 501301, Telangana, India
[b] Malla Reddy Engineering College, Gundlapochampally, Telangana, 500100, India
[c] Kesava Memorial Institute of Technology, Narayanguda, Hyderabad, India

ARTICLE INFO

Communicated by Y.E. Lozovik

Keywords:
Nanocomposites
Ferrites
Paraformaldehyde
X-band
Ku-band
Reflection loss
Shielding effectiveness

ABSTRACT

A series of nanocomposite materials were developed to study microwave absorption properties in 8.2–12.4 GHz (X-band) and 12.4–18 GHz (Ku-band) regions. Nanocomposites of ferrite and polymer constituents with ordered combination (x) wt% $Ni_{0.48}Cu_{0.12}Zn_{0.4}Fe_2O_4$ + (1-x) wt% paraformaldehyde, (x = 1, 0.9, 0.7, 0.5, 0.3, 0.1, 0) were prepared by mechanical alloying method. Microwave digestion system was used to prepare nanopowders of $Ni_{0.48}Cu_{0.12}Zn_{0.4}Fe_2O_4$ by microwave hydrothermal method. Microwave absorption studies revealed that synergistic combination of ferrite and paraformaldehyde phases in the synthesized composites enhanced the ability to absorb electromagnetic waves screening maximum of 99.7% power of incident electromagnetic waves in X and Ku band frequency regions. The results proved that maximum reflection coefficient of 0.925 and minimum absorption coefficient of 0.072 at 12 GHz were achieved and maximum shielding effectiveness of 26.7 dB was obtained with significant contribution from absorption. The studies proved that maximum synergistic effects were achieved for 50% polymer phase of the sample wherein balanced combination of dielectric and magnetic losses gives rise to minimum reflection loss. The results confirmed that the prepared absorbent dominant materials are found to be potential candidates for designing microwave filters in radar, stealth and satellite applications.

1. Introduction

The development of new materials capable of absorbing electromagnetic waves is a significant research area in rapid advanced technologies in various fields such as electronics, telecommunications, aerospace, military, medical, environmental and commercial applications due to increased use of electromagnetic devices in microwave frequency regions. The widespread usage of electromagnetic devices in GHz frequencies over long time causes unwanted electromagnetic interference pollution leading to malfunctioning of other electronic components [1,2]. Furthermore, prolonged exposure of microwave radiation can give rise to serious health hazards to human beings and harmful effects on environment. Hence, suppression of unwanted electromagnetic interference radiation is a major task to be addressed [3–6]. Creation and designing of materials capable of dissipating electromagnetic interference pollution efficiently, gained major attraction in recent years [7–11]. In general, a good microwave absorbing material should satisfy conditions: impedance matching and electromagnetic wave attenuation which depend on complex permittivity and complex permeability [12,13]. In addition to superior microwave absorption performance, the materials designed for electromagnetic interference filters should possess the features of wide bandwidth, mechanical strength, lightweight, good thermal stability, miniaturization, corrosion resistant and low cost, etc. Hence, new materials with superior microwave absorption properties along with the above requirements is still a challenging task [14]. Earlier, metal sheets were used as shielding materials to reflect unwanted electromagnetic interference radiation, but these materials were found to be limited practical applications due to several factors like processing difficulty, heavy weight, low flexibility, easy corrosion and oxidation, high cost, etc [15,16]. Later, ferrites were considered to be good absorbing materials with high absorption performance, excellent magnetic and dielectric properties. However, these materials suffer drawbacks of natural ferromagnetic resonance occurring at low frequencies, narrow absorption bandwidth [17]. To overcome these difficulties, polymers have been used in combination with ferrites and achieved improved microwave absorption performance

* Corresponding author.
E-mail address: mallavarapudurga@gmail.com (M. Kanakadurga).

https://doi.org/10.1016/j.ssc.2022.114790
Received 13 January 2022; Accepted 31 March 2022
Available online 18 April 2022

[18–21]. Nanocomposites of $Ni_{0.48}Cu_{0.12}Zn_{0.4}Fe_2O_4$, prepared by hydrothermal method using microwave energy, and conducting polymer, polyaniline were prepared and analysed microwave absorption properties by our earlier reports [22].

The present work deals with the preparation of nanocomposites by varying combination of $Ni_{0.48}Cu_{0.12}Zn_{0.4}Fe_2O_4$(NCZ) nanopowders, that were prepared by microwave hydrothermal method, and an insulating polymer, paraformaldehyde (PFD), and then studies of synergistic effects of the nanocomposites over X-band (8.2–12.4 GHz) and Ku band (12,4–18 GHz) microwave frequency regions. The purpose of selecting present materials is due to favourable characteristics of NCZ ferrite like good chemical stability, corrosion resistant and high saturation magnetization and encouraging features of thermosoftening polymer, PFD, such as easy processing, flexibility, lightweight, low processing cost, hight strength and environmentally stable. Prepared samples were tested by XRD and SEM techniques to confirm spinel ferrite and polymer PFD phases of the nanocomposites. The shielding performance of the nanocomposites, studies of reflection coefficient, absorption coefficient, transmission coefficient and reflection loss as function of frequency were investigated.

1.1. Experimental

Among all chemical methods for synthesis of nanopowders, microwave assisted hydrothermal method, a method that uses electromagnetic energy in microwave frequencies to hydrothermal reaction system, was considered as superior synthesis process. In this method heating process is uniform and takes place in a closed reaction system for a time of short period which enhances reaction kinetics resulting in saving of time and energy. Furthermore, the crystal size and morphology can be tuned by appropriately selecting the operating parameters [23–25].

The NCZ nanopowder was prepared by microwave hydrothermal method using microwave digestion system, MARS-5, CEM Corp., Mathews, NC. The advantage of using microwave hydrothermal method, description of microwave digestion system and NCZ ferrite nanopowder preparation were elaborately explained in our earlier reports [22]. Paraformaldehyde in solid form was purchased from Sigma Aldrich chemicals limited with 99% purity. The paraformaldehyde (PFD) powder was characterized by SEM and XRD. The nanocomposites of NCZ nanopowders and PFD with different proportions are prepared using mechanical alloying method and the details are as follows. As synthesized NCZ ferrite nanopowder and commercially purchased PFD powder are dried separately at 60 °C in an oven and then cooled to room temperature. The powders are mixed in different proportions, (x) wt% $Ni_{0.48}Cu_{0.12}Zn_{0.4}Fe_2O_4$ + (1-x) wt% Paraformaldehyde, (x = 1, 0.9, 0.7, 0.5, 0.3, 0.1, 0) and labelled as NCZ, NF1, NF2, NF3, NF4, NF5, PFD, respectively. Powders of each combination are grounded separately using a RetschCo high energy planetary ball mill for 30 h with interruptions of 15 min after every 40 min. The speed of the mill and ball to powder mass charge ratio are optimized and set at 400 rpm and 14:1, respectively. The grounded powders are annealed at temperature 110 °C for half an hour time in air atmosphere. Characterization of each nanocomposite sample is performed using X-ray diffraction technique (Philips PW-1730), and scanning electron microscopy (SEM, LEICA, S440i, UK).

To examine absorption properties in X and Ku-band microwave regions, powders are pressed into cylindrical pellets with measurements suitable for rectangular X-band wave-guide (WR90, height = 10.16 mm and width = 22.86 mm) and Ku-band wave guide (WR62, height = 7.8994 mm and width = 15.7988 mm). The complex reflection scattering parameters (S_{11} and S_{22}) and complex transmission scattering parameters (S_{21} and S_{12}) are determined in X and Ku-band regions, using Agilent 8722 ES vector network analyser [26].

2. Results and discussion

XRD patterns of crystalline NCZ ferrite, polymer and nanocomposite samples are shown in the Fig. 1, reproduced from earlier report [27]. The XRD of NCZ ferrite shows characteristic peaks that are matched with standard values confirming the spinel structure. The intensity of ferrite peaks reduces and PFD peaks intensity rises, as amount of polymer phase increases in the composites, this feature can be observed from the figure. Moreover, the width of the ferrite peaks increases as PFD content increases in the composites which can be observed in the figure. The average crystallite size of each sample is calculated from Scherrer formula, ($L = K\lambda/\beta \cos\theta$, K is a constant, λ wavelength of X-rays, β the full-width half maximum and θ the diffraction angle) [28] and the obtained values are reported in Table 1. The reported values show that crystallite size and lattice parameter of composites reduce as amount of PFD content increases in the composites confirming that amorphous nature of PFD polymer chains decreases crystalline nature of composites. This feature indicates the presence of synergy between polymer and ferrite phases [29].

Fig. 2 depicts morphological microstructures of the samples, which are taken from earlier reports [27]. From the figures it can be observed that the polymer existence breaks the connectivity of ferrite grains. Moreover, the strong interaction between ferrite particles causes the agglomeration of grains, as ferrite phase increases, leading to uneven distribution of PFD in composites. The average value of grain size was estimated by line intercept method, and obtained in the range 24 nm–40 nm. Fig. 3 gives information about relative amounts of elements exist in the samples by energy dispersive X-ray spectroscopy (EDS), EDS spectra of SEM images. From Fig. 3 (b), the distribution of elements of ferrite phase and elements of PFD phase in composite samples can be found. Fig. 3(a) confirms that no peaks of other elements are seen except the

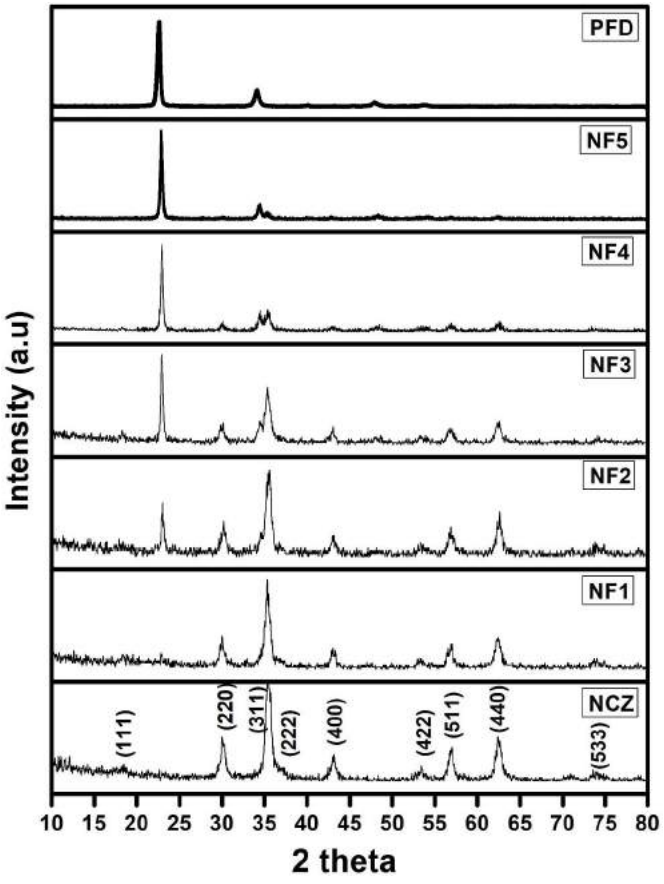

Fig. 1. XRD of NCZ – PFD nanocomposites.

Table 1
Structural parameters of NCZ + PFD nanocomposites.

Sample	XRD Crystallite size (nm)	Lattice parameter (Å)	Grain size (nm)
NCZ	35	8.439 ± 0.001	40
NF1	31	8.423 ± 0.001	37
NF2	28	8.422 ± 0.001	33
NF3	23	8.412 ± 0.001	29
NF4	21	8.404 ± 0.001	26
NF5	21	8.371 ± 0.001	24

only ones corresponding to ferrite and PFD.

To examine how effectively electromagnetic waves have been attenuated by the composite materials, microwave absorption properties have been studied in X-band and Ku-band frequencies. Reflection coefficient, absorption coefficient, transmission coefficient and absorption efficiency were calculated from scattering parameters S_{11} (or S_{22}), S_{12} (or S_{21}) that are measured by vector network analyzer using following formulae [30,31]:

When electromagnetic waves strike the material surface, sum of reflection coefficient R, absorption coefficient A, and transmission coefficient T, must be equal to one, i.e.,

$$A + R + T = 1 \text{or} A = 1 - R - T \text{and}$$

Absorption efficiency A_{eff}, A_{eff} = (1-R-T)/(1-R) such that

$$R = |S_{11}|^2 = |S_{22}|^2,\ T = |S_{12}|^2 = |S_{21}|^2$$

Figs. 4 and 5 show variations of reflection coefficient, absorption coefficient, transmission coefficient, absorption efficiency of composite

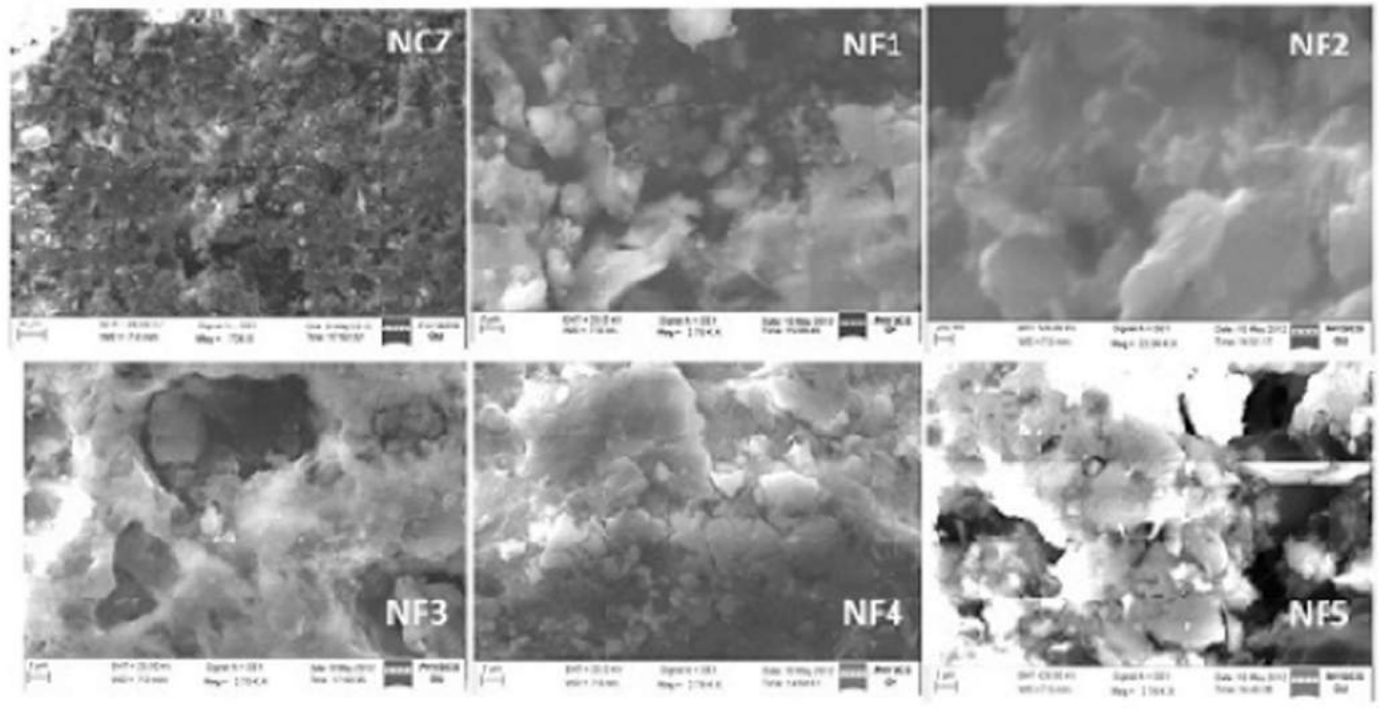

Fig. 2. SEM images of NCZ – PFD nanocomposites.

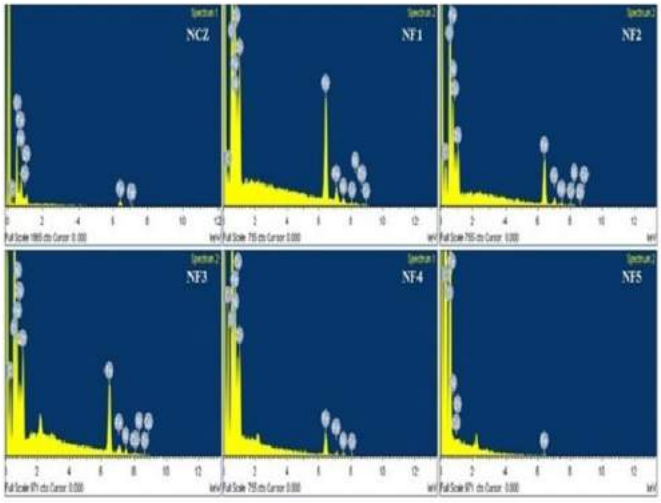

(a)

NCZ		
Element	Weight%	Atomic%
C K	12.99	28.31
O K	26.95	44.11
Fe L	46.76	21.92
Ni L	6.97	3.11
Cu L	0.47	0.19
Zn L	5.86	2.35
Total	100	100

NF1		
Element	Weight%	Atomic%
C K	10.08	23.48
O K	26.15	45.71
Fe L	41.15	20.61
Ni L	10.56	5.03
Cu L	1.74	0.76
Zn L	10.32	4.41
Totals	100.00	100

NF2		
Element	Weight%	Atomic%
C K	15.49	34.42
O K	22.00	36.69
Fe L	40.80	19.50
Ni L	11.13	5.06
Cu L	2.24	0.94
Zn L	8.34	3.40
Totals	100.00	100

NF3		
Element	Weight%	Atomic%
C K	39.94	51.10
O K	47.34	45.48
Fe L	9.38	2.58
Ni L	2.02	0.53
Cu L	0.10	0.02
Zn L	1.22	0.29
Totals	100.00	100

NF4		
Element	Weight%	Atomic%
C K	47.63	55.66
O K	49.80	43.69
Fe L	2.30	0.58
Ni L	0.23	0.05
Cu L	0.03	-0.01
Zn L	0.07	0.01
Totals	100.00	100

NF5		
Element	Weight%	Atomic%
C K	54.50	63.72
O K	39.72	34.86
Fe L	4.77	1.20
Ni L	0.08	0.02
Cu L	0.50	0.11
Zn L	0.43	0.09
Totals	100.00	100

(b)

Fig. 3. (a) EDS spectra and (b) EDS elemental analysis of NCZ – PFD nanocomposites.

samples in X–band and Ku–band frequency regions respectively. The plots revealed that reflection coefficient rises with increase of PFD amount in the composites throughout X and Ku-bands. The sample NF5 with 90% polymer content shows maximum reflection coefficient of 0.84 and remains almost constant over entire frequency range. The absorption coefficient decreases from 0.45 to 0.15 with increase of polymer phase, with 0.45 shown by pure ferrite. Transmission coefficient increases from 0.002 to 0.005 with increase of PFD up to 70% polymer (NF4) amount and then reduced for NF5 composite. Lower values of transmission coefficient and larger of reflection coefficient confirm higher attenuation and absorption dominated electromagnetic waves in both X and Ku-band regions. Absorption efficiency is found to increase with polymer phase up to 50% PFD content (NF3) and then decreases. This feature is observed in both X and Ku frequencies. All samples exhibit absorption efficiency of above 95% throughout X-band and Ku-band regions.

Moreover, the synergy between two phases enhances reflection and absorption coefficients of nanocomposites which are found to be 0.925 and 0.0721, respectively, for NF5 sample at 12 GHz. Hence, the composite NF5 is able to shield 99.713% power of incident electromagnetic wave that is shared by 92.503% absorption and 7.21% reflection. In Ku-band frequency region, at 17.8 GHz, NF5 composite exhibits reflection coefficient of 0.91886 and absorption coefficient of 0.07824 which contributes 91.886% of absorption and 7.824% of reflection and hence able to shield maximum of 99.71% power of incident electromagnetic wave. This indicates that there exists balanced combination of magnetic and polymer phases (10% ferrite and 90% polymer) in NF5 composite at which synergistic effects between magnetic losses and dielectric losses are maximum which results in the excellent shielding of electromagnetic waves. The obtained results are in agreement with earlier reports [32, 33].

Shielding effectiveness caused by reflection and absorption can be written from the measurements of vector network analyzer as [34,35].

$$SE_R = 10\log_{10}(1 - R)$$

$$SE_A = 10\log_{10}(1 - A_{eff}) = 10\log_{10}[(T / (1 - R)]$$

Figs. 6–8 represent variations of total shielding effectiveness SE_T, shielding effectiveness due to reflection SE_R, shielding effectiveness due to absorption, SE_A, respectively, in 8.2–18 GHz regions. It can be seen that addition of polymer enhances SE_T from 23 dB (NCZ) to 26.7 dB (NF3) and on further increment of polymer, shielding effectiveness decreases. Fig. 7 shows variation of reflection of shielding effectiveness and one can observe that these are low values as compared shielding

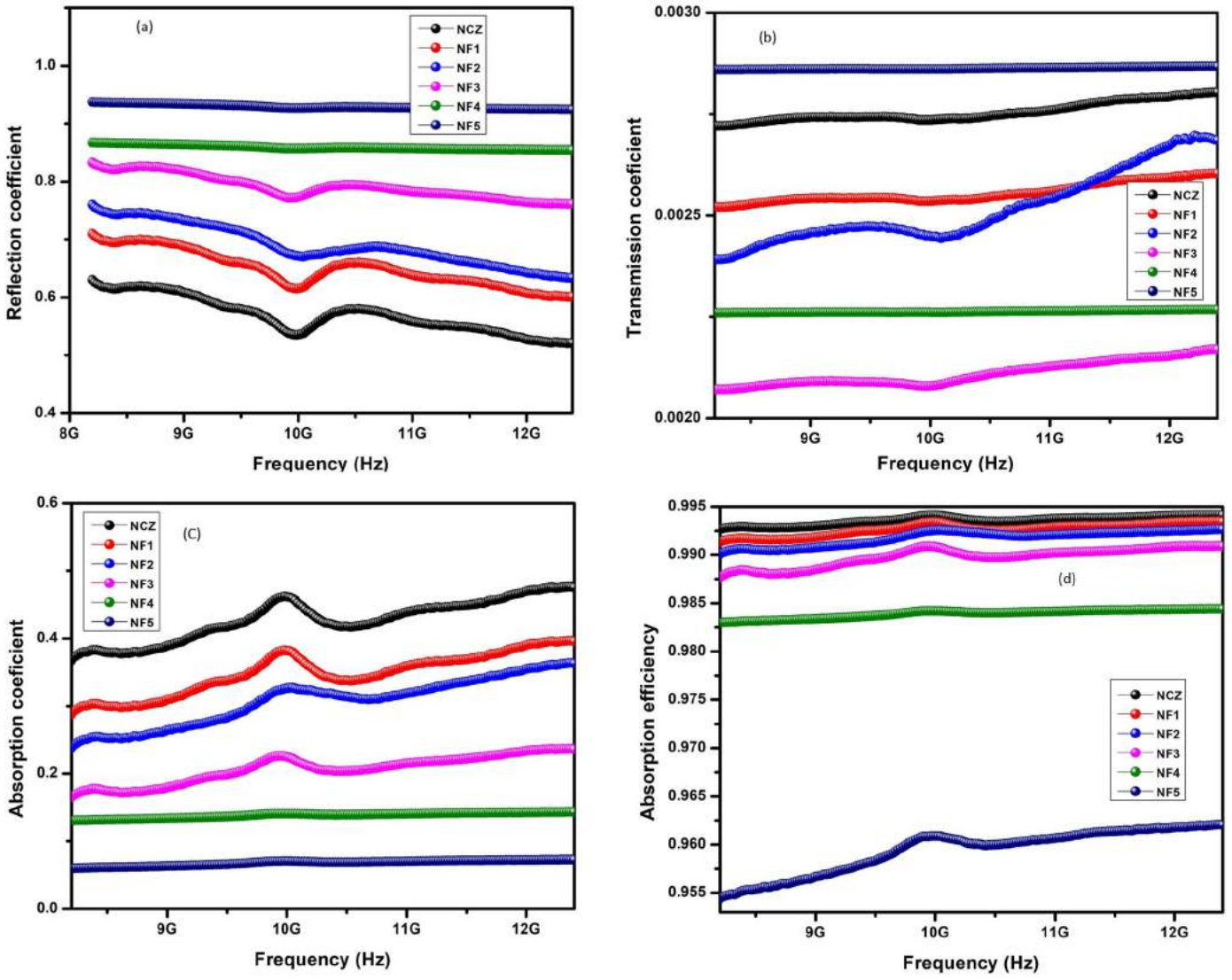

Fig. 4. Variation of (a) Reflection Coefficient (b) Transmission Coefficient (c) Absorption Coefficient and (d) Absorption efficiency of NCZ – PFD nanocomposites in X-band frequency region.

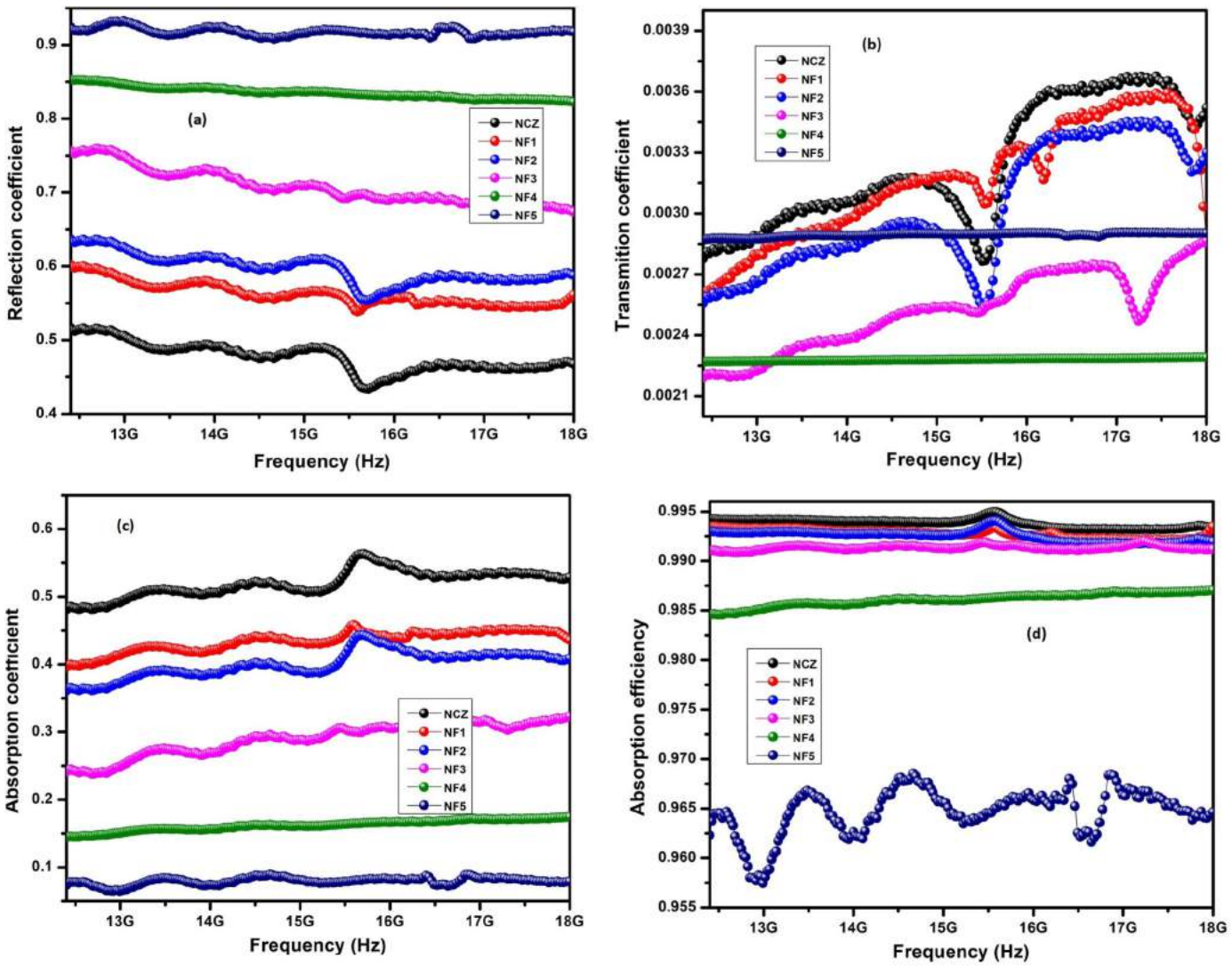

Fig. 5. Variation of (a) Reflection Coefficient (b) Transmission Coefficient (c) Absorption Coefficient and (d) Absorption efficiency of NCZ – PFD nanocomposites in Ku-band frequency region.

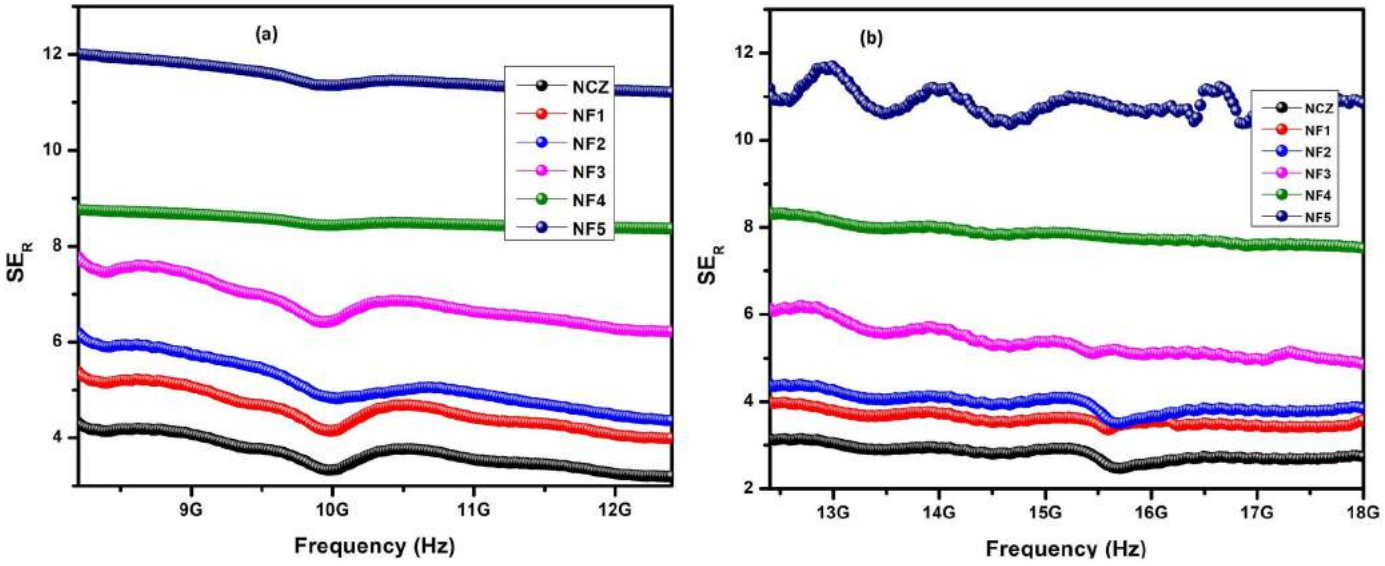

Fig. 6. Variation of shielding effectiveness due to reflection, SE_R with frequency in (a) X-band and (b) Ku-band regions.

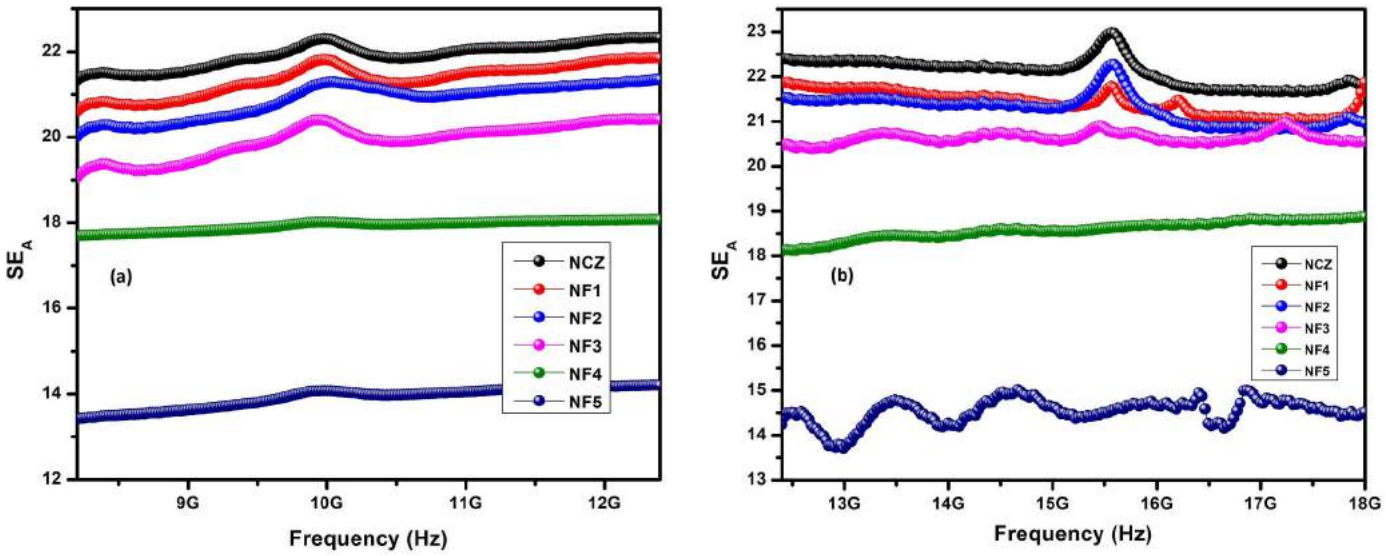

Fig. 7. Variation of shielding effectiveness due to absorption, SE_A with frequency in (a) X-band and (b) Ku-band regions.

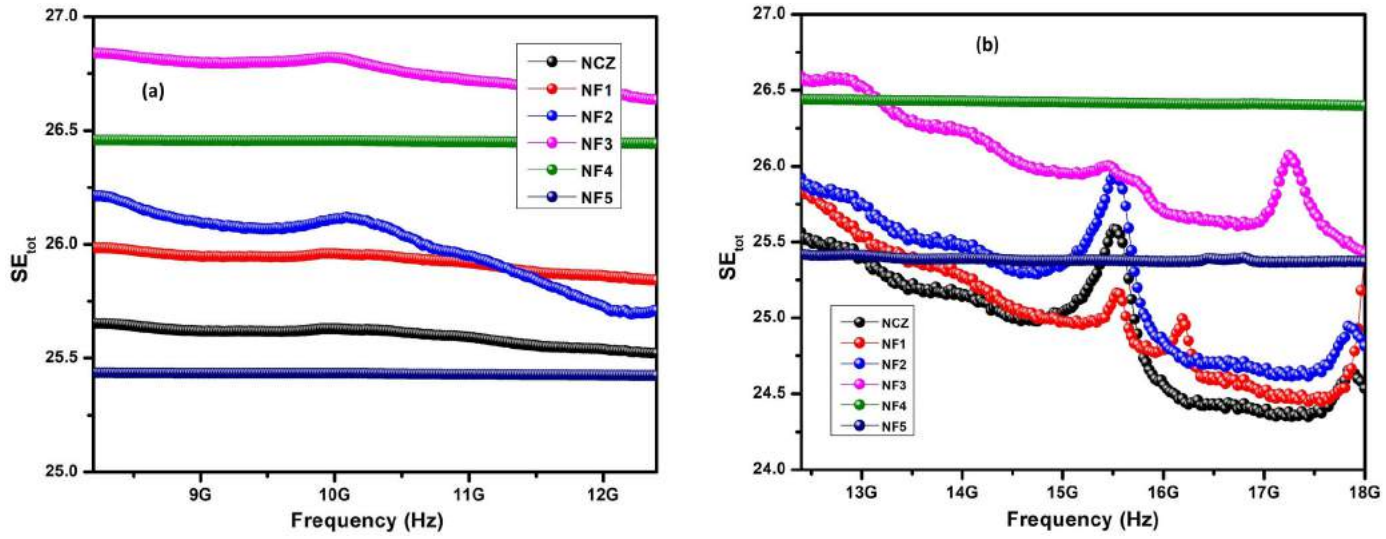

Fig. 8. Variation of total shielding effectiveness, SE_T with frequency in (a) X-band and (b) Ku-band regions.

effectiveness due to absorption, as shown in the Fig. 8. SE_R increases with the addition of PFD and lies in the range 4 dB–7.9 dB. From the Figs. 6–8, we can conclude that the major contribution to shielding effectiveness comes from SE_A. This is due to the presence of large number of dipoles rather than mobile charge carriers in the composites. Table 2 depicts SE_R, SE_A, SE_T values at 8.2 GHz and 12.4 GHz for all the samples.

To further investigate synergistic effects of present nanocomposites, variation of reflection loss has been explored for all the samples. Figs. 9 and 10 indicate variation of reflection loss with frequency in X and Ku-bands. From the figures it can be observed that the sample NF3 with 50% PFD phase shows minimum reflection loss of – 31.18 at 11.98 GHz with bandwidth 3.11 GHz and −27.95 dB at 17.8 GHz, of all other samples. The present results are consistent with the earlier reports [21]. Table 2 gives minimum RL values along with bandwidth. Minimum reflection loss varies from −28.5 dB (NCZ) to −31.18 dB (NF3) and then decreases with further increase of PFD phase. Among all samples, NF3 with 50% PFD phase is optimized to study reflection loss variation for different

Table 2
Shielding effectiveness and reflection loss properties of NCZ-PFD nanocomposites.

S. No	Sample	At 8.2 GHz (X-band)			At 12.4 GHz (Ku-band)			Minimum reflection loss (dB) and frequency (GHz)	Bandwidth over −10 dB (GHz)
		SE_R	SE_A	SE_{tot}	SE_R	SE_A	SE_{tot}		
1	**NCZ**	4.32	18.76	23.08	3.15	19.87	23.03	−28.5 dB at 9.14 GHz	8.78–10.8
2	**NF1**	5.53	19.00	24.53	3.99	20.45	24.45	−29.2 dB at 9.6 GHz	8.99–10.67
3	**NF2**	6.38	19.29	25.67	4.43	20.95	25.38	−29.94 at 8.68, −28.97 at 17.3	8.2–10.65, 16.15–18
4	**NF3**	7.05	19.68	26.74	5.73	20.80	26.53	−31.18 at 11.98, 27.95 at 17.83	10.88–13.99, 16.96–18
5	**NF4**	7.45	19.41	26.86	7.06	19.77	26.84	−14.18 dB at 11.91 GHz	9.08–14.99
6	**NF5**	7.88	18.21	26.09	7.54	18.53	26.07	−8.67 at 9.75	–

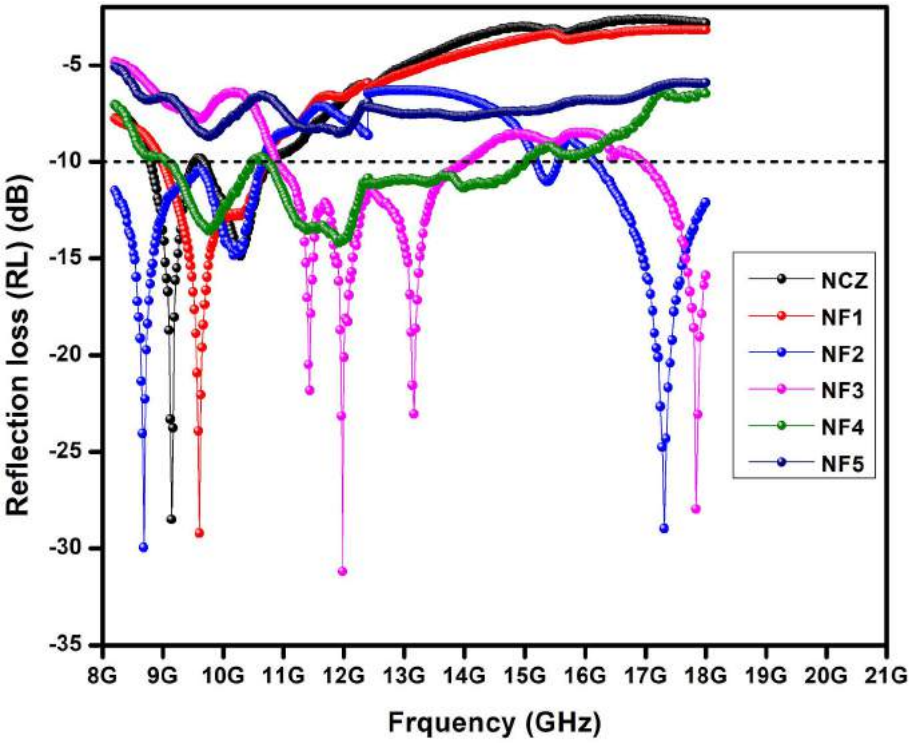

Fig. 9. Variation of reflection loss of NCZ – PFD nanocomposites in X-band and Ku-band frequency regions.

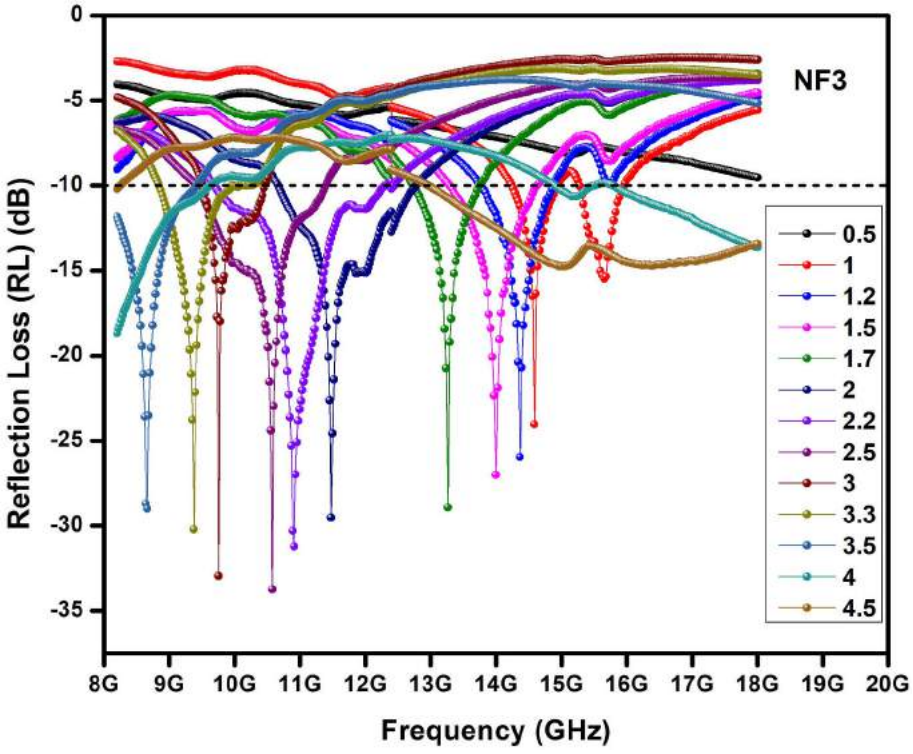

Fig. 10. Variation of reflection loss of NF3 nanocomposite for multiple thickness values in X-band and Ku-band frequency regions.

thickness values in the range 0.5 mm–4.5 mm, which is shown in the Fig. 10. RL_{min} increases initially and then decreases with sample thickness 2.1 mm.

The present results revealed that by tailoring the amount of PFD phase in magnetic composites EMI shielding properties can be tuned in X and Ku-bands regions. Hence, it can be concluded that the current materials are potential candidates for designing microwave absorbers in radar, stealth applications and satellite applications [36,37].

3. Conclusions

Microwave hydrothermally prepared nanopowders of nickel copper zinc ferrites were combined with paraformaldehyde polymer successfully to constitute nanocomposites. The synergistic combination between ferrite and polymer phases results in the improved performance of microwave absorption in X-band and Ku-band regions. The present samples are able to shield effectively, 99.7% of incident electromagnetic waves distributed by 92.503% absorption and 7.21% reflection in X-band and 91.886% of absorption and 7.824% of reflection in Ku-band regions. The present studies confirmed that the nanocomposite materials are potential candidates for fabricating and designing microwave absorbers in radar, stealth and satellite applications.

Declaration of competing interest

The authors declare that they have no known competing financial interests or personal relationships that could have appeared to influence the work reported in this paper.

Acknowledgments

Authors are thankful to the department of physics, Osmania University, Hyderabad, India and University of Hyderabad, Hyderabad, India, for providing experimental facilities to complete the present work successfully.

References

[1] Sharbati Ali, Verdi Khani Javad Mola, Amiri Gholam Reza, Microwave absorption studies of nanocrystalline $SrMn_{x/2}(TiSn)_{x/4}Fe_{12-x}O_{19}$ prepared by the citrate sol–gel method, Solid State Commun. 152 (2012) 199–203.
[2] C.J.v. Klemperer, D. Maharaj, Composite electromagnetic interference shielding materials for aerospace applications, Compos. Struct. 91 (2009) 467–472.
[3] Y.C. Qing, W.C. Zhou, F. Luo, D.M. Zhu, Titanium carbide (MXene) nanosheets as promising microwave absorbers, Ceram. Int. 42 (14) (2016) 16412–16416.
[4] R. Baan, Y. Grosse, B. Lauby-Secretan, F. El Ghissassi, V. Bouvard, L. Benbrahim-Tallaa, N. Guha, F. Islami, L. Galichet, K. Straif, Carcinogenicity of radio frequency electromagnetic fields, Lancet Oncol. 12 (2011) 624–626.
[5] H.L. Lv, Z.H. Yang, B. Liu, G.L. Wu, Z.C. Lou, B. Fei, R.B. Wu, A flexible electromagnetic wave-electrivity harvester, Nat. Commun. 12 (2021) 834.
[6] J. Schüz, A. Ahlbom, Exposure to electromagnetic fields and the risk of childhood leukaemia: a review, Radiat. Protect. Dosim. 32 (2008) 202–211.
[7] Shaohui Su, Jiahao Yu, Xianguo Liu, Jieyi Yu, Solid, Fe nanoparticles embedded in polyaniline-derived carbon fibers as broad bandwidth microwave absorbers for GHz electromagnetic wave, Solid State Commun. 334–335 (2021) 114400.
[8] T.Q. Hou, Z.R. Jia, A.L. Feng, Z.H. Zhou, X. H liu, H.L. Lv, G.L. Wu, Hierarchical composite of biomass derived magnetic carbon framework and phytic acid doped polyanilne with prominent electromagnetic wave absorption capacity, J. Mater. Sci. Technol. 68 (2021) 61–69.
[9] Y.C. Zhou, B. Zhao, H. Chen, H.M. Xiang, F.Z. Dai, S.J. Wu, W. Xu, Electromagnetic wave absorbing properties of TMCs (TM¼Ti, Zr, Hf, Nb and Ta) and highentropy (Ti0.2Zr0.2Hf0.2Nb0.2Ta0.2) C, J. Mater. Sci. Technol. 74 (2021) 105–118.
[10] Bo Zhang, Ibrahim Mahariq, Ngo Tran, Mustafa Z. Mahmoud, Majid Niaz Akhtar, Enhanced electromagnetic wave dissipation features of magnetic Ni microspheres by developing core-double shells structure, Ceram. Int. (2021), https://doi.org/10.1016/j.ceramint.2021.09.120.
[11] X.F. Zhou, Z.R. Jia, X.X. Zhang, B.B. Wang, W. Wu, X.H. Liu, B.H. Xu, G.L. Wu, Controllable synthesis of Ni/NiO@porous carbon hybrid composites towardsremarkable electromagnetic wave absorption and wide absorption bandwidth, J. Mater. Sci. Technol. 87 (2021) 120–132.
[12] G. Tong, Q. Hu, W. Wu, W. Li, H. Qian, Y. Liang, Submicrometer-sized NiO octahedra: facile one-pot solid synthesis, formation mechanism, and chemical conversion into Ni octahedra with excellent microwave-absorbing properties, J. Mater. Chem. 22 (2012) 17494–17504.
[13] H. Sun, R. Che, X. You, Y. Jiang, Z. Yang, J. Deng, L. Qiu, H. Peng, Cross-stacking aligned carbon-nanotube films to tune microwave absorption frequencies and increase absorption intensities, Adv. Mater. 26 (2014) 8120–8125.
[14] C. Tong, Advanced Materials and Design for Board Level EMI shielding·Principle of Board Level Shielding (BLS). C. Tong. Advanced Materials and Design for Board Level EMI Shielding · Principle of Board Level Shielding, BLS), 2012, 2012.
[15] B.C. Jackson, G. Shawhan, Current review of the performance characteristics of conductive coatings for EMI control, in: 1998 IEEE EMC Symposium Internationalsymposium on Electromagnetic Compatibility Symposium Record (catNo98CH36253), vol. 1, 1998, pp. 567–572.
[16] S. Geetha, K.K. Satheesh Kumar, C.R.K. Rao, M. Vijayan, D.C. Trivedi, EMI shielding:methods and materials—a review, J. Appl. Polym. Sci. 112 (2009) 2073–2086.
[17] X. Zhou, D. Chuai, D. Zhu, Electrospun synthesis of reduced graphene oxide (RGO)/NiZn ferrite nanocomposites for excellent microwave absorption properties, J. Supercond. Nov. Magnetism 32 (2019) 2687–2697.
[18] A. Ohlan, K. Singh, A. Chandra, S.K. Dhawan, Microwave absorption behavior of core shell structured poly (3, 4-ethylenedioxy thiophene) - barium ferrite nanocomposites, ACS Appl. Mater. Interfaces 2 (2010) 927–933.
[19] B.W. Li, Y. Shen, Z.X. Yue, C.W. Nan, Influence of particle size on electromagnetic behavior and microwave absorption properties of Z-type Ba-ferrite/polymer composites, J. Magn. Magn Mater. 313 (2007) 322–328.
[20] H. Qiu, X. Luo, J. Wang, et al., Synthesis and characterization of ternary polyaniline/barium ferrite/reduced graphene oxide composite as microwave-absorbing material, J. Electron. Mater. 48 (2019) 4400–4408.
[21] Shan Jiang, Qian Kun, Yu Kejing, Zhou Hongfu, Weng Yunxuan, Zhang Zhongwei, Study on ultralight and flexible Fe3O4/melamine derived carbon foam composites for high-efficiency microwave absorption, Chem, Phys. Lett. 779 (2021) 138873.
[22] P. Raju, P. Neelima, G. Neeraja Rani, M. Kanakadurga, Enhanced microwave absorption properties of $Ni_{0.48}Cu_{0.12}Zn_{0.4}Fe_2O_4$ + polyaniline nanocomposites, J. Phys. Chem. Solid. 154 (2021) 110048.
[23] S. Komarneni, R. Roy, Q.H. Li, Microwave-hydrothermal synthesis of ceramicpowders, Mater. Res. Bull. 27 (1992) 1393–1405.
[24] K. Sadhana, S.R. Murthy, K. Praveena, Structural and magnetic properties of Dy3+ doped $Y_3Fe_5O_{12}$ for microwave devices, Mater. Sci. Semicond. Process. 34 (2015) 305–311.
[25] G. Yang, S.-J. Park, Conventional and microwave hydrothermal synthesis andapplication of functional materials: a review, Materials 12 (7) (2019) 1177.
[26] Hewlett-Packard, Microwave Network Analyser Catalogue 8510 and Product Note 8510-3, 1987.
[27] P. Raju, J. Shankar, J. Anjaiah, Ch Kalyani, G Neeraja Rani, Complex permittivity and permeability properties analysis of NiCuZn Ferrite-Polymer nanocomposites for EMI suppressor applications, J. Phys. Conf. 1495 (2020), 012001.
[28] B.D. Cullity, Elements of X-Ray Diffraction, second ed., Addison-Wesley, 1978.
[29] J. van den Boomgaard, R.A.J. Born, A sintered magnetoelectric composite material $BaTiO_3$-Ni(Co, Mn) Fe_2O_4, J. Mater. Sci. 13 (1978) 538–1548.
[30] American Society for Testing and Materials, ASTMD5568-1: Standard Test Method for Measuring Relative Complex Permittivity and Relative Magnetic Permeability of Solid Materials at Microwave Frequencies, ASTM, WestConshohoken, PA, 2001.
[31] A.M. Nicolson, G.F. Ross, Measurement of the Intrinsic Properties of materials by time domain techniques, Instrumentantion and Measurement 19 (1970) 377–382.
[32] Shivam Gupta, Chih-HuangLai ChingChang, Tai Nyan-Hwa, Hybrid composite mats composed of amorphous carbon, zinc oxide nanorods and nickel zinc ferrite for tunable electromagnetic interference shielding, Compos. B Eng. 164 (2019) 447–457.
[33] Yang Fan, Jimei Xue, Yujie Ma, Xiaomeng Fan, Shaobo Zhang, Shangwu Fan, Wenke Ma, Qingfeng Zeng, Laifei Cheng, Impedance matching optimization of SiCf/Si3N4–SiOC composites for excellent microwave absorption properties, Ceram. Int. 9 (2021) 273.
[34] P. Saini, V. Choudhary, B.P. Singh, R.B. Mathur, S.K. Dhawan, Synth. Met. 161 (2011) 1522.
[35] D.D.L. Chung, Materials for electromagnetic interference shielding, Mater. Chem. Phys. 255 (2020) 123587.
[36] X. Li, H. Yi, J. Zhang, J. Feng, F. Li, D. Xue, H. Zhang, Y. Peng, N.J. Mellors, Fe 3 O 4–graphene hybrids: nanoscale characterization and their enhanced electromagnetic wave absorption in gigahertz range, J. Nanoparticle Res. 15 (2013) 1472.
[37] Yi-WenBai, Guimei Shi, Jun Gao, Fa-Nian Shi, Synthesis, crystal structure of a iron-manganese bimetal MOF and its graphene composites with enhanced microwave absorption properties, J. Phys. Chem. Solid. 148 (2021) 109657.

Available online at www.sciencedirect.com

ScienceDirect

journal homepage: www.elsevier.com/locate/he

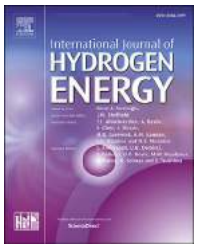

Enhanced photocatalytic hydrogen evolution from reduced graphene oxide-defect rich TiO_{2-x} nanocomposites

Jagadeesh Babu S. [a,b], *Murthy Muniyappa* [a,c], *Navakoteswara Rao V.* [d], *Ravi Mudike* [a], *Mahesh Shastri* [a,c], *Sardar Tathagata* [a], *Prasanna D. Shivaramu* [a], *Shankar M.V.* [e], *Ananda Kumar C.S.* [a,**], *Dinesh Rangappa* [a,*]

[a] *Department of Applied Sciences (Nanotechnology), Center for Post Graduate Studies, Visvesvaraya Institute of Advance Technology (VIAT), Visvesvaraya Technological University, Muddenahalli Campus, Chikkaballapur District 56 2101, India*

[b] *Department of Physics, Malla Reddy Engineering College(A), Maisammaguda, Hyderabad, Telangana, India*

[c] *Department of Electronics & Communication, Nagarjuna College of Engineering & Technology, Devanahalli, Bengaluru, India*

[d] *Center for Material Science and Nanotechnology, Yogivemana University, Kadapa, Andhra Pradesh, India*

[e] *Nanocatalysis and Solar Fuels Research Laboratory, Department of Materials Science & Nanotechnology, Yogi Vemana University, Kadapa 516005, Andhra Pradesh, India*

HIGHLIGHTS

- One pot synthesis of defect engineered TiO_{2-x} and RGO/TiO_{2-x} nanocomposites.
- The influence of RGO on defect-rich TiO_{2-x} shown significant improvement in opto-electronic properties.
- Addition of RGO in TiO_{2-x} enhances the charge transfer by reducing electron hole recombination.
- RGO/TiO_{2-x} nanocomposite remarkably enhances rate of Hydrogen evolution under solar and visible spectrum.

ARTICLE INFO

Article history:
Received 23 March 2022
Received in revised form
3 June 2022
Accepted 13 July 2022
Available online 14 August 2022

Keywords:
TiO_{2-x}
RGO/TiO_{2-x}
Defect rich TiO_2
Photocatalyst

ABSTRACT

Solar-driven photocatalytic hydrogen generation by splitting water molecules requires an efficient visible light active photocatalyst. This work reports an improved hydrogen evolution activity of visible light active TiO_{2-x} photocatalyst by introducing reduced graphene oxide via an eco-friendly and cost-effective hydrothermal method. This process facilitates graphene oxide reduction and incorporates intrinsic defects in TiO_2 lattice at a one-pot reaction process. The characteristic studies reveal that RGO/TiO_{2-x} nanocomposites were sufficiently durable and efficient for photocatalytic hydrogen generation under the visible light spectrum. The altered band gap of TiO_{2-x} rationally promotes the visible light absorption, and the RGO sheets present in the composites suppresses the electron-hole recombination, which accelerates the charge transfer. Hence, the noble metal-free RGO/TiO_{2-x} photocatalyst exhibited hydrogen production with a rate of 13.6 mmol $h^{-1}g^{-1}_{cat.}$ under solar illumination. The appreciable photocatalytic hydrogen generation activity of 947.2 μmol $h^{-1}g^{-1}_{cat}$ with 117 μAcm^{-2} photocurrent density was observed under visible light (>450 nm).

* *Corresponding author.*
** *Corresponding author.*
E-mail addresses: csanandakumar@gmail.com (A.K. C.S.), dineshrangappa@gmail.com (D. Rangappa).
https://doi.org/10.1016/j.ijhydene.2022.07.115

Photo anode
Solar hydrogen generation

Introduction

Exploitation of natural resources as a raw material for hydrogen production is an admissible strategy in the sustainable energy era. Water splitting has been recognized as a clean way to produce hydrogen energy [1]. Many metal oxides, sulfides and nitride compounds have been identified as photocatalytic materials since the discovery of TiO_2 [2–11]. However, the unique characteristics of TiO_2 such as non-corrosive, non-toxic, durable and high photocatalytic performance have made it TiO_2 as the most promising catalyst [12–15]. On the contrary, from a visible light absorption perspective, TiO_2 has not thrived due to its wide optical bandgap. So far, enormous efforts have been accomplished to overcome these glitches with appreciable ideas like metal ion doping, preparation of composites, loading of noble metals, fabrication of heterojunctions, and dye sensitization [16–18]. However, all these approaches involve bandgap alteration and improving its charge mobility to hinder the electron-hole recombination via charge separation in the TiO_2 [19,20]. Recently, the intrinsic defects in the TiO_2 lattice evidenced a significant change in colour and optoelectric properties [21–27]. Improved visible light-harvesting efficiency of TiO_2, with the incorporation of Ti^{3+} and oxygen vacancies (Ti^{3+}/O_v), are reported [21,28]. Contrasting to traditional doping methods, the formation of defects in the lattice can create unremitting new energy levels just below the conduction band of TiO_2 and reduces thermal instability due to other doping impurities [29]. Furthermore, efficient charge transfer is possible at stable Ti^{3+} medium intervals [21,28,30]. However, owing to charge recombination, the photocatalytic activity of pristine TiO_{2-x} remains restricted.

One of the most effective methods to counteract the charge carrier recombination in TiO_2 is graphene insertion. Graphene entails with sp2 hybridized carbon atoms in a 2D layered structure with unique characteristics such as high specific surface area, electrical and thermal conductivity. These unique features made graphene explored in sensors, drug delivery, supercapacitors, and Li-ion batteries [31–36]. So far, many researchers have been exploring graphene-based composites to enhance photocatalytic activity [37–43]. Due to its high conductivity and large surface area, reduced graphene oxide rapidly mobilizes photogenerated charge carriers to enhance photoreactions [44]. As a result, graphene is a potential material to increase the photocatalytic hydrogen generation efficiency. Recently, B. Qiu et al. have reported that Ti^{3+} doped TiO_2 and graphene composite has significantly improved over methyl orange dye (MO) degradation under visible light. There it seems the RGO/TiO_{2-x} nanocomposite system is a promising approach to enhance photocatalytic activity towards water splitting. A sufficient interaction between TiO and RGO layers is essential for the efficient separation of photogenerated e^-/h^+ in the hybrid TiO/RGO nanocomposites [44–47]. However, there are not many efforts in the literature on the TiO_{2-x}/RGO nanocomposites. The only report on this TiO_{2-x}/RGO materials that was prepared by vacuum calcination method evidenced a limited hydrogen evolution of 400 μmol h^{-1} [48]. The "firm" combination of anatase TiO_2 (P25) particles and RGO confined the photocatalytic activity. Hence, the poor hydrogen evolution from the TiO_{2-x}/RGO photocatalyst was reported [48]. Furthermore, the cost of commercial P25 is considerably high, making large-scale production of TiO_{2-x}/RGO and usage unfeasible at low cost. Therefore, there is need for developing TiO_{2-x}/RGO nanocomposites without any doping or any high temperature treatment.

This report mainly focusses on enhancing the photocatalytic activity of defective TiO_{2-x} by incorporating intrinsic defects using low-cost starting materials and decorating with RGO sheets through an eco-friendly, cost-effective one pot hydrothermal route. The reduction of graphene oxide and incorporation of intrinsic defects in the TiO_2 network occurs in a one-pot reaction. As expected, the prepared defect rich TiO_{2-x}/RGO nanocomposite triggered the absorption capability to visible-IR region of solar spectrum and also suppressed the recombination and charge mobility issues. As a result, the enhanced hydrogen evolution was achieved under solar light irradiation.

Experimental section

Materials used

Graphite flakes were purchased from fisher scientific. Phosphoric acid (H_3PO_4), sulfuric acid (H_2SO_4), Hydrogen Peroxide (H_2O_2), Ethanol, $TiCl_4$ (99%), and L-Ascorbic Acid of 99% purity from Merck. Potassium permanganate ($KMnO_4$) was obtained from Sigma Aldrich. *N*-methyl-pyrrolidine (NMP), polyvinylidene fluoride (PVDF).

Synthesis of TiO_{2-x}/RGO nanocomposite photocatalysts

The synthesis of TiO_{2-x}/RGO nanocomposites was followed as earlier reported [49]. The GO sheets were initially prepared using the modified hummers method [50]. The obtained GO sheets were taken in various weight concentrations, which vary from 1% to 5% in each 10 mL of de-ionized water. Graphene oxide solution was ultrasonicated for 1 h to obtain nicely dispersed graphene oxide sheets (sol A). On other hand, under stirring the L-ascorbic acid of 0.05 M was dissolved in 25 mL of de-ionized water. Further, a $TiCl_4$ solution of 1.5 mL

was added drop wisely to the L-ascorbic solution. The pH of titanium precursor was maintained at four by adding 1 M NaOH solution and stirred for 30 min (sol B).

Dispersed graphene oxide solution (sol A) was added to sol B, followed by continuous stirring. The resulting solution was transferred to a 60 mL stainless steel autoclave with a Teflon-coated container. The hydrothermal reaction was carried out by placing autoclave in a hot air oven at 180 °C for hydrothermal treatment for 12 h. The resulting obtained product was rinsed thoroughly with de-ionized water and ethanol, followed by centrifugation and sonication. The washed material was dried in a hot air oven at 90 °C for 10 h, and the collected sample was ground in a mortar to get a fine powder. The resultant powder was labelled as RBT1, RBT2, RBT3, RBT4, and RBT5 where x = 1,2,3,4 and 5% weight percentage of graphene oxide. This process was repeated without adding GO precursor, and the obtained powder was labelled as TiO_{2-x}. Pristine TiO_2 was obtained without using L-ascorbic acid and graphene oxide precursor.

Fabrication of photoanodes

For the fabrication of photoanodes, 8 mg of as-synthesized nanomaterial was mixed with 1 mg of carbon powder and 1 mg of Polyvinylidene fluoride in an *N*-methyl-pyrrolidine (NMP) medium. The obtained slurry paste was further coated on fluorine-doped tin oxide (FTO) substrate using a doctor blading process. The coated films were dried in a vacuum furnace at 70 °C for 12 h.

Characterization

The crystal and structural information of the samples was investigated using X-ray diffractometer (Model- Rigaku Ultima IV), and Raman spectrometer (Model- EZRaman-N Series Raman Analyzers). The optical behavior of the samples was examined using UV/Vis/NIR spectrometer (Model- PerkinElmer lamda 750). The morphological and Elemental analysis was obtained using High Resolution Transmission Electron Microscope (HR-TEM) (Model- Jeol/JEM 2100) and X-ray Photoelectron Spectroscopy (XPS) (Model- ULVAC-PHI, PHI 5000 Versa probe II). The defect sites of the samples were investigated with Electron Spin Resonance Spectroscopy (ESR) (Model- JEOL Model JES FA200).

Photocatalytic H_2 evolution process

The photocatalytic H_2 evolution study was assessed by using natural solar light. Solar light intensity was recorded for every hour from 10:00 to 15:00 with the Newport power meter (model 843-R) digital exposure meter. During the experiments, the average light intensity observed was about 300 ± 10 mW cm^{-2}. The reaction was performed in a quartz reactor containing 47.5 mL DI water and 2.5 mL glycerol and 10 mg of photocatalyst. The reactive solution was purged for 35 min with pure nitrogen gas under dark conditions to eradicate dissolved oxygen. After light irradiation, the evolved gases were analyzed every 1 h, using gas chromatography (GC) (Model- Shimadzu GC-2014) with thermal conductivity detector, 5Å column molecular sieve and N_2 carrier gas.

Photocurrent measurements

The photocurrent transient measurements were recorded in an aqueous medium of 0.5 M Na_2SO_4 using three-electrode electrochemical work station. Fabricated photoanodes, platinum is the working electrode and counter electrodes. Ag/AgCl (3 M KCl) was used as reference electrodes. The input voltage bias of 0.5 V vs Ag/AgCl was employed under a 300 mW cm^{-1} Xe lamp solar simulator with UV-cutoff filter for transient photocurrent measurements.

Results and discussion

The strategy followed in preparation RGO/TiO_{2-x} nanocomposite was dispersion of graphene oxide sheets in the TiO_2 network under ambient conditions by taking advantage of L-ascorbic acid to reduce the TiO_2 and graphene oxide using the hydrothermal method. During hydrolysis, the titanium tetrachloride forms Ti^{4+} ions along $4Cl^-$ with H_2O. L-ascorbic acid is a source of OH group forms HCl and Ti(IV)-oxo species. The Ti(IV)-oxo species converts into TiO_{2-x} nanocrystals [51]. The diffraction peaks of pristine and defect rich TiO_2 (TiO_{2-x}), and all RGO/TiO_{2-x} nanocomposites correspond to the anatase phase TiO_2 with the tetragonal structure are well-indexed with standard JCPDS Card 21-1272. The crystal planes (101), (004), (200), (105), (211), (204), and (116) of all synthesized samples were reflected at 25.1°, 37.8°, 47.9°, 55.0°, 62.5°, and 68.3°, respectively. On the other side, no characteristic peaks of GO species were observed in Fig. 1, indicating the formation of reduced graphene oxide in all the composite materials. The domination of anatase TiO_2 peak over the weak characteristic peak of RGO at 24.5° could hinder RGO in RBT samples [52]. The crystalline size of all synthesized nanomaterials was obtained using the Debye-Scherer formula, and the same was tabulated in Table 1. The obtained crystallite sizes were well correlated with TEM images. Further, the crystallite size, lattice strain, and disorder density were calculated to analyze the

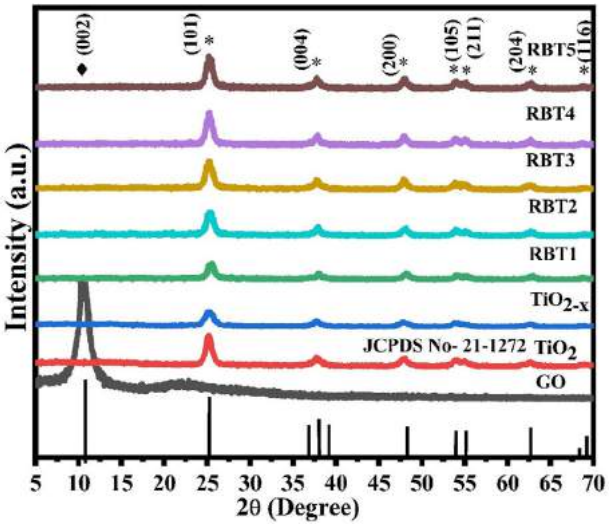

Fig. 1 – XRD characteristic patterns of a) TiO_2, TiO_{2-x}, and RBT samples with different GO concentrations.

Table 1 – The average crystallite (D) size, lattice micro strain, and dislocation densities of pristine TiO_2, TiO_{2-x}, and RGO/TiO_{2-x} (RBT) samples with different GO weight concentrations.

S.No	Sample	Crystallite size(D) nm	Lattice micro strain x (10^{-3})	Dislocation density
1.	TiO_2	9.84	6.54	0.01030
2.	TiO_{2-x}	6.95	5.70	0.02064
3.	RBT1	8.20	1.32	0.01290
4.	RBT2	8.62	2.33	0.01484
5.	RBT3	8.80	3.64	0.01343
6.	RBT4	9.21	3.81	0.01178
7.	RBT5	9.26	4.67	0.01164

crystallographic changes caused by the defect formation and graphene introduction using XRD data shown in Table 1.

In Fig. 2, the Raman-active modes E_g at 144 cm^{-1}, B_{1g} at 400 cm^{-1}, and A_{1g} at 515 cm^{-1} frequencies were noticed in all investigated samples. The Eg peaks of TiO_{2-x} and RBT samples exhibited a blue shift compared with pristine TiO_2. The concentration of defective sites and lattice distortion could be responsible for the blue shift [51,53,54]. The D and G bands of graphene were observed at 1346 and 1598 cm^{-1}, respectively. Where D is accompanied by sp^3 carbon atom vibrations of reduced graphene oxide, and band G is accompanying with plane vibrations of sp^2 carbon atoms. This change suggests that the regular size of the sp^2 domain in the plane decreases during the hydrothermal process [52]. It is reasonable to assume that the partial reduction of the GO sheet will cause a disruption along with the reaction site and lead to the appearance of a new graphite domain, resulting in a smaller size of the RGO sheet. The small size of the RGO sheet will create many edges, which act as defects and reflects in the increase of the D band intensity [55]. The Raman spectra of RBT composites reveal that the partial reduction of GO escalates the mobility of electrons and suppresses more recombination photogenerated e^-/h^+ [56].

Fig. 3(a) shows the TEM image of the RBT2 sample, demonstrating that the RGO was finely dispersed in the TiO_{2-x} host matrix of average particle size 6 nm. The HRTEM image of

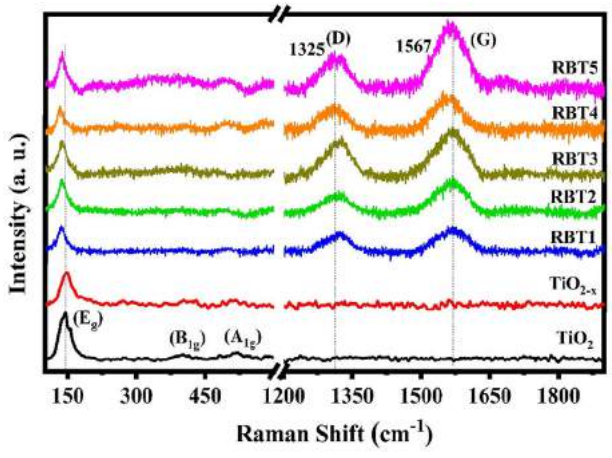

Fig. 2 – Raman spectra of TiO_2, TiO_{2-x}, and RBT (1, 2, 3,4, and 5) samples with different GO concentrations.

the RBT2 sample in Fig. 3(b) revealed the interplanar distance of RGO in TiO_{2-x} crystalline network was 0.39 nm corresponds to (002) plane, and 0.30 nm reflects (100) plane of anatase TiO_{2-x}. The sheets of RGO were indicated the nature of the composite structure among them, respectively. SAED pattern depicted the multi-crystalline nature of nanoparticles and was shown in Fig. 3(c). Furthermore, elemental mapping images from scanning transmission electron microscope (STEM) showed in Fig. 3(c, d, and e) the track of three elements, Ti, O, and C, which elementally confirms the RGO/TiO_{2-x}.

Fig. 4(a) shows the UV–Vis/NIR DRS spectra of the pristine TiO_2, TiO_{2-x}, and RBT composites with different weight concentrations of GO varies from 1% to 5%. In Fig. 4(a), the absorbance capability of TiO_{2-x} and RBT nanocomposites was protracted towards higher wavelengths of the visible regime. The incorporation of intrinsic defects and dispersion of RGO could be the reason for the redshift in optical absorption of TiO_{2-x} and RBT composite samples [53,56]. Fig. 4(b) shows the tauc plots for estimated bandgaps of the samples plotted from the absorption spectra of as-synthesized samples. The energy gaps were calculated using tauc plots by pointing the x-axis intercept of an extended tangential line from the curve's linear regime. These results indicated a bandgap reduction of TiO_{2-x} and RBT samples due to the intrinsic defects in TiO_{2-x} lattice, and additional interfacial interaction of RGO could be the reason for RBT nanocomposites. From Fig. 4, it is projected that the light absorption could be more efficient in TiO_{2-x} and RBT samples since the expanded absorbance of light in the visible-NIR region and bandgap narrowing.

A significant bandgap alteration in the TiO_{2-x} and RBT samples indicates that a defect layer is formed below the conduction level. ESR spectra at room temperature were recorded to investigate defects formation in samples. It has been noticed that except pristine TiO_2, all the samples received a resonance signal at 1.998 g-value. The resonance signals would be attributed to surface defects (unsaturated Ti^{3+} sites) characteristically owing trapped electrons on oxygen vacancies (O_v) [57]. The insight of ESR spectra confirms that there is no stable Ti^{3+} defects on the sample surface. However, at the surface, Ti^{3+} would act to absorb ambient O_2, which would be converted to O_2^- and displays resonance signal at $g \approx 1.998$ [58].

Fig. 6(a) illustrates the full XPS survey spectra of RBT2 nanocomposite, the peaks of Ti, O, and C are detected, and no other impurity elements were observed. The Ti 2p peaks of pristine TiO_2, TiO_{2-x}, and RBT2, the Ti 2p peaks of pristine TiO_2 were located around 459.59 and 465.35 eV. These peaks Ti $2p_{3/2}$, and Ti$2p_{1/2}$ spin-orbital doublet corresponding to Ti^{4+}–O, were shown in Fig. 6(b), respectively [59]. The same peaks were observed in TiO_{2-x} at 459.49 and 465.24, whereas RBT2 sample peaks were observed around 459.39 and 465.16 eV. Compared with pristine TiO_2. The Ti2p peaks shifted to lower binding energies along with a simultaneous reduction in the peak area. Both of these observations suggest the articulation of Ti^{3+} defects in TiO_{2-x} [2,53]. In the RBT2 sample, the redshift indicates the consequences of forming Ti–C bonds and defects compared to pristine TiO_2 [60].

As we know, XPS detection of chemical bonds limited to top few atomic layers of the material. In the case of the Ti element, the Ti2p peaks were not deconvoluted into Ti^{3+} 2p

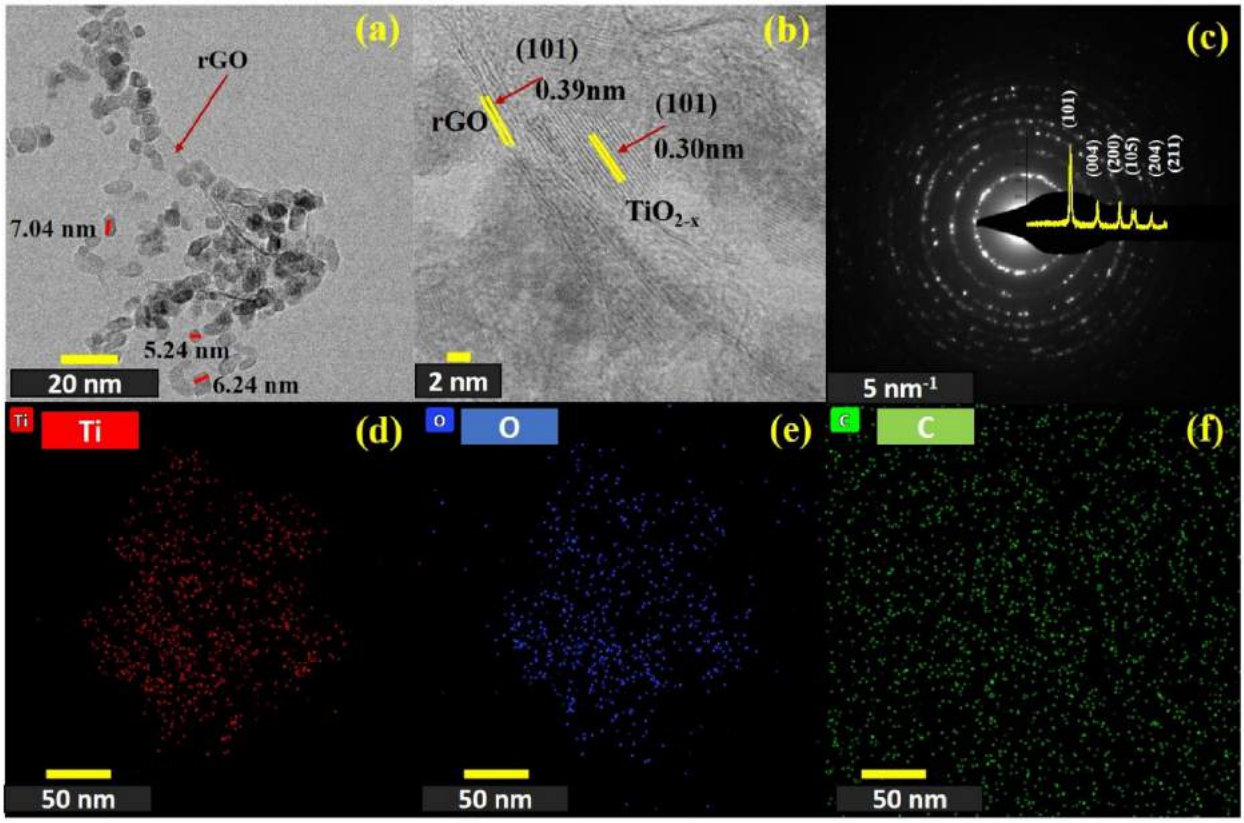

Fig. 3 – (a, b) TEM images of RBT2 sample and Figure (c) SAED patterns of RBT2 sample. Figure (d, e, and f) STEM images of RBT2 sample.

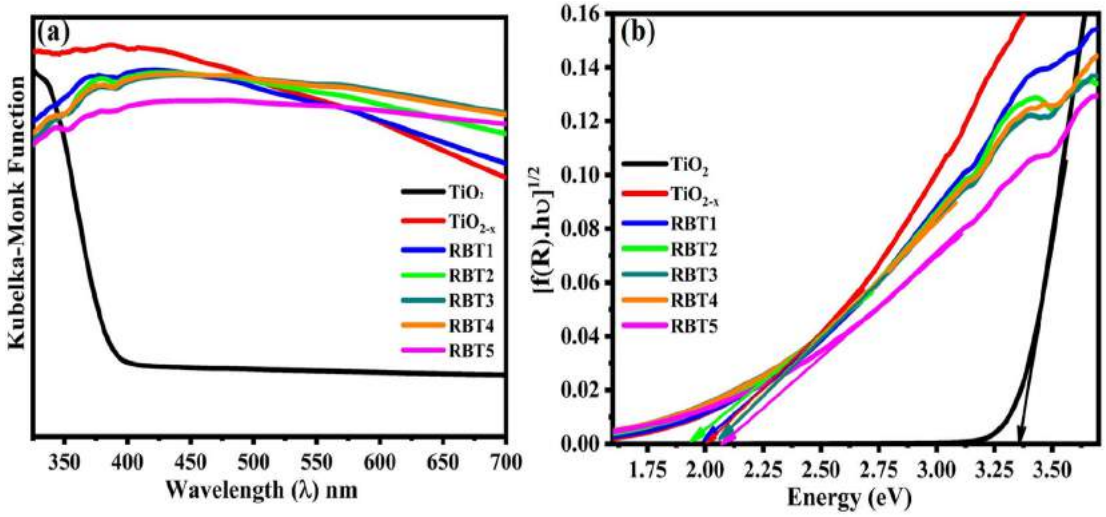

Fig. 4 – (a) Diffuse Reflectance UV–Visible spectra. (b) Tauc plots of pristine TiO_2, TiO_{2-x}, and RBT samples with different GO concentrations.

and Ti^{4+} 2p. Suggesting stable Ti^{3+} defects are not present in the TiO_{2-x} and RBT2 samples. Fig. 5(c) shows the C1s region of the RBT2 nanocomposite. The C=C and C–C bonds are assigned to the deconvoluted peak at 285.0 eV. Furthermore, the oxidized carbon peaks located at 286.2, 287.3, and 288.5 eV are ascribed to the O–C=O, C–O and C=O bonds, respectively [48].

The XPS analysis confirms a strong interface of TiO_{2-x} and RGO in the RBT2 nanocomposite, which is more accommodating in establishing electron transport channels and

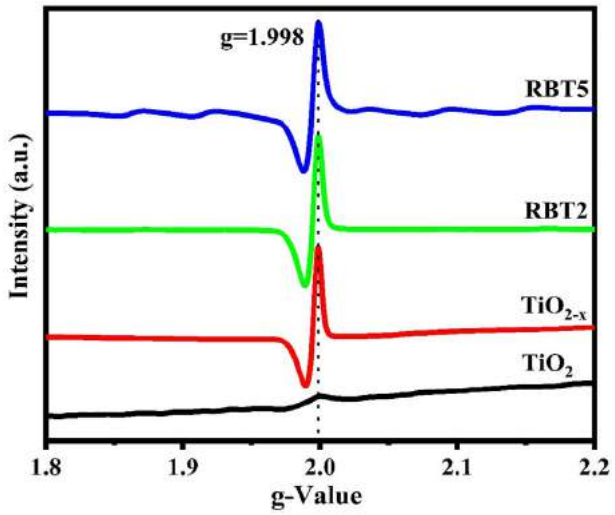

Fig. 5 – ESR recorded spectra of TiO_2, TiO_{2-x}, RBT2, and RBT5 samples.

enhancing photo generated charge separation during the photocatalytic H2 evolution reaction.

Photocatalytic hydrogen evolution

The enhanced optical properties of TiO_{2-x} and RBT samples showed tremendous improvement in photocatalytic water splitting under natural solar light. The hydrogen evolution was investigated using glycerol as a sacrificial reagent. The hydrogen evolved from aqueous suspensions containing hydrothermally prepared TiO_2, TiO_{2-x}, and RGO/TiO_{2-x} composite samples were shown in Fig. 7(a). It should be noted that photocatalytic hydrogen evolution performance of pristine TiO_2, TiO_{2-x}, and RBT (1, 2, 3, 4, and 5) nanocrystals were investigated by directly suspending in the reactor, without any metal dopant. It was found that the photocatalytic activity of the RBT2 sample shows the highest hydrogen evolution, i.e., 13.6 mmol. h^{-1} $g^{-1}_{cat.}$ compared to RBT (1, 3, 4, and 5) samples. The pristine TiO_2 sample showed poor photocatalytic H_2 generation activity than the TiO_{2-x} and RBT (1, 2, 3, and 4) samples. The wide bandgap and high rate of recombination sites could be the reason for the poor photocatalytic activity of pristine TiO_2. In the TiO_{2-x} sample, the defects in the lattice increase the visible range absorption and enhance photocatalytic activity by twofold compared with pristine TiO_2.

In comparison with reported data (listed in Table 2), RBT2 composite was demonstrated an improved hydrogen production rate under solar light illumination. The introduction of RGO could explain the increase in hydrogen evolution with a large surface area and excellent electronic conductivity, which can more easily promote the photogenerated charge to the surface of the composite. The free mobility of charge carriers results in suppressing the recombination process [61]. In contrast, introducing RGO with a large surface area can increase the number of active sites [62]. The photocatalytic

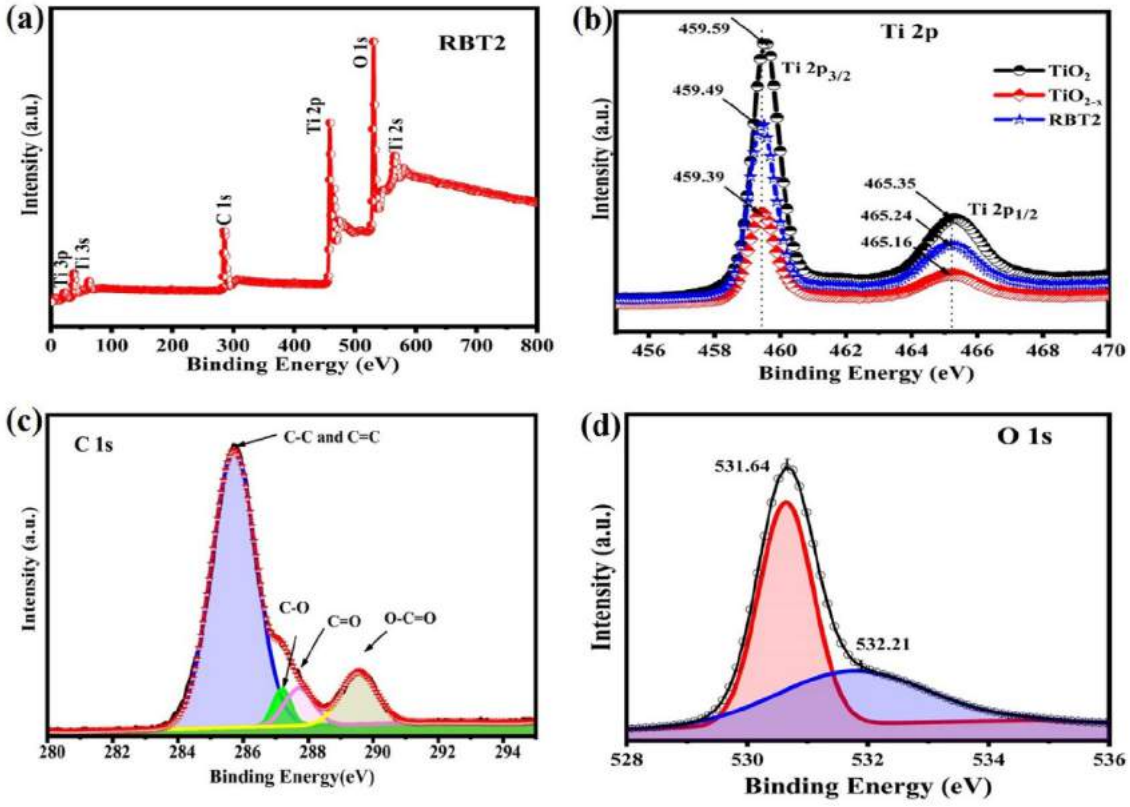

Fig. 6 – (a). Shows the complete survey XPS spectra of the RBT2 sample. Figure (b) shows the Ti 2p peaks of the TiO_2, TiO_{2-x}, and RBT2 samples. Figure (c) shows the C 1s deconvoluted peaks. Figure (d) shows O 1s peaks of RBT2 sample.

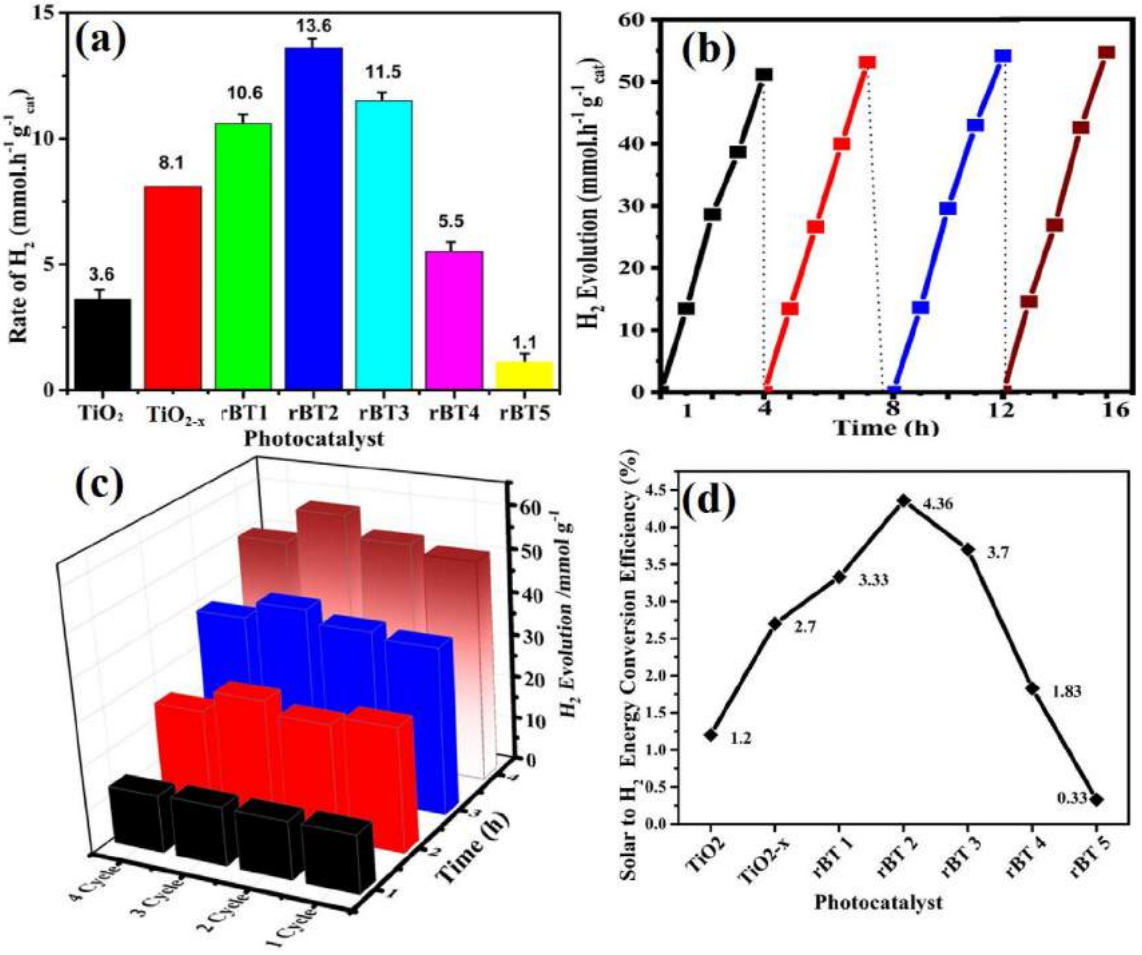

Fig. 7 – (a) Photocatalytic H_2 evolution of TiO_2 and TiO_{2-x} and RBT (1, 2, 3, 4, and 5) samples with different GO weight concentrations under solar irradiation. Figure (b) shows the cycle test of the RBT2 photocatalyst.

activity is enhanced at the optimum 2% of GO content in the catalyst. The amount of hydrogen evolution increases at a rate of 13.6 mmol $h^{-1}g^{-1}_{cat,}$ with 4-h constant irradiation, which is much higher than TiO_{2-x} (8.1 mmol $h^{-1}g^{-1}_{cat}$). Photocatalytic activity decreased with a further increase of RGO content due to unfavorable occupation of TiO_{2-x} active centers with an excess of RGO. Thus a decrease of active sites of the catalyst results to a decrease in the photocatalytic activity [63].

Furthermore, the content of RGO has a substantial influence on photon absorption. The photons absorbed by the photocatalysts improve as the RGO concentration increases. As a result, the photons cannot be constantly fed into photocatalysts resulting in a decrease in photoinduced charge carriers [64]. These conflicting aspects are compromised when RGO is loaded by 2 wt%, at which point the shielding of active sites balances the impact of increased surface area. As a result, a composite containing 2% by weight had the highest photocatalytic activity.

Further, the photocatalytic and Photoelectrochemical activity was carried out for pristine TiO_2, $TiO_{2-x,}$ and optimized composite RBT2 using xenon lamp 300 mW cm^{-1} with a UV-Cutoff filter (≥450 nm). Fig. 8(a) and (b) show the hydrogen evolution rate and transient photocurrent response curves of pristine TiO_2, TiO_{2-x}, and RBT2 samples. The RBT2 composite exhibits the highest H2 evolution rate of 947.2 μmol $h^{-1}g^{-1}_{cat}$ and photocurrent density of 117 μA cm^{-2}, and it is almost two times larger than that of TiO_{2-x}. These results confirm that incorporating oxygen vacancies and insertion of RGO played a vital role in the TiO_2 system for achieving visible activity and overcoming the recombination issues.

A plausible mechanism for photocatalytic hydrogen generation

From the optoelectronic studies of TiO_{2-x} and RGO/TiO_{2-x} nanocomposites, the absorbance of the proposed samples protracts towards higher wavelengths of the visible NIR regime the light utilization could be more efficient. Additionally, the role of RGO in the RBT composite promotes the rapid transportation of photogenerated charge carriers. Which significantly prevents direct recombination of electron-hole pairs [74,75]. Fig. 8(a) and (b) show the visible light photocatalytic H2 evolution and transient photocurrent response curves of TiO_2, TiO_{2-x}, and RBT2 samples. The RBT2 composite

Table 2 – The List of Hydrogen Evolution from reported defective TiO_2 and its composite forms synthesized by various methods.

S. No	Photocatalyst/Co-catalyst	Method	Sacrificial reagent	Light Source	H_2 evolution (mmol h^{-1} g^{-1})	Ref
1.	N-Black TiO_2/RGO	Vacuum Sintering	100 mL 5 vol% Glycerol	250 W Xenon Lamp	11.4	[65]
2.	10LBT/CdS	$NaBH_4$ Reduction	50 mL of 0.35 M Na_2SO_3 and 0.25 M Na_2S (50/50/v/v) aqueous solution	300 W Xenon lamp λ > 420 nm	9.9	[66]
3.	H–TiO2	Ar- Annealing	20 vol% MeOH and 1.78 wt% Pt co-catalyst	UV–vis irradiation (380–780 nm)	0.14	[67]
4.	Black TiO_2/Pt 1 wt%	Ti O oxidation	100 mL 20 vol% methanol	300 W Xenon Lamp (Cutoff filter 400 nm)	0.0225	[68]
5.	Black TiO_2/Pt 0.6 wt%	$TiCl_3$ oxidation	100 mL/methanol 10 vol %	Xenon Lamp 300 W (cutoff filter 420 nm)	0.1167	[69]
6.	Black TiO_2/Pt 1 wt %	Imidazole reduction	120 mL 25 vol% methanol	Xenon Lamp 300 W (cutoff filter 40 0 nm)	0.115	[70]
7.	Black TiO_2/Pt 0.5 wt%	TiH_2 assisted reduction	200 mL 20 vol% methanol	300 W Xenon lamp	5.8	[71]
8.	Black TiO_2/Pt 0.5 wt%	Bio-template method combined with an ethane diamine encircling process	100 mL 20 vol% methanol	Xenon lamp 15 A (Filter of A.M 1.5 G)	3.3	[72]
9.	Black TiO_2/Pt 1 wt%	Solvothermal method	120 mL/methanol 30 vol %	Xenon Lamp 300 W (cutoff filter 420 nm)	0.08	[73]
10.	Black TiO_2/0.6 wt% Pt	Hydrothermal method ($TiCl_3$)	100 mL 10 vol% methanol	Xenon Lamp 300 W (cutoff filter 420 nm)	0.116	[51]
11.	Brown TiO2	Hydrothermal method ($TiCl_4$)	50 mL/2.5 mL Glycerol	Natural solar light (Intensity −300 ± 10 mW cm^{-2})	8.1	[53]
12.	RGO/Def-ect rich TiO_{2-x}	Hydrothermal method	50 mL/2.5 mL Glycerol	Solar Light	13.6	Present work
				Xenon Lamp 300-mWcm^{-1} (≥450 nm)	0.94	

exhibits the highest photocurrent density of 117 μA cm^{-2}, almost two times larger than TiO_{2-x}. It confirms that including an optimum percentage of 2% RGO in the RBT composite improves light absorption and significantly accelerates the composite photogenerated charge separation and transportation. Likewise, RGO can serve as an acceptor for TiO_{2-x} photogenerated electrons. Because of its high conductivity, it facilitates rapid charge transfer, effectively preventing charge recombination in composites.

Fig. 9(a and b) shows the proposed H_2 production mechanism of TiO_{2-x} and RBT. During the exposure to visible light, for TiO_{2-x} systems, in the absence of RGO, the photo-excited electrons in the conduction band recombine rapidly without participating in the evolution of H_2 due to poor charge transfer. Thus, poor evolution of H_2 can occur. Whereas, in RGO/TiO_{2-x}, the excited conduction band electrons of TiO_{2-x} transferred to RGO via intimate interface contacts to H_2 reaction sites [76]. As in the presence of RGO, when electrons are transferred from the conduction band to the RGO layer, the sheet-like structure of the RGO can help the electrons move freely; there was a scarcer opportunity for electron/hole recombination. Thus, RGO acts as a fast charge transfer of photogenerated electrons and suppresses the possibility of recombination of electron holes. As a result, water can be reduced to hydrogen at the RGO surface and oxidized at the TiO_{2-x} surface. In addition, the feasible enhancement in photocatalytic activity of RBT2 relative to its counterparts of RGO/TiO_{2-x} can be explained by the reduction of the bandgap, the improvement of electron transfer, and charge separation through RGO, and the reduction of recombination rate. Thus, the formation of RGO/TiO_{2-x} heterojunction interfaces can rationally enhance the H_2 production activity than TiO_{2-x} and pristine TiO_2.

Conclusion

In summary, pristine TiO_2, oxygen vacancy defects rich TiO_{2-x}, and RGO/TiO_{2-x} samples with different GO concentrations from 1% to 5% were synthesized at a low-cost hydrothermal method. The influence of RGO on defect-rich TiO_{2-x} over structural, morphological, and optical properties was systematically explored. The as-prepared RBT2 photocatalyst (without any cocatalyst) exhibits remarkable enhancement in photocatalytic in the rate of hydrogen evolution 13.6 mmol h^{-1} $g^{-1}_{cat.}$, compared to the pristine TiO_2, TiO_{2-x}, and other already reported RGO/TiO_{2-x}. The present work may be strong evidence that the optimal content of RGO enhances the charge transfer, which suppresses the electron-hole recombination problem.

Declaration of competing interest

The authors declare that they have no known competing financial interests or personal relationships that could have appeared to influence the work reported in this paper.

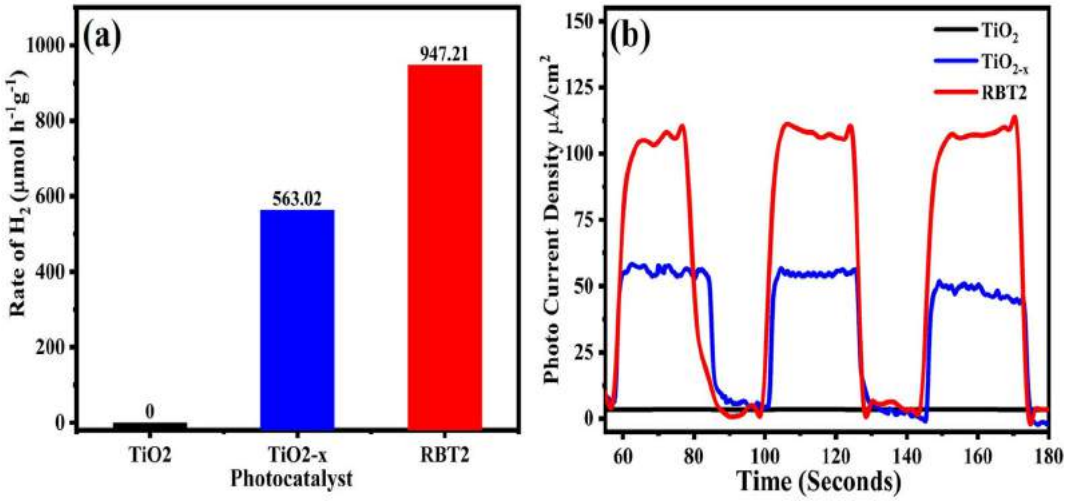

Fig. 8 – (a) H2 Evolution. (b) The transient Photocurrent response of TiO_2, TiO_{2-x}, and RBT2 samples under visible light (≥450 nm).

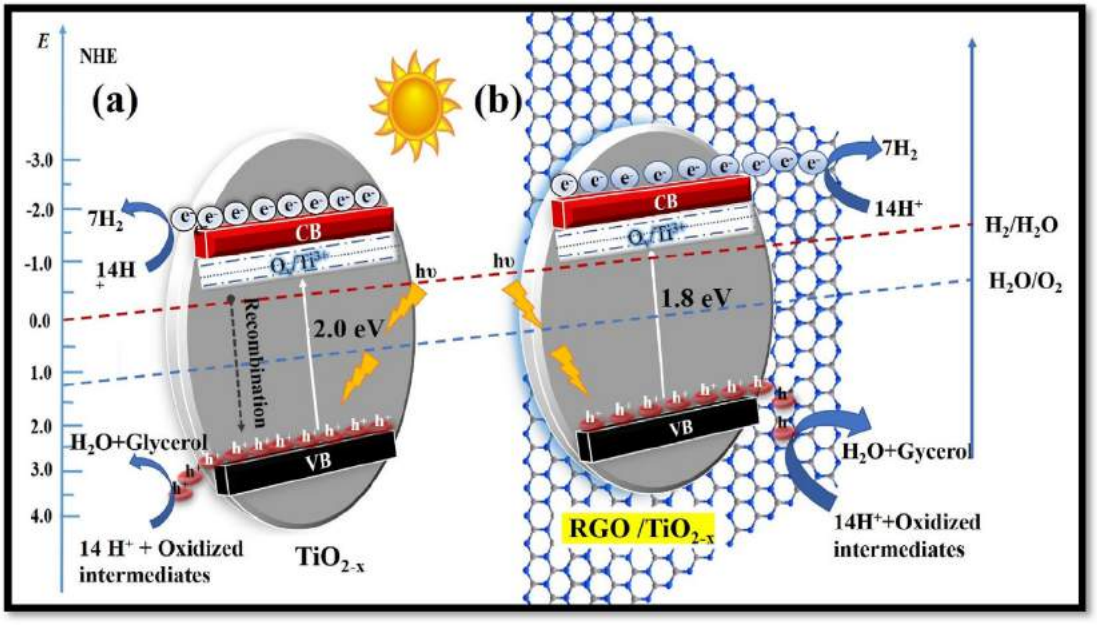

Fig. 9 – (a) Proposed H_2 evolution mechanism of TiO_{2-x}, (b) RGO/TiO_{2-x} under solar irradiation.

Acknowledgments

This work is partially supported by the Dept. of IT, BT & ST, Govt. of Karnataka under grant No. VGST/CESEM/2012-13/182. The authors would like to thank Y. Gambe, I. Honma, Tohoku University, Japan, CeNs Bangalore, IISc Bangalore for INUP program CeNSE, SAIF Cochin, and SAIF IIT Madras for providing characterization facilities.

REFERENCES

[1] Fujishima A, Honda K. Electrochemical photolysis of water one and two-dimensional structure of poly (L-alanine) shown by specific heat measurements at low. Nature 1972;238:37–8. https://doi.org/10.1038/238037a0.

[2] Zuo F, Bozhilov K, Dillon RJ, Wang L, Smith P, Zhao X, et al. Active facets on titanium(III)-doped TiO2: an effective strategy to improve the visible-light photocatalytic activity.

Angew Chem Int Ed 2012;51:6223–6. https://doi.org/10.1002/anie.201202191.
[3] Lu X, Wang G, Xie S, Shi J, Li W, Tong Y, et al. Efficient photocatalytic hydrogen evolution over hydrogenated ZnO nanorod arrays. Chem Commun 2012;48:7717–9. https://doi.org/10.1039/c2cc31773g.
[4] Li S, Chen D, Zheng F, Zhou H, Jiang S, Wu Y. Water-soluble and lowly toxic sulphur quantum dots. Adv Funct Mater 2014;24:7133–8. https://doi.org/10.1002/adfm.201402087.
[5] Dom R, Govindarajan S, Joshi SV, Borse PH. A solar-responsive zinc oxide photoanode for solar-photon-harvester photoelectrochemical (PEC) cells. Nanoscale Adv 2020;2:3350–7. https://doi.org/10.1039/D0NA00139B.
[6] Pareek A, Thotakuri R, Dom R, Kim HG, Borse PH. Nanostructure Zn–Cu co-doped CdS chalcogenide electrodes for opto-electric-power and H2 generation. Int J Hydrogen Energy 2017;42:125–32. https://doi.org/10.1016/j.ijhydene.2016.10.029.
[7] Martin DJ, Qiu K, Shevlin SA, Handoko AD, Chen X, Guo Z, et al. Highly efficient photocatalytic H2 evolution from water using visible light and structure-controlled graphitic carbon nitride. Angew Chem Int Ed 2014;53:9240–5. https://doi.org/10.1002/anie.201403375.
[8] Wang X, Maeda K, Thomas A, Takanabe K, Xin G, Carlsson JM, et al. A metal-free polymeric photocatalyst for hydrogen production from water under visible light. Nat Mater 2009;8:76–80. https://doi.org/10.1038/nmat2317.
[9] Jia Q, Iwashina K, Kudo A. Facile fabrication of an efficient BiVO4 thin film electrode for water splitting under visible light irradiation. Proc Natl Acad Sci USA 2012;109:11564–9. https://doi.org/10.1073/pnas.1204623109.
[10] Muniyappa M, Kalegowda S N, Shetty M, Sriramoju JB, Shastri M, NR SV, et al. Cocatalyst free nickel sulphide nanostructure for enhanced photocatalytic hydrogen evolution. Int J Hydrogen Energy 2022;47:5307–18. https://doi.org/10.1016/j.ijhydene.2021.11.171.
[11] Chandrappa S, Murthy DHK, Reddy NL, Babu SJ, Rangappa D, Bhargav U, et al. Utilizing 2D materials to enhance H2 generation efficiency via photocatalytic reforming industrial and solid waste. Environ Res 2021;200:111239. https://doi.org/10.1016/j.envres.2021.111239.
[12] Linsebigler AL, Lu G, Yates JT. Photocatalysis on TiO 2 surfaces: principles, mechanisms, and selected results. Chem Rev 1995;95:735–58. https://doi.org/10.1021/cr00035a013.
[13] Zhang J, Xu Q, Feng Z, Li M, Li C. Importance of the relationship between surface phases and photocatalytic activity of TiO2. Angew Chem Int Ed 2008;47:1766–9. https://doi.org/10.1002/anie.200704788.
[14] Ni M, Leung MKH, Leung DYC, Sumathy K. A review and recent developments in photocatalytic water-splitting using TiO 2 for hydrogen production. Renew Sustain Energy Rev 2007;11:401–25. https://doi.org/10.1016/j.rser.2005.01.009.
[15] Higashi M, Abe R, Takata T, Domen K. Photocatalytic overall water splitting under visible light using ATaO 2 N (A = Ca, Sr, Ba) and WO 3 in a IO 3 −/I − shuttle redox mediated system. Chem Mater 2009;21:1543–9. https://doi.org/10.1021/cm803145n.
[16] Kamegawa T, Matsuura S, Seto H, Yamashita H. A visible-light-harvesting assembly with a sulfocalixarene linker between dyes and a Pt-TiO2 photocatalyst. Angew Chem Int Ed 2013;52:916–9. https://doi.org/10.1002/anie.201206839.
[17] Chen X, Shen S, Guo L, Mao SS. Semiconductor-based photocatalytic hydrogen generation. Chem Rev 2010;110:6503–70. https://doi.org/10.1021/cr1001645.
[18] Basavarajappa PS, Patil SB, Ganganagappa N, Reddy KR, Raghu AV, Reddy CV. Recent progress in metal-doped TiO2, non-metal doped/codoped TiO2 and TiO2 nanostructured hybrids for enhanced photocatalysis. Int J Hydrogen Energy 2020;45:7764–78. https://doi.org/10.1016/j.ijhydene.2019.07.241.
[19] Li X, Yu J, Low J, Fang Y, Xiao J, Chen X. Engineering heterogeneous semiconductors for solar water splitting. J Mater Chem A 2015;3:2485–534. https://doi.org/10.1039/c4ta04461d.
[20] Marschall R. Semiconductor composites: strategies for enhancing charge carrier separation to improve photocatalytic activity. Adv Funct Mater 2014;24:2421–40. https://doi.org/10.1002/adfm.201303214.
[21] Chen X, Liu L, Yu PY, Mao SS. Increasing solar absorption for photocatalysis with black hydrogenated titanium dioxide nanocrystals. Science 2011;331:746–51 (80-).
[22] Zuo F, Wang L, Wu T, Zhang Z, Borchardt D, Feng P. ChemInform abstract: self-doped Ti3+ enhanced photocatalyst for hydrogen production under visible light. ChemInform 2010;41:11856–7. https://doi.org/10.1002/chin.201049012.
[23] Wendt S, Sprunger PT, Lira E, Madsen GKH, Li Z, Hansen J, et al. The role of interstitial sites in the Ti3d defect state in the band gap of titania. Science 2008;320:1755–9. https://doi.org/10.1126/science.1159846 (80-).
[24] Chen CC, Say WC, Hsieh SJ, Diau EWG. A mechanism for the formation of annealed compact oxide layers at the interface between anodic titania nanotube arrays and Ti foil. Appl Phys Mater Sci Process 2009;95:889–98. https://doi.org/10.1007/s00339-009-5093-6.
[25] Su J, Zou X-X, Zou Y, Li G, Wang P, Chen J. Porous titania with heavily self-doped Ti 3+ for specific sensing of CO at room temperature. Inorg Chem 2013;52:5924–30. https://doi.org/10.1021/ic400109j.
[26] Xia T, Zhang Y, Murowchick J, Chen X. Vacuum-treated titanium dioxide nanocrystals: optical properties, surface disorder, oxygen vacancy, and photocatalytic activities. Catal Today 2014;225:2–9. https://doi.org/10.1016/j.cattod.2013.08.026.
[27] Liu L, Chen X. Titanium dioxide nanomaterials: self-structural modifications. Chem Rev 2014;114:9890–918. https://doi.org/10.1021/cr400624r.
[28] Chen X, Liu L, Huang F. Black titanium dioxide (TiO_2) nanomaterials. Chem Soc Rev 2015;44:1861–85. https://doi.org/10.1039/C4CS00330F.
[29] Li K, Gao S, Wang Q, Xu H, Wang Z, Huang B, et al. In-situ-reduced synthesis of Ti^{3+} self-doped TiO_2/g-C_3N_4 heterojunctions with high photocatalytic performance under LED light irradiation. ACS Appl Mater Interfaces 2015;7:9023–30. https://doi.org/10.1021/am508505n.
[30] Xu H, Ouyang S, Liu L, Reunchan P, Umezawa N, Ye J. Recent advances in TiO_2-based photocatalysis. J Mater Chem A 2014;2:12642. https://doi.org/10.1039/C4TA00941J.
[31] Eda G, Chhowalla M. Chemically derived graphene oxide: towards large-area thin-film electronics and optoelectronics. Adv Mater 2010;22:2392–415. https://doi.org/10.1002/adma.200903689.
[32] Lee C, Wei X, Kysar JW, Hone J. Measurement of the elastic properties and intrinsic strength of monolayer graphene. Science 2008;321:385–8. https://doi.org/10.1126/science.1157996 (80-).
[33] Balandin AA, Ghosh S, Bao W, Calizo I, Teweldebrhan D, Miao F, et al. Superior thermal conductivity of single-layer graphene. Am Chem Soc Nano 2008;8:902–7.
[34] Zhu Y, Murali S, Cai W, Li X, Suk JW, Potts JR, et al. Graphene and graphene oxide: synthesis, properties, and applications. Adv Mater 2010;22:3906–24. https://doi.org/10.1002/adma.201001068.
[35] Shetty M, Schüßler C, Shastri M, Sabbanahalli C, Chitrabhanu CP, Murthy M, et al. One-pot supercritical water

synthesis of Bi2MoO6-RGO 2D heterostructure as anodes for Li-ion batteries. Ceram Int 2021;47:10274–83. https://doi.org/10.1016/j.ceramint.2020.12.061.
[36] Jang J-H, Rangappa D, Kwon Y-U, Honma I. Direct preparation of 1-PSA modified graphenenanosheets by supercritical fluidic exfoliation and its electrochemical properties. J Mater Chem 2011;21:3462–6. https://doi.org/10.1039/C0JM02472D.
[37] Xiang Q, Yu J, Jaroniec M. Synergetic effect of MoS 2 and graphene as cocatalysts for enhanced photocatalytic H 2 production activity of TiO2 nanoparticles. J Am Chem Soc 2012;134:6575–8. https://doi.org/10.1021/ja302846n.
[38] Fan W, Lai Q, Zhang Q, Wang Y. Nanocomposites of TiO2 and reduced graphene oxide as efficient photocatalysts for hydrogen evolution. J Phys Chem C 2011;115:10694–701. https://doi.org/10.1021/jp2008804.
[39] Xiang Q, Yu J, Jaroniec M. Graphene-based semiconductor photocatalysts. Chem Soc Rev 2012;41:782–96. https://doi.org/10.1039/c1cs15172j.
[40] Zhang XY, Li HP, Cui XL, Lin Y. Graphene/TiO2 nanocomposites: synthesis, characterization and application in hydrogen evolution from water photocatalytic splitting. J Mater Chem 2010;20:2801–6. https://doi.org/10.1039/b917240h.
[41] Iwase A, Ng YH, Ishiguro Y, Kudo A, Amal R. Reduced graphene oxide as a solid-state electron mediator in Z-scheme photocatalytic water splitting under visible Light.Pdf. JACS 2011;133:11054–7.
[42] Wang Y, Wang W, Mao H, Lu Y, Lu J, Huang J, et al. Electrostatic self-assembly of BiVO 4 -reduced graphene oxide nanocomposites for highly efficient visible light photocatalytic activities. ACS Appl Mater Interfaces 2014;6:12698–706. https://doi.org/10.1021/am502700p.
[43] Xiang Q, Yu J, Jaroniec M. Enhanced photocatalytic H2-production activity of graphene-modified titania nanosheets. Nanoscale 2011;3:3670–8. https://doi.org/10.1039/c1nr10610d.
[44] Zhang Hao, Lv Xiaojun, Li Yueming, Ying Wang JL. P25-Graphene composite as a high performance photocatalyst. ACS Nano 2009;4:380–6. https://doi.org/10.1021/nn901221k.
[45] Zhang Yanhui, Tang Zi-Rong, Fu Xianzhi, Xu Yi-Jun. TiO2-graphene nanocomposites for gas-phase photocatalytic degradation of TiO2-Graphene nanocomposites for other TiO2-Carbon composite TiO2-Graphene truly different from volatile aromatic pollutant: is TiO_2–Graphene Truly Different from Other TiO_2–Carbon Composite Materials?. ACS Nano 2010;4:7303–14. https://doi.org/10.1021/nn1024219.
[46] Zhang Y, Tang ZR, Fu X, Xu YJ. Engineering the unique 2D mat of graphene to achieve graphene-TiO 2 nanocomposite for photocatalytic selective transformation: what advantage does graphene have over its forebear carbon nanotube? ACS Nano 2011;5:7426–35. https://doi.org/10.1021/nn202519j.
[47] Xu L, Yang L, Johansson EMJ, Wang Y, Jin P. Photocatalytic activity and mechanism of bisphenol a removal over TiO2–x/rGO nanocomposite driven by visible light. Chem Eng J 2018;350:1043–55. https://doi.org/10.1016/j.cej.2018.06.046.
[48] Qiu B, Zhou Y, Ma Y, Yang X, Sheng W, Xing M, et al. Facile synthesis of the Ti3+self-doped TiO2-graphene nanosheet composites with enhanced photocatalysis. Sci Rep 2015;5:2–7. https://doi.org/10.1038/srep08591.
[49] Sriramoju JB, Muniyappa M, Marilingaiah NR, Sabbanahalli C, Shetty M, Mudike R, et al. Carbon-based TiO2-x heterostructure nanocomposites for enhanced photocatalytic degradation of dye molecules. Ceram Int 2021;47:10314–21. https://doi.org/10.1016/j.ceramint.2020.12.014.
[50] Chen J, Yao B, Li C, Shi G. An improved Hummers method for eco-friendly synthesis of graphene oxide. Carbon NY 2013;64:225–9. https://doi.org/10.1016/j.carbon.2013.07.055.
[51] Wajid Shah M, Zhu Y, Fan X, Zhao J, Li Y, Asim S, et al. Facile synthesis of defective TiO 2-x nanocrystals with high surface area and tailoring bandgap for visible-light photocatalysis. Sci Rep 2015;5:1–8. https://doi.org/10.1038/srep15804.
[52] Qu Y, Gao Y, Kong F, Zhang S, Du L, Yin G. Pt–rGO–TiO2 nanocomposite by UV-photoreduction method as promising electrocatalyst for methanol oxidation. Int J Hydrogen Energy 2013;38:12310–7. https://doi.org/10.1016/j.ijhydene.2013.07.038.
[53] S. Jagadeesh Babu, V. Navakoteswara Rao, Dharmapura H.K. Murthy, Shastri Mahesh, M Murthy, Shetty M, et al. Significantly enhanced cocatalyst-free H2 evolution from defect-engineered Brown TiO2. Ceram Int 2020;47(10):14821–8. https://doi.org/10.1016/j.ceramint.2020.10.026.
[54] Dong J, Han J, Liu Y, Nakajima A, Matsushita S, Wei S, et al. Defective black TiO2 synthesized via anodization for visible-light photocatalysis. ACS Appl Mater Interfaces 2014;6:1385–8. https://doi.org/10.1021/am405549p.
[55] Wang J, Hernandez Y, Lotya M, Coleman JN, Blau WJ. Broadband nonlinear optical response of graphene dispersions. Adv Mater 2009;21:2430–5. https://doi.org/10.1002/adma.200803616.
[56] Li L, Yu L, Lin Z, Yang G. Reduced TiO2-graphene oxide heterostructure as broad spectrum-driven efficient water-splitting photocatalysts. ACS Appl Mater Interfaces 2016;8:8536–45. https://doi.org/10.1021/acsami.6b00966.
[57] Liu W, Sun W, Borthwick AGL, Wang T, Li F, Guan Y. Simultaneous removal of Cr(VI) and 4-chlorophenol through photocatalysis by a novel anatase/titanate nanosheet composite: synergetic promotion effect and autosynchronous doping. J Hazard Mater 2016;317:385–93. https://doi.org/10.1016/j.jhazmat.2016.06.002.
[58] D'Arienzo M, Carbajo J, Bahamonde A, Crippa M, Polizzi S, Scotti R, et al. Photogenerated defects in shape-controlled TiO 2 anatase nanocrystals: a probe to evaluate the role of crystal facets in photocatalytic processes. J Am Chem Soc 2011;133:17652–61. https://doi.org/10.1021/ja204838s.
[59] Scotti R, Bellobono IR, Canevali C, Cannas C, Catti M, D'Arienzo M, et al. Sol-gel pure and mixed-phase titanium dioxide for photocatalytic purposes: relations between phase composition, catalytic activity, and charge-trapped sites. Chem Mater 2008;20:4051–61. https://doi.org/10.1021/cm800465n.
[60] Liu Y, Shi Y, Zhang S, Liu B, Sun X, Yang D. Optimizing the interface of C/titania@reduced graphene oxide nanofibers for improved photocatalytic activity. J Mater Sci 2019;54:8907–18. https://doi.org/10.1007/s10853-019-03454-3.
[61] Meng F, Li J, Cushing SK, Zhi M, Wu N. Solar hydrogen generation by nanoscale p-n junction of p-type molybdenum disulfide/n-type nitrogen-doped reduced graphene oxide. J Am Chem Soc 2013;135:10286–9. https://doi.org/10.1021/ja404851s.
[62] Sher Shah MSA, Park AR, Zhang K, Park JH, Yoo PJ. Green synthesis of biphasic TiO 2-reduced graphene oxide nanocomposites with highly enhanced photocatalytic activity. ACS Appl Mater Interfaces 2012;4:3893–901. https://doi.org/10.1021/am301287m.
[63] Chen J, Xu X, Li T, Pandiselvi K, Wang J. Toward high performance 2D/2D hybrid photocatalyst by electrostatic assembly of rationally modified carbon nitride on reduced graphene oxide. Sci Rep 2016;6:37318. https://doi.org/10.1038/srep37318.
[64] Li Q, Guo B, Yu J, Ran J, Zhang B, Yan H, et al. Highly efficient visible-light-driven photocatalytic hydrogen production of

CdS-cluster-decorated graphene nanosheets. J Am Chem Soc 2011;133:10878–84. https://doi.org/10.1021/ja2025454.
[65] Ida S, Samuel Justin SJ, Wilson P, Neppolian B. Visible light active black TiO2 nanostructures and its RGO based nanocomposite for enhanced hydrogen generation and electrochemical potency. Appl Surf Sci Adv 2022;7:100215. https://doi.org/10.1016/j.apsadv.2022.100215.
[66] Devaraji P, Gao R, Xiong L, Jia X, Huang L, Chen W, et al. Usage of natural leaf as a bio-template to inorganic leaf: leaf structure black TiO2/CdS heterostructure for efficient photocatalytic hydrogen evolution. Int J Hydrogen Energy 2021;46:14369–83. https://doi.org/10.1016/j.ijhydene.2021.01.198.
[67] Jia G, Wang Y, Cui X, Zhang H, Zhao J, Li LH, et al. Wet-chemistry hydrogen doped TiO2 with switchable defects control for photocatalytic hydrogen evolution. Matter 2022;5:206–18. https://doi.org/10.1016/j.matt.2021.10.027.
[68] Pei Z, Ding L, Lin H, Weng S, Zheng Z, Hou Y, et al. Facile synthesis of defect-mediated TiO2-x with enhanced visible light photocatalytic activity. J Mater Chem A 2013;1:10099–102. https://doi.org/10.1039/c3ta12062g.
[69] Amano F, Nakata M, Yamamoto A, Tanaka T. Effect of Ti3+ ions and conduction band electrons on photocatalytic and photoelectrochemical activity of rutile titania for water oxidation. J Phys Chem C 2016;120:6467–74. https://doi.org/10.1021/acs.jpcc.6b01481.
[70] Zou X, Liu J, Su J, Zuo F, Chen J, Feng P. Facile synthesis of thermal- and photostable titania with paramagnetic oxygen vacancies for visible-light photocatalysis. Chem Eur J 2013;19:2866–73. https://doi.org/10.1002/chem.201202833.
[71] Liu X, Xu H, Grabstanowicz LR, Gao S, Lou Z, Wang W, et al. Ti3+ self-doped TiO2-x anatase nanoparticles via oxidation of TiH2 in H2O2. Catal Today 2014;225:80–9. https://doi.org/10.1016/j.cattod.2013.08.025.
[72] Zhang K, Zhou W, Zhang X, Qu Y, Wang L, Hu W, et al. Large-scale synthesis of stable mesoporous black TiO2 nanosheets for efficient solar-driven photocatalytic hydrogen evolution: via an earth-abundant low-cost biotemplate. RSC Adv 2016;6:50506–12. https://doi.org/10.1039/c6ra06751d.
[73] Zhao Z, Tan H, Zhao H, Lv Y, Zhou LJ, Song Y, et al. Reduced TiO2 rutile nanorods with well-defined facets and their visible-light photocatalytic activity. Chem Commun 2014;50:2755–7. https://doi.org/10.1039/c3cc49182j.
[74] Hafeez HY, Lakhera SK, Bellamkonda S, Rao GR, Shankar MV, Bahnemann DW, et al. Construction of ternary hybrid layered reduced graphene oxide supported g-C3N4-TiO2 nanocomposite and its photocatalytic hydrogen production activity. Int J Hydrogen Energy 2018;43:3892–904. https://doi.org/10.1016/j.ijhydene.2017.09.048.
[75] Lin P, Hu H, Lv H, Ding Z, Xu L, Qian D, et al. Hybrid reduced graphene oxide/TiO2/graphitic carbon nitride composites with improved photocatalytic activity for organic pollutant degradation. Appl Phys A 2018;124:510. https://doi.org/10.1007/s00339-018-1933-6.
[76] Xu Y, Wang X, Jin M, Kempa K, Shui L. Water splitting performance enhancement of the TiO 2 nanorod array electrode with ultrathin black phosphorus nanosheets. Chemelectrochem 2020;7:96–104. https://doi.org/10.1002/celc.201901456.

Available online at www.sciencedirect.com

ScienceDirect

journal homepage: www.elsevier.com/locate/he

Cocatalyst free nickel sulphide nanostructure for enhanced photocatalytic hydrogen evolution

Murthy Muniyappa [a], *Sagara N. Kalegowda* [a], *Manjunath Shetty* [b], *Jagadeesh Babu Sriramoju* [c], *Mahesh Shastri* [a], *Navakoteswara Rao S.V.* [d], *Debasis De* [e], *Shankar M.V.* [d], *Dinesh Rangappa* [a,*]

[a] *Department of Applied Sciences (Nanotechnology), Visvesvaraya Technological University, Center for Postgraduate Studies, Muddenahalli, Chikkaballapur, India*

[b] *Department of Aeronautical and Automobile Engineering, Manipal Institute of Technology, Manipal Academy of Higher Education (MAHE), Manipal, Karnataka, India*

[c] *Department of Physics, MallaReddy Engineering College, Maisammaguda, Hyderabad, Telangana, India*

[d] *Nanocatalysis and Solar Fuels Research Laboratory, Department of Material Science and Nanotechnology, Yogi Vemana University, Vemanapuram, Kadapa, Andhra Pradesh, India*

[e] *Energy Institute, Bengaluru (Centre of R.G.I.P.T.), Bangalore, India*

HIGHLIGHTS

- Synthesized NiS-α/β phase by simple solvothermal method.
- By changing the water to ethanol ratio bandgap of NiS varied from 1.83 to 1.53 eV.
- NiS-α phase exhibited H_2 generation of 13.413 mmol $h^{-1}g^{-1}$.
- NiS acts as alternative photocatalyst to binary or ternary photocatalysts.

GRAPHICAL ABSTRACT

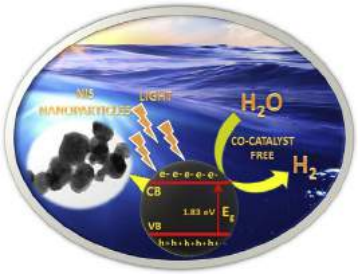

ARTICLE INFO

Article history:
Received 5 August 2021
Received in revised form
4 November 2021
Accepted 22 November 2021
Available online 16 December 2021

Keywords:
Nanostructure
NiS
Solvothermal process

ABSTRACT

Metal chalcogenides are highly active, inexpensive, and earth-abundant materials for photocatalytic hydrogen evolution. This work presents cocatalyst-free Nickel Sulphides (α and β phases) nanostructures for photocatalytic hydrogen generation. NiS nanostructures are synthesized by the solvothermal method by varying the water to ethanol ratio. The synthesized sample has shown an optical bandgap of 1.83 eV, which is favorable for H_2 generation. X-ray diffractometer (XRD) patterns confirm the formation of hexagonal and rhombohedral crystal structures with high phase purity for both NiS-α and NiS-β nanostructures. The multifaceted regular-shaped morphology with 50 nm sized particles was confirmed by high-resolution transmission electron microscopy (HR-TEM). The photocatalytic H_2 generation studies reveal that the NiS-α phase exhibited better H_2 generation

* *Corresponding author.*
E-mail addresses: dineshrangappa@gmail.com, dinesh.rangappa@vtu.ac.in (D. Rangappa).

https://doi.org/10.1016/j.ijhydene.2021.11.171

Bandgap
Hydrogen generation
Photocatalysis

activity of 13.413 m mol $h^{-1}g^{-1}$ than the NiS-β phase of 12.713 m mol $h^{-1}g^{-1}$ under UV–Vis light irradiation without any cocatalyst.

Introduction

Hydrogen is an alternative and renewable fuel for the substitution of conventional fossil fuel. For sustainable development of society, green energy generation and storage technologies should be encouraged. Photocatalytic H_2 generation is a straightforward and cost-effective approach [1–3]. Photocatalytic H_2 generation by water splitting is a promising and sustainable technology as it is environmentally friendly and commercially viable [4–9]. This process draws the attention of many researchers due to its high efficiency, low cost, more stable, less toxic, and long-range active semiconductor materials. Recently, there have been many efforts to synthesize photocatalyst composites containing binary and ternary metal oxides to explore a wide range of materials such as oxides and nitrides. These materials show better results but still lag inefficiencies and stability of photocatalysis for practical purposes [10]. Therefore, it is essential to look for an alternative class of materials to overcome these limitations.

Metal sulfides are an attractive group of materials because of their earth abundance, relatively cheap, visible light active, lower bandgap, interesting optical and electrical properties [11]. Most of the dichalcogenides have a wide absorbance range and their electronic properties can be tuned by varying the size, morphology, and stoichiometry. This class of materials are very suitable for hydrogen generation because of less carrier diffusion time, more stability, and electrical conductivity [12].

Among various metal sulfides dichalcogenides, the MoS_2, CoS_2, FeS_2, and NiS_2 are more commonly explored as catalysts and cocatalysts in electrocatalytic and photocatalytic water splitting applications [13–18]. However, there is limited work reported on NiS_2 material as a photocatalyst due to its unsuitable band positions to the redox potential of water [19]. Recently, Bhosale et al. reported sulfur deficient $NiS_{1.97}$ as a photo-electrocatalyst for water splitting applications [19]. It opens up space for photocatalytic applications of nickel sulfide.

Nickel sulfide exists in different phases such as NiS (α and β), NiS_2, Ni_3S_2, Ni_3S_4, Ni_7S_6, and Ni_9S_8 [20]. Synthesizing single-phase nickel sulfide is very difficult using low-temperature wet chemical processes. Various synthesis methods such as microwave [21], solvothermal [22], hot injection method [23] have been explored for synthesizing controlled phases of nickel sulfides. However, mixed-phase formation is the major challenge in synthesizing this material. Roffey et al. reported the phase-controlled synthesis of NiS by single-source square-planar nickel bis(dithiocarbonate) complexes, $[Ni(S_2CNR_2)_2]$ where, they observed that phase transformation from α to β phase at higher temperature (280 °C) [24]. Yang et al. has reported the synthesis of α and β phase NiS by solvothermal method for dye-sensitized solar cell applications and found that the α phase outperformed the β phase [22]. By changing the temperature and capping agents such as citric acid, β cyclodextrin, and polyvinylpyrrolidone through a solvothermal method, Aniruddha et al. studied tuneable bandgap NiS for photocatalytic organic dye degradation application [25]. There are several reports on other phases of NiS such as NiS_2, Ni_3S_2, Ni_3S_4, Ni_7S_6, and Ni_9S_8. However, so far the α and β phases of NiS nanostructures have not been employed in photocatalytic H_2 generation as photocatalyst. Therefore, it is imperative to study the photocatalytic hydrogen evolution of α and β phase NiS nanostructures.

In this study, α and β phase NiS nanostructures were prepared by green synthesis protocol by utilizing ethanol and ethanol: water (1:2) ratio through the solvothermal method. For the first time, photocatalytic H_2 generation of α and β phase of highly crystalline, monophase NiS nanostructures were studied without cocatalyst. Moreover, the stability of NiS nanostructures before and after the photocatalytic hydrogen generation was studied. The photoelectrochemical properties were exploited to further substantiate the photocatalytic water splitting of synthesized NiS nanostructures.

Experimental details

Materials and characterization

Nickel acetate tetra-hydrate [Ni $(CH_3COO)_2{\cdot}4H_2O$], thiourea $[(NH_2)_2CS]$, and sodium dodecyl sulfate $[NaC_{12}H_{25}SO_4]$ were purchased from Merck Chemicals. The procured chemicals were analytical grade and used without any purification. Ethanol $[C_2H_5OH]$ and DI water were used throughout the experiment. All other chemicals and solvents were used without any further purification.

Crystal structures and phase purity of the synthesized samples were carried out using powder X-Ray diffractometer (XRD) (Rigaku Ultima-IV) ranging from 20 to 70° in 2-theta with 0.02 steps/sec using Cu-K*a* as radiation source (λ = 0.15406 nm) at room temperature. The morphology and elemental analyses of the prepared samples were analyzed by scanning electron microscopy (SEM) SU1510 and energy dispersive X-Ray spectroscopy (EDX), respectively. The high-resolution transmission electron microscopy (HRTEM) images were captured using JEOL, JEM 2100. The UV–Vis spectra of the samples were carried out using a PerkinElmer spectrometer. The photoluminescence (PL) spectra of the samples were recorded in JASCO FP 3600 fluorescence spectroscopy. X-ray photoelectron spectra were analyzed by Shimadzu, ESCA 3100 spectroscopy. The photoelectrochemical measurements were performed in OrigaLys electrochemical workstation. All

the measurements were made on a standard three-electrode system consisting of Ag/AgCl as the reference electrode, Pt wire as counter electrode and FTO coated photocatalysts (3×6 cm^2) were used as a working electrode. 0.1 M Na_2SO_4 was used as an electrolyte. The photocurrent was measured under a 300 W Xenon lamp at 0.2 V biasing conditions with manual ON/OFF. Electrochemical impedance spectra were recorded at − 0.2 V bias at the range of 0.01–10^6 Hz. The Mott–Schottky measurements were carried out at 1 kHz frequency with 0.1 M Na_2SO_4 electrolyte.

Preparation of nickel sulphide (NiS)

NiS nanostructures were synthesized by a simple solvothermal technique as shown in Scheme 1. Under typical synthesis conditions, 4.0 mmol of Ni $(CH_3COO)_2 \cdot 4H_2O$, 750 mg of $(NH_2)_2CS$, and 57 mg of $NaC_{12}H_{25}SO_4$ (SDS) were dissolved in a beaker with pure ethanol (NiS-α) and ethanol: DI water ratio of 1:2 (NiS- β) separately, under continuous stirring. Further, stirring was continued for ~30 min at room temperature until it becomes green colour. Finally, each green precursor solution was poured into a 60 ml Teflon-lined hydrothermal autoclave and kept for 8 h at 200 °C temperature. Later the autoclave was cooled down to room temperature and the samples in the form of solid-precipitates were collected by centrifugation. The collected dark brown powders were washed and dried at 70 °C for 8 h. The sample was prepared only in pure ethanol named as NiS-α. Similarly, NiS sample prepared using ethanol: DI water ratio of 1:2 is referred to as NiS-β. NiS samples prepared with different ratios of solvents (water: ethanol) were found to be mixed α and β phases with some impurities but only the 1:2 ratio resulted in β phase NiS.

Photocatalytic activity

The Photocatalytic activity was performed in a quartz reactor under irradiance of a light source of 260 W Xenon lamps (wavelength of 200–800 nm). In a typical experimental setup, the distance between the source of light and the reactor was maintained at 25 cm in cold water circulation to the reactor to maintain a stable temperature. In a 185 ml of quartz reactor, 5 mg of NiS nanoparticles were suspended as photocatalyst in a 50 ml mixture solution of (0.3 M) Na_2S and (0.3 M) Na_2SO_4. The final concentration of NiS nanoparticles was 0.1 g/l. The rubber septum was used to seal the reactor and a magnetic stirrer was used for stirring. Before irradiation nitrogen gas was purged to remove oxygen. The generated H_2 gas was collected and monitored periodically using an off-line gas chromatograph with N_2 carrier gas (Shimadzu GC-2014 with Molecular Sieve/5 Å column). The photocatalytic quantum efficiency was calculated.

Results and discussion

Structural analysis

The crystal structure of the NiS powder sample synthesized by the simple hydrothermal method was characterized by the XRD technique. Fig. 1 shows the XRD patterns of NiS-α and NiS-β samples. The peaks observed in the XRD pattern of the NiS-α sample correspond to those of the standard hexagonal crystal structure with α phase (D.B Card number: 9009240). The diffraction peaks at 2θ values of 30.06°, 34.59°, 45.815°, and 53.49° corresponds to (100), (101), (102) and (110) planes, respectively. On the other hand, NiS-β shows a rhombohedral crystal structure with β-phase. At 200 °C the saturation vapor pressure of pure ethanol is 2.95 Mpa, which favours the

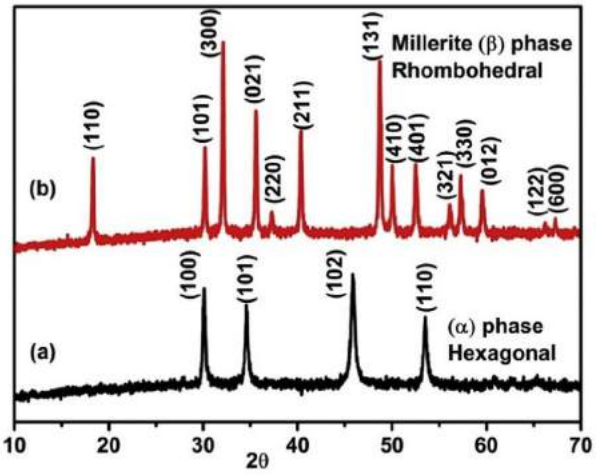

Fig. 1 – XRD patterns of (a) NiS-α (b)NiS-β synthesized by hydrothermal method at 200 °C.

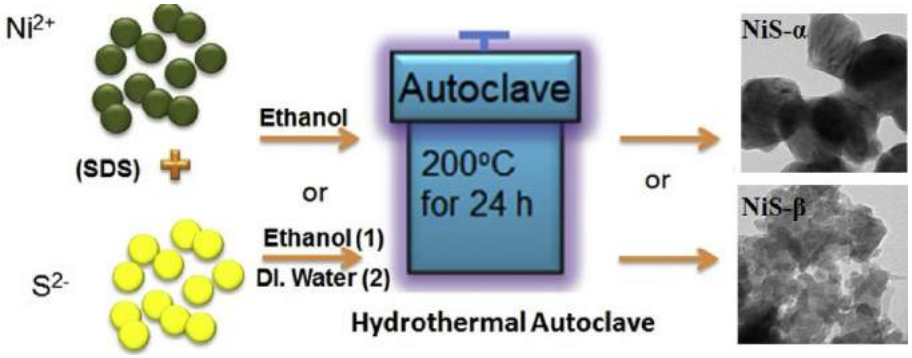

Scheme 1 – Schematic of NiS nanostructures synthesized by a simple solvothermal technique.

formation of the α phase [22]. Whereas for water, it is 1.55 Mpa renders the formation of the NiS-β phase. According to NiS phase diagram, the NiS-α phase is formed at a higher temperature compared to the NiS-β phase [24,26]. This finding is consistent with the NiS phase diagram. All the diffraction peaks in the XRD pattern of NiS-β are matched with the standard rhombohedral NiS-β phase (D.B Card number 5000114). The diffraction peaks at 2θ values of 18.38°, 30.22°, 32.21°, 35.60°, 37.26°, 40.355°, 48.85°, 49.99°, 52.48°, 56.08°, 57.26°, 59.5°, 66.32°, and 67.19° correspond to the (110), (101), (300), (021), (220), (211), (131), (410), (401), (321), (330), (012), (122) and (600) planes, respectively. The average crystallite size (D) was calculated by Scherer's equation [27].

$$D = 0.9\lambda/B \cos\theta \quad (1)$$

where, λ-is the wavelength of the X-Rays, B is the full width at half maxima, and θ is the diffraction angle of the characteristic peak. The D-value of the NiS-α sample was found to be ~25 nm, whereas, for the NiS-β, the D-value (~50 nm) was found larger than NiS-α. A larger D-value for the NiS-β sample may be due to Ostwald ripening during the crystal growth stage in the reaction under ethanol: water (1:2) mixed solvents condition [28,29].

Morphology of nanostructured NiS

The surface morphology of synthesized nanostructured NiS was analyzed through SEM images. Fig. 2 shows SEM images in two different magnifications for (a-b) NiS-α phase and (c-d) NiS-β phase. In Fig. 2(a and b), it is observed that the nanostructured NiS-α particles are well distributed and are in regular multifaceted shaped particles with size of ~40 nm. On the other hand, from Fig. 2(c and d), it is observed that NiS-β particles are agglomerated in nature. The magnified image in Fig. 2(d) clearly shows the agglomeration of two different types of nanostructures-elongated oval-shaped particles. The average length of these particles is ~200 nm and these particles are oriented randomly in different directions.

The morphology, crystallinity, and particle size of synthesized nanostructured NiS were analyzed using HRTEM. Fig. 3(a and b) clearly shows images of multifaceted regular-shaped NiS-α phase nanoparticles with an average size ~50 nm which is correlated with the images obtained from SEM images [Fig. 2(a and b)]. Fig. 3(c) shows the image of lattice fringes from the (101) plane of a thin NiS-α polycrystalline grain of hexagonal crystal structure. On the other hand, Fig. 3(d–f) represent HRTEM images of the NiS-β sample. Similar to the SEM images [Fig. 2(c and d)], HRTEM images in Fig. 3(d and e) show the agglomeration of oval and needle-shaped particles. The average diameter and length of the needles are 100 nm and 20 nm, respectively. Lattice fringes from two different planes of (101) and (110) for thin NiS-β polycrystalline grain of rhombohedral crystal structure were shown in Fig. 3(f). Results are correlated with the interplanar spacing (d-value) in XRD patterns.

Optical properties of nanostructured NiS

Fig. 4(a) and (b) shows the absorption spectra and Tauc-Mott plots of NiS-α and NiS-β, respectively. The bandgap energy of synthesized NiS-α and NiS-β were calculated by the Tauc-Mott equation [30].

$$(\alpha h\nu) = A(h\nu - Eg)^n \quad (2)$$

where α is absorption coefficient, h is Plank's Constant, ν is the frequency of light, A is proportional constant and n value depends upon the type of semiconductors [31]. As the nanostructured NiS sample is direct bandgap material, the calculated bandgap energy for the NiS-α phase is 1.83 eV, whereas, the bandgap energy was decreased to 1.53 eV for the sample NiS-β phase as the absorption band edge was increased to 515 nm. This decrease in bandgap energy for NiS-β may be due

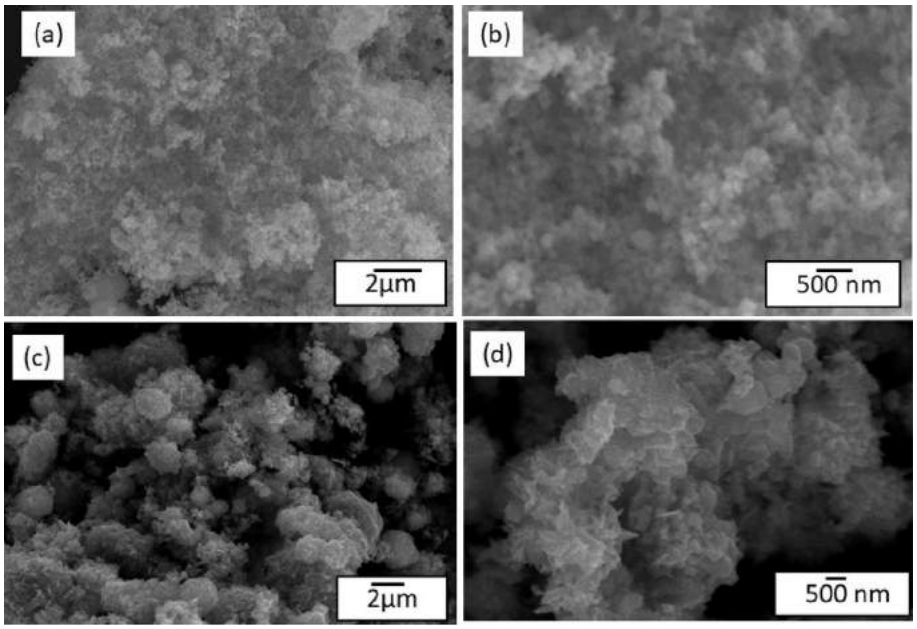

Fig. 2 – SEM images of (a–b) NiS-α and (c–d) NiS-β nanostructures synthesized by hydrothermal method at 200 °C.

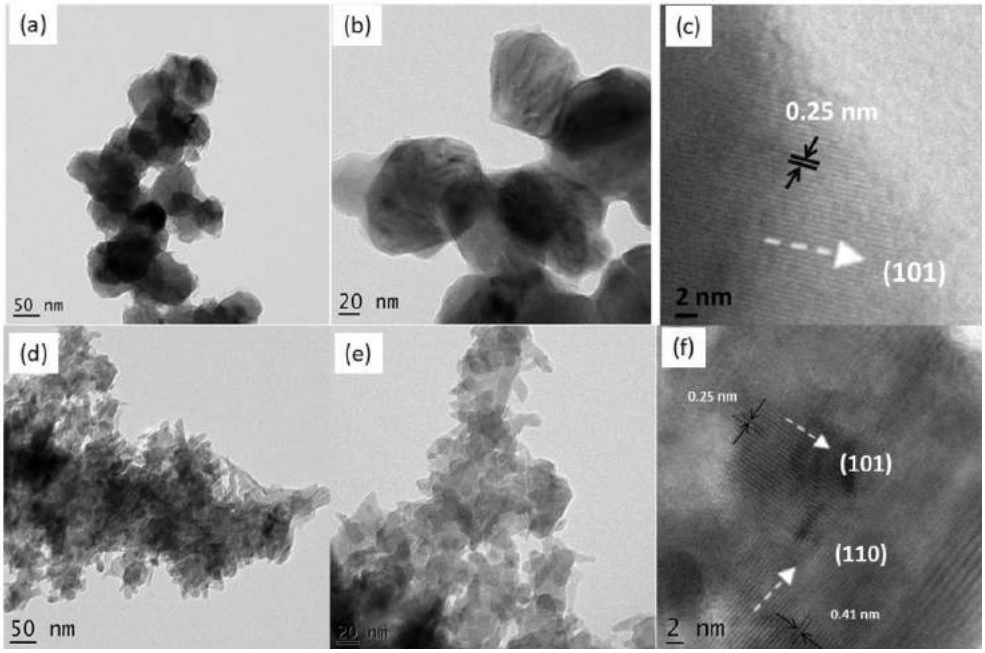

Fig. 3 – HRTEM images of (a–c) NiS-α and (d–f) NiS-β nanostructures synthesized by hydrothermal method at 200 °C.

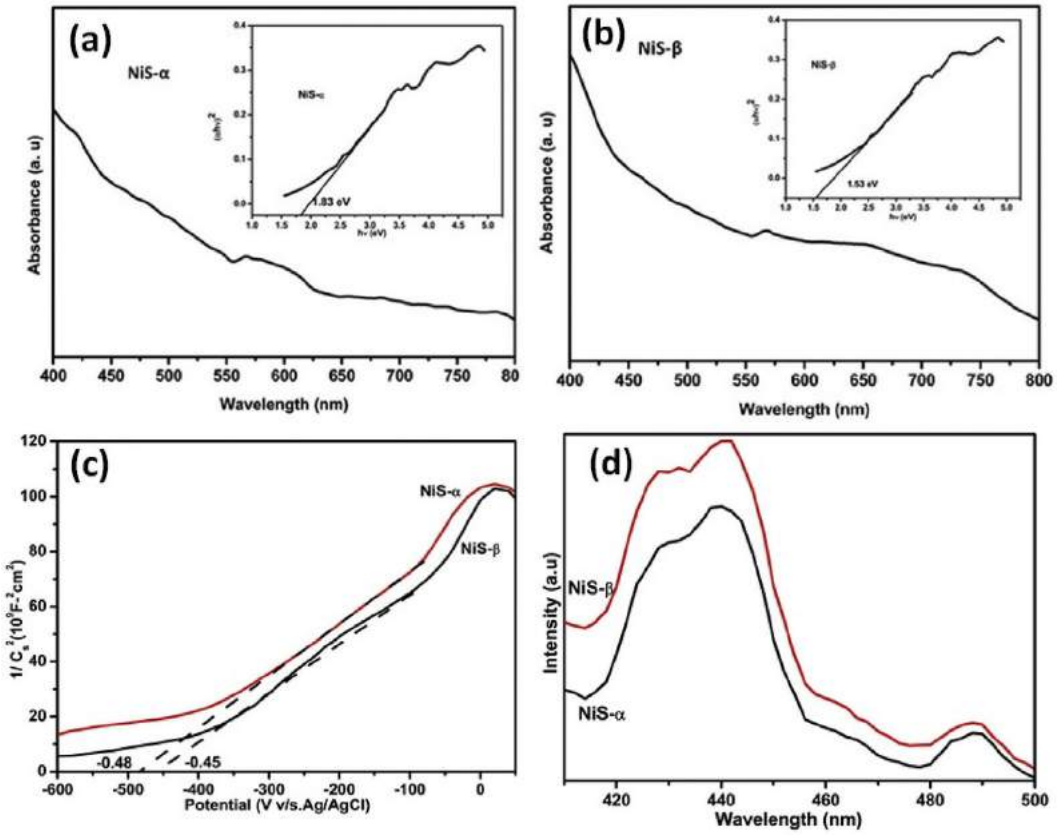

Fig. 4 – (a)–(b) Absorption Spectra and Tauc-Mott plots (insets) (c) Mott-Schottky plots (d) photoluminescence spectra of NiS-α, NiS-β, synthesized by hydrothermal method at 200 °C.

to structural change and/or the nonstoichiometric nature of the sample [19]. This may be correlated with the XPS spectra as shown in Fig. 6. The Mott–Schottky (M–S) analysis was carried out to know the electronic band structure and charge transfer mechanism [32]. The inverse square space charge ($1/Cs^2$) vs. potential shows a positive slope which, indicates the n-type behaviour as shown in Fig. 4(c) [33]. The flat band potential of NiS-α and NiS-β samples were determined by extrapolating the linear portion of the curves to the intercept at the x-axis. The obtained potentials were further converted to reversible hydrogen scale and corresponding flat band potentials were calculated to be 0.13 V,0.16 V (vs. RHE), respectively. The conduction edge position of NiS-α and NiS-β samples were tallied to be −0.17 V, −0.14 (vs. NHE, pH 0) by using the equation, $E_{fb} = E_{Ag/Agcl} + 0.059 \times pH + E^0_{Ag/Agcl}$ (pH = 7, $E^0_{Ag/Agcl} = 0.197$ V) [32,34–36]. The results indicated that, the E_{fb} potential of the NiS-β sample shifts towards a cathodic or negative direction from −0.45 V to −0.48 V (vs. Ag/Agcl) due to more negative surface charge carriers present in the NiS-β sample [36]. Then, the Valance band edge (Evb) was found to be 1.66 V and 1.39 V for NiS-α and NiS-β samples (Evb = Eg-Ecb) [34].

Further, PL spectroscopy was performed to check the charge carrier behaviour of photocatalyst. The PL emission spectra from (a) NiS-α phase and (b) NiS-β phase, shown in Fig. 5(d). The spectra were recorded in the range of 300–500 nm after exciting the samples at 371 nm at room temperature. The emission peaks at 410 nm and 440 nm observed for both the samples were attributed to the different defects states [37]. There were no significant changes in the peak positions of the PL spectra for both samples, whereas, a reduced PL intensity observed in the NiS-α sample may be due to the presence of non-radiative recombination sites as defects. The presence of non-radiative recombination sites enhances the active sites on the photocatalysts which, obviously enhances the hydrogen evolution rate [19]. At ~490 nm wavelength, a broad emission peak of low intensity was observed due to interband transition in both the NiS-α and NiS-β samples band structure [38].

The transient photocurrent and electrochemical impedance spectroscopy experiments were carried out to find out the charge separation and charge carrier behaviour of the synthesized NiS-α and NiS-β samples as shown in Fig. 5(a and b) the NiS-α shows the highest photocurrent (82 μA/cm^2) compared to NiS-β (47 μA/cm^2) which, indicates a higher charge separation rate [39]. The smallest arcs in the EIS spectra in Fig. 5(b) represent the lower charge transfer resistance in NiS-α than NiS-β samples, which is following the photocurrent results of the samples. The lower charge resistance indicates prolonged charge recombination as well as enhanced electron transfer rate [40]. Which are consistent with the photocatalytic activity of the synthesized NiS-α and NiS-β samples.

Fig. 6(a) shows the survey scan of the NiS-α sample which indicates the presence of Ni and S elements on the surface. Fig. 6(b) and (c) show the narrow spectrum of Ni-2p and S-2p, respectively, of the NiS-α sample. The binding energy (E_b) appeared at 161.8 eV and 162.8 eV in the spectrum were attributed to S-$2p^{3/2}$ and S-$2p^{1/2}$ orbitals of S^{2-} [41,42]. The E_b-value at 168.8 eV was corresponded to the surface adsorbed O_2, which may be incorporated at the time of processing the sample [43]. The E_b-values at 855.68 eV and 872.82 eV were attributed to Ni-$2p^{3/2}$ and Ni-$2p^{1/2}$, respectively [39,44]. The XPS spectra of the NiS-α sample confirm the bonding of Ni^{2+} and S^{2-} without any Ni (O) state. Fig. 6(d) and (e) show a similar spectrum of Ni-2p and S-2p, respectively, for the NiS-β sample. The E_b values at 162 and 163.12 eV were represented S-$2p^{3/2}$ and S-$2p^{1/2}$ orbitals of S^{2-}. The E_b values at 855.77 (satellite peak at 860.76 eV) and 873 eV were appeared due to Ni-$2p^{3/2}$ and Ni-$2p^{1/2}$, respectively.

Photocatalytic hydrogen generation of nanostructured NiS

The Photocatalytic H_2 generation activity was carried out for both NiS-α and NiS-β samples using Na_2S and Na_2SO_3 (1:1 mol ratio) as the sacrificial agent. Fig. 7(a) shows that the NiS-α phase sample generated 13.413 mmol $h^{-1}g^{-1}$ of H_2 gas whereas, the NiS-β phase sample generated 12.731 mmol $h^{-1}g^{-1}$ of H_2

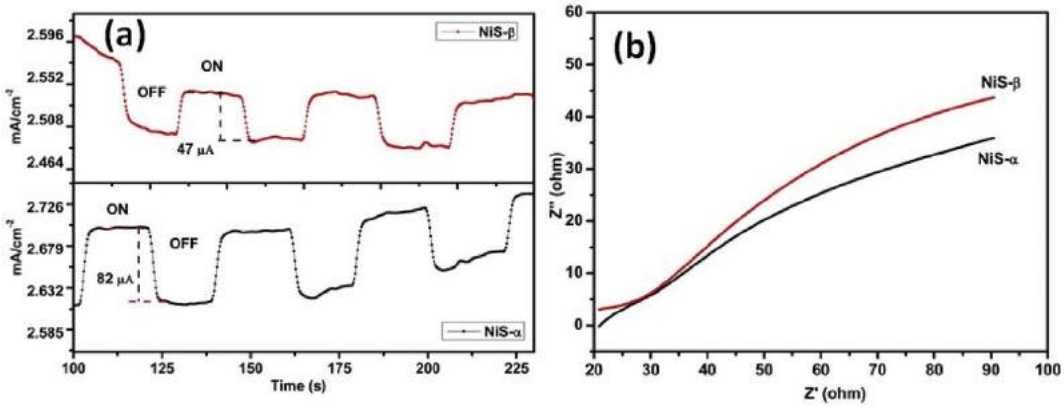

Fig. 5 – (a) Transient photocurrent response and (b) Electrochemical impedance spectra of NiS-α, NiS-β synthesized by hydrothermal method at 200 °C.

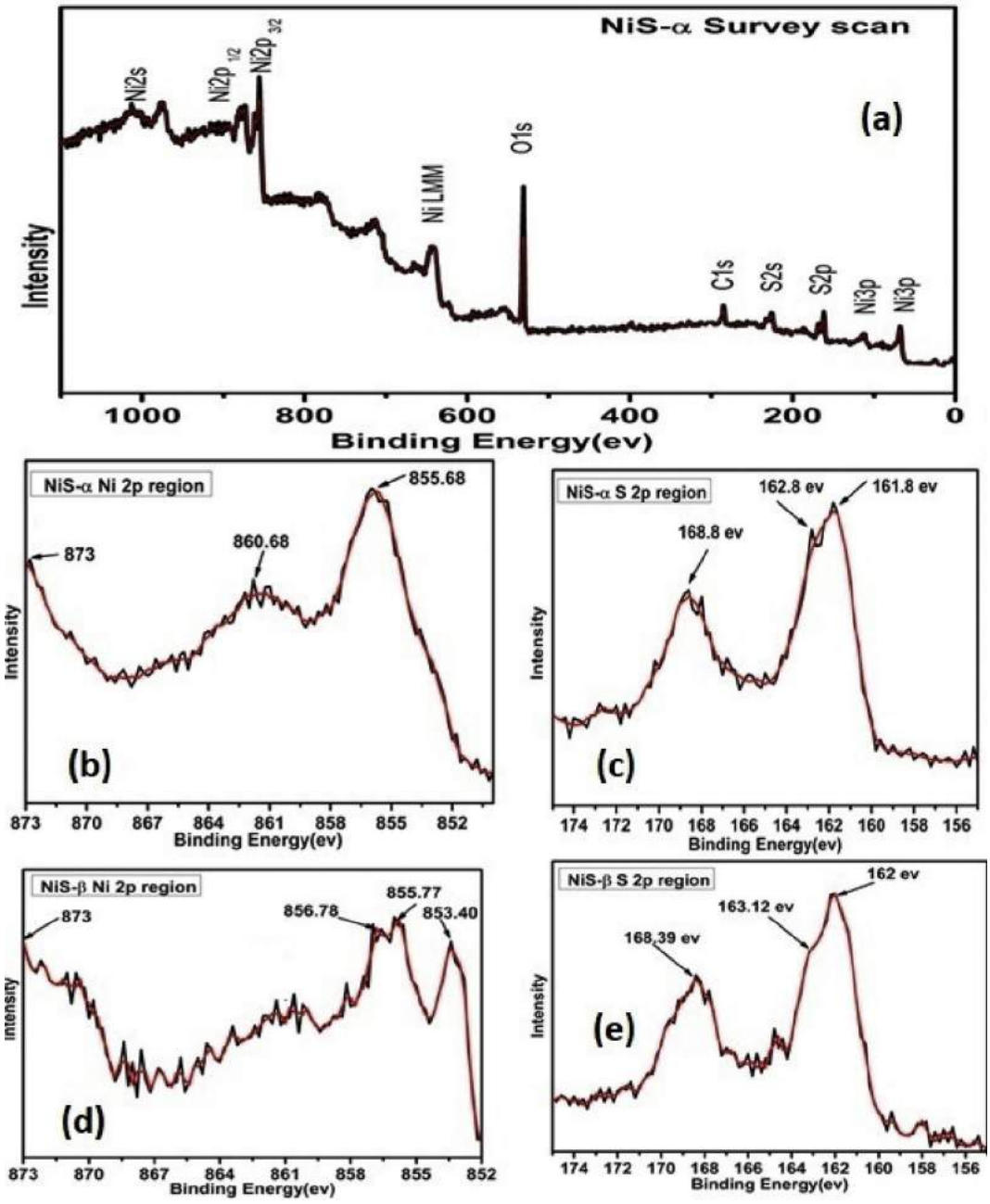

Fig. 6 – XPS Spectrum of NiS-α phase (a) survey scan (b)Ni 2p region (c) S 2p region, and NiS-β phase (d) Ni 2p region, (e) S 2p region.

gas. The H_2 gas production rate is shown in Fig. 7(b). To the best of our knowledge, synthesized NiS shows the highest H_2 generation compared to previously reported binary, ternary composites of metal oxides, sulfides, and carbon nitrides as listed in Table 1).

The NiS-α phase was showing better photocatalytic activity than the NiS-β phase due to the following reasons; (I) The photoabsorption capacity of the NiS-α phase was more than the NiS-β phase, which was confirmed from the UV–Vis Spectra as shown in Fig. 4(a). (II) The long-range and high photoabsorption capacity of the NiS-α phase shows a compatible band edge potential of 1.83 eV for water splitting. These properties influence a greater number of e^- and h^+ charge carriers' generation which are responsible for better photocatalytic water splitting. The presence of nonradiative recombination sites as defects in the NiS-α phase causes charge separation as well as reaction sites for photocatalytic water splitting [19]. This result correlates with the PL spectrum of the NiS-α phase.

The stability of the NiS-α phase was tested for five cycles under the same conditions as carried out at earlier H_2 generation activity over 4 h which is shown in Fig. 7(c). The reaction

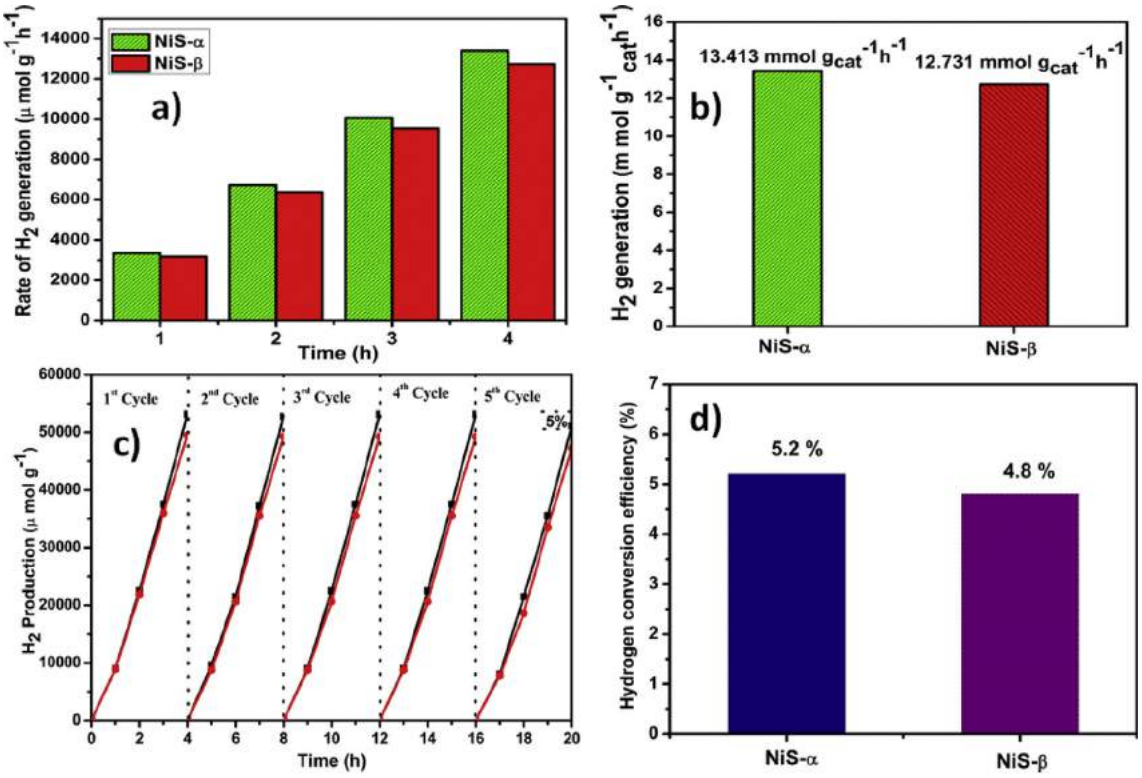

Fig. 7 – (a) Photocatalytic hydrogen generation rate of NiS-α and NiS-β phase samples. (b) Comparison of hydrogen generation activity under 260 W Xe lamp for 4 h for NiS-α and NiS-β samples. (c) Reusability of NiS-α and NiS-β samples for five-run cycles. (d) The hydrogen conversion efficiency of NiS-α and NiS-β samples.

Table 1 – List of recent studies on photocatalytic activities of NiS as co-catalyst under 300 W Xenon lamp with 420 nm Filter in different samples.

Sl. No	Sample name	Co catalyst	H_2 evolution mmol·g^{-1} h^{-1}	Reference & Year
1	NiS/HNb_3O_8	NiS	1.519	[45],2018
2	$NiS/CQDs/ZnIn_2S_4$	NiS	0.568	[46],2019
3	TiO_2/NiS	NiS	0.018	[47],2019
4	$ZnIn_2S_4/In(OH)_3$–NiS	NiS	7.010	[48],2020
5	$NiS/WO_3/g\text{-}C_3N_4$	NiS	2.929	[40],2020
6	MgAl-LDH/NiS	NiS	0.358	[49],2020
7	$NiS/g\text{-}C_3N_4$	NiS	1.346	[50],2020
8	NiS/Zn0.5Cd0.5Se-DETA	NiS	13.89	[51],2020
9	$NiS–CuS–C_3N_4$	NiS	1.6	[52],2020
10	**NiS-α**	-	**13.413**	**This work**

was carried out consecutively for five days and before starting the reaction on each day, the reactor was always purged by N_2 gas. From Fig. 7(c), it was observed that the 5th cycle of H_2 generation is reduced by 5% due to the loss of photocatalyst in recovering process. After five cycles, the recovered samples were characterized by XRD and SEM analysis to elucidate any structural and morphological changes that occurred on the samples as shown in Figs. 8 and 9. XRD and SEM analysis show that the samples were stable by retaining their structure as well as morphology which, represents free from any photo corrosion. Photocatalytic hydrogen conversion efficiency was found to be 5.2% for NiS-α samples with a 13.413 mmol $g^{-1}h^{-1}$ hydrogen evolution rate. the photocatalytic hydrogen conversion efficiency of the NiS-β sample was found to be 4.8% which is significantly lower compared to the NiS-α sample as shown in Fig. 7(d).

A plausible mechanism for H_2 evolution using nanostructured NiS

The direct bandgap of 1.83 eV for nanostructured NiS-α prepared only using ethanol was measured using the Tauc-Mott equation. This low bandgap nanostructured NiS alone as a photocatalyst can separate photogenerated charge carriers.

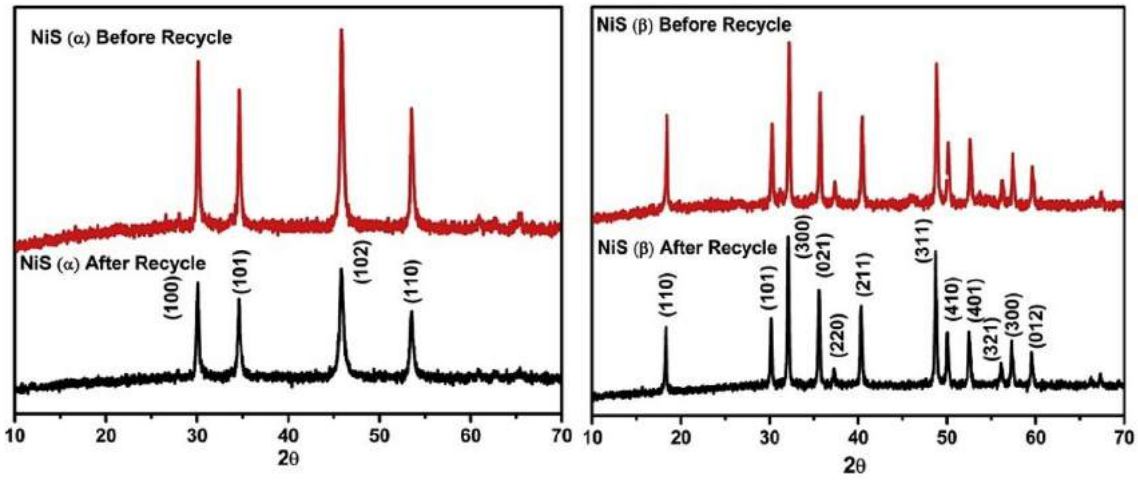

Fig. 8 – XRD patterns of NiS-α and NiS-β phase samples before and after photocatalytic reactions.

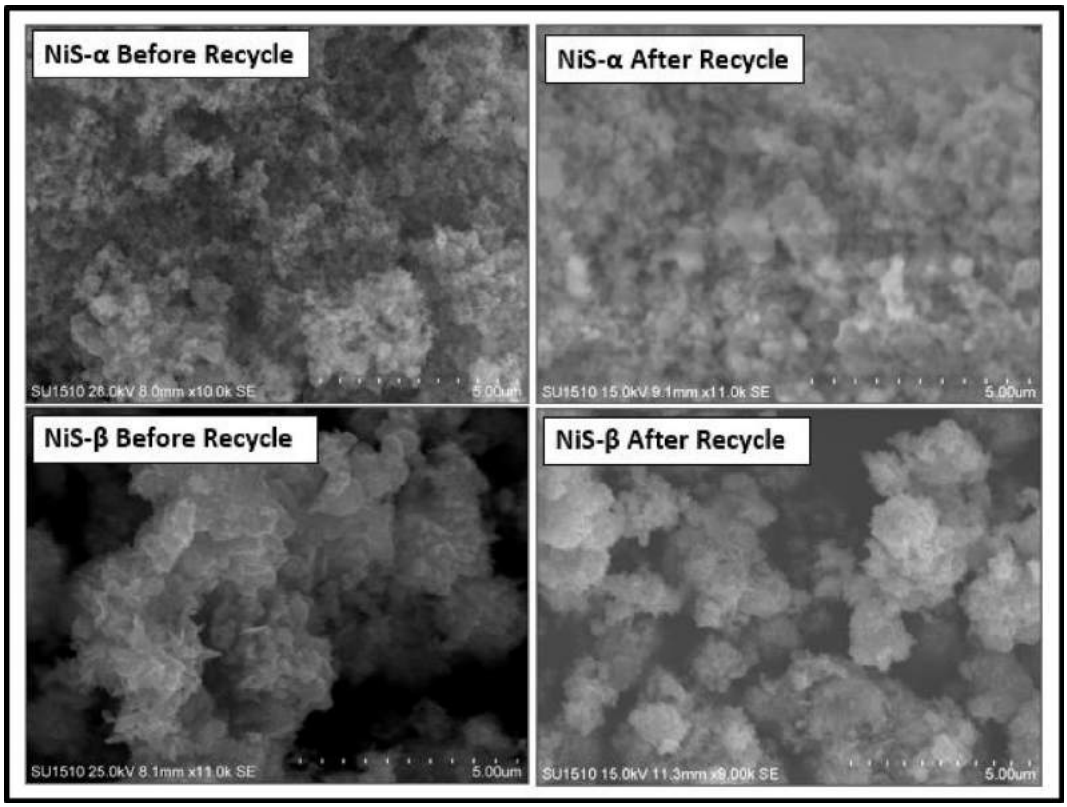

Fig. 9 – SEM Images of NiS-α and NiS-β phase samples before and after photocatalytic reactions.

The conduction band (CB) and valence band (VB) edges were calculated from Milliken electronegativity theory [53] given in Eqs. (3) and (4)

$$E_{VB} = \chi - E^C + 0.5\ E_g \quad (3)$$

$$E_{CB} = E_{VB} - E_g \quad (4)$$

where, E_{VB} and E_{CB} are the valence band and conduction band edge potentials, respectively, χ is the absolute electronegativity of nanostructured NiS (5.23 eV), E^C is the energy of free electrons on the hydrogen scale (4.5 eV), E_g is the bandgap of NiS-α (1.83 eV). The E_{VB} potential of 1.645 eV is calculated using Eq. (3). Similarly, the E_{CB} potential of – 0.185 eV is found from Eq. (4). The band structures and mechanism of hydrogen production are shown schematically in Fig. 10. It is observed that the E_{CB} potential is above the hydrogen evolution potential for splitting water. The protons (H^+) are reduced by the conduction band electrons to generate hydrogen. On the other hand, the holes trapped in the valence band were scavenged by hole scavenger Na_2SO_3 in the solution to produce H^+, and that further reduced by photo-excited electrons to produce hydrogen again.

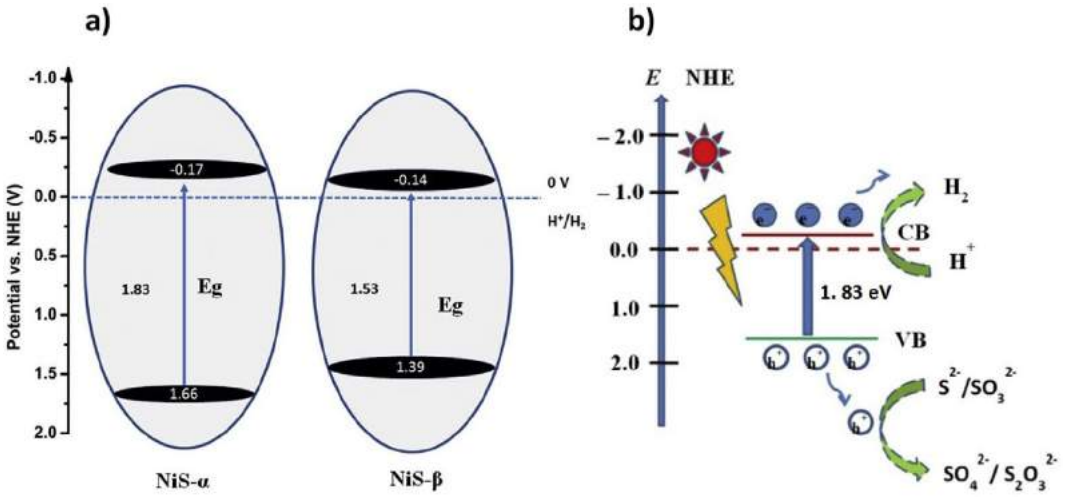

Fig. 10 – a) The band structure of NiS-α and NiS-β. b) probable mechanism of photocatalytic hydrogen evolution using nanostructured NiS- α under UV–Vis light irradiation.

Conclusions

Nanostructured NiS samples synthesized were used as a catalyst for photocatalytic H_2 generation without any cocatalyst. NiS- α and β stable phases were obtained by just varying solvent ratios through the solvothermal method. The NiS-α phase was exhibited a better H_2 generation of 13.413 mmol $h^{-1}g^{-1}$ in 4 h with better stability. As synthesized, NiS- α and β samples would be a better option compared to binary or ternary compounds for photocatalytic H_2 generation. This study opens space for cocatalyst-free photocatalytic hydrogen generation.

Declaration of competing interest

The authors declare that they have no known competing financial interests or personal relationships that could have appeared to influence the work reported in this paper.

Acknowledgment

We acknowledge the support given by the Vision Group of Science and Technology, Department of Information Technology, Biotechnology and Science & Technology, Government of Karnataka, Grant No.: VGST/CESEM/2012-13/GRD-182.

REFERENCES

[1] Kudo A, Miseki Y. Heterogeneous photocatalyst materials for water splitting. Chem Soc Rev 2009;38:253–78. https://doi.org/10.1039/b800489g.
[2] Rosseler O, Shankar MV, Du MK Le, Schmidlin L, Keller N, Keller V. Solar light photocatalytic hydrogen production from water over Pt and Au/TiO_2(anatase/rutile) photocatalysts: influence of noble metal and porogen promotion. J Catal 2010;269:179–90. https://doi.org/10.1016/j.jcat.2009.11.006.
[3] Li Y, Gou H, Lu J, Wang C. A two-step synthesis of $NaTaO_3$ microspheres for photocatalytic water splitting. Int J Hydrogen Energy 2014;39:13481–5. https://doi.org/10.1016/j.ijhydene.2014.03.023.
[4] Navarro RM, Peña MA, Fierro JLG. Hydrogen production reactions from carbon feedstocks: fossil fuels and biomass. Chem Rev 2007;107:3952–91. https://doi.org/10.1021/cr0501994.
[5] Palo DR, Dagle RA, Holladay JD. Methanol steam reforming for hydrogen production. Chem Rev 2007;107:3992–4021. https://doi.org/10.1021/cr050198b.
[6] Rostrup-Nielsen JR, Sehested J, Nørskov JK. Hydrogen and synthesis gas by steam- and $C0_2$ reforming. Adv Catal 2002;47:65–139. https://doi.org/10.1016/s0360-0564(02)47006-x.
[7] Bockris JOM. The origin of ideas on a Hydrogen Economy and its solution to the decay of the environment. Int J Hydrogen Energy 2002;27:731–40. https://doi.org/10.1016/S0360-3199(01)00154-9.
[8] Hafeez HY, Lakhera SK, Bellamkonda S, Rao GR, Shankar MV, Bahnemann DW, et al. Construction of ternary hybrid layered reduced graphene oxide supported g-C_3N_4-TiO_2 nanocomposite and its photocatalytic hydrogen production activity. Int J Hydrogen Energy 2018;43:3892–904. https://doi.org/10.1016/j.ijhydene.2017.09.048.
[9] Mamathakumari M, Praveen Kumar D, Haridoss P, Durgakumari V, Shankar MV. Nanohybrid of titania/carbon nanotubes - nanohorns: A promising photocatalyst for enhanced hydrogen production under solar irradiation. Int J Hydrogen Energy 2015;40:1665–74. https://doi.org/10.1016/j.ijhydene.2014.11.117.
[10] Navarro Yerga RM, Consuelo Álvarez Galván M, del Valle F, Villoria de la Mano JA, Fierro JLG. Water splitting on semiconductor catalysts under visiblelight irradiation. ChemSusChem 2009;2:471–85. https://doi.org/10.1002/cssc.200900018.
[11] Faber MS, Dziedzic R, Lukowski MA, Kaiser NS, Ding Q, Jin S. High-performance electrocatalysis using metallic cobalt pyrite (CoS 2) micro- and nanostructures. J Am Chem Soc 2014;136:10053–61. https://doi.org/10.1021/ja504099w.
[12] Singh N, Jabbour G, Schwingenschlögl U. Optical and photocatalytic properties of two-dimensional MoS_2. Eur Phys J B 2012;85:2–5. https://doi.org/10.1140/epjb/e2012-30449-7.

[13] Faber MS, Lukowski MA, Ding Q, Kaiser NS, Jin S. Earth-abundant metal pyrites (FeS_2, CoS_2, NiS_2, and their alloys) for highly efficient hydrogen evolution and polysulfide reduction electrocatalysis. J Phys Chem C 2014;118:21347–56. https://doi.org/10.1021/jp506288w.
[14] Du P, Eisenberg R. Catalysts made of earth-abundant elements (Co, Ni, Fe) for water splitting: recent progress and future challenges. Energy Environ Sci 2012;5:6012–21. https://doi.org/10.1039/c2ee03250c.
[15] Chen Z, Forman AJ, Jaramillo TF. Bridging the gap between bulk and nanostructured photoelectrodes: the impact of surface states on the electrocatalytic and photoelectrochemical properties of MoS_2. J Phys Chem C 2013;117:9713–22. https://doi.org/10.1021/jp311375k.
[16] Pang H, Wei C, Li X, Li G, Ma Y, Li S, et al. Microwave-assisted synthesis of NiS_2 nanostructures for supercapacitors and cocatalytic enhancing photocatalytic H2 production. Sci Rep 2014;4:1–8. https://doi.org/10.1038/srep03577.
[17] Yin L, Yuan YP, Cao SW, Zhang Z, Xue C. Enhanced visible-light-driven photocatalytic hydrogen generation over g-C_3N_4 through loading the noble metal-free NiS 2 cocatalyst. RSC Adv 2014;4:6127–32. https://doi.org/10.1039/c3ra46362a.
[18] Xu K, Xu H, Feng G, Feng J. Photocatalytic hydrogen evolution performance of NiS cocatalyst modified $LaFeO_3$/g-C_3N_4 heterojunctions. New J Chem 2017;41:14602–9. https://doi.org/10.1039/c7nj03120c.
[19] Bhosale R, Kelkar S, Parte G, Fernandes R, Kothari D, Ogale S. NiS1.97: a new efficient water oxidation catalyst for photoelectrochemical hydrogen generation. ACS Appl Mater Interfaces 2015;7:20053–60. https://doi.org/10.1021/acsami.5b05077.
[20] Karthikeyan R, Navaneethan M, Archana J, Thangaraju D, Arivanandhan M, Hayakawa Y. Shape controlled synthesis of hierarchical nickel sulfide by the hydrothermal method. Dalton Trans 2014;43:17445–52. https://doi.org/10.1039/c4dt02059f.
[21] Idris NH, Rahman MM, Chou SL, Wang JZ, Wexler D, Liu HK. Rapid synthesis of binary α-NiS-β-NiS by microwave autoclave for rechargeable lithium batteries. Electrochim Acta 2011;58:456–62. https://doi.org/10.1016/j.electacta.2011.09.066.
[22] Yang X, Zhou L, Feng A, Tang H, Zhang H, Ding Z, et al. Synthesis of nickel sulfides of different phases for counter electrodes in dye-sensitized solar cells by a solvothermal method with different solvents. J Mater Res 2014;29:935–41. https://doi.org/10.1557/jmr.2014.74.
[23] Karthikeyan R, Thangaraju D, Prakash N, Yasuhiro A, Hayakawa. Single-step synthesis and catalytic activity of structure-controlled nickel sulfide nanoparticles. CrystEngComm 2015;17:5431–9. †,‡,*Manuscript A.
[24] Roffey A, Hollingsworth N, Islam HU, Mercy M, Sankar G, Catlow CRA, et al. Phase control during the synthesis of nickel sulfide nanoparticles from dithiocarbamate precursors. Nanoscale 2016;8:11067–75. https://doi.org/10.1039/c6nr00053c.
[25] Molla A, Sahu M, Hussain S. Synthesis of tunable band gap semiconductor nickel sulphide nanoparticles: rapid and round the clock degradation of organic dyes. Sci Rep 2016;6:1–11. https://doi.org/10.1038/srep26034.
[26] Liu X. Hydrothermal synthesis and characterization of nickel and cobalt sulfides nanocrystallines. Mater Sci Eng B Solid-State Mater Adv Technol 2005;119:19–24. https://doi.org/10.1016/j.mseb.2004.12.051.
[27] Navya Rani M, Murthy M, Shyla Shree N, Ananda S, Yogesh S, Dinesh Rx. Ceram Int 2019;45:25020–6. https://doi.org/10.1016/j.ceramint.2019.04.195.
[28] Li H, Chai L, Wang X, Wu X, Xi G, Liu Y, et al. Hydrothermal growth and morphology modification of β-NiS three-dimensional flowerlike architectures. Cryst Growth Des 2007;7:1918–22. https://doi.org/10.1021/cg0703588.
[29] Roosen AR, Carter WC. Simulations of microstructural evolution: anisotropic growth and coarsening. Phys A Stat Mech Its Appl 1998;261:232–47. https://doi.org/10.1016/S0378-4371(98)00377-X.
[30] Zhao X, Feng J, Liu J, Shi W, Yang G, Wang GC, et al. An efficient, visible-light-driven, hydrogen evolution catalyst NiS/ZnxCd1−xS nanocrystal derived from a metal–organic framework. Angew Chem Int Ed 2018;57:9790–4. https://doi.org/10.1002/anie.201805425.
[31] Khiew PS, Huang NM, Radiman S, Ahmad MS. Synthesis of NiS nanoparticles using a sugar-ester nonionic water-in-oil microemulsion. Mater Lett 2004;58:762–7. https://doi.org/10.1016/j.matlet.2003.07.006.
[32] Vamvasakis I, Papadas IT, Tzanoudakis T, Drivas C, Choulis SA, Kennou S, et al. Visible-light photocatalytic H_2 production activity of β-Ni(OH)2-Modified CdS mesoporous nanoheterojunction networks. ACS Catal 2018;8:8726–38. https://doi.org/10.1021/acscatal.8b01830.
[33] Li X, Yu J, Low J, Fang Y, Xiao J, Chen X. Engineering heterogeneous semiconductors for solar water splitting. J Mater Chem 2015;3:2485–534. https://doi.org/10.1039/c4ta04461d.
[34] Liu Q, Huang J, Tang H, Yu X, Shen J. Construction 0D TiO_2 nanoparticles/2D CoP nanosheets heterojunctions for enhanced photocatalytic H2 evolution activity. J Mater Sci Technol 2020;56:196–205. https://doi.org/10.1016/j.jmst.2020.04.026.
[35] Shen R, Zhang L, Chen X, Jaroniec M, Li N, Li X. Integrating 2D/2D CdS/α-Fe_2O_3 ultrathin bilayer Z-scheme heterojunction with metallic β-NiS nanosheet-based ohmic-junction for efficient photocatalytic H_2 evolution. Appl Catal B Environ 2020;266:118619. https://doi.org/10.1016/j.apcatb.2020.118619.
[36] He Kelin, Xie Jun, Liu Zhao-qing, Li Neng, Chen Xiaobo, Hu Jun, Li Xin. Multi-functional Ni_3C Cocatalyst/g-C3N4 nanoheterojunctions for robust photocatalytic H_2 evolution under visible light kelin. J Mater Chem 2018;8:8726–38. https://doi.org/10.1021/acscatal.8b01830.
[37] Li Y, Wang H, Zhang H, Liu P, Wang Y, Fang W, et al. A {0001} faceted single crystal NiS nanosheet electrocatalyst for dye-sensitised solar cells: sulfur-vacancy induced electrocatalytic activity. Chem Commun 2014;50:5569–71. https://doi.org/10.1039/c4cc01691b.
[38] Akbarzadeh R, Dehghani H, Behnoudnia F. Sodium thiosulfate-assisted synthesis of NiS_2 nanostructure by using nickel(ii)-Salen precursor: optical and magnetic properties. Dalton Trans 2014;43:16745–53. https://doi.org/10.1039/c4dt02232g.
[39] Xiao X, Zheng S, Li X, Zhang G, Guo X, Xue H, et al. Facile synthesis of ultrathin Ni-MOF nanobelts for high-efficiency determination of glucose in human serum. J Mater Chem B 2017;5:5234–9. https://doi.org/10.1039/c7tb00180k.
[40] Zhang L, Hao X, Li Y, Jin Z. Performance of WO_3/g-C_3N_4 heterojunction composite boosting with NiS for photocatalytic hydrogen evolution. Appl Surf Sci 2020;499:143862. https://doi.org/10.1016/j.apsusc.2019.143862.
[41] Zhang L, Huang Y, Zhang Y, Gu H, Fan W, Liu T. Flexible electrospun carbon nanofiber@NiS core/sheath hybrid membranes as binder-free anodes for highly reversible lithium storage. Adv Mater Interfaces 2016;3:1–10. https://doi.org/10.1002/admi.201500467.
[42] Sahoo S, Mondal R, Late DJ, Rout CS. Electrodeposited Nickel Cobalt Manganese based mixed sulfide nanosheets for high performance supercapacitor application. Microporous

Mesoporous Mater 2017;244:101–8. https://doi.org/10.1016/j.micromeso.2017.02.043.

[43] Pu J, Wang T, Wang H, Tong Y, Lu C, Kong W, et al. Direct growth of $NiCo_2S_4$ nanotube arrays on nickel foam as high-performance binder-free electrodes for supercapacitors. Chempluschem 2014;79:577–83. https://doi.org/10.1002/cplu.201300431.

[44] Liu SQ, Wen HR, Ying-Guo, Zhu YW, Fu XZ, Sun R, et al. Amorphous $Ni(OH)_2$ encounter with crystalline CuS in hollow spheres: a mesoporous nano-shelled heterostructure for hydrogen evolution electrocatalysis. Nanomater Energy 2018;44:7–14. https://doi.org/10.1016/j.nanoen.2017.11.063.

[45] Xia Y, Liang S, Wu L, Wang X. Ultrasmall NiS decorated HNb_3O_8 nanosheets as highly efficient photocatalyst for H_2 evolution reaction. Catal Today 2019;330:195–202. https://doi.org/10.1016/j.cattod.2018.03.061.

[46] Wang B, Ding Y, Deng Z, Li Z. Rational design of ternary NiS/CQDs/$ZnIn_2S_4$ nanocomposites as efficient noble-metal-free photocatalyst for hydrogen evolution under visible light. Chinese J Catal 2019;40:335–42. https://doi.org/10.1016/S1872-2067(18)63159-6.

[47] Shi X, Kim S, Fujitsuka M, Majima T. In situ observation of NiS nanoparticles depositing on single TiO_2 mesocrystal for enhanced photocatalytic hydrogIn situ observation of NiS nanoparticles depositing on single TiO_2 mesocrystal for enhanced photocatalytic hydrogen evolution activity en evolu. Appl Catal B Environ 2019;254:594–600. https://doi.org/10.1016/j.apcatb.2019.05.031.

[48] Ye L, Wen Z, Li Z, Huang H. Hierarchical architectured ternary nanostructures photocatalysts with $in(OH)_3$ nanocube on ZnIn 2 S 4/NiS nanosheets for photocatalytic hydrogen evolution. Sol RRL 2020;2000027:2000027. https://doi.org/10.1002/solr.202000027.

[49] Chen J, Wang C, Zhang Y, Guo Z, Luo Y, Mao CJ. Engineering ultrafine NiS cocatalysts as active sites to boost photocatalytic hydrogen production of MgAl layered double hydroxide. Appl Surf Sci 2020;506:144999. https://doi.org/10.1016/j.apsusc.2019.144999.

[50] Lin X, Du S, Li C, Li G, Li Y, Chen F, et al. Consciously constructing the robust NiS/g-C_3N_4 hybrids for enhanced photocatalytic hydrogen evolution. Catal Lett 2020;150:1898–908. https://doi.org/10.1007/s10562-020-03118-x.

[51] Li X, Mei F, Zhang J, Dai K, Liang C. Noble-metal-free NiS decorated organic-inorganic hybrid ZnxCd1−xSe-diethylenetriamine solid solution for hydrogen evolution. Appl Surf Sci 2020;507:145213. https://doi.org/10.1016/j.apsusc.2019.145213.

[52] Xu Y, Du C, Zhou C, Yang S. Ternary noble-metal-free heterostructured NiS–CuS–C_3N_4 with near-infrared response for enhanced photocatalytic hydrogen evolution. Int J Hydrogen Energy 2020;45:4084–94. https://doi.org/10.1016/j.ijhydene.2019.12.040.

[53] Butler MA. Prediction of flatband potentials at semiconductor-electrolyte interfaces from atomic electronegativities. J Electrochem Soc 1978;125:228. https://doi.org/10.1149/1.2131419.

J Mater Sci: Mater Electron

Study on the DC supply and charging effect on the growth of carbon nanotubes and their electrochemical properties

S. Chetana[1,2], Manjunath Shetty[4], Kunal Roy[1], Jagadeesh Babu Sriramoju[3], Guddappa Halligudra[1], Prasanna D. Shivaramu[1], C. S. Ananda Kumar[1], K. G. Basavakumar[5,*], and Dinesh Rangappa[1,*]

[1] Department of Applied Sciences (Nanotechnology), Center for Postgraduate Studies, Visvesvaraya Technological University, Muddenahalli, Chikkaballapur, Karnataka 562101, India
[2] Research and Development Department, Uttaranchal University, Arcadia Grant, Chandanwari, Prem Nagar, Dehradun, Uttarakhand 248007, India
[3] Department of Physics, Malla Reddy Engineering College (A), Secunderabad, Telangana 500100, India
[4] Department of Aeronautical and Automobile Engineering, Manipal Institute of Technology, Manipal Academy of Higher Education (MAHE), Manipal 576104, Karnataka, India
[5] C Byregowda Institute of Technology, Kolar 563101, Karnataka, India

Received: 23 March 2022
Accepted: 21 July 2022

ABSTRACT

Preparation of chirality-defined few-walled CNT (FWCNT) is one of the major challenges in the carbon nanotube (CNT) fields. In the last two decades, significant progress has been made in preparing chirality-controlled synthesis (CCS) of FWCNT through both a direct synthesis approach and a post-synthesis separation approach due to insignificant changes in the tube diameter and twist angle. Hopefully, the present study will encourage further research on the preparation of FWCNT and also utilize key research and practical applications of FWCNTs. In this study, the SEM images of as-grown nanotubes show that applying electric field during the growth process affects the growth of the nanotubes and nanotubes properties can be achieved and altered by changing the supplied electrical DC bias. Raman spectroscopy has been used to analyze the structure and forms of grown FWCNTs samples. The Raman spectrum from all obtained CNTs samples shows the presence of major two peaks, corresponding to the 1350 cm^{-1} and 1570 cm^{-1} bands as well as characteristic Raman bands for metallic or semi-conductive CNTs and their corresponding electrochemical performance also have been performed.

Address correspondence to E-mail: bkumarkg@gmail.com; dinesh.rangappa@vtu.ac.in

https://doi.org/10.1007/s10854-022-08813-6
Published online: 26 August 2022

1 Introduction

Carbon nanotube (CNT)-based devices have been produced consecutively, which implies a bright future for CNT electronics and arouses the desire for direct growth of identical semiconducting CNTs together with the semiconductor industry standard. For various approaches to control the chirality of CNTs, the solution is to deepen the understanding of the growth mechanism in chemical vapor deposition. A physical picture focused on carbon atoms transfer in CVD growth of CNTs has been established for two decades. However, the charge transfer in the growth process can be systematically studied [1].

In the last 15 years, chirality control is considered the biggest challenge in this area of research which is related to the initiation of graphitization of CNTs [2]. When the catalytic substrate bonding reaction is weak, hydrocarbon decomposition occurs at the top of the metal surface having a sharp contact angle with the substrate. The hydrocarbon (C_2H_2) spreads down through the metal and the CNTs precipitate from the bottom, pushing the metal particles from the substrate to the tip of the CNTs, which then precipitate from the bottom, while the upper part of the CNTs continues the C_2H_2 decomposition. This model is known as Tip Growth Model [3]. Subsequent hydrocarbon deposition takes place in the lower peripheral surface of the metal and dissolved carbon diffuses upward, while the CNTs grow with the catalyst particle in their base. Such a mechanism is named the base-growing model [3].

Recent advances in the selective synthesis of SWCNT by epitaxial growth model [4], in this same mechanism same other SWCNTs synthesis by bimetallic catalyst (7–8), and also same other techniques used to control mechanisms magnetic field [5] and electric field to control the chirality of SWCNTs. This model faced main challenges of catalyst size, chirality specific growth [4], and stability of the nanosize SWCNTs growth processes. The key to the various approaches to controlling the chiral index of CNTs is to expand our understanding of the mechanisms of catalytic growth in chemical vapor deposition. We recently reported on CNT's vertical growth by serving magnetic and electric fields [5] but hear difficulty for chirality controlling also we reported the development of SWCNTs by novel electric field controlling mechanism and also by changing the orientation of the substrate concerning the direction of the electric field or by applying an electric current during the growth process, the desired carbon nanotubes are formed.

The generation of charge during the growth formation of CNTs has already been studied and reported preciously. But the variation in applied DC bias and its effects on the resistive behavior during the growth of CNTs and their electrochemical properties have not been studied previously. Herein, we investigated the effect of DC voltage on Fe/Al-catalyzed CNT growth, their properties (including semiconductive, or metallic), and their electrochemical properties also. The additional electrons arise from the generation and transfer of charge during the growth of CNTs, indicating that electrochemical processes take place during the surface reaction step. The field measurement equipment was then subsequently designed to confirm that CNT's CVD growth could be considered a basic battery system. Moreover, it was found that changes in Fermi levels in Fe–Al-based catalysts have a significant effect on the chirality of CNTs when different external electric fields were applied. These discoveries not only provide new insights into the growth of CNTs but also open up new possibilities to control the growth of CNTs using electrochemical methods.

2 Methodology

2.1 Catalyst preparation

Catalyst preparation was carried out by the simple sol–gel method, as reported elsewhere [6]. 0.5 (M) of $Fe(NO_3)_3{\cdot}9H_2O$ was added into 100 ml deionized water and stirred for 30 min to get a clear homogeneous solution followed by the addition of 0.8 (M) of $Al(NO_3)_3{\cdot}9H_2O$. The whole solution mixture was initially stirred at room temperature for 24 h and 12 h more at 90 °C to get dried material. Finally, the dried sample was annealed at 450 °C to obtain a Fe_2O_3/Al_2O_3 catalyst.

2.2 CNTs growth mechanism

The furnace (KejiaFurnace KJ-1600G) temperature was increased to 950 °C to grow CNTs, with a ramp rate of 10 °C/min with an Ar atmosphere containing 5% H_2 with a flow rate of 100 sccm, followed by 100 sccm of C_2H_2 gas was supplied to initiate the growth.

Finally, after growing for 60 min, the sample was cooled down to room temperature gradually. During the CVD process, the growth of CNT may follow the following mechanism as reported elsewhere [4, 6, 7].

2.2.1 Phase 1

Initially, near 500–600 °C, the Fe_2O_3 phase gets changed into unstable α-Fe_2O_3 and then gets reduced to α-Fe_3O_4 by absorbing some moisture content. After phase change, the unstable α-Fe_3O_4 again transformed into α-Fe_2O_3 by reaching the growth temperature at 700 °C with increasing crystallinity.

$$Fe_2O_3 \xrightarrow{500-600^{\circ}C} \alpha - Fe_2O_3 \xrightarrow{H_2O} \alpha - Fe_3O_4 \sim \xrightarrow{700^{\circ}C} \alpha - Fe_2O_3 \quad (1)$$

2.2.2 Phase 2

Above 800 °C, both α-Fe_2O_3 and acetylene start to decompose because of the reduction of α-Fe_2O_3 into its unstable Fe_3O_4 phase by hydrogen atoms (from C_2H_2) (Eq. 2). The reduced unstable Fe_3O_4 instantly transformed into metallic α-Fe according to Eq. (3). Similarly, Al_2O_3 has also been converted into metallic α-Al because of the temperature increment above 900 °C, since Al_2O_3 gets reduced at higher temperature of 900–950 °C as shown in Eq. (4).

$$C_2H_2 \xrightarrow{800^{\circ}C} 2C + 2H \quad (2)$$

$$3\alpha - Fe_2O_3 \xrightarrow{2H,900^{\circ}C} 2\alpha - Fe_3O_4 + H_2O \rightarrow \alpha - Fe \quad (3)$$

$$Al_2O_3 \xrightarrow{950^{\circ}C} \alpha - Al_2O_3 \xrightarrow{H,950^{\circ}C} \alpha - Al \quad (4)$$

2.2.3 Phase 3

In the final phase, decomposed C atoms meltdown and nucleation were initiated after reaching supersaturation level on the surface of α-Fe and α-Al to form Fe–C and Al–C orientation followed by the transformation into their carbides (such as Fe_3C and Al_4C_3), respectively. Consequently, CNTs growth was also confirmed via precipitation according to Eqs. (5–6).

$$\alpha - Fe + C \xrightarrow{800-900^{\circ}C} Fe - C \xrightarrow{2Fe,800-900^{\circ}C} Fe_3C \quad (5)$$

$$\alpha - Al + C > \xrightarrow{900^{\circ}C} Al - C \xrightarrow{3Al/2C,\ >\ 900^{\circ}C} Al_4C_3 \quad (6)$$

Thus, by the combined catalytic effect of Fe_2O_3/Al_2O_3 catalysts, the controlled growth and formation of CNTs can be carried out because Fe_2O_3 helps to catalyze the reaction up to 800 °C and Al_2O_3 helps to catalyze the reaction above 900 °C in a suitable way.

a. In situ power supply installation and measurement

During the growth reaction, in situ measurement of DC electrical bias influence on CNT (double-walled and multi-walled) synthesis has been carried out using a continuous DC power supply (VRR 3002). The growth of double-walled and multi-walled CNTs was examined within the bias range from 0.5 to 3.5 V having 0.5 V of increment. By minimizing environmental noise and connecting Keithley 2401 sourcemeter, charge generation on the surface of CNTs has been observed in terms of electrical resistance at different biases which was quite similar to the traditional emf measurement (Fig. 1).

3 Results and discussion

Figure 2 represents the variation of resistance on CNTs growth and temperature effect on the process. It was observed that initially, the resistance decreased with increasing temperature from room temperature to 950 °C (operating temperature) which was according to the Ohmic rule. Since the substrate surface and oxide catalysts were both semi-conductive, resistance came down with a steeper profile up to an initial 190 min. After reaching the operating temperature (950 °C), 100 sccm Ar/H_2 flow was begun and it was found that the resistance became stable for 20 min. But as the 100 sccm C_2H_2 was added as a feed gas into the reaction chamber at 60 min, the resistance again started to come down slowly and after an hour, a 0.0002 Ω of resistance was dropped. This gradual resistance drop phenomenally attributes to the growth of semi-conductive CNTs.

The diffraction pattern of few-walled CNT is displayed in Fig. 3. The major characteristic peaks of the few-walled CNT samples were observed at 2*θ* (deg.) of 26.25, 53.8, and 57.2° corresponding to the lattice planes (h k l) of (0 0 2), (0 0 4), and (1 0 2), respectively, with a hexagonal arrangement [8]. Peak position at 31.87° corresponding to the Al_4C_3 at (2 0 1) plane [9]. The diffraction peak at 43.1° indicated the presence of α-Fe_2O_3 corresponding to the (0 1 1) plane [10]. The peak at 36° corresponds to the (1 1 1) plane was of γ″-FeN [11]. Diffraction peak at 37.6° was

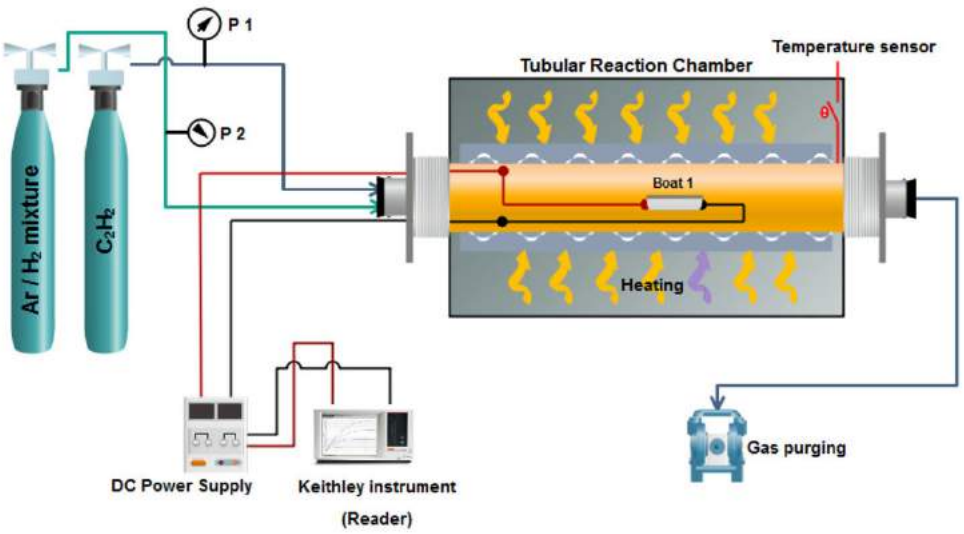

Fig. 1 Schematic of in situ DC supply-assisted chemical vapor deposition technique for the synthesis of CNTs

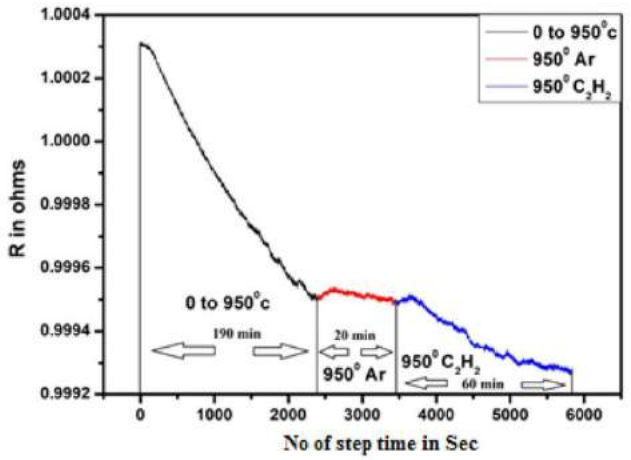

Fig. 2 In situ measurement of DC bias on CNTs growth showing the change of electrical resistance with feed gas

attributed to Fe_3C at (2 2 1) [9]. 44.75° was attributable to the α-Fe and Fe_3C overlapping at (1 1 0) and (2 2 0) planes and 63° was attributed to the appearance of α-Fe at the (2 0 0) [9]. A peak at 66° was corresponding to α-Al_2O_3 at the (4 4 0) plane [12]. In Fig. 4, it has been observed that the major characteristic diffraction peak of as-synthesized CNTs has been shifted slightly by lowering the applied potential which signifies the enhancement of growth of semi-conductive few-walled CNTs at lesser resistance [13].

The FTIR spectral illustration is displayed in Fig. 5. It showed the presence of weak vibration of α-Fe_2O_3 and α-Al_2O_3 phases between 500 and 700 cm^{-1} [14] and also it revealed that the samples are not

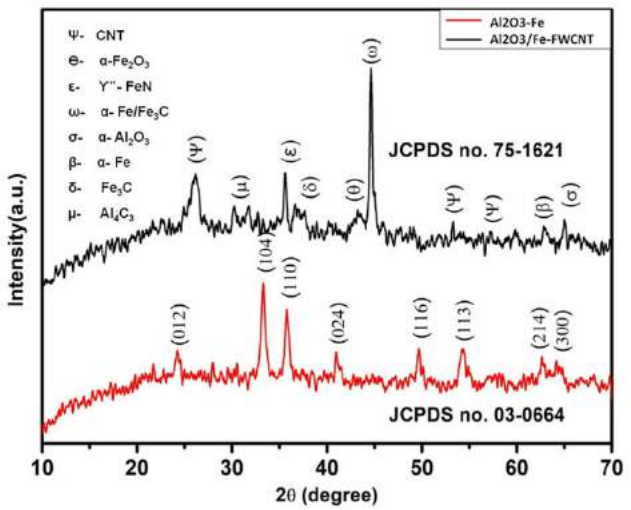

Fig. 3 XRD pattern of CNT, including metal carbides and nitride

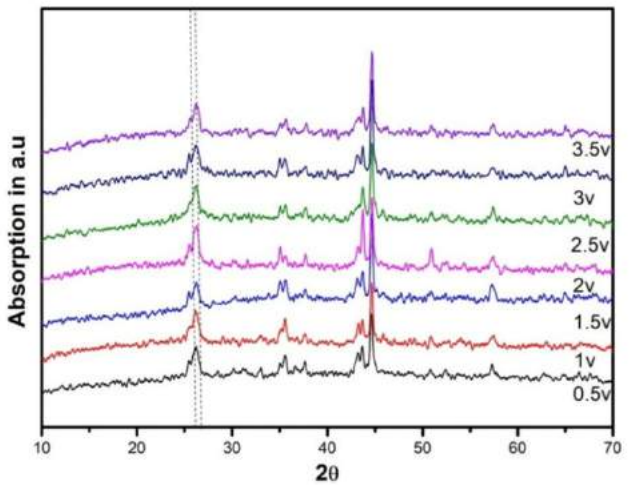

Fig. 4 Diffraction patterns of CNTs synthesized at different applied electrical biases

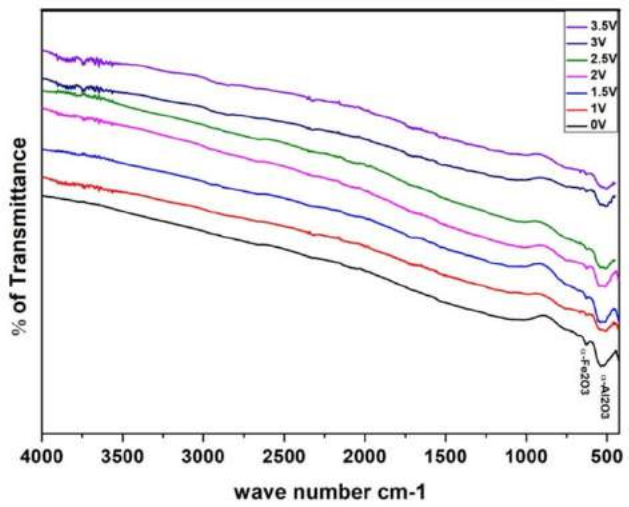

Fig. 5 FTIR spectral profiles of CNTs synthesized at different applied electrical biases

functionalized, i.e., pure CNTs. Some peaks appearance has been observed near 3700 cm^{-1} attributable to the presence of surface hydroxyl groups (–OH) because of the absorption of atmospheric moisture [15].

Figure 6 displays the recorded Raman profiles of FWCNT samples synthesized at different applied electrical biases from 0 to 3.5 V indicating the presence of characteristic peak intensities of RBM (radial breathing mode) (Fig. 6b and d) and G-band. However, RBM is a distinct quantum characteristic of SWCNT because of their radial vibration, and it cannot be overlooked for FWCNTs completely because of their diameters below 2 nm [16]. Moreover, the RBM is strongly correlated with the tube diameter distribution which can be extracted using the following relation [17]:

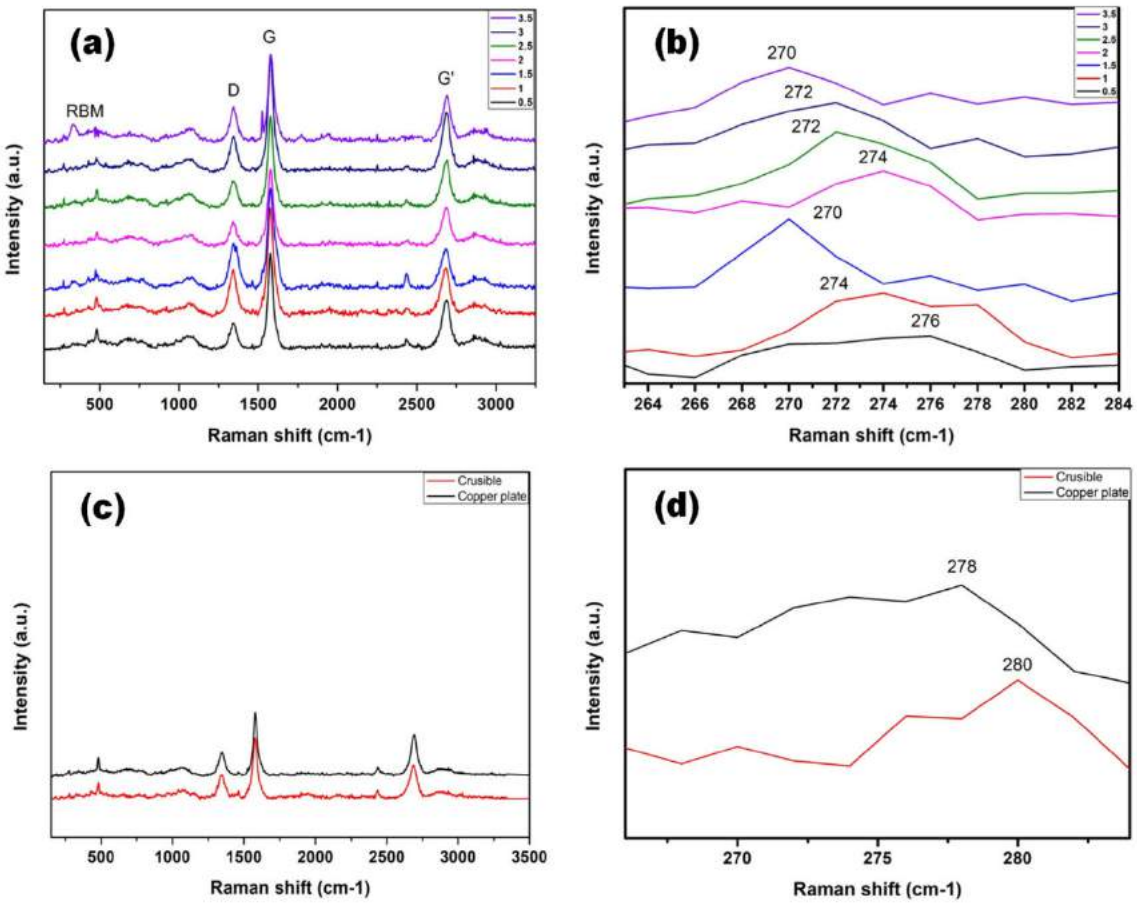

Fig. 6 Raman spectra of FWCNTs **a** synthesized at different applied potentials, **b** RBM regions at different applied potentials, **c** synthesized in alumina crucible and copper plate, respectively, and **d** RBM regions for alumina and copper plate-synthesized FWCNTs

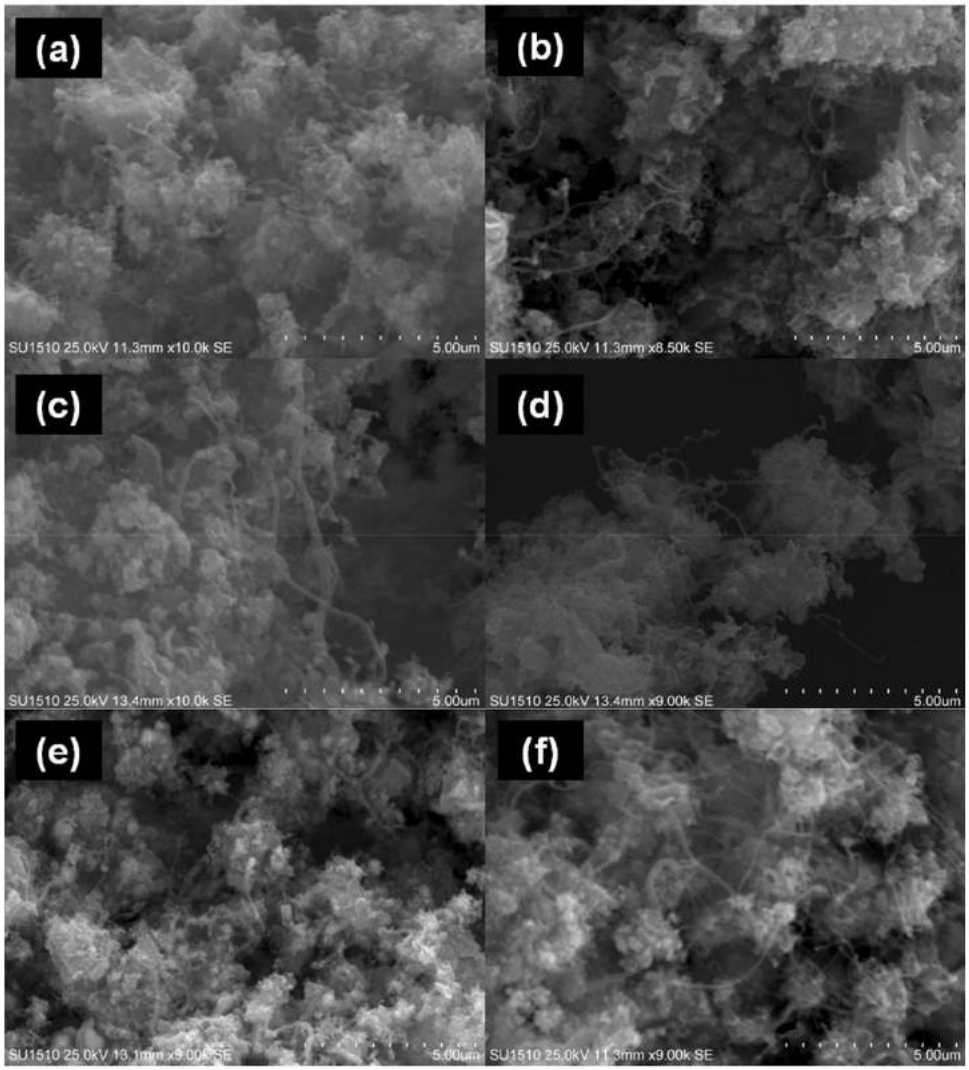

Fig. 7 SEM photographs of entangled CNTs bundles synthesized at **a** 0.5 V, **b** 1.0 V, **c** 1.5 V, **d** 2.0 V, **e** 2.5 V, and **f** 3.0 V

$$f_{\mathrm{RBM}} = \frac{c_1}{d_{\mathrm{CNT}}} + c_2 \tag{7}$$

where f is the frequency of RBM (cm^{-1}), d_{CNT} is the diameter of CNT (nm), and c_1 and c_2 are constants having the value of 235 (cm^{-1} nm) and 9 (cm^{-1}), respectively. From Fig. 6a and c, it can be observed that the D-band and G-band resonated near 1350 cm^{-1} and 1570 cm^{-1} in all the spectrums with the D/G ratio ranging between 0.4 and 0.5 representing the graphitization of the samples with the good agreement [18]. With increasing applied potential, the average diameter of the FWCNTs also increased gradually from 0.87 to 0.9 nm because of the redshift of the RBM region which was estimated using Eq. (7). Most importantly, a strong characteristic peak of the BWF band (Breit–Wigner–Fano) was found at a higher electrical bias (3.5 V) near 1535 cm^{-1} frequency which was attributed to the formation of metallic CNT [19]. Further, the inclusion of G′-bathe nd nandr 2700 cm^{-1} intensified the formation of fewer walls as well as the metallicity of the FWCNTs [16].

Figure 7a–f displays the SEM photographs of as-synthesized CNTs at different applied potentials; hence, densely entangled nanotubes were observed in all the images which were likely to be strongly connected bundles of ropes as shown. Aggregation and compaction of these nanotubes may be enhanced by the strong Van der Waal's interaction and π–π stacking [20, 21].

The electron transfer efficiency, i.e., redox efficiency by exchanging cation–anion between electrolyte and electrode material is mainly analyzed by cyclic voltammetry. In the particular potential window, these redox phenomena get influenced by the

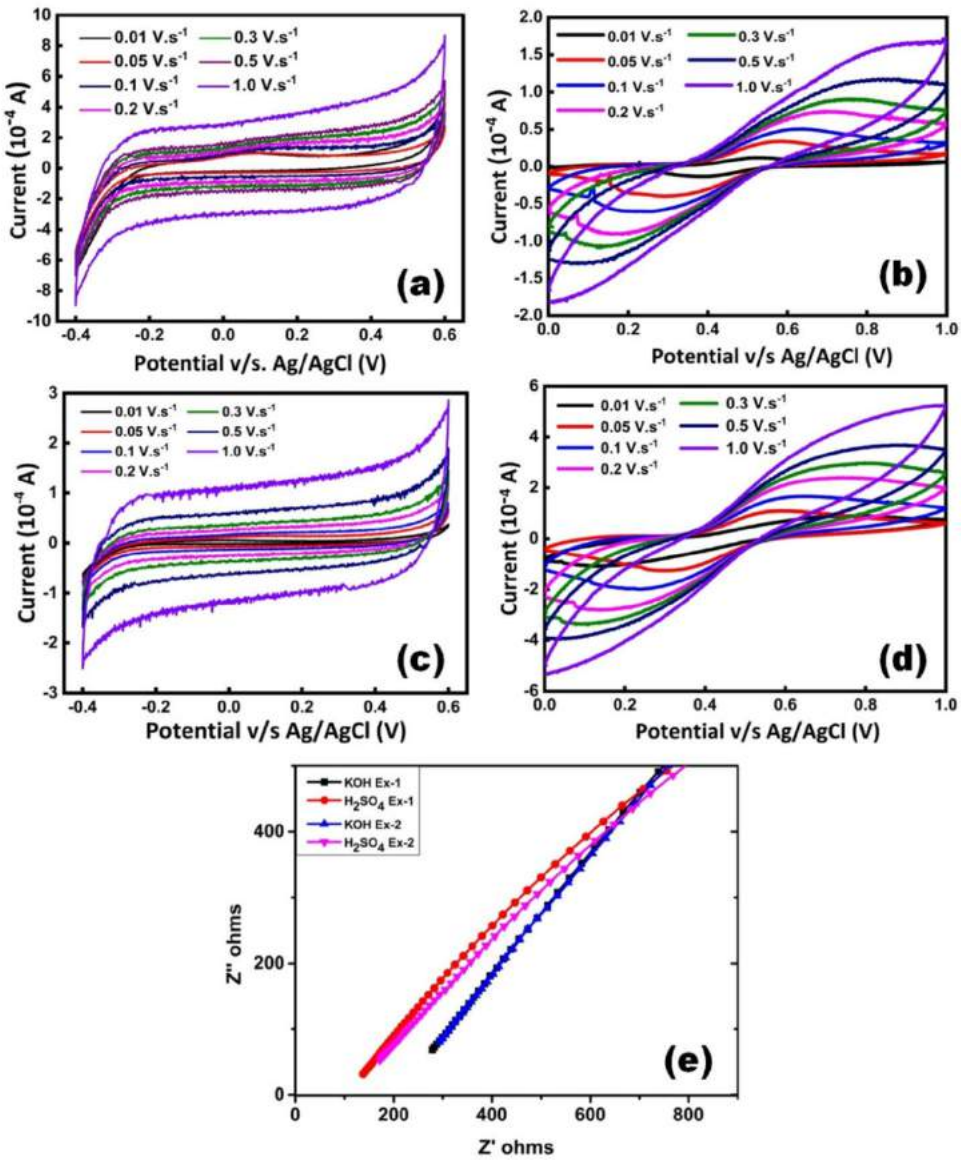

Fig. 8 Cyclic voltammograms of electrode material using **a** CNT synthesized at 0 V and 1(M) KOH electrolyte, **b** CNT synthesized at 0 V and 1(M) H_2SO_4 electrolyte, **c** CNT synthesized at 3.5 V and 1(M) KOH electrolyte, **d** CNT synthesized at 3.5 V and 1(M) H_2SO_4 electrolyte, and **e** electrochemical impedance (Nyquist) plot for CNT-based capacitive electrode at different electrolytes

Table 1 The specific capacitance of CNT-based electrodes at different electrolyte and scan rates

Scan rate (V s^{-1})	Specific capacitance (F g^{-1})			
	CNT-0 V		CNT-3.5 V	
	H_2SO_4	KOH	H_2SO_4	KOH
0.01	67.167	49.473	70.436	18.288
0.05	1.134	1.39	38.144	0.094
0.1	2.099	0.771	5.092	0.142
0.2	1.622	0.627	5.507	0.121
0.3	1.503	0.587	4.798	0.141
0.5	1.018	0.449	3.184	0.12
1	0.579	0.272	1.721	0.098

electron cloud density and based on that energy storage capability of a material can be explored. CV measurements of CNTs synthesized at 0 V and 3.5 V against Ag/AgCl standard electrode and two different electrolyte solutions are (KOH and H_2SO_4) as shown in Fig. 8a–d within the potential window of −0.4 to 6.0 V (for KOH electrolyte) and 0 V to 1.0 V (for H_2SO_4 electrolyte) at the different scan rates from 0.01 to 1.0 V s^{-1}. In both the cases of CNT-0 V and 3.5 V, it can be observed that CV profiles for KOH electrolytes (Fig. 8a and c) are quite smooth compared to H_2SO_4-based electrolytes (Fig. 8b and c). This implies a very less oxidation–reduction reaction happening between electrolyte and CNTs which can be reflected from the specific capacitance value

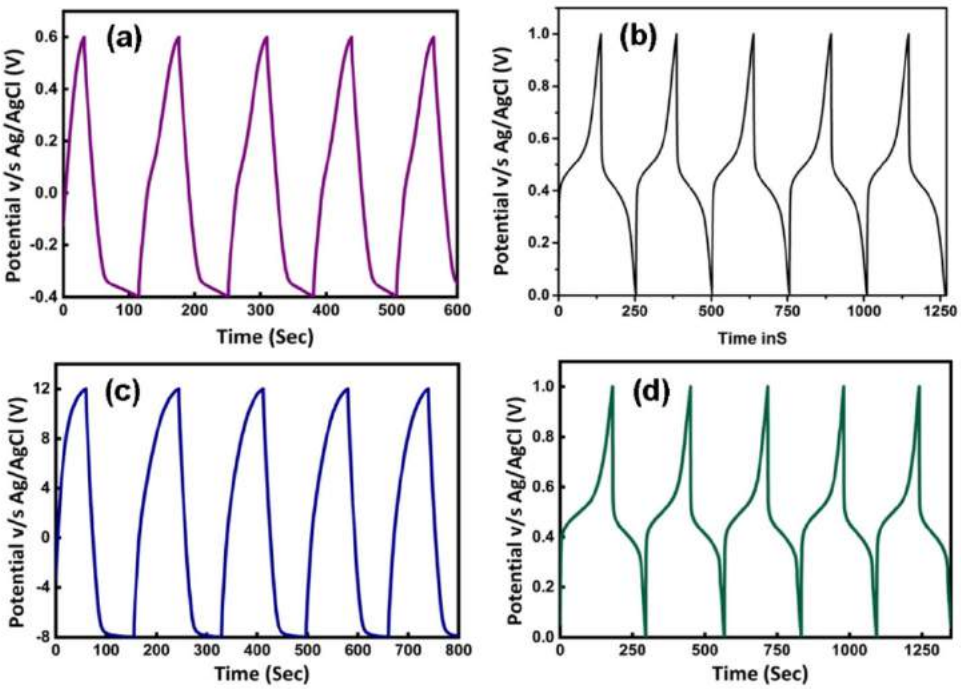

Fig. 9 Charge–discharge profiles of **a** CNT synthesized at 0 V and 1(M) KOH electrolyte, **b** CNT synthesized at 0 V and 1(M) H_2SO_4 electrolyte, **c** CNT synthesized at 3.5 V and 1(M) KOH electrolyte, and **d** CNT synthesized at 3.5 V and 1(M) H_2SO_4 electrolyte

(KOH) in Table 1 also. The reason might be the generation of lesser numbers of electrons and less interaction on the surface of CNTs compare to H_2SO_4. Furthermore, in both the CV profiles of H_2SO_4-based electrolytes, small oxidation–reduction peaks were observed at 0 to 0.2 V and 0.8 to 1.0 V. Impedance profiles of the CNT-electrodes in Fig. 8e confirmed the pseudocapacitive nature of the material which supported the literature report also [22] having strong possibilities of development of the CNTs and CNT-based materials for the application of electrochemical energy storage system. Charge–discharge performances in Fig. 9a–d also supported the previous literature with the good agreement of possible development of pseudocapacitor [22].

4 Conclusion

In this study, we have observed the changes in the CNT growth phase and its physicochemical properties with the variation of applied DC potential from 0.5 to 3.0 V. At higher potential (> 3.0 V), it was found that the metallic CNT was formed and below 3.0 V, semi-conductive CNTs were grown. All the Raman spectral analyses have supported the formation of a FWCNT because of the presence of a very weak RBM region attributing the predictive diameter approx. below 1.5 nm. The electrochemical performance showed the possibility of application of synthesized FWCNTs in semiconductor-based energy storage systems. Thus, the improvement and growth-controlled CNTs synthesis with desired chirality can be deemed in upcoming time with specific findings and new species. The main focus of this study was to investigate the effect of applied DC bias during the growth of CNTs in its semi-conductive and metallic formation and their corresponding effect on the electrochemical energy storage system (supercapacitor), which has been successfully represented. These discoveries not only provide new insights into the growth of CNTs but also open up new possibilities to control the growth of CNTs depending on the requirement for the application in electrochemical energy storage systems.

Acknowledgements

The authors would like to acknowledge the Department of IT, BT and S&T, Government of Karnataka for sponsoring the research work under VGST, CESEM 18.2. The authors also like to acknowledge the Research & Development Cell, Uttaranchal University for carrying out some characterizations.

Author contributions

All authors equivalently contributed to the study, conception, and methodological designing of the present work. Materials preparation, data collection, measurement, and analysis have been carried out by CS, MS, KR, and MM. Draft of the manuscript was written by CS and KR. Modifications, new insertions, commenting, and reviews were done by MS, VG, JSB, GH, PDS, and AKCS. The work has been supervised and monitored by KGB and DR.

Funding

Funding was provided by the Department of Science and Technology for Social Development (Grant No. VGST, CESEM 18.2).

Data availability

All the data generated and analyzed during this study were included in this article during its preparation.

Declarations

Conflict of interest The authors declare no conflict of interest.

References

1. M.P. Kumar, S. Raga, S. Chetana, D. Rangappa, Realization of anomalous microwave absorption characteristics of PVB-PEDOT:PSS with electromagnetic data-driven discovery. IEEE Trans. Dielectr. Electr. Insul (2022). https://doi.org/10.1109/TDEI.2022.3148440
2. E. Plaza, H. Briceño-Fuenmayor, J. Arévalo, R. Atencio, L. Corredor, Electric field effect in the growth of carbon nanotubes. J. Nanopart. Res. (2015). https://doi.org/10.1007/s11051-015-3055-9
3. R.T.K. Baker, M.A. Barber, P.S. Harris, F.S. Feates, R.J. Waite, Nucleation and growth of carbon deposits from the nickel catalyzed decomposition of acetylene. J. Catal. (1972). https://doi.org/10.1016/0021-9517(72)90032-2
4. F. Yang, X. Wang, D. Zhang, J. Yang, D. Luo, Z. Xu, J. Wei, J.Q. Wang, Z. Xu, F. Peng, X. Li, R. Li, Y. Li, M. Li, X. Bai, F. Ding, Y. Li, Chirality-specific growth of single-walled carbon nanotubes on solid alloy catalysts. Nature (2014). https://doi.org/10.1038/nature13434
5. M. Baghgar, Y. Abdi, E. Arzi, Effects of magnetic and electric fields on the growth of carbon nanotubes using plasma enhanced chemical vapor deposition technique. EPJ Appl. Phys. (2009). https://doi.org/10.1051/epjap/2009162
6. D.U. Zuru, Z. Zainal, M.Z. Hussein, A.M. Jaafar, H.N. Lim, S.K. Chang, Theoretical and experimental models for the synthesis of single-walled carbon nanotubes and their electrochemical properties. J. Appl. Electrochem. **48**, 287–304 (2018). https://doi.org/10.1007/S10800-018-1158-6/FIGURES/11
7. B. Liu, W. Ren, L. Gao, S. Li, S. Pei, C. Liu, C. Jiang, H.M. Cheng, Metal-catalyst-free growth of single-walled carbon nanotubes. J. Am. Chem. Soc. (2009). https://doi.org/10.1021/ja8093907
8. B.V. Mohan Kumar, R. Thomas, A. Mathew, G. Mohan Rao, D. Mangalaraj, N. Ponpandian, C. Viswanathan, Effect of catalyst concentration on the synthesis of MWCNT by single step pyrolysis. Adv. Mater. Lett. (2014). https://doi.org/10.5185/amlett.2014.592
9. V. Krisyuk, A.N. Gleizes, L. Aloui, A. Turgambaeva, B. Sarapata, N. Prudhomme, F. Senocq, D. Samélor, A. Zielinska-Lipiec, D. de Caro, C. Vahlas, Chemical vapor deposition of iron, iron carbides, and iron nitride films from amidinate precursors. J. Electrochem. Soc. (2010). https://doi.org/10.1149/1.3430105
10. W.J. Yu, P.X. Hou, L.L. Zhang, F. Li, C. Liu, H.M. Cheng, Preparation and electrochemical property of Fe_2O_3 nanoparticles-filled carbon nanotubes. Chem. Commun. (2010). https://doi.org/10.1039/c0cc02121k
11. L. Dumée, K. Sears, J. Schütz, N. Finn, M. Duke, S. Gray, Influence of the sonication temperature on the debundling kinetics of carbon nanotubes in propan-2-ol. Nanomaterials (2013). https://doi.org/10.3390/nano3010070
12. P.S. Santos, H.S. Santos, S.P. Toledo, Standard transition aluminas. Electron microscopy studies. Mater. Res. (2000). https://doi.org/10.1590/s1516-14392000000400003
13. J. Wang, P. Liu, B. Xia, H. Wei, Y. Wei, Y. Wu, K. Liu, L. Zhang, J. Wang, Q. Li, S. Fan, K. Jiang, Observation of charge generation and transfer during CVD growth of carbon nanotubes. Nano Lett. (2016). https://doi.org/10.1021/acs.nanolett.6b00841
14. P.X. Hou, C. Liu, H.M. Cheng, Purification of carbon nanotubes. Carbon N. Y. (2008). https://doi.org/10.1016/j.carbon.2008.09.009
15. M.H. Razali, A. Ahmad, M.A. Azaman, K.A.M. Amin, Physicochemical properties of carbon nanotubes (CNT's) synthesized at low temperature using Simple hydrothermal method. Int. J. Appl. Chem. **12**, 273–280 (2016)
16. M.S. Dresselhaus, G. Dresselhaus, R. Saito, A. Jorio, Raman spectroscopy of carbon nanotubes. Phys. Rep. (2005). https://doi.org/10.1016/j.physrep.2004.10.006

17. D.Y. Kim, C.M. Yang, Y.S. Park, K.K. Kim, S.Y. Jeong, J.H. Han, Y.H. Lee, Characterization of thin multi-walled carbon nanotubes synthesized by catalytic chemical vapor deposition. Chem. Phys. Lett. (2005). https://doi.org/10.1016/j.cplett.2005.07.064
18. R. Kamalakannan, K. Ganesan, S. Ilango, N. Thirumurugan, V.N. Singh, M. Kamruddin, B.R. Mehta, A.K. Tyagi, The role of structural defects on the transport properties of a few-walled carbon nanotube networks. Appl. Phys. Lett. (2011). https://doi.org/10.1063/1.3583583
19. S.M. Bose, S. Gayen, S.N. Behera, Theory of the tangential G-band feature in the Raman spectra of metallic carbon nanotubes. Phys. Rev. B (2005). https://doi.org/10.1103/PhysRevB.72.153402
20. N. Saifuddin, A.Z. Raziah, A.R. Junizah, Carbon nanotubes: a review on structure and their interaction with proteins. J. Chem. (2013). https://doi.org/10.1155/2013/676815
21. D.A. Britz, A.N. Khlobystov, Noncovalent interactions of molecules with single walled carbon nanotubes. Chem. Soc. Rev. (2006). https://doi.org/10.1039/b507451g
22. C. Zhong, Y. Deng, W. Hu, J. Qiao, L. Zhang, J. Zhang, A review of electrolyte materials and compositions for electrochemical supercapacitors. Chem. Soc. Rev. (2015). https://doi.org/10.1039/c5cs00303b

Molecular Crystals and Liquid Crystals

ISSN: (Print) (Online) Journal homepage: https://www.tandfonline.com/loi/gmcl20

Rheological investigations on cholesterol derivative mesogens

Bindu Madhavi A., Sreehari Sastry S., Umadevi C. & Soma Sundar L.N.V.H.

To cite this article: Bindu Madhavi A., Sreehari Sastry S., Umadevi C. & Soma Sundar L.N.V.H. (2022) Rheological investigations on cholesterol derivative mesogens, Molecular Crystals and Liquid Crystals, 745:1, 16-25, DOI: 10.1080/15421406.2022.2069911

To link to this article: https://doi.org/10.1080/15421406.2022.2069911

MOLECULAR CRYSTALS AND LIQUID CRYSTALS
2022, VOL. 745, NO. 1, 16–25
https://doi.org/10.1080/15421406.2022.2069911

Taylor & Francis
Taylor & Francis Group

Rheological investigations on cholesterol derivative mesogens

Bindu Madhavi A.[a], Sreehari Sastry S.[b], Umadevi C.[c], and Soma Sundar L.N.V.H.[d]

[a]Freshmen Engineering Department, Potti Sriramulu Chalavadi Mallikarjuna Rao College of Engineering and Technology, Vijayawada, Andhra Pradesh, India; [b]Department of Physics, Acharya Nagarjuna University, Nagarjunanagar, Andhra Pradesh, India; [c]Department of Physics, SPW Degree College, Tirupati, Andhra Pradesh, India and [d]Department of Humanities and Science, Malla Reddy Engineering College (A), Secunderabad, Telangana, India

ABSTRACT

The rheological investigations on cholesteryl bromide (CB) and cholesteryl 2-(ethoxy-ethoxy) ethyl carbonate (CEEEC) were carried out. The viscoelastic properties of both mesogens are strongly temperature dependent. In CB, the temperature scans on moduli discovered an abrupt change which is an indication of Smectic phase. In frequency sweep, the CEEEC is characterized by a prevalent viscous behavior while for CB a cross-over of moduli with dominating storage modulus. A shear thinning followed by Newtonian flow is found in CB and Newtonian flowin CEEEC. This study infers the usefulness as lubricants and additive in tribology.

KEYWORDS

Lubrication; mesogens; non-Newtonian behavior; shear thinning; viscoelastic

1. Introduction

The rheological behavior of liquid crystals has been the center of attention in many engineering applications such as lubrication. Liquid crystals (LCs) are one of the delicate and beautiful states of matter. Liquid crystals are also called mesogens as they maintain some of the structure characteristics during flow. The organic compounds with elongated molecules exhibit the cholesteric phase. Cholesteric mesophase is found in derivatives of cholesterol but not in cholesterol (cholest-5-en-3β-ol) itself [1]. The cholesterol conjugates have much scientific interest in the field of materials science on account of their unique self-assembling property, which can be driven by an external stimulus. Cholesterol-based mesogens have a great interest for their intrinsic mechanical, electrical or optical, biological and chemical properties [2–8]. LCs is a recent addition to the materials library used in 4D additive manufacturing [9].

Rheology is the study of mechanical properties under different deformations of complex bodies that appear over a range of applied shear [10]. Several rheological tests like steady and oscillatory tests were performed on complex materials like mud samples, drilling fluids, surfactants, colloids, *etc.*, in order to analyze the rheological fingerprint of the material [11–13]. The very nature of liquid crystals invites the development and correlation of rheological properties. Liquid crystals may flow as

CONTACT S. Sreehari Sastry sreeharisastry@yahoo.com Department of Physics, Acharya Nagarjuna University, Nagarjunanagar, Andhra Pradesh, India.

(anisotropic) liquids, and present a highly complex rheological behavior. The rheological characterization of cholesteric materials is the subject of continuing work. The rheological behavior of LCs is catching the attention of researchers due to their strange physical properties and technological importance of some materials based on them. Rheological and tribological properties were investigated for thermotropic cholesterics, lamellar LCs [14].

When LCs are introduced as additives then they are able to optimize the tribological properties oils and greases [15]. The application of some cholesterol esters as additive positively affects the antifriction properties of mineral industrial oil [16]. Liquid crystals have good load-bearing properties and can reduce friction, wear [17]. Liquid crystalline compounds of the rod-like structures were tested as lubricating agents [18]. Rheological properties of cholesteric esters were studied to check their suitability as lubricant additives [19] and are found to be efficient as oil additives [20]. Consistency and viscosity are the important factors that affect the efficiency of LCs in lubrication [21].

It is of great practical importance to achieve the rheological characterization of liquid crystals for the apprehension of their tribological properties. As part of our continuing effort for a better understanding of the rheological behavior of liquid crystals and their role in tribology, two derivatives of cholesterol were paid attention. The aim of this work is to investigate the rheological behavior of two cholesterol derivative mesogens. Furthermore, the study highlights the importance and influence of rheological behavior on the tribological application.

2. Materials and methods

The two cholesterol derivatives viz., cholesteryl bromide (CB), cholesteryl 2-(ethoxyethoxy) ethyl carbonate (CEEEC) are monotropic cholesterogens belonging to the cholestarene groups of steroids and are obtained from Eastman Kodak Co., USA.

An optical polarizing microscope equipped with crossed polarizers and a hot-stage is used to examine transition temperatures, mesomorphic textures. The rheological measurements were made with ARG2 rheometer from TA Instruments in both steady-shear and oscillation mode. The magnetic bearing and wide gap induction motor technology associated with the rheometer provides a low torque performance of the order of $\mathrm{nN} \times \mathrm{m}$. The maximum permitted deviation in temperature for Peltier plate is $0.1^{\circ}\mathrm{C}$. A 40 mm parallel plate sensor was used. The sample is loaded after setting zero gaps at test temperatures. After loading, the mesogens were maintained at their clearing temperature for few minutes to minimize the thermal history fluctuations. All testes were repeated to ensure the reproducibility of data. The rheology advantage software enables data recording and analysis. Initially controlled stress measurements were performed. Later on, time sweep, temperature sweep (with heating rate $0.2^{\circ}\mathrm{C/min}$), frequency sweep tests are done to achieve the least disturbance of the internal structures. Subsequently steady-shear measurements were performed in which stress was varied.

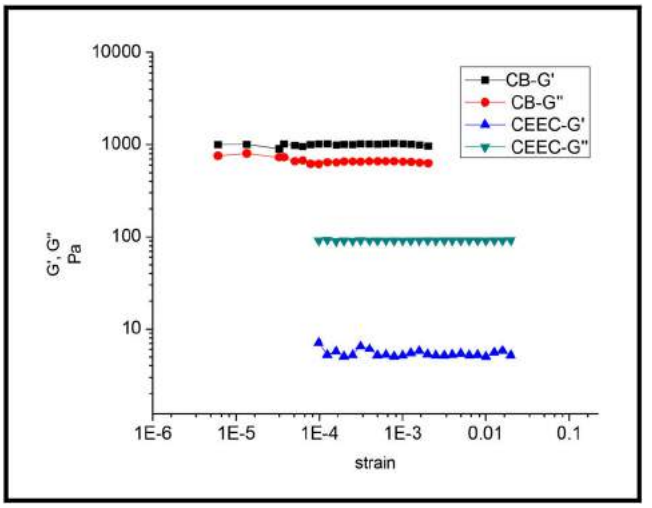

Figure 1. Determination of the linear regime.

3. Results

3.1. Thermotropic mesomorphism

Traditionally, the rheology of thermptropic liquid crystals has been studied by first investigating the phase transition temperatures. The cholesteric phases and transition temperatures were obtained from a polarizing optical microscope. The derivative CEEEC exhibits the cholesteric mesophase between 15–32 °C with a layer of the Grandjean plane cholesteric structures. Cholesteric phase for CB has occurred between 100 and 110°C. The phase transition temperatures are in acceptable concurrence with literature values [22].

3.2. Viscoelastic properties

The most important physical parameters for the use of liquid crystals in Tribology are their mesomophic range and rheological behavior. All the measurements were performed strictly within the cholesteric mesomorphic temperatures. The linear viscoelastic results are obtained by small amplitude oscillatory shear at a constant frequency of 6.283 rad/s. The evolution of storage modulus and loss modulus as function of the applied strain is shown in Figure 1.

CB is exhibiting solid-like behavior and CEEEC is liquid-like to the strain applied. The response is similar for both the moduli and linear up to a definite value known as the limit of strain amplitude (γ_c). A further increase above this level causes a sharp breakdown of the micro structure. The two derivatives showed linear viscoelastic behavior at small strain amplitude. This limit of strain amplitude or the onset of non-linearity is lower for derivative CB. With the onset of non-linearity, the flow history would perturb the structural configuration of the mesogens. Both the moduli of CB are exhibiting a higher value than CEEEC. Nevertheless, for both the derivatives the range of linear viscoelastic limit is almost short and is due to the rod shape of molecules and the cholesteric structure. Thus, the critical percentage of strain value is useful in observing the

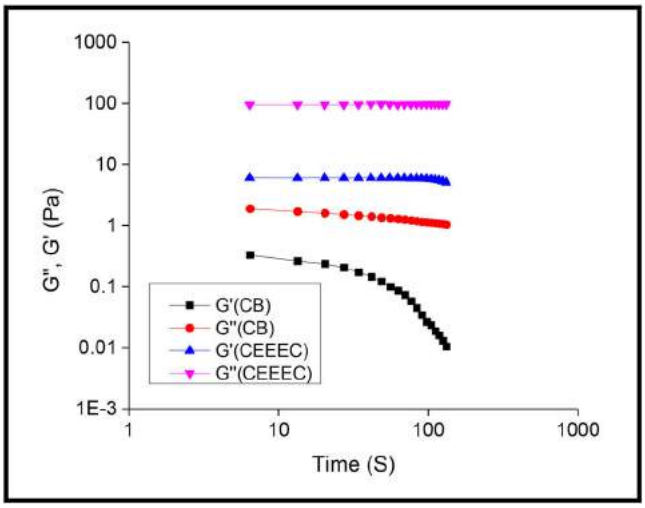

Figure 2. Time sweep measurement.

structural reorganization and relaxation times ($\sim 1/\omega_c$) at different frequencies. When the applied strain exceeds the critical strain amplitude then the cholesteric phase shows a marked rheotropy ever since the change in superstructure of the cholesteric phase.

The second test to perform before any other test is dynamic time sweep in LVR limit. The thermal stability of the derivatives is checked by keeping frequency fixed at 6.283 rad/s. Such time sweeps on LCs are important for polymer processing and other industrial applications. The results summarized in Figure 2 suggest that CEEEC had no viscoelastic property and formed liquid-like situation in testing time (5 min). Such a behavior was understood as a weak cohesion between liquid layers [23]. Langelaan and Gotsis [24] hypothesized such a result as the stability of the sample and substantiate that no re-crystallization or chemical degradation occurs. And for CB, G'' is steady with time as it corresponds to its relaxed state.

Temperature is a key parameter influencing LC structure and rheological behavior. We know that temperature can largely influence not only the movement of molecules but the viscoelastic properties also. Temperature-dependent dynamic viscoelastic measurements were carried out at frequency 6.238 rad/s and presented in Figure 3.

The temperature scans on G' and G'' of CB discovered an abrupt change in moduli at temperature range 100 °C to 100.2°C. This seems to suggest a phase change or existence of sub phase if any. Vani and Vijayan [25] have proposed a latent Smectic C or twisted smectic C in CB due to its layered arrangement at this temperature. This observation was also supported by dominant solid behavior of CB as the Smectic phase of a pure compound is rather solid-like. Both moduli are characterized by the same type of mechanical spectrum. A storage modulus reduction leads to less resistant structures in the solid phase. No significant change in the storage modulus of CEEEC with temperature is noticed, whereas the loss modulus G" decreased exponentially with time but still dominate over the elastic modulus demonstrating a weakly structured system.

The dynamic moduli measured in a frequency sweep at fixed temperature are able to reveal the microstructure existing in the system. Normally this test is done for

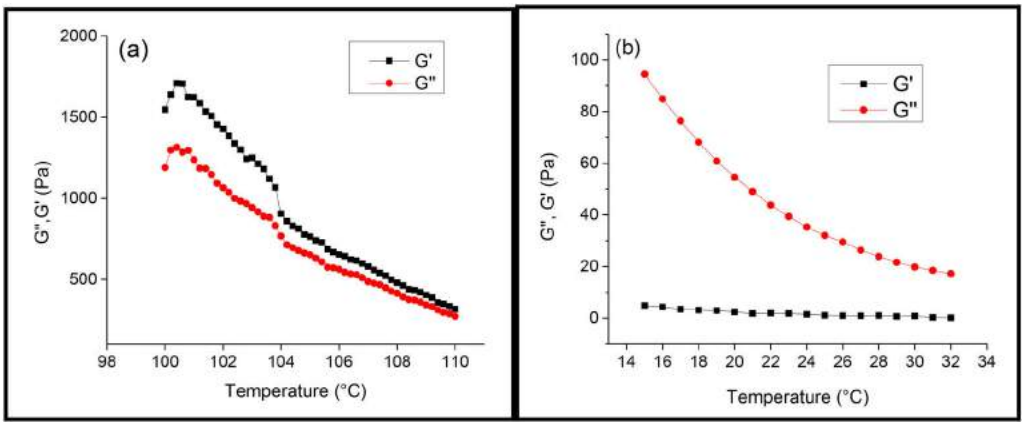

Figure 3. Temperature dependence of viscoelastic parameters. (A) Cholesteryl bromide and (B) cholesteryl 2-(ethoxy-ethoxy) ethyl carbonate.

contemplating the mechanical properties of the materials without upsetting the structure [10]. The relaxation behavior of shear deformations is shown in Figure 4.

The values of the storage modulus G' and the loss modulus G'' have different behaviors as the frequency increases. From the figures, it is depicted that the viscoelastic behavior was not qualitatively similar for the two derivatives. The molecular orientation in LCs can greatly influence the viscoelastic nature. In Figure 4 (A) for CB, in the beginning, G' has a lower value than G''. Hence the response is viscous-like. But with increasing frequency, both G' and G'' started increasing, and eventually at a frequency $\omega_c = 0.31$ rad/s (G' $= G'' = 645$ Pa) G' is equal to G''. At this cross-over frequency the derivative is no longer viscous but rather exhibits a viscoelastic behavior. After this cross-over frequency, the elastic modulus overtakes loss modulus and reached a rubbery plateau regime. Indeed, G' tends to level off to a rubber plateau value, demonstrating the elasticity of solid-like material. Qualitatively similar data have been observed in lyotropic solutions, thermotropic main-chain liquid crystal polymers [26], and in other cholesteric liquid crystals [27].

In the literature, the leveling off of the storage modulus is generally linked to such macrostructure that could enhance the material's elasticity. The reciprocal of the cross-over frequency here is 3.22 s which is numerically equal to characteristic longest relaxation time of CB. The loss modulus, storage modulus curves for CEEEC display a clear upward concavity over the applied frequencies. The G' and G'' profiles evidence the viscous behavior of CEEEC ($G'' > G'$) at all frequencies. In general, the cholesteric liquid crystal becomes liquid-like when they are subjected to many cycles of strain.

3.3. Flow properties

Viscosity is another important thermo-physical property which is a measure of internal friction or ability to flow, and largely determines suitability for any particular application. The Viscosities of the two derivatives are measured over a given temperature range with shear rate fixed at 50 1/s and presented in Figure 5.

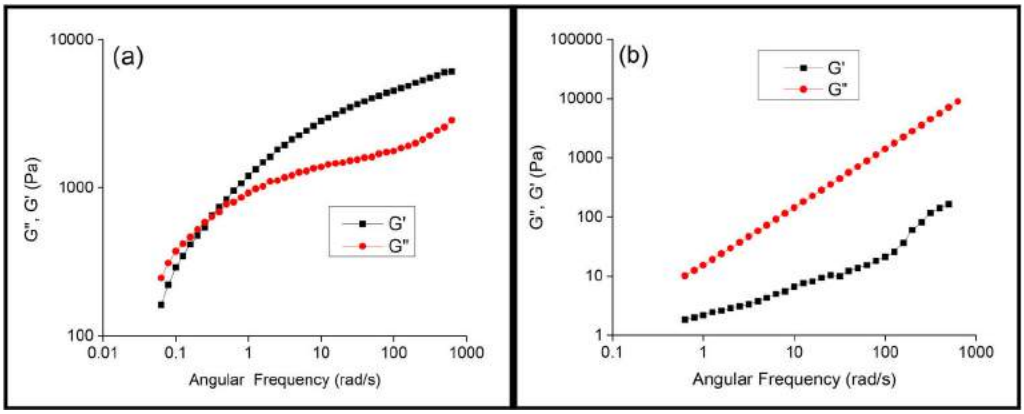

Figure 4. Frequency dependent dynamic viscoelastic curves. (A) Cholesteryl bromide and (B) cholesteryl 2-(ethoxy-ethoxy) ethyl carbonate.

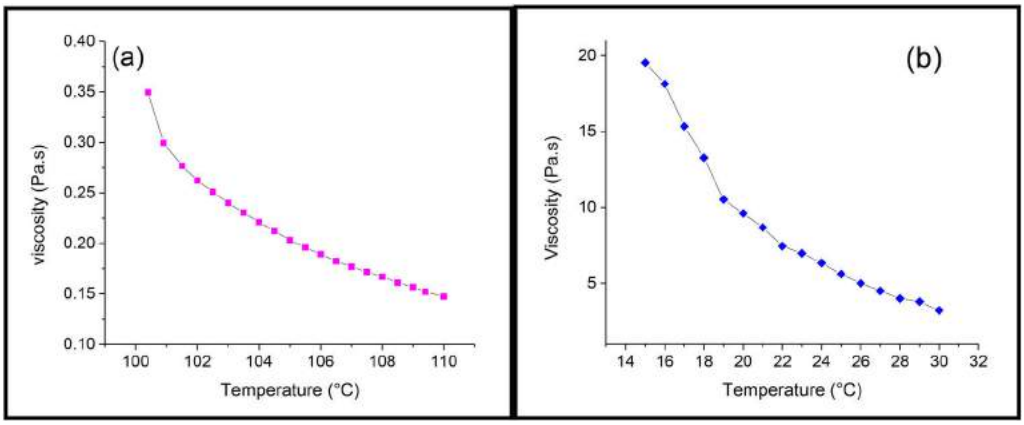

Figure 5. Dynamic temperature sweeps at Shear rate 50/s. (A) Cholesteryl bromide and (B) cholesteryl 2-(ethoxy-ethoxy) ethyl carbonate.

Both the derivatives have shown a decrease in viscosity, which is common in fluids. Generally, an anomaly in the viscosity dependence of temperature reveals a phase transition or existence of sub phase [28]. Evidence for existence of any sub phases or blue phases is not found. Here, authors could not find any indication of smectic phase in CB which was spoken in our viscoelastic measurements. The shear rate considered here might be high enough to suppress the viscosity peaks. In this work, shear rate was chosen high bearing in mind that any anomaly in the viscosity at low shears makes it difficult to handle and limits its application. Also, such a shear thinning behavior expands their application in many fields.

A typical response of the shear stress to shear rate is represented in Figure 6. These plots of shear rate *versus* stress taken on logarithmic scale can be used to emphasize the generally observed power law behaviors ($\sigma = K\ \gamma^m$) and m is the slope of the curve [29]. As the shear rates chosen are $\sim 1–10^3\ s^{-1,}$ the power-law description does well for CB. A fair straight line seen for the two derivatives corresponds to different temperatures in their cholesteric phase. CB has shown a tendency for non-Newtonian which

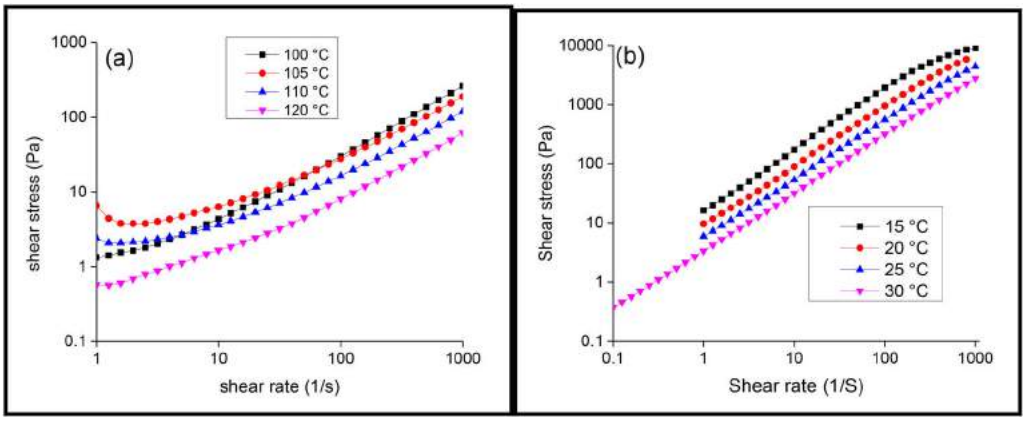

Figure 6. Steady-shear measurements. (A) Cholesteryl bromide and (B) cholesteryl 2-(ethoxy-ethoxy) ethyl carbonate.

becomes increasingly pronounced at lower temperatures. CB has shown shear thinning behavior with the power law index values 0.79 ($T = 100^{\circ}$C), 0.57 ($T = 105^{\circ}$C), 0.61 ($T = 110^{\circ}$C), and 0.69 ($T = 120^{\circ}$C). In LCs, the particle orientation makes the flow mechanism complicated than that of isotropic fluids.

For CEEEC, the power law exponent value is 0.99 and is independent of temperatures considered, showing that it is rheological behavior independent of temperature, and remains Newtonian. Both the lower and higher shear rate behavior has become difficult to see, and then only the Newtonian region (2) is seen in the steady-state flow plots. Also, any anomalous thermal dependency of shear viscosities was not observed. Data for both derivatives reveal that the sample becomes less viscous upon heating. Such a shear thinning behavior and shape of molecules lead to high mobility of molecules such that their layers slide readily when added as additives in lubricants. LCs, when used as additives improve the lubricating capacity of lubricants resulting in the reduction of coefficient of friction and wear [30].

The shear rate dependence of viscosity is intended in steady-state flow and presented in Figure 7. Both the lower and higher shear rate behavior has become difficult to see for both the derivatives.

The power-law region flow curves for CB follow a shear thinning behavior because of its layered structure. The non-bonded Vander Waal's forces which stabilize the three-dimensional structure of CB are suppressed when the shear rate is increased, giving rise to a shear thinning effect. A strong non-Newtonian behavior with temperature thickening effect is observed ionic liquid crystals [31]. The main mechanism assumed for shear thinning reduction of viscosity by the stimulated orientation of cholesteric superstructure with shear rate [32–34]. It also can be explained as the increased molecular mobility due to interruption of interactions and entanglement of molecules. A number of previous rheological studies on cholesteric liquid crystal systems have shown that materials in the cholesteric state are non-Newtonian up to a significant shear stress, and show Newtonian limiting viscosity behavior thereafter. Preparatory trend for Newtonian limiting viscosity at high shear can be clearly seen the graph for CB. During flows, the flexible rod-like molecules of liquid crystals align in the flow direction. As a result of

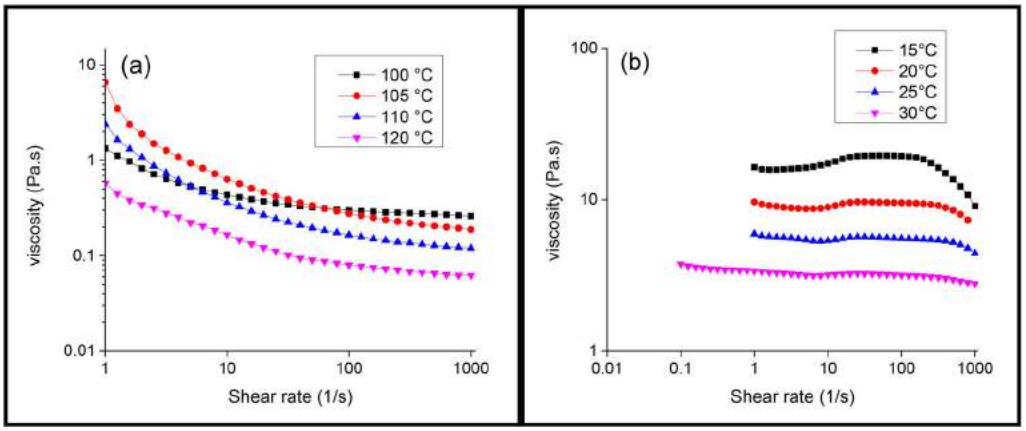

Figure 7. Effect of temperature on the steady-shear flow. (A)Cholesteryl bromide and (B) cholesteryl 2-(ethoxy-ethoxy) ethyl carbonate.

their tendency to return to the random coil configuration they exert a force perpendicular to the flow direction. Furthermore, the viscous behavior of CB showed an intriguing reliance with temperature.

Typically, a Newtonian behavior is observed for CEEEC within the shear rates range from 0.1 to 10^3/S. This may be understood as the orientation of liquid crystal molecules in hydrodynamic flow. The Newtonian behavior of viscosity results from the arrangement of molecules along the lines of action even at small forces. This constant viscosity regime seems to be the plateau regime (region 2) of 'three regions flow curve' as proposed by Onogi and Asada [35]. The texture of liquid crystals may be broken in region 1, and hence the wall effect is anticipated to be observed in this region 2. One can be obliged to use this as some characteristic viscosity of the material.

The viscoelastic, flow properties of these two cholesterics are quite interesting and are as good as rheological properties of members of homologous series of fatty acid cholesteryl esters and other commercial liquid crystal additives [19, 36, 37]. The tribological investigations on the homologous series of fatty acid cholesteryl esters [20, 38] have shown that they significantly reduced coefficient of friction. The influence of rheological properties of lubrication compositions of fatty acid cholesteryl esters on their tribological characteristics has also been determined [39]. The rheological measurements on ionic liquids were performed to analyze their relationship with friction coefficient [40]. Keeping in mind all these observations we assume that this study might be promising for the use of liquid crystals in tribology.

4. Conclusions

To summarize the experimental findings, the cholesterol derivative mesogens have exhibited a rich variety of rheological behavior. It has been observed that cholesteric phase for CEEEC and CB has occurred between 100 °C and 110 °C, and 15 °C and 32 °C, respectively. The linear viscoelastic span is comparable for the two derivatives. Insignificant impact of time on the rheological parameters of CEEEC is observed in the dynamic time sweep measurements. The temperature scans on G′ and G″ for CB

discovered an abrupt change in moduli at temperature range 100 °C to 100.2 °C suggesting a phase change or existence of sub phase. For CEEEC, the temperature could not effect on storage modulus, *G*', and its value is always less than loss modulus. Both the moduli are sensitive to frequency variation for two derivatives. The temperature–viscosity curves exhibited typical exponential decay and could not reflect the existence of sub phases or blue phases because of high shear applied. Steady-shear flow curves for CB exhibited typical shear thinning and the non-Newtonian flow affinity is prominent at lower temperatures. The CEEEC, within the measured shear rates range is Newtonian owing to the hydrodynamic flow orientation. It is worth highlighting that the rheology is an important issue for tribology and the two derivatives with such rheological behavior, when considered as potential lubricant additives may enhance ability of lubricants to reduce the coefficients of friction and the wear.

Conflicts of interest

The authors declare no conflict of interest.

Acknowledgments

Author S.S.S. is grateful to University Grants Commission's BSR Faculty fellowship.

Funding

University Grants Commission's BSR Faculty fellowship- No.F.18-1/2011(BSR) Dt:04/01/2017 and No. F4-5(11)/2019(BSR) dated 18 August 2020 and University Grants Commission Departmental Special Assistance at Level I program No.: F.530/1/DSA-1/2015 (SAP-1), dated 12 May 2015.

References

[1] Chilaya, G. S. and Lisetski, L. N. (1986). *Mol.Cryst. Liq.Cryst.*, *140*(2–4), 243. doi:10.1080/00268948608080157
[2] Mallia, V. A. and Tamaoki, N. (2004). *Chem. Soc. Rev.*, *33*(2), 76. doi:10.1039/b106617j
[3] Bhattacharya, S. and Krishnan-Ghosh, Y. (2002). *Mol. Cryst. Liq. Cryst.*, *381*(1), 33. doi:10.1080/713738738
[4] Tamaoki, N. (2001). *Adv. Mater.*, *13*(15), 1135. doi:10.1002/1521-4095(200108)13:15<1135::AID-ADMA1135>3.0.CO;2-S
[5] Rebecca, J., *et al.* (2013). *Liq. Cryst. Rev.*, *1*, 29. https://doi.org/10.1080/21680396.2013.769310
[6] Popov, P., *et al.* (2016). *Sens. Bio-Sens. Res.*, *8*, 31. doi:10.1016/j.sbsr.2016.03.008
[7] Popov, P., Mann, E. K. and Jákli, A. (2017). *J. Mater. Chem B*, *5*(26), 5061. doi:10.1039/c7tb00809k
[8] Guo, C. *et al.* (2010). *Drug Discov. Today*, *15*(23–24), 1032. doi:10.1016/j.drudis.2010.09.006
[9] del Pozo, M. *et al.* (2022). *Adv. Mater.*, *34*(3), 2104390. doi:10.1002/adma.202104390
[10] Özdemir, Y. *et al.* (2017). *Acta Phys. Pol. A*, *132*(3-II), 825. doi:10.12693/APhysPolA.132.825
[11] Shakeel, A., Kirichek, A. and Chassagne, C. (2020). *J. Nonnewton Fluid Mech.*, *286*, 104434. doi:10.1016/j.jnnfm.2020.104434
[12] Rodrigues, R. K. *et.al.* (2020). *J. Nonnewton Fluid Mech.*, *286*, 104397. doi:10.1016/j.jnnfm.2020.104397

[13] Rothstein, J. P. and goushki, H. M. (2020). *J. Nonnewton Fluid Mech.*, *285*, 104382. doi:10.1016/j.jnnfm.2020.104382
[14] Chen, L. *et al.* (2019). *Langmuir*, *35*(11), 4037. doi:10.1021/acs.langmuir.8b04144
[15] Usol'tseva, N. V. and Smirnova, A. I. (2019). *Lubricants*, *7*(12), 111. doi:10.3390/lubricants7120111
[16] Vekteris, V. and Mokshin, V. (2008). *Mater. Sci.*, *44*(5), 730. doi:10.1007/s11003-009-9125-3
[17] Noroozi, N. and GrecovLiq, D. (2013). *Crystal*, *40*(7), 871. doi:10.1080/02678292.2013.792127
[18] Wazynska, B., Tykarska, M. and Okowiak-Chinalska, J. (2011). *Mol. Cryst. Liq. Cryst.*, *542*(1), 213. 10.1080/15421406.2011.570594
[19] Bindu Madhavi, A. and Sastry, S. S. (2019). *Int. J. Mod. Phys. B*, *33*(05), 1950014. doi:10.1142/S0217979219500140
[20] Mokshin, V. (2020). *Adv. Mech. Eng.*, *12*(7), 168781402094547. doi:10.1177/1687814020945474
[21] Mang, T. and Dresel, W. (2007). *Lubricants and Lubrication*, Wiley VCH Verlag GmbH & Co. KGaA, Germany.
[22] Baessler, H. *et al.* (1969). *Mol. Cryst.*, *6*(3-4), 329. doi:10.1080/15421407008083470
[23] Somma, E. and Nobile, M. R. (2004). *J. Rheol.*, *48*(6), 1407. doi:10.1122/1.1795194
[24] Langelaan, H. C. and Gotsis, A. D. (1996). *J. Rheol.*, *40*(1), 107. doi:10.1122/1.550733
[25] Vani, G. V. and Vijayan, K. (1979). *Mol. Cryst. Liq. Cryst.*, *51*(3-4), 253. doi:10.1080/00268947908084711
[26] Hongladarom, K., Secakusuma, V. and Burghardt, W. R. (1994). *J. Rheol.*, *38*(5), 1505. doi:10.1122/1.550556
[27] Ramos, L. *et al.* (2002). *Phys. Rev. E Stat. Nonlin. Soft Matter. Phys.*, *66*(3 Pt 1), 031711. doi:10.1103/PhysRevE.66.031711
[28] Jadâyn, J. and Czechowski, G. (2004). *Acta Phys. Pol. A*, *105*(4), 59. doi:10.12693/APhysPolA.105.459
[29] Steffe, J. F. (1996). *Rhelogical Methods in Food Processing Engineering*, Freeman Press, USA.
[30] Gribailo, A. P., Kupreev, M. P. and Zamyatnin, V. O. (1983). *Chem. Technol. Fuels Oils*, *19*(7), 342. doi:10.1007/BF00731562
[31] Avilés, M. D. *et al.* (2020). *J. Mol. Liq.*, *301*, 112406. doi:10.1016/j.molliq.2019.112406
[32] Alcantara, M. R. and Dias, L. C. F. (1998). *Colloids Surf. A*, *136*(1-2), 155. doi:10.1016/S0927-7757(97)00319-1
[33] Larson, R. G. (1999) *Structure and Rheology of Complex Fluids*, Oxford University Press, NY.
[34] Porter, R. S. and Johnson, J. F. (1963). *J. Appl. Phys.*, *34*(1), 55. doi:10.1063/1.1729089
[35] Onogi, S. and Asada, T. (1980) *Rheology Principles*, Plenum Press,NY.
[36] Waters E. P. J., *et al***et al**. (2009). *Asia-Pac. J. Chem. Eng.*, *4*(1), 80. doi:10.1002/apj.220
[37] Chapoy, L. L. and Duke, R. W. (1979). *Rheol. Acta*, *18*(4), 537. 10.1007/BF01736958
[38] Ermakov, S. F., *et al.* (2015). *J. Frict. Wear*, *36*(6), 496. 10.3103/S1068366615060033
[39] Berezina, E. V., *et al.* (2016). *Procedia Eng.*, *150*, 579. doi:10.1016/j.proeng.2016.07.044
[40] Amann, T., Dold, C. and Kailer, A. (2012). *Soft Matter*, *8*(38), 9840. doi:10.1039/c2sm26030a

micromachines

IMPACT FACTOR 3.523

Indexed in: PubMed

Article

FPGA Implementation of AI-Based Inverter IGBT Open Circuit Fault Diagnosis of Induction Motor Drives

Nagalingam Rajeswaran, Rajesh Thangaraj, Lucian Mihet-Popa, Kesava Vamsi Krishna Vajjala and Özen Özer

MDPI

https://doi.org/10.3390/mi13050663

micromachines

MDPI

Article

FPGA Implementation of AI-Based Inverter IGBT Open Circuit Fault Diagnosis of Induction Motor Drives

Nagalingam Rajeswaran [1,*], Rajesh Thangaraj [1], Lucian Mihet-Popa [2,*], Kesava Vamsi Krishna Vajjala [3] and Özen Özer [4]

[1] Electrical and Electronics Engineering, Malla Reddy Engineering College, Secunderabad 500100, India; rajesh.t@mrec.ac.in
[2] Faculty of Information Technology, Engineering, and Economics, Oestfold University College, 1757 Halden, Norway
[3] Department of Physics, Malla Reddy Engineering College, Secunderabad 500100, India; media@mrec.ac.in
[4] Department of Mathematics, Faculty of Science and Arts, Kırklareli University, Kırklareli 39100, Turkey; ozenozer39@gmail.com
* Correspondence: rajeswarann@gmail.com (N.R.); lucian.mihet@hiof.no (L.M.-P.); Tel.: +91-73822211597 (N.R.)

Abstract: In modern industrial manufacturing processes, induction motors are broadly utilized as industrial drives. Online condition monitoring and diagnosis of faults that occur inside and/or outside of the Induction Motor Drive (IMD) system make the motor highly reliable, helping to avoid unscheduled downtimes, which cause more revenue loss and disruption of production. This can be achieved only when the irregularities produced because of the faults are sensed at the moment they occur and diagnosed quickly so that suitable actions to protect the equipment can be taken. This requires intelligent control with a high-performance scheme. Hence, a Field Programmable Gate Array (FPGA) based on neuro-genetic implementation with a Back Propagation Neural network (BPN) is suggested in this article to diagnose the fault more efficiently and almost instantly. It is reported that the classification of the neural network will provide the output within 2 µs although the clone procedure with microcontroller requires 7 ms. This intelligent control with a high-performance technique is applied to the IMD fed by a Voltage Source Inverter (VSI) to diagnose the fault. The proposed approach was simulated and experimentally validated.

Keywords: condition monitoring; Induction Motor Drive; fault diagnosis; FPGA; Back Propagation Neural Network; Discrete Wavelet Transforms

Citation: Rajeswaran, N.; Thangaraj, R.; Mihet-Popa, L.; Krishna Vajjala, K.V.; Özer, Ö. FPGA Implementation of AI-Based Inverter IGBT Open Circuit Fault Diagnosis of Induction Motor Drives. *Micromachines* **2022**, *13*, 663. https://doi.org/10.3390/mi13050663

Academic Editor: Piero Malcovati

Received: 22 March 2022
Accepted: 21 April 2022
Published: 23 April 2022

1. Introduction

Industrial induction motors are highly reliable and easy to operate; hence, they are extensively used as industrial drives [1,2]. They work under harsh and severe conditions, and as a result, they are subject to both internal and exterior faults and breakdowns [3]. These faults must be sensed at the earliest stage; otherwise, catastrophic failure of the machine may result in disruptions to production [4,5]. It was this need that necessitated online supervision and fault analysis design to be integrated with the drive system [6,7].

According to conventional wisdom, the maintenance of Induction Motor Drive (IMD) happens at a certain interval. However, the performance of IMD may decline at irregular intervals as a result of environmental and operational factors. As a result, online monitoring of instant messaging is required to increase efficiency. In new evolving methodologies, predictive maintenance via condition monitoring (CM) is a critical component, intending to project the maintenance schedule based on the state of the plant or process [8–10]. It is possible to improve the performance and efficiency of an IMD by using condition-based monitoring. Such monitoring also extends the life and productivity of the system and reduces internal and external damages. It has become vital to use CM and fault detection in IMDs to prevent unexpected failures and reduce unplanned downtime. There are many

ways for condition monitoring of IM, including Acoustic Emission (AE) monitoring, vibration signature analysis, and Motor Current Signature Analysis (MCSA). However, these monitoring techniques are complicated and need costly sensors [10]. When a CM system is efficient, it is capable of delivering early warning and forecasting errors. The CM system obtains basic data information from the motor via the use of signal processing or data analysis methods as described before. Although the method does not need human interpretation, it does have a fundamental downside [11–13]. The automation of the fault detection and diagnosis process is a natural evolution in the development of CM technologies [14,15]. An intelligent system, such as artificial intelligence methods, Genetic Algorithms (GA), Fuzzy Logic (FL), Artificial Neural Networks (ANN), and expert systems, is required for the autonomous fault detection system [16]. In an industry-based comprehensive assessment of high voltage IMD failures, multiple types of classification were used to identify the causes of the failures [17]. These categories included protection system, machine size, age, number of poles, maintenance regime, and operating hours. Induction machines have been subjected to an investigation into the causes of both stator and bearing failures, which together account for about 75% of all failures [18].

To gather information regarding CM and diagnostic measures, a survey on IM drives for industrial applications was conducted [19]. The research focused on the challenges that are now being addressed and those that will be addressed in the future in the development of autonomous diagnostic methods. The LabVIEW platform was used to produce cutting-edge capabilities for online control of induction motors [20–22]. It has been determined that the use of stator current analysis-based demodulation methods is the most suited method for diagnosing bearing faults.

There are many noncontact CM approaches that may be used to diagnose inductor motor failures. Specifically, it was discovered that the park vector analysis and instantaneous power analysis procedures are the most effective methods for recognizing motor failure signals. The Support Vector Machine (SVM)-based algorithms have demonstrated that they provide improved results for the classification and fault diagnosis of a three-phase induction motor [23]. The Bearing Damage Index (BDI), which is based on the wavelet packet node energy coefficient analysis method, has been proposed not only to detect faults in bearings but also to detect the severity level of the fault [24]. The Bearing Damage Index (BDI) is based on the wavelet packet node energy coefficient analysis method. A review of the most current literature has been published on the automation of condition monitoring in IMD [25]. When it comes to directing maintenance for electrical machines, one of the factors that has been identified as a barrier is the cost-to-benefit ratio between capital and operating expenses [26–28].

In the last two decades or so, condition supervision and fault identification of IMD attracted the attention of many researchers who developed AI-based control schemes such as expert systems, fuzzy interference systems, neural network and neuro-fuzzy techniques. All these techniques when implemented in real time are computationally complex, time-consuming, and lacking in optimal switching strategies. Hence, a new method, neuro-genetic design and implementation of fault diagnosis of induction motors based on a FPGA are proposed in this article [29,30]. The measured signals are processed through DWT for feature extraction. These features are used to detect the type of fault that occurred in the system.

The remaining article is structured as follows. The proposed test system model is presented in Section 2. Section 3 details the proposed method, and Section 4 presents the experimental results. Lastly in Section 5 the conclusions are presented.

2. Proposed System Description

The schematic diagram of the IMD with a FPGA-based neuro-genetic implementation is shown in Figure 1. The proposed system consists of a power supply block having an AC to DC converter node and a DC to AC inverter node, a squirrel cage induction motor, a flux and signal estimation (Programmable Cascaded Low Pass Filter (PCLPF)) block, a

neuro-genetic based fault diagnosis block, a controller block, a neuro-genetic-based Space Vector Pulse Width Modulation (SVPWM) block, and a binary block. The input signals corresponding to the induction motor's terminal voltages and currents are transformed into output signals indicating torque and flux by the lux and signal estimation block. These signals are sent into the controller block, which creates input signals for the SVPWM block, which processes and generates suitable pulses for the binary logic block. The fault diagnosis block receives signals matching the Insulated Gate Bipolar Transistor (IGBT) inverter's output voltages.

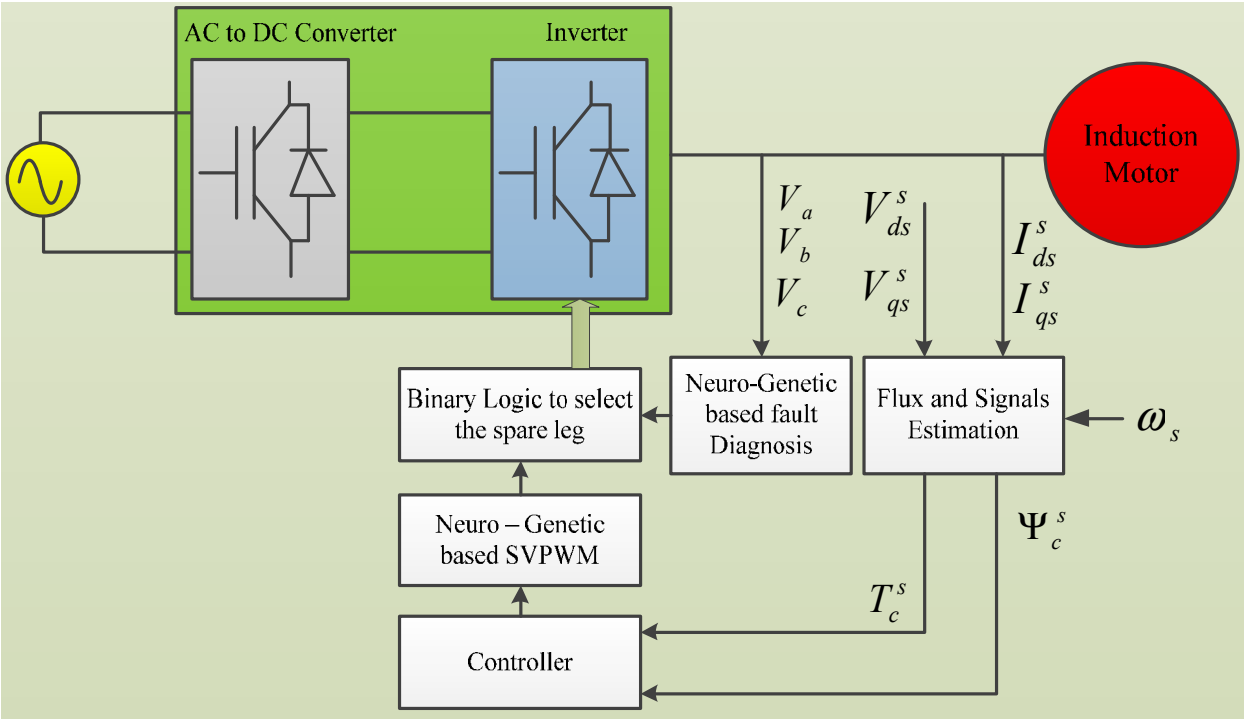

Figure 1. Schematic of Neuro-Genetic-based fault diagnosis drive system.

It processes them in the neural network to produce TRIAC signals for the modified structure of the IGBT inverter. These, together with the output signal of the SVPWM block, are input to the binary logic block, the output signals of which are utilized to transfer the jurisdiction from the faulty leg to the backup leg.

2.1. Reconfiguration of Inverter Topology

IGBT inverter topology is shown in Figure 2. The inverter structure has three legs, with every leg carrying two switches, **S1**, **S2**, **S3**, **S4**, and **S5**, **S6**, correspondingly. The fourth leg has another two switches, **S7** and **S8**. Three Triacs, **T1**, **T2** and **T3**, are utilized for configuring the inverter later fault existence and its elimination. If there is a misfiring in power switch **Sn**, the fault identification part finds this fault and separates the corresponding fault leg by disconnecting the gate signals to the switch **Sn**. The phase current '$\mathbf{i_{sn}}$' is reduced to zero by the freewheeling diodes **Dn** in the faulted leg. Then the restructuring module fires **Tn** which interconnects '**n**' (Leg) and '**o**' (**C1** and **C2**).

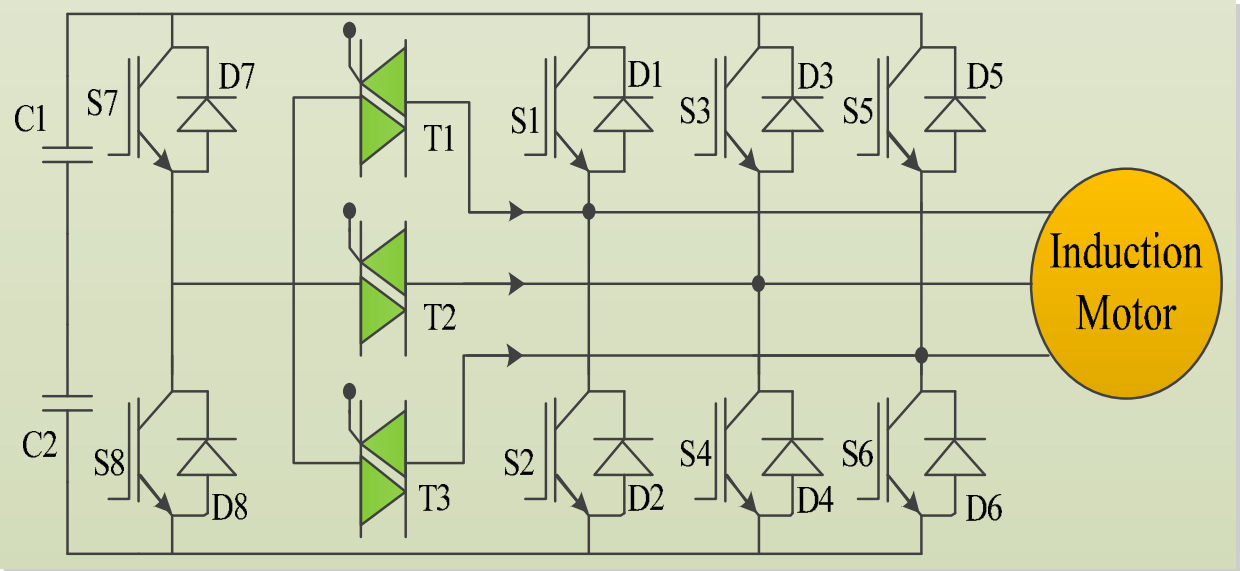

Figure 2. IGBT Inverter topology.

2.2. Fault Diagnosis Based on a FPGA

To accurately diagnose the fault when it occurs, the trend or changes in the monitoring signals must be sensed unambiguously so that the same could be converted into binary code. These coded signals could be used to translate the fault category and its position. Then appropriate gate signals can be generated for suitable action on the system. To carry out the above processes, the control scheme should consist of facilities such as a signal or feature eradication, neural network regulation, fault identification, and gating signals. For the drive system under consideration, the fault diagnosis is performed as follows. The backfire in any one of the switches in a leg of the inverter can be recognized by an error in the corresponding leg voltage. The neural network is experienced with ordinary and extraordinary data for the inverter operation, and so outputs of the neural network are almost '0' and '1' as binary code. Then, corresponding to the error signal of the faulty leg voltage, binary code is generated and sent to the fault identification structure which senses and decodes the fault category and its location. Thereupon, the neural network selects the switches to isolate the faulty leg and bring in the spare leg so that the inverter regains its normal state as a three phase **VSI** to supply the IMD, making it fault tolerant. Suppose if the fault occurred in leg '**n**', causing a deviation in the leg voltage $\pm\Delta Vno$. Then, the leg voltage after fault occurrence can be given as Equation (1),

$$V'no = Vno \pm \Delta Vno \quad (1)$$

This signal may not distinguish itself from Vno, and so a signal transformation technique is required to accurately diagnose the fault. The feature or signal extractor should be such that it provides adequate and significant details about the trend of the signal to enable the neural network to diagnose the fault type and its location with a high degree of accuracy. To achieve this, a feature extractor using a Discrete Wavelet Transform (DWT) technique is employed. The Register Transfer Language (RTL) schematic diagram of the DWT technique is shown in Figure 3. Discrete wavelet transformation is good in time resolution of high frequencies [11].

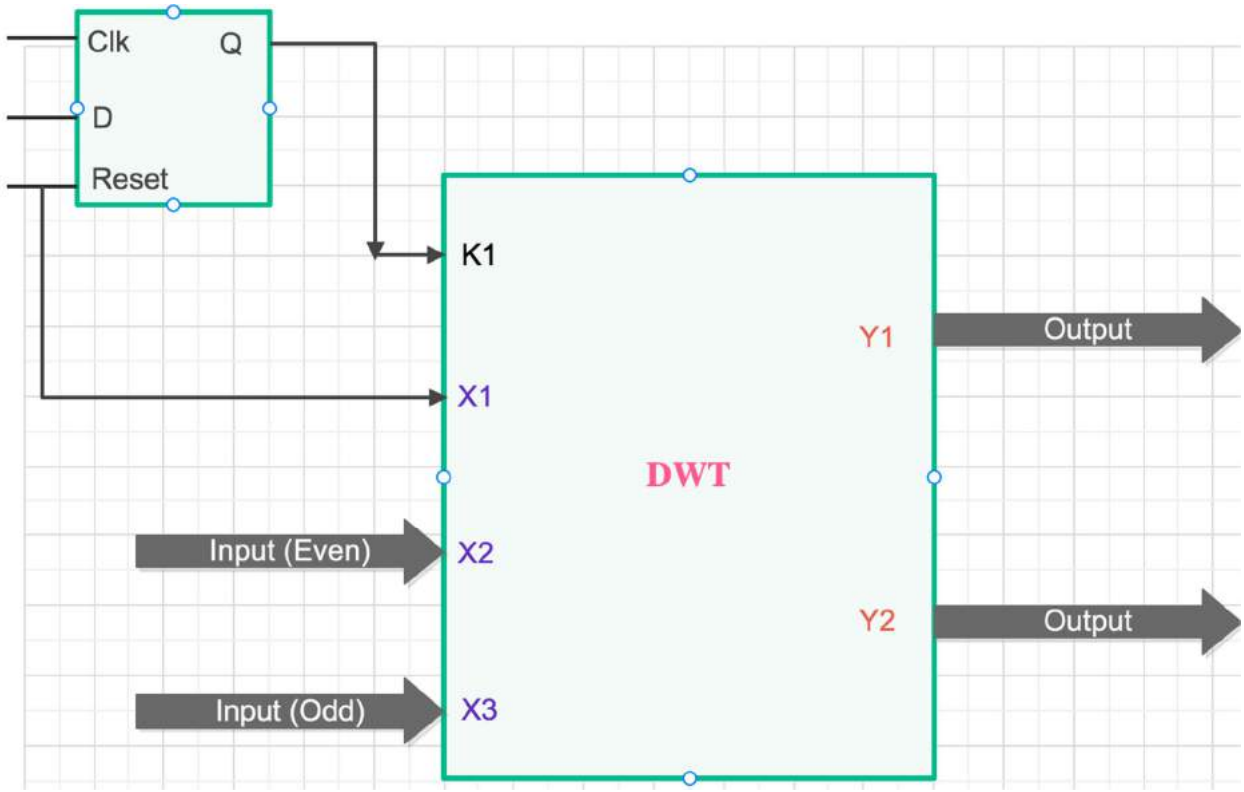

Figure 3. Schematic view of DWT.

3. Neuro-Genetic Approach for Fault Classification

For accurate fault isolation, the signals (voltage, current, and speed) are transformed with the DWT technique for feature extraction [8]. After transformation, the output voltage variations are classified by using the neuro-genetic approach which continues to feedback the signals until desired (target) output is obtained representing the fault situation.

Neuro-Genetic Architecture Design

The structure of the BPN classification based on a FPGA is shown in Figure 4. For the given drive system fed by a **VSI**, there are seven states to represent the conditions, i.e., normal, fault on **S1**, fault on **S2**, fault on **S3**, fault on **S4**, fault on **S5**, fault on **S6**, and fault on **S7**. It requires a seven-layer neural structure. In addition, there are three hidden nodes and one yield node.

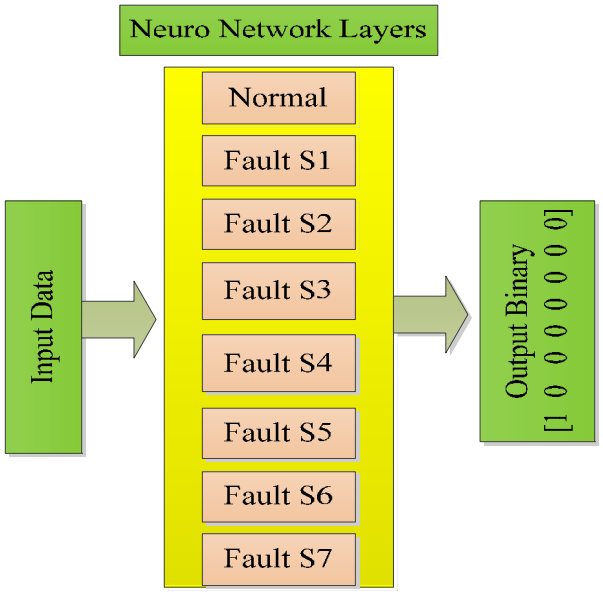

Figure 4. Development of BPN classification structure.

The neuro-genetic-SVPWM has double subnets. One is the voltage amplitude subnet with a 1-3-1 structure, and the other is the angle subnet with the architecture of 1-18-3 to produce a three-phase yield. The sigmoid activation function is used. Every structure is experienced with one set of normal data and four sets of faulted data.

The use of GA helps achieve an optimized weight value for BPN to obtain the desired output for the fault situation. Thus, the neuro-genetic technique based on a FPGA when implemented functions in such a way that the control scheme is capable of fast processing to achieve fault diagnosis almost instantly [12,13]. Here, the mixed design of neural networks and genetic algorithms is developed and implemented in the FPGA process as given by the flow diagram in Figure 5. The idle, birth, selection, crossover, mutation, and store states are used in GA. Linear feedback shift register (LFSR) is used to produce arbitrary numbers [13,14]. A fitness value is designated to every part in the community depending on the discrepancy in the set and original output of the structure. The total number of Pins in the FPGA appliance is 208 and utilized pins in the suggested structure are only 49. The experimental setup presented in Figure 6 is verified on the xc3s500e-4-pq208 board (Xilinx, San Jose, CA, USA). The three-phase induction motor specifications are listed in Table 1.

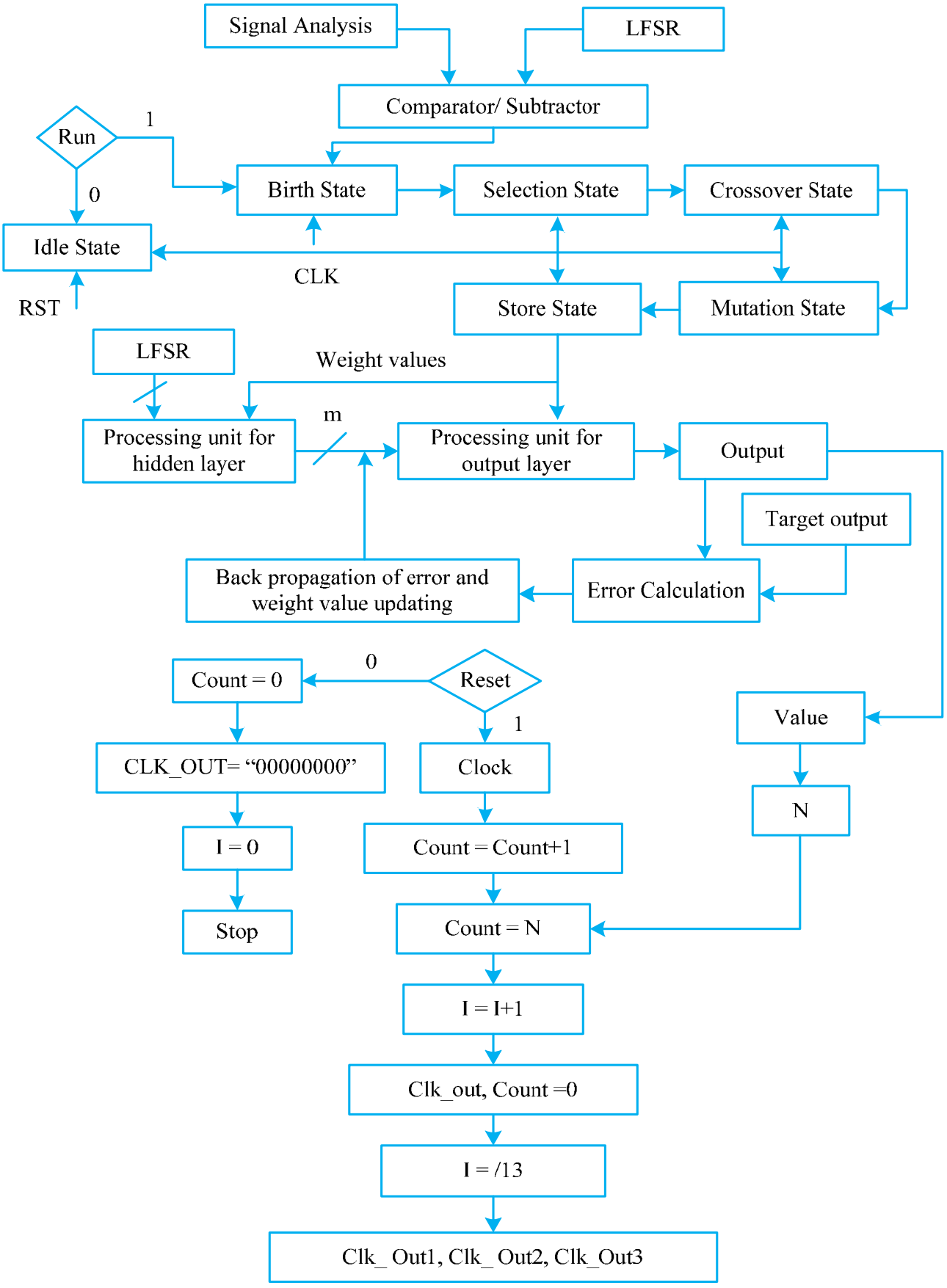

Figure 5. Flow chart of neuro-genetic design.

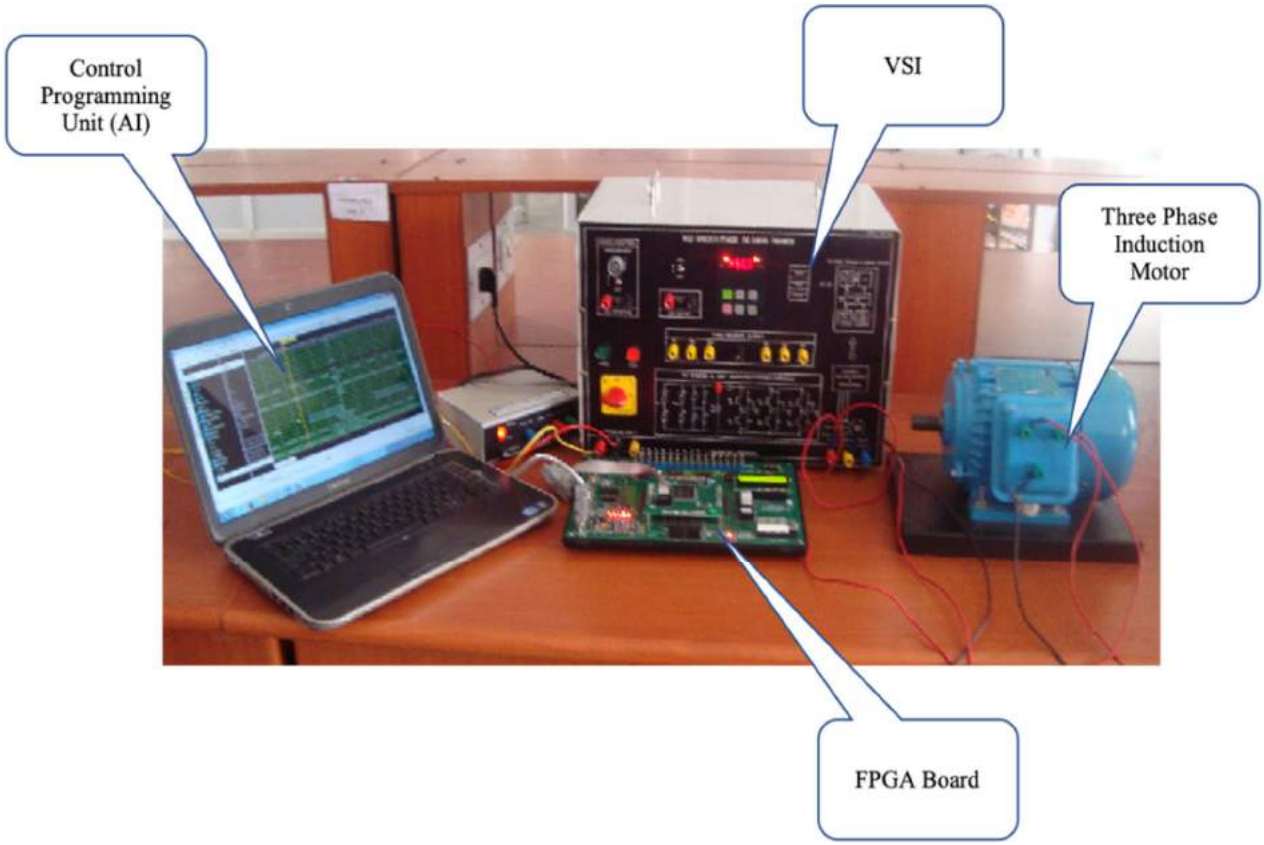

Figure 6. Neuro-genetic implementation based on a FPGA.

Table 1. Induction motor specifications.

Parameter	Range
Speed	1390 rpm
Volts	415 V
Frequency	50 Hz
Power	0.75 kW
Pole	4

4. Results and Discussion

The problem associated with ANN concerning weight optimization to train the network is adequately addressed using GA. The use of DWT as a feature extractor provides significant details in the pattern set to the neural network, enabling it to perform with a high degree of accuracy in fault diagnosis.

With successful configuration by a FPGA, the neuro-genetic-SVPWM processes the signals such that the variation of the neural network provides the yield with minimum and maximum time of 10.85 ns and 11.99 ns. It is reported that the classification of the neural network will provide the output within 2 µs although the clone procedure with a microcontroller requires 7 ms [17]. However, the neuro-genetic approach obtained the low and high period of yield as 10.857 ns (7.440 ns logic, 3.417 ns route, 68.5% for logic and 31.5% for route) and 11.99 ns (8.042 ns for logic, 3.952 ns for route, 67.1% for logic and 32.9% for route), respectively. The result simulations are performed by using integer numbers. The selected device power information is shown in Table 2. The prototype requirement of the proposed method device utilization summary is provided in Table 3. According to the defective and normal conditions, the output voltage waveform reveals how quickly the neuro-genetic process will produce the switching wave shape. A total of 173,524 kilobytes of RAM are used. The suggested design achieves the use of hardware and efficiency to

minimize power consumption in different aspects. Table 4 shows the full clock reports and timing summary. The simulation timing and real-time clock utilization by VHDL is a hardware description language (HDL) software and is tabulated below in Table 5.

Table 2. Power summary.

Parameter	Power (W)	Voltage	Range	Icc (A)	Iccq (A)
Vccint	0.031	1.20	1.14 to 1.25	0.000	0.026
Vccaux	0.045	2.5		0.000	0.018
Vcco25	0.005	2.5		0.000	0.002

Table 3. Device utilization summary.

Logic Utilization	Used	Available	Range
Total number of slice registers	188	9312	2%
Number used as flip flops	105		
Number used as latches	83	2.5	
Number of 4 input LUTs	270	9312	2%
Logic Distribution	**Used**	**Available**	**Range**
Number of occupied slices	217	4656	4%
Number of slices containing only related logic	217	217	100%
Number of slices containing unrelated logic	0	217	0%
Total Number of 4 input LUTs	303	9312	3%
Number used as logic	270		
Number used as a route-through	33		
Number of bonded IOBs	81	159	51%
IOB latches	11		
Number of BUFGMUXs	3	24	12%
Number of M | ULT | I18X18SIOs	4	20	20%

Table 4. Clock Report.

Clock Net	Resource	Locked	Fanout	Net Skew (ns)	Max Delays (ns)
X4/y0_not001	BUFGMUX_X2Y10	No	12	0.011	0.142
Clk1_BUFGP	BUFGMUX_X2Y11	No	75	0.076	0.196
State_out1_1_OBUF	BUFGMUX_X1Y10	No	11	0.030	0.148
x3/ov4	Local		16	0.045	1.249
x3/ov1	Local		6	0.211	1.988
x3/ov3	Local		5	0.460	1.124
x3/ov2	Local		6	0.224	2.235

Table 5. Timing Summary.

Parameters	Frequency
Minimum period	10.857 ns
Maximum frequency	92.108 MHz
Minimum input arrival time before clock	20.18 ns
Maximum output required time after clock	11.99 ns
Maximum combinational path delay	8.610 ns
Total REAL time to Xst completion	11.00 s
Total CPU time to Xst completion	10.41 s

5. Conclusions

Fault diagnosis of IMD has been attempted for fault occurrence in VSI by using a neuro-genetic technique based on a FPGA. The neuro-genetic algorithm (BPN with GA)

processes the error to diagnose the fault type and its location to transfer the switching from faulty leg to spare leg of the IGBT inverter, thereby making the system a fault tolerant IMD. The implementation of this technique is found to increase the speed of response for situational observation and fault identification, thereby enhancing the reliability of the drive system in modern industrial processes. With successful configuration by a FPGA, the neuro-genetic-SVPWM processes the signals such that the variation of the neural network provides the yield with minimum and maximum time of 10.85 ns and 11.99 ns. The proposed techniques can be extended in the near future with various machine-learning methods and switching response can be improved.

Author Contributions: N.R. and R.T.; methodology, N.R.; software, R.T.; validation N.R., L.M.-P. and K.V.K.V.; formal analysis, L.M.-P.; investigation, R.T.; resources, N.R.; data creation, R.T.; writing—original draft preparation, Ö.Ö.; writing—review and editing, N.R., R.T. and K.V.K.V.; visualization, N.R.; supervision, K.V.K.V. and L.M.-P.; project administration, R.T.; funding acquisition. All authors have read and agreed to the published version of the manuscript.

Funding: This research received no external funding.

Institutional Review Board Statement: Not applicable.

Informed Consent Statement: Not applicable.

Conflicts of Interest: The authors declare no conflict of interest.

References

1. Gangsar, P.; Tiwari, R. Signal based condition monitoring techniques for fault detection and diagnosis of induction motors: A state-of-the-art review. *Mech. Syst. Signal Process.* **2020**, *144*, 106908. [CrossRef]
2. Khoualdia, T.; Lakehal, A.; Chelli, Z.; Khoualdia, K.; Nessaib, K. Optimized multi-layer perceptron artificial neural network-based fault diagnosis of induction motor using vibration signals. *Diagnostyka* **2021**, *22*, 65–74.
3. Popa, L.M.; Jensen, B.B.; Ritchie, E.; Boldea, I. Condition monitoring of Wind Generators. In Proceedings of the 38th IAS Annual Meeting on Conference Record of the Industry Applications Conference, Salt Lake City, UT, USA, 12–16 October 2003; Volume 3, pp. 1839–1846. [CrossRef]
4. Al-Janabi, S.; Rawat, S.; Patel, A.; Al-Shourbaji, I. Design and evaluation of a hybrid system for detection and prediction of faults in electrical transformers. *Int. J. Electr. Power Energy Syst.* **2015**, *67*, 324–335. [CrossRef]
5. Sica, F.C.; Guimarães, F.G.; de Oliveira Duarte, R.; Reis, A.J. A cognitive system for fault prognosis in power transformers. *Electr. Power Syst. Res.* **2015**, *127*, 109–117. [CrossRef]
6. Uddin, M.N.; Hao, W. Development of a self- tuned neuro-fuzzy controller for induction motor drives. *IEEE Trans. Ind. Appl.* **2007**, *43*, 1108–1116. [CrossRef]
7. Mihet-Popa, L.; Bak-Jensen, B.; Ritchie, E.; Boldea, I. Current Signature Analysis to Diagnose Incipient Faults in Wind Generator Systems. In Proceedings of the 5th International Symposium on Advanced Electromechanical Motion Systems-Electromotion, ELECTROMOTION 2003, Marrakech, Morocco, 26–28 November 2003; Volume 2, pp. 647–652.
8. Zhong, B. Developments in intelligent condition monitoring and diagnostics in System Integrity and Maintenance. In Proceedings of the 2nd Asia-Pacific Conference (ACSIM2000), Nanjing, China, 1 January 2000; Queensland University of Technology: Brisbane, Australia, 2000; pp. 1–6.
9. Naber, N.; Getz, T.; Kim, Y.; Petrosky, J. Real-Time Fault Detection and Diagnostics Using FPGA-Based Architectures. In Proceedings of the 2010 International Conference on Field Programmable Logic and Applications, Milan, Italy, 31 August–2 September 2010; IEEE Computer Society. pp. 346–351.
10. Mihet-Popa, L.; Pacas, J.M. Failure Detection in Converter Fed Induction Machines under Different Operation Conditions. In Proceedings of the International Electric Machines and Drives Conference (IEMDC), San Antonio, TX, USA, 15–18 May 2005; Volume 3, pp. 967–974.
11. Verucchi, C.J.; Acosta, G.G. Fault Detection and Diagnosis Techniques in Induction Electrical Machines. *Lat. Am. Trans.* **2007**, *5*, 41–49. [CrossRef]
12. Qiao, Z.; Elhattab, A.; Shu, X.; He, C. A second-order stochastic resonance method enhanced by fractional-order derivative for mechanical fault detection. *Nonlinear Dyn.* **2021**, *106*, 707–723. [CrossRef]
13. Mihet-Popa, L.; Prostean, O.; Szeidert, I.; Filip, I.; Vasar, C. Fault Detection Methods for Frequency Converters Fed Induction Machines. In Proceedings of the 12th IEEE Conference on Emerging Technologies and Factory Automation-ETFA, Patras, Greece, 25–28 September 2007; pp. 161–168. [CrossRef]
14. Zidani, F.; Diallo, D.; Benbouzid, M.E.H.; Said, R.N.A. Fuzzy-based approach for the diagnosis of fault modes in a voltage-fed PWM inverter induction motor drive. *IEEE Trans. Ind. Electron.* **2008**, *55*, 586–593. [CrossRef]

15. Wu, Y.; Jiang, B.; Wang, Y. Incipient winding fault detection and diagnosis for squirrel-cage induction motors equipped on CRH trains. *ISA Trans.* **2020**, *99*, 488–495. [CrossRef]
16. Mihet-Popa, L. Current Signature Analysis as Diagnosis Media for incipient fault detection. *J. Adv. Electr. Comput. Eng.* **2007**, *7*, 11–15. [CrossRef]
17. Tatikonda, S.; Agarwal, P. Field Programmable Gate Array (FPGA) based neural network implementation of Motion Control and fault diagnosis of induction motor drive. In Proceedings of the 2008 IEEE International Conference on Industrial Technology, Chengdu, China, 21–24 April 2008; pp. 1–6.
18. Toma, R.N.; Prosvirin, A.E.; Kim, J.M. Bearing fault diagnosis of induction motors using a genetic algorithm and machine learning classifiers. *Sensors* **2020**, *20*, 1884. [CrossRef] [PubMed]
19. Ali, M.Z.; Shabbir, M.N.S.K.; Zaman, S.M.K.; Liang, X. Single-and multi-fault diagnosis using machine learning for variable frequency drive-fed induction motors. *IEEE Trans. Ind. Appl.* **2020**, *56*, 2324–2337. [CrossRef]
20. Kumar, P.; Hati, A.S. Review on machine learning algorithm-based fault detection in induction motors. *Arch. Comput. Methods Eng.* **2021**, *28*, 1929–1940. [CrossRef]
21. Zaman, S.M.K.; Liang, X. An effective induction motor fault diagnosis approach using graph-based semi-supervised learning. *IEEE Access* **2021**, *9*, 7471–7482. [CrossRef]
22. Kabul, A.; Ünsal, A. A diagnosis method of multiple faults of induction motors based on vibration signal analysis. In Proceedings of the 2021 IEEE 13th International Symposium on Diagnostics for Electrical Machines, Power Electronics and Drives (SDEMPED), Dallas, TX, USA, 22–25 August 2021; Volume 1.
23. Bazan, G.H.; Goedtel, A.; Duque-Perez, O.; Morinigo-Sotelo, D. Multi-Fault Diagnosis in Three-Phase Induction Motors Using Data Optimization and Machine Learning Techniques. *Electronics* **2021**, *10*, 1462. [CrossRef]
24. Zamudio-Ramirez, I.; Antonino-DAVIU, J.A.; Osornio, R.A.; Dunai, L. Tracking of high-order stray-flux harmonics under starting for the detection of winding asymmetries in wound-rotor induction motors. *IEEE Trans. Ind. Electron.* **2021**, *69*, 8463–8471. [CrossRef]
25. Wong, P.K.; Biao, J.S. Fault Diagnosis of Induction Motors Under Untrained Loads with a Feature Adaptation and Improved Broad Learning Framework. *IEEE/ASME Trans. Mechatron.* **2021**, 1–12. [CrossRef]
26. Mauricio, A.; Smith, W.A.; Randall, R.B.; Antoni, J.; Gryllias, K. Improved Envelope Spectrum via Feature Optimization-gram (IESFOgram): A novel tool for rolling element bearing diagnostics under non-stationary operating conditions. *Mech. Syst. Signal Process.* **2020**, *144*, 106891. [CrossRef]
27. Mohammed, O.A.; Abed, N.Y.; Ganu, S. Modelling and Characterization of Induction Motor Internal Faults Using Finite Element and Discrete Wavelet Transforms. *IEEE Trans. Magnet.* **2006**, *42*, 3434–3436. [CrossRef]
28. AlShorman, O.; Alkahatni, F.; Masadeh, M.; Irfan, M.; Glowacz, A.; Althobiani, F.; Kozik, J.; Glowacz, W. Sounds and acoustic emission-based early fault diagnosis of induction motor: A review study. *Adv. Mech. Eng.* **2021**, *13*, 1687814021996915. [CrossRef]
29. Cerda, J.C.; Martinez, C.D.; Comer, J.M.; Hoe, D.H.K. An efficient FPGA random number generator using LFSRs and cellular automata. In Proceedings of the 2012 IEEE 55th International Midwest Symposium on Circuits and Systems (MWSCAS), Boise, ID, USA, 5–8 August 2012; pp. 912–915.
30. Choudhary, A.; Goyal, D.; Shimi, S.L.; Akula, A. Condition monitoring and fault diagnosis of induction motors: A review. *Arch. Comput. Methods Eng.* **2019**, *26*, 1221–1238. [CrossRef]

HEAT TRANSFER

ORIGINAL ARTICLE

Analysis of Joule heating and chemical reaction effects in electroosmosis peristaltic transport of couple-stress and micropolar fluids

Kattamreddy Venugopal Reddy, Machireddy Gnaneswara Reddy, Oluwole Daniel Makinde

First published: 03 April 2022 | https://doi.org/10.1002/htj.22533

Abstract

This article features the reaction of electroosmosis peristaltic transport of combined couple-stress and micropolar fluid in an inclined asymmetric channel through a porous medium. Mathematical modeling is given in the presence of Joule heating, thermal radiation, and heat flux effects. The relevant equations are computed subject to long wavelength and small Reynolds number approximation. The coupled system resulting equations have been executed computationally to plot different effects graphically. A detailed analysis of the results is given through graphs. Graphs are plotted for velocity, temperature, concentration, and pumping characteristics. The impact of each significant parameter on flow, species, and thermal characteristics is enumerated in these studies. The influence of couple stress and electroosmosis parameters are also simulated. This problem is very significant to the discussion of chemical separation/fraternization procedures and bio-microfluidics devices for the resolution of the diagnosis.

Volume 51, Issue 6
September 2022
Pages 4992-5014

micromachines

MDPI

Article

Recent Development of Heat and Mass Transport in the Presence of Hall, Ion Slip and Thermo Diffusion in Radiative Second Grade Material: Application of Micromachines

V. V. L. Deepthi [1], Maha M. A. Lashin [2], N. Ravi Kumar [3], Kodi Raghunath [4], Farhan Ali [5,*], Mowffaq Oreijah [6], Kamel Guedri [6,7], El Sayed Mohamed Tag-ElDin [8], M. Ijaz Khan [9] and Ahmed M. Galal [10,11]

[1] Department of Mathematics, CVR College of Engineering, Hyderabad 500039, India
[2] College of Engineering, Princess Nourah Bint Abdulrahman University, Riyadh 84428, Saudi Arabia
[3] Department of Mathematics, Malla Reddy Engineering College (Autonomous), Medchal 500100, India
[4] Department of Humanities and Sciences, Bheema Institute of Technology and Science, Adoni 518301, India
[5] Department of Mathematical Sciences, Federal Urdu University of Arts, Sciences & Technology, Gulshan-e-Iqbal Karachi 75300, Pakistan
[6] Mechanical Engineering Department, College of Engineering and Islamic Architecture, Umm Al-Qura University, Makkah 21955, Saudi Arabia
[7] Research Unity: Materials, Energy and Renewable Energies, Faculty of Science of Gafsa, University of Gafsa, Gafsa 2100, Tunisia
[8] Faculty of Engineering and Technology, Future University in Egypt, New Cairo 11835, Egypt
[9] Department of Mechanical Engineering, American Lebanese University, Beirut 1102, Lebanon
[10] Mechanical Engineering Department, College of Engineering, Prince Sattam Bin Abdulaziz University, Wadi Addawaser 11991, Saudi Arabia
[11] Production Engineering and Mechanical Design Department, Faculty of Engineering, Mansoura University, Mansoura 35516, Egypt
* Correspondence: farhanali.ali15@gmail.com

Citation: Deepthi, V.V.L.; Lashin, M.M.A.; Ravi Kumar, N.; Raghunath, K.; Ali, F.; Oreijah, M.; Guedri, K.; Tag-ElDin, E.S.M.; Khan, M.I.; Galal, A.M. Recent Development of Heat and Mass Transport in the Presence of Hall, Ion Slip and Thermo Diffusion in Radiative Second Grade Material: Application of Micromachines. *Micromachines* **2022**, *13*, 1566. https://doi.org/10.3390/mi13101566

Academic Editor: Kwang-Yong Kim

Received: 18 August 2022
Accepted: 15 September 2022
Published: 21 September 2022

Publisher's Note: MDPI stays neutral with regard to jurisdictional claims in published maps and institutional affiliations.

Abstract: This article describes the incompressible two-dimensional heat and mass transfer of an electrically conducting second-grade fluid flow in a porous medium with Hall and ion slip effects, diffusion thermal effects, and radiation absorption effects. It is assumed that the fluid is a gray, absorbing–emitting but non-scattering medium and the Rosseland approximation is used to describe the radiative heat flux in the energy equation. It is assumed that the liquid is opaque and absorbs and emits radiation in a manner that does not result in scattering. It is considered an unsteady laminar MHD convective rotating flow of heat-producing or absorbing second-grade fluid across a semi-infinite vertical moving permeable surface. The profiles of velocity components, temperature distribution, and concentration are studied to apply the regular perturbation technique. These profiles are shown as graphs for various fluid and geometric parameters such as Hall and ion slip parameters, radiation absorption, diffusion thermo, Prandtl number, Schmidt number, and chemical reaction rate. On the other hand, the skin friction coefficient and the Nusselt number are determined by numerical evaluation and provided in tables. These tables are then analysed and debated for various values of the flow parameters that regulate it. It may be deduced that an increase in the parameters of radiation absorption, Hall, and ion slip over the fluid region increases the velocity produced. The resulting momentum continually grows to a very high level, with contributions from the thermal and solutal buoyancy forces. The temperature distribution may be more concentrated by raising both the heat source parameter and the quantity of radiation. When one of the parameters for the chemical reaction is increased, the whole fluid area will experience a fall in concentration. Skin friction may be decreased by manipulating the rotation parameter, but the Hall effect and ion slip effect can worsen it. When the parameter for the chemical reaction increases, there is a concomitant rise in the mass transfer rate.

Keywords: diffusion thermo effect; radiation absorption; porous media; Hall and ion slip effects

1. Introduction

A few decades ago, the majority of academics focused more of their attention on MHD fluid flow difficulties. Still, they overlooked the Hall current and the Ion-slip current in Ohm's law. The flow of MHD heat and mass transfer in the presence of a high magnetic field is essential in solving a wide variety of engineering issues, including those involving astronomy, chemical engineering, and geophysics. There is a good chance that Hall and ion-slip currents play an essential role in the flow of laboratory plasma. As a result, a recent suggestion has been made to investigate the heat and mass transfer of a free-convection MHD flow that goes through an infinite vertical porous plate while considering Hall and ion slip currents. Recent research on magnetohydrodynamic (MHD)-driven flows, on the other hand, is focused on the firm application of a magnetic field since this causes many other complicated phenomena, such as the Hall current, ion slip, Joule heating, and so on (Sutton and Sherman [1]). This application's relevance may be observed in many different engineering processes, such as magnetic fusion systems, energy generators, Hall sensors, and Hall accelerators, as well as in specific astrophysical applications. Abo-Eldahab et al. [2] investigated the combined effects of the hall and ion-slip currents on free convective flow across a semi-infinite vertical plate. Ref. [2] Srinivasacharya and Kaladhar [3] used the homotopy analysis method to investigate the effect of Hall and Ion-slip currents on fully developed electrically conducting fluid flow between vertical parallel plates in the presence of a temperature-dependent heat source. This study was conducted in the presence of a temperature-dependent heat source. After that, Darbhasayanam et al. [4] looked at how Hall and ion slip currents affect the flow of electrically conducting couple stress fluid between two circular cylinders when a temperature-dependent heat source is present. Tani [5] researched the steady motion of an electrically conducting viscous liquid in the presence of Hall current. Motsa and Shateyi [6] performed a numerical analysis on magnetomicropolar fluid flow, heat and mass transfer with suction through porous material to determine the impacts of Hall currents, ion-slip currents, and changing thermal diffusivity on these processes. Attia [7] used an analytical approach to research the flow of a dusty fluid when Hall and ion slip current were present. The flow of a magnetohydrodynamic boundary layer was examined by Ghosh [8] across a stretched sheet while a chemical reaction was taking place. The chemically reactive second grade via porous saturated space was investigated by Raghunath et al. [9] using a perturbation technique. Raghunath et al. [10] have investigated the effects of Soret, Rotation, Hall, and Ion Slip on the unsteady flow of a Jeffrey fluid through a porous medium. At the same time, heat is absorbed, and chemical reactions occur. Sibanda and Makinde [11] have investigated the hydromagnetic steady flow and heat transfer characteristics of an incompressible viscous electrically conducting fluid past a rotating disk in a porous medium with ohmic heating, Hall current and viscous dissipation.

The study of magnetohydrodynamics in the presence of heat and mass transfer, as well as radiation and diffusion, has captured the interest of a sizable number of academics as a result of the wide variety of applications it may be put to use. In the fields of astrophysics and geophysics, it is used to examine the structures of stars and the sun, radio transmission via the ionosphere, and other such phenomena. Its uses may be found in engineering, such as in MHD pumps, MHD bearings, and other places. The process of mass transfer is also quite prevalent in theoretical discussions on the structure of stars, and its effects may be noticeable on the sun's surface. The investigation of the impact of a magnetic field plays a significant role in free convection flow, particularly in the case of liquid metals, electrolytes, and ionized gases. The thermal physics of hydromagnetic issues with mass transport has vast implications in the field of power engineering. Various industrial and environmental activities involve the presence of radiative fluxes. A few examples of this are heating and cooling chambers, energy processes involving the burning of fossil fuels, evaporation from huge open water reservoirs, astrophysical flows, solar power technologies, and the re-entry of space vehicles. Seth and Sarkar [12] investigated the influence of an induced magnetic field on the hydromagnetic natural convection flow

of a chemically reacting fluid across a moving vertical plate with ramping wall temperature. The effects of an induced magnetic field on the flow of a free convective channel were studied by Sarveshanand and Singh [13]. Sarma and Pandit [14] investigated the effects of thermal radiation, chemical reactions, and generated magnetic fields on MHD mixed convection flow across a vertical porous plate. Following that, Ojjela et al. [15] investigated the effects that thermophoresis and an induced magnetic field had on a mixed convective Jeffrey fluid contained between two porous plates. Jha and Aina [16] show the interplay of conducting and non-conducting walls on the MHD natural convection flow in a vertical micro-channel with an induced magnetic field. Shaw et al. [17] have studied impact of Entropy Generation and Nonlinear Thermal Radiation on Darcy–Forchheimer Flow of $MnFe_2O_4$-Casson/Water Nanofluid due to a Rotating Disk. Very recently Sharma [18] has studied FHD flow and heat transfer over a porous rotating disk accounting for Coriolis force along with viscous dissipation and thermal radiation. Ram et al. [19] have possessed a Ferrofluid flow over a moving plate in a porous medium is theoretically investigated by solving the boundary layer equations with boundary conditions using Neuringer–Rosensweig model. Mahantesh et al. [20] have studied impacts of a novel exponential space dependent heat source on MHD slip flow of carbon nanoliquids past a stretchable rotating disk. The flow is created due to rotation and stretching of the disk. Vijay and Sharma [21] have studied heat and mass transfer of ferrofluid flow between corotating stretchable disks with geothermal viscosity.

The investigation of first-order chemical reactions that include simultaneous heat and mass transfer has attracted many researchers in recent years. It has been the focus of considerable stress in recent times. Evaporation at the surface of a water body and heat and mass transfer all take place concurrently in several different processes, including energy transfer in a wet cooling tower, flow in a desert cooler, and energy transfer in a desert cooler. Some of the uses of this flow may be found in many different sectors, such as the power industry. One of the techniques of producing electrical energy is to directly extract it from moving conducting fluid, which is one of the applications of this flow. Studying heat production or absorption in flowing fluids is vital in issues involving chemical processes that dissociate fluids. These problems may be broken down into two categories: The effects that the creation of heat might cause could potentially change the temperature distribution and, as a result, the pace at which particles are deposited in nuclear reactors, electronic chips, and semiconductors wafers. It is interesting to study the effects of a magnetic field on the temperature distribution and heat transfer when the fluid is not only an electrical conductor but also capable of emitting and absorbing radiation because some fluids are also capable of emitting and absorbing thermal radiation. Because of this, heat transmission through thermal radiation is becoming more significant as we become more concerned with space applications and higher operating temperatures. Recent research conducted by Raghunath and colleagues [22–24] investigated the impact of chemical reactions on different flow geometries. The effects of Soret on the unsteady free convection flow of a viscous incompressible fluid through a porous medium with high porosity bounded by a vertical infinite moving plate have been discussed by Ramachandra et al. [25]. This flow occurs under thermal diffusion, a chemical reaction, and a heat source. Raghunath and Mohanaramana [26] have researched Hall, Soret, and rotational effects on unsteady MHD rotating flow of a second-grade fluid through a porous media in the presence of chemical reaction and aligned magnetic field. Their findings were published not too long ago.

In the fields of geophysics, petrochemical engineering, meteorology, oceanography, and aeronautics, the notion of fluid flow, heat and mass transfer inside a rotating environment plays a very significant part in the applications of these sciences. Applications in geophysics and fluid engineering are where the impetus for scientific study on rotating fluid systems first began. This is where the field has been propelled forward. The effect of rotation significantly impacts the motion of the atmospheres of both planets and the earth. This has implications for several different elements of atmosphere motion. The theory of

rotational flow is used for figuring out the fluid's viscosity, constructing centrifugal devices like the turbine, and other similar activities. Ali et al. [27] have studied Saleel, Entropy Generation Analysis of Peristaltic Flow of Nanomaterial in a Rotating Medium through Generalized Complaint Walls of Micro-Channel with Radiation and Heat Flux Effects. Ali et al. [28] have analyzed the slippage phenomenon in hydromagnetic peristaltic rheology with Hall current and viscous dissipation. Awais et al. [29] possessed Convective and peristaltic viscous fluid flow with variable viscosity, J. Engin. Thermophys. Ali et al. [30] investigated Oscillatory Flow in a Porous Channel with Porous Medium and Small Suction. Ali et al. [31] have studied Oscillatory flow of second grade fluid in cylindrical tube. Ilya et al. [32] have possessed Heat source and sink effects on periodic mixed convection flow along the electrically conducting cone inserted in porous medium.

Raghunath et al. [10] conducted research not too long ago in which they studied the effect of Hall and ion-slip currents on the unsteady MHD flows of a viscous, incompressible, and electrically conducting fluid that was occurring between two vertical plates in a rotating system when the lower plate was impulsively started. The work done by Raghunath et al. [10] for the diffusion thermal and Second grade fluid cases will be extended even further with the help of this effort. After obtaining the flow equations in a dimensionless form using the perturbation technique, the flow equations are then analytically solved under the appropriate conditions. The graphical representation and subsequent discussion of the influence of various flow parameters on the fluid velocity, volume flow rate, and surface friction are shown below. The significance of the findings acquired from this research is that they provide the criteria for verifying the accuracy of various numerical or empirical methodologies. In addition, the results that were produced from this study have the potential to be used in the fields of fluid mechanics and heat transport.

2. Formulation of the Problem

We considered the heat and mass transfer of an unsteady two-dimensional MHD convective flow of a viscous laminar heat initiating second-grade liquid over a semi-infinite longitudinal moveable porous layer engrained in consistent permeable material. We adapted to a homogeneous transverse magnetic field. We do this while considering Hall and ion slip consequences. The Cartesian coordinate system is selected so that the x-axis is maintained along the wall in the direction of upward movement, and the z-axis is perpendicular to this orientation. A magnetic field with strength of B_0 and a uniform intensity is moving in a direction that is perpendicular to the flow. In their original, undisturbed states, the fluid and the plate are both rotating in a fixed orientation relative to the perpendicular to the plate at a constant angular velocity. At the surface, the temperature and concentration are subject to random fluctuations; this is true for both the fluid and the plate. The investigational challenge may be seen by looking at the physical model shown in Figure 1.

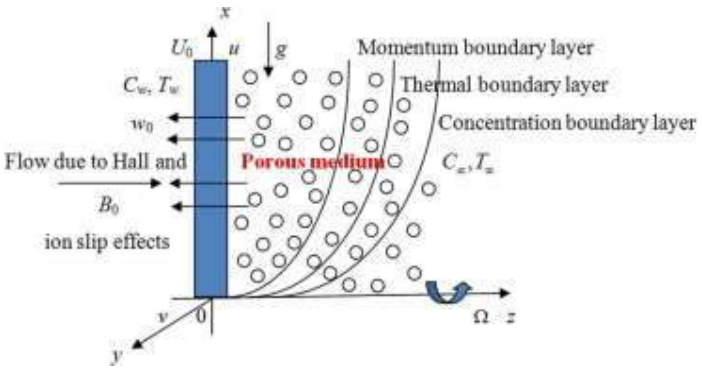

Figure 1. Flow diagram.

The fluid properties are assumed to be constant except that the influence of density variation with temperature has been considered only in the body-force term. The concentration of diffusing species is very small in comparison to other chemical species, the concentration of species far from the wall, C_α s infinitesimally small and hence the Soret and Dufour effects are neglected. The chemical reactions are taking place in the flow and all thermophysical properties are assumed to be constant of the linear momentum equation which is approximated according to the Boussinesq approximation. Due to the semiinfinite plane surface assumption, the flow variables are functions of z and the time t only. The flow governing equations and boundary conditions as followed by Raghunath et al. [10].

$$\frac{\partial u}{\partial x}+\frac{\partial u}{\partial y}=0 \tag{1}$$

$$\frac{\partial u}{\partial t}+w\frac{\partial u}{\partial z}-2\Omega v=-\frac{1}{\rho}\frac{\partial p}{\partial x}+\nu\frac{\partial^2 u}{\partial z^2}+\frac{\alpha}{\rho}\frac{\partial^3 u}{\partial z^2\partial t}+\frac{B_0 J_y}{\rho}-\frac{\nu}{k}u+g\beta(T-T_\infty^{**})+g\beta^*(C-C_\infty) \tag{2}$$

$$\frac{\partial v}{\partial t}+w\frac{\partial v}{\partial z}+2\Omega u=-\frac{1}{\rho}\frac{\partial p}{\partial y}+\nu\frac{\partial^2 v}{\partial z^2}+\frac{\alpha}{\rho}\frac{\partial^3 v}{\partial z^2\partial t}-\frac{B_0 J_x}{\rho}-\frac{\nu}{k}v \tag{3}$$

$$\frac{\partial T}{\partial t}+w\frac{\partial T}{\partial z}=\frac{k_1}{\rho C_p}\frac{\partial^2 T}{\partial z^2}-\frac{1}{\rho C_p}\frac{\partial q_r}{\partial z}-\frac{Q_0}{\rho C_p}(T-T_\infty)+Q_1(C-C_\infty)+\frac{DK_T}{C_s C_p}\frac{\partial^2 C}{\partial z^2} \tag{4}$$

$$\frac{\partial C}{\partial t}+w\frac{\partial C}{\partial z}=D\frac{\partial^2 C}{\partial z^2}-K_c(C-C_\infty) \tag{5}$$

The proper boundary requirements for the velocity, temperature, and concentration distributions are provided if the assumptions outlined above hold.

$$u=U_0,\quad v=0,\ T=T_w+\varepsilon(T_w-T_\infty)e^{iwt},\ C=C_w+\varepsilon(C_w-C_\infty)e^{iwt}\ \text{ at } z=0 \tag{6}$$

$$u\to U_\infty,\ \ v\to 0,\ \ T\to T_\infty \qquad C\to C_\infty \qquad \text{as} \quad z\to\infty \tag{7}$$

In light of the fact that the solution to the continuity equation is either a constant or a function of time, we will assume that.

$$w=-w^1{}_0(1+A\varepsilon e^{iwt}) \tag{8}$$

where A is a real positive constant, ε and Aε are small, less than unity, w_0 is the scale of the suction velocity which has a non-zero positive constant.

The Rosseland approximation can be used for the radiative heat flux vector q_r because, for an optically thick fluid, in addition to emission, there is also self-absorption. Since the absorption coefficient is typically wavelength dependent and significant, we can use the Rosseland approximation. Therefore, q_r may be deduced from

$$q_r=\frac{-4\sigma_1}{3k_1}\frac{\partial^2 T^4}{\partial z} \tag{9}$$

where k_1 is the Rosseland mean absorption co-efficient and σ_1 is the Stefan–Boltzmann constant.

We assume that the temperature differences within the flow are sufficiently small so that T^4 can be expressed as a linear function. Using Taylor's series, we expand T^4 to the free stream temperature T and neglect higher order terms. This results in the following approximation:

$$T^4 \approx 4T_\infty^3 T - 3T_\infty^4 \tag{10}$$

As a result, we have

$$\frac{\partial q_r}{\partial z} = \frac{-16\sigma_1 T_\infty^3}{3k_1}\frac{\partial^2 T}{\partial z^2} \tag{11}$$

Equation (4), derived from Equations (10) and (11), may be simplified to

$$\frac{\partial T}{\partial t} + w\frac{\partial T}{\partial z} = \frac{k_1}{\rho C_p}\frac{\partial^2 T}{\partial z^2} - \frac{Q_0}{\rho C_p}(T - T_\infty) + \frac{1}{\rho C_p}\frac{16\sigma_1 T_\infty^3}{3k_1}\frac{\partial^2 T}{\partial z^2} + Q_1(C - C_\infty) + \frac{DK_T}{C_s C_p}\frac{\partial^2 C}{\partial z^2} \tag{12}$$

Because it is presumed that the frequency of electron–atom collisions is very high, it is impossible to ignore Hall and ion slip currents. Therefore, the velocity in the y-direction is caused by Hall currents and ion slip currents. When the magnitude of the magnetic field is exceptionally great, the generalised law of Ohm is adjusted such that it takes into account the Hall effect as well as the ion slip effect (Sutton and Sherman [1]),

$$J = \sigma\left(E + V \times B\right) - \frac{\omega_e \tau_e}{B_0}\left(J \times B\right) + \frac{\omega_e \tau_e \beta_i}{B_0^2}\left(\left(J \times B\right) \times B\right) \tag{13}$$

Further it is assumed that $\beta_e = \omega_e \tau_e \sim O(1)$ and $\beta_i = \omega_i \tau_i \ll 1$, In the Equation (13) the electron pressure gradient, the ion-slip and thermo-electric effects are neglected. We also assume that the electric field $E = 0$ under assumptions reduces to

$$\left(1 + \beta_i \beta_e\right) J_x + \beta_e J_y = \sigma B_0 v \tag{14}$$

$$\left(1 + \beta_i \beta_e\right) J_y + \beta_e J_x = -\sigma B_0 v \tag{15}$$

On solving above Equations (14) and (15), we get

$$J_x = \sigma B_0\left(\alpha_2 u + \alpha_1 v\right) \tag{16}$$

$$J_y = -\sigma B_0\left(\alpha_2 v - \alpha_1 u\right) \tag{17}$$

$$Where\ \alpha_1 = \frac{1 + \beta_e \beta_i}{\left(1 + \beta_e \beta_i\right)^2 + \beta_e^2}, \alpha_2 = \frac{\beta_e}{\left(1 + \beta_e \beta_i\right)^2 + \beta_e^2}$$

when Equations (16) and (17) are introduced into (2) and (3), respectively, the equations that are produced are,

$$\frac{\partial u}{\partial t} + w\frac{\partial u}{\partial z} - 2\Omega v = -\frac{1}{\rho}\frac{\partial p}{\partial x} + v\frac{\partial^2 u}{\partial z^2} + \frac{\alpha}{\rho}\frac{\partial^3 u}{\partial z^2 \partial t} + \frac{\sigma B_0^2\left(\alpha_2 v - \alpha_1 u\right)}{\rho} - \frac{v}{k}u + g\beta(T - T_\infty^{\cdot\cdot}) + g\beta^*(C - C_\infty) \tag{18}$$

$$\frac{\partial v}{\partial t} + w\frac{\partial v}{\partial z} + 2\Omega u = -\frac{1}{\rho}\frac{\partial p}{\partial y} + v\frac{\partial^2 v}{\partial z^2} + \frac{\alpha}{\rho}\frac{\partial^3 v}{\partial z^2 \partial t} - \frac{\sigma B_0^2\left(\alpha_2 u + \alpha_1 v\right)}{\rho} - \frac{v}{k}v \tag{19}$$

Fusing Equations (2) and (3), let $q = u + iv$ and $\xi = x - iy$, we obtain

$$\frac{\partial q}{\partial t} + w\frac{\partial q}{\partial z} + 2i\Omega q = -\frac{1}{\rho}\frac{\partial p}{\partial \xi} + v\frac{\partial^2 q}{\partial z^2} + \frac{\alpha}{\rho}\frac{\partial^3 q}{\partial z^2 \partial t} + \frac{\sigma B_0^2\left(\alpha_2 v - \alpha_1 u\right)}{\rho} - \frac{v}{k}q + g\beta(T - T_\infty^{\cdot\cdot}) + g\beta^*(C - C_\infty) \tag{20}$$

Beyond the border layer, Equation (20) provides

$$-\frac{1}{\rho}\frac{\partial p}{\partial \xi}=\frac{dU_\infty}{\partial t}+\frac{v}{k}U_\infty+\frac{\sigma B_0^2}{\rho}U_\infty \tag{21}$$

To standardise the mathematical representation of the physical issue, we will introduce the non-dimensional quantities and parameters listed below.

$$\begin{aligned}
&q^*=\frac{q}{w_0}, w^*=\frac{w}{w_0},\ z^*=\frac{w_0 z}{v},\ U_0^*=\frac{U_0}{w_0}, U_\infty^*=\frac{U_\infty}{w_0},\ t^*=\frac{t\,w_0^2}{v}, \theta=\frac{T-T_\infty}{T_w-T_\infty}, \phi=\frac{C-C_\infty}{C_w-C_\infty},\\
&M^2=\frac{\sigma B_0^2 v}{\rho w_0^2}, \Pr=\frac{v\,\rho C_p}{k_1}=\frac{v}{\alpha}, r=\frac{vg\beta(T_w-T_\infty)}{w_0^3}, Gm=\frac{vg\beta^*(C_w-C_\infty)}{w_0^3},\\
&K=\frac{w_0^2 k}{v^2}, Sc=\frac{v}{D}, R=\frac{\Omega v}{w_0^2}, H=\frac{vQ_0}{\rho C_p w_0^2}, S=\frac{w_0^2\,\alpha_1}{\rho v^2},\ K_c=\frac{K_c v}{w_0^2}, F=\frac{16\sigma^* T_\infty^3}{3kk_1}\\
&Du=\frac{DK_T}{vC_sC_p}\frac{(C_w-C_\infty)}{(T_w-T_\infty)}, Q_1=\frac{vQ_1(C_w-C_\infty)}{(T_w-T_\infty)w_0^2}
\end{aligned} \tag{22}$$

By exploiting variables that are not dimensional, the three governing Equations (5), (12), and (20), reduced to

$$\frac{\partial q}{\partial t}-(1+A\varepsilon e^{iwt})\frac{\partial q}{\partial z}=\frac{dU_\infty}{dt}+\frac{\partial^2 q}{\partial z^2}+S\frac{\partial^3 q}{\partial z^2\partial t}-\lambda q+Gr\,\theta+Gm\,\phi \tag{23}$$

$$Where\,\lambda=M^2(\alpha_1+i\alpha_2)+2iR+\frac{1}{K}$$

$$\frac{\partial \theta}{\partial t}-(1+A\varepsilon e^{iwt})\frac{\partial \theta}{\partial z}=-\frac{(1+F)}{\Pr}\frac{\partial^2\theta}{\partial z^2}-H\,\theta+Q_1\phi+D_u\frac{\partial^2\phi}{\partial z^2} \tag{24}$$

$$\frac{\partial \phi}{\partial t}-(1+A\varepsilon e^{iwt})\frac{\partial \phi}{\partial z}=\frac{1}{Sc}\frac{\partial^2\phi}{\partial z^2}-K_c\phi \tag{25}$$

The equations that relate to the boundary conditions are as follows:

$$q=U_0,\ \ \theta=1+\varepsilon e^{iwt},\ \phi=1+\varepsilon e^{iwt} \qquad \text{at } z=0 \tag{26}$$

$$q=0,\ \ \theta=0,\ \ \phi=0 \qquad \text{as} \quad z\to\infty \tag{27}$$

3. Solution of the Problem

The expressions (23) and (25) portray a set of partial differential equations that cannot be solved in closed form; nonetheless, if the equations can be reduced to a set of ordinary differential equations in dimensionless form, then the equations can be solved analytically. This can be accomplished by expressing the velocity, temperature, and concentration as,

$$q=q_0(z)+\varepsilon e^{nt}q_1(z)+O(\varepsilon^2) \tag{28}$$

$$\theta=\theta_0(z)+\varepsilon e^{nt}\theta_1(z)+O(\varepsilon^2) \tag{29}$$

$$\phi=\phi_0(z)+\varepsilon e^{nt}\phi_1(z)+O(\varepsilon^2) \tag{30}$$

The following pairs of equations are obtained by substituting the Equations (28)–(30) into the Equations (23)–(25) by equating the harmonic and non-harmonic components, as well as the neglecting and higher order terms of, and by obtaining the following:

$$\frac{\partial^2 q_0}{\partial z^2}+\frac{\partial q_0}{\partial z}-\lambda q_0=-Gr\,\theta_0-Gm\,\phi_0 \tag{31}$$

$$(1+Siw)\frac{\partial^2 q_1}{\partial z^2}+\frac{\partial q_1}{\partial z}-(\lambda+iw)q_1=-Gr\,\theta_1-Gm\,\phi_1-A\frac{\partial q_0}{\partial z} \tag{32}$$

$$\frac{\partial^2 \theta_0}{\partial z^2}+\Pr\frac{\partial \theta_0}{\partial z}-(H+F)\Pr\theta_0=-\Pr\left(Q_1\phi_0+D_u\frac{\partial^2\phi_0}{\partial z^2}\right) \tag{33}$$

$$\frac{\partial^2 \theta_1}{\partial z^2}+\Pr\frac{\partial \theta_1}{\partial z}-(iw+H+F)\Pr\theta_1=-\Pr\left(A\frac{\partial \theta_0}{\partial z}+Q_1\phi_1+D_u\frac{\partial^2\phi_1}{\partial z^2}\right) \tag{34}$$

$$\frac{\partial^2 \phi_0}{\partial z^2}+Sc\frac{\partial \phi}{\partial z}-Sc\,Kc\,\phi_0=0 \tag{35}$$

$$\frac{\partial^2 \phi_1}{\partial z^2}+Sc\frac{\partial \phi_1}{\partial z}-(iw+K_c)Sc\,\phi_1=-A\,Sc\frac{\partial \phi_0}{\partial z} \tag{36}$$

The requirements that relate to each border are as follows:

$$q_0=U_0, q_1=0,\ \ \theta_0=1,\ \theta_1=1, \phi_0=1,\ \phi_1=1 \qquad \text{at } z=0 \tag{37}$$

$$q_0=0, q_1=0,\ \ \theta_0=0,\ \theta_1=0, \phi_0=0,\ \phi_1=0 \qquad \text{as} \quad z\to\infty \tag{38}$$

By applying the initial conditions (37) and (38) and then solving Equations (31)–(36), one obtains the following approach:

$$\varphi_0=\exp(-m_1 z) \tag{39}$$

$$\varphi_1=b_1\exp(-m_1 z)+b_2\exp(-m_2 z) \tag{40}$$

$$\theta_0=b_3\exp(-m_1 z)+b_4\exp(-m_3 z) \tag{41}$$

$$\theta_1=b_5\exp(-m_1 z)+b_6\exp(-m_2 z)+b_7\exp(-m_3 z)+b_8\exp(-m_4 z) \tag{42}$$

$$q_0=b_9\exp(-m_1 z)+b_{10}\exp(-m_3 z)+b_{11}\exp(-m_5 z) \tag{43}$$

$$q_1=b_{12}\exp(-m_1 z)+b_{13}\exp(-m_2 z)+b_{14}\exp(-m_3 z)+b_{15}\exp(-m_4 z)+ b_{16}\exp(-m_5 z)+b_{17}\exp(-m_6 z) \tag{44}$$

Substituting Equations (39)–(44) into Equations (28)–(30), we acquire the velocity temperature and concentration

$$q=b_9\exp(-m_1 z)+b_{10}\exp(-m_3 z)+b_{11}\exp(-m_5 z)+ \varepsilon e^{iwt}\begin{pmatrix} b_{12}\exp(-m_1 z)+b_{13}\exp(-m_2 z)+b_{14}\exp(-m_3 z)+\\ b_{15}\exp(-m_4 z)+b_{16}\exp(-m_5 z)+b_{17}\exp(-m_6 z)\end{pmatrix} \tag{45}$$

$$\theta=b_3\exp(-m_1 z)+b_4\exp(-m_3 z)+\varepsilon e^{iwt}\,(b_5\exp(-m_1 z)+b_6\exp(-m_2 z)+b_7\exp(-m_3 z)+b_8\exp(-m_4 z)) \tag{46}$$

$$\phi = \exp(-m_1 z) + \varepsilon e^{iwt} \left(b_1 \exp(-m_1 z) + b_2 \exp(-m_2 z)\right) \tag{47}$$

For this particular boundary layer flow, the skin friction co-efficient, the Nusselt number, and the Sherwood number are all crucially significant physical characteristics. The following is a definition and determination of each of these parameters:

3.1. Skin Friction

Very important physical parameter at the boundary is the skin friction which is given in the non-dimensional form and derives as

$$\tau = \left(\frac{\partial q}{\partial z}\right)_{z=0} = -\left(\left(b_9 m_1 + b_{10} m_3 + b_{11} m_5\right) + \varepsilon e^{iwt} \begin{pmatrix} b_{12} m_1 + b_{13} m_2 + \\ b_{14} m_3 + b_{15} m_4 + b_{16} m_5 + b_{17} m_6 \end{pmatrix}\right) \tag{48}$$

3.2. Nusselt Number

Another physical parameter like rate of heat transfer, in the form of Nusselt number, is expressed by

$$Nu = -\left(\frac{\partial \theta}{\partial z}\right)_{z=0} = \left(\left(b_3 m_1 + b_4 m_3\right) + \varepsilon e^{iwt} \left(b_5 m_1 + b_6 m_2 + b_7 m_3 + b_8 m_4\right)\right) \tag{49}$$

3.3. Sherwood Number

The rate of mass transfer in the form of Sherwood number is also derived by

$$Sh = -\left(\frac{\partial \phi}{\partial z}\right)_{z=0} = m_1 + \varepsilon e^{iwt} \left(b_1 m_1 + b_2 m_2\right) \tag{50}$$

4. Results and Discussion

The present investigation aims to investigate the effects of radiation absorption, Hall, and ion slip on the uncertain free convective flow of an electrically conducting fluid that is viscous and incompressible over an unbounded vertical porous plate. At the same time, a uniform transverse magnetic field is present. A regular perturbation approach is used to find solutions to the governing equations of the flow field when the Eckert number Ec is small. The closed-form solutions for the velocity, temperature, and concentration have been derived analytically. Its behaviour is computationally addressed concerning various flow characteristics such as the Hartmann number (M), the Hall parameter (e), the ion slip parameter (e), the thermal Grashof number (Gr), the mass Grashof number (Gm), the permeability of porous media (K), the radiation absorption criterion (Q_1), the diffusion thermo criterion (Du), the Prandtl number (Pr). For computational intention, we are setting up the values A = 2, ε = 0:001; U_0 = 0.1, while the parameters being M = 2, K = 0.5, R = 1, S = 0.5, Gr = 5, Gm = 3, be = 1, bi = 0.2, Pr = 0.71, H = 1, Sc = 0.22, Kc = 1, Du = 2, Q_1 = 0.5, t = 2 fixed over the range. Figures 2–18 are shown here, with their respective velocities, temperatures, and concentrations represented as distributions. The stresses, Nusselt number, and Sherwood number at the plate are analyzed numerically, explained with governing factors, and summarized in the Tables 1–3. The outcomes of this investigation, as indicated in Table 4, are consistent with the findings of the prior study [10], which Raghunath and his colleagues conducted.

Figures 2 and 3 illustrate the consequences of the thermal buoyancy force, denoted by Gr, and the concentration buoyancy force, characterized by Gm. Increasing the thermal and mass Grashof numbers causes fluid velocity in the principal flow direction inside the boundary layer area. This is the case regardless of whether the Grashof number is increased. This is because an increase in both the thermal and the solutal Grashof number causes a rise in buoyancy effects, and these effects cause more flow in the direction that is

already the dominant flow. There is a reverse flow occurring in the direction of the secondary flow. When the temperature and concentration of Grashof numbers are increased, the secondary velocity profiles rise in the boundary layer area further away from the plate. At the same time, they fall closer to the plate. It should also be observed that there is no reversal flow in the secondary flow direction when neither heat nor concentration buoyancy forces are present. This is something that should be taken into consideration. This indicates that the forces associated with buoyancy and the movements of the free stream are to blame for the induction of reverse flow.

We see a decrease in the size of the velocity components u and v, as well as a reduction of the velocity of resultant velocity when the strength of the magnetic field is increased, as shown in Figure 4. Because the effects of a transverse magnetic field on an electrically conducting fluid generate a piezoresistive force (also known as the Lorentz force), which is analogous to the drag force, growing M causes the drag force to raise, which in turn causes the motion of the fluid to slow down as a direct result of the increased drag force. As the passage of time causes the permeability factor (K) to grow, Figure 5 demonstrates that the subsequent velocity component u becomes more concentrated while increasing in height. When K is made higher, the consequent velocity is also pushed higher, increasing the thickness of the momentum boundary layer. A decrease in porosity leads to an increase in fluid speed that is less visible once measured within the flow zone filled by the liquid.

Both Figures 6 and 7 illustrate how the Hall current parameters, denoted by (βe), and the ion-slip parameter, denoted by (βi), affect the fluid velocity. It is clear from looking at Figures 4 and 5 that as the Hall and ion-slip parameters are increased, the fluid velocity in the primary flow direction decreases in the boundary layer region that is close to the plate, but it increases in the boundary layer region that is further away from the plate. This phenomenon can be seen in both of these figures. The fluid velocity in the secondary flow direction increases everywhere in the boundary layer area due to an increase in the hall parameter, except for a narrow region where it disappears. This is because the Hall current is generated as a result of the spiralling of conducting fluid particles around magnetic lines of force, which have the potential to create secondary motion in the flow field. The nature of the ion-slip current on the fluid flow in the secondary flow direction is shown to be the exact opposite of that of the Hall current.

The influence of the diffusion thermo specification can be seen in Figures 8 and 9, which depict the velocity and temperature profiles, respectively. Figure 8 demonstrates the effect of the Dufour number on the primary and secondary velocities, which may be found on this page. It shows that greater values of the Dufour number cause the initial momentum to increase, but it indicates that the behaviour of the second velocity is the exact reverse of what one would expect. This pattern is a direct result of the generation of energy flow, which makes it possible for the rate of motion to pick up speed. Figure 9 makes it clear that an elevation in the values of the Dufour number leads to an accompanying rise in the temperature of the fluid. This is shown by the fact that an increase in the importance of the Dufour number can be seen. The generation of energy flow, which causes a temperature rise, is responsible for this occurrence.

The impact of the radiating absorption characteristic is seen in Figure 10 in both the primary and secondary velocity directions. According to the statistics, the main velocity graphs increase when there is an increase in radiating absorption. Still, the secondary velocity graphs go down when there is a drop in radiating absorptions over the whole liquid region. It was interesting to see how an increase in the radiating absorption characteristics might result in a rise in velocity. Inside the border layers, a description of the effects of the radiation-absorption parameter on the temperatures is depicted. As seen in Figure 11, it has become abundantly clear that the temperature distributions are rising functions of the absorbed radiation. In contrast, the inverse pattern was found when the rotation parameter was used, as shown in Figure 12.

The influence of the radiation factor on the velocity and temperature is shown in Figures 13 and 14. It is clear from looking at Figure 13 shows that a rise in the radiation parameter causes a decrease in the essential velocity, but it has the opposite effect on the secondary velocity. As a consequence of this, the resulting velocity decreases as the value of R increases over the whole of the area that is occupied by the fluid. The influence of the thermal radiation parameter is quite essential when it comes to temperature profiles. It has been discovered that there is a negative correlation between the increase in the radiation parameter and the temperature (Figure 14). As a result of the action of the radiation parameter, it is also possible to observe that the thickness of the thermal boundary layer quickly decreases.

Figure 15 illustrates how the Prandtl number (Pr) influences temperature profiles when certain fluids are present. These fluids include hydrogen (Pr = 0.684), air (Pr = 0.71), carbon dioxide (Pr = 0.72), and water (Pr = 1.0). According to the data in this figure, a rise in the Prandtl number results in a drop in temperature over the whole flow field. This agrees with the theory that the thickness of the thermal boundary layer decreases as the Prandtl number increases. Figure 16 displayed the differences in temperature profiles that resulted from using various values for the heat source specification H. Bringing down the temperature of the flow field, increasing the value of the heat source parameter. This may occur because of the fluid's elastic quality.

Figures 17 and 18 illustrate the chemical reaction parameter Kc's influence and the effect that the Schmidt number has on the concentration distribution. Figure 17 demonstrates an increase in the value of the parameter for the chemical reaction. The concentration profiles were quickly decreased due to Kc. As the number of chemically responsive factors increases, the number of chemical reactions that influence the quantities of solutal particles also increases, which causes the concentration domain to decrease. The end effect of the chemical reaction is a reduction in the breadth of the solute border stratum. In Figure 18, the concentration gradient is shown as having decreased over the whole flow field as the Schmidt number Sc increased. This demonstrates that heavier diffusing species have a higher impact on inhibiting the concentration dispersion of the flow field.

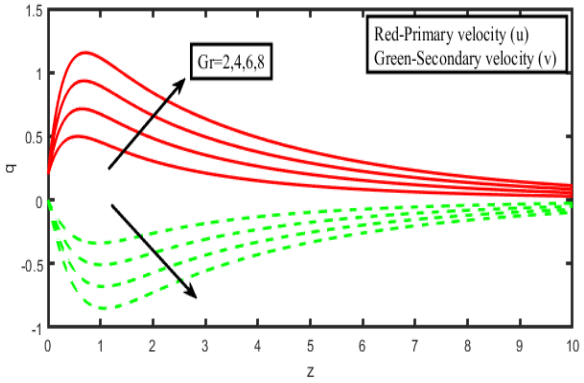

Figure 2. Velocity profiles for u and v for thermal Grashof number (Gr).

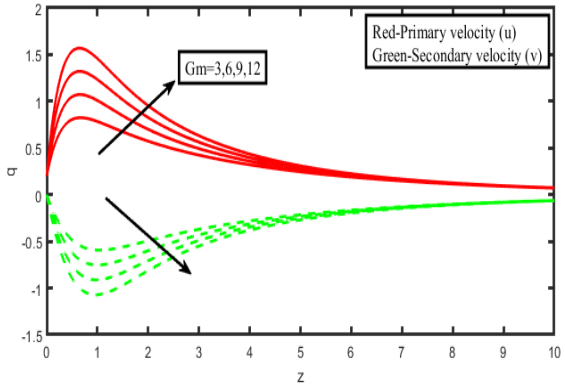

Figure 3. Velocity profiles for u and v for modified Grashof number (Gm).

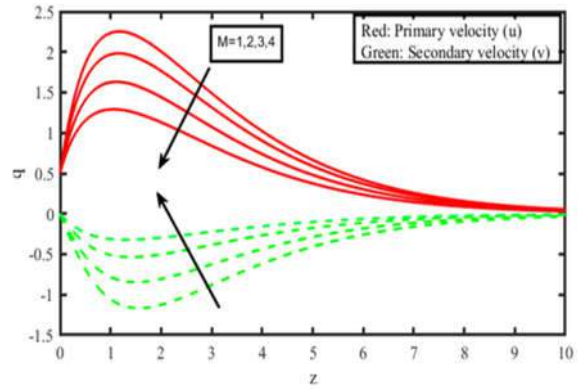

Figure 4. Velocity profiles for u and v for Magnetic field parameter (M).

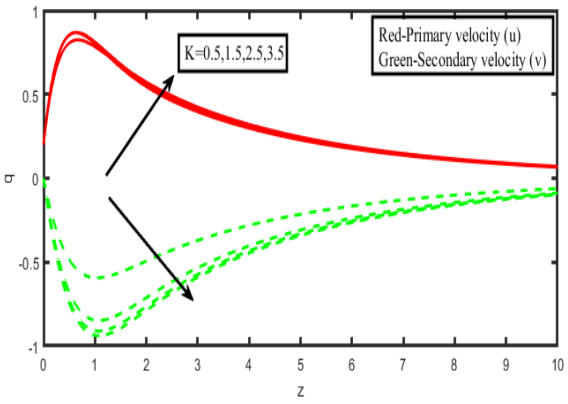

Figure 5. Velocity profiles for u and v for Permeability of porous media (K).

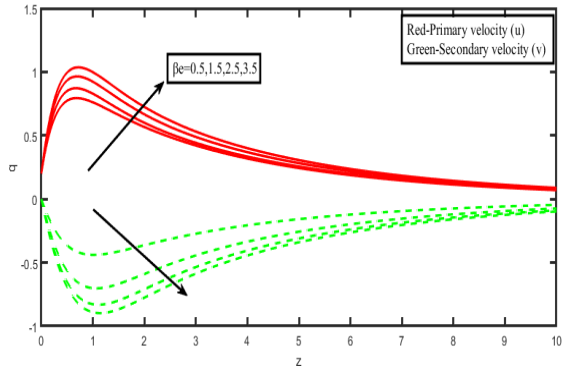

Figure 6. Velocity profiles for u and v for Hall parameter (β_e).

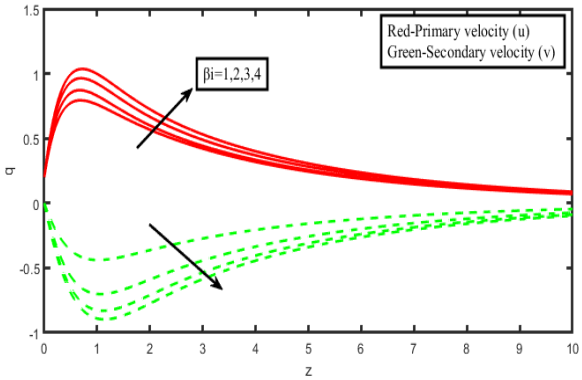

Figure 7. Velocity profiles for u and v for Hall parameter (β_i).

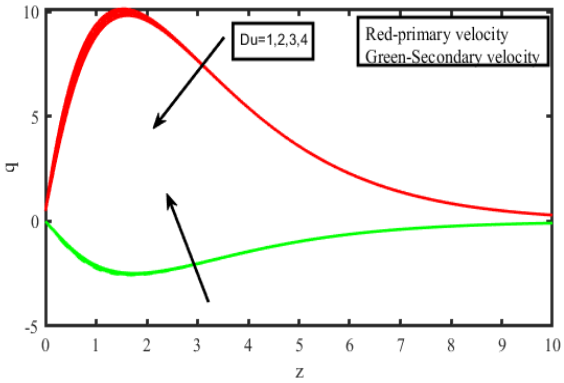

Figure 8. Velocity profiles for u and v for Diffusion thermo specification (D_u).

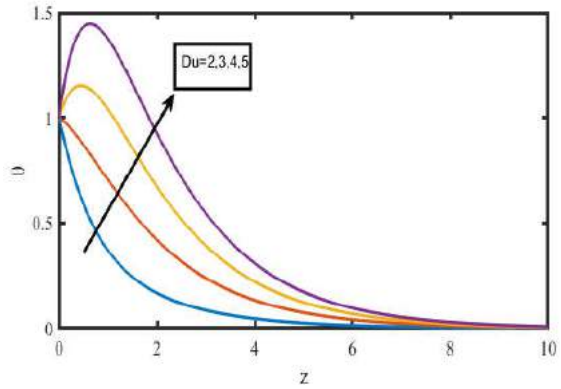

Figure 9. Temperature profiles for Diffusion thermo specification (D_u).

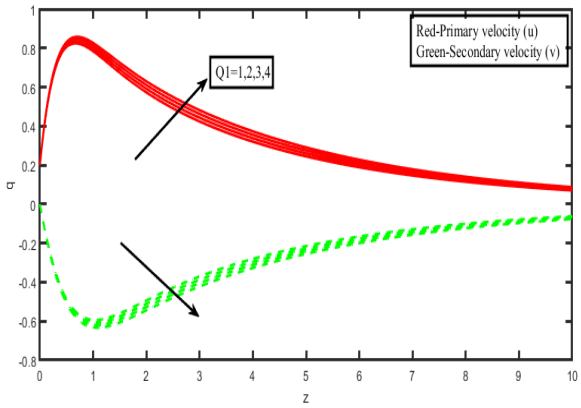

Figure 10. Velocity profiles for u and v for Radiation Absorption (Q_1).

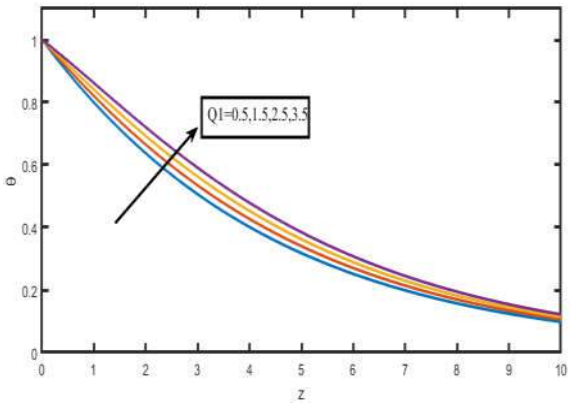

Figure 11. Temperature profiles for Radiation absorption (Q_1).

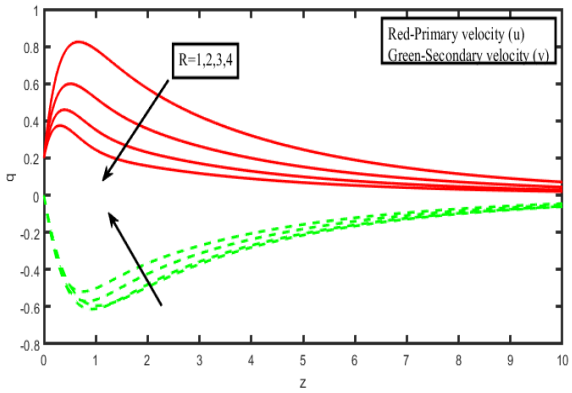

Figure 12. Velocity profiles for u and v for Rotation specification (R).

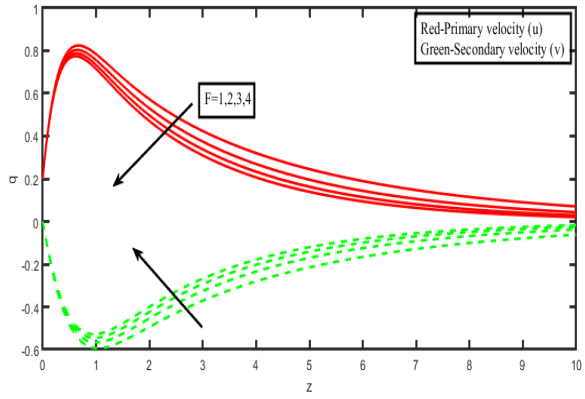

Figure 13. Velocity profiles for u and v for Radiation parameter (F).

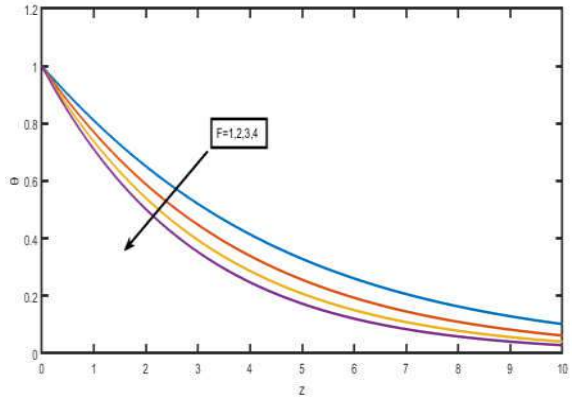

Figure 14. Temperature profiles for Radiation parameter (F).

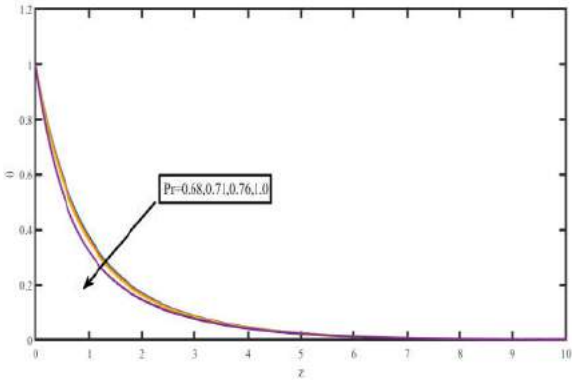

Figure 15. Temperature profiles for Prandtl number (Pr).

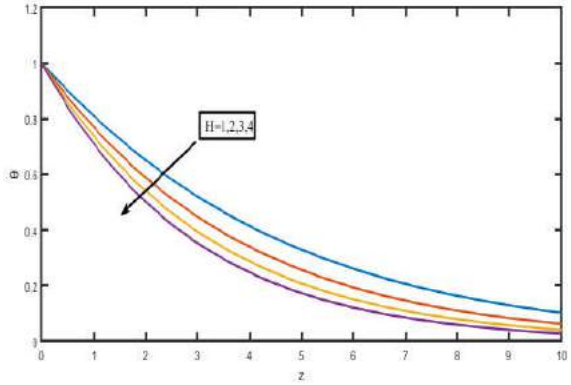

Figure 16. Temperature profiles for Heat absorption Parameter (H).

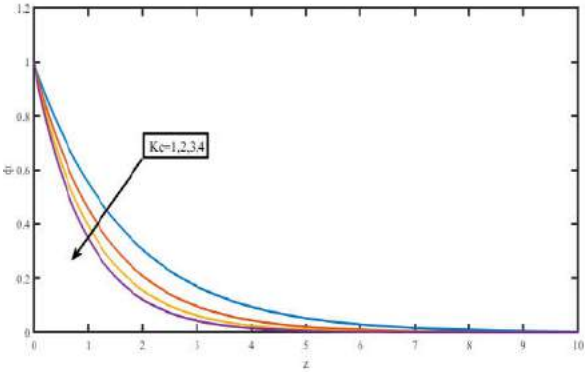

Figure 17. Concentration profiles for Chemical reaction (K_c).

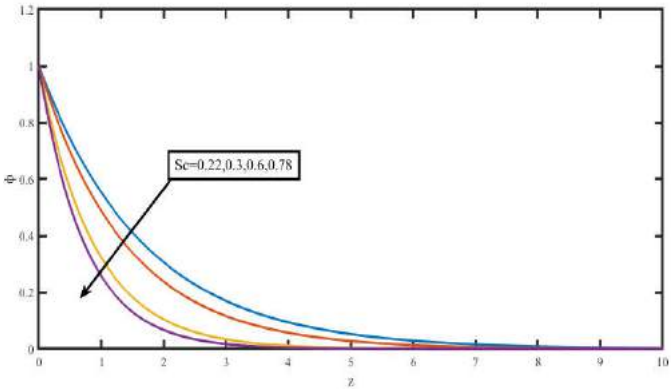

Figure 18. Concentration profiles for Schmidt number (S_c).

The values for the magnitudes of skin friction are summarized in Table 1, which may be found below. An increase in the Hartmann number will be introduced to decrease the amount of skin friction. This application uses second-grade fluid because of its elastic nature, which reduces the frictional drag caused by the liquid. It is explored what happens to similar behavior when the rotation factor, the Prandtl number, the heat source factor, the Schmidt number, the chemical reaction factor, and the amount of time are all enhanced. An increase in the permeability parameter or the second-grade fluid parameter will further improve the expansion of skin friction in intensity on the edge of the surface. The analogous activity is explored for the same when an increase in the thermal Grashof number, mass Grashof number, Hall and ion aspects that affect them are enhanced on the boundary of the surface.

As a consequence, a rise in the Nusselt number also results from an increase in the radiation parameter, the Prandtl number, and the heat source parameters, as shown in Table 2. The radiation absorption parameter and the frequency oscillations of the radiation need to be increased for it to be diminished. According to Table 3, an increase in the Schmidt number, the chemical reaction parameter, the frequency of fluctuations, or non-dimensional time all contribute to strengthening the Sherwood number as time proceeds. In Table 4 expressed as the results of the present study are pretty congruent with the findings of the previous study by Raghunath and colleagues [10]. Recently, investigations regarding nanomaterials are listed in Refs. [33,34].

Table 1. Skin friction.

Gr	Gm	βe	βi	Pr	H	Sc	Kc	R	Du	M	K	S	Q_1	τ
5	3	1	0.2	0.71	1	0.22	1	1	1	2	0.5	0.5	0.5	2.1521
5	3	1	0.2	0.71	1	0.22	1	1	1	3	0.5	0.5	1	2.7852
5	3	1	0.2	0.71	1	0.22	1	1	1	2	1.0	05	1	1.4521
5	3	1	0.2	0.71	1	0.22	1	1	1	2	1.5	0.5	1	3.7852
5	3	1	0.2	0.71	1	0.22	1	1	1	2	0.5	0.5	2	3.5211
5	3	1	0.2	0.71	1	0.22	1	1	1	2	0.5	1.0	3	2.0332
5	3	1	0.2	0.71	1	0.22	1	1	1	2	0.5	1.5	1	2.7852
9	3	1	0.2	0.71	1	0.22	1	1	1	2	0.5	0.5	1	3.7852
12	3	1	0.2	0.71	1	0.22	1	1	1	2	0.5	0.5	1	2.7852
5	6	1	0.2	0.71	1	0.22	1	1	1	2	0.5	0.5	1	5.4621
5	9	1	0.2	0.71	1	0.22	1	1	1	2	0.5	0.5	1	3.3221
5	3	2	0.2	0.71	1	0.22	1	1	1	2	0.5	05	1	3.0214
5	3	3	0.2	0.71	1	0.22	1	1	1	2	0.5	0.5	1	4.7852
5	3	1	0.4	0.71	1	0.22	1	1	1	2	0.5	0.5	1	2.0324
5	3	1	0.6	0.71	1	0.22	1	1	1	2	0.5	0.5	1	3.7852
5	3	1	0.2	5.0	1	0.22	1	1	1	2	0.5	0.5	1	3.0125
5	3	1	0.2	7.0	1	0.22	1	1	1	2	0.5	05	1	2.7852
5	3	1	0.2	0.71	2	0.22	1	1	1	2	0.5	0.5	1	1.3214
5	3	1	0.2	0.71	3	0.22	1	1	1	2	0.5	0.5	1	1.7852
5	3	1	0.2	0.71	1	0.25	1	1	1	2	0.5	0.5	1	2.7852
5	3	1	0.2	0.71	1	0.30	1	1	1	2	0.5	0.5	1	2.1255
5	3	1	0.2	0.71	1	0.22	2	1	1	2	0.5	05	1	2.7852
5	3	1	0.2	0.71	1	0.22	4	1	1	2	0.5	0.5	1	2.1254
5	3	1	0.2	0.71	1	0.22	1	2	1	2	0.5	0.5	1	2.7852
5	3	1	0.2	0.71	1	0.22	1	2	2	2	0.5	0.5	1	2.7852
5	3	1	0.2	0.71	1	0.22	1	2	3	2	0.5	0.5	1	2.6221

Table 2. Nusselt number.

F	Q_1	H	Pr	ω	Du	Nu
2	0.5	1	0.71	π/6	1	1.1251
3	0.5	1	0.71	π/6	1	1.7852
1	1	1	0.71	π/6	1	−0.12541
1	2	1	0.71	π/6	1	−1.65514
1	0.5	2	0.71	π/6	1	1.4521
1	0.5	3	0.71	π/4	1	1.4021
1	0.5	1	5.0	π/3	1	1.2785
1	0.5	1	7.0	π/6	1	1.3210
1	0.5	1	0.71	π/4	1	1.4521
1	0.5	1	0.71	π/3	1	1.0321
1	0.5	1	0.71	π/3	2	1.7520
1	0.5	1	0.71	π/3	3	1.0321

Table 3. Sherwood number.

Sc	Kc	ω	Sh
0.3	1	π/6	0.6521
0.6	1	π/6	0.9852
0.22	2	π/6	0.1201
0.22	3	π/6	0.5200

0.22	1	π/4	0.4520
0.22	1	π/3	1.4520

Table 4. Comparison of results for primary velocity (A = 5, n = 0.5, t = 0.5, ϵ = 0.01, U_0 = 0.5, Sc = 0.22, Kc = H = Q_1 = F = 1, Du = 0).

M	K	Gr	Gm	Previous Results Raghunath et al. [10]	Present Values
2	0.5	5	3	0.703484	0.752100
3				0.452455	0.452114
4				0.302545	0.302144
	1.0			0.797822	0.785210
	1.5			0.835478	0.842011
		8		0.934587	0.962214
		12		1.161458	1.122348
			5	0.780458	0.788752
			7	0.851458	0.852147

5. Conclusions

i. By increasing the magnetic field's strength, the rotating speed, or the properties of the second-grade fluid, the velocity produced may be reduced.
ii. Permeability of the porous medium may be enhanced to have the same effect as increases.
iii. The velocity is intended to decrease if the pore size of a porous medium decreases, which is the same behaviour seen in the case of radiation.
iv. An increase in the Hall parameter and the ion slip parameter over the fluid region contribute to the rise in the ultimately produced velocity.
v. The resultant velocity is affected by the thermal and solute buoyancy forces, and it will continue to increase in intensity until it hits a significant threshold.
vi. As the diffusion thermo and radiation absorption parameter, the resulting velocity and temperature.
vii. When both the heat source parameter and radiation increase, the temperature distribution becomes more concentrated. The fluid medium has decreased concentration due to the chemical reaction and the Schmidt number.

Author Contributions: Conceptualization, V.V.L.D. and M.M.A.L.; methodology, N.R.K.; software, N.R.K.; validation, M.I.K., K.R. and F.A.; formal analysis, M.O.; investigation, K.G.; resources, K.G.; data curation, M.I.K.; writing—original draft preparation, V.V.L.D.; writing—review and editing, E.S.M.T.-E.; visualization, A.M.G.; supervision, M.I.K.; project administration, M.M.A.L.; funding acquisition, E.S.M.T.-E. All authors have read and agreed to the published version of the manuscript.

Funding: The authors would like to thank the Deanship of Scientific Research at Umm Al-Qura University for supporting this work by Grant Code: 22UQU4331317DSR85. The authors express their gratitude to Princess Nourah bint Abdulrahman University Researchers Supporting Project (Grant No. PNURSP2022R152), Princess Nourah bint Abdulrahman University, Riyadh, Saudi Arabia.

Data Availability Statement: All the data are clearly available in the manuscript.

Conflicts of Interest: The authors declares no conflict of interest.

Nomenclature

x, y	dimensional co-ordinates (m)
u, v	velocity components along x,y directions (m/s)
A	real positive constant
B_0	applied magnetic field (A/m)
C	non- dimensional fluid concentration (kg/m^3)
C_P	specific heat at a constant pressure (J/kg. K)

C_w	the uniform concentration of the fluid at the plate (kg m^{-3})
C_∞	the concentration of the fluid far away from the plate (kg m^{-3})
D	coefficient of mass diffusivity (m^2/s)
D_M	Chemical molecular diffusivity; $m^{-2}{\cdot}s^{-1}$
g	acceleration due to gravity (m s^{-2})
Gr	thermal Grashof number
Gm	mass Grashof number
B	magnetic field vector (A/m)
E	electric field vector (c)
V	velocity vector (m/s)
Q_0	heat source parameter
J	current density vector (A/m^2)
J_x, J_y	current densities along x and y directions
k	permeability of porous medium (m^2)
k_1	thermal conductivity (W/m K)
K	permeability parameter
Kc	chemical reaction parameter (w/mk)
K_l	chemical reaction rate constant
m	Hall parameter
M	Hartmann number
N	constant
Nu	local Nusselt number
P_e	electron pressure (Pascal)
Pr	Prandtl number
q_m	local surface mass flux (kg s^{-1} m^{-2})
q_w	local surface heat flux (W m^{-2})
R	rotation parameter
S	second grade fluid
Sc	Schmidt number
Sh	local Sherwood number
Q_1	radiation absorption parameter
t	time (s)
T_w	the uniform temperature of the fluid at the plate (K)
T_∞	the temperature of the fluid far away from the plate (K)
u_0	plate velocity (m s^{-1})
w	slip velocity (m s^{-1})
w_0	scale of suction velocity
q_r	radiative heat flux

Greek symbols

β	coefficient of thermal expansion of the fluid
β*	coefficient of mass expansion of the solid
θ	non-dimensional temperature (K)
ϕ	non-dimensional concentration (mol/m^3)
ν	kinematic viscosity (m^2/s)
ρ	fluid density (Kg/m^3)
σ	electrical conductivity (S/m)
Ω	angular velocity (s^{-1})
τ_w	local wall shear stress (pascal)
τ	local skin friction coefficient
τ_e	electron collision time (s)
ω_e	cyclotron frequency (e/mB)

Subscripts and superscripts

e	electrons
i	ions
w	conditions on the wall
∞	free stream conditions

References

1. Sutton, G.W.; Sherman, A. *Engineering Magnetohydrodynamics*; McGraw-Hill Book Comp: New York, NY, USA, 1965.
2. Abo-Eldahab, E.M.; Aziz, M.A. Hall and ion-slip effects on MHD free convective heat generating flow past a semi-infinite vertical plate flat plate. *Phys. Scr.* **2000**, *61*, 344–348.
3. Srinivasacharya, D.; Kaladhar, K. Mixed convection flow of couple stress fluid between parallel vertical plates with Hall and Ion-slip effects. *Commun. Nonlinear Sci. Numer. Simul.* **2012**, *17*, 2447–2462.
4. Srinivasacharya, D.; Kaladhar, K. Analytical solution of mixed convection flow of couple stress fluid between two circular cylinders with Hall and ion-slip effects. *Turkish J. Eng. Env. Sci*. **2012**, *36*, 226–235.
5. Tani, I. Steady flow of conducting fluids in channels under transverse magnetic fields with consideration of Hall effects. *J. Aerosp. Sci.* **1962**, *29*, 297–305.
6. Motsa, S.S.; Shateyi, S. The Effects of Chemical Reaction, Hall, and Ion-Slip Currents on MHD Micropolar Fluid Flow with Thermal Diffusivity Using a Novel Numerical Technique. *J. Appl. Math.* **2012**, *2012*, 30.
7. Attia, H.A. Transient Hartmann flow with heat transfer considering the Ion-slip. *Phys. Scr.* **2002**, *66*, 470–475.
8. Ghosh, S. Magnetohydrodynamic boundary layer flow over a stretching sheet with chemical reaction. *Int. J. Educ. Sci. Res.* **2015**, *2*, 78–83.
9. Kodi, R.; Ravuri, M.; Gulle, N.; Ganteda, C.; Khan, S.U.; Khan, M.I. Hall and ion slip radiative flow of chemically reactive second grade through porous saturated space via perturbation approach. *Waves Random Complex Media* **2022**, 1–17. https://doi.org/10.1080/17455030.2022.2108555.
10. Raghunath, K.; Ganteda, C.; Lorenzini, G. Effects of Soret, Rotation, Hall, and Ion Slip on Unsteady MHD Flow of a Jeffrey Fluid Through A Porous Medium in The Presence of Heat Absorption and Chemical Reaction. *J. Mech. Eng. Res. Dev.* **2022**, *45*, 80–97.
11. Sibanda, P.; Makinde, O.D. On steady MHD flow and heat transfer past a rotating disk in a porous medium with ohmic heating and viscous dissipation. *Int. J. Numer. Methods Heat Fluid Flow* **2010**, *20*, 269–285. https://doi.org/10.1108/09615531011024039.
12. Seth, G.S.; Sarkar, S. Hydromagnetic natural convection flow with induced magnetic field and nth order chemical reaction of a heat absorbing fluid past an impulsively moving vertical plate with ramped temperature. *Bulg. Chem. Commun.* **2015**, *47*, 66–79.
13. Sarveshanand; Singh, A.K. Magnetohydrodynamic free convection between vertical parallel porous plates in the presence of induced magnetic field. *Springer Plus* **2015**, *4*, 333. https://doi.org/10.1186/s40064-015-1097-1.
14. Sarma, D.; Pandit, K.K. Effects of thermal radiation and chemical reaction on steady MHD mixed convective flow over a vertical porous plate with induced magnetic field. *Int. J. Fluid Mech. Res.* **2015**, *42*, 315–333.
15. Ojjela, O.; Raju, A.; Kambhatla, P.K. Influence of thermophoresis and induced magnetic field on chemically reacting mixed convective flow of Jeffrey fluid between porous parallel plates. *J. Mol. Liq.* **2017**, *232*, 195–206.
16. Jha, B.; Aina, B. Interplay of non-conducting and conducting walls on magnetohydrodynamic(MHD) natural convection flow in vertical micro-channel in the presence of induced magnetic field. *Propuls. Power Res.* **2018**, *7*, 296–307.
17. Shaw, S.; Dogonchi, A.S.; Nayak, M.K.; Makinde, O.D. Makinde, Impact of Entropy Generation and Nonlinear Thermal Radiation on Darcy–Forchheimer Flow of $MnFe_2O_4$-Casson/Water Nanofluid due to a Rotating Disk: Application to Brain Dynamics. *Arab. J. Sci. Eng.* **2020**, *45*, 5471–5490. https://doi.org/10.1007/s13369-020-04453-2.
18. Sharma, K. FHD flow and heat transfer over a porous rotating disk accounting for Coriolis force along with viscous dissipation and thermal radiation. *Heat Transf.* **2022**, *51*, 4377–4392. https://doi.org/10.1002/htj.22504.
19. Ram, P.; Sharma, K.; Bhandari, A. Effect of porosity on revolving Ferrofluid flow with rotating disk. *Int. J. Fluids Eng.* **2010**, *6*, 67–76.
20. Mahanthesh, B.; Gireesha, B.J.; Animasaun, I.L.; Muhammad, T.; Shashikumar, N.S. Shashikumar, MHD flow of SWCNT and MWCNT nanoliquids past a rotating stretchable disk with thermal and exponential space dependent heat source. *Phys. Scr.* **2019**, *94*, 085214. https://doi.org/10.1088/1402-4896/ab18ba.
21. Vijay, N.; Sharma, K. Heat and mass transfer study of ferrofluid flow between co-rotating stretchable disks with geothermal viscosity: HAM analysis. *Chin. J. Phys.* **2022**, *78*, 83–95. https://doi.org/10.1016/j.cjph.2022.05.014.
22. Raghunath, K.; Gulle, N.; Vaddemani, R.R.; Mopuri, O. Unsteady MHD fluid flow past an inclined vertical porous plate in the presence of chemical reaction with aligned magnetic field, radiation, and Soret effects. *Heat Transf.* **2021**, *51*, 2742–2760. https://doi.org/10.1002/htj.22423.
23. Raghunath, K.; Obulesu, M. Unsteady MHD oscillatory Casson fluid flow past an inclined vertical porous plate in the presence of chemical reaction with heat absorption and Soret effects. *Heat Transf.* **2021**, *51*, 733–752. https://doi.org/10.1002/htj.22327.
24. Raghunath, K.; Obulesu, M.; Sujatha, S.; Venkateswaraju, K. Investigation of MHD Casson fluid flow past a vertical porous plate under the influence of thermal diffusion and chemical reaction. *Heat Transf.* **2021**, *51*, 77–394. https://doi.org/10.1002/htj.22311.
25. Vaddemani, R.R.; Kodi, R.; Mopuri, O. Characteristics of MHD Casson fluid past an inclined vertical porous plate. *Mater. Today: Proc.* **2022**, *49*, 2136–2142. https://doi.org/10.1016/j.matpr.2021.08.328.
26. Raghunath, K.; Mohanaramana, R. Hall, Soret, and rotational effects on unsteady MHD rotating flow of a second-grade fluid through a porous medium in the presence of chemical reaction and aligned magnetic field. *Int. Commun. Heat Mass Transf.* **2022**, *137*, 106287. https://doi.org/10.1016/j.icheatmasstransfer.2022.106287.
27. Ali, A.; Sajid, M.; Anjum, H.J.; Awais, M.; Nisar, K.S.; Saleel, C.A. Saleel, Entropy Generation Analysis of Peristaltic Flow of Nanomaterial in a Rotating Medium through Generalized Complaint Walls of Micro-Channel with Radiation and Heat Flux Effects. *Micromachines* **2022**, *13*, 375. https://doi.org/10.3390/mi13030375.

28. Ali, A.; Mumraiz, S.; Anjum, H.J.; Asghar, S.; Awais, M. Slippage phenomenon in hydromagnetic peristaltic rheology with hall current and viscous dissipation. *Int. J. Nonlinear Sci. Numer. Simul.* **2022**, *23*, 635–659. https://doi.org/10.1515/ijnsns-2019-0226.
29. Awais, M.; Bukhari, U.; Ali, A.; Yasmin, H. Convective and peristaltic viscous fluid flow with variable viscosity. *J. Eng. Thermophys.* **2017**, *26*, 69–78. https://doi.org/10.1134/S1810232817010088.
30. Ali, A.; Asghar, S. Oscillatory Flow in a Porous Channel with Porous Medium and Small Suction. *J. Mech.* **2014**, *30*, 153–159. https://doi.org/10.1017/jmech.2014.7.
31. Ali, A.; Asghar, S.; Alsulami, H.H. Oscillatory flow of second grade fluid in cylindrical tube. *Appl. Math. Mech.* **2013**, *34*, 1097–1106. https://doi.org/10.1007/s10483-013-1730-8.
32. Ilya, A.; Ashraf, M.; Ali, A.; Shah, Z.; Kumam, P.; Thounthong, P. Heat source and sink effects on periodic mixed convection flow along the electrically conducting cone inserted in porous medium. *PLoS ONE* **2021**, *16*, e0260845. https://doi.org/10.1371/journal.pone.0260845.
33. Abbasi, A.; Farooq, W.; Tag-ElDin, E.S.M.; Khan, S.U.; Khan, M.I.; Guedri, K.; Elattar, S.; Waqas, M.; Galal, A.M. Heat Transport Exploration for Hybrid Nanoparticle (Cu, Fe_3O_4)-Based Blood Flow via Tapered Complex Wavy Curved Channel with Slip Features. *Micromachines* **2022**, *13*, 1415.
34. Thejas, R.; Naveen, C.S.; Khan, M.I.; Prasanna, G.D.; Reddy, S.; Oreijah, M.; Guedri, K.; Bafakeeh, O.T.; Jameel, M. A review on electrical and gas-sensing properties of reduced graphene oxide-metal oxide nanocomposites. Biomass Conversion and Biorefinery **2022**, 1–11. https://doi.org/10.1007/s13399-022-03258-7.

energies

MDPI

Article

Experimental Investigation and Performance Characteristics of Francis Turbine with Different Guide Vane Openings in Hydro Distributed Generation Power Plants

Megavath Vijay Kumar [1,*], T. Subba Reddy [2], P. Sarala [3], P. Srinivasa Varma [4], Obbu Chandra Sekhar [5], Abdulrahman Babqi [6], Yasser Alharbi [6], Basem Alamri [6,*] and Ch. Rami Reddy [3,5]

1 Department of Mechanical Engineering, Malla Reddy Engineering College, Maisammaguda, Secunderabad 500100, India
2 Department of Mechanical Engineering, Andhra Loyola Institute of Engineering and Technology, Vijayawada 520008, India
3 Department of Electrical and Electronics Engineering, Malla Reddy Engineering College, Secunderabad 500100, India
4 Department of Electrical and Electronics Engineering, Koneru Lakshmaiah Education Foundation, Vaddeswaram 522502, India
5 Department of Electrical Engineering, National Institute of Technology, Srinagar 190006, India
6 Department of Electrical Engineering, College of Engineering, Taif University, P.O. Box 11099, Taif 21944, Saudi Arabia
* Correspondence: vijaykumar.084@mrec.ac.in (M.V.K.); b.alamri@tu.edu.sa (B.A.)

Abstract: This article presents a study on the performance characteristics of a Francis turbine operating with various guide vane openings to determine the best operating point based on unit quantities. The guide vane openings were specified based on the width between the vanes at their exit, i.e., 10 mm, 13 mm, 16 mm, and 19 mm. The performance characteristic curves of the Francis turbine—head versus speed, torque versus speed, discharge versus speed, and efficiency versus speed—were obtained at various input power and guide vane openings. From these data, unit curves were plotted and the corresponding best efficiency points were obtained. The highest efficiency of 50.25% was obtained at a guide vane opening of 19 mm. The values of head, discharge, speed, and output power at BEP were 7.84 m, 13.55 lps, 1250 rpm, and 524 W, respectively.

Keywords: renewable energy; Francis turbine; guide vane opening; performances & unit quantities

Citation: Vijay Kumar, M.; Reddy, T.S.; Sarala, P.; Varma, P.S.; Chandra Sekhar, O.; Babqi, A.; Alharbi, Y.; Alamri, B.; Reddy, C.R. Experimental Investigation and Performance Characteristics of Francis Turbine with Different Guide Vane Openings in Hydro Distributed Generation Power Plants. *Energies* **2022**, *15*, 6798. https://doi.org/10.3390/en15186798

Academic Editor: Chirag Trivedi

Received: 28 July 2022
Accepted: 10 September 2022
Published: 17 September 2022

1. Introduction

The motive energy found in water is known as hydropower. By using hydroelectric power plants, it can be transformed into electrical energy. All that is needed is a constant inflow of water and a height difference between the location where the water is found and the location where it can be released. The potential for hydropower is impressive. It is a free resource that is perpetually renewable and nonpolluting. Hydropower plays a significant role in the multipurpose use of water resources in many situations. The destructive forces of flood flows and the energy of normal flows are harnessed by hydropower projects to provide useful electrical energy. The economy of different power sources is reflected in the cost of electricity. Countries that have a large proportion of hydropower in their systems have the lowest tariffs. Upgrading existing hydropower plants is frequently more economical than building new ones. High initial investment-prone hydropower plants hold the substantial potential of uprating at the time of renovation, thereby making upgrading proposals cost-effective [1]. Due to the rising demand for electricity, hydropower plants are now more necessary than ever. Therefore, modernizing hydroelectric facilities is crucial to meeting public demand.

1.1. Selection of Turbines

The head under which a turbine is going to be operated gives guidance for the selection of the type of turbine. The range of operation of each type is shown concerning the head (H) and specific speed (ns) [2]. The total power to be installed must be known and the number of machines then are chosen by economic consideration of load factor, the extent of water storage, if any, cost of powerhouse, the convenience of operation, and maintenance. Once the output per machine has been decided, information must be obtained concerning the suitable speeds for which the generator can be constructed economically. From these data, the coupling power, effective head, and speed of the turbine are known. Hence, the specific speed is calculated. From the previous table, the suitable turbine is selected. Since the speed of the generator can generally be selected from several suitable numbers of pairs of poles, the appropriate specific speed is not limited to one value. In many cases, the overlap is considerably extended and the problem arises of selecting from two types of turbines, either of which could be used [3]. Here, knowledge of the advantages and disadvantages of each type will assist, especially concerning efficiency when running at part load. If the machine is required to operate for long periods of part loads, the Pelton turbine would be preferred to the Francis turbine. Similarly, if the choice lay between two Francis turbines, that with the lower specific speed would be more suitable, whereas if the choice lay between a Kaplan turbine or a propeller turbine or a Francis turbine with a high specific speed, the Kaplan turbine would be preferred. This is because of the flattest efficiency curve being obtained from the Kaplan turbine, followed by the Pelton turbine, the low-specific-speed Francis turbine, the high-specific-speed Francis turbine, and finally the propeller turbine, which has the most peaked form of the efficiency curve. It must not be assumed that the highest possible specific speed is always desirable [4,5].

1.2. Francis Turbine

Francis turbines can be built to handle a wide range of head and flow rates. This, combined with their high efficiency, has resulted in them being the most widely used turbine in the world. The Francis-type units have a head range of 20 m to 700 m, a specific speed of 60 to 400 rpm, and an output power ranging from a few kilowatts to one gigaton. Large Francis turbines are custom-built for each location to achieve the highest possible efficiency, typically exceeding 90% [6]. The water initially needs to enter the scroll (volute), which is an annular channel that surrounds the runner, and then flows between the stationary vanes and adjustable guide vanes, which provide the water with the best flow direction. It then enters the completely submerged runner, altering the momentum of the water and causing a reaction in the turbine. Water flows in a radial direction towards the center. The water is impinged upon by curved vanes on the runner. The guide vanes are configured in such a way that the energy of the water is largely converted into rotary motion, rather than being consumed by eddies and other undesirable flow phenomena that cause energy losses. The guide vanes are typically adjustable to provide some adaptability to variations in the water flow rate and turbine load. The Francis turbine's guide vanes are the elements that direct the flow of water [7]. The authors investigated flow parameters, such as flow angles at the runner's inlet and outlet, flow velocities, and guide vane angles, to derive flow characteristics. The goal was to analyze the pressure distribution and flow behavior to achieve the level of accuracy required for the concept design of a revitalized turbine. The obtained results are in good agreement with the on-site experiments, particularly for the characteristic curve [8].

For three different specific speed turbines, the authors predicted the accuracy and compared it to the model test results. It was demonstrated that the numerical model test presented in this investigation could predict important characteristics of the Francis turbine with high accuracy not only quantitatively but also qualitatively by comparing simulation results with model test results for pressure-fluctuation characteristics, efficiency characteristics, and cavitation characteristics. As a result, it was determined that numerical model testing would be a more realistic estimation tool for Francis turbine hydraulic

performance, contributing to cost reduction in the development of the Francis turbine [9]. The authors investigated Francis turbine guide vanes with pivoted support and an external control mechanism for converting pressure to kinetic energy and directing it to runner vanes. It has been discovered that increasing the clearance gap of the guide vane opening increases leakage, lowering energy conversion and turbine efficiency and resulting in a larger secondary vortex [10].

Many simulated results on hydroturbines have been conducted using various turbulence models to identify their performance parameters [11]. Three distinct turbulence models were explored in this work to measure the sensitivity of the model for the derivation of Francis hydroturbine performance characteristics. To evaluate the performance of the turbine, three different operating circumstances were chosen: part load, overload, and best efficiency point. The highest velocity fluctuation inside the Francis runner was anticipated by the model. The turbulence model can be used to capture the vortex rope that appears at the runner's output [12]. The influence of blade thickness on hydraulic performance was investigated numerically using six types of impellers with varied blade thicknesses that were integrated into the same pump to compare head and efficiency under design point [13]. The effect of clearance on the performance of a Francis turbine was investigated, and it was discovered that as transverse flow and loss increased, efficiency decreased significantly. When considering a specific degree of erosion, the pressure on both sides of the blade and at the outflow of the blade was precisely proportional to the erosion state [14–16]. The flow conditions in the runner inlet of a low-speed-number Francis turbine are found to be identical when a cascade with one guide vane between two flow channels is optimized [17].

Guide vane (GV) clearance gaps grow larger due to abrasive wear, which worsens the flow and reduces efficiency. In order to reduce potential consequences of an eroded guide vane on the performance of the turbine, this research evaluates several guide vane profiles. It is discovered that the pressure differential between the neighboring sides causes the clearance gap to create a leakage flow. A vortex filament is created when the leaky flow combines with the main flow and is forced within the runner [18]. The authors offer a methodology for the design, optimization, and additive manufacture of turbine blade rows and other components of highly stressed turbomachinery. The technique subsequently produces final geometries that have been suitably represented for additive manufacturing. A few aluminum prototypes of the newly improved turbine blade have been produced in order to undergo mechanical and fatigue testing [19]. The mechanical power turbine's torque varies with its size. With a peak value of 3249.7 Nm at pitch angle 17°, significant torque was obtained in the pitch angle range of 15–20°. As turbines grow in size and their pitch angle range increases, they will produce more power, reaching a maximum of 124,987.1 W or 125 kW [20]. The findings demonstrated that in operating conditions involving substantial flow rates, severe sand abrasion might be seen close to the blade head and outlet. In working conditions with low flow rates, there may be very minor abrasion found close to the blade flange. The runner is severely abraded and its effectiveness is lowered in proportion to the sediment concentration and sand diameter [21]. While the flow separation on the suction side close to the blade tip merges, the flow characteristics on the blade pressure side are often stable. The flow-separation phenomenon manifests itself more visibly with larger tip clearance. The tip leakage vortex, which is also a spatial three-dimensional spiral structure created by the entrainment effect of the tip leakage flow and main flow, becomes more pronounced as the tip clearance rises [22].

After detailed review of the literature, it was apparent that lots of research has been carried out on hydroturbines, but few studies have made an attempt at different guide vane openings and no literature was found on best operating point based on unit quantities. As such, the present work focuses the best operating point based on unit quantities by studying the performance characteristics of the Francis turbine at various input powers and guide vane openings.

2. Experimental Setup

2.1. Experimental Setup of Francis Turbine

The model Francis turbine available at Hydro Turbo Machines Lab was designed and built by Nilavalagan (1973) and was used for these experiments, as shown in Figures 1 and 2.

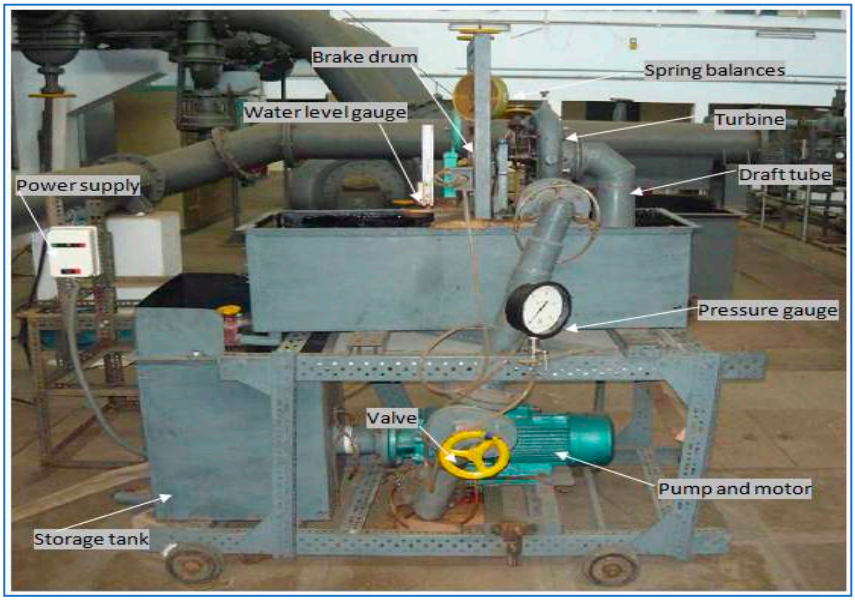

Figure 1. The Francis turbine test setup.

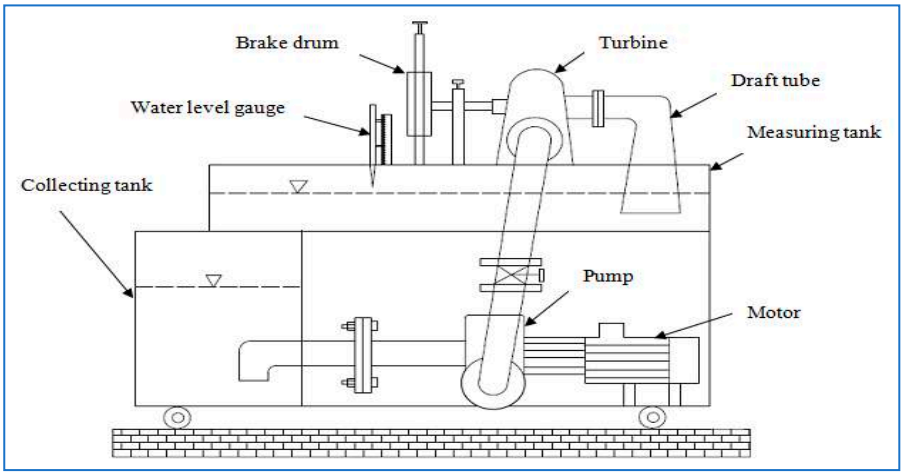

Figure 2. Schematic of Francis turbine test setup.

The Francis turbine is a machine that uses the energy of water and converts it into mechanical energy. Thus, it becomes the prime mover to run the electrical generators to produce electricity. The head is generated using a pump that draws water from the storage tank and supplies it to the inlet of the turbine. The torque generated by the turbine is measured using a brake drum. The water outlet flow of the turbine is sent to the measuring tank through the draft tube. The excess water from the measuring tank flows to the storage tank.

Four pressure tapings made near the inlet of the turbine were made to form a piezo-ring and were connected to a pressure gauge (range 0–2.5 kg/cm^2). The tachometer was used to measure the speed (N) of the turbine. The turbine was loaded with the help of a brake drum connected to a loading belt. The tension in the belt on both sides of the brake drum was measured with spring balances. The load on the turbines was altered with the help of hand wheels connected to balances. The diameter of the brake drum was 225 mm

and the thickness of the belt 5 mm. At the back of the turbine casing, there is a guiding vane mechanism. The distance between the two successive guide vanes can be altered by rotating a hand wheel. The maximum distance between one guide vane's tip to another was measured using a vernier caliper. It was found to be 19 mm maximum.

2.2. Specification of the Instruments Required for Measuring

(a) Discharge

The discharge measurement in this experiment was done using a rectangular notch, shown in Figure 3, fitted in the measuring tank. The discharge formula found by the Indian Standard (IS: 9108-1979) was used and is discussed below.

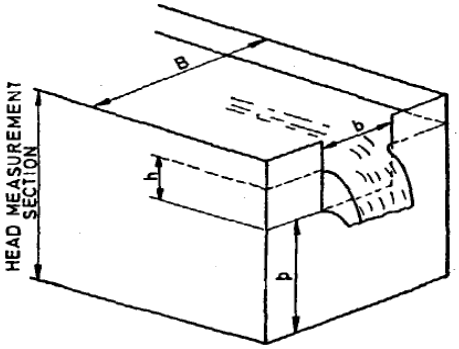

Figure 3. Rectangular notch.

The Kindsvater–Carter rectangular weir formula is

$$Q = C_e \frac{2}{3} \sqrt{2g} b_e h_e^{3/2} \quad (1)$$

where,

Q = discharge, m^3/sec

C_e = coefficient of discharge,

b_e = effective width, in mm, and

h_e = effective head in mm.

The coefficient of discharge was determined by experiment as a function of two variables from the formula:

$$C_e = f(\frac{b}{B}, \frac{h}{p}) \quad (2)$$

The effective width and head are defined by the equations:

$$b_e = b + k_b = b + 3.6 \quad (3)$$

$$h_e = h + k_h = h + 0.0012 \quad (4)$$

Which and are experimentally determined quantities, in meters, which compensates for the combined effects of viscosity and surface tension.

From the value of b/B, formula for C_e can be written as

$$(b/B = 0.6): = 0.593 + 0.018 \quad (5)$$

The water-level gauge was used to measure the height of the water level in a rectangular notch. This water-level gauge was fixed with the scale. This gauge mechanism has a rotating device for making adjustments.

(b) Speed

The digital tachometer was used to measure the speed of the turbine. Its range is 0–5000 rpm. This tachometer is kept at the back of the brake drum to find the speed of the turbine.

(c) *Pressure*

A Bourdon tube pressure gauge was used to find the pressure at the inlet of the turbine. The pressure gauge range was 0 to 2.5 kg/cm^2.

(d) *Load*

The spring balance was used to find the loads applied on the brake drum. The spring-balance range was 10 kg × 50 gm and 20 kg × 100 gm.

2.3. Experimental Methodology

- Connect the supply-pump motor unit to 3 ph, 440 V, 30 A, electrical supply, with neutral and earth connection and ensure the correct direction of pump motor unit. Keep the gate closed before the pump is on. Later, press the green button of the supply-pump starter and then release. The guide vane distance is maintained at 19 mm initially for fully open guide vane position and altered to 16 mm, 13 mm, and 10 mm distance with the help of a hand wheel. For each of the above guide vane openings, the speed of the turbine is maintained initially at 1000, 1500, 2000, and 2500 rpm by adjusting the pump outlet valve. Later, the load is applied in steps of 250 g till the lowest possible speed at which the turbine can run continuously. For each corresponding set of readings, the pressure at the inlet of the turbine, speed, load on the brake drum, and head over notch are noted. Then, the gate valve is closed and the supply-water pump switched off.
- The performances of the turbine were calculated, i.e., discharge, head, torque, input power, output, efficiency, and unit quantities. Later, the performance characteristics of the turbine were plotted.

3. Results and Discussion

The best efficiency point of the Francis laboratory scale was found by operating the water pump at different guide vane openings. The performance characteristics were plotted for these conditions. For each water supply, the reading was obtained and respective characteristics curves plotted for four different guide vane openings. The guide vane openings were specified based on the width between the vanes at their exit, i.e., 10 mm, 13 mm, 16 mm, and 19 mm. For each water supply and respective guide vane opening, an experiment was conducted as per the procedure indicated in Section 2.3. Each experiment was repeated and performance curves for discharge versus speed, head versus speed, torque versus speed, and efficiency versus speed were plotted.

A polynomial curve fit was done for the two individual sets of readings that were repeated for the same experimental condition to check repeatability. Then, the two individual experimental results were merged as one single set and fitted as a polynomial curve. The correlation coefficient was found to be not less than 0.98. The respective polynomial equation for each of torque, discharge, and head with speed were substituted in the efficiency formula and corresponding efficiency was calculated.

3.1. Performance Characteristics of Francis Turbine

The performance characteristics of discharge versus speed, head versus speed, torque versus speed, and efficiency versus speed for 10 mm guide vane opening are shown in Figures 4–11. At lower input power, few points could be obtained. The turbine came to a halt at higher loads, but starting the turbine at higher power enables taking a large number of readings. The discharge appears to be less at high speeds compared to low speeds; this may be because the machine is vibrating and fluctuating while it is functioning.

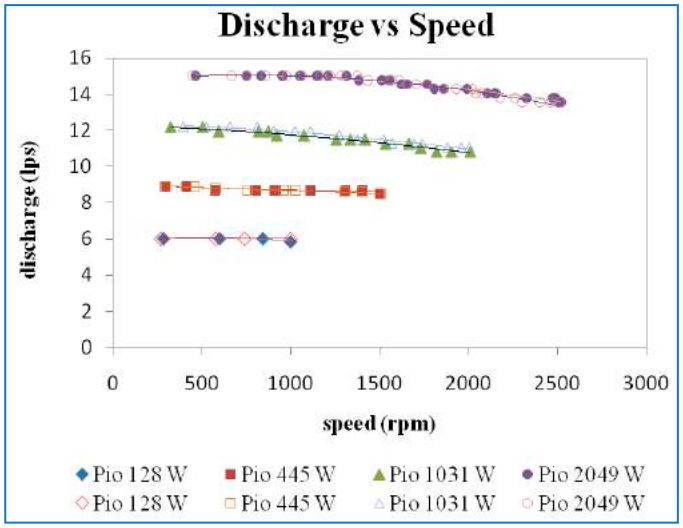

Figure 4. Discharge vs. speed at a guide vane opening of 10 mm.

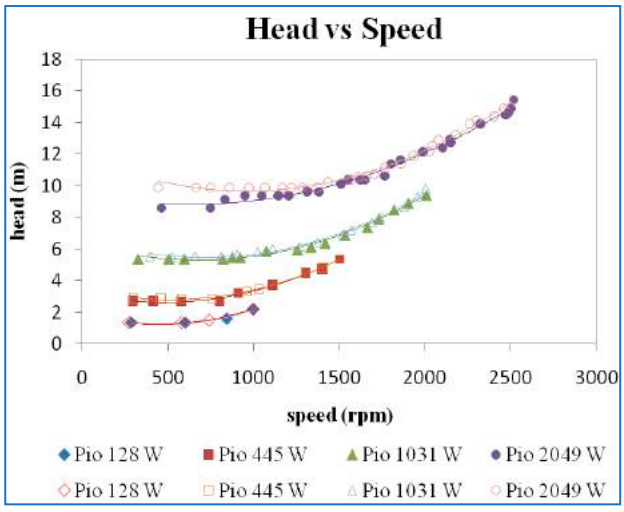

Figure 5. Head vs. speed at a guide vane opening of 10 mm.

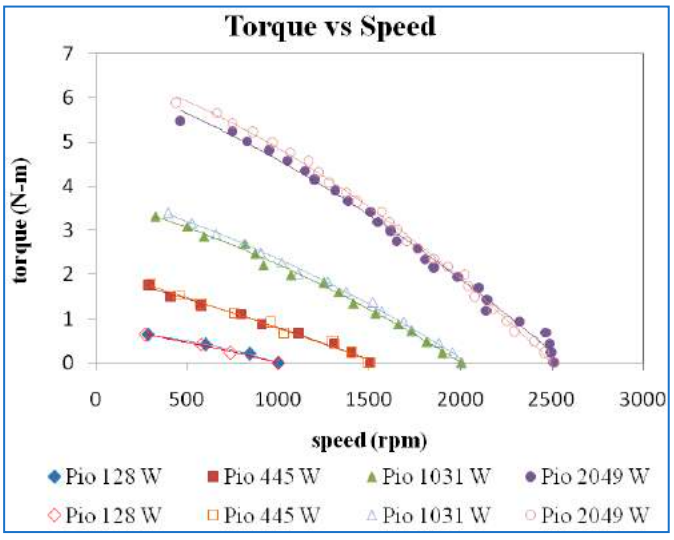

Figure 6. Torque vs. speed at a guide vane opening of 10 mm.

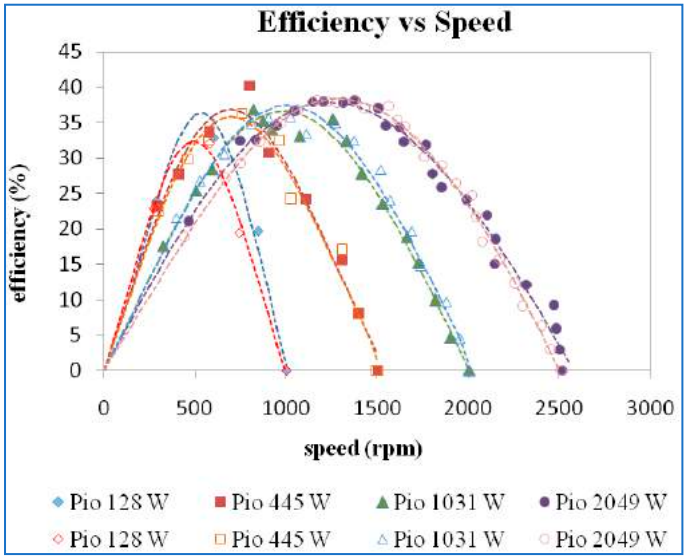

Figure 7. Efficiency vs. speed at a guide vane opening of 10 mm.

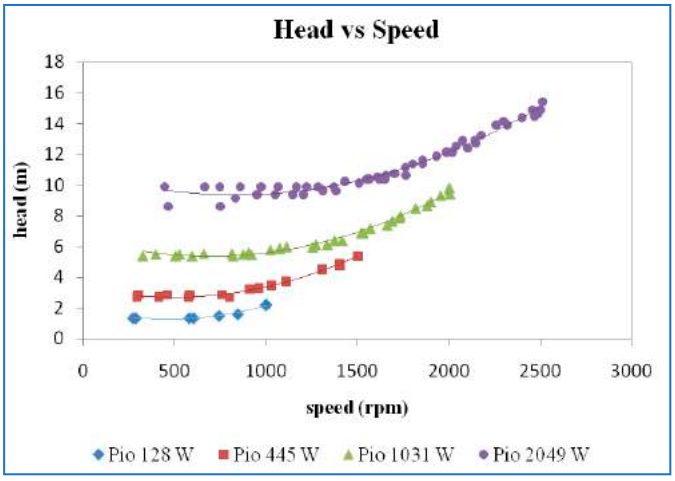

Figure 8. Head vs. speed at a guide vane opening of 10 mm.

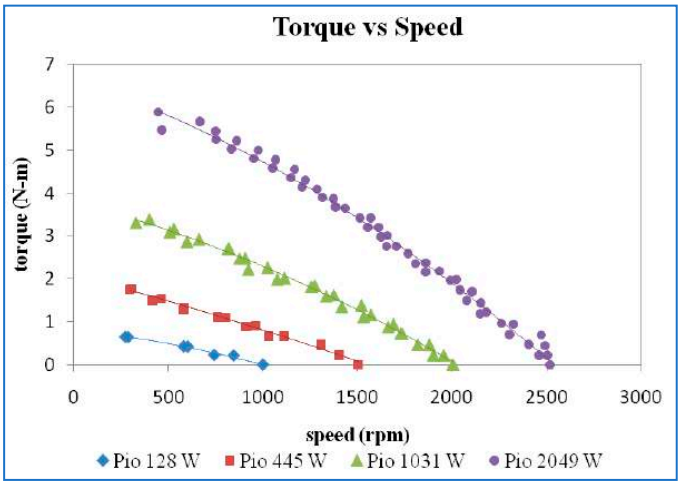

Figure 9. Torque vs. speed at a guide vane opening of 10 mm.

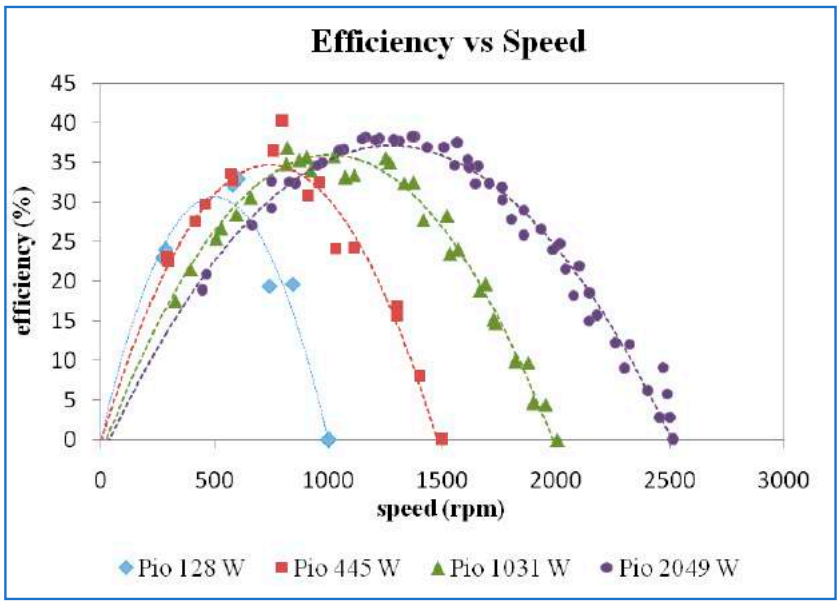

Figure 10. Efficiency vs. speed at a guide vane opening of 10 mm.

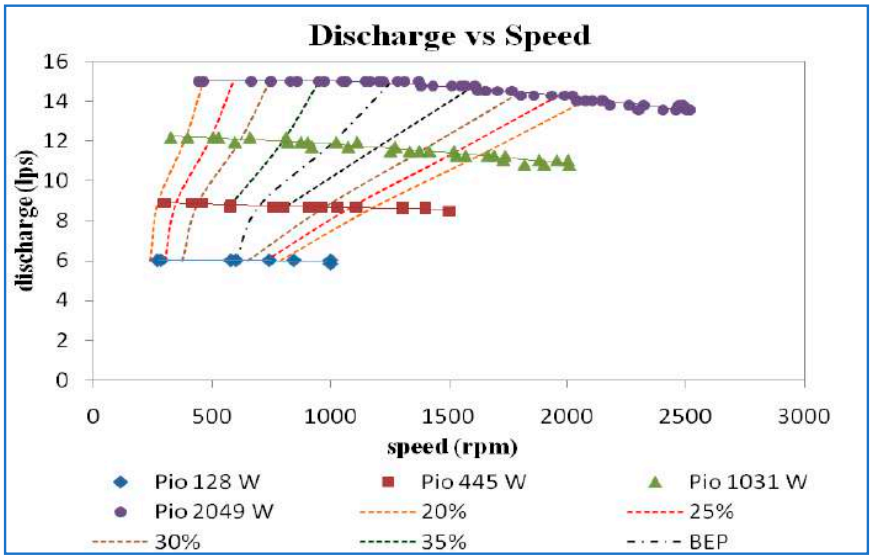

Figure 11. Discharge vs. speed and iso-efficiency line at 10 GVO.

Figure 5 shows the plot of the variation of the head concerning the speed for different power inputs. The head increases with an increase in the power inputs. The head is almost constant at lower speeds and then increases with speed. There is a slight increase in the head curves even during the lower speeds for the power input of 2049 (W). In this plot also, it may be observed that the repeatability of the readings is good.

A study of Figure 6 showing the plot of torque versus speed shows that at no load conditions, the speed of the turbine is about 2500 rpm for the power input of 2049 (W). This is the maximum speed that was achieved for the highest possible power input. The speed at no load came down to 2000 rpm, 1500 rpm, and 1000 rpm, respectively, as the input power was decreased. In fact, during the experiments, the input valve that changes the power input to the turbine was fixed based on the speed in the no-load condition. When a load is applied, the torque rises, increasing the frictional forces acting between the brake drum and the belt. This causes heat to be released, reducing speed. The repeatability of the readings can also be seen in the two sets plotted in Figure 6.

Efficiency versus speed for different power inputs is shown in Figure 7. It may be seen that higher maximum efficiency was obtained for higher inputs and efficiency increased

to a maximum then decreased as speed increased. This is because the output power is contributed by the torque and speed. The speed decreases with increases in torque; thereby, the overall output power increases, reaches a maximum, and then decreases. One can argue that the effect of input power may also contribute to the variation in efficiency. This is true, but only at higher speeds. The discharge and the head were almost constant at lower speeds, so the variation of input power becomes insignificant. That is the reason that the efficiency curves show the increasing and decreasing trend.

The two sets of points in Figures 4–7 indicate clearly that the results are repeatable and hence they were considered together and a single curve fitted for every value of input power.

Figure 8 shows the plot of the variation of the head concerning the speed for different power inputs. Trial 1 and trial 2 were combined and plotted as a single curve. It can be seen that head decreases with a decrease in the power inputs.

Figure 9 shows that when the load is applied, the torque increases the frictional forces acting between the brake drum and the belt increase and dissipate the energy in the form of heat; therefore, the speed comes down. The torque is increased by decreasing the speed.

The efficiency versus speed for different power inputs is shown in Figure 10. The higher maximum efficiency was obtained for higher input power. However, there is only a slight variation of maximum efficiency at 445 W, 1031 W, and 2049 W input power.

The iso-efficiency lines plotted on discharge versus speed curves are shown in Figure 11. From the efficiency curves, horizontal lines corresponding to efficiencies of 20%, 25%, 30%, 35%, and best efficiency point (BEP) were drawn and the speed and the discharge corresponding to the point where the efficiency curves intersect the horizontal iso-efficiency lines were noted and plotted, as shown in the above figure. It may be noted that the value of discharge and speed at maximum efficiency is 32%, 36%, 37%, and 38% at input power of 77 W, 243 W, 647 W, and 1414 W for guide vane opening of 10 mm.

The head versus speed curve shown in Figure 12 was obtained at a guide vane opening of 13 mm. The head is decreasing with decreasing the speed. When input power is more, the head seems to be more.

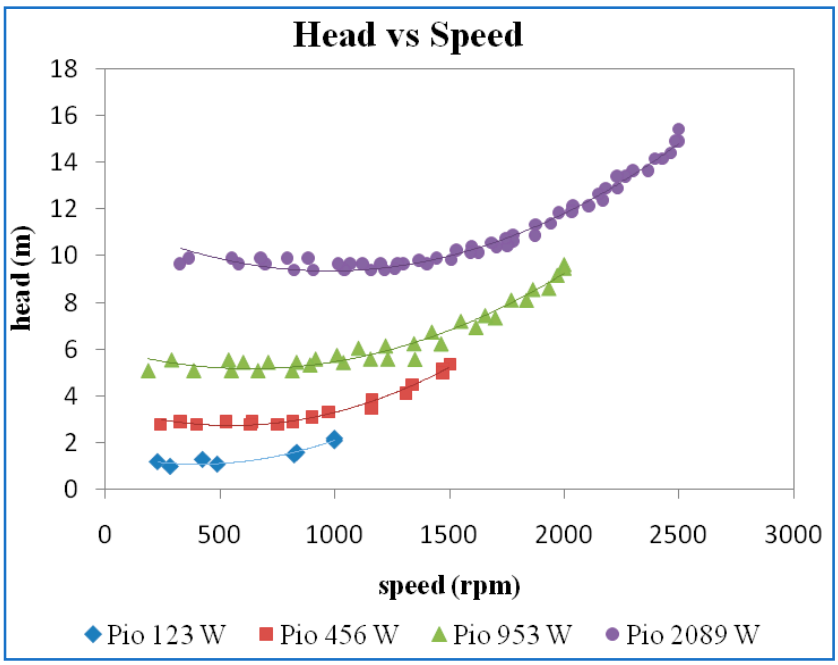

Figure 12. Head vs. speed at a guide vane opening of 13 mm.

From Figure 13, it may be seen that as speed decreases, the torque starts to increase when the load is applied to the brake drum. There is not much variation in these curves between guide vane openings of 13 mm and 10 mm, as seen in Figures 9 and 13.

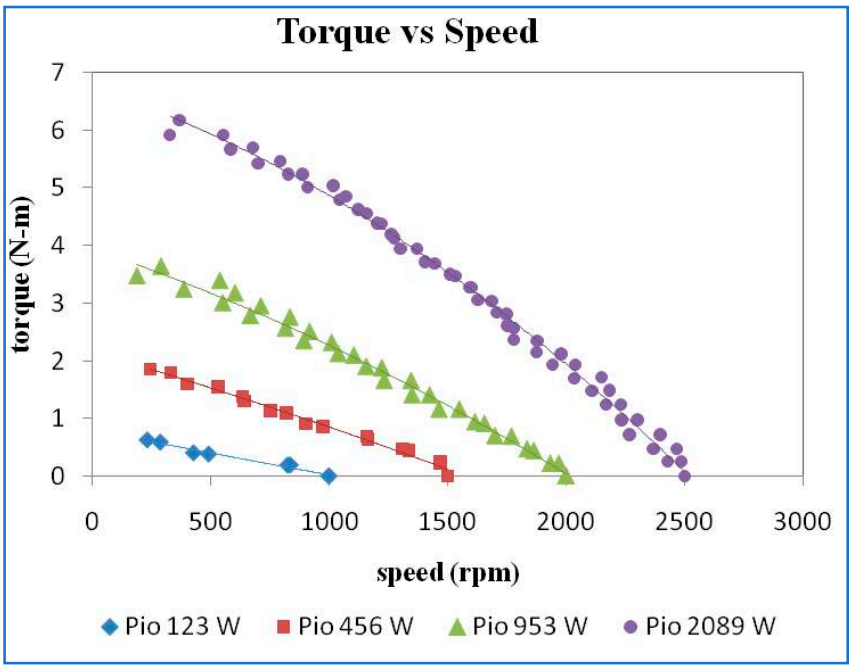

Figure 13. Torque vs. speed at a guide vane opening of 13 mm.

The maximum efficiency was observed at a power input of 953 W for a guide vane opening of 13 mm, as seen in Figure 14. At input power of 123 W, 456 W, and 953 W the maximum efficiency increases gradually, but at power input 2089 W it is decreased slightly due to the vibration, which leads to cavitations within the turbine.

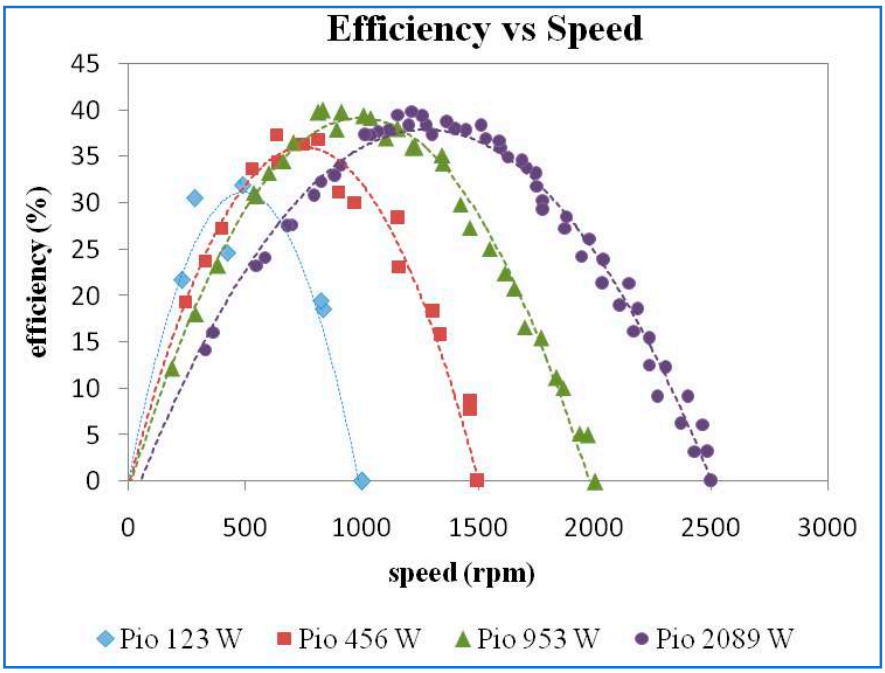

Figure 14. Efficiency vs. speed at a guide vane opening of 13 mm.

Figure 15 shows that the discharge is more or less constant at different input power. The iso-efficiency plot seems not much different between the guide vane openings of 10 mm and 13 mm. The values at best efficiency points are 33%, 37%, 40%, and 39%.

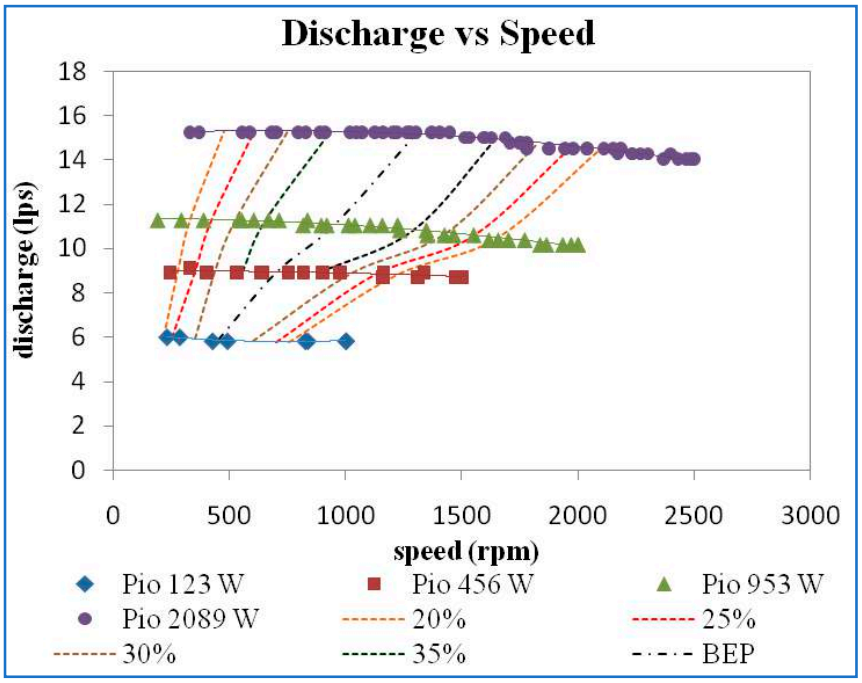

Figure 15. Discharge vs. speed and iso-efficiency line at 13 GVO.

The plot of the variation between the head and speed for different power input at 16 mm GVO is shown in Figure 16. The head decreases with decreasing power input. A notable variation may be observed at higher speeds.

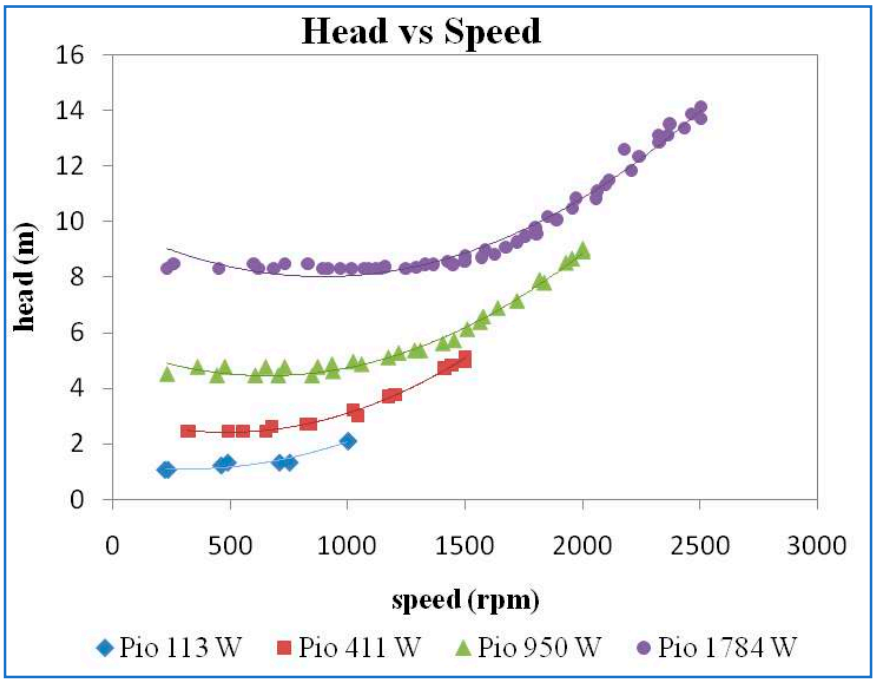

Figure 16. Head vs. speed at a guide vane opening of 16 mm.

From Figure 17, it may be concluded that at a GVO of 16 mm, when the torque increases the speed starts decreasing when the load is applied on the brake drum. There is not much variation from guide vane openings of 16 mm, 13 mm, and 10 mm.

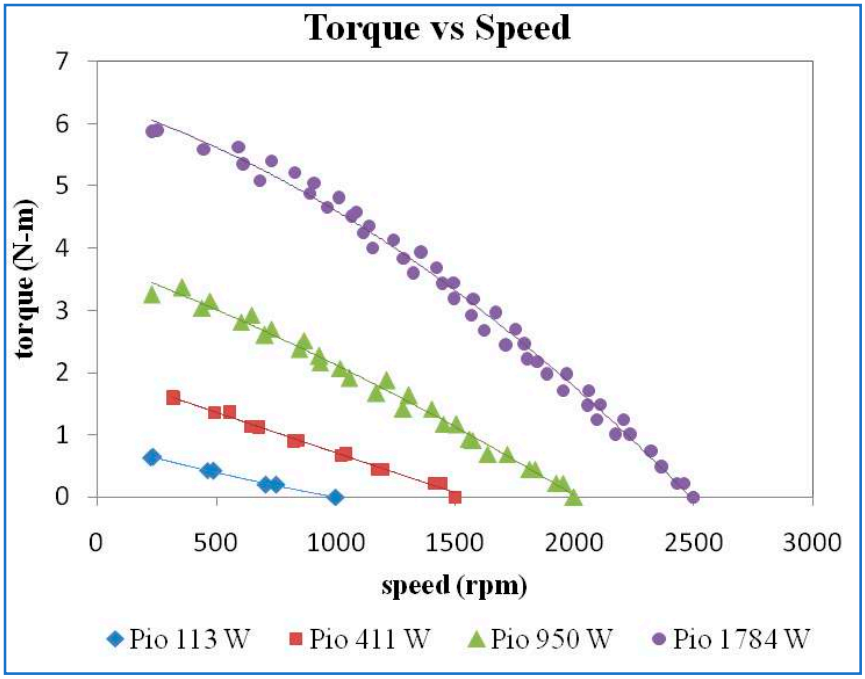

Figure 17. Torque vs. speed at a guide vane opening of 16 mm.

From Figure 18, it is observed that the maximum efficiency at 16 mm GVO was seen at a power input of 1784 W. The maximum efficiency decreases as input power is decreased. As there is an increase in guide vane opening, the efficiency improves compared to the low guide vane opening due to there being no impediment or vibration.

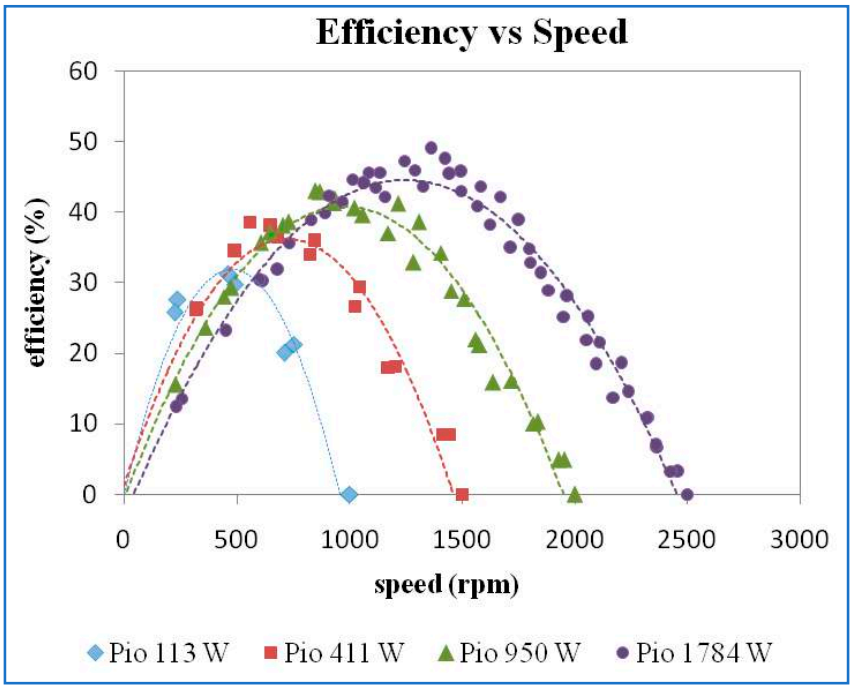

Figure 18. Efficiency vs. speed at a guide vane opening of 16 mm.

From Figure 19, it is seen that at 113 W power input, the discharge was constant. At other input power, the discharge was slightly decreased as speed increased at 16 mm GVO. The iso-efficiency lines plotted seem to be a straight line with different slopes. The discharge versus speed at BEP is 32%, 38%, 42%, and 46%.

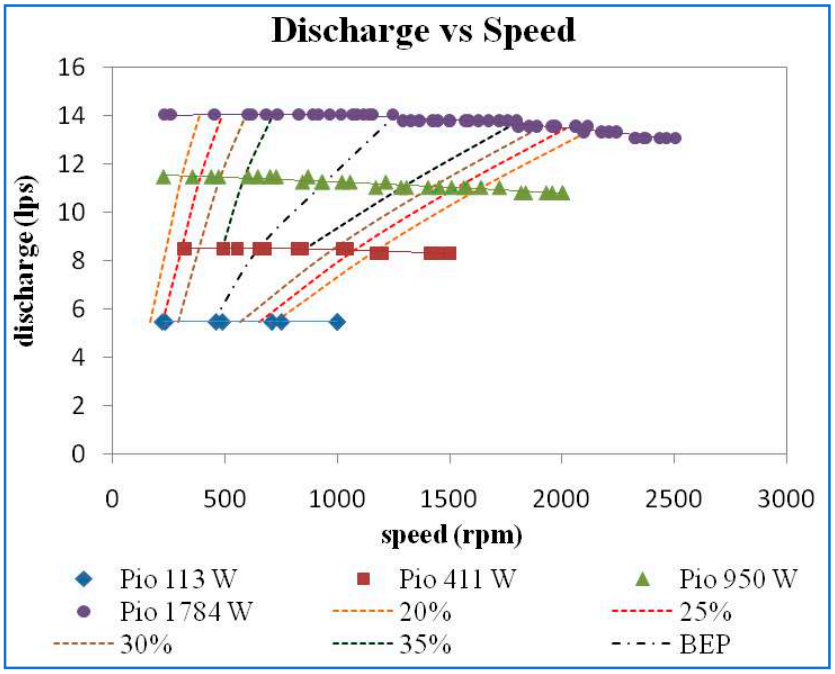

Figure 19. Discharge vs. speed and iso-efficiency line at 16 GVO.

Figure 20 shows the plot of the variation of head with respect to the speed for different power input at a GVO of 19 mm. The head increases with increase in the power input. There is a variation in the head curves at higher speed for all the four power inputs.

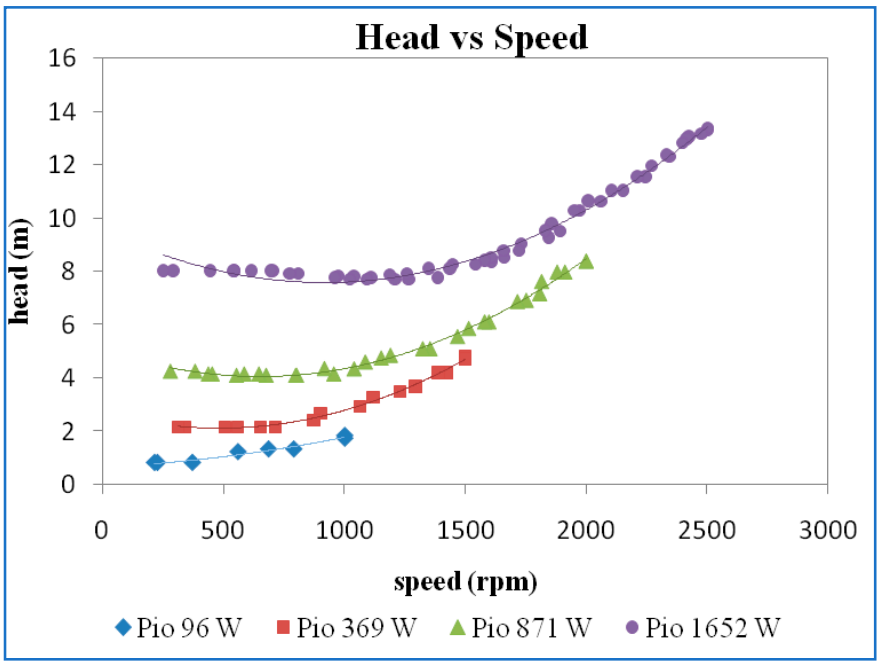

Figure 20. Head vs. speed at a guide vane opening of 19 mm.

According to Figure 21, when the load is applied the torque increases the frictional forces acting between the brake drum and the belt increases and dissipates the energy in the form of heat, and thus the speed comes down. The torque is increased with increased input power. There is a large variation in torque at 1652 W power input compared to other lower input power.

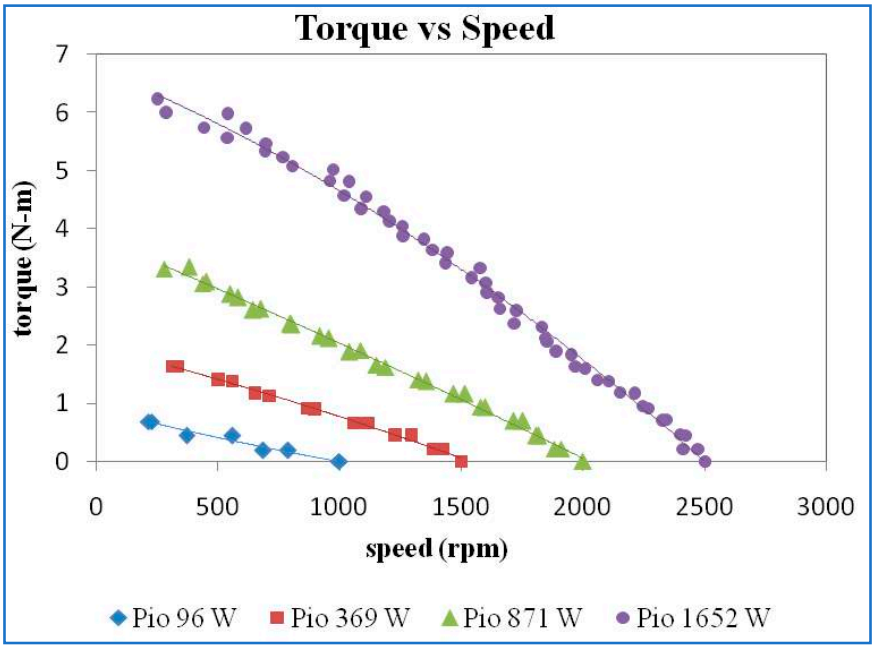

Figure 21. Torque vs. speed at a guide vane opening of 19 mm.

From Figure 22, maximum efficiency is observed at 1652 W. Maximum efficiency observed at 871 W was higher compared to the 96 W and 369 W power inputs. Compared to all other guide vane openings, the 19 mm guide vane opening showed the best efficiency due to no obstruction and vibration compared to low guide vane openings. As per the standard of this turbine, it could not achieve more efficiency at 19 mm guide vane opening due to some of the drawbacks, such as leakages between the blades and the casing and vibrations of the turbine.

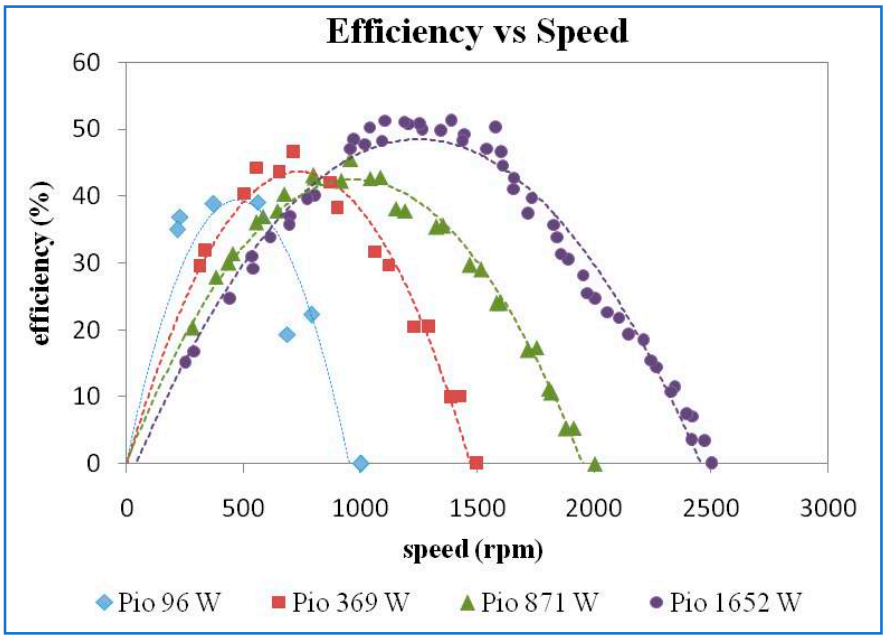

Figure 22. Efficiency vs. speed at a guide vane opening of 19 mm.

Discharge was found to be constant as speed was varied at different input powers, as shown in Figure 23 at a GVO of 19 mm. The iso-efficiency was plotted and seems not much different between guide vane openings of 10 mm, 13 mm, 16 mm and 19 mm. The bp values are 41%, 46%, 47% and 50%.

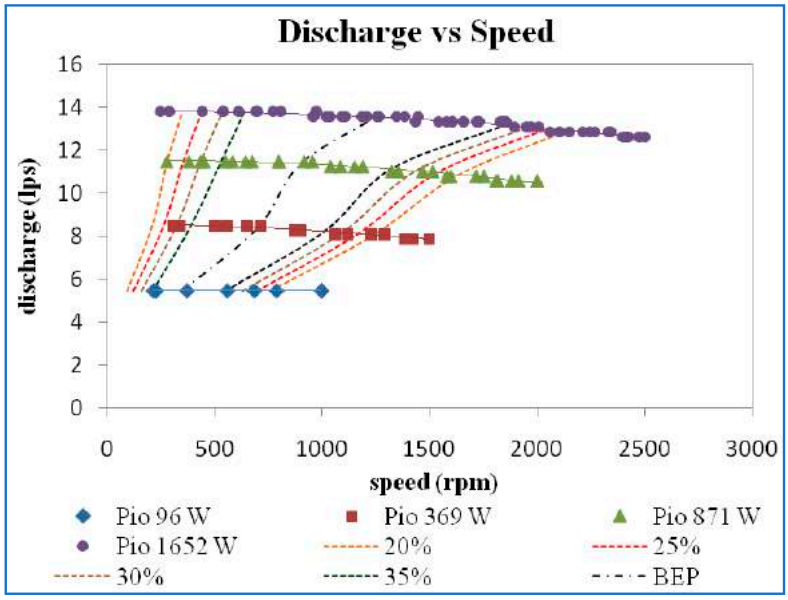

Figure 23. Discharge vs. speed and iso-efficiency line at 19 GVO.

3.2. Best Efficiency Point Curves

Figure 24 shows that all the best efficiency points with different guide vane openings are plotted in 10 mm guide vane opening. The four best efficiency points combined are intersecting at 930 speed and 11 discharge. They all split at higher discharge and lower discharge. All the discharge curves seem to be constant. As the guide vane opening was varied, there was a variation in the line of best efficiency, as shown in Figure 10. This plot indicates that all these lines merge at speed of 920 rpm.

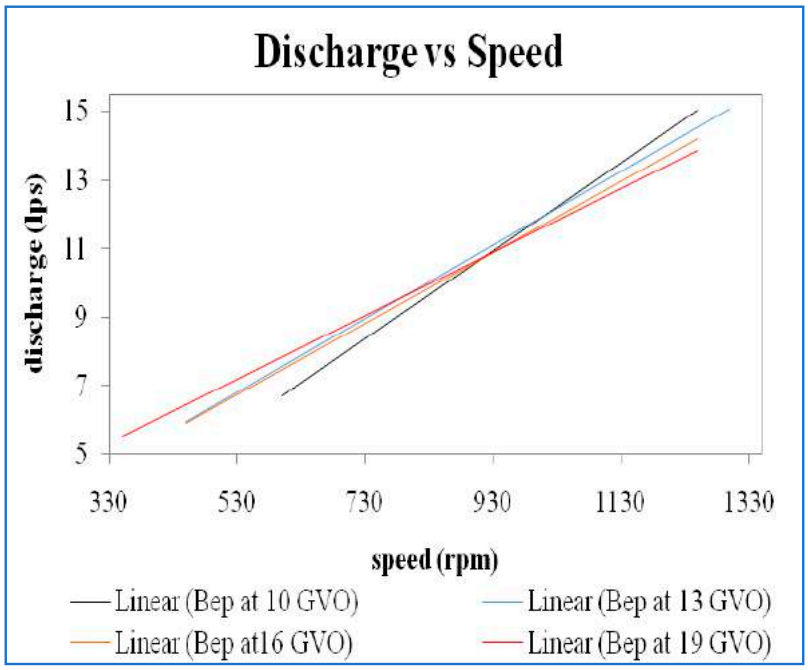

Figure 24. Discharge vs. speed for best efficiency point at 10 mm GVO.

3.3. Unit Curves

The unit discharge versus unit speed curve is shown in Figure 25. For all trial 1 and trial 2 readings at various input power, the points seem to coalesce, so one universal trend line was drawn for all the data indicating the variation of the unit discharge with respect to

unit speed. Compared to characteristic curves of discharge versus speed, the unit discharge decreases with increase in unit speed.

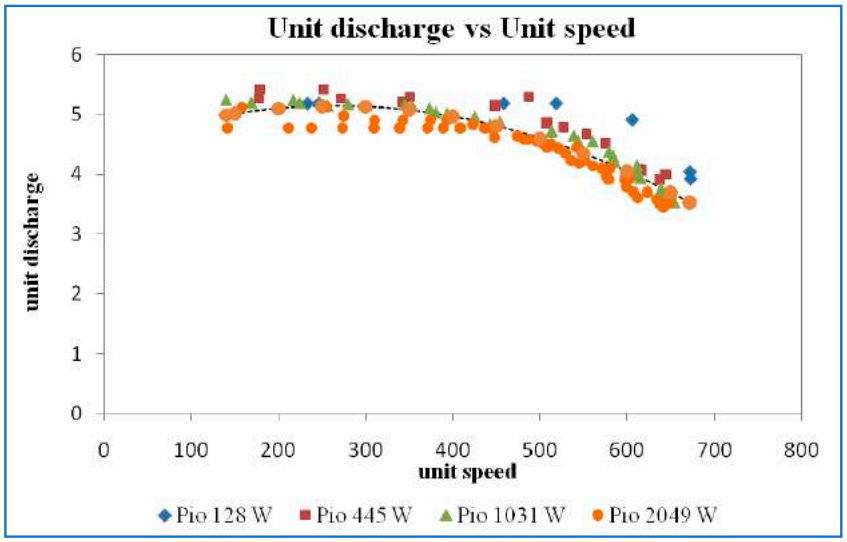

Figure 25. Unit discharge vs. unit speed at a guide vane opening of 10 mm.

The variation of output power versus unit speed operating at different power inputs is shown in Figure 26. These points form a second-order polynomial curve fit with correlation coefficients near one. The maximum unit output power is found at a unit speed of 396 rpm.

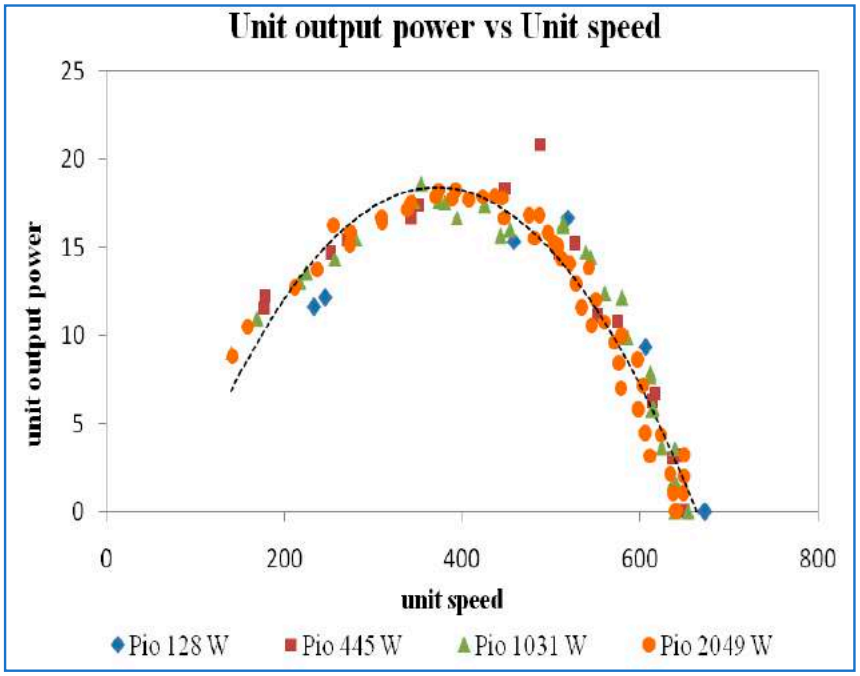

Figure 26. Unit output power vs. unit speed at a guide vane opening of 10 mm.

For the 10 mm guide vane opening, the maximum efficiency is obtained for unit speed of 400, as shown in Figure 27. The highest efficiency is about 38%.

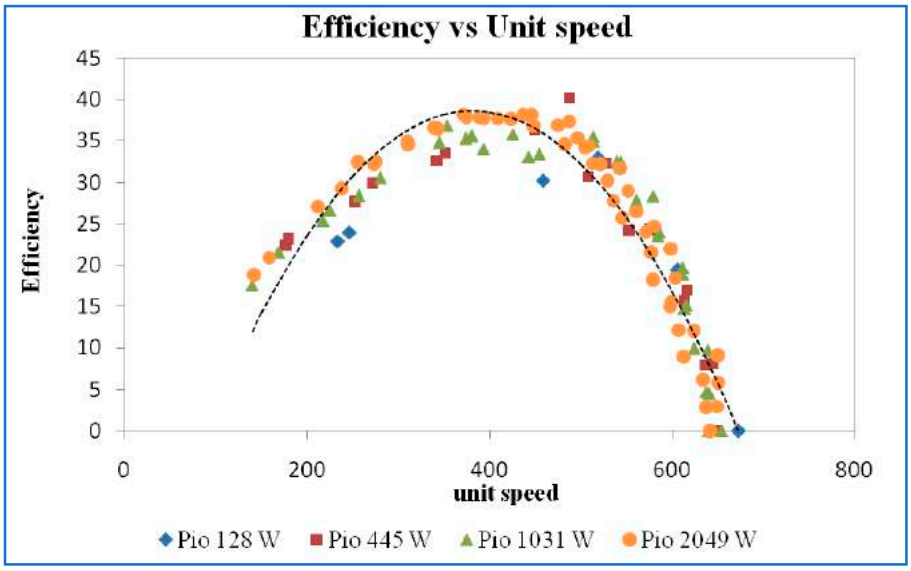

Figure 27. Efficiency vs. unit speed at a guide vane opening of 10 mm.

For a guide vane opening of 13 mm, the unit discharge versus unit speed curve is shown in Figure 28. The unit discharge decreases with increase in unit speed at this guide vane opening also. When compared to that for 10 mm, the unit discharge increases and decreases with increasing speed.

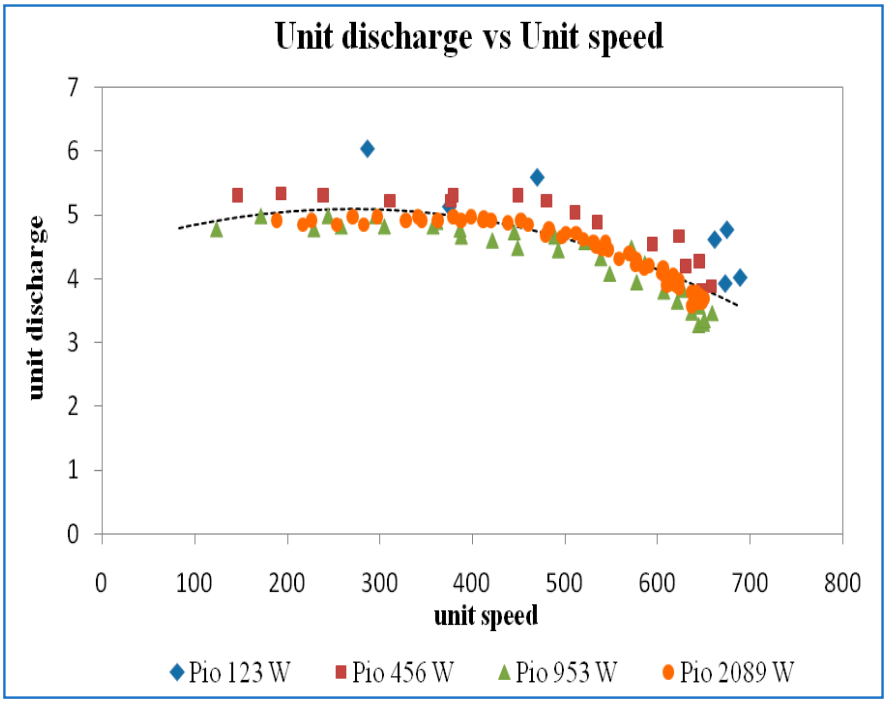

Figure 28. Unit discharge vs. unit Speed at a guide vane opening of 13 mm.

The variation in unit output power versus unit speed operating at different power inputs is shown in Figure 29. The maximum output power is found at a unit speed of 396 rpm, the same as that at a GVO of 10 mm.

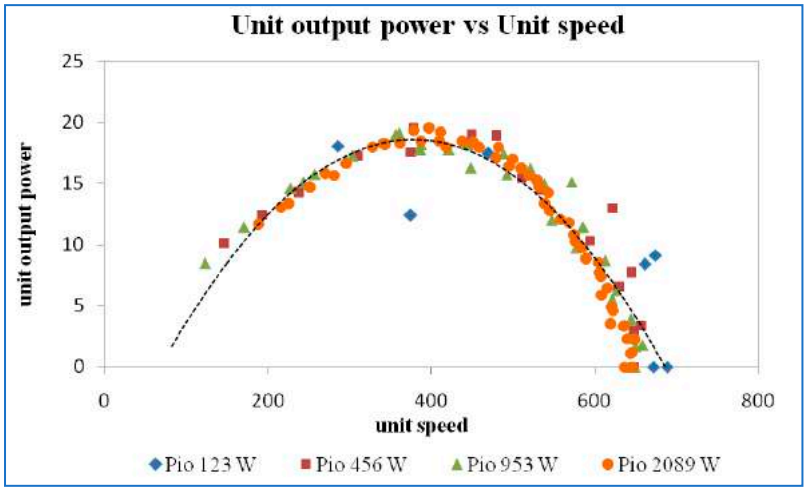

Figure 29. Unit output power vs. unit speed at a guide vane opening of 13 mm.

Variation in efficiency versus unit speed is shown in Figure 30. The efficiency gradually increases and decreases. The maximum efficiency is attained at a unit speed of 400 rpm.

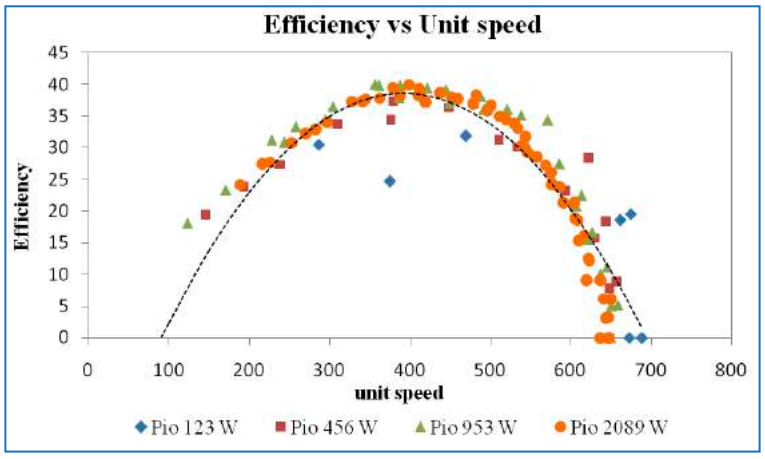

Figure 30. Efficiency vs. unit speed at a guide vane opening of 13 mm.

For a guide vane opening of 16 mm, the unit discharge versus unit speed curve is shown in Figure 31. The unit discharge decreases with an increase in unit speed.

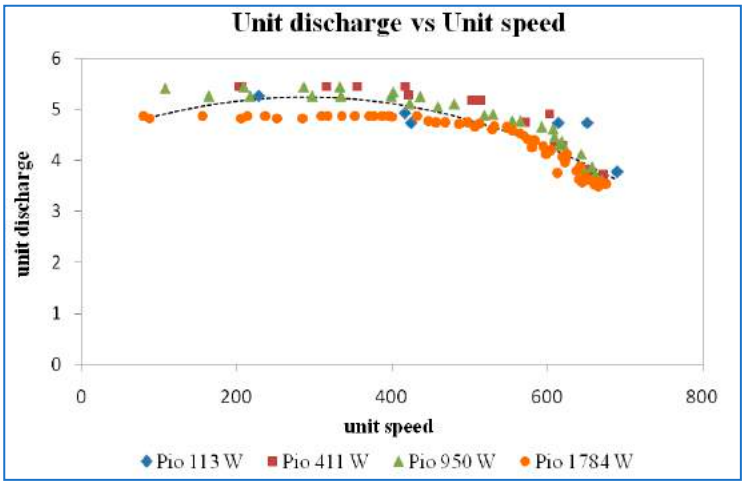

Figure 31. Unit discharge vs. unit speed at a guide vane opening of 16 mm.

The variation in unit output power versus unit speed operating at different power inputs is shown in Figure 32. The maximum output power is found at a unit speed of 396 rpm, the same as that at a GVO of 10 mm and 13 mm.

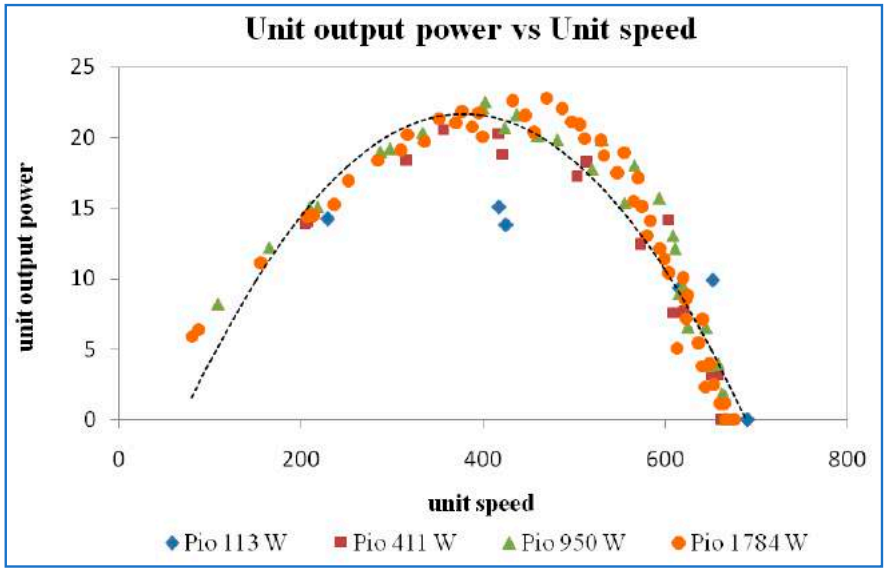

Figure 32. Unit output power vs. unit speed at a guide vane opening of 16 mm.

Figure 33 shows that a higher maximum efficiency is obtained at 45% with a guide vane opening of 16 mm. This curve at a unit speed value of 400 rpm attained maximum efficiency.

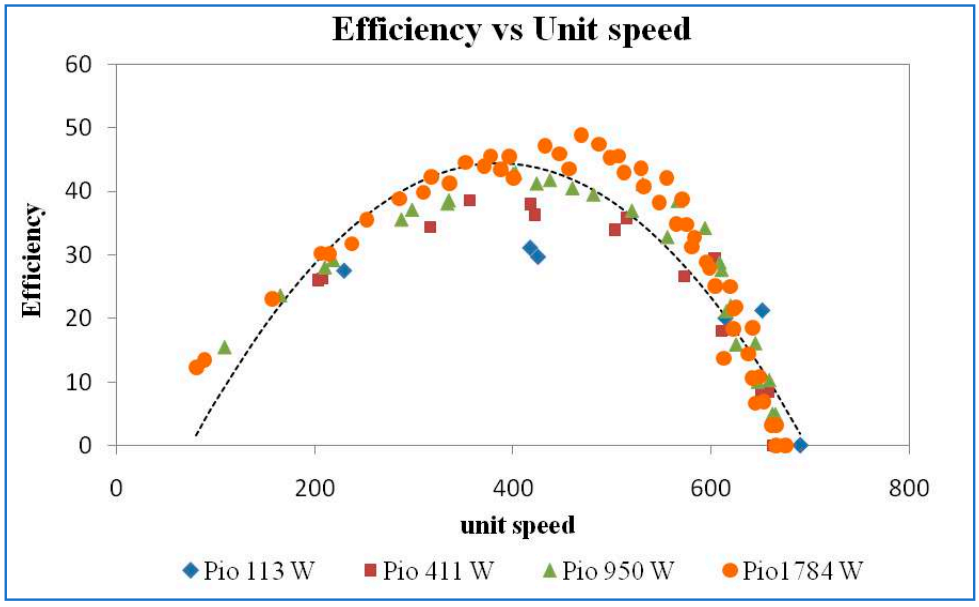

Figure 33. Efficiency vs. unit speed at a guide vane opening of 16 mm.

The unit discharge versus unit speed curve is shown in Figure 34. The unit discharge decreases with increasing unit speed. The unit discharge decreases with increasing unit speed. The unit discharge curve looks similar to GVO of 13 mm, 16 mm, and 19 mm.

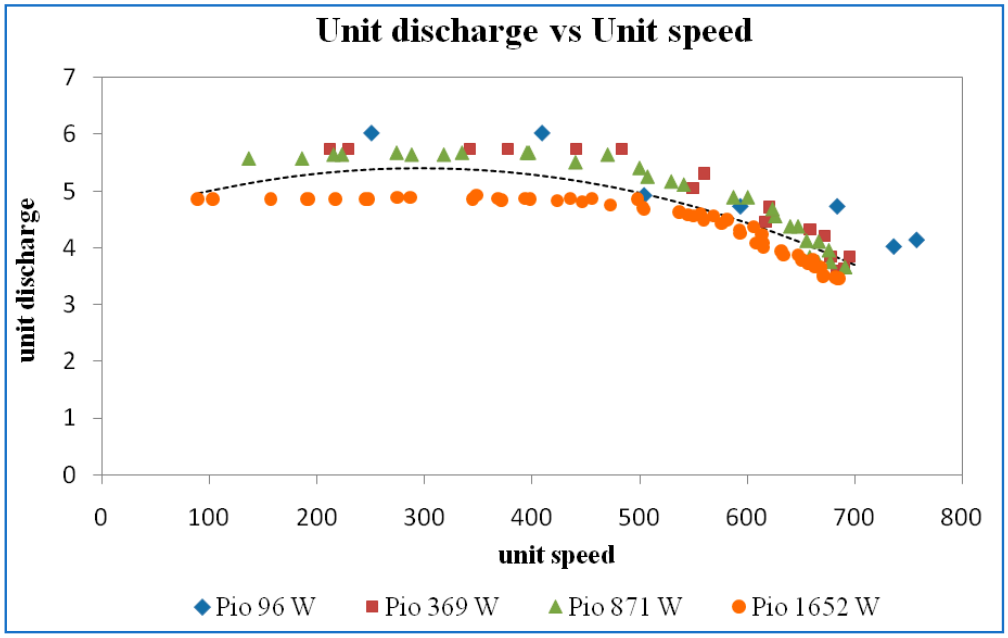

Figure 34. Unit discharge vs. unit speed at a guide vane opening of 19 mm.

The variation in unit output power versus unit speed operating at different power inputs is shown in Figure 35. The maximum output power is found at a unit speed of 400 rpm, the same as that at a GVO of 10 mm, 13 mm, and 19 mm.

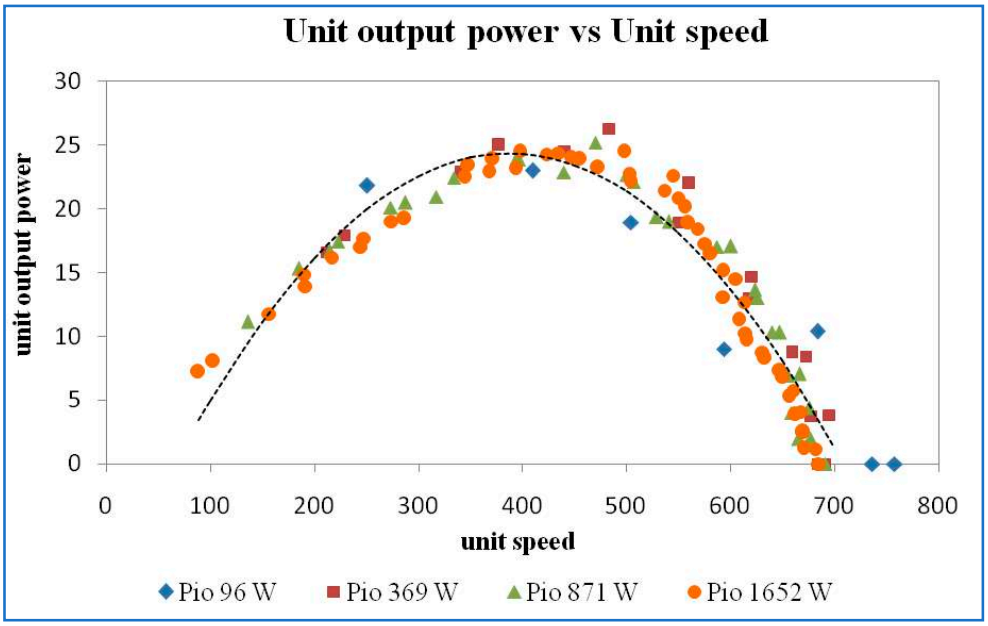

Figure 35. Unit output power vs. unit speed at a guide vane opening of 19 mm.

Figure 36 shows the variation in efficiency with unit speed for GVO of 19 mm. It shows that the unit speed at BEP is 400 rpm.

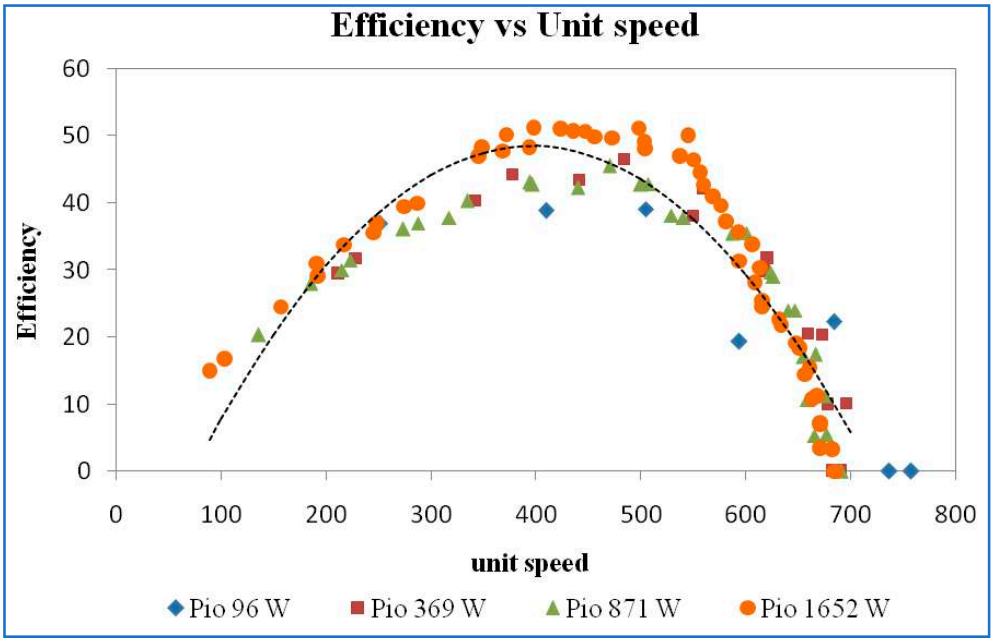

Figure 36. Efficiency vs. unit speed at a guide vane opening of 19 mm.

Using results obtained for other GVOs, as mentioned in Table 1, variations of unit quantities at the best efficiency point were plotted concerning GVO. The results presented in Figure 37 show the values to be more or less constant for all guide vane openings.

Table 1. Best efficiency points from characteristics of Francis turbine.

S. No	Guide Vane Opening GVO (mm)	Speed N (rpm)	Discharge Q (lps)	Head Given to Turbine H (m)	Brake Output Power (W)	Power Input to the Turbine (W)	Efficiency (%)
1	10	600	6.02	1.31	25.08	77.44	32.39
2		700	8.77	2.82	88.15	242.86	36.30
3		1000	11.83	5.58	239.34	647.33	36.97
4		1250	14.89	9.68	537.68	1414.14	38.02
5	13	450	5.86	1.09	20.90	62.89	33.24
6		700	8.92	2.81	92.36	245.79	37.58
7		950	11.06	5.39	236.09	584.55	40.39
8		1300	15.14	9.61	558.15	1427.69	39.09
9	16	450	5.47	1.14	20.57	61.33	33.54
10		650	8.49	2.47	78.64	205.51	38.27
11		950	11.29	4.67	220.64	517.26	42.66
12		1250	13.94	8.29	522.94	1134.04	46.11
13	19	350	5.47	0.91	19.99	48.89	40.88
14		700	8.40	2.25	85.26	185.57	45.94
15		900	11.38	4.19	209.13	468.15	44.67
16		**1250**	**13.55**	**7.84**	**524.00**	**1042.79**	**50.25**

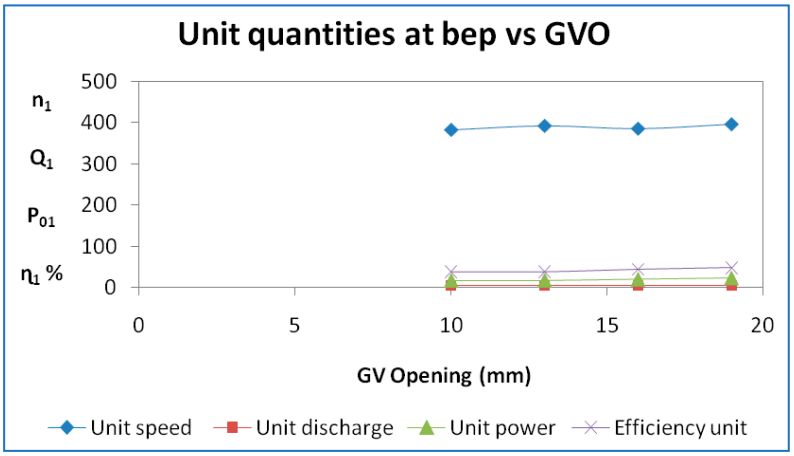

Figure 37. BEP unit quantities vs. GVO.

4. Conclusions

In the current work on the best operating point based on unit quantities by studying the performance characteristics of the Francis turbine at various input powers and guide vane openings, the important conclusions are revealed below.

The performance characteristic curves were plotted within the available range of variation of guide vane openings (10 mm to 19 mm) and input power (96 W to 2089 W). From these available data, unit curves were plotted and corresponding best efficiency points obtained. The highest efficiency of 50.25% was obtained at a guide vane opening of 19 mm. The values of head, discharge, speed, and output power at BEP were 7.84 m, 13.55 lps, 1250 rpm, and 524 W, respectively. As per the condition of this Francis turbine, the main reason for not obtaining more than the higher efficiency of 50.25% was leakage flow that passed through the clearance gap between the guide vanes' high-pressure and low-pressure sides. To determine how much leakage flow there is, finding the velocity vectors inside the gap can be used.

Author Contributions: Conceptualization, M.V.K., T.S.R. and P.S.; methodology, C.R.R., P.S.V. and O.C.S.; software, B.A., Y.A. and A.B.; validation, M.V.K., P.S.V. and C.R.R.; formal analysis, B.A. and Y.A.; investigation M.V.K. and A.B.; resources, M.V.K.; data curation, T.S.R.; writing—original draft preparation, M.V.K. and C.R.R.; writing—review and editing, M.V.K., T.S.R., C.R.R., P.S., P.S.V. and O.C.S.; visualization, Y.A.; supervision, C.R.R.; project administration, C.R.R.; funding acquisition, B.A. All authors have read and agreed to the published version of the manuscript.

Funding: The authors would like to acknowledge the financial support received from the Taif University Researchers Supporting Project (TURSP-2020/278), Taif University, Taif, Saudi Arabia.

Institutional Review Board Statement: Not applicable.

Informed Consent Statement: Not applicable.

Data Availability Statement: Not applicable.

Conflicts of Interest: The authors declare no conflict of interest.

References

1. Logan, E., Jr. *Turbomachinery: Basic Theory and Applications*; CRC Press: Boca Raton, FL, USA, 1993. Available online: https://books.google.co.in/books?hl=en&lr=&id=s4Qfa1AWGGkC&oi=fnd&pg=PR5&dq=1.%09Logan+Jr,+Earl.+Turbomachinery:+Basic+theory+and+applications (accessed on 25 June 2022).
2. Yannopoulos, S.I.; Lyberatos, G.; Theodossiou, N.; Li, W.; Valipour, M.; Tamburrino, A.; Angelakis, A.N. Evolution of Water Lifting Devices (Pumps) over the Centuries Worldwide. *Water* **2015**, *7*, 5031–5060. [CrossRef]
3. Reynolds, T.S. *Stronger than a Hundred Men: A History of the Vertical Water Wheel*; No. 7; JHU Press: Baltimore, MD, USA, 1983.
4. Pang, J.; Liu, H.; Liu, X.; Yang, H.; Peng, Y.; Zeng, Y.; Yu, Z. Study on sediment erosion of high head Francis turbine runner in Minjiang River basin. *Renew. Energy* **2022**, *192*, 849–858. [CrossRef]

5. Zhang, W.; Zhu, B.; Yu, Z.; Yang, C. Numerical study of pressure fluctuation in the whole flow passage of a low specific speed mixed-flow pump. *Adv. Mech. Eng.* **2017**, *9*, 1687814017707651. [CrossRef]
6. Gatte, M.T.; Rasim, A.K. Hydro Power. *Energy Conserv.* **2012**, *9*, 95–124. Available online: https://books.google.co.in/books?hl=en&lr=&id=DASaDwAAQBAJ&oi=fnd&pg=PA95&dq=Gatte,+Mohammed+Taih,+and+Rasim+Azeez+Kadhim.+%22Hydro+power (accessed on 30 June 2022).
7. Norquest, P.E. Ambient Pressure Water Turbine. U.S. Patent No. 4,416,584, 22 November 1983. Available online: https://patents.google.com/patent/US4416584A/en (accessed on 7 July 2022).
8. Choi, H.-J.; Zullah, M.A.; Roh, H.-W.; Ha, P.-S.; Oh, S.-Y.; Lee, Y.-H. CFD validation of performance improvement of a 500 kW Francis turbine. *Renew. Energy* **2013**, *54*, 111–123. [CrossRef]
9. Kurosawa, S.; Lim, S.M.; Enomoto, Y. Virtual model test for a Francis turbine. In *IOP Conference Series: Earth and Environmental Science*; IOP Publishing: Bristol, UK, 2010; Volume 12.
10. Sahu, R.K.; Gandhi, B.K. Erosive flow field investigation on guide vanes of Francis turbine—A systematic review. *Sustain. Energy Technol. Assess.* **2022**, *53*, 102491.
11. Li, G.; Ma, F.; Guo, J.; Zhao, H. Case Study of Roadway Deformation Failure Mechanisms: Field Investigation and Numerical Simulation. *Energies* **2021**, *14*, 1032. [CrossRef]
12. Kamal, M.; Abbas, A.; Prasad, V.; Kumar, R. A numerical study on the performance characteristics of low head Francis turbine with different turbulence models. *Mater. Today Proc.* **2021**, *49*, 349–353. [CrossRef]
13. Shigemitsu, T.; Fukutomi, J.; Kaji, K. Influence of Blade Outlet Angle and Blade Thickness on Performance and Internal Flow Conditions of Mini Centrifugal Pump. *Int. J. Fluid Mach. Syst.* **2011**, *4*, 317–323. [CrossRef]
14. Koirala, R.; Zhu, B.; Neopane, H.P. Effect of Guide Vane Clearance Gap on Francis Turbine Performance. *Energies* **2016**, *9*, 275. [CrossRef]
15. Koirala, R.; Thapa, B.; Neopane, H.P.; Zhu, B.; Chhetry, B. Sediment erosion in guide vanes of Francis turbine: A case study of Kaligandaki Hydropower Plant, Nepal. *Wear* **2016**, *362–363*, 53–60. [CrossRef]
16. Koirala, R.; Neopane, H.P.; Zhu, B.; Thapa, B. Effect of sediment erosion on flow around guide vanes of Francis turbine. *Renew. Energy* **2019**, *136*, 1022–1027. [CrossRef]
17. Thapa, B.S.; Trivedi, C.; Dahlhaug, O.G. Design and development of guide vane cascade for a low speed number Francis turbine. *J. Hydrodyn.* **2016**, *28*, 676–689. [CrossRef]
18. Chitrakar, S.; Dahlhaug, O.G.; Neopane, H.P. Numerical investigation of the effect of leakage flow through erosion-induced clearance gaps of guide vanes on the performance of Francis turbines. *Eng. Appl. Comput. Fluid Mech.* **2018**, *12*, 662–678. [CrossRef]
19. Amedei, A.; Meli, E.; Rindi, A.; Romani, B.; Pinelli, L.; Vanti, F.; Arnone, A.; Benvenuti, G.; Fabbrini, M.; Morganti, N. Innovative design, structural optimization and additive manufacturing of new-generation turbine blades. Turbo Expo: Power for Land, Sea, and Air. *Am. Soc. Mech. Eng.* **2020**, *84089*, V02CT35A004. [CrossRef]
20. Sosilo, A.K.; Hadi, H.; Soehartanto, T. Design of Hydro Power by Using Turbines Kaplan on The Discharge Channel Paiton 1 and 2. *E3S Web Conf.* **2018**, *42*, 01008. [CrossRef]
21. Weili, L.; Jinling, L.; Xingqi, L.; Yuan, L. Research on the cavitation characteristic of Kaplan turbine under sediment flow condition. *IOP Conf. Ser. Earth Environ. Sci.* **2010**, *12*, 012022. [CrossRef]
22. Ma, Y.; Qian, B.; Feng, Z.; Wang, X.; Shi, G.; Liu, Z.; Liu, X. Flow behaviors in a Kaplan turbine runner with different tip clearances. *Adv. Mech. Eng.* **2021**, *13*, 16878140211015879. [CrossRef]

sustainability

MDPI

Article

Impact of a Thermal Barrier Coating in Low Heat Rejection Environment Area of a Diesel Engine

Megavath Vijay Kumar [1,*], Thumu Srinivas Reddy [2], Ch. Rami Reddy [3,*], S. Venkata Rami Reddy [4], Mohammad Alsharef [5], Yasser Alharbi [5] and Basem Alamri [5]

[1] Department of Mechanical Engineering, Malla Reddy Engineering College, Secunderabad 500100, India
[2] Department of Electronics and Communication Engineering, Malla Reddy Engineering College, Secunderabad 500100, India
[3] Department of Electrical and Electronics Engineering, Malla Reddy Engineering College, Secunderabad 500100, India
[4] Department of Electrical and Electronics Engineering, JNTUA College of Engineering, Pulivendula 516390, India
[5] Department of Electrical Engineering, College of Engineering, Taif University, P.O. Box 11099, Taif 21944, Saudi Arabia
* Correspondence: vijaykumar.084@mrec.ac.in (M.V.K.); crreddy229@mrec.ac.in (C.R.R.)

Abstract: The most recent developments in Thermal Barrier Coating (TBC) relate to engine performance, manufacturing and other related challenges. TBC on the piston crown and valves to enhance engine characteristics while using diesel and Mahua Methyl Ester (MME) as a petroleum fuel has a great sustainable development. For this utility, a Direct Injection (DI) conventional diesel engine was renewed to an LHR engine by applying 0.5 mm thickness of $3Al_2O_3$-$2SiO_2$ (as TBC) onto the piston crown and valves. The MME is used in the LHR (Low Heat Rejection) engine. For examination, the fuel injector pressure is set at 200 bar. Compared to a standard DI diesel engine, the results demonstrate that the application of TBC boosts brake thermal efficiency to 13.65% at 25% load. The LHR engine's SFC and BTE significantly improved at full load while using MME fuel. The lower temperature of exhaust gases is achieved by combining MME and diesel fuels with TBC. It was observed that both MME with and without TBC significantly reduced the smoke density. In addition, it was exposed that using MME fuel with TBC very slightly reduced carbon monoxide emissions under all loads. It was also shown that MME with TBC significantly reduced environmental hydrocarbon emissions at all loads.

Keywords: mahua methyl ester biodiesel; diesel fuel; thermal barrier coating; low heat rejection engine; environment; renewable energy

Citation: Vijay Kumar, M.; Srinivas Reddy, T.; Rami Reddy, C.; Rami Reddy, S.V.; Alsharef, M.; Alharbi, Y.; Alamri, B. Impact of a Thermal Barrier Coating in Low Heat Rejection Environment Area of a Diesel Engine. *Sustainability* **2022**, *14*, 15801. https://doi.org/10.3390/su142315801

Academic Editor: Jacopo Bacenetti

Received: 13 October 2022
Accepted: 23 November 2022
Published: 28 November 2022

1. Introduction

In India, the production of inedible oil is poor, leading to some development work undertaken by the Government of India for the production of alternative fuel to inedible oils, such as Jatropha, Mahua, Karanja, Linseed, Cotton, Mustard, Neem, etc. In India, most of the states are tribal regions where Mahua seeds are found in abundance [1,2]. The Mahua tree can provide sources from the seventh year of the plantation onward. Mahua seed oil is a common ingredient of Indian hydrogenated fat. The Mahua raw oil is extracted from the seed kernels and its oil appears similarly to semi-solid fat at room temperature, pale yellow due to the high viscosity in oil. Mahua crude oil contains 30 to 40% free acids. During biodiesel production, the manufacturer can produce various products from glycerin [3,4]. Generally, the raw Mahua Oil (MO) has a high percentage of Free Fatty Acids (FFA) and the change in FFA to biodiesel is very much essential in employing the transesterification or esterification process [5,6]. It is also observed that MO's properties and chemical composition are approximately similar to other inedible oil such as Cotton, Neem, Karanja, etc.,

but the Mahua has a high content of viscosity and FFA. Some renowned processes such as transesterification, esterification, dilution, microemulsion and pyrolysis are utilized to reduce the viscosity in order to produce biodiesel. However, transesterification is one of the best processes for obtaining maximum yield with some effective properties compared to diesel properties [7,8]. The impact of n-butanol/diesel blended fuels on the performance and emissions of heavy-duty diesel engines was investigated. The results showed that the engine performed better when 10% n-butanol was combined with diesel [9]. The effect of n-butanol/diesel fuel on engine performance and emission parameters was investigated and the results revealed that n-butanol at 2% and 4% in the blended fuel reduced emission levels [10]. The impact of n-butanol blended fuels on Euro VI diesel engines was investigated. The findings revealed that diesel/n-butanol mixed fuels increased CO and HC emissions while having no influence on NOx emissions [11]. The combustion and exhaust characteristics of an n-butanol/diesel fuel blend were investigated. The results revealed that the 20% n-butanol/diesel blend reduced soot, NOx, and CO emissions by 56.52%, 17.19%, and 30.43%, respectively, when compared to diesel [12]. The combustion and exhaust characteristics of a blended n-butanol/diesel fuel engine were investigated. The results revealed that n-butanol reduced CO and soot emissions while increasing NOx emissions in n-butanol/diesel fuel [13]. Particulate matter emissions from vehicles can be produced directly throughout fuel combustion or through condensation in the air and nucleation during the dilution and cooling of hot tailpipe exhaust [14]. The majority of particles produced by engine combustion are graphitic carbon, with minor amounts of metallic ash, sulfur compounds, and hydrocarbons [15]. Particle number size distributions (PNSDs) and PM emissions from vehicles are influenced by several factors, including engine type such as SI or CI Engines, type of fuel and engine specifications, vehicle operating conditions, particulate filter technology, and atmospheric conditions (temperature, wind speed, and humidity) [16,17]. One of the physical methods for using vegetable oil in a diesel engine that does not require any chemical treatment is microemulsion [18]. Microemulsions are made by combining esters and dispersants (solvents) with or without diesel fuel to form clear, thermodynamically stable oil-surfactant dispersion [19]. As a result of their higher alcohol content, microemulsions have a lower calorific value than diesel; however, these alcohols have a higher latent heat property and can cool the combustion chamber, reducing nozzle coking. The effects of microemulsification and transesterification on the performance of vegetable oil engines using methanol were examined. The effectiveness of methanol/vegetable oil microemulsions is based on employing methanol-based biodiesel as a surfactant. Previous research focused on the impact of co-surfactants and the effect of catalysts in water oil microemulsions produced from various refined and high-free fatty acid (FFA) oils [20,21]. A few thermos-chemical liquefication studies have focused on using waste sludge mixed with various co-surfactants to develop diesel fuel via microemulsion in enhancing its use and the physicochemical properties of the emulsified fuel. However, due to the high carbon waste and low efficiency, more research is required to enhance this technology for large-scale use [22,23]. As per the authors view, during the combustion of IC engines it was noticed that heat loss is one of the major problems and plays a vital role in all aspects of engine operation such as engine efficiency, fuel consumption, and emissions. Due to the loss of heat energy, the engine's performance and efficiency will be reduced. When the combustion gases take place inside the combustion chamber, the heat energy will be rejected to the atmosphere and pass through the other heat transfer modes. The gas temperature and pressure will be lost due to the engine output.

According to the Global Energy Statistical Yearbook 2020, India consumed 1230 TWh of energy in 2019. In comparison to 2018, global consumption increased by 0.7%. Global energy consumption is expected to skyrocket in the coming century. New industrial power generation equipment materials have resulted in more efficient and long-lasting engines to meet increasing energy demands [24]. Turbines generate energy over a long period. Gas turbines are widely used in energy generation and transportation. The material used in turbine engines has a longevity of over 50,000 h when operated at temperatures ranging

from 900 to 1100 °C. The materials will oxidize regardless of how good they are. Protective coatings are commonly used to keep the fabric from further oxidation and corrosion. Surface modification aims to improve or enhance surface properties that aid in corrosion and oxidation resistance. Coatings have become more resistant to deterioration under operational conditions in recent years [25].

Thermal barrier coatings act as heat barriers, preventing heat from spreading throughout the material. TBC plays an important role in safeguarding parts of gas turbines, internal combustion engines, and other high-temperature machines. TBC is a patterned framework that is layered over metallic segments, such as gas turbine blades. TBCs are distinguished by their low heat conductivity; the coating withstands extremely high temperatures when subjected to a heat stream [26,27]. The need for a higher working temperature in today's gas turbines is an ever-increasing process to improve their work productivity. As a result, the extended working temperatures exceed the melting point of nickel-based super alloys, which is deleterious to the chemical and heat-resistant properties of these composites. As a result, it is critical to protect these substrate materials from high operating temperature levels by providing heat protection via TBC's. Many years ago, ceramics were used before the LHR Engines. Cerium is also used in a thermal barrier coating with a high melting point that is spattered on the outside of alloy parts and has a thickness of 120–400 µm. Ceramic materials have a lower heat conduction coefficient and weight than the other materials used in conventional methods [28]. Nowadays, it is observed that ceramic materials have grown to achieve a better performance in diesel engines [29,30]. Lanthanum zirconate (LaZrO) is well-known in aircraft engines for its high melting point and good thermal stability. The thermal properties and failure mechanisms of these advanced TBCs remain difficult to understand [31]. Due to TBC's capacity to shield, which permits greater working temperatures and lowers the cost of cooling systems, this trend will undoubtedly continue, improving component efficiency overall [32]. The significant lengthening of YSZ TBC lifetime with the application of particular transient regimes with medium cooling/heating rates. This would enable the usage of YSZ at surface temperatures much higher than 1200 °C [33,34]. This paper examines the current state of TBCs, including the most recent developments in terms of their performance and manufacture, associated difficulties, and suggestions for their potential usage in severe settings such as diesel engines, aerospace, nuclear, high-temperature, or other.

Consequently, the loss of heat transfer energy in the engine decreases the overall performance. Many experimental studies have been conducted to gain a better understanding of the mechanisms that affect heat transfer within the combustion chamber. Each of these fundamental studies has contributed to understanding heat transfer in the IC engine, with the ultimate goal of improved engine performance and efficiency. Thus, many have demonstrated that the most essential factors affecting heat transfer include engine load, speed, compression ratio, ignition timing, fuel pressure variation, and equivalence ratio. By applying TBC onto the piston crown and valve, the direct injection (DI) conventional diesel engine is transformed into an LHR engine to reduce heat loss [24]. Enhancing the LHR engine with effective TBC promises lower fuel consumption, higher thermal efficiency, lowering emissions and elimination of the cooling system [25]. Several ceramic coatings such as Mullite, AL_2O_3, TiO_2, CaO/MgO–ZrO_2 and Yttria-stabilized Zirconia (YSZ), have been used in several engine applications [26,27].The key contributions of this paper are summarized as follows:

- The system was designed to improve the diesel engine with certain modified parameters such as Thermal Barrier Coating on the piston crown and valve surface based on a thorough literature review;
- The conventional diesel engine was aimed renewed to an LHR engine by applying 0.5 mm thickness of $3Al_2O_3$-$2SiO_2$ (as TBC) onto the piston crown and valves;
- In addition, an alternative fuel was used to reduce emissions with a low heat rejection system;

- Mahua oil was selected for investigation with TBC due to more O_2 content present in Mahua oil.

As per the literature survey, further criteria are discussed in choosing the TBC for diesel engines and the Mullite material characteristics are covered in Section 2. The transesterification procedure for creating Mahua Methyl Ester from its raw oil is described in Section 3. The comparison of the various fuel attributes is discussed in Section 4, along with an analysis. The experimental photography and the engine parameters are described in Section 5, alongside their specifications.

2. Low Heat Rejection Engine

Selection of TBC Material for IC Engines

To fulfill the requirement of a suitable TBC, we have to find an appropriate TBC with a good attachment of coating materials that can resist rigorous conditions in the diesel combustion chamber. The essential requirements for an excellent quality TBC are outlined below.

- Chemical inertness;
- Good adherence capability with a metallic substrate;
- Higher melting point of a material;
- Lower thermal conductivity of a material;
- At room temperature, no phase changes take place;
- Same thermal expansion coefficient with the metallic substrate [35,36].

Even though numerous ceramic materials are used as TBC in diesel engines, the physical properties of Mullite, such as thermal conductivity, high corrosion resistance, high hardness, good thermal shock resistance below 1273 K, etc., are promising. There are some physical properties of Mullite as TBC as shown in the below Table 1. From the below table, we can expect that a quality outside layering material is quite suitable for an internal combustion engine's purpose.

Table 1. Properties of Mullite.

Name	Properties				
Mullite ($3Al_2O_3$-$2SiO_2$)	Melting Point	Poisson's Ratio	Thermal Conductivity (λ)	Young's Modulus (E)	Thermal Expansion Coefficient (α)
	2123 K	0.25	3.3 W/mk (1400 K)	127 GPa (293 K)	5.3×10^{-6} (293–1273 K)

The conventional engine was converted into an LHR engine with a Mullite coating in order to improve the engine. For this purpose, one bore diesel engine is transformed into LHR engine by applying the Mullite of 0.5 mm thickness onto the valves and piston crown as shown in Figure 1.Later, experimental work was carried out with standard diesel and biodiesel with and without TBC to analyze the performance and emission characteristics.

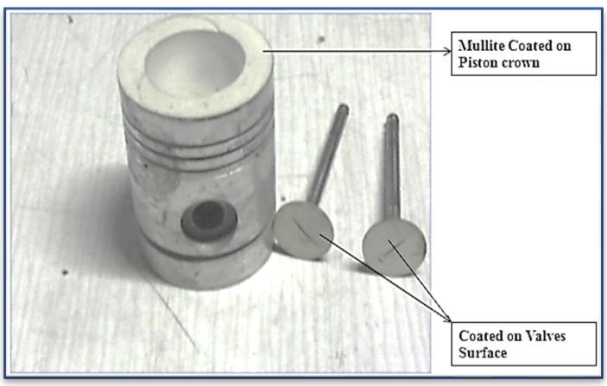

Figure 1. Mullite coated to Piston crown and valves surface.

3. Transesterification Process

In this section, the transesterification process is presented. Initially, the Mahua oil is preheated at 65 °C to 70 °C for 30 min to remove the moisture content. After the preheating process, 1000 mL of Mahua oil is taken with 14 g of potassium hydroxide and 300 mL of methanol. The potassium hydroxide and methanol are added to 1000 mL of Mahua oil, then it is heated at 55 °C and simultaneously the solution has to be stirred for 60 min. During the process, the chemicals react with the Mahua oil and produce the MME. After finishing the process, the mixture is allowed to settle down in a separating flask for 24 h. Once the reaction process is completed, the glycerin must be settled down and the methyl ester should be separated in a separate container. After the separation, the MME should be washed with distilled warm water. The distilled water is heated at 45 °C; then, the heated distilled water is mixed with MME and after mixing the solution, it must be shaken gently to remove residual catalyst or soap content. Then, the distilled water is removed. The MME is then heated at 100 °C for 30 min to remove the trace of water left over in it. Finally, the Mahua biodiesel was obtained as per the methodology of the reference article [37] as shown in Figure 2.

Figure 2. Final Product of Pure Mahua Biodiesel.

4. Fuel Properties

Various physical properties of diesel and MME fuels are mentioned in Table 2. Some of the physical properties, such as density, specific gravity, kinematic viscosity, calorific value, flash point, fire point, Cloud point, pour point and colour, were tested in the fuel laboratory of Malla Reddy Engineering College, India and the rest of the properties were cited [38]. The properties of the MME fuel are within the standard of ASTM D 6751 and EN 14214.

Table 2. Properties of the Fuels.

Properties	Diesel	MME	Test-Method	Instruments Used
Density(15 °C), kg/m^3	835	872	EN ISO 3675/EN ISO 12185	Hydrometer
Specific gravity	0.850	0.916	ASTM D792	Hydrometer
Kinematic viscosity at 40 °C, mm^2/s	2.4	4.0	EN ISO 3104/EN 14105	Redwood Viscometer
Calorific value (KJ/kg)	42,930	39,400	ASTM D240	Bomb Calorimeter
FlashPoint °C	70	127	EN ISO 2719/EN ISO 3679	Pensky-Martens
FirePoint °C	76	136	EN ISO 2719/EN ISO 3679	Pensky-Martens
Cloud point °C	−10 to −15	6	ASTM D2500	Cloud Point
Pour point °C	−35 to −15	1	ASTM D97	Pour Point
Colour	Light brown	Dark yellow	NM	Based on eye visibility
Cetane number	51	46	EN ISO 5165	[38]
Aniline point °C	69	63	EN 14111	[38]
Iodine value	NM	60	ASTM D1959-97	[38]
Diesel index	150	145	NM	[38]

Note: NM = Not measured.

5. Experimental Setup Description

5.1. Engine Test

A 3.5 kW single bore diesel engine (Table 3) with a fixed speed 1500 rpm water cooled is used for the investigation to progress the performance and to diminish the harmful emissions. The layout of the experimentation setup has been depicted in Figure 3. For loading the engine, the eddy current dynamometer has been used for investigation.

Table 3. Engine Specifications.

Name of the Specifications	Values
Name of Engine	Kirloskar
Stroke	4
Type of cooling	Water Cooled
Loading Type	Eddy Current Dynamometer
BHP	5
Stroke length	110 mm
Bore	80 mm
No. of Cylinder	1
Compression Ratio	16.5:1
Speed	1500 rpm
Fuel Injection Pressure	200 bar
Rated output	3.68 kw (5.0 hp)
Connecting Rod Length	230.0 mm
Exhaust Valve Open	20° BBDC [39]
Exhaust Valve Closes	20° ATDC [39]
Inlet Valve Open	20°BTDC [39]
Inlet Valve Close	25° ATDC [39]
Injection Advance	27° BTDC

The fuel has been injected into a cylinder with a pressure of 200 bar. The timing made for valve opening and closing is the exhaust valve opens at 20° BBDC, the exhaust valve closes at 20° ATDC, the inlet valve opens at 20° BTDC and the inlet valve closes at 25° ATDC. The fuel injection timing was maintained at 27° before Top Dead Center. Emission gas analyzers and smoke analyzers were used to find the content of HC, CO, NO_x, and smoke opacity.

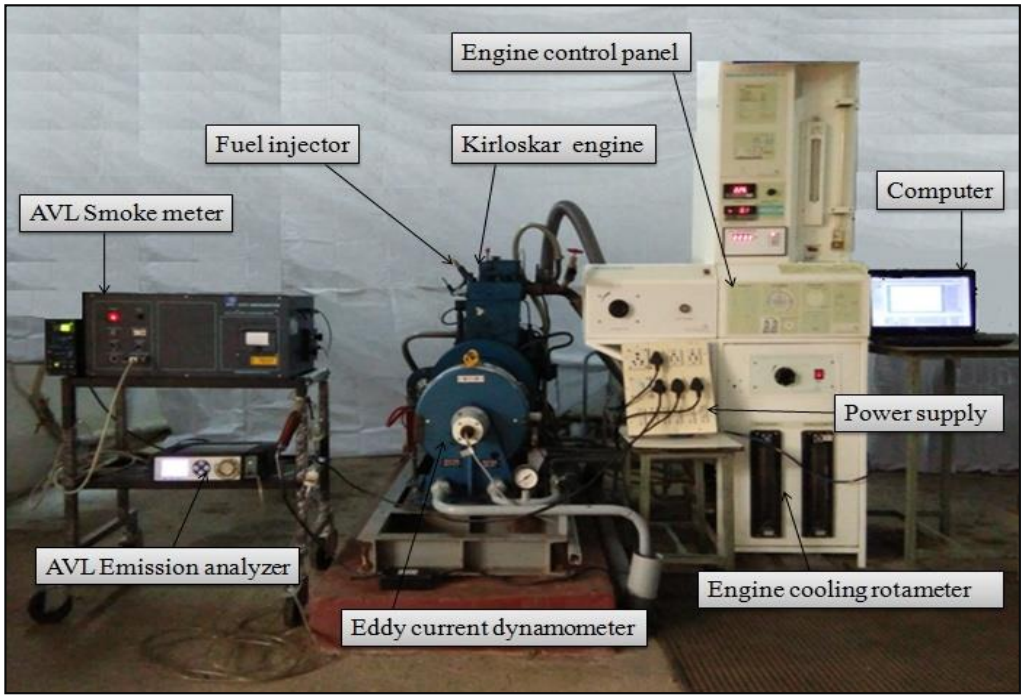

Figure 3. Photograph view of an experimental setup.

5.2. AVL 444 Gas Analyzer

This procedure must be performed on gas analyzers after they have been field-commissioned and for subsequent calibration. The accuracy and measuring ranges are presented in Tables 4 and 5.

Table 4. Gas Analyzer Measuring Range.

S. No.	Measured Parameter	Specification
1	Oxygen	0–22% vol.
2	Carbon monoxide	0–10% vol.
3	Carbon dioxide	0–20% vol.
4	Hydro carbon	0–20,000 ppm
5	Nitrogen oxide	0–5000 ppm
6	Engine speed	400–6000 rpm
7	Oil temperature	30–125 °C
8	Lambda	0 to 9.999

Table 5. Gas Analyser Accuracy.

S. No.	Measured Parameter	Specification
1	Oxygen	<2% vol.: ±0.1% vol. >2% vol.: ±1% vol.
2	Carbon monoxide	<0.6% vol.: ±0.03% vol. >0.6% vol.: ±5% vol.
3	Carbon dioxide	<10% vol.: ±0.5% vol. >10% vol.: ±5% vol.
4	Hydro carbon	<200 ppm: ±10 ppm >200 ppm ±5% of ind. value
5	Nitrogen oxide	<5000 ppm: ±50 ppm
6	Engine speed	±1% of ind. value
7	Oil temperature	±4 °C

The test procedure for gas analyzers is as follows:

- Ensure that the power supply meets the manufacturer's specifications and that the electrical earthing is correct;
- Ensure that all of the accessories specified by the manufacturer are present and functional;
- Validate the span and zero calibration with suitable CO and HC sample gases;
- Examine the electrical calibration;
- Ensure that the sampling system is leak-free;
- The printer is operational, and the printout details are correct;
- Using this analyzer, check one vehicle for idling emission measurement.

5.3. Specification of AVL Smoke Meter and its Operating Conditions

The specifications of AVL smoke meter are presented in Table 6. Operating conditions:

- Warm-up time:20 min (max.) at 220 V Supply;
- Operating temperature:0–50 °C;
- Relative humidity:90% at 50 °C relative humidity (non condensing).

Table 6. Specification of AVL smoke meter.

Type	Values/Model
Make and Model	AVL 437C Smoke meter
Sampling type	Partial flow
Light source	Halogen Lamp, 12 V/5 W
Range	0–100% opacity, 0–99.99 m^{-1} absorption
RPM	400–6000 in

5.4. Percentage Uncertainties of Calculated Parameters

The uncertenities of calculated parameters are shown in Table 7.

Table 7. Uncertainties for Calculated parameters.

Parameters	Percentage Uncertainties
Brake power	±0.5
Brake specific fuel consumption	±1.5
Brake thermal efficiency	±1.0

6. Results and Discussion

At different loadings, the LHR engine was investigated for different diesel and biodiesel with TBC and without TBC. The result was analyzed and is presented in the following sections.

6.1. Performance and Emission Parameters

6.1.1. Brake Specific Fuel Consumption

The variation of brake specific fuel consumption (BSFC) with a load at 200 bar pressure, which shows the results both with and without TBC for different fuels, is presented in Figure 4. Here, the fuel consumption of diesel is lower when compared to biodiesel. The BSFC without TBC of diesel at full load is 0.40 kg/kWh and for biodiesel is 0.44 kg/kWh. The comparison of TBC of diesel at full load is 0.37 kg/kWh and for biodiesel is 0.42 kg/kWh. At 25% load diesel with TBC, fuel consumption was found to be lower. The use of with and without TBC increases biodiesel fuel consumption because of its lower calorific value.

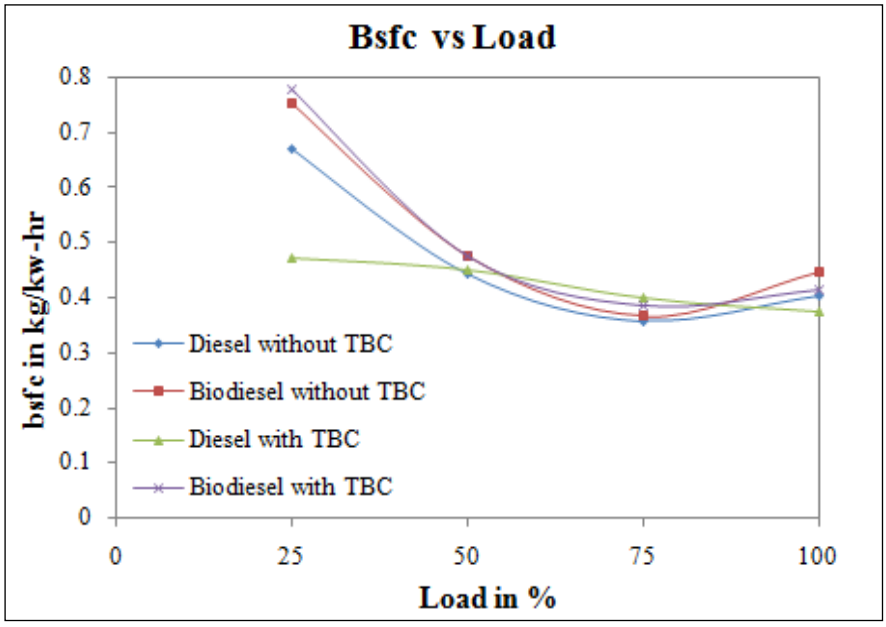

Figure 4. BSFC vs. Load.

6.1.2. Brake Thermal Efficiency

The Figure 5 shows the variation of brake thermal efficiency (BTE) with load at 200 bar pressure. The experiment was conducted with and without TBC for different fuels. At 25% load condition, diesel with TBC was found to be improved. At full load conditions, not much remarkable improvement was observed because higher viscosity leads to poor atomization, fuel vaporization and combustion. Hence, there was not much improvement in thermal efficiency.

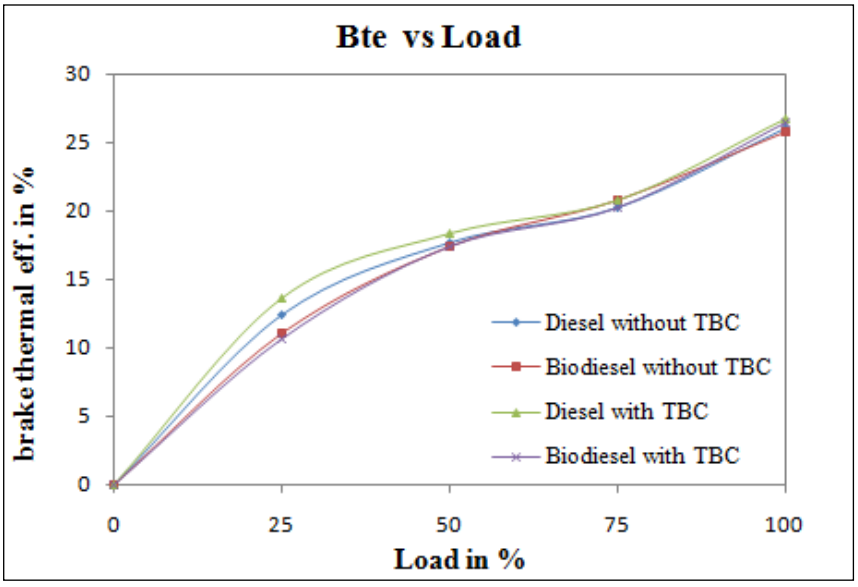

Figure 5. BTE vs. Load.

6.1.3. Exhaust Gas Temperature

Figure 6 shows the variation of exhaust gas temperature with a load at 200 bar injection pressure. The results showed that, in all cases, the exhaust gas temperature increased with the increase in load. For the diesel and biodiesel fueled without TBC, the biodiesel was the highest value of exhaust gas temperature of 265 °C, whereas the corresponding value with diesel was found to be 255 °C; for biodiesel with TBC, the highest value of exhaust gas temperature

was 427 °C, whereas the corresponding value with diesel was found to be 337 °C only. The exhaust temperature having a higher percentage of biodiesel was found to be higher at the entire load in comparison to diesel oil with TBC. The MME and diesel without TBC were found to lower exhaust gas temperature compared to others with TBC. This may be due to the higher combustion temperature of TBC, which gains more heat during the combustion process, and the presence of more oxygen in biodiesel, resulting in a higher peak combustion temperature; this, therefore, increases the exhaust gas temperature for biodiesel at full load.

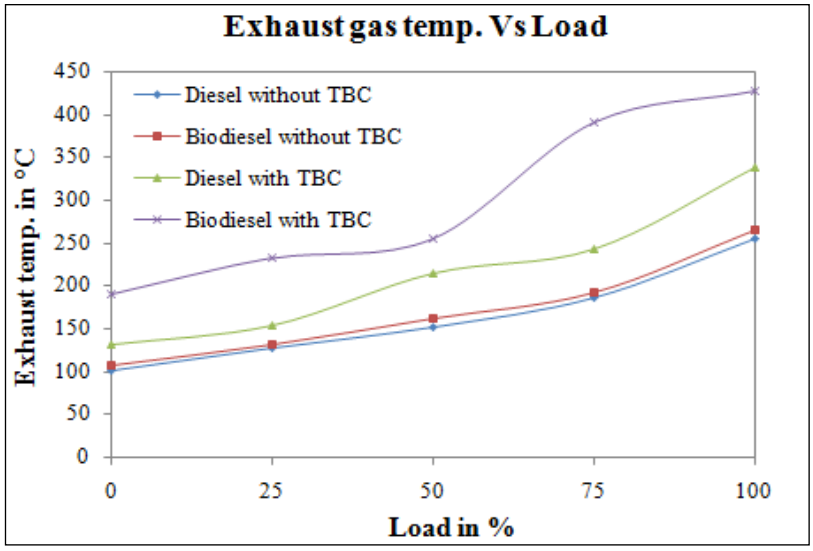

Figure 6. Exhaust Gas Temperature vs. Load.

6.1.4. Smoke Density

The variation of smoke density with load is shown in Figure 7. The smoke density of biodiesel with and without TBC was found significantly reduced compared to diesel with TBC and without TBC. This is because biodiesel has a better vaporization effect at higher combustion temperatures, and there is more oxygen in biodiesel. In comparison to all other trends, the particulate matter has been reduced for biodiesel with TBC because TBC has the ability to resist heat in the combustion chamber, which has aided in the burning of smoke particles.

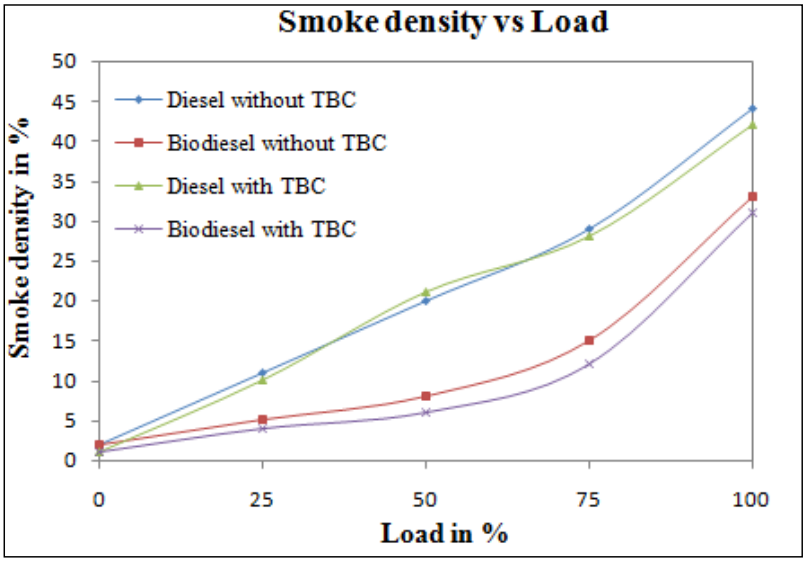

Figure 7. Smoke Density vs. Load.

6.1.5. CO Emissions

Figure 8 shows the variation of carbon monoxide emission with load at 200 bar injection pressure. The results were compared with and without TBC which was fueled with diesel and biodiesel. At 100% load condition, the results were found to increase the CO emissions compared to the different loads such as 0%, 25%, 50% and 75%. At 1% to 75% load, the CO emission was found to be lower because of improvements in combustion and because more oxygen molecules are contained in biodiesel [40]. At all load conditions, the flow rate of the air will be constant, but the fuel flow rate will vary as the load varies. So, as the fuel flow rate increases, the mixture keeps becoming rich. However, in the case of high load, with more amount of fuel and a lower amount of air present, and also as a result of the improper mixing, more carbon monoxide will be released.

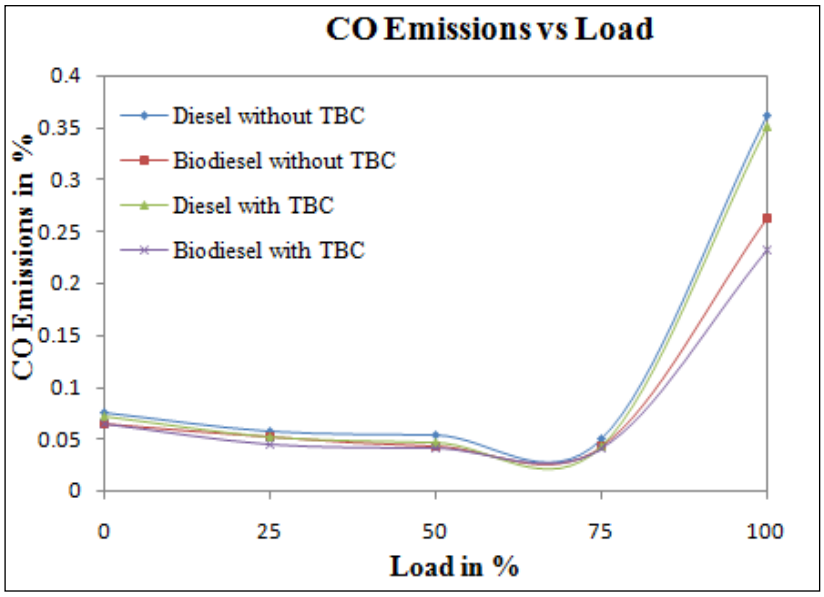

Figure 8. CO Emissions vs. Load.

6.1.6. HC Emissions

The comparisons of hydrocarbon emissions of diesel and biodiesel at 200 bar injection pressure with and without TBC are shown in Figure 9. Biodiesel was found to emit much fewer HC emissions compared to the baseline fuel. At maximum load without TBC, the HC emissions are 90 (PPM) for diesel and for biodiesel 47 (PPM). At 100% load without TBC, biodiesel emits much fewer CO emissions compared to diesel. At maximum load, there was a remarkable reduction in HC emissions: 63 (PPM) for diesel and 45 (PPM) for biodiesel with TBC. The use of thermal barrier coating inside the cylinder resists the high temperature at the surface of the cylinder due to the high temperature, the formation of hydrocarbon will reduce. Additionally, the use of biodiesel with TBC enhances in the reduction in HC due to the oxygen present in biodiesel. This may be owing to an increase in combustion gas temperature as a result of a decline in heat losses.

6.1.7. NOx Emissions

The variation of oxide of nitrogen (NOx) with load at 200 bar pressure, which is shown with and without TBC for diesel and biodiesel fuels, is presented in Figure 10. NOx is formed by oxidizing nitrogen in the atmosphere at a sufficiently high temperature, depending on the number of oxygen ions present. It was well noted that the biodiesel with and without TBC causes more NOx emissions because more O_2 levels are present in biodiesel which helps in better combustion and results in increasing the temperature. The diesel without TBC was found to lower NOx emissions.

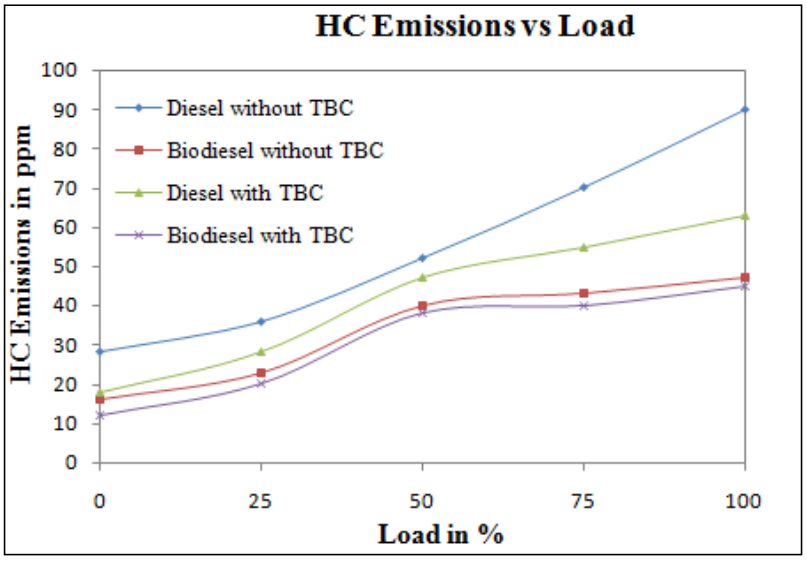

Figure 9. HC Emissions vs. Load.

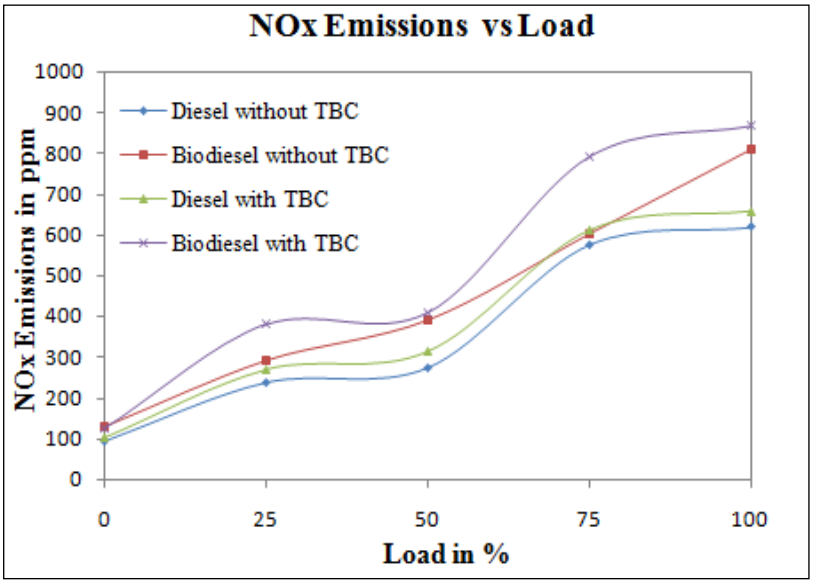

Figure 10. NOx vs. Load.

7. Conclusions

In the current work, to improve engine performance with Mahua biodiesel in CI engines, different technologies with and without TBC have been studied and compared with baseline fuel. Here, experiments were conducted with biodiesel and TBC technologies and have been studied extensively through performance and emissions. The experiments were demonstrated with constant fuel injector pressure of 200 bar and at a constant speed of 1500 rpm. Now that we have conducted the investigation and analysis of the LHR engine, we reveal the important conclusions below.

The Mahua methyl ester properties of density, fire point, flash point, and kinematic viscosity were observed to be within the limits of ASTM D 6751 and EN 14214 specifications. The property value is observed to be sealed and higher than the diesel. The calorific value (CV) of the alternative fuel is seen to be lower than diesel. This will cause an increase in ignition delay during the combustion process in LHR engine.

DI diesel engine was transformed to an LHR engine with the modification of 0.5 mm thickness of $3Al_2O_3$-$2SiO_2$ as TBC onto the piston crown and valves. Later, the engine characteristics were investigated and analyzed.

The fuel consumption of diesel is lower when compared to MME biodiesel. Due to the low calorific value, using and not using the TBC will increase the fuel consumption of biodiesel.

A significant increase in brake thermal efficiency at 25% load condition diesel with TBC was found to be improved due to the TBC.

Using TBC, good results for exhaust gas temperature with diesel and MME were obtained at all loads. The use of thermal barrier coating inside the cylinder resists the high temperature at the surface of the cylinder due to this more heat is attained during combustion by the TBC. A temperature of 427 °C was achieved by biodiesel with TBC high load and 337 °C by diesel with TBC at a high load. The smoke density of MME with and without TBC was found significantly reduced due to the greater amount of O_2 atoms present in the biodiesel and as well as the use of thermal barrier coating inside the cylinder resist the high temperature at the surface.

CO emissions were observed to decrease with the combination of biodiesel and TBC at all loads. This was due to the resistance of heat in a combustion chamber, as well as the biodiesel being given an extra dose of oxygen content in burning. At all loads, MME biodiesel with TBC was found a remarkable reduction in HC emissions. At maximum load, there was a remarkable reduction in HC emissions: 63 (PPM) for diesel and 45 (PPM) for biodiesel with TBC. This happened due to the O_2 molecules present in the MME oil.

It is observed that biodiesel with and without TBC causes more NOx emissions, and that biodiesel with TBC has increased to 870 ppm of NOx emission at high load conditions. High-temperature fuel combustion occurs when a fuel is burned at a temperature high enough (over 1300 °C or 2370 °F) to cause some of the nitrogen in the air to oxidize and produce NOx emissions. The diesel without TBC was found to lower NOx emissions.

As a result, MME biodiesel can be used as a substitute fuel for diesel engines, rather than modified and unmodified diesel fuel. For added benefit, the TBC can be used as a diesel engine substitute fuel.In future works, we can go to further enhance the engine with different alternative fuels and fuel additives. Moreover, to reduce the NOx, it can be investigated with the exhaust gas recirculation system.

Author Contributions: Conceptualization M.V.K., C.R.R.; methodology, S.V.R.R., M.V.K.; software, M.V.K., C.R.R.; validation M.A., Y.A. and B.A.; formal analysis, M.V.K.; investigation, M.V.K. and C.R.R.; resources, M.V.K.; data curation, C.R.R. and T.S.R.; writing—original draft preparation, M.V.K.; writing—review and editing, C.R.R., S.V.R.R., T.S.R., M.A., Y.A. and B.A.; visualization, B.A.; supervision, C.R.R. and T.S.R.; project administration, M.V.K.; funding acquisition, B.A. All authors have read and agreed to the published version of the manuscript.

Funding: The authors would like to acknowledge the financial support received from Taif University Researchers Supporting Project Number (TURSP-2020/278), Taif University, Taif, Saudi Arabia.

Institutional Review Board Statement: Not applicable.

Informed Consent Statement: Not applicable.

Data Availability Statement: Not applicable.

Conflicts of Interest: The authors declare no conflict of interest.

References

1. Nandi, S. Performance of CI engine by using biodiesel-mahua oil. *Am. J. Eng. Res.* **2013**, *2*, 22–47.
2. Padhi, S.K.; Singh, R.K. Optimization of esterification and transesterification of Mahua (Madhuca Indica) oil for production of biodiesel. *J. Chem. Pharm. Res.* **2010**, *2*, 599–608.
3. Agarwal, A.; Das, L.M. Biodiesel Development and Characterization for Use as a Fuel in Compression Ignition Engines. *J. Eng. Gas Turbines Power* **2001**, *123*, 440–447. [CrossRef]
4. Padhi, S.K.; Singh, R.K. Non-edible oils as the potential source for the production of biodiesel in India: A re-view. *J. Chem. Pharm. Res.* **2011**, *3*, 39–49.
5. Vijay Kumar, M.; Veeresh Babu, A.; Ravi Kumar, P. Producing biodiesel from crude Mahua oil by two steps of trans-esterification process. *Aust. J. Mech. Eng.* **2019**, *17*, 2–7. [CrossRef]
6. Azam, M.M.; Waris, A.; Nahar, N. Prospects and potential of fatty acid methyl esters of some non-traditional seed oils for use as biodiesel in India. *Biomass Bioenergy* **2005**, *29*, 293–302. [CrossRef]

7. Chauhan, P.S.; Chhibber, V.K. Non-edible oil as a source of bio-lubricant for industrial applications: A re-view. *Int. J. Eng. Sci. Innov. Technol.* **2013**, *2*, 299–305.
8. Sirurmath, S.; Vikram, P.M.; Das, G. Transesterification of Fish Oil and Performance Study on 4-Stroke CI Engine with Blends of Fish Biodiesel. *IJRET Int. J. Res. Eng. Technol.* **2014**, *3*, 608–612.
9. Tipanluisa, L.; Fonseca, N.; Casanova, J.; López, J.-M. Effect of n-butanol/diesel blends on performance and emissions of a heavy-duty diesel engine tested under the World Harmonised Steady-State cycle. *Fuel* **2021**, *302*, 121204. [CrossRef]
10. Şahin, Z.; Aksu, O.N. Experimental investigation of the effects of using low ratio n-butanol/diesel fuel blends on engine performance and exhaust emissions in a turbocharged DI diesel engine. *Renew. Energy* **2015**, *77*, 279–290. [CrossRef]
11. Lapuerta, M.; Hernández, J.J.; Rodríguez-Fernández, J.; Barba, J.; Ramos, A.; Fernández-Rodríguez, D. Emission benefits from the use of n-butanol blends in a Euro 6 diesel engine. *Int. J. Engine Res.* **2018**, *19*, 1099–1112. [CrossRef]
12. Nayyar, A.; Sharma, D.; Soni, S.L.; Mathur, A. Experimental investigation of performance and emissions of a VCR diesel engine fuelled with n-butanol diesel blends under varying engine parameters. *Environ. Sci. Pollut. Res.* **2017**, *24*, 20315–20329. [CrossRef] [PubMed]
13. Siwale, L.; Kristóf, L.; Adam, T.; Bereczky, A.; Mbarawa, M.; Penninger, A.; Kolesnikov, A. Combustion and emission characteristics of n-butanol/diesel fuel blend in a turbo-charged compres-sion ignition engine. *Fuel* **2013**, *107*, 409–418. [CrossRef]
14. Maricq, M.; Chase, R.; Podsiadlik, D.; Vogt, R. Vehicle exhaust particle size distributions: A comparison of tailpipe and dilution tunnel measure-ments. *SAE Trans.* **1999**, *108*, 721–732.
15. Shi, J.P.; Mark, D.; Harrison, R.M. Characterization of Particles from a Current Technology Heavy-Duty Diesel Engine. *Environ. Sci. Technol.* **2000**, *34*, 748–755. [CrossRef]
16. Myung, C.L.; Park, S. Exhaust nanoparticle emissions from internal combustion engines: A review. *Int. J. Automot. Technol.* **2011**, *13*, 9–22. [CrossRef]
17. Vu, T.V.; Delgado-Saborit, J.M.; Harrison, R.M. Review: Particle number size distributions from seven major sources and implications for source apportionment studies. *Atmos. Environ.* **2015**, *122*, 114–132. [CrossRef]
18. Fangrui, M.; Hanna, M.A. Biodiesel production: A review. *Bioresour. Technol.* **1999**, *70*, 1–15.
19. Yusuf, N.; Kamarudin, S.; Yaakub, Z. Overview on the current trends in biodiesel production. *Energy Convers. Manag.* **2011**, *52*, 2741–2751. [CrossRef]
20. Wellert, S.; Karg, M.; Imhof, H.; Steppin, A.; Altmann, H.J.; Dolle, M.; Richardt, A.; Tiersch, B.; Koetz, J.; Lapp, A.; et al. Structure of biodiesel based bicontinuous microemulsions for environmentally compatible decontamina-tion: A small angle neutron scattering and freeze fracture electron microscopy study. *J. Colloid Interface Sci.* **2008**, *325*, 250–258. [CrossRef]
21. de Jesus, A.; Silva, M.M.; Vale, M.G.R. The use of microemulsion for determination of sodium and potassium in biodiesel by flame atomic absorption spectrometry. *Talanta* **2008**, *74*, 1378–1384. [CrossRef] [PubMed]
22. Ding, X.; Yuan, X.; Leng, L.; Huang, H.; Wang, H.; Shao, J.; Jiang, L.; Chen, X.; Zeng, G. Upgrading Sewage Sludge Liquefaction Bio-Oil by Microemulsification: The Effect of Ethanol as Polar Phase on Solubilization Performance and Fuel Properties. *Energy Fuels* **2017**, *31*, 1574–1582. [CrossRef]
23. Leng, L.; Han, P.; Yuan, X.; Li, J.; Zhou, W. Biodiesel microemulsion upgrading and thermogravimetric study of bio-oil produced by liquefaction of different sludges. *Energy* **2018**, *153*, 1061–1072. [CrossRef]
24. Karaoglanli, A.C.; Dikici, H.; Kucuk, Y. Effects of heat treatment on adhesion strength of thermal barrier coating systems. *Eng. Fail. Anal.* **2013**, *32*, 16–22. [CrossRef]
25. Buyukkaya, E.; Cerit, M. Experimental study of NOx emissions and injection timing of a low heat rejection diesel engine. *Int. J. Therm. Sci.* **2008**, *47*, 1096–1106. [CrossRef]
26. Cao, X.Q.; Vassen, R.; Stoever, D. Ceramic materials for thermal barrier coatings. *J. Eur. Ceram. Soc.* **2004**, *24*, 1–10. [CrossRef]
27. MohamedMusthafa, M.; Sivapirakasam, S.; Udayakumar, M. Comparative studies on fly ash coated low heat rejection diesel engine on performance and emission characteristics fueled by rice bran and pongamia methyl ester and their blend with diesel. *Energy* **2011**, *36*, 2343–2351. [CrossRef]
28. Jia, L.; Wen, T.; Tian, C.; Liu, Z.; Yu, J.; Yuan, L. Preparation and thermophysical properties of RE2CrTaO7 (Y, Sm, Dy, Yb) ceramics for thermal barrier coating applications. *Ceram. Int.* **2022**, *48*, 23814–23820. [CrossRef]
29. Lima, C.; Guilemany, J. Adhesion improvements of Thermal Barrier Coatings with HVOF thermally sprayed bond coats. *Surf. Coatings Technol.* **2007**, *201*, 4694–4701. [CrossRef]
30. Gatowski, J.A. Evaluation of a selectively-cooled single-cylinder 0.5-l Diesel engine. *SAE Trans.* **1990**, *99*, 1580–1591.
31. Shen, Z.; Liu, G.; Dai, J.; He, L.; Mu, R. LaNdZrO thermal barrier coatings by electron beam physical vapor deposition: Morphology, thermal property and failure mechanism. *Chem. Eng. J. Adv.* **2022**, *11*, 100328. [CrossRef]
32. Mondal, K.; Nuñez, L., III; Downey, C.M.; van Rooyen, I.J. Recent advances in the thermal barrier coatings for extreme environments. *Mater. Sci. Energy Technol.* **2021**, *4*, 208–210. [CrossRef]
33. Vaßen, R.; Bakan, E.; Mack, D.E.; Guillon, O. A Perspective on Thermally Sprayed Thermal Barrier Coatings: Current Status and Trends. *J. Therm. Spray Technol.* **2022**, *31*, 685–698. [CrossRef]
34. Mondal, K.; Nuñez, L., III; Downey, C.M.; Van Rooyen, I.J. Thermal barrier coatings overview: Design, manufacturing, and applications in high-temperature industries. *Ind. Eng. Chem. Res.* **2021**, *60*, 6061–6077. [CrossRef]
35. Kamo, R.; Assanis, D.N.; Bryzik, W. Thin Thermal Barrier Coatings for Engines. *SAE Trans.* **1989**, *98*, 131–136. [CrossRef]
36. Abedin, M.J.; Masjuki, H.H.; Kalam, M.A.; Sanjid, A.; Ashraful, A.M. Combustion, performance, and emission characteristics of low heat rejection engine operating on various biodiesels and vegetable oils. *Energy Convers. Manag.* **2014**, *85*, 173–189. [CrossRef]

37. Kumar, M.V.; Veeresh Babu, A.; Ravi Kumar, P. Experimental investigation on mahua methyl ester blended with diesel fuel in a compression ignition diesel engine. *Int. J. Ambient. Energy* **2019**, *40*, 304–316. [CrossRef]
38. Vijay Kumar, M.; Babu, A.V.; Kumar, P.R.; Reddy, S.S. Experimental investigation of the combustion characteristics of Mahua oil biodiesel-diesel blend using a DI diesel engine modified with EGR and nozzle hole orifice diameter. *Biofuel Res. J.* **2018**, *5*, 863–871. [CrossRef]
39. Basaran, H.U.; Ozsoysal, O.A. Effects of application of variable valve timing on the exhaust gas tem-perature improvement in a low-loaded diesel engine. *Appl. Therm. Eng.* **2017**, *122*, 758–767. [CrossRef]
40. Hegab, A.; Dahuwa, K.; Islam, R.; Cairns, A.; Khurana, A.; Shrestha, S.; Francis, R. Plasma electrolytic oxidation thermal barrier coating for reduced heat losses in IC engines. *Appl. Therm. Eng.* **2021**, *196*, 117316. [CrossRef]

Case Studies in Thermal Engineering 40 (2022) 102557

Contents lists available at ScienceDirect

Case Studies in Thermal Engineering

journal homepage: www.elsevier.com/locate/csite

Investigation of the combustion of exhaust gas recirculation in diesel engines with a particulate filter and selective catalytic reactor technologies for environmental gas reduction

Megavath Vijay Kumar [a,**], Alur Veeresh Babu [b], Ch. Rami Reddy [c], A. Pandian [d], Mohit Bajaj [e], Hossam M. Zawbaa [f,g,h,*], Salah Kamel [i]

[a] Department of Mechanical Engineering, Malla Reddy Engineering College, Maisammaguda, Secunderabad, 500100, Telangana, India
[b] Department of Mechanical Engineering, National Institute of Technology Warangal, Warangal, 506004, Telangana, India
[c] Department of Electrical and Electronics Engineering, Malla Reddy Engineering College, Maisammaguda, Secunderabad, 500100, Telangana, India
[d] Department of Electrical and Electronics Engineering, Koneru Lakshmaiah Education Foundation, Guntur, Andhra Pradesh, India 522502
[e] Department of Electrical Engineering, Graphic Era (Deemed to Be University), Dehradun, 248002, India
[f] Faculty of Computers and Artificial Intelligence, Beni-Suef University, Beni-Suef, Egypt
[g] Technological University Dublin, Dublin, Ireland
[h] Applied Science Research Center, Applied Science Private University, Amman, Jordan
[i] Electrical Engineering Department, Faculty of Engineering, Aswan University, 81542, Aswan, Egypt

ARTICLE INFO

Keywords:
Diesel engine
Diesel particulate filter
Selective catalytic converter
Exhaust gas recirculation
Harmful emissions
Environment
Gas reduction
Sustainable development

ABSTRACT

The use of diesel engines has increased dramatically in recent years, as has the number of exhaust emissions. These emissions have the potential to endanger Mother Nature and the living species within it. Governments all over the world have introduced legislative rules on exhaust emission reduction in order to limit the number of emissions released into the environment through the use of global sustainable development technologies. This has compelled automobile manufacturers to create a variety of diesel emission reduction systems, the most important of which are the Diesel Particulate Filter (DPF), Exhaust Gas Recirculation (EGR), and Selective Catalytic Reactor (SCR). The primary goal of this research work is to reduce diesel engine exhaust gas emissions by utilizing emission reduction systems such as DPF, EGR, and SCR. Here, various combinations of the aforementioned emission reduction systems were tested to determine the best possible combination that had the greatest impact on the exhaust gases. The best possible combination depends on the performance of what gases are to be eliminated, keeping the EGR rate at an optimum value between 10% and 20%. If preference is given to reduce NOx, then we will combine 10–20% EGR with SCR, but if the preference is given to reduce HC, CO, and soot, we will use 10% - 20% EGR in combination with a DPF. Overall, the DPF + SCR with 10% EGR rates seems to be an appreciable result.

* Corresponding author. Faculty of Computers and Artificial Intelligence, Beni-Suef University, Beni-Suef, Egypt.
** Corresponding author. Department of Mechanical Engineering, Malla Reddy Engineering College, Secunderabad, 500100, India
E-mail addresses: vijaykumar.084@mrec.ac.in (M.V. Kumar), avbabu@nitw.ac.in (A.V. Babu), crreddy229@mrec.ac.in (Ch.R. Reddy), pands07@kluniversity.in (A. Pandian), thebestbajaj@gmail.com (M. Bajaj), hossam.zawbaa@gmail.com (H.M. Zawbaa), skamel@aswu.edu.eg (S. Kamel).

https://doi.org/10.1016/j.csite.2022.102557
Received 21 September 2022; Received in revised form 1 November 2022; Accepted 12 November 2022
Available online 17 November 2022

1. Introduction

The Diesel Engine, invented by the German engineer Rudolf Diesel, was a marvelous creation that changed the way the automobile industry worked. It is an internal combustion engine that compresses air to elevate its pressure and temperature so high that the atomized diesel fuel undergoes combustion almost instantaneously when it is sprayed into the combustion chamber. The Major advantage of a Compression Ignition (CI) engine compared to a Spark Ignition (SI) engine is the higher compression ratio achieved in the former, making it more efficient. This makes diesel engines more suitable for heavy-duty vehicles, which require more torque to overcome rough terrain. In a 4-stroke Diesel engine, a certain mass of air is taken in through the inlet valve into the combustion chamber as the piston in the cylinder moves towards the Bottom Dead Center (BDC). At the BDC, the piston reverts its direction to compress the air inside the cylinder to very high pressure and temperature. The compression ratio values may range from 15 to 20 in a typical CI engine. The diesel fuel is then sprayed in an atomized form just before the piston arrives at the Top Dead Center (TDC) to account for the ignition delay. The high temperature and pressure of the air cause the fuel to ignite almost spontaneously, forcing the piston to move back toward the BDC. This is known as the power stroke of the engine, as it is where the engine provides the necessary torque to move the vehicle. In the last stroke, as the piston moves back up, the exhaust valve is opened to let out all of the exhaust gases. The intake valve opens again to take in a fresh charge of air, and the cycle is repeated so on. Heavy road trucks, ships, many buses, many commercial boats, heavy tractors, military vehicles, passenger cars, many large vans, large-scale portable generators, many agricultural and mining vehicles, and many long-distance engines use the majority of diesel engines.

1.1. Exhaust gas recirculation (EGR)

The EGR is a method used nowadays in the automotive industry to reduce the Oxides of Nitrogen (NOx). The nitrogen oxides are released by the engine during the operational period due to high combustion temperature. A high concentration of NOx is formed when the combustion temperature exceeds temperatures of 2400–2500 °C. The main principle of the EGR system works by recirculation of a small amount of exhaust gas back into the combustion chamber via the intake manifold. This small amount is combined with the incoming air/fuel charge. By this method, the high temperatures are minimized by diluting the air/fuel mixture. The Exhaust gas recirculation flow comprises 3 different working conditions. The first condition is a high flow which is essential for mid to increasing/cruising accelerating ranges. The combustion temperature is considerably high here. The 2nd requirement is the low EGR flow. This kind of flow is needed for low speeds and lesser loading conditions. The 3rd condition is no flow condition. No flow should occur when the engine is slightly warming up, and the throttle is idle. Therefore, these three operations through which the EGR takes place can have a considerable impact on vehicle efficiency/derivability. As stated above, the EGR mainly works on recirculating a small portion of the exhaust gas back into the combustion chamber. Firstly, the air mixture is brought into the cylinder. The supply of the exhaust gas is completed. The use of EGR is needed for NOx emission control. Having discussed the working principle of Exhaust Gas Recirculation, the following are the main factors by which the target pollutant NOx is controlled:

- The heat capacity (Cp) of air is lower than that of the exhaust gas. Thus, there will be a small number of energy releases during the combustion, and the lower limit of the temperature increases.
- The partial pressure of oxygen is reduced; thus, the concentration of oxygen inside the cylinder also goes down. This is because of the replacement of the combustion mixture with an exhaust gas with a lower proportion of oxygen.
- The speed at which the combustion is taking place is also reduced, and the lower limit of temperature rises as a result.

If the combustion temperature is way too high, the formation of NOx takes place. Any attempt to reduce the NOx. The implementation of the EGR will increase the particulate matter in the loading oil. The re-introduction of exhaust gas that is acidic in nature will increase the Total Acidic Number (TAN) of the lubricant.

1.1.1. Theory of operation

The main function of an EGR method is to control the flow under different working conditions. It also has to override flow which would otherwise compromise the performance of the engine. As the load changes the engine, the amount of exhaust that must be supplied into the intake manifold changes. The result is an operational system working on a thin line between the performance of the engine and the control of NOx. Again, too much metering of the exhaust gas can lead to a decline in engine performance. The knocking of the engine can occur if the emission standards are not met and there is little EGR flow. The EGR ratio is defined as the theatrical volume of recirculated exhaust gas.

1.1.2. EGR cooling system

The exhaust gas that has been recirculated should be cooled down. 50% of the reduction of the radiators is possible if the design is followed accordingly. Cooling down the recirculated gas is one of the ways to reduce the emission levels which cause pollution. The generation of NOx can be reduced by decreasing the temperature of the gas in the combustion chamber. An EGR cooler is installed between the valve and the intake manifold. Water is used as the cooling medium and has proven to be very effective than using air. The heating time for quick warm-up of after-treatment devices has been demonstrated to decrease in a system with a controlled EGR cooling system, improving engine temperature control. The amount of air entering the combustion chamber is increased by the intake of the cooled EGR system, which also makes the air denser. Thus, complete combustion is accomplished, which lowers the number of particles produced.

1.2. Diesel particulate filter (DPF)

A DPF, short for DPF, is a device that can be fitted to the exhaust section of an automobile to reduce the number of soot particles/

Particulate Matter which is released into the atmosphere. It does this so by filtering the exhaust gases out and, in the process, traps the Particulate Matter (PM). A DPF consists of an enclosed structure that contains a certain type of filter to trap that particulate matter. It can also consist of a burner in order to burn the soot in a process called regeneration. Different types of Filters can be found within the DPF, all designed to similar requirements. A good DPF filter should be able to;

- Carry out fine filtration
- Creates a Minimum Pressure drop
- Cost low
- Should be durable to withstand the rough conditions

Some of the filters used in the DPF include;

- Cordierite wall flow filter: This is one of the most common types of filters used in DPFs. They are cheap, easy to install, and provide exceptional filtration efficiency. The major drawback of this system is that it is not durable as its melting temperature is low (about 1200 °C). Some of the filters have melted off during the regeneration process due to their low temperature.
- Silicon Carbide wall Flow Filter: This type of filter is made by joining many small silicon carbide segments together to form one big piece. The advantages of this type of filter are similar to the ones listed above, except that the melting temperature of a silicon carbide wall flow filter is about 1000 °C higher than the common Cordierite wall-flow filter.
- Metal Fibre flow through the filter: The filters made from this type of material consist of metal wire-like fibers knitted together to form one large monolith. Such types of filters are expensive compared to the former two. The major advantage of this type of filter is that, even at a low temperature, electric current can be passed through the filter to perform the regeneration process.

1.2.1. Working on a DPF

The Exhaust gasses from the engine combustion chamber are made to pass through the DPF, which can be fitted either before or after the catalytic converter based on preference. The exhaust gases flow through the porous holes in the filter. The soot particles are larger than the porous holes of the filter; hence they get trapped as they pass through the filter. The treated exhaust gases then pass through the exit of the DPF out into the atmosphere. The soot particles Accumulate slowly inside the filter till the backpressure reduces to a certain minimum value, after which the differential pressure sensor sends a signal to the Electronic Control Unit (ECU). The ECU then sends a signal to the burner to carry out the regeneration process. In the regeneration process, the accumulated soot is burnt off in any of the following ways;

Active regeneration- After the particulate build-up reaches a certain level, the exhaust gas temperature is increased to above 600°. The temperature can be increased by engine throttling, the use of a burner upstream, and electrical regeneration.

- In engine throttling, the air-fuel mixture is made leaner to increase the amount of oxygen available for combustion. This causes the exhaust gases to be at a higher temperature which may then burn off the accumulated soot.
- A burner may be employed such that whenever a signal is given to it by the ECU, it can combust the accumulated soot around the filter.
- Electric regeneration is specifically for the ones containing a metal fiber flow through a filter. Electricity is passed through the filter, which heats and burns the unwanted soot.

Passive regeneration-these systems employ a catalyst that reduces the overall oxidation temperature of the soot particles to the level of exhaust gas temperatures. By reducing the oxidation temperature, the soot can easily be regenerated at lower temperatures.

1.3. Selective catalytic reduction (SCR)

The selective catalytic reduction, also known as SCR, is one of the effective ways of incorporating the conversion of NOx with the help of catalysts in Nitrogen (N_2) and Water (H_2O). Mostly a reductant in its gaseous form is mixed with exhaust gas and adsorbed onto a catalyst. The by-product of the reaction is Carbon Dioxide (CO_2) if the reductant used is urea. The SCR of NOx with the usage of ammonia as the reducing agent was first developed in the United States by the Engelhard Corporation in 1957. The advancement in this technology was spread in Japan and US in the early 60s, with the primary emphasis being on low-cost catalyst agents. The first real-time large-scale Selective catalytic reduction unit was installed by the IHI Corporation in 1978.

The major applications of SCR are found in boilers (industrial and utility) and importantly in municipal units to reduce solid waste. This has been effective to an extent (70–95%) reduction. In recent years automobiles have been using this technology, as well as gas turbines and locomotives.

1.3.1. Chemistry of the process

The reduction reaction of NOx takes place with the influx of gas via the catalytic chamber. First, a reductant like Urea is mixed with the other gas components before passing through the catalytic chamber. The reaction carried out in the SCR is as follows.

$$4NO + 2(NH_2)_2CO + O_2 \rightarrow 4N_2 + 4H_2O + 2CO_2$$

$$4NO + 4NH_3 + O_2 \rightarrow 4N_2 + 6H_2O_2$$

$$NO_2 + 4NH_3 + O_2 \rightarrow 3N_2 + 6H_2O$$

$$NO + NO_2 + 2NH_3 \rightarrow 2N_2 + 3H_2O$$

The secondary reactions are as follows:

$$2SO_2 + O_2 \rightarrow 2SO_3$$

$$2NH_3 + SO_3 + H_2O \rightarrow (NH_4)2SO_4$$

The following is the reaction is when urea is used instead of aqueous ammonia.

$$NH_3 + SO_3 + H_2O \rightarrow NH_4HSO_4$$

The most preferred temperature to carry out the reactions is in the range of 600–700 K, but the range can be increased with longer reaction times. The various factors which affect the minimum temperature for the reaction are the components of the gas and the geometrical structure of the catalyst. An alternative reductant commonly used is Ammonium Sulphate. The catalysts used in selective catalytic reduction are derived from ceramics, mainly used as a carrier and oxides of metals such as Tungsten and molybdenum. Recently activated carbon has been used to develop a catalyst. This helps in the depletion of NOx at lower limits of temperatures as well. Each catalyst has its advantages and disadvantages. The base metal catalysts do not possess sufficient thermal durability but are budget-friendly and are functional in temperature limits mostly seen in the power plants and boilers. Thermal durability is an important factor when the combination of SCR and DPF is used in automobile applications. Especially with forced regeneration, the base metal catalysts have a high potential of being catalyzed, which in turn can oxidize SO_2 to SO_3 and can cause considerable damage. Another commonly used catalyst is the Zeolite catalyst, with the main advantage being the operation at elevated temperature ranges, which the base catalysts lack. They possess the ability to sustain operations carried out at temperature ranges of 900 K–1100 K. Also, the probability of damage from SO_2 oxidation is much lesser.

1.3.2. Reductants

With catalysts, the different reductants being incorporated in the Selective catalytic reduction applications are urea and ammonia in aqueous form. These are widely available. The purest form of anhydrous ammonia is toxic and safe storage is not feasible. The biggest advantage being no further conversion is required when used in the SCR. Large industries are in favor of this and are used by industrial operators. Compared to anhydrous ammonia, ammonia in an aqueous form is relatively safe for storage and transport. Urea is the safest when it comes to storage, but thermal decomposition is required for further conversion to be used as a feasible reductant.

2. Literature review

The different areas of research that have taken place to reduce diesel emissions will be cited in this chapter. The main focus will be put on diesel emissions, the reduction systems such as the Diesel Particulate Filter, Selective Catalytic Reactant, and Exhaust gas recirculation. The different studies that have taken place on both the emissions and the reduction systems led us to the objectives of our detailed study.

The authors studied the various exhaust gases from diesel engines at various loads. They described that among the pollutant emissions, Carbon Monoxide (CO) and Hydrocarbons (HC) are emitted due to incomplete combustion and unburned fuel, but NOx emissions occur due to high combustion temperatures above 1600 °C. About PM emissions, the reason for PM emissions is the agglomeration of partially burned fuel, partially burned lubricant, fuel oil, and cylinder lubricant [1]. The author has described the parameters of the Emission of various oxides of nitrogen concerning temperature and their control. He briefly looked at the history of emission reduction at a glance. He concluded that NOx emissions should be reduced immediately and effectively since the level is still serious and an issue. The level of Euro-VI is set to 0.08 g/km now, a phenomenal 55% reduction from the current Euro-V standard for passenger cars and 75% in the case of a large car. This study was done based on the Euro-VI General Standard and Euro -V standard [2]. The researcher has carried out repeated investigations and has concluded that the injection of solutions in the aqueous form (urea) in the exhaust manifold for NO reductions is an age-old technology, at least 2 decades old. Since then, many methods have been developed which have been commercially viable. Urea solution of varying concentrations from 10 to 30% with variable flow rates was tested by using vanadium as a catalyst which improves the rate of the chemical reaction even at the lower limit of the temperatures of even 190 °C Results showed that a maximum of 26.41% of NOx reduction was achieved with a regulated flow rate of 0.76 lit/hr. with 9% urea concentration [3]. The authors have studied that carrying out the SCR technique using urea as the primary agent is an optimum method for application on stationary diesel engines. The journal talks about the fundamental drawbacks and challenges of extending the Urea-SCR applications to the mobile domain. The steps involved in the reduction process included the endothermic decomposition of liquid urea, hydrolysis of the isocyanic acid, and a selective reduction of NOx [4]. The authors have done experiments and investigations on the performance characteristics, combustion, and emission characteristics of SI engines with blends of cotton seed oil of 20%, 40%, 70%, and 100% in volume. There was an increase in the oxides of nitrogen compared to the diesel in its homogeneous form; the SCR system was implemented in the exhaust pipe. The results showed that with the injection of a 30% concentration of urea solution, there was a rapid decrease in the rate of the number of oxides of nitrogen [5]. The usage of Pongamia pinata methyl ester (PPME) as a substitute fuel for diesel engines has been researched by the authors. For the reduction of nitrogen oxides, aqueous urea solutions were injected into the tail end of a diesel engine's pipe along with PPME. Four different observations were made for the various concentrations of urea solution 0%, 10%, 20%, and 30% by mass, along with various rates of flow of urea solution as the reductant, which enhances the chemical reactions. With a urea flow rate of 0.58 lit/hr, 25% concentration of urea solution and marine ferromanganese nodule, 62% NOx reduction was attained [6]. The survey on NOx treatment is major in the present years due to rising environmental awareness. Selective Catalytic Reduction (SCR) and Exhaust Gas Recirculation (EGR) are the

proven technology for reducing NOx. The other treatment methods offer higher NOx. The authors have investigated the effect of EGR (10%, 15%, 20%, and 25%) on 3 cylinders, constant speed, and air-cooled CI diesel engine, from this investigation they have concluded that at lower loads the higher rate of EGR can be applied to CI engine without any drawback of its fuel economy and efficiency, thus the NOx reduction is attained [7]. The authors have proved that EGR combined intake heating promisingly reduces the total hydrocarbon emission with an enhancement of BTE at lower load conditions [8]. The EGR was employed in an indirect injection spark ignition engine and showed to be more efficient in terms of fuel economy [9,10]. By using Methanol blended fuels, the adjustment of exhaust port parameters has a greater impact on mean indicated pressure, trapping efficiency, and scavenging efficiency [11]. The study's conclusions state that innovative coal-fired units should be adopted and their performance pledged at a range of loads, including minimal loads. To increase efficiency and lower carbon dioxide emissions, Vietnam should employ ultra-supercritical technology in new units [12]. Variable valve actuation (VVA) can be an effective approach to boost performance while reducing emissions by raising the in-cylinder charge temperature [13]. The developed multivariable engine controller's performance is demonstrated on a six-cylinder diesel-E85 RCCI engine. In comparison to open-loop control, the stable and safe operating range is increased from 25 to 35 °C intake manifold temperature, and the ultimate load range is increased by 14.7% up to BMEP = 14.8 bar [14]. Due to better performance and emission characteristics, B20 mahua biodiesel at 8 lpm of biogas flow rate in dual fuel mode is determined to be the best combination [15]. SCR creates a substantial reduction in the correlation coefficients between NOx emissions and air-fuel ratio (0.76 vs 0.47 for China V truck; 0.72 vs 0.05 for China VI truck), although not in the correlation coefficients between CO2 emissions and air-fuel ratio, which can be used to determine whether SCR is working effectively [16]. The SCR reaction was shown to proceed proficiently via either surface NH_3 or NH_4 species, attempting to solve a long-standing debate about their involvement in the SCR reaction [17]. Managing active DPF regeneration must consider the effect of the fast regeneration time frame on emission and input energy, as well as the influence of flow rate and regeneration temperature [18]. The hierarchical microstructure of Co/CZ@M/C, combined with high-efficiency filtration and low-temperature catalytic oxidation of soot particles, seems to have possible uses in the diesel particulate filter (DPF) field [19]. With a diesel oxidation catalyst (DOC), CO and HC are reduced drastically to zero, and NOx is reduced by 24.3% [20]. For the studies, a single-cylinder direct injection compression ignition engine that had been suitably modified to run in dual fuel mode with EGR was employed. The results of the trials showed that, at higher engine loads, the NOx-smoke emission trade-off was improved by the dual fuel mode with EGR without losing the characteristics of engine combustion and performance [21]. The main outcome of this study is that CO and HC emissions, two major issues for RCCI engines operating at part load, were reduced while NOx reduction increased with 8% EGR. Even though smoke emission is slightly greater with EGR than without EGR, it is still lower than in traditional mode (Diesel alone). Their work offered the novel idea that EGR can be utilized to lower the CO and HC emissions of RCCI engines operating at part load [22]. SCR technology should be developed for marine low-speed engines to meet the demands of high thermal efficiency, low pollutant emissions, and high sulphur fuel. Under the concomitant limitations of high sulphur fuel and low exhaust temperature, the low-speed diesel engine SCR systems will eventually give up some engine economy to obtain increased denitrification efficiency and operational reliability [23].

Based on the aforementioned literature review, it is clear that it is challenging to control the PM and NOx values in the environment. In this case, EGR lowers NOx, DPF collects PM, and SCR also lowers NOx emission. Therefore to control the PM and NOx, we have implemented the present framework with EGR combined with SCR & DPF to manage the emission.

3. Experimental setup and methodology

3.1. Modifications to an after-treatment process for engine

3.1.1. Engine with EGR system

Firstly, the EGR system was initially fitted to the diesel engine EGR gases, which also include water vapor, HC, CO, NOx, and CO_2, redirect some of the clean air entering the combustion chamber.

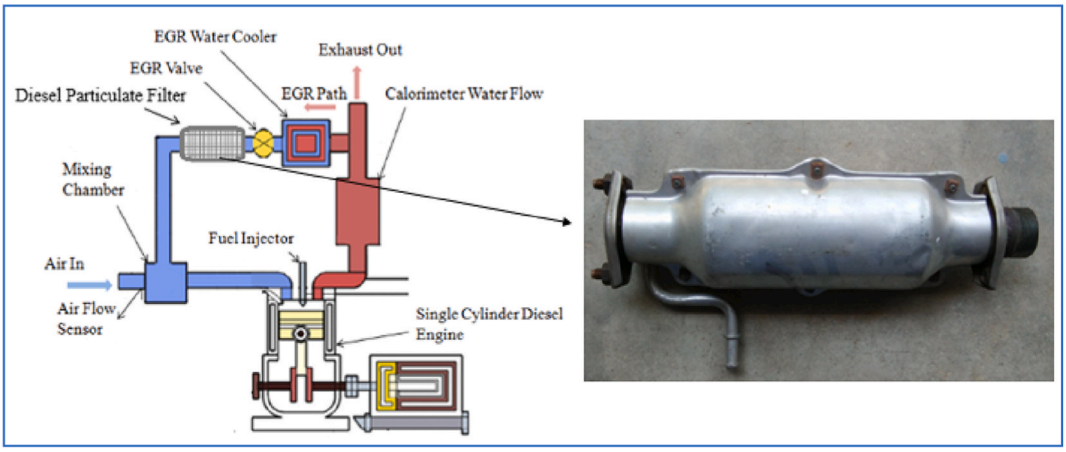

Fig. 1. Schematic diagram of EGR + DPF system.

The valve is typically used to control the rate at which EGR flows. The mixing chamber was utilized to ensure the correct mixing of exhaust and fresh air. The equation (i) is used to compute the EGR (%).

$$\text{EGR rate } (\%) = \frac{Q_{\text{without EGR}} - Q_{\text{with EGR}}}{\text{QwithoutEGR}} \text{ x } 100 \quad \text{(i)}$$

where $Q_{\text{without EGR}}$ is the airflow rate without EGR and it is equal to 26 kg/h and $Q_{\text{with EGR}}$ is 23.4 kg/h (10%), 20.8 kg/h (20%) and 18.2 kg/h (30) %. The dropdown of the airflow is 2.6 kg/h (10%), 5.2 kg/h (20%) & 7.8 kg/h (30%)

3.1.2. Engine with DPF + EGR system

Secondly, to capture the soot particles, the DPF system was installed. DPF has a wall thickness of 0.30 mm and a 200-CPSI construction. The installation of the EGR and DPF systems ensures that no PM is introduced into the combustion chamber during the recirculation of exhaust gases. It made use of the non-catalyzed cordierite wall-flow DPF. This Cordierite wall flow doesn't undergo any chemical reactions; it only traps the soot. Fig. 1 displays the schematic with EGR and DPF.

3.1.3. Engine with DPF + SCR system

Thirdly, the SCR system was set up as depicted in Fig. 2. The installation of the EGR and SCR systems results in the recirculation of exhaust gases being supplied to the combustion chamber together with CO_2, H_2O, and PM. A two-way catalytic converter, the SCR performs two jobs at once:

- Oxidation of CO to CO_2: $2CO + O_2 \rightarrow 2CO_2$
- Oxidation of HC (unburnt and partially burnt fuel) to $CO_2$and water: $C_xH_{2x}+2 + [(3x+1)/2]\ O_2 \rightarrow xCO_2 + (x+1)\ H_2O$ (a combustion reaction)

The schematic diagram with EGR and SCR is shown in Fig. 2.
Fig. 2 displays the schematic with EGR and SCR.

3.2. Diesel engine setup

In this study, a computerized TV1-Kirloskar diesel engine with a 3.5 kW output and a constant speed of 1500 rpm was used. An eddy current dynamometer is connected to the engine to regulate engine torque. The control panel regulates the load and engine speed. Table 1 provides information on the engine's specifications. NOx, HC, and CO are measured using an AVL gas analyzer.

3.3. Measuring devices

Table 2. Shows the ranges and accuracy of measuring devices. These measuring devices are used during the experimentation.

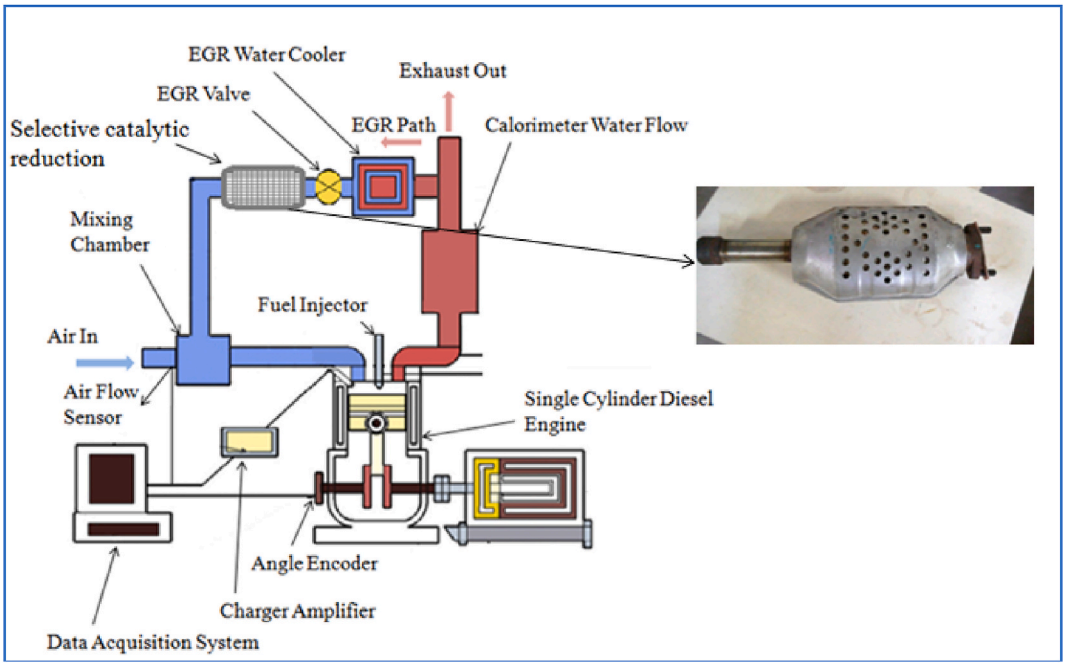

Fig. 2. Schematic diagram of EGR + SCR system.

Table 1
Information on diesel engine specifications.

Parameters	Details
Engine supplier	Apex Innovations Pvt. Ltd.
Engine type	TV1-KIRLOSKAR
Engine software	Internal combustion engine analyzer software (Version 9.0)
Loading type	An eddy current dynamometer model
No. of cylinder	1
No. of strokes	4
Rated power (kW)	3.5 at 1500 rpm
Timing of Injection (°CA. bTDC)	23
Swept volume (cc)	661
Stroke length (mm)	110
Cylinder bore (mm)	87.5
Compression ratio	17.5:1
Connecting rod length (mm)	234
Engine cooling type	Cooling water
Piston bowl	Hemispherical
Nozzle opening pressure (bar)	210

Table 2
Accuracy and ranges of measuring devices.

Quantity	Range	Accuracy
AVL gas analyzer	NO_x: 0–5000 ppm	±50 ppm
	CO: 0–10% by vol.	±0.03%
	HC: 0–20000 ppm	±10 ppm
AVL smoke meter	0–100%	±0.2%
Pressure Sensor	(0–110 bars)	±0.05 bar
Fuel flow sensor	0-5 psi	±0.1 psi
Crank angle encoder	0°–720°	±1°
Speed measuring	0–5000 rpm	±10 rpm
Air flow sensor	0–3.500 mm of H_2O	±1 mm of H_2O
Alternator	0–20 A, 0–450 V	±0.55 A, ± 1 V
Thermocouples	0–1000 °C	±1 °C

3.4. *Experimental testing procedure*

The baseline, EGR, EGR + DPF, and EGR + SCR are connected to the engine. The experimental work was done as explained above.

- The engine is connected to the battery. The water values are opened to circulate water for cooling the engine.
- The engine is started with no load applied to it and made to run at a constant rate of 1500 RPM. The engine is let to run so that it can be heated up and reach a steady state.
- The Exhaust Gas recirculation valve is opened to let only 10%, 20%, and 30% of the exhaust gas to be circulated. Caution is kept to keep the valve in that position throughout the experiment.

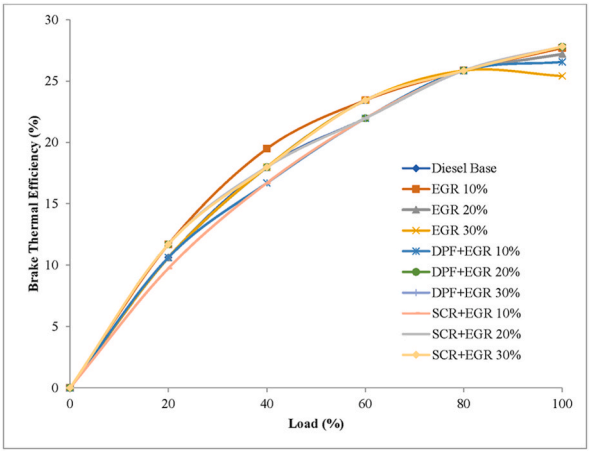

Fig. 3. Variation of BTE vs. Load.

- The fuel knob is turned towards the neutral position to let fuel flow to the burette. The amount of this fuel consumed in 1 min will be used to carry out the required measurements.
- The Emission analyzer is then connected to the secondary exhaust outlet, and the corresponding smoke readings are noted.
- The above steps are repeated thrice to reduce human error while taking readings.
- All the above steps are then repeated at 20%, 40%, 60%, 80% and Full load conditions. Caution is kept to keep the engine speed running at a constant rate of 1500 RPM.
- The above experiment will be conducted for conditions 20% EGR and 30% EGR.
- The above method is repeated same for the combination of EGR + DPF and EGR + SCR.

4. Results and discussion

Performance, combustion and emissions characteristics have been plotted from the data obtained based on the above procedure. Different comparisons are made in the graphs to decide the best possible combination.

4.1. Engine performance analysis

4.1.1. Brake thermal efficiency

The successful conversion of chemical energy present in fuel into heat energy and transformation into mechanical energy at the engine shaft is shown by brake thermal efficiency. With an increase in the load placed on the engine, BTE rises as shown in Fig. 3. BTE is mainly dependent on fuel heating value and fuel consumption. BTE for diesel as a fuel is 29.22 at 10% EGR at peak load. The other values of BTE at peak load are 27.28 at 20% EGR, and 25.41 at 30% EGR. We can therefore observe that BTE decreases with an increase in the EGR rate. Additionally, compared to lower EGR rates, the decrease in BTE at higher EGR rates is significant. This may be because the amount of fresh oxygen available for combustion decreases due to replacement by exhaust gases. The BTE of EGR + DPF is decreasing with further EGR rates level due to the back pressure that occurred in DPF. This is mainly due to the replacement of exhaust gases, which increases the soot levels and accumulate in DPF. Here, the soot particles are not vanishing in DPF because the temperature of the gases in DPF could not be able to generate more than 500 °C; due to this, the flow of the exhaust gases is not passing freely from the DPF system. In fact, the soot particles have the ability to get burn at 500 °C–600 °C. The combination of EGR + SCR is also performing poor performance due to the replacement of H_2O, CO_2, PM, and other gases; due to this, the combustion temperature is reducing and lowering the NOx levels.

4.1.2. Brake-specific fuel consumption

Fig. 4 shows the variation of BSFC with respect to the load. BSFC is decreased with an increment in load. This is an indication of the effective combustion of fuel. The BSFC is decreased by EGR 10% due to the return of unburned hydrocarbons. The further rise of EGR rates seems to increase in BSFC. When EGR and DPF are utilized together, the BSFC is increased because of the back pressure brought on by the soot deposit in the DPF. As the soot particles accumulate in the DPF, the flow of the exhaust gases falls flowing freely from the DPF, especially at low Load conditions because at low load conditions, the temperature of the exhaust will be low, and the trapped soot particles in DPF may not vanish. So, this is how it causes back pressure. Moreover, the flow rate of the fresh air from the atmosphere will reduce significantly as the EGR rate increases. The reintroduction of CO_2, water vapor, and PM into the combustion chamber develops incomplete combustion, which in turn increases the BSFC when EGR + SCR is used.

4.2. Engine combustion analysis

4.2.1. In-cylinder pressure

Fig. 5 shows the variation of In-cylinder pressure with the crank angle at full load conditions. Compared to the diesel baseline, the

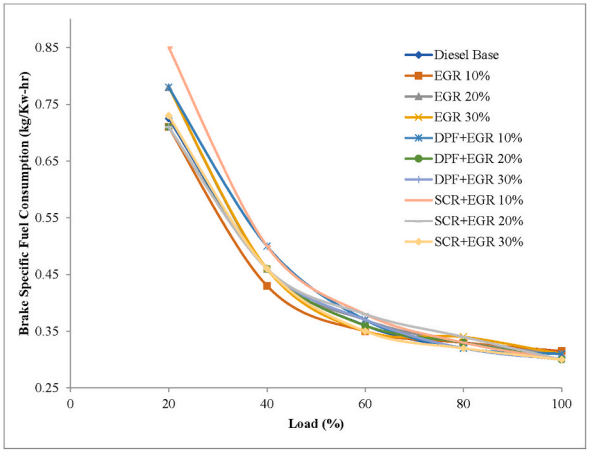

Fig. 4. Variation of BSFC vs Load.

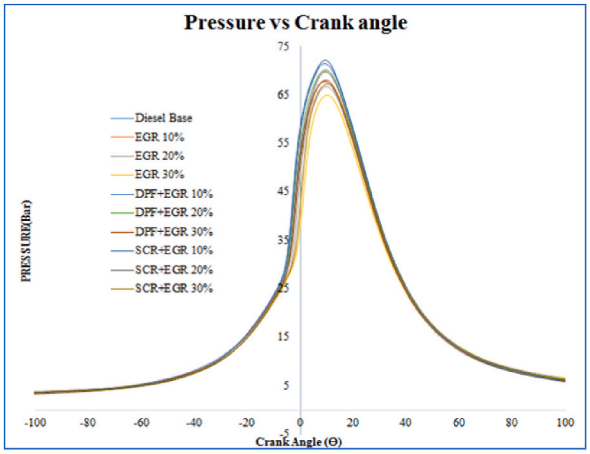

Fig. 5. In-cylinder pressure with the crank angle at the full load condition.

EGR application and with the EGR rate increase, the pressure rise is seen to be decreased. When compared to different EGR rates and their combinations with DPF and SCR, it is found that the 10% EGR rate with DPF and SCR combo performs best [24]. These drawbacks are observed to be due to the back pressure with DPF caused by and recirculating of H_2O, soot, and CO_2.

4.2.2. *In-cylinder gas temperature*

The variations of In-cylinder gas temperature concerning load are shown below in Fig. 6. The temperature is reduced by increasing the EGR rates. The reason for lowering the exhaust gas temperature is that the utilization rate of oxygen for combustion is relatively low and the specific heat of the intake air-fuel mixture is high. The temperature is slightly increased at higher load conditions for the combination of 10% EGR + DPF. The rest of the EGR rates with DPF are decreased in gas temperature. The maximum In-cylinder temperature is reduced for 10%, 20%, and 30% EGR with SCR; this is mainly due to the recirculating of exhaust gases which leads to incomplete combustion.

4.2.3. *Heat release rate*

Fig. 7 shows the variation of HRR with the crank angle at full load conditions. The late HRR is observed for 10%, 20%, and 30% EGR rates and shows a higher HRR due to the slow rate of combustion. The HRR for 10% EGR + DPF is observed to be early HRR and cannot attain a maximum HRR. For all EGR rates with the SCR combination, the early HRR is achieved and could not reach the maximum HRR. The HRR mainly relates to the Ignition delay and combustion process.

4.3. *Engine emission analysis*

4.3.1. *Carbon Monoxide*

Fig. 8 shows the CO change with load for various EGR rates and its DPF and SCR combo. Most of this CO is produced as a result of inadequate combustion. Components, including the fuel-air ratio, compression ratio, delay time, fuel type, and injection timing, all affect how CO develops. For each particular combination, the level of CO emissions is maximal at full load. However, it was observed that at 30% EGR + SCR, the CO generation increased considerably. It is primarily caused by incomplete combustion. CO increases with increasing EGR rates. The combinations of EGR + DPF are observed to be lower as compared to the other application of SCR and EGR.

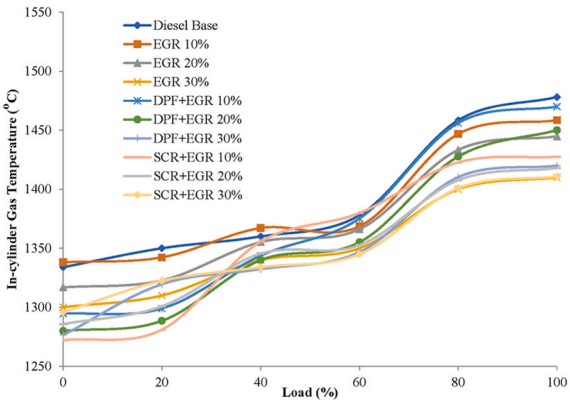

Fig. 6. In-cylinder gas temperature vs. Load.

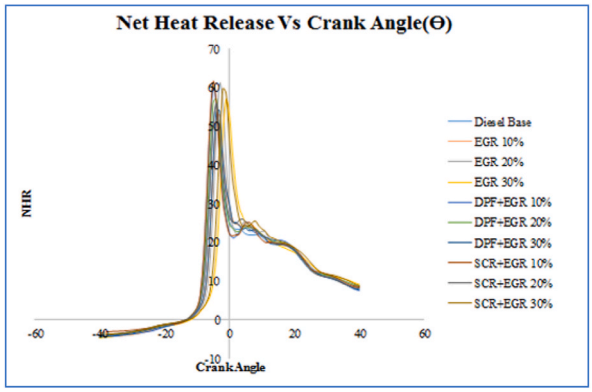

Fig. 7. Heat release rate with the crank angle at the full load condition.

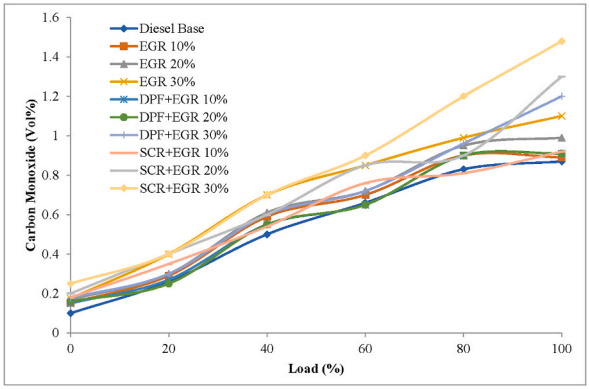

Fig. 8. Variation of Carbon monoxide vs. Load.

At higher EGR rates, CO emissions are increased due to the low availability of oxygen by EGR.

4.3.2. Hydrocarbon

As shown in Fig. 9, the HC emissions increase as the load increases. They are primarily formed as a result of insufficient fuel combustion and are fortified with a rich mixture. The temperature of the cylinder wall during mixture formation influences HC formation, particularly at the cylinder boundary. Furthermore, the fuel flowing into the combustion chamber is not involved in combustion along these lines, resulting in higher HC emissions for diesel, particularly at full engine load. It can be noted that the maximum amount of HC emission is at a full load of 30% EGR. The HC emission increases with EGR rates. Because there is less oxygen in the combustion chamber, the rich mixture results in incomplete combustion, which results in higher HC emissions in the exhaust. Because soot is accumulated in the DPF, the combination of EGR and DPF appears to be more effective in reducing HC emissions. The SCR, with a combination of EGR rates, appears to be ineffective in reducing HC emissions.

4.3.3. Oxides of nitrogen

Fig. 10 depicts the NOx variation for all tested systems as a function of the load on a compressed ignition engine. One of the most hazardous harmful exhaust pollutants from a diesel engine is NOx, which is sensitive to fuel quality, oxygen content, and combustion temperature. An increase in NOx was observed for the various systems as the load increased. Additionally, due to the buildup of carbon on the cylinder surface, burning chamber, and valve walls that serves as an insulator and raises the temperature in the engine cylinder, insufficient fuel ignition results in greater NOx outflow. In comparison to the other parameters, the NOx emission is highest at full load for 10% EGR. However, throughout all load operations, the application of EGR dramatically reduced NOx emissions. It can be seen that 30% EGR results in a greater reduction in NOx emissions. The graph of In-cylinder gas temperature demonstrates that the main cause of the decrease in NOx emissions is a lower combustion chamber temperature. The EGR + DPF is not so effective in reducing NOx compared to the other data. With the combination of SCR + EGR at different rates, the NOx levels are decreasing compared to all other parameters.

4.3.4. Smoke opacity

Fig. 11 depicts the variation in smoke opacity concerning load for all tested systems using a compressed ignition engine. One of the major toxic exhaust emissions from diesel engines is smoke opacity. The increase in load caused an increase in smoke opacity for the

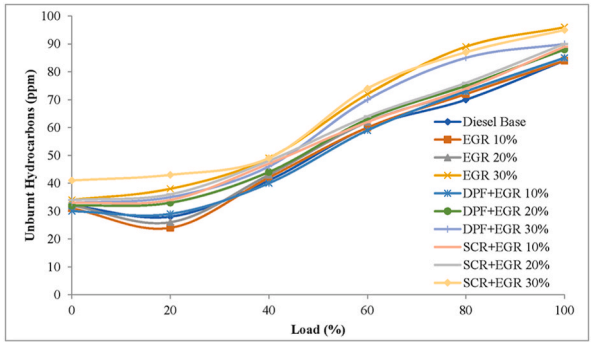

Fig. 9. Variation of Unburnt hydrocarbon vs. Load.

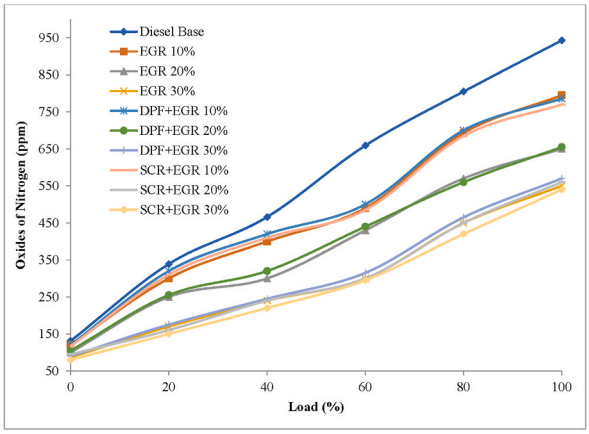

Fig. 10. Variation of Oxides of nitrogen vs. Load.

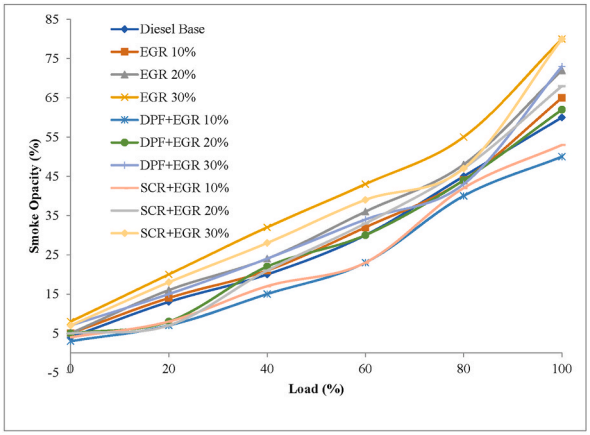

Fig. 11. Variation of Smoke Opacity vs. Load.

various systems. Furthermore, insufficient fuel ignition causes more smoke to escape due to incomplete combustion, which leads to the formation of soot particles at lower temperatures and higher load conditions. The soot particles are high at full load for increasing EGR rates. But by the use of DPF, the soot particles seem to decrease with EGR. The combination of DPF + SCR with EGR application soot particles is observed to be increased due to the recirculation of exhaust of H_2O and N_2. The SCR mainly covers the NO_X into H_2O and N_2. The DPF + SCR with 10% EGR application is having an appreciable reduction in emissions and without much affecting the performances.

5. Conclusions

Based on the obtained results from this study and by taking into consideration the first goal, which looks to reduce gas emissions, it is possible to mention that the outcomes of this work are: the brake thermal efficiency has a higher value when the EGR rate is 10% when compared to the other combinations, and fuel consumption is also reduced especially at partial load conditions.

As the rate of EGR increases the NOx level reduces but due to insufficient oxygen supply, the air-fuel ratio decreases hence reducing the brake thermal efficiency at higher loads. Here, as the EGR flow rate is increasing, the fresh air from the atmosphere flow rate is decreasing, and the mixture becomes a more lean mixture due to the lack of fresh air and more amount of fuel it is leading to a drop in the performance of the engine.

With the combination of EGR and DPF, the soot particle gets trapped hence allowing only the clean gases to pass through the EGR back into the combustion chamber. The level of HC and CO enters the combustion chamber, where they are completely burned, but because of the high temperature inside the combustion chamber, NOx levels also rise at the same time. Therefore, trapping the PM in the DPF and allowing the other gases in the combustion chamber has a positive effect at an EGR rate of 10%. In the DPF system, where the soot is trapped, higher EGR rates cause back pressure. Due to the soot buildup in the DFP, where the soot in the DPF cannot be eliminated at lower load circumstances because of the low temperature of the gases, the back pressure is continued.

With the combination of an SCR and EGR, the NOx levels get reduced due to the conversion of the NOx to nitrogen gas. But with the combination of an SCR and EGR the amount of CO_2 entering the combustion chamber also does increase, resulting incomplete combustion, which increases the value of HC and CO in the exhaust gases. The EGR 10% with SCR shows a good impact without damaging the performance of the engine.

The best possible combination depends on the performance of what gases are to be eliminated, keeping the EGR rate at an optimum value between 10% and 20%. If preference is given to reduce NOx, then we will combine 10–20% EGR with the SCR system, but if the preference is given to reduce HC, CO and soot, we need to utilize 10% - 20% EGR in combination with a DPF system which gives a little good impact in reducing the emissions. The implementation of the work can be utilizing the EGR system with the combination of DPF and SCR for reducing the Soot and NOx at low EGR rates only.

For further work, the combination of EGR + DPF + SCR may give appreciable results for controlling the Soot and NOx at a time.

Institutional review board statement

Not applicable.

Informed consent statement

Not applicable.

Author statement

Megavath Vijay Kumar: Conceptualization, Software, Review, Editing, Writing, Original Draft, **Alur Veeresh Babu**: Conceptualization, Software, Review, Editing, Writing, Original Draft, **Ch. Rami Reddy**: Investigation, Formal Analysis, Supervision, Writing, **A. Pandian**: Conceptualization, Investigation, Supervision, Writing, **Mohit Bajaj**: Writing, Review, Editing, **Hossam M. Zawbaa**: Resources, Writing, Review, Editing, **Salah Kamel**: Supervision, Writing, Review, Editing.

Declaration of competing interest

The authors declare that they have no known competing financial interests or personal relationships that could have appeared to influence the work reported in this paper.

Data availability

Data will be made available on request.

Acknowledgment

The work of Hossam M. Zawbaa was supported by the European Union's Horizon 2020 Research and Enterprise Ireland under the Marie Skłodowska-Curie Grant 847402. This work is also supported by the LINTE$\hat{\text{A}}$2 Laboratory, Gdansk University of Technology.

References

[1] İ. Reşitoğlu, The pollutant emissions from diesel-engine vehicles and exhaust aftertreatment systems, Clean Technol. Environ. 17 (2015) 15–27. A, Altinişik, K, Keskin, A.
[2] M.V. Kumar, A.V. Babu, P.R. Kumar, Influence of metal-based cerium oxide nanoparticle additive on performance, combustion, and emissions with biodiesel in a diesel engine, Environ. Sci. Pollut. Control Ser. 26 (8) (2019) 7651–7664.
[3] E. Tronconi, I. Nova, F. Marchitti, G. Koltsakis, D. Karamitros, B. Maletic, N. Markert, D. Chatterjee, M. Hehle, Interaction of NO x reduction and soot oxidation in a DPF with Cu-zeolite SCR coating, Emission Control Sci. Technol. 1 (2) (2015) 134–151.
[4] M. Koebel, G. Madia, M. Elsener, Selective catalytic reduction of NO and NO2 at low temperatures, Catal. Today 73 (3–4) (2002) 239–247.
[5] R. Sheshathri, A. Avinash, Study of the emission characteristics of the SCR system on CI engine fuelled with diesel-ethanol blends and an optimised urea injection system, in: Applied Mechanics and Materials, vol. 812, Trans Tech Publications Ltd, 2015, pp. 33–43.

[6] C.E. Romero, X. Wang, Key technologies for ultra-low emissions from coal-fired power plants, in: Advances in Ultra-low Emission Control Technologies for Coal-Fired Power Plants, Woodhead Publishing, 2019, pp. 39–79.
[7] J. Hussain, K. Palaniradja, N. Alagumurthi, R. Manimaran, Retracted: Effect of Exhaust Gas Recirculation (EGR) on Performance and Emission Characteristics of a Three Cylinder Direct Injection Compression Ignition Engine, 2012.
[8] T.D. Kumar, S.S. Hussain, D.K. Ramesha, Effect of a zinc oxide nanoparticle fuel additive on the performance and emission characteristics of a CI engine fuelled with cotton seed biodiesel blends, Mater. Today Proc. 26 (2020) 2374–2378.
[9] G. Fontana, E. Galloni, Experimental analysis of a spark-ignition engine using exhaust gas recycle at WOT operation, Appl. Energy 87 (7) (2010) 2187–2193.
[10] Y.L. Bai, Z. Wang, J.X. Wang, Part-load characteristics of direct injection spark ignition engine using exhaust gas trap, Appl. Energy 87 (8) (2010) 2640–2646.
[11] W. Yang, F. Li, F. Ma, D. Xu, J. Xu, F. Wang, Influence of the port height to stroke ratio on the performance of an OP2S engine fueled with methanol/diesel, Energies 15 (6) (2022) 2186.
[12] A.T. Hoang, T.V. Nguyen, B.T. Nguyen, The experimental evaluation of energy efficiency and carbonic emission rates for all stable loads of larger-scale (+ 600 MW) coal-fired power generation units in Vietnam, Energies 15 (6) (2022) 2185.
[13] P. Kumar, Y. Zhang, Variable valve strategy evaluation for low-load operation in a heavy-duty gasoline compression ignition engine, Energies 15 (6) (2022) 2017.
[14] J. Verhaegh, F. Kupper, F. Willems, Data-driven air-fuel path control design for robust RCCI engine operation, Energies 15 (6) (2022) 2018.
[15] A.S. Kshatriya, P. Tiwari, T.M. Yunus Khan, S.D. Abdul Khadar, M. Mansour, Investigations into the combined effect of mahua biodiesel blends and biogas in a dual fuel engine, Energies 15 (6) (2022) 2057.
[16] B. Song, J. Gong, W. Tang, G. Zeng, M. Chen, P. Xu, M. Shen, S. Ye, H. Feng, C. Zhou, Y. Yang, Influence of multi-walled carbon nanotubes on the microbial biomass, enzyme activity, and bacterial community structure in 2, 4-dichlorophenol-contaminated sediment, Sci. Total Environ. 713 (2020), 136645.
[17] M. Guo, B.M. Lis, M.E. Ford, I.E. Wachs, Effect of redox promoters (CeOx and CuOx) and surface sulfates on the selective catalytic reduction (SCR) of NO with NH3 by supported V2O5-WO3/TiO2 catalysts, Appl. Catal. B: Environ. (2022), 121108.
[18] Z. Meng, B. Zeng, J. Tan, Z. Chen, J. Ou, Study of gas and particulate emission characteristics during the fast regeneration period of DPF, Fuel 317 (2022), 123353.
[19] C. Ai, Y. Du, B. Wen, R. Shu, L. Cao, W. Wang, Preparation and characterization of diesel particle filter (DPF) with hierarchical microstructure for catalytic combustion of soot, Ceram. Int. 48 (7) (2022) 9304–9312.
[20] S. Hu, B. Deng, D. Wu, K. Hou, Energy flow behavior and emission reduction of a turbo-charging and EGR non-road diesel engine equipped with DOC and DPF under NRTC (non-road transient cycle), Fuel 305 (2021), 121571.
[21] S.K. Mahla, A. Dhir, K.J. Gill, H.M. Cho, H.C. Lim, B.S. Chauhan, Influence of EGR on the simultaneous reduction of NOx-smoke emissions trade-off under CNG-biodiesel dual fuel engine, Energy 152 (2018) 303–312.
[22] S.S. Kalsi, K.A. Subramanian, Experimental investigations of effects of EGR on performance and emissions characteristics of CNG fueled reactivity controlled compression ignition (RCCI) engine, Energy Convers. Manag. 130 (2016) 91–105.
[23] Y. Zhu, W. Zhou, C. Xia, Q. Hou, Application and development of selective catalytic reduction technology for marine low-speed diesel engine: trade-off among high sulfur fuel, high thermal efficiency, and low pollution emission, Atmosphere 13 (5) (2022) 731.
[24] S. Saravanan, Effect of EGR at advanced injection timing on combustion characteristics of diesel engine, Alex. Eng. J. 54 (3) (2015) 339–342.

How Can Machine Tool Parameters Influence Tool Life and Wear Characteristics? An Experiment Design Approach

Balaji Krushna Potnuru, Vasishta Bhargava Nukala, Satya Prasad Maddula, A. C. Uma Maheshwara Rao, Praveen Ronad, P. Chinmaya Prasad, and Suresh Akella

Abstract In this work, we implement a response surface method, for investigating the impact of machining parameters on tool life and wear characteristics. The influence variables also include the temperature on the degradation of tool material. Taylor's tool life equation based on the cutting speed is evaluated for different tool lift exponents which represent the type of work piece material. Three different types of cooling mediums have been considered for the series of experiments, and hexagonal boron nitride with maximum of 1.25% by volume was used as nano particle lubricant material. The tool life for different materials has been compared to verify the accuracy of tool life predictions. The results showed that with increase in cutting speed, feed rate and depth of cut, the tool life and wear reduced exponentially for cutting speeds between 50 mm/min and 100 mm/min and the maximum tool life was found when the cutting speed was 70 mm/min and feed rate of 0.15 mm/rev. Despite low cutting speeds, the depth of cut increased the tool wear and temperature by 11.1% and 10.4% respectively.

Keywords Tool life · Tool wear · Depth of cut · Feed rate · Cutting speed · Temperature

B. K. Potnuru (✉)
Department of Mechanical Engineering, Malla Reddy Engineering College (Autonomous)-Main Campus, Maisammaguda, Telangana State, India

V. B. Nukala · A. C. Uma Maheshwara Rao · P. Ronad · S. Akella
Department of Mechanical Engineering, Sreyas Institute of Engineering and Technology, Bandlaguda, Nagole, Telangana, India

S. P. Maddula
Department of Aerospace Engineering, GITAM Deemed to be University, Hyderabad, Telangana, India

P. Chinmaya Prasad
Department of Mechanical Engineering, GITAM Deemed to be University, Hyderabad, Telangana, India

P. K. Chaurasiya et al. (eds.), *Technology Innovation in Mechanical Engineering*,
Lecture Notes in Mechanical Engineering,
https://doi.org/10.1007/978-981-16-7909-4_9

1 Introduction

In field of manufacturing technology, machining processes are usually a sequence of operations which determine how a work piece material can be transformed to a finished industrial product by using high strength cutting tools. Metal cutting is one of the foremost techniques used in industry to shape or remove unwanted material from work piece. The most important variables in metal cutting processes include spindle speed, temperature, feed rate, lubrication, cutting forces, power consumption, and vibration. During such processes, tool wear and tool life are important considerations which take account of the forces and rely on the feed rate, cutting speed, and depth of cut involved in a single operation. In metal cutting operation, tool wear becomes dominant when the process conditions require maximum productivity and is achieved at an economical cost consideration. According to [1–4] nature of any tool wear is not clear due to high contact temperatures and pressures formed at the tool-chip and tool-work piece interfaces. It is result of physical, chemical, and thermo-mechanical phenomenon caused due to adhesive, abrasive, diffusive, and oxidative properties. Research in metal cutting techniques vary with material characteristics and the condition of machining operation, steel alloys are by far the most multifunctional and adaptable materials in manufacturing processes.

In the present study, we examine the effect of machining parameters such as the speed, feed rate and depth of cut on the cemented carbide tool insert for various cooling medium conditions. Hexagonal boron nitride nano particles are added to improve the lubrication properties during machining process. In Sect. 2, we discuss the tool life and wear characteristics using the basic and extended empirical tool life equations. The empirical constants in tool life equations are obtained using experimental data analysis for cemented carbide and steel alloys. A response surface methodology using regression-based equation has been implemented for the data obtained through a series of 16 experiments carried on turning operations on lathe bed and boring operations. Tool life and wear was determined for cutting speeds that ranged between 40 mm/min and 120 mm/min and for maximum value of 0.25 mm/rev and 0.6 mm, respectively. Finally, we present a conclusion on suitable tool life for range of machining parameters studied.

2 Methods

2.1 Tool Life Calculation

Taylor, 1906 developed an empirical correlation between cutting speed and tool life through a series of experiments and found that tool life varied exponentially with cutting speed [5]. In metal cutting operations, tool deforms the work piece material and produces chips during the deformation process under the action of mechanical forces, temperature, and tribological characteristics. The basic Taylor model as given

by Eq. (1) provides relatively quick results that can be evaluated manually, but the extended Taylor model takes significantly longer time to evaluate manually. Hence, in the present study we used MATLAB 2019b software to evaluate the extended tool life equation given by Eq. (3) for different machining conditions.

$$v_s \cdot T_l^n = C \tag{1}$$

$$v_s \cdot h^x \cdot T_l^n = C \tag{2}$$

$$v_s \cdot T_l^n \cdot d^x \cdot f^y = C \tag{3}$$

$$T = C^{\frac{1}{n}} \cdot v^{-\frac{1}{n}} \cdot d^{\frac{x}{n}} \cdot f^{\frac{y}{n}} \tag{4}$$

where v_s is cutting speed expressed in m/min, T_l is tool life expressed in minutes, C and n are constants, which will be based on work piece and tool material. The value of n selected for ceramic inserts as 0.4. Tool life equation of Taylor may be extended by the influence of feed as shown in Eq. (2) where, f is feed rate mm/rev, C, x, and y are empirical constants, which will be based on tool and work piece material characteristics. Another empirical formula for tool life commonly used in case of turning process is given by Eqs. (3) and (4). Equation (3) is dependent on two additional parameters, feed rate, f, mm/rev depth of cut, d, mm. Hexagonal boron nitride (HBN) is anisotropic refractory substance which consists of primarily boron and nitrogen and used essentially as dry lubricant. Due to good thermal and chemical stability they are applied in ceramics parts production which can resist high temperatures. The cubic form of boron nitride has exceptional adhesive properties and often used as binders.

2.2 Response Surface Methodology

In the simulation of manufacturing systems, there is a widespread use of simulation to design and optimization. Response surface methodology (RSM) is one such technique in which optimized values for design variables are sought by using a possible set of input–output factor combinations in the design space. The search procedures for optimized values according to the optimization technique adopted and involves complex calculations for machine tool and manufacturing industry. Hence, design of experiment process consists of factor inputs from experiments which produce model response outputs that vary with simulation runs. Hence, factor responses are estimated using model simulation runs iteratively and depend on new values of independent variables [6, 7]. This method also consists of metamodel normally, is a first- or second-order polynomial equations to determine the responses for different model

parameters. Using the metamodel we can obtain a set of factor values which optimizes the response [8]. The important objective of experiment design is to find the key parameters that have strongest influence on outcomes and require least amount of computation cost of simulation. This is sometimes known as factor screening or sensitivity analysis. Schruben and Cogliano [9] introduced a method for dynamic simulation in which values of inputs are varied to find simulated outputs at different frequencies. The output process parameters are examined whenever the input parameters frequencies variation changed. This is known as *factor's oscillation* to determine the change in output response at a given frequency. As a result the test models can be obtained at a reduced cost of simulation which is substantially lower than conventional experiment design approaches. Additionally statistically obtained values correlate well with RSM simulation outputs [9–11]. It also means optimization time for whole simulation runs are small enough to evaluate factor inputs and corresponding model response outputs. In case of manufacturing systems the product data used for mass production of components is validated using parametric data obtained from the metamodel [12]. The statistical fitness of metamodel responses can be tested reliably using ANOVA approach. It is especially useful when the population means are computed for more than two sets of groups. For such cases, correlation coefficient, R square is used to check accuracy among the model responses for discrete simulation runs and interactions are sought among factor variables [13]. Hence interactions are never determined by single factor variable approach [11, 12]. After a metamodel is obtained, RSM can evaluate the relationship as well as interactions among the several parameters using quantitative data. Common approach to RSM implementation is as shown below.

- Factor screening of parameters
- Finding the optimum region of interest
- Model the optimum response using polynomial or factor equations.

The screening procedure consists of listing all the factor parameters and performing an initial guess towards the region of optimum. Next, a first order model is fitted using the least squares. The path of steepest ascent is related to models regression coefficients. The direction of ascent is shown by signs. Higher order models, such as second-order model, also consists of stationary point that shows a point of maximum or minimum response known as *saddle point*. A second-order model in experiment design method can be evaluated using one of following ways.

- Box Behnken
- Central Composite Design (CCD)
- Face centred design
- Equiradial design
- Hybrid design

Parameters or variables for optimization carried out through model equation [14, 14]. In the present study we develop model equations which represent response surface modelling. Using the regression-based curve fitting method to the data obtained from series of 16 experiments, we obtain a polynomial expression given by

Table 1 Empirical constants used for different tool material inserts

C	n	Material
160	0.4	Ceramic
350	0.125	HSS (non-steel)
200	0.125	Steel
2700	0.25	Cemented carbide (non steel)
1500	0.25	Steel
10,000	0.6	Ceramic

Eq. (4) based on the extended tool life equation given by Eq. (3) which is a function of all three machining parameters discussed earlier. As mentioned before, the correlation coefficient, R^2 is given by Eq. (5) and found to be 0.9704 which represents an excellent fit with the experiment data and those obtained from model simulation runs. The model response equations are usually a second-order polynomial which are fitted by means of regression approach.

$$T = -0.0053 \cdot V^3 + 0.322 \cdot F^2 V^2 - 6.1279 \cdot V \cdot D + 41.471 \tag{5}$$

$$R^2 = 0.9704 \tag{6}$$

Similarly, we can obtain the regression equation and its correlation coefficient based on basic tool life Eq. (1) and given by Eqs. (7) and (8) respectively.

$$T = 0.0981 \cdot V^2 - 2.8676 \cdot V + 23.446 \tag{7}$$

$$R^2 = 0.9156 \tag{8}$$

where V is Cutting speed, F is feed, D is depth. A general second-order equation for tool life as function of machine spindle speed, feed and cut depth can be written according to Eq. (9) (Tables 1 and 2)

$$\begin{aligned} T(F, V, d) = T_o + T(F) \cdot V(F) + T(D) \cdot V(D) \\ + T(F \cdot D) \cdot V(F) \cdot V(D) + T(F) \cdot V^2 \end{aligned} \tag{9}$$

3 Results

See Figs. 1, 2, 3, 4, 5 and 6.

Table 2 Computed actual and predicted tool life using Eqs. (1) and (2), actual and predicted chip thickness

S. No	Tool life (min) (Actual)	Predicted Tool life [min] using Eq. (1)	Predicted tool Life (min) using Eq. (2)	Chip thickness, mm	Predicted Chip thickness, mm
1	25.3	24.93	46.49	0.182	0.20
2	21.5	24.93	41.29	0.191	0.20
3	16.4	24.93	38.04	0.210	0.20
4	11.9	24.93	35.71	0.216	0.20
5	33.2	10.75	19.70	0.184	0.17
6	36	10.75	18.11	0.181	0.17
7	14	10.75	16.28	0.173	0.17
8	11.23	10.75	15.51	0.169	0.17
9	34	5.74	10.41	0.157	0.14
10	25.4	5.74	9.33	0.153	0.14
11	32	5.74	8.99	0.147	0.14
12	13	5.74	8.36	0.145	0.14
13	37	3.47	6.26	0.142	0.13
14	29	3.47	5.69	0.139	0.13
15	23	3.47	5.35	0.138	0.13
16	15	3.47	5.15	0.140	0.13

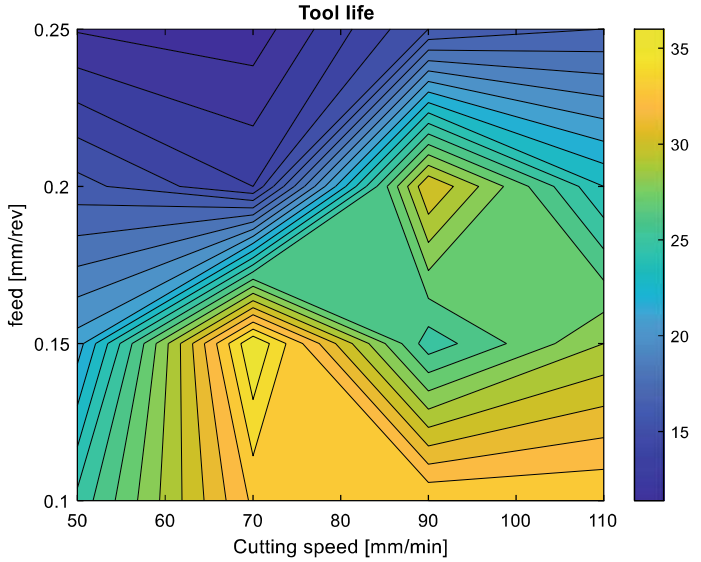

Fig. 1 Contour graph depicting desing life of tool for changing rates in feed and speed of cutting

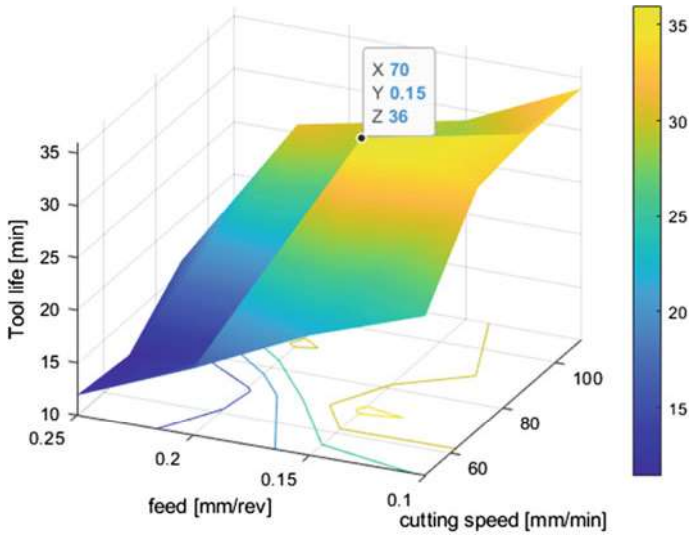

Fig. 2 Response surface of life of cutting tool at multiple rates applied to feed and cutting speed

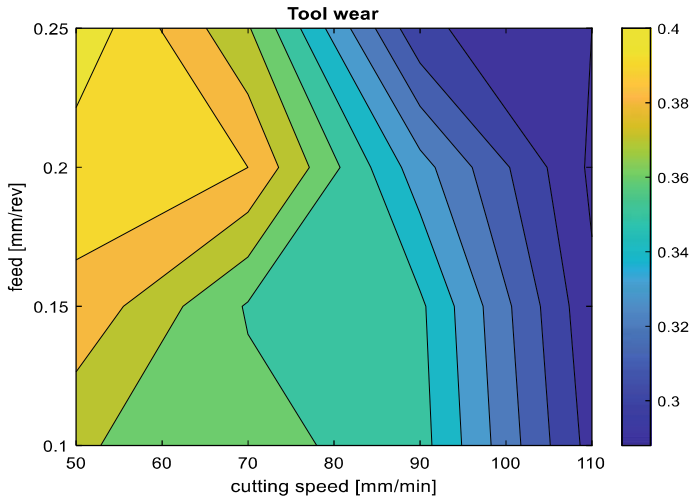

Fig. 3 Contour plot of tool wear for different feed rates and cutting speed values

4 Conclusions

It is observed that the effect of machining parameters feed rate (mm/rev), depth of cut (mm), and cutting speed (mm/min) have a significant influence on the tool life of the cutting tool. A response surface methodology was adopted on experiment data

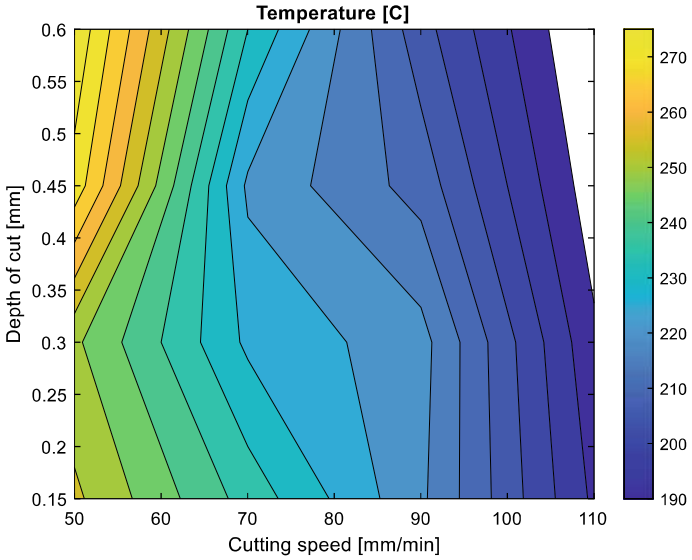

Fig. 4 Temperature distribution on tool face for different values of depth of cut and cutting speeds

Fig. 5 Comparison of tool life when the tool life exponent, n is 0.4 and C value of 185, $x = 0.01$ and $y = 0.1$ (HSS non-steel) material using Eqs. (1) and (2)

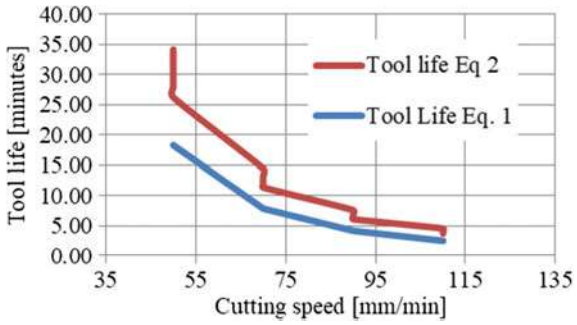

Fig. 6 Comparison of tool life for varying cutting speed values and at different tool life constants

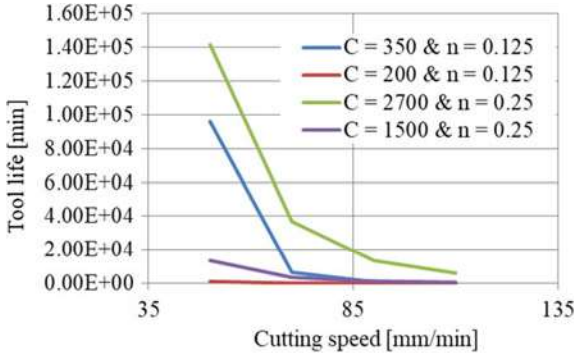

to determine the effects of machining parameters on tool life and wear for various cooling medium conditions.

Few important observations from the present study are:

1. It is observed that by plotting the graph between tool life, varying cutting speed and feed rates, at low cutting speed tool life will increase and a high feed velocity will reduce the cutting time per work piece.
2. Graph of surface degradation of tool for changing feed rate, cutting speeds reveals that when cutting speed increases the cutting temperature also increases which will reduce the tool life.
3. The tool wear for different feed rates and cutting speed values demonstrates that tool wear is affected lowest when the feed rate at 0.15 mm/rev. Smooth surface roughness was produced due to the high values of speed and low values for feed rate.
4. The analyses were done on temperature distribution on tool face for different values of depth of cut and cutting speeds. It is observed that the temperature of tool flank (side face) during the machining process is varied directly with speed and caused due to abrasion while the land (top face) is caused due to adhesive wear. At a higher value of spindle speeds, the temperature recorded at the tool face increased exponentially.
5. Temperature distribution on tool face is also affected when the depth of cut and cutting speeds was increased. Hardness of work piece material strongly influences cutting speed and tends to reduce tool life significantly. By increasing cutting speed to ~20% the expected tool life is reduced to half but when cutting speed is increased by 50% the expected tool life is reduced to 1/5th of original life.

Further research on the variable tool geometry provides better understanding of tool life and wears characteristics.

References

1. Talib, A.N.: Studying the effect of cutting speed and feed rate on tool life in the turning processes. In: First Engineering Scientific/Conference College of Engineering, University of Diyala, 22–23 Dec (2010)
2. Kale, S.A., Chaudhari, N.B.: Effect of cutting parameters on tool life. Int. J. Curr. Eng. Technol. **6**(6), 2178–2182 (2016)
3. Ayodeji, O.O., Abolarin, S.M., Yisa, J.J., Olaoluwa, P.S., Kehinde, A.C.: Effect of cutting speed and feed rate on tool wear rate and surface roughness in lathe turning process. Int. J. Eng. Trends Technol. **22**(4), 173–175 (2015)
4. Astakhov, V.P.: Effects of the cutting feed, depth of cut, and workpiece (bore) diameter on the tool wear rate. Int. J. Adv. Manuf. Technol. **34**(631–640). https://doi.org/10.1007/s00170-006-0635-y (2007)
5. https://amtil.com.au/mathematical-models-effectively-calculate-tool-life/-:~:text=The%20equation%20for%20Taylor%E2%80%99s%20basic%20model%20is%20vC,result%20in%20a%20tool%20life%20of%20one%20minute. Mathematical models effectively calculate tool life - AMTIL, September 2, Industry news, Source: https://amtil.com.au/ (2016)

6. Meilgaard, B.T., Civille, M., Carr, G.V.: Sensory Evaluation Techniques, 2nd edn. CRC Press, Boca Raton, FL (1991)
7. A.V.A. Resurreccion: Quantitative of quality attributes as perceived by the consumer. In: Consumer Sensory Testing for Product Development. Aspen Publishers, Inc., Gaithersburg, MD (1998)
8. Box, K.G., Wilson, G.E.P.: On the experimental attainment of optimum conditions. J. R. Stat. Soc. **13**, 1–45 (1951)
9. Schruben, L.W., Cogliano, V.J.: An experimental procedure for simulation response surface model identification. Commun. Assoc. Comput. Mach. **30**, 716–730 (1987)
10. Schruben, L.W., Margolin, B.H.: Pseudo random number assignment in statistically designed simulation and distributing sampling experiments. J. Am. Statist. Assoc. **73**, 504–520 (1978)
11. Schruben, L.W.: Establishing the credibility of simulations. SIMULATION **34**, 101–105 (1980)
12. Tan, C.-H., Ghazali, H.M., Kuntom, A., Tan, C.-P., Ariffin, A.A.: Extraction and physicochemical properties of low free fatty acid crude palm oil. Food Chem. **113**, 645–650 (2009). https://doi.org/10.1016/j.foodchem.2008.07.052
13. Moskowaitz, H.R.: Product optimization approaches and applications. In: Measurement Food Prefer. Blackie Academie & Professional, Glasgow, UK, pp. 97–136 (1994)
14. Schutz, H.G.: Multiple regression approach to optimization. Food Technol. **37**, 46–48, 62 (1983)
15. Law, A.M.: Simulation Modelling and Analysis, 4th edn. McGraw Hill Publishers, New Delhi (2010)

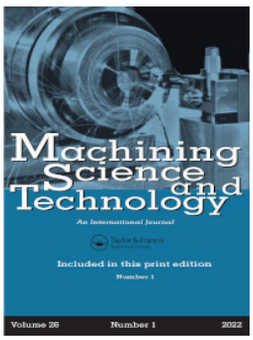

Machining Science and Technology

An International Journal

ISSN: (Print) (Online) Journal homepage: https://www.tandfonline.com/loi/lmst20

Influence of milling process parameters and significance of tools to improve the surface quality of GFRP composites

I. S. N. V. R. Prasanth, D. V. Ravishankar, M. Manzoor Hussain & Chandra Mouli Badiganti

To cite this article: I. S. N. V. R. Prasanth, D. V. Ravishankar, M. Manzoor Hussain & Chandra Mouli Badiganti (2022) Influence of milling process parameters and significance of tools to improve the surface quality of GFRP composites, Machining Science and Technology, 26:1, 120-136, DOI: 10.1080/10910344.2021.1998830

To link to this article: https://doi.org/10.1080/10910344.2021.1998830

Published online: 02 Dec 2021.

MACHINING SCIENCE AND TECHNOLOGY
2022, VOL. 26, NO. 1, 120–136
https://doi.org/10.1080/10910344.2021.1998830

Taylor & Francis
Taylor & Francis Group

Influence of milling process parameters and significance of tools to improve the surface quality of GFRP composites

I. S. N. V. R. Prasanth[a], D. V. Ravishankar[b], M. Manzoor Hussain[c], and Chandra Mouli Badiganti[d]

[a]Department of Mechanical Engineering, Malla Reddy Engineering College, Hyderabad, India; [b]Department of Mechanical Engineering, TKR College of Engineering & Technology, Hyderabad, India; [c]Department of Mechanical Engineering, JNTUH, Hyderabad, India; [d]Department of Mechanical Engineering, RISE Krishna Sai Prakasam Group of Institutions, Ongole, India

ABSTRACT

The anisotropic nature of polymer composites presents many challenges for manufacturers to adopt appropriate machining processes. In the present investigation, end milling experiments were conducted on glass fiber reinforced polymer laminates with five varieties of customized cutting tools with different angles of rake and clearance. The performance of the tools was evaluated in terms of their machining force, surface roughness and delamination factor at spindle speeds in the range of 690–2500 rpm. From the observations, relatively high rake and angled clearance tools performed better than the rest of the tools under consideration in terms of delamination and machined surface finishing. The milling operations performed at a spindle speed of 1950 rpm produced better surface quality. Observations from SEM graphs, exposed surface defects due to milling, generated at lower spindle speeds of 690 rpm and at higher spindle speeds of 2500 rpm with the tool signature of low angle rake and angled clearance tools out of all five tools considered for the experiments.

KEYWORDS

Bi-directional glass fiber reinforced polymers; conventional milling; customized carbide tipped tools; surface integrity; SEM

Introduction

Manufacturing techniques commonly used in glass fiber reinforced polymer (GFRP) composites do not require much machining to manufacture a finished product other than trimming and finishing. However, in special cases such as large pipeline fittings and aircraft parts, the milling and drilling of the components cannot be eliminated. As well as end milling is also used in the development of fiber reinforced polymer (FRP) molding tooling systems. Machining is inevitable in special situations where riveted holes and slots are used for mating one component (composite) with others

CONTACT Chandra Mouli Badiganti badiganti1@gmail.com Department of Mechanical Engineering, RISE Krishna Sai Prakasam Group of Institutions, Ongole, India.

(traditional isotropic material). Machining operations, such as turning, drilling, milling and trimming operations, have traditionally been used to make keyholes (Lopresto et al., 2016). Abrão et al. (2007) has observed that maintaining closer dimensional accuracy is necessary in assembly of parts to obtain a high degree of geometrical tolerance and surface finish. In wide and relatively dense composite parts, milling is carried out extensively, especially in jet engine casings, wind turbine blades, racing car bodies and marine hulls (An et al., 2021; Azmi et al., 2012). In machining the reinforcements, orientations may be disturbed due to abnormal cutting reaction forces. Zhang et al. (2001) has found fiber-matrix de-bonding takes place at a depth of cut range between 0.125 and 0.25 mm.

The current study examines ways to minimize damages to machined surface, focusing on FRP composites. Thus, understanding the machinability characterization and mechanism of machining of GFRP composites is an important research area in the field of secondary manufacturing. Cai et al. (2019) investigated precision machining mechanism in orthogonal cutting of carbon fiber reinforced polymer (CFRP) materials. An optimum cutting speed of 200 mm/min and small depth of cut 20 µm were recommended to achieve lower machining force and better surface finish. An et al. (2015) carried out orthogonal machining operations with five varieties of cutting tools (with different tool rake and clearance angle). Results showed large rake angle tool (25°) helps to ease separation of chips from machining surface, considerably reducing machining force. Additionally, use of larger rake angle produces defect-free machining surface. Cutting responses of CFRP materials is investigated (An et al., 2019; An et al., 2020). Can (2019) reported performance of four varieties of end milling tools on sheet mold compound (SMC) composites. Taguchi L16 OA experiments were conducted and repeated thrice. Latha et al. (2011) has modeled and performed optimization using Taguchi Method on a GFRP composite for various process parameters. Optimization of GFRP during drilling process and the effect of deamination factor by the process parameters is performed and found that feed rate influences the most in the delamination (Srinivasan et al., 2017).

Slamani et al. (2019) also reported on the effect of cutting process parameters in edge trimming of CFRP composites on machined surface quality. Researchers have used condensation vapor deposition diamond coated tool to examine surface integrity and tool wear. Better results (namely minimized delamination) were seen at lower feed rates and higher spindle speeds. Previous researchers (Wang et al., 1995; Calzada et al., 2012; Slamani et al., 2015) found machining forces were affected by few input factors, such as machining process conditions, properties of cutting tool and tool nomenclature. Chatelain and Zaghbani (2012) reported on

the influence of tool nomenclature on machining force, surface roughness and damage mechanism in trimming of CFRP materials. The experiments were carried out with three carbide Chemical vapor deposition (CVD) coating tools having varieties of tool angles under different machining conditions. They found surface quality was poor when axial cutting forces were high. Study on hole quality of a fiber metal composite is conducted during dry drilling by varying the parameters and coating on the tool (Giasin et al., 2019). Effect of machining parameters in abrasive water jet machining of carbon glass fiber hybrid composite is studied and a mathematical relationship was also developed to validate the results (Ming et al., 2018). Palanikumar (2007) has modeled the surface roughness through response surface method of a GFRP composites and ANOVA is used to validate the results obtained in his study.

Arola et al. (1996) and Ramulu (1997) undertook orthogonal machining studies using Physical vapor deposition (PVD) coated tools on Bi-Directional and Uni-Directional CRRP composites having different fiber ply orientations. The authors found cutting mechanism was highly dependent on type of fiber used while tool geometry and machining conditions had less impact. Arola and Ramulu (1997) studied the effect of slot milling operations on UD-GFRP composites. The authors found cutting force was influenced by fiber angle and chip thickness followed by other machining process parameters (spindle speed and feed rate). Cutting forces were increased from 0° to 90° and then decreased from 90° to 180° while chip thickness was increased.

Arola et al. (1996) and Arola and Ramulu (1997) investigated chip formation mechanism in orthogonal cutting of CFRP composites with varied tool rake and clearance angles, tool materials, and various combination of cutting process parameters. They found chip formation mechanism was affected by direction of cutting tool on work piece angles followed by machining process parameters. Shojaeefard et al. (2019) used Taguchi DOE 4 ○4 to optimize machining process parameters and avoid surface roughness in machining of sheet metal using 3 helical forming tools. They found surface quality was proportionate to quality and cost. They noted larger diameters of tool provided lower surface roughness and that had no definite effect on other process parameters (cutting speed and feed rate). Findings showed machined damages were influenced by change of fiber arrangement in UD-GFRP composites (Iliescu et al. 2010; Calzada et al. 2012; Jahromi et al. 2014). Optimization of milling process parameters of GFRP composites is carried out by author in his earlier study (Prasanth et al., 2018; Prashanth et al., 2018).

Studies, hence, indicate a poor understanding of tool performance on machined surface damage. This study therefore addresses by examining five

Table 1. Physical properties of GFRP composite constituents.

Type	Density (g/cm^3)	Tensile strength (GPa)	Young's modulus (GPa)
E-glass	2.58	1.75	72.3
Polyester resin	1.2	0.055	2.4

varieties of customized tools to understand surface integrity. In the present research work, the objective is to develop special purpose tools to be adapted to the milling of FRP composite materials to achieve a better milled surface. Further investigations in these directions could lead to the establishment of ISO standards. Existing conventional tools have limitations on tool signature variations. The improvement in clearance angles contributes to a hypothesized reduction in friction between the milling surface and the cutting edge in the current competition. The increase in the angle of the rake also provides the space for the reinforcement to be easily cut, which even contributes to a reduction of the cutting power. The tool signature of the customized tool rake angle is therefore increased by 5° and the clearance angle by 2°. Five types of customized tools were considered for experimentation, i.e., tool-1 rake angle was 15° and its clearance angle 6°; tool-2 rake angle 20° and its clearance angle 8°; tool-3 rake angle 25° and its clearance angle 10°; tool-4 rake angle 30° and its clearance angle 12° and tool-5 rake angle 35° and its clearance angle 14°.

Experimental set up and procedure

In the present investigation, woven roving glass fiber (450GSM and diameter of fiber 25 µm) supplied by Saint Gobain is used. Matrix material used for fabrication of composite laminate is general purpose polyester resin and the hardener used with the combination of catalyst (methyl ethyl ketone peroxide) and cobalt naphthalene as accelerator purchased from local vendor. The polymer laminates were fabricated using hand layup compression molding technique and glass fiber is considered in Bi-Direction $[0°/90°]_{10}$. A mixture of polyester resin (matrix) and hardener taken in the ratio of 10:1 and stirred in a glass mug and ready mixture is poured into the mold of E-Glass preform under the pressure of 200 kgf. Resin was cured for 5 hours to form a composite laminate. Physical properties of GFRP composite constituents are represented in Table 1.

Work pieces of 100 × 100 × 10 mm blocks were cut using diamond abrasive wheel cutter for milling operations. Burn-off tests were conducted to discover the fiber volume fraction (55%) of experimental GFRP work pieces as per ASTM D2584-68. Mechanical properties (tensile and flexural strength tests) of glass composite laminates are tests on a universal testing machine and the investigation is carried out as per the ASTM D790 and ASTM D 638 standards and tabulated in Table 2. Acid digestion test has

Table 2. Mechanical Properties of GFRP composite laminate.

Tensile test results for GFRP composite laminate				
Sample name	Thickness (mm)	Ultimate tensile load (KN)	Ultimate tensile strength (N/mm^2)	
Bi-directional Woven roving composite laminate	5.88	8.59	180	
Flexural test results for GFRP composite laminate				
Specimen name	Force (Kgf)	Deflection (mm)	Flexural strength (N/mm^2)	Flexural modulus (N/mm^2)
Bi-directional Woven roving composite laminate	2	0.01	264.5	65690

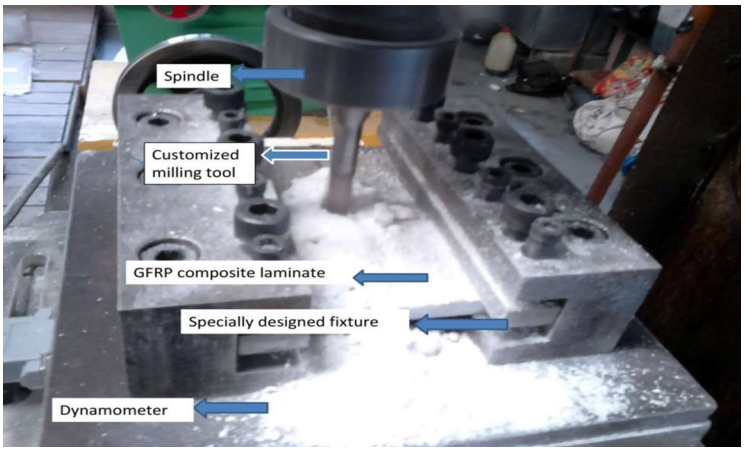

Figure 1. Experimental set up for performing milling operations on GFRP composite laminates.

been performed as per ASTM D3171-99, to know the void content in GFRP composite laminate and voids were found to be in the range of 4%–5%.

End milling operations were conducted using conventional universal milling machine to produce work piece slots as shown in Figure 1 (Prasanth et al. 2017b). Five varieties of customized carbide tipped end milling tools of 10 mm diameter were selected and tool specifications are presented in Table 3: tool-1 rake angle was 15°, and its clearance angle was 6°; tool-2 rake angle was 20°, and its clearance angle was 8°; and tool-3 rake angle was 25°, and its clearance angle was 10°, tool-4 rake angle was 30°, and its clearance angle was 12°, and tool-5 rake angle was 35°, and its clearance angle was 14° (see Figure 2). Five spindle speeds were selected: 690, 960, 1153, 1950 and 2500 rpm, and constant feed rate were 120 mm/min while depth of cut was 3 mm.

Machining forces were considered in the direction of tool travel using three axis strain gauge type milling tool dynamometer. Computerized data acquisition system was also used. The work pieces were centrally fixed on the special purpose fixture over the milling tool dynamometer to avoid

Table 3. Tool specifications.

Cutting tool	Diameter in 'mm'	Number of cutting edges	Rake angle	Clearance angle	Cutting tool over view	Cutting edge view of the tool
Customized carbide tipped tool-1	10	2	15°	6°		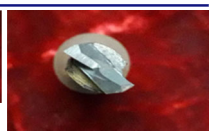
Customized carbide tipped tool-2	10	2	20°	8°		
Customized carbide tipped tool-3	10	2	25°	10°		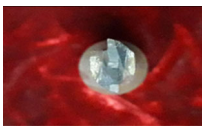
Customized carbide tipped tool-4	10	2	30°	12°		
Customized carbide tipped tool-5	10	2	35°	14°	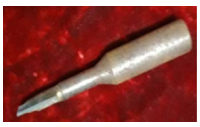	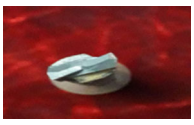

Figure 2. Five varieties of customized carbide tipped tools.

machining vibrations. Cutting component forces were recorded as per Langari et al. (2016).

There was customized strain gauge type dynamometer to determine cutting forces during milling. The cutting tool was fed over work piece in x-

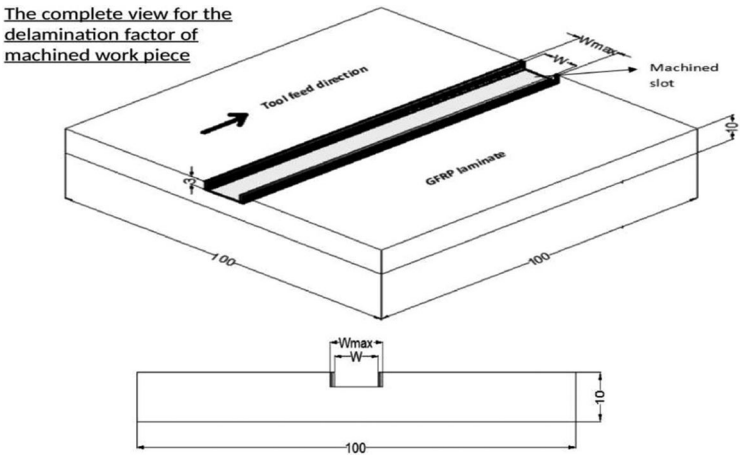

Figure 3. The complete view of delamination factor.

direction (F_x-feed force), F_y-cutting force and F_z-thrust force. The resultant force 'F_R' was considered as machining force $F_m = \sqrt{F_x^2 + F_y^2 + F_z^2}$. The data analogue device was connected to milling tool dynamometer and output readings were displayed on personal laptop.

Mitutoyo taly surf test (Make-Japan-Model-SJ210) with diamond stylus tip was used to measure surface roughness using center line average method. The surface of machined slot was cleaned so it was free from abrasive particles. To ensure accurate readings, the device was set at 2.5 mm transverse length and 0.8 mm cutoff value. The stylus was kept in contact with the grooved surface to avoid skidding. The surface roughness (R_a) values were measured at three different places and the readings displayed on the screen.

The machined slot widths at three different places were measured using a traveling microscope (Model RVM-201) with an accuracy of 10 µm. To determine the value of $W_{Max,}$ first, the vernier scale (traveling microscope) was counted as 0.01 mm. These values are substituted in Equation (1). Delamination factor (F_D) was calculated by taking the average value as per Davim and Reis (2005).

Delamination was measured using traveling microscope. Delamination factor (F_D) was determined based on the formulae,

$$F_D = W_{Max}/W \tag{1}$$

Where W_{Max} = width of the slot after machining in millimeters and W = actual width of slot in millimeters. The complete detail of delamination factor specimen is shown in Figure 3 (Prasanth et al. 2017a). The measurable outcomes in this experiment were F_m, R_a, and F_D as well as surface topology. The machining conditions are shown in Table 4.

Table 4. Experimental plan for milling.

Trial number	Spindle speed in 'rpm'	Tool type	Feed rate in 'mm/min'	Depth of cut in 'mm'
1 to 5	690	1/2/3/4/5	120	3
6 to 10	960	1/2/3/4/5	120	3
11 to 15	1153	1/2/3/4/5	120	3
16 to 20	1950	1/2/3/4/5	120	3
21 to 25	2500	1/2/3/4/5	120	3

Experiment number	Trial number	Spindle speed in 'rpm'	Tool type	Feed rate in 'mm/min'	Depth of cut in 'mm'
	1	690	1	120	3
	2	960	1	120	3
1	3	1153	1	120	3
	4	1950	1	120	3
	5	2500	1	120	3

Four sets of experiments conducted at spindle speeds of 960, 1153, 1950 and 2500 rpm with four tools.

Table 5. Experimental results.

	Machining force 'F_m' in N					Surface roughness 'Ra' in Microns					Delamination Factor 'F_D' in mm/mm				
Spindle speed 'N' in 'rpm'	Tool 1	Tool 2	Tool 3	Tool 4	Tool 5	Tool 1	Tool 2	Tool 3	Tool 4	Tool 5	Tool 1	Tool 2	Tool 3	Tool 4	Tool 5
690	30	27.8	28.2	28	26.5	3.61	3.52	3.3	3.23	2.9	1.28	1.26	1.27	1.23	1.2
960	30.8	28.1	28.4	28.2	27.1	3.55	3.4	3.25	3.19	2.7	1.25	1.24	1.23	1.2	1.16
1153	31.5	28.6	30.1	29.3	27.5	3.46	3.25	3.2	3.15	2.54	1.21	1.2	1.17	1.15	1.12
1950	32.8	30.2	30	30.1	28.2	3.4	3.1	3	2.8	2.41	1.18	1.18	1.15	1.13	1.1
2500	34.1	32.1	30.5	30.8	28.8	3.5	3.21	3.22	3	2.49	1.27	1.26	1.25	1.2	1.14

Results and discussion

Obtaining the desired machined surface quality is a major issue in milling of GFRP composites. Hence, choosing suitable machining process parameters is important to obtain better surface finish with minimal surface damages. It must be emphasized machined surface quality of polymer matrix composites depends on spindle speed and tool rake angle.

Machining effects on surface roughness

The effect of type of tool on surface roughness is evaluated using five end milling tools with varied geometries and other machining conditions as shown in Table 4. The results of the experiments are shown in Table 5. Figure 4a shows the effect of spindle speed on surface roughness with five different end milling tools.

The effect of spindle speed on surface roughness is described in two stages. The experiments are shown in Table 4 (trials from 1 to 20) while their results are displayed in Table 5. Spindle speed was increased from 690 to 1950 rpm and surface roughness was decreased continuously from 3.61 to 2.47 µm. Surface roughness became smoother at higher spindle speeds. These desirable spindle speeds are sufficient for material deformation,

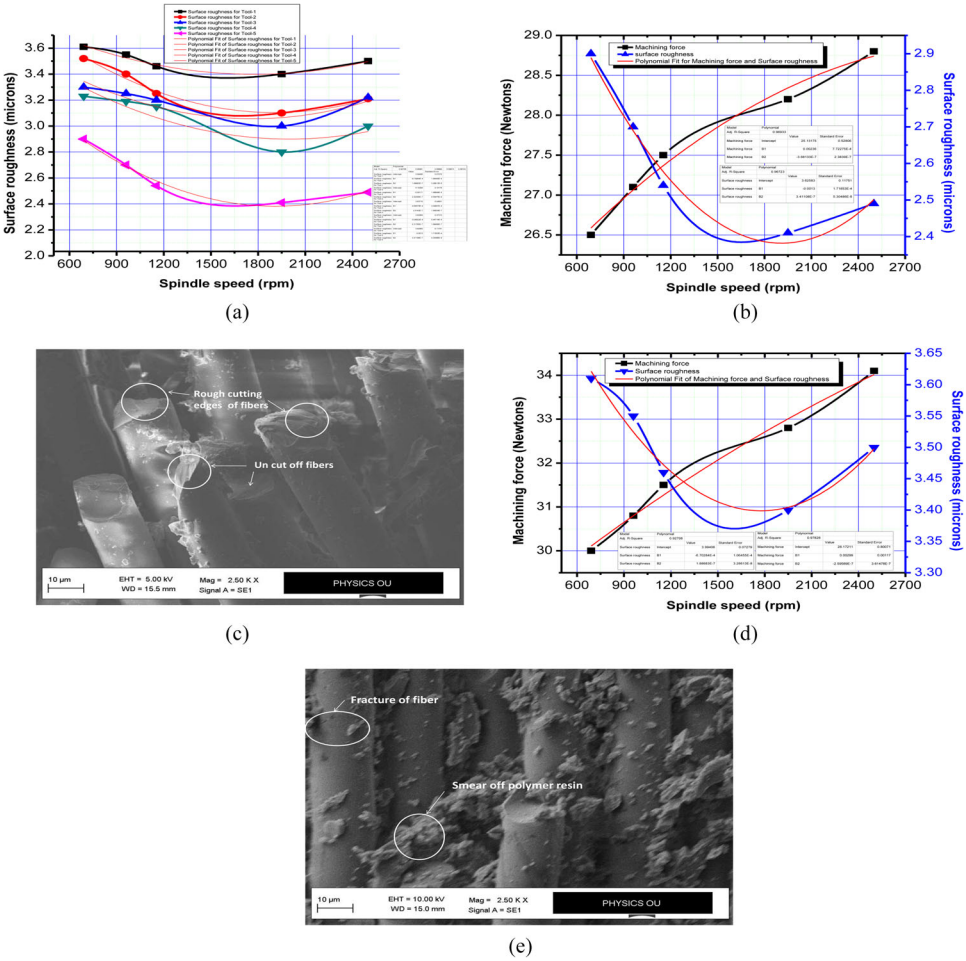

Figure 4. (a) Spindle speed versus roughness with five tools. (b) The interaction effect of machining force and surface roughness at five spindle speeds with tool-5. (c) SEM image for machined surface damages of GFRP laminate, when milling with tool-1 at a spindle speed of 960 rpm. (d) The interaction effect of machining force and surface roughness at five spindle speeds with tool-1. (e) SEM image for machined surface damages of GFRP laminate, when milling with tool-1 at a spindle speed of 2500 rpm.

namely, to form a cutting chip. There was easy withdrawal of chips from milled slot and cutting mechanism was uncomplicated.

The interaction effect between machining force and surface roughness at five different spindle speeds when milling with tool-5 is shown in Figure 4b. Among the five end milling tools, type-5 tool provided the smoothest surface finish at spindle speeds of 1950 rpm with sufficient machining forces (28.2 N). It carried away the chips from the milling surface. Larger tool rake angle held up the fiber shear failures to some extent. There was also less friction between rake face and work piece. Hence, reasonably

better surface roughness (2.41 μm) and an attractive surface finish were obtained.

Table 4 (trial number 1–15) and Table 5 show the experiments and results, respectively. At lower parametric conditions i.e., lower spindle speeds between 690 and 1153 rpm and low rake and clearance angled tool produced greater surface roughness (3.61 μm). At lower spindle speed (between 690 rpm and 1153 rpm), fiber chip layers were not easily separated from the machining surface. Chip disposal was difficult due to smaller rake and clearance angle of tools. Ineffective machining forces were generated, and material layer separation became complicated when cracks begun to form. This resulted in greater surface irregularities and rougher finishing. Figure 4c shows visible damages, namely rough cutting edges and uncut of fibers when milling with tool-1.

With increased spindle speed from 1153 to 1950 rpm, surface roughness was decreased from 3.46 to 2.41 μm and no visible damages were observed. The outcome is smoother machined surface.

Machining conditions (trial number 21–25 in Table 4) and results are shown in Table 5. Beyond the spindle speeds of 1950 rpm, particularly at 2500 rpm, surface roughness was greatly increased from 2.41 to 3.5 μm pointing to rough machined surface. This is because at higher spindle speeds, high compressive and thrust forces are generated which leads to material deformation and fracture of fibers, indicating greater failures at producing rougher machined surface.

The interaction effect between machining force and surface roughness at five different spindle speeds when milling with tool-1 is shown in Figure 4d.

Higher tangential forces at a higher spindle speed of 2500 rpm resulted in deflecting of cutting tool on the work pieces. Hence, large, segmented chip zones were formed without any uniform chips. Milling surface deteriorated leading to sub-surface damages.

It has been noted higher spindle speeds of 2500 rpm with maximized resultant forces (34.1 N), low rake and clearance angle of tool-1, did not reduce surface roughness. At maximum spindle speed, high friction was generated which then produced more thermal stresses. It led to tool clogging problem which needed to be addressed by tool plowing on milling surface. Consequently, glass resin and fiber were fractured while the tool rotated toward the rake face of the work piece 4. Greater thrusting resulted in thermo-mechanical action which in turns resulted in friction between tool and work piece interface due to high plowing action of tool on the fibers. This surface roughness (3.5 μm) meant the surface finish was poor. Figure 4e shows smears in glass resin and fracture of fibers.

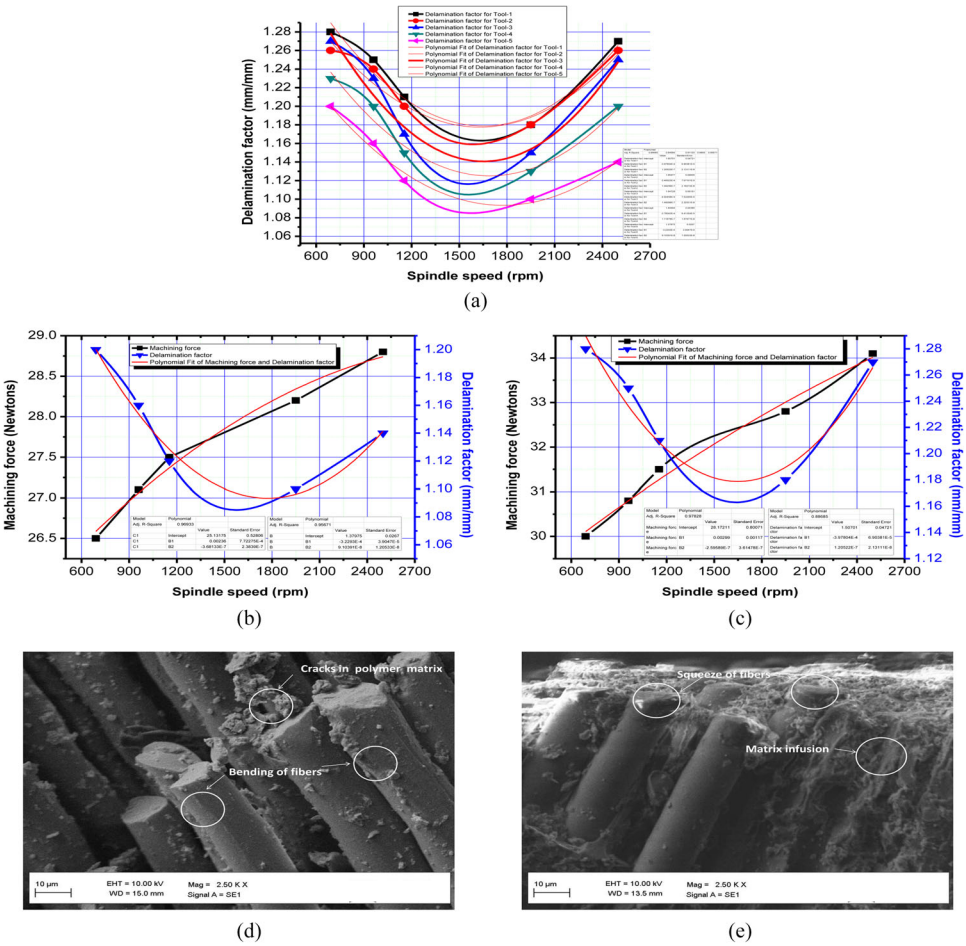

Figure 5. (a) Spindle speed versus delamination factor using five types of tools. (b) The interaction effect of machining force and delamination factor at five spindle speeds with tool-5. (c) The interaction effect of machining force and delamination factor at five spindle speeds with tool-1. (d) SEM image for machined surface damages of GFRP laminate when milling with tool-1 at a spindle speed of 690 rpm. (e) SEM image for machined surface failures of GFRP laminate when milling with tool-1 at a spindle speed of 2500 rpm.

Machining effects on delamination factor

Figure 5a shows the effect of spindle speed on delamination factor using five types of tools.

Figure 5b shows the interaction effect between machining force and delamination factor at five different spindle speeds when milling with tool-5. The effect of spindle speed on delamination factor is described below.

The experimental arrangement is shown in Table 4 (trial number 1 to 20) and its results are shown in Table 5. Calculated delamination factor is decreased from 1.28 to 1.1 considerably when spindle speed was increased from 690 to 1950 rpm. At spindle speed of 1950 rpm, larger rake angle

tool-5 was used with both adjacent vertical wall surface of milling slot resulting in significant cutting action between tool rake face and work piece at aggressive machining forces (28.2 N). At the shortest time of cutting action of tool i.e., if the tool is disengaged from work piece quickly there is a possibility of smoother fiber cuts due to tool rake and clearance angles. Continuous chips were produced in a fine powder form. Hence, no discernible delamination was seen.

The interaction effect between machining force and delamination factor at five different spindle speeds when milling with tool-1 is shown in Figure 5c.

Table 4 shows experimental trial 1 to 5 at lower spindle speed of 690 rpm and lower cutting force at 30 N. This force was inadequate which resulted in uncut fiber passing below tool-1 rake face near matrix material. Here, lesser deformation of fiber was seen. There is therefore matrix withdrawal in the form of segments. Matrix separation was difficult and partial cracking of matrix and bending of fiber was observed. There was peeling of fibers and cracking of matrix which degraded surface quality. Maximized delamination was at 1.21. Damages, such as matrix crack and bending of fibers, are shown in SEM Figure 5d.

Machining conditions are shown in Table 4 (trial number 21 to 25) and it indicates beyond 1950 rpm i.e., at higher spindle speeds of 2500 rpm using tool-1, the work piece is penetrated rapidly due to high compressive and thrust forces. High friction was created between tool rake face and work piece. The thrusting forces were increased which resulted in shear zone rubbing due to low clearance angle of the tool. Thereby, fibers tended to bend easily and get crushed. It was evident maximum delamination was achieved at 1.27. Figure 5e shows damage mechanisms due to fiber squeezing and matrix infusion.

Machining effects on cutting force

The effect of spindle speed on machining force is described below:

Figure 6a shows the effect of spindle speed on machining force with five different end milling tools. The machining force interaction effect with surface roughness and delamination factor is shown in Figures 4b, d, 5b, and c.

The experimental conditions are shown in Table 4 (trial number 1–20) and their results are shown in Table 5. When spindle speed was increased from 690 rpm to 1950 rpm, the machining force was considerably increased from 30 N to 32.8 N. The measurable outcomes i.e., surface roughness and delamination factor were considerably decreased from 3.61 µm to 2.41 µm

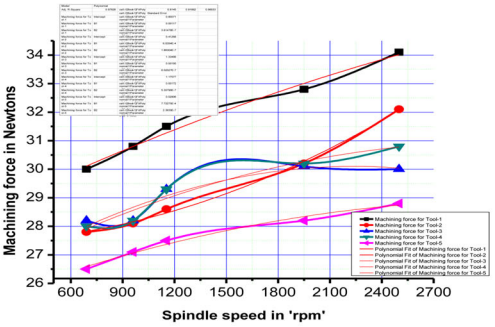

(a)

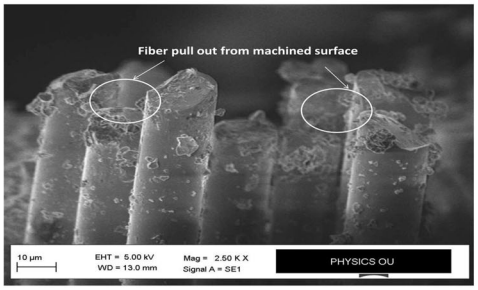

(b)

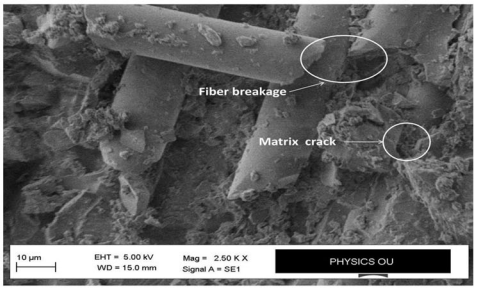

(c)

Figure 6. (a) Spindle speed versus machining force using five tools. (b) SEM image for machined surface damages of GFRP laminate when milling with tool-2 at a spindle speed of 690 rpm. (c) SEM image for machined surface damages of GFRP laminate when milling with tool-2 at a spindle speed of 2500 rpm.

and 1.28 to 1.1. Therefore, with increased spindle speeds, the cutting forces were laterally and linearly increased.

When milling with low rake and clearance angle tools (1,2,3, and 4) at low spindle speeds from 690 rpm to 1153 rpm, there was a withdrawal of chips having brush-like fibers with minimum chip thickness. Elastic recovery was difficult and matrix fracture more complex resulting in larger chip segments. The cutting action became complicated, distinctly bulkier chips were formed, tool clogging and complicated chip formation mechanism. There was also fiber pull out and other sub-surface damages. The machined surface became asymmetrical and surface quality deteriorated. Further, machined surface became rougher and delamination was experienced. The failure mechanism is shown in Figure 6b which details failure modes, such as fiber pull out and subsurface damages.

At the optimal spindle speed of 1950 rpm (trials from 16 to 20) and sufficient machining force at 28.2 N milling with tool-5 having larger rake and clearance angle facilitate cutting action and quicker impairing of chips. Therefore, the chips were extracted quickly along the cutting direction. These desirable deformations of continuous chips happened due to less bouncing action of the high clearance angle tool. The material removal rate

was increased and there was no obstruction during extraction of chips from milling surface. Thus, machined surface became smoother at 2.8 µm and delamination factor was less at 1.1.

Milling conditions are shown in Table 4 (trial number 21 to 25). When spindle speed was varied from 1950 rpm to 2500 rpm, the machining forces were drastically increased from 32.8 N to 34.1 N in tool advancement before chips were removed from the milled area.

It was difficult to obtain shear deformation to remove the chips away from the surface at low rake angle tool-1 with increased machining force (34.1 N).

Inter-laminar shear forces were observed at fiber matrix interface due to high compressive machining forces in tool advancement mechanism. Severe damages were seen, namely bending of fibers, bending, matrix cracks and delamination. Figure 6c shows surface failures, such as matrix crack and fiber breakage.

Conclusion

The current study is focused on the tool performances and effect of input process parameters on milling surface quality of GFRP composite laminates.

1. The cutting mechanism was influenced by spindle speed and tool geometries.
2. The machined surface quality was significantly influenced by tool angles and spindle speeds. The following were noted:
   - Moderate spindle speed of 1950 rpm generated machining force around 23.5 N for improved surface quality.
   - Neither lower spindle speed at 690 rpm nor higher spindle speed at 2500 rpm is recommended for desirable machined surface quality.
   - Higher tool rake angled, and clearance angled tool-5 is recommended for better performance i.e., minimal surface damages.
   - Lower tool rake angled and clearance angled tools (tool-1, 2, 3, and 4) did not provide attractive results.
3. The SEM evaluation based on milling surface quality of GFRP composites at different phases are described below.
   - Milling conditions of spindle speed at 1950 rpm, feed rate 120 mm/min, and depth of cut 3 mm with tool-5 helped to avoid thermo-mechanical failures and minimized machined surface damages.
   - More surface damages were noted, when milling with low rake and clearance angled tools (tool-1, 2, 3, and 4).

4. Varying of other factors, such as work piece characteristics (fiber volume fraction, fiber ply orientation, properties of work piece material) and conditions may be influenced results related to desirable machined surface quality.
5. Further investigations in these directions could lead to established ISO standardization.

Nomenclature

GFRP	glass fiber reinforced polymer
FRP	fiber reinforced polymer
CFRP	carbon fiber reinforced polymer
SMC	sheet mold compound
CVD	chemical vapor deposition
PVD	physical vapor deposition
F_x	feed force
F_y	cutting force
F_z	thrust force
F_R	resultant force
F_m	machining force
R_a	surface roughness
F_D	delamination factor
W_{Max}	width of the slot after machining in mm
W	actual width of the slot in mm

ORCID

Chandra Mouli Badiganti http://orcid.org/0000-0002-8213-6555

References

Abrão, A.M.; Faria, P.E.; Rubio, J.C.C.; Reis, P.; Davim, J.P. (2007) Drilling of fiber reinforced plastics: A review. *Journal of Materials Processing Technology*, 186(1–3): 1–7. doi: 10.1016/j.jmatprotec.2006.11.146

An, Q.; Cai, C.; Cai, X.; Chen, M. (2019) Experimental investigation on the cutting mechanism and surface generation in orthogonal cutting of UD-CFRP laminates. *Composite Structures*, 230: 111441. doi:10.1016/j.compstruct.2019.111441

An, Q.; Chen, J.; Ming, W.; Chen, M. (2021) Machining of SiC ceramic matrix composites: A review. *Chinese Journal of Aeronautics*, 34(4): 540–567. doi:10.1016/j.cja.2020.08.001

An, Q.; Dang, J.; Li, J.; Wang, C.; Chen, M. (2020) Investigation on the cutting responses of CFRP/Ti stacks: With special emphasis on the effects of drilling sequences. *Composite Structures*, 253(May): 112794. doi:10.1016/j.compstruct.2020.112794

An, Q.; Ming, W.; Cai, X.; Chen, M. (2015) Effects of tool parameters on cutting force in orthogonal machining of T700/LT03A unidirectional carbon fiber reinforced polymer laminates. *Journal of Reinforced Plastics and Composites*, 34(7): 591–602. doi:10.1177/0731684415577688

Arola, D.; Ramulu, M. (1997) Orthogonal cutting of fiber-reinforced composites: A finite element analysis. *International Journal of Mechanical Sciences*, 39(5): 597–613. doi:10.1016/S0020-7403(96)00061-6

Arola, D.; Ramulu, M.; Wang, D.H. (1996) Chip formation in orthogonal trimming of graphite/epoxy composite. *Composites Part A: Applied Science and Manufacturing*, 27(2): 121–133. doi:10.1016/1359-835X(95)00013-R

Azmi, A.I.; Lin, R.J.T.; Bhattacharyya, D. (2012) Experimental study of machinability of GFRP composites by end milling. *Materials and Manufacturing Processes*, 27(10): 1045–1050. doi:10.1080/10426914.2012.677917

Cai, X.; Zhou, R.; Shen, L.; Tang, H.; An, Q. (2019) An experimental investigation on precision machining mechanism of carbon fibre reinforced polymer. *International Journal of Abrasive Technology*, 9(1): 16–30. doi:10.1504/IJAT.2019.097965

Calzada, K.A.; Kapoor, S.G.; Devor, R.E.; Samuel, J.; Srivastava, A.K. (2012) Modeling and interpretation of fiber orientation-based failure mechanisms in machining of carbon fiber-reinforced polymer composites. *Journal of Manufacturing Processes*, 14(2): 141–149. doi:10.1016/j.jmapro.2011.09.005

Can, A. (2019) Study on the machinability of SMC composites during hole milling: Influence of tool geometry and machining parameters. *Arabian Journal for Science and Engineering*, 44(9): 7599–7616. doi:10.1007/s13369-019-03865-z

Chatelain, J.F.; Zaghbani, I. (2012) A comparison of special helical cutter geometries based on cutting forces for the trimming of CFRP laminates. *International Journal of Mechanics*, 6(1): 52–59.

Davim, J.P.; Reis, P. (2005) Damage and dimensional precision on milling carbon fiber-reinforced plastics using design experiments. *Journal of Materials Processing Technology*, 160(2): 160–167. doi:10.1016/j.jmatprotec.2004.06.003

Giasin, K.; Gorey, G.; Byrne, C.; Sinke, J.; Brousseau, E. (2019) Effect of machining parameters and cutting tool coating on hole quality in dry drilling of fibre metal laminates. *Composite Structures*, 212(15): 159–174. doi:10.1016/j.compstruct.2019.01.023

Iliescu, D.; Gehin, D.; Iordanoff, I.; Girot, F.; Gutiérrez, M.E. (2010) A discrete element method for the simulation of CFRP cutting. *Composites Science and Technology*, 70(1): 73–80. doi:10.1016/j.compscitech.2009.09.007

Jahromi, A.S.; Bahr, B.; Krishnan, K. (2014) An analytical method for predicting damage zone in orthogonal machining of unidirectional composites. *Journal of Composite Materials*, 48(27): 3355–3365. doi:10.1177/0021998313509862

Langari, J.; Kolahan, F.; Aliakbari, K. (2016) Effect of tool speed on axial force, mechanical properties and weld morphology of friction stir welded joints of A7075-T651. *International Journal of Engineering*, 29(3): 403–410. doi:10.5829/idosi.ije.2016.29.03c.15

Latha, B.; Senthilkumar, V.S.; Palanikumar, K. (2011) Modeling and optimization of process parameters for delamination in drilling glass fiber reinforced plastic (GFRP) composites. *Machining Science and Technology*, 15(2): 172–191. doi:10.1080/10910344.2011.579802

Lopresto, V.; Caggiano, A.; Teti, R. (2016) High performance cutting of fibre reinforced plastic composite materials. *Procedia CIRP*, 46: 71–82. doi:10.1016/j.procir.2016.05.079

Ming, I.W.M.; Azmi, A.I.; Chuan, L.C.; Mansor, A.F. (2018) Experimental study and empirical analyses of abrasive waterjet machining for hybrid carbon/glass fiber-reinforced composites for improved surface quality. *The International Journal of Advanced Manufacturing Technology*, 95(9–12): 3809–3822. doi:10.1007/s00170-017-1465-9

Palanikumar, K. (2007) Modeling and analysis for surface roughness in machining glass fibre reinforced plastics using response surface methodology. *Materials & Design*, 28(10): 2611–2618. doi:10.1016/j.matdes.2006.10.001

Prasanth, I.S.N.V.R.; Ravishankar, D.V.; Hussain, M.M. (2017a) Comparative evaluation on milled surface quality of GFRP composites by different end mill tools. *International*

Journal of Machining and Machinability of Materials, 19(5): 483–504. doi:10.1504/IJMMM.2017.087622

Prasanth, I.S.N.V.R.; Ravishankar, D.V.; Hussain, M.M.; Badiganti, C.M.; Sharma, V.K.; Pathak, S. (2018) Investigations on performance characteristics of GFRP composites in milling. *The International Journal of Advanced Manufacturing Technology*, 99(5–8): 1351–1360. doi:10.1007/s00170-018-2544-2

Prasanth, I.S.N.V.R.; Ravishankar, D.V.; Hussain, M.M. (2017b) Analysis of milling process parameters and their influence on glass fiber reinforced polymer composites. *IJE TRANSACTIONS A: Basics*, 30(7): 1074–1080. 10.5829/ije.2017.30.07a.17

Prashanth, I.S.N.V.R.; Ravi Shankar, D.V.; Manzoor Hussain, M.; Chandra Mouli, B. (2018) Critical analysis in milling of GFRP composites by various end mill tools. *Materials Today: Proceedings*, 5(6): 14607–14617. doi:10.1016/j.matpr.2018.03.052

Ramulu, M. (1997) Machining and surface integrity of fibre-reinforced plastic composites. *Sadhana*, 22(3): 449–472. doi:10.1007/BF02744483

Shojaeefard, M.H.; Khalkhali, A.; Shahbaz, S.O. (2019) Low-carbon steel sheet asymmetric single-point incremental forming: Analysis and optimization of the surface roughness. *International Journal of Engineering, Transactions C: Aspects*, 32(6): 866–871. 10.5829/ije.2019.32.06c.10

Slamani, M.; Chatelain, J.F.; Hamedanianpour, H. (2019) Influence of machining parameters on surface quality during high speed edge trimming of carbon fiber reinforced polymers. *International Journal of Material Forming*, 12(3): 331–353. doi:10.1007/s12289-018-1419-2

Slamani, M.; Gauthier, S.; Chatelain, J.F. (2015) A study of the combined effects of machining parameters on cutting force components during high speed robotic trimming of CFRPs. *Measurement*, 59: 268–283. doi:10.1016/j.measurement.2014.09.052

Srinivasan, T.; Palanikumar, K.; Rajagopal, K.; Latha, B. (2017) Optimization of delamination factor in drilling GFR-polypropylene composites. *Materials and Manufacturing Processes*, 32(2): 226–233. doi:10.1080/10426914.2016.1151038

Wang, D.H.; Ramulu, M.; Arola, D. (1995) Orthogonal cutting mechanisms of graphite/epoxy composite. Part I: Unidirectional laminate. *International Journal of Machine Tools and Manufacture*, 35(12): 1623–1638. https://doi.org/10.1016/0890-6955(95)00014-O doi:10.1016/0890-6955(95)00014-O

Zhang, L.C.; Zhang, H.J.; Wang, X.M. (2001) A force prediction model for cutting unidirectional fibre-reinforced plastics. *Machining Science and Technology*, 5(3): 293–305. doi:10.1081/MST-100108616

JMEPEG
https://doi.org/10.1007/s11665-022-07717-0

1059-9495/$19.00

TECHNICAL ARTICLE

Influence of Post-heat Treatment on Friction Stir-Processed AA7075/SiC Surface Composite Properties

D.S. Chandra Mouli, R. Umamaheswara Rao, A. Raveendra, P. Saritha, and G. Parthasarathi

Submitted: 5 June 2022 / Revised: 2 November 2022 / Accepted: 11 November 2022

The effect of post-aging treatment on the evolution of microstructure and the properties of silicon carbide-reinforced AA7075 surface composite manufactured by friction stir processing (FSP) were explored in this study. For this purpose, FSPed surface composites were subjected to aging treatment at 150, 180, and 210 °C for 8 and 16-h duration. The microstructure and properties such as microhardness and wear resistance were evaluated after aging treatment. The results showed that the grain refinement and homogenous distribution of SiC in matrix together with the precipitation strengthening enhanced the properties of FSPed surface composites. Hardness was found to be decreased at higher aging temperature and duration, due to the abnormal grain growth and the formation of stable precipitated particles in the microstructure. Surface composite samples age-treated to 180 °C for 8 h, and 150 °C for 16 h have exhibited good wear resistance and frictional characteristics. This study demonstrated that the FSP process combined with aging treatment had a significant influence on the microhardness and wear resistance of AA7075/SiC surface composite.

Keywords AA7075/SiC surface composite, Aging treatment, Friction stir processing, Microstructure, Microhardness, Wear resistance

1. Introduction

The most widely used structural materials are aluminum alloys because of their excellent properties. Among aluminum alloys, AA7075 alloy is preferred in aerospace and automobile industries owing to its high-strength-to-weight ratio (Ref 1-3). It is also sensitive to aging heat treatment; therefore, it can be strengthened by the precipitation hardening mechanism (Ref 4). However, they exhibit poor surface characteristics which restricted their use in several tribological applications (Ref 5). In the past few years, many research attempts have been made for improving surface properties of aluminum alloys, and they suggest processes like reinforcing the surface with hard particles and grain refinement methods. Among the various grain refinement methods mentioned in the literature, friction stir processing (FSP) gained popularity, as it can be effectively used to improve the surface characteristics of aluminum alloys by refining grain by dynamic recrystallization mechanism (Ref 6-8). It has been demonstrated that the surface properties of FSPed aluminum alloys can also be enhanced by reinforcing the microstructure with ceramic particles like aluminum oxide and silicon carbide (Ref 9, 10).

The post-heat treatment process has been performed by many investigators to further improve the mechanical properties of the aluminum alloy after FSP (Ref 11-13). Enhancement in the properties was ascribed to grain boundary hardening and precipitate hardening mechanisms (Ref 14). It has been reported that the post-aging process after FSPed aluminum alloy increased the hardness due to the existence of metastable precipitates and their pinning effect at the grain boundaries (Ref 15-17). The number of metastable precipitates was found to increase with the increase in the aging duration which was accountable for the increase in strength (Ref 18).

Recent researches have proposed the possibility of combining the effect of reinforcement and heat treatment such as annealing and artificial aging for improving the properties of the surface composite produced by the FSP process (Ref 19-27). The improvement in the properties such as hardness, wear resistance, and thermal stability of post-heat-treated FSPed aluminum surface composite was achieved due to the combined effect of inhibition of grain growth, the existence of reinforcement particles and the formation of fine precipitates in the microstructure. Owing to the advantages of post-heat treatment after FSP, a detailed study is required to explore the effect of post-heat treatment on the properties of FSPed aluminum alloy surface composite. Thus far, no research work has been performed to investigate the effect of post-aging treatment on the properties of FSPed AA7570/SiC surface composite. In our previous work (Ref 28), the microhardness and the wear resistance of AA7570 alloy were enhanced by incorporating SiC particles on the surface by the FSP process and successfully optimized the processed parameter. The present study focuses mainly to study the outcome of post-aging heat treatment on the mechanical and tribological properties of the FSPed AA7570/SiC surface

D.S. Chandra Mouli, Department of Mechanical Engineering, JNTUK, Kakinada, Andhra Pradesh 533005, India; and Department of Mechanical Engineering, MREC(A), Hyderabad, Telangana 500100, India; **R. Umamaheswara Rao**, Department of Mechanical Engineering, CEC, Visakhapatnam, Andhra Pradesh 530048, India; **A. Raveendra**, Department of Mechanical Engineering, MREC(A), Hyderabad, Telangana 500100, India; and **P. Saritha** and **G. Parthasarathi**, Department of Mechanical Engineering, Anurag University, Hyderabad 500088, India. Contact e-mail: dkmouli1986@gmail.com.

Published online: 09 December 2022

composite. Post-aging treatment was performed with different temperatures and durations, and their effects were systemically analyzed by examining microstructure evolution, microhardness, and wear resistance of the surface composite.

2. Experimental Procedure

In this study, rolled plates of age-hardenable AA7075-T651 alloy having dimensions of 150 × 50 × 6 mm were selected as the base metal. Silicon carbide (SiC) particles with an average size of 37 μm and a density of 3.21 g/cm3 were selected as reinforcing material. SiC particle was preferred as reinforcement owing to its superior mechanical properties, corrosion resistance, low density, and good thermal stability and proved to improve the properties of aluminum and its alloy (Ref 29-31).

Blind holes of size 2 mm with a depth of 3.5 mm were drilled and arranged in an array of 2 × 2 mm for placing the SiC particles. A spacing of 4 mm was provided between the holes, for the uniform distribution of reinforcing particles. Along the work piece length of 150 mm, 50 such holes are made. An automatic vertical milling machine (HMT Ltd. Pinjore, India) with suitable alteration was used in the fabrication of AA7075/SiC surface composites. A flat shoulder FSP tool with a square pin made of an H13 steel tool was used. The shoulder diameter and the length of the tool were 20 and 100 mm, respectively. The size and height of the square pin were 6 and 6 mm, respectively. The photograph and the schematic drawing of the tool are shown in Fig. 1. A pinless tool made of H13 steel was used for the capping process had a diameter and length of 20 and 100 mm, respectively. For concealing the SiC particles in the drilled hole and preventing them from scattering while FSP, the capping process was performed with a rotational speed of 560 rpm, a traverse speed of 25 mm/min, and a plunging depth of 0.3 mm.

After the capping process, AA7075/SiC surface composites were made with a single-pass FSP with the rotational speed, traverse speed, and tilt angle of 1125 rpm, 50 mm/min, and 3°, respectively. These parameters were chosen based on the previous study by authors (Ref 28) that optimized these parameters for enhancing the tribological properties of AA7075/SiC surface composites. During FSP, 8 KN of axial load and 15 s of initial dwelling period were maintained. To avoid the defects like tunneling and voids in the stir zone (Ref 32), FSP was performed with 0.24 mm shoulder penetration depth. Through this process, surface composite with 10% (vol%) SiC was produced. Calculation of volume percentage of reinforcement is provided in Appendix A. After the FSP process, six samples of the surface composite were subjected to the artificial aging process. As the solidus temperature of AA7075 is 477 °C, artificial aging was performed below this temperature. According to the literature (Ref 17), the artificial aging of FSPed surface composite specimen was done. First, the specimen was heated to an elevated temperature and maintained at that temperature for the specified aging time for the formation of the precipitate particles. After the aging time, the specimen was cooled to room temperature in the air. The aging temperatures and time durations selected in this study are presented in Table 1. After the aging process, the samples were cooled to room temperature inside the furnace.

Microhardness was measured with a neighboring indentation distance of 0.5 mm along the transverse section of each surface composite sample using the Vickers microhardness tester (VH-IMDX). Specimens with dimensions of 10 × 10 × 6 mm were used for microhardness test. Hardness measurement was taken according to ASTM E-384 with a load of 500 g and a dwelling time of 20 s. At each location, hardness was measured three times and the average value was considered for hardness data. The wear test was conducted on specimens having dimensions 25 × 5 × 6 mm according to ASTM-G99 using the pin-on-disc tester (DUCOM). The wear test was conducted for 300 s at room temperature in dry conditions. A disc made of hardened chromium steel was used as a counterface. The track diameter of 120 mm, a sliding speed of 175 rpm, and a normal load of 30 N were used during the wear test. The specimens used for microhardness and wear test were machined from the surface composite using wire EDM process. To examine the microstructure and to observe the SiC

Table 1 Artificial aging process schedule for AA7075/SiC surface composite

Sample designation	Temperature, °C	Time, Hrs
150/8	150°	8
150/16	150°	16
180/8	180°	8
180/16	180°	16
210/8	210°	8
210/16	210°	18

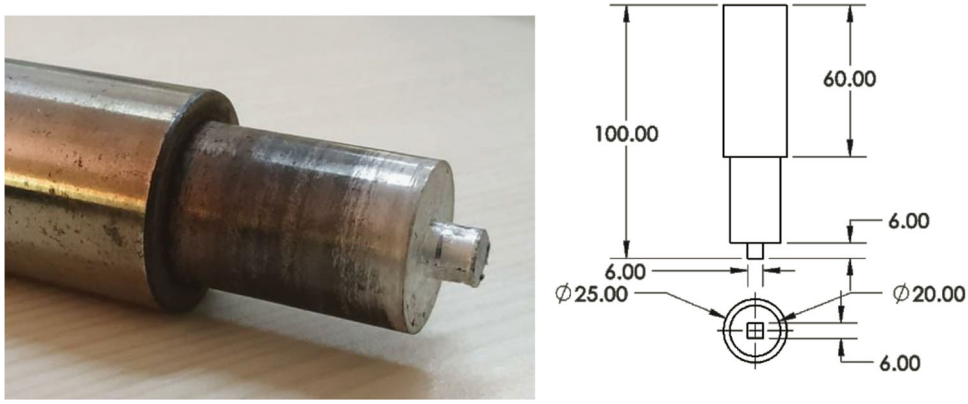

Fig. 1 Photograph and the dimension of FSP tool (all dimensions are in mm)

distribution on the stir zone surface, a scanning electron microscope (JSM-6330) with built-in energy-dispersive spectroscopy (EDS) was used.

3. Results and Discussion

3.1 Microstructure

Figure 2 presents the microstructure at the stir zone surface of the FSP samples after artificial aging treatment at different temperatures and times. Homogeneous distribution of SiC particles without any traces of agglomeration was observed in the matrix of all the FSP samples. Interestingly, ring-shaped white spots were noticed in the microstructure. These white rings were found to increase with the increase in aging temperature and time. They were analyzed by EDS, and the spectrum and the element composition are presented in Fig. 3. EDS result indicated the formation of precipitates. During the early phase of the artificial aging process, the precipitates of $MgZn_2$ formed along the grain boundaries help to prevent the dislocation movement and thereby improve the strength of the 7075 aluminum alloy by precipitation strengthening mechanism (Ref 4, 15, 33, 34). When the aging temperature and time are increased further, these precipitates grow in size and get increased in volume fraction, thus enhancing the precipitation strengthening.As seen in Fig. 3, when the alloy over-aged at a temperature of more than 180 °C, these precipitates are incoherent with the matrix material and they became ineffective in resisting the dislocation movement. This leads to the reduction in the strength of the 7075 aluminum alloy (Ref 12, 18, 35).

3.2 Microhardness

The effect of aging treatment on the microhardness at base metal, thermomechanically affected zone (TMAZ), heat-affected zone (HAZ), and stir zone (SZ) of artificially aged samples in comparison with the non-aged FSP sample is pictorially shown in Fig. 4. In all the cases, microhardness was found to be lesser in the base metal, whereas it was increased gradually from HAZ and reached a high value at the stir zone. The lower hardness at HAZ and TMAZ is attributed to the grain growth that occurred during FSP. The maximum hardness of 125 Hv was obtained at the stir zone when the aging treatment was performed at 180 °C for 8 h.

The microhardness profile of the FSP samples after the artificial aging process conducted at various temperatures for 8 and 16 h is shown in Fig. 5(a) and (b), respectively. These figures show that the values of hardness across the transverse section of the FSP samples vary depending on the selected artificial aging temperature and duration. The microhardness profiles of all the samples showed a general increase in hardness at the stir zone when compared to the other zones. The fine grains formed owing to dynamic recrystallization and the presence of uniformly distributed SiC particles are responsible for the increase in hardness at the stir zone. At 8-h aging duration (Fig. 5a), as the aging temperature increased, hardness increased initially up to 180 °C and then decreased. For 16 h of aging duration (Fig. 5b), the hardness at the stir zone tends to decrease with the increase in aging temperatures considered in this study. At the higher aging duration, the hardness increases by the formation of fine precipitates as explained earlier. At higher aging temperature and duration, hardness decreased because of the occurrence of over aging. Over-aging normally occurs for AA7075 alloy beyond 180 °C. Hence at 180 °C, microhardness reached the highest value. Beyond 180 °C (i.e., 210 °C), over-aging occurred which resulted in abnormal grain growth and an increase in the precipitated particles (Ref 11, 36). It was reported elsewhere (Ref 12) that increase in aging time and temperature results in over-aging, which caused the decrease in hardness. As the aging time increases, the precipitation formation becomes more prevalent, resulting in

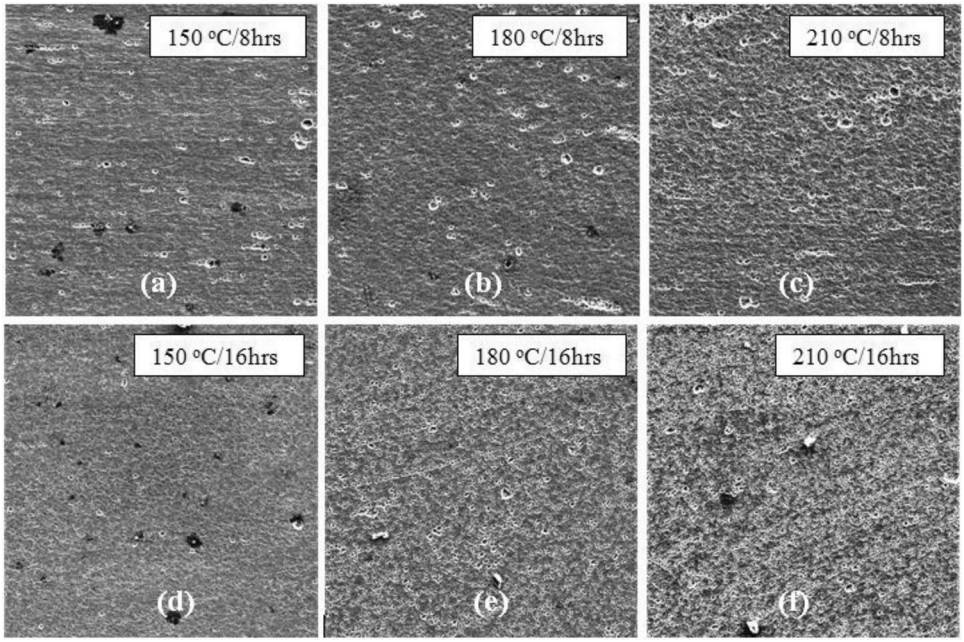

Fig. 2 Surface microstructure of stir zone of the FSP samples obtained at different aging temperatures and times (magnification: 500X, Scale: 100 μm)

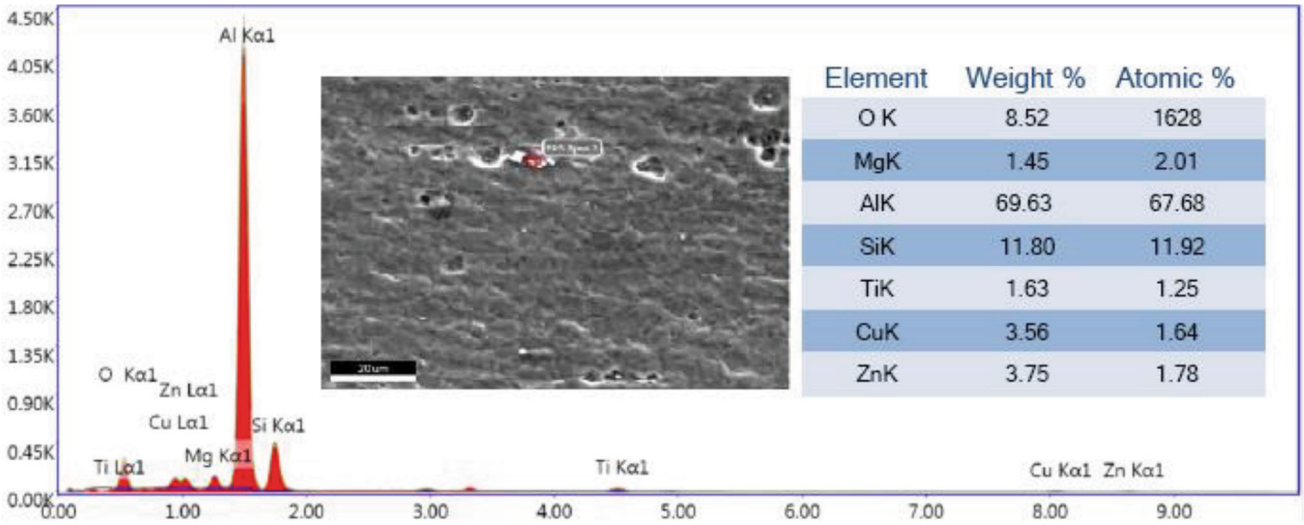

Element	Weight %	Atomic %
O K	8.52	1628
MgK	1.45	2.01
AlK	69.63	67.68
SiK	11.80	11.92
TiK	1.63	1.25
CuK	3.56	1.64
ZnK	3.75	1.78

Fig. 3 Result of the EDS analysis on 210/8 FSP specimen showing the spectrum and the elemental composition

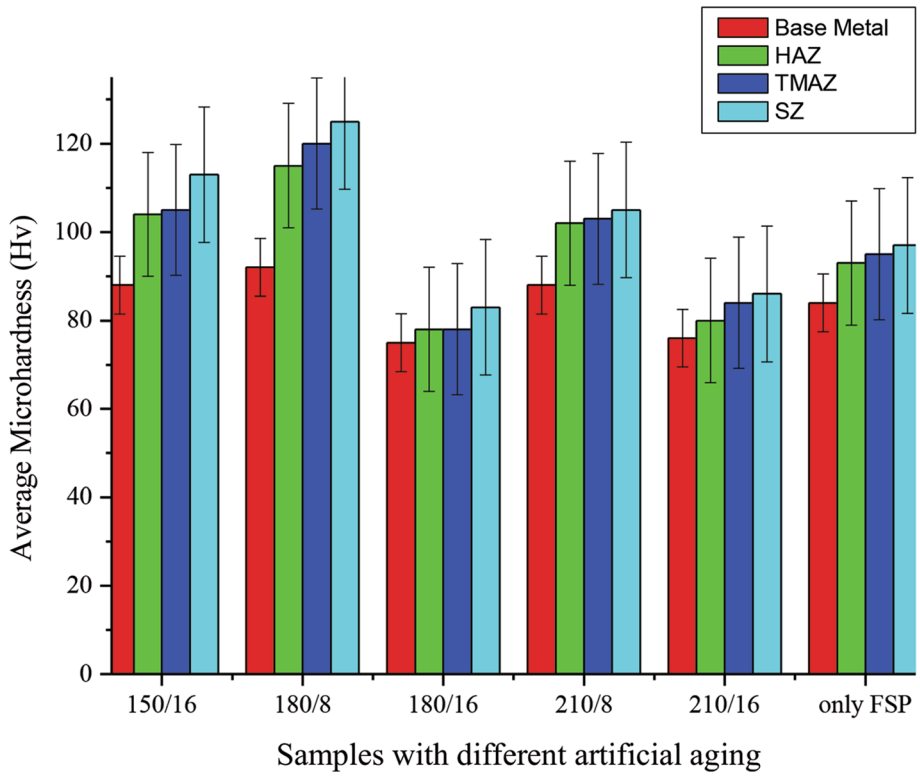

Fig. 4 Average microhardness at different zones of the aged and non-aged FSP samples

the hardness reduction of the aluminum alloy. Even though reinforcing particles are present in the microstructure, due to high aging temperature they could not effectively increase pinning force for restricting the grain growth (Ref 37).

4. Wear Characteristics

Figure 6(a) and (b) presents the variation of specific wear rate with time for different FSP samples aged at 8 and 16 h, respectively.

From Fig. 6 (a) and (b), it was evident that the specific wear rate of all the age-treated FSP samples gradually increased as the time duration of the wear test increased. Among the age-treated FSP samples, samples aged to 180 °C for 8 h and 150 °C for 16 h have exhibited lower wear rate. These two samples had higher microhardness because of the reasons explained earlier. The hardened surface of the samples permitted less plastic deformation due to the SiC reinforcement, grain refinement, and the formation of hard precipitates in the matrix. All these phenomena resulted in lower wear rate. However, as the time duration of the wear test increased, there was a frictional heat generation at the interface which caused the

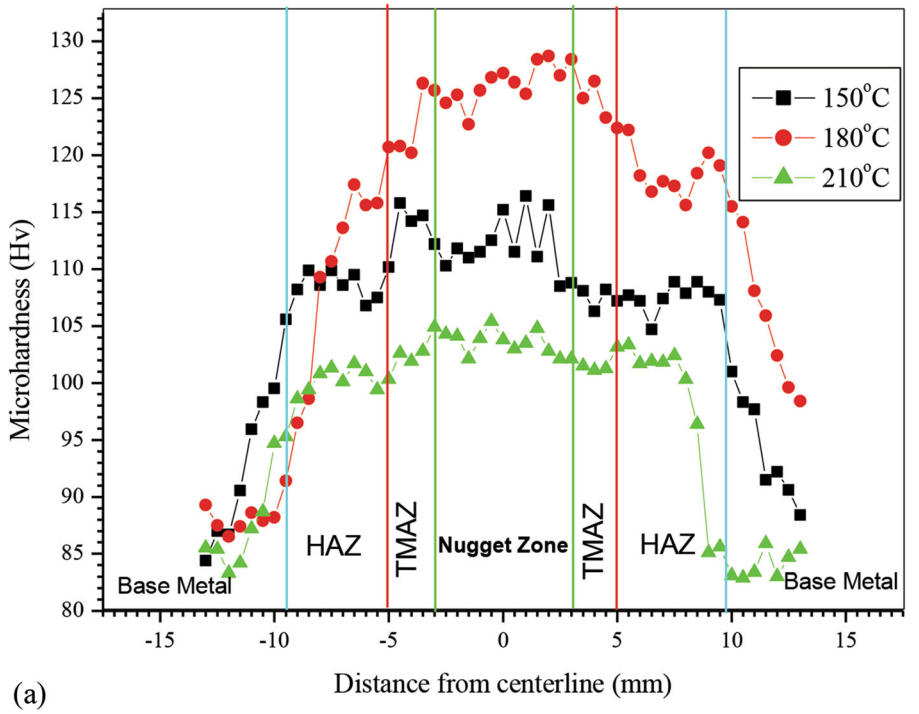

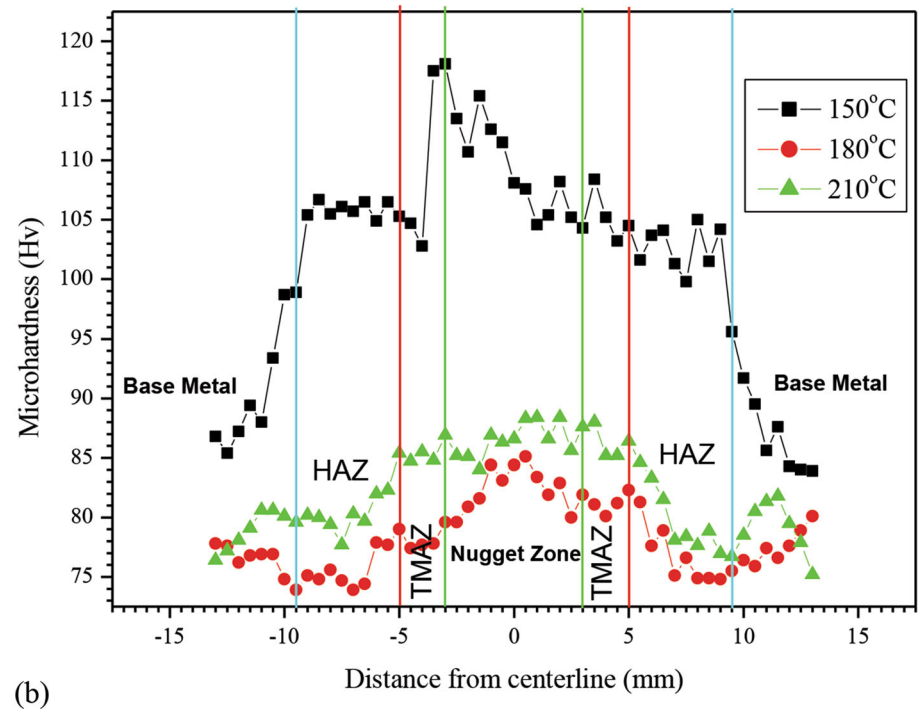

Fig. 5 Variation of the microhardness of FSP samples at different aging temperatures for (a) 8 h and (b) 16 h

thermal softening of the surface. As a consequence of this, there was an increase in wear rate with time.

Figure 7(a) and (b) represents the variation of friction coefficient with sliding time of the age-treated FSP samples for 8 and 16 h, respectively, under sliding wear test. The average coefficient of friction at each temperature for 8 and 16 h is presented in Table 2. The coefficient of friction was found to be fluctuating over the entire time duration of the test for all the FSP samples. These fluctuations may have resulted from the variation of contact surface area between FSP samples and the disc counterface of the wear tester due to the presence of SiC reinforcement and the precipitates in the matrix. From Fig. 7(a) and (b) and Table 2, it was clear that samples with high microhardness, namely 180/8 and 150/16, have shown lower wear rate and coefficient of friction. Hence, it can be concluded that these samples have good wear resistance and frictional characteristics.

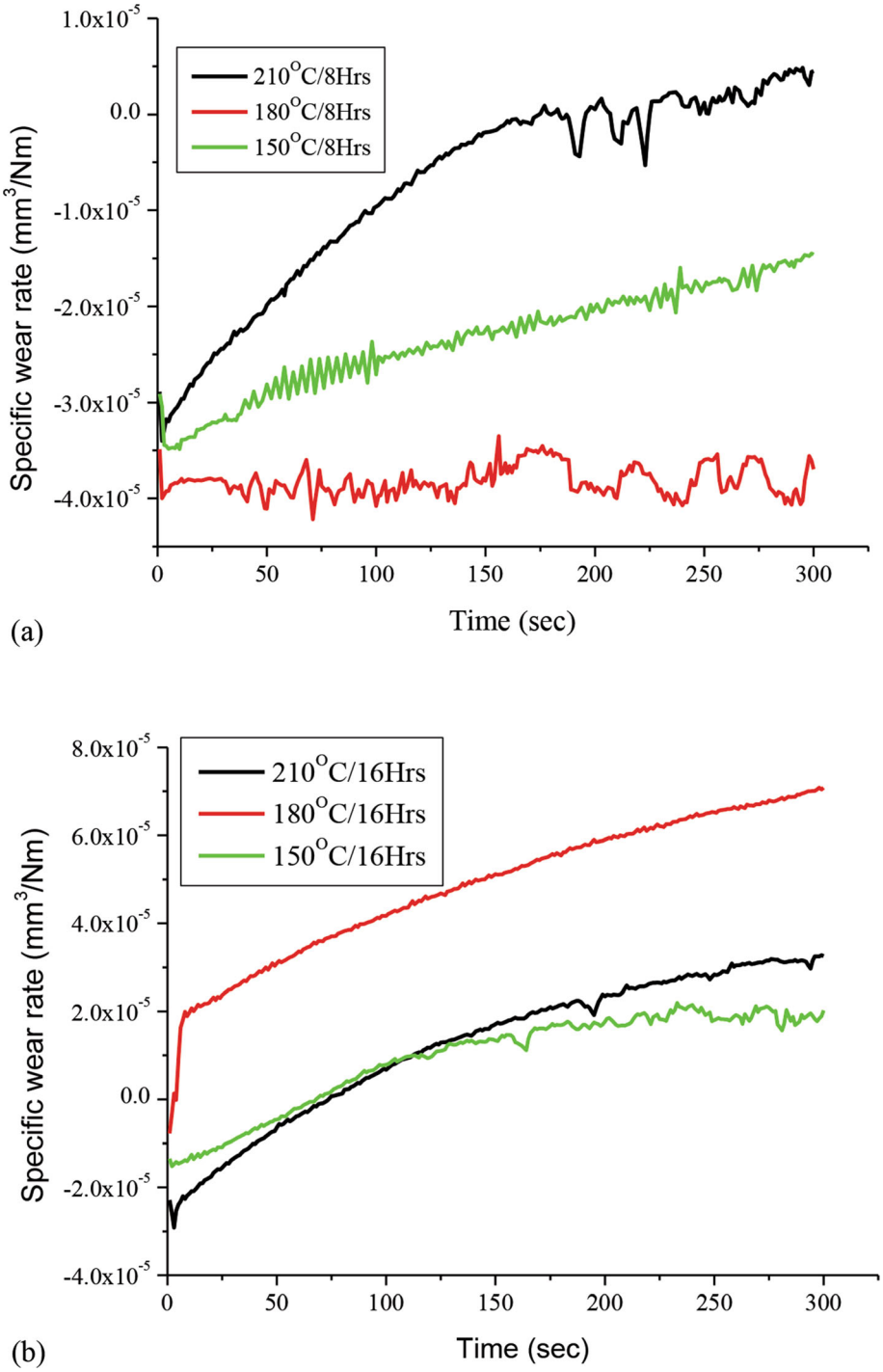

Fig. 6 Variation of specific wear rate with time of the FSP samples aged at different temperatures for (a) 8 h and (b) 16 h

5. Conclusions

The effect of post-aging heat treatment on the mechanical and tribological properties of the FSPed Al7570/Sic surface composite was studied in this research work. The influence of temperature and duration of the aging process were analyzed by examining microstructure, microhardness, and specific wear rate of the surface composite. The research findings are as follows:

1. Homogeneous distribution of SiC particles was observed in the microstructure of all the FSP samples without any traces of agglomeration.
2. EDS analysis revealed that the artificial aging process performed after FSP formed $MgZn_2$ precipitate along the grain boundary.
3. The microhardness and wear resistance of AA7075/SiC surface composite are improved by the particle strengthening and precipitation strengthening mechanisms.

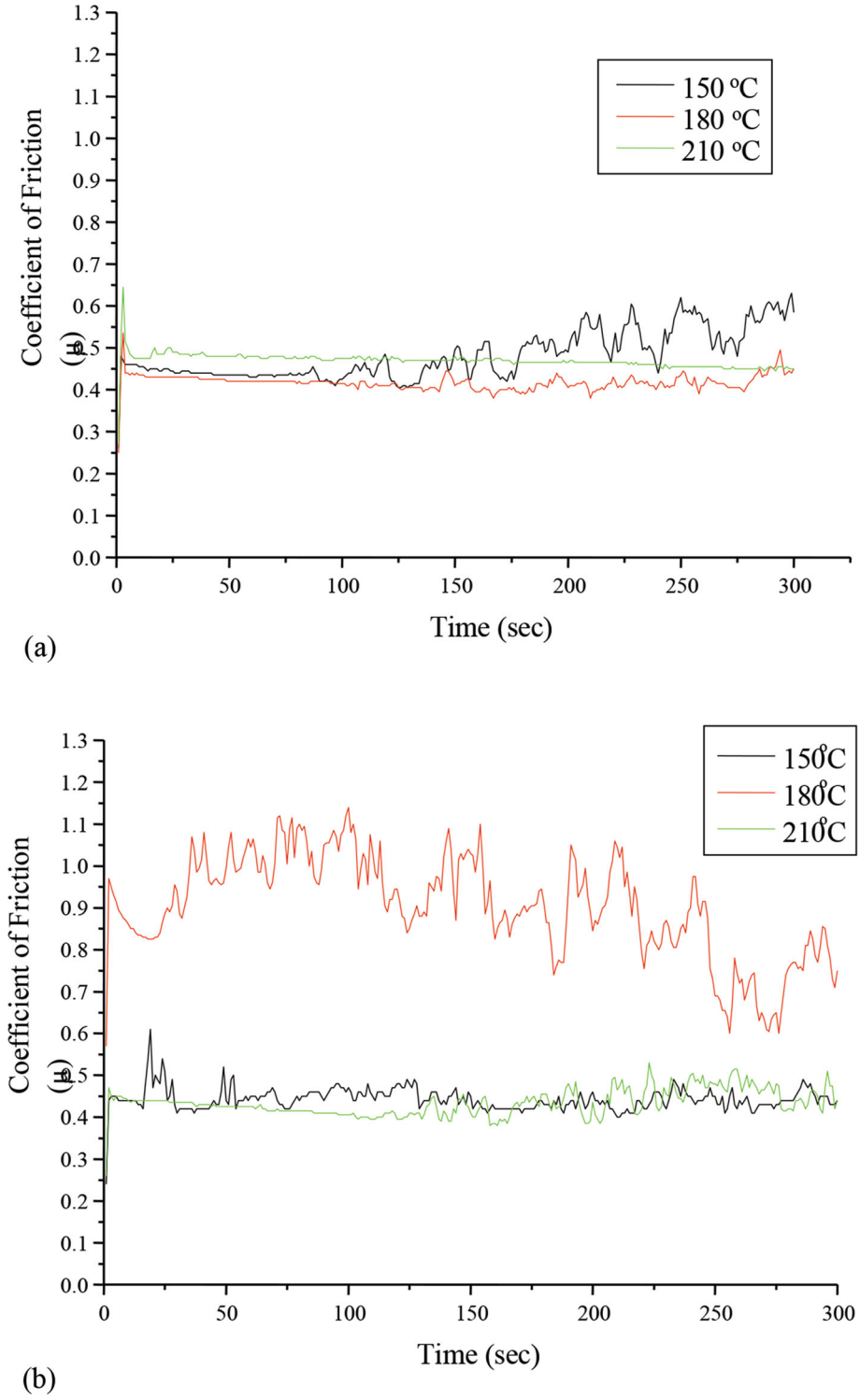

Fig. 7 Variation of coefficient of friction for (a) 8 h and (b) 16 h of age treatment

4. At 8 h of aging, hardness increases up to 180 °C due to the formation of fine precipitates.
5. At higher aging temperature and duration, hardness decreased because of the abnormal grain growth and the formation of stable precipitated particles in the microstructure.
6. FSPed AA7075/SiC surface composite samples age-treated to 180 °C for 8 h and 150 °C for 16 h have exhibited good wear resistance and frictional characteristics. This is attributed to the SiC reinforcement, grain refinement, and the formation of hard precipitates in the matrix.

Table 2 Average coefficient of friction at different aging temperatures and times

Aging temperature, °C	Aging time	
	8 h	16 h
150	0.48	0.42
180	0.44	0.90
210	0.47	0.43

Appendix

Volume fraction of reinforcement in FSP can be easily calculated by taking the volume of the base metal on which FSP is to be performed (without holes) as the total volume. Then, the volume fraction of reinforcement can be calculated as the sum of the volume of holes divided by total volume. In this research work, blind holes of size 2 mm were drilled arranged in an array of 2 × 2 mm with a depth of 3.5 mm. Fifty such holes are made along the work piece length of 150 mm. Total volume of all holes are 549.78 mm^3. Volume of the base metal on which FSP was done is 150 × 6 × 6 mm = 5400 mm^3. Hence, the volume percentage of the reinforcement is calculated as follows:

$$\begin{aligned}&\text{Volume percentage of the reinforcement}\\&= (\text{Total volume of holes}/\text{Volume of the base metal on which FSP was done}) \times 100\\&= (549.78/5400) \times 100\\&= 10.18\%\,(\text{Approx. as } 10\%)\end{aligned}$$

References

1. Y.D. Zhang, S.B. Jin, P.W. Trimby, X.Z. Liao, M.Y. Murashkin, R.Z. Valiev, J.Z. Liu, J.M. Cairney, S.P. Ringer, and G. Sha, Dynamic Precipitation, Segregation and Strengthening of an Al–Zn–Mg–Cu Alloy (AA7075) Processed by High-Pressure Torsion, *Acta Mater.*, 2019, **162**, p 19–32.
2. S.K. Patel, V.P. Singh, B.S. Roy, and B. Kuriachen, Recent Research Progresses in Al-7075 based In-situ Surface Composite Fabrication Through Friction Stir Processing: A Review, *Mater. Sci. Eng., B*, 2020, **1**(262), 114708
3. A.T. Guner, D. Dispinar, and E. Tan, Microstructural and Mechanical Evolution of Semisolid 7075 Al Alloy Produced by SIMA Process at Various Heat Treatment Parameters, *Arab. J. Sci. Eng.*, 2019, **44**(2), p 1243–1253.
4. O.Z. Gokhan and A. Karaaslan, Properties of AA7075 Aluminum Alloy in Aging and Retrogression and Reaging Process, *Trans. Nonferrous Met. Soc. China.*, 2017, **27**(11), p 2357–2362.
5. A. Baradeswaran and P.A. Elaya, Effect of Graphite on Tribological and Mechanical Properties of AA7075 Composites, *Tribol. Trans.*, 2015, **58**, p 1–6.
6. V. Sharma, U. Prakash, and B.M. Kumar, Surface Composites by Friction Stir Processing: A Review, *J. Mater. Process. Technol.*, 2015, **224**, p 117–134.
7. V. Sudhakar, G. Madhu, K.M. Reddy, and R. Srinivasa, Enhancement of Wear and Ballistic Resistance of Armour Grade AA7075 Aluminium Alloy using Friction Stir Processing, *Def. Technol.*, 2015, **11**, p 10–17.
8. V.V. Patel, V. Badheka, and A. Kumar, Friction Stir Processing as a Novel Technique to Achieve Superplasticity in Aluminum Alloys: Process Variables, Variants, and Applications, *Metallogr. Microstruct. Anal.*, 2016, **5**(4), p 278–293.
9. N. Pol, G. Verma, R.P. Pandey, and T. Shanmugasundaram, Fabrication of AA7005/TiB2-B4C Surface Composite by Friction Stir Processing: Evaluation of Ballistic Behavior, *Def. Technol*, 2018, **15**, p 1–6.
10. H. Rana and V. Badheka, Elucidation of the Role of Rotation Speed and Stirring Direction on AA 7075–B4C Surface Composites Formulated by Friction Stir Processing, *Proc. Inst. Mech. Eng. Part L J. Mater. Des. Appl.*, 2019, **233**(5), p 977–994.
11. Y.F. Hou, C.Y. Liu, B. Zhang, L.L. Wei, H.T. Dai, and Z.Y. Ma, Mechanical Properties and Corrosion Resistance of the Fine Grain Structure of Al–Zn–Mg–Sc Alloys Fabricated by Friction Stir Processing and Post-Heat Treatment, *Mater. Sci. Eng., A*, 2020, **21**(785), 139393
12. S. Kilic, I. Kacar, M. Sahin, F. Ozturk, and O. Erdem, Effects of Aging Temperature, Time, and Pre-strain on Mechanical Properties of AA7075, *Mater. Res.*, 2019, **12**, p 22.
13. Chauhan K, Satyanarayana MV, Kumar A. Effect of tool geometry and heat treatment on friction stir processing of AA6061. In: Advances in Applied Mechanical Engineering 2020 (pp. 947–953). Springer, Singapore
14. X.H. Zeng, P. Xue, L.H. Wu, D.R. Ni, B.L. Xiao, and Z.Y. Ma, Achieving an Ultra-High Strength in a Low Alloyed Al Alloy Via a Special Structural Design, *Mater. Sci. Eng. A*, 2019, **755**, p 28–36.
15. S. Gholami, E. Emadoddin, M. Tajally, and E. Borhani, Friction Stir Processing of 7075 Al Alloy and Subsequent Aging Treatment, *Trans. Nonferrous Met. Soc. China*, 2015, **25**(9), p 2847–2855.
16. Y.F. Hou, J.J. Xiao, C.Y. Liu, and B. Zhang, Effect of Heat Treatment on the Microstructure, Mechanical Properties, and Corrosion Resistance of Friction Stir Processed Al-Zn-Mg-Cu-Sc-Zr Alloy, *J. Mater. Eng. Perform.*, 2021, **30**(5), p 3398–3405.
17. P.K. Mandal, R.J. Kumar, and J.M. Varkey, Effect of Artificial Ageing Treatment and Precipitation on Mechanical Properties and Fracture Mechanism of Friction Stir Processed MgZn2 and Al3Sc Phases in Aluminium Alloy, *Mater. Today Proc.*, 2021, **1**(46), p 4982–4987.
18. I. Charit and R.S. Mishra, Effect of Friction Stir Processed Microstructure on Tensile Properties of an Al-Zn-Mg-Sc Alloy Upon Subsequent Aging Heat Treatment, *J. Mater. Sci. Technol.*, 2018, **34**(1), p 214–218.
19. Z. Chen, J. Li, A. Borbely, G. Ji, S.Y. Zhong, Y. Wu, M.L. Wang, and H.W. Wang, The Effects of Nanosized Particles on Microstructural Evolution of an In-situ TiB2/6063Al Composite Produced by Friction Stir Processing, *Mater. Des.*, 2015, **25**(88), p 999–1007.
20. D. Ghanbari, M.K. Asgarani, K. Amini, and F. Gharavi, Influence of Heat Treatment on Mechanical Properties and Microstructure of the Al2024/SiC Composite Produced by Multi–Pass Friction Stir Processing, *Measurement*, 2017, **1**(104), p 151–158.
21. L. Ke, C. Huang, L. Xing, and K. Huang, Al–Ni Intermetallic Composites Produced In situ by Friction Stir Processing, *J. Alloy. Compd.*, 2010, **503**(2), p 494–499.
22. F. Khodabakhshi, A. Simchi, A.H. Kokabi, A.P. Gerlich, and M. Nosko, Effects of Post-annealing on the Microstructure and Mechanical Properties of Friction Stir Processed Al–Mg–TiO2 Nanocomposites, *Mater. Des.*, 2014, **1**(63), p 30–41.
23. M.S. Khorrami, M. Kazeminezhad, and A.H. Kokabi, Thermal Stability of Aluminum After Friction Stir Processing with SiC Nanoparticles, *Mater. Des.*, 2015, **5**(80), p 41–50.
24. I.S. Lee, P.W. Kao, C.P. Chang, and N.J. Ho, Formation of Al–Mo Intermetallic Particle-Strengthened Aluminum Alloys by Friction Stir Processing, *Intermetallics*, 2013, **1**(35), p 9–14.
25. D.R. Ni, J.J. Wang, Z.N. Zhou, and Z.Y. Ma, Fabrication and Mechanical Properties of Bulk NiTip/Al Composites Prepared by Friction Stir Processing, *J. Alloy. Compd.*, 2014, **15**(586), p 368–374.
26. J. Qu, H. Xu, Z. Feng, D.A. Frederick, L. An, and H. Heinrich, Improving the Tribological Characteristics of Aluminum 6061 Alloy by Surface Compositing with Sub-micro-size Ceramic Particles Via Friction Stir Processing, *Wear*, 2011, **271**(9–10), p 1940–1945.
27. J. Mohamadigangaraj, S. Nourouzi, and H.J. Aval, The Effect of Heat Treatment and Cooling Conditions on Friction Stir Processing of A390–10 wt% SiC Aluminium Matrix Composite, *Mater. Chem. Phys.*, 2021, **15**(263), 124423
28. D.S. Mouli and R.U. Rao, Optimization of Friction Stir Process Parameters for Micro-Hardness and Wear Characteristics of Silicon Carbide-Reinforced Al-7075 Surface Composite, *Trans. Indian Inst. Met.*, 2021, **24**, p 1–9.
29. A.P. Reddy, P.V. Krishna, R.N. Rao, and N.V. Murthy, Silicon Carbide Reinforced Aluminium Metal Matrix Nano Composites-A Review, *Mater. Today Proc.*, 2017, **4**(2), p 3959–3971.

30. M.H. Rahman and H.M. Al Rashed, Characterization of Silicon Carbide Reinforced Aluminum Matrix Composites, *Proc. Eng.*, 2014, **1**(90), p 103–109.
31. M.S. Surya and G. Prasanthi, Manufacturing, Microstructural and Mechanical Characterization of Powder Metallurgy Processed Al7075/SiC Metal Matrix Composite, *Mater. Today Proc.*, 2021, **1**(39), p 1175–1179.
32. D.K. Lim, T. Shibayanagi, and A.P. Gerlich, Synthesis of Multi-walled CNT Reinforced Aluminium Alloy Composite via Friction Stir Processing, *Mater. Sci. Eng. A*, 2009, **507**(1–2), p 194–199.
33. M.H. Shaeri, M.T. Salehi, S.H. Seyyedein, M.R. Abutalebi, and J.K. Park, Microstructure and Mechanical Properties of Al-7075 Alloy Processed by Equal Channel Angular Pressing Combined with Aging Treatment, *Mater. Des.*, 2014, **57**, p 250–257.
34. T. Hu, K. Ma, T.D. Topping, J.M. Schoenung, and E.J. Lavernia, Precipitation Phenomena in an Ultrafine-Grained Al Alloy, *Acta Mater.*, 2013, **61**, p 2163–2178.
35. L. Zhang, Y.F. Hou, C.Y. Liu, H.F. Huang, and H.M. Sun, Effects of Short-Time Heat Treatment on Microstructure and Mechanical Properties of 7075 Friction Stir Welded Joint, *J. Mater. Eng. Perform.*, 2021, **19**, p 1–9.
36. J. Chen, L. Zhen, S. Yang, W. Shao, and S. Dai, Investigation of Precipitation Behavior and Related Hardening in AA 7055 Aluminum Alloy, *Mater. Sci. Eng. A*, 2009, **500**(1–2), p 34–42.
37. M.M. Attallah and H.G. Salem, Friction Stir Welding Parameters: a Tool for Controlling Abnormal Grain Growth During Subsequent Heat Treatment, *Mater. Sci. Eng. A*, 2005, **391**, p 51–59.

applied sciences

MDPI

Article

XG Boost Algorithm to Simultaneous Prediction of Rock Fragmentation and Induced Ground Vibration Using Unique Blast Data

N. Sri Chandrahas [1,2], Bhanwar Singh Choudhary [1,*], M. Vishnu Teja [3], M. S. Venkataramayya [2] and N. S. R. Krishna Prasad [2]

[1] Department of Mining Engineering, IIT (ISM) Dhanbad, Dhanbad 826004, India; srichandrahas@mrec.ac.in
[2] Department of Mining Engineering, Malla Reddy Engineering College, Hyderabad 500100, India; iiic@mrec.ac.in (M.S.V.); nsrkprasad@mrec.ac.in (N.S.R.K.P.)
[3] Mai-Nefhi College of Engineering and Technology, Mai-Nefhi P.O. Box 5230, Eritrea; mvteja1995@gmail.com
* Correspondence: bhanwarschoudhary@iitism.ac.in

Abstract: The two most frequently heard terms in the mining industry are safety and production. These two terms put a lot of pressure on blasting engineers and crew to give more while consuming less. The key to achieving the optimum blasting results is sophisticated bench analysis, which must be combined with design blast parameters for good fragmentation and safe ground vibration. Thus, a unique solution for forecasting both optimum fragmentation and reduced ground vibration using rock mass joint angle and blast design parameters will aid the blasting operations in terms of cost savings. To arrive at a proper understanding and a solution, 152 blasts were carried out in various mines by adjusting blast design parameters concerning the measured joint angle. The XG Boost, K-Nearest Neighbor, and Random Forest algorithms were evaluated, and the XG Boost outputs were shown to be superior in terms of Mean Absolute Percentage Error (MAPE), Root Mean Squared Error (RMSE), and Co-efficient of determination (R^2) values. Using XG Boost, the decision-tree-based ensemble Machine Learning algorithm that uses a gradient-boosting framework and a simultaneous formula was developed to predict both fragmentation and ground vibration using joint angle and the same set of parameters.

Keywords: rock joints; drones; XG Boost; fragmentation; PPV

Citation: Chandrahas, N.S.; Choudhary, B.S.; Teja, M.V.; Venkataramayya, M.S.; Prasad, N.S.R.K. XG Boost Algorithm to Simultaneous Prediction of Rock Fragmentation and Induced Ground Vibration Using Unique Blast Data. *Appl. Sci.* **2022**, *12*, 5269. https://doi.org/10.3390/app12105269

Academic Editor: Lina M. López

Received: 25 April 2022
Accepted: 22 May 2022
Published: 23 May 2022

1. Introduction

The use of explosive energy in blasting affects both rock fragmentation and induced ground vibration. Rock movement may be desired, and manifests in amuck profile suitable for the loading equipment. The complete and proper utilization of explosive energy is the main objective in this process; energy used in achieving proper fragmentation automatically reduces negative aspects such as ground vibration. Positive blast results can be obtained by equalizing the energy of the explosive to the strength of the rock, optimum design parameters, and geospatial positioning of the blast holes.

There are many equations in blasting to make use of explosive energy properly to yield a safe and effective blast, but most formulas are designed based on controllable parameters such as burden, spacing, bench height, hole diameter, stemming, decking, firing pattern, and quantity of explosive, etc. Many researchers have revealed that uncontrollable parameters such as joints and bedding planes, rock compressive and tensile strengths also significantly affect the performance of the blast in terms of fragmentation and ground vibration. The daunting task of any blasting engineer is to ensure that the selected blast design parameters meet all post-blast requirements and the targeted fragmentation of an enterprise. Blast-induced ground vibrations are a major issue to be tackled.

The presence of geological discontinuities in a rock mass can significantly influence both rock fragmentation and ground vibration [1–3]. Joints are among the most common

defects in the rock mass and are also defined as planes of weakness. Jointed rock gives poorer fragmentation than un-jointed rock, as stress waves dissipate and gases escape from joints and create an imbalance in attenuation and produce uneven fragmentation [4]. Likewise, rock joint angles have a substantial impact on shockwave propagation post blasting [5]. There is a pronounced impact of joint orientation on mean fragmentation size and ground vibration [6–10]. Good fragmentation is obtained when the orientation of the free face is parallel to and on the dip side of the principle joint planes [11,12]. Similarly, the rate of attenuation depends on the incidence angle of the joint face [13–15]. Usually, a joint angle of 90° generates the very fast attenuation of stress wave [16]; however, with an increase in joint angle, the attenuation rate of vibration velocity increases and decreases the efficiency of fragmentation. Thus, alteration in joint angle has a potential effect on the blast results [10,17]. Joint intensity also influences blasting results [16].

Blast design parameters such as spacing burden ratio, firing pattern, and explosive quantity pose a substantial impact on both rock fragmentation and ground vibration [17]. Poor blast design results in desensitization of explosives and detonator damage [18]. Geological aspects such as open joints, discontinuities, and voids are the cause behind the premature detonation and detonator damage due to the merging of side-by-side blast holes; in the case of surface, blasting would explain the cause–effect relationship. Similarly, excessive burden results in fly rock; therefore, burden and/or spacing of the decks should be sufficient to avoid the risk of fly rock and over ground vibrations. According to thumb rules, considering a minimum 8 to 25 ms delay between charges in the same row and between rows prevents blast shock overlap and could result in fewer ground vibrations [18].

A firing pattern provides a synchronized opportunity for the explosive charges to exercise their combined effect. Thus, firing pattern provides a free face, to the upcoming blast holes in some order, with the blast progression. A firing pattern determines the movement and direction of the rock throw. The firing pattern reflects a substantial effect on twin products of blasting, i.e., fragmentation and ground vibration. During the blast trials, it was observed that the V pattern had better fragmentation, probably due to in-flight collision between broken rock fragments [18]. Analogously, investigations found that firing patterns can significantly influence and govern both fragmentation and ground vibration results [19].

Soft computing approaches such as self-learning, adaptive recognition, and nonlinear dynamic processing can substantially aid in the resolution of intractable and perplexing geotechnical problems [20–26]. Many researchers have employed artificial intelligence-based algorithms such as ANN, FIS, GEP, Regression, XG Boost, Random Forest, AMC, and K-NN to solve and predict rock fragmentation and resultant ground vibration [27–30]. Nevertheless, none of these models have delivered a unique formula for predicting fragmentation and ground vibration using joint angle and blast design parameters, so an attempt has been made by the authors in this direction.

Two models—FIS, an artificial intelligence approach, and regression—were developed to forecast rock fragmentation using 415 blast design datasets in an Iranian mine and the research indicated that the FIS model performed well in predicting results [23]. Similarly, various methods showed that models can accurately forecast rock fragmentation based on input factors such as burden, spacing, and explosive quantity, among others [31]. Analogously, the Gene Expression Programming (GEP) model was used to predict Peak Particle Velocity (PPV) in Malaysian mines. A total of 102 datasets of blast design parameters such as burden-to-spacing ratio, stemming, hole-depth, a maximum charge per delay, and powder factor were fed into the trained model, and the GEP produced good R^2 and Random Mean Square Error (RMSE) metrics and predicted well [32]. On 93 blasts of data, algorithms such as SVM, XG Boost, Random Forest, and K-NN were employed, and the results showed that XG Boost predicted the closest PPV value among all of them [33,34].

Objectives

The main objectives of the research are to predict the ground vibration and fragmentation using tools such as XG Boost, K-Nearest Neighbor, and Random Forest algorithms.

2. Materials and Methods

2.1. Predictability and Assessment of Blast Results

Traditionally, the blast results are assessed mostly after observing the muck profile and the fragments by way of estimation. After the excavator handles the blast material, the time taken for handling the material is noted, too; the rock fragments that are too difficult to handle are kept aside. Thus, the post-blast analysis is not properly quantified, and is prone to error, due to non-standard methods used. Nowadays, in mining, Artificial Intelligence (AI) and Machine Learning (ML) are being used for quick and accurate analysis. STRAYOS software is used for the analysis of the video input of the blast area, producing a joint pattern after analysis. Fragmentation is analyzed through STRAYOS software and O-PITBLAST software is used in designing the blast.

2.2. A Brief of the Mine and Blast Site

Opencast mine I of Ramagundam III Area, Singareni Collieries Company Limited, Telangana, India is the mine where the studies were conducted. Figures 1–3 shows the site location on an Indian map, its Google map position, and experimental overburden benches.The mine was previously worked through underground methods but later was converted to an opencast mine. In the study area, overburden benches were 12 m high. Rock strata are comprised of sandstone and alluvium soil. The average density of sandstone was 2.3 g/cc.

a. Identification of bench structural geo-property through UAV:

For the reconfiguration of the new blast design, extensive work was under taken to determine the rock condition and joint intensity. DJI Mavic Unmanned Aerial Vehicle (UAV) was used to detect joint planes.

The UAV was capable of capturing and recording photos and videos at 4K resolution. It can run for 25 min in the air with a single battery charge and weighs 258 g. Calibration was performed to fix signal problems, allowing for a better take-off of the drone placed on the helipad shown in Figure 4a, as well as the bench scanning test shown in Figure 3.

The drone operated with mobile application LITCHI in FIRST-PERSON VIEW (FPV) mode with 18 satellite signal poles, as shown in Figure 4b.

The UAV flew through the bench range at a height of 100 feet, with a 75 percent overlap. To get error-free images, the camera angle was set to 45 degrees so as to focus on the bench's top edge and the beginning of the bench floor. In order to maintain accuracy, at least four to five images were taken at the same time in order to generate multiple point cloud data for use in STRAYOS software to generate a 3D model. In total, 580 photos were captured from 1 de-coaled,2B seam, 3A coal seam, and 3A de-coaled.

b. Geo–technical properties of the site:

To design blasts in O-PITBLAST SOFTWARE, geo-rock attributes are required. To complete the task, rock samples were collected from each proposed site and tested in a laboratory. Table 1 shows the results of various tests, such as uniaxial compressive, Young Modulus, and Poisson's tests. The average mineralogical composition of sandstone was calcite 43–50%, quartz 14–18%, feldspar 13–15%, and the remaining 20–25% in a combination of clay, mica, and dolomite.

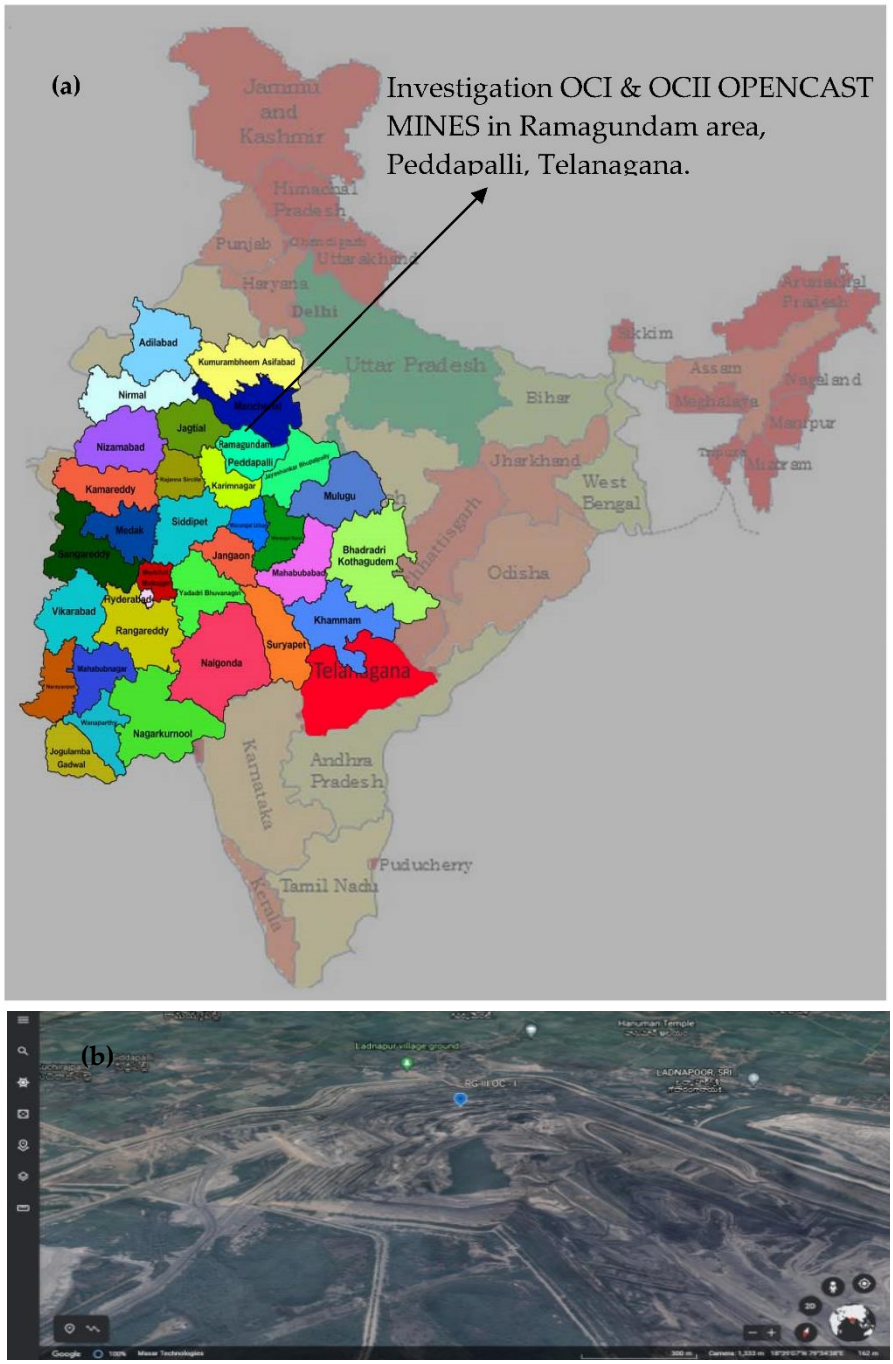

Figure 1. (**a**,**b**) Indian Map and Google Earth image indicating Ramagundam mines.

2.3. AI Tools for Rock Characterization

STRAYOS, Artificial Intelligence (AI)-based software has been used to analyze joint intensity and joint pattern at the target bench. Images of rock joints are analyzed repeatedly to see if characteristic patterns can be found in the picture data.

Joints in rock mass break the propagation of blast waves; hence, fragmentation may be affected. Under certain circumstances, there may not be any back-break or over-break, and fragmentation may be aided by joints, improving overall performance. There may be excessive sapling towards free faces at joints when rock is weak and explosive gases give a push effect without actually shattering them. Because of this complex relationship, the characterization of bench cracks is important for designing the spatial disposition of blast holes and the placement of decks.

Figure 2. Drone image of RGIII-OCI Mine.

Figure 3. Drone take-off and scan.

Figure 4. (**a**,**b**): Drone helipad and drone interface.

STRAYOS Software requires a minimum of 10 drone photographs to create a 3D model. When data is successfully fed into the software, the interface displays a 3D model of a bench, as shown in Figure 5. After enabling different clusters suggested by software with the aid of AI, planes and lines will be visible on a 3D bench. Lines and planes are two ways in which the software helps the user to analyze discontinuities. When the cluster lines and planes option is activated, the DIP direction, STRIKE direction, and DIP angle of joints on the bench can be identified. A wire-framed bench with lines is shown in Figure 6. Table 2 shows the results of using 580-point cloud data to detect joints in four benches.

Table 1. Averaged values of geo-technical properties of the rock samples.

Mine	Name of Bench	Density, g/cm^3	Uni-Axial Compressive Strength, MPa	Young Modulus, GPa	Poisson's Ratio	Joint Angle, Degree	Joint Spacing, m
OC I	1 De-Coaled	2.490	67	22.58	0.290	DIP—48 to 74 STRIKE–110 to 180	0.2–0.49
	2A Coaled	2.28	61	31.00	0.156	DIP—27 to 61 STRIKE–94 to 172	0.15–0.76
	3A Seam	2.35	52	27.55	0.310	DIP—50 to 84 STRIKE–121 to 179	0.2–0.5
OC II	2B OB Seam	2.28	52	20.65	0.250	DIP—34 to 85 STRIKE–120 to 183	0.23–0.49
	1B OB Seam	2.41	71	21.67	0.356	DIP—52 to 73 STRIKE–121 to 175	0.39–0.51

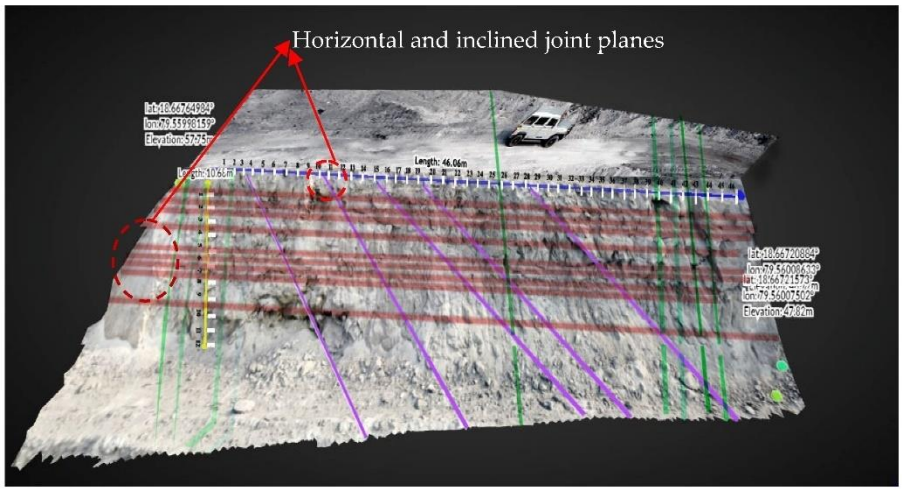

Figure 5. 3D bench with planes.

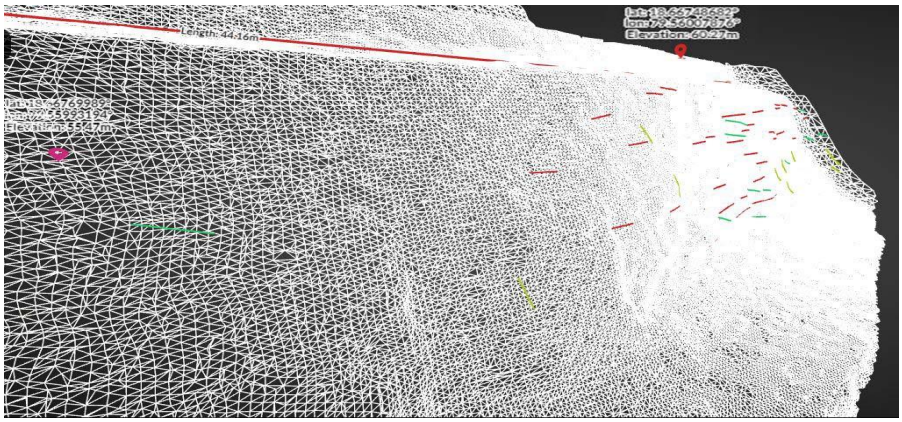

Figure 6. Wire-framed bench with line.

Table 2. Model training and testing datasets.

S.No	Spacing Burden Ratio (Se/Be), m	Total Explosive, kg	Firing Pattern	Joint Angle, Degree	Fragmentation	PPV	MaximumCharge/Delay, Kg
Training Data (80%) 118 Samples							
1	1.3	7425	1	86	0.67	5.33	200
2	1.2	10,125	1	83	1.4	5.29	195
3	1.3	8100	1	85	0.91	4.94	187
4	1.3	8230	2	85	1.2	4.56	180
5	1.3	8100	3	80	0.89	5.15	195
6	1.3	8100	1	74	0.55	4.79	186
7	1.3	5670	3	86	0.55	3.91	155
8	1.2	5690	1	31	0.45	3.8	140
9	1.3	8100	2	84	0.97	4.61	180
10	1.3	5130	1	90	0.44	3.21	145
11	1.3	7100	1	39	0.38	2.8	125
12	1.3	5940	3	38	0.31	2.21	122
13	1.2	6110	3	90	0.88	3.52	145
14	1.3	7290	3	82	1.1	3.78	149
15	1.3	4500	3	46	0.91	3.94	146
16	1.3	6210	2	85	1.2	3.96	158
17	1.3	5940	1	86	0.82	4.51	180
18	1.3	6615	3	36	0.47	3.55	141
19	1.3	6210	3	80	0.56	2.9	128
20	1.2	6885	2	41	0.33	4.18	148
21	1.3	7290	1	29	0.97	5.39	210
22	1.3	5400	1	90	0.38	2.55	120
23	1.3	4995	3	80	0.38	2.03	130
24	1.3	6210	3	35	0.34	2.85	110
25	1.3	6480	3	85	0.57	4.11	145
26	1.3	9280	3	45	0.56	3.96	170
27	1.4	7020	3	68	0.91	4.21	195
28	1.2	6000	1	38	0.34	4.9	120
29	1.3	7420	2	78	0.45	4.54	180
30	1.2	7290	3	75	0.65	4.28	185
31	1.3	7105	2	88	0.35	3.7	145
32	1.3	5940	3	35	0.44	3.26	147
33	1.3	7020	2	90	0.97	3.5	142
34	1.3	5265	3	84	0.29	2.11	135
35	1.3	4725	3	86	0.38	1.85	119
36	1.3	5670	1	77	0.33	1.49	121
37	1.3	5240	1	91	0.39	3.11	155
38	1.3	7132	1	37	0.36	2.9	115
39	1.3	5940	3	36	0.333	2.2	150
40	1.2	6110	3	90	0.88	3.52	165
41	1.3	7290	3	82	1.1	3.78	135
42	1.3	4500	3	46	0.91	3.94	125
43	1.3	6220	2	84	1.19	3.86	125
44	1.3	5940	1	86	0.82	4.51	185
45	1.3	6615	3	36	0.47	3.55	130
46	1.3	6210	3	80	0.56	2.9	130
47	1.2	6886	2	42	0.34	4.19	175
48	1.3	7290	1	29	0.97	5.39	195
49	1.3	5401	1	93	0.36	2.32	130
50	1.3	4995	3	80	0.366	2.08	123
51	1.3	7420	2	78	0.42	4.57	186
52	1.2	7290	3	74	0.64	4.31	178
53	1.3	7105	2	88	0.35	3.7	160
54	1.3	5940	3	35	0.44	3.43	150

Table 2. *Cont.*

S.No	Spacing Burden Ratio (Se/Be), m	Total Explosive, kg	Firing Pattern	Joint Angle, Degree	Fragmentation	PPV	MaximumCharge/Delay, Kg
55	1.3	7425	1	86	0.67	5.33	210
56	1.2	10,222	1	80	1.5	5.2	198
57	1.3	8100	1	85	0.91	4.94	190
58	1.3	8230	2	85	1.2	4.56	187
59	1.3	8100	3	80	0.89	5.15	200
60	1.3	8100	1	74	0.55	4.79	195
61	1.3	5120	1	91	0.44	3.3	155
62	1.3	7100	1	39	0.38	2.8	135
63	1.3	5940	3	38	0.31	2.21	128
64	1.2	6110	3	90	0.88	3.52	175
65	1.3	7290	3	82	1.1	3.78	179
66	1.2	6110	3	90	0.88	3.52	160
67	1.3	7260	3	82	1.1	3.78	178
68	1.3	4500	3	45	0.92	3.9	184
69	1.3	6210	2	85	1.2	3.96	185
70	1.3	5940	1	86	0.82	4.51	190
71	1.25	7230	3	79	1.1	4.26	179
72	1.25	7110	3	78	0.92	3.41	160
73	1.25	8222	3	55	1.5	5.2	195
74	1.25	8900	3	57	0.98	3.22	139
75	1.3	8240	3	89	1.6	4.56	185
76	1.25	8500	3	51	0.77	3.78	170
77	1.3	9500	3	54	0.55	4.67	185
78	1.2	8125	1	60	1.5	5.29	210
79	1.3	8100	1	82	0.91	4.94	190
80	1.3	8230	2	59	1.2	4.56	183
81	1.3	7880	3	69	1.2	2.5	125
82	1.3	8100	1	74	0.55	4.79	170
83	1.3	7688	3	72	0.85	4.2	160
84	1.2	5690	1	70	1.3	3.9	145
85	1.3	8100	2	58	0.97	4.61	165
86	1.3	6130	1	90	1.2	4.23	155
87	1.3	7555	1	42	1.1	2.1	122
88	1.3	5988	3	57	0.31	4.21	170
89	1.2	6121	3	94	0.88	2.33	143
90	1.3	7356	3	59	1.1	2.31	137
91	1.3	4200	3	46	0.99	2.67	150
92	1.3	6345	2	73	0.89	5.1	205
93	1.3	5789	1	86	0.99	3.6	138
94	1.3	6618	3	42	0.59	3.22	137
95	1.3	6220	3	81	0.73	2.9	132
96	1.2	6845	2	57	0.99	4.18	176
97	1.3	7256	1	77	0.73	4.5	182
98	1.3	5400	1	55	0.92	2.9	135
99	1.3	4998	3	34	0.67	1.2	110
100	1.3	6240	3	54	0.34	1.66	115
101	1.3	6480	3	67	0.57	1.59	112
102	1.3	8956	3	34	0.69	2.33	129
103	1.4	7455	3	54	0.8	2.41	132
104	1.25	6890	1	60	0.82	4.9	194
105	1.35	4789	2	87	0.45	4.54	185
106	1.25	6800	3	89	1.33	3.55	155
107	1.32	8905	2	87	0.57	3.41	145
108	1.32	6000	3	56	0.78	2.2	132
109	1.25	6800	2	74	0.97	2.78	143

Table 2. *Cont.*

S.No	Spacing Burden Ratio (Se/Be), m	Total Explosive, kg	Firing Pattern	Joint Angle, Degree	Fragmentation	PPV	MaximumCharge/Delay, Kg
110	1.25	6580	3	35	0.99	2.57	137
111	1.25	5890	3	46	0.78	1.85	125
112	1.25	6001	1	45	0.68	1.56	120
113	1.3	5240	1	67	0.39	3.14	139
114	1.2	7800	1	54	0.79	2.2	120
115	1.3	6570	3	58	1.4	2.2	123
116	1.2	6777	3	43	1.2	3.52	145
117	1.3	7833	3	56	1.45	3.78	155
118	1.3	6544	3	45	1.28	3.33	139
119	1.3	8000	2	423	1.23	3.66	134
Testing Data (20%) 28 Samples							
120	1.31	7665	1	32	0.82	3.51	144
121	1.31	6502	3	69	0.61	3.55	149
122	1.35	6300	3	80	0.72	2.9	132
123	1.26	6211	2	42	0.34	3.61	155
124	1.36	6733	1	29	0.97	3.87	145
125	1.36	7500	1	69	0.66	2.32	130
126	1.36	6744	3	80	0.59	2.08	127
127	1.3	6500	2	48	0.71	3.6	145
128	1.2	7580	3	74	0.64	3.91	156
129	1.3	6900	2	56	0.77	3.7	155
130	1.3	5900	3	50	0.53	3.43	140
131	1.3	7425	1	48	0.89	3.74	155
132	1.2	10,222	1	92	1.5	3.88	158
133	1.3	8100	1	60	1.1	4.94	195
134	1.36	8900	2	778	1.2	4.56	190
135	1.3	8700	3	92	1.21	3.61	155
136	1.3	8600	1	74	1.25	2.24	135
137	1.3	5120	1	91	0.44	3.3	148
138	1.3	7300	1	68	0.28	2.8	148
139	1.36	6400	3	89	0.51	2.21	132
140	1.25	6500	3	83	0.88	3.52	151
141	1.35	7300	3	79	1.1	3.78	159
142	1.25	6544	3	69	0.88	3.52	151
143	1.35	7559	3	82	1.1	3.78	155
144	1.3	5200	3	45	0.32	3.9	160
145	1.3	6300	2	85	0.43	3.96	163
146	1.3	6400	1	86	0.82	4.51	192
147	1.25	7111	3	79	0.31	3	142
148	1.25	7390	3	66	0.92	3.22	157
149	1.25	7890	3	56	0.27	2.67	132
150	1.25	8234	3	87	0.98	3.22	142
151	1.3	8240	3	34	0.46	4.56	179
152	1.25	8221	3	45	0.77	3.78	155

2.4. Blast Modeling Using Software

A 12 m bench with SME explosive was designed with alternative decking at 0.5 m, 2.5 m, and 1 m and was fired with a V pattern in the presence of joints, as shown in Figure 7. By a manual method it is difficult to include all of the parameters; therefore, computer software called O-PITBLAST SOFTWARE was used for designing the blast round. Similarly, blast check and charging-checking are shown in Figure 8a,b.

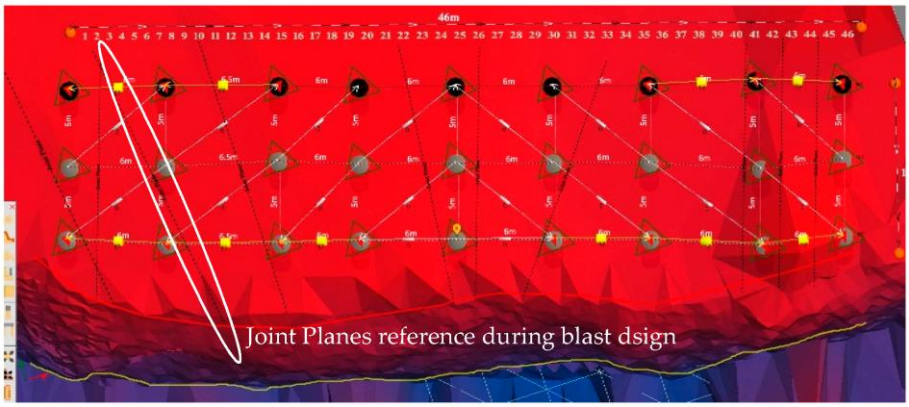

Figure 7. Blast design in O-PITBLAST.

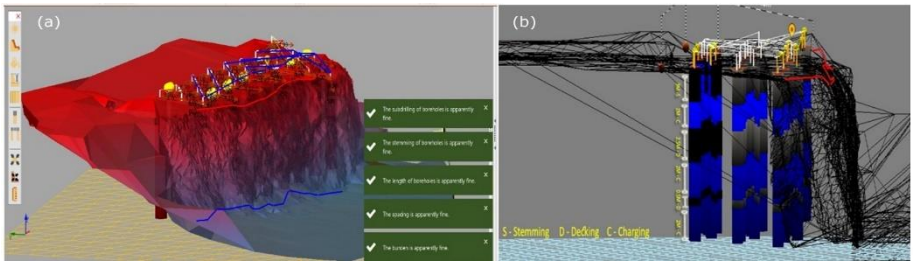

Figure 8. (**a**,**b**) Blast Verification and Wire Mesh model with charging.

2.5. Blast Experimentation

1. The four OB benches chosen for experimentation were 1 de-coaled, 3A coal seam, and 3A de-coaled with bench heights of 12 m, 10.5 m, 11 m, and 9.5 m, respectively. Because the mine was previously worked underground, there was a high risk of disturbances in strata and induction of cracks. To address this issue, benches were initially cleaned to a depth of 0.3 m for improved visibility and identification of cracks and joint planes, as shown in Figure 9a,b.

Figure 9. (**a**,**b**) Bench leveling and preparation for drilling.

2. The joint planes of the benches were identified by STRAYOS software and marked with white powder on the bench top surface to avoid the seizing-up of drilling bits in joints and to have a reference in deciding blast pattern and connections, as shown in Figure 10. Table 1 shows the design burden and spacing values in the O-PITBLAST that yielded good predicted results. The drill bit diameter was 150 mm, which was adequate for the existing bench height, burden, and spacing, and the drilled holes are shown in Figure 11.

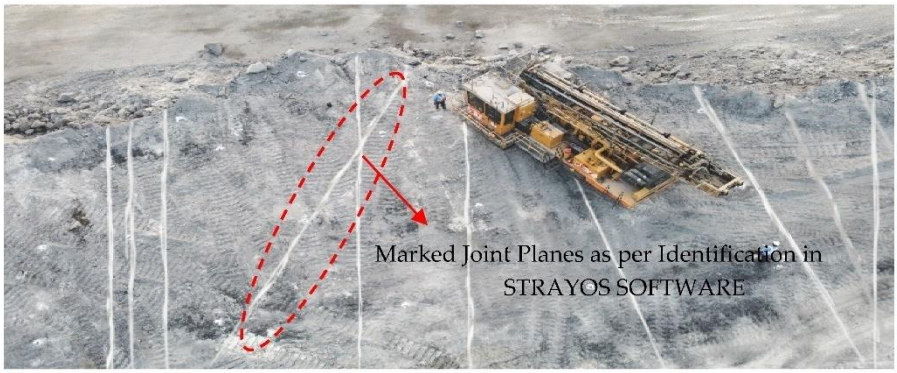

Figure 10. Bench–joint planes marking.

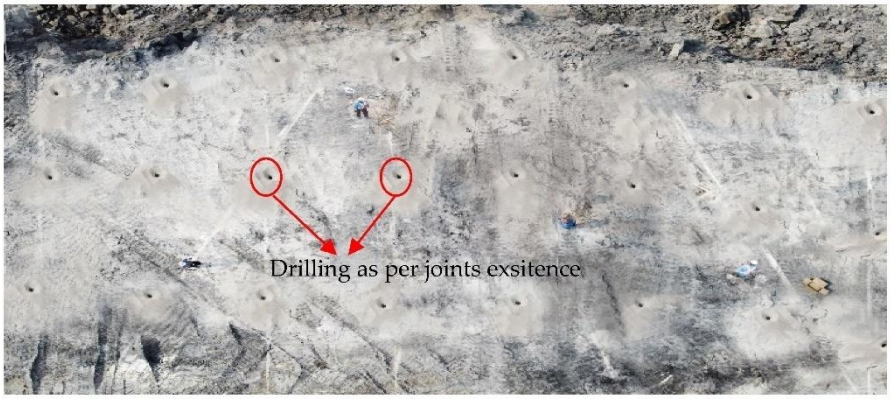

Figure 11. Bench photograph after drilling.

A total of 152 blasts were performed to determine the effect of Se/Be ratio, total explosive quantity, and firing pattern on rock fragmentation and ground vibration. In all these blasts, site mixed emulsion (SME) explosive was used with a booster-nonel combination, and Down hole delays of 425 and 450 ms were chosen, with hole-to-hole delays of 17 milliseconds and row-to-row delays of 25 and 42 ms, adopted, respectively, according to rock conditions. The average explosive quantity was between 45–55 kg and 2 boosters per 1 m of the hole were used.

152 blasts were performed in four phases in 27 benches. The phases are A, B, and C, as shown below.

Phase A: All blast design parameters were maintained the same, but the firing pattern was altered with respect to joint angle.

Phase B: All blast design parameters were maintained the same, but the Spacing Burden Ratio was altered with respect to joint angle.

Phase C: All blast design parameters were maintained the same, but the Explosive Quantity was altered with respect to joint angle.

2.6. Assessment of Fragmentation

STRAYOS software, with the help of AI, can identify from the orthophotograph the entire dataset for all the rock sizes. When the border is identified, the rocks within the border are sorted by diameters. D10, D20 . . . D80, D90 values are generated based on the concepts of KUZ-RAM and SWEBREC.

The drone flew at a height of 90 feet, with a 90° camera angle, i.e., perpendicular to the ground and with 80% capturing overlap, immediately after the blast at noon over the blasted muck pile to avoid the settling of dust layer on rock and the shadows, one over the other.

AI automatically detects the boundary of a muck pile and allows the user to change the edge points as desired; different rock fragmentation sizes will be marked with dif-

ferent colors in the configured boundary, as shown in Figure 12a,b. All blasts produced fragmentation graphs similar to the one shown in Figure 13.

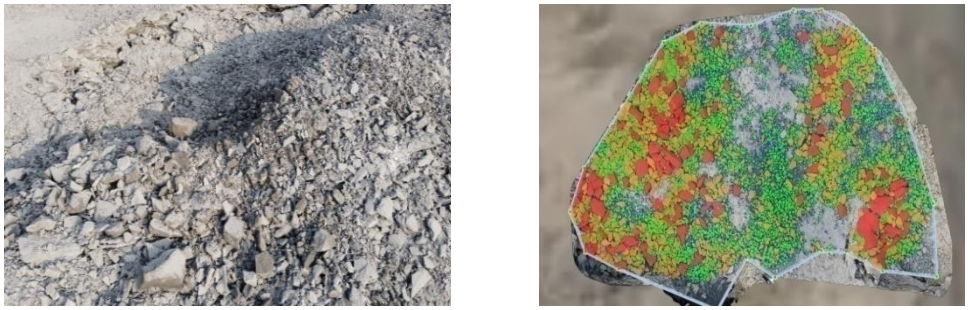

(**a**) (**b**)

Figure 12. (**a**,**b**) Blast fragmentation and muck pile Detection.

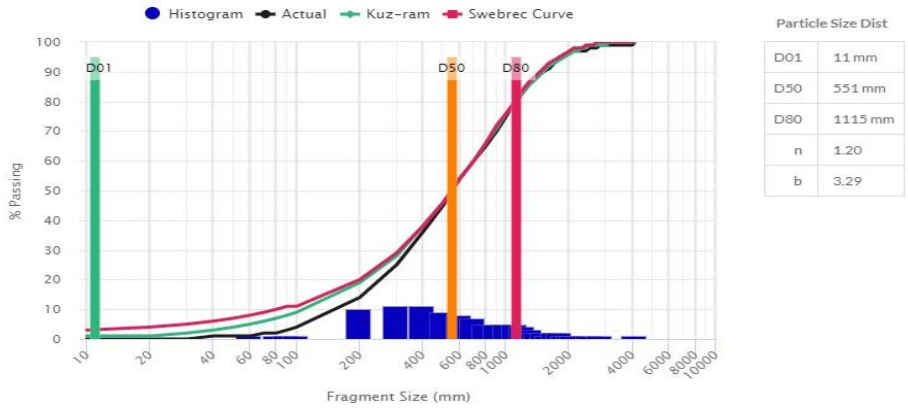

Figure 13. Fragmentation graph.

2.7. Ground Vibration

As shown in Figure 14a, the ground vibration was monitored using NOMIS, an engineering seismograph. The transducer was attached to spikes and firmly pressed into the ground surface to maintain direct contact with the earth. The maximum charge per delay was between 110 and 210 kg, since the distance between the blast location and the monitoring station remained constant throughout the research. The measuring distance was 500 m. To establish a precise distance between the blasting site and the monitoring spot, drone geo-coordinates were used, as shown in Figure 14b. Vibration data produced by each blast is exported and saved. PPV for longitudinal (R), vertical (V), and transverse (T) components, vector sum velocity (VS) were reported by the seismograph during the blasts, as shown in Table 2.

(**a**) (**b**)

Figure 14. (**a**,**b**) NOMIS seismograph and satellite-based DJI remote controller.

2.8. XG Boost Regression Algorithm

XG Boost provides a scalable, portable, and Distributed Gradient Boosting Library, and thus an enhanced method based on gradient boosting decisions [35–37]. XG Boost model can effectively generate boosted trees, work in parallel, and tackle classification and regression problems [38]. The optimization of the value of the objective function lies at the heart of the method. It uses the gradient boosting framework to construct machine learning algorithms. With parallel tree boosting, XG Boost can handle various engineering issues quickly and accurately.

$$\text{Obj}\ (\theta) = \frac{1}{n}\sum_{i}^{n} L(y_i - Y_i) + \sum_{j=1}^{j} \Omega\ (fj) \tag{1}$$

L is the training loss function, while Ω denotes the regularization term. The training loss is used to assess the performance of the model on training data. The regularization term seeks to regulate the model's complexity by preventing over-fitting [39]. In the formula, fj means a prediction coming from the jth tree.

It makes use of gradient (the error term) and hessian to create the trees. Hessian is a second-order derivative of the loss at the present estimate, which is provided as:

$$h_m(x) = \frac{\partial^2 L(Y,\ f(x))}{\partial f(x)^2} \tag{2}$$

where $f(x) = f^{(m-1)}(x)$ and L is Loss of function

$$\text{Similarity Score}\ = \frac{(Sum of residuals)^2}{(N + \lambda\ )} \tag{3}$$

where λ is the L2 regularization term of weights.

Gain of the root node:

$$Gain = Left\ similarity + Right\ similarity - Root\ similarity \tag{4}$$

$$\text{Output Value} = \frac{(\Sigma \text{Residual}_i)}{\Sigma[\ \text{Previous Probability}_i \times (1 - \text{Previous Probability}_i)] + \lambda} \tag{5}$$

2.9. Random Forest Algorithm

The decision tree method was initially introduced by Breiman [40]. It is popular for being a reliable non-parametric statistical approach for both regression and classification issues. It was an ensemble approach for achieving prediction accuracy based on the outcomes of various trees [41]. RF combines the projected values from each tree in the forest to provide the best result for each new observation. Each tree in the forest serves as an important member of the RF's ultimate decision [42].

Three phases summarize the crux of the RF model for regression:

1. Based on the dataset, generate bootstrap samples that are the number of trees in the forest (ntree).
2. Create an unpruned regression tree for each bootstrap sample by picking predictors at random (mtry). Choose the optimal split among those factors.
3. Assemble the anticipated values of the trees to forecast fresh observations (ntree). The average value of the projected values by each tree in the forest was utilized to solve the regression problem as well as forecast fragmentation and blast-induced PPV.

The error rate can be obtained from the training dataset in two ways, using out-of-bag (OOB) and aggregate of OBB.

K-NN Algorithm

It is a popular approach in machine learning for tackling regression and classification problems. It was developed by Altman NS [43]. The K-NN method finds the testing point and classifies it based on its nearest neighbors (k-neighbors). From the training data, the algorithm teaches nothing. It solely retains the weights of its functional space neighbors. When anticipating a new observation, it looks for comparable findings and computes the closeness to those neighbors.

In geosciences, the K-NN algorithm has been widely utilized to predict rock fragmentation, back break, and ground vibration [33]. KNN primarily employs the weighted average value of the k-nearest neighbors; the computation begins by calculating the distance between the uncertain and labeled neighbors using Equation (6), and then the neighbors' numbers are re-arranged by raising the distance and RMSE using the cross-validation method. Finally, the average inverse distance between K-Nearest Neighbors will be computed.

$$D(x_{tr},\ x_t) = \sum_{i=1}^{n} w_n(x_{tr,n} - x_{t,n}) \quad (6)$$

Above n denotes the number of features, $x_{tr,n}$ & $x_{t,n}$ represent the nth feature of training and testing data, and W_n presents the weight of the nth feature.

3. Results and Discussions

The data in this study were split into two sections: a training dataset and a testing dataset. The majority of the datasets (about 118 blasting events) are utilized for training, and the remaining (28 observations) are used for testing. The training dataset is utilized to create the aforementioned models, as shown in Figure 15. The testing dataset is used to evaluate the performance of the built models.

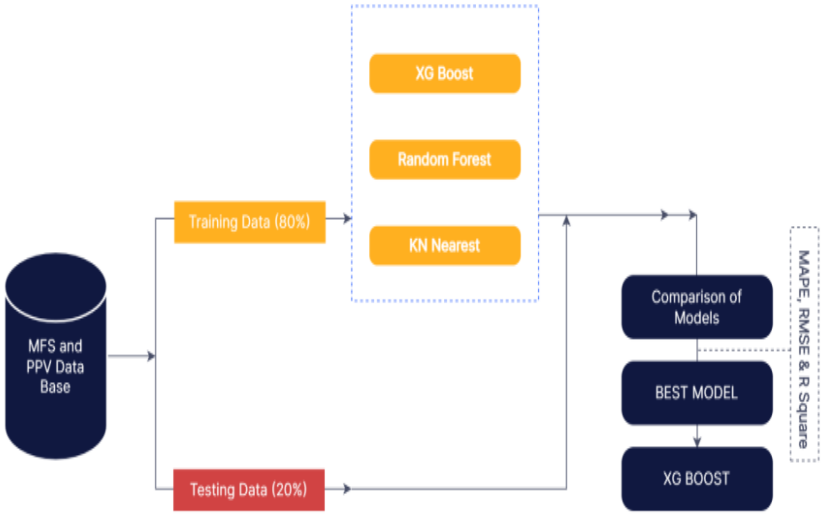

Figure 15. Model execution and best model selection.

Two statistical metrics, MAPE and RMSE were used in this research to evaluate the performance of XG Boost, KNN, and Random Forest constructed the models shown in Figure 15. The most often-used measure for determining the accuracy is the Mean Absolute Percentage Error. This falls within the category of scale-independent percentage errors, which may be used to compare series on different scales. Likewise, MSE is used to measure the degree of inaccuracy in the statistical models. The average squared difference between observed and expected values is calculated. The MSE equals zero when a model has no errors and the value rises as the model inaccuracy rises.

The following equations were used to calculate MAPE and MSE in this study.

$$\text{MSE} = \frac{1}{\text{n}} \sum_{\text{i}=1}^{\text{n}} (y_i - Y_i)^2 \tag{7}$$

Here, n represents a number of data points; y_i denotes observed values and Y_i are the predicted values. Hence, MSE is the average squared difference between the actual and predicted value.

$$\text{MAPE} = \frac{100\%}{\text{n}} \sum_{\text{t}=1}^{\text{n}} \left| \frac{A_t - F_t}{A_t} \right| \tag{8}$$

where A_t denotes the current value and Ft denotes the predicted value. The difference between them is divided by the actual value of A_t. This ratio's absolute value is added for each projected point in time and divided by the number of fitted points (n).

$$\text{R}^2 = 1 - \frac{\sum \text{i} \left(\text{y}_\text{i} - \hat{\text{y}}_1 \right)^2}{\sum \text{i} \left(\text{y}_\text{i} - \bar{\text{y}} \right)^2} \tag{9}$$

A number of data here represented by n, yi & $\hat{\text{y}}_\text{i}$ denote the actual and forecasted vales and $\bar{\text{y}}$ denotes the mean. Metrics such as MAPE, RMSE, and R^2 were computed on both training and testing datasets to evaluate the performance and accuracy of the model to decide the final algorithm and to develop a formula to predict fragmentation and ground vibration. The values are presented in Table 3.

Table 3. MAPE, RMSE, and R^2 results.

Metric Type	XG Boost Regression		Random Forest		KN Nearest	
	Fragmentation					
	Training	**Testing**	**Training**	**Testing**	**Training**	**Testing**
MAPE	24	22.5	21.2	20.1	19.2	18.1
RMSE	0.0854	3.873	0.0021	4.221	0.0031	5.321
R^2	0.953	0.9125	0.89	0.67	0.9	0.87
	Peak Particle Velocity					
MAPE	19	18.4	17.5	15.8	16.9	14.32
RMSE	0.0056	2.8890	0.0041	3.78	0.0886	4.88
R^2	0.96	0.932	0.79	0.65	0.83	0.72

According to Table 3 and Figure 16, XG Boost algorithms perform well in both fragmentation and peak particle velocity based on metric values of MAPE, RMSE, and R^2 in both 80% training and 20% testing data. Fragmentation and peak particle velocity were measured in the field, and the XG Boost, Random Forest, and KNN models predicted values using the testing data shown in Figure 17. The predicted values of the XG Boost model were very close to the measured values of both fragmentation and peak particle velocity. In this study, the XG Boost regression method was finalized and utilized to forecast the simultaneous formula for fragmentation and PPV.

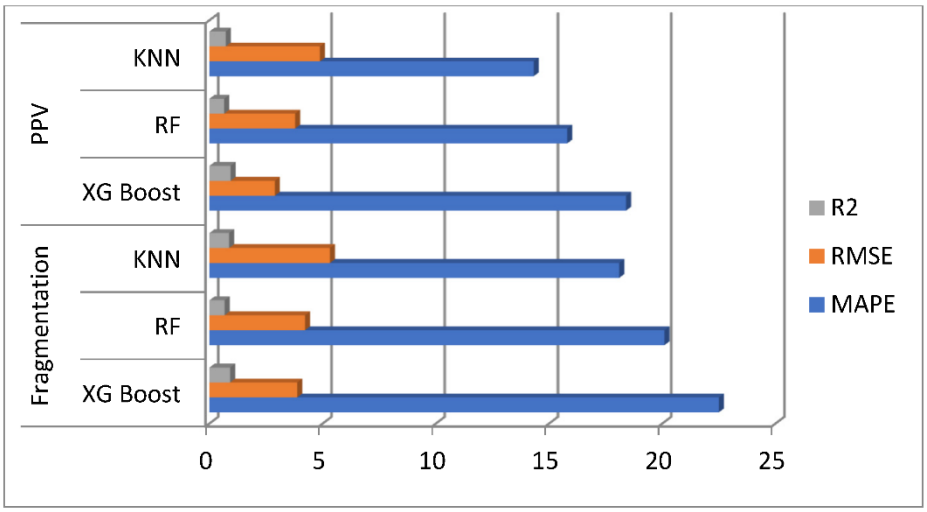

Figure 16. Performance of MAPE, RMSE, and R^2 on testing data.

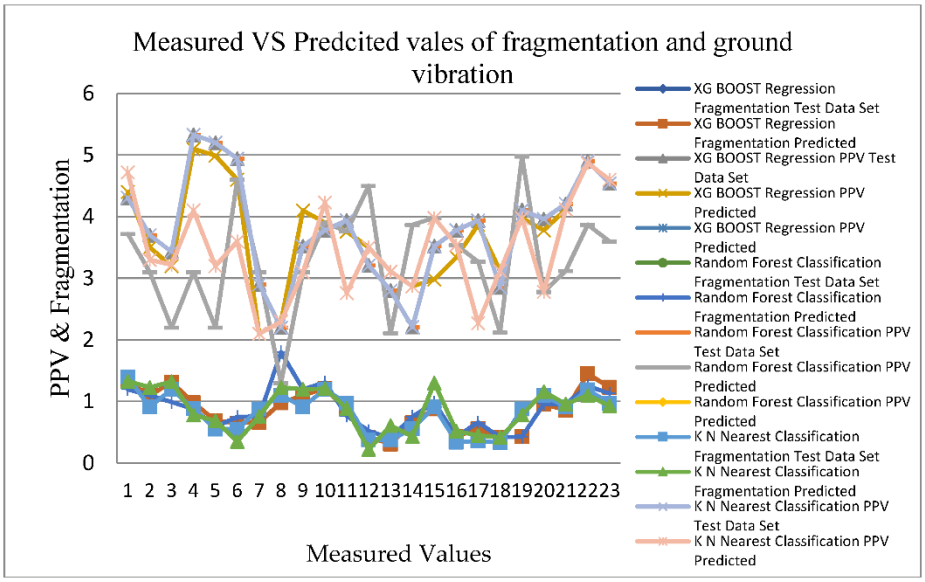

Figure 17. Fragmentation and PPV results comparison between measures models and predicted.

XG Boost Regression

To avoid modeling complexity, two stopping methods, maximum tree depth and n rounds, were selected in the current XG Boost Regression Model. Choosing significant numbers for maximum tree depth and n rounds would result in excessive development of the tree and an over-fitting issue. Therefore, to avoid this problem, the maximum tree depth was set to 1–3 and n rounds to 50, 100, and 150. A trial-and-error approach was used with a range of two values to get the best combination of these two parameters. The dataset was randomly sorted into training (80%) and testing (20%). For the training set, K-fold cross-validation was used to determine the optimum model parameters. The training set was divided into 10 parts of about equal size for 10-fold cross-validation, of which 9 parts were used for training and 1 part utilized for validation. This method was repeated 10 times repeatedly, and the average of these values was used to get the predicted forecast accuracy.

The initial prediction began by taking into account the mean of the dependent variables, MFS and PPV, from the dataset. The residual values from the previous prediction points were then computed. Furthermore, utilizing (80%) of the data, the model was trained to build an XG Boost tree using Equations (1)–(3). As illustrated in Figures 18–21 the tree

divided the data into two portions. The similarity score and gain were calculated by taking the average of the two nearest leaves and moving the residue to the leaf with the highest score and gain. To avoid model complexity, the learning rate and maximum depth were set to 1.0 and 3. After acquiring predictions (residuals) from model 1, all data points were run through model 1 to obtain h1(x) and the F1(x) prediction and residuals of model 2. Similarly, the technique for obtaining h2(x) for model 3 was carried out.

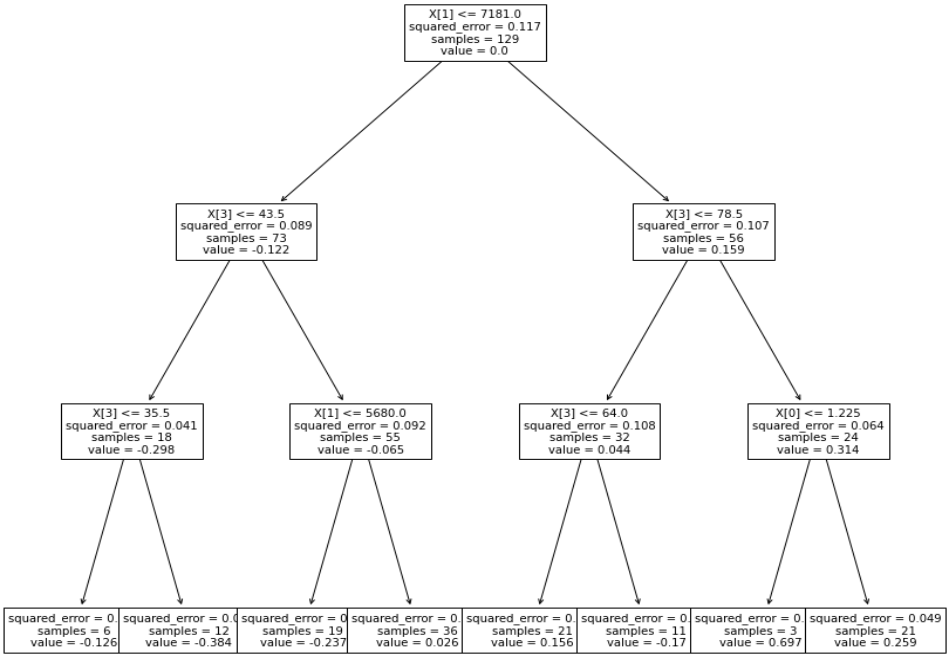

Figure 18. Tree 1 fragmentation.

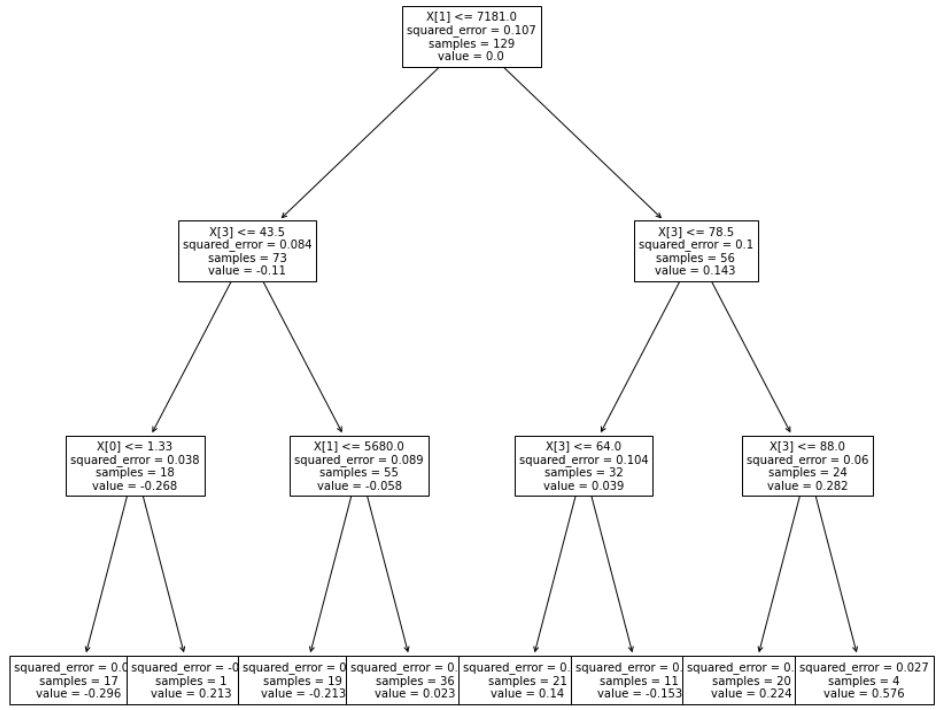

Figure 19. Tree 2 fragmentation.

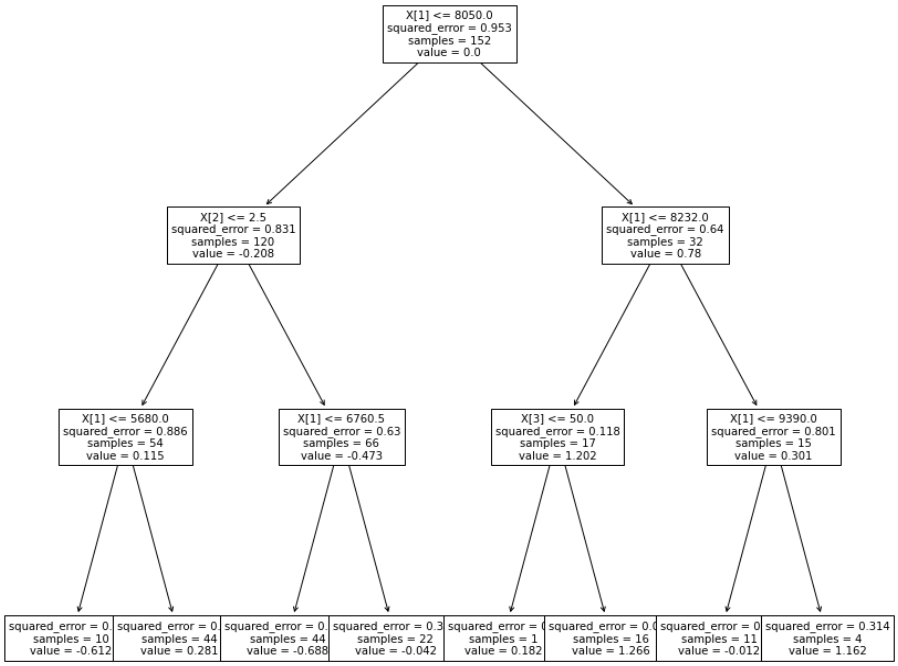

Figure 20. Tree 1 PPV.

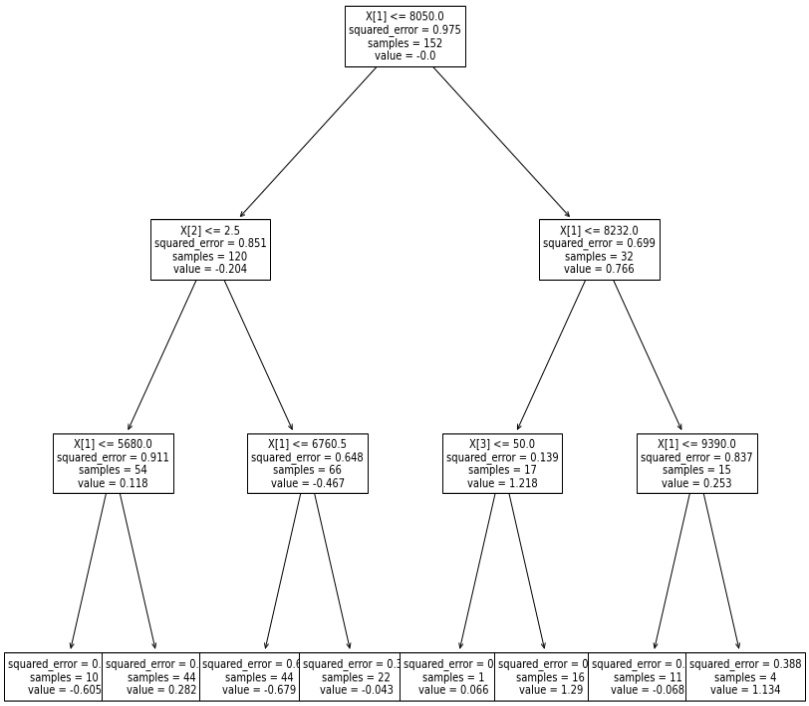

Figure 21. Tree 2 PPV.

The final empirical formulas for predicting fragmentation and peak particle velocity are provided in Equations (10) and (11), which were generated from the trained model using Figure 18. The flow chart created utilizing the weight–age of the Se/Be ratio, Total explosive quantity (TE), Firing Pattern (FP), and joint angle degree (JAD) in terms of squared errors, samples, and prediction values from the trees shown in Figures 18–21. Maximum Charge per Delay was not considered since the output iterations did not balance

accuracy in anticipating fragmentation and PPV as the numbers ranged from 110 to 210 kg with little fluctuation, as shown in Table 2.

$$\text{Fragmentation} = 0.77 + 0.1(\text{Tree 1}) + 0.1(\text{Tree 2}) \quad (10)$$

$$\text{PeakParticleVelocity} = 3.60 + 0.1(\text{Tree 1}) + 0.1(\text{Tree 2}) \quad (11)$$

where tree 1 and 2 are final prediction values of models.

Using Figure 22, one can predict the simultaneous results of fragmentation and PPV. The process depicted in Figure 18 can be used to run the predetermined values of Se/Be, TE, FP, and JAD based on the geo-mechanical condition of the rock mass. Both fragmentation and PPV tree models produced TE as the root node. If the predetermined value of TE is less than or equal to 7181, the pattern continued to the left (Yes); otherwise, it proceeded to the right (No). Furthermore, the final prediction value of tree 1 was chosen based on the comparison values of pre-decided blast parameters and actual parameters derived by the models shown in Figure 22. Tree 2 of fragmentation and PPV trees 1 and 2 were predicted using similar step.

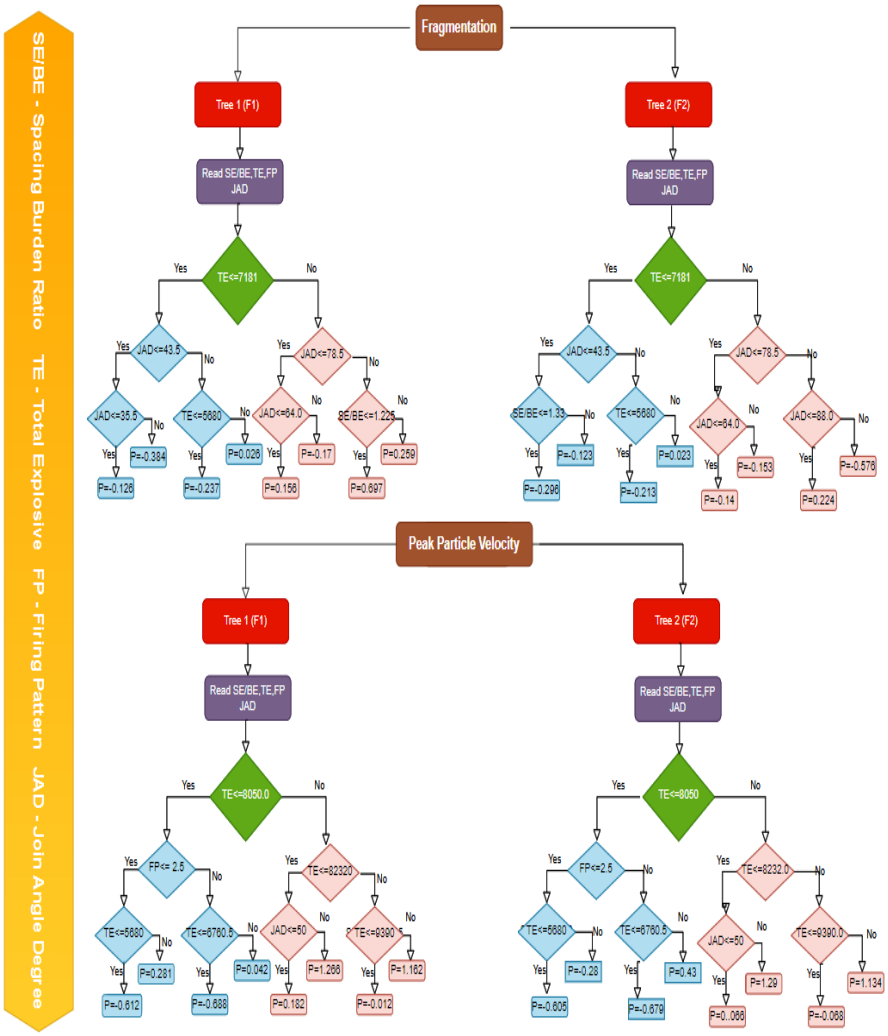

Figure 22. Tree reading process to opt prediction value.

Figures 23 and 24 demonstrate the relationship between the characteristics Se/Be, FP, TE, and JAD and target both fragmentation and peak particle velocity. The PYTHON Seaborn module was used to build correlation heat maps. The association between the

dependent and independent variables is strong. Se/Be ratio, TE, and JAD are coefficients mapped with fragmentation, while FP, TE, and JAD are coefficients mapped with PPV, the same characteristics generated from both trees in fragmentation and PPV segments.

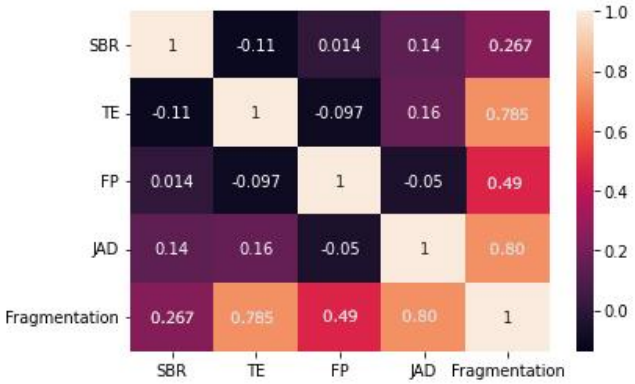

Figure 23. Correlation matrix of fragmentation.

Figure 24. Correlation matrix of PPV.

A Taylor diagram, shown in Figure 25, was used for rigorous evolution, which allows for more robust comparisons between models. Taylor multi-metrics outperform a single model in terms of accuracy. It may exhibit several criterion outputs in a single figure, which is a great way to grasp the findings. An XG Boost model depicts a good coefficient value among the other two models.

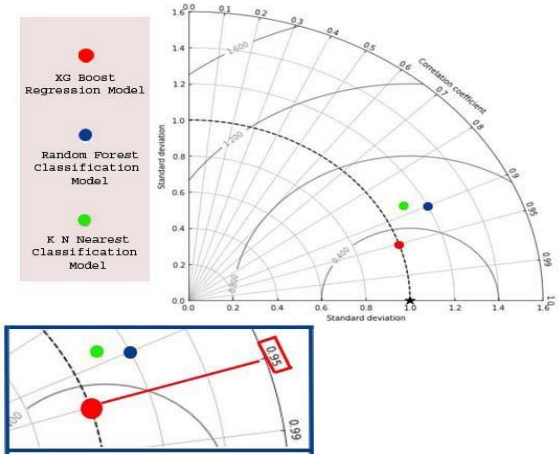

Figure 25. Taylors Diagram.

Using Python's seaborn function, a pair grid was utilized to depict pair-wise connections in datasets. Pair grid provides greater versatility than the pair plot shown in

Figures 26 and 27. Pair grid assigned each variable in a dataset to a column and row on a multi-axes grid. A variety of axes level-plotting functions were employed to create a bivariate plot in the upper and lower triangles, with the marginal distribution of each variable in the diagonals. Furthermore, the hue parameter was utilized to express an extra level of conditions that plots various subplots in different hues.

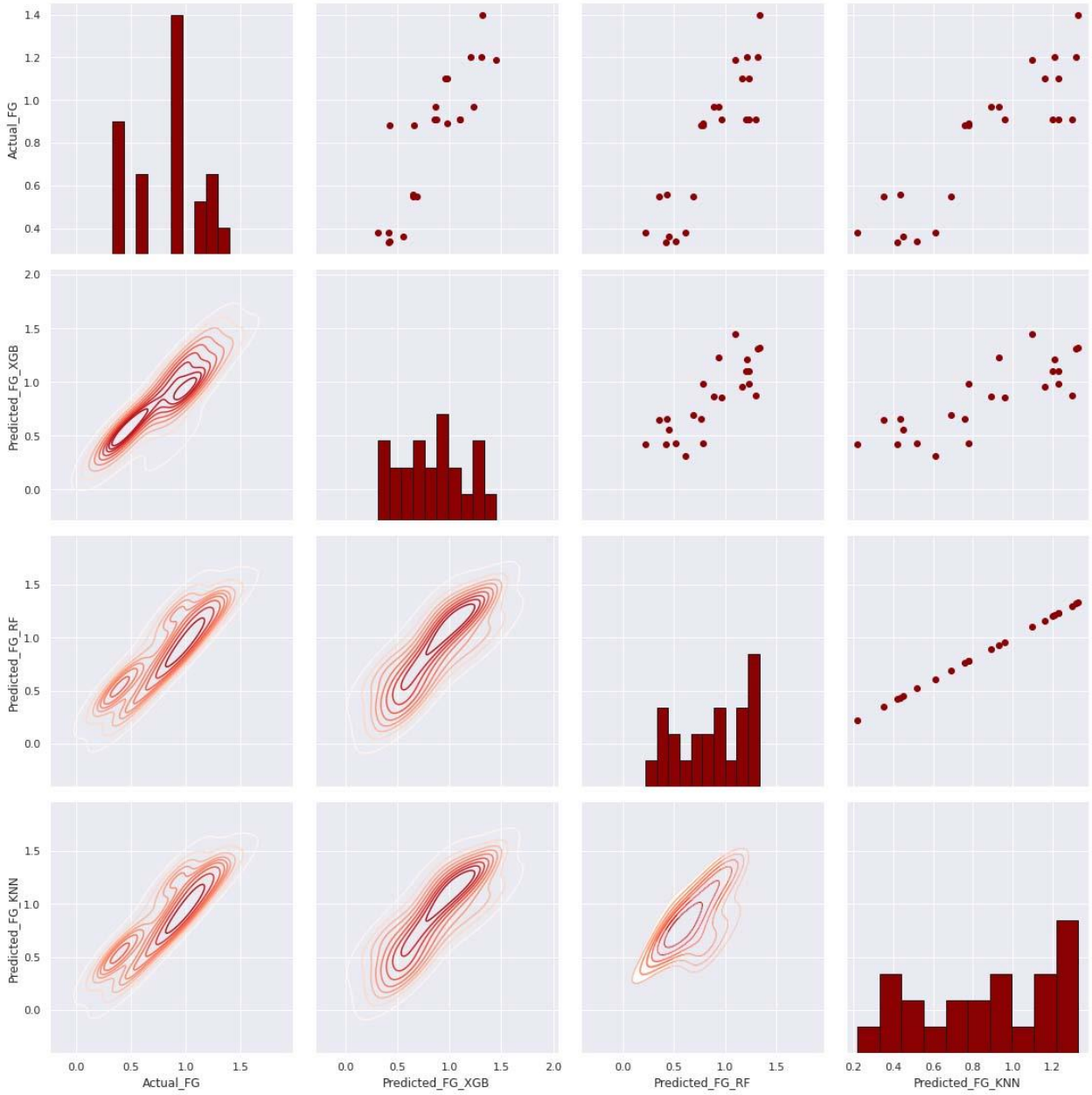

Figure 26. Fragmentation Pair Grid Function.

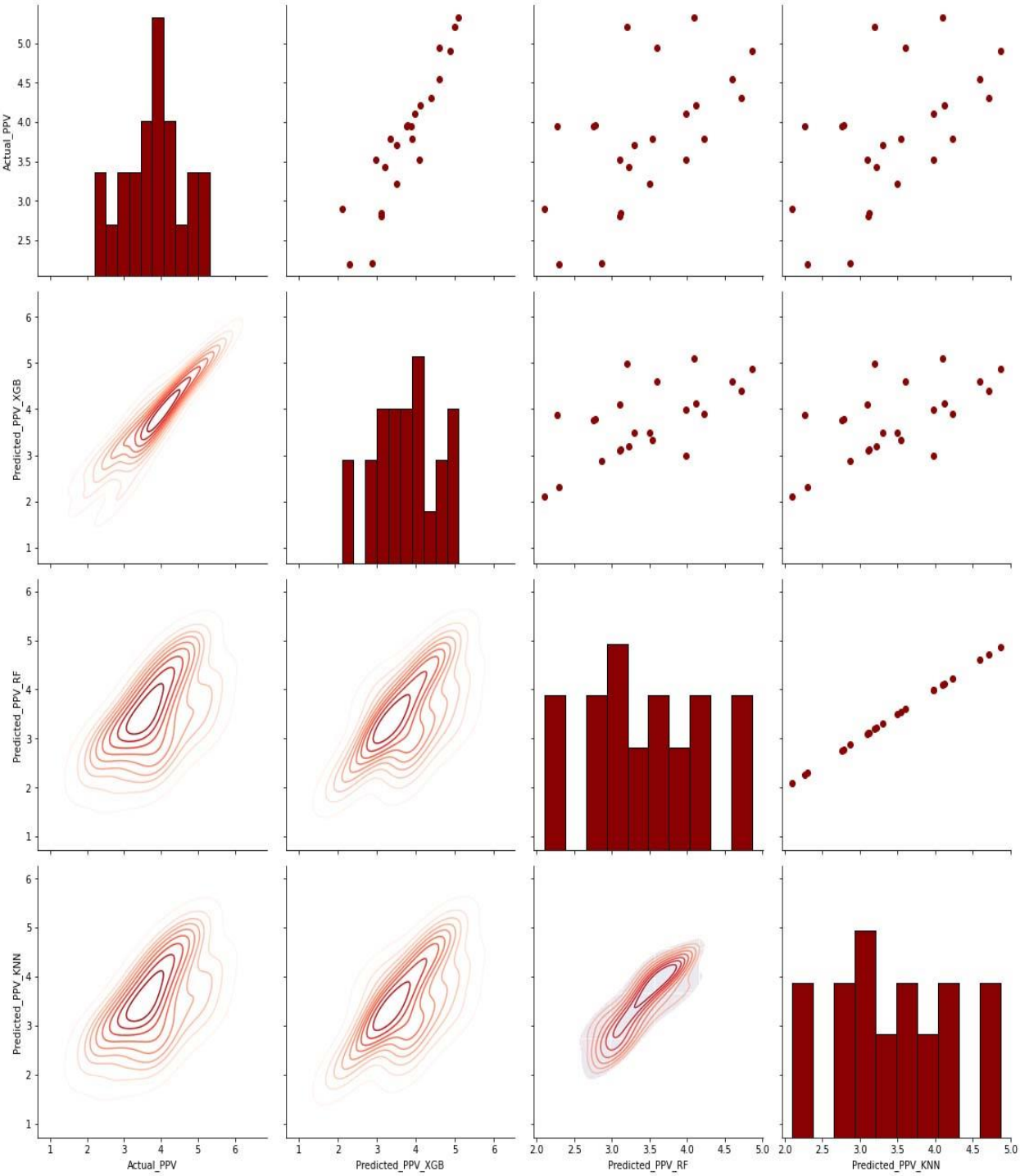

Figure 27. PPV Pair Grid Function.

4. Conclusions

The study's goal was to develop a unique empirical formula using algorithms to simulate the simultaneous prediction of fragmentation and ground vibration using the same set of blast design parameters, including joint angle. There was no fruitful blast design parameters database accessible that included the proper joint angle to direct input to the algorithm, thus achieving the purpose. One hundred and fifty-two blasts were conducted in various opencast mines in the Singareni coal mines of Telangana, measuring the Se/Be ratio, firing pattern, and total explosive, and recording the joint angle. The data

was used to train three models: XG Boost, Random Forest, and KNN, which were then evaluated using three metrics: MAPE, RMSE, and R^2. XG Boost model was selected.

- Use of O-PITBLAST SOFTWARE aided in the design of blasting and provided preliminary warnings for iterations.
- Available technical tools such as STRAYOS SOFTWARE are helpful in identifying the joint angle for rock mass characterization as well as fragmentation analysis
- A Correlation matrix was used to understand relationships between dependent and independent variables, and it proved to be quite useful.
- The XG Boost Regression Algorithm was found to be useful for creating an empirical formula to forecast simultaneous fragmentation and peak particle velocity utilizing joint angle and other blast design parameters such as Se/Be ratio, Total Explosive, and Firing Pattern while keeping the charge per delay constant.
- Empirical formulas of fragmentation and ground vibration are substantial in predicting results.

  Fragmentation = 0.77 + 0.1(Tree 1) + 0.1 (Tree 2)
  Peak Particle Velocity = 3.60 +0.1(Tree 1) +0.1(Tree 2)

Author Contributions: Conceptualization, methodology, investigation, software and writing—original draft preparation has been conducted by N.S.C.; supervision and formal analysis have been conducted by B.S.C., writing—review and editing done by M.V.T., M.S.V. and N.S.R.K.P. All authors have read and agreed to the published version of the manuscript.

Funding: This research received no external funding.

Informed Consent Statement: Informed consent was obtained from all subjects involved in the study.

Data Availability Statement: Available in https://github.com/SriChandrahas/XGBoost-Public/blob/6c14d4a4ae26f6c8f3c6e2763594235c5145eee2/XGBOOST_FRAG.ipynb (accessed on 20 April 2022).

Acknowledgments: I would like to express my heartfelt gratitude to my mentor, B.S. Choudhary, Associate Professor, IIT (ISM) Dhanbad, for meticulously tracking and adding his research inputs to this paper. I am always grateful to my college IIT (ISM) Dhanbad. I would like to express my gratitude to the Principal, Director, and management of Malla Reddy Engineering College, Hyderabad for allocating adequate time to carry out research.

Conflicts of Interest: The authors declare no conflict of interest.

References

1. Aziznejad, S.; Esmaieli, K. Effects of joint intensity on rock fragmentation by Impact. In Proceedings of the 11th International Symposium on Rock Fragmentation by Blasting, Sydney, Australia, 24–26 August 2015.
2. Ash, R.L. The Influence of Geological Discontinuities on Rock Blasting. Ph.D. Thesis, University of Minnesota, Minneapolis, MN, USA, 1973.
3. Hakan, A.K.; Konuk, A. The effect of discontinuity frequency on ground vibrations produced from bench blasting: A case study. *Soil Dyn. Earthq. Eng.* **2008**, *28*, 686–694. [CrossRef]
4. Yahyaoui, S.; Hafsaoui, A.; Aissi, A.; Benselhoub, A. Relationship of the discontinuities and the rock blasting results. *J. Geol. Geogr. Geoecol.* **2018**, *26*, 208–218. [CrossRef]
5. Wu, Y.; Hao, H.; Zhou, Y.; Chong, K. Propagation characteristics of blast-induced shock waves in a jointed rock mass. *Soil Dyn. Earthq. Eng.* **1998**, *17*, 407–412. [CrossRef]
6. Chakraborty, A.; Jethwa, J.; Paithankar, A. Effects of joint orientation and rock mass quality on tunnel blasting. *Eng. Geol.* **1994**, *37*, 247–262. [CrossRef]
7. Bakar Abu, M.Z.; Tariq, S.M.; Hayat, M.B.; Zahoor, M.K.; Khan, M.U. Influence of Geological Discontinuities Upon Fragmentation by Blasting. *Pak. J. Sci.* **2013**, *65*, 414–419.
8. Singh, P.; Roy, M.; Paswan, R.; Sarim, M.; Kumar, S.; Jha, R.R. Rock fragmentation control in opencast blasting. *J. Rock Mech. Geotech. Eng.* **2016**, *8*, 225–237. [CrossRef]
9. Lyana, K.N.; Hareyani, Z.; Shah, A.K.; Hazizan, M.H. Effect of Geological Condition on Degree of Fragmentation in a Simpang Pulai Marble Quarry. *Procedia Chem.* **2016**, *19*, 694–701. [CrossRef]
10. Singh, D.P.; Apparao, V.; Saluja, S.S. A laboratory study on effect of joints on rock fragmentation. American rock mechanics association. In Proceedings of the 21st U.S. Symposium of Rock Mechanics (USRMS), Rolla, MO, USA, 28–30 May 1980.
11. Belland, J.M. Structure as a Control in Rock Fragmentation Coal Lake Iron Ore Deposited. *Can. Min. Met. Bull.* **1968**, *59*, 323–328.

12. Talhi, K.; Bensaker, B. Design of a model blasting system to measure peak p-wave stress. *Soil Dyn. Earthq. Eng.* **2003**, *23*, 513–519. [CrossRef]
13. Lewandowski, T.H.; Luan Mai, V.K.; Danell, E. Influence of discontinuities on presplitting effectiveness. In *Rock Fragmentation by Blasting: Proceedings of the Fifth International Symposium on Rock Fragmentation by Blasting, FRAGBLAST-5*; Mohanty, B., Ed.; CRC Press: Montreal, QC, Canada, 1996; pp. 217–232. [CrossRef]
14. Worsey, P.N.; Qu, S. Effect of joint separation and filling on pre-split blasting. In Proceedings of the 3rd Mini Symposium on Explosives and Blasting Research, Miami, FL, USA, 5 February 1987; pp. 26–40.
15. Whittaker, B.S.; Singh, R.N.; Sun, G. Fracture Mechanics Applied to Rock Fragmentation due to blasting. In *Rock Fracture Mechanics. Principles, Design and Applications Development in Geotechnical Engineering*; Elsevier Science Ltd.: Amsterdam, The Netherlands, 1992; Chapter 13; Volume 71, pp. 443–479.
16. Li, J.; Ma, G. Analysis of blast wave interaction with a rock joint. *Rock Mech. Rock Eng.* **2010**, *43*, 777–787. [CrossRef]
17. Chandrahas, S.; Choudhary, B.S.; Krishna Prasad, N.S.R.; Musunuri, V.; Rao, K.K. An Investigation into the Effect of Rockmass Properties on Mean Fragmentation. *Arch. Min. Sci.* **2021**, *66*, 561–578. [CrossRef]
18. Choudhary, B.S. Firing Patterns and Its Effect on Muckpile Shape Parameters and Fragmentation in Quarry Blasts. *Int. J. Res. Eng.* **2013**, *2*, 32–45. [CrossRef]
19. Sasaoka, T.; Takahashi, Y.; Hamanaka, A.; Wahyudi, S.; Shimada, H. Effect of Delay Time and Firing Patterns on the Size of Fragmented Rocks by Bench Blasting. In *Proceedings of the 28th International Symposium on Mine Planning and Equipment Selection—MPES 2019*; Springer: Berlin/Heidelberg, Germany, 2019; pp. 449–456. [CrossRef]
20. Atici, U. Prediction of the strength of mineral admixture concrete using multivariable regression analysis and an artificial neural network. *Expert Syst. Appl.* **2011**, *38*, 9609–9618. [CrossRef]
21. Tonnizam Mohamad, E.; Hajihassani, M.; Jahed Armaghani, D.; Marto, A. Simulation of blasting—Induced air overpressure by means of artificial intillegene neural networks. *Int. Rev. Model. Simul.* **2012**, *5*, 2501–2506.
22. Xie, C.; Nguyen, H.; Bui, X.N.; Choi, Y.; Zhou, J.; Nguyen Trang, T. Predicting rock size distribution in mine blasting using various novel soft computing models based on meta-heuristics and machine learning algorithms. *Geosci. Front.* **2021**, *12*, 101108. [CrossRef]
23. Monjezi, M.; Rezaei, M.; Yazdian Varjani, A. Prediction of rock fragmentation due to blasting in Gol-E-Gohar iron mine using fuzzy logic. *Int. J. Rock Mech. Min. Sci.* **2009**, *46*, 1273–1280. [CrossRef]
24. Singh, T.N.; Verma, A.K. Sensitivity of total charge and maximum charge per delay on ground vibration. *Geomat. Natl. Hazards Risk* **2010**, *1*, 259–272. [CrossRef]
25. Sharma, L.K.; Singh, R.; Umrao, R.K.; Sharma, K.M.; Singh, T.N. Evaluating the modulus of elasticity of soil using soft computing system. *Eng. Comput.* **2016**, *33*, 497–507. [CrossRef]
26. Bahrami, A.; Monjezi, M.; Goshtasbi, K.; Ghazvinian, A. Prediction of rock fragmentation due to blasting using artificial neural network. *Eng. Comput.* **2011**, *27*, 177–181. [CrossRef]
27. Sayadi, A.; Manojezi, M.; Talebi, N.; Khandelawal, M. A comparative study on the application of various artificial neural networks to simultaneous prediction of rock fragmentation and back break. *J. Rock Mech. Geotech. Eng.* **2013**, *5*, 318–324. [CrossRef]
28. Dindarloo, S.R. Peak particle velocity prediction using support vector machines: A surface blasting case study. *J. S. Afr. Inst. Min. Metall.* **2015**, *115*, 637–643. [CrossRef]
29. Ebrahimi, E.; Monjezi, M.; Khalesi, M.R.; Armaghani, D.J. Prediction and optimization of back-break and rock fragmentation using an artificial neural network and a bee colony algorithm. *Bull. Eng. Geol. Environ.* **2015**, *75*, 27–36. [CrossRef]
30. Monjezi, M.; Bahrami, A.; Yazdian Varjani, A. Simultaneous prediction of fragmentation and flyrock in blasting operation using artificial neural networks. *Int. J. Rock Mech. Min. Sci.* **2010**, *47*, 476–480. [CrossRef]
31. Shirani Faradonbeh, R.; Armaghani, D.J.; Majid, M.A.; Tahir, M.M.; Murlidhar, B.R.; Monjezi, M.; Wong, H.M. Prediction of ground vibration due to quarry blasting based on gene expression programming: A new model for peak particle velocity prediction. *Int. J. Environ. Sci. Technol.* **2016**, *13*, 1453–1464. [CrossRef]
32. Longjun, D.; Xibing, L.; Ming, X.; Qiyue, L. Comparisons of random forest and support vector machine for predicting blasting vibration characteristic parameters. *Procedia Eng.* **2011**, *26*, 1772–1781. [CrossRef]
33. Nguyen, H.; Bui, X.-N.; Bui, H.-B.; Cuong, D.T. Developing an XGBoost model to predict blast-induced peak particle velocity in an open-pit mine: A case study. *Acta Geophys.* **2019**, *67*, 477–490. [CrossRef]
34. Friedman, J.H. Greedy function approximation: A gradient boosting machine. *Ann. Stat.* **2001**, *29*, 1189–1232. [CrossRef]
35. Friedman, J.H. Stochastic gradient boosting. *Comput. Stat. Data Anal.* **2002**, *38*, 367–378. [CrossRef]
36. Chen, M.; Liu, Q.; Chen, S.; Liu, Y.; Zhang, C.-H.; Liu, R. XGBoost-Based Algorithm Interpretation and Application on Post-Fault Transient Stability Status Prediction of Power System. *IEEE Access* **2019**, *7*, 13149–13158. [CrossRef]
37. Friedman, J.; Hastie, T.; Tibshirani, R. Additive logistic regression: A statistical view of boosting (with discussion and a rejoinder by the authors). *Ann. Stat.* **2000**, *28*, 337–407. [CrossRef]
38. Chen, T.; He, T. Xgboost: Extreme Gradient Boosting; R Package Version 04-2; 2015. Available online: https://cran.microsoft.com (accessed on 12 April 2022).
39. Gao, W.; Wang, W.; Dimitrov, D.; Wang, Y. Nano properties analysis via fourth multiplicative ABC indicator calculating. *Arab. J. Chem.* **2018**, *11*, 793–801. [CrossRef]
40. Breiman, L. Random forests. *Mach. Learn.* **2001**, *45*, 5–32. [CrossRef]

41. Vigneau, E.; Courcoux, P.; Symoneaux, R.; Guérin, L.; Villière, A. Random forests: A machine learning methodology to highlight the volatile organic compounds involved in olfactory perception. *Food Qual. Prefer.* **2018**, *68*, 135–145. [CrossRef]
42. Gao, W.; Guirao, J.L.; Basavanagoud, B.; Wu, J. Partial multidividing ontology learning algorithm. *Inf. Sci.* **2018**, *467*, 35–58. [CrossRef]
43. Altman, N.S. An introduction to kernel and nearest-neighbor nonparametric regression. *Am. Stat.* **2019**, *46*, 175–185.